NASA/CP-1998-207671/PT1

Nineteenth International Laser Radar Conference



Edited by
Upendra N. Singh and Syed Ismail
Langley Research Center, Hampton, Virginia

Geary K. Schwemmer
Goddard Space Flight Center, Greenbelt, Maryland

July 1998

The NASA STI Program Office . . . in Profile

Since its founding, NASA has been dedicated to the advancement of aeronautics and space science. The NASA Scientific and Technical Information (STI) Program Office plays a key part in helping NASA maintain this important role.

The NASA STI Program Office is operated by Langley Research Center, the lead center for NASA's scientific and technical information. The NASA STI Program Office provides access to the NASA STI Database, the largest collection of aeronautical and space science STI in the world. The Program Office is also NASA's institutional mechanism for disseminating the results of its research and development activities. These results are published by NASA in the NASA STI Report Series, which includes the following report types:

- TECHNICAL PUBLICATION. Reports of completed research or a major significant phase of research that present the results of NASA programs and include extensive data or theoretical analysis. Includes compilations of significant scientific and technical data and information deemed to be of continuing reference value. NASA counter-part or peer-reviewed formal professional papers, but having less stringent limitations on manuscript length and extent of graphic presentations.

- TECHNICAL MEMORANDUM. Scientific and technical findings that are preliminary or of specialized interest, e.g., quick release reports, working papers, and bibliographies that contain minimal annotation. Does not contain extensive analysis.

- CONTRACTOR REPORT. Scientific and technical findings by NASA-sponsored contractors and grantees.

- CONFERENCE PUBLICATION. Collected papers from scientific and technical conferences, symposia, seminars, or other meetings sponsored or co-sponsored by NASA.

- SPECIAL PUBLICATION. Scientific, technical, or historical information from NASA programs, projects, and missions, often concerned with subjects having substantial public interest.

- TECHNICAL TRANSLATION. English-language translations of foreign scientific and technical material pertinent to NASA's mission.

Specialized services that help round out the STI Program Office's diverse offerings include creating custom thesauri, building customized databases, organizing and publishing research results . . . even providing videos.

For more information about the NASA STI Program Office, see the following:

- Access the NASA STI Program Home Page at ***http://www.sti.nasa.gov***

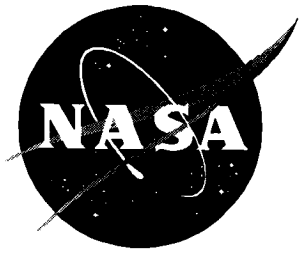
- Email your question via the Internet to help@sti.nasa.gov

- Fax your question to the NASA Access Help Desk at (301) 621-0134

- Phone the NASA Access Help Desk at (301) 621-0390

- Write to:
  NASA Access Help Desk
  NASA Center for AeroSpace Information
  7121 Standard Drive
  Hanover, MD 21076-1320

NASA/CP-1998-207671/PT1



Nineteenth International Laser Radar Conference

Edited by
Upendra N. Singh and Syed Ismail
Langley Research Center, Hampton, Virginia

Geary K. Schwemmer
Goddard Space Flight Center, Greenbelt, Maryland

Abstracts of papers presented at a Conference sponsored by the National Aeronautics and Space Administration, Washington, D.C.; the United States Naval Academy, Annapolis, MD; the Naval Research Laboratory, Washington, D.C.; the Integrated Program Office, Silver Spring, MD; the Optical Society of America, Washington, D.C.; the American Meteorology Society, Boston, MA; the University of Maryland Baltimore County, Catonsville, MD; and Hampton University, Hampton, VA, and held at the United States Naval Academy, Annapolis, Maryland
July 6–10, 1998

National Aeronautics and
Space Administration

Langley Research Center
Hampton, Virginia 23681-2199

July 1998

The use of trademarks or names of manufacturers in this report is for accurate reporting and does not constitute an official endorsement, either expressed or implied, of such products or manufacturers by the National Aeronautics and Space Administration.

Available from the following:

NASA Center for AeroSpace Information (CASI)
7121 Standard Drive
Hanover, MD 21076-1320
(301) 621-0390

National Technical Information Service (NTIS)
5285 Port Royal Road
Springfield, VA 22161-2171
(703) 487-4650

Preface to 19th ILRC Proceedings

This publication contains the written submissions to the 19th International Laser Radar Conference (ILRC), held at the United States Naval Academy and the Loews Annapolis Hotel, in Annapolis, Maryland, July 6-10, 1998. Held biennially under the auspices of the International Coordination Group for Laser Atmospheric Studies, the ILRC brings together an interdisciplinary group of researchers working in the field of laser remote sensing, and is perhaps the largest regular gathering dedicated solely to lidar in the world. Included are over 260 papers from around the world, covering a wide range of lidar subjects including new lidar techniques and component technologies, atmospheric profiling, terrestrial, and marine applications, space based and future lidar systems. We have also included a small session to address subjects such as commercialization, safety and legal issues involving lidar, areas not normally associated with research, but ones that will nevertheless influence the development of lidar into the next century.

The ILRC is unique among professional technical conferences in that it is run by a different group of individuals within the lidar community every time it is held, rather than by a quasi-permanent team sponsored by a large professional society or organization. Each venue is located in a different part of the world and each group imparts its own culture and personal ideas to it. The 19th ILRC committee members proudly present our best efforts to the lidar community, hoping that this ILRC is among your most fruitful and memorable experiences. We feel that you will find the content of the ILRC to be of high interest and quality, and that is due mainly to the high quality of your research contributions.

In putting together the 19th ILRC, we strove to encourage and highlight as many new research topics and researchers as possible while keeping a balance with more mature applications and lidar veterans. The framework for the technical program is given by the parent organization ICLAS. It contains no parallel sessions other than poster sessions, which are held separately from the oral sessions. This allows for approximately 100 oral and 160 poster presentations. The majority of the papers are given in the poster sessions, which are more conducive to personal and information interchange. To further emphasize the poster presentations, the conference award committee is offering two prizes to help highlight this important part of the ILRC. To miss the poster sessions is to miss most of the content of the ILRC.

We would like to acknowledge the innumerable contributions of the conference support staff at Jorge Scientific Corporation, in particular, Mr. Brit Griswold and Mr. Todd R. Del Priore for graphics and web page designs. Acknowledgments are also due to Mr. Vince Bracket and Mr. Anthony Notari of SAIC for their commendable efforts in receiving the electronic submissions and posting them on the 19th ILRC website. We are also grateful to Dr. Reza Malek-Madani for arranging the United States Naval Academy facilities for this conference. We also thank our many sponsors and supporters for their generous contributions, which made this conference possible.

This two-part document was prepared for publication through the efforts of the staff of the Data Analysis and Imaging Branch of the Information Systems & Services Division, NASA Langley Research Center, including the entire staff of the NCI Information Systems, Inc. Technical Publications group.

Dr. Upendra N. Singh
Editor
NASA LaRC

Dr. Syed Ismail
Co-Editor
NASA LaRC

Mr. Geary K. Schwemmer
Co-Editor
NASA GSFC

Mr. Geary K. Schwemmer, Conference Chairman
NASA Goddard Space Flight Center
Dr. Upendra N. Singh, Conference Co-Chairman
NASA Langley Research Center

Technical Program Committee

Dr. Syed Ismail, Program Committee Chairman
NASA Langley Research Center
Dr. Tom McGee, Program Committee Co-Chairman
NASA Goddard Space Flight Center
Dr. Richard A. Ferrare, Program Committee Co-Chairman
NASA Langley Research Center

Dr. James Abshire, GSFC
Mr. James Barnes, LaRC
Dr. Jens Bösenberg, MPI, Germany*
Dr. Edward Browell, LaRC
Dr. Wynn Eberhard, NOAA/ETL
Dr. Edward Eloranta, Univ. of Wisconsin
Dr. Christopher Fields, USNA
Dr. Pierre H. Flamant, Ecole Poly., France*
Dr. Chester Gardner, U. Illinois*
Mr. Bruce Gentry, GSFC
Dr. William Grant, LaRC
Dr. Chris Grund, NOAA/ETL
Dr. Michael Hardesty, NOAA/ETL*
Dr. Raymond Hoff, AES, Toronto, Canada*
Dr. H. Hu, Chinese Acad. of Sci., China*
Dr. Michael Kavaya, MSFC
Dr. Philippe Keckhut, CNRS, France
Dr. T. Kobayashi, Fukui Univ., Japan*
Dr. C. Laurence Korb, GSFC
Dr. Patrick McCormick, Hampton Univ.*
Dr. S. Harvey Melfi, UMBC*
Dr. Robert Menzies, JPL
Dr. Pamela Millar, GSFC
Dr. L. Stefanutti, IROE-CNR, Firenze, Italy*
Dr. I. Stuart McDermid, JPL
Dr. Jacques Pelon, CNRS, France*
Dr. C. Martin Platt, CSIRO, Australia*
Dr. Wolfgang Renger, DLR, Germany*
Mr. Geary K. Schwemmer, GSFC
Dr. Upendra N. Singh, LaRC
Dr. James Spinhirne, GSFC
Dr. Ulla Wandinger, ITR, Germany
Dr. Christian Werner, DLR, Germany
Mr. David Whiteman, GSFC
Dr. David Winker, LaRC
Dr. Jean-Pierre Wolf, Univ. of Lyon, France
Dr. Vladimir Zuev, Inst. Atmo. Opt., Russia*

* ICLAS Working Group Member

Acronyms
AES (Atmospheric Environment Service)
CSIRO (Commonwealth Scientific and Industrial Research Organization)
DLR (Deutsche Forschungsanstalt für Luft- und Raumfahrt)
ETL (Environmental Technology Laboratory)
GSFC (NASA/Goddard Space Flight Center)
IROE (Istituto di Ricerca Onde Elettromagnetiche)
ITR (Institute for Tropospheric Research)
JPL (NASA/Jet Propulsion Laboratory)
JSC (Jorge Scientific Corporation)
LaRC (NASA/Langley Research Center)
MPI (Max-Planck-Institut für Meteorologie)
MSFC (NASA/Marshall Space Flight Center)
NASA (National Aeronautics and Space Adm.)
NOAA (National Oceanic and Atmospheric Adm.)
NRL (Naval Research Laboratory)
SSAI (Science Systems and Applications, Inc.)
UMBC (University of Maryland Baltimore County)
USNA (United States Naval Academy)

Organizing Committee

Dr. William Heaps, Organizing Committee Chairman
NASA Goddard Space Flight Center
Dr. John Degnan, Organizing Committee Co-Chairman
NASA Goddard Space Flight Center
Mr. Leonard R. McMaster
NASA/Langley Research Center
Dr. Edward V. Browell, Senior Advisor
NASA/Langley Research Center
Dr. Patrick McCormick, Senior Advisor
Hampton University
Dr. Harvey Melfi, Senior Advisor
University of Maryland Baltimore County
Mr. David Whiteman, Social Committee Chairman
NASA/Goddard Space Flight Center
Mr. Keith Evans, Social Committee Co-Chairman
University of Maryland Baltimore County
Dr. Thomas D. Wilkerson
Utah State University

Mr. Willie Benjamin, JSC
Dr. Gilbert Davidson, Visidyne
Dr. Christopher Fields, USNA
Dr. David Guerra, W. Maryland College
Dr. William Hooper, NRL
Ms. Kathy Keller, JSC
Dr. Reza Malek-Madani, USNA
Mr. Stephen Palm, SSAI
Mr. Eric Shettle, NRL
Ms. Kelly Whetzel, JSC

Publication Committee

Dr. Upendra N. Singh, Editor
NASA/Langley Research Center
Dr. Syed Ismail, Co-Editor
NASA/Langley Research Center
Mr. Geary K. Schwemmer, Co-Editor
NASA Goddard Space Flight Center

Travel Grant Award Committee

Dr. Richard A. Ferrare, Chairman, Student Travel Grant
NASA/Langley Research Center
Dr. Upendra N. Singh, Chairman, Foreign Visitors Travel Grant
NASA/Langley Research Center

The Nineteenth International Laser Radar Conference Sponsors

National Aeronautics and Space Administration

International Committee on Laser Atmospheric Studies

United States Naval Academy

Naval Research Laboratory

Integrated Program Office

Mission to Planet Earth Office

Optical Society of America

American Meteorological Society

University of Maryland Baltimore County

Hampton University

CONTENTS

Introduction iii

Sponsors vii

Appendix—Author Index ..... AI

Part 1

Plenary Session (PL)
Monday, July 6, 8:00 a.m. to 12:00

1. Invited Talk:
Laser Development from Carbon Dioxide to FEL and Their Applications to Remote Sensing and Pollution Monitoring
C. Kumar N. Patel, University of California Los Angeles, Los Angeles, CA 1-1

2. Chemical Composition of the Atmosphere: What Have We Learned and What Should We Measure?
Guy Brasseur, Atmospheric Chemistry Division, National Center for Atmospheric Research, Boulder, CO (e-mail: brasseur@ucar.edu) ..... *

3. The Greenhouse Effect and Global Warming
Robert Cess, Institute for Terrestrial and Planetary Atmospheres, State University of New York, Stony Brook, NY (e-mail: rcess@notes.cc.sunysb.edu) ..... *

Oral Session 1 (OS1)
Aerosol, Clouds, and Multiple Scattering
Session Chairs: E. Eloranta and U. Wandinger
Monday, July 6, 1:30 to 5:30 p.m.

1. Invited Talk:
Role of Lidar in Climate-Related Aerosol Characterization Experiments
A. Ansmann, D. Althausen, D. Müller, I. Mattis, F. Wagner, and U. Wandinger 7-2

2. LASE Measurements of Aerosols and Water Vapor During TARFOX
Richard A. Ferrare, Syed Ismail, Edward V. Browell, Vincent G. Brackett, Susan A. Kooi, Marian B. Clayton, S. Harvey Melfi, David N. Whiteman, Geary Schwemmer, Keith D. Evans, Peter V. Hobbs, J. Pepijn Veefkind, Philip B. Russell, John M. Livingston, Philip Hignett, Brent N. Holben, and Lorraine A. Remer 11-3

3. Retrieval of the Extinction Coefficient and Microphysical Parameters of Dense Stratocumulus Clouds From Backscatter Lidar Observations: Application to Leandre 1 Measurements During EUCREX '94.
J. Pelon, V. Trouillet, and P.H. Flamant 15-4

4. Lidar Evidence of Desert Dust Layers in the North Atlantic and Mediterranean and Assessment of their Infrared Radiative Impact
P. Chazette, J. Pelon, F. Dulac, V. Trouillet, I. Carrasco, and E. Hamonou 19-5

5. A Lidar Network for the Establishment of an Aerosol Climatology
Jens Bösenberg, Matthias Alpers, Christine Böckmann, Horst Jäger, Volker Matthias, Thomas Trickl, Ulla Wandinger, and Matthias Wiegner 23-6

* No abstract.

6. Validation of POLDER/ADEOS Data Using a Ground-Based Lidar Network: Preliminary Results for Semi-Transparent and Cirrus Clouds
H. Chepfer, L. Sauvage, P.H. Flamant, J. Pelon, P. Goloub, G. Brogniez, J. Spinhirne, M. Lavorato, and N. Sugimoto 25

7. Routine Dual-Wavelength Raman Lidar Observations at Leipzig as Part of an Aerosol Lidar Network in Germany
Ina Mattis, Ulla Wandinger, Detlef Müller, Albert Ansmann, and Dietrich Althausen 29

8. Observations of Stratospheric Aerosols Using a Global Lidar Network
Tomohiro Nagai, Michio Hirota, Toshifumi Fujimoto, Osamu Uchino, Toshikazu Itabe, Kohei Mizutani, Motoaki Yasui, Takashi Shibata, Ben Liley, W. Andrew Mathews, Sri Kaloka, and Saipul Hamdi 33

9. Lidar Measurements of Stratospheric Aerosol at Hefei, China During 1991–1997
Huanling Hu 37

10. Comparison of Lidar and Radar Cloud Measurements at Geesthacht: An Example for Active-Instrument Synergy in Studies of Atmospheric Processes
Claus Weitkamp, Olaf Danne, Holger Flint, Wilhelm Lahmann, Markus Quante, and Felix A. Theopold 41

11. Midlatitude Cirrus Clouds: A Climatology from the 10-Year Polarization Lidar Observation Program at FARS
Kenneth Sassen, James R. Campbell, and Jennifer M. Barnett 45

12. Circular Depolarization Lidar Measurements of Cirrus Clouds
Ryan Woodard, Richard L. Collins, Robert S. Disselkamp, Takashi Shibata, and Yasurobu Iwasaka 47

13. Cloud Measurements with a Multiple-Field-of-View, Dual Polarization Lidar System
Luc R. Bissonnette and Gilles Roy 51

14. Off-Beam (Multiply-Scattered) Lidar Returns from Stratus, 2: Space-Time Measurements in a Laboratory Simulation
Anthony B. Davis, Cheng Ho, and Steven P. Love 55

Poster Session 1
Session Chairs: R. Hoff and W. Grant
Monday, July 6, 7:30 to 9:30 p.m.

Part 1—Aerosols and Clouds (PS1.1)

1. Examination of the Nonlinear Lidar-Operator—An Inverse Ill-posed Problem
Claudia Bernutat, Christine Böckmann, and Ronny Ramlau 59

2. Lidar Observation of Gravity Waves in the Troposphere and Low Stratosphere Above Sofia
George V. Kolarov, Ivan V. Grigorov, and Orlin I. Vankov 63

3. Separation of Rayleigh and Aerosol Scattering Using Pure Rotational Raman Scattering
D.M. Simonich and B.R. Clemesha 65

4. Two-Wavelength Laser Sounding of Stratospheric Aerosol Layer After Pinatubo Eruption
A.P. Chaikovsky, A.P. Ivanov, M.M. Korol, F.P. Osipenko, and V.N. Shcherbakov 69

5. 12 years of Stratospheric Aerosol Measurements by Lidar Sounding over Obninsk, Russia (58°N, 38°E)
S.S. Khmelevtsov, Yu. G. Kaufman, and A.S. Khmelevtsov 73

6. Large Antropogenic Burning Events and Cirrus as Observed by Lidar in Southern Hemisphere at Buenos Aires, Argentina
Mario Lavorato, Javier Fochesatto, Pablo Cesarano, Eduardo Quel, Laurent Sauvage, Pierre Flamant, and Jacques Pelon 75

7. Lidar and Radiometer Sounding of Cloud Properties
C.M.R. Platt, S.A. Young, R.T. Austin, and M.C. Pickett 77

8. Fluctuation Characteristics of the Cloud Top Height
V. Shamanaev, I. Penner, and G. Kokhanenko 79

9. Monitoring of Atmospheric Aerosols in Seoul using a Micro Pulse Lidar
Soon-Chang Yoon and Jae Gwang Won 83

10. Airborne Lidar Observations of Smoke Haze During SCAR-B 1995
William D. Hart and James D. Spinhirne 87

11. Off-Beam (Multiply-Scattered) Lidar Returns from Stratus, 1: Cloud-Information Content and Sensitivity to Noise
Anthony B. Davis and Robert F. Cahalan 91

12. Combining Data from Lidar and In Situ Instruments to Characterize the Vertical Structure of Aerosol Optical Properties
J. Redemann, R.P. Turco, R.F. Pueschel, E.V. Browell, and W.B. Grant 95

13. High Spectral Resolution Lidar at 532 nm for Simultaneous Measurement of Aerosol and Atmospheric State Parameters
Johnathan Hair, David A. Krueger, and C.Y. She 99

14. High Spectral Resolution Lidar Using an Iodine Filter for Measuring Temperature and Optical Characteristics of Aerosols and Clouds
Zhaoyan Liu, Ichiro Matusi, and Nobuo Sugimoto 103

15. Lidar Network and Airborne Observations of the Cloud Street over Tokyo in Summer
Kenji Kai, Kanji Wakiyama, Masamitsu Fujii, Keiko Niwano, Daisuke Muramatsu, Makoto Abo, Chikao Nagasawa, Toshiyuki Murayama, Kikuo Okada, Hiroshi Hara, and Hayato Nakajima 107

16. Lidar Observations of Aerosols at Bandung, Indonesia
K. Mizutani, T. Itabe, M. Yasui, T. Aoki, T. Nagai, T. Fujimoto, M. Hirota, O. Uchino, A. Nuryanto, S. Kaloka, and S. Hamdi 111

17. Constraint Inversion Algorithm for Deriving Aerosol Optical Property From Lidar Observation and its Application
Qiu Jinhuan 113

18. Cirrus and Mid-clouds Programme for Climatology Purposes and Studies of Processes at the Mesoscale
Sauvage Laurent, Hélène Chepfer, Salem Elouragini, Pierre H. Flamant, and Jacques Pelon 115

19. Operational Processing and Cloud Boundary Detection from Micro Pulse Lidar Data
James R. Campbell, Dennis L. Hlavka, James D. Spinhirne, V. Stanley Scott III, and David D. Turner 119

20. Lidar and Radiometric Observations of Aerosols in a Tropical Urban Environment
P.C.S. Devara, R.S. Maheskumar, G. Pandithural, P.E. Raj, and K.K. Dani 123

21. Two Approaches to Derive Aerosol Extinction Coefficient Profiles From Backscatter Lidar Measurements
Matthias Wiegner and Volker Freudenthaler 127

22. The Structure of the Mixed Layer and Aerosal Layer Over Tokyo Metropolitan Area in Summer
Kenji Kai, Kazunobu Manome, Masamitsu Fujii, Daisuke Muramatsu, Makoto Abo, Chikao Nagasawa, Toshiyuki Murayama, Yuichi Ohno, Takeshi Yokozawa, and Hiroshi Hara.....131

23. Retrieval of Droplets Size Density Distribution from Multiple Field of View Cross Polarized Lidar Signals
Gilles Roy and Luc Bissonnette 135

24. Cloud Properties Derived by the RIVM High Temporal Resolution Lidar and the Vaisala CT75K Lidar Ceilometer
Arnoud Apituley, André van Lammeren, and Ronald Sok 139

25. Calibration of the Vertical Lidar Measurement of Tropospheric Aerosol Extinction Coefficients
Hideki Kinjo, Hiroaki Kuze, Mitsuo Minomura, and Nobuo Takeuchi 143

26. Lidar Observations of Atmospheric Aerosol Near Black Sea
T. Skakalova, I. Kolev, O. Parvanov, and B. Kaprielov 147

27. Long-Term Monitoring of Aerosol and Cloud in Sukhothai, Thailand and Chiba/Tsukuba, Japan
N. Takeuchi, H. Kuze, T. Uezono, A.Tadaishi, T. Takamura, and T. Nakajima 151

28. Aerosol Analysis Techniques and Results from Micro Pulse Lidar
Dennis L. Hlavka, James D. Spinhirne, James. R. Campbell, John A. Reagan, and Donna Powell 155

29. Lidar Studies of Cirrus Clouds Above Western Siberia
V.V. Zuev, M.I. Andreev, V.D. Burlakov, A.V. El'nikov, and S.V. Smirnov 159

30. Depolarization Measurements of Cirrus Cloud at Chung-Li (25°N, 121°E)
Wei-Nai Chen and Jan-Bei Nee 165

31. Imaging of a Multiple Scattered Laser Beam Passing through Clouds: Experiment and Computer Simulation
Y. Saito, M. Ishizuka, S. Nagao, T.D. Kawahara, A. Nomura, and K. Noguchi 169

32. Aerosols, Cirrus Clouds and Temperature Measurements With Lidar in Camagüey, Cuba
René Estevan, Roberto Aroche, Ismael Pomares, Sonia Cervantes, Juan Carlos Antuña 173

33. Statistical Characteristics of the Maritime Cloud Base Height
V. Shamanaev, G. Kokhanenko, and I. Penner 177

34. Average and Fluctuation Characteristics of the Transparency of Lake Baikal Water from Airborne Lidar Data
G. Ludbrook, A. Scott, G. Kokhanenko, I. Penner, and V. Shamanaev 181

35. Lidar Studies of the Cirrus Cloud Optical Properties Anisotropy
B.V. Kaul, D.N. Romashov, and I.V. Samokhvalov 185

36. Synergetic Simulation of the Earth Radiation Mission Lidar and Other Instruments
Shiv R. Pal, David Donovan, Mark Cann, Ralph Girard, P.S. Park, J.P. Blanchet, and M. Laroque 189

37. Optical Extinction in Clouds at Multiple Wavelengths
G.L. Schuster, S.T. Esposito, and C.R. Philbrick 193

38. Backscattering Mueller Matrix Derived from Lidar Polarization Measurements: Theory
Avishai Ben-David 195

39. Lidar Observations at the Manila Observatory During the 1997 Indonesian Forest Fire
Lorenzo de la Fuente, Jaime Bucoy, John Holdsworth, and Minella Alarcon.....199

40. Mie Backscatter Intensity and Depolarization Measurements of Tropical Clouds, 14.64 N, 121.07 E in the Philippines
Susana V. Dorado, Nofel C. Lagrosas, Emmanuel Agcropra, Jordan Cañete, and Minella C. Alarcon 203

41. CART and GSFC Raman Lidar Measurements of Atmospheric Aerosol Backscattering and Extinction Profiles for EOS Validation and ARM Radiation Studies
R.A. Ferrare, D.D. Turner, S.H. Melfi, D.N. Whiteman, G. Schwemmer, K.D. Evans, J.E.M. Goldsmith, and T. Tooman.....207

Poster Session 1
Part 2— Lidar Altimeter and Space Lidar Systems (PS1.2)

1. The Geoscience Laser Altimeter System (GLAS)
James B. Abshire, James C. Smith, and Bob E. Schutz 211

2. Laser Pointing Determination for the Geoscience Laser Altimeter System
Pamela S. Millar and J. Marcos Sirota.....215

3. Airborne Laser Mapping: Topographic and Bathymetric Applications
J. Green and A.G. Cunningham.....219

4. New Instrumentation Developed for Mater Laser Ranging Observatory
M. Selden, C. Steggerda, R. Stringfellow, T. Oldham, D. McClure, and G. Bianco 223

5. Development of a Mediam Repetition Rate (10 Hz–500 Hz) Diode Pumped Laser Transmitter for Airborne Scanning Altimetry
D.B. Coyle, Steven J. Lindauer II, and Richard B. Kay 225

6. Calculations of Multiple Scattering-Induced Errors in the GLAS Mission
David P. Duda, James D. Spinhirne, and Edwin W. Eloranta.....229

7. SLR2000: A Microlaser-Based Single Photoelectron Satellite Laser Ranging System
John J. Degnan and Jan F. McGarry 233

8. The Detection of Clouds, Aerosols and Marine Atmospheric Boundary Layer Characteristics from Simulated GLAS Data
Stephen P. Palm and James D. Spinhirne 237

9. Russian Compact Lidar for NASA "Mars Surveyor Program 98"
A.V. Bukharin, V.M. Linkin, A.N. Lipatov, A.N. Lyash, V.S. Makarov, S.M. Pershin, and A.V. Tiurin 241

10. Calibration of LITE Data
Mary T. Osborn 245

11. LITE Data Processing
Kathleen A. Powell and David M. Winker.....249

12. Observations of High Altitude Clouds Over the Equator in Regions Exhibiting Extremely Cold Temperatures
Ali H. Omar and Chester S. Gardner 253

Oral Session 2 (OS2)
Tropospheric Profiling
Session Chairs: H. Melfi and J. Bösenberg
Tuesday, July 7, 8:00 a.m. to 12:00

1. Invited Talk:
Global Tropospheric Ozone Investigations
Edward V. Browell 257

2. LASE Measurements of Convective Boundary Layer Development During SGP97
Syed Ismail, Edward V. Browell, Richard A. Ferrare, Christoph Senff, Kenneth J. Davis, Donald H. Lenschow, Susan Kooi, Vince Brackett, and Marian Clayton 261

3. Water Vapor and Aerosol Distribution Over the Atlantic Ocean as Observed by LEANDRE II During ACE 2
Cyrille Flamant, Jacques Pelon, and Didier Bruneau 265

4. Airborne Lidar Measurements of Ozone and Aerosols During the Pacific Exploratory Mission—Tropics A
Marta A. Fenn, Edward V. Browell, William B. Grant, Carolyn F. Butler, Susan A. Kooi, Marian B. Clayton, Vincent G. Brackett, and Gerald L. Gregory 269

5. Rotational Vibrational-Rotational (RVR) Raman DIAL for Ozone Measurements in Clouds: Methodology and Experiment
Jens Reichardt, Scott E. Bisson, Susanne Krumbholz, Rudolf Baumgart, Claus Weitkamp, and Bernd Neidhart 273

6. Daytime Measurements of Aerosol Particle Extinction and Ozone Profiles with a Combined Elastic DIAL/Raman DIAL
Volker Matthias and Jens Bösenberg 277

7. Daytime Raman Lidar Measurements of Water Vapor During the ARM 1997 Water Vapor Intensive Observation Period
D.D. Turner and J.E.M. Goldsmith 281

8. Comparison of Measurements by the NASA/GSFC Scanning Raman Lidar and the DOE/ARM CART Raman Lidar
David Whiteman, David Turner, Keith Evans, Belay Demoz, Harvey Melfi, Geary Schwemmer, Martin Cadirola, Richard Ferrare, John Goldsmith, Tim Tooman, and Stacy Wise 285

9. Raman Lidar Capability to Measure Tropospheric Properties
C. Russell Philbrick 289

10. Raman-DIAL: Application to Areas Characterized by Varying Aerosol Burden
Arthur J. Sedlacek III and Mark D. Ray 293

11. Tropospheric Temperature Profiling Based on Detection of Stokes and Anti-Stokes Rotational Raman Lines at 532 nm
Ulla Wandinger, Ina Mattis, Albert Ansmann, Yuri Arshimov, Sergey Bobrovnikov, and Ilya Serikov 297

12. Initial Development of a Fiber-Based Lidar System for Atmospheric Water Vapor Measurements
Liesl M. Little, Peter D. Dragic, S. David Roh, James J. Coleman, and George C. Papen 301

13. Water Vapour and Aerosol Observations by Lidar in the Nocturnal Boundary Layer
Paola Di Girolamo, Paola F. Ambrico, Aldo Amodeo, Antonella Boselli, Roberta Capobianco, Gelsomina Pappalardo, and Nicola Spinelli 305

14. Lidar Observations of a Land-Breeze Circulation
E. W. Eloranta, R. Kuehn, and S. Mayor 309

Oral Session 3 (OS3)
Stratospheric/Mesopheric Profiling
Session Chairs: C. Gardner and S. McDermid
Tuesday, July 7, 1:30 to 5:30 p.m.

1. Invited Talk:
Contribution of Stratospheric and Mesospheric Lidar Measurements to Climate Issues
Philippe Keckhut and Alain Hauchecorne 313

2. Study of the Arctic Polar Vortex Erosion From Ozone Lidar Measurements at OHP (44°N, 6°E)
S. Godin and A. Hauchecorne 317

3. Analysis of Record-Breaking Low Ozone Values During the 1997 Winter Over NDSC-Station Lauder, New Zealand
E.J. Brinksma, Y.J. Meijer, B.J. Connor, G.L. Manney, J.B. Bergwerff, G.E. Bodeker, I.S. Boyd, J.B. Liley, W. Hogervorst, J.W. Hovenier, and D.P.J. Swart 319

4. Comparison of Airborne Lidar Measurements with Contour Advection Simulations
H. Flentje, M. Wirth, W. Renger, and W.A. Lahoz.....323

5. Lidar Measurements of Stratospheric Ozone at the Eureka NDSC Station, 1993 to 1998
A.I. Carswell, J.C. Bird, D.P. Donovan, T.J. Duck, S.R. Pal, and D. Velkov 327

6. Integrated Experiment on Optical Monitoring of Atmospheric Ozone at the Siberian Lidar Station
V.V. Zuev, M.V. Grishaev, A.V. El'nikov, V.N. Marichev, and S.V. Smirnov 331

7. A New Aerosol Background Level in the Stratosphere? Lidar Observations of the Period 1976 to 1997
H. Jäger and F. Homburg.....335

8. Temperature Climatology of the Middle Atmosphere From Long-Term Lidar Measurements at Mid- and Low-Latitudes
I. Stuart McDermid, Thierry Leblanc, Philippe Keckhut, Alain Hauchecorne, C.Y. She, and David A. Krueger 339

9. Lidar Temperature Measurements at Ny-Ålesund (79N) During Winter, 1998
T.J. McGee, M. Gross, P. Newman, G. Beyerle, I. Beninga, A. Dahl, R. Neuber, P. Wahl, and O. Schrems.....343

10. Results of the Ny-Ålesund Ozone Measurements Intercomparison NAOMI
W. Steinbrecht, M. Gross, T. McGee, R. Neuber, P.v.d. Gathen, P. Wahl, U. Klein, and J. Langer.....347

11. Resonance Lidar and Airglow Observations of Wave Activity in the Arctic Mesopause
Richard L. Collins and Roger W. Smith 351

12. Comparison of an Fe Boltzmann Lidar with a Na Narrowband Lidar
George C. Papen and Daniel Treyer.....355

13. Mesopause Temperature Variations from Observations of More Than 24 Hours
David A. Krueger, Huailin Chen, and C.Y. She.....359

14. A Frequency-Agile Lidar with Concurrent Frequency Monitor for Simultaneous Measurement of Temperature and Line-of-Sight Wind in the Mesopause Region
Michael White, David A. Krueger, and C.Y. She.....363

Poster Session 2
Session Chairs: M. Platt and R. Ferrare
Tuesday, July 7, 7:30 to 9:30 p.m.

Part 1—Tropospheric Profiling (PS2.1)

1. Upper Tropospheric Water Vapor: A Field Campaign of Two Raman Lidars, Airborne Hygrometers, and Radiosondes
S. Harvey Melfi, Dave Turner, Keith Evans, Dave Whiteman, Geary Schwemmer, and Richard Ferrare 367

2. A Compact Water Vapor Raman Lidar
Coorg R. Prasad and Savyasachee Mathur 371

3. Lidar Profiling of Ozone and Aerosol in the SCOS97-NARSTO Experiment
Y. Zhao, R.D. Marchbanks, C.J. Senff, H.D. Johnson, and L. Dolislager 375

4. Chemistry and Dynamics of the Lower Troposphere over North America and the North Atlantic Ocean in Fall 1997 Observed Using an Airborne UV DIAL System
William B. Grant, Carolyn F. Butler, Marta A. Fenn, Susan A. Kooi, Edward V. Browell, and Henry Fuelberg 379

5. Measurement of Various Minor Species Near Ground Surface Using Differential Absorption Lidar
S.L. Jain, B.C. Arya, S. Sharma, and Arun Kumar 383

6. Lidar Observation of the Nocturnal Inversion Transition in the Lower Atmosphere over Hong Kong
T.M. Mok, K.M. Leung, J.C.L. Chan, A.H.P. Ho, and C.N. Ng 387

7. Multiwavelength DIAL for Trace SO_2 Measurement
Tetsuo Fukuchi, Naohiko Goto, Takashi Fujii, and Koshichi Nemoto 391

8. Airborne Lidar Studies of the Entrainment Zone
Christoph Kiemle, Gerhard Ehret, and Kenneth J. Davis 395

9. The EPFL UV Ozone DIAL: Results and Upgradings
Valentin Simeonov, François Jeanneret, Philippe Quaglia, Hubert van den Bergh, and Bertrand Calpini 399

10. Towards Quantifying Mesoscale Flows in the Troposphere Using Raman Lidar and Sondes
B. Demoz, D. Starr, K. Evans, D. Whiteman, S. Mel, D. Turner, R. Ferrare, J. Goldsmith, G. Schwemmer, and M. Cadirola 403

11. Raman/DIAL Techniques for Ozone Measurements
Steven T. Esposito and C. Russell Philbrick 407

12. Lidar Observation of the Atmospheric Boundary Layer over Jakarta, Indonesia
Mego Pinandito, Imam Rosananto, Ii Hidayat, Muharyan Syamsudin, Santoso Sugondo, Nobuo Sugimoto, Ichiro Matsui, and Takao Kobayashi 411

13. Lidar Measurements of the Atmospheric Boundary Layer (ABL) Dynamics at Buenos Aires, Argentina
Javier Fochesatto, Mario Lavorato, Pablo Cesarano, Eduardo Quel, Cyrille Flamant, Jacques Pelon, and Pierre Flamant 415

14. Water Vapour Mixing Ratio Measurements Using the Purple Crow Raman-Scattering Lidar
C. Bryant, P.S. Argall, R.J. Sica, and R.M. Hoff 417

15. Issues Effecting the Signal-to-Noise Ratio for Airborne CO_2 DIAL Measurements
Richard G. Vanderbeek, Avishai Ben-David, Francis M. D'Amico, and Steven W. Gotoff 421

16. Multiple Wavelength Rotational Raman Lidar For Calibration Free Determination of Tropospheric Temperatures
D. Waite, S. Frey, F. Immler, M. Mueller, P. Rairoux, M. Rodriguez, B. Stein, C. Wedekind, H. Wille, L. Wöste, and W. Zimmer 425

17. Atmospheric Lidar EXperiment (ALEX): A New Raman Lidar System at the University of Maryland Baltimore County
Martín P. Cadirola, S. Harvey Melfi, David N. Whiteman, and A. Dan Wooten 429

18. Retrieval of Ozone and Water Vapor in the Lower Troposphere by Raman DIAL
Benoît Lazzarotto, Valentin Simeonov, Philippe Quaglia, Gilles Larcheveque, Hubert van den Bergh, Bertrand Calpini, Max Frioud, and Valentin Mitev 433

19. Raman Lidar Calibration of the DMSP SSM/T-2 Microwave Water Vapor Sensor
John Wessel, Steven Beck, Yat Chan, Robert Farley, and Jerry Gelbwachs 437

20. Is the PBL Height Well Determined by Aerosol Lidar in Very Clean Boreal Conditions?
G. Larchevêque, V. Simeonov, H. Van den Bergh, and B. Calpini 441

21. Modeling Technique of Processing Raman-Lidar Returns from a Stack Emission to Extract Data on Its Composition and Total Outcome
I.B. Serikov, Yu.F. Arshinov, S.M. Bobrovnikov, and A.I. Nadeev 445

22. Towards Water Vapor Profiling with BELINDA
Holger Flint, Felix A. Theopold, and Claus Weitkamp 449

23. Broadband Lidar Measurements of Tropospheric Constituent Profiles
I.M. Povey, A.M. South, C. Hill, and R.L. Jones 453

24. Comparison of Aerosol Properties Derived from Lidar, Sun Photometer, and In Situ Observations During the Aerosol Characterization Experiment 2
Frank Wagner, Detlef Müller, Albert Ansmann, Diana Weise, and Dietrich Althausen 457

25. A New Technique to Derive Mixed Layer Depth and Entrainment Zone Thickness from Lidar Profiles
D.G. Steyn, M. Baldi, and R.M. Hoff 461

26. LASE Validation Experiment: Preliminary Processing of Relative Humidity from LASE Derived Water Vapor in the Middle to Upper Troposphere
Vincent G. Brackett, Syed Ismail, Edward V. Browell, Susan A. Kooi, Marian B. Clayton, Richard A. Ferrare, Patrick Minnis, Brian J. Getzewich, and Jennifer Staszel 465

27. Summary of Volume Imaging Lidar (VIL) Preliminary Results from the Lake-Induced Convection Experiment (Lake-ICE)
Shane D. Mayor, Edwin W. Eloranta, Ralph Kuehn, and Patrick Ponsardin 469

28. On the Contribution of Water-Vapor DIAL to the Investigation of Turbulent Transport Processes
Volker Wulfmeyer 473

Poster Session 2

Part 2—Stratospheric/Mesospheric Profiling (PS2.2)

1. First Results from the Aerosol Lidar and Backscatter Sonde Intercomparison Campaign STRAIT '97 at Table Mountain Facility During February–March 1997
G. Beyerle, M.R. Gross, D.A. Haner, N.T. Kjome, I.S. McDermid, T.J. McGee, J.M. Rosen, H.J. Schafer, and O. Schrems 477

2. Evaluation and Optimization of Lidar Temperature Analysis Algorithms Using Simulated Data
Thierry Leblanc, I. Stuart McDermid, Alain Hauchecorne, and Philippe Keckhut 481

3. High-Resolution Lidar Studies of Stratospheric Air Intrusions
Holger Eisele, Rudolf Sladkovic, and Thomas Trickl 485

4. Comparison of Temperature and Ozone Profiles Derived from DIAL and SAGE II Measurements over Toronto
J.C. Bird, D. Velkov, D.P. Donovan, A.I. Carswell, S.R. Pal, and S. Guo 489

5. The Winter Evolution of the Polar Stratospheric Vortex Thermal Structure
Thomas J. Duck, James A. Whiteway, and Allan I. Carswell 493

6. Rayleigh/Raman Scattering Lidar for Measuring Atmospheric Parameters
Shunsheng Gong, Wengang Zheng, Hongjun Li, Guotao Yang 497

7. Stratospheric Aerosol Climatology in North and South Hemisphere
Donatella Guzzi, Marco Morandi, Vincenzo Santacesaria, Leopoldo Stefanutti, Pietro Agostini, and Vicenzo Cuzzola 501

8. ILE Lidar Measurements of Ozone Concentration Over Suwon, Korea
Chan Bong Park and Choo Hie Lee 505

9. Results of Lidar Data Application to Climatic Studies of the Stratospheric Ozone Field Above Western Siberia
V.S. Komarov, V.V. Zuev, N. Ya. Lomakina, V.N. Marichev, and Yu. B. Popov 509

10. Observations of Gravity Waves in the Stratospheric Polar Vortex
James A. Whiteway, Thomas J. Duck, and Allan I. Carswell 511

11. Observation of the Middle Atmospheric Thermal Tides Using Lidar Measurements Over Mauna Loa Observatory (19.5°N, 155.6°W).
Thierry Leblanc and I. Stuart McDermid 513

12. The Ny-Ålesund Aerosol and Ozone Measurements Intercomparison Campaign 1997/98 (NAOMI-98)
R. Neuber, G. Beyerle, I. Beninga, P. von der Gathen, P. Rairoux, O. Schrems, P. Wahl, M. Gross, Th. McGee, Y. Iwasaka, M. Fujiwara, T. Shibata, U. Klein, and W. Steinbrecht 517

13. Multiwavelength Measurements of Arctic Lower Stratospheric Aerosol at Eureka
D.P. Donovan, J.C. Bird, A.I. Carswell, T.J. Duck, T. Itabe, T.Nagai, S.R. Pal, O. Uchino, T. Shibata, and J.A.Whiteway 521

14. Japanese Mesopause Physics Program with a Sodium Temperature Lidar at Syowa Station, Antarctica
T.D. Kawahara, A. Nomura, T. Kitahara, F. Kobayashi, and Y. Saito 525

15. The Purple Crow Lidar at the University of Western Ontario
P.S. Argall, R.J. Sica, A.R. Russell, O.N. Vassiliev, and C.R. Bryant 529

16. The Purple Crow Sodium Resonance Fluorescence Lidar
O.N.Vassiliev, P.S. Argall, M. Mwangi, and R.J. Sica 533

17. Rayleigh Lidar Observations of Temperature and Gravity Waves in the Middle Atmosphere
S. P. Namboothiri, N. Sugimoto, H. Nakane, I. Matsui, and Y. Murayama 537

18. Observations of Mesospheric Sodium over Italy
Piero Di Carlo, Vincenzo Rizi, and Guido Visconti 541

19. Lidar Measurements of Mesospheric Potassium Layers with a Injection Seeded Flashlamp Pumped Ti:Sapphire Laser
Tatsuya Kyomitsu, Makoto Abo, Chikao Nagasawa, and Yasukuni Shibata 545

20. Faraday Metal Vapor Filters For Daytime Observation of the Mesopause Region
Songsheng Chen, David A. Krueger, and C.Y. She 549

21. Characteristics of Mesospheric Sodium Layers Observed by a TMU Lidar
Chikao Nagasawa and Makoto Abo ..... *

22. The ALOMAR Ozone DIAL System
David Rees ..... *

Part 2†

Oral Session 4 (OS4)
Wind Profiling
Session Chair: M. Hardesty and R. Menzies
Wednesday, July 8, 8:00 to 11:40 a.m.

1. Invited Talk:
Tropospheric Wind Measurements From Space: The SPARCLE Mission And Beyond
Michael J. Kavaya and G. David Emmitt 553

2. Estimating SPARCLE Shuttle Lidar Performance with Ground Based Doppler Lidar
R. Michael Hardesty, W. Alan Brewer, and Barry J. Rye 557

3. Multi-Channel Doppler Lidar for Remote Sensing of Wind in the Troposphere
Takao Kobayashi, Dengxin Hua, Takeshi Murae, and Ryuzo Tanaka 561

4. Combined Wind And Water-Vapor Measurements Using the NOAA Mini-MOPA Doppler Lidar
W. Alan Brewer, Volker Wulfmeyer, R. Michael Hardesty, and Barry J. Rye 565

5. Comparison of Doppler Lidar Wind Measurements with the German Forecast Model (DM)
Stephan Rahm, Christian Werner, Susanne Lehner, and Michael Buchhold 569

6. Performance and Applications of the NOAA 2 μm High Resolution Doppler Lidar
Volker Wulfmeyer, W. Alan Brewer, Christoph Senff, Shane Mayor, Richard Marchbanks, Jim Howell, Ann Weickmann, Ron Richter, Chris Grund, and R. Michael Hardesty 573

7. A New Instrumented Site at Ecole Polytechnique (France) With Lidars and Radars
Claude Loth, Pierre H. Flamant, Jacques Pelon, and Jacques Testud 577

8. Design and Performance of a Miniature Lidar Wind Profiler (MLWP)
Donald M. Cornwell, Jr. and Mariusz J. Moidek 581

9. Invited Talk:
The Double Edge Aerosol and Molecular Techniques for Doppler Lidar Wind Measurement
C. Laurence Korb and Christina Flesia 585

10. Lidar Measurements of Tropospheric Wind Profiles with the Double Edge Technique
Bruce M. Gentry, Steven X. Li, C. Laurence Korb, Savyasachee Mathur, and Huailin Chen 587

---

* Abstract not available at time of publication.

† Part 2 is presented under separate cover.

11. Spaceborne Simulations of Two Direct-Detection Doppler Lidar Techniques
Matthew J. McGill and Steve X. Li 591

12. Direct Detection Doppler Wind Lidar for Spaceflight
Jack A. McKay 595

Oral Session 5 (OS5)
Lidar Techniques and Technology
Session Chairs: C. Werner and J. Barnes
Thursday, July 9, 8:00 a.m. to 12:00

1. Invited Talk:
Advanced Solid State Lasers for Lidar Systems
P. F. Moulton 601

2. 2-Micron Diode-Pumped Pulsed Laser Transmitter for SPARCLE: A Coherent Wind Lidar Shuttle Mission
Upendra N. Singh, Jirong Yu, Mulugeta Petros, Norman P. Barnes, and Mark W. Phillips 603

3. Yb:YAG Lasers for Space Based Remote Sensing
J.J. Ewing and T.Y. Fan 609

4. Laser Transmitter Design for the Geoscience Laser Altimeter System
R.S. Afzal, A.W. Yu, W. Mamakos, A. Lukemire, J.L. Dallas, B. Schroeder, and J.W. Green 613

5. Compact, Ruggedized Eyesafe Laser Transmitter
J.C. McCarthy, P.A. Ketteridge, R. Day, Ian Lee, and Evan Chicklis 617

6. Solid State Laser Technology Development For Atmospheric Sensing Applications
James C. Barnes 619

7. Holographic Airborne Rotating Lidar Instrument Experiment (HARLIE)
Geary K. Schwemmer 623

8. Femtosecond White Light Lidar
P. Rairoux, R. Neuber, S. Niedermeier, M. Rodriguez, F. Ronneberger, R. Sauerbrey, H. Schillinger, B. Stein, D. Waite, C. Wedekind, H. Wille, and L. Wöste 627

9. Sequential Tilted Interference Filter Polychromator as a Lidar Receiver for Rotational Raman Temperature Measurements in the Troposphere and Stratosphere
Andreas Behrendt, Jens Reichardt, Claus Weitkamp, and Bernd Neidhart 631

10. Diode Laser Seeded Optical Parametric Oscillator for Airborne Water Vapor DIAL Application in the Upper Troposphere
G. Ehret, A. Fix, and V. Weib 635

11. Automated All-Weather Lidar with Scanning Option
Wynn L. Eberhard, Raul J. Alvarez II, Janet M. Intrieri, Scott P. Sandberg, Keith W. Koenig, and Kathleen R. Healy 639

12. Two Wavelength Ti:Sapphire Laser for Ozone DIAL Measurements from Aircraft
Wen Situ and Russell J. DeYoung 643

13. A Pulsed Kilowatt Class Coherent CO_2 Laser Radar System
V. Hasson, M. Kovacs, F. Corbett, R. Eng, H. Chou, P. Lewis, Y. Wang, D. Ruffatto, R. Pohle, T.R. Glesne, and R. Wendt 647

14. Air Force Research Laboratory Long-Range Airborne CO_2 DIAL Chemical Detection System
N. Scott Higdon, Marsha J. Fox, David R. Dean, James A. Dowling, Brian T. Kelly, Daniel C. Senft, Diego K. Pierrottet, Carla M. Hamilton, Dale A. Richter, and Ronald R. Bousek 651

Oral Session 6 (OS6)
Lidar Applications including Marine and Trace Gas Measurements
Session Chairs: J. Abshire and R. Madani
Thursday, July 9, 1:30 to 4:10 p.m.

1. Invited Talk:
Importance of Moisture in Cyclone Track Prediction
T.N. Krishnamurti 655

2. Chemical Detection Results From Ground Tests of an Airborne CO_2 Differential Absorption Lidar System
D.C. Senft, B.T. Kelly, M.J. Fox, R.R. Bousek, and N.S. Higdon 657

3. Lidar Measurement of Launch Vehicle Exhaust Plumes
Phan D. Dao, Anthony Dentamaro, Robert Farley, Philip Soletsky, Richard Garner, Patrick Connolly, Ronald Frelin, Gilbert Davidson, Jerry Gelbwachs, and Martin Ross 661

4. Pump-and-Probe Lidar: OH Kinetics Study for Determining a New Indicator for the Ozone Production
François Jeanneret, Frank Kirchner, Alain Clappier, Hubert van den Bergh, and Bertrand Calpini 665

5. Range Resolved Measurements for Standoff Detection of Chemical Agents
Jay Fox, Jeffrey Ahl, Avishai Ben-David, Francis D'Amico, Richard Vanderbeek, and Cynthia Swim.....669

6. Scanning Lidar Imaging of Marine Aerosol Fields Generated by Breaking Waves
Shiv K. Sharma, Barry R. Lienert, John N. Porter, Antony D. Clarke, and James Howell 673

7. Mini Raman Laser-Radar System for In Situ, Stand-off Interrogation of Surface Contamination
Mark D. Ray and Arthur J. Sedlacek III 677

8. An Operational Wake Vortex Sensor Using Pulsed Coherent Lidar
Ben C. Barker, Jr., Grady J. Koch, and D. Chi Nguyen 681

9. Validation of Saharan Dust Layer Characteristics With Lidar Observations
V. Mohan Karyampudi, Steve Palm, John Reagan, W.B. Grant, Harold Pierce, E.V. Browell, and S.H. Melfi 685

Poster Session 3
Session Chairs: H. Hu and J. Pelon
Thursday, July 9, 7:30 to 9:30 p.m.

Part—1 Wind Profiling (PS3.1)

1. The Double Edge Technique for Doppler Lidar Wind Measurement
C. Laurence Korb, Bruce M. Gentry, S. Xingfu Li, Cristina Flesia, Huailin Chen, and S. Mathur.....691

2. Double-Edge Molecular Technique for Doppler Lidar Wind Measurement
Cristina Flesia and C. Laurence Korb 695

3. Analysis of a Multistatic Coherent Doppler Lidar for Remote Wind Measurements
Eric P. Magee and Timothy J. Kane 699

4. Design and Operational Characteristics of the Shuttle Coherent Wind Lidar
Farzin Amzajerdian, Gary D. Spiers, Bruce R. Peters, Ye Li, Timothy S. Blackwell, and Joseph M. Geary 703

5. Transportable Wind Lidar for Meteorological Applications
Patricia Delville, Ph. Drobinski, X. Favreau, A. Dabas, C. Boitel, J.M. Donnier, B. Romand, C. Loth, P.H. Flamant, and J. Pelon 707

6. Spectral Asymmetry of TEA-CO_2 Laser Pulses—Application in Coherent Lidars with Low Frequency Stability
Vladimir Stoykov Marinov and Dimitar Vassilev Stoyanov 711

7. Derivation of Wind Spectra from Doppler Wind Lidar Velocity Measurements
P. Drobinski, A. Dabas, and P.H. Flamant 715

8. Retrieval of 2D and 3D Windfield over Complex Orography by Airborne Doppler Lidar
Philippe Drobinski, Julie Périn, Alain M. Dabas, Pierre H. Flamant, and Jacques Pelon 719

9. Wind-Driven Angular Dependence of Sea-Surface Reflectance Measured with an Airborne Doppler Lidar
David M. Tratt, Robert T. Menzies, and Dean R. Cutten 723

10. Measurement of Turbulence Parameters in the Atmospheric Boundary Layer with a CW Doppler Lidar
V.A. Banakh, N.P. Krivolutsky, and I.N. Smalikho, F. Köpp, and Ch. Werner 727

11. Performance of Measurement of Turbulence Parameters by Pulsed Doppler Lidar
V.A. Banakh and I.N. Smalikho .....*

12. Simulation of Scanning CW Doppler Lidar Run
V.A. Banakh, N.P. Krivolutsky, I.N. Smalikho, and Ch. Werner 731

13. Efficient Third Harmonic Generation for Wind Lidar Applications
David W. Mordaunt, Eric C. Cheung, James G. Ho, and Stephen P. Palese 735

14. Lidar Measurements of Wind Velocity Profiles in the Low Troposphere
O. Parvanov, I. Kolev, and B. Kaprielov 739

15. Lidar Measurements of Wind Profiles in the Boundary Layer by Using Correlation Technique
Qiu Jinhuan, Yang Liquang, Zheng Siping, and Huang Qirong 743

16. Statistical Characteristics of Light Helical Fields in Turbulent Media
M.S. Maganova and M.V. Lomonosov 745

Poster Session 3

Part 2—Lidar Techniques and Technology (PS3.2)

1. Shipborne Lidar Sensing of the Upper Water Layer In the Middle Atlantic
V. Shamanaev, G. Kokhanenko, and I. Penner 747

2. Reduction of PMT Signal-Induced Noise in Lidar Receivers
Cynthia K. Williamson and Russell J. DeYoung 751

3. Fade Statistics and CNR Improvement of an Equal-Gain Coherent Receiver Array
J. Xu, A. Delaval, G. Sellar, A. Al-Habash, D. Kelly, S. Frederick, R. Phillips, L. Andrews, and J. Stryjewski 755

* Abstract not available at time of publication.

4. Heterodyne DIAL at High Repetition Rate: A Solution for the Data Acquisition Problem
Holger Linné and Jens Bösenberg 759

5. All Solid State Heterodyne DIAL System for Simultaneous Water Vapor and Wind Measurements
Stefan Lehmann, Jens Bösenberg, Friedhelm Jansen, and Holger Linné 763

6. Efficient Field-of-View Control for Multiple-Field-of-View Lidar Receivers
Gilles Roy, Luc Bissonnette, and Christian Bastille 767

7. Standardization of DAS Lidar Measurements
Derk Weidauer, Karl-Heinz Eickel, Wilhelm Lahmann, Ljuba Nikowa, Matthias Ulbricht, Konradin Weber, Claus Weitkamp, and Jean-Pierre Wolf 771

8. Design and Preliminary Results from Simultaneous Upward/Downward Airborne Lidar System
Michael G. Harwood and Kevin B. Strawbridge 775

9. Development of a Compact, Ground-Based Ozone DIAL System
T.H. Chyba, T. Zenker, C.L. McCray, H.R. Lee, B. Thomas, R. Elivert, N. Scott Higdon, and D.A. Richter 779

10. Comparison of Lidar and Meteorological Data with a Model in a Case of Destruction of Temperature Inversions in Mountain Valleys
Ivan Kolev, Plamen Savov, Boyan Tatarov, and Boiko Kaprielov 783

11. Injection-Seeded Pulsed Ti:Sapphire Ring Laser for Atmospheric Water Vapour Measurements in the Region from 922 nm to 942 nm
G. Poberaj and H.H. Klingenberg 787

12. Diode Pumped Nd: YAG Rod Oscillator with Cr4+:Yag Passive Q-Switch Operating up to 1.5 kHz and 1 Watt average power
Mark Kushina and Christian Dinolfo 791

13. Laser Pulse Amplification Characteristics of Chromium-Doped Forsterite
Takashi Fujii, Tetsuo Fukuchi, and Koshichi Nemoto 795

14. New Frequency Conversion Schemes for Pulsed Optical Parametric Oscillators to Efficiently Generate Continuously Tunable Ultraviolet Radiation
Andreas Fix and Gerhard Ehret 799

15. Single Frequency, Pulsed Laser Diode Transmitter for Dial Water Vapor Measurements at 935 nm
Gregg W. Switzer, Donald M. Cornwell Jr., Michael A. Krainak, James B. Abshire, and Jonathan A.R. Rall 803

16. Extractable Energies in Tm,Ho:YAG and Tm,Ho:YLF 2 μm-Lasers With Multiple-Pulse Operation
Didier Bruneau, Stéphane Delmonte, and Jacques Pelon 807

17. Simultaneous Upward/Downward Airborne Lidar Observations Including Depolarization Measurements During Two Recent Field Studies
Kevin B. Strawbridge, Michael G. Harwood, and I. Gultepe 811

18. Performance Improvements to the Lidar Atmospheric Sensing Experiment (LASE)
W.C. Edwards, L.P. Petway, and C.W. Antill, Jr. 815

19. Conversions to the Lidar Atmospheric Sensing Experiment (LASE) Instrument for Nadir and Zenith Measurements
Alvah S. Moore, Jr. and Leroy F. Matthews 819

20. Characterization of White Light Generated in the Atmosphere and the Use for Atmospheric Remote Sensing With Lidar
H. Wille, S. Niedermeier, P. Rairoux, M. Rodriguez, F. Ronneberger, R. Sauerbrey, H. Schillinger, B. Stein, D. Waite, C. Wedekind, and L. Wöste 823

21. Experimental Studies on A ΔK Lidar for Atmospheric Temperature Measurement Using Longitudinal Mode Spacing and Acoustic Wave
Yasukuni Shibata, Chikao Nagasawa, and Makoto Abo 827

22. A Modeling of Noise in Lidar-Returned Signal Using Non-linear Autoregressive Models Based on Kalman Filtering Techniques
J.L. Gao, C.N. Ng, J.C.L. Chan, K.M Leung, and A.H.P. Ho 829

23. On the Calculation of Received Power for Lidar Imaging Systems
Bernhard Bundschuh, Holger Richter, Dietrich Althausen, Detlef Müller, and Albert Ansmann 833

24. M-Squared Laser Beam and Telescope Overlap Factors for a 1.5 micron KTP OPO Lidar
Priyavadan Mamidipudi and Dennis Killinger 837

25. Bidirectional Reflectance Factors Used in Lidar Calibration
David A. Haner and Robert T. Menzies 841

26. Advanced Detector and Waveform Digitizer for Water Vapor DIAL Systems
Tamer F. Refaat, William S. Luck, Jr., and Russell J. DeYoung 845

27. Signal-Induced Noise Effects in a Photon Counting System for Stratospheric Ozone Measurement
David B. Harper and Russell J. DeYoung 849

28. An OPO-Based Lidar System for Differential Absorption Measurements of Methane in the 3 μm Region
S.W. Lee, T. Zenker, and T. H. Chyba 853

29. A Fiber-Optic Coupled Telescope for Water Vapor DIAL Receivers
Fredrik Lonn and Russell J. DeYoung 857

30. UV Generation of 25mJ/pulse at 289 nm for Ozone Lidar
Mark E. Storm, Waverly Marsh, and James C. Barnes 861

31. Characterization of a 16-bit Digitizer System for Lidar Data Acquisition
Cynthia K. Williamson and Russell J. DeYoung 863

32. Daytime PRN-cw Backscatter Lidar Demonstration with Narrow-band Diode Laser MOPA and FADOF
G. Mileti, R. Matthey, and V. Mitev 867

33. Tunable Lidar System Based on OPA Laser Sources
G. Pappalardo, P.F. Ambrico, A. Amodeo, S. Amoruso, M. Armenante, V. Berardi, A. Boselli, R. Capobianco, N. Spinelli, and R. Velotta 871

34. Atmospheric Depolarization Lidar Experimental Receiver: A Space Shuttle Hitchhiker Payload
Matthew J. McGill, V. Stanley Scott, and James D. Spinhirne 875

35. Operation of the Prototype Holographic Atmospheric Scanner for Environmental Remote Sensing (PHASERS)
David V. Guerra, Albert D. Wooten Jr., Sandipan S. Chaudhuri, and Geary K. Schwemmer 879

36. PRN-cw Lidar with Broadband Powerful Diode Laser for Cloud and Target Detection
Renaud Matthey and Valentin Mitev 883

37. Thermal Lens Measurement in Diode-Pumped Nd:YAG Zig-Zag Slab
M.C. Smoak, R.B. Kay, D.B. Coyle, and D. Hopt 887

38. Differential Absorption Lidar (DIAL) Measurements of Atmospheric Water Vapor Utilizing Robotic Aircraft
Ngoc Hoang, Russell J. DeYoung, Coorg R. Prasad, and Gabriel Laufer 891

Poster Session 3

Part 3—Lidar Applications (PS3.3)

1. Average and Fluctuation Characteristics of the Transparency of Littoral Waters of Northern Scotland from the Data of Airborne Lidar Sensing
G. Ludbrook, A. Scott, G. Kokhanenko, I. Penner, and V. Shamanaev 895

2. Lidar Measurements of Chlorophyll Content in Vegetation
Gennadii G. Matvienko, Tatjana P. Astafurova, Anatolii I. Grishin, Olga V. Kharchenko, Vladimir M. Klimkin, and Vladimir G. Sokovikov 897

3. Shipborne Lidar Sensing of the Upper Water Layer in the Middle Atlantic
V. Shamanaev, G. Kokhanko, and I. Penner 901

4. Operation of the Mobile Lidar Trailer
Anthony V. Dentamaro, Phan D. Dao, Robert Farley, Philip Soletsky, Richard Garner, Ronald Frelin, Gilbert Davidson, Patrick Connolly, Jerry Gelbwachs, and Martin Ross 905

5. Noncooperative Target Classification of Airborne Threats
Wilfred Otaguro, Chyau Shen, Lee Pratt, and Kathleen Gainey 909

6. Capacitively Stabilized Etalon Technology for Spaceborne Wind Lidar Application
Steven X. Li, Bruce M. Gentry, C. Laurance Korb, Savyasachee Mathur, and Huailin Chen 915

7. Characteristics of an Ozone Dial Receiver for Operation on an Unpiloted Atmospheric Vehicle
Soendeke Goldschmidt and Russell J. DeYoung 919

8. Increased Capabilities for Conventional Lidars Using Holographic Optics
Thomas D. Wilkerson, Marc Hammond, and Vincent B. Wickwar 923

Oral Session 7 (OS7)
Space and Future Lidar Systems
Session Chairs: P. McCormick and V. Zuev
Friday, July 10, 8:00 a.m. to 12:00

1. Invited Talk:
Initial Mars Orbiter Laser Altimeter (MOLA) Measurements of the Mars Surface and Atmosphere
James B. Abshire, Xiaoli Sun, and Robert S. Afzal 925

2. Multi-Beam Surface Lidar for Lunar and Planetary Mapping
Jack L. Bufton and James B. Garvin 927

3. Development of Miniature Lidar Using Narrow Linewidth Semiconductor Lasers for Mars Boundary Layer Wind and Dust Opacity Profiles
Robert T. Menzies, Greg Cardell, Carlos Esproles, Siamak Forouhar, Hamid Hemmati, and David Tratt 929

4. Preliminary Results of the ALISSA Cloud Lidar On Board the MIR Space Station
Alain Hauchecorne, Marie-Lise Chanin, Christian Malique, Dusan Nedeljkovic, Jacques-Emile Blamont, Michael Desbois, Gueorgui Tulinov, and Vladimer Melnikov 931

5. Earth-Satellite-Eearth Laser Long-path Absorption Experiments Using the Retroreflector in Space (RIS) on the ADEOS Satellite
Nobuo Sugimoto, Nobuhiko Koga, Atsushi Minato, Kenichi Ozawa, Yasunori Saito, Akio Nomura, Tetsuo Aoki, Toshikazu Itabe, and Hiroo Kunimori 935

6. Wind Lidar Edge Technique Shuttle Demonstration Mission—Anemos
Stephen J. Leete, David J. Bundas, Anthony J. Martino, Timothy M. Carnahan, and Barbara J. Zukowski 939

7. Pathfinder Instruments for Cloud and Aerosol Spaceborne Observations (PICASSO)
M. Patrick McCormick and David M. Winker 943

8. Ozone Research with Advanced Cooperative Lidar Experiment (ORACLE) Implementation Study
John H. Stadler, Edward V. Browell, Syed Ismail, Alexander E. Dudelzak, and Donald J. Ball 945

9. Invited Talk:
ELISE (Experimental Lidar In Space Equipment) Development and Science Application Plan: NASDA Mission Demonstration Satellite Lidar (MDS-lidar) Project
Yasuhiro Sasano 949

10. Cloud Distribution Statistics from LITE
David M. Winker 955

11. Intercomparison of LITE Tropospheric Aerosol Retrievals with a Regional Aerosol Climate Model
R.M. Hoff, A. Vandermeer, L. Spacek, J.P. Blanchet, C. Ro, R. Vet, P. Liu, S.L. Gong, and L.A. Barrie 959

12. Comparisons of LITE Observations with Ground-Based Lidar and SAGE II Profiles over SE Australia.
Stuart A. Young and Mary T. Osborn 963

13. Correction of Spaceborne Lidar Signal for Multiple Scattering From High Clouds
A.V. Starkov and C. Flesia 967

Oral Session 8 (OS8)
Lidar Commercialization and Eye Safety
Session Chairs: T. Kobayashi and L. Stefanutti
Friday, July 10, 1:30 to 3:00 p.m.

1. Invited Talk:
Commercialization of Lidar: Review and Perspective
Stephen E. Moody 971

2. Invited Talk:
Research Lasers and Air Traffic Safety: Issues, Concerns, and Responsibilities of the Research Community
Phillip J. Nessler, Jr. 975

3. Micro Lidar for Aerosol Measurement
I. H. Hwang, Matthew K. Nam, and Belthur Ranganayakamma 979

4. A Radar Safety Device for Lidars Probing the Atmosphere
J.M. Alvarez, W.H. Fuller, Jr., and R. M. Lawerence 983

Laser Development from Carbon Dioxide to FEL and their Applications to Remote Sensing and Pollution Monitoring

C. Kumar N. Patel
University of California, Los Angeles, Box 951405, Los Angeles, CA 90095, USA
Phone (310) 825-7943; Fax: (310) 206-4997; E-mail: patel@research.ucla.edu

Introduction

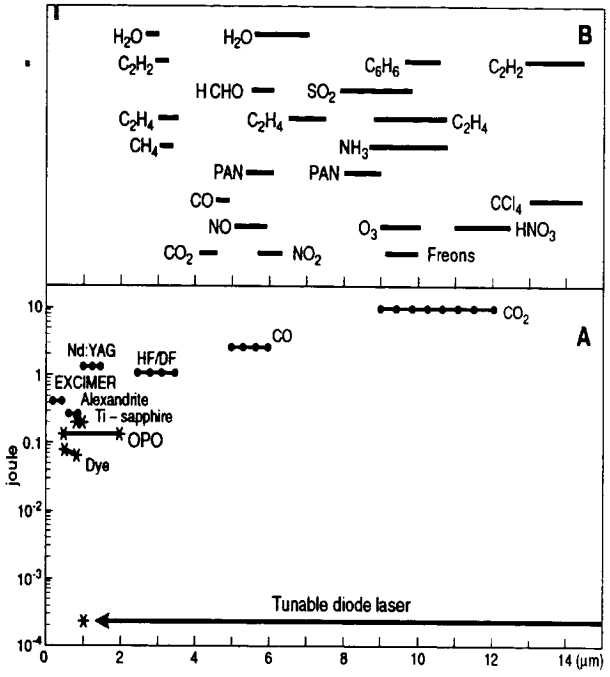
Optical spectroscopic methods, including scattering, absorption and fluorescence, are well established for determination of various species of known properties both in the air as well as in water. Progress in the fields of active remote sensing and pollution monitoring is closely linked with the advances in tunable high power lasers (e.g., Patel 1978; Manheimer 1994). In the past decade, development of high-efficiency CO-oxidation catalysts for the extended operation of CO_2 lasers, and advances in tunable Ti-sapphire and optical parametric oscillators (OPO) and amplifiers (OPA) have significantly enhanced the capabilities of laser radars used for a variety of remote sensing applications including environmental monitoring from airborne and space-borne platforms as well as from ships. For large scale applications, however, it remains the case that the extent of the deployment of laser remote sensing systems is inhibited by tunability and power limitations. In this context, development of kilowatt-class free electron lasers (FEL) that are tunable over a wide spectral range (UV to mid-infrared) offers an exciting opportunity for use of this technology as an optical transmitter for range gated detection (e.g., Madey 1971; Benson 1995).

This paper discusses the current state of a brief sample of remote sensing lasers, in conjunction with examples of their uses for environmental studies and pollution monitoring both in the atmosphere and the ocean. With the status of these conventional laser systems as background, the paper summarizes a proposed FEL-based, mobile platform that would achieve orders-of-magnitude increases in tunability and power, promising major gains in the scientific yield for a number of large-scale active remote sensing applications.

Overview of Some Principal Remote Sensing Lasers

Figure 1A summarizes approximate output pulse energy (J) as a function of wavelength for a variety of continuously and discretely tunable lasers, while Figure 2 shows the projected performance of a kW-class FEL, tunable from near-UV through the mid-IR. Spectral regions of absorption arising from vibrational-rotational transitions of some typical molecules of interest in environmental and pollution monitoring are shown in Fig. 1B.

Figure 1. (A) Summary of approximate average power



output plotted against wavelength for a variety of continuously and discretely tunable lasers in the visible and the near-infrared region. The output powers denoted on the figure are for typical laboratory-sized lasers. (B) Spectral regions of absorption arising from vibrational-rotational transitions for some typical molecules of interest in pollution detection.

The CO_2 laser operates at lines spaced by ~2 cm^{-1} in 9.5 to 11μm (Patel 1964; see also Fig. 1A). Isotope substitution in the CO_2 molecules further increases the number of discrete lines. This is an important region of the spectrum, where strong fundamental absorption bands of a number of pollutants and green house gases are present in the atmosphere. CO_2 lidars have been used to detect specific chemicals at ppm to ppb level in the atmosphere using differential absorption lidar (DIAL) techniques (e.g., Patel 1978). CO_2 laser-based coherent lidar systems have shown great utility in the area of Doppler wind measurement (e.g., Bilbro *et al.* 1986; Intrieri *et al.* 1990), while a high-power

injection-seeded Ho,Tm:YLF laser operating at 2.05 μm with output of 600 mJ at 10 Hz has recently been developed for accurate and precise measurements of tropospheric winds from space (Appell 1998; Singh 1998).

Combination and overtone vibrational-rotational modes of molecular species in the 700-2500 nm region (not shown in Fig. 1B) also have absorption strengths adequate for detecting profiles of moderate to high concentrations of water vapor, the most important greenhouse gas, and various other gaseous species produced by volcanic and industrial pollution in the troposphere and lower stratosphere. Injection-seeded, tunable and line-narrowed alexandrite and Ti-sapphire laser systems have been successfully used for measuring profiles of water vapor using both ground-based and airborne DIAL systems (e.g., Ismail and Browell 1994).

In addition, the electronic-vibrational absorption of molecular species in the 220-440 nm spectral region have proven useful for DIAL measurements of O_3, SO_2, H_2S, etc. (e.g., Zanzottera 1990). Fluorescence (both atomic and molecular) and Raman lidars usually require suitable short wavelength monochomatic lasers in UV and visible region but the short wavelength tunable sources could be useful in remote resonance fluorescence and resonance Raman lidars and could significantly increase (by several orders of magnitude) the detection limits of the fluorophores and chromophoric-Raman species in oceanic lidars. Diode-pumped solid state lasers are finding increasing applications in underwater fluorescence and reflection imaging as well as in airborne laser transmitters, where the electric power requirements and mass of the system are critical considerations.

Despite low Raman cross-sections, advanced high power UV lasers (both excimer and frequency-tripled Nd:YAG) are successfully used for water-Raman lidar (e.g., Grant 1991; Whiteman *et al.* 1992). One of the attractive features of Raman scattering relates to the ease with which the concentration of species relative to reference species such as N_2 in the atmosphere can be evaluated from the ratio of respective Raman signals provided relevant cross-sections are known. Hybrid UV-DIAL and Raman lidar systems have been developed for measurement of stratospheric ozone with high power and high repetition rate excimer lasers (e.g., McGee *et al.* 1995). The Raman augmentation of ozone-DIAL has allowed accurate measurements of stratospheric ozone in the presence of volcanic aerosol.

Cloud and aerosol particles suspended in the atmosphere are a major determinant of climate forcing, so that knowledge of the chemical and microphysical properties of clouds and aerosols is critical. In particular, solar blocking by stratospheric sulfate aerosols (primarily volcanic in nature) is now believed to be important in mitigating global warming processes. Development of high power laser transmitters from the UV to IR has opened up the possibility of using multiwavelength lidar systems for providing a better understanding of these primary aerosol properties, and for differentiating between hygroscopic and non-hygroscopic aerosol types. At present, the need to use multiple laser systems, however, makes it difficult to operate multiwavelength Mie-Rayleigh lidar systems on a routine basis.

The following subsections expand the detail of the foregoing discussion for two of the principal lasers and remote-sensing areas. This is followed by a summary of the potential contributions of a continuously tunable (UV-IR) FEL transmitter. In the IR region, the FEL would improve the detection limits as well as the number of chemical species that can be monitored with IR DIAL systems.

CO_2 lidar applications

One of the more versatile coherent sources is the CO_2 laser, which is characterized by exceptionally high gain and efficiency and is particularly tolerant toward an extensive and diverse array of excitation schemes (e.g., Patel 1964; Patel *et al.* 1965). This has resulted in the CO_2 laser family being very well represented in the laser remote sensing arena. Furthermore, the 9-11 μm operational wavelength range overlaps prominent molecular spectral features in both natural and foreign (i.e., pollutant) atmospheric constituents of interest to a broad spectrum of research and monitoring activities. Measurement of atmospheric water vapor by means of the differential absorption lidar (DIAL) technique is one such application to which CO_2 systems have been notably successful (e.g., Hardesty 1984), with the ongoing need to understand the detailed behavior of the global hydrologic cycle being the primary driver. CO_2 DIAL systems have also been used to remotely detect important trace species such as CO, NO, and C_2H_4, etc. (Killinger and Menyuk 1981; Carlisle *et al.* 1995). CO_2 lidar systems have also been used to elucidate the optical and microphysical properties of clouds (Gross *et al.* 1984; Platt and Takashima 1987) and entrained aerosols (Post 1984), these being critical parameters in understanding the impact of trends in the Earth's radiation budget on global climate change processes. The typical range of CO_2 laser pulse energies utilized by lidar researchers has been 0.1 to 2.0 J. However, CO_2 lasers can

be and have been constructed, if desired, to generate pulse energies in excess of 1 kJ. These very high CO_2 laser energies, though, have not been used for lidar studies. The anticipated ~30J wavelength-tunable pulse energies in the thermal IR possible with a high performance FEL transmitter therefore represent at least an order of magnitude increase in range performance compared to the capability of typical systems in use at present.

Resonance Fluorescence Lidars and Remote Sensing of Global Change

Climate studies of the upper atmosphere suggest that this region of the atmosphere may be much more sensitive to global changes in greenhouse gas concentrations than the lower atmosphere (Roble and Dickinson 1989). Resonance lidar techniques provide a unique tool for probing the upper mesosphere and lower thermosphere (70-120 km) due to the presence of free metal atoms ablated from meteors (Gardner 1989). More recently, narrow band dye laser systems have been developed that employ Doppler-free fluorescence spectroscopy to precisely probe the hyperfine structure of Na atoms and hence determine the temperature and wind profiles in this region (Bills *et al.* 1992; She *et al.* 1992).

These systems have been used to study the thermal structure of the region and determine the roles of dynamic and chemical processes in maintaining the observed structure which is far from radiative equilibrium (Yu and She 1995). Furthermore, high resolution measurements of the winds and temperatures have been used to study how small scale wave breaking contributes to the thermal structure of the region (Tao and Gardner 1995).

Given these successes, considerable effort has been given to developing solid state lidar systems to carry out these measurements. Currently, measurements are underway with alexandrite systems that probe free potassium atoms at the same altitudes as the sodium layer (von Zahn and Hoffner 1996). Advanced line-narrowed FEL sources will be very promising for monitoring minor constituents of the metallic layer and the dynamics of the upper atmosphere.

Mobile FEL Platform

The special characteristics of the free electron laser (FEL) have the potential to make a remote sensing instrument of extraordinary power (Manheimer, 1994). Its unique potential for continuous wavelength tuning over a wide bandwidth makes it possible for a single laser to observe an unprecedented number of species. The FEL is also capable of high peak and average power, which would allow either or both making observations over much-increased distances and decreasing the times for observations that can take many minutes with conventional lasers to seconds, or less.

To exploit this potential a consortium led by UCLA and the University of Hawaii is proposing a mobile remote sensing platform based on a FEL on a large oceanographic vessel (Sharma *et al.* 1997). The performance features of this laser will include tunability over the entire range of near-UV to mid-IR wavelengths that have useful atmospheric transmission; GHz switching between wavelengths; pulse power of megawatts, and kilowatt-class average power (Fig. 2); and flexible amplitude and frequency modulation for high range resolution.

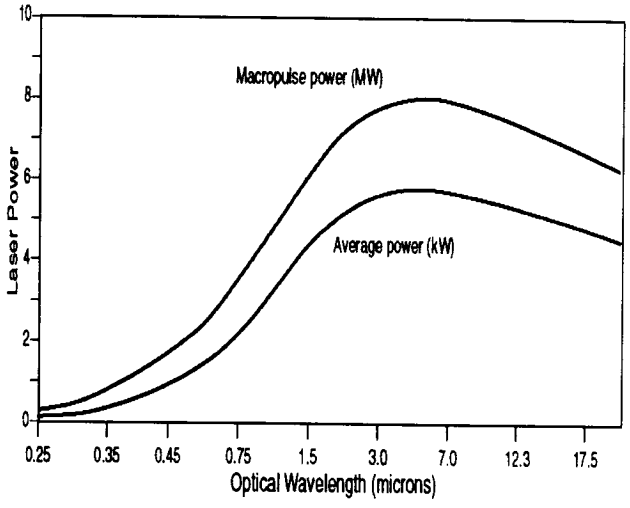


Figure 2. Projected output power of the proposed FELDAR at an operating PRF of 180 Hz.

The laser output mimics the temporal structure of the electron beam lasing medium, producing picosecond pulses that have had relatively large linewidth in the past (6 - 40 cm^{-1}). However, interferometric (Szarmes *et al.* 1996) and injection seeding (Amir *et al.* 1991) techniques have been successfully applied in recent years to spectrally narrow FEL output ($\leq$ 210 MHz; 0.003 cm^{-1} at 3 μm). In a recent development, operation with phase-locked pulses has demonstrated a 100-MHz linewidth, and experiments are underway on the Mk III FEL with an intracavity Fox-Smith interferometer to achieve single mode (sub-MHz linewidth) output appropriate for Doppler-free spectroscopy (Madey, private communication, 1998). Implementation of these techniques to a kilowatt FEL will render this class of laser system a very powerful tool for resonance fluorescence lidar, as well as for narrow-line

DIAL systems. In addition to this new narrow-line capability, broadband FELDAR (free electron laser detection and ranging) in conjunction with an imaging spectrograph and 2D-CCD detector will offer opportunities for simultaneous measurements of multiple molecular species by the differential optical absorption spectroscopy (DOAS) technique (Povey *et al.* 1998).

The output characteristics of this laser transmitter would be valuable for an extremely wide variety of applications. An early survey (Helsley *et al.* 1996) identified uses ranging from near real-time mapping of pollution in the entire Los Angeles Basin, to the study of the origin of noctilucent clouds, the effect of volcanic emissions on the Earth's temperature and albedo, and primary production in the oceans. High average power and the ability to rapidly switch the output wavelength will give the proposed system the ability to operate in a time-sharing mode, supporting simultaneous observations for diverse purposes, as well as for integrated observations such as coupled studies of the atmosphere and upper ocean.

Because of their size and pulse characteristics, FELDAR systems pose important questions about the deployment platforms, and will require innovative receiver design. For the proposed FEL platform, a large oceanographic vessel was chosen as the most suitable means of providing mobility to a FEL, which are large and massive in current embodiments. The areas where innovations are needed in receiver designs include means to exploit the output pulse modulations in order to enable high range resolution. The proposed schemes include frequency and amplitude modulations, and 'micropulse formatting' with arbitrary arrangements of present or missing pulses on a GHz time scale, for use with a pseudorandom coding scheme (e.g., Takeuchi *et al.* 1983).

Conclusions

Orders-of-magnitude advances in the capabilities of tunable laser systems will greatly expand the uses of active remote sensing. With growing global environmental and pollution problems, a ship-based FELDAR system will provide a needed tool for long-term monitoring of coastal areas, large ocean expanses and the atmosphere, including an increased ability to complement observations by satellites. To fully realize the benefits of such a development, extensive cooperation is anticipated between numerous institutions, funding agencies, private companies, and interdisciplinary teams of scientists.

Acknowledgments

The author would like to thank a number of colleagues who contributed to the preparation of this paper, particularly Drs. Shiv K. Sharma (University of Hawaii), Robert J. Burke (Arcata Systems, Santa Cruz, CA), David M. Tratt (Jet Propulsion Laboratory, Pasadena, CA), and Richard L. Collins (University of Alaska, Fairbanks).

References

Amir, A., J. F. Knox-Seith, and M. Warden (1991): Narrow-bandwidth operation of a free-electron laser enforced by seeding. *Phys. Rev. Lett.* **66**, 29-32.

Appell, D. (1998): Shuttle laser to measure atmospheric winds. *Laser Focus World* **34**, March 30, 29-31.

Benson, S. V. (1995): Tunable free-electron lasers, in F. J. Duarte (ed.), *Tunable Laser Handbook*, Academic Press, New York, pp. 443-470.

Bilbro, J. W., C. DiMarzio, D. Fitzjarrald, S. Johnson, and W. Jones (1986): Airborne Doppler lidar measurements. *Appl. Opt.* **25**, 3952- 3960.

Bills, R. E., C. S. Gardner, and C. Y. She (1991): Narrow band lidar technique for Na temperature and Doppler wind observations in the upper atmosphere. *Opt. Eng.* **30**, 13-21.

Carlisle, C. B., J. E. van der Laan, L. W. Carr, R. Adam, and J.-P. Chiaroni (1995): CO_2 laser-based differential absorption lidar system for range-resolved and long-range detection of chemical vapor plumes. *Appl. Opt.* **34**, 6187-6200.

Gardner, C. S. (1989): Sodium resonance fluorescence lidar applications in the atmospheric sciences and astronomy. *Proc. IEEE*, **77**, 408-418.

Grant, W. B. (1991): Differential absorption and Raman lidar for water vapor profile measurements: a review. *Opt. Eng.* **30**, 40-48.

Gross, A., M. J. Post, and F. F. Hall, Jr. (1984): Depolarization, backscatter, and attenuation of CO_2 lidar by cirrus clouds. *Appl. Opt.* **23**, 2518-2522.

Hardesty, R. M. (1984): Coherent DIAL measurement of range-resolved water vapor concentration. *Appl. Opt.* **23**, 2545-2553.

Helsley, C. E., S. K. Sharma, R. J. Burke, and C. K. N, Patel (1996): Pan-Oceanic Environmental and Atmospheric Research Laboratory (PEARL), A Consortium Proposal for a National Facility for Marine and Atmospheric Research, January 17, 1996, unpublished.

Intrieri, J. M., A. J. Bedard, Jr., and R. M. Hardesty (1990): Details of colliding thunderstorm outflows as observed by Doppler lidar. *J. Atmos. Sci.* **47**, 1081-1098.

Ismail, S., and E. V. Browell (1994): Recent lidar technology developments and their influence on measurements of tropospheric water vapor. *J. Atmos. Oceanic Technol.* **11**, 76-84.

Killinger, D. K., and N. Menyuk (1981): Remote probing of the atmosphere using a CO_2 DIAL system. *IEEE J. Quantum Electron.* **QE-17**, 1917-1929.

Madey, J. M. J. (1971): Stimulated emission of bremsstrahlung in a periodic magnetic field. *J. Appl. Phys.* **42**, 1906-1913.

Manheimer, W. M. (1994): Gyrotron and free electron lasers as atmospheric sensors. *Phys. Plasma* **1**, 1721-1729.

McGee, T. J., M. R. Gross, U. N. Singh, J. J. Butler, and P. E. Kimvilakani (1995): Improved stratospheric ozone lidar. *Opt. Eng.* **34**, 1421-1430.

Patel, C.K.N. (1964): Interpretation of CO_2 optical maser experiments. *Phys. Rev. Lett.* **12**, 588-590.

Patel, C. K. N. (1978): Laser Detection of pollution. *Science* **202**, 157-173.

Patel, C.K.N., P. K.Tien, J. H. McFee (1965): CW high power CO_2-N_2-He laser. *Appl. Phys. Lett.* **7**, 290-292.

Platt, C. M. R., and T. Takashima (1987): Retrieval of water cloud properties from carbon dioxide lidar soundings. *Appl. Opt.* **26**, 1257-1263.

Post, M. J. (1984): Aerosol backscattering profiles at CO_2 wavelengths: the NOAA data base. *Appl. Opt.* **23**, 2507-2509.

Povey, I. M., A. M. South, A. t'Kint de Roodenbeke, C. Hill, R. A. Freshwater, and R. L. Jones (1998): A broadband lidar for the measurement of tropospheric constituent profiles from the ground. *J. Geophys. Res.* **103**, 3369-3380.

Roble, R. G., and R. E. Dickinson (1989): How will changes in carbon dioxide and methane modify the mean structure of the mesosphere and thermosphere? *Geophys. Res. Lett.* **16**, 1441-1444.

Sharma, S. K., C. E. Helsley, R. J. Burke, D. M. Tratt, R. L. Collins and C. K. N. Patel (1997): Ship-based free electron laser (FEL) lidar for oceanic and atmospheric research. In N. K. Saxena (ed.), *Recent Advances in Marine Science and Technology, 96*, PACON International, Honolulu, Hawaii, pp. 191-204.

She, C. Y., J. R. Yu, H. Latifi, and R. E. Bills (1992):. High-spectral-resolution fluorescence light detection and ranging for mesospheric sodium temperature measurements, *Appl. Opt.* **31**, 2095-2106.

Singh, U. N. (1998): Development of high-pulse energy Ho,Tm:YLF coherent transmitter (to be published).

Szarmes, E. B., A. D. Madden and J. M. J. Madey (1996): Optical phase locking of a 2.86 GHz Harmonically mode locked free-electron laser. *J. Opt. Soc. Amer. B* **13**, 1588-1597.

Tao, X., and C. S. Gardner (1995): Heat flux observations in the mesopause region above Haleakala. *Geophys. Res. Lett.* **22**, 2829-2832.

von Zahn, U., and J. Hoffner (1996): Mesopause temperature profiling by potassium lidar. *Geophys. Res. Lett.* **23**, 141-144.

Whiteman, D. N., S. H. Melfi and R. A. Ferrare (1992): Raman lidar system for the measurement of water vapor and aerosols in the Earth atmosphere. *Appl. Opt.* **31**, 3068-3082.

Takeuchi, N., N. Sugimoto, H. Baba, and K. Sakurai (1983): Random modulation cw lidar. *Appl. Opt.* **22**, 1382-1386.

Yu, J. R., and C. Y. She (1995): Climatology of a midlatitude mesopause region by a lidar at Fort Collins, Colorado (40.6°N, 105°W). *J. Geophys. Res.* **100**, 7441-7452.

Zanzottera, E. (1990): Differential absorption lidar techniques in the determination of trace pollutants and physical parameters of the atmosphere. *Critical Rev. Anal. Chem.* **21**, 40-48.

Role of Lidar in Climate–related Aerosol Characterization Experiments

A. Ansmann, D. Althausen, D. Müller, I. Mattis, F. Wagner, and U. Wandinger
Institute for Tropospheric Research
Permoserstrasse 15, D–04318 Leipzig, Germany
Phone: ++49 341 235 2149, FAX: ++49 341 235 2361, E-mail: ilrc@tropos.de

1 Introduction

In order to quantify the impact of anthropogenic and natural aerosols on climate, large international field campaigns such as the first and second Aerosol Characterization Experiment (ACE 1, Tasmania, 1995; ACE 2, Portugal/Canaries, 1997), the Tropospheric Aerosol Radiative Forcing Experiment (TARFOX, USA, 1996), the Lindenberger Aerosol–Charakterisierungs–Experiment (LACE 98, Germany, 1998), ACE ASIA (southeast Asia, 1998), and comprehensive aerosol studies within the framework of the Indian Ocean Experiment (INDOEX, Indian Ocean, 1999) have been or will be conducted. In these observations the physical state and the chemical composition of the aerosol (layers) as well as the resulting optical, radiative, and cloud nucleating properties of the particles, including their changes with humidity, are quantified and the relationships between all these parameters are investigated. The overall goal of the characterization is to determine and to understand the properties and controlling factors of the aerosol in the anthropogenically modified atmosphere and assess their relevance for radiative forcing.

The needed complete aerosol data sets can only be obtained in so–called aerosol closure experiments. In section 2, the definition and tasks of closure studies and the role of lidar in this context is briefly described. Because the most important optical aerosol parameter, that can be derived from lidar observations, is the particle scattering or extinction coefficient, the available aerosol lidar techniques are critically reviewed in section3.

2 Column closure experiment

The defintion of a closure experiment is as follows: In a closure experiment an overdetermined set of observations is obtained, where the measured value of a dependent variable is compared with the value that is calculated from measured values of independent variables, using a model or operation. A close agreement between measured and calculated results demonstrates that the model is a suitable representation of the observed system and is appropriate for the use as a component in other (higher order) models. The main question behind all climate–related column closure experiments is: Can measured physical and chemical properties of the aerosol in the vertical be used to accurately predict the column–integrated direct effect of aerosols on radiative transfer?

In well–designed column closure experiments, lidar observations play an important role. In order to form a consistent impression of the aerosol impact on climate, airborne measurements of aerosol properties and radiative fluxes at the top and bottom of present aerosol layers should be conducted in the vicinity of a lidar beam. Only in this way, ground-based lidar, sunphotometer, in–situ measurements and airborne and satellite observations of aerosol and radiation properties are really comparable, can really be combined.

Beside the information about presence, height, structure, and thickness of aerosol layers, the most important quantity, expected by the aerosol community to be derived from lidar observations, is the particle (volume) extinction coefficient and its vertical distribution, and this, if possible, at several wavelengths within the spectral range from the UV to the IR region. Furthermore, physical parameters retrieved from the spectral slope of scattering coefficients are of great interest in closure studies. In this context, it may be useful to review available lidar techniques for the determination or estimation of the height profile of the particle extinction coefficient. This is done in this paper on the basis of aerosol data measured with the scanning six–wavelength aerosol lidar and the dual–wavelength Raman lidar of the Institute for Tropospheric Research (Müller et al., 1998; Mattis et al., 1998). The six–wavelength lidar also detects Raman signals of nitrogen (607 nm) and of water vapor (660 nm).

3 Particle extinction retrieval

3.1 Elastic backscatter lidar

As well known but often ignored in aerosol lidar publications, the main disadvantage of the Klett method (Klett, 1981; Fernald, 1984), that is used to solve the elastic–backscatter lidar equation, is that two unknowns (the backscatter and the extinction coefficient) have to be determined from one measured signal. The problem seems to be tackled by introducing the extinction/backscatter ratio (lidar ratio). However, as a result of changing aerosol properties with height (size distribution, chemical composition), the lidar ratio estimates are very inaccurate and thus prohibit a proper estimation of the extinction profile and the particle optical depth.

Two examples of measurements during ACE 2 will underline this. In Figs 1 and 2 a six–wavelength and a four–wavelength lidar measurement are shown. The backscatter coefficient profiles indicate an optically very thin aerosol layer which was advected from North America to Portugal during the past four days before the observation (Fig. 1) and a thick layer of polluted air which was advected from central Europe according to backtrajectory analyses.

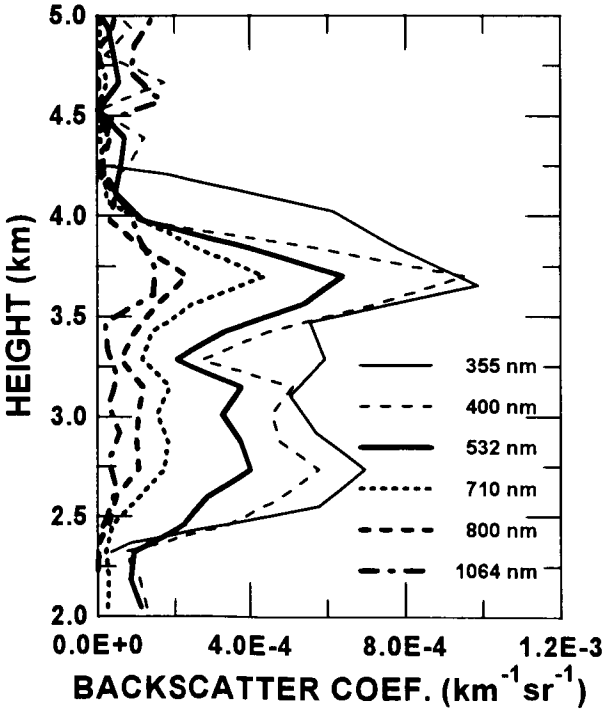


Fig. 1: Particle backscatter coefficient measured at six wavelengths in the free troposphere at Sagres, Portugal, during ACE 2 on 16 June 1997 between 2015 and 2215 UTC. The optical depth of the layer was about 0.02 at 532 nm. The relative humidity in that layer was less than 1%. Due to detection problems, the 355–nm backscatter profile is not very reliable.

The optical depth of the thin layer was only 0.02 at 532 nm (determined from N_2 Raman signals). In this case the lidar backscatter signal is more or less not affected by particle extinction. As a direct consequence, the backscatter coefficient profile is not sensitive to the lidar ratio but the extinction coefficient profile is very sensitive to that estimate.

Even in the case shown in Fig. 2 (pollution outbreak) with a considerable impact of light extinction on the signal strength, the uncertainty in the solution of the particle extinction coefficient is unacceptably high. By assuming different, but reasonable lidar ratios a large range of 'realistic' results can be produced. Solutions varying by a factor of three or more can easily be calculated. As mentioned above, due to changing aerosol physical and chemical properties and, thus, changing (total and backward) scattering conditions with height, the Klett method cannot be used to determine particle extinction profiles. Only the backscatter coefficients are reliable and thus shown here.

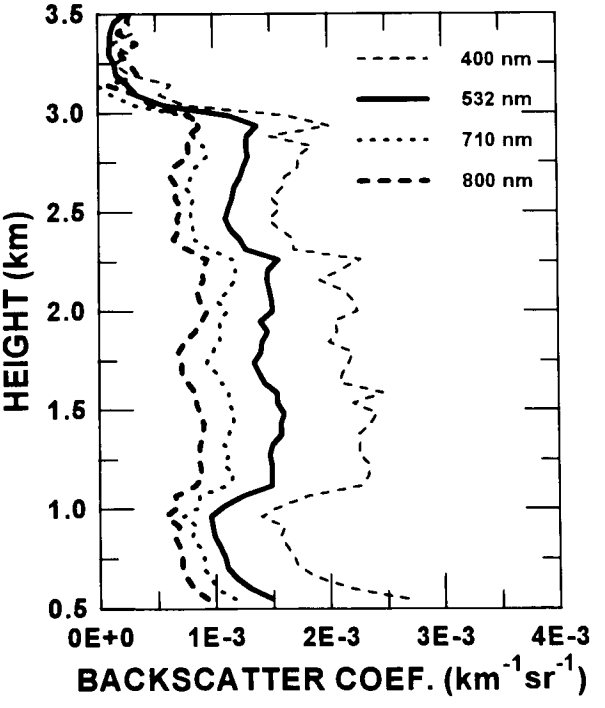


Fig. 2: Particle backscatter coefficient measured with the multiple–wavelength aerosol lidar at Sagres on 20 July 1997 between 430 and 500 UTC. According to sunphotometer observations 50 km north of the lidar site at an altitude of 900 m, the optical depth of the pollution layer between 1000 and 3000 m was about 0.4, 0.25, and 0.15 at 400, 532, and 800 nm, respectively.

3.2 Scanning elastic–backscatter lidar

The situation is much better, if a scanning lidar is available and horizontally homogeneous aerosol conditions are present. By taking data under different zenith angles θ_1 and θ_2, the particle optical depth between the lidar (!) and height z above the altitude for which the overlap between the laser beam and the receiver field is complete (for both beams) can directly be retrieved from the signal ratio $P(z,\theta_1)/P(z,\theta_2)$ (Gutkowicz–Krusin, 1993). Neither a lidar–ratio profile nor the overlap functions have to be known. The derivation of the particle optical depth then yields the extinction coefficient.

An example is shown in Fig. 3. Laser beams were alternately transmitted at zenith angles of 30 and 60 degrees. Every five minutes the angle was changed. Six five–minute–averages for each angle had been further averaged before the signal ratio P(z,30°)/P(z,60°) was formed and the optical parameters were calculated. Fig. 4 presents a comparison with sunphotometer observations. The optical–depth values determined from the sunphotometer are, on the average, a bit larger than the ones calculated from the lidar signals. This systematic difference may be caused by the fact that the lidar data cover the range up to 3500 m only.

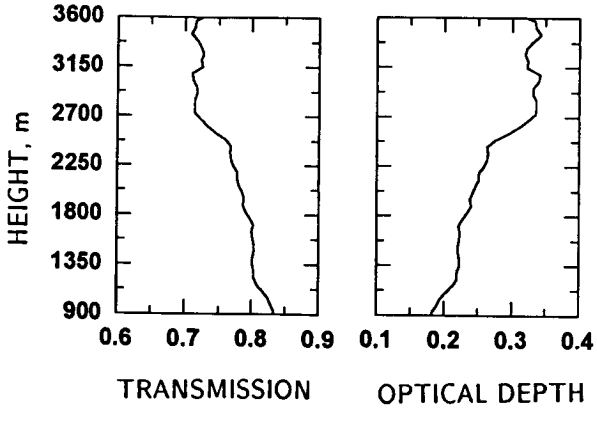


Fig. 3: Height profiles of the particle transmission and the optical depth determined from a two–zenith–angle lidar observation at 400 nm. The lidar measurement was taken at Sagres, Portugal, on 18 July 1997 between 2109 and 2221 UTC. Sunphotometers at Sagres and at an altitude of 900 m (50 km north of Sagres) around 1900 UTC yield values of 0.4 and 0.16, respectively. This is in good agreement with the lidar observations.

We can conclude from the ACE–2 observations that this differential extinction method works well under clear sky and thermodynamically stable conditions which are typically present at night–time. However, for a successful application of this method it is essential that the zenith angle is changed every few minutes and that averaging periods are about 30 min for each zenith angle. Then, effects due to backscatter and extinction fluctuations should be suppressed to a large extent. Whereas the optical depth of present aerosol layers can often be determined with sufficiently good accuracy, the extinction–coefficient profile is usually noisy due to remaining backscatter variations.

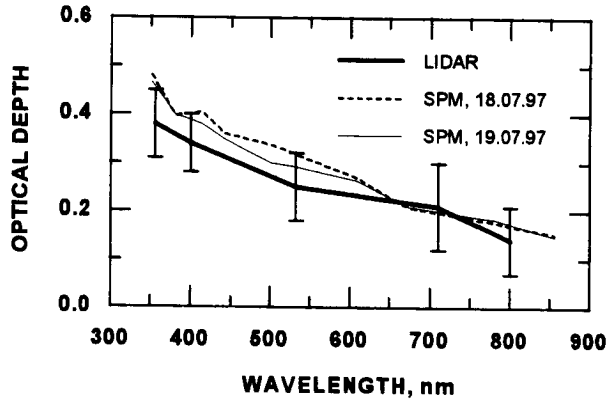


Fig. 4: Spectral optical depth derived from scanning lidar data on 18 July 1997 between 2109 and 2221 UTC and sunphotometer (SPM) observations at Sagres on 18 July 1997 (1900 UTC) and on 19 July 1997 (800 UTC). The large error bars indicate statistical and systematic uncertainties.

3.3 Raman lidar

The only method left for a proper retrieval of the extinction coefficient is the determination from signals purely backscattered by molecules (Shipley et al., 1983; Ansmann et al., 1990). The Raman lidar method has already intensively been applied to study the extinction properties of tropospheric (Ferrare et al., 1996) and stratospheric aerosols (Ansmann et al., 1997). The determination is based on nitrogen or oxygen Raman backscatter profiles. In contrast to the Klett method, only one unknown has to be derived from the measured signal because the molecular backscatter characteristics is sufficiently well known.

Unfortunately, Raman signals are about three orders of magnitude smaller than aerosol backscatter signals. Thus, although daytime observations are possible (up to heights of a few kilometers), Raman measurements are mainly restricted to night–time hours. The advantage of a Raman lidar is its

simple configuration when interference filters are used to separate the Raman from aerosol signals. Furthermore, by employing a Nd:YAG laser two extinction–coefficient profiles at 355 and 532 nm can easily be determined so that a good estimate of the climate–relevant spectral slope of the extinction coefficient in the solar wavelength region is obtained in addition. An example of such a dual–wavelength Raman lidar measurement is shown in Fig. 5. Since Raman lidars usually also allow to measure the water–vapor mixing ratio, this lidar technique seems to be the most useful one for atmospheric aerosol studies. The relative humidity which strongly influences the optical properties of aerosols can be computed from the mixing–ratio value by using a radiosonde temperature information.

Concerning the inversion of the optical data into physical parameters it should finally be mentioned that recent investigations show that the uncertainties in the physical parameters are significantly reduced if, in addition to the spectrally resolved backscatter characteristics, extinction information is available (Müller, 1997).

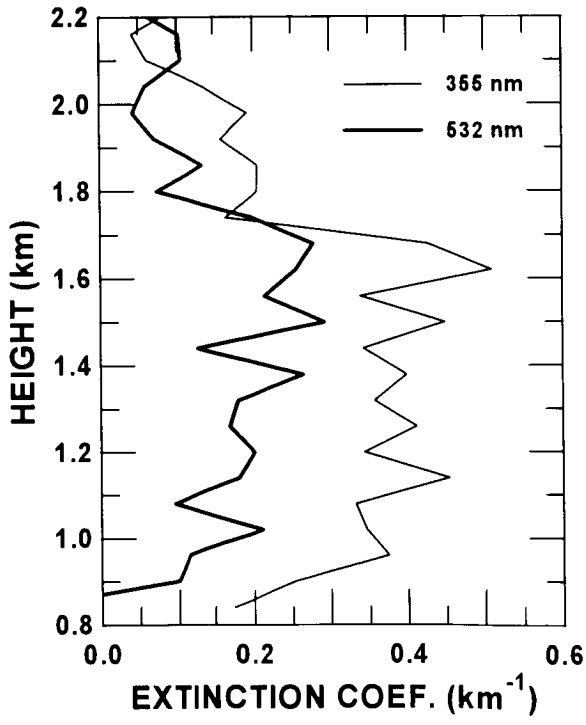


Fig. 5: Extinction coefficient for 355 and 532 nm derived from nitrogen Raman signals backscattered at 387 and 607 nm. The measurement was taken with the dual–wavelength Raman lidar at Leipzig on 17 March 1997.

References

Ansmann, A., Mattis, I., Wandinger, U., Wagner, F., Reichardt, J., and Deshler, T. (1997). Evolution of the Pinatubo aerosol: Raman lidar observations of the particle optical depth, effective radius, mass, and surface area over central Europe at 53.4° N. *J. Atmos. Sci.*, 54, 2630–2641.

Ansmann, A., Riebesell, M., and Weitkamp, C. (1990). Measurements of atmospheric aerosol extinction profiles with a Raman lidar. *Opt. Lett.*, 15, 746–748.

Ferrare, R.A., Whiteman, D.N., Melfi, S.H., Evans, K.D., and Holben, B.N. (1995). Raman lidar and sun photometer measurements of aerosols and water vapor during the ARM RCS experiment. in *Optical Remote Sensing of the Atmosphere*, 2, OSA Technical Digest Series, 206–208.

Fernald, F.G. (1984). Analysis of atmospheric lidar observations: some comments. *Appl. Opt.*, 23, 652–653.

Gutkowicz–Krusin, D. (1993). Multiangle lidar performance in the presence of horizontal inhomogeneities in atmospheric extinction and scattering. *Appl. Opt.*, 32, 3266–3272.

Klett, J.D. (1981). Stable analytic inversion solution for processing lidar returns. *Appl. Opt.*, 20, 211–220.

Mattis, I., Wandinger, U., Müller, D., Ansmann, A., Wagner, F., and Althausen, D. (1998). Routine dual–wavelength Raman lidar observations at Leipzig as part of an aerosol lidar network in Germany. 19th ILRC Proceedings.

Müller, D., Wandinger, U., Althausen, D., Mattis, I., and Ansmann, A. (1998). Retrieval of physical particle properties from lidar observations of extinction and backscatter at multiple wavelengths. *Appl. Opt.*, 37, 20 April issue.

Müller, D. (1997). Inversionsverfahren zur Bestimmung physikalischer Partikeleigenschaften aus Mehrwellenlängen–Lidarmessungen. Ph.D. dissertation, University of Leipzig, 99 pages.

Shipley, S.T., Tracy, D.H., Eloranta, E.W., Trauger, J.T., Sroga, J.T., Roesler, F.L., and Weinman, J.A. (1983). High spectral resolution lidar to measure optical scattering properties of atmospheric aerosols. 1: Theory and instrumentation. *Appl. Opt.*, 22, 3716–3724.

LASE Measurements of Aerosols and Water Vapor During TARFOX

Richard A. Ferrare[1], Syed Ismail[1], Edward V. Browell[1], Vincent G. Brackett[2], Susan A. Kooi[2], Marian B. Clayton[2],S. Harvey Melfi[3], David N. Whiteman[4], Geary Schwemmer[4], Keith D. Evans[3], Peter V. Hobbs[5], J. Pepijn Veefkind[6], Philip B. Russell[7], John M. Livingston[8], Philip Hignett[9] Brent N. Holben[4], and Lorraine A. Remer[10]

[1]NASA Langley Research Center, MS-401A, Hampton, Virginia 23681-0001, USA, 757-864-9443, 757-864-7790 (fax), r.ferrare@larc.nasa.gov
[2]Science Applications International Corporation, Hampton, Virginia, USA
[3]University of Maryland Baltimore County, Baltimore, Maryland, USA
[4]NASA Goddard Space Flight Center, Greenbelt, Maryland, USA
[5]University of Washington, Seattle, Washington, USA
[6]TNO Physics and Electronics Laboratory, The Hague, The Netherlands
[7]NASA Ames Research Center, Moffett Field, California, USA
[8]SRI International, Menlo Park, California, USA
[9]UK Meteorological Office, Farnborough, Hampshire, UK
[10]Science Systems and Applications, Inc., Greenbelt, Maryland, USA

Introduction

The TARFOX (Tropospheric Aerosol Radiative Forcing Observational Experiment) intensive field campaign was designed to reduce uncertainties in estimates of the effects of anthropogenic aerosols on climate by measuring direct radiative effects and the optical, physical, and chemical properties of aerosols [1]. TARFOX was conducted off the East Coast of the United States between July 10-31, 1996. Ground, aircraft, and satellite-based sensors measured the sensitivity of radiative fields at various atmospheric levels to aerosol optical properties (i.e., optical thickness, phase function, single-scattering albedo) and to the vertical profile of aerosols.

The LASE (Lidar Atmospheric Sensing Experiment) instrument, which was flown on the NASA ER-2 aircraft, measured vertical profiles of total scattering ratio and water vapor during a series of 9 flights. These profiles were used in real-time to help direct the other aircraft to the appropriate altitudes for intensive sampling of aerosol layers. We have subsequently used the LASE aerosol data to derive aerosol backscattering and extinction profiles. Using these aerosol extinction profiles, we derived estimates of aerosol optical thickness (AOT) and compared these with measurements of AOT from both ground and airborne sun photometers and derived from the ATSR-2 (Along Track and Scanning Radiometer 2) sensor on ERS-2 (European Remote Sensing Satellite-2). We also used the water vapor mixing ratio profiles measured simultaneously by LASE to derive precipitable water vapor and compare these to ground based measurements.

LASE Instrumentation

LASE is the first fully engineered, autonomous airborne DIAL (Differential Absorption Lidar) system to measure water vapor, aerosols, and clouds throughout the troposphere [2,3]. This system uses a double-pulsed Ti:sapphire laser, which is pumped by a frequency-doubled flashlamp-pumped Nd:YAG laser, to transmit light in the 815-nm absorption band of water vapor. The Ti:sapphire laser wavelength is controlled by injection seeding with a diode laser that is frequency locked to a water vapor line using an absorption cell. LASE operates by locking to a strong water vapor line and electronically tuning to any spectral position on the absorption line to choose the suitable absorption cross-section for optimum measurements over a range of water vapor concentrations in the atmosphere. LASE operated by alternating between strong (line center) and weak (side of strong line) water vapor cross sections for the on-line DIAL wavelength in order to measure water vapor throughout the troposphere. Typical horizontal and vertical resolutions for water vapor profiles extending between 0.2-18 km are 5 km and 300 m, respectively. Comparisons of water vapor measurements made by airborne dew point and frost point hygrometers, NASA/GSFC Raman lidar, and radiosondes during the LASE Validation Experiment, which was conducted in September, 1995 near Wallops Island, Virginia, showed the LASE water vapor mixing ratio measurements to have an accuracy of better than 6% or 0.01 g/kg, whichever is larger, across the troposphere [4].

In addition to measuring water vapor mixing ratio profiles, LASE simultaneously measures aerosol backscattering profiles at the off-line wavelength near 815 nm. Assuming a region with very low aerosol loading can be identified, profiles of the total scattering ratio, defined as the ratio of total (aerosol+molecular) scattering to molecular scattering, are determined by normalizing the scattering in the region containing enhanced aerosol scattering to the expected scattering by the "clean" atmosphere at that altitude. The aerosol backscatter coefficient is then computed from the total scattering ratio and the molecular backscattering cross section derived from radiosonde and/or model pressure and temperature profiles. These aerosol profiles, which span the altitude range between 0.03-18 km, typically have horizontal and vertical resolutions of 200 m and 30 m, respectively.

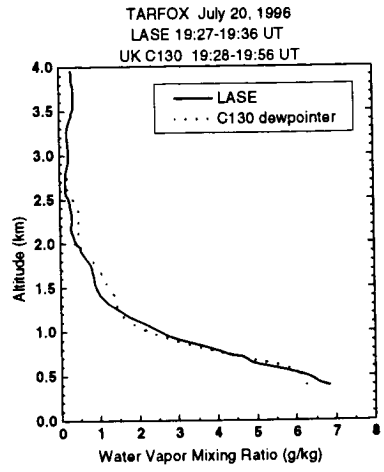


Figure 1. Water vapor mixing ratio profiles measured by LASE and a dew point hygrometer on the UK C-130 aircraft.

Measurements

During TARFOX, LASE collected a total of 24 flight hours of data over 9 flights between July 14 and July 26, 1996. These flights were coordinated with overflights of the NOAA-14, ERS-2, and LANDSAT satellites, and with flights by the other TARFOX aircraft including the University of Washington (UW) C-131A, the United Kingdom (UK) Meteorological Research Flight C-130, and the Center for Interdisciplinary Remotely Piloted Aircraft Studies (CIRPAS) Pelican. These flights occurred predominantly over the Atlantic Ocean 100-300 km east of Wallops Island, Virginia, although several flight legs were flown over surface sites at Wallops Island and other East Coast sites. A complete description of TARFOX operations is given in reference [5].

LASE profiles of water vapor mixing ratio were compared with those measured by dew point hygrometers flown on the UK C-130 and the UW C-131. Figure 1 shows an example of the water vapor mixing ratio profiles measured by LASE and the C-130 dewpoint hygrometer on July 20; these profiles, which were acquired within 30 minutes and 30 km of each other, show excellent agreement. Similar comparisons between the water vapor profiles measured by LASE and the C-131 dewpoint hygrometer showed the dewpoint hygrometer water vapor profiles to be about 13% drier than those measured by LASE. However, some of this difference may be due to an intermittent problem in the C-131 dew point hygrometer that caused the C-131 dewpoint temperatures occasionally being shifted by about 1.5 degrees C toward lower temperatures. This produced a periodic dry bias of 10-12% in the C-131 water vapor mixing ratios.

The aerosol scattering ratios measured by LASE over Wallops Island were compared with those measured by the NASA Goddard Space Flight Center (GSFC) Scanning Raman Lidar (SRL). The GSFC lidar measured aerosol profiles at 355 nm during daytime operations [6]. Figure 2 shows a comparison of the aerosol scattering ratios measured by both lidar systems on July 17. Since LASE and the GSFC lidar measure aerosol profiles at different wavelengths, the LASE aerosol scattering ratio profiles were scaled to 355 nm using the wavelength dependence of aerosol optical thickness between 340 nm and 1020 nm measured at Wallops Island by a ground based Cimel sun photometer. This wavelength dependence, which is expressed as the exponent α in the expression $\lambda^{-\alpha}$, varied between 1.0 to 1.7 during the five days of coincident LASE and GSFC lidar measurements. As shown in figure 3, the aerosol scattering ratios derived from the two lidar datasets in this manner show good agreement.

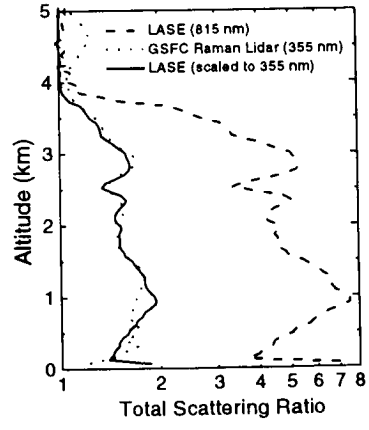


Figure 2. Total scattering ratios measured by LASE and the GSFC Raman lidar at 21:25 UT on July 17, 1996.

Aerosol extinction coefficient profiles were derived from the LASE aerosol backscattering profiles using an extinction/backscattering ratio of $S_a = 60$ sr. This value was derived from simultaneous measurements of aerosol extinction and backscattering by the SRL during TARFOX. Measurements of AOT derived from SRL data using this value of S_a and measurements of AOT by ground based sun photometers agreed to within 10-15% [6]. The good agreement between the aerosol scattering ratios measured by the two lidars, when scaled using the wavelength dependence of aerosol optical thickness, indicated that S_a was relatively constant between these two wavelengths.

Examples of both aerosol extinction coefficient and water vapor mixing ratio profiles measured by LASE

during the return flight leg to Wallops Island on July 20 are shown in figure 4. These water vapor mixing ratio and aerosol extinction coefficient profiles were integrated to derive the precipitable water vapor and aerosol optical thickness measurements shown in figure 5. Measurements of aerosol optical thickness and precipitable water vapor by ground based sun photometers at Wallops Island and Cheritan, and measurements of aerosol optical thickness by the Ames sun photometer on the UW C-131 while flying below the ER-2, are also shown. The AOT at 815 nm for the Ames sun photometer was determined by interpolating the AOT measured at 525 nm and 1021 nm. These results show that there is generally good agreement in the aerosol and water vapor measurements among these sensors and that aerosol optical thickness and precipitable water vapor were highly correlated on this day.

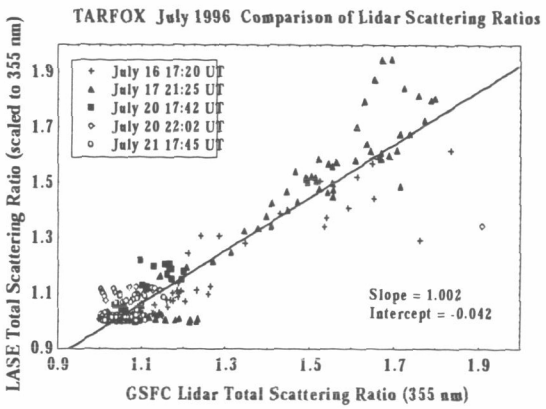


Figure 3. Comparison of total scattering ratios measured by LASE and GSFC Raman lidar during TARFOX.

Figure 6 shows a comparison of AOT measured by LASE and the ATSR-2 satellite sensor on July 25. The ATSR-2 sensor has four spectral bands in the visible and near infrared which are used to derive AOT over cloud-free regions [7]. This figure shows measurements of AOT derived from ATSR-2 radiances measured directly under the ER-2 flight track when the satellite passed over the TARFOX area at 15:52 UT. The difference in AOT measured by the two techniques in the southern portion of the flight track is thought to result from clouds interfering with the ATSR-2 measurements, since the LASE profiles showed scattered clouds in this region. ATSR-2 measurements of AOT on July 25 in another, less cloudy, region of the TARFOX area 50-100 km away from the ER-2 flight track agreed well with those measured by the Ames sun photometer on the C-131.

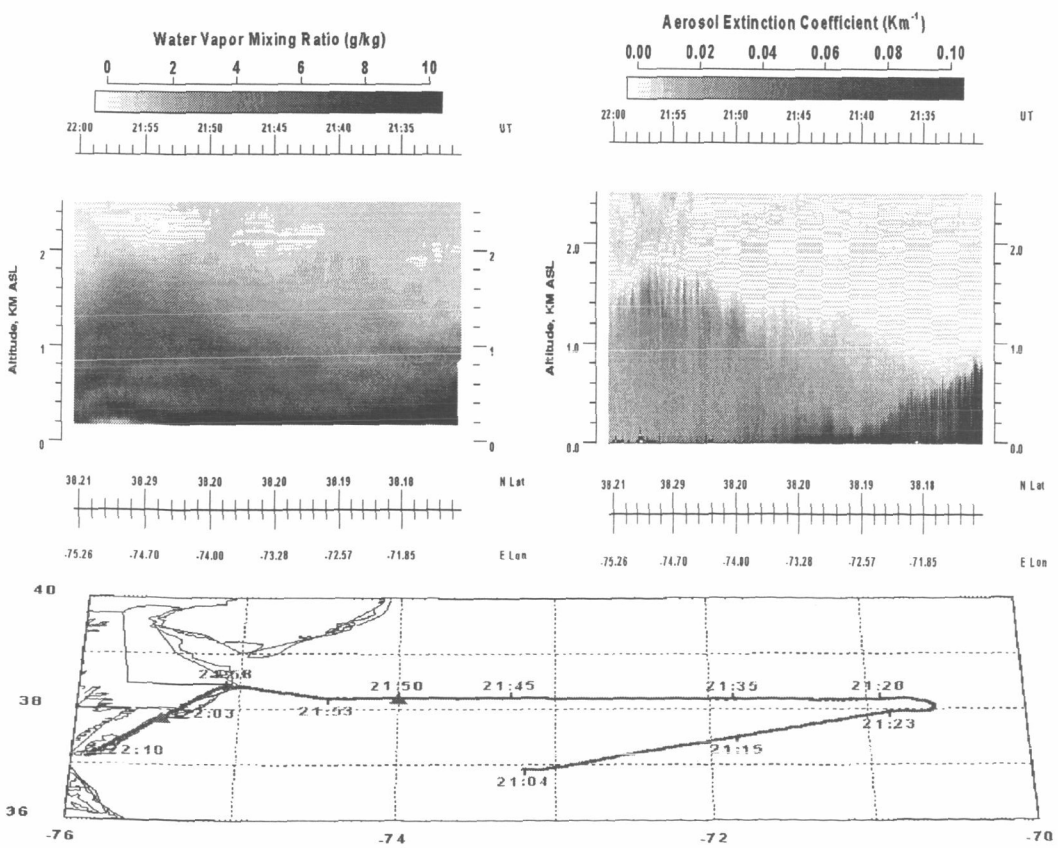


Figure 4.Water vapor mixing ratio (top left) and aerosol extinction (top right) profiles acquired by LASE during the return flight of the ER-2 to Wallops Island on July 20, 1996. The bottom panel shows the east to west flight path of the ER-2 during this time.

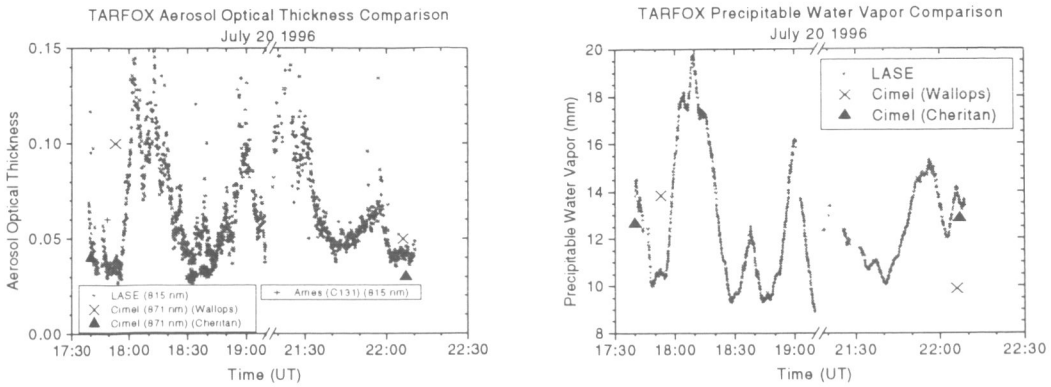


Figure 5. Aerosol optical thickness measured by LASE and sun photometers on July 20 (left), same except for precipitable water vapor (right). Note that the latter part of this figure corresponds to the period shown in figure 4.

Summary

Measurements of aerosols and water vapor acquired by LASE during the TARFOX experiment were compared with ground, airborne, and satellite based measurements. Aerosol extinction profiles were derived from the LASE aerosol backscatter profiles using an extinction/backscattering ratio of S_a = 60 sr derived from coincident Raman lidar measurements. Estimates of AOT derived from the LASE data agreed well with those measured by ground and airborne sun photometers and derived from the ATSR-2 satellite sensor. Precipitable water vapor derived from the LASE water vapor mixing ratio profiles agreed with simultaneous measurements from ground based sun photometers. The ability of LASE to simultaneously measure water vapor and aerosol profiles indicates that this lidar system will be also valuable for investigating the relationships between water vapor and aerosol optical characteristics.

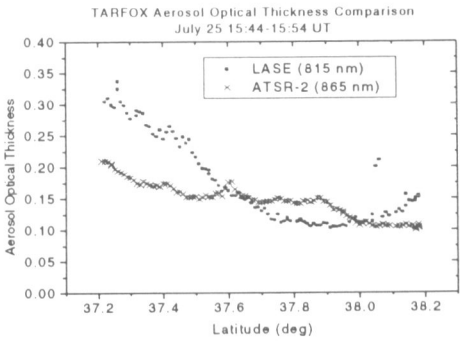


Figure 6. LASE and ATSR-2 measurements of aerosol optical thickness below the ER-2 flight track on July 25, 1996.

References

1. Russell, P.B., P.V. Hobbs, and L.L. Stowe, Aerosol properties and radiative effects in the United States east coast haze plume: An overview of the Tropospheric Aerosol Radiative Forcing Observational Experiment (TARFOX), submitted to *J. Geophys. Res.,* (1998)
2. Browell, E.V., and S. Ismail, First lidar measurements of water vapor and aerosols from a high-altitude aircraft, OSA Optical Remote Sensing of the Atmosphere Technical Digest, vol. 2, 212-214, (1995).
3. Moore, A.S., Jr., K.E. Brown, W.M. Hall, J.C. Barnes, W.C. Edwards, L.B. Petway, A.D. Little, W.S. Luck, Jr., I.W. Jones, C.W. Antill, Jr., E.V. Browell, and S. Ismail, Development of the Lidar Atmospheric Sensing Experiment (LASE), an advanced airborne DIAL instrument, Advances in Atmospheric Remote Sensing with Lidar, A. Ansmann, R. Neuber, P. Rairoux, and U. Wandinger, eds., Springer-Verlag, Berlin, 281-288, (1997).
4. Browell, E.V., S. Ismail, W.M. Hall, A.S. Moore, Jr., S.A. Kooi, V.G. Brackett, M.B. Clayton, J.D.W. Barrick, F.J. Schmidlin, N.S. Higdon, S.H Melfi, and D.N. Whiteman, LASE validation experiment, in Advances in Atmospheric Remote Sensing with Lidar, A. Ansmann, R. Neuber, P. Rairoux, and U. Wandinger, eds., Springer-Verlag, Berlin, 289-295, (1997).
5. Whiting, W., P.B. Russell, P.V. Hobbs, and L.L. Stowe, TARFOX Operations Summary, NASA Ames Research Center, Moffett Field, CA, USA, 140 pp., (1996).
6. Ferrare, R.A., G. Schwemmer, S.H. Melfi, K.D. Evans, D.N. Whiteman, Y.J. Kaufman, D. Guerra, and D. Wooten, Scanning Raman lidar measurements of aerosol backscatter and extinction profiles during TARFOX, Spring AGU Meeting, Baltimore, MD, (1997).
7. Veefkind, J.P., G. de Leeuw, P. Russell, P.V. Hobbs, and P. Durkee, Aerosol optical depth retrieval using ATSR-2 and AVHRR data during TARFOX, submitted to *J. Geophys. Res.,* (1998).

RETRIEVAL OF THE EXTINCTION COEFFICIENT AND MICROPHYSICAL PARAMETERS OF DENSE STRATOCUMULUS CLOUDS FROM BACKSCATTER LIDAR OBSERVATIONS: APPLICATION TO LEANDRE 1 MEASUREMENTS DURING EUCREX'94.

J. PELON [1], V. TROUILLET [1] AND P. H. FLAMANT [2]

[1] Service d'Aéronomie du CNRS, 4 Place Jussieu, B 104, F-75252 Paris, France
[2] Laboratoire de Météorologie Dynamique, Ecole Polytechnique, 91128 Palaiseau, France.

I. Introduction

Stratocumulus clouds are frequently observed in mid-and high latitudes to extend over large ocean areas. They are strongly reducing the solar flux to the surface, and increase earth-atmosphere albedo. Their occurrence may thus lead to a strong modification of the radiation budget. The most significant parameters used to analyze the cloud-radiation interactions are the cloud structure (broken or continuous, top and base heights), the effective radius and liquid water. Remote sensing is the only way to derive quantitative information about their occurrence and properties on scales large enough to be used as inputs for general circulation models. Passive measurements have been widely used for such a purpose. It has however been shown that the retrieval of cloud properties may be biased due to the presence of thin cirrus clouds, or when albedo difference are small between the surface and the Sc. Airborne measurements have confirmed the ability of backscatter lidar to analyze cloud structure at the meso-scale, such as cloud top altitude fluctuations in relation with entrainement. They have also been previously used in complement to passive observations to retrieve microphysical parameters for low to medium optical thickness clouds (Spinhirne et al., 1989). In the case of dense Sc, lidar retrieval of such properties may be in error due to the strong in-cloud extinction which may imply to account for a correction of the detection bandwidth. The purpose of this paper is to present a method to derive stratocumulus cloud properties in such a case. The methodology is first presented, results are discussed in the last section.

II. Methodology

The backscattered lidar signal S(z,t) can be written as the double convolution taking into account the laser pulse emission function $P_e(t)$ and the detection response D(t)

$$S(z,t) = K\left[B(z) \otimes P_e(t) + P_b(t)\right] \otimes D(t) + S_b(t) \qquad (1)$$

where K is the overall detection efficiency of the lidar system. P_b and S_b are additive optical and electical noises respectively. B(z) is the impulse response of the atmosphere, written as

$$B(z) = \frac{1}{(z - z_e)^2} \beta(z) T^2(z) \qquad (2)$$

where $\beta(z)$ is the atmospheric backscatter coefficient, and T(z) the transmission between the measurement altitude z and the emission altitude z_e. When the pulse duration is very short as compared to the signal sampling only the second convolution in Eq. (1) needs to be considered. Time and altitude (distance) are then equivalent. In the case of a clear atmosphere, or when the rate of change of B(z) is small as compared to the inverse of the time decay of the detection system

$$\frac{1}{B}\frac{dB}{dz} << \frac{2}{c}\frac{1}{D}\frac{dD}{dt} \qquad (3)$$

we obtain the classical lidar equation, which has been widely used for retrieving properties of aerosols and clouds. For dense clouds, or when Eq. (3) is not satisfied, the detected signal is more representative of the detection system impulse function D(t). The convolution needs to be calculated to retrieve atmospheric properties. We will use here a simple formalism which allows to make analytical calculations, and derive simple expressions which can generally be used with a good approximation. The detection system design leads to assume that D(t) corresponds to a first order filtering so that $D(t) = 1/t_S \exp(-t/t_S)$, where t_S is the time constant related to the detection bandwidth. We will consider the time or altitude origin as the time when the laser pulse reaches the cloud top height. Neglecting the molecular and particular extinction and scattering as compared to the droplet contribution, the lidar signal in the cloud S_c (z) as given by Eq. (1) can be written as

$$S_c(z) = K\frac{cE_0}{(z-z_e)^2}\frac{\beta_c}{(1-2\eta\alpha_c z_s)}\left[\exp(-2\eta\alpha_c z) - \exp-\frac{z}{z_s}\right] \qquad (4)$$

where Eo is the emitted laser energy. β_c and α_c are the in-cloud backscatter and extinction coefficient. The electronic time constant t_s has been translated into the equivalent height $z_s=ct_s/2$. Equation (4) has been derived using a simple model where the cloud extinction is assumed to be constant inside the cloud. The depth of the transition zone at the cloud top is considered as negligibly small. As we are aiming at a dense cloud detection, equation (4) accounts for multiple scattering contribution. We have introduced the multiple scattering factor η (see Spinhirne et al., 1989 for example) to account for the reduction in optical thickness due to multiple scattering ($\alpha_{ca} = \eta\alpha_c$). We have furthermore assumed η to be constant with height, so that the apparent backscatter to extinction ratio in the cloud $k_{ca}=\beta_c/\alpha_{ca}=k_c/\eta$. One can see that when the product $\alpha_c.z_s$ is much smaller than one, Eq. (4) corresponds to the classical lidar equation in a semi-transparent cloud. On the contrary when $\alpha_c.z_s >> 1$, only the last term remains, and as expected, the signal shape is defined by the detection system function. A maximal apparent backscatter coefficient equal to k_{ca}/z_s is reached at the signal peak. This is an interesting property in the case of warm clouds which present the highest extinction coefficients as k_c is known to be equal to 0.055 sr^{-1} (Pinnick et al., 1983). Measuring z_s in the lab (or from Eq.(4) from the logarithmic derivative of the signal after its maximum in a very dense cloud) thus allows the determination of η.

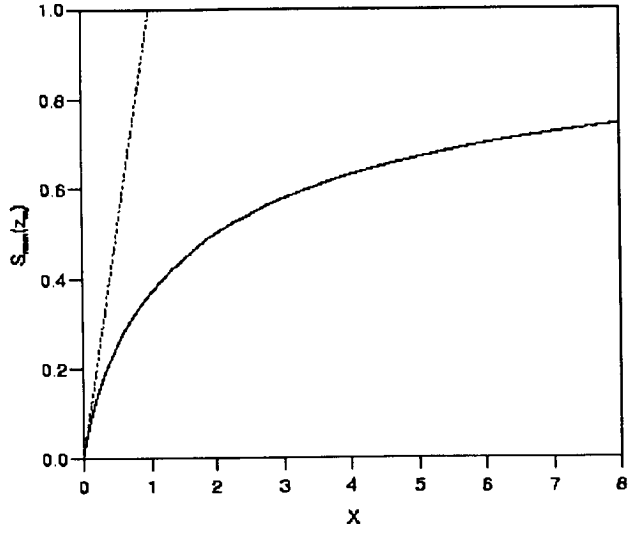


Figure 1 : Variation of the normalized cloud extinction retrieved by lidar as a function of the true normalized cloud extinction. The straight line corresponds to a high bandwith detection system.

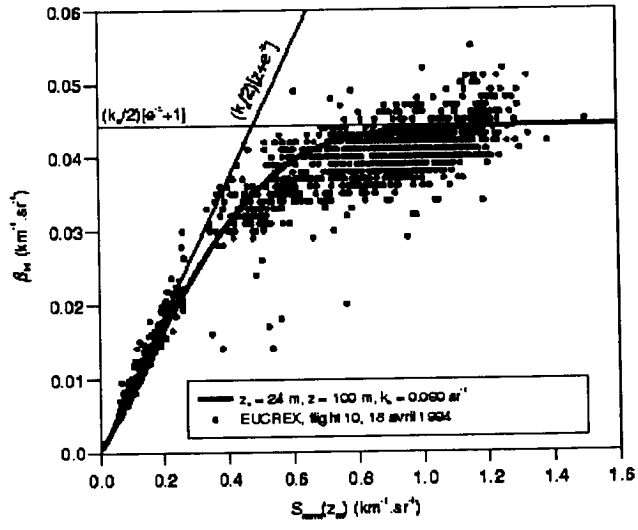


Figure 2: Integrated cloud backscatter coefficient as a function of the maximal apparent backscatter. Results are reported for a penetration of 100 m in the cloud (see text).

This procedure however requires to perform the signal analysis in terms of extinction, which is one of the unknowns. We have thus aimed at deriving a procedure using only the measured parameters as a function of the unknown α_c. To this respect we have rewritten the lidar equation with reduced parameters $\hat{z} = z/z_s$ and $X = 2\alpha_c.z_s$. After having normalized the backscattered signal to a reference backscatter value above the cloud (using lidar calibration or an inversion method), we obtain a signal directly related to the apparent backscatter coefficient

$$S(\hat{z}) = C\frac{k_{ca}}{2z_s}\frac{X}{1-X}\left[\exp- X\hat{z} - \exp-\hat{z}\right] \qquad (5)$$

where C is the normalizing signal value. C should be very close to 1, if the system parameters (K, Eo) are known, or if aerosol properties are known outside the cloud, so that the true backscatter value can be derived from the lidar equation inversion from the source emission point to the cloud.

The main parameters we have identified are the maximal signal obtained from the first derivative of S and the integrated backscatter coefficient. The maximum in-cloud signal is expressed as

$$S_m(\hat{z}_m) = C\frac{k_{ca}}{2z_s}\frac{X}{1-X}\left[X^{(\frac{X}{1-X})} - X^{(\frac{1}{1-X})}\right] \quad (6)$$

It is a increasing function of X, as shown in Figure 1, allowing to derive X when kca and zs are known. In order to determine such parameters the backscatter signal integrated from the cloud edge to a normalized altitude $\hat{z}$ in the cloud is used. It is expressed as

$$\beta_{int}(\hat{z}) = C\frac{k_{ca}}{2(1-X)}[1-X+X\exp-\hat{z}-\exp-X\hat{z}] \quad (7)$$

As seen from Equation (7), the integrated backscatter is expressed somewhat differently as the in the classical equation (see Spinhirne et al., 1989 for example) due to the introduction of the time constant of the detection. It is only equivalent for small X values. It can be also expressed as a function of the maximal normalized signal, and converges towards $k_{ca}/2$ at large X or S_m values.

III. Cloud parameter analysis

The objectives of the EUCREX'94 campaign were focused on remote sensing of both high and low cloud properties. During this campaign lidar observations were dedicated to the study of both cirrus clouds (Sauvage et al., 1997) and stratocumulus clouds (Descloitres et al., 1996). The 18 April 1994 case was selected as the most interesting for the study of stratocumulus, and was used to test the method. Figure 2 shows the integrated backscatter coefficient obtained as a function of the maximal signal during the selected flight of Eucrex, as the aircraft was flying at an altitude of about 4 km, observing stratocumulus clouds, which top height was located at about 1 km, in the nadir viewing mode. Calculations have been made for $\hat{Z}=4$, leading to a value $k_{ca} = 0.088$ and thus to $\eta = 0.61$. These values were determined from both the plateau and the slope.

Flights were performed on a leg (AM) about a hundred kilometers long, north west of Brittany above a dense Sc deck. Backscatter lidar data have shown cloud top altitude increase from 800 m at the NE (point A) to 1100 m at the SW (point M). The base altitude was also observed by lidar during a first leg below the Sc to be rather constant near 450 m. This altitude corresponds to the lifting condensation level obtained from in-situ measurements. results are reported on Figure 3. Cloud top and base height fluctuations evidence larger cell structure near point M (about 5 km). Apparent cloud extinction coefficient was deduced from maximum signals as detailed in previous section. It shows an exponential increase at the cloud base up to about 700 m, where the apparent extinction reaches 0.05 m^{-1}. The maximal value was about 0.2 m^{-1} near the cloud top.

Under the hypothesis of adiabatic increase of the liquid water content W inside the convective cells evidenced by their higher top altitude and extinction (or optical thickness on figure 4), we can write W=Az. In the shortwave domain, the effective radius r_e can be obtained from W and the cloud extinction coefficient α_c through the relationship $r_e = \frac{3}{2}\frac{W}{\rho\alpha_c}$, where ρ is the liquid water density. In the two cells we obtain 5.5 μm < re < 7.5 μm on average, assuming z corresponds to the altitude difference between the LCL altitude and the measured cloud top (about 550 m). This value is close to the value re = 6.5 μm measured in situ. The number of droplets deduced from our measurements is about N = 600 cm^{-3}. The optical thickness has then been estimated from the retrieved extinction coefficient at the cloud top assuming the liquid water content increase is adiabatic and the effective radius is constant and equal to 6.5 μm. Results are reported in Figure 4.

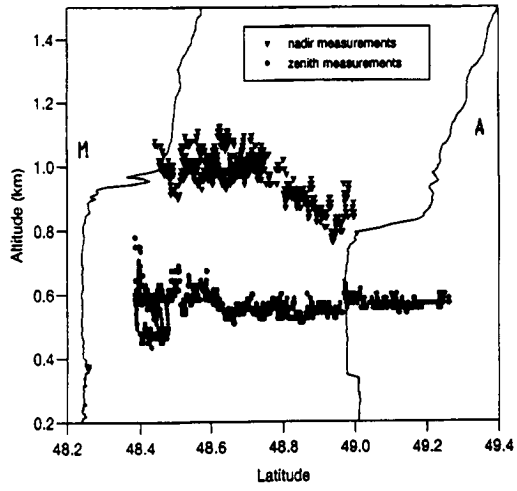


Figure 3 : Cloud top and base altitudes of the stratocumulus retrieved by the airborne backscatter lidar LEANDRE 1, as compared to potential temperature profiles measured by the ARAT during ascent and descent.

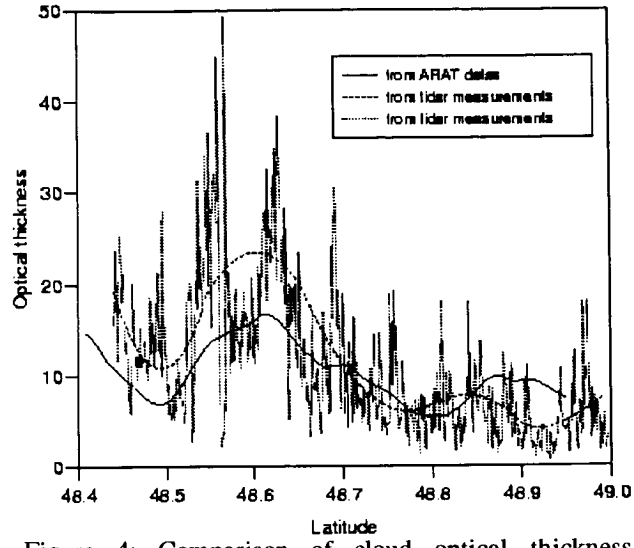


Figure 4: Comparison of cloud optical thickness estimated by lidar and by radiometry over the AM leg.

The two main convective cells near 48,6 degrees in latitude which were previously characterized by their cloud top altitude increase are here more clearly evidenced. The optical thickness in this region is larger than 30 at scales smaller than a kilometer. This optical thickness averaged over a larger scale is in rather good agreement with the one retrieved from passive measurements (upward and downward shortwave fluxes measured by the aircraft) using an analytical approximation derived from a two stream radiation transfer calculations. Although the absolute values are somewhat different in the denser part of the cloud (possibly due to errors in both methods) it is found comparable mesoscale features. Optical thickness deduced from in situ measurements is larger than 20 in the same area (Descloîtres et al., 1996).

V. Conclusion and future work

A new method has been tested to retrieve optical and microphysical cloud properties from lidar measurements in dense stratocumulus clouds (optical thickness larger than 10). Results are encouraging and the method will be used to analyze cloud parameter variability in more details.

Acknowledgements

Financial support for the flights and for the study was received from the European Communities and from the Programme Atmosphère et Océan à Moyenne Echelle of INSU-CNRS which are acknowledged.

References

Descloîtres J., H. Pawlowska, J. Pelon, J.-L. Brenguier, F. Parol, J.-C. Buriez, and P. H. Flamant, Experimental retrieval of cloud optical thickness during Eucrex : comparison of three approaches, *Preprints 12th Int. Conf. on Clouds and Precip* Zurich, août 1996, 394-397.

Pinnick R. G., S. G Jennings., P. Chyleck, C. Ham, W. T. Grandy, Backscatter and extinction in water clouds, J. Geophys. Res, 88, 6787-6796, 1983.

Spinhirne J., D., R. Boers, and W. Hart, Cloud top liquid water from lidar observations of marine stratocumulus, J. Appl. Meteor., 28, 81-90, 1989.

Sauvage L., H. Chepfer, V. Trouillet, P. H. Flamant, G. Brogniez, J. Pelon, F. Albers, Remote sensing of cirrus radiative properties during EUCREX'94. Case study of 17 April 1994. Part 1 : Observations, En révision à Monthly Weather Review, 1997.

LIDAR EVIDENCE OF DESERT DUST LAYERS IN THE NORTH ATLANTIC AND MEDITERRANEAN AND ASSESSMENT OF THEIR INFRARED RADIATIVE IMPACT

P. CHAZETTE,[1] J. PELON,[2] F. DULAC,[1] V. TROUILLET,[2] I. CARRASCO,[2] AND E. HAMONOU[1]

[1] Laboratoire des Sciences du Climat et de l'Environnement, Laboratoire mixte CEA-CNRS, F-91191 Gif-Sur-Yvette, France
[2] Service d'Aéronomie du CNRS, 4 Place Jussieu, B 104, F-75252 Paris, France

I. Introduction

Aerosols have a significant impact on the Earth direct radiative forcing as they increase atmospheric absorption and scattering (Charlson et al., 1992). Satellite observations at solar (Husar et al., 1997) and infrared (Legrand et al., 1992) wavelengths suggest that Saharan dust has one of the strongest effect on regional radiative forcing. An accurate determination of the aerosol optical properties as a function of altitude is necessary to compute the aerosol longwave forcing (Egan, 1994), particularly for African dust which is known to experience long range transport in the free troposphere over the Atlantic Ocean (Prospero and Carlson, 1972). For this purpose, ground-based lidar measurements have been obtained during several Saharan dust transport events in the Mediterranean area between January and June 1997 in the frame of the European MEDUSE program (Hamonou et al., 1997). Other observations had been made from aircraft in the frame of the SOFIA/ASTEX campaign (Weill et al., 1995; Albrecht et al., 1995) in June 1992 near the Azores in the mid Atlantic Ocean. These direct lidar observations of the vertical structure of African dust plumes are presented here. We also discuss observations and model calculations of the radiative impact of dust during SOFIA/ASTEX.

II. Observation of dust events

Aerosol vertical soundings were performed with backscatter lidar systems emitting at 532 nm at two stations during MEDUSE campaigns: Observatoire de Haute Provence (OHP France, 43.94°N 5.72°E) and University of Thessaloniki (Greece, 22.97°E, 40.52°N). Lidar vertical profiles were obtained with a filtered vertical resolution of about 300 m and a temporal average of about 10 minutes. The aerosol extinction coefficient was derived using the Klett inversion procedure (1985). The upper boundary condition has been taken from the Lowtran-6 model (Kneizys et al., 1983) at an altitude larger than 5 km. The backscatter phase function has been calculated from the background desert dust aerosol model defined by Shettle (1984) with a Mie scattering model. The calculated normalized backscatter phase function is equal to 0.035 sr^{-1}. During SOFIA/ASTEX campaign lidar (532 nm) and nephelometer (550 nm) extinction vertical profiles, and pyrgeometer upward longwave flux measurements were obtained with the French research aircraft ARAT (Avion de Recherche Atmosphérique et de Télédétection) (Chazette et al., 1997). The same normalized backscatter phase function was used, but in this case a reference value given by the nephelometer at the airplane altitude was used for the inversion.

Table 1 summarizes these observations. Dust transport occurred in two well-defined layers located at about the same altitudes, and with similar optical thicknesses. These structures correspond to layers in which dust particles are trapped and transported, as shown by trajectory analysis. All these events were identified using Meteosat visible images. Likely sources of dust identified by infrared Meteosat observations (Legrand et al., 1994) are West Sahara, South Tunisia and East Libya for OHP events, South Algeria and Southeast Libya for Thessaloniki events, and northwestern Africa for SOFIA/ASTEX event.

Table 1: lidar sounded dust transport events.

Date	8 May 1997	14-17 May 1997	2 June 1997	17 June 1992
Location	Thessaloniki	OHP	Thessaloniki	Azores
Dust layer altitude	3 and 5 km	2 and 4 km	2.5 and 4 km	1.5 and 3.5 km
Dust optical thickness (532 nm)	0.1 to 0.2	≈ 0.1	≈ 0.15	0.1 to 0.16

In Figures 1 and 2, the lidar-derived extinction coefficient profiles for both 8 May over Thessaloniki, and 15 May over OHP are plotted. Morning and afternoon profiles are shown. Two main aerosol layers are observed, located between 2 and 5 km in altitude. Profiles above 5 km are less precisely retrieved over Thessaloniki because

of a lower signal-to-noise ratio. Available meteorological soundings showed that these layers were associated with sharp relative humidity minima and southern winds.

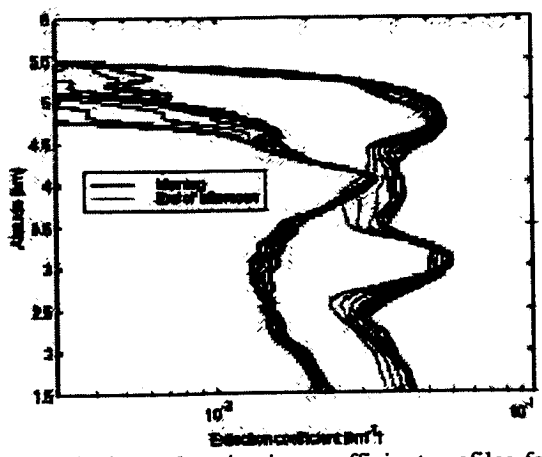


Figure 1: Aerosol extinction coefficient profiles for the May 8, 1997 at Thessaloniki. Morning profiles were obtained between 9:30 and 10:30 UT, and afternoon profiles between 16:30 and 17:30 UT.

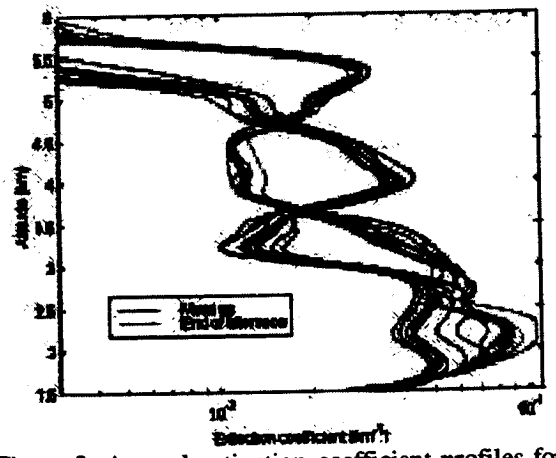


Figure 2: Aerosol extinction coefficient profiles for the May 15, 1997 at OHP. Morning profiles were obtained between 6 and 8 UT, and afternoon profiles between 17 and 19 UT.

Figure 3 shows the extinction vertical profile obtained from lidar measurements between 1.3 and 4.3 km height . A dense Stratocumulus (Sc) layer was observed below 1.3 km height (not shown). Over clouds a relatively turbid and dry air layer was present up to 5 km with two maxima, as for the events observed over the Mediterranean. The optical thickness (0.14) was also comparable.

III. Radiative impact of the dust event of SOFIA/ASTEX campaign

Desert aerosols are absorbing and have a significant radiative impact in the longwave (LW) region (Ackermann and Chung, 1992). As radiometer measurements were performed simultaneously with lidar over the Azores region, we may look at their forcing in this part of the spectrum. On 17 June 1992, the LW upward flux is stemming from the stratocumulus cloud. From coincidentshortwave flux measurements, we derived the cloud albedo and deduced that the Sc cloud optical thickness was greater than 10. Flux variability is thus expected to be weak in the longwave domain, as it can be considered as a blackbody emitting at the temperature of its top. In order to refer to a comparable Sc cloud cover observed in dust-free conditions, we used measurements taken on June 19. The upward LW flux measured at an altitude of 5 km during the flights performed on 17 and 19 June are reported in Table 2, as well as respective cloud top characteristics. The Sc top heights were close to each other, although their temperatures were slightly different. We can see significant differences in upward fluxes between the two days, which are mainly due to differences in temperature and water-vapor content.

Table 2: Sc cloud top conditions and upward infrared radiation fluxes measured for the aerosol free case of 19 June and the desert aerosol case of June 17, 1992, and modeled for the two days without desert aerosol.

	Stratocumulus layer top			Upward LW flux (W m^{-2})		
	height (km)	T (°C)	r (g/kg)	Measured	Modeled (no aerosol)	Difference
19 June (no aerosol)	1.2	11	7.5	335.1	335.9	0.8
17 June (aerosol)	1.1-1.2	10	9.5	321.0 to 323.1	324.2	1.1 to 3.2

Upward LW fluxes have also been calculated using the ECMWF radiative transfer model (Morcrette, 1989. Aircraft soundings of pressure, temperature (T), water-vapor mixing ratio (r) have been used as inputs along with standard carbon dioxide and ozone profiles. Results are also reported in Table 2. Small differences between

modeled and measured fluxes are found. The 0.8 W m^{-2} difference in clear conditions is assumed to be due to some bias in flux measurements and/or modeling and also to apply to June 17 computations. The dust aerosol forcing can be estimated from the 17 June difference between model calculations in aerosol free conditions and measurements. The decrease in exiting LW radiance varies between 0.3 and 2.4 W m^{-2}. The uncertainty, however, is relatively large (estimated to be within ± 3 W m^{-2}) due to multiple error sources mainly from measurements,

IV. Modeling of aerosol LW forcing over ocean clear sky condition

In order to compare this estimate with more refined computations, the line by line model which has been used in Chazette et al. (1998) has been modified to include dust aerosol LW radiative forcing. For this first assessment, mid-latitude summer climatological vertical profiles of temperature, water-vapor (H_2O), carbon dioxide (CO_2), methane (CH_4), ozone (O_3) and nitrous oxide (N_2O) have been considered. The mean water-vapor mixing ratio in the marine boundary layer is between 9 and 10 g kg^{-1}. The sea surface temperature of 19.5 °C measured during SOFIA/ASTEX has been used as boundary condition for the surface equivalent blackbody. The ocean emissivity has been taken equal to 1.

To determine the aerosol extinction as a function of wavelength, the refractive indices of Volz (1973) have been used in a Mie scattering model. The vertical distribution of aerosols obtained from lidar extinction coefficient at 532 nm shown in Figure 3 has been used. The result of our radiative forcing simulation is shown in Figure 4 for the aircraft altitude as well as the spectral irradiance where the main interfering gases are located. The integrated dust aerosol LW radiative forcing deduced from the spectral aerosol radiative forcing is about 0.23 Wm^{-2} and corresponds, as for the measurements, to a reduction in the outgoing flux. The main spectral regions which do not overlap with absorption lines associated with interfering gases and thus contributed to this effect are found in the two atmospheric windows between 8 and 9.5 µm, and 10 and 13 µm, as discussed by Ackermann and Chung (1992).

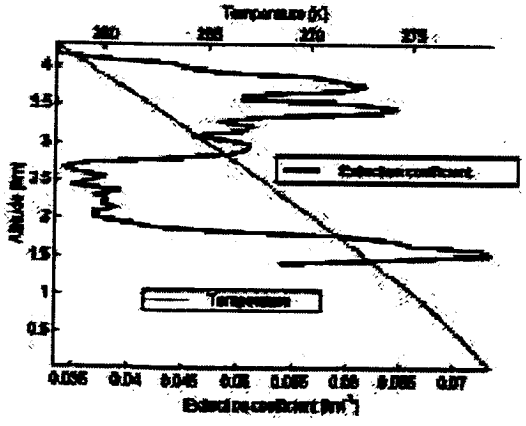


Figure 3: Airborne lidar extinction vertical profile as a function of the altitude for the June 17, 1992. The climatic temperature profile used is also given.

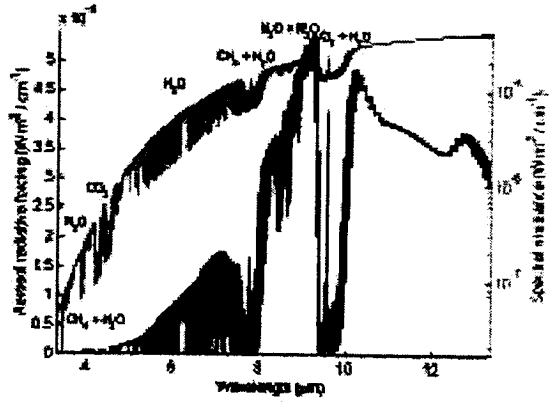


Figure 4: Calculated spectral aerosol LW radiative forcing as a function of wavelength at 4.3 km height (black curve and left scale). The spectral irradiance is also given with the main gaseous absorption bands (right scale).

V. Conclusive remarks

The vertical distribution of desert dust particles transported northwards from Africa was deduced from lidar measurements during several events in the North Atlantic and western and eastern Mediterranean. Vertical profiles are close for all observations, and correspond to an optical thickness of the order of 0.15. The LW forcing due to desert aerosol observed over North Atlantic has been estimated from measurements and calculations. Line by line modeling of the LW forcing was also performed for the observed case over the Azores. The reduction in LW flux over the Azores was estimated to be about 1±3 W m^{-2}, in agreement with the modeled dust forcing. Due to the observed similarities in dust vertical distribution and sea surface temperature, result should also apply to the

Mediterranean. Our results were obtained in cloudy conditions, with cloud top about 10 °C colder than the sea surface. It is however expected that the forcing measured over clouds would be smaller than the one observed over a warm sea surface, but larger than the one over a sea surface at 10 °C (cloud top temperature), as the LW impact of aerosol is modified by the greenhouse gases below cloud top altitude. The values obtained here are smaller than the ones previously reported (5-15 $W.m^{-2}$) over a clear seawater area at warmer temperature over the tropics (Ackermann and Chung, 1992; Egan, 1994) but these applied to optical depths larger than 0.5. Further analyses will be performed on data gathered during other campaigns.

Acknowledgments

Part of the measurements presented here are from the MEditerranean DUSt Experiment (MEDUSE) project, which was principally funded by the DG XII of the European Union Commission, through the 1994-1998 Environment and Climate Program. We would like to acknowledge D. Balis, A. Papayannis and E. Galani from the Laboratory of Atmospheric Physics, Thessaloniki, and G. Ancellet from the Service d'Aéronomie, Paris, for lidar measurements.

References

Ackermann S.A. and H. Chung (1992), Radiative effects of airborne dust on regional energy budgets at the top of the atmosphere, *J. Appl. Met.*, 31, 223-233.

Albrecht, B. A., C. S. Bretherton, D. W. Johnson, W. H. Schubert, and A. S. Frisch (1995), The Atlantic Stratocumulus Transition Experiment-ASTEX., *Bull. Am. Meteorol. Soc.*, 76, 889-904.

Charlson R.J., S.E. Schwartz, J.M. Hales, R.D. Cess, J.A. Coakley, J.E. Hansen and D.J. Hofman (1992), Climate forcing by anthropogenic aerosol, *Science*, 255, 423-430.

Chazette P., J. Pelon, C. Moulin, V. Trouillet, I. Carrasco, F. Dulac, W. Guelle, P. Bousquet, and P.H. Flamant (1997), Synergy between lidar and Meteosat measurements for a Saharan dust event during SOFIA/ASTEX, *J. Aerosol Sci.*, 28/suppl. 1, S659-S660.

Chazette P., C. Clerbaux, and G. Mégie (1998), Radiative forcing of methane estimated using nadir spectral radiances, *App. Opt.*, in press.

Egan G.E., Radiative transfer properties of the Saharan Region, R*emote Sens. Environ.*, 50, 182-193, 1994.

Hamonou E., P. Chazette, A. Papayannis, D. Balis, F. Marenco, V. Santacesaria, G. Ancellet, (1997), Ground-based measurements of Saharan dust optical properties in the frame of the European MEDUSE Project, *J. Aerosol Sci.* 28/Suppl. 1, S695-S696.

Husar R.B., J.M. Prospero and L.L. Stowe (1997), Characterization of tropospheric aerosols over the oceans with the NOAA advanced very high resolution radiometer optical thickness operational product, *J. Geophys. Res.*, 102, 16889-16909.

Klett.J. D (1985), Lidar inversion with variable backscatter/extinction ratios. *Appl. Opt.*, 24, 1638-1643.

Kneizys F.X., E.P. Shettle, W.O. Gallery, J.H. Chetwynd J.R., L.W. Abreu, J.E.A Selby, S.A. Clough and R.W. Fenn (1983), Atmospheric transmittance/radiance: computeur code LOWTRAN 6.

Legrand M., G. Cautenet and J.C Buriez (1992), Thermal impact of Saharan dust over land. Part II: Application to satellite IR remote sensing, *J. Appl. Meteor.*, 31, 181-193.

Legrand, M., C. N'doumé, and I. Jankowiak, (1994), Satellite derived climatology of the Saharan aerosol, in Passive Infrared Remote Sensing of Clouds and the Atmosphere II, edited by D.K. Lynch, *Proc. SPIE. Int. Soc. Opt. Eng.*, 2309, 127-135.

Morcrette J.J. (1989), Description of the radiation scheme in the ECMWF model, European Centre for Medium Range Weather Forecasts Technical Memo. 165.

Prospero J.M. and T.N. Carlson (1972), Vertical and a real distribution of Saharan dust over the western equatorial north Atlantic Ocean, *J. Geophys. Res.*, 77, 5255-5265.

Shettle E.P. (1984), Optical and radiative properties of a desert aerosol model, in Proc. Symp. on Radiation in the Atmosphere, G. Fiocco ed., A. Deepak Publishing Company, 74-77.

Volz F.E. (1973), Infrared optical constants of ammonium sulfate, Saharan dust, volcanic pumice, and flyash, *Appl. Opt.*, 12, 564-568.

Weill A. et al. (1995), SOFIA 1992 experiment during ASTEX, The Global Atmosphere and Ocean System, 3, 355-395.

A Lidar Network for the Establishment of an Aerosol Climatology

Jens Bösenberg [1], Matthias Alpers [2], Christine Böckmann [3], Horst Jäger [4], Volker Matthias [1], Thomas Trickl[4], Ulla Wandinger [5], and Matthias Wiegner [6]

1: Max-Planck-Institut für Meteorologie, Bundesstraße 55, D-20146 Hamburg, Germany
Phone: +49 40 41173-257, Fax: +49 40 41173-269, E-mail: boesenberg@dkrz.de
2: Institut für Atmosphärenphysik, Kühlungsborn
3: Institut für Mathematik der Universität Potsdam
4: Fraunhofer Institut für Atmosphärische Umweltforschung, Garmisch-Partenkirchen
5: Institut für Troposphärenforschung, Leipzig
6: Meteorologisches Institut der Universität München

1 Introduction Aerosol plays an important role in atmospheric physics and chemistry and therefore has a significant influence on weather and climate. It modifies the radiation field directly through scattering and has a large indirect influence on the radiation field and on the atmospheric water cycle because it is one key for cloud nucleation. The formation, aggregation, and sedimentation also has a major impact on the composition of trace gases in the atmosphere, and the presence of liquid or solid surfaces gives rise to a whole class of heterogeneous chemical processes. In view of the great importance of aerosol in atmospheric processes the availability of data describing its main statistical properties is rather poor, in particular with respect to the vertical distribution. With the establishment of a lidar network as presented below we intend to make a significant contribution to improve this situation.

2 Goals In view of the lack of a reliable and representative dataset concerning the vertical distribution of aerosol optical properties the main goal of the German lidar network is to provide these data, based on regular observations at some selected sites. These sites have been chosen to characterize both rather unpolluted air entering the continent from the northwesterly sector as well as more polluted air in the middle and southern part of Germany. Since a better understanding of causes for and effects of temporally and spatially inhomogeneous aerosol fields requires a systematic study of correlation between aerosol properties and meteorological conditions, the planned measurements will provide such data for an extended period of time to cover a large variety of conditions and to provide sufficient statistical significance. Many additional aspects of the influence of long-range transport on aerosol properties will be covered as well, such as impact of mediterranean airmasses in particular on central Europe, deposition by blocking mountain areas, influence of Föhn-situations, stratosphere-troposphere exchange, and boundary layer - free troposphere exchange, especially in the Alps.

3 Methods Lidar is an excellent tool for providing data on the vertical distribution of aerosol scattering properties. In order to come up with well defined physical parameters it was decided to use a combination of several methods. The standard backscatter lidar is still a valuable means to retrieve aerosol parameters for small optical depths, e.g. in clean areas, the upper troposphere, and the stratosphere. Since it is rather easy to operate and is at least a byproduct of any lidar measurement, this method is used to a large extent.

But it is well known that the backscatter lidar method has its limits. The retrieval does not yield a unique solution because only one set of signals is measured while two sets of parameters, backscatter and extinction, determine the signal. Additional problems are caused by the need to calibrate the signals , preferentially at the far end, and by the fact that the inversion is an ill-

posed problem in a mathematical sense. Two methods will be used to overcome these problems, Raman lidar and multiple-zenith-angle measurements. The use of Raman scattering from nitrogen or oxygen in addition to measuring the elastic backscatter has proven to be a very valuable tool for determining the extinction profile separately from the backscatter profile. This method will be employed at most of the stations of the lidar network using at least one wavelength around 350 nm.

The second method used to retrieve the extinction profile independently is to perform measurements at two different zenith angles simultaneously or at least alternating. When sufficient temporal averaging is applied it may be assumed that for a large variety of meteorological conditions the aerosol properties are the same for both directions. Then the set of two lidar equations can be solved directly to yield extinction and backscatter profiles. This method will also be used at some of the network stations.

In addition to the quantitative retrieval of optical parameters for at least one UV-wavelength as described above simultaneous measurements at 0.53 and 1.06 μm will be used to provide a phenomenological description of the aerosol type. The results of separate experiments where both lidar and in situ instruments are used to yield a more detailed description of the aerosols will serve to classify the aerosol type from the wavelength dependence of backscatter and/or extinction.

The main purpose of the measurements within the lidar network is to build up a database to derive statistical properties of aerosol vertical distribution over Germany, which may form the basis of a real aerosol climatology provided that the measurements are continued for a sufficiently long time. The limited resources and the status of lidar instrument development do not allow continuous operation, but rather a very limited sample of data can be collected. In order to make this sample unbiased it was decided to operate the lidars on fixed preselected times, presently three times a week. In case that lidar measurements are impossible during this time for reasons of precipitation or fog, this observation will be included in the dataset.

Some special situations will also be addressed: the modification of aerosol properties after passage of extended frontal systems, mainly cold fronts approaching from the northwesterly sector, and the diurnal cycle. It is expected that the modification of aerosol properties after cold-front passage will include the influence from industrialized regions, since two stations, Hamburg and Kühlungsborn, are located close to the sea shore at the entrance of rather unpolluted airmasses from the North-Atlantic region, while Leipzig and Munich are sufficiently downstream to be markedly influenced by man-made pollution.

4 Organization The following institutions participate in the operation of this network:

- MPI für Meteorologie, Hamburg
- Institut für Atmosphärenphysik, Kühlungsborn
- Institut für Troposphärenforschung, Leipzig
- Meteorologisches Institut der Universität München, München
- Fraunhofer Institut für Atmosphärische Umweltforschung, Garmisch-Partenkirchen

In addition to these measurement groups the Institut für Mathematik der Universität Potsdam provides support on solving the ill-posed retrieval problem.

At the stations mentioned above regular measurements at 3 wavelengths around 0.35, 0.53, and 1.06 μm are performed each Monday and Thursday around noon as well as each Monday after sunset. These measurements will form the basis for the climatological dataset. Additional measurements will be performed for selected periods to study the modification of airmasses during frontal passage over Germany and to characterize the diurnal cycle of aerosol properties for different meteorological conditions.

Data quality will be assured by performing special intercomparison experiments among the lidar systems as well as an intercomparison of retrieval algorithms.

5 Summary The establishment of a small lidar network for routine observation of the vertical distribution of aerosol optical properties will serve to collect a sufficiently large dataset to study causes and effects of inhomogeneous aerosol fields. In addition a number of special studies concerning transport and transformation of aerosols will be carried out with the collected data. It is hoped that this small set of stations will form the nucleus for a larger network covering at least major parts of Europe or even the globe.

Validation of POLDER/ADEOS data using a ground-based lidar network : preliminary results for semi-transparent and cirrus clouds.

H. Chepfer[1], L. Sauvage[1], P. H. Flamant[1], J. Pelon[1],
P. Goloub[2], G. Brogniez[2], J. Spinhirne[3], M. Lavorato[4], N. Sugimoto[5]

(1) Institut Pierre Simon Laplace, L.M.D, Ecole Polytechnique, 91128 Palaiseau. France
Phone: (33) 1 69 33 36 06 Fax: (33) 1 69 33 30 05 E-mail: chepferalmd.polytechnique.fr
(2) Laboratoire d'Optique Atmosphérique, Université de Lille 1. 59655 Villeneuve d'Ascq Cedex. France.
(3) NASA/GSFC, Greenbelt, MD 20771 USA.
(4) CEILAP, Villa Martelli - Argentina.
(5) NIES,Tsukuba, Japan.

1. Introduction

At mid and tropical latitudes, cirrus clouds are present in more than 50% of the time in satellites observations. Due to their large spatial and temporal coverage, and associated low temperatures, cirrus clouds have a major influence on the Earth-Ocean-Atmosphere energy balance through their effects on the incoming solar radiation and outgoing infrared radiation (Liou 1986). At present the impact of cirrus clouds on climate is well recognized but remains to be asserted more precisely (Hansen et al, 1984), for their optical and radiative properties are not very well known. In order to understand the effects of cirrus clouds on climate, their optical and radiative characteristics of these clouds need to be determined accurently at different scales in different locations i.e. latitude.
Lidars are well suited to observe cirrus clouds, they can detect very thin and semi-transparent layers, and retrieve the clouds geometrical properties i.e. altitude and multilayers, as well as radiatuve properties i.e. optical depth, backscattering phase functions of ice crystals. Moreover the linear depolarization ratio can give information on the ice crystal shape (Sassen 1991). In addition, the data collected with an airborne version of POLDER (POLarization and Directionality of Earth Reflectances) instrument have shown (Chepfer 1996) that bidirectional polarized measurements can provide with informations on cirrus cloud microphysical properties (crystal shapes, preferred orientation in space).
The spaceborne version of POLDER-1 has been flown on ADEOS-1 platform during 8 months (October 96 - June 97), and the next POLDER-2 instrument will be launched in 2000 on ADEOS-2. The POLDER-1 cloud inversion algorithms are currently under validation. For cirrus clouds, a validation based on comparisons between cloud properties retrieved from POLDER-1 data and cloud properties inferred from a ground-based lidar network is currently under consideration. We present the first results of the validation.

2. POLDER-1/ADEOS data and inversion algorithms for clouds.

POLDER-1/ADEOS measures the bidirectional reflectances in the shortwave wavelengths, and provides polarization measurements in 3 spectral band centered at 443 nm, 670 nm and 864 nm (Deschamps 1994). The first step of POLDER cloud algorithms have been defined, they are presented in Buriez et al (1997). The cloud products are: (i) cloud thermodynamical phase, (ii) cloud altitude, and (iii) cloud optical depth. The different inversion methods are presented in Table 1:

	Inversion method	Inputs
Altitude	- Rayleigh pressure (Goloub et al 1994) - Differential absorption (Parol et al 1994)	-Bidirectional polarized reflectances at 443 nm and 864 nm -Bidirectional reflectances at 765 nm (broad and narrow band channels)
Water phase (ice/liquid)	- Absence/presence of rainbow at scattering angle θ=140° (Goloub et al 1994) - Particle shape signature for scattering angles lower than 110°	-Bidirectional polarized reflectances at 864nm around scattering angle θ=140°. -Bidirectional polarized reflectances at 864nm for scattering angles lower than 110°
Optical depth	given microphysical model	Bidirectional reflectances at 443 nm, 670 nm, 864 nm.

Table 1: POLDER cloud inversion algorithms.

Two methods are used to derive the cloud altitude: (i) one so called " Rayleigh pressure method " consists in measuring the partial column of molecules above the cloud using bidirectional polarization measurements at 443 and 864 nm,(ii) the second is based on the differential absorption method in the oxygene band, and it uses bidirectional reflectances measured in a narrow and a broad band around the oxygen absorption line spectrum.
The cloud thermodynamic phase is inferred from bidirectional polarization reflectances in the 864 nm channel, for it is strongly sensitive to the particle shape (Goloub et al 1997, Chepfer et al 1997). The distinction between spherical particles corresponding to liquid water clouds and non-spherical crystals corresponding to ice clouds, can be identified by observing the bidirectional polarized reflectances in two ranges of scattering angles ($70°<\theta<120°$ or $130°<\theta<150°$).
The cloud optical depth is derived from the bidirectional reflectances. It assumes homogeneous plane-parallel cloud layer composed of water droplets with an effective radius of 10 µm and an effective variance of 0.15. Even if these assumptions are not conclusive in the case of ice clouds, for instance, the first step algorithm of POLDER cloud optical depth do apply the same microphysical model to the different types of clouds.

3. Lidars measurements

Cirrus cloud radiative and optical properties are strongly dependent on temperature, humidity, and altitude of the cloud. They are also dependent on meteorological conditions, large scale and meso-scale circulation, and so on latitude. In order to conduct a significant validation, we considere five different ground-based lidar sites spread around the world, three of them are located in the Northern hemisphere, two in the Southern hemisphere. The characteristics of the different sites and ground-based lidars are presented in Table 2:

	PALAISEAU (France)	CART_site (USA)	MANUS	BUENO AIRES	TSUKUBA (Japan)
Latitude	48.43° N	36.61° N	2.06° S	34.36° S	36.0° N
Longitude	2.15° E	97.41° W	147.44° W	57.6° W	140.1° E
Altitude		315 m	5 m		
Caracteristics	Continental Sub-urban	Continental Great plaines	Pacific Ocean	Coastal Urban	Coastal
Lidar	Medium lidar	Micro-lidar	Micro-lidar	Medium lidar	Micro-lidar
Wavelength	0.532 µm	0.523 µm	0.523 µm	0.532 µm	0.532 µm
Power	150 mJ	10 µJ	10 µJ	250 mJ	10 µJ
Frequency	20 Hz	2500 Hz	2500 Hz	10 Hz	2500 Hz
Depolarization	Yes	No	No	No	No

Table 2: Lidar network

The optical depth are corrected of multiple scattering effects using a multiple scattering factor equal to 0.50. Thermodynamical cloud phase are inferred from polarization measurements when available. In addition pressure and temperature profiles provided by radiosoundings are used to assess the cloud phase.

4. Comparisons

The validation of POLDER cloud products by lidars, bears on the following parameters: cloud altitudes, optical depth, and thermodynamical phase. The main uncertainties come from the difference in footprints between ground-based measurements and satellites measurements. The POLDER pixel resolution is 6x6 km whereas the lidar footprint is about 30m. In order to account for these differences, we proceeded in two steps:
(i) comparison of altitude, phase, and optical depth of POLDER measurements in the single pixel corresponding to the lidarsite with the value derived from lidar measurements at the time of ADEOS overpass.
(ii) comparison of the POLDER products corresponding to an area of 15x15 pixels (ie, 100x100 km), with the values derived from lidar measurements collected during a 2 hours time period about the time of POLDER overpass.
Moreover, when lidar measurements show instable atmospheric conditions i.e. variable multilayers, strong horizontal inhomogeneities, the cloud case is not considered. And when the POLDER histogram of 15x15 pixels is highly dispersed and clearly shows evidence of inhomegeities in the cloud, the cloud case has been rejected.
There are 40 cloud cases available for the validation purposes. An example of comparisons is presented in the Fig. 1 to 3. Figure 1 corresponds to the lidar backscattered profiles collected on the 10th of November 1996 at Cart site (ARM). It shows a stable cirrus layer between 10 and 13 km of altitude. On this day, POLDER/ADEOS overpassed the Cart site at 1808 UT. This cloud is optically thin, the optical depth from lidar ranges between few hundres and 0.5.

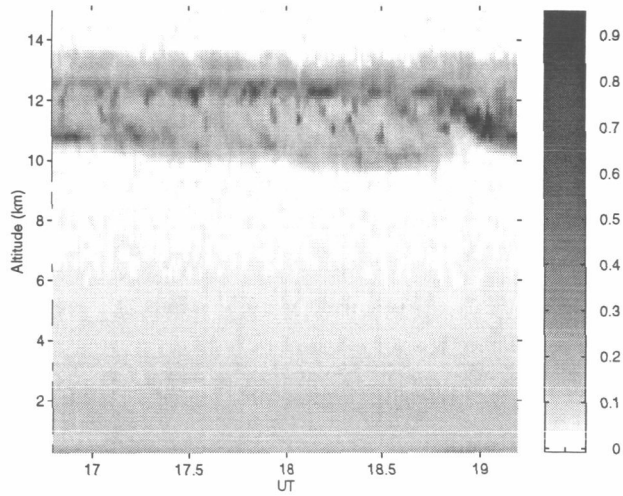


Figure 1: Backscattered lidar signal at Cart site on the 10th of November 1996

-The altitudes retrieved using the POLDER "Rayleigh method " in a 15x15 pixels area around the Cart site are presented in Fig. 2. They are range between 4 and 6 km, and the value corresponding to the single pixel located on the lidar Cart site is equal to 4.5 km. In this instance, the difference between POLDER and lidar altitudes seems be due to an intrinsic limitation of the "Rayleigh inversion method": for thin cloud, POLDER detects both molecules located below and above the cloud, and that lead to an underestimation of the cloud altitude.
- In addition the "Oxygen pressure" method provides with altitudes higher than 14 km. This conclusion is only preliminary, for this POLDER algorithm is currently under modification.
- The cloud phase is correctly identified as ice cloud by the appropriate POLDER algorithm.
- The optical depth obtained with POLDER (Fig. 3) ranges between 1 and 2, whereas the lidar gives an optical depth lower than 1. The overestimation of POLDER can be explained by an a priori microphysical model which is not suitable for ice clouds.

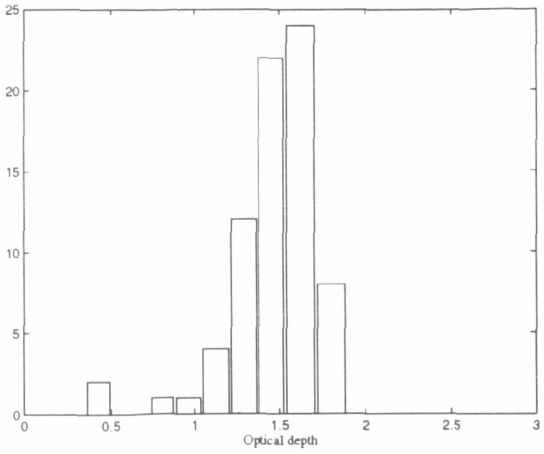


Figure 2: POLDER cloud altitude (15x15 pixels)

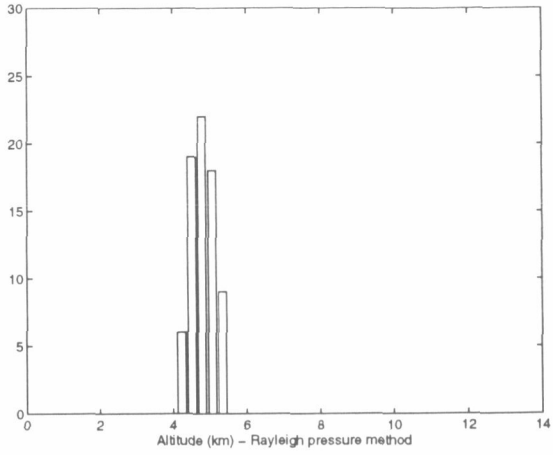


Figure 3: POLDER optical depth (15x15 pixels)

At present, 9 cloud cases have been analysed so far. They show that the optical depths retrieved from POLDER are frequently overestimated, it might be concluded that the microphysical model used to inverse ice cloud POLDER data (spheres with r_e=10 μm) should be modified in the next future. The Rayleigh pressure method to inferre the cloud altitude works satisfactorily for optical depths greater than 1.5, but it tends to underestimate the cloud altitude for lower optical depths for the reasons given above.The cloud phase test seems to work satisfactorily, even for optically thin clouds.

In one hand, these preliminary results have to be confirmed by using the complete data set of lidar measurements. In the other hand, we plan to enlarged the lidar network both in number of sites and capabilities, for the launch of POLDER-2/ADEOS-2 in 2000.

References

Buriez J. C., C. Vanbauce, F. Parol, P. Goloub, M. Herman, B. Bonnel, Y. Fouquart, P. Couvert, G. Sèze, 1997: " Cloud detection and derivation of cloud properties from POLDER " , *Int. J. Rem. Sens.*, **18**, 2785-2813.

Chepfer H., R. Valentin, V. Trouillet, G. Brogniez, P. H. Flamant, J. Pelon, and Y. Fouquart, 1996 : " Determination of a radiatively equivalent microphysic for cirrus clouds during EUCREX'94 - Sensitivity of radiative fluxes to the microphysic. " , *Proceedings of the IRS*, Fairbanks, Alaska, USA, August 19-24 1996.

Chepfer H., G. Brogniez, Y. Fouquart, 1997 : " Cirrus clouds microphysical properties deduced from POLDER observations " , *SCANOP*, Helsinki, June 9-11 1997.

Deschamps P-Y., F-M. Bréon, M. Leroy, A. Podaire, A. Brickaud, J-C. Buriez, and G. Sèze, 1994 : ' The POLDER Mission : Instrument Characteristics and Scientific Objectives ' *IEEE*, **32**, 3.

Goloub P., JL Deuzé, M. Herman, and Y. Fouquart, 1994 : ' Analysis of the POLDER Polarization Measurements Performed Over Cloud Covers ', *IEEE*, **32,** 1.

Goloub P., H. Chepfer, M. Herman, G. Brogniez, and F. Parol, 1997 : " Use of polarization for clouds study " , SPIE, San Diego, August 1997, 3121, 330-341.

Hansen, J. E., A. Lacis, D. Rind, G. Russel, P. Stone, I. Fung, R. Ruedy, and J. Lerner, 1984 : Climate sensitivity : Analysis of feedback mechanisms. Climate processes and climate sensitivity. J. E. Hansen and Takahashi, Eds. Geophys.Monogr. Ser., **29**, M. Ewing Vol.5, Amer. Geophys. Union, 130 - 163 pp.

Liou, K. N., 1986 : Review. Influence of cirrus clouds on weather and climate processes : A global perspective. *Mon. Wea. Rev.*, **114**, 1167 - 1199.

Parol F., P. Goloub, J. Descloitres, J. Pelon P. H. Flamant, 1996 : " Comparison between four independent methods of cloud pressure derivation using POLDER and lidar measurements during EUCREX'94 " , *Proceedings of the IRS*, Fairbanks, Alaska, USA, August 19-24 1996.

Sassen K., 1991 : "The polarization lidar technique for cloud research : A review and current assessment." *Bull. Amer. Meteor.Soc.*, **72**, 1848-1866.

Routine Dual-Wavelength Raman Lidar Observations at Leipzig as part of an aerosol lidar network in Germany

Ina Mattis, Ulla Wandinger, Detlef Müller, Albert Ansmann, Dietrich Althausen
Institute for Tropospheric Research
Permoserstr. 15, D-04303 Leipzig, Germany
Phone: (++49)341 235-2941, Fax: (++49)341 235-2361, E-mail: ina@tropos.de

1 Introduction

Atmospheric aerosols have an appreciable effect on Earth's radiation budget, air quality, cloud properties and precipitation. These processes influence the climate directly and indirectly and are not well understood. Thus, the German research department BMBF (Bundesministerium für Bildung, Wissenschaft, Forschung und Technologie) set up the research program AFS (Aerosol Forschungs-Schwerpunkt) in order to study physical and chemical aerosol properties, their spatial and temporal distribution and variation. As part of the research program a lidar network has been established (Bösenberg *et al.*, 1998). Table 1 shows the participating groups which are situated in northern, central, and southern Germany. Comparisons between the derived aerosol properties at these different sites allow not only a general characterization of the vertical aerosol distribution and its dependence on season, weather regime, diurnal cycle and local effects, but also investigations of the temporal and spatial development of the aerosol properties. Analytical backtrajectories yield information about the origin of the observed aerosols. The trajectories are calculated and provided by the German Weather Service for all lidar-network stations and six height levels two times a day.

2 Instrumental setup

Two lidar systems at the Institute for Tropospheric Research in Leipzig, Germany, participate in the lidar network. The main work horse is a dual-wavelength aerosol Raman lidar that was developed during the past three years. Figure 1 illustrates its general setup. A seeded Nd:YAG laser emits pulses at wavelengths of 1064, 532, and 355 nm with an overall power of 1.6 J and a repetition rate of 30 Hz. A tenfold beam expander reduces the divergence to less than 0.1 mrad. The backscattered light is collected with a 1-m Cassegrain telescope that has a variable field of view between 0.1 and 0.7 mrad. Within a 9-channel receiver (figure 2) the elastically backscattered signals at the three laser wavelengths and the Raman signals of nitrogen at 387 nm and 607 nm and of water vapor at 407 nm are separated by the use of dichroic beamsplitters and interference filters. A polarizer discriminates the parallel- and cross-polarized components of the 532-nm backscatter signal. Two pure rotational Raman signals are separated by a double-grating monochromator. All signals are detected by photomultiplier tubes and recorded using the photon-counting technique. Altogether 9 signals

Table 1: Lidar stations within the AFS lidar network (Bösenberg *et al.*, 1998). Routine aerosol observations three to four times a week (at noon and at sunset, on Monday and Thursday) will be performed at least until August 2000.

Lidar stations	Latitude	Longitude
Kühlungsborn	54° 7′ N	11° 46′ E
Hamburg	53° 34′ N	9° 58′ E
Leipzig	51° 21′ N	12° 26′ E
Munich	48° 9′ N	11° 34′ E
Garmisch-Partenkirchen	47° 30′ N	11° 6′ E

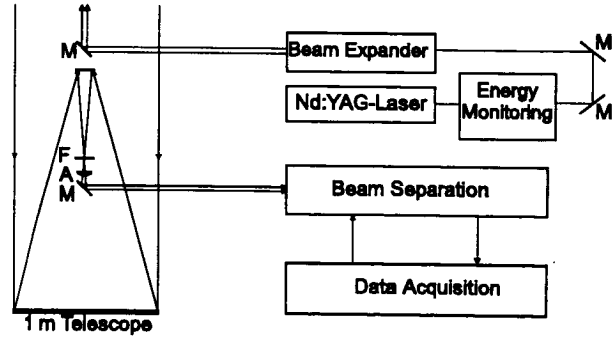


Figure 1: Schematic view of the dual-wavelength aerosol Raman lidar. M, F, and A indicate mirrors, the field stop determining the receiver field of view, and an achromatic lense, respectively.

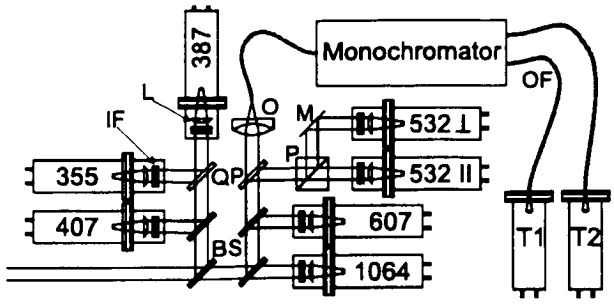


Figure 2: Schematic view of the beam separation unit of the Raman lidar. Optical elements are: beam splitters (BS), quartz plates (QP), a mirror (M), interference filters (IF), lenses (L), a polarizer (P), an objective (O) and optical fibres (OF).

are measured and the optical aerosol properties and meteorological data listed in table 2 are determined.

The double-grating monochromator was installed in co-operation with the Institute for Atmospheric Optics of the Siberian Branch of the Russian Academy of Sciences at Tomsk, Russia (Wandinger *et al.*, 1998). Goal is to determine temperature profiles by means of the pure rotational Raman technique. Four lines, with the rotational quantum numbers J of 6 and 12 at both wings of the pure rotational Raman spectrum of nitrogen at 529.0, 530.3, 533.7, and 535.0 nm, are spectrally separated and spatially combined to only two signals for $J = 6$ and $J = 12$.

Additional maesurements are carried out with the transportable multiple-wavelength lidar of the Institute for Tropospheric Research at special weather conditions. With this lidar profiles of backscatter coefficients at 355, 400, 532, 710, 800, and 1064 nm and the extinction coefficient at 607 nm (at nighttime) can be determined (Müller *et al.*, 1996, 1998). Besides lidar measurements, sun photometer observations of the aerosol optical thickness in a spectral range between 351 nm and 1064 nm at 18 channels are conducted as often as possible.

3 Measurement strategy

To obtain an extensive set of observed profiles the measurement strategy is as follows: Except under precipitation conditions profiles of aerosol properties will be determined at all lidar-network stations at least three times a week (one nighttime and two daytime measurements). Additional coordinated measurements are planned when cold fronts cross Germany or when high pressure systems determine the weather and aerosol conditions. Before a cold-front passage the air in the warm sector is usually humid and polluted. After the front passage dryer and cleaner air is typically advected into the lidar-net area from the North-Atlantic region. If the front moves from north to south, an increasing anthropogenic effect on the aerosol behind the front should be observable when data taken at Hamburg (close to the North Sea) and Kühlungsborn (close to Scandinavia and the Baltic Sea) are compared with those taken at Leipzig, about 400 km southeast of Hamburg or those measured at Munich and Garmisch-Partenkirchen, about 800 km south of Hamburg. During high-pressure situations, pollution steadily increases, especially in winter time. It is of interest whether this accumulation effect is similar at all stations and thus representative for a large area or if it is different indicating strong effects of local sources of pollution.

4 Measurement example

A measurement example is shown in figure 3. According to backtrajectories (figure 4) air was advected from Africa over south Europe to Germany.

The profiles of aerosol properties as well as the meteorological data show the boundary-layer height at 2 km. Note that in the free troposphere up to 7 km height the quite high extinction coefficients are nearly equal at both wavelengths, but the backscatter values at 355 nm are larger than these at 532 nm.

Table 2: Data provided by the Raman lidar. Data in parentheses are determined in the lower troposphere only. The 1064-nm channel will be operational from April 1998.

Aerosol Properties			
Parameter	Wavelength, nm	Day	Night
Backscatter Coefficient	1064	x	x
	532	x	x
	355	x	x
Extinction Coefficient	532	(x)	x
	355	(x)	x
Depolarization Ratio	532	x	x

Meteorological Data		
Parameter	Day	Night
Water-Vapor Mixing Ratio		x
Temperature		x
Relative Humidity		x

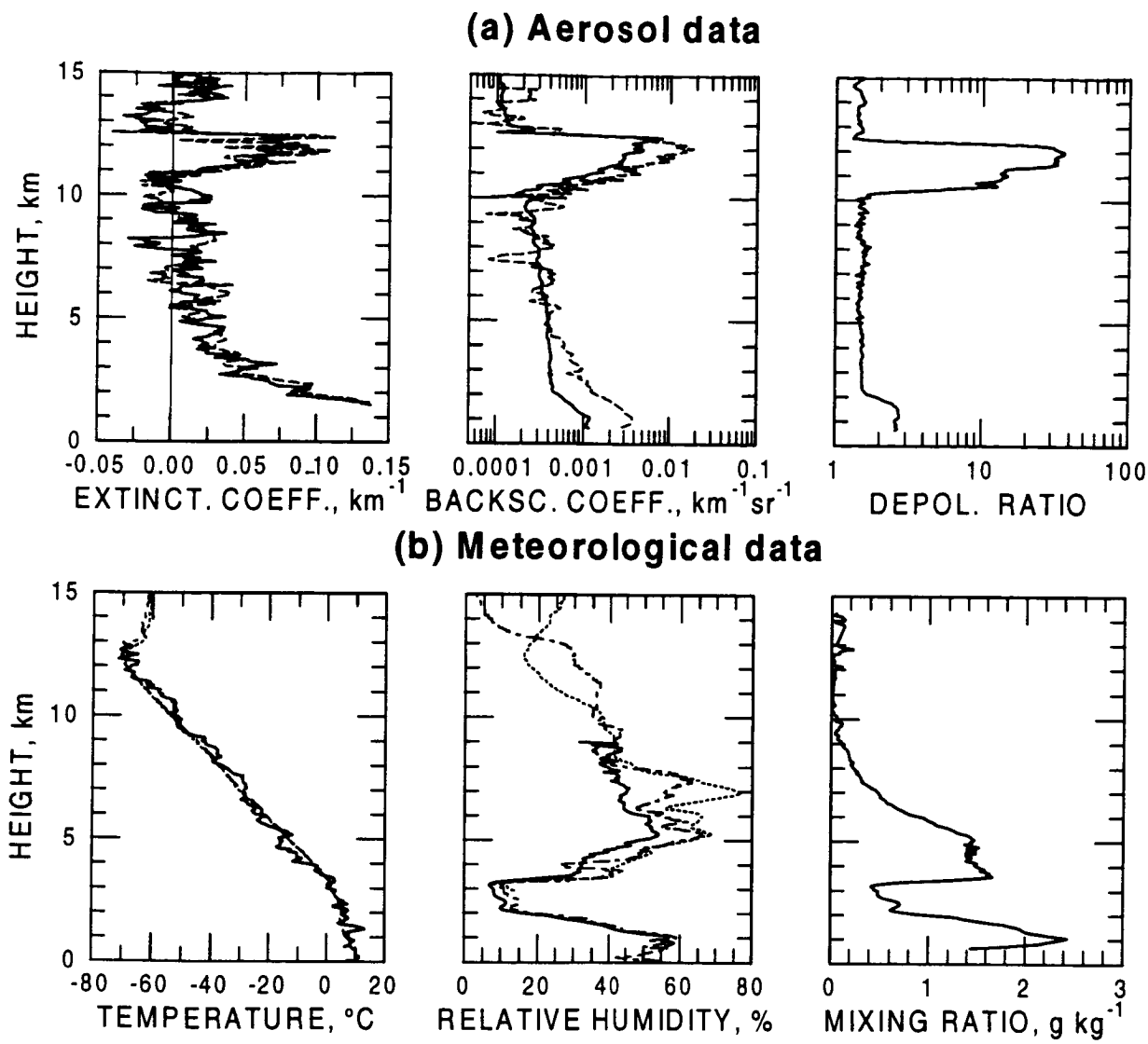


Figure 3: (a) Particle extinction and backscatter coefficients, depolarization ratio at 532 nm (solid lines) and at 355 nm (dashed lines) measured on 12 January 1998 between 18:30 and 20:30 local time. (b) Meteorological data from the Raman lidar (solid lines) and radio sounding. Dashed lines indicate the data of ascending sonde and dotted lines those of descending one. Values below 1 km are not shown, because careful correction of effects caused by the incomplete overlap between the laser beam and the receiver field of view has not been done yet.

A similar spectral behavior was observed in the cirrus cloud between 10 and 12 km height. Its depolarization ratio at 532 nm was about 30%. The profiles of water-vapor mixing ratio and relative humidity show a dry layer with relative humidity values less than 10% below the 700 hPa height level where the back-trajectories indicate an advection from the arid areas of north Africa. In the free troposphere the water vapor content again increased up to 50%. In this height range more humid air arrived from the Tropics. The temperature profile measured with lidar reaches up to the tropopause at 12 km height.

5 Outlook

Within the framework of the AFS research program a lidar network was set up in Germany in order to investigate the dependence of aerosol properties on season, weather regimes, and local effects. Since December 1997 the dual-wavelength aerosol Raman lidar of the Institute for Tropospheric Research in Leipzig takes part in the regular measurements of this network.

During the next three years a dense set of aerosol data will be produced so that local and general features of aerosol conditions over Germany can be stud-

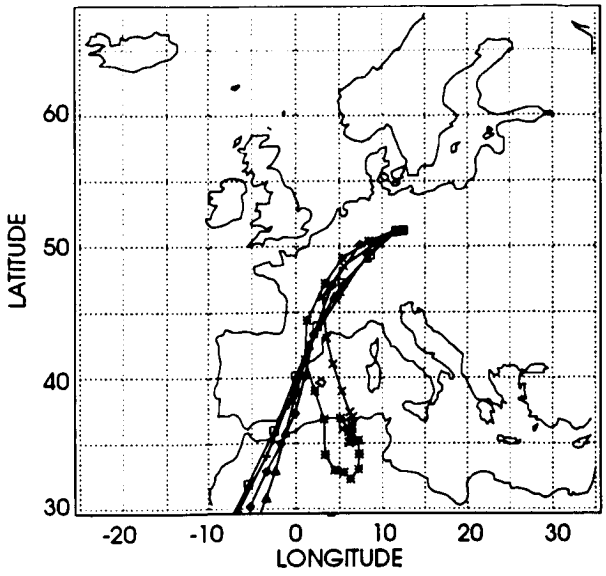


Figure 4: Analytical backtrajectories arriving at Leipzig at 20:00 local time on 12 January 1998 at different height levels of 975 hPa (×), 850 hPa (*), 700 hPa (◇), 500 hPa (△), 300 hPa (□), and 200 hPa (+). The distances between the symbols correspond to a time step of 6 hours. The trajectories are provided by the German Weather Service.

ied in detail. In combination with trajectory analyses and meteorological observations an aerosol climatology for different tropospheric height levels will be performed.

6 References

Bösenberg, J., Alpers, M., Böckmann, C., Jäger, H., Matthias, V., Wandinger, U., and Wiegner, M. (1998) A Lidar Network for the Establishment of an Aerosol Climatology. *This proceedings* .

Müller, D., Althausen, D., Wandinger, U., and Ansmann, A. (1996) Multiple-Wavelength Aerosol Lidar. In *Advances in Atmospheric Remote Sensing with Lidar* (Edited by Ansmann, A., Neuber, R., Rairoux, P., and Wandinger, U.). Springer Verlag, Berlin/Heidelberg/New York.

Müller, D., Wandinger, U., Althausen, D., Mattis, I., and Ansmann, A. (1998) Retrieval of physical particle properties from lidar observations of extinction and backscatter at multiple wavelengths. *Appl. Opt.* **37**, in press.

Wandinger, U., Mattis, I., Ansmann, A., Arshinov, Y., Bobrovnikov, S., and Serikov, I. (1998) Tropospheric Temperature Profiling Based on Detection of Stokes and Anti-Stokes Rotational Raman Lines at 532 nm. *This proceedings* .

Observations of Stratospheric Aerosols using a Global Lidar Network

Tomohiro Nagai, Michio Hirota, and Toshifumi Fujimoto
Meteorological Research Institute
1-1, Nagamine, Tsukuba, Ibaraki, 305-0052, Japan
Phone : +81-298-53-8582, FAX : +81-298-56-0644, E-mail : tnagai@mri-jma.go.jp

Osamu Uchino
Japan Meteorological Agency

Toshikazu Itabe, Kohei Mizutani, and Motoaki Yasui
Communications Research Laboratory

Takashi Shibata
Solar-Terrestrial Environmental Laboratory, Nagoya University

Ben Liley, and W. Andrew Matthews
National Institute of Water and Atmospheric Research, New Zealand

Sri Kaloka, and Saipul Hamdi
National Institute of Aeronautics and Space (LAPAN), Indonesia

Abstract To measure the stratospheric aerosol layer, five lidar stations have been established at Eureka in Canadian Arctic, Tsukuba and Naha in Japan, Bandung in Indonesia and Lauder in New Zealand and extensive lidar measurement have been done. Both the stratospheric aerosols and polar stratospheric clouds were measured. The evolution of the stratospheric aerosol layer and high temperature PSC event are discussed.

1. Introduction

Stratospheric change, such as Ozone holes, ozone depletion in the Antarctic and Arctic stratosphere, is one of the most serious concerns in global environmental studies, and studies on this change must necessarily include measurement of the stratospheric aerosol. Stratospheric aerosols, including polar stratospheric clouds (PSCs), play an important role in the climate system through the radiative processes and heterogenous chemical reactions happened on their surface. Background aerosol layer in the lower stratosphere is independent of the season, but it is markedly enhanced for a few years after large volcanic eruptions such as the 1991 Mt. Pinatubo eruption (Uchino et al., 1995). Polar stratospheric clouds (PSCs) appear in the stratosphere during polar night under low temperature conditions. PSCs are thought to play an essential role, through heterogeneous chemical reactions, in stratospheric ozone depletion processes during polar spring. The characteristics of PSCs are therefore of great interest (e.g. Solomon, 1990), and many Arctic experiments to measure them have been carried out (Turco et al., 1990; McCormick et al., 1990; Browell et al., 1990; Anderson and Toon, 1993; Pyle et al., 1994).

To clarify the global distribution and time evolution of the stratospheric aerosol layer, a global lidar network have been developed. Five lidar stations have been established at Eureka (80°N) in Canadian Arctic, Tsukuba (36°N) and Naha (26°N) in Japan, Bandung (7°S) in Indonesia and Lauder (45°S) in New Zealand and extensive lidar measurement have been carried out.

2. Lidar Network

The stations of the lidar network are shown in Figure 1. This network cover the Arctic, northern and southern mid latitude, northern sub-tropical and equatorial region. At all stations, a Nd:YAG laser is employed for the transmitter and systems installed in three overseas stations had been calibrated in Japan and the system at Naha had been calibrated at Tsukuba before shipping out. The second harmonics of 532 nm is used at all locations, the fundamental wavelength of 1,064 nm is used at Eureka, Tsukuba and Bandung, and the third harmonics of 355 nm is used at Tsukuba and

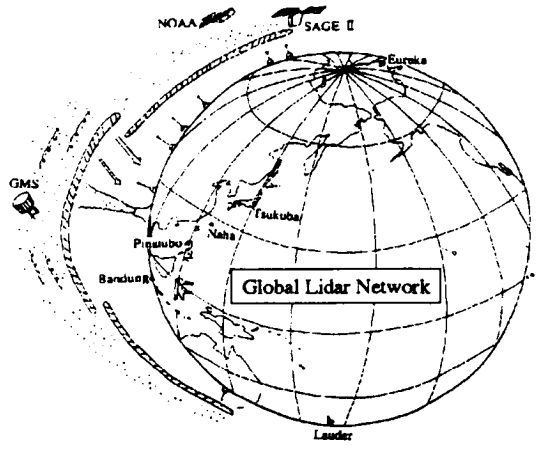


Figure 1. Location of the stations of the lidar network.

Bandung. Observations started before the Pinatubo eruption at Tsukuba, have been made since September 1991 at Naha, November 1992 at Lauder, February 1993 at Eureka, and December 1996 at Bandung. At the Arctic station Eureka, the measurement were done only in winter seasons since the winter season is the most important for PSC measurement and also it is very difficult to measure the stratospheric aerosols during daytime.

3. Stratospheric Aerosols Measurement

Time evolution of the integrated backscattering coefficient (IBC) of the five lidar stations are shown in Figure 2. The integration range of the IBCs shown in Figure 2 is just above the tropopause to around 30 to 33 km (depend on the data quality and altitude of the aerosol top) so that the IBCs are almost proportional to the total column amount of aerosols in

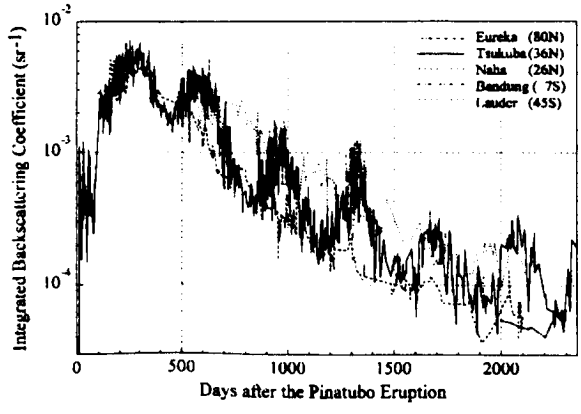


Figure 2. Time evolution of the integrated backscattering coefficient at five lidar stations by 532 nm.

entire stratosphere. The total amount of the stratospheric aerosols increased evidently about 3 months after the 1991 Mt. Pinatubo volcanic eruption, reached maximum on February 1992 and decreased thereafter. It takes about 5 years to return to calm stratosphere from the violently disturbed by the Pinatubo eruption. However, the amount of the aerosols in the calm condition of 5 years after the Pinatubo eruption is less than that condition just before the Pinatubo eruption. Clear seasonal variation can be seen in mid latitude station of Tsukuba and Lauder. On the other hand, no clear seasonal variation on sub-tropical station of Naha. This seasonal variation could be thought to be from the variation of the tropopause altitude. Also, biannual variation, just like QBO, can be seen at Tsukuba.

Figure 3 shows the time evolution of the maximum scattering ratio. Maximum scattering ratios of all stations shows very similar value except for the early phase of the Pinatubo event. This shows the density of the stratospheric aerosols originated from the Pinatubo eruption were well dispersed within one year and the density of the aerosols became uniform globally. From this figure, we can also find 5 years recovery time from the Pinatubo eruption.

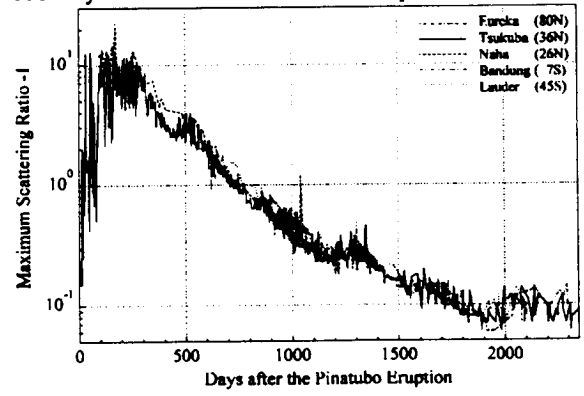


Figure 3. Time evolution of the maximum scattering ratio minus 1 (R-1) at five stations.

4. Polar Stratospheric Clouds

In this series of observations, many PSC events was measured over the Arctic station Eureka. In Eureka, five winter campaigns had been carried out since February 1993, and the PSCs have been observed in three winter campaigns of 1994/1995, 1995/1996 and 1996/1997.

The PSC, which was firstly observed at Eureka on December 12, 1994, is shown in Figure 4. Clear enhancement of the depolarization ratio can be seen

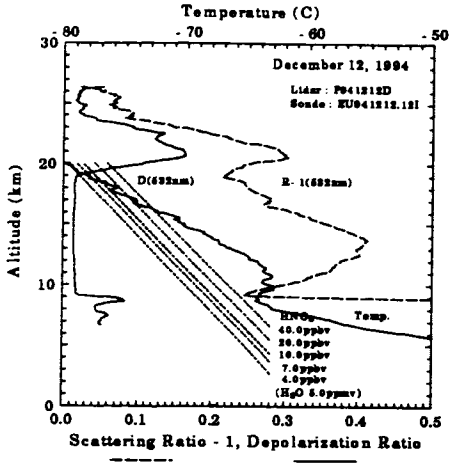


Figure 4. Scattering ratio (R) and depolarization ratio (D) profiles of the PSCs observed at 532 nm on December 12, 1994. The temperature profile (Temp.) was observed by radiosonde operated at the Eureka weather station. The radiosonde was launched at 12 UT on December 12, 1994. The frosting temperatures of the nitric acid trihydrate particles are also overlapped by the dashed line. The mixing ratio of the water vapor is assumed to be 5 ppmv [Hanson and Mauersberger, 1988].

19 to 24 km. Also enhancement of the scattering ratio can be seen at same altitude range. Since the stratospheric aerosols originated from the Mt. Pinatubo eruption still remained at that time (Fig. 1), the scattering ratio enhancement is not so clear comparing with the depolarization. From the optical property, this PSC can be classified to the type 1a PSC (Browell et al., 1990) and is thought to be composed of crystallized nitric acid trihydrate (NAT) particles since the temperature of the stratosphere was cold enough to create the NAT particles.

Figure 5 shows the PSCs observed on January 6, 1995. Clear enhancement of depolarization ratio and small enhancement on scattering ratio can be seen around 20 km. Also the layer in which the depolarization ratio was enhanced smaller extended down to about 14 km. This kind of smaller depolarization enhancement was not observed in the previous PSC event in the December 1994. During this event, the temperature at altitudes between 14.3 and 16 km was not below the frost point of NAT for 10 ppbv HNO_3 (Figure 5), while the temperature at altitudes above 16 km was below the NAT frost point. Although the temperature at altitudes from 14 to 15 km decreased 1 K from 00 UT to 12 UT on 6 January, at 12 UT, they were still 1 K higher than the frost point. The temperature at the lower extent, 14.3 to 16 km, was between 199 K and 202 K and could be higher than the NAT frost point considering the temperature error of sonde measurement is about 1 K.

Similar kind of PSCs were observed on February 26, 1997 (Figure 6). In this event, depolarization ratio enhancement can be seen down to 13 km where the temperature was about 5 degrees higher than the expected NAT frost point. If these kind of PSCs are composed of NAT particles, the nitric acid density must be much higher than the observed value. So that this suggests that there must be some kinds of PSCs other than NAT, could be sulfuric acid tetrahydrate (SAT) and/or sulfuric acid hemihexahydrate (SAH), those can exist in higher temperature

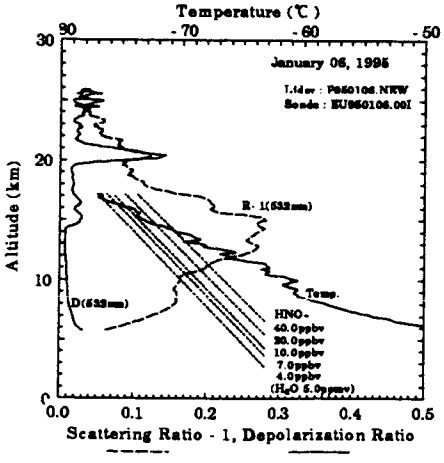


Figure 5. This is similar to Fig. 4 but for lidar data observed on January 6, 1995 and radiosondes launched at 00 UT on January 6, 1995.

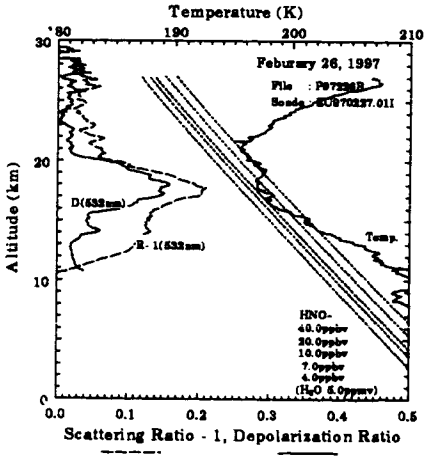


Figure 6. This is similar to Fig. 4 but for lidar data observed on February 26, 1997 and radiosondes launched at 01 UT on February 26, 1997.

than NAT from laboratory experiment and theoretical study.

5. Summary

Extensive lidar measurement for stratospheric aerosols and polar stratospheric clouds were carried out using a global lidar network. Impressive time evolution of the stratospheric aerosol layer from the Mt. Pinatubo volcanic eruption was observed. From the observation of the Arctic station, some PSCs appeared in higher temperature of expected NAT formation temperature and this suggests that PSCs which are composed of SAT and/or SAH must exist in Arctic stratosphere.

6. Acknowledgments

This work was financially supported by the Science and Technology Agency of Japan (STAJ). The authors would like to thank Dr. Hans Fast of the Atmospheric Environment Service (AES), Canada, and Prof. Allan I. Carswell of York University for their cooperation in these lidar observations at Eureka. The observatory AStrO (Arctic Stratospheric Ozone observatory) at Eureka was constructed and maintained by the AES of the Canadian Government.

References

Anderson, J. G. and Toon, O. B. (1993). Airborne Arctic stratospheric expedition II: an overview, *Geophys. Res. Lett.*, 20: 2499-2502.

Browell, E. V., Butler, C. F., Ismail, S., Robinette, P. A., Carter, A. F., Higdon, N. S., Toon, O. B., Schoeberl, M. R., and Tuck, A. F. (1990). Airborne lidar observations in the wintertime Arctic stratosphere: Polar stratospheric clouds, *Geophys. Res. Lett.*, 17:385-388.

Hanson, D. and Mauersberger, K. (1988). Laboratory studies of the nitric acid trihydrate: Implications for the south polar stratosphere, *Geophys. Res. Lett.*, 15,:855-858.

McCormick, M. P., Kent, G. S., Hunt, W. H., Osborn, M. T., Poole, L. R., and Pitts, M. C. (1990). Arctic polar stratospheric cloud observations by airborne lidar, *Geophys. Res. Lett.*, 17:381-384,.

Pyle, J. A., Harris, N. R. P., Farman, J. C., Arnold, F., Braathen, G., Cox, R. A., Faucon, P., Jones, R. L., Megie, G., O'Neill, A., Platt, U., Pommereau, J-P., Schmidt, U., and Stordal, F. (1994) An overview of the EASOE campaign, *Geophys. Res. Lett.*, 21:1191-1194.

Solomon, S. (1990). Progress towards a quantitative understanding of Antarctic ozone depletion, *Nature*, 347:347-354.

Turco. R., Plumb, A., and Condon, E. (1990). The airborne Arctic stratospheric expedition: Prologue, *Geophys. Res. Lett.*, 17:313-316.

Uchino, O., Nagai, T., Fujimoto, T., Matthews, W. A., and Orange, J. (1995). Extensive lidar observations of the Pinatubo aerosol layers at Tsukuba (36.1°N), Naha (26.2°N), Japan and Lauder (45.0°S), New Zealand, *Geophys. Res. Lett.*, 22:57-60.

Lidar Measurements of Stratospheric Aerosol at Hefei, China during 1991-1997

Huanling Hu
Anhui Institute of Optics and Fine Mechanics
Chinese Academy of Sciences
P.O.Box 1125, Hefei, Anhui 230031, China
Tel. +86-551-5591012 Fax +86-551-5591572
Email: hlhu@aiofm.hfcas.ac.cn

Abstract -- The violent eruption of Philippine volcano Pinatubo in mid June of 1991 caused a serious perturbation on the stratospheric aerosols for a long period. In the paper, we report observational results by our L625 lidar during the period of 1991-1997, including evolution of volcano Pinatubo cloud. The vertical profiles of stratospheric aerosol, their peak scattering ratio, the time variation of integrated backscattering coefficients (IBC) will be analyzed. L625 lidar measurement data of stratospheric aerosol reveal the characteristics of background period before the volcanic eruption, the evolution of the Pinatubo volcanic cloud, and the present new background level.

I. INTRODUCTION

Variation of stratospheric aerosol affects atmospheric minor constituents and climate through changes in the radiation field as well as by dynamic and chemical processes. In order to estimate the impact quantitatively, it is very important to observe stratospheric aerosol vertical distributions and their time variations. Lidar is a very powerful remote sensing technique for monitoring the stratospheric aerosols with a high vertical and temporal resolution. This paper will analyze the variations of the stratospheric aerosol profiles measured by a L625 lidar at Hefei (31.9°N, 117.17°E), China, during the period of 1991-1997.

II. L625 LIDAR AND MEASUREMENTS

L625 lidar system consists of a double frequency YAG laser (wavelength 532nm), emitting 100mJ per pulse at a repetition rate of 10Hz, a receiving telescope of diameter 625mm, and a photon counting unit. A mechanical chopper can cut the strong-intensity signal before it is amplified by the PMT (EMI9817B). The height resolution of measurement was 600m, normally, before 1996, and 120m after then. The whole system, which is controlled by a PC computer, is set on the top floor of a building with a dome ceiling at the suburb of Hefei city.

In order for one PMT to cover the whole signal range of about three orders of magnitude from 6km to 35km or higher, the measurement is divided into two steps. In the first step, an averaged profile, for about 1000 laser shots, of return signal is obtained at relatively low altitude (about 6-25km), when the chopper opens at 6km and a neutral attenuator with transmittance of 5% is inserted in front of the PMT. Thus, the photon arrival rate is small enough to eliminate the pulse-pair error. At the second step, the chopper is adjusted to cut off the return signals from the altitudes below 10km, and the attenuator is taken away, so that the return signal can be recorded from higher altitudes (10-35km). Whole measurement takes about 30 minutes. A 'grand composite' profile spanning the altitude region of interest between 6km and 35km can be formed by matching the above two profiles. The lidar back-scattering ratio, R(z), is defined as

$$R(z) = [B_a(z) + B_m(z)] / B_m(z) = 1 + B_a(z) / B_m(z) \qquad (1)$$

where $B_a(z)$, $B_m(z)$ are aerosol and molecular back scattering functions, respectively. The $B_m(z)$ can be calculated from radiosonde data or Elterman model. The backscattering ratio R(z) is calculated by evaluating

$$R(z) = k\, N_s(z)\, Z^2 / B_m(z) / Q^2(z) \qquad (2)$$

where $N_s(z)$ is photon number of return signal, $Q^2(z)$ is the two-way atmospheric transmittance, and k is a system constant determined by normalizing the right-hand side of Eq. (2) to an expected minimum value (R_{min}=1.01) of R over a specified altitude range (28-32km). In calculation of the transmittance $Q^2(z)$, molecular extinction is from radiosonde or model, and aerosol extinction is calculated directly from the aerosol backscattering function by using

extinction-backscattering ratio values[1] of 22, 40, 43 during the period of Pinatubo volcanic cloud (June of 1991 - June of 1994), and 34, 52, 58 during the period with normal situation, over the height ranges of 15-20, 20-25, and 25-30 km, respectively. The Eq.(2) is solved by using updated value of aerosol extinction for iterations.

III. VARIATION OF STRATOSPHERIC AEROSOLS DURING 1991-1997

The violent eruption of Philippine volcano Pinatubo in mid June of 1991 caused a serious perturbation on the stratospheric aerosols for a long period. Our L625 lidar was used at Hefei for measurement of nearly 400 backscatter profiles of stratospheric aerosol during the period of 1991-1997, including evolution of volcano Pinatubo. The integrated backscattering coefficient (IBC) represents the total loading of aerosols. Fig.1 and Fig.2 show the variations of monthly averaged and half-yearly averaged IBC(16-27km), respectively, during the period of 1991-1997. The seven years from 1991 to 1997 may be divided into three periods: (i) the background period from January to mid-June, 1991 before the eruption, (ii) the volcanic cloud evolution period from June of 1991 to mid-1994, and (iii) the present new background period since mid 1994. The averaged values of IBC are 2.02×10^{-4} sr^{-1} and 3.12×10^{-4} sr^{-1} for the pre-background period from January to May of 1991, and present background

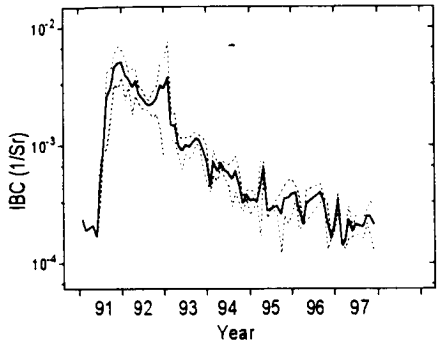


Fig.1 Variation of monthly averaged IBC In the range of 16-27km

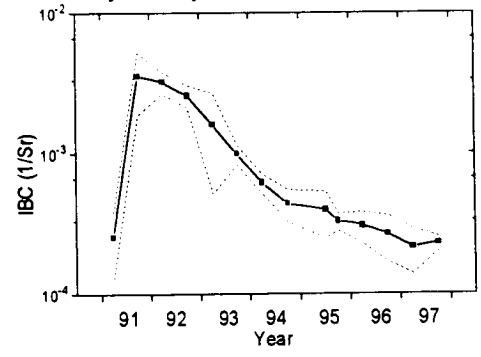


Fig. 2 Variation of half-yearly averaged IBC in the range of 16-27km

period from July of 1994 to present, respectively. During the effective period of Pinatubo volcano, the observed maximum value of IBC is 9.24×10^{-3} sr^{-1} on November 25, 1991. The maximum value of monthly averaged IBC is 5.10×10^{-3} sr^{-1} for December of 1991. The e-folding decay time of IBC was estimated to be approximately 15 months. Fig. 2 shows the variation of half-yearly averaged IBC from 1991 to 1997. The maximum value emerged at the second half of 1991, and it decreased monotonously as time goes on, which reveals the evolution of Pinatubo volcanic cloud.

Fig. 3 shows some typical profiles of stratospheric aerosols. A profile taken on May 15, 1991 represents the background prior to the Pinatubo eruption, whose peak scattering ratio, R_{max} is 1.21 only at 18.3 km altitude. The first increase of the aerosols from Pinatubo eruption was observed at 15.9 km with R_{max} of 4.54 at Hefei on June 27, 1991, just 12 days later after the eruption. On July 19, about a month after the eruption, a strong scattering layer

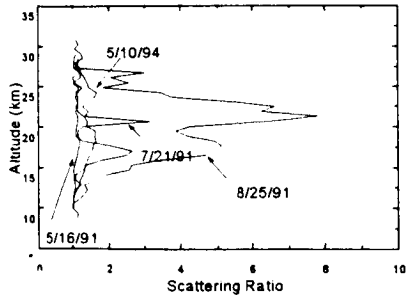


Fig.3 Back scattering ratio profiles

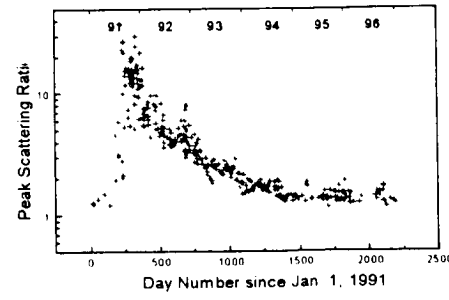


Fig.4 Maximum back scattering ratio

Was observed around 21 km. These results are similar with the data observed by MRI lidar system[2] at Tsukuba, Japan. On August 8, the value of R_{max} increased up to 37.62 at 22.5 km. From August 1991, the upper layer grew

day by day over Hefei and merged into a broad layer together with the lower layer. Until the end of August of 1991, a double-layered structure could be observed, and since early September same year it was replaced by a single layer with a peak near 22 km. A profile taken on October 3, 1996 represents the nature in new background period, whose value of R_{max} is 1.27 at 17.6 km. Fig. 4 shows the evolution of the maximum scattering ratio over Hefei. The values of R_{max} initially showed large fluctuation, reflecting inhomogeneity of the cloud distribution. It was confirmed by SAGE II measurements[3] from June to August of 1991 that the major part of the cloud was confined to an equatorial band 20°S to 30°N. Hefei is just located on the north boundary of the band. The large fluctuation was probably related to the forward and backward movement of the cloud around the equator. After August of 1991, the cloud was transported towards the north, the fluctuation became smaller and the peak scattering ratio generally varied between 10 and 20. It was about 10 in the early 1992, then decreased to about 5 in summer of 1992. The altitude of the peak scattering ratio over Hefei was mostly about 22 km.

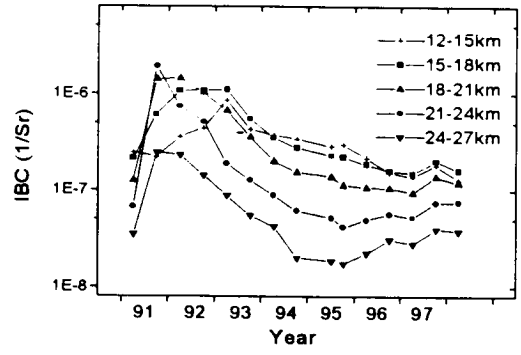


Fig.5 Variation of half-yearly averaged IBC In five sub-layers from 12 to 27km

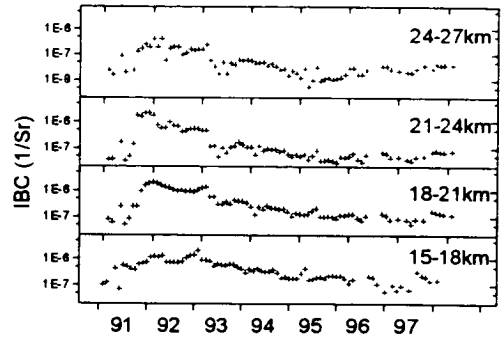


Fig.6 Variation of monthly averaged IBC in four sub-layers from 15 to 27km

Fig.5 and Fig.6 show the time variations of both the half-yearly averaged and the monthly averaged IBC in 5 sub-layers from 12 to 27km. The thickness is 3km for the all 5 sub-layers. It can be seen from Fig.5 for the pre-background and present new background periods: (a) the IBC values are nearly same with each other for the both sub-layers of 12-15km and 15-18km; (b) the sub-layer IBC decreases gradually with altitude for the others. The revolution of the volcanic cloud can be seen from Figures 5 and 6 during the volcanic period from mid-1991 to mid-1994. The maximum loading emerged before the end of 1991 for the three sub-layers of 18-21, 21-24, and 24-27km, in the spring of 1992 for the sub-layer of 15-18km, and in January of 1993 for the sub-layer of 12-15km. The loading of the volcanic cloud decreased gradually for every sub-layer since the beginning of 1993.

REFERENCES

[1] H. Jager and D. Hofmann, "Midlatitude lidar backscatter to mass, area, and extinction conversion model on in situ aerosol measurements from 1980 to 1987" , App. Opt., Vol.30, No.1, pp127-138, January 1991.

[2] O. Uchino "Lidar observations of the Pinatubo aerosol layers" , Review of Laser Engineering, Vol. 23, No.2, pp161-165, February 1995.

[3] M. P. McCormick and R. E. Veiga, "SAGE II measurements of early Pinatubo aerosols" , Geophys. Res. Lett., Vol.19, No.2, pp155-158, January 1992.

Comparison of lidar and radar cloud measurements at Geesthacht: an example for active-instrument synergy in studies of atmospheric processes

Claus Weitkamp, Olaf Danne, Holger Flint, Wilhelm Lahmann, Markus Quante, and Felix A.Theopold
GKSS-Forschungszentrum Geesthacht GmbH, D-21494 Geesthacht, Germany
Phone: +49 4152 87 1854, Fax: +49 4152 87 1888, E-mail: claus.weitkamp@gkss.de

1 Introduction

When in the early days of lidar clouds were one of the first targets of the new technique, few of the measurements that were to be carried out later on various types of clouds could be imagined. Instruments of increased complexity such as differential-absorption lidar, multiple-wavelength elastic-backscatter lidar, Raman lidar, and Raman DIAL helped solve some of the problems that could not be investigated with elastic-backscatter lidar alone. Progress, however, came slowly, and up to our days clouds continue to bear mysteries in geometric, radiometric, chemical and dynamical behavior. For thick clouds lidars can, in particular, only measure properties in those parts of the clouds that are close to the surface, and even if looked at with lidars from below and from above, processes that occur inside thick clouds evade the investigation with lidars.

The range of wavelengths used for lidars spans little more than one and a half orders of magnitude, much less than the range of droplet and particle diameters in clouds. To significantly increase this range towards longer wavelengths necessarily leads to the use of radars. In the present contribution an attempt is made to show that the combination of the two types of systems yields more information than the mere addition of data from the individual devices.

2 Lidar instruments

At GKSS four lidars can actually be utilized for cloud sensing. ARGOS is a classical differential-absorption lidar (Goers, 1995) with two dye lasers emitting between 280 and 450 nm. Designed and used predominantly for gas concentration measurements, ARGOS can also be operated in a mode in which the fundamental or frequency-doubled Nd:YAG-laser radiation is directly transmitted into the atmosphere; this mode lends itself particularly well for cloud measurements up to the tropopause.

ATLAS was built for rotational-Raman temperature measurements and rotation-vibration Raman moisture profiling at a primary wavelength of 277 nm (Zeyn et al., 1996). For cloud measurements the hydrogen Raman-shift cell can be bypassed, and 248-nm radiation is transmitted. Because of this short wavelength system range is limited to little more than 2 km.

BELINDA, like ARGOS a differential-absorption lidar, relies on measurements near the center of an absorption line for the signal wavelength and, unlike conventional DAS lidars, on absorption measurements in the wings of the same line as a reference (Theopold et al., 1996). The system presently in operation at GKSS is equipped with a $Ti:Al_2O_3$ laser that emits in the 720-780 nm wavelength region. Clouds can be measured at least up to the tropopause.

Best suited for nighttime cloud measurements is the Combined Raman Lidar, a 308/355/532-nm multiple-primary-wavelength system (Reichardt et al., 1996). Designed to also measure ozone, moisture, and temperature, it not only provides geometric cloud parameters, but radiative (backscatter coefficient, extinction coefficient, lidar ratio) and some microphysical properties of clouds as well; part of its performance relies on the additional use of wavelengths from inelastic (Raman) scattering from nitrogen at 332, 387 and 608 nm. Range is up to 100 km, so not only low, medium and high-altitude tropospheric clouds can be measured, but stratospheric aerosol from volcano emissions, polar stratospheric clouds and even noctilucent clouds around 90 km height have been observed and analyzed. Subvisible clouds of solid material are particularly well seen in the cross-polarized elastic return channel at 355 nm.

Although most measurements of clouds and in clouds have until now been made with the Raman lidar, only the BELINDA lidar system has been used for the simultaneous lidar-radar measurements reported here.

3 The 95-GHz radar

MIRACLE, a *MIllimeter-wave RAdar for Cloud Layer Explorations*, works in the W band at 95 GHz (Quante et al., 1998). With its polarization, Doppler analysis and azimuth-elevation scanning capabilities, MIRACLE was specially designed for cloud studies. The first three moments of the Doppler spectrum (total backscattered power, mean velocity and velocity variance) are derived from the return signals either by the pulse-pair algorithm or by a 64-point fast-Fourier-transform full spectrum analysis. The most important polarimetric quantities derived from the data are differential reflectivity (which in first approximation vanishes in zenith measurements), linear depolarization ratio, and the copolarized correlation coefficient. Beam divergence is 3 mrad, depth resolution is 7.5 to 75 m, range is 15 km, and sensitivity varies from -40 dBZ at 1 km and -30 dBZ at 10 km height.

4 Lidar-radar comparisons

In some instances the comparison measurements made at Geesthacht with the radar and one of the lidars agree quite well, sometimes there are considerable differences.

For the sake of conciseness only two examples are shown here for which the lidar and radar results differ markedly. On 29 September 1997 12:36 GMT a cirrostratus of 4.5 km geometric thickness that had reached a thickness of 6 km thirty minutes later was observed with the radar (Fig. 1a). Because of the high optical density of the cloud, the lidar senses only the lowest 1 to 2 km of the cloud (Fig. 1b). Its dynamics, however, with condensed matter disappearing at the bottom and new material forming at the top, leading to a downward motion inside the cloud, is clearly visible with both systems. No rain is observed at ground level. Yet the apparent cloud bottom as obtained from the radar is lower than that from the lidar (Fig. 2). This is interpreted as particles that are large enough to backscatter the radar beam, but provide relatively little optical backscattering. This interpretation is supported by the analysis of the velocity distribution of the lidar-invisible part of the cloud from the radar. It yields a downward-directed speed of the scatterers of up to 1.5 m/s, typical for crystals of about 1 mm diameter as are known to occur in fall streaks (Fig. 3).

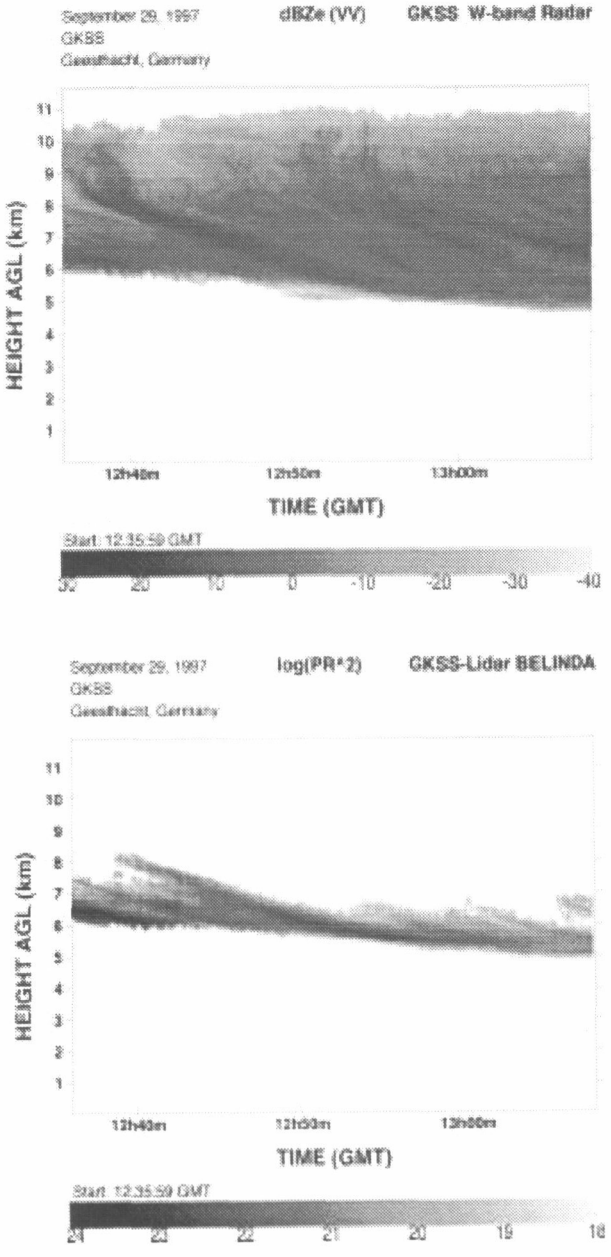


Figure 1. Time-height profile of a cirrostratus taken with the GKSS 94-GHz cloud radar (top) and the 720-nm lidar system BELINDA (bottom). Time and altitude resolution of the two systems have been matched at 2 s and 75 m, respectively.

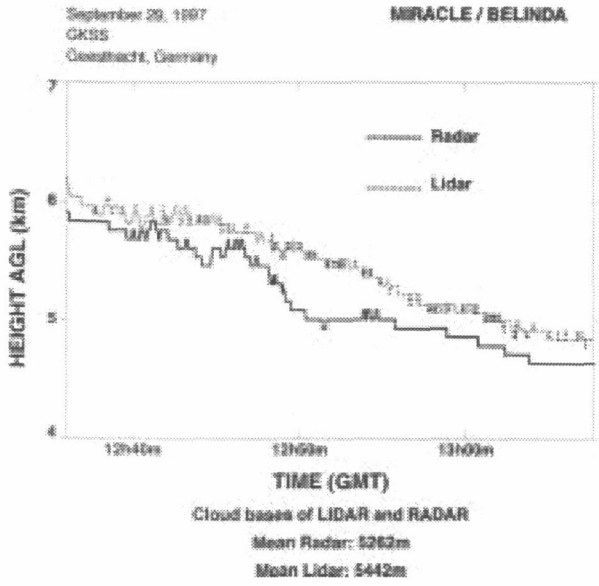


Figure 2. Lower boundary of the cirrostratus of Fig. 1 as determined from the lidar (dashed) and radar data (solid line).

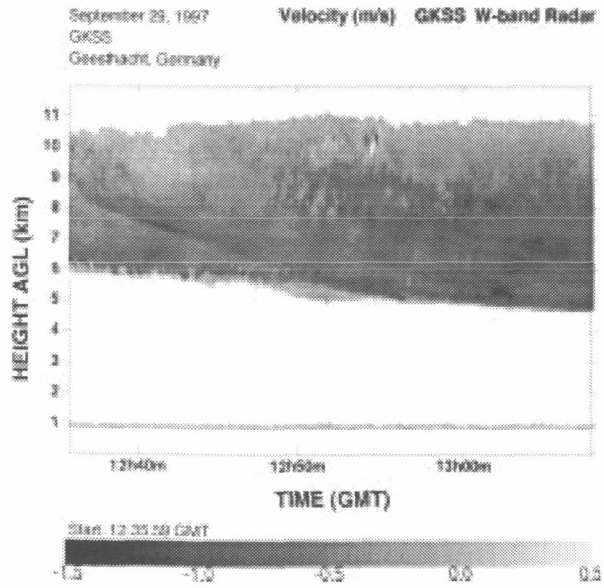


Figure 3. Downward speed in cirrostratus of Fig. 1

Another example is a cirrus observed on 4 November 1997 between 15:57 and 16:27 GMT. Between one and four layers, extending from about 7 to 11 km altitude, are seen with the lidar (Fig. 4). No signal is obtained from the radar. This is a clear indication that not just the number density but also the size of the ice crystals is too small to scatter the radar beam to a significant extent.

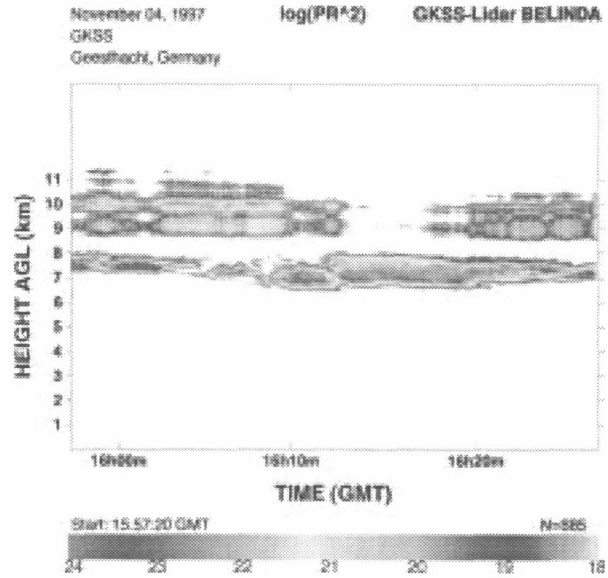


Figure 4. Time-height distribution of the backscatter signal of a cirrus measured with the BELINDA lidar. The cirrus is too thin to be visible in the radar signal.

5 Conclusions

In summary it can be stated that, although the radar and lidar data often coincide, cloud base heights determined with the lidar and with the radar sometimes do not agree. This is due to the microphysical state and resulting backscattering conditions for radiation that differs in wavelength by 3 to 4 orders of magnitude. The internal structure of the lower part of the cloud and its dynamic behavior as determined with the two systems usually agree quite well. For thick clouds the cloud top cannot be located with the lidar because of the much stronger attenuation of the laser light as compared to the 3-mm-wave radiation.

Whereas the radar is better suited for the determination of the total vertical extent of a thick cloud structure, the lidars are more sensitive to thin layers of clouds and to small variations in optical depth at and near the cloud lower boundary, in agreement with similar conclusions obtained from recent collocated lidar-radar measurements elsewhere (van Lammeren et al., 1998).

If both a radar and a lidar are available, then from the combination of the results information can be obtained that cannot be extracted from either of the two measurements alone. How to fully exploit this possibility is only now being investigated.

References

Goers, U.B. (1995). Laser remote sensing of sulfur dioxide and ozone with the mobile differential absorption lidar ARGOS. Optical Engineering 34(11):3097-3102.

van Lammeren, A., Russchenberg, H., Apituley, A., ten Brink, H., and Feijt, A. (1998). CLARA: a data set to study sensor synergy. In: M. Quante, J.P.V.Poiares Baptista, and E. Raschke, eds.: Proceedings of the Workshop on Synergy of Active Instruments in the Earth Radiation Mission. Report ESA EWP-1968 / GKSS 98/E/10:157-160.

Quante, M., Danne, O., Lemke, H., Milferstädt, D., and Raschke, E. (1998). The GKSS 95-GHz cloud radar: system description and potential contributions in support of the Earth Radiation Mission. In: M. Quante, J.P.V. Poiares Baptista, and E. Raschke, eds.: Proceedings of the Workshop on Synergy of Active Instruments in the Earth Radiation Mission. Report ESA EWP-1968 / GKSS 98/E/10:75-80.

Reichardt, J., Wandinger, U., Serwazi M., and Weitkamp, C. (1996): Combined Raman Lidar for Aerosol, Ozone, and Moisture Measurements. Optical Engineering 35(5): 1457-1465.

Theopold, F.A., Behrendt, A., Flint, H., and Weitkamp, C. (1996). First Results of the BELINDA Approach. In: A. Ansmann, R. Neuber, P. Rairoux, U. Wandinger, eds.: Advances in Atmospheric Remote Sensing with Lidar. Selected Papers of the International Laser Radar Conference (18ILRC), Berlin, 22-26 July 1996. Springer, Berlin Heidelberg New York: 325-328.

Zeyn, J., Lahmann, W., and Weitkamp, C. (1996). Remote daytime measurements of tropospheric temperature profiles with a rotational Raman lidar. Optics Letters 21(16):1301-1303.

Midlatitude Cirrus Clouds: A Climatology from the 10-Year Polarization Lidar Observation Program at FARS

Kenneth Sassen, James R. Campbell*, and Jennifer M. Barnett
Department of Meteorology, University of Utah

Corresponding Author: K. Sassen, 819 Browning, University if Utah, Salt Lake City. UT: 801-585-9492: 801-585-3681: ksassen @atmos.met.utah.edu

*Current Affiliation: Science Systems and Applications Inc, Code 912 NASA/GSFC, Greenbelt, MD 20771

Abstract

Ruby (0.694 μm) lidar systems have long been relied on to conduct long-term studies of the stratospheric aerosol, for example. At the University of Utah Facility for Atmospheric Remote Sensing (FARS), a ruby lidar high cloud observation program designed for both basic research and to support the Project FIRE Extended Time Observations satellite validation effort, has been underway since December 1986. From this ~2,500-hour dataset the climatological properties of the cirrus clouds prevailent over the eastern Great Basin of the western US are examined. The FARS cirrus cloud climatological dataset described here is comprised of 1,389 hourly polarization lidar zenith measurements collected within ±3-h of the 0000 UTC local National Weather Service radiosonde launches to provide accurate cloud temperature, pressure, and wind data, along with various supporting radiometric and some radar data. In particular, a narrow-beam midinfrared (9.5-11.5 μm) PRT radiometer has been coalinged with the lidar to provide important supporting information using the LIRAD technique. The 10-min average data periods used in this study correspond to hourly GOES imagery.

In characterizing the monthly means and variability of cirrus cloud macrophysical properties, cloud generation is shown to be controlled by synoptic scale upper air circulations mainly related to seasonally persistent Intermountain Region ridge/trough systems in the upper troposphere. Cirrus cloud top heights tend to follow the seasonal variations in the height of the tropopause, except during the summer season due to the relatively weak summer monsoonal convective activity in this semiarid locale, which typically does not generate thunderstorms strong enough to reach the elevated summer topopause. Although a considerable degree of variabilty exits, 10-y average values for cirrus cloud base/top heights, pressures, temperatures, and wind speeds and directions are, respectively, 8.79 / 11.2 km, 336.3 / 240.2 mb, -34.4 / -53.9°C, 16.4 / 20.2 m/s, and 276.3 / 275.7°. The overall average cirrus cloud physical thickness is 1.81 km.

Estimates of cloud visible optical thickness τ based on the "thin" (i.e., bluish) visual appearance of most of the cirrus clouds in our sample indicate that τ <~0.3 occur about 50% of the time, implying that midlatitude cirrus, at least in our region, may be too tenuous to be effectively sampled using current satellite methods, and that their climatic impact needs to be reexamined to more accurately reflect the effects of cirrus clouds that are both optically and physically thin. The τ of opaque cirrus increase up to a limit of ~3.0, where the transition to the midlevel altostratus clouds occurs. Cirrus cloud emissivities derived with the LIRAD method show a dependence on both cloud temperature and thickness, a consequence of the adiabatic process controlling cloud formation. Supercooled liquid water clouds detected with lidar depolarization data may be present in a transient manner in lower cirrus cloud regions, but are not responsible for cirrus cloud generation. These findings provide for an effective definition for cirrus, which conforms with the traditional view based on visual inspection: cirrus are upper tropospheric ice clouds with cloud top temperatures colder than ~-40°C and τ that range from about 0.03 (for visible cirrus) to 3.0 (for altostratus). Finally, and importantly, since cirrus are a product of regional weather patterns, the global representativeness of this and other extended cirrus cloud datasets is discussed.

Circular Depolarization Lidar Measurements of Cirrus Clouds

Ryan Woodard and Richard L. Collins
Geophysical Institute, University of Alaska Fairbanks
903 Koyukuk Dr., Fairbanks, AK 99775-7320 USA
Phone: (907)474-7578, FAX: (907)474-7290, E-mail: ryan.woodard@gi.alaska.edu

Robert S. Disselkamp
Pacific Northwest National Laboratory
MS K8-88, 902 Batelle Blvd., PO Box 999, Richland, WA 99352 USA

Takashi Shibata and Yasunobu Iwasaka
Solar Terrestrial Environment Laboratory
Nagoya University, Chikusa-ku, Nagoya 464, Japan

1 Introduction

Cloud optical properties obtained from field measurements have been used in atmospheric radiation models to estimate cloud radiative forcing as a function of cloud type [Hobbs, 1993; Hartmann et al., 1992]. These optical properties, though, are not accurately known. Polarization sensitive lidar systems have made unique contributions to the study of optically thin clouds, however laboratory studies have shown [Sassen, 1977] that different ice particle types produce the same linear depolarization ratio and thus linear polarization techniques alone cannot uniquely determine cloud particle size and shape. Mishchenko and coworkers [Mishchenko et al., 1996] have shown that consideration of backscattering of both linear and circular polarized light provides a more sensitive measure of the non-sphericity of the cloud particles than the linear polarization technique alone.

While the complete Stokes polarization vector may be determined by measuring four backscatter polarization parameters, few studies of this complexity have been carried out. A recent review by Sassen [1991] cites only one study of lidar field measurements of four components of the polarization of the backscattered light [Houston and Carswell, 1978]. In this work we present preliminary lidar observations of linear and circular depolarization ratios of optically thin clouds in the upper troposphere.

2 Experimental Details

Following the standard Stokes vector (S = (I,Q,U,V)) conventions adopted by Bohren and Huffman [1983], the relationship between the Stokes vector of the incident light, S_i, and scattered light, S_S, can be written as a matrix multiplication, $S_S = \mathbf{S}.S_i$, where the scattering matrix $\mathbf{S}$ is a 4x4 matrix. For an anisotropic distribution of particles, Perrin [1942] shows that the general backscattering matrix reduces to:

$$\mathbf{S} = \begin{pmatrix} S_{11} & 0 & 0 & S_{14} \\ 0 & S_{22} & 0 & 0 \\ 0 & 0 & -S_{22} & 0 \\ S_{14} & 0 & 0 & S_{44} \end{pmatrix}$$

Therefore, only four independent scattering matrix elements need to be determined. An isotropic distribution of particles has $S_{14}=0$, whereas an anisotropic distribution of particles may yield $S_{14}\neq 0$. A linear polarization lidar deployed at Poker Flat Research Range (PFRR) near Fairbanks, Alaska has been modified to make three of these four measurements. A fourth measurement made concurrently is used to calibrate the observations. Following standard processing techniques [e.g. Collins et al., 1996], the background and dark counts are estimated from the high altitude returns where no significant signal was recorded ($\approx$ 75 km) and subtracted from the photon count profiles to yield the actual lidar photon count signals in the parallel and

perpendicular receiver channels, Ip and Is respectively. The ratio of these two signal profiles yield the system depolarization ratio profiles,

$$\tilde{\delta} = \frac{I_S}{I_P}.$$

To make measurements of the depolarization of circular light we place quarter-wave plates in the transmitter beam path and also in the receiver beam path after the telescope turning mirror. We have the following set of four measurements; linear transmission and linear reception (i.e. no quarter wave plates in the system), circular transmission and linear reception (i.e. quarter wave plate in the transmitter only), circular transmission and circular reception (i.e. quarter wave plates in the transmitter and receiver) and linear transmission and circular reception (i.e. quarter wave plate in the receiver only). Under the assumption of perfect metallic Fresnel reflections in the telescope and at the beam steering mirrors, and complete rejection of the orthogonal polarization in each of the receiver polarizers we have four distinct system depolarization ratios. Under the assumption of single scattering, these ratios may be written in terms of the cloud scattering matrix elements:

1. Linear Transmission and Linear Reception (i.e. Linear Depolarization Ratio)

$$\tilde{\delta}_{LL} = K_L \frac{S_{11} - S_{22}}{S_{11} + S_{22}}$$

2. Circular Transmission and Linear Reception

$$\tilde{\delta}_{CL} = K_C$$

3. Circular Transmission and Circular Reception (i.e. Circular Depolarization Ratio)

$$\tilde{\delta}_{CC} = K_C \frac{S_{11} - S_{44}}{S_{11} + S_{44} - 2S_{14}}$$

4. Linear Transmission and Circular Reception

$$\tilde{\delta}_{LC} = K_C \frac{S_{11} + S_{14}}{S_{11} - S_{14}}.$$

The coefficients K_i are ratios of the relative gain in each of the channels. Different attenuators are used in each mode to prevent overloading of the detectors and maintain the different signal levels within similar ranges.

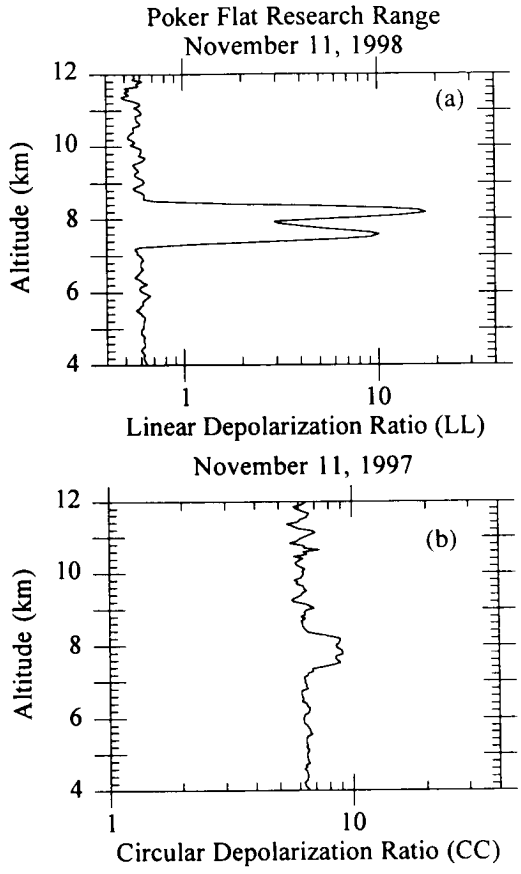


Figure 1. (a) Linear depolarization ratio profile on November 11, 1997. (b) Circular depolarization profile on November 11, 1997.

3 Results

On the nights of November 12, 1997 and February 6, 1998 the lidar was operated at PFRR. The range is a dark rural site 30 miles north of Fairbanks. Thin clouds were noted by the observers (i.e. most stars were visible but the Milky Way could not be clearly distinguished). Lidar profiles were taken over 10 minutes (6000 laser shots) with 60 m resolution in each of the four configurations. The linear depolarization measurement is made as at the start of the observations and repeated at the end to determine if the structure of the clouds had evolved during the ≈50 minute observation period. Two of the four system depolarization ratios, linear (LL) and circular (CC), for each night are shown in Figures 1 and 2.

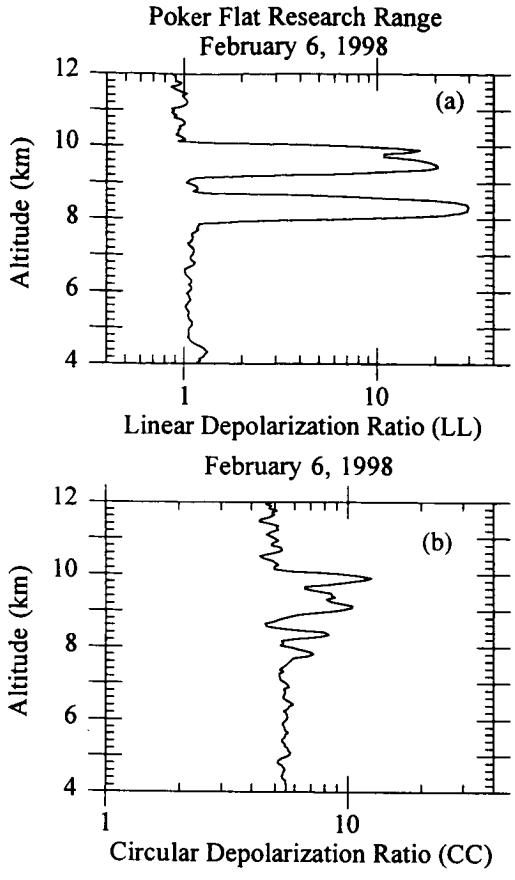


Figure 2. (a) Linear depolarization profile on February 6, 1998. (b) Circular depolarization profile on February 6, 1998.

The CL profile on both nights was constant with altitude, as expected. The LC profile showed no distinct signature associated with the clouds, suggesting that S_{14} was negligible.

A cloud is clearly detected on both nights. Given the strong depolarization, the optical thinness, and the winter conditions, we conclude that these clouds are Cirrus. We assume that at other altitudes the backscatter is dominated by Rayleigh scatter. The system depolarization ratio did not change significantly between the first and last profiles (both LL), so for the purposes of this presentation we assume the characteristics of these clouds were relatively constant over the observation period. From the figures we note that while the linear depolarization ratio profiles are similar on both nights, the circular depolarization ratio profiles differ considerably. On November 11 the circular depolarization profile is uniform throughout the cloud. However, on February 6 the circular depolarization ratios differ in the upper and lower cloud layers and show considerable structure that is not evident in the November data.

4 Summary

This work presents new depolarization lidar observations of Cirrus clouds in the upper troposphere. These observations suggest that the combination of linear and circular depolarization techniques provides additional insight into the structure of the cloud particles. Analysis of these observations is currently in progress and more detailed results, showing the retrieval of backscattering matrix elements, will be presented.

References

Bohren, C.F., D.R. Huffman, *Absorption and Scattering of Light by Small Particles*, John Wiley & Sons, 1983.

Collins, R. L., Lummerzheim, D., R. W. Smith, Analysis of lidar systems for profiling aurorally excited molecular species, *Appl. Opt*, 33:4906, 1997.

Hartmann, D.L., M.E. Ockert-Bell, M.L. Michelsen, The Effect of Cloud Type on Earth's Energy Balance: Global Analysis, *J. Climate*, 5:1281 1992.

Hobbs, P. V., *Aerosol-Cloud-Climate Interactions*, Academic Press Inc., New York, 1993.

Houston, J. D., and A. I. Carswell, Four-component polarization measurement of lidar atmospheric scattering, *Appl. Opt.*, 17:614, 1978.

Mishchenko, M.I., L.D. Travis, D.W. Mackowski, T-Matrix Computations of Light Scattering by Non-Spherical Particles: A Review, J. Quant. Spect. Rad. Trans., 55:535, 1996.

Perrin, F., Polarization of Light Scattered by Isotropic Opalescent Media, *J. Chem. Phys.*, 10:415, 1942.

Sassen, K., The Polarization Lidar Technique for Cloud Research: A Review and Current Assessment, *Bull. Am. Meteorol. Soc.*, 72:1848, 1991.

Sassen, K., Ice Crystal Habit Discrimination with the Optical Backscatter Depolarization Technique, *J. Appl. Meteor.*, 16:425, 1977.

Cloud Measurements with a Multiple-Field-of-View, Dual Polarization Lidar System

Luc R. Bissonnette and Gilles Roy

DREV-Defence Research Establishment Valcartier
2459, Pie XI Blvd. North, Val-Bélair, Québec, Canada, G3J 1X5
Tel.: +418-844-4437 • *Fax*: +418-844-4511 • *E-mail*: luc.bissonnette@drev.dnd.ca

Lidar probing of clouds gives rise to significant multiple-scattering contributions. The early preoccupations were for correcting these effects but it was soon recognized[1–3] that retrievable information on cloud droplet size and concentration is contained in multiply scattered signals. At Defence Research Establishment Valcartier, we have built multiple-field-of-view (MFOV) lidar receivers[4] to take advantage of multiple scattering and recover at least part of the additional available information. The gain over conventional single-scattering lidar measurements is substantial in dense scattering media: access to droplet size, and less ambiguity on the relative importance of the backscatter and extinction coefficients on signal fading.

Our current MFOV lidar transceiver is made up of a 100 Hz, 60 mJ, 12 ns Nd:YAG laser and a 200 mm diameter, 760 mm focal length reflective optics receiver. The receiver field of view (FOV) is changed at the laser pulse rate by means of a rotating aluminized glass disc, placed in the image plane, on which 32 different-size irises were etched. The laser Q-switch is slaved to the rotating disc velocity. The disc comprises 4 different series of 8 irises that define FOVs varying between 0.1 and 12 mrad full angle. Hence, a FOV scan at low angular resolution is completed every 0.08 s and a high resolution one, every 0.32 s. Therefore, meaningful cloud MFOV measurements require that time fluctuations be slower than 12 Hz in the first case, and 3 Hz in the second case. Previous measurements by Roy *et al.*[5] showed that most stratus cloud events satisfy the 3 Hz limit.

Vertical probings of stratus clouds were routinely made. Figures 1 and 2 illustrate the type of additional information that can be derived from MFOV measurements.

In Fig. 1 are plotted the return signals and the depolarization ratios at a small and a large FOV for a rather complex event involving precipitation and cloud layers. The depolarization curves show important depolarization at low altitudes and between the three well defined peaks of the return signals, but a sharp drop at the onset of the peaks. The particles causing large depolarization are snowflakes, but the peaks have to be cloud layers of spherical water droplets because of the small depolarization. Within the cloud layers, there is in addition a marked difference between the small and the large FOVs. While the depolarization drops to a low level at the base of the layers in both cases, it remains low at the small FOV but starts to increase again at the large FOV as particularly evident in the main cloud layer based at 660 m. This is a clear evidence of depolarization caused by multiple scattering. Although the cloud layers are made up, for the most part, of spherical water droplets, the radiation collected at large FOVs is depolarized because it is backscattered at angles slightly less than 180° owing to multiple forward scatterings in the forward and return propagation paths. The depolarization caused by multiple scattering is therefore proportional to the strength of the multiple scattering contributions and, consequently, increases with penetration depth and FOV as shown in Fig. 1 for vertical ranges greater than 660 m.

Figures 2a and 2b show MFOV returns from two different stratus cloud layers. In Fig. 2a, the large and small FOV cloud returns drop to the receiver noise level at the same range while, in Fig. 2b, the large FOV return clearly outlasts the small FOV return by more than 50 m. We can thus infer with good confidence that the returns go to zero because of vanishing backscatter in the first case, but increasing extinction in

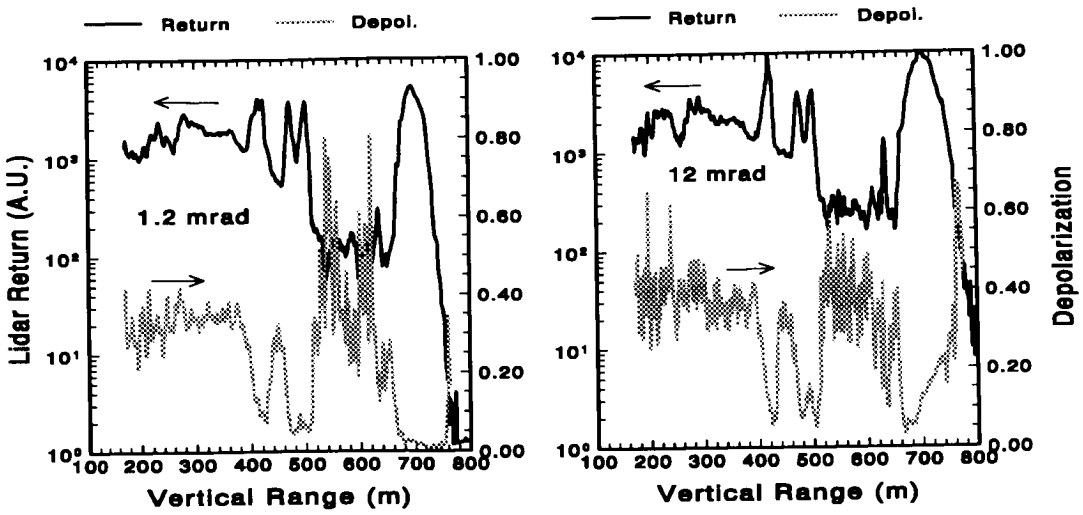


Figure 1: Example of MFOV cloud lidar returns and depolarization ratios for small (1.2 mrad) and large (12 mrad) receiver fields of view

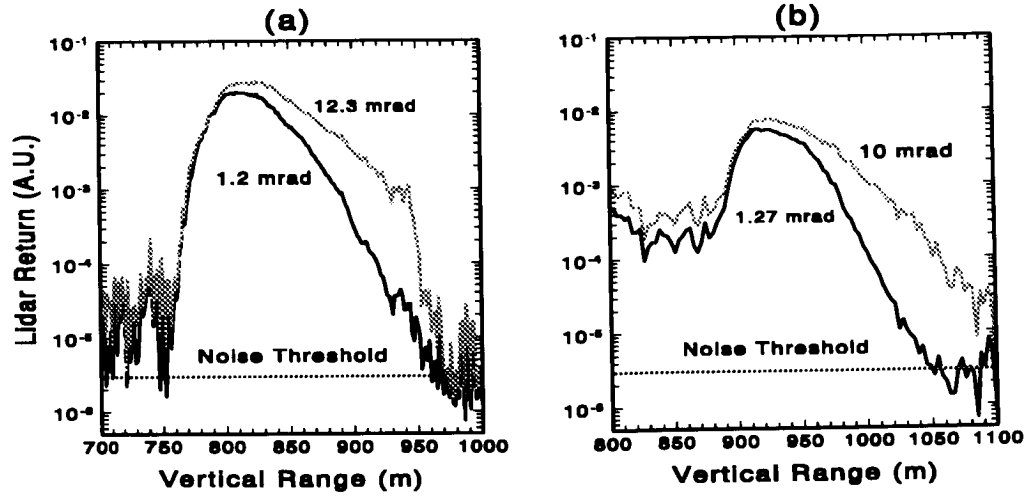


Figure 2: MFOV lidar returns from two different stratus cloud layers

the second case. In other words, the lidar pulse has reached the cloud top for the event of Fig. 2a but not for that of Fig. 2b. Such a conclusion is not possible with conventional single FOV measurements because of the ambiguity on whether signal fading is caused by decreasing backscatter or increasing extinction. The below-cloud signals of Fig. 2b are due to falling snow.

Our lidar inversion method for exploiting multiple scattering is outlined in Bissonnette and Hutt.[6] It is applicable to scattering particles greater than the lidar wavelength, which is the case for cloud and precipitation water droplets or ice crystals at 1.06 μm. Under this condition, approximately half of the particulate extinction is due to diffraction scattering which is concentrated in a narrow peak centered on the laser axis. This means that a large fraction of the scattered radiation remains within the receiver FOV and can thus contribute substantially to the measured signal. Because half or more of all scatterings are in the near forward direction, it follows that the multiply scattered radiation collected by the receiver in the co-axial configuration of our system has, for the most part, undergone a single backscattering at an angle close to 180° preceded and followed by near forward scatterings.[7] Hence, the FOV dependence of lidar returns is strongly related to the profile of the scattering diffraction peak. Diffraction theory tells us that the width of the peak is inversely proportional to the mean diameter of the droplets. This forms the basis for determining the mean droplet diameter from the relative strength of the MFOV returns. Finally, the multiple scattering contributions provide sufficient information to eliminate the need for a boundary value on the extinction coefficient. More details are given in Ref. 6.

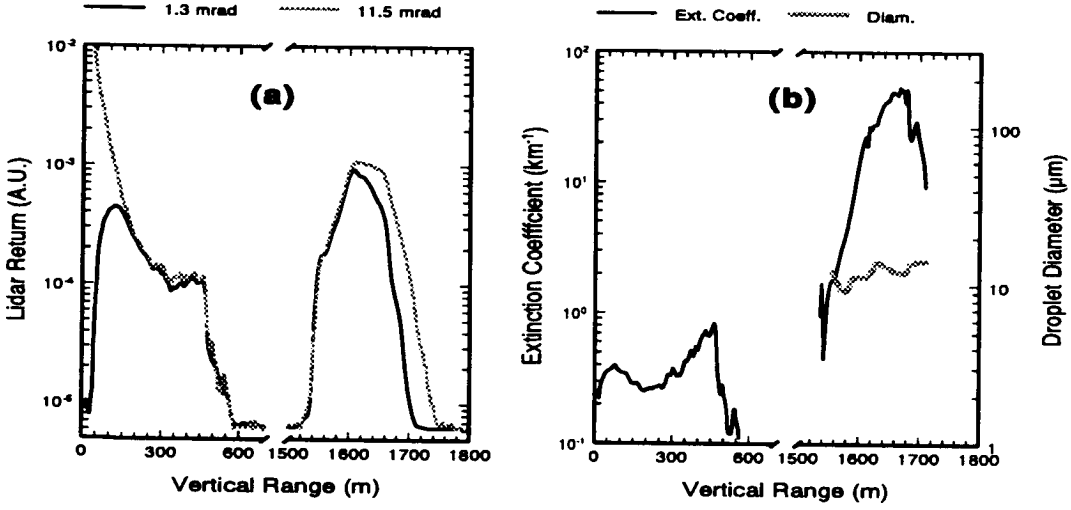


Figure 3: MFOV returns (a) from a stratus cloud layer and corresponding solutions (b) for extinction coefficient and mean droplet diameter

Figure 3 shows an example of inversion results. Plotted in the left panel are the raw lidar returns at the smallest and largest fields of view used for analysis, and in the right panel the corresponding retrieved solutions for the extinction coefficient and mean droplet diameter. The measurements were made under conditions of a nearly uniform stratus ceiling. The raw returns show three distinct regions: a ground haze capped at 600 m, a clear air gap between 600 and 1500 m, and a cloud layer with a base at $\sim$ 1540 m. In the haze layer, the small and large FOV signals are almost exactly superimposed; there is no sign of multiple scattering contributions. The large FOV return is somewhat noisier but this is to be expected because of the much greater quantity of background radiation falling on the detector and of the residual electronic noise caused by the near-saturation impulse at close range. The latter effect results from the faster 'overlap'

function at the large FOV as clearly illustrated in Fig. 3. In the clear air gap, the return signals fall below the noise level at both FOVs. They rise simultaneously at the cloud base but begin to diverge about 60 m into the cloud, indicating the onset of measurable multiple scattering contributions. The inversion solutions are plotted in the right-hand-side panel. They were calculated with a more current version of the method of Ref. 6. No boundary value was specified, the multiple scattering information provided by the relative strength of the large to the small FOV returns has superseded that requirement. The solutions are terminated where the small FOV signal drops to the noise level and, of course, there is no size retrieval where no multiple scattering contributions are measured. The retrieved extinction coefficient is 30-50 km^{-1} in the cloud layer and 0.3-0.5 km^{-1} in the haze layer; these values are quite typical for clouds and haze. Hence, the inversion method seems to work well over a wide range of extinction values. On the other hand, the size solution gives a mean cloud droplet diameter of 10-14 μm. This agrees well with the values of 10-20 μm most often quoted for clouds. We are currently participating in an extensive program to validate our solutions against *in situ* aircraft data.

In conclusion, the inversion of MFOV cloud lidar returns gives, at each range bin, good estimates of the cloud average droplet diameter and extinction coefficient. From these two simultaneous solutions and a suitable hypothesis on the form of the droplet size distribution, for example a two-parameter gamma function as used in many cloud models, we can calculate other cloud parameters such as the droplet concentration, the liquid water content, the infrared transmittance and emissivity, etc. The MFOV technique, therefore, has great potentials for extending the usefulness of lidars in the remote sensing of cloud properties. We are currently developing an eyesafe MFOV lidar to make simultaneous return measurements at 7 FOVs. Simultaneous detection at all FOVs and eyesafety are prerequisites for ground based scanning and airborne operations.

REFERENCES

[1] R.J. Allen and C.M.R. Platt, "Lidar for multiple backscattering and depolarization observations," Appl. Opt., Vol., 16, pp. 3193-3199 (1977).

[2] S.R. Pal and A.I. Carswell, "Polarization properties of lidar scattering from clouds at 347 nm and 694 nm," Appl. Opt., Vol. 17, pp. 2321-2328 (1978).

[3] K. Sassen and R.L. Petrilla, "Lidar depolarization from multiple scattering in marine stratus clouds," Appl. Opt., Vol. 25, pp. 1450-1459 (1986).

[4] G. Roy, L.R. Bissonnette, and C. Bastille, "Efficient field-of-view control for multiple-field-of-view lidar receivers," submitted to 19th Intl Laser Radar Conference, Annapolis, Maryland, July 6-10,1998.

[5] G. Roy and L.R. Bissonnette, "Non-simultaneous measurement of multiple-field-of-view lidar returns in clouds: time correlation lengths," Proc. of 18th Intl. Laser Radar Conference, Springer Verlag Berlin, 1996.

[6] L.R. Bissonnette and D.L. Hutt, "Multiply scattered aerosol lidar returns: inversion method and comparison with *in situ* measurements," Appl. Opt., Vol. 34, pp. 6959-6975 (1995).

[7] F. Nicolas, L.R. Bissonnette, and P.H. Flamant, "Lidar effective multiple-scattering coefficients in cirrus clouds," Appl. Opt., Vol. 36, pp. 3458- 3468 (1997).

OFF-BEAM (MULTIPLY-SCATTERED) LIDAR RETURNS FROM STRATUS, 2: SPACE-TIME MEASUREMENTS IN A LABORATORY SIMULATION

Anthony B. Davis, Cheng Ho, and Steven P. Love
Los Alamos National Laboratory, Space & Remote Sensing Science Group (NIS-2)
PO Box 1663 (Mail Stop C-323), Los Alamos, NM 87545, USA.
Tel: (505) 665 6577; Fax: (505) 667 3815; E-mail: adavis@lanl.gov

Abstract

We present preliminary results from a simulation of off-beam lidar observations of an *in vitro* "cloud" of constant physical thickness and optical depth varying over 2.4 orders of magnitude. The key element in the instrumental suite is an imaging/ranging device that uses single-photon counting based on Micro-Channel Plate/Crossed Delay Line (MCP/CDL) technology. In the time domain, these measurements closely mimic LITE returns from marine stratocumulus. In the spatial domain, they confirm the main points of the analytical theory of diffusing wave propagation in a finite medium. Most importantly, they demonstrate the feasibility of real cloud applications —physical and optical thickness retrieval— with existing technology, at least from ground and by night.

1. Introduction

In a companion paper (Davis and Cahalan, 1998), we survey the theory of off-beam cloud lidar which relies heavily on multiply scattered light emerging from the cloud at considerable distances from the laser beam. At present, we only need to recall that, for typical stratus (optical thickness $\tau \approx 8$-16, physical thickness $\Delta \approx 0.3$–0.5 km), the root-mean-square horizontal photon transport from incidence to escape is $\langle \rho^2 \rangle \approx 0.2$–0.5 km, with many scatterings in the interim. Indeed, the photons' average dwelling time $\langle t \rangle$ associated with this horizontal transport is equivalent to about twice the cloud's thickness. This means that the number of scatterings involved is on the order of twice the optical depth. Given the asymmetry factor ($g = 0.85$) of the forward-peaked scattering phase function for cloud droplets, $1/(1-g) = 7$ or so scattering events is enough for the photon to forget its original direction of propagation. In such circumstances, the radiation field is dominated almost everywhere by multiply-scattered photons and the relevant theoretical framework is diffusion theory, equivalently, photon random-walk theory.

Off-beam lidar has tremendous potential in cloud remote sensing, as can be seen in the following first-order asymptotic formulas:

$$\langle t \rangle \sim \Delta / c,$$

$$\sqrt{\langle \rho^2 \rangle} \sim \Delta / \sqrt{(1-g)\tau}$$

(asymptotic radiative transfer theory is routinely invoked in passive cloud remote sensing in the solar spectrum). The above scaling relations can be derived from elements of random walk theory (Davis *et al.*, 1997a). A more detailed Green-function analysis of the diffusion equation with the appropriate boundary conditions makes specific predictions for the numerical constants and pre-asymptotic correction terms; see Davis and Marshak (1996) for a simplified presentation.

In view of the importance of the atmospheric application in mind (physical cloud thickness Δ is not readily accessible by any existing remote sensing technique), it is paramount to validate experimentally the above-mentioned body of theory. The most effective way to do this is in the lab, where we can control all the parameters.

There is a long history of bringing atmospheric optics into the laboratory, although rarely when multiple scattering is involved. A notable exception to this is the work of Craig Bohren at Penn State, e.g., Bohren *et al* (1995). Most "lidar-in-the-lab" experiments with an emphasis on multiple scattering were conducted by the Florence group using streak-camera technology to achieve the very high temporal resolution required to obtain the time-gated observations on a necessarily small sample (Gai *et al*, 1996; and references therein). Experiments involving multiply-scattered near-IR light propagating in laboratory samples have been performed in the context of "diffusing-wave" spectroscopy, with various applications in mind including non-intrusive 3D medical imaging (Yodh and Chance, 1995; and references therein). Detection of diffusing lidar photons in real clouds (escaping hundreds of meters away from the beam) has been reported elsewhere (Davis *et al.*, 1997b); however, the spatial sampling is poor and no photon-path discrimination was obtained.

As far as we know, there has never been a simultaneous space-time detection of photons diffusing in a medium with continuous sampling in all dimensions, neither in the lab nor in the field. In this paper, we present results from such an experiment recently conducted at Los Alamos National Laboratory where remotely observable transects of radiative Green functions are accurately measured.

2. Description of Experiment

2.1 Instrumentation

This experiment is a direct application of a project in sensor technology development at Los Alamos National Laboratory's Nonproliferation and International Security Division funded by the U.S. Department of Energy. In its final configuration, the Micro-Channel Plate/Crossed Delay Line (MCP/CDL) detector system with Pulse Absolute Timing (PAT) fast electronics is expected to offer the following performance:

- 30 μm FWHM for point-source resolution (i.e., ≈1300 pixels across the 4 cm diameter of the MCP's active area);
- better than 100 ps timing accuracy (i.e., less than 3 cm in photon flight);
- sustainable random count rate of 5 10^6 counts/s (which determines the saturation level of the device).

Priedhorsky, Smith and Ho (1996) proposed that such a system, coupled with a sharply pulsed laser, can be used for remote ranging and 3D mapping. An end-to-end prototype system has been constructed. Using this system, the 3D imaging and mapping concept has been demonstrated in the laboratory and in the field (Ho *et al.*, in preparation).

For this experiment, we used a solid-state pulsed laser at 655 nm with a regular pulse width of 83 ps as the illumination source. The pulses are triggered at a period of 640 ns (1.6 MHz rep-rate), giving an average power of about 7 μW. Light from the target scene is collected by a commercial f/5 Matsukov telescope (50 cm focal length), roughly collocated with the laser. The MCP/CDL detector is located at the focal plane with a narrow-band filter of 10 nm bandpass in the optical train to reject ambient light.

2.2 Cloud Model

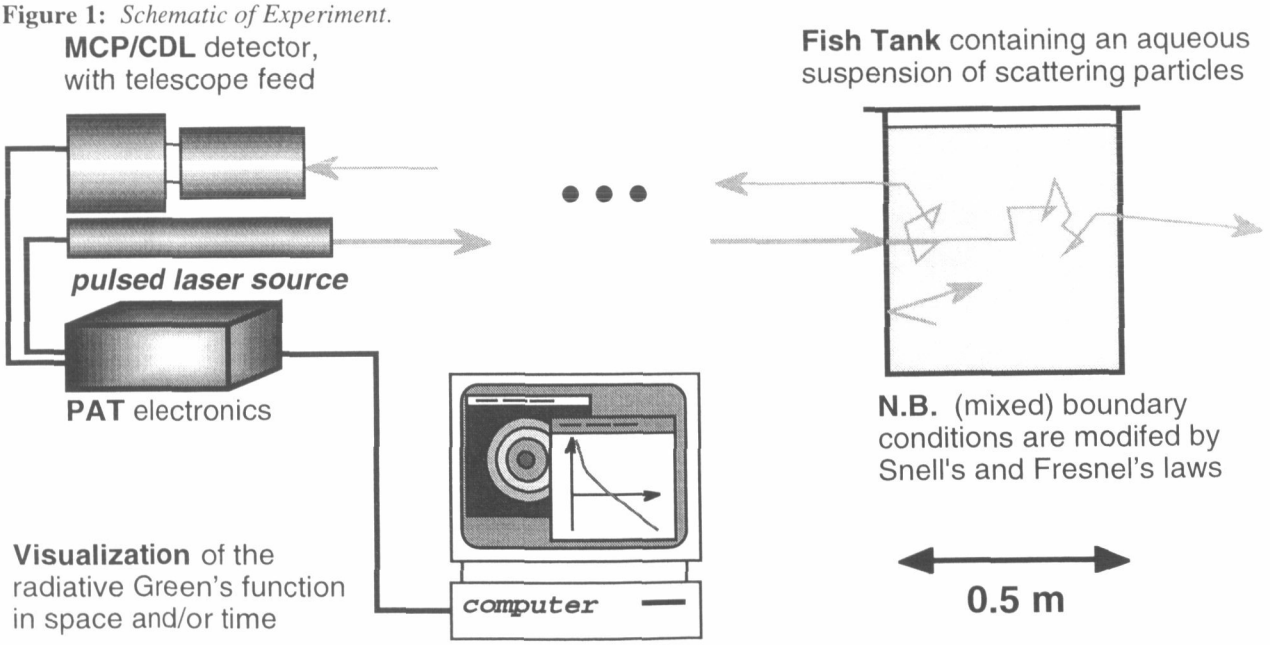
To model a plane-parallel cloud in the lab, we require a rigid transparent container with one dimension (parallel to the optical axis) smaller than the other two. Furthermore, that dimension needs to be as large as possible with respect light-flight during the smallest instrumentally definable interval (say, 6 cm). We settled on a commercial fish tank fashioned in tempered glass, dimensions 0.88×0.66×0.44 m^3. To produce the surrogate cloud, we needed to create a homogeneous conservatively scattering optical medium in the aquarium with a controllable extinction coefficient. This was done by filling the tank with (tap) water, progressively adding a popular fabric softener (uncolored/unscented Downy®), and stirring the mixture. Mixing ratio was varied from 2 10^{-4} (43 ml of softener), producing a slight haziness, to 4 10^{-2} (≈10 l of softener), resulting in an opaque cloudy medium.

2.3 Experimental Set-Up and Procedure

The experiment was conducted in a large dark room. The laser was tightly focused on the model cloud described above, located at a distance of about 6 m. The beam was aimed close to the center of the broad face of the tank and the detector's FOV was centered more-or-less on the impact point. Figure 1 shows a schematic of the experiment which is scaled-down approximately 1000÷1 with respect to a real cloud observation from an aircraft.

Illumination was slightly off-normal to avoid a direct return of the beam into the instrument by specular reflection. Short (1–10 s) exposures were taken for quick looks at the data, followed by one-minute exposures which were archived for post-processing. We describe the latter in the following section.

Figure 1: *Schematic of Experiment.*



3. Preliminary Account of Experimental Results

Results for just water and very low Downy® concentration are not trivial to interpret because of specular and diffuse reflections of the directly transmitted (or forward scattered) beam inside the tank. As the optical thickness is increased, the picture gets simpler to understand.

Figure 2 shows spatially-summed returns for three *large* optical depths, increasing by factors of two. The similarity with LITE returns from marine stratocumulus (Winker, 1997) is remarkable and the exponential tail that

stretches far beyond the cloud thickness is theoretically predicted for off-beam lidar signals. Note that the decay rate is not very sensitive to optical depth. In this aspect, we are reproducing work by the Florence group using radically different methodology.

Figure 3 shows the spatial counterpart of Fig. 2: the path-integrated spatial radiance pattern excited by the laser beam, as if it were CW. Here again we find asymptotically exponential behavior, as predicted. Note that the decay rate is clearly dependent on optical depth. In this aspect, there is currently an effort at NASA's GSFC to measure the spatial radiative Green function with more standard instrumentation than used here.

For a more comprehensive overview of our experimental results for these three and other "clouds", the interested reader can go to the following URL: http://www.rulli.lanl.gov/cloud/cloud.htm. At this web-site, animated "movies" (sequential time-slices of spatial data) can be viewed that dramatically illustrate the outward propagation of the diffusing wave of photons.

The instrumental parameters that will have to be changed in a night-time field experiment are: stronger source, lower rep-rate, narrower interference filter, faster optics. It is likely that we can perform within the confines of eye-safety. The faster optics are only required for ground-based cloud observations where the cloud is likely to be at relatively close range; this may pose a problem in the filtering.

4. Conclusions and Future Plans

We have successfully measured radiative Green functions of dense optical media resembling homogeneous plane-parallel clouds with continuous space-time sampling. The Green function is simply the space-time response of the medium in back-scatter to external illumination with a laser pulse. The detector is essentially a photon-counting 2D radiometer with ultra-fast electronics that enable absolute arrival time measurement for each photon.

The preliminary results presented here validate the main points of the diffusion equation-based theory that was been discussed elsewhere. A more definitive account is in preparation. The success of this experiment proves that there is no severe technological barrier preventing performance of such off-beam lidar measurements on real clouds at night. We are currently preparing for off-beam lidar observations in the field with an upgraded transmitter and better adapted optics. At present, observations by day are not an option since sunlight would jeopardize the integrity of the MCP/CDL detector. Even if it were adequately protected, solar photons would overwhelm the weak off-beam signal for commonly used sources and filtering techniques (see companion paper for the alternatives under consideration).

Acknowledgments

This work is funded by the Laboratory Directorate Research and Development (LDRD) program at Los Alamos National Laboratory (Remote Sensing Science Thrust). We thank the sensor project team led by Clayton Smith for the development and use of the detector system. Miles Hindman and Alan Bird from the sensor team assisted in the experiment. We thank Sig Gerstl and Bill Priedhorsky for fruitful discussions.

References

Bohren, C., J. Linskens, and M. Churma, 1995: At what optical thickness does a cloud completely obscure the Sun? *J. Atmos. Sci.*, **52**, 1257–

Davis, A., and A. Marshak, 1996: Cloud Responses from CW and Pulsed Lasers as Green's Functions: What do They Tell us? & Can we Measure Them? In *8th International Worskshop on MUltiple SCattering Lidar Experiments (MUSCLE 8 – Extended Abstract Volume)*, March 04–06, 1996, Québec (Qc), pp. 67–71, Def. Res. Est.Valcartier (DREV).

Davis, A., D. M. Winker, A. Marshak, J. D. Spinhirne, R. F. Cahalan, S. P. Love, S. H. Melfi, and W. J. Wiscombe, 1997b: Retrieval of physical and optical cloud thicknesses from space-borne and wide-angle lidar. In *Advances in Atmospheric Remote Sensing with Lidar*. Eds. A. Ansmann, R, Neuber, P. Rairoux, and U. Wadinger, Springer-Verlag, pp. 193–196.

Davis, A., J. D. Spinhirne, M. McGill, and R. F. Cahalan, 1997a: Off-beam cloud lidar: First detection of diffusing photons. In *Proceedings of Winter Topical Meeting on "Optical Remote Sensing of the Atmosphere"*, February 10–14, 1997, Santa Fe (NM), pp. 39–41, Optical Society of America, Washington (DC).

Davis, A., and R. F. Cahalan, 1998: Off-beam (multiply-scattered) lidar returns from stratus, 1: Cloud-information content & sensitivity to noise, *19th International Laser Radar Conference*, Annapolis (Md), July 6–10, 1998, (submitted).

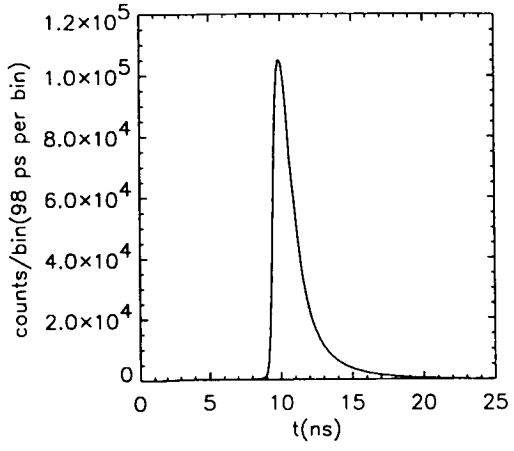
Gai, M., M. Gurioli, P. Bruscaglioni, A. Ismaelli, and G. Zaccanti, 1996: Laboratory simulations of lidar returns from clouds. *Appl. Opt.*, **35**, 5435-5442.

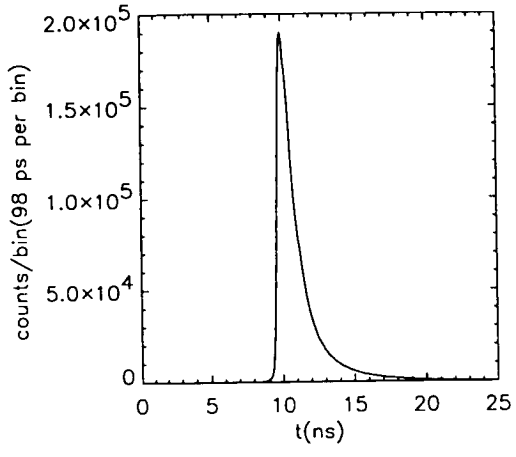
Priedhorsky, W. C., R. C. Smith, and C. Ho 1996: Laser ranging and mapping with a photon-counting detector. *Appl. Opt.*, **35**, 441–452.

Winker, D. M., 1996: Simulation and modeling of the multiple scattering effects observed in LITE data. In *Advances in Atmospheric Remote Sensing with Lidar*. Eds. A. Ansmann, R, Neuber, P. Rairoux, and U. Wadinger, Springer-Verlag, pp. 185–188.

Yodh, A., and B. Chance, 1995: Spectroscopy/imaging with diffusing light. *Phys. Today*, **48**, No. 3, 34-40.

Figure 2: *Spatially-Integrated Pulse Shapes (Impulse Responses).* From top to bottom, Downy® amount (hence optical thickness) increases from 1.375 l to 5.5 l, by factors of 2.





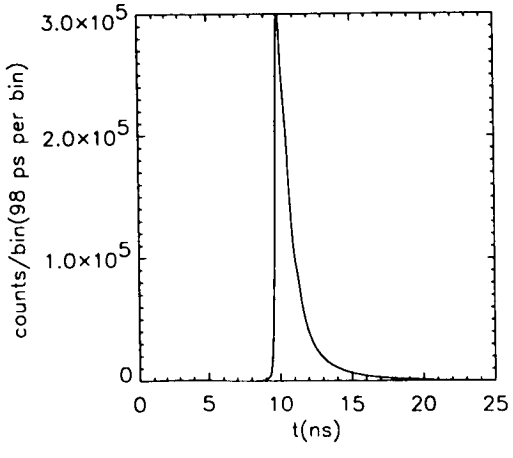
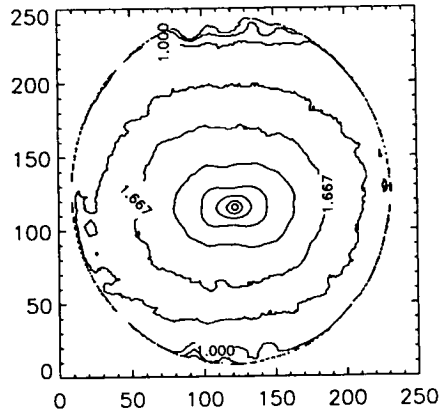
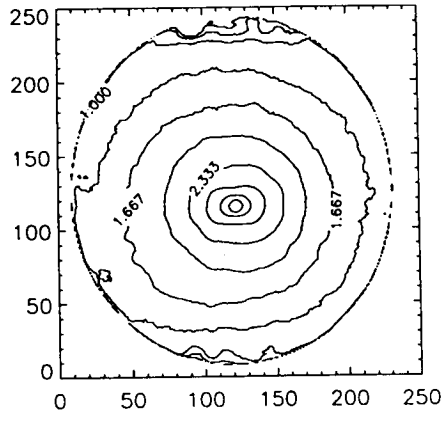
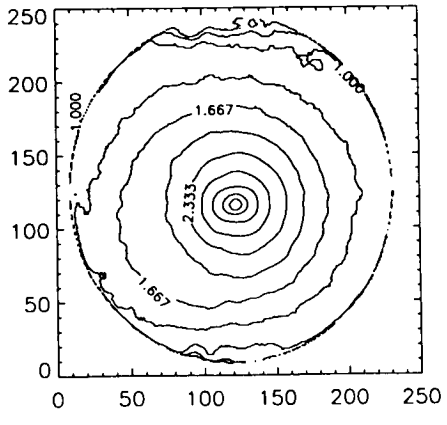


Figure 3: *Time-Integrated Spot Shapes (Point-Spread Functions).* Same ordering/concentrations as in Fig. 2.







Examination of the Nonlinear LIDAR-Operator - an Inverse Ill-posed Problem

Claudia Bernutat, Christine Böckmann
Institut für Mathematik, Universität Potsdam
Am Neuen Palais 10, Potsdam, D-14415, Germany
Phone: 0049-331-977-1743, FAX: 0049-331-977-1578, E-mail: bockmann@rz.uni-potsdam.de

Ronny Ramlau
Department of Computer Science, University of Utah
Salt Lake City, Utah 84112

1 Introduction

Atmospheric aerosols play an important role for climate and for atmospheric chemistry. They have appreciable influence on the earths radiation budget, air quality, clouds and precipitation as well as the chemistry of the troposphere and stratosphere, see (McCormick and Thomason, 1995). One of the key aspects in a further understanding of the importance of aerosols is the investigation of the spatial and temporal variability of the particles microphysical properties, such as parameters describing their mean size, mass and surface-area concentrations. Microphysical properties of aerosols can be measured by optical ranging methods; here we deal with the lidar method, where backscattered light from laser pulses at various discrete wavelengths is collected simultaneously on the emitted wavelengths. The measured backscatter intensity depends on the backscatter and extinction properties of aerosols, which in turn depend on their abundance, size distribution, refractive index $m(\lambda)$, phase and on the wavelength.
The mathematical model for such a LIDAR messuring process consists of one nonlinear and two linear integral equations. These are the LIDAR-equation, see (Measures, 1984),

$$P(\lambda,z) = C(\lambda)P_e(\lambda)\beta(\lambda,z)\tfrac{1}{z^2} \cdot \exp\{-2\int_0^z \alpha(\lambda,\tilde{z})d\tilde{z}\}, \quad (1)$$

(where λ is the wavelength, z the height, C is a specific quantity of the measuring apperatus, P_e the intensity of the emitted signal, P the intensity of the detected signal, β and α are the backscattering and extinction coefficients) and the Fredholm integral equations of the first kind for backscattering and extinction coefficients β^{Aer} and α^{Aer}

$$\beta^{Aer}(\lambda,z) = \int_{r_a}^{r_b} \pi r^2 Q_\pi(r,\lambda;m)n(r,z)\,dr, \quad (2)$$

$$\alpha^{Aer}(\lambda,z) = \int_{r_a}^{r_b} \pi r^2 Q_{ext}(r,\lambda;m)n(r,z)\,dr, \quad (3)$$

where r is the particle radius, m the refractive index, n the aerosol size distribution we are looking for, Q_π the backscattering and Q_{ext} the extinction efficiencies. We have

$$\beta = \beta^{Aer} + \beta^{Ray} \quad \text{and} \quad \alpha = \alpha^{Aer} + \alpha^{Ray} \quad (4)$$

with known β^{Ray} and α^{Ray}. The kernel functions of the integral equations (2) and (3) reflect shape, size and material composition of particles. We assume Mie-particles. Following formulas hold for backscattering and extinction efficiencies, see (Bohren and Huffmann, 1983),

$$Q_\pi = \frac{1}{k^2r^2}\left|\sum_{n=1}^{\infty}(2n+1)(-1)^n(a_n - b_n)\right|^2, \quad (5)$$

$$Q_{ext} = \frac{2}{k^2r^2}\sum_{n=1}^{\infty}(2n+1)Re(a_n + b_n), \quad (6)$$

where k is the wave number defined by $k = 2\pi/\lambda$ and a_n and b_n are the coefficients which we get over the boundary conditions for the tangential components of the waves. We substitute the equations (2), (3) and (4) into the LIDAR-equation (1) and we get the so called nonlinear LIDAR-operator L

$$L(n) = P \quad (7)$$

which is advantageous since we do not need the LIDAR-ratio.

2 Modified Landweber-method for the nonlinear ill-posed LIDAR-operator

As a product of a compact integral operator and the exponential of a compact integral operator, the inverse problem of finding a solution for the nonlinear LIDAR-operator (7) is ill-posed. This problems may be interpreted as finding the cause of a given effect. Inverse problems of determination of system parameters from input-output

measurements are often ill-posed in the sense that distinct cause can account for the same effect and small changes in a perceived effect can correspond to very large changes in a given cause. A common feature of inverse problems posed in function spaces is their instability, that is, small changes in the data may give rise to large changes in the solution. Because the measured data might be highly contamined by noise, i.e.

$$\|P - P^\delta\| \leq \delta$$

one has to use *regularization methods* for controlling the data noise. Although the theory for the regularization of linear ill-posed problems is well developed, see e.g. (Louis, 1989), there are only few general results for nonlinear operators, see (Engl, Hanke and Neubauer, 1996). A common method for the inversion of ill-posed problems is Tikhonov regularization, where as an approximation to a solution of the equation $L(n) = P$ is used the minimizing element of the functional

$$J_\gamma(n) = \|L(n) - P^\delta\|^2 + \gamma\|n - n_0\|^2 \ ,$$

where n_0 is an a-priori-guess to the solution and γ is the regularization parameter. However, it is difficult to find an appropriate parameter γ as well as to minimize the functional J_γ. From the computational point of view, it is more convenient to make use of iterative algorithms. For our test computations the Landweber-method see (Hanke, Neubauer and Scherzer, 1995) was used.

Regularization methods assume certain properties of the operator like the existence of the Fréchet-derivative and weakly closedness. We consider the LIDAR-operator first as a mapping between $\mathcal{L}^2$-spaces (spaces of quadratic integrable functions):

$$L \quad : \quad \mathcal{L}^2(I_r \times I_z) \longmapsto \mathcal{L}^2(I_\lambda \times I_z)$$

with $I_r = [r_a, r_b]$,$I_z = [0, z_1]$ und $I_\lambda = [\lambda_0, \lambda_1]$.
$L(n)(\lambda, z) = c(\lambda, z)\beta(\lambda, z) \cdot \exp\{-2\int_0^z \alpha(\lambda, \tilde{z})d\tilde{z}\}$
where $c(\lambda, z) := C(\lambda)P_e(\lambda)\frac{1}{z^2}$.

Let X and Y be Banach-spaces. A continuous nonlinear operator $L : \mathcal{D}(L) \subset X \to Y$ is said to be Fréchet-differentiable at $n \in X$ if there exists a bounded linear operator $L'(n)$ with

$$\frac{\|L(n+h) - L(n) - L'(n)h\|_Y}{\|h\|_X} \to 0 \text{ for } \|h\|_X \to 0.$$

The Fréchet-derivative of the LIDAR-operator with respect to the function n is given by
$(L'(n)h)(\lambda, z) = c(\lambda, z) \int_{I_r} K_\pi(r, \lambda; m)h(r, z)dr$

$$\cdot \exp\{-2\int_0^z \alpha(\lambda, y)dy\} - 2c(\lambda, z)\beta(\lambda, z)$$

$$\cdot \exp\{-2\int_0^z \alpha(\lambda, y)dy\} \int_0^z \int_{I_r} K_{ext}(r, \lambda; m)h(r, y)dr\,dy$$

with $K_{ext}(r, \lambda; m) = \pi r^2 Q_{ext}(r, \lambda; m)$
and $K_\pi(r, \lambda; m) = \pi r^2 Q_\pi(r, \lambda; m)$ for the kernel functions. The adjoint of the Fréchet-derivative is by definition the operator $L'(n)^*$ for which holds

$$\langle L'(n)h, g\rangle_{\mathcal{L}^2(I_\lambda \times I_z)} = \langle h, L'(n)^* g\rangle_{\mathcal{L}^2(I_r \times I_z)}$$

for all functions $g \in \mathcal{L}^2(I_r \times I_z)$ where

$$\langle f, g\rangle = \int_X \int_Y f(x, y)g(x, y)dy\,dx$$

is the $\mathcal{L}^2$-scalar product. This is given by

$(L'(n)^* g)(r, z) =$

$$\int_{I_\lambda} c(\lambda, z) \exp\{-2\int_0^z \alpha(\lambda, y)dy\} K_\pi(r, \lambda, m)g(\lambda, z)d\lambda$$

$$-2\int_z^{z_1} \int_{I_\lambda} c(\lambda, y)\beta(\lambda, y) \exp\{-2\int_0^y \alpha(\lambda, x)dx\}$$

$$\cdot K_{ext}(r, \lambda; m)g(\lambda, y)d\lambda dy.$$

To proof the weakly sequentially closedness we consider L as a mapping $L : H^s \hookrightarrow \mathcal{L}^2 \mapsto H^s$. The Sobolev-spaces

$$H^s := \{f \in \mathcal{L}^2 : (1 + |\xi|^2)^{s/2}\mathcal{F}f(\xi) \in \mathcal{L}^2\}$$

contain $\mathcal{L}^2$-functions with certain smoothness properties e.g. infinitely differentiable functions with compact support, $\mathcal{F}$ means the Fourier transformation, see e.g. (Triebel, 1978). The embedding operator i from the Sobolev-spaces H^s into $\mathcal{L}^2$ is compact and linear for all $s > 0$ and thus the composition $L \circ i$ is compact and continuous. Now we can formulate the following

Lemma: The operator $\tilde{L} = L \circ i$ is weakly (sequentially) closed, i.e.

$$(n_k) \rightharpoonup n \wedge \tilde{L}(n_k) \rightharpoonup P) \Rightarrow (n \in \mathcal{D}(\tilde{L}) \wedge P = \tilde{L}(n)).$$

This is a common result that the composition of a continuous nonlinear operator and a compact linear operator is weakly sequentially closed. The proof uses the well known Banach-Steinhaus-theorem, see e.g. (Triebel, 1978). We identify $L \circ i$ again by L. Hence the LIDAR-operator fulfills the essential conditions for using regularization methods. We used the Landweber iteration method. For nonlinear operators, it is defined by

$$n_{k+1}^\delta = n_k^\delta + L'(n_k^\delta)^*(P^\delta - L(n_k^\delta)) \ ,$$

where $L'(n_k^\delta)^*$ denotes the adjoint operator of

the Fréchet-derivative at point n_k^δ of the LIDAR–operator L. A fast discretization of Landweber's method was developed in (Ramlau, 1998). The implementation of the algorithm is done as follows: A finite dimensional subspace

$$X_l = \text{span } \{e_k\}_{k=1,\dots,l}$$

with orthonormal basis e_k is chosen; usually the functions e_k will be step functions:

$$e_k(x) := \begin{cases} 1 \text{ for } x \in [(k-1)/n,\ k/n] \\ 0 \text{ otherwise.} \end{cases}$$

Then, the new iterate is assumed to belong to X_l and computed by

$$\begin{aligned} n_{k+1}^\delta &= \sum_{j=1}^{l} \langle n_{k+1}^\delta, e_j \rangle e_j \\ \langle n_{k+1}^\delta, e_j \rangle &= \langle n_k^\delta, e_j \rangle + \langle L'(n_k^\delta) e_j,\ P^\delta - L(n_k^\delta) \rangle \ . \end{aligned}$$

In contrary to linear problems, where the values of $L'(n_k^\delta)e_j$, $j = 1, ..., l$ must be computed only once, for the nonlinear problem one must compute it within every iteration step, which leads to a much higher computational effort.

3 Numerical Results

We computed for different complex refractive indices the kernel efficiencies Q_{ext} and Q_π. The kernel functions in (2) and (3) are square integrable in $[r_a, r_b] \times [\lambda_0, \lambda_1]$. The degree of ill-posedness depends on the smoothness of the kernel function. So the two integral equations (2) and (3) are extremly different from each other, see Figure 3 and Figure 5. Test computations will be done by assuming the following log-normal size distribution

$$n(r,z) = \frac{n_{total}}{r\sqrt{2\pi}\ln\sigma(z)} \exp\{-\frac{(\ln r - \ln r_{med}(z))^2}{2\ln^2\sigma(z)}\}$$

where n_{total} is the sum of particles per m^3 (we assume $10^6 m^{-3}$), r_{med} is the radius where the half of particles has a radius less then r_{med}, and σ is a relative measure for the width of the distribution. We choose $r_{med} \in [0.1, 0.6]\,\mu m$ and $\sigma \in [1.3, 2]$, see (Müller, 1997). In Figure 1 is shown the simulated twodimensional size distribution in dependence of particle radius and height. Figure 2 shows the size distributions for three constant heights which are lognormal distributions with different parameters. For our running test computations we used data generated by the forward problem; the perturbation of the data was done by adding Gaussian noise. The belonging data are shown in Figure 4. At the moment the implementation of the reconstruction algorithm is always in process, but we are looking forward to present numerical results.

4 Outlook

A sensitivity study for the inversion algorithm will be performed next. The question on the minimum number and kind of optical data has to be further examined. This will help to inverse LIDAR measurements without LIDAR-ratio. Special attention will be paid to the accuracy of deriving the parameters in dependence of measurement errors.

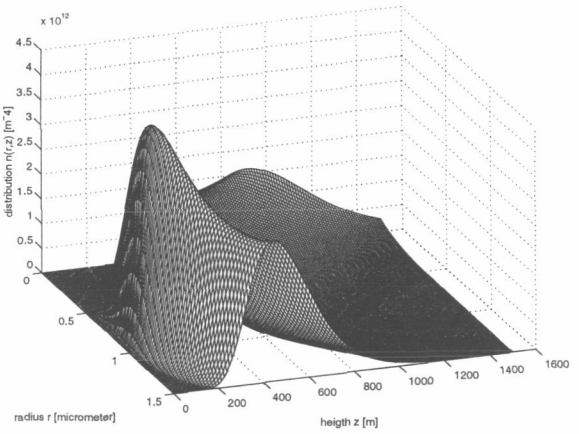


Figure 1: Particle size distribution $n(r, z)$

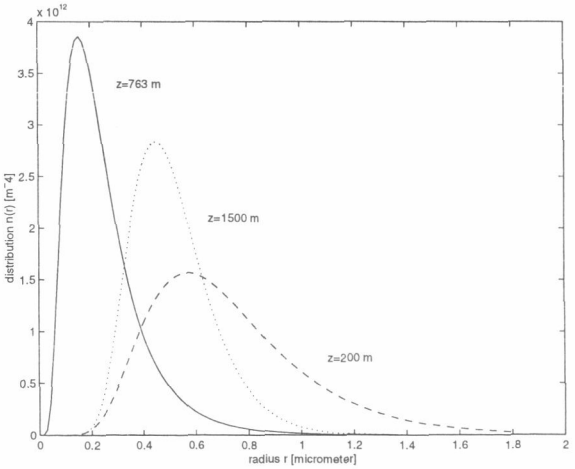


Figure 2: Sectional drawing for 3 constant heights

5 Acknowledgments

This work has been supported by the Bundesministerium für Bildung, Wissenschaft, Forschung und Technologie (BMBF) under grant 03-MA7PO1-5.

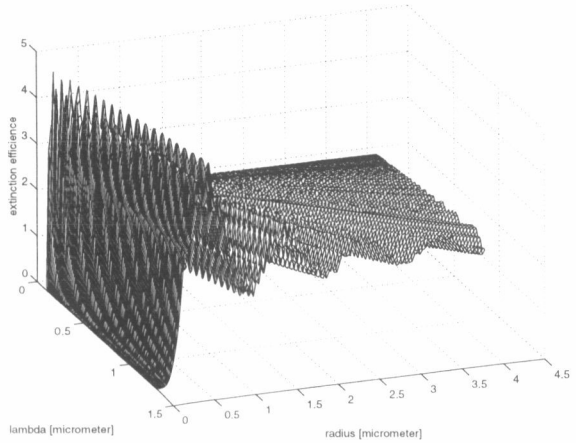


Figure 3: Efficience Q_{ext} for $m = 1.44 + 0.01i$

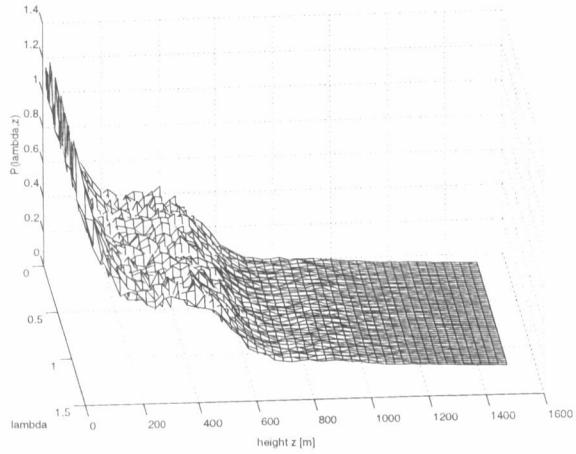


Figure 4: Generated data for reconstruction

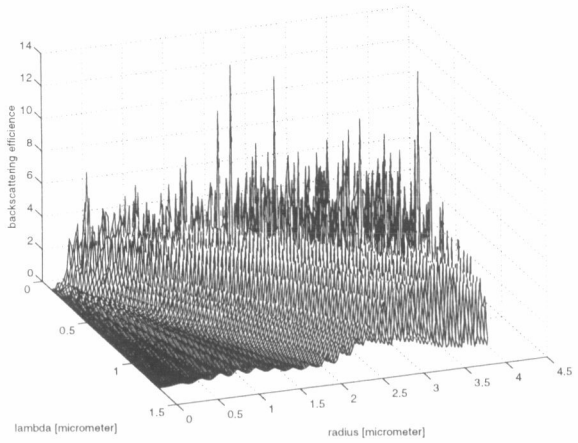


Figure 5: Efficience Q_π for $m = 1.44 + 0.01i$

References

Ansmann A., Wandinger U., Riebesell M., Weitkamp C. and Michaelis W. (1992). Independent measurement of extinction and backscatter profiles in cirrus clouds by using a combined Raman elastic–backscatter lidar. *Applied Optics* 33: 7113-7131.

Böckmann C. and Niebsch J. (1996). Mollifier Methods for Aerosol Size Distribution. In *Advances in Atmospheric Remote Sensing with Lidar.*, Eds A. Ansmann, et al. New York, Berlin, Heidelberg. Springer: 67-70.

Bohren G. F. and Huffman D. R. (1983) *Absorption and Scattering of Light by Small Particles.* New York: John Wiley and Sons.

Engl H. W., Hanke M. and Neubauer A. (1996). *Regularization of Inverse Problems.* Dordrecht, Boston and London: Kluwer Academic Publishers.

Hanke M., Neubauer A. and Scherzer O. (1995). A convergence analysis of the Landweber iteration for nonlinear ill-posed problems. *Numer. Math.* 72: 21-37.

Louis A. K. (1989). *Inverse und schlecht gestellte Probleme.* Stuttgart: Teubner.

McCormick M. P. and Thomason L. W. (1995). Atmospheric effects ot the Mt. Pinatubo eruption. *Nature* 373: 399-404.

Measures R. M. (1984). *Laser remote sensing, Fundamentals and Applications.* New York: John Wiley and Sons.

Müller D. (1997). Inversionsalgorithmus zur Bestimmung physikalischer Partikeleigenschaften aus Mehrwellenlängen-Lidarmessungen. PhD Thesis Universität Leipzig.

Ramlau R. (1998). A modified Landweber method for nonlinear ill-posed problems. *Inverse Problems*, submitted.

Stein B., Del Guasta M., Kolenda J., Morandi M., Rairoux P., Stefanutti L., Wolf J. P. and Wöste L. (1994). Stratospheric aerosol size distribution from multispectral lidar measurements at Sodankylä during EASOE. *Geophys. Res. Lett.* 21: 1311-1314.

Triebel H. (1978). *Interpolation Theory, Function Spaces, Differential Operators.* Berlin: VEB Deutscher Verlag der Wissenschaften.

LIDAR OBSERVATION OF GRAVITY WAVES IN THE TROPOSPHERE AND LOW STRATOSPHERE ABOVE SOFIA

George V. Kolarov , Ivan V. Grigorov and Orlin I. Vankov
Institute of Electronics - Bulgarien Academy of Sciences
72, Tzarigradsko shosse, 1784 Sofia, BULGARIA
Phone: (0359 2) 743-1487, FAX:(0359 2) 975-3201, E-mail: kolarov@phys.acad.bg

The atmospheric gravity waves propagate in both vertical and horizontal directions and arise depending on the thermodynamic state of the atmosphere. Their amplitude and frequency characteristics are parameters which can be used in the estimate of the energetics and momentum budget of the atmospheric masses, and of the turbulent eddy diffusion. Knowing these characteristics results in a better understanding of the atmospheric processes. [1,2]. Regular fluctuations in the atmospheric transparency that are due to the wave processes can find practical applications in the astrophysics [3]. The predominant part of the lidar gravity waves studies are carried out in the stratosphere and middle atmosphere in the 70 - 100 km range [4,5]. However, elucidating the genesis of this type of waves necessitates investigations in the troposphere and lower stratosphere [6]. Covering the range of altitudes from the ground layer to the stratopause calls for special lidar equipment.

Using a lidar with high sounding repetition rate, we detected wave processes in the troposphere and lower stratosphere. The lidar makes use of a copper-vapor laser with a pulse repetition rate of 5 kHz. It also has the advantage of covering a sounding range of 200 m - 30 km, which is made possible by the use of a receiver operating in the photon counting mode in combination with multichannel accumulation and averaging. Since 1989, we have repeatedly employed the same lidar for similar observations.

The vertical atmospheric sounding experiment was carried out during the night of July 3, 1997, in the city of Sofia. We obtained 256 lidar profiles from layers with $\Delta H = 300$ m at an averaging time of 1 min. The data from each sounded layer was used to build discrete series. These were spectrally analyzed following a classical procedure that included obtaining of periodograms after normalization of the random fluctuations, filtration by a Tukey window, fast Fourrier transformation, and smoothing of the spectrum by means of a rectangular window.

All periodograms obtained from the first ($H = 250$ m) to the 43-rd ($H = 12900$ m) atmospheric layers exhibited a well expressed frequency maximum with a 40-min. period within a 95 % confidence interval. Figure 1 shows periodograms constructed by averaging the data series obtained from each ten consecutive layers. In contrast, the periodograms from altitudes over 15 km, had no expressed lines that could be related to wave processes.

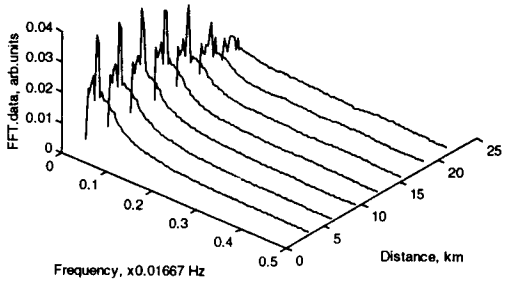


Figure1. Power specters of lidar signals from atmospheric layers whit thickness 3000 m.

The assumption of a single wave process within the entire range of the troposphere and the stratopause was confirmed via combining the lidar signals from neighboring layers up to 15 km and processing the single data series thus obtained following the same spectral analysis procedure (Figure.2).

The atmospheric wave process, shown by us, has practically the same period for all altitudes, including the tropopause and part of the stratosphere. The measured ground wind velocity

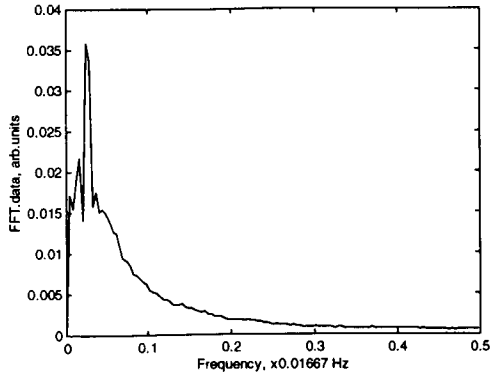


Figure2. Power specter of lidar signals integrated from all sounding atmospheric layers

was 2 m s^{-1}. The lidar was located at a distance of 10 km on the leeward side of a mountain with an altitude of 1600 m above the lidar point. It is possible that the gravity wave have orographic origin. On the other hand, the low wind velocity makes this hypothesis doubtful.

References

1. Gossard E.E. end Hooke W.H.,(1975), Waves in the Atmosphere, Elsevier Scien.Pub.Co, Amsterdam.

2. Manson, A.H., (1990), Gravity Wave Horizontal and Vertical Wavelengths:An Update of Measurements in the Measopause Region(~80-100 km), J. Atmos.Sci.,**41**, 2765-2773.

3. Dermendjiev, V.N., Kolarov, G.V., Mitsev, Ts.A., (1992), Intensity Oscillations of the Fe XIV (λ=530.3nm) Solar Corona: Disturbances Due to the Wave Processes in the Earth's Atmosphere, Solar Physics, **137**,199-202.

4. Chanin, M.L. and Hauchecorne, A. (1981), lidarobservation of gravityand tidal waves in the stratosphere and mesosphere, J.Geophys.Res.,**86**,9715

5. Stefanutti, L., M. Morandi, F. Castagnoli, B. Radicati, (1984), Lidar stratospheric aerosol measurements from 1982 to today. Analysis of short-time aerosol fluctuations, SPIE,**492**, ECOOSA'84,186-193

6. Lyadjin, V.A., (1990), Possibility of Reveal Orographic Perturbations in the Stratosphere by Lidar Techniques, 15 ILRC, Tomsk, USSR, part 1, 288-290

Separation of Rayleigh and Aerosol Scattering Using Pure Rotational Raman Scattering

D. M. Simonich and B. R. Clemesha
Aeronomy Department, Instituto Nacional de Pesquisas Espaciais – INPE
C.P. 515, São José dos Campos, SP, 12201-970, Brazil
Phone: (12) 345-6954, FAX: (12) 345-6952, E-mail: simonich@laser.inpe.br

1. Introduction

One of the major problems in determining atmospheric temperature from laser radar measurements of Rayleigh backscatter is the elimination of the contribution from volcanic aerosols. We normally estimate this factor by comparing our data to a standard atmosphere derived from 2 years of atmospheric sounding data at our location. This procedure is adequate for use in determining atmospheric density and aerosol scattering ratios but to use it to derive the atmospheric temperature profile could lead to errors. For this reason we currently only reduce our data for temperature down to 35 km. so that there is no aerosol contribution. One technique, which has been used by Keckhut et al. (1990), measures vibrational Raman scattering and, since Raman scattering is only from molecules, they obtained the Rayleigh scattering in the region 12 to 30 km. This technique can only be used with low aerosol scattering since the wavelength of vibrational Raman scattering is sufficiently removed from the laser emission line to suffer different extinction. To calculate this difference one must make some assumptions about the aerosol characteristics. If one uses pure rotational Raman scattering this problem does not arise since the Raman scattering wavelengths for rotational Raman are extremely close to the stimulating wavelength.

Nedeljkovic et al. (1993) used a rotational Raman lidar that measured the intensity of the scattered signal from the anti-Stokes spectrum in 2 narrow bands separated by 1.3 nm. Since the shape of the anti-Stokes spectrum depends upon the atmospheric temperature, the ratio of the two signals at a given height is proportional to the temperature at that height. The disadvantage of this technique is that it requires two complete photon-counting channels just for the rotational Raman part of the measurement.

2. Single Raman channel

We have developed a scheme that uses only one photon counting channel to obtain the Raman scattering in the region 10 to 35 km. Since modern interference filters are low loss, almost all of what is not transmitted by the filter is reflected. Thus our receiver uses one interference filter for the laser line and as well as acting as a wavelength separator by reflecting the Raman scattered signal. This gives a substantial reduction in the intensity of the Rayleigh-aerosol scattering sent to the Raman channel. Figure 1 shows the total transmission of both channels using reflection and transmission data supplied by the manufacturer plotted on a linear scale.

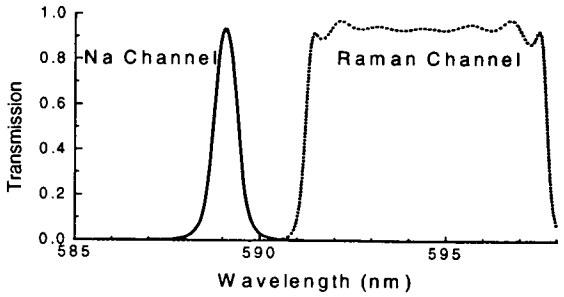


Figure 1. Total transmission of the receiver channels.

In order to get sufficient rejection of the Rayleigh-Aerosol scattered signal, the Raman channel filter cuts off some of the lines close to 589 nm. Figure 2 shows the Total transmission of the Raman channel on a log scale as well as the scattered lines for N_2 and O_2 at a temperature of 220°K.

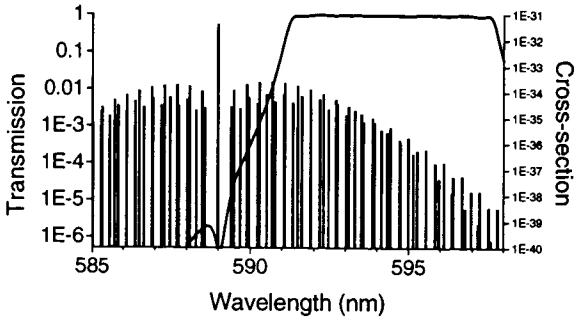


Figure 2 Total transmission of the Raman channel on a log scale and the scattering cross sections for N_2 and O_2 at a temperature of 220°K.

We see that the Rayleigh-Aerosol scattered signal present in the Raman channel is decreased by at least 10^{5}. Thus there should be almost no contamination

of the Raman channel due to aerosol scattering. This is an essential part of the scheme.

3. Scattering Simulation

Because the Raman channel does not respond uniformly to all the Raman lines in the scattered spectrum, the measured signal can not directly determine the density of $N_2 + O_2$. It is possible to choose a filter passband such that the variation of the signal with temperature is quite small (around 1 %) over the range of temperatures of interest (about 190 to 260 °K). Unfortunately a filter which meets the necessary cutoff and bandwidth conditions costs about 13,000 dollars which is hard to justify. Since we can't just use the scattering from the Raman channel to get the Rayleigh density over the region of interest, we use the total transmission of the Raman channel in an iterative process to obtain the temperature distribution in the region 10 to 35 km. The procedure is to first construct a table of effective scattering cross sections including both N_2 and O_2 and the total Raman channel transmission at each of these wavelengths for all temperatures in the range of interest. We then start with a standard temperature profile and from it derive the $N_2 + O_2$ density profile. Assuming that the atmosphere is in hydrostatic equilibrium and obeys the ideal gas law we derive a temperature profile from this density profile fixing the pressure at the highest height and use the procedure of Hauchecorne and Chanin (1980). We then use this new temperature profile to execute another iteration and repeat the process until the profile has converged to a stable value.

In order to test this procedure we did some simulations of the lidar operation. We started with a temperature profile obtained from a July average of radiosonde data at the Sao Paulo airport (about 100 km from our location). From this we derived a atmospheric density profile using the method described in Hauchecorne and Chanin (1980). This density profile served as the atmosphere for our simulation.

We then simulated the passage of our laser beam through this atmosphere. Our laser is used to measure atmospheric sodium so the wavelength is 589 nm. and the bandwidth is about 6 pm. The atmosphere was assumed to have a constant composition with height of 78% N_2 and 20.9% O_2. The computation of the scattering cross sections follows the work of Penney et al. (1974) and Inaba (1976). Using the temperature profile which was used to derive the atmospheric density profile, we calculated the effective scattering cross section profile for Raman scattering including the total transmission of the Raman channel. This together with the atmospheric density profile and the N_2 and O_2 ratios above was used to calculate a received signal for the Raman channel. The Rayleigh channel simulation included a scattering ratio profile of trapezoidal shape with a constant maximum value over a 5 km. range to simulate aerosol scattering. The resulting scattering profiles were then used in the data reduction program to obtain the Rayleigh density, the scattering ratio and the Raman temperature profiles.

In figure 3 we present the results of a simulation which had a maximum scattering ratio of 10. The crossed points are the input temperature profile derived from the Sao Paulo radiosonde data. The dashed curve is the standard temperature profile used to start the reduction of the Raman channel data. The solid curve is the calculated temperature profile after 10 iterations of the procedure described above. The largest error below 40 km (which is the region for which we would use this data) is at the tropopause and is 3% less than the data input used for the simulation. One can see that even starting with a substantially different temperature to reduce the Raman data the resulting temperature profile is quite close to the original one. This temperature is only used as part of the reduction to determine the $N_2 + O_2$ density profile. The final temperature profile is derived from the Rayleigh data after the aerosol scattering contribution has been removed.

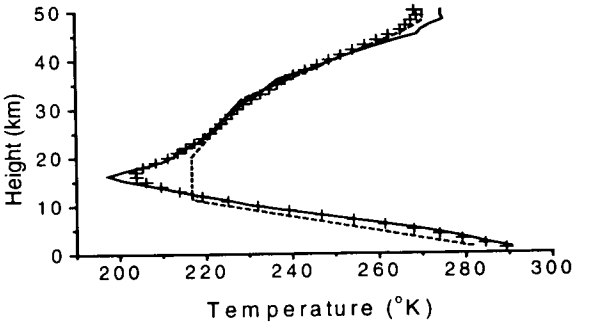


Figure 3 Temperature versus height for the simulation. The crosses are the temperature profile from Sao Paulo used as the input to the simulation. The dashed line is the initial temperature profile used in the reduction. The solid curve is the result of the data reduction.

Figure 4 shows the result of the scattering ratio retrieval. The values are extremely close to the input data the largest error being a half of a percent. Dividing the recovered Rayleigh density by the original input density gave errors of less than 2% above 40 km and less than 1% from 35 km downward.

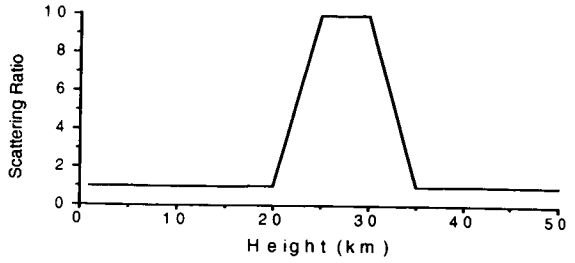


Figure 4. The retrieved scattering ratio profile for this simulation.

4. Conclusions

We have shown that it is possible to obtain the atmospheric density of only N_2 + O_2 using Raman scattering which can then be used to remove the aerosol scattering from the Rayleigh scattering channel profile giving a pure Rayleigh density profile. This density profile can then be used to derive the temperature profile for the atmosphere from low altitudes to the upper limit of reliable Rayleigh data.

5. Acknowledgements

This work was partially funded by the Fundação de Amparo À Pesquisa do Estado de São Paulo – FAPESP under grant number 96/6346-9.

References

Hauchecorne, A. and Chanin, M. L. (1980). Density and temperature profiles obtained by lidar between 35 and 70 km.*Geophys. Res. Lett.* 7(8):565-568.

Inaba, H. (1976). Detection of atoms and molecules by Raman scattering and resonance fluorescence. In (1976) *Laser monitoring of the atmosphere: Topics in applied physics Vol 14*, pages 153-236, Springer-Verlag, New York,N.Y.

Keckhut, P., Chanin, M. L. and Hauchecorne, A. (1990). Stratosphere temperature measurement using Raman lidar.*Appl. Opt.*, 29(34):5182-5186.

Nedeljkovic, D., Hauchecorne, A., and Chanin, M. L. (1993). Rotational Raman lidar to measure the atmospheric temperature from the ground to 30 km.*IEEE Trans. Geosci. Rem. Sensing* 31(1):90-101.

Penney, C. M., St. Peters, R. L. and Lapp,M. (1974). Absolute rotational Raman cross sections for N_2, O_2 and CO_2.*J. Opt. Soc. Am.* 64(5):712-716.

Two-Wavelength Laser Sounding of Stratospheric Aerosol Layer After Pinatubo Eruption

A.P. Chaikovsky, A.P. Ivanov, M.M. Korol, F.P. Osipenko, V.N. Shcherbakov,
Stepanov Institute of Physics, National academy of sciences of Belarus.
pr. F. Skoriny 68, Minsk, 220602 Belarus
Phone: (375 17) 268-5891, FAX: (375 17) 239-3131, E-mail: chaikov@ifanbel.bas-net.by

1. Introduction

The lidar station of the Institute of Physics, Belarus Academy of Sciences (Minsk, 53.85 N, 27.5 E) is providing systematic lidar monitoring of the stratospheric aerosol layer (SAL) since 1985. Immediately after the Pinatubo eruption, stratospheric sounding was by a two-wavelength lidar (532 and 1064 nm) with synchronous measurements of backscatter depolarization. Previous work (Ivanov et al., 1997) gave the results on the dynamics of altitude profiles of aerosol concentration by the data on 532-nm laser sounding. This investigation evaluates the set comprising the profiles of the two-wavelength ratio of aerosol backscatter coefficients to study the microstructural variability of aerosol particles. The methodology of two-wavelength sounding data processing and the results on the processing of the measurements are given here.

The operational utility of a two-wavelength lidar to monitor the SAL depends on some features in a relationship between microstructural parameters of aerosol particles and ratio $\gamma(h) = \beta_a(h,\lambda_2)/\beta_a(h,\lambda_1)$ of aerosol backscatter coefficients $\beta_a(h,\lambda_1)$ and $\beta_a(h,\lambda_2)$ at two wavelengths λ_1=532 and λ_2=1064 nm. The calculations of γ value for several stratospheric aerosol models have been made at some expected parameters of particle size distribution. Figure 1 illustrates typical dependencies of γ on parameter r_0 for the model of single-mode log-normal aerosol particles' size distribution $n(r)$

$$n(r) = \frac{1}{\sqrt{2\pi}\, r \ln\sigma} \exp\left(\frac{\ln^2 r/r_0}{2\ln^2\sigma}\right) \quad (1)$$

with σ equal to 1.60 and 1.92. The tendency to γ increase with r_0 is seen, but it is not monotonic in the vicinity of r_0=0.1 μ m value, which is typical of background conditions. For different size distribution models, optical parameter γ would be similar if the efficient parameters of the distribution function, $r_{3/2}$ and $\sigma_{eff} = (r_{4/3}/r_{3/2}) - 1$, are close to each other.

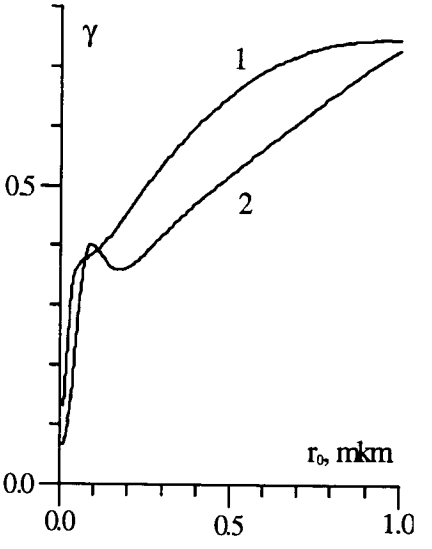


Figure 1. The ratio γ vs r_0; σ =1.604 (1) and σ = 1.92 (2).

Measurement of particles' size distributions show that in some cases stratospheric aerosols were, in fact, a mixture of several fractions. In the absence of any additional information on aerosol size distribution, measurements of γ are only an indicator of changes in particle sizes and just demonstrate the tendency in variations of particles' efficient radius.

Thus, although there is a little possibility to solve the inverse problem on the reconstruction of aerosol size distribution by two-wavelength sounding data, one can detect particles' changes and describe their tendencies. This information is, certainly, significant for practice, if lidar observations serve for just monitoring purposes.

2. Technique for measuring aerosol optical parameters

We process data of two-wavelength polarization sounding to retrieve profiles of the following SAL parameters: 1) the backscatter ratio $R(h,\lambda_1) = [\beta_a(h,\lambda_1) + \beta_m(h,\lambda_1)]/\beta_m(h,\lambda_1)$, where $\beta_m(h,\lambda_1)$ is the molecular backscatter coefficient at

wavelength λ_1=532 nm; 2) the ratio of aerosol backscatter coefficients at two wavelengths, $\gamma(h)$, 3) the aerosol extinction coefficient, $\varepsilon_a(h,\lambda_i)$ i=1,2. The processing algorithm used should rather correctly take aerosol extinction into account as far as the stratospheric aerosol depth was high enough (about 0.1 to 0.2 at 532 nm) for a long time after the Pinatubo eruption. Moreover, estimations of aerosol layer optical depth values in the stratosphere from lidar data immediately are interesting for a wide range of atmospheric optical problems.

The atmospheric optical parameters $\beta_a(h,\lambda_i)$ and $\varepsilon_a(h,\lambda_i)$, i=1,2, were found as the solutions to the set of four differential equations by the iterative method (Ivanov et al., 1996). The two equations are routine lidar equations for wavelengths λ_i, i=1,2. The two remaining equations represent a relationship between $\beta_a(\lambda_i)$ and $\varepsilon_a(\lambda_i)$.

From a physical viewpoint, an opportunity to determine such a relationship is that both these parameters are related to the size distribution of aerosol particles and their composition. If the spectral dependence of one of the parameters was measured rather correctly, then the aerosol size distribution can be reconstructed quite certainly on this basis to provide, at the next step, the calculation of the spectrum of the second parameter. Owing to insufficient information content in two-wavelength sounding data for our case, we are solving essentially less general problem on searching the relations of the kind $\varepsilon_a(\lambda_i)=F(\beta_a(\lambda_i),\beta_a(\lambda_j))$, i,j = 1,2, $i \neq j$. To this end, we have used the elaborated methodology (Chaikovsky et al., 1994; Tauroginskaya et al., 1994) giving the desired relations as linear regressions of the following form

$$\varepsilon(\lambda_i)=\sum_{j=1}^{2} a_{ij}\beta_a(\lambda_j), \qquad (2)$$

A set of expected distributions $n(r)$ determines the statistical ensemble of $\beta_a(\lambda_i)$ quantities, for which optimal values of coefficients a_{ij} are derived by methods elaborated in mathematical statistics. There is no an absolute right-hand term in Eqs.(2), so these relations are valid irrespective of aerosol particles' concentration.

To find coefficients a_{ij}, we have preliminary constructed a statistical model of stratospheric aerosols by evaluating available reference data on the microstructure of these aerosols after volcanic eruptions. This has enabled us to isolate background, fine, and coarse aerosol fractions, to relate corresponding log-normal size distributions with them, and to determine ranges of expected variations in the parameters of the distributions and in the relative concentration values.

It turned out that the error in Eqs.(2) was below 20%, and the original statistical ensemble should be divided by two ensembles. The criterion for such a division was γ value ($\gamma \leq 0.38$ and $\gamma > 0.38$, respectively).

So, we have obtained four equations with four unknowns, two sets of coefficients a_{ij} being used in Eqs.(2) as a function of a γ value.

The main source of errors in estimated $\beta_a(\lambda_i)$ by processing the experimental two-wavelength sounding data was inaccuracy in calibration procedure that was being made routinely by the atmospheric layer above 30 km. The errors in regression equations (2) made the decisive contribution to the errors in estimated optical depth values of stratospheric layers.

3. Experimental results

Routine observations by using the two-wavelength lidar were being made since the end of 1991. The evaluations of the variability in backscatter ratio $R(h,\lambda_1)$ were given in (Ivanov et al., 1997) to characterize, in the first turn, the dynamics of the altitude profiles of aerosol particles' concentration. The next basic results were obtained by processing the set of ratio profiles $\gamma(h)$.

There were observed variations in profiles $\gamma(h)$ during the formation of the SAL to be due to the volcanic eruption and its relaxation to the background conditions. Figure 2 shows ratio profiles $\gamma(h)$ and $R(h,\lambda_1)$ that are the arithmetic means of the observations during about a month and correspond to different stages of the SAL variability process. The ratio γ was seen to grow with altitude from 10 to 25 km during the SAL formation at the end of 1991 and the beginning of 1992. Thereafter, $\gamma(h)$ profiles show a tendency to decreasing γ with altitude increasing that is, probably, related with the decreasing effective radius of aerosol particles. Ratio $\gamma(h)$ is featured by a largest gradient at altitudes above the maximum of $R(h,\lambda_1)$.

Figure 3 illustrates yearly distributions of the integral backscatter coefficient within the 13-30 km layer and of ratio γ. These distributions were averaged over four stratospheric layers. Decreasing γ four all four layers, except that for 10-13 km

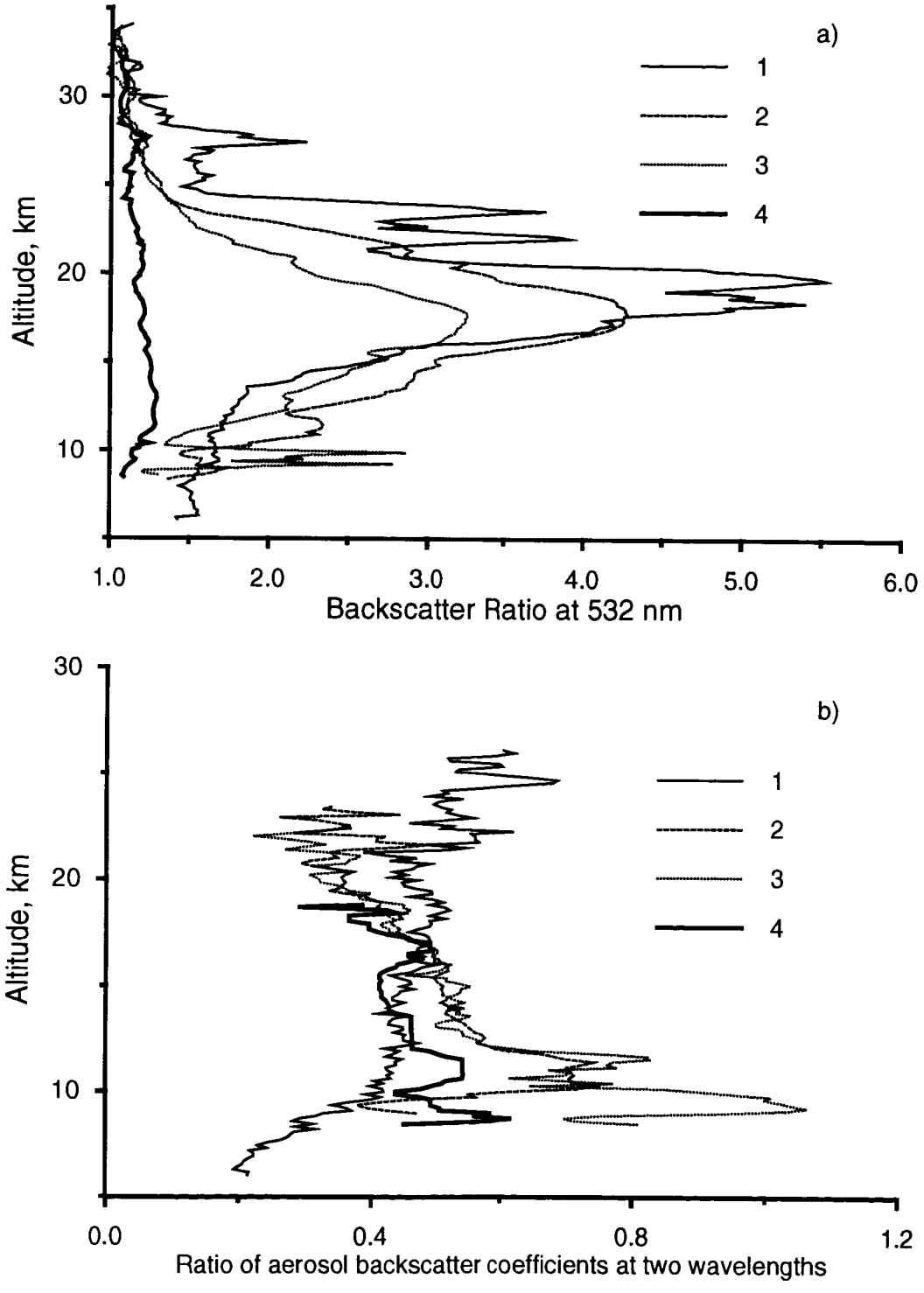


Figure 2. The profiles ratio profiles $\gamma(h)$ (a) and $R(h,\lambda_1)$ (b) observed on 1 - December , 1991; 2 - June, 1992; 3 - February, 1993; 4 - February, 1994;

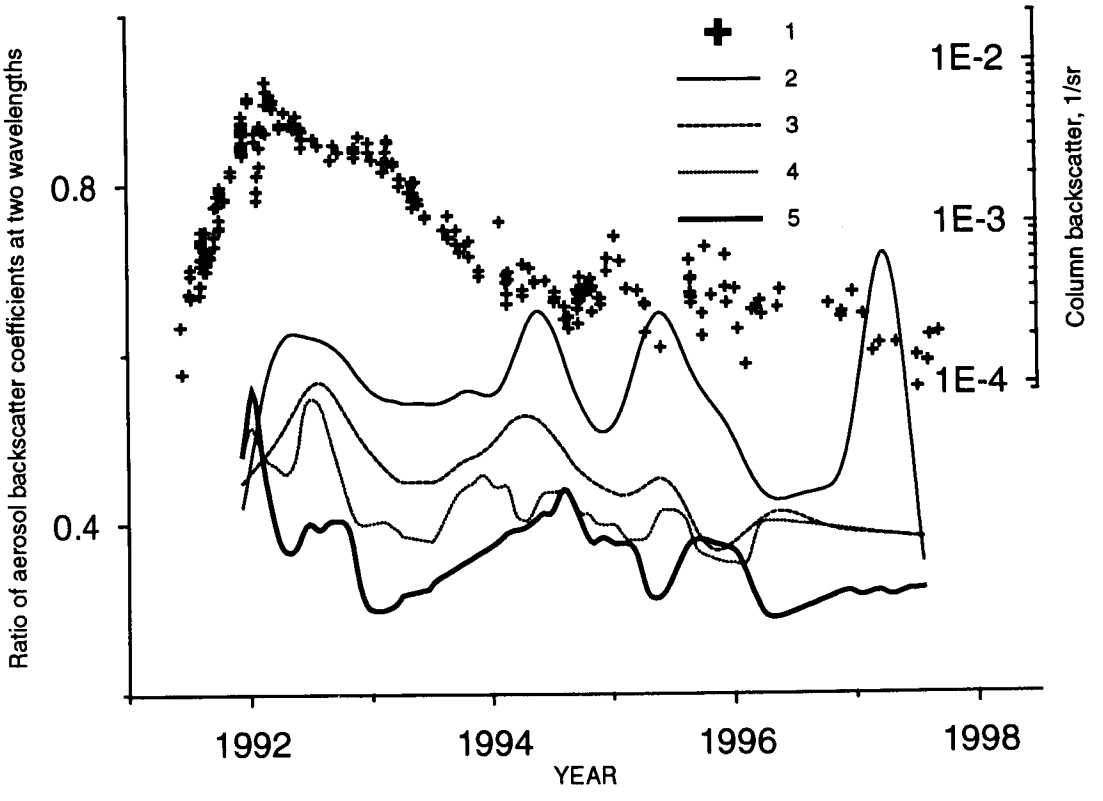


Figure 3 The time transformation of the SAL optical parameters: 1) - integral aerosol backscatter coefficient 2-5) - the ratio γ that are the arithmetic means at layers 10-13, 13-14, 15-20, 20-25 km, respectively

layer, is seen after the optical depth has gained a maximum at the beginning of 1992. Unstable γ values within the lowest layer can be mainly explained by the effects of *Cirrus* clouds during observations. In some situations, however, the joint analysis of two-wavelength lidar data, depolarization of sounding signals, and meteorological parameters' profiles gives certain evidences on the appearance of a coarse non-spherical aerosol fraction in the lowest region of the SAL.

Above 13 km, γ values decreased gradually to the level characteristic of the background condition of the SAL. This was accompanied by strong temporal fluctuations of γ that may be related with the seasonal rearrangement of stratospheric air mass circulation.

References

Chaikovsky A.P., Shcherbakov V.N., Tauroginskaya S.B. (1994). Technique for determining atmospheric aerosol optical parameters by multi-wavelength laser sounding. *17 ILRC* (1994) 17-19.

Ivanov A.P., Chaikovsky A.P., Shcherbakov A.P., Osipenko F.P., Korol M.M., and Tauroginskaya S.B. (1996). Two-wavelength lidar measurement technique and data on stratospheric aerosol optical parameters. *Atmos. Oceanic Opt.*, **9**(12): 1009-1014.

Ivanov A.P., Osipenko F.P., Chaikovsky A.P., Shcherbakov A.P., and Tauroginskaya S.B. (1997). Dynamics of optical parameters of Stratospheric aerosol layer following the eruotion of Mt.Pinatubo from liddr data. *Izvestiya, Atmos. Oceanic Phys.*,**33**(2): 184-189.

Tauroginskaya S.B., Chaikovsky A.P., and Shcherbakov A.P.. (1994). Optimized linear estimated of integral parameters of multifricomponent aerosol. *Izvestiya, Atmos. Oceanic Phys.*,**7**(2).

12 years of Stratospheric Aerosol Measurements by Lidar Sounding over Obninsk, Russia (55° N, 38° E)

S. S. Khmelevtsov, Yu. G. Kaufman, A. S. Khmelevtsov

Institute of Experimental Meteorology, Lenin St 82 Obninsk Kaluga Reg. Russia
FAX: +7 (095)-255-22-25 E-mail: eridan@meteo.ru

Abstract. The results of stratospheric aerosol measurements by lidar sounding over Obninsk, Russia since 1985 are presented.

1 Introduction

Laser sounding was testified by the numerous researchers as one of the most adequate method to obtain the data on aerosol radiative forcing for climate investigation and for preparation radiative parts for climate models (Kaufman et al., 1982).

Vertical profiles of stratospheric aerosol backscattering ratio were measured over Obninsk (Russia) by two lidars "Maket-1" (Kaufman et al., 1993) and "LD-2" since 1985. Both of them were designed as multifunctional devices, intended for research of SA concentration. Nd:YAG lasers (532 nm, 40 mJ/pulse, 25 Hz) and multichannel photon counter detecting system are used in them. "Maket-1" receiving telescope is 50 cm diameter and "LD-2" – 30 cm.

There were no measurements during the period from November 1989 to January 1990 because the lidar was used for research expedition on Hawaii and Samoa to conduct intercalibration measurements jointly with the USA lidar (Kaufman et al., 1993).

2 Observations

The backscattering ratio vertical profiles of SA after Mt. Pinatubo eruption, measured over Obninsk by the lidar, are shown in Figure 1.

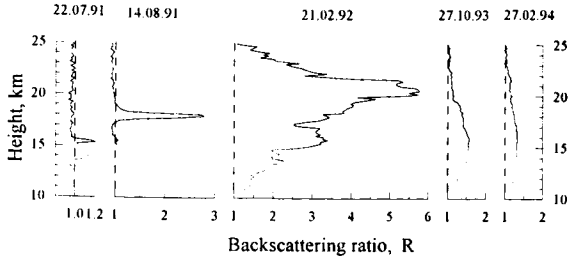


Figure 1. The backscattering ratio vertical profiles of SA after Mt. Pinatubo eruption, measured over Obninsk

First arrival of volcanic aerosol just above the tropopause was measured on 22 July. New aerosol cloud with large concentration appeared in August 14, 1991. Main body of the volcanic aerosol layer reached Obninsk in February 1992. From January 5, 1992 to January 25, 1992 the decay of SA was due to the huge stratospheric warming.

Integrated backscattering coefficient for the range of altitudes from 15 to 30 km (Figure 2) was calculated using backscattering ratio profiles, some of them are shown in Figure 1. It contains the "background" aerosol during 1988-1989, decay of Mt. Pinatubo eruption after 1991 and new "background" period in 1995-1997.

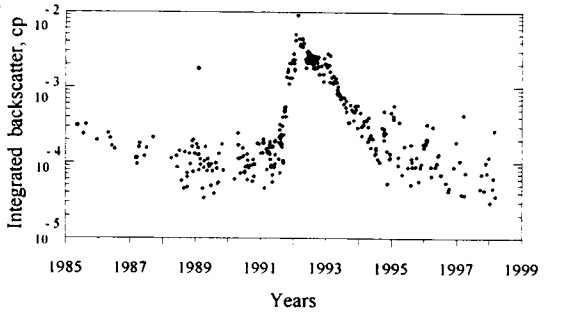


Figure 2. Integrated backscattering coefficient for the range of the altitudes from 15 to 30 km

Obninsk measurement data supplements the data of laser sounding in Garmish-Partenkirchen and other lidar sites (Hayashida et al., 1993; Jager et al., 1994).

Some values integrated backscattering coefficient measured in February – March 1989, 1995 – 1998 significantly exceed background level. Most probable reason of this phenomenon is the forming the polar stratospheric clouds in the moderate latitudes in that season.

Obninsk lidar data sets were used for evaluation of decay time and dispersal of the stratospheric aerosol. For Mt. Pinatubo the decay (1/e) following maximum of integrated aerosol backscatter was 11 months.

Optical depth of the stratospheric aerosol layer from 15 to 30 km over Obninsk was also evaluated. Extinction/backscattering convertion factors necessary to assess the optical depth were taken from (Jager et al., 1994). They are shown in Figure 3.

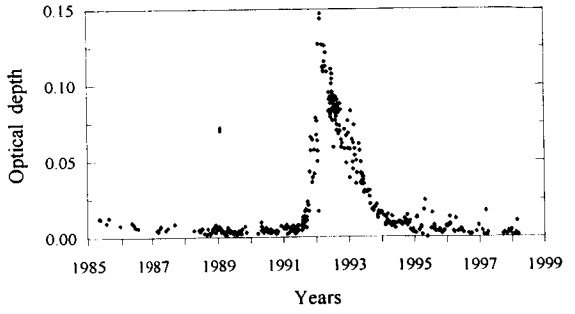


Figure 3. Optical depth of the SA layer from 15 to 30 km over Obninsk

Carbonyl sulphide (OCS) is considered to be responsible for background level of stratospheric aerosol (Crutzen, 1976). OCS diffuses into the stratosphere and produces sulphuric acid vapour. But the measured concentration of this gas in the stratosphere doesn't increase and presents at the 0.5 ppbv since at least 1976.

The suggestion that the source of aerosol mass increase by 5% per year might be aircrafts flying near or up of tropopause in the North was discussed in (Hofmann, 1990). The assessments, made in (Jager, 1991), indicate the dramatically increase of the mass of SA (12% per year), whereas the total stratospheric particle number is similar in 1979 and 1988.

On the contrary, the authors (Hitchman et al., 1994) created a global climatology of the stratospheric aerosol by combining the observations from the SAGE I, SAGE II and SAM I instruments and suggested that aerosol layer is distinctly volcanic in nature and background stratospheric layer was never achieved within the period from 1979 to 1990.

Data analysis of Figure 1 points out that the background aerosol grew slightly from 1989 to 1997.

References

Crutzen, P.J. (1976). The possible importance of CSO for the sulphate layer of the stratosphere. *Geophys. Res. Lett.*, **3**, p. 73-76.

ayashida, S., Sasano, Y. (1993). Stratospheric aerosol change in the early stage of volcanic disturbance by the Pinatubo eruption observed over Tsukuba, Japan. *Geophys. Res. Lett.*, **20**, p. 575-578.

Hitchman, D.J., McKay, M., Trepte, C. R. (1994). *Journ. Geophys. Res.*, **99**, N D10, p. 20,689-20,700.

Hofmann, D.J. (1990). Increase in the Stratospheric Background Sulphuric Acid Aerosol mass in the Past 10 Years. *Science*, **248**.

Jager, H., Freudenthaler, V., Homburg, F. (1994). Stratospheric aerosols and Pinatubo eruption clouds. 17 ILRC, Abstracts of Papers, Sendai, Japan (1994, July 25-29), p. 371-374.

Jager, H. (1991). Stratospheric aerosols: Observations, trends, and effects. *J. Aerosol Sci.*, **22,** Suppl. 1, p. S517-S520.

Kaufman, Yu.G., Khmelevtsov, S.S., DeFoor T.E. (1993). Lidar measurements of stratospheric aerosol during the SAGA III expedition. *J. Geophys. Res.*, **98,** p. 16,909-16,913.

Kaufman, Yu.G., Kolomeev, M.P., Khmelevtsov, S.S. (1982). Stratospheric aerosol and it impact on the Earth climate. *Izv. AN SSSR, Phys. Atmos. and Ocean*, **18**, N 12, p. 1256-1260.

Large Antropogenic Burning Events and Cirrus as Observed by Lidar in Southern Hemisphere at Buenos Aires (Argentina).

Mario Lavorato, Javier Fochesatto, Pablo Cesarano, Eduardo Quel
División Radar Láser-CEILAP (CITEFA-CONICET)-
Zufriategui 4380-1603 Villa Martelli-Argentina
lavorato@udceilap.edu.ar.

Laurent Sauvage, Pierre Flamant
Laboratoire de Météorologie Dynamique. Ecole Polytechnique.Palaiseau. France.
flamant@lmdx04.polytechnique.fr

Jacques Pelon
Servicie d'Aeronomie du CNRS. Universitè Paris-6. France
jacques.pelon@aero.jussieu.fr

Abstract. Large antropogenic burning events and cirrus clouds were measured with two backscatetter lidar systems operating simultaneously: one operating at 532 nm and the second at 308 nm, both located at the same site in a urban area in the Buenos Aires suburb (34.6 S, 58.5 W). The two lidar systems pointing vertically. The downward solar radiation flux at the surface is also measured by a pyranometer. In addition to these measurements daily information of radiosoundings at the nearby international airport are collected. Biomass burnings taking place in the tropical South America were observed, due to the large scale circulation, that brings the airmasses from the tropical area over Argentina and Buenos Aires. Several events have been recorded. In addition, cirrus optical parameters were documented during the same period.

Lidar and Radiometer Sounding of Cloud Properties

C. M. R. Platt*, S. A. Young†, R. T. Austin*, and M. C. Pickett†
*Department of Atmospheric Science, Colorado State University, Fort Collins, Colorado 80523-1371, USA
†CSIRO Division of Atmospheric Research, Aspendale, Victoria, Australia
Corresponding author: C. M. R. Platt, Phone: (970) 491-8259, Fax: (970) 491-8449
E-mail: martin@reef.atmos.colostate.edu

Clouds at various altitudes and latitudes have been investigated extensively in the southern hemisphere during the past two decades with lidar and infrared radiometry (LIRAD) (Platt et al., 1987). Data obtained in the late nineteen-seventies and eighties have been extended more recently by observations of mid-latitude boundary layer and mixed phase clouds and equatorial and tropical cirrus and storm anvils. The LIRAD method has been augmented by observations of water vapor path with microwave radiometry. Further analyses are being made from simultaneous millimeter radar soundings, data that will not be discussed in this paper.

Observations are made by a high-power pulsed visible lidar (694 or 532 nm) and a narrow-beam infrared radiometer with channels typically at 10.84 and 8.62 microns. The cloud height and structure is measured at 1 to 10 Hz by the lidar and the infrared radiance is measured continuously by the radiometer. A microwave radiometer, designed by the Environmental Technology Laboratory, NOAA, Boulder (Westwater et al., 1995), measures the water vapor path and liquid water path at 23.87 and 31.65 GHz. This instrument was available for observations of equatorial and tropical cirrus.

Radiosonde data are needed to obtain temperature and humidity profiles through the clouds in order to calculate the infrared emittance and optical depth. The visible optical depth is retrieved by various methods from the calibrated lidar profiles. Correlation of the lidar integrated attenuated backscatter with the infrared emittance leads to further information on the cloud microphysical structure, cloud particle effective radius and (for cirrus clouds) the ice crystal habit. A modified two-component forward iterative integration is used to retrieve the cloud backscatter coefficients and optical depth. The cloud visible optical depth is also retrieved in thin cirrus by calculating the transmittance of scattered radiation from above the cloud, using a model of Rayleigh molecular backscatter with allowances for aerosol scatter (Young, 1995). Multiple scattering effects in the lidar beam are significant. They have been studied by Platt (1981) among others.

The data are enhanced considerably by the addition of a detection channel to measure the depolarized component of the scattered radiation, the transmitted laser pulse radiation being linearly polarized. Data obtained on mid-level mixed phase clouds indicate the considerable variability obtained in these clouds (Young et al., 1998). Lidar depolarization observations indicate the different signatures from oriented hexagonal plates, fall-streaks, more "normal" ice clouds, and water clouds. The latter signature arises from multiple scattering within water clouds.

Observations on cirrus clouds within 2 degrees of the equator revealed deep layers of clouds, even in the absence of thunderstorms in the vicinity. These observations were taken in the ARM-sponsored Pilot Radiation Observation Experiment (PROBE) at Kavieng, New Ireland, Papua New Guinea (Platt et al., 1998). These clouds appeared to form in deep moist layers that were often observed in the upper troposphere. The infrared emittance, for a given temperature, was found to be higher than in mid-latitude clouds. Cirrus cells appeared to develop during the morning and early afternoon and to dissipate towards nightfall.

Tropical clouds at 12°S in Northern Australia were investigated in the ARM-sponsored Maritime Continent Thunderstorm Experiment (MCTEX). Observations revealed frequent low-density stratified layers of cirrus just below, and sometimes at, the tropopause. These layers persisted for many hours both before and after thunderstorms had developed and dissipated. An example is shown in Figure 1. Several storm anvils were also observed in various stages of dissipation.

The LIRAD method has also been used to observe the properties of marine stratocumulus clouds. Groundbased observations were made at Cape Grim, Tasmania during the Southern Hemisphere Cloud Experiment. *In situ* aircraft measurements of cloud drop distribution were also made which could be compared with the LIRAD results. This enabled values for the multiple scattering factor to be retrieved. Retrieved values were comparable with calculated values. An unexpectedly large fraction of the clouds had emittances well below unity.

When collated, values of the emittance and IR optical depth showed marked trends with temperature, as would be expected, based on the decrease in the supply of moisture with increasing altitude in the troposphere. Similarly, values of the cloud particle visible backscatter to extinction ratio, retrieved from the integrated attenuated backscatter in optically thick clouds, showed a trend with

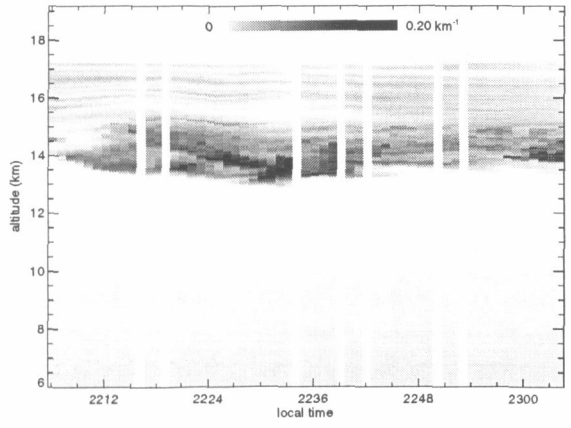


Figure 1: Thin cirrus near the tropopause (17 km) at MCTEX, 4 December 1995.

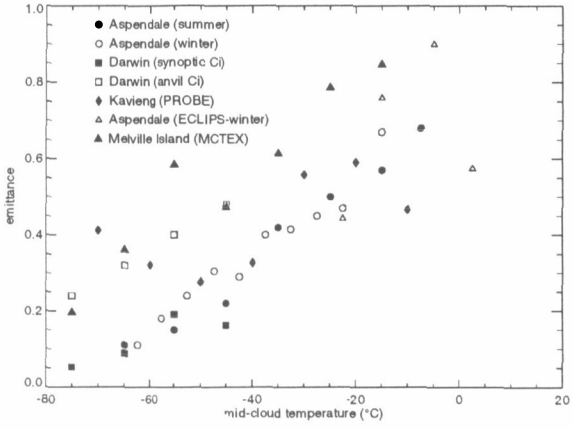


Figure 2: IR emittance variation with temperature for seven experiments.

temperature. This was associated with changing ice crystal habit with temperature, as found in past laboratory and field experiments. The trends in the cloud emittance (10.84 microns) is shown in Figure 2. The Aspendale and Darwin synoptic data are from Platt et al. (1987). The Darwin anvil cirrus data are from Platt et al. (1984). The PROBE data are from Platt et al. (1998), and the ECLIPS data are from Young et al. (1998).

Future progress relies on the availability of *in situ* aircraft data of cloud size distribution, phase, and habit with simultaneous lidar observations. An international program of ground-based lidar observations would be of great benefit to the atmospheric science community. Simultaneous use of other instruments is also desirable. The US Department of Energy Atmospheric Radiation Measurement Program (ARM) is a good example of a program that is making observations with a variety of ground-based instruments and with the aim of making continuous measurements over a period of ten years, augmented by intensive observation periods (IOPs) with aircraft obtaining *in situ* data. Such sites in Oklahoma; Manus Island, Papua New Guinea; and Barrow, Alaska are excellent examples of successful cloud measurement stations.

A more extensive network of measurements is needed. Sites in such a network could be arranged to measure aerosol properties as well as clouds. The observations could be made at sites that are already measuring surface radiative fluxes and other quantities. The networks could also be used for validation of data taken from future passive and active satellite systems.

Acknowledgments

The PROBE and MCTEX observations were sponsored by ARM. Parts of the work were supported by the U. S. Department of Energy, Office of Health and Environmental Research, Grants DE-FG02-92ER61373, DE-FG02-96ER62569, and DE-FG03-94ER61748.

References

Platt, C. M. R., 1981: Remote sounding of high clouds, III: Monte Carlo calculations of multiple-scattered lidar returns. *J. Atmos. Sci.*, **38,** 156–167.

Platt, C. M. R., A. C. Dilley, J. C. Scott, I. J. Barton, and G. L. Stephens, 1984: Remote sounding of high clouds, V: Infrared properties and structure of tropical thunderstorm anvils. *J. Clim. and Appl. Meteor.*, **23,** 1296–1308.

Platt, C. M. R., J. C. Scott, and A. C. Dilley, 1987: Remote sounding of high clouds. Part VI: Optical properties of mid-latitude and tropical cirrus. *J. Atmos. Sci.*, **44,** 729–747.

Platt, C. M. R., S. A. Young, P. J. Manson, G. R. Patterson, S. C. Marsden, and R. T. Austin, 1998: The optical properties of equatorial cirrus from observations in the ARM Pilot Radiation Observation Experiment. *J. Atmos. Sci.*, in press.

Westwater, E. R., J. H. Churnside, J. A. Shaw, J. B. Snider, K. S. Gage, Y. Han, W. Ecklund, A. Riddle, and A. C. Williams, 1995: Ground-based remote sensor observations during the PROBE experiment in the tropical western Pacific. *Proc. IGARSS'95*, Florence, Italy, 10–14 July 1995, 882–886.

Young, S. A., 1995: Analysis of lidar backscatter profiles in optically thin clouds. *Applied Optics*, **34,** 7019–7031.

Young, S. A., C. M. R. Platt, R. T. Austin, and G. R. Patterson, 1998: Optical properties and microphysics of some mid-latitude, mid-level clouds in ECLIPS. To be submitted to *Monthly Weather Review.*

FLUCTUATION CHARACTERISTICS OF THE CLOUD TOP HEIGHT

V. Shamanaev, I. Penner, and G. Kokhanenko

Institute of Atmospheric Optics,
1, Akademicheskii Ave, Tomsk 634055, Russia
Tel: +7 3822 258516
Fax: +7 3822 259086
E-mail: shvs@losa.iao.tomsk.ru

The Institute of Atmospheric Optics has been carrying out airborne lidar sensing of the cloud top height (CTH) primarily of stratocumulus clouds with the average CTH no more than 3 km for some years. The distance from an aircraft to a cloud was determined by several criteria for the CTH based on analysis of a lidar return signal [1]. The flight altitude was measured with the aircraft navigation system and was taken constant. In all measurements we used an excess of the signal amplitude coming from the cloud over a given threshold followed by the increase of the signal amplitude at least for two subsequent range gates as a criterion for the cloud boundary. The threshold was set as the level of the signal from the atmosphere plus the doubled rms noise level.

Thus, a series of the CTH values after preliminary processing represents a random process of the CTH fluctuations about zero mean with unit variance. Low-frequency components that fell outside realistic spatial scales of an individual realization were filtered out. High-frequency components caused by extremal overshoots occurring in the process of determination of the cloud boundary for low signal-to-noise ratios were smoothed with the use of a sliding median filter. In case of sensing of broken cloudiness, discontinuities and omissions arose in the series of the CTH data. Therefore, the procedure for preliminary preparation of lidar sensing data to their further processing by statistical methods comprised formatting of continuous series of the discrete CTH values recorded in a single run.

The initial data are burdened with trends and low-frequency components with periods much longer than the sensing period. Direct combination of individual realizations in the continuous series of the CTH values for a single run in the presence of discontinuous trends would result in significant distortions of the estimated probability density and spectral characteristics. Such trends were filtered out from realizations of limited lengths by fitting of the data with a lower-order polynomial with the use of the least squares method. For the most part, linear trends were filtered out.

Even though the data series were obtained by us for cloud fields that differed greatly, the probability densities of the CTH fluctuations were always close to normal. The data series with the large number of individual CTH measurements in a single run obtained for separate horizontal sections of the sensing path when the aircraft flew along straight lines in different directions above the same cloud field are best described with the Gaussian model of the probability density. For example, this can be seen from Fig. 1 that illustrates the scheme of a flight above the Barents Sea. Real flight routs were somewhat distorted due to the drift of the aircraft.

In general during all our experiments (above the sea surface and above Western Siberian plains) the spectrum of the CTH fluctuations for low stratocumulus clouds had no specific features and obeyed $-5/3$ power law for the significant wavelength range (40 m$<\lambda<$20 km). This agrees with the Kolmogorov-Obukhov theory of the stationary turbulence in the inertial subrange of spatial wavelengths. At the same time, significant deviations toward smaller or larger exponents were observed in individual experiments.

The power densities of the CTH fluctuations shown in Fig. 2 were derived from the data of lidar sensing of cloud formations in the same region but at different stages of their evolution on 27 and 29 November. They characterize the dynamic state and the spatial structure of the cloud field. Thus, for the developing (from the data of meteorological satellite) stratified cloud field on 27 November (Fig. 2a) we obtained the classical ($-5/3$ power law) spectrum of turbulent processes in the entire examined inertial wavelength range (40 m$<\lambda<$10 km). The spectrum shown in Fig. 2b was obtained on 29 November for the stratocumulus cloudiness at the stage of filling (cloud field destruction). The wavelength range for which $-5/3$ power law preserves, is limited from above by the inflection point located at a wavelength of ~100 m and from below by the clearly pronounced outer scale (of the order of 2-4 km). For wavelengths larger than 100 m the rate of decrease of the power spectrum caused by destruction of cloudy cells within the entire decaying cloud field becomes higher.

The outer scale here characterizes the recurrence of the spatial structure of convective clouds that form the examined cloud field.

Reference

1. Shamanaev V. S. On Estimation of the Light Scattering Coefficient within the Region of Cloud Boundary. Atmospheric and Oceanic Optics, v. 5, No. 7, 702-707 (1992).

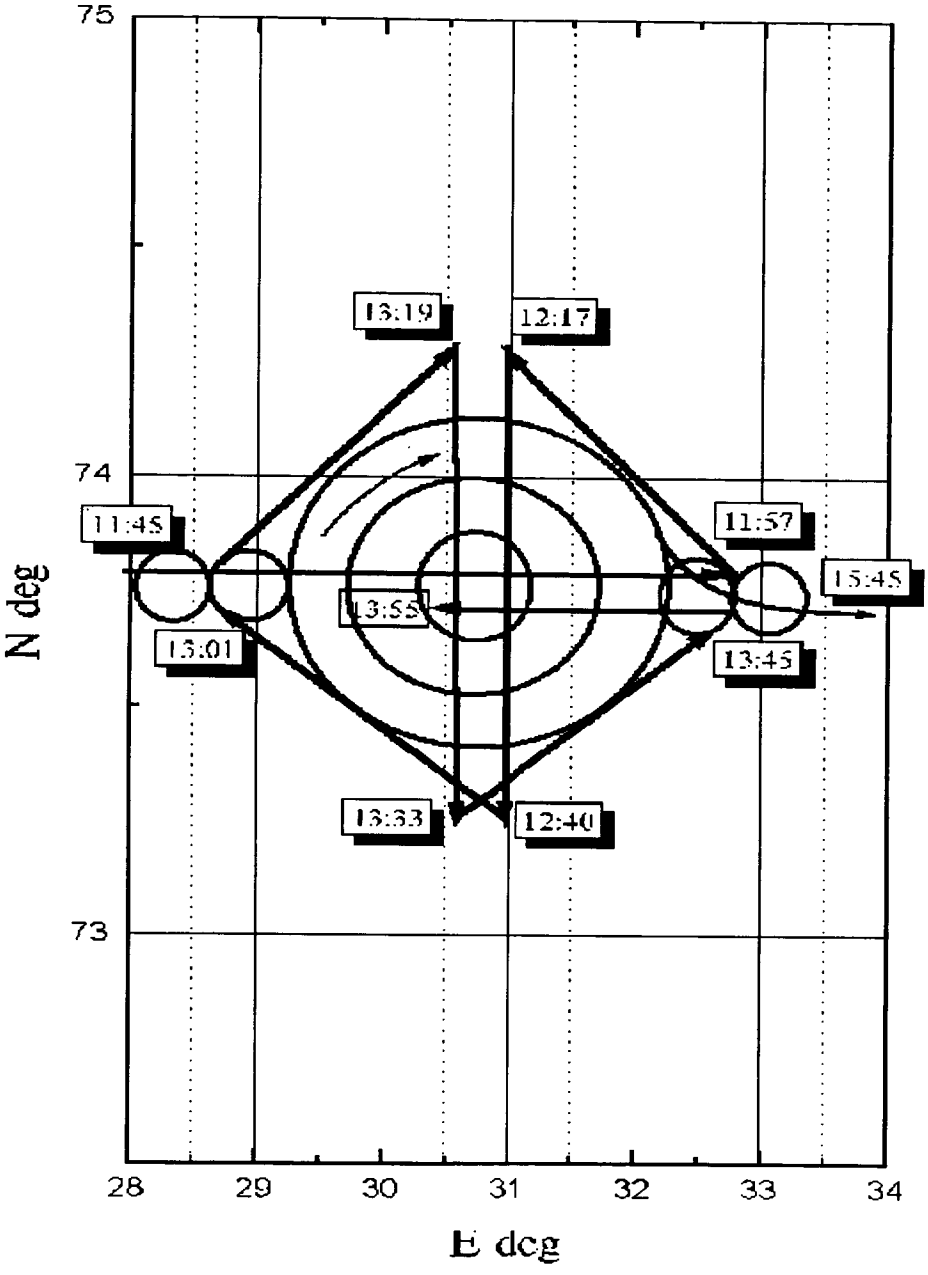
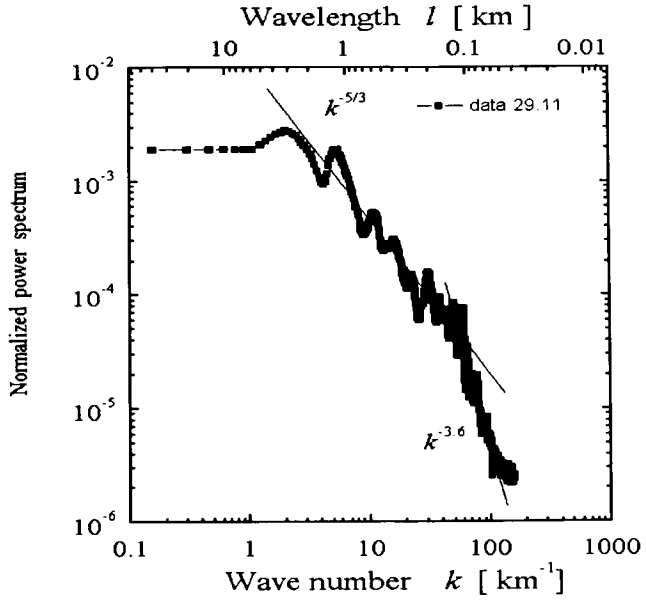
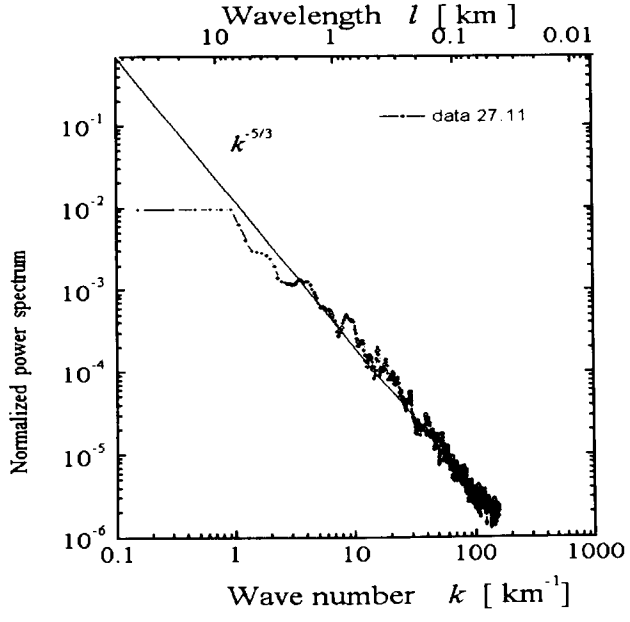


Fig. 1. Flight region and the scheme of the flight route.


Wavelength l [km]
10
1
0.1
0.01
10^{-2}
10^{-3}
10^{-4}
10^{-5}
10^{-6}
$k^{-5/3}$
data 29.11
$k^{-3.6}$
Normalized power spectrum
0.1
1
10
100
1000
Wave number k [km^{-1}]

b


Wavelength l [km]
10
1
0.1
0.01
10^{-1}
10^{-2}
10^{-3}
10^{-4}
10^{-5}
10^{-6}
data 27.11
$k^{-5/3}$
Normalized power spectrum
0.1
1
10
100
1000
Wave number k [km^{-1}]

a

Fig. 2

Monitoring of Atmospheric Aerosols in Seoul using a Micro Pulse Lidar

Soon-Chang Yoon, Jae Gwang Won
Department of Atmospheric Sciences, Seoul National University
Shinrim-dong, Kwanak-ku, Seoul 151-742, Korea
Phone:+82 (2) 880-6717, Fax:+82 (2) 872-1992, E-mail: syoon@air.snu.ac.kr

I Introduction

A micro pulse lidar(MPL) is used to monitor the atmospheric aerosols day and night in Seoul. One of the major parameters required for the computation of light extinction coefficient from the lidar signal is the ratio of the light extinction coefficient to the backscattering coefficient. In order to compute the vertical profiles of light extinction by atmospheric aerosols, the ratio of the light extinction coefficient to the backscattering coefficient is calculated from the Mie theory with the aerosol characteristics measured in Seoul. Assuming the extinction to backscattering ratio is constant in the troposphere the light extinction coefficient by aerosols in each layer of 30m thick is calculated up to 5km height.

From the numerous vertical profiles of light extinction coefficient the temporal variation of the planetary boundary layer(PBL) height is obtained, which reveals the development of residual layer in PBL in the evenings that can hardly be identified with the conventional soundings such as air sondes.

This paper presents the computation procedure for the light extinction to backscattering ratio, and the detection of residual layer in PBL from the lidar signal.

2 Measurements

The MPL system is manufactured by the SES Inc. and the details of the system are given in Lee et al.(1997). The monitoring site is located at the skirt of Mt. Kwanak in the campus of Seoul National University. Continuous day and night measurements were done except on rainy days during September to November 1997. The pulse repetition rate is 2,000Hz, and a shut sum of 1,200,000(10 minutes) is averaged for each profile. Basic meteorological variables i.e. temperature, humidity, wind speed and wind directionare measured simultaneously with an automatic weather station.

In order to compute the refractive index of aerosols, aerosol characteristics measured at the same site in previous years are analyzed. Aerosols are sampled by a high volume sampler and analysed by ion chromatography for the ion component analysis. Aerosol size distributions are measured with an optical particle counter (HIAC/ROYCO Inc., Model 5230), which measures the number concentration of the particles ranging 0.32□ □ 25□ into 8 channels.

3 Data analysis

One of the major parameters required for the computation of light extinction coefficient from the lidar data is the ratio of the light extinction coefficient to the backscattering coefficient, which is typically in a range of 15 to 60 in many applications of aerosol lidars. Light extinction and backscattering coefficients for a single spherical particle can be computed numerically for a given wavelength if the refractive index of aerosols and the relative humidity are provided(Bohren and Huffman, 1983).

Table 1 shows typical ion components of aerosols analysed by ion chromatography in Seoul. Using the refractive index of each aerosol component given in Reist(1993) and in Pitts and Pitts(1986), the mean refractive index of aerosols is obtained by a weighted averaging of refractive indices for each aerosol components as in Table 2. The arithmetic mean of the refractive index of aerosols in Seoul turns out to be 1.510-0.612i, which is similar to the result of Kim et al.(1990) for urban air when the relative humidity is about 50%.

With the mean refractive index of aerosols and the mean particle size of each size interval, the extinction to backscattering ratio is computed for a single particle from the Mie scattering theory, the subroutine BHMIE in Bohren & Huffman(1983). Multiplying this value by the number of particles in each size range the extinction to backscattering ratio is computed for each value of relative humidity.

Fig. 1 shows the extinction to backscattering ratio vs relative humidity. Its mean value turns out about 25±10% when the relative humidity is below 70%, and it decreases down to 20 as the relative humidity approaches 100%. Since the relative humidity tends to decrease with height on clear days, we have used the constant value of 25 for the extinction to backscattering ratio. However, this ratio is supposed to vary with height because of the variation of refractive index of aerosols and their size distribution with height. But, since we have no such data in the upper air, we are forced to use the constant value.

Table 1. Volume ratios of aerosol components in Seoul. TOC stands for total organic carbon, and IC does for inorganic carbon.

Ions(%) / Date	NO_3^-	SO_4^{2-}	Cl^-	TOC	IC
95/10/13	35.2	26.7	7.8	21.4	3.4
95/10/14	18.2	30.5	12.1	19.9	13.9
95/10/16	10.1	42.8	10.0	21.1	12.1
95/10/17	21.2	26.1	13.7	25.4	8.6
95/10/18	14.1	23.8	13.7	21.2	22.0
95/10/19	7.0	28.8	19.5	20.2	21.1
95/10/21	22.1	24.2	9.8	27.2	11.3
95/10/23	25.8	22.6	11.1	23.3	11.6
95/10/25	32.4	25.1	16.1	13.3	7.6
96/10/12	28.6	27.9	6.1	23.0	9.8
96/10/13	20.1	35.8	6.0	22.8	9.7
96/10/14	16.7	38.1	7.9	23.0	9.8
96/10/15	10.1	34.7	12.1	22.0	16.5
96/10/16	16.1	30.3	11.1	22.3	16.7
96/11/12	10.3	40.5	12.0	22.7	9.7
96/11/15	10.4	34.7	12.4	22.2	16.7
96/11/22	26.7	27.1	9.6	23.0	9.8
96/11/25	26.3	25.9	9.3	22.3	9.5

Table 2. Refractive indices of aerosols in Seoul.

Date	Real	Imaginary	Date	Real	Imaginary
95/10/13	1.514	-0.0169	**96/10/12**	1.518	-0.0492
95/10/14	1.511	-0.0698	**96/10/13**	1.515	-0.0488
95/10/16	1.509	-0.0605	**96/10/14**	1.511	-0.0491
95/10/17	1.502	-0.0429	**96/10/15**	1.509	-0.0825
95/10/18	1.513	-0.1100	**96/10/16**	1.512	-0.0835
95/10/19	1.502	-0.1054	**96/11/12**	1.503	-0.0486
95/10/21	1.508	-0.0565	**96/11/15**	1.508	-0.0833
95/10/23	1.511	-0.0583	**96/11/22**	1.512	-0.0492
95/10/25	1.510	-0.0383	**96/11/25**	1.513	-0.0479

The boundary condition for the computation of lidar constant is given as $\beta_p = 0.2\beta_m$ at 5 km, where β_p and β_m are the backscattering coefficients by the particles and by the molecules, respectively. The lidar constant is computed by the iteration method introduced in Fernald et. al(1972). The decay of raw data caused by the unfocused lidar signal near the ground is corrected by the overlap correction method introduced by Spinhirne(1995) and SES Inc.(1996).

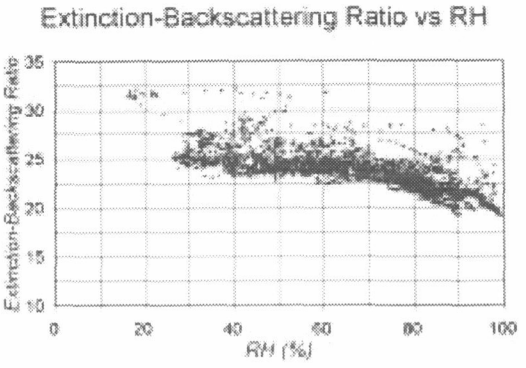


Figure 1. Dependency of the ratio of extinction coefficient to backscattering coefficient on the relative humidity(RH) computed from Mie theory using the aerosol characteristics measured in Seoul.

A comparison of the light extinction coefficient thus obtained at the ground level with the those computed from the Mie scattering theory is shown in Figure 2. The extinction coefficient obtained fron the MPL data is much higher than the ones computed from the Mie theory. We can not tell which one is closer to the true value. However, their temporal variation tendency matches very well.

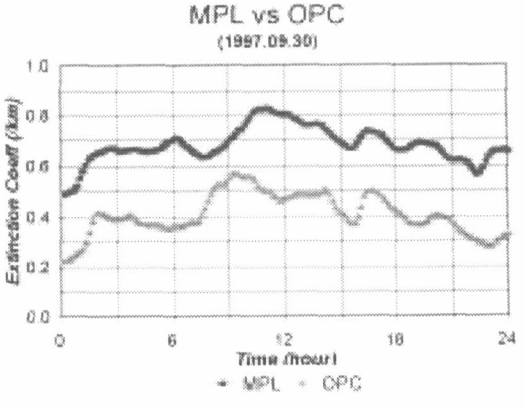


Fig 2. Comparison of extinction coefficients: (-- --) measured by MPL, and (-- --) computed from Mie theory with OPC data.

4 Temporal variation of PBL height

Since most of the aerosol mass emitted from ground sources is mostly confined in the planetary boundary

layer(PBL), the aerosol concentration tends to decrease abruptly across the PBL top. Therefore, the PBL height can be determined from each profile of light extinction, and the temporal variation of the PBL height can be obtained from the numerous consecutive profiles for each day. Figure 3 shows a diurnal variation of PBL height. The residual layer in the upper part of the PBL can be identified in the evenings, which develops starting at 7:00 p.m. in Figure 3. This residual layer can hardly be detected by conventional soundings such as air sondes. Once the residual layer develops, air pollution piles up in the PBL since it stays there in the residual layer until next day.

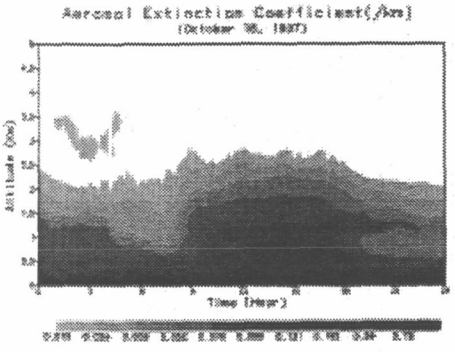


Fig 3. Diurnal variation of aerosol extinction coefficient profile.

5 Summary

The ratio of light extinction to backscattering coefficient is computed from the Mie scattering theory for the chemical composition and size distribution of aerosols measured in Seoul. The extinction to backscattering ratio is found to be 25±2.5 when the relative humidity is below 70%, and decreases toward 20 at higher relative humidity.

Temporal variations of PBL height are obtained from the numerous consecutive profiles, and the residual layers in the upper part of PBL are detected from MPL profiles, which cause the buildup of air pollutants in PBL for a few days.

References

Bohren, C. F. and Huffman, D. R., 1983 ; *Absorption and Scattering of Light by Small Particles*, John Wiley & Sons, Inc.

Fernald, F. G., Merman, B. M. and Reagan, J. A., 1972 ; Determination of Aerosol Height Distribution by Lidar, *J. Appl. Meteor.* Vol. 11, 482-489.

Kim, Y. J. and Boatman, J. F., 1990 ; Size Calibration Corrections for the Forward Scattering Spectrometer Probe (FSSP) for Measurement of Atmospheric Aerosols of Different Refractive Indices, *J. Atmospheric and Oceanic Technology*, Vol. 7, 681-688

Lee, H. S. et al., 1997 ; Micro Pulse Lidar for Aerosol and Cloud Measurement, Advances in Atmospheric Remote Sensing with Lidar, *Advances in Atmospheric Remote Sensing with Lidar*, Springer-Verlag, 7-10.

Pitts, B. J, and Pitts, J. N, 1986 ; *Atmospheric Chemistry : Fundamentals and Experimental Techniques*, John Wiley & Sons.

Reist, P. C., 1993 ; *Aerosol Science and Technology*, McGraw-Hill, Inc.

SES Inc., 1996 ; *Micro Pulse Lidar Instruction Manual*, SES Inc., 4032 Blackburn Lane, Burtonsville, MD 20866, U. S. A.

Spinhirne, J. D., 1995 ; Compact Eye Safe Lidar Systems., *The Review of Laser Engineering*, Vol. 23, No. 2, 112-118.

Airborne Lidar Observations of Smoke Haze During SCAR-B 1995

William D. Hart
Science Systems and Applications Inc
NASA Goddard Space Flight Center Laboratory for Atmospheres,Code 912
Greenbelt, Md 20771 USA
Phone: (301) 286-4936, FAX (301) 286-1762,E-mail billhart @virl.gsfc.nasa.gov
James D. Spinhirne
NASA Goddard Space Flight Center Laboratory for Atmospheres, Code 912
Greenbelt, MD 20771 USA

I. Introduction

The Smoke, Clouds, Aerosol, and Radiation Brazil(SCAR-B) field campaign was conducted to study the effects that widespread and persistent biomass burning have upon radiative and chemical processes in the atmosphere. The radiative transfer characteristics of the atmosphere are altered by the introduction of particulate and gaseous materials which are the products of the combustion of vegatative material at ground level. These substances are transported and distributed horizontally and vertically by atmospheric dynamical processes which may be perturbed by the heat energy from the fires. As the pollutants disperse, their physical and chemical properties change substantially. A complete description of the effects of smoke requires that the evolution back to the natural situation be fully examined.

A most important component of smoke haze investigation is finding its vertical and horizontal distribuition in relation to the driving factors of dynamics and the related horizontal transport. In this presentation, we employ data from the Cloud Lidar System(CLS), carried aboard the NASA ER-2 aircraft, to provide a unique view of the particulate or aerosol loading produced by fires, especially with regard to the geometrical distribution of the aerosols in the vertical plane. The lidar has the ability to measure aerosol optical properties in a continuous fashion at quite fine vertical and horizontal resolution. The results from the lidar provide measurements that are largely independent of influences that corrupt passive instruments and thus it can serve to corroborate their results. The extended horizontal and vertical range of lidar results can also augment ground based and airborne in situ measurements which have limited horizontal and vertical scope.

We present the results of our analysis of CLS observations taken during the SCAR-B field campaign. Observations of the the aerosol optical thickness from the Aerosol Robotic Network(AERONET) of solar photometers are employed in conjunction with CLS data to derive extinction to backscatter ratio values which are used to convert the lidar backscatter coefficient into extinction coefficient. The extinction coefficient is integrated vertically to find aerosol optical thickness along ER-2 flight tracks. We use images of the CLS derived extinction coefficient to depict its horizontal and vertical distribution. Multispectral photometer optical thickness is used to compute the Angstrom exponent. With these, we examine the hypothesis that the values of extinction to backscatter ratio can be related to the Anstrom coefficient since both of these would be a function of the refractive index and size distribution of the aerosols.

II. Computational Procedure

The computation of extinction coefficient proceeds as follows. Profiles, (based upon 10-shot, 1 second lidar averages) of the attenuated backscatter coefficient are computed from [see Spinhirne, 1996]

$$\beta'_a(z) = P_n(z) = \beta_a(z) T_a^2(z) \qquad (1)$$

where β'_a is aerosol attenuated backscatter coefficient, β_a is backscatter coefficient, P_n is the normalized and calibrated lidar signal, T_a is the transmission from the aircraft to the altitude Z. Extinction to backscatter parameters are computed at solar photometer sites using the relationships

$$S_a = \frac{(1 - e^{-2\tau_a})}{2\gamma'} \qquad (2)$$

and

$$\gamma' = \int_{z_t}^{z_a} P_n(z)\,dz \qquad (3)$$

where $e^{-2\tau_a}$ is the two-way aerosol vertical columnar transmission derived from a solar photometer, $P_n(z)$is defined in equation (1), and z is height. Inherent in this analysis is the assumption of a constant S_a. The limits of the integration z_t and z_b are the altitudes of the top of the aerosol layer and the earth's surface, respectively. In use of this relationship, we ignore the influence of molecular scattering because the total molecular atmospheric optical thickness at 1.064μm is less than 0.01. The extinction coefficient is given by

$$\sigma_a(z) = S_a\beta_a(z). \quad (4)$$

The backscatter coefficient profile $\beta_a(z)$ is derived from a lidar profile by using

$$\beta_a(z) = \frac{P_n(z)}{T_a^2(z_-)} \quad (5)$$

and $$T_a(z_-) = e^{-S_a\int_{z_t}^{z_-}\beta_a(z)dz} \quad (6)$$

The transmission $T_a(z_-)$ is computed from the top of the layer to a level just above z. The computation uses a numerical integration from the top of the layer to the bottom. The lidar optical thickness, τ_a, is the value of at the bottom of the layer. That is

$$\tau_a = \int_{z_t}^{z_b}\sigma_a(z')dz' \quad (7)$$

The Angstrom exponent is an optical parameter which is related to the particle size structure of the constituent aerosols. The value can be obtained directly from multispectrral photometer observations. We used the relationship

$$\alpha_a = \frac{\ln(\tau_1/\tau_2)}{\ln(\lambda_2/\lambda_1)} \quad (8)$$

where τ_1 and τ_2 are the aerosol optical depths at wavelengths λ_1 and λ_2 ,respectively. In this study, λ_1=0.438μm and λ_2=0.871μm.

III. Observations

. In Fig. 1, we show the the distribution of aerosols observed by the CLS along a representative flight track from the 07SEP 95 ER-2 flight. The solar photometer optical thickness which was used in the computation of S_a was a value exptrapolated to the laser wavelength, 1.064μm. The image shows the extinction coefficient of the smoke haze. These computations of extinction coefficient are based upon the value of S=26.8sr calculated at 18.36UTC when the ER-2 flew within 10km of Alta Floresta.

The smoke aerosol structure of Fig.1 exhibits several interesting features. A ground level smoke source is located at about 17.7 UTC. A region of relatively high smoke density near the ground spreads to both sides of this feature. A layer of enhanced concentration extends from about 17.85UTC to the end of the segment at 18.4UTC. This layer has a top which slopes up from left to right. The sloping of the top results from convection of the billowing smoke as it advects downwind. Immediately above that layer is a band of lower density. The top of the well mixed boundary layer is at about 3.5 km from 17.5UTC to 17.85UTC. At that point is a discontinuity where the top of the layer drops to about 3.1km. The top of these layers are bounded by a capping temperature inversion.

A second rendition of the smoke aerosol concentration is shown in the lower portion of Fig. 1 as a plot of columnar aerosol optical thickness. The plot shows local maxima where low level sources are located. It also shows a grandual increase in the optical depth corresponding to the thickening of the sloping layer. The value of optical thickness deternined by the solar photometer is indicated on the plot by the notation Alta Floresta.

A third depiction of the aerosol loading is shown in Fig. 2. It is a plot of the horizontally averaged profile of the extinction coefficient for the segment. The highest average concentrations are in the layer from the ground to about 2.25km. where a local minimum is found. A layer of almost constant average concentration is found above that up to about 3.5km. Above that height, the value quickly falls to nearly zero.

Computations of S_a were made for each of the 22 high quality ER-2 solar photometer overpassess that occurred during eight observation days. The value of $S_a$is a function of the physics of the interaction of laser light photons with the aerosol particles that is strongly influenced by the sizes, shapes, and refractive indices of the particles. The characteristics of the aerosols change as the aerosols age. An interesting hypothesis concerning the values of S_a from different photometer sites was that a systematic relationship could be found between S_a and an optical parameter obtained from the photometers. The parameter we chose to test was Angstrom exponent as defined in equation (8).

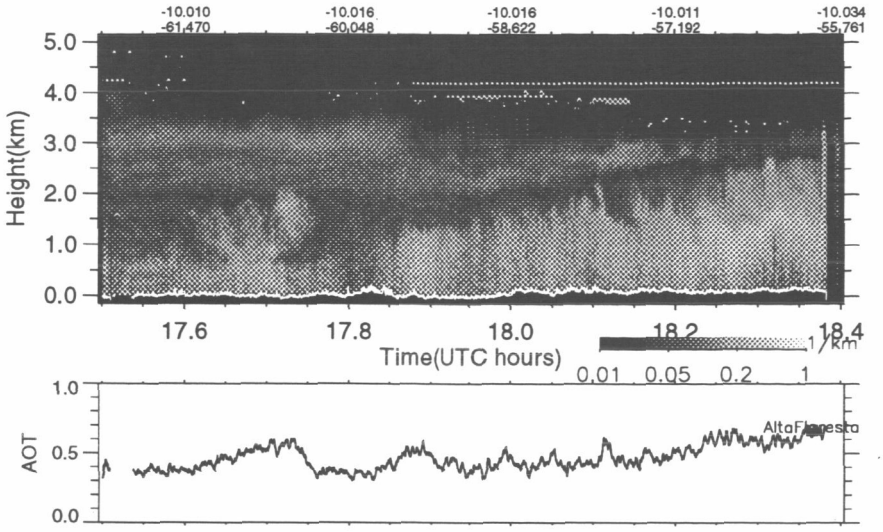


Figure 1. Image of CLS extinction coefficient(σ_a) juxtaposed with a plot of the aerosol optical thickness from 07Sep95.

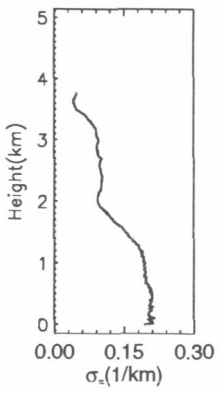


Figure 2. Averaged profile of extinction coefficient from the 07Sep95,17.5-18.4UTC segment.

Others [Holben, 1996] have shown that aerosol origin and age and particle morphology influence the value of α_α. The values of α_a were also computed for each ER-2 overpass. The results of these computations are shown in Fig. 3. The values of S_a span a range of about 20sr to 40sr. This range backets values found in other lidar studies of other types of aerosols[Spinhirne, 1980, Reagan, 1988]. Values in this range are somewhat unexpected for smoke. The increased absorption, which is typical of smoke particles which have high carbon content, should decrease the relative backscatter which would result in larger values of S_a. Instead, our observed values are characteristic of those found in other investigations. The plot shows no correlation between the parameters and suggests that they independent of each other for these products of biomass buring. Perhaps the phyical properties of these aerosols are too convoluted to be revealed in such a simplified analysis. The radiative transfer modelling which would help resolve this question are left for future work.

IV. Conclusions

The volumetric nature of the observations which are obtained from the ER-2 CLS provides at least three valuable data products which are important to the boundary layer aerosol investigation. First the spatial distribution of boundary layer aerosols, which in the present case are the product of large scale biomass burning, is detectable by airborne lidar. The distribution is mapped in the vertical plane at a high resolution. Lidar signal displays show vertical structure which are difficult or impossible to derive from other data sources Compelling features revealed by lidar could advance studies involving the use of other instrumentation. Second, the optical thickness can be computed for extended horizontal segments. Finally, horizontally averaged vertical profiles of σ_a can be computed at any resolution to obtain characteristics of the vertical distribution of σ_a. These profiles can provide valuable information for studies which describe the transport of the aerosols or the effects that the aerosol loading has

upon the radiative transfer processes in the boundary layer

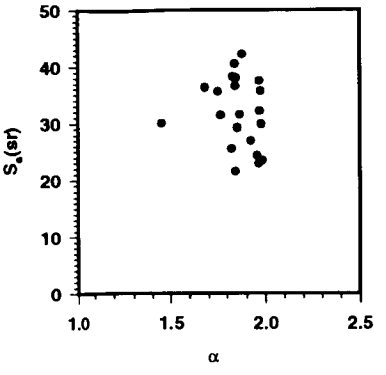


Figure 3. Plot of the extinction to backscatter coefficient vs. Angstrom exponent. The lack of a discernible correlation suggests that scattering and absorbing properties of the aerosols are not directly related to the age of the smoke particles.

The range of extinction to backscatter values which were computed at the overflown solar photometer locations during eight ER-2 sorties are consistent with values derived in other boundary layer aerosols studies in a wide variety of locations and conditions. The values of the ratio varied from near 20sr to greater than 40sr. It was expected that the values for smoke aerosols would be larger than this. However, the majority clustered near 30sr. Previously, the values have been thought to be nearly twice as large due to the absorbing nature expected for smoke haze. The fact that no correlation was found between the Angstrom exponent derived from the solar photometer observations and S_a suggests that the scattering properties of the aerosols are too comlex to be readily characterized by this single optical parameter. The mixtures of aerosol types together with the complex size distributions of the particles precludes any simple characterization using a single parameter.

Future spaceborne lidars will have the capability to monitor anthropogenic aerosols on a routine and systematic basis. This will permit investigators to develop a climatology of these on a global scale. Furthermore, episodic events at remote locations, such as drought induced biomass fires, will be observed. We have shown here that the optical thicknesses and the horizontal and vertical extinction distribution of the aerosol loading can be determined from the lidar observations in quantitative analysis of the aerosols. This will enhance observations of these phenomena made with passive instrumentation.

REFERENCES

Holben, B.N., A. Setzer, T. F. Eck, A. Pereira,and I. Slutsker, Effect of dry-season biomass burning on Amazon basin aerosol concentrations and optical properties, *J. Geophys. Res,*101,19,465-19,481,1996

Reagan, J.A., M.V. Apte, A. Ben-David, and B.M. Herman, Assessment of aerosol extinction to backscatter ratio measurements made at 694.3 nm in Tucson, Arizona, *Aerosol Sci. and Tech,* 8,215-226,1988

Spinhirne,J.D., J.A. Reagan, and B.M. Herman,Vertical distribution of aerosol extinction cross section and inference of aerosol imaginary index in the troposphere by lidar technique, *J. Appl. Met.*, 19,426-438,1980

Spinhirne, J.D.,W.D.Hart and D.L.Hlavka, Cirrus Infrared Parameters and Shortwave Reflectance Relations from Observations, *J. Atmos. Sci,*53,1438-1458,1996

OFF-BEAM (MULTIPLY-SCATTERED) LIDAR RETURNS FROM STRATUS, 1: CLOUD-INFORMATION CONTENT & SENSITIVITY TO NOISE

Anthony B. Davis,
Los Alamos National Laboratory, Space & Remote Sensing Science Group (NIS-2)
P.O. Box 1663 (Mail Stop C-323), Los Alamos, NM 87545, USA.
Tel: (505) 665 6577, Fax: (505) 667 3815, E-mail: adavis@lanl.gov

and Robert F. Cahalan
NASA's Goddard Space Flight Center, Climate & Radiation Branch (Code 913)
Greenbelt, Md 20771, USA.

Abstract

We review the basic multiple scattering theory of off-beam lidar returns from optically thick clouds using the diffusion approximation. The shape of the temporal signal —the stretched pulse— depends primarily on the physical thickness of the cloud whereas its spatial counterpart —the diffuse spot— conveys specific information on the cloud's optical thickness, as do the absolute returns. This makes observation of the weak off-beam lidar returns an attractive prospect in remote sensing of cloud properties. By estimating the signal-to-noise ratio, we show that night-time measurements can be performed with existing technology. By the same criterion, day-time operation is a challenge that can only be met with a combination of cutting-edge techniques in filtering and in laser sources.

1. Context

In the atmospheric lidar context, the Lidar-In-space-Technology-Experiment (LITE) that flew on Space-Shuttle mission STS-64 in 09/94 (Winker *et al.*, 1996) is a precursor of off-beam lidar in the sense that all orders-of-scattering —hence maximum pulse-stretching— are present in the returns from dense boundary-layer clouds (Winker, 1997). Indeed, at 260 km range the night-time 3.5 mrad field-of-view (FOV) subtends 0.9 km, i.e., 3–4 times the horizontal photon transport scale defined in a passive remote sensing context by Davis *et al.* (1997a). This underscores the limitations of approaches based on the (single-scattering) lidar equation, even with semi-empirical corrections for multiple (forward) scatterings; in essence, the need for 2-way penetration sets the maximum optical depth at about 3 (Platt *et al.*, 1994). Multiple scattering is now considered more as a resource than a nuisance in atmospheric lidar (Flesia and Schwendimann, 1995); however, because of the emphasis on forward-scattering in the current models, off-beam ("multiple FOV") measurements have been confined a degree or so from the axis.

In the broader context of imaging science, off-beam lidar is the first projected atmospheric application of diffusing-wave phenomenology; Yodh and Chance (1995; and references therein) describe promising new applications of 3D diffusing-wave imaging in non-intrusive medical diagnostics.

2. Theoretical Background: Diffusing-Wave Propagation in a Finite Medium

Atmospheric lidar can be modeled mathematically as a Green-function problem. The radiative transfer equation is linear in its source term which, in this case, is a Dirac δ-function in space, time and direction. So, by definition, the resulting radiance field is a Green's function. This re-formulation of the lidar problem is particularly useful in the description of highly-scattered off-beam responses from dense clouds (Davis and Marshak, 1996). Physically, we are observing the propagation of a "diffusing" wave of photons away from an initial burst released at the cloud's boundary. Rather than ballistic motion which characterizes standard photon propagation, propagation is far slower here, being mediated by the photon's Brownian motion in the cloud (Davis *et al.*, 1997b).

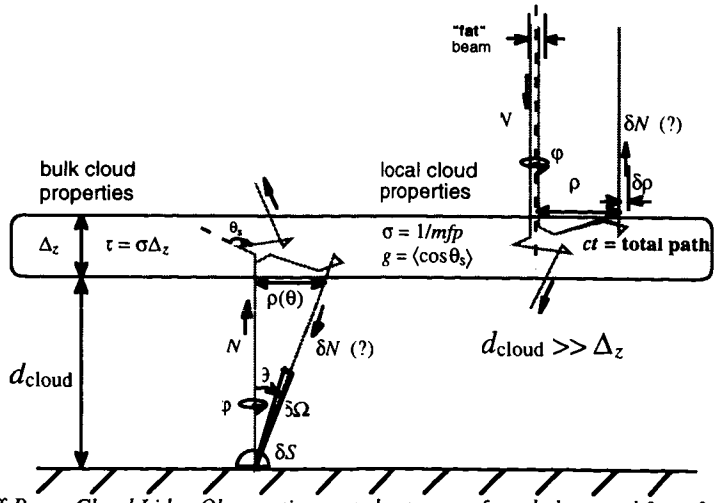


Figure 1: *Schematic of Off-Beam Cloud Lidar Observations, at short range from below, and from far above.*

Let $G_R(x,y,t)$ be the cloud's Green function as observed in reflection (there is also one in transmission). Horizontal coordinates x,y are centered on the beam and time t is measured after the laser pulse crosses the cloud's boundary. $G_R(\cdot)$ can be either a radiance measured at the instrument, in which case x,y are functions of the view angle $\Omega(\theta,\varphi)$ or a flux (Ω_z-weighted integral of radiance) measured at the cloud boundary. The former is relevant to remote-sensing, the latter to theory where closed-form results are obtainable within the diffusion approximation (Davis and Marshak, 1996).

The following asymptotic formulas are representative of diffusion-based off-beam lidar theory in absence of absorption:

$$\langle t \rangle = \iiint t G_R(x,y,t)\mathrm{d}x\mathrm{d}y\mathrm{d}t \;/\; \iiint G_R(x,y,t)\mathrm{d}x\mathrm{d}y\mathrm{d}t \;\sim\; \Delta\,/c, \tag{1}$$

$$\langle \rho^2 \rangle = \iiint (x^2+y^2) G_R(x,y,t)\mathrm{d}x\mathrm{d}y\mathrm{d}t \;/\; \iiint G_R(x,y,t)\mathrm{d}x\mathrm{d}y\mathrm{d}t \;\sim\; \Delta^2/(1-g)\tau \tag{2}$$

where Δ is cloud's physical thickness, τ its optical thickness, and g the asymmetry factor of the scattering phase function (cf. Fig. 1). Equation (2) defines Davis *et al.*'s (1997a) horizontal transport scale for *solar* photons.

For typical stratus ($\Delta \approx 0.2$–0.5 km, $\tau \approx 8$–16, $g = 0.85$), the root-mean-square horizontal transport, $\sqrt{\langle \rho^2 \rangle}$, is 0.2–0.5 km. A detailed Green-function analysis of the time-dependent diffusion problem with the appropriate boundary- and initial-conditions yields specific numerical constants and non-negligible pre-asymptotic correction terms for the above formulas. Figure 2 is a log-log plot of numerical results for $c\langle t \rangle/\Delta$ and $\sqrt{\langle \rho^2 \rangle}/\Delta$ for cloud of variable τ and Δ when $G_R(\cdot)$ is flux; notice the good agreement with Eqs. (1–2) at large τ.

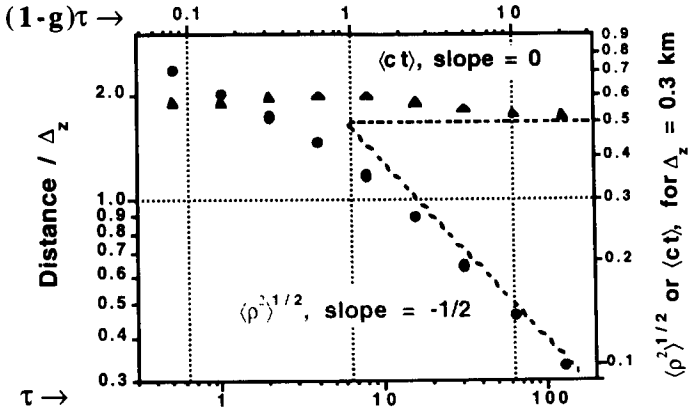


Figure 2: *Scaling of Low-Order Moments of Marginal Spatial and Temporal Signals with Basic Cloud Parameters, Δ & $(1\text{-}g)\tau$.* Thick-cloud asymptotic slopes predicted by diffusion theory are indicated.

3. Application to Remote Sensing: Off-Beam Cloud Lidar

Figure 1 is a schematic of off-beam lidar observation, from ground (note the necessity of wide-angle optics) and from space (where the beam can no longer be considered infinitesimally narrow, with respect to $\sqrt{\langle \rho^2 \rangle}$). Since g is not expected to be highly variable, Eqs. (1–2) have an immediate appeal to cloud remote sensing: measurements of $G_R(\cdot)$ lead to Δ and τ (note that no existing remote-sensing technique yields the former quantity reliably).

Table 1 describes the kind of radial/azimuthal integration scheme that can be implemented in practice by software or hardware: 13 zones are defined with increasing radial (zenith-angle) increments that (over)compensate for the sharp decrease in signal with distance from the beam. Figure 3 shows the exponential decay of (average) path-integrated radiance going from one zone to the next. The close agreement between the exact computation and the flux-based estimate assuming isotropic surface radiance validates the diffusion approximation used to derive Eqs. (1–2). The exponential decay in Fig. 3 was actually observed in real clouds in a "reciprocal" experiment where, using an otherwise unmodified research lidar system, the beam was deflected away from zenith by as much as 12° before losing the signal altogether (Davis *et al.*, 1997c).

Figure 4 shows the simulated time-dependence in each zone of Fig. 3, essentially the highly discretized representation of $G_R(\cdot)$ that we could hope to measure with the scheme described in Table 1. Close to the beam —hence to standard lidar— the time-scale of the signal is determined by photon mean-free-path ($1/\sigma = \Delta/\tau$, where σ is extinction and $\tau = 13$), far from the beam, the time-constant is on the order of a few Δ's. In a companion paper (Davis *et al.*, 1998), we present first-ever laboratory measurements of space-time Green's functions for simulated clouds of various optical depths using an ultra-sensitive (single photon-counting) imaging/ranging device.

4. Signal-to-Noise Ratio Estimates: Night & Day

Can the measurements of Davis *et al.* (1998) under near-ideal laboratory conditions be reproduced in the field? The answer depends on how high we can keep the signal-to noise (*S/N*) ratio. Signal strength is obtained directly from the data in Fig. 4. In the far-field (bins #10–13), a typical signal for a doubled Nd:YAG (0.532 μm) laser with 50 μJ ($\approx 10^{14}$ photon) pulses is $\approx 10^{11}$ photons/pulse/m^2/st/s. Under an overcast sky, ambient radiance in

absence of moonlight and light pollution is $\approx 10^{8.5}$ photons/m^2/st/s for a 1 nm band-pass filter at lidar wavelengths (W. Priedhorsky, priv. com.). Thus,

$$S/N \approx 10^{2.5} \times (E/50) \times (1/\delta\lambda) \times n^{1/2} \qquad (3)$$

where E is pulse-energy in μJ, $\delta\lambda$ is filter band-pass in nm, and n is the number of pulses averaged to produce the signal. By full-moon, there is $\approx 10^3$ times more ambient light, but the ensuing reduction of single-pulse *S/N* in Eq. (3) can be defeated by pulse averaging: at rep-rate 10^4 pulses/s, a second yields a factor of 100 in *S/N*. So, night-time off-beam lidar seems to be within current technological reach (eye-safe micro-pulse lasers, interference filters).

In day-time, there is $\approx 10^9$ times more ambient light than used in Eq. (3). So we need to improve *S/N* by at least a factor of $\approx 10^{6.5}$. Apart from pulse-averaging, this calls for non-standard technology in lidar applications: atomic-line filters with $\delta\lambda \approx 0.001$ nm (Yeh, 1982) centered at solar absorption lines (Na doublet, N down by more than an order of magnitude), and strong sources (possibly jeopardizing eye-safety) tunable to the filter wavelength. If necessary, one may abandon $G_R(\cdot)$ measurement and use a spatial filter that will give only the ratio in Eq. (2).

5. Conclusions

We reviewed diffusing-wave Green function theory for finite optical media from the standpoint of off-beam cloud lidar. Sensitivity of the basic off-beam quantities to cloud parameters makes their measurement attractive for remote sensing; indeed, optical *and* physical cloud thicknesses can be retrieved. However, until new technologies in filtering and laser sources are fully tested, *a priori* signal-to-noise ratios favor night-time observations.

References

Davis, A., and A. Marshak, 1996: Cloud Responses from CW and Pulsed Lasers as Green's Functions: What do They Tell us? & Can we Measure Them? In *8th International Worskshop on MUltiple SCattering Lidar Experiments (MUSCLE 8 – Extended Abstract Volume)*, March 04–06, 1996, Québec (Qc), pp. 67–71, Def. Res. Est.Valcartier (DREV).

Davis, A., A. Marshak, R. F. Cahalan, and W. J. Wiscombe, 1997a: The LANDSAT scale-break in stratocumulus as a three-dimensional radiative transfer effect, implications for cloud remote sensing. *J. Atmos. Sci.*, **54**, 241–260.

Davis, A., D. M. Winker, A. Marshak, J. D. Spinhirne, R. F. Cahalan, S. P. Love, S. H. Melfi, and W. J. Wiscombe, 1997b: Retrieval of physical and optical cloud thicknesses from space-borne and wide-angle lidar. In *Advances in Atmospheric Remote Sensing with Lidar*. Eds. A. Ansmann, R, Neuber, P. Rairoux, and U. Wadinger, Springer-Verlag, pp. 193–196.

Davis, A., J. D. Spinhirne, M. McGill, and R. F. Cahalan, 1997c: Off-beam cloud lidar: First detection of diffusing photons. In *Proceedings of Winter Topical Meeting on "Optical Remote Sensing of the Atmosphere"*, February 10–14, 1997, Santa Fe (NM), pp. 39–41, Optical Society of America, Washington (DC).

Davis, A., C. Ho, and S. P. Love, 1998: Off-beam (multiply-scattered) lidar returns from stratus, 2: Space-time measurements in a laboratory simulation, *19th International Laser Radar Conference*, Annapolis (Md), July 6–10, 1998 (submitted).

Flesia, C., and P. Schwendimann (Eds.), 1995: Special section on MUltiple SCattering in Lidar Experiments (MUSCLE). *Applied Physics B – Lasers and Optics*, **B60**, pp. 315–362.

Platt, C. M., *et al.* (27 authors), 1994: The Experimental Cloud LIdar Pilot Study (ECLIPS) for Cloud Radiation Research, *Bull. Amer. Meteor. Soc.*, **75**, 1635–1654.

Winker, D. M., 1997: Simulation and modeling of the multiple scattering effects in LITE data. In *Advances in Atmospheric Remote Sensing with Lidar*. Eds. A. Ansmann, R, Neuber, P. Rairoux, and U. Wadinger, Springer-Verlag, pp. 185–188.

Winker, D. M., R. H. Couch, and M. P. McCormick, 1996: An overview of LITE: NASA's Lidar-In-space Technology Experiment, *Proc. IEEE*, **84**, 164–180.

Yeh, P., 1982: Dispersive magneto-optic filters, *Appl. Opt.*, **21**, 2069–2075.

Yodh, A., and B. Chance, 1995: Spectroscopy/imaging with diffusing light. *Phys. Today*, **48**, No. 3, 34-40.

#	inner radius (outer$_{13}$ = 1)	θ, from	... to (°)	solid angle (st)	ρ, from	... to (m)	area (m^2) at 1 km range	radiative flux (pulse^{-1}m^{-2})	average radiance (pulse^{-1}m^{-2}st^{-1})
1	0.00000	0.00	0.03	7.49e-07	0.00	0.43	5.89e-01	2.47e-08	3.30e-02
2	0.00075	0.03	0.04	7.49e-07	0.43	0.79	1.36e+00	2.98e-09	3.98e-03
3	0.00137	0.04	0.08	4.49e-06	0.79	1.43	4.51e+00	3.12e-09	6.94e-04
4	0.00248	0.08	0.15	1.50e-05	1.43	2.61	1.50e+01	3.70e-09	2.47e-04
5	0.00452	0.15	0.27	4.94e-05	2.61	4.75	4.95e+01	4.26e-09	8.63e-05
6	0.00823	0.27	0.49	1.64e-04	4.75	8.65	1.64e+02	5.34e-09	3.26e-05
7	0.01498	0.49	0.90	5.44e-04	8.65	15.74	5.43e+02	7.12e-09	1.31e-05
8	0.02726	0.90	1.64	1.80e-03	15.74	28.64	1.80e+03	9.54e-09	5.31e-06
9	0.04961	1.64	2.98	5.94e-03	28.64	52.13	5.96e+03	1.27e-08	2.13e-06
10	0.09029	2.98	5.42	1.96e-02	52.13	94.87	1.97e+04	1.71e-08	8.75e-07
11	0.16432	5.42	9.80	6.35e-02	94.87	172.67	6.54e+04	2.29e-08	3.64e-07
12	0.29907	9.80	17.45	1.97e-01	172.67	314.26	2.17e+05	2.38e-08	1.24e-07
13	0.54431	17.45	30.00	5.53e-01	314.26	577.35	7.37e+05	1.31e-08	2.60e-08

Table 1: *A 13-Element Focal Plane Zenithal/Azimuthal (ZEN/AZI) Integration Scheme.* Path-integrated signals (average radiance and radiative flux at the instrument) are entered for an idealized homogeneous cloud of optical thickness $\tau = 13$ and "C1" scattering properties (asymmetry factor $g \approx 0.84$) at $\lambda = 1.06$ μm, leading to $R = 1-T = 0.52$. The model cloud, physical thickness $\Delta = 300$ m, is observed from a range of 1 km. Extinction in the cloud is $\sigma = \tau/\Delta = 43$ km^{-1}, hence the transport mean free path $\ell_t = 1/[(1-g)\sigma] = 0.14$ km and the "rescaled" optical depth $(1-g)\tau = \Delta/\ell_t = 2.1$.

Figure 3: *ZEN/AZI Summation Scheme and Validation of Diffusion Approximation.* Boundaries of most of the 13 zenith-angle zones described in Table 1 are indicated near the lower axis. Exact radiance at the instrument and its Lambertian surface flux approximation for the cloud model described in Table 1 are plotted on the l.h. axis; their agreement validates the diffusion (photon random walk) assumption used to derive Eqs. (1–2). Solid angles subtended by the 13 zones are plotted on the r.h. axis. Note how the product of radiance and solid angle (the element of radiative flux, hence the current in a PMT) is roughly constant from zone to zone, as shown in Table 1. This is the purpose of the nonlinear decimation in radial distance.

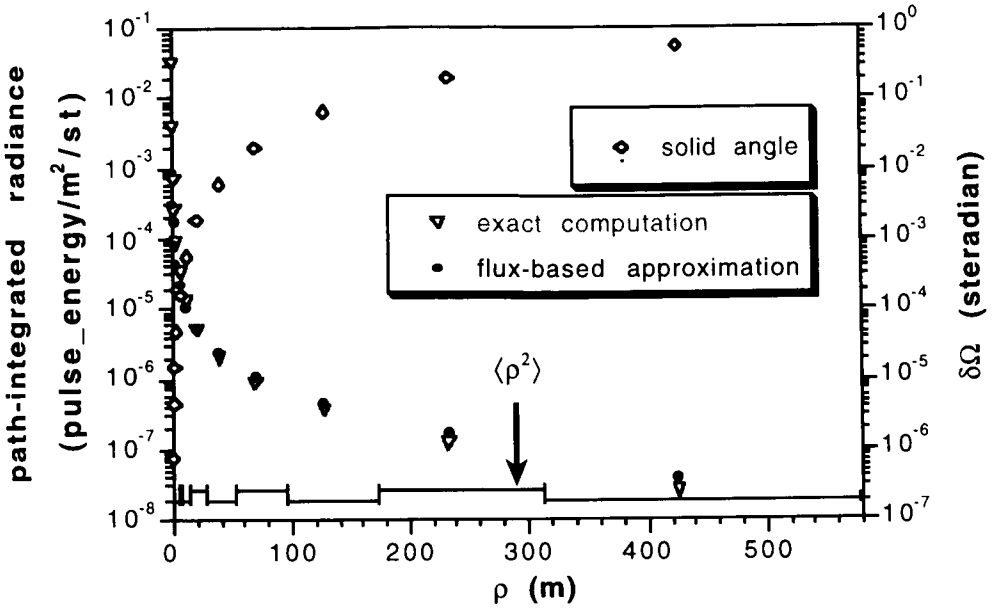
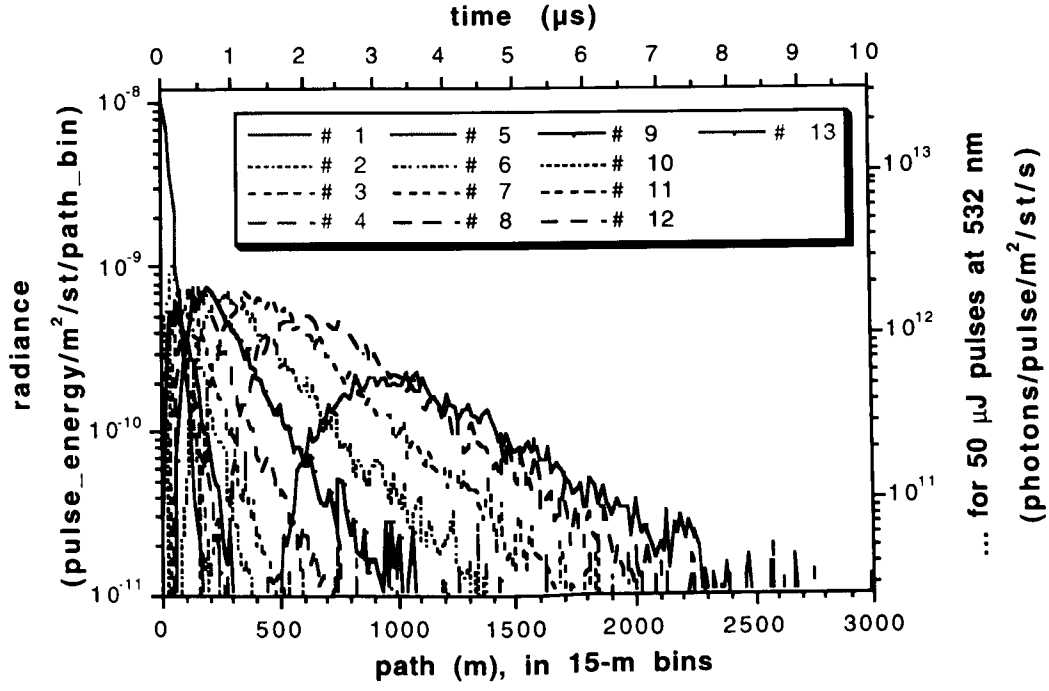


Figure 4: *Numerical Simulation of a Space-Time (Angle-Path) Observation using the ZEN/AZI Summation Described in Table 1.* Notice the numerical noise resulting from the (forward) Monte Carlo computation with 10^9 photon-histories. Path-bins are 15 m ($5\ 10^{-8}$ s) wide and 200 are used along the abscissa. See Table 1 for a description of the cloud model.



Combining Data from Lidar and In Situ Instruments to Characterize the Vertical Structure of Aerosol Optical Properties

J. Redemann[1], R. P. Turco[1], R. F. Pueschel[2] , E.V. Browell[3], W. B. Grant[3]

[1]University of California, Dept. of Atmospheric Sciences, 7221 Math Sciences,
405 Hilgard Ave., LA, CA 90095-1565,
ph.: (310) 825-9230, fax: (310) 206-5219, em: redemann@atmos.ucla.edu

[2]NASA Ames Research Center, Moffett Field, CA 94035-1000

[3]NASA Langley Research Center, Hampton, VA 23681-0001

1 Introduction

Over the last decade, the quantification of tropospheric aerosol abundance, composition and radiative impacts has become an important research endeavor. For the most part, the interest in tropospheric aerosols is derived from questions related to the global and local (instantaneous) radiative forcing of climate due to these aerosols.

One approach is to study local forcing under well-defined conditions, and to extrapolate such results to global scales. To estimate local aerosol forcing, appropriate radiative transfer models can be employed (e.g., the Fu-Liou radiative transfer code, [Fu and Liou, 1993]). In general, such models require information on *derived* aerosol properties [Toon, 1994]; namely the aerosol optical depth, single-scattering albedo, and asymmetry factor (phase function), all of which appear in the equations of radiative transfer.

In this paper, we report on a method that utilizes lidar data and *in situ* aerosol size distribution measurements to deduce the vertical structure of the aerosol complex index of refraction in the near IR, thus identifying the aerosol type. Together with aerosol size distributions obtained *in situ*, the aerosol refractive index can be used to calculate the necessary *derived* aerosol properties.

The data analyzed here were collected during NASA's PEM West-B (Pacific Exploratory Mission) experiment, which took place in February/March 1994. The platform for the measurements was the NASA DC-8 aircraft. The primary goal of the PEM West missions [Browell et al., 1996] was the assessment of potential anthropogenic perturbations of the chemistry in the Pacific Basin troposphere. For this purpose the timing of PEM West-B corresponded to the seasonal peak in transport from the Asian continent into the Pacific basin [Merrill et al., in press]. This period normally occurs during Northern Hemisphere spring, when the Japan jet is well-developed.

2 Experimental Details

While the main focus of PEM West-B was the investigation of ozone chemistry, a number of instruments onboard the mission aircraft measured aerosol properties. The *in situ* aerosol instruments consisted of a Forward Scattering Spectrometer Probe, FSSP-300, as well as the NASA Ames wire impactor system [Pueschel et al., 1994]. The NASA Langley Research Center airborne UV DIAL (DIfferential Absorption Lidar) system, operating at 280 nm, 300 nm, 600 nm and 1064 nm, provided remote observations in both zenith and nadir configurations. Especially for radiative transfer calculations, it is desirable to have information about aerosol optical properties within the entire atmospheric column. In principle, lidar is capable of providing some of the required information along the vertical viewing path.

The scenarios for the comparison of the *in situ* and the lidar data are depicted in Fig.1. Prior to the descent of the research aircraft, the lidar continuously samples in the nadir as well as in the zenith direction, providing data that

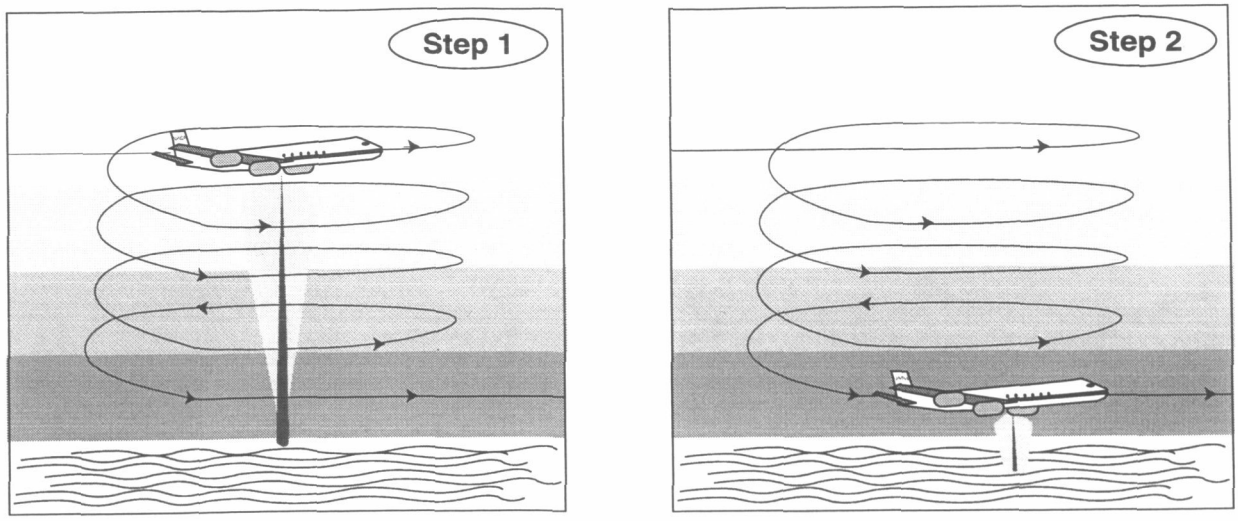


Fig.1 : Experimental setup for the comparison of lidar-derived with FSSP derived aerosol backscatter

can be inverted to yield local backscatter profiles. At the same time, the onboard FSSP continuously measures the local aerosol size distribution in the radius range of 0.21 - 11.84 µm along the entire flight track. The *in situ* data are then used to calculate aerosol optical coefficients at the lidar wavelengths using a standard Mie-scattering code, and assumptions regarding the particle refractive index. This analysis yields the height-dependent aerosol backscatter and extinction profiles, which may then be compared to the inverted lidar profiles obtained aloft. For this study, we used a 50-s binning interval for the FSSP data before calculating the optical parameters.

The NASA Langley DIAL system operated at four wavelengths from the UV to the near-IR at a pulse rate of about 8.6 Hz. The system contained a pair of Nd:YAG lasers each pumping a dye laser [Browell, 1989; Browell et al., 1996]. The atmospheric backscatter return was recorded with 30-m vertical resolution and a horizontal averaging interval of 1.75 s, resulting in a horizontal resolution of approximately 400-m at a nominal aircraft speed of 14 km/min. Simultaneous zenith and nadir measurements were taken with a standoff range of 750 m above and below the aircraft to avoid problems with the "overlap" function. A detailed description of the DIAL system is found in Browell et al.[1983] and Browell [1989].

The lidar data was inverted using a modified Klett algorithm [Mielke et al., 1992] to obtain the scattering ratio, $R(z)$, from the lidar signal in the form:

$$R(z) = \frac{\dfrac{F(z)}{\beta_{mol}(z)}}{\dfrac{1}{R(z_0)} + 2\int_z^{z_0} F(z')g(z')dz'} \qquad (1)$$

where $F(z)$ is defined as follows:

$$F(z) = \frac{z^2 P(z)}{z_0^{\,2} P(z_0)} \beta_{mol}(z_0) \qquad \times$$

$$\exp\left\{2\int_z^{z_0} [\beta_{mol}(z')g(z') - \alpha_{mol}(z')]dz'\right\} \quad . \qquad (2)$$

$P(z)$ is the lidar signal from a distance z, while $P(z_0)$ is the lidar signal at a reference distance z_0. The aerosol scattering parameters required to calculate $R(z_0)$ and the lidar ratio $g(z)$ were derived from the *in situ* size distribution measurements.

3 Data comparison

Our basic assumption in comparing the lidar- and *in situ* - derived backscatter profiles is that the aerosol index of refraction is constant over specific altitude intervals. To divide the local atmosphere into such layers - with different refractive indices - we first use the structure of the raw lidar data to choose the

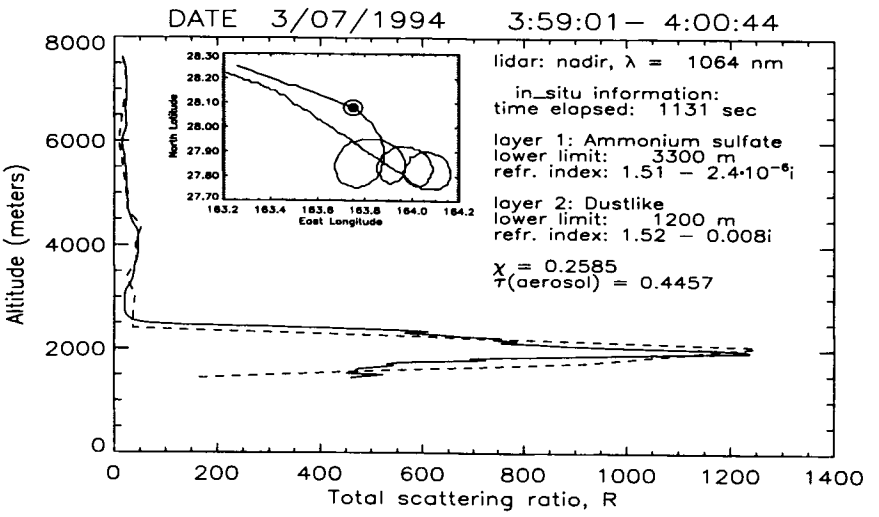


Fig. 2: Comparison of lidar derived aerosol scattering ratio (solid line) with *in situ* aerosol scattering ratio (dashed line) at 1.064 μm for case study 3 on March 7, 1994

number and location of these layers. In the subsequent lidar inversion, we then seek to minimize the altitude-averaged, relative difference between the lidar scattering ratio and the FSSP-derived scattering ratio:

$$\chi = \frac{1}{N}\sum_{i=0}^{N}\frac{R_{FSSP}(z_i) - R_{lidar}(z_i)}{R_{lidar}(z_i)} \qquad (3)$$

given here in terms of the discretized scattering ratio profiles, where N is the number of data points along the profile. In this sense, the quantity χ serves as an estimate of the accuracy of the aerosol refractive index in the calculation of R_{FSSP}.

Table 1: Complex index of refraction for the seven aerosol types considered in this study according to a classification by Kent et al. [1983].

Aerosol type	Complex index of refraction at 1.064 μm
Maritime	1.405 - 0.004i
Maritime/rural	1.463 - 0.009i
Rural/urban	1.56 - 0.089i
Urban	1.600 - 0.163i
Dustlike	1.52 - 0.008i
75% H_2SO_4	1.42 - $1.5\cdot10^{-6}$i
$(NH_4)_2SO_4$	1.51 - $2.4\cdot10^{-6}$i

For the purpose of this study we confined our possible choices of refractive indices to the seven aerosol types listed in Table 1.

4 Results

At three locations in the Pacific Basin troposphere, we compared altitude profiles of aerosol backscattering at 1.064 μm as derived from *in situ* aerosol size distribution and lidar measurements.

For all three case studies, we achieved reasonable agreement when we assumed two distinct layers of differing aerosol refractive index. In particular, two of the three cases studied gave excellent agreement when we included an upper layer of aqueous sulfuric acid aerosols (above 3.4 km and 4.7 km, respectively) and a lower layer similar to rural or rural/urban type aerosols [Redemann et al., submitted]. A third case study (Fig. 2) yielded an upper aerosol layer composed of ammonium sulfate particles (3.3 km - 7.6 km) and a lower layer of dust-like aerosol (1.2 km - 3.3 km).

A back-trajectory analysis for this latter case study indicated a similar history of the airmasses in the different layers [Merrill et al., in press]. The airmasses representing both the upper and lower layers originated southeast of the Caspian Sea and passed over the Gobi desert at some time during the 2 days prior to sampling. In particular, the lowest level airmass crossed the Gobi Desert at its northern

edge 36 hours before the measurements took place. Accordingly, the finding of an aerosol with dustlike refractive index in the lower portion of this profile is very much consistent with the airmass origin and history.

5 Conclusions

In almost every case investigated, the combined PEM-West B aerosol observations (lidar, FSSP, impactor) could not be explained on the basis of a compositionally homogeneous aerosol layer. However, most of the data could be interpreted using a multi-layer aerosol model with reasonable choices of aerosol types (and corresponding refractive indices). The main layers could be identified using the intensity profile of the raw lidar data. Indeed, we note that in the three cases presented here, the assumption of two distinct layers was adequate to provide an accurate interpretation of the measurements. This begins to define the limitations of current observations in resolving aerosol structure, both vertically and horizontally. We conclude that the combination of aerosol *in situ* size distribution data and lidar backscatter data in the fashion shown here is a suitable technique to retrieve the vertical structure of the aerosol refractive index.

Acknowledgments. The authors would like to thank Dr. John T. Merrill (University of Rhode Island) for the analysis of airmass trajectories beyond the archived case studies. We would like to express our gratitude towards Guy Ferry (NASA Ames), Steve Howard (Symtech Corp.) and Sunita Verma (SSAI) for helpful discussions regarding the *in situ* data analysis and Marta Fenn (SAIC) for help with the lidar data. This work was partly funded under NASA Earth System Science Fellowship 95-0344, and NSF grant ATM-96-18425.

References:

Browell, E.V. et al., NASA multipurpose airborne DIAL system and measurements of ozone and aerosol profiles, *Appl.Opt.*, 22, 522-534, 1983

Browell, E.V., Differential Absorption Lidar sensing of ozone, *Proc.IEEE*, 77, 419-432,1989

Browell, E.V. et al., Large-scale air mass characteristics observed over Western Pacific during summertime, *J.Geophys.Res.*, 101, 1691-1712, 1996

Fu, Q. , K.N. Liou, On the correlated k-distribution method for radiative transfer in nonhomogeneous atmospheres, *J.Atmos.Sci.* 49, 1992

Kent, G.S., G.K. Yue, U.O. Farrukh, A. Deepak, Modeling atmospheric aerosol backscatter at CO_2 laser wavelengths. 1: Aerosol properties, modeling techniques, and associated problems, *Appl.Opt.*, 22, 1655-1665, 1983

Merrill, J.T., R.E. Newell, A.S. Bachmeier, A meteorological overview for the Pacific Exploratory Mission-West, Phase B, *J.Geophys.Res.*, PEM-West B special issue, submitted

Mielke, B., V.N. Cherbakov, B. Stein, J. Kolenda, P. Rairoux, J.-P. Wolf, Error analysis of restoring stratospheric aerosol parameters from single frequency lidar sounding, *SPIE*, 1688, 212-218, 1992

Pueschel, R.F., J.M. Livingston, G.V. Ferry, T.E. DeFelice, Aerosol abundances and optical characteristics in the Pacific basin free troposphere, *Atmos.Environ.*, 28, 951-960, 1994

Redemann, J., R.P. Turco, R.F. Pueschel, M.A. Fenn, E.V. Browell, W.B. Grant, A multi-instrument approach for characterizing the vertical structure of aerosol properties: Case Studies in the Pacific Basin troposphere, *JGR*, submitted

Toon, O.B., Modeling the relationships between aerosol properties and the direct and indirect effects of aerosols on climate, in: *Aerosol forcing of climate*, Charlson, R.J., Heintzenberg, J.(eds.), 197-213, John Wiley & Sons, New York, 1994

High Spectral Resolution Lidar at 532 nm for Simultaneous Measurement of Aerosol and Atmospheric State Parameters

Johnathan Hair, David A. Krueger, and C.Y. She
Physics Department, Colorado State University, Fort Collins, CO. 80523
Phone: (970) 491-5880, FAX: (970) 491-7947, E-mail:jwhair@lamar.colostate.edu

Abstract

We report the first field measurement of a high spectral resolution lidar system at 532 nm with an injection seeded doubled Yag laser and the use of molecular iodine vapor filter in the receiver to measure both atmospheric state parameters (temperature, pressure, and density) and aerosol properties simultaneously. With input of both pressure and temperature at a reference altitude, the system measures vertical profiles of aerosol optical properties and atmospheric state parameters.

1. Introduction

Measurements of vertical profiles of aerosol optical properties and atmospheric state parameters including temperature are of considerable importance to atmospheric physics. It is therefore one of the principal goals of lidar measurements in the troposphere to measure directly the backscatter ratio and temperature profiles (She, 1990), thereby determining all relevant vertical profiles of aerosol optical properties and state parameters of a troposphere in hydrostatic and local thermal equilibrium. The scattering spectrum from molecules, Rayleigh scattering, which depends on the temperature and pressure, can be used to measure the atmospheric temperature and pressure at different altitudes. Light scattered from the atmosphere also has contributions from aerosols, which vary in size, shape, and distribution. A high spectral resolution lidar (HSRL), with the use of atomic or molecular vapor filters, can spectrally separate molecular and aerosol scattering return signals to allow measurements of vertical aerosol properties and temperature profiles (Shimizu et al., 1983). Using a barium vapor filter operated near 537 nm, initial measurements with this technique have been reported (Alvarez et al., 1993). Measurements of optical aerosol properties have been measured using an iodine vapor filter by the Wisconsin group (Piironen et al., 1994). More recently, measurements of tropospheric temperature profiles using an iodine vapor filter to deduce simultaneously measured aerosol optical properties and state parameters were conducted at 589 nm (Caldwell, 1995). Although the photon signal to noise of the system at 589 nm was marginal due to a relatively low linear count rate that were achievable with the photomultiplier tube that was available, the measurement results were in agreement with the concurrent balloon sonde. The HSRL technique for measuring atmospheric temperature and aerosol properties is self consistent in that it only requires the pressure at one altitude as an independent input. The development of the HRSL at different stages has been summarized and compared (Hair et al., 1996).

2. Lidar System at 532 nm

The complexity of the 589 nm HSRL system based on several inter-related lasers has prompted the development of a lidar system to be operated at 532 nm, using the popular, commercially available doubled YAG laser. Since the lidar system uses the spectral information from the scattered returns that pass through an iodine vapor filter for frequency discrimination, the laser transmitter must have high spectral resolution (~100 MHz) and be tunable over a few GHz so that it can be operated within a selected iodine absorption band. In addition the laser must be capable of being locked to an absolute frequency. As shown in Figure

1, a Lightwave model 142 cw dual wavelength laser having 50 mW of both 1064 nm and 532 nm light is used. The 1064 nm light is used to seed a pulsed doubled YAG laser (Spectra Physics model DCR-3D) producing tunable and Fourier transform limited transmitting laser pulses. The cw 532 nm light is frequency locked to provide an absolute frequency reference using iodine Doppler-free saturated absorption spectroscopy, with an active feedback control loop (Arie et al., 1992).

The detection system in our case uses a relatively small 8-inch Cassegrain telescope. A Daystar filter with a FWHM of 130 GHz has been installed in the receiving system to eliminate rotational and vibrational Raman scattered light from the return signal, eliminating the need to include them in data analysis. In addition, this removes significant background light which also allows measurements to be made near dusk and dawn. The signal is then split into three channels. Two molecular scattering channels have iodine vapor filters, while an unfiltered channel measures the total Rayleigh-Mie scattering as shown in Figure 1. This system is an improvement over that at 589 nm for two main reasons (Caldwell, 1995). The system at 532 nm reduces the error due to photon counting statistics and simplifies the lidar transmitter to a more desirable and robust system. As demonstrated previously for the 589 nm system, an iodine vapor filter can accurately be used to separate molecular and aerosol scattering for atmospheric temperature measurements and with a transmitter consisting of only stable solid state lasers that are commercially available, atmospheric temperature and aerosol measurements with high range and temporal resolution can be conducted routinely.

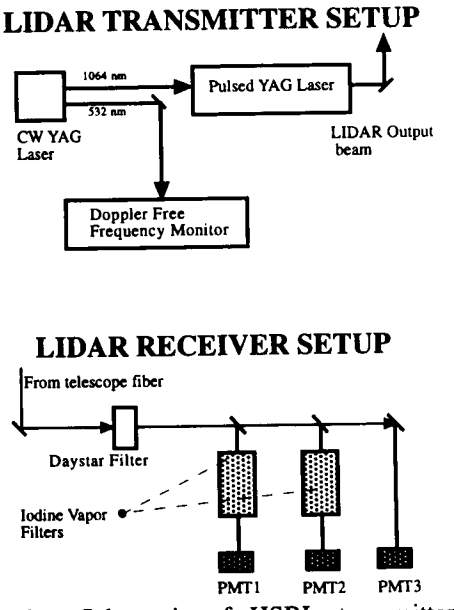


Figure 1. Schematic of HSRL transmitter and receiver. The transmitter system consists of the cw YAG laser to seed the pulsed YAG laser allowing a single longitudinal mode with 74 MHz linewidth. The receiver setup consists of the collected light being split into three channels, two with iodine filters.

3. Initial Field Results

In the spring of 1997, the lidar system at 532 nm was in operation. Data taken on the night of May 4 demonstrated reduction of the photon counting error as experienced in the 589 nm system, giving an hourly average temperature profile with ~ 6.5 K/km lapse rate up between 2 and 10 km with good signal-to-noise. As reported in a recent conference paper (Hair et al., 1998), the data obtained on September 6, 1997 has demonstrated the lidar's ability for cloud dynamic studies and for temperature profile measurements with modest aerosol or cloud backscatter present (backscatter ratio less than 5). Unfortunately, there exists a systematic temperature bias making the lidar measured temperatures consistently ~ 8 K warmer than the reading from balloon sonde. The exact nature of this bias is still under study, although most likely it is due to insufficient spectral purity in the laser system at 532 nm.

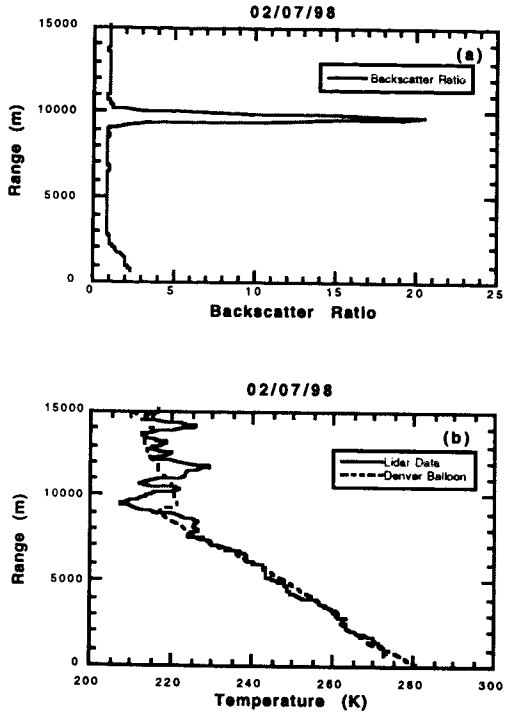


Figure. 2 Observed hourly mean backscatter ratio (a) and temperature (b) profiles taken at Fort Collins, CO. on Feb. 7, 1998, along with a Denver balloon sounding (bold dash line).

The HSRL originally conceived assumes that only a pressure input at one altitude is needed for data analysis (Alvarez, et al, 1993) to retrieve profiles of aerosol and atmospheric state parameters. Until a laser transmitter of better spectral purity is available there are two alternatives. First we may correct the temperature bias by using both pressure and temperature at the reference level. Alternatively, we assume that the transmitted laser light has a 1% broad band radiation (over a 35 GHz range) in addition to the main narrowband (measured to be ~ 75 MHz FWHM) output. With this broadband radiation accounted for in the data analysis program, the temperature bias is removed. A recent example using this analysis procedure on data taken Feb. 7, 1998 is shown in Fig. 2. The lidar measured temperature profile tracks the balloon sonde very well up to ~ 10 km where a layer of cloud with backscatter ratio of 20 was present The temperature data is a bit noisy above 10 km, but considering the photon noise, it is still in agreement with the balloon sonde taken 60 miles away.

4. Conclusion and Future Prospect

The field measurements shown in Figure 2 revealed the salient features and demonstrated the uniqueness of our HSRL lidar system under development. The lidar is capable of simultaneous measurements of aerosol and atmospheric state parameters. With such a modest lidar system (5 W transmitter and an 8-inch receiving telescope), hourly mean temperature profiles can be made up to a range of 15 km, even under modest aerosol/cloud contamination. If laser spectral purity can be increased, higher backscatter ratios can be tolerated, making dynamical and thermal studies of cirrus cloud structure possible with our lidar.

Though with poor signal-to-noise, the interim lidar at 589 nm did not show observed systematic temperature bias because the laser transmitter only used the pulsed YAG laser to pump a dye amplifier. The small fraction of broadband light in the pump does not significantly impact the frequency spectrum of the PDA output (Caldwell, 1995). During the course of the development, it became clear that the spectral purity of our current YAG system is, unexpectedly, lower than that is required for the HSRL transmitter for atmospheric temperature profiles to be exactly determined without the correction for the ~1% broadband frequency component in the transmitted laser signal. Before the laser transmitter is improved, a normalization factor will be introduced into data analysis for temperature measurements. This can be done by a simple measurement of pressure and temperature at one convenient altitude or by introducing an appropriate fraction of broadband component light into the transmitter spectrum in data analysis depending on the laser system used.

5. Acknowledgment

This work is supported in part by DOD Center for Geoscience, Phase II (DAAH04-94-G-0420) at Colorado State University.

References

Alvarez II, R. J., Caldwell, L. M., Wolyn, P. G., Krueger, D. A., McKee, T. B., and She, C. Y., "Profiling Temperature, Pressure, and Aerosol Properties Using a High Spectral Resolution Lidar Employing Atomic Blocking Filters", *J. Atm. Oceanic Tech.*, 10, pp. 546-556, 1993.

Arie, A., Schiller, S., Gustafson, E. K., Byer, R. L., "Absolute frequency stabilization of diode-laser-pumped ND:YAG lasers to hyperfine transitions in molecular iodine", *Opt. Lett.*, 17, pp. 1204-1206, 1992.

Caldwell, L. M., *A High Spectral Resolution Lidar using an Iodine Vapor Filter at 589 nm*, Ph.D. thesis, Dept. of Physics, Colorado State University, Ft. Collins, Co., 1995.

Hair, J. W., L. M. Caldwell, D. A. Krueger, and C.Y. She, "High Spectral Resolution Lidar for Measuring Aerosol and Atmospheric State Parameters Using an Iodine Vapor filter at 532 nm", in pp. 241-250, Application of Lidar to Current Atmospheric Topics, Sedlacek Ed., *SPIE Proceedings* 2833 (1996).

Hair, J. W., D. A. Krueger, and C.Y. She, "High Spectral Resolution Lidar for Measuring Aerosol and Atmospheric State Parameters and Aerosol Properties", *Proceedings of the 1997 Battlespace Atmospherics Conference 2-4 December*, Eds. K.D. Anderson and J.H. Richter, Space and Naval Warfare Systems Center Technical Document 2989, December 1997.

Piironen, P., and Eloranta, E. W., "Demonstration of a High-Spectral-Resolution Lidar based on an Iodine Absorption Filter", *Opt. Lett.*, 19, 3, pp. 234-236, 1994.

She, C.Y. "Remote measurement of atmospheric parameters: new applications of physics with lasers", *Contemp. Phys.*, 31, pp. 247-260,1990.

Shimizu, H. S., Lee, S. A., and She, C. Y., "High spectral resolution lidar system with atomic blocking filters for measuring atmospheric parameters", Appl. Opt., 22, pp. 1373-1381, 1983.

High Spectral Resolution Lidar Using an Iodine Filter for Measuring Temperature and Optical Characteristics of Aerosols and Clouds

Zhaoyan Liu, Ichiro Matsui, and Nobuo Sugimoto

National Institute for Environmental Studies
Onogawa 16-2, Tuskuba, 305 Japan

Phone: (081) 0298-502477, FAX: (081) 0298-502575, Email: liu@nies.go.jp

1 Introduction

Although a basic Mie lidar is able to provide the information of distributions of atmospheric aerosols, it requires an assumption on the relationship between the extinction and back scattering coefficients of aerosols to solve the lidar equation (Collis and Russell, 1976, Reagan *et al.*, 1989). It was suggested (Shipley et al., 1983) that when the Rayleigh and the Mie scattering signals are measured separately the aerosol optical roperties can be directly deduced with the knowledge of air molecular scattering parameters. A high spectral resolution lidar (HSRL) using a monochromatic laser and a narrow band blocking filter such as the high resolution Fabry-Perot etalon and the atomic vapor cell can provide such a direct determination of the two backscattering components based on their spectral difference without the need for additional assumptions.

In 1983 Shimizu *et al.* proposed a HSRL using atomic blocking filters for measuring atmospheric parameters and She *et al.* (1992) demonstrated the simultaneous HSRL measurements of tropospheric temperature and aerosol extinction coefficient profiles using two barium atomic vapor filters. These studies have shown several advantages of an atomic absorption filter over an interferometer filter: the spectral characteristics of an atomic absorption filter are stable and its transmission characteristics are not dependent on the mechanical alignment, which makes the alignment of the filter much easier and can eliminate the well known range dependence of lidar signal along with an interferometer filter; furthermore, high rejection against aerosol scattering can be obtained with an atomic absorption filter so that the separation of the Rayleigh and Mie scattering signals becomes more easy and more perfect.

Piironen and Eloranta (1994) demonstrated HSRL measurements of aerosol scattering properties based on an iodine absorption filter and reported that strong absorption is obtained with a short length of the iodine vapor cell at room temperature.

In this paper we report a HSRL using an iodine filter for measuring clouds and aerosols. One of the purposes of the HSRL is to construct models of clouds and aerosols which can be useful for developing data reduction algorithms for space lidar observation. We also present the measurement of the atmospheric temperature profile with the HSRL.

2 Lidar System Description

A block diagram of the HSRL is shown in Fig.1. The lidar transmitter employs a pulsed, frequency doubled Nd:YAG laser at 532 nm (Continuum Powerlite 7010) as a light source. The laser oscillator is injection seeded with a single frequency cw Nd:YAG laser so that the laser has a narrow spectral band width of 0.003 cm^{-1}. Maximum frequency doubled output is 400 mJ per pulse at a repetition rate of 10 Hz. Pulse energy is changeable by adjusting the Q-switch delay time. Pulse duration is 5-7 ns. The laser wavelength is tunable by thermally scanning the seeder frequency.

Since the laser wavelength should be tuned to and kept at the center of an iodine absorption line for completely blocking the Mie scattering component, a wavelength monitor was developed. It consists of an acoustooptic (AO) modulator, an 20 cm iodine cell, and two power monitor detectors with peak holding circuit. A small portion of transmitted laser beam is picked off with a partial mirror and directed to the wavelength monitor. Both zeroth and first order beams from the AO modulator are transmitted through the iodine cell and detected with the detectors. The frequency of the first order beam is shifted by 270 MHz while the zeroth order beam does not receive the shift. When the laser wavelength is tuned to the center of an absorption line of iodine, the shifted wavelength is located at the shoulder of the absorption line. The change of the laser frequency and the direction of the change can be thus detected from the changes of the outputs of the two detectors.

The receiver uses a 40 cm iodine cell as a high resolution blocking filter and the laser wavelength is tuned to the 1111 absorption line center. Because the transmission of the iodine vapor cell is dependent on the cell temperature, the iodine cell is thermally stabilized.

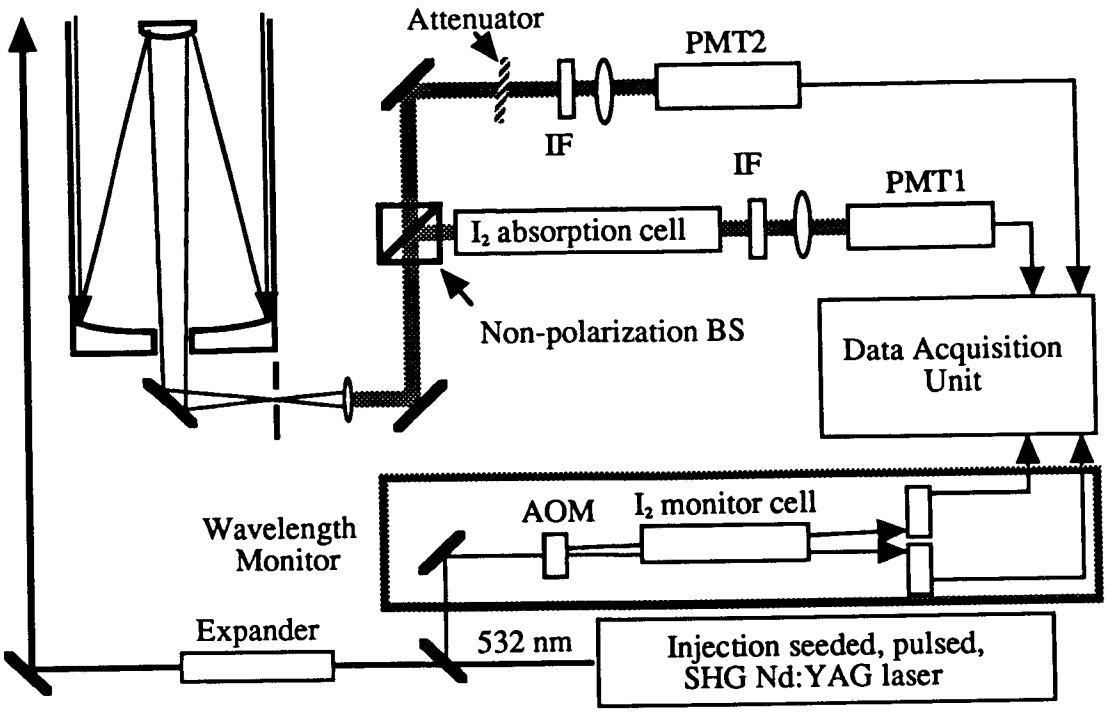


Fig. 1 Daigram of the iodine absorption Blocking filter based HSRL.

A 56 cm Cassegrain type telescope is used in the receiver. A non-polarization cube beamsplitter is used for dividing the collected lidar return to eliminate the effect of depolarization in cloud measurements. Two photomultiplier tubes, PMT1 and PMT2, are used for optical detection and photon counting mode is utilized. Table 1 lists the lidar specifications.

Table 1 Lidar specifications

Transmitter	
Laser :	pulsed, injection seeded SHG Nd:YAG
Wavelength: 532 nm	
Maximal output:	400 mJ / pulse
Repetition Rate:	10 Hz
Receiver	
Telescope:	56 cm, Cassegrain type
FOV:	0.3 mrad.
Detector:	photomultiplier tube
Detection mode:	photon counting
Bandwidth:	3 nm

3 Experimental Results

To test the characteristics of the iodine filter, we firstly measured the absorption spectrum of the iodine cell for the wavelength monitor by scanning the laser wavelength. Fig. 2 shows the results. By comparing the measured iodine spectrum with the published spectrum (Gerstenkorn *et al.*, 1978) we identified the absorption lines. We chose 1111 line for HSRL experiments, because it has strong absorption.

We then measured the spectrum of lidar return signal by scanning laser wavelength over 1110 and 1111 lines. Fig. 3 shows the ratio of the outputs of PMT1 and PMT2 as a function of laser wavelength. In Fig. 3, spectra at a height of 7.5, 12.3 and 18.3 km (solid line) and simultaneously measured iodine absorption spectrum (dotted line) are shown. For comparison we calculated the convolution of the iodine spectrum and Rayleigh spectrum, and fitted the result to the measured spectra of different heights.

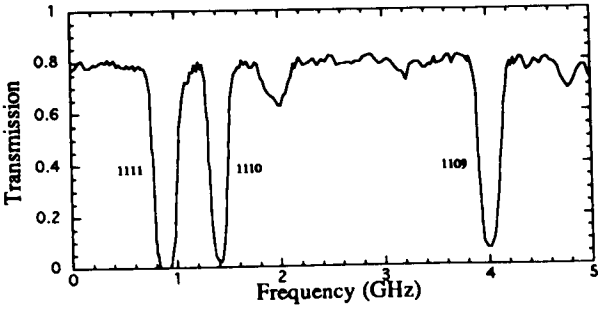


Fig. 2 Absorption lines of monitor iodine cell measured by scanning laser wavelength.

We obtained the temperature profile from the spectral widths of the fitted Rayleigh spectra for different heights . We also retrieved a temperature profile by inverting the Rayleigh profile derived with PMT1 in Fig.1 using the algorithm by Elterman (1953) and Hauchecorne and Chanin (1980). Both temperature profiles are compared in Fig. 4 with a sonde measurement at a station close to the lidar site. Temperature profiles are generally agreed. The temperature profile retrieved from the Rayleigh profile is higher than sonde data at the lower height. This is due to the saturation of the photocounting system. The profile obtained with the Rayleigh spectral width is less sensitive to the saturation.

Mie-to-Rayleigh backscatter ratio and backscattering coefficient distributions of the stratospheric aerosols can also be derived at the same time with the temperature profile measurement. Figure 5 shows an example of the scattering ratio in stratosphere which was measured on the nights of January 26, 1998. Integrated backscattering coefficient from tropopause to 30 km was currently observed to be 0.00015~0.00025 (sr^{-1}).

Preliminary observation of clouds has be started. Figure 6 shows an example of measured backscatter coefficient (a), optical depth (b), extinction coefficient (c) and lidar ratio (d) (i.e., the ratio of the extinction

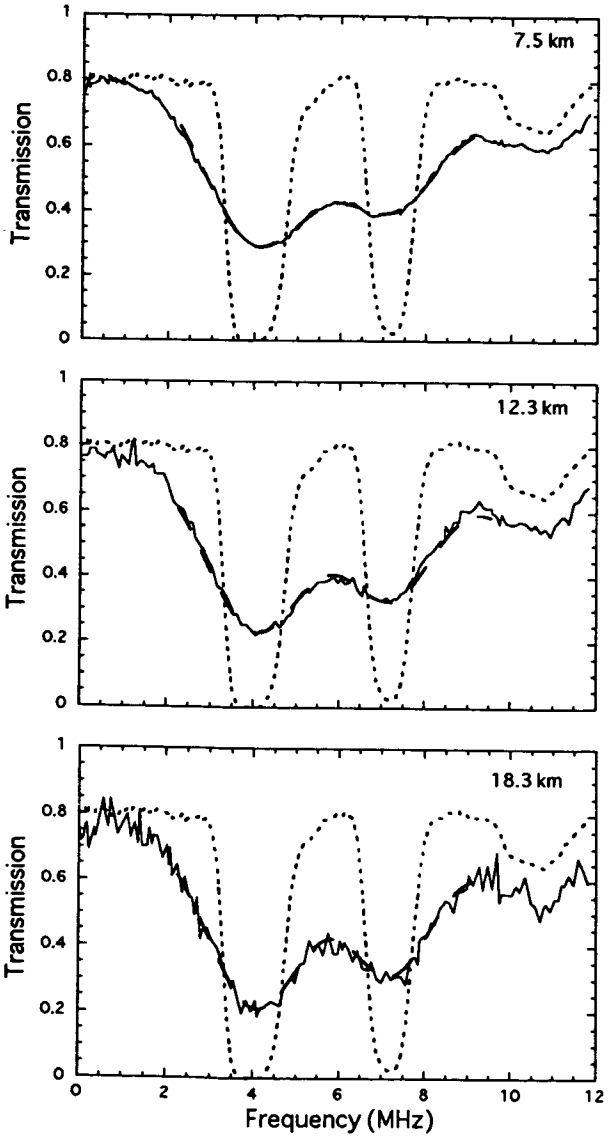


Fig.3 Measured spectra of returns backscattered from the height of 7.5, 12.3 and 18.3 km (thin line), and simultanuoesly measured absorption spectrum of monitor iodine cell (dotted line), and calculated convolutions of iodine absorption spectrum and Rayleigh spectrum for different heights (dashed line). Range resolution is 600 m.

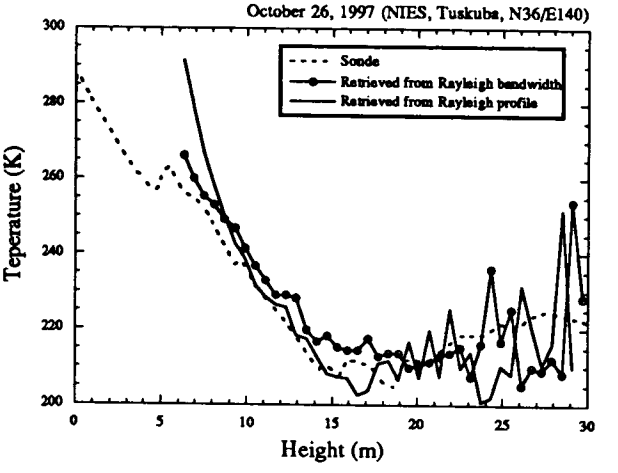


Fig. 4 Comparisons of measured temperature profiles with a sonde data.

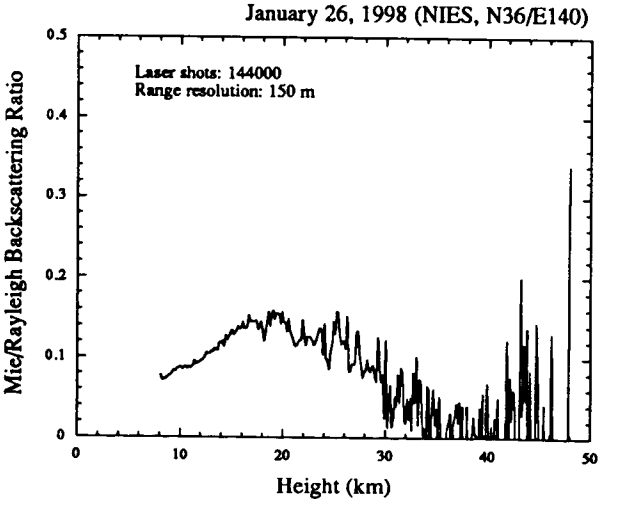


Fig. 5 An example of observed Mie-to-Rayleigh backscattering ratio in stratosphere.

coefficient to the backscattering coefficient of the Mie scatterers) of an optically thin cloud.

4 Conclusions

A HSRL using an iodine absorption filter has been developed and reported. The preliminary observations showed that a HSRL is a useful tool for measurements of aerosol and cloud optical properties. It was also demonstrated that a HSRL can be used for simultaneous measurements of the profiles of backscattering coefficient and temperature of the stratosphere and upper troposphere.

This lidar is currently being used for measuring the aerosols, clouds and temperature profiles at NIES.

References:

Collis, R. T., and P. B. Russell (1976). Lidar measurement of particles and gases by elastic backscattering and differential absorption, in *Laser Monitoring of the Atmosphere*, E. Hinkley, Ed. (spring, New York), p.71.

Elterman, L. B. (1953). A series of stratospheric temperature profiles obtained with the searchlight technique. *J. Geophys. Res.* **58**, p.519.

Gerstenkorn, S., and P. Luc (1978). *Atlas du spectre d'absorption de la molecule d'iode* (Centre National de las Recherche Scientifique, Paris).

Hauchecorne, A., and M. L. Chanin (1980). Density and temperature profiles obtained by lidar between 35 and 70 km. *Geophys. Res. Lett.* **7**, p.565.

Piironen, P. and E. W. Eloranta. Demonstration of a high-spectral-resolution lidar based on an iodine absorption filter (1994). *Opt. Lett.* **19**, p.234.

Reagen, J. A., M. P. McCormick, and J. D. Sphinhirne (1989). Lidar sensing of aerosols and clouds in the troposphere and stratosphere. *Proc.IEEE* **77**, p.433.

She, C. Y, R. J. Alvarez II, L. M. Caldwell, and D. A. Krueger (1992) High- spectral-resolution Rayleigh-Mie lidar measurement of aerosol and atmospheric profiles. *Opt. Lett.* **17**, p.541.

Shimizu, H., S. A. Lee, and C. Y. She (1983) High spectral resolution lidar system with atomic blocking filters for measuring atmospheric parameters. *Appl. Opt.* **22**, p.1373.

Shipley, S. T, D. H. Tracy, E. W. Eloranta, J. T. Trauger, J. T. Sroga, F. L. Roesler and J. A. Weinman (1983). High spectral resolution lidar to measure optical scattering properties of atmospheric aerosols. 1: theory and instrumentation.*Appl. Opt.* **22**, p.3716.

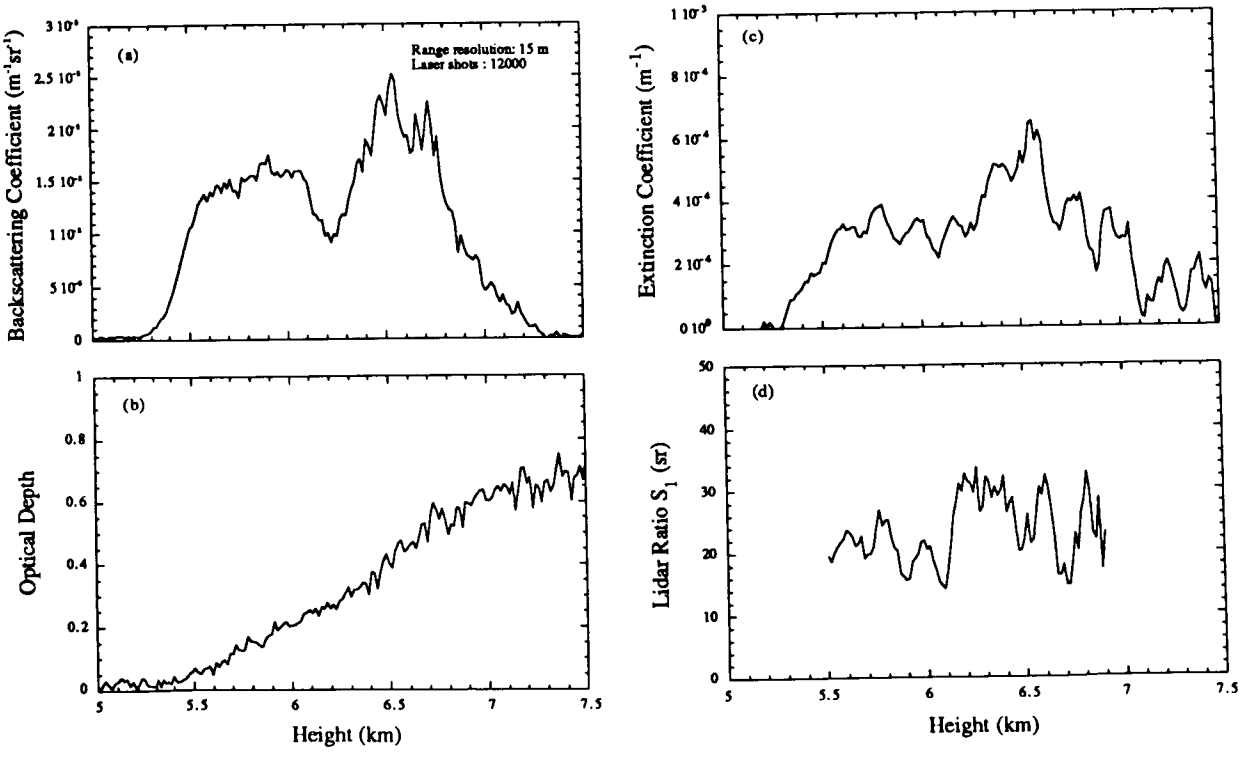


Fig. 6 An example of retrieved optical parameters of a thin could.

Lidar Network and Airborne Observations of the Cloud Street over Tokyo in Summer

Kenji Kai*, Kanji Wakiyama, Masamitsu Fujii, Keiko Niwano, and Daisuke Muramatsu,
Institute of Geoscience, University of Tsukuba
Phone & FAX:81-298-53-6704, E-mail: kai@sky.envr.tsukuba.ac.jp
Makoto Abo, and Chikao Nagasawa
Department of Electrical Engineering, Tokyo Metropolitan University
Toshiyuki Murayama
Tokyo University of Mercantile Marine
Kikuo Okada
Meteorological Research Institute/ JMA
Hiroshi Hara, and Hayato Nakajima
Ishikawajima-Harima Heavy Industries Co., Ltd

* (After April 1998) Corresponding author address: Kenji Kai, Unit of Environmental Informatics, Graduate School of Human Informatics, Nagoya University, Chikusa-ku, Nagoya 464-8601, Japan. Phone & FAX: 81-52-789-4257. E-mail: kai@info.human.nagoya-u.ac.jp

1 Introduction

Recently, a street of cumulus clouds (the so-called "Kampachi Cloud") was frequently observed over the Metropolitan Loop Road No.8 in Tokyo in summer (Figure 1). People living along the Loop 8 are interested in the cloud street: What is the mechanism of the cloud street? Is the cloud street formed by the aerosols released by cars on the Loop 8, or by the heat island in Tokyo ? To answer these questions, the lidar network and airborne observations were carried out at three lidar stations from 1994 to 1996. The radiosonde soundings were also made at the second lidar station.

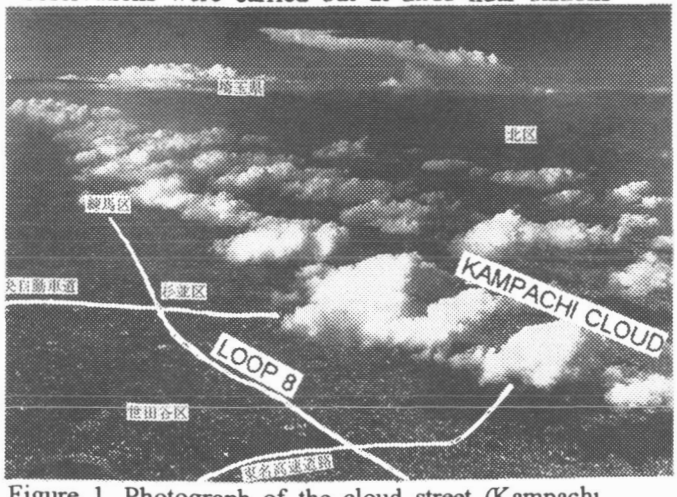


Figure 1. Photograph of the cloud street (Kampachi Cloud) on 21 August 1989 (by the Asahi Shimbun).

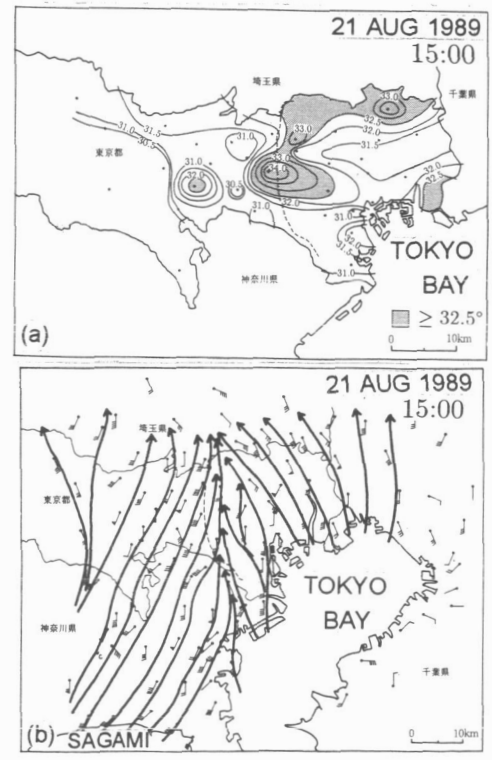


Figure 2.(a) Surface temperature, and (b) surface wind and stream line in Tokyo and its surround area at 15 JST on 21 August 1989.

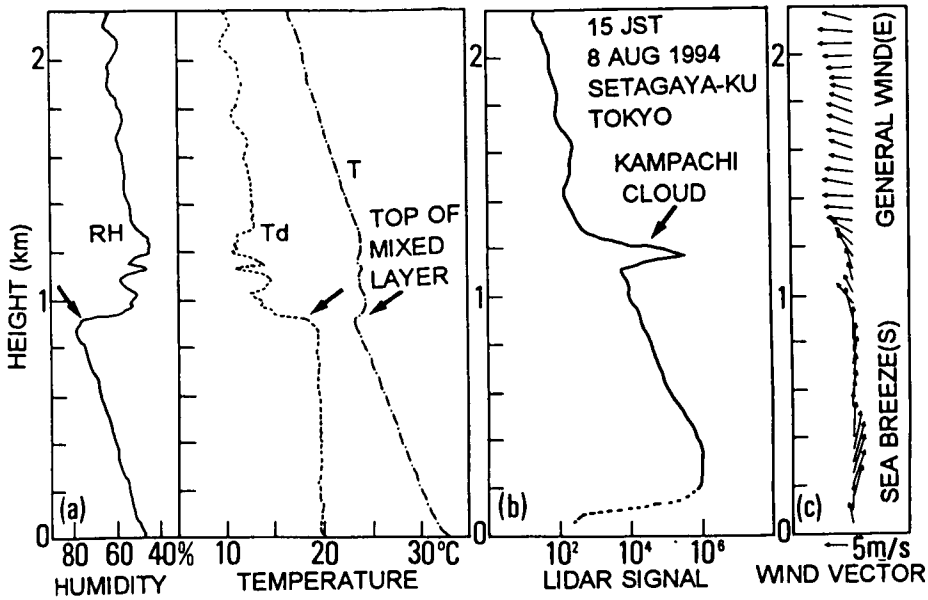


Figure 3. Lidar and radiosonde observation of the cloud street over Setagaya-ku, Tokyo at 15 JST on 8 August 1994. (a) Relative humidity (RH), dew-point temperature (Td) and air temperature (T), (b) backscattered lidar signal, and (c) horizontal wind vector.

2 Case Study of the Cloud Street in August 1989

The analysis of the surface wind and temperature measured at a hundred of monitoring stations in Tokyo and its surrounding area is shown in Figure 2.These figures show that the Kampachi Cloud occurred over the convergence zone of surface winds.The convergence zone coincides with the heat island of Tokyo. The analysis suggested that the geographical location of the cloud street may be determined by the interaction between the heat island circulation and the land and sea breeze circulation in Tokyo.

3 Lidar Network Observation in 1994

The lidar network and radiosonde observations of the cloud were carried out in Tokyo during 5-8 August 1994 in order to investigate the structure of the cloud. The fist station was located at Koto-ku, near the Bay of Tokyo. The second station, Setagaya-ku, was just west of the center of Tokyo, 15 km inland from the seashore. The third station, Hachioji, was 45 km inland.

A typical cloud street was observed at 1200 m just above the mixed layer in the afternoon on 8 August 1994, when the sea breezes from the Tokyo and Sagami Bays were blowing into the heat island of Tokyo. It is suggested that the cloud street was formed by the thermal convection in the unstable shear flow.

4 Airborne Observation in 1996

The airborne, lidar and radiosonde observations were carried out in the summer of 1996, in order to investigate the structure of the atmosphere over Tokyo.

A laser particle counter, an impactor and a thermometer-hygrometer were installed in a helicopter. The airborne observation by the helicopter provided vertical profiles of number density of aerosols, aerosol samples, air temperature and humidity from 300 m to 2500 m.

Simultaneously, lidar and radiosonde observations were conducted. A compact and removable eye-safe lidar developed by IHI (Ishikawajima-Harima Heavy Industries Co., Ltd.) was used to monitor the atmospheric environment.

Figure 4(a) shows a schematic illustration of an aerosol layer and the free atmosphere over Tokyo. The airborne observation demonstrated that there was

an aerosol layer over Tokyo due to the anthropogenic sources. The visibility was bad in the aerosol layer and very good in the free atmosphere. In the daytime, the aerosol layer corresponded to the mixed layer at height of about 1 km. There were cumulus clouds at the top of the mixed layer.

Figure 4(b) are electron micrographs of the aerosols collected at heights of 300 m, 1000 m and 2500 m. The anthropogenic aerosols were well mixed in the mixed layer, and were trapped at the capping inversion. An abrupt change of aerosol density exists between the mixed layer (Z=1000 m) and the free atmosphere (Z=2500 m). Several water-soluble aerosols can be seen in the electron micrograph at height of 1000 m, where the relative humidity is high.

Figure 5 shows a comparison of simultaneous lidar, radiosonde, and airborne observations at 15 JST on 9 August 1997 over Tokyo. There was a top of mixed layer at height of 1600 m. Potential temperature and specific humidity are almost constant in the mixed layer. Relative humidity is maximum at the top of mixed layer. Intensity of back scattering is constant in the mixed layer, and increases near the top of mixed layer. Number density of the aerosols at various radii increases gradually from the surface to the top of the mixed layer, and then decreases suddenly. The figure demonstrated that the mixed layer controlled the vertical distribution of the aerosols.

5 Concluding Remarks

We proposed an observational model of the atmospheric environment and the Kampachi Cloud over Tokyo in Figure 6 (Kai et al., 1995a). Sea breezes from the Tokyo and Sagami Bays, the heat island along the Loop 8, the aerosol layer and the Kampachi Cloud characterize the atmospheric environment over Tokyo in summer. The observational results suggested that the condensation nuclei and water vapor for the Kampachi Cloud were supplied from the mixed layer. The compact and removable eye-safe lidar developed by IHI was applicable to monitoring the atmospheric environment over a populated area such as Tokyo.

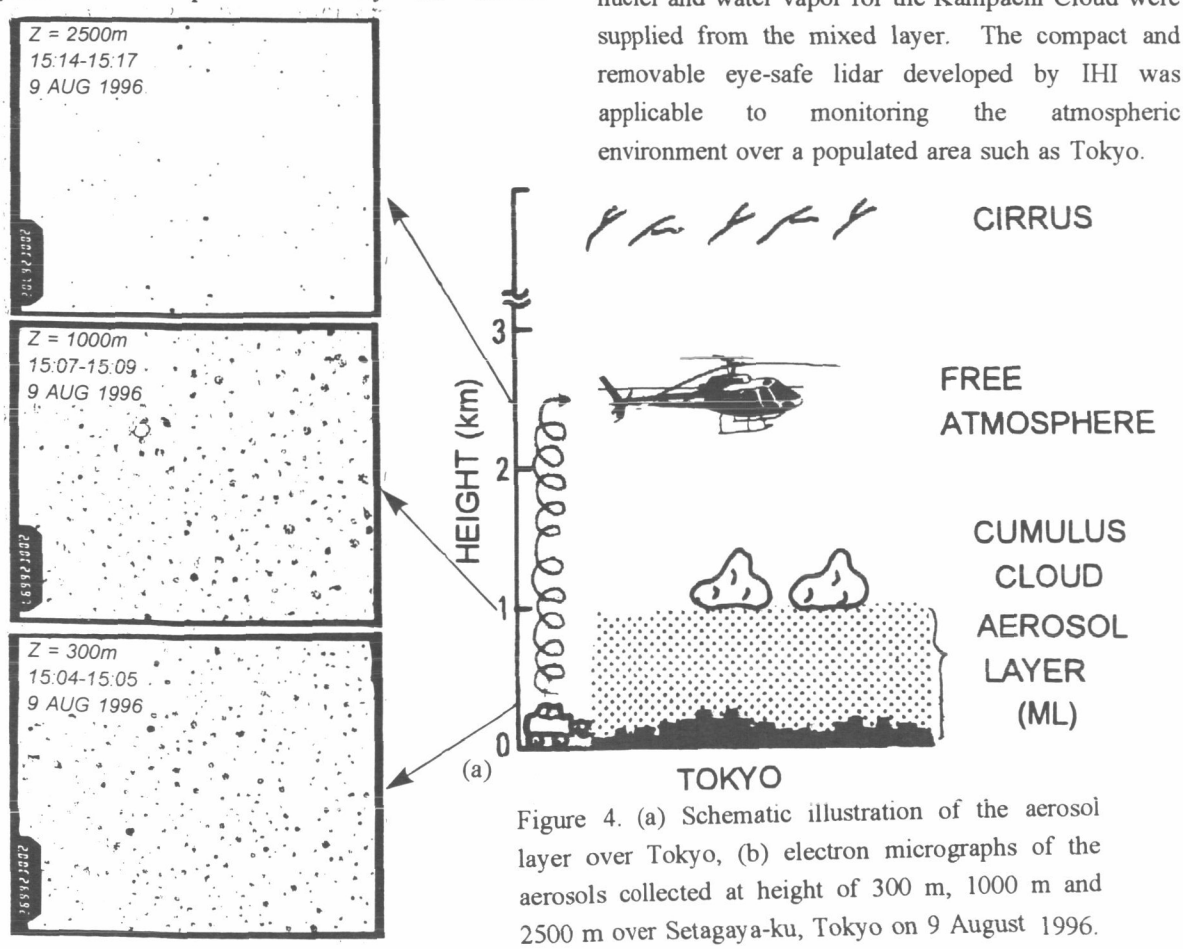


Figure 4. (a) Schematic illustration of the aerosol layer over Tokyo, (b) electron micrographs of the aerosols collected at height of 300 m, 1000 m and 2500 m over Setagaya-ku, Tokyo on 9 August 1996.

References

Kai, K. et al.(1995). A case study on the Kampachi Cloud Street over Tokyo (in Japanese). *Tenki*, 42(7):417-427.

Kai K. et al.(1995). Observation of the Kampachi Cloud over Setagaya-ku, Tokyo in the summer of 1994 (in Japanese). *Tenki*, 42(10):715-719.

Kai K. et al.(1997). Lidar network and airborne observations of the cloud street over Tokyo in summer. *Proceedings of the 12th Symposium of Boundary Layers and Turbulence, 28 July - 1 August 1997, Vancouver, Canada*, 465-466.

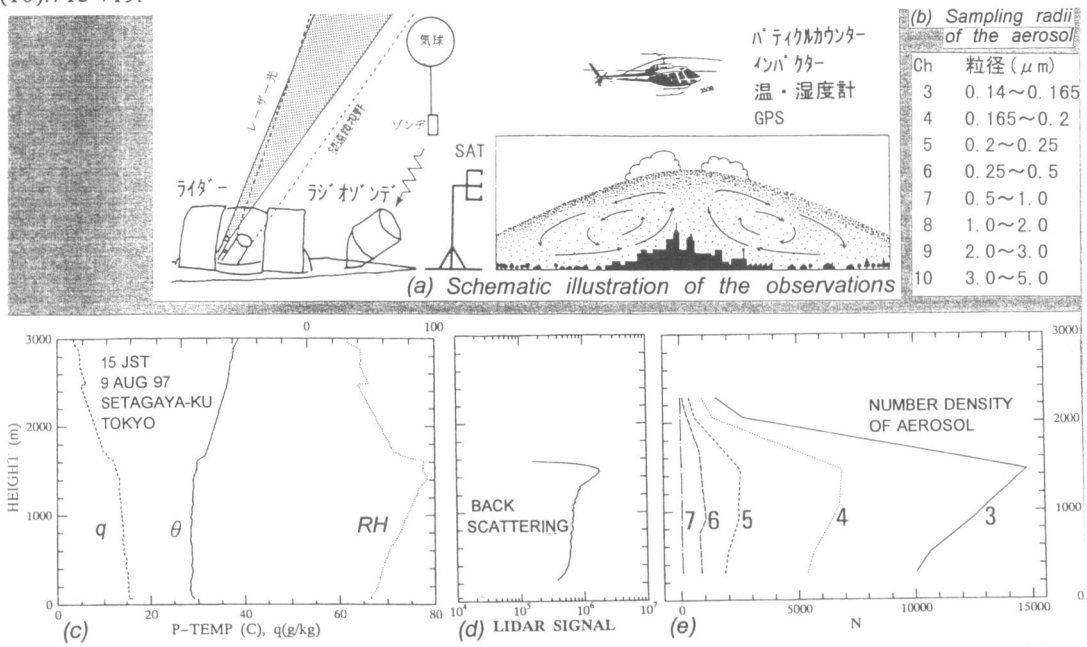


Figure 5. Comparison of simultaneous lidar, radiosonde and airborne observations. (a) Schematic illustration of the observations, (b) sampling radii of the aerosol, (c) specific humidity, potential temperature and relative humidity, (d) lidar signal, and (e) number of the aerosols at various radii.

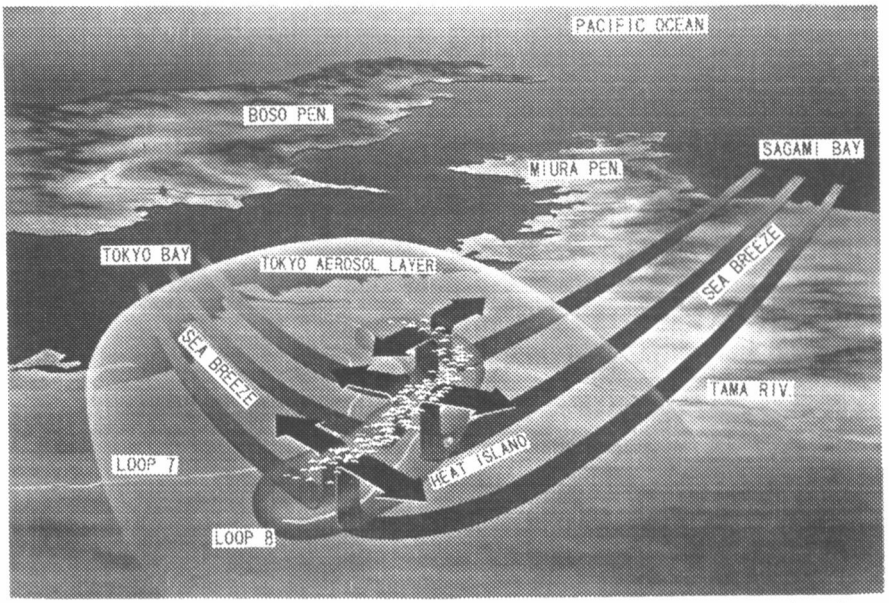


Figure 6. Model of the atmospheric environment and the Kampachi Cloud over Tokyo in summer.

Lidar Observations of Aerosols at Bandung, Indonesia

K.Mizutani, T.Itabe, M.Yasui, T.Aoki
Communications Research Laboratory, Ministry of Posts and telecommunications
4-2-1 Nukui-kita, Koganei, Tokyo 184--8795, Japan
Phone:+81-423-27-6955 ,FAX:+81423-27-6667, E-mail:mizutani@crl.go.jp

T.Nagai, T.Fujimoto, M.Hirota
Meteorological Research Institute, Japan Meteorological Agency
1-1 Naganine, Tsukuba, Ibaraki 305, Japan
Phone:+81-298-53-8582 ,FAX:+81-298-56-0644, E-mail:tnagai@mri-jma.go.jp

O.Uchino
Observations Department, Japan Meteorological Agency
1-3-4 Ote-machi, Chiyoda-ku, Tokyo 100, Japan
Phone:+81-3-3212-8341 ,FAX:+81-3211-4640, E-mail:ouchino@hq.kishou.go.jp

A.Nuryanto, S.Kaloka, S.Hamdi
National Institute of Aeronautics and Space, Bandung, Indonesia
Jl.Dr.Djundjunan 133,Bandung 40173, Indonesia
FAX:+62-22-601-4998

1. Introduction

Aerosols in the atmosphere take an important role in the global climate change through radiation and chemical processes. Information of aerosol scattering magnitude is also necessary for the development of spaceborne lidar because required system parameters (laser power, telescope diameter, detector sensitivity) depend on the strength of aerosol backscattering. Though lidar is the best tool to measure height profiles of the atmospheric aerosols, the equatorial region where raw materials of the stratospheric aerosols are supplied through active convection is a blank area as for lidar observations. Then, we installed a lidar system at Bandung, Indonesia to observe height profiles of aerosol distribution and to study the transportation mechanism of the aerosols in the global scale.

2. Lidar System

A lidar system is installed at Bandung (-7N, 108E), Indonesia on November 1996. Fundamental (1064nm), 2nd harmonic (532nm), and 3rd harmonic (355nm) wavelengths of Nd:YAG laser are transmitted. 2nd harmonic backscatter light and its N_2 raman backscatter light (607nm) are collected by a 28cm telescope and a 35cm diameter telescope. Fundamental and 3rd harmonic light are used in other receiving system which is described by Nagai et al. (1997).

In 35cm telescope system, upper troposphere and stratospher are observed by photon counting. 532nm light components polarized parallel and perpendicular to the laser light are separately observed to get information about shape of aerosols. the parallel component is divided to lower altitude channel and upper altitude channel to expand dynamic range of detection system. The upper and lower altitude channels data are connected around 20km and combined to form a height profile of parallel component. The raman backscatter channel includes only the signal from molecular N_2 and is used as a reference for the atmospheric molecule distribution and extinction.

In 28cm telescope system, the signal is measured by A/D converter to observe the troposphere. Parallel and perpendicular components to the laser light are also separately observed. The system parameters are listed in Table 1.

3. Result

A height profile of scattering ratio and depolarization ratio after applying an iterative method for correction of extinction is shown in Figure 1 together with that at Wakkanai (45N, 142E). Tropopause of this day is 17.6km which is just up a small peak seen at 17.2km. The stratospheric aerosols are distributed between 18km and about

Table 1. Lidar system at Bandung

Transmitter			
Laser	Nd:YAG laser with SHG and THG		
wavelength	1064 nm*	532 nm	355nm*
Output energy	400 mJ	200 mJ	580 mJ
Repetition Rate		10 Hz	
Beam divergence		<0.1 mrad	
Receiver(532nm and 607nm system)			
Telescope	35cm Φ	28cm Φ	
Field of view	1.0 mrad	1.4 mrad	
Height resolution	60 m	15m	
Detector	PMT(R3234x4)	PMT(R3234x2)	
	Px2,S, Raman (N_2)	P,S	
Method of detection	photon counting	A/D	

*1064nm and 355nm laser light are used for backscattering measurement at each wavelengths and for raman backscattering measurement at 386nm by H_2O and at 408nm by N_2.

35km. Clouds are always observed between 10km and tropopause and area around tropopause is clear except for cloud-like structures. The stratospheric aerosols are seen from 12km and decrease around 30km at Wakkani. As the aerosols observed at Bandung appear from higher altitude than that at Wakkani, the integrated backscattering coefficients (IBC) are a few times smaller than at Wakkani. Time variation of IBC is shown at Figure 2. Variation of IBC at Bandung seems to be small and IBC is about $6x10^{-5}sr^{-1}$ level. In this observation period, Soufriere Hill at West Indies erupted and it is reported that plumes of ash have reached heights of 12km. Though there is a small increase of IBC after the eruption, the relation is not clear.

An example of height profiles of scattering ratio and depolarization measured by A/D are shown in Figur 3. Aerosol layer or thin clouds exist up to 6km, but upper troposphere seems to be very clear except for cirrus clouds which is always seen in higher altitude than 10km. Except for cloud-like structures, this clear upper troposphere is always observed at Bandung.

References

Nagai, T., et al. (1997). Lidar measurement of the stratospheric temperature at Bandung, Indonesia, in proceeding of the Tsukuba International Workshop on Stratospheric Change and Its Role in Climate and on the ATMOS-C1 Sattellite Mission: 121-123.

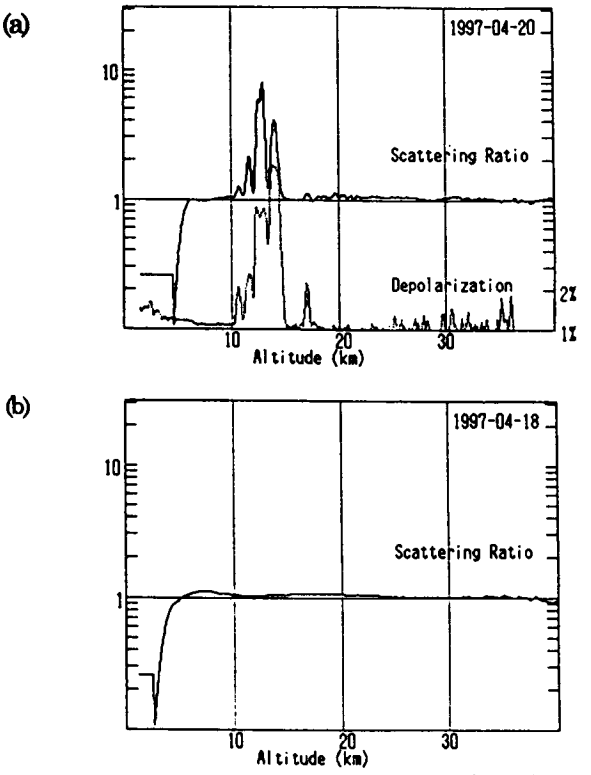


Figure 1 (a) Height profiles of scattering ratio and depolarization ratio at Bandung. (b) Height profile of scattering raio at Wakkanai.

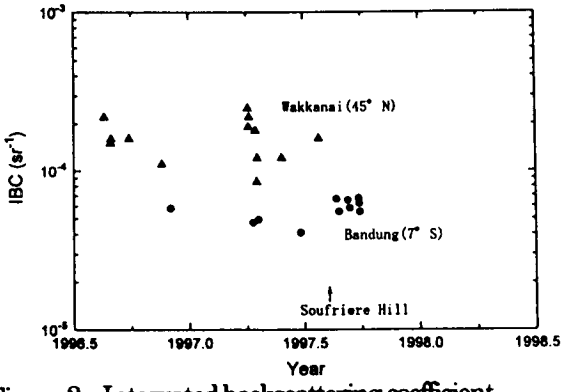


Figure 2 Integrated backscattering coefficient.

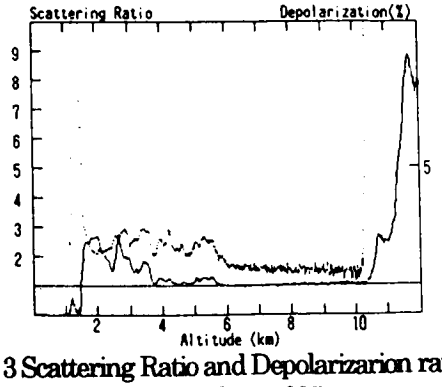


Figure 3 Scattering Ratio and Depolarizarion ratio at Bandung on April 21, 1997.

Constraint Inversion Algorithm for deriving Aerosol Optical Property from Lidar Observation and its Application

Qiu Jinhuan
Institute of Atmospheric Physics,Chinese Academy of Sciences,Beijing 100029, China
Email:jhqiu@mimi.cnc.ac.cn

Abstract

A key question of the backward integration (Klett) algorithm to lidar equation is how to determine the far-end extinction coefficient. This paper develops a Constraint Inversion Algorithm (CIA) for deriving the coefficient and then aerosol extinction profile from lidar return signals. The algorithm demands lidar return signals along both Horizontal path and slant (or vertical) path, and it uses *Horinzontal* signals as constraint information in determining far-end aerosol extinction coefficient and then extinction profile $\sigma_a(r)$ along the *slant* path. It is found that the smaller the wavelength is, and the larger the aerosol optical depth is, the more sensitive to the variation of the aerosol extinction to backscatter ratio k_a the solution by CIA. According to the property a method is proposed to simultaneously retrieve $\sigma_a(r)$ and k_a from multi-wavelength or multi-path lidar observations. Numerical simulations and some applications by CIA will be presented. Its application includes a ruby lidar measurements of $\sigma_a(r)$ during a dust storm event and a Nd-YAG lidar measurements of $\sigma_a(r)$ in the boundary layer. lidar-detected aerosol extinction profile will be compared with aerosol concentration profile measured on a tower with a height of 344m.

1. Constraint Inversion Algorithm (CIA) for deriving aerosol extinction coefficient profile and its extinction to backscatter ratio

The lidar equation can be written as

$$P(r) = \frac{CE[\beta_m(r) + \beta_a(r)]}{r^2} e^{-2\int_0^r [\sigma_m(r') + \sigma_a(r')]dr'} \quad (1)$$

where P(r) is the lidar return signal from the atmosphere at the distance r, C is a constant of lidar system, E is laser output energy, $\beta_m(r)$ and $\sigma_m(r)$ are molecular backscatter coefficient and extinction coefficient, and $\beta_a(r)$ and $\sigma_a(r)$ are aerosol backscatter and extinction coefficients, respectively.

It can be derived from Eq.1 that

$$f(r) = \int_{r_0}^{r} k_a(r) S(r) \exp\left\{\int_0^r [1-\alpha(r'')]\sigma_m(r'')dr''\right\}dr$$
$$= \frac{CE}{2}\left\{\exp[-2\alpha(r_0)\tau_m(0,r_0) - 2\tau_a(0,r_0)] - \exp[-2\tau_a(0,r) - 2\alpha(r)\tau_m(0,r)]\right\}, \quad (2)$$

where $\alpha(r)=k_a(r)/k_m$, $k_a(r)$ and k_m are aerosol and molecular extinction to backscatter ratios. τ_a and τ_m are aerosol and molecular optical depths, and $S(r)=P(r)r^2$.

Combining Eqs.1-2 can yield expression on the far-end extinction coefficient $\sigma_a(r_1)$ as:

$$\sigma_a(r_1) = -\frac{k_a(r_1)}{k_m}\sigma_m(r_1) + S(r_1)k_a(r_1)\{\exp[2\tau_m(0,r_1) + 2\tau_a(r_0,r_1) - \frac{2k_a(r_0)}{k_m}\tau_m(0,r_0)] - \exp[2\tau_m(0,r_1) - 2\frac{k_a(r_1)}{k_m}\tau_m(0,r_1)]\}/f(r_1). \quad (3)$$

It is difficult to consider or derive height-dependent $k_a(r)$ according to lidar return signals.

Molecular parameters can be known. Neglecting the variation of $k_a(r)$ with r ($k_a(r)=k_a$), the far-end extinction coefficient $\sigma_a(r_1)$ can be determined if k_a and $\tau_a(r_0,r_1)$ are known. Then the aerosol extinction coefficient solution by backward integration algorithm using the $\sigma_a(r_1)$ is:

$$\sigma_a(r) = -\alpha\sigma_m(r) + \frac{S(r)\exp\left[2(\alpha-1)\int_r^{r_1}\sigma_m(r')dr\right]}{S(r_1)/\left[\sigma_a(r_1)+\alpha\sigma_m(r_1)\right]+2\int_r^{r_1}S(r)\exp\left[2(\alpha-1)\int_r^{r_1}\sigma_m(r'')dr''\right]dr} \quad (4)$$

A key question is how to determine aerosol optical depth $\tau_a(r_0, r_1)$ between near-end r_0 and far-end r_1. So-called Constraint Inversion Algorithm (CIA) proposed in this paper uses additional lidar return signals and some aerosol parameters derived from the signals alone the *horizontal* path as constraint information in determining $\tau_a(r_0, r_1)$ alone *slant* or *vertical* path. In the algorithm $\tau_a(r_0, r_1)$ can be derived according to Eqs.1-2 as:

$$\tau_a(r_0,r_1) = -\frac{k_a(r_1)}{k_m}\tau_m(r_0,r_1) - 0.5\ln\left[1-\frac{\bar{G}Ef(r_1)b}{\bar{E}\bar{f}(\bar{r}_1)\bar{b}}\right], \quad (5)$$

$$\bar{G} = 1-\exp\left[-2\bar{\tau}_a(\bar{r}_0,\bar{r}_1) - 2\bar{\alpha}\bar{\tau}_m(\bar{r}_0,\bar{r}_1))\right], \quad (6)$$

$$b = \exp\left[-2\tau_a(0,r_0) - 2\alpha\tau_m(0,r_0)\right], \quad (7)$$

$$\bar{b} = \exp\left[-2\bar{\tau}_a(0,\bar{r}_0) - 2\bar{\alpha}\bar{\tau}_m(0,\bar{r}_0)\right]. \quad (8)$$

where parameters with the bar are the horizontal ones, definition of both $f(r_1)$ and $\bar{f}(\bar{r}_1)$ are shown in Eq.2.

As shown in Eq.5, five parameters such as $f(r_1)$, $\bar{f}(\bar{r}_1)$, $\bar{G}$, b and $\bar{b}$ must be known in order to determine $\tau_a(r_0, r_1)$. If $k_a(r)$ is known, $f(r_1)$ and $\bar{f}(\bar{r}_1)$ can be calculated using lidar return signals. $\bar{G}$ can be derived through determining the optical depth $\bar{\tau}_a(\bar{r}_0,\bar{r}_1)$ from horizontal lidar signals. In the case of small r_0 or basically homogeneous aerosol extinction coefficient between 0 and r_0, $b/\bar{b}\approx 1$. So, in the case of height-independent aerosol extinction to backscatter ratio k_a, if the k_a is known, $\tau_a(r_0, r_1)$ can be determined. Then in the case of height-independent aerosol extinction to backscatter ratio and no molecular scatter, the value k_a is not needed, and the ratio of $f(r_1)$ to $\bar{f}(\bar{r}_1)$ can be simplified as :

$$f(r_1)/\bar{f}(\bar{r}_1) = \int_{r_0}^{r_1}S(r)dr \Big/ \int_{r_0}^{\bar{r}_1}\bar{S}(r)dr. \quad (9)$$

It is found that the smaller the wavelength is, and the larger the aerosol optical depth is, the more sensitive to the variation of the value k_a the solution by CIA. According to the property a method is proposed to simultaneously retrieve $\sigma_a(r)$ and k_a from multi-wavelength or multi-path lidar observations.

2. Numerical simulations and Some applications

In numerical simulations, effect of errors in the constraint information, lidar return signals, and height-dependent k_a on the solution by CIA is analyzed. CIA is used in deriving aerosol extinction coefficient profile $\sigma_a(r)$ from a ruby lidar observations during a dust storm event. It will also be used in a Nd-YAG lidar measurements of $\sigma_a(r)$ in the boundary layer during March to June of 1998, and lidar-detected aerosol extinction profile will be compared with aerosol concentration profile measured by a particle sampler on a tower with a height of 344m. Some results will be presented.

Cirrus and mid - clouds programme for climatology purposes and studies of processes at the mesoscale

Sauvage Laurent [1], Hélène Chepfer[1], Salem Elouragini[2], Pierre H. Flamant[1], Jacques Pelon[1]

(1) Institut Pierre Simon Laplace, LMD, Ecole Polytechnique, 91128 Palaiseau, France

Phone : +33 1 69333199, Fax. : +33 1 69333005, E-Mail : sauvage@stathp.polytechnique.fr

(2) Institut Préparatoire aux Etudes d'Ingénieurs (IPEIM), Monastir, Tunisia

1. Introduction

Upper tropospheric clouds play a key role in the earth's radiation balance and therefore in global climate. For instance, cirrus clouds can modulate the heating and cooling rates of the atmosphere and earth's surface by greenhouse and albedo effects, respectively (Liou, 1986). Until recently, our knowledge on the radiative, physical and microphysical properties of cirrus clouds were rather deficient despite some attemps conducted in the past. The experimental problem hamper our capability to come up with a relevant set of parameters for modelling. Recently, several field experiments have been conducted involving various remote sensors i.e. lidar, radar, radiometers, and in situ microphysical probes, that result in comprehensive data sets for the optical, radiative and microphysical properties of cirrus clouds. In addition, dedicated sites instrumented in remote sensors provide the oportunity to document the cirrus clouds properties over long periods of time.
In the recent years, we have been involved in both types of activities i.e. field campaigns and longer term climatology in the framework of a Cirrus and mid-clouds programme conducted at Institut Pierre Simon Laplace for the purpose of radiative transfer studies. Field campaigns such as EUCREX (European Cloud and Radiation Experiment) in 1994 put an amphasis on the parametrisation of processes while a longer term climatology undertaken at Palaiseau since 1993 is intended to provide with relevant parameters of mid - latitude cirrus clouds.

2. Data set and data inversion

During EUCREX in 1994 (Raschke et al., 1996) conducted off the coast of Brittany (France) over the Atlantic Ocean, natural cirrus have been documented from both remote sensors and in situ measurements. Backscatter lidars with depolarization measurements capability were deployed on board an aircraft and from the ground. The aircraft was also equiped with in situ probes and radiometers looking up and down (microphysical FSSP probes, Barnes PRT-5 (Precision radiation Thermometer), Eppley visible and infrared radiometers) above and below the cloud (Fig. 1). At present, the data set includes four flights conducted on extended cirrus decks on April 17 an April 21, and three time series recorded from the ground.
In addition, routine measurements are conducted at Palaiseau (48°.43°N, 2.15° E) since 1993. The site is instrumented with a backscatter lidar with depolarization capability and visible and infrared radiometers . Radiosoundings are available nearby from the 12 km far meteo station. Many cases of cirrus have been recorded for periods of time of more than 6 hours .

The lidar data inversion is conducted according to Fernald (1984), Spinhirne et al. (1990) and Young (1995). The clouds properties to be retrieved are the following : base and top height, structure in cloud, apparent optical thickness, backscatter profile, apparent backscatter-to-extinction ratio., depolarisation ratio. The apparent parameters are corrected for multiple scattering.using a multiplying factor η equal to 0.5 (Nicolas et al, 1997).
The lidar linear depolarization ratio is (Sassen 1979) : $\Delta = P_{\perp}(z)/P_{//}(z)$, where $P_{\perp}(z)$ and $P_{//}(z)$ are the backscattered power with perpendicular- and parallel polarization with respect to the transmitted laser polarization, respectively. It requires a normalization to the molecular depolarization at reference altitudes assuming the existence of "clear air" zones below and/or above the cirrus cloud. The depolarization ratio for a purely molecular signal is taken as Δ=2.8% (Young, 1980 and 1981). The cirrus depolarization ratio Δp is corrected for molecular contribution. Δp allows to discriminate water phase from ice and also to give an information on orientation of ice crystals. We obtain depolarisation ratio between 0.4 and 0.5 for cirrus clouds as Spinhirne and Hart,1990), except during some occasions as presented below.

3. Seeding of an altostratus by a cirrus cloud

On 11 April 1994, during the Eucrex campaign, a ground based lidar observed a seeding event of an altostratus by a cirrus (Fig. 2a).
The meteo analysis indicates a cold front coming from the north west. The wind velocity was 30 ms^{-1} between 7 and 8 km and it decreased to 20 ms^{-1} at 5 km. The radiosounding show the presence of a moisture layer between 6.5 and 9 km at 12:00 UT.
Depolarisation values of 0.5 were measured in the first part of the cirrus cloud with clear atmosphere below. Then high values of Δp near or greater than 100 % indicating randomly oriented particles (Platt, 1981).The altostratus layer at 5

km was supercooled liquid water as Δp was almost zero and temperature was -23°C. After the seeding of cirrus particles into this lower layer begining at 17:30 UT, we observed high values of depolarization mixed with low values, significant of mixed phase water (Fig. 2b).
A complete study of the seeding case will be proceeded containing a radiative study by comparison of radiative models outputs and flux measurements deduced from AVHRR and radiometers at the ground. We also will get information on dynamics forcing (vertical motion and turbulence) which is a very important feature in cloud formation (Ström, et al 1997).

4. Statistical properties

From a first analysis of lidar data available from EUCREX campaign and permanent site Palaiseau in France, we obtained distribution of height and optical thicknesses for cirrus clouds as shown in table 1.

	base	top	ΔH	δ
EUCREX				
FLIGHT 8				
leg OM1	8,37±0,59	9,67±0,46	1,29±0,36	0,64±0,54
leg MO1	8,71±0,55	10,135±0,475	1,42±0,29	0,44±0,25
leg MO2	8,53±0,59	9,74±0,5	1,21±0,34	0,44±0,38
FLIGHT 9				
leg AC	7,5±0,88	9,88±0,72	2,38±0,86	0,56±0,55
FLIGHT 13				
leg AB1	8,45±0,4	10,88±0,27	2,43±0,347	0,77±0,436
leg AB2	8,163±0,6	11,182±0,153	2,95±0,63	0,48±0,245
leg BA1	7,95±0,55	10,814±0,2	2,86±0,67	0,60±0,38
FLIGHT 14				
leg BA1	8,67±0,68	11,49±0,156	2,81±0,68	0,63±0,48
PALAISEAU				
081094			2,94±1,40	1,0±0,9
101094			2,54±0,62	0,70±0,66
111094			3,27±0,15	1,54±0,36

table 1 :Statistical results of some lidar data for geometrical and optical parameters : base, top, height ΔH and optical thickness δ of cirrus clouds.

We can distinguish between thin heterogenous cirrus with a negative exponential distribution of the optical thickness (Fig. 3a and 3b) and thick cirrus described by both gaussian thickness and optical thickness distributions (Fig. 3c and 3d).

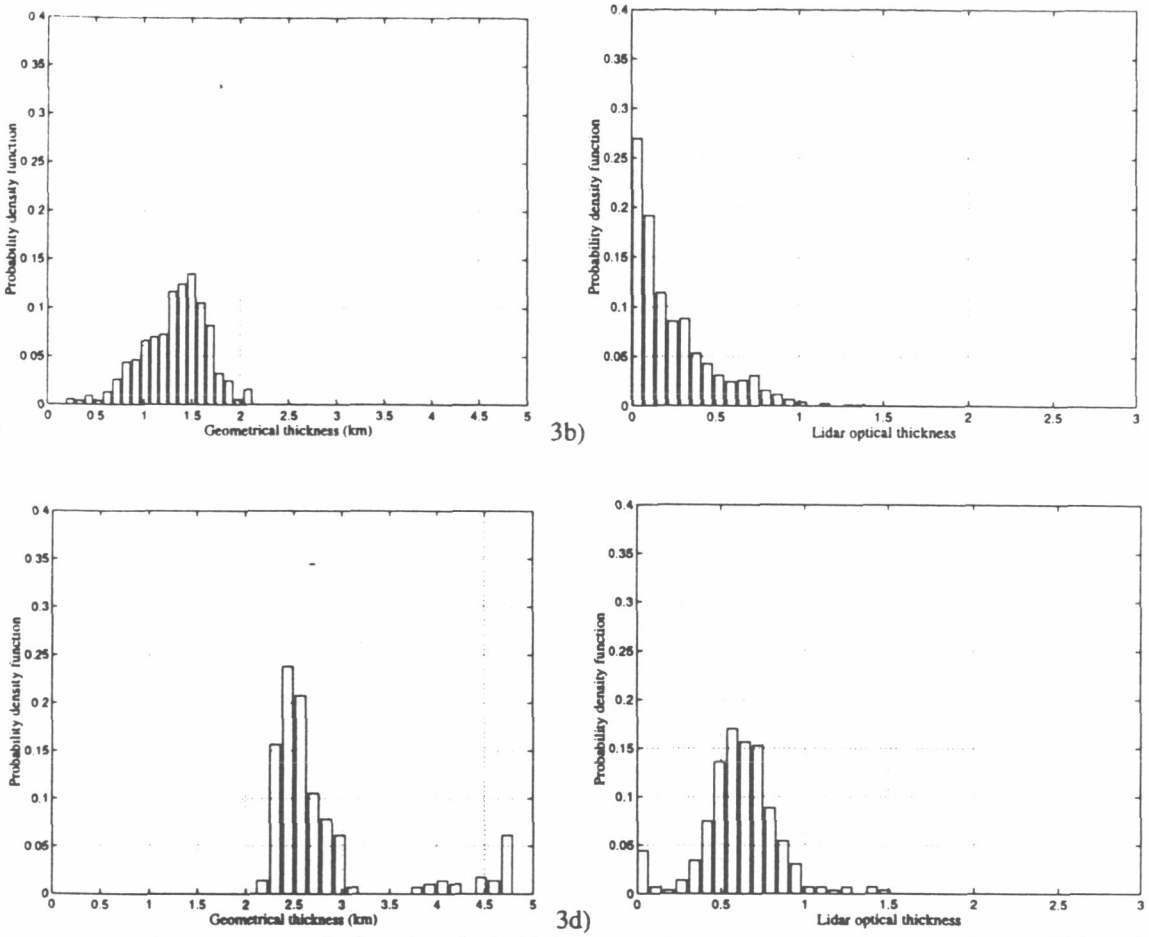


Figure 3 : Distribution of geometrical and optical thicknesses of an optically thin cirrus (3a and 3b); a thick homegenous cirrus cloud (3c and 3d).

5. summary

Using a well documented lidar data set we retrieved some relevant properties : the structure of high level clouds, their apparent optical thickness, extinction coefficient, and depolarization ratio. This last parameter will allow us to make some conclusion on microphysics by comparison with models data.
A large data set elaborated from a lidar network at midlatitudes and tropics in both hemispheres is currently under examination. We aim to give a climatology of high clouds by lidars.

References

1. Fernald F.G., 1984, Analysis of atmospheric lidar observations : some comments, Appl. Opt., 23, 652 - 653.
2. Liou K , 1986, Influence of cirrus clouds on weather and climate processes : a global perspective, A.Meteor.Soc., 114, 1167 - 1197.
3. Nicolas F., L.R.Bissonnette, P.H.Flamant, 1997, Lidar effective multiple scattering coefficients in cirrus clouds, App. Opt., 36, 3458 - 3468.
4. Platt C.M.R., 1981, Observed Temperatures variations in cirrus optical properties, J. Atm. Sc., 38, 1069 - 1082.
5. Raschke E., D. Hemmings, R. Sefzig and M. Quante, 1990 : International Cirrus Experiment : Field Phase Plan, Institut f¸r Geophysik und Meterologie, Universität zu Köln, 129 pp.
6. Sassen K., 1979 : Scattering of polarized laser light by water droplet, mixed-phase and ice crystal clouds. Part I, J. Atmos. Sci., 36, 838- 851.
7. Spinhirne J.D, and W.D. Hart, 1990, Cirrus structure and radiative parameters from airborne lidar and spectral radiometer observations : The 28 October 1986 FIRE study, Mon. Wea. Rev., 118, 2329 - 2343.
8. Ström J., B. Strauss, T. Anderson, F. Schröder, J. Heintzenberg, P. Wendling,1997, In situ Observations of the Microphysical Properties of Young Cirrus Clouds,J.Atm.Sci., Vol. 54, n∞23, 2542 - 2553.
9. Young S.A. , 1995, Analysis of backscatter profiles in optically thin clouds, Appl. Opt.34, 7019-7031.

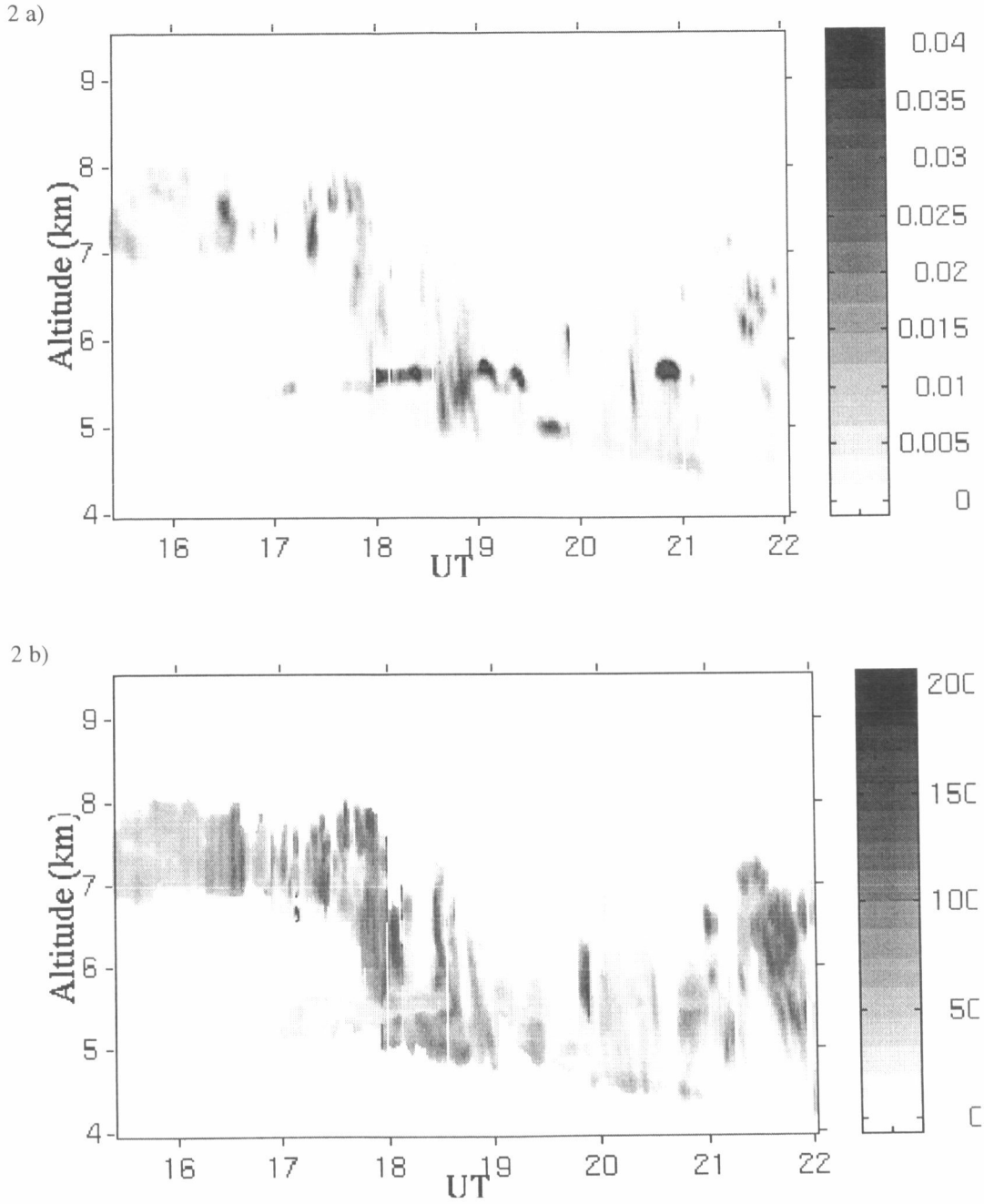


Figure 2 : a) Backscatter coefficient in $km^{-1}sr^{-1}$; b) Depolarization ratio in cloud (%). We observe high values of Δp in the cirrus cloud and in altostratus after seeding by the cirrus cloud.

Operational Processing and Cloud Boundary Detection from Micro Pulse Lidar Data

James R. Campbell, and Dennis L. Hlavka
Science Systems and Applications Inc.
Code 912 NASA Goddard Space Flight Center, Greenbelt, MD 20708 USA
Phone: (301) 286-4631, FAX: (301) 286-1768, E-mail: campbell@virl.gsfc.nasa.gov

James D. Spinhirne, and V. Stanley Scott, III
Mesoscale and Atmospheric Processes Branch
Code 912 NASA Goddard Space Flight Center, Greenbelt, MD 20708 USA

David D. Turner
Pacific Northwest National Laboratories
PO Box 999, MSIN K7-28, Richland, Washington, 99352 USA

1. Introduction

Micro Pulse Lidar (MPL) was developed at NASA-Goddard Space Flight Center (GSFC) as the result of research on space-borne lidar techniques. It was designed to provide continuous, unattended observations of all significant atmosperhic cloud and aerosol structure with a rugged, compact system design and the benefit of eye safety (Spinhirne 1993). The significant eye safety feature is achieved by using low pulse energies and high pulse repetition rates compared to standard lidar systems. MPL systems use a diode pumped 10 μj, 2500 Hz doubled Nd:YLF laser. In addition, a solid state Geiger mode avalanche photo diode (GAPD) photon counting detector is used allowing for quantum efficiencies approaching 70%. Other design features have previously been noted by Spinhirne (1995).

Though a commercially available instrument, with nearly 20 systems operating around the world, the most extensive MPL work has come from those operated by the Atmospheric Radiation Measurement (ARM) (Stokes and Schwartz 1994) program. The diverse ability of the instrument relating to the measurement of basic cloud macrophysical structure and both cloud and aerosol radiative properties well suits the ARM research philosophy. MPL data can be used to yield many parameters including cloud boundary heights to the limit of signal attenuation, cloud scattering cross sections and optical thicknesses, planetary boundary layer heights and aerosol scattering profiles, including those into the stratosphere in nighttime cases (Hlavka et al 1996). System vertical resolution ranges from 30 m to 300 m (i.e. high and low resolution respectively) depending on system design.

The lidar research group at GSFC plays an advisory role in the operation, calibration and maintenance of NASA and ARM owned MPL systems. Over the past three years, processing software and system correction techniques have been developed in anticipation of the increasing population of systems amongst the community. Datasets produced by three ARM-owned systems have served as the basis for this development. With two operating at the southern Great Plains Cloud and Radiation Testbed Site (SGP CART) since December 1993 and another at the Manus Island Atmospheric Radiation and Cloud Station (TWP ARCS) location in the tropical western Pacific since February 1997, the ARM archive contains over 4 years of observations. In addition, high resolution systems planning to come on-line at the North Slope, AK CART shortly with another scheduled to follow at the TWP ARCS-II will diversify this archive with more extensive observations.

2. Data Processing

MPL systems record one minute shot averages in one of three possible byte arrays depending on system and vertical resolution. The prototype instrument used a byte length of 825, low resolution systems use 836 and high resolution systems vary based on desired vertical setting. From the lidar equation, raw count rates take the form:

$$n(r) = \frac{\left(O_c(r)CE\beta(r)T^2\right)}{r^2} + n_b + n_{ap}(r) \qquad (1)$$
$$DTC[n(r)]$$

where n equals the measured signal return in photo electron counts per second at range r, O_c is the overlap correction as a function of range caused by

field of view conflicts in the transmitter-receiver system, C represents a dimensional system calibration constant, E is the transmitted laser pulse energy, β is the backscatter cross section due to all types of atmospheric scattering, T is atmospheric transmittance, n_b is background contribution from ambient light, n_{ap} is the afterpulse correction for detector run on, and DTC is the detector offset deadtime correction as a function of raw count rate. This equation can be taken to the form

$$\frac{\left[\left[n(r) * DTC[n(r)]\right] - n_b - n_{ap}(r)\right] r^2}{O_c(r)E} = C\beta(r)T^2 \quad (2)$$

which is referred to as normalized relative backscatter (NRB). Operational data products produced for the ARM community use this value as output (Campbell et al., 1998). Going a step further, attenuated backscatter can be calculated by dividing C through the left-hand side of this equation, though C must be calculated subjectively on a case by case basis.

Solving equation (2) requires calibrating each MPL for signal and range dependent deadtime, afterpulse and overlap corrections. Deadtime corrections are provided as a function of raw count rate by the photon detector manufacturer. Linear interpolation of this chart in the form of a look-up table, or a curve-fitting equation to the function aptly handles this correction in processing code. Overlap correction is developed by recording an extended period of data with the MPL where aerosol backscatter is constant with distance (i.e. horizontally aimed profile where target aerosol layer is assumed homogeneous). Implicitly at some range r_o the overlap ceases to exist and the correction factor become 1.0. Equation (1) can be written as:

$$P(r) = \left[(n(r) * DTC[n(r)]) - n_b - n_{ap}(r)\right] r^2 = O_c(r)CE\beta(r)T^2 \quad (3)$$

Knowing that $T = e^{-\tau}$ and $\tau = \sigma r$, where τ is the optical thickness through the layer and σ is the extinction cross section, equation (3) can be rewritten as:

$$P(r) = O_c(r)CE\beta(r)e^{-2r\sigma} \quad (4)$$

For the section of this function where $r > r_o$ and $O_c = 1.0$ taking the natural log of both sides of equation (4) yields:

$$\ln[P(r)] = \ln[CE\beta(r)] - 2r\sigma \quad (5)$$

Since this layer is assumed homogeneous CEβ becomes constant. Plotting ln[P] versus r takes the form of $y = mx + b$ with -2σ as the slope m. Fitting a line to the points where $r > r_o$, as in Figure 1, and calculating the slope value equation (4) can be solved for O_c as:

$$O_c(r) = \frac{P(r)}{CE\beta(r)e^{-2r\sigma}} \quad (6)$$

However, since CEβ is a constant we can solve for it with equation (5) where $r > r_o$ and $O_c = 1.0$ and plug this value into equation (6) to solve for the overlap correction as a function of range. The afterpulse correction is developed taking data while pointing the system at a hard target preferably 300 m in range. By blocking the laser pulse detector readings past the target range yield the residual afterpulse signature. Once again a curve-fit equation can be developed for this function for use in processing code.

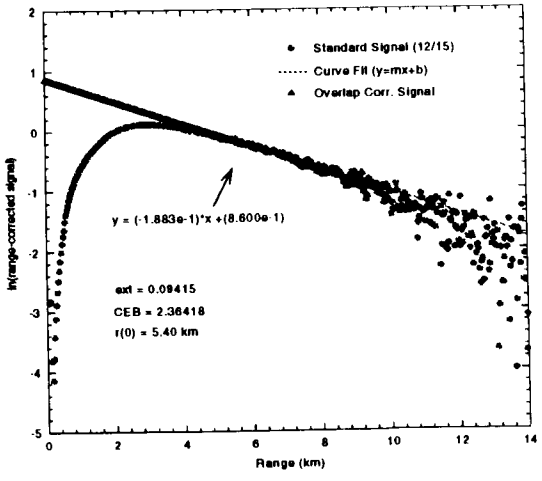


Figure 1. Overlap correction development.

3. Cloud Boundary Height Algorithm

The GSFC cloud boundary height algorithm developed for MPL data uses bi-directional vertical differencing of adjacent range bins of one minute shot averages compared to a similarly analyzed clear-sky baseline. Differences between the two may then be analyzed for possible cloud boundaries. Days are divided into 12 separate analyzing periods from which averaged shots can be examined for both possible baseline inclusion and cloud boundary search. The cloud threshold is combination of a relative signal and signal-to-noise ratio (SNR) increase varying upon observed background count rates.

For each averaged shot a running three point sum of the derivative of the natural log of NRB is taken from the first data range bin vertically to search for areas of deviance, whereby any bin summing over 1.0 is thought to possess cloud. This process discriminates between clear and cloudy shots within a period to produce baseline updates. A varying minimum of clear shots, based on locale, is required to warrant an update. Additionally, as larger variations in signal structure take place in the boundary layer on the scale of 2 hours (one period) the section of the baseline below 3 km can be updated irrespective of the remainder if the minimum clear shot standard is reached amongst its region. Therefore despite cases of prolonged high cloudiness the boundary layer portion of the baseline continues to update. A linear bridge is built between the two sections to smooth out discontinuities in relative signal differencing which may occur. The baseline consists of NRB and SNR averages for each bin. SNR is obtained by reverting NRB back to raw count rates as

$$SNR(r) = \frac{\frac{N(r)O_c(r)N_s E}{r^2}}{\sqrt{\frac{N(r)O_c(r)N_s E}{r^2} + B_s N_s}} \qquad (7)$$

where N is NRB as a function of range, N_s is the number of shots in a one minute average (normally 150,000) and B_s is the solar background count.

Figure 2 displays algorithm output for the first 2 km of a shot average taken by the TWP unit. The first column refers to the height AGL of the center of the corresponding range bin and the second notes the NRB value recorded for that bin. The third column is the percentage increase of backscatter between the bin below and the subject bin, with the same calculation from the bin above to the subject bin listed below. The fourth column is the same process done for the clear sky baseline, and the fifth column is cumulative difference between the values. Note that the first and last bin (not shown) use the baseline value to calculate upwards and downwards increases respectively. The next four columns show the same process for SNR values. The final two columns contain cloud boundary markers and the direction of signal spikes responsible for them respectively.

HGHT	BS	BSDF	BADF	DIFF	SNR	SNDF	BSND	DIFF	CLD	SPK
0.27	0.609	1.665	0	1.665	763.06	0.546	0	0.546	Base	yes
		-0.333	0.149	-0.481		0.261	0.605	-0.344		no
0.57	0.913	0.499	-0.129	0.628	605.04	-0.207	-0.377	0.17	Mid	yes
		-0.143	-0.037	-0.106		0.115	0.167	-0.053		no
0.87	1.065	0.167	0.039	0.128	542.79	-0.103	-0.143	0.04	Mid	no
		0.447	-0.043	0.49		0.503	0.132	0.371		yes
1.17	0.736	-0.309	0.045	-0.354	361.24	-0.334	-0.116	-0.218	Top	no
		0.591	-0.052	0.643		0.637	0.109	0.528		yes
1.47	0.462	-0.372	0.055	-0.426	220.72	-0.389	-0.098	-0.291	n/a	no
		0.351	0.018	0.333		0.489	0.138	0.351		no
1.77	0.342	-0.26	-0.018	-0.242	148.27	-0.328	-0.121	-0.207	n/a	no
		0.344	0.174	0.17		0.502	0.213	0.289		no
2.07	0.255	-0.256	-0.148	-0.108	98.71	-0.334	-0.176	-0.158	n/a	no
		0.247	0.34	-0.093		0.418	0.265	0.152		no

Figure 2. Cloud boundary detection algorithm statistical output for the first 2 km of an averaged shot.

For a cloud boundary to be observed a one or two bin relative NRB increase (either upward or downward) of at least 55% and an SNR increase greater than approximately 42% (the number becomes slightly less near the ground) is required. Because this relationship is not fixed due to variance in solar background rates requiring both increases results in an elastic threshold. For example during daytime where background values are relatively high, a 55% increase in NRB will see a corresponding SNR increase of well over 42%. However at night where background rates are very low, a 55% increase in NRB corresponds to an SNR increase much less than required, thus demanding greater relative NRB increases (than 55%) for detecting cloud. Thus, the threshold becomes the NRB increase in cases of little noise and SNR increase when background rates are high.

Working upward from the base range bin once an "upspike" is detected (as in the 0.27 km bin on Fig. 2), signaling an upwards relative increase in NRB and SNR meeting the threshold requirement, the algorithm sets a cloud base at the corresponding height. A "downspike" is then sought signaling the cloud top. While searching the algorithm ignores other upspikes until the cloud top is found. Additionally, once a cloud top is conditionally found

the following bin above is examined in case of another downspike marking a continued downtrend in signal strength and the true cloud top. Figure 3 plots NRB and cloud boundary height data for a cirrus cloud observed on 23 January 1998 at SGP between 0400 and 0700 GMT. Due to the rather coarse resolution of the currently operational MPLs, gaps between clouds of one range bin (i.e. 300 m) are smoothed requiring at least 600 m of separation between a cloud top and new base. The anticipated availability of processed high-resolution datasets in the near future will likely change this condition.

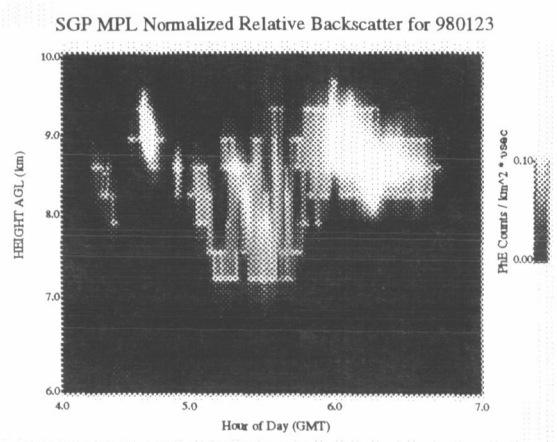


Figure 3. Cloud boundary algorithm heights superimposed on processed MPL data on 23 January 1998 between 0400 and 0700 GMT.

4. Summary

Continuous atmospheric profiling by a growing population of MPL systems will provide numerous time extensive datasets over the coming years from various climatic regions. The current archive of MPL data recorded by ARM-owned systems includes over 4 years of nearly uninterrupted observations over north-central Oklahoma and Manus Island, Papua New Guinea. Data processing techniques and algorithms have been developed at GSFC to produce real-time value added data products for MPL related research. This work includes algorithms for normalizing raw uncorrected data and multiple cloud boundary detection. The ability of MPL data to yield many atmospheric radiative and macrophysical properties places emphasis on the need for such algorithms in order to realize the full potential of datasets. In particular, extensive cloud frequency and thermodynamical climatologies are expected to result from MPL observations aiding in the knowledge of regional cloud variations.

5. Acknowledgments

The authors wish to thank Ms. Robin Perez (ARM) for her efforts in coordinating the extensive computer processing of the ARM MPL datasets.

References

Campbell, J.R., Hlavka, D.L., Spinhirne, J.D., Turner, D.D., Flynn, C.J. (1998). Operational cloud boundary detection and analysis from micro pulse lidar data. In *Abstracts of the 1998 ARM Science Team Meeting*, ARM, submitted.

Hlavka, D.L., Spinhirne, J.D., Scott, V.S., Galbraith, A.E., and Reagan, J.A. (1997). Full time lidar cloud and aerosol height distribution data sets to support radiation/climate forcing studies. In *Abstracts Of the 9th Conference on Atmospheric Radiation*, AMS, 1.15.

Spinhirne, J.D. (1993). Micro pulse lidar, *IEEE Trans. Geo. Rem. Sens.*, 31: 48-55.

Spinhirne, J.D., Rall, J.A.R., and Scott, V.S. (1995). Compact eye safe lidar systems, *Rev. Laser Eng.*, 23: 112-118.

Stokes, G.M., and Schwartz, S.E., (1994). The Atmospheric Radiation Measurement (ARM) Program: Programmatic background and design of the cloud and radiation test bed, *Bull. Amer. Meteorol. Soc.*, 75: 1201-1221.

LIDAR AND RADIOMETRIC OBSERVATIONS OF AEROSOLS IN A TROPICAL URBAN ENVIRONMENT

P.C.S. DEVARA, R.S. MAHESKUMAR, G. PANDITHURAI, P.E. RAJ and K.K. DANI
Physical Meteorology and Aerology Division, Indian Institute of Tropical Meteorology,
Dr. Homi Bhabha Road, Pashan, Pune 411 008, India
Tel : +91-0212-330846; Fax : +91-0212-347825; e-mail : devara@tropmet.ernet.in

INTRODUCTION

Aerosols which present in the atmosphere in different sizes (from 10^{-3} to 10^{3} μm) with varying chemical composition play important role in human health, atmospheric boundary layer and electricity, weather, climate, air and water quality, satellite remote sensing and in the cycling of trace substances. As the aerosol characteristics exhibit a high degree of variability in space and time, and as the anthopogenic share of the total aerosol loading is quite substantial, it is also essential to monitor systematically the aerosol features over longer time scales [1,2].

As aerosols in the troposphere dominate optical properties of the atmosphere, significant contribution to the studies in the field of aerosol science has come from the optical remote sensing techniques. Lidar and radiometry have evolved as the most powerful and versatile techniques for atmospheric aerosol monitoring. While passive radiometers have a longer history of operation of atmospheric studies, including operation from space, for a number of years, active lidar systems are playing important roles in recent years. Because of the excellent spatial resolution which is unattainable with any other remote sensor, lidar technique attracted many scientists for the study of aerosols in different environments. Today, the lidar and radiometric methods are used in a variety of aerosol measurement and monitoring roles, providing information that can be unique or complementary to measurements made by *in-situ* instruments [3].

Despite the importance of tropics and potentiality of the lidar and radiometric techniques, aerosol measurements are sparse over tropics and more so in India. Besides general build-up of aerosols over urban environments (mainly due to anthropogenic activities), the treatment of tropospheric aerosols, particularly in the boundary layer, has become a difficult task due to their shorter residence time in the atmosphere. A computer-controlled, bistatic Argon ion lidar (operating since October 1986) and PC-based spectroradiometer and sunphotometer (both operating since 1992) at the Indian Institute of Tropical Meteorology (IITM), Pune (18°32'N, 73°51'E, 559 m AMSL), India have been used for regular monitoring of aerosol climatological and associated meteorological parameters over this urban station. At present, the IITM lidar and radiometers are also being used for validating the IRS-P3 polar orbiting satellite data and for making Indian Ocean Experiment (INDOEX) correlative measurements. More than 800 vertical profiles of lidar observed aerosol number density in the atmospheric boundary layer during October 1986-September 1996, and radiometric observations of aerosol optical depths obtained on about 350 cloud-free days during February 1993-April 1997 have been utilized in the study. The experi-mentation, data archival and analysis procedures, and results of the above specific experiments are presented in this paper.

TOPOGRAPHY AND INSTRUMENTATION

The experimental site is located at an elevation of about 573 m AMSL, ~100 km inland from the west coast and is surrounded by hillocks as high as 760 m AMSL forming a valley-like configuration. The meteorological conditions at Pune vary considerably from continental (winter) to maritime (summer) environment. The transport and dispersion of pollutants, particularly those in the lower levels of the atmosphere, are believed to be affected by the circulation processes that evolve because of the typical terrain. Also, the stone quarries (east side) and brick-kilns (west side) situated within 1 km distance on either side of the experimental site are considered to be the major local anthropogenic sources contributing to aerosol observations. A significant contribution is also expected due to the major urban activity from the eastern part of the site. The western side is a sparsely populated area.

The data for the present study were obtained with a bistatic lidar, high-spectral resolution radiometer (spectroradiomenter) and multi-wave-

length solar radiometer (sunphotometer). The lidar consists of a tunable Argon ion laser as transmitter, and a 250-mm Newtonian telescope equipped with condensing-collimating lenses, narrow-band interference filter (1nm FWHM) and Peltier-cooled PMT, as receiver. The optical lay-out of this lidar is shown in Fig. 1. The transmitter and receiver are

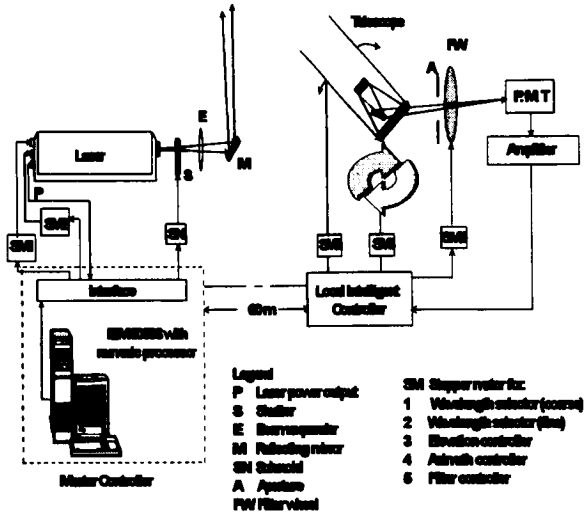


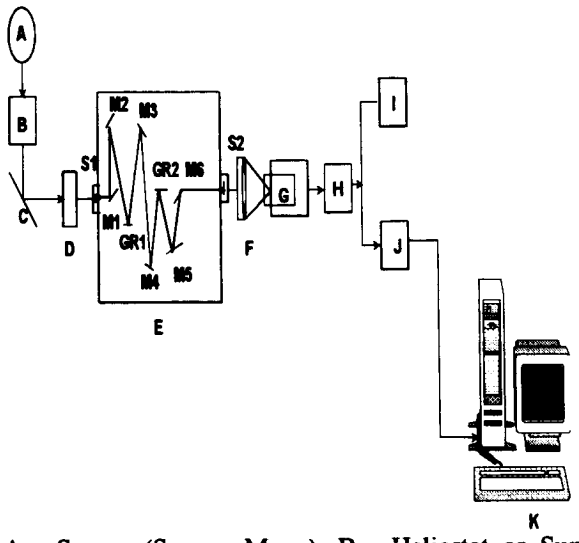
Fig. 1. Optical lay-out of the computer-controlled bistatic lidar system.

coaxially separated by a distance of 60 m in order to operate the system in bistatic mode, the unique configuration which provides angular distribution of scattered intensity for obtaining aerosol size distribution. The on-line control and digital data system provides real-time acquisition, analysis and display of lidar data [4].

The spectroradiometer composed of a double monochromator tailored with holographic gratings and associated detection and data acquisition systems [5]. A line diagram of this radiometer is depicted in Fig. 2. The system can be operated in the spectral range between 200 nm and 720 nm, at sampling interval as low as 0.1 nm. For the present study, a sampling interval of 5 nm for each spectrum was used. The sunphotometer which was operated in conjunction with the spectroradiometer is a conventional filter-wheel-based photometer and it detects quasi-continuous solar irradiance at thirteen wavelengths ranging between UVA and NIR.

OBSERVATIONS AND ANALYSIS

Over 800 profiles (covering the altitude range between 20 m and 1380 m) of aerosol number



A : Source (Sun or Moon); B : Heliostat or Sun (Moon) tracker; C : Reflecting mirror; D : Shutter; E : Double monochromator; F: Condensing lens; G : Photomultipler with cooler housing; H : Amplifier (analog or photon counting); I : Multipen chart recorder; J : Interface;, K : Data acquisition, analysing and plotting system; M_1, M_2, M_4, M_6 : Reflecting mirrors; M_3 & M_5 : Collimating mirrors; S_1 : Entrance slit; S_2 : Exit slit; GR_1 & GR_2 : Holographic gratings

Fig. 2. Line diagram of the spectroradiometer for the measurement of fine-scale atmospheric aerosol optical depths.

density obtained during the 10-year period (October 1986 - September 1996) using an Argon ion lidar, and aerosol optical depth data collected on about 350 cloud-free days from February 1993 through April 1997, except the south-west (SW) monsoon months (June-September), using the spectroradiometer and sunphotometer formed the database for the results reported here. The data retrieval and inversion methods for obtaining aerosol number density from lidar scattered signal strength profiles and height-integrated aerosol optical depth from radiometer observations have been published in the literature [5-8]. The methods of computation of lidar-derived aerosol column content for studying the long-term trends and ventilation coefficients for studying air quality have also been published [6,7]. The aerosol vertical profiles obtained with lidar on all observational days (usually vary from 5 to 7) in each month have been used to construct time series of weekly and monthly mean aerosol column content. The aerosol optical depths obtained with the radiometers on all the clear-sky days, covering the

lidar experimental days, in each month have been averaged and the monthly mean optical depth data series have been constructed for spectroradiometer and sunphotometer separately.

RESULTS AND DISCUSSION

In order to investigate the recent cliamtological trends in the aerosol concentration over Pune, both

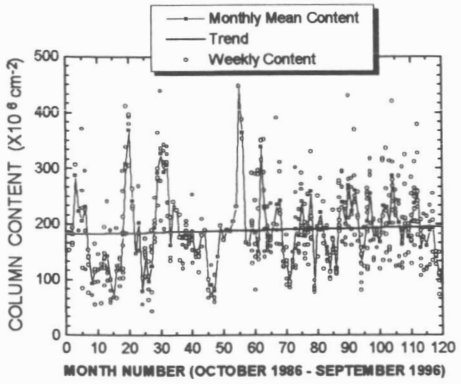


Fig. 3. Long-term trend in the lidar-observed aerosol loading at Pune

weekly as well as monthly mean values of boundary-layer aerosol column content, computed from the aerosol climatological data archived during October 1986-September 1996 have been subjected to the polynomial regression analysis. These data along with their long-term trend (thick line) are shown in Fig. 3. A close examination of the figure reveals an increase of about 9 % in the monthly mean aerosol loading at the station over a period of 10 years. This increase is considered to be due to growth in urbanization, industrialization and changes in land-use patterns in proximity to the experimental station. It has been found that the long-term trend in aerosol loading is not monotonic, but changes from year to year depending on meteo-rological parameters (precipitation, in particular) and local anthropogenic activities.

The aerosol optical depths determined at wave-length of 550 nm from spectroradiometer and 400 nm from sunphotometer observations recorded during February 1993-April 1997 are shown in Fig. 4. As these data represent aerosol extinction (function of aerosol loading) up to about 50 km and cover more than 4-year period, the long-term trends derived from it can be compared, in some sense, with those observed from lidar- recorded aerosol data.

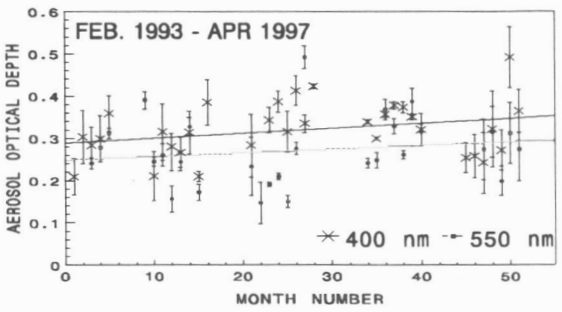


Fig. 4. Long-term trend radiometer-derived aerosol optical depth at Pune. Dotted and solid line in the figure denote trends observed with spectroradiometer and sunphotometer, respectively. Vertical bars indicate standard errors.

The percentage increase in long-term trends exhibited by both spectroradiometer and sun-photometer data were about 16% and 24%, respectively. The difference between the slopes is considered to be due to the response of different sizes of aerosol particles to the wavelength of observations. The trends in aerosol size distribution, derived from the wavelength dependence of aerosol optical depths, are also shown in Fig. 5. The higher Junge exponents observed by the spectroradiometer and smaller exponents by the sunphotometer are considered to be due to the range of wavelengths involved in the measurements.

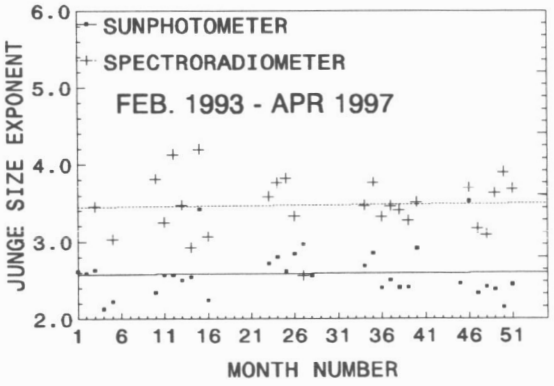


Fig. 5. Trends in aerosol size index observed from spectroradiometer (dashed) and sunphotometer (solid)data.

The aerosol column content and monsoon precipitation relationship has been examined with long-term data recorded during the 10-year period (1987-1996) in Fig. 6. The results show a fairly good agreement between the pre-monsoon (March-April) aerosol content and ensuing SW monsoon rainfall. Such an association has been clearly seen during the contrasting monsoon seasons of 1987

(weak) and 1988 (active). This is ascribed to the combined effect of atmospheric dynamics induced by the changes in radiation field vis-à-vis cloud micro-physics in relation to the variations in the distributions of aerosol physico-chemical characteristics prevailing over the experimental station. The monthly mean ventilation coefficients, computed from the lidar-derived mixing depths and concurrent pibal winds during the period from October 1986 through September 1996 are shown plotted in Fig. 7. It can be seen from the figure that the ventilation coefficients are low during early winter period which indicates higher pollution potential, while the low coefficients observed during

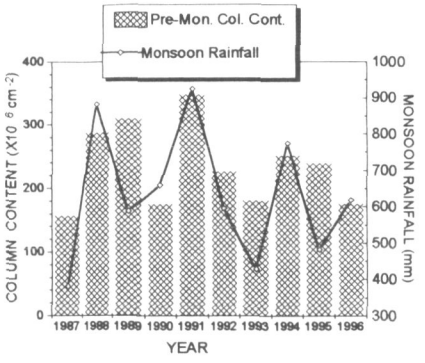


Fig. 6. Association between lidar-derived pre-monsoon aerosol column content and monsoon precipitation

SW monsoon months may not be significant mainly due to rainout and washout processes taking place over the station during that period.

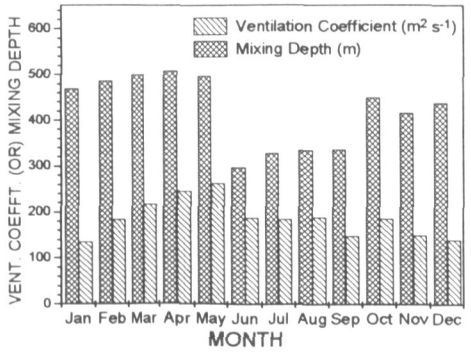


Fig. 7. Lidar-derived mixing depths and associated ventilation coefficients over Pune.

CONCLUSIONS

The results of the study of an aerosol climatology, built with the lidar and radiometric observations carried out in an urban environment, indicate an increasing trend of aerosol loading, correspondence with monsoon precipitation and tendency of higher pollution potential over the experimental station. Observations are being continued to investigate these aspects in detail.

ACKNOWLEDGEMENT

The authors are grateful to the Director, IITM, Dr. A.S.R. Murty for valuable suggestions and to the IMD, Pune for meteorological data support.

REFERENCES

1. WCRP (World Climate Research Program) : Aerosols, clouds and the climatically important parameters : lidar application and networks (Final Report, Meeting of Experts), Geneva, Switzerland, 10-12 December 1985 (WMO/TD-No. 233).
2. IPCC (Intergovernmental Panel for Climate Change) : Climate Change 1995, University Press (1996), Cambridge, Great Britain.
3. IGAP (The International Global Aerosol Program Plan) : Report of the Experts Meeting on Space Observations of Tropospheric Aerosols and Complementary Measurements (1991) 51p.
4. Devara, P.C.S., Raj, P.E., Sharma, S. and Pandithurai, G. : Real-time monitoring of atmospheric aerosols using a computer-controlled lidar. Atmos. Environ., 29 (1995) 2205-2215.
5. Devara, P.C.S., Pandithurai, G., Raj, P.E. and Sharma, S. : Investigations of aerosol optical depth variations using spectroradiometer at an urban station, Pune, India. J. Aerosol Sci., 27 (1996) 621-632.
6. Sharma, S. : Remote sensing of the atmosphere using the lidar technique, Ph.D. Thesis (1994), University of Pune, Pune , 167p.
7. Devara, P.C.S. : Laser remote sensing techniques for atmospheric pollution surveillance. Commun. Instrum., 4 (1994) 97-114.
8. Devara, P.C.S. and Raj, P.E. : A bistatic lidar for aerosol studies. Inst. Electron. Telecommun. Engrs. Tech. Rev. , 4 (1987) 412-415.
9. Devara, P.C.S. and Raj, P.E. : Remote sounding of aerosols in the atmosphere using a bistatic CW Helium-Neon lidar. J. Aerosol Sci., 20 (1989) 37-44.

Two Approaches to Derive Aerosol Extinction Coefficient Profiles From Backscatter Lidar Measurements

Matthias Wiegner and Volker Freudenthaler
Ludwig-Maximilians-Universität München, Meteorologisches Institut
Theresienstraße 37, D - 80 333 München, Germany
Phone: ++49 89 2394 4344, Fax: ++49 89 2394 4381, E-mail: m.wiegner@lrz.uni-muenchen.de

1. Introduction

The disagreement between the observed and the predicted global temperature increase has drawn attention to atmospheric aerosols again. The discrepancies certainly were partly caused by the very crude parameterizations or even neglect of the aerosol forcing in climate models. However, simple conclusions concerning a possible compensation of greenhouse warming and aerosol cooling must be avoided because of the different spatial and temporal scales and the non-linear interactions between these atmospheric constituents.

To understand the radiative forcing of aerosols, it is required to measure their distributions in time and space as well as their optical and microphysical properties. Among others, statistics of the vertical distribution of particles are lacking. For this purpose the operation of a lidar is a promising tool, especially when utilized for several years and in the frame of a network. Steps towards this goal were made in 1996 and 1997 within the Bavarian climate research program where the lidar of the Meteorological Institute of the University of Munich (MIM) was operated. In December 1997 a German network of five lidar stations begun a joint effort to establish a statistical basis of an aerosol climatology (Bösenberg et al., 1998).

In the following, results from a field-campaign in May 1997 near Hohenpeißenberg (Upper-Bavaria) and preliminary results from measurements at Munich are reported where two different approaches to overcome the underdetermination of the lidar equation were investigated.

2. Hohenpeißenberg measurements

The lidar of the MIM (Wiegner et al., 1995) operates at the three Nd:YAG wavelengths. Special features of the lidar are its compact design so that it is mobile, and the scanning capability.

The measurements at Hohenpeißenberg (47.8° N, 11.0° E) were made between May 9 and 17, 1997 (field-campaign 'OPAP'97'). The lidar site was at the southern slope of the mountain at 721 m above sea level, the height of the mountain itself being 985 m. At certain times sun photometer measurements were performed simultaneously to the lidar measurements. On May 15, nephelometer measurements onboard of a balloon were made which were used for comparison.

To calculate aerosol extinction coefficients, the normalization method (e.g., Russell et al., 1979) was applied to the lidar measurements. In general, a backscatter ratio of 1.2 was assumed above 5 km where the lidar signal was close to a hypothetical Rayleigh signal. The optical depth determined from the retrieved lidar profile was adjusted to the optical depth from the sun photometer measurements by varying the lidar ratio. To reduce the 'missing range' between the lidar site and full overlap of receiver's filed-of-view and laser beam, the following approach was made: The normalization method was applied to lidar measurements under small zenith angles ($\vartheta < 14°$) between the free troposphere and a height z_l, where the overlap was complete. The retrieved aerosol extinction coefficient at height z_l was then used as boundary value for Klett's backward algorithm (Klett, 1985) which was applied to measurements under large zenith angles ($66° < \vartheta < 76°$). As a result, extinction coefficients could be determined down to 100 m above the surface, sometimes even lower. Consequently, a pre-requisite for a reasonable comparison between lidar integrated extinction coefficients and sun photometer data was fulfilled well.

Special emphasis of the data evaluation was put on three subsequent days of sunny weather (May 15 to 17). The diurnal cycles of the aerosol distribution were found to be similar. The aerosol optical depth at $\lambda = 0.532$ μm in the morning was around 0.2 increasing to about 0.35 at sunset. The increase was attributed to particle production on the one hand and the increasing rela-

tive humidity in the afternoon on the other hand. The first and the last profile measured on May 15 are shown in Fig. 1 as an example. The sharp decrease of particle extinction at the top of the boundary layer (940 m above msl) (Fig. 1, left panel) in the morning was smoothed out in the following three hours. At about 1400 hours, a second layer with its maximum between 1.5 km and 2 km built up with developing convection and the upper boundary of significant aerosol load rised in the course of the day from 3 km to 4.5 km (Fig. 1, right panel).

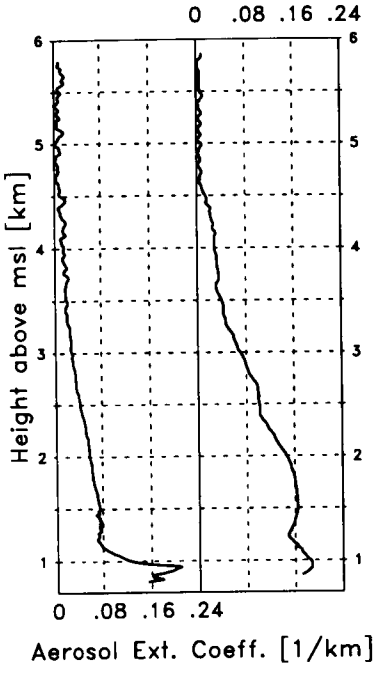


Figure 1: Aerosol extinction coefficient profile for λ=0.532 μm, May 15, 1997, 0700 (left) and 1745 (right) local time at Hohenpeißenberg.

The balloon-board nephelometer measurements were used as an independent check. The balloon was launched at 0700 local time at the lidar site and reached a height of 3.4 km within 35 minutes. The lidar's measurement direction followed the flight track of the balloon as close as possible. The agreement was quite good: The scattering coefficients from the nephelometer were lower than the lidar's extinction coefficients by 15% in the planetary boundary layer (PBL), which is a reasonable value. Both layers in the PBL (at 820 m and 940 m) were clearly resolved. Slight discrepancies in the height assignment of the latter aerosol layer were caused by the 30 seconds integration time of the nephelometer and the fast ascend of the ballon. In the very clear troposphere above the PBL both instruments show very low values near their detection limits.

3. Munich measurements

The problem of the underdetermination of the lidar equation was overcome in the above mentioned cases by combining lidar and sun photometer measurements. In principle, a method using exclusively lidar data is advantageous because no sampling problems occur. For this reason, the joint evaluation of lidar measurements under different zenith angles is a promising approach in case of sufficient homogeneity of the aerosol distribution.

If the backscatter coefficient is assumed to be constant in a plane at height z and also the transmission between the surface and that plane, the optical depth τ from the surface to z can be directly determined from the lidar signals P at height z at two zenith angles ϑ_1 and ϑ_2 via

$$\tau(z) = A \left[B - \ln \left(\frac{P(z,\vartheta_1)}{P(z,\vartheta_2)} \right) \right]$$

with:

$$A = \frac{\cos\vartheta_2 \cos\vartheta_1}{2\,(\cos\vartheta_2 - \cos\vartheta_1)}$$

and

$$B = \ln \left(\frac{\cos^2\vartheta_1}{\cos^2\vartheta_2} \right)$$

The mean aerosol extinction coefficient can be derived by differentiation within adequate layers after subtraction of the Rayleigh contribution.

This two-angle approach was not applicable during the Hohenpeißenberg measurements because of the inhomogeneity of the aerosol distribution. This inhomogeneity was clearly visible in subsequent measurements at 19 different scan angles. Considering the location of the lidar which was at the foot of the mountain, this was not surprising.

To test the two-angle approach over a less structured terrain, measurements in Munich were investigated. First results of the evaluation of February 98-data for wavelengths 0.532 μm and 0.355 μm show that averaging 2000 lidar shots (200 seconds measuring time) was sufficient to estimate the aerosol optical depth of layers several hundred of meters thick under very stable

meteorological conditions. Knowing the optical depth, inversion results from the Klett algorithm (or normalization method) can again be adjusted by variation of the lidar ratio. The resulting lidar ratios were within the typical range known from the literature. In summary, the actual inversion of the lidar data was done by conventional algorithms (Klett, normalization) and the information from the two measurement directions only served for finding 'mean' lidar ratios appropriate for certain layers.

A direct application of the two-angle approach, i.e. differentiation of the retrieved optical depths to obtain extinction coefficients, requires longer integration times, in particular, if a spatial resolution of some tens of meters is desired.

4. Acknowledgements

The project was partly funded by the Bavarian Climate Research Program (BayFORKLIM) under contract G6. The authors wish to thank Dr. Michael Weller from the German Weather Service, Potsdam, for supplying the nephelometer data and Dr. Jörg Ackermann (MIM) for the sun photometer measurements.

5. References

Bösenberg, J., Alpers, M., Böckmann, C., Jäger, H., Matthias, V., Wandinger, U., and Wiegner, M. (1998). A Lidar Network for the Establishment of an Aerosol Climatology. *this volume*

Klett, J.D. (1985). Lidar inversion with variable backscatter/extinction ratios. *Appl. Opt., 24, 514-515*

Russell, P.B., Swissler, T.J., and McCormick, M.P. (1979). Methodology for error analysis and simulation of lidar aerosol measurements. *Appl. Opt., 18, 3783-3797*

Wiegner, M., Quenzel, H., Rabus, D., Völker, W., Völger, P., Ackermann, J., Kähler, C., Fergg, F., Wildgruber, G. (1995). The mobile three-wavelength backscatter lidar of the Meteorological Institute of the University Munich, in: Lidar and Atmospheric Sensing. *SPIE Vol. 2505, 2-10*

The Structure of the Mixed layer and Aerosol layer over Tokyo Metropolitan Area in Summer

Kenji Kai*, Kazunobu Manome, Masamitsu Fujii, and Daisuke Muramatsu,
Institute of Geoscience, University of Tsukuba, Tsukuba, Ibaraki 305, Japan
Phone & FAX:81-298-53-6704, E-mail: kai@sky.envr.tsukuba.ac.jp
Makoto Abo, and Chikao Nagasawa
Department of Electrical Engineering, Tokyo Metropolitan University
Toshiyuki Murayama
Tokyo University of Mercantile Marine
Yuichi Ohno
Communications Research Laboratory (CRL)
Ministry of Posts and Communications
Takeshi Yokozawa, and Hiroshi Hara
Ishikawajima-Harima Heavy Industries Co., Ltd (IHI)

* (After April 1998) Corresponding author address: Kenji Kai, Unit of Environmental Informatics, Graduate School of Human Informatics, Nagoya University, Chikusa-ku, Nagoya 464-8601, Japan. Phone & FAX: 81-52-789-4257. E-mail: kai@info.human.nagoya-u.ac.jp

1. Introduction

There live 30,000,000 people in the Tokyo Metropolitan Area. The atmospheric environment over Tokyo is influenced by human activity. The urbanization produces a heat island, and a dust island. In sunny days, the mixed layer plays a dominant role in the transport and diffusion of pollutants in the lower atmosphere. It is important to study a three dimensional structure of an urban mixed layer over Tokyo, as well as a land-sea breeze circulation, because the mixed layer control the vertical diffusion of pollutants and the land-sea breeze transports them horizontally (Kai et al., 1997).

In the summer of 1997, the University of Tsukuba, Tokyo Metropolitan University, Tokyo University of Mercantile Marine, CRL and IHI carried out a network of cooperative observations of the mixed layer and aerosol layer over Tokyo by use of three lidars, a wind profiled and a radiosonde at four stations. The purpose of the present study is to investigate the three-dimensional structure of the mixed layer and aerosol layers over Tokyo.

2. Network of cooperative observations

The network of cooperative observations was operated at four stations in Tokyo from 6 to 8 August 1997 (Figure 1). The first site was located at Koto-ku, near the Tokyo Bay. A Nd:YAG (λ =

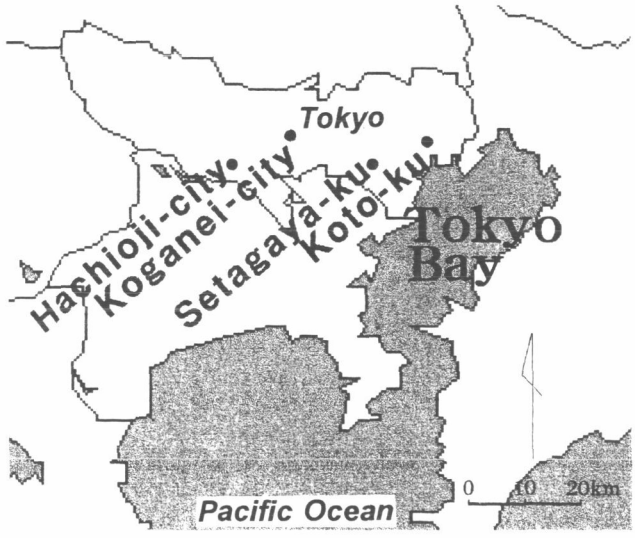


Figure 1. Location map of the four stations of Koto-ku Setagaya-ku, Koganei-city and Hachioji-city.

532 nm) lidar was used. The second site, Setagaya-ku, was just west of the center of Tokyo, 15 km inland from the seashore. An eye-safe Ho:YAG (λ = 2100 nm) lidar was used (Nagajima et al., 1997). Simultaneously, the radiosonde observation was made at the second station. The radiosonde provided vertical profiles of temperature, humidity and wind. The third station was located on Koganei-city, 30 km inland from the seashore. The wind profiler (λ = 22 cm) was used. It provided the vertical profiles of wind speed and direction in the lower troposphere. The echo power data by the wind profiler have information of the mixed layer structure. The fourth station, Hachiouji-city, was located 43 km inland from the seashore. A Nd:YAG (=532 nm) lidar was used.

3. Analysis of lidar and windprofiler data

In the mixed layer, conservable scalars, such as potential temperature, are distributed uniformly by the convective motions in the unstable conditions. To a lesser extent, the aerosols also have uniform distribution in the mixed layer (Arya, 1988). The lidar-derived mixed layer height was defined as the height where the scattering intensity by the lidar drastically decreased.

We determined objectively the mixed-layer height by the vertical gradient of lidar backscattering signals as follows:

$$G(z) = dC(z)/dz \; / \; C(z) \qquad (1)$$

where Z is altitude, C(z) range-corrected lidar signal and G(z) the gradient of C(z). In this scheme, the lowest aerosol layer was assumed to the mixed layer.

This scheme was verified by the radiosonde data, and applied to the wind profiler. The mixed-layer height derived by the wind profiler corresponded to a wind shear layer between the mixed layer and the free atmosphere.

We estimated 10-minute mixed-layer heights at the four stations in Tokyo from the seashore to 43 km inland.

4. Results and discussion

4.1 Aerosol layers and wind profile

Figure 2 shows diurnal variations of the mixed layer, the aerosol layer and the wind vector at Setagaya-ku on 7 August 1997. The mixed layer gradually developed from 7 JST (z=500 m) to 12 JST (z=1300 m). The aerosol layer at about 1000 m was a cloud during the morning hours. In the afternoon, the mixed layer kept a height of about 1300 m. The

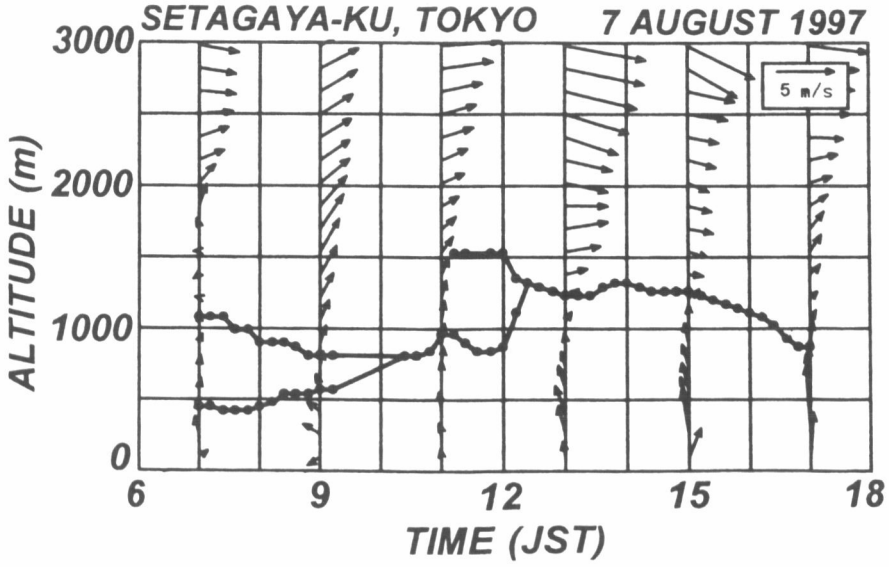


Figure 2. Mixed layer, aerosol layer and wind vector at Setagaya-ku, Tokyo, on 7 August 1997.

southerly sea breeze blew in the mixed layer, and the westerly wind prevailed in the free atmosphere. There was a layer of strong wind shear, which was a boundary between the mixed layer and the free atmosphere.

4.2 Diurnal variations of the mixed layer and the aerosol layers

Figure 3 shows diurnal variations of the mixed layer and the aerosol layers over Tokyo Metropolitan Area.. It was cloudy in the morning and clear in the afternoon on 7 August 1997. There were double aerosol layers at the four stations in the morning. The upper aerosol layer was due to the cloud, and the lower aerosol layer corresponded to the mixed layer. In the afternoon, the cloud layer disappeared. The mixed layers at inland three stations

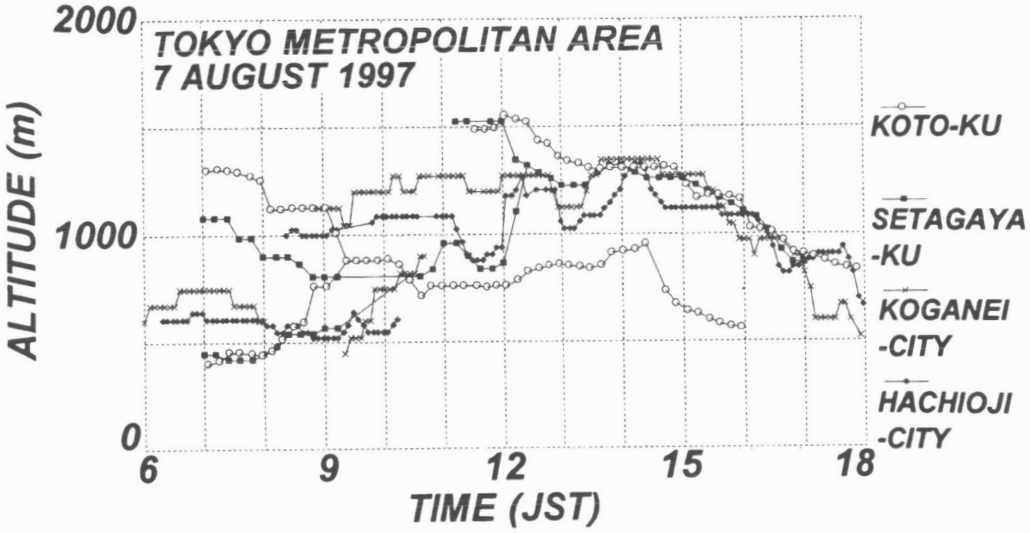


Figure 3. Diurnal variations of the mixed layer and the aerosol layer over the Tokyo Metropolitan Area on 7 August 1997.

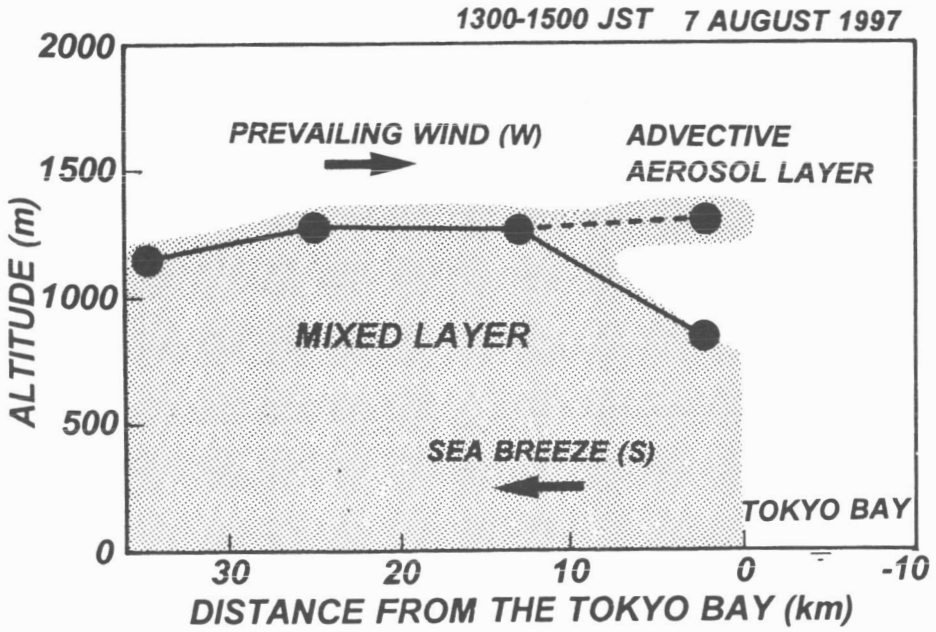


Figure 4. Cross-section of the mixed layer and the aerosol layer over the Tokyo Metropolitan Area at 13-15 JST on 7 August 1997. The mixed and aerosol layers are shaded. The prevailing wind was westerly, and the sea breeze was southerly. There was an advective aerosol layer over the Koto-ku.

(Setagaya-ku, Koganei-city and Hachioji-city) extended to 1200-1300 m from 13 JST to 15 JST, and decreased to 800m at 17 JST. The height of the mixed layer at Koto-ku was about 400 m lower than those at other stations.

Figure 4 illustrates a cross-section of the mixed and aerosol layers from 13 JST to 15 JST. The horizontal axis is a distance from the Tokyo Bay. The prevailing wind above the mixed layer was westerly, and the sea breeze in the mixed layer was southerly. The height of the mixed layer at three inland stations was 1200 - 1300 m, but that at the first station was 800 m, which was 400 m lower than other stations. This is an effect of the Tokyo Bay. There was also an upper aerosol layer at a height of 1300 m at the first station. Comparing Figures 1 to 3, the upper aerosol layer is considered to be formed by a transport of aerosols by the upper westerly wind.

5. Conclusion

The lidar-derived height of the mixed layer was defined as the height of the abrupt change in the profile of lidar-backscattering. It was determined objectively from gradients of backscattering signal. This scheme was verified by the radiosonde data, and applied to the echo power data obtained by the wind profiler. The network of the three lidars, the windprofiler and the radiosonde provided the cross-section of the structure of the mixed layer and the aerosol layer over the Tokyo Metropolitan area in summer. The advection of the aerosols by the prevailing wind was observed above the mixed layer.

References

Arya, S.P. (19889. Introduction to micrometeorology. Academic Press, Inc., 307p.

Kai K. et al.(1997). Lidar network and airborne observations of the cloud street over Tokyo in summer. Proceedings of the 12th Symposium of Boundary Layers and Turbulence, 28 July - 1 August 1997, Vancouver, Canada, 465-466.

Nakajima et al.(1997). Atmospheric environmental monitoring by an eye-safe laser radar. The Review of Laser Engineering, 25(1):50-54.

Retrieval of Droplets Size Density Distribution from Multiple Field of View Cross Polarized Lidar Signals.

Gilles Roy and Luc Bissonnette
Defence Research Establishment Valcartier, 2459 Pie XI Blvd North, Val Belair, Qc, G3J 1X5
Tel: 418 844 4335, Fax: 418 844 4511, email: gilles.roy@drev.dnd.ca

Abstract: The multiple field of view (MFVO) secondary polarization lidar signals are used to calculate the particle size density distribution (PSD) at the base of the cloud. At cloud base, multiple scattering is weak and single backscattering is predominant by many orders of magnitude. Because the secondary polarization is a direct measure of multiple scattering it is therefore advantageous to use the secondary polarization. To do so a mathematical relation is worked out between the lidar fields of view (FOV), the water droplets, the scattering angles and the angular depolarization. The model is supported by experimental MFOV lidar measurements done in a control environment.

Introduction

Recent theoretical and experimental work on multiple scattering and on MFOV lidar detection have made possible the retrieval of cloud droplet size. Basically, the enhanced lidar signal caused by multiple scattering and measured with the MFOV lidar contains information on the droplet size. In our previous theoretical model[1], we used the total (sum of both polarizations) MFOV lidar signal which limits the analysis to cloud depths large enough for multiple scattering contribution to be significantly above the noise. This meant that droplet size retrieval was not possible at small penetration depths into the cloud. In this paper, we show, both theoretically and experimentally, that the use of the secondary polarization makes possible the retrieval of the droplet size density function at the very edge of clouds.

In the absence of multiple scattering, the lidar signal consists of backscattered light at exactly 180°, and a linearly polarized light source produces no secondary polarization lidar signal since, for spherical droplets, the depolarization ratio is zero at 180°. To illustrate this, Fig. 1 shows the phase function and the depolarization ratio of linearly polarized light obtained from Mie calculations. The high peak values of the phase function near 0° are attributed to diffraction and, therefore, contain particle size information. Diffraction does not cause depolarization as clearly show in Fig.1, but the multiple internal reflections cause strong depolarization at large scattering angle. However, as stated earlier, the depolarization ratio rapidly drops to zero at exactly 180°.

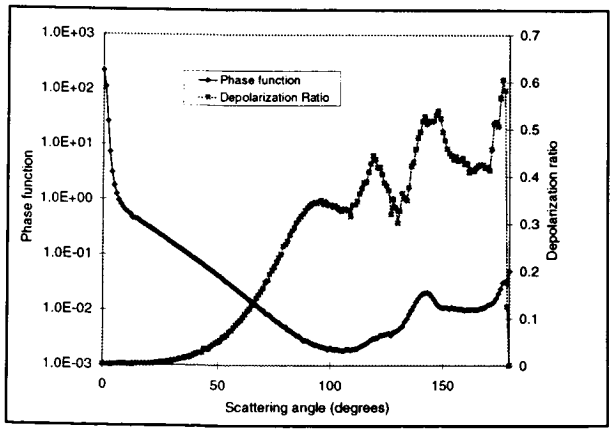


Fig.1 Phase function and depolarization of a C2 type cloud

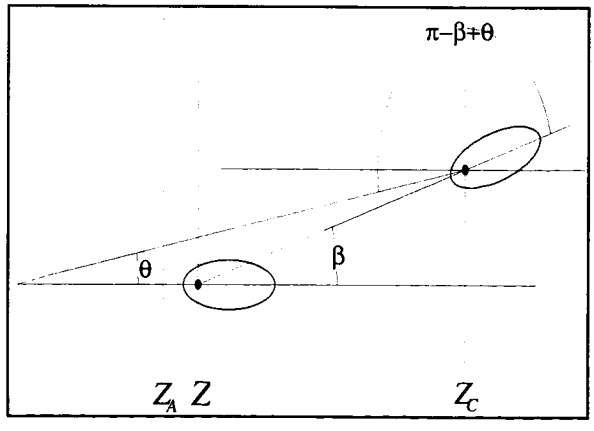


Fig. 2 Scattering process that leads to secondary polarization

Model

Figure 2 illustrates the scattering processes that lead to secondary polarization in the presence of multiple scattering and defines the geometry of the problem. The cloud is located at the distance z_a and a first forward

scattering , along β, occurs at a distance z followed by a backscattering, along $\pi - \beta + \theta$, in the plane z_c. The FOV θ and the scattering angle β are related as follows :

$$\tan\beta = (\frac{z_c}{z_c - z})\tan\theta \qquad [1]$$

Given a cloud with extinction coefficient $\alpha(z)$, the measured secondary-polarization received lidar power between the FOVs θ_{j+1} and θ_j is obtained by summing all the scattering contributions between the distances z_a and z_c over the particle size density distribution $q_0(x)$, x being the particles diameter, i.e.

$$S(z_c, \theta_{j+1} - \theta_j) = P_0 e^{-2\alpha(z_c - z_a)} \frac{c\tau}{2} \frac{\rho A}{z_c^2} \int_{x_{min}}^{x_{max}} q_0(x) \int_{z_a}^{z_c} [\int_{\beta_j}^{\beta_{j+1}} x^2 I(z,\beta,n)\sin\beta d\beta]\alpha(z)\delta(z,x,<\beta>,n)dzdx , \qquad [2]$$

where $I(z,\beta,n)$ is the forward scattering phase function, $\delta(z,x,<\beta>,n)$ is the depolarization ratio at angle $\pi - <\beta> + \theta$, $<\beta> = (\beta_{j+1}(z) + \beta_j(z))/2$, n is the refractive index, P_0 is the laser power, $c\tau$ the product of the speed of light and the pulse width, ρ is the backscattering coefficient at z_c and $\alpha(z)$ the extinction coefficient. The number density distribution $q_0(x)$ can be changed to a volume density distribution[2] $q_3(x)$ via the equation

$$q_0(x) = \frac{x^{-3} q_3(x)}{\int_{x_{min}}^{x_{max}} x^{-3} q_3(x) dx} , \qquad [3]$$

and the integral over x is divided into M particle size intervals with $q_3(x)$ constant in each interval. We thus rewrite Eq.2 as:

$$S(z_c, \Delta\theta_j) z_c^2 = \sum_{i=1}^{M} C_3 \bar{q}_3(\bar{x}_i) \int_{x_i}^{x_{i+1}} \int_{z_a}^{z_c} [\int_{\beta_j}^{\beta_{j+1}} x^{-1} I(z,x,\beta,n)\sin\beta d\beta]\alpha(z)\delta(z,x,<\beta>,n)dzdx . \qquad [4]$$

Equation 4 is rewritten in matrix form as: $\mathbf{S} = \mathbf{A}\mathbf{q}_3$, [5]

where the matrix coefficients are given by

$$A_{ij} = C_3 \int_{x_i}^{x_{i+1}} \int_{z_a}^{z_c} [\int_{\beta_j}^{\beta_{j+1}} x^{-1} I(z,\beta,x,n)\sin\beta d\beta]\alpha(z)\delta(z,x,<\beta>,n)dzdx , \qquad [6]$$

with C_3 being a constant with respect to z, x and β.

From equations 5 and 6 the PSD $\mathbf{q}_3$, is obtained through matrix inversion. However, as in many inverse problems in physics, the direct inversion of Eq. 5 does not lead to satisfactory results. It is necessary to use a constrained linear inversion technique[3]. Equation 6 contains the unknown range-dependent extinction coefficient $\alpha(z)$. However, since the system is not calibrated and the constant C_3 unspecified, the PSD can only be

determined in relative units. Therefore, we need only the relative strength of $\alpha(z)$. Because the method is applicable at small penetration depths, we can take $\alpha(z)$ proportional to the measured total lidar signal.

Figure 3 shows the calculated (Eq. 4) range-corrected "s" polarization lidar return within the FOVs θ_i and θ_{i+1} as a function of θ_{i+1} for a uniform cloud beginning at a distance of 95m and a penetration depth of 5m. The assumed water droplet size density distributions are two log-normal distributions with 10 and 20 μm mean diameters and geometric standard deviation of 0.2. Figure 4 shows the corresponding signals integrated over the FOV.

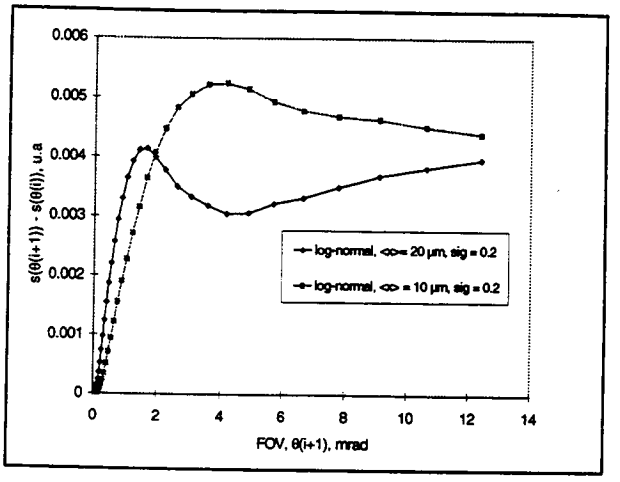


Fig. 3 Range corrected "s" polarization lidar return within FOV θ_i and θ_{i+1} as a function of fov θ_{i+1}

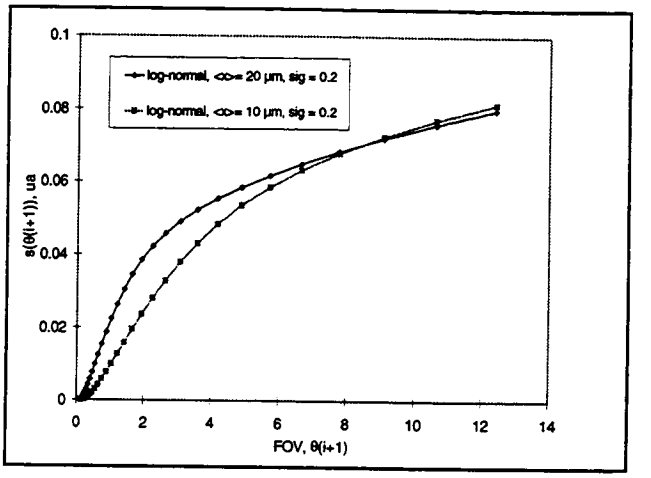


Fig. 4 Range corrected "s" polarization lidar return within FOV θ_{i+1} as a function of fov θ_{i+1}

Experimental validation

MFOV lidar measurement were made under a controlled environment using a 22-m long aerosol chamber in which longitudinally distributed pneumatic nozzles produced a fine water droplet cloud. The MFOV lidar measurements were made sequentially wiyh a 100 Hz repetition rate Nd-YAG laser synchronized with a rotating aluminized glass disk etched at the periphery with 32 ring masks. The laser beam is 2.5 cm in diameter and 0.2 mrad in divergence while the collection optic FOVs cover the range 0.1 to 12 mrad. See paper "Efficient field-of-view control for multiple-field-of-view lidar receivers", 19th ILRC, for further details.

Figure 5 shows the total lidar signal (p+s) and secondary "s" polarization lidar returns as functions of distance for 1 and 12 mrad total FOVs. Clearly at the beginning of the cloud, the "p" polarization measurement values are over 3 orders of magnitudes higher than the "s" polarization measurement values. Without polarization separation, the multiple scattering signal would be lost in the main polarization signal fluctuations.

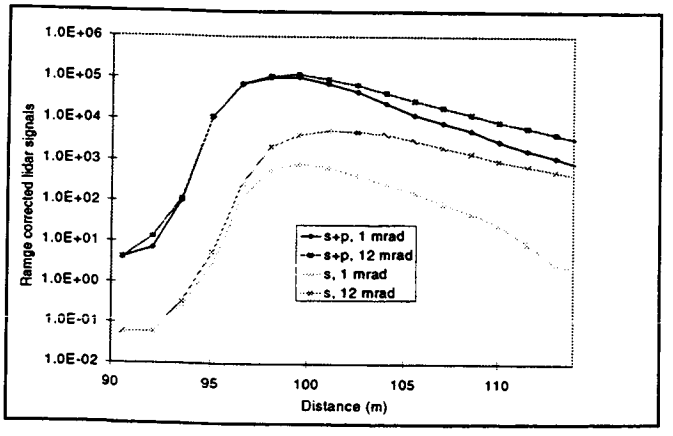


Fig.5 - Total lidar signal "p+s" and secondary "s" polarization lidar returns as a function of distance for 1 and 12 mrad total FOV's.

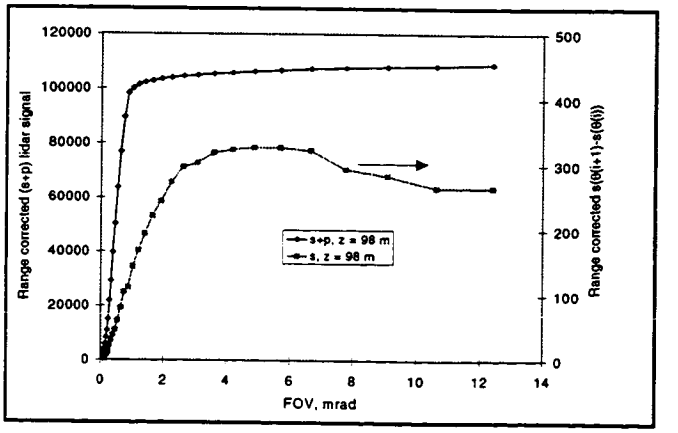


Fig.6 - Total lidar signals "p+s" and "s" polarization lidar within FOV θ_i and θ_{i+1} as a function of FOV θ_{i+1} for the 99.5 m distance.

Figure 6 shows the total lidar signal (p+s) and secondary "s" polarization ring signal as functions of the FOV θ_{j+1} at the distance 99.5 m (i.e. 4.5 m into the cloud). The total lidar signal shows only the laser beam footprint at the edge of the cloud and contains no information on droplet size because the multiple scattering signal is submerged by the single scattering signal. However, the "s" polarization measurement profile is a pure multiple scattering measurement and is clearly compatible with the modelized signals shown in Figure 4.

The "s" polarization individual ring measurements were used as the $\mathbf{S}$ vector of Eq. 5 and the matrix elements of Eq. 6 were calculated with $z_a = 95$m and $z_c = 98$m and $z_c = 99.5$m. The particle size density distributions, $\mathbf{q}_3$, were obtained through the matrix inversion of Eq. 5 using a conventional second difference constrained linear inversion technique. Figure 7 shows a very good consistency between the results obtained at 98 and 99.5 m.

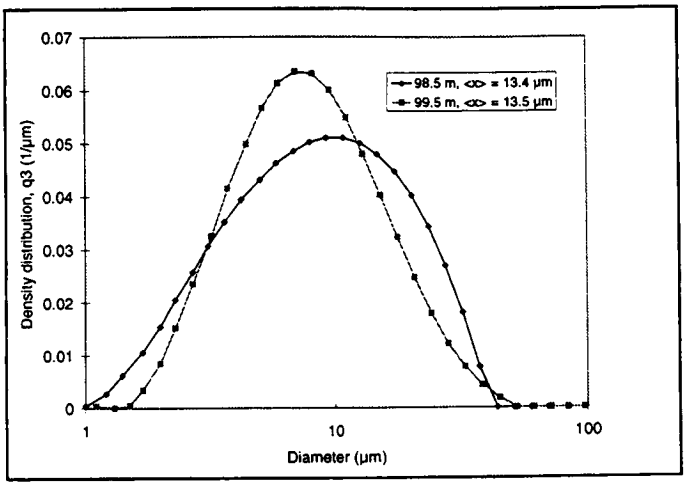


Fig 7. Particle size density distribution obtained by application of matrix inversion to the secondary polarization ring measurements at distances of 98 and 99.5 m.

Discussion and conclusion

The proposed technique based on the use of the secondary polarization offers great potential for the determination of the PSD of clouds. The method is only applicable at small penetration depths and does not require the absolute knowledge of the extinction coefficient $\alpha(z)$ witch is set proportional to the measured total lidar signal. The model is relatively simple of application and the measurements are easily done with FOV segmentation. However since the technique uses a unique characteristic of spherical droplets (zero depolarization at 180°), it cannot be applied to non-spherical particles or very large droplets that are frequently found to be oblate.

References

1. G. Roy, L.C. Bissonnette, C. Bastille and G. Vallée, "Estimation of cloud droplet size density distribution from multiple-field-of-view lidar returns", Opt. Eng. 36(12) 3404 -3415 (December 1997)

2. T. Allen, "Particle Size Measurement", Chapman and Hall, New York, 1981

3. S.Twomey, "Introduction to the mathematics of inversion in remote sensing and indirect measurements", Elsevier Scientific Publishing, 1977

Cloud Properties derived by the RIVM High Temporal Resolution Lidar and the Vaisala CT75K Lidar Ceilometer

Arnoud Apituley†, André van Lammeren‡ and Ronald Sok† and ‡

† *National Institute of Public Health and the Environment (RIVM),*
P.O. Box 1, 3720 BA Bilthoven, The Netherlands, E-mail: Arnoud.Apituley@rivm.nl

‡ *Royal Netherlands Meteorological Institute (KNMI),*
P.O. Box 201, 3720 AE De Bilt, The Netherlands

Introduction

Optical properties of clouds are a factor of great uncertainty in present day computational climate and weather models. In particular, the parameterization of the small scale (microphysical) cloud parameters needs to be improved. Aimed at obtaining a high quality data set for the development and testing of algorithms for cloud parameter retrieval from remote sensing data three measurement campaigns, within the CLouds And RAdiation (CLARA) project were carried out in the Netherlands in 1996 [1]. A number of active and passive remote sensing instruments were simultaneously operated. These instruments measured different parameters related to the interaction of clouds with radiation. In addition, in-situ measurements of the droplet spectra in stratocumulus clouds were made. Lidar and radar systems obtained the vertical structure of the clouds. The CLARA data set is used as a test bed for the development of new sensor synergy algorithms that will yield cloud parameters unavailable from each of the instruments alone [2, 1, 3].

Lidars have been used in the past for cloud studies and have proven adequate in obtaining geometrical cloud parameters [4, 5] and also to retrieve optical cloud parameters [6, 7, 8, 9]. Nowadays, commercially available lidar systems traditionally used in airports as cloud base height sensors (ceilometers) have been enhanced to give backscatter profiles and cloud properties beside just the cloud base height. However, the eye-safety requirements for such systems have their impact on the measurement characteristics. For instance, the typical integration time of such a ceilometer that is usually based on a high repetition rate (a few kHz), low power (μJ/pulse) laser diode influences the observed variability of the clouds and the retrieved optical parameters due to "smearing".

The temporal and spatial variability of clouds are among the key issues in the CLARA project. In many lidar applications such as trace gas detection, the atmosphere can be considered "frozen" in the sense that the quantity being measured does not vary significantly over a certain period of time. However, the structure of clouds (i.e. the distribution of the clouds droplets within a certain volume) is usually very variable as the droplets move with the turbulent structures in the atmosphere and are dynamically formed and removed by condensation, evaporation and coagulation processes. These differences are significant. The optical properties of clouds are directly coupled to the droplets' size distribution and number density. For this reason, lidar echo of each laser pulse will be different. Further, the backscatter of cloud droplets is so large, that the lidar echo can be detected with good signal-to-noise ratio (SNR) even for single laser pulses, provided of course the laser pulse energy and the sensitivity of the lidar receiver both are sufficient. The high temporal and spatial resolution attainable by lidars makes these instruments valuable for variability studies of cloud geometrical and optical properties.

This paper shows some results of the comparison of the collocated measurements from a "classical" backscatter lidar based on a high-power pulsed Nd:YAG laser and a commercial lidar ceilometer based on a pulsed laser diode.

Table 1: *Instrument parameters of the RIVM-HTRL and the Vaisala CT75K Lidar Ceilometer. Half-range mode values for the CT75K are indicated by †.*

	HTRL	CT75K
Laser type	Nd:YAG	4 × InGaAs Diode laser
Wavelength (nm)	1064	905
Pulse energy (J)	300e-3	4 × 1.6e-6 †
Pulse repetition rate (Hz)	10	5.13e3 †
Beam divergence (mrad)	≈ 0.5	0.53 × 0.75
Beam diameter (mm)	6	145
Receiver area (m^2)	31.42e-3	4 × 66e-3
Receiver FOV (mrad)	10	0.66
Photodetector	APD	4 × APD
Geometry	bi-axial	co-axial
Maximum altitude (km)	6.8	11.8 †
Vertical resolution (m)	7.5	15.24 †

High Temporal Resolution Lidar (HTRL)

The emitter of the HTRL is based on a Quanta-Ray DCR-11 pulsed Nd:YAG laser. For the generation of 532 nm from the 1064 nm fundamental wavelength, a thermostated type-I (polarisation preserving) second harmonic generation (SHG) crystal is installed. Two separate detectors are used to register the lidar echoes at 1064 nm and 532 nm. Here, only 1064 nm data is considered, because this wavelength is relatively close to the operating wavelength of the CT75K at 905 nm.

To capture the high variability of the clouds, the HTRL stored individual lidar returns up to an altitude of 6750 m at a spatial resolution of 1.5 m or 7.5 m resolution. Storage of raw 8-bit data samples on DDS-tapes was limited to a rate of about 1.6 Hz. All raw data were afterwards transcribed to CD-ROM. The instrument parameters are summarised in Tab.1.

The sensitivity of the HTRL had to be adjusted manually by an operator changing the combination of neutral density filters in the detection. Most of the time the combination was set to allow for the entire signal — particularly the peak reflection of the clouds — to be within the digitisers range and never to exceed 1.8 V, based on the linearity properties of the avalanche photo diode (APD) detector. During episodes with clouds only above ≈ 3 km digitiser overload was allowed in the altitude range below the clouds to increase the SNR in the upper regions.

Before interpretation, the lidar signals were normalised to the emitted laser power by taking the signal value in the sample in the data record

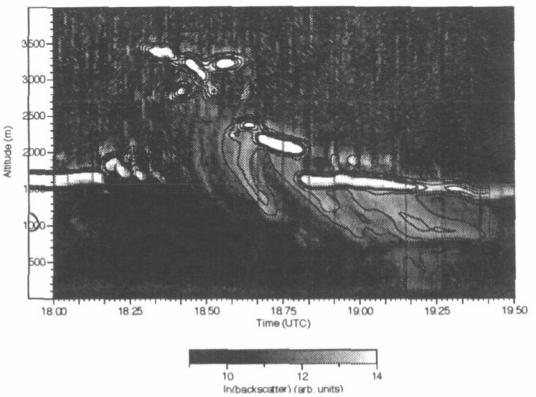


Figure 1: *Density plot of HTRL data with a contour overlay of CT75K data for December 6, 1996. The delay between HTRL an CT75K was about 4 minutes, due to non-synchronised system clocks.*

representing the reflection by the exit window. The reflection can be assumed to be directly proportional to the emitted laser power. Since the raw data was recorded on a single shot basis, the normalisation is done (off-line) for each individual lidar echo. Background subtraction and normalisation were the only pre-processing operations carried out.

CT75K Lidar Ceilometer

The Vaisala CT75K Lidar Ceilometer was designed as a fully automated, stand-alone system. The CT75K was required to be completely eye-safe. For this reason a laser diode emitting 1.6 μW/pulse at 905 nm is used. Moreover, the laser beam diameter is expanded before emission to 145 mm. The CT75K is composed of four emitter/receiver units. The maximum range of the system is 21 km, but the instrument was used in half-range mode during the CLARA campaigns for higher altitude resolution and a shorter measurement cycle. Data acquisition and all further processing is done in embedded software. A software package supplied by Vaisala called "CT-View" running on a host computer was used to retrieve the backscatter profiles, cloud base height and instrument status information. The range resolution in half-range mode is 15.24 m. In this paper a resolution of 30.48 m (100 ft) is used. The calibrated backscatter profiles are given in $Sr^{-1}km^{-1}$ [10]. The instrument parameters are summarised in

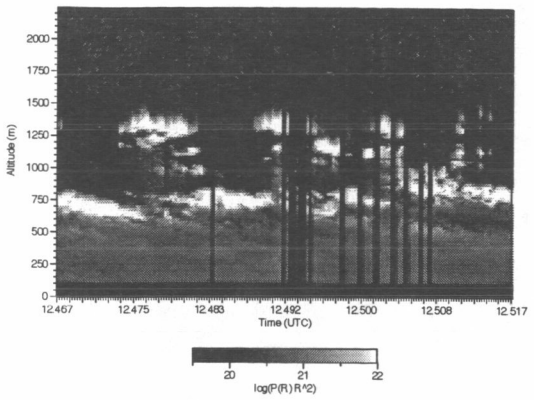


Figure 2: *Density plot of single shot HTRL data for a 3 min. period between 12:28 and 12:31 UTC on November 26, 1996. The time axis is in fractional hours. Vertical dark lines appear where no data is available.*

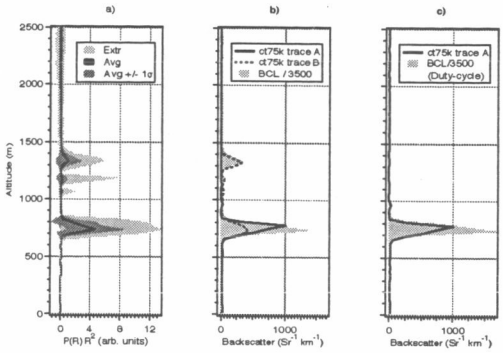


Figure 3: *a) Average range corrected HTRL lidar return averaged over 30 seconds starting at 12.4856 or 12:29.08 UTC (see Fig.2). The lighter shaded areas indicate extremes, darker shades indicate standard deviation. b) The lighter shaded area representing the average HTRL lidar return shown in a) together with the two consecutive traces of the CK75K closest in time to the HTRL data after synchronisation. c) Again, the lighter shaded area representing the average HTRL lidar return shown in a), now taking into account the CT75K duty cycle. Also shown is CT75K trace A.*

Tab.1.

The acquisition time of the ceilometer in half-range mode is 30 seconds. However, it is very important to note that data is collected only in part of this interval. The measurement cycle is divided into two: a 12.8 second interval in which data is recorded and averaged (65536 laser pulses) followed by a 17.2 second period during which data is processed and transferred to the host computer for storage [10].

Comparison

Before comparison of backscatter profiles, the HTRL and CT75K data had to be synchronised. Since both systems were located within 15 m from each other and both were pointing at the zenith sky, near identical measurement volumes were observed. Any time lag between the data can therefore be attributed to non-synchronised system clocks. The data synchronisation, in a first approximation, was done visually by means of overlaying contour plots of the CT75K data on averaged HTRL data (Fig.1). Then, fine tuning was accomplished by integrating the backscatter profiles from both systems within a certain time interval over a cloud free region (i.e. the boundary layer or below the cloud) and above the partial overlap of the HTRL, and correlating these values. The time shift yielding the best correlation was used to synchronise the data. The regression parameters were also used to scale the HTRL data to the CT75K backscatter profiles. This synchronisation procedure gave satisfactory results for most circumstances. Reiteration may improve synchronisation. This was not done so far.

Since all raw HTRL data were stored on a shot-by-shot basis, averaging of the data to different time and altitude resolutions (i.e. those of the CT75K) could be done. In addition to the average backscatter, the standard deviation was calculated and the unaveraged absolute minimum and maximum (the envelope) backscatter values were saved (Fig.3a). Two modes of averaging were implemented: one taking all HTRL data within the averaging time bins and one taking into account the duty cycle used by the CT75K.

An example of the effects of averaging are illustrated using a highly variable situation on November 26, 1996 (see Fig.2). The 3 minute interval shown in the plate clearly reveals a broken lower cloud cover that it is optically thick, and a second cloud layer that is seen only when the lower cloud disappears. When averaging over 30 seconds (the time between two labeled tick marks in Fig.2) the optical depth of the lower cloud seems smaller because two cloud layers

are observed (see Fig.3a, b). Depending on the retrieval method used, it is quite possible that false optical depth values for clouds in situations like these are obtained. Due to the highly variable cloud cover, marked differences arise between the normal average and the averages taking into account the duty-cycle of the CT75K as can be seen in Fig.3. Note that the cloud base height and shape of the backscatter profiles compare very well once the CT75K duty-cycle is taken into account (Fig.3c). The observed penetration depth is very similar for this example.

Conclusions

In general, good resemblance between the cloud base height detected by both systems was found. Also, the backscatter profiles compared well for lower clouds and mid-range clouds, with comparable penetration depths. However, for higher clouds sometimes large discrepancies were found. More investigations are necessary to establish the cause of these differences.

Under highly variable cloud conditions it becomes apparent that temporal averaging of lidar return signals has great influence on derived cloud parameters. Especially when retrieving cloud optical depths from lidar data, high time resolution data is necessary, or at least the information about the variability of the observations has to be retained.

Acknowledgements

This work was carried out as part the Dutch National Research Programme on Global Air Pollution and Climate Change (NOP). Ronald Sok was a trainee from Hogeschool Enschede. During the CLARA measurement campaigns in April and November 1996, a Vaisala CT75K was on loan from ESA/ESTEC.

References

[1] A. van Lammeren, H. Russchenberg, A. Apituley, H. ten Brink, and A. Feijt. CLARA: a Data Set to Study Sensor Synergy. In P. Ingman and E. Raschke, editors, *Synergy of Active Instruments in the Earth Radiation Mission, 12-14 November 97, Geesthacht*, pages 157–160. ESA/GKSS, 1997.

[2] A. van Lammeren and A. Feijt. The Emissivity of Cirrus Clouds Derived from LITE and Meteosat Measurements. In A. Ansmann, R. Neuber, P. Rairoux, and U. Wandinger, editors, *Advances in Atmospheric Remote Sensing with Lidar*, pages 201–204. Springer-Verlag, Berlin, 1997.

[3] H.W.J. Russchenberg V.K.C Venema A.C.A.P van Lammeren and A. Apituley. Radar-Lidar observations of Clouds During the CLARA-Campaigns. In P. Ingman and E. Raschke, editors, *Synergy of Active Instruments in the Earth Radiation Mission, 12-14 November 97, Geesthacht*, pages 161–165. ESA/GKSS, 1997.

[4] S.R. Pal, W. Steinbrecht, and A.I. Carswell. Automated method for lidar determination of cloud-base height and vertical extent. *Applied Optics*, 31(10):1488–1494, 4 1992.

[5] A.I. Carswell, A. Fong, S.R. Pal, and I. Pribluda. Lidar-Derived Distribution of Cloud Vertical Location and Extent. *Journal of Applied Meteorology*, 34:107–120, 1 1995.

[6] J.D. Lindberg, W.J. Lentz, E.M. Measure, and R. Rubio. Lidar determinations of extinction in stratus clouds. *Applied Optics*, 23(13):2172–2177, 7 1984.

[7] W. Carnuth and R. Reiter. Cloud extinction profile measurements by lidar using Klett's inversion method. *Applied Optics*, 25(17):2899–2907, 1986.

[8] A. Ansmann, U. Wandinger, M. Riebesell, C. Weitkamp, and W. Michaelis. Independent measurement of extinction and backscatter profiles in cirrus clouds by using a combined Raman elastic-backscatter lidar. *Applied Optics*, 31(33):7113–7131, 1992.

[9] S.A. Young. Analysis of lidar backscatter profiles in optically thin clouds. *Applied Optics*, 34(30):7019–7031, 10 1995.

[10] T. Kähkönen, A.M. Kärkkäinen, and S. Torikka. *Lidar ceilometer CT75K User's Guide, CT75K-U118en-1.2.* Vaisala Oy, Helsinki, Finland, 5 1996.

Calibration of the vertical lidar measurement of tropospheric aerosol extinction coefficients

Hideki Kinjo, Hiroaki Kuze, Mitsuo Minomura and Nobuo Takeuchi
Center for Environmental Remote Sensing, Chiba University
1-33 Yayoi-cho, Inage-ku, 263-8522 Japan
Phone: (042)290-3852, FAX: (043)290-3857, E-mail: wood@rsirc.cr.chiba-u.ac.jp

1. Introduction

Recently we have constructed an atmospheric data collection lidar (ADCL) to obtain the aerosol data needed to perform the atmospheric correction to satellite remote-sensing data. Figure 1 shows extinction profiles derived from ADCL data measured at four wavelengths (0.355, 0.532, 0.756, 1.064m). The extinction coefficients below the lidar overlapping point are assumed to be constant.

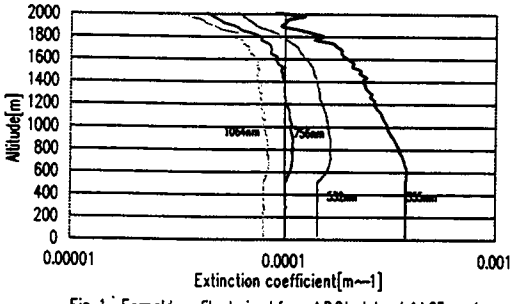


Fig. 1 Fernald profile derived from ADCL data at 14:25 on 4 March 1998. The boudnary values are determined utilizing atmospheric model.

To obtain good precision in inverting the ADCL data for the case where the condition of a large optical thickness cannot be fulfilled, here we propose to use the calibration value obtained with an integrating nephelometer set at ground level. In the case of our atmospheric data collection lidar the lowest altitude determined by the overlapping of the laser beams with telescope field-of-view is approximately 400 m above ground level in vertical measurements with 3 mrad field-of-view. This lower limit, which is introduced to prevent the saturation of the detection system, can be alleviated by employing a larger field-of-view angle, but cannot be eliminated completely. In order to obtain the relevant information between the ground level and the overlapping point we make use of data from slant observation using a portable lidar. In the actual process it is assumed that the medium between the laboratory level (about 60 m above sea level) and the full overlap point of the portable lidar (about 160 m above sea level) is homogeneous.

2. Experimental situation

Aerosol vertical profile measurement at the Nd:YAG laser wavelength of 532 nm has been performed using our atmospheric data collection lidar. Simultaneously a portable lidar with a Nd:YAG laser (wavelength 532 nm) at an elevation angle of 20 degree has been employed to collect the information in the lower troposphere. To calibrate the lidar-derived extinction coefficient, an integrating nephelo-meter is operated continuously at the ground level. All the instruments are located in our laboratory at Chiba University, about 30 km east of Tokyo.

3. Portable lidar measurement

First we examine whether it is reasonable to calibrate the portable lidar data by means of the ground level extinction coefficient measured with the integrating nephelometer. Fig. 2 is the plot of aerosol extinction at the ground level measured with the two instruments. In the analysis of lidar data with Fernald's inversion method[1], the boundary value is assumed to be constant, 0.00022 m^{-1}. The reference altitude is chosen to be 500 m (1462 m slant range). For the extinction-to-backscattering ratio we have assumed S_1=30 all through the lidar path. The lowest altitude of the interval considered is 100 m (292 m slant range) with a receiver field-of-view of 4 mrad. Assuming homogeneous atmosphere below 100 m, we can expect a value at the lowest altitude in agreement with the nephelometer-derived extinction data. This gives rise to a constraint with regard to the choice of the boundary value in the Fernald analysis.

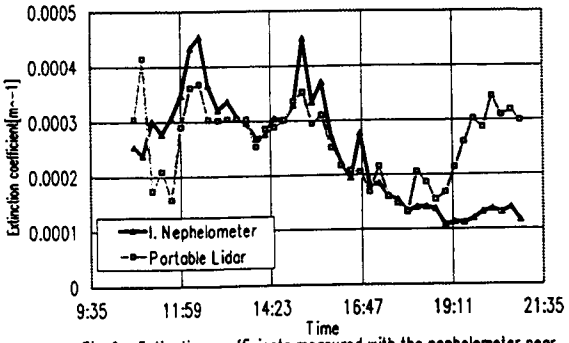


Fig. 2 Extinction coefficients measured with the nephelometer near ground level (60 m ASL) and the portable lidar. The latter is at 160 m altitude derived from Fernald method. (12 August 1997. S1=30.)

Two results agree well around 14:00, when the atmospheric condition at the reference altitude (500 m) is considered to be stable with time. Since the mean value of the relative humidity observed on the experimental day at our laboratory is approximately 92% (Fig. 3), a large value of single-scattering albedo (more than 90%) is expected for aerosol scattering. Thus it would be reasonable to use the ground-level scattering coefficient as the calibration value for the extinction coefficient in the analysis of the portable lidar data.

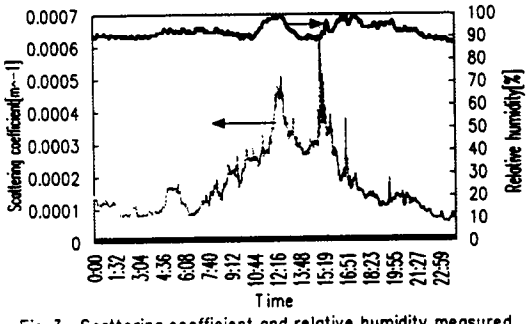


Fig. 3 Scattering coefficient and relative humidity measured with the integrating nephelometer on 12 August 1997.

4. Calibration of the ADCL data

The vertical extinction profiles in Figs. 4 (19:15JST, 13 August, 1997) and 5 (19:30JST, 13 August, 1997) have been composed from the ADCL measurements in the altitude between 400 m and 3500 m and the portable lidar measurements between 100 m and 400 m. The boundary value at 400 m altitude for the inversion of the portable lidar data is chosen utilizing the ground-level calibration value. This boundary value also serves as a calibration value for the inversion of the ADCL data. Below 100 m the aerosol extinction coefficient is assumed to be constant. The mean value of the relative humidity observed on the relevant day at our laboratory is approximately 93%.

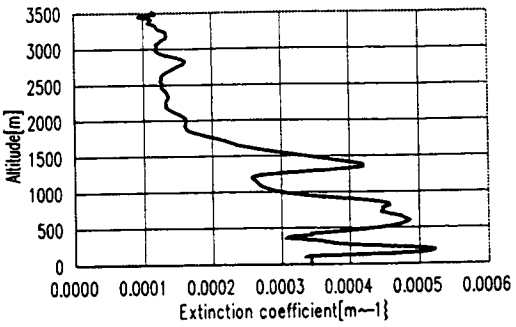


Fig. 4 Aerosol extinction coefficint with Fernald method from multi-wavelength and portable lidar return measured at 19:15 on 13 August 1997. S1=30.

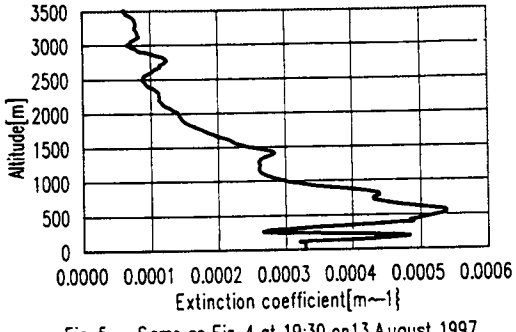


Fig. 5 Same as Fig. 4 at 19:30 on13 August 1997.

Comparing these two figures, we can see a multi-layered structure of aerosols which changes rapidly with time. The growth of the layer thickness between the altitude of 300 m to 1000 m is explained by the descent of the concentrated aerosol layer.

5. S_1 dependence of optical thickness

The two profiles shown in Figs. 4 and 5 are calculated with the extinction-to-backscatteri-ng ratio of 30 in the lidar path. In this section, we investigate the S_1 dependence of the optical thickness. The optical thickness between 0 and 3500 m is calculated with the S_1 value between 30 and 60. The results show an increase of 3.6% in the case of 19:15 data (Fig. 4), while there is 2.2% increase in the case of 19:30 data (Fig. 5). Owing to the high value of the relative humidity, it appears that the change of S_1 parameter does not affect the resulting optical thickness significantly. It is also found that under relatively low humidity, the S_1 dependence becomes more significant.

6. Wavelength dependence of extinction

In regard to the atmospheric correction of satellite remote sensing data in the visible and infrared region, aerosol extinction plays an important role. For each spectral band of satellite sensors it is desirable to have the aerosol information to derive the relevant optical thickness. The advantage of the multi-wavelength lidar, when compared with conventional instruments such as a sun-photometer, is that its capability of observing aerosol optical properties layer by layer. An example of such observation is shown in Fig. 6. In Fig. 6(a) range-corrected A-scope signals are exhibited for the four wavelength, and in Fig. 6(b) the wavelength dependence of aerosol extinction coefficient is summarized for the lower troposphere. This latter result can be interpreted with the help of detailed Mie calculation. The stronger wavelength dependence at the lower altitude than the higher altitude in Fig. 6(b) can be attributed to the larger amount of so-called accumulation particles (smaller than 1m).

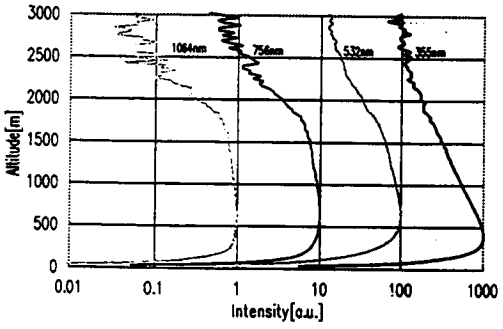


Fig. 6(a) Range-Ascope signals. 14:25, 4 March 1998.

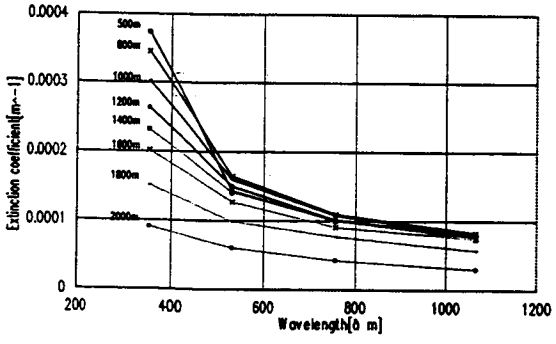


Fig. 6(b) Wavelength dependence of extinction coefficient at each altitude. 14:25, 4 March 1998.

7. Summary

We have demonstrated the improvement of the lidar-data processing utilizing the nephelometer-derived extinction data. Even under the situation where the inverted profile is sensitive to the choice of the boundary value of the aerosol extinction (optical thickness is less than unity), the aerosol distribution can be inverted accurately from lidar data with this type of calibration method. The applicability of ADCL to derive the wavelength dependent feature of aerosol profile has also been discussed briefly.

Reference

1) F.G.Fernald , "Analysis of Atmospheric Lidar Observations: Some Comments", Appl. Opt. 23, 652 (1984)

LIDAR OBSERVATIONS OF ATMOSPHERIC AEROSOL NEAR BLACK SEA

T. Skakalova, I. Kolev, O. Parvanov, B. Kaprielov
Institute of Electronics - Bulgarian Academy of Sciences
72 Trakia blvd., Sofia 1784, Bulgaria
Fax: + 359 (2) 973201; E-mail: blteam@phys.acad.bg

1. Introduction

The different thermal regimes of water and land, determined by their thermal capacities and heat conductivities lead to a horizontal pressure gradient in the coastal area. Therefore the air masses over the warmer surface move towards the cooler one. At greater heights a flow in the opposite direction exists, which closes the circulation pattern and thus the so-called breeze cell is formed. The particular size and development of the cell are influenced by the concrete relief of the region. It was found that time and spatial resolution of the lidars present an opening for detailed observations of the orography determined cell's dynamics and aerosol stratification.

In the last decades the coastal area of lakes, seas and oceans has been a place of urbanization and industrialization and therefore an object of a lof meteorological and ecological investigations. Investigation of air pollutants circulation and the existence of elevated pollution layers over Los Angelis were performed during the BASIN project (Wakimoto, 1986). The formation of organized convection during cold air penetration over a warm sea surface was studied using airborne lidars in the MASEX experiment (Melfi, 1985). Similar experiments were carried out in Bulgarian Black Sea coastal zone (Kolev, 1994, Parvanov, 1988).

The paper presents investigations of the influence of the underlying surfaces over the aerosolstratification during different parts of the breeze circulation.

2. Method and apparatus

The data discussed in the present paper was taken during an experiment carried out in September9-14, 1992, in the region of the village Shkorpilovtzi (in the station, belonging to the Institute of Oceanography, Bulgarian Academy of Sciences). The groundbased elastic backscattering lidar (Kolev,1994), used during the experiment, was installed at 12 m above the sea level and about 120 m away from the shoreline. A meteorological surface layer station and pilot balloons (Kolev, 1994) were used for obtaining the basic meteorological parameters: temperature and humidity diurnal behavior and wind profiles. The lidar data considered in the paper were obtained by vertical scanning at different step, depending on the scale and duration of the observed phenomenon (1°, 3.5°, 10° corresponding to scanning of land-to-sea breeze, the vice versa and well developed convective layer) along various azimuths.

The lidar experimental results are presented as 2-D images of the backscattered laser signals as aunction of the height and distance along the sounded path at different elevations. A 2-D pattern/cross-sections is constructed compiling data from a vertical scanning at a certain azimuth (Az).

3. Results and discussion

The synoptic conditions during the experiment were typical for the Bulgarian Black sea coast in summer - quiet, sunny weather (anticyclone) with consequently well-presented breeze circulation:

In fig.1a, 1b wind profiles from September 12 and 14, 1992 respectively are shown. The diurnal behaviour of the temperature, humidity and horizontal wind speed, measured near the surface are presented on fig.2. As it can be seen from the wind profiles in the morning till 09:30 up to heights of about H=200 m land-to-sea breeze exists, while at greater heights the change of the wind direction occurs and at heights H>600 m well-presented sea-to-land wind is observed.

During the same period of time the temperature and humidity values near the surface are low. After a calm period (09:30-10:30) a change in wind direction (fig.1a) along with a maximum of horizontal wind speed and humidity is observed. around 14:00 the temperature near the land surface reaches it's diurnal maximum (fig.2), while a minimum in the horizontal wind speed is recorded. In the afternoon (16:00-18:00) a second maximum

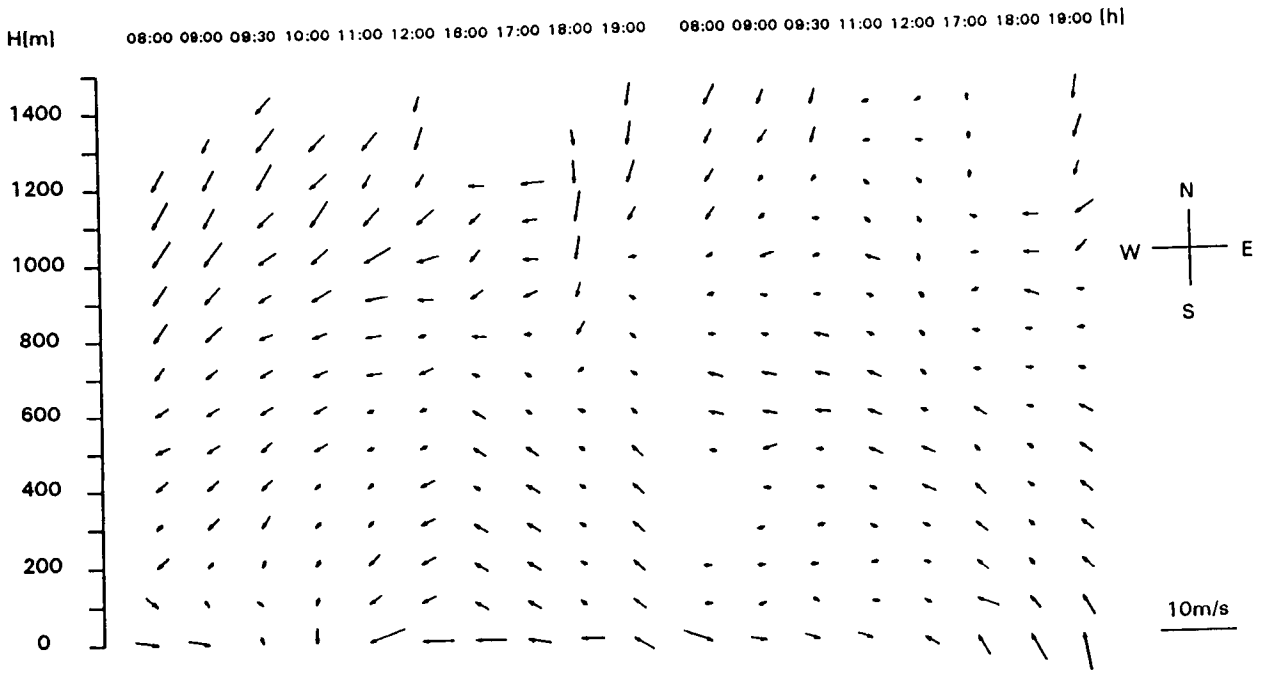


Fig.1 Pilot balloon wind profiles (1a - 12.09.1992; 1b - 14.09.1992)

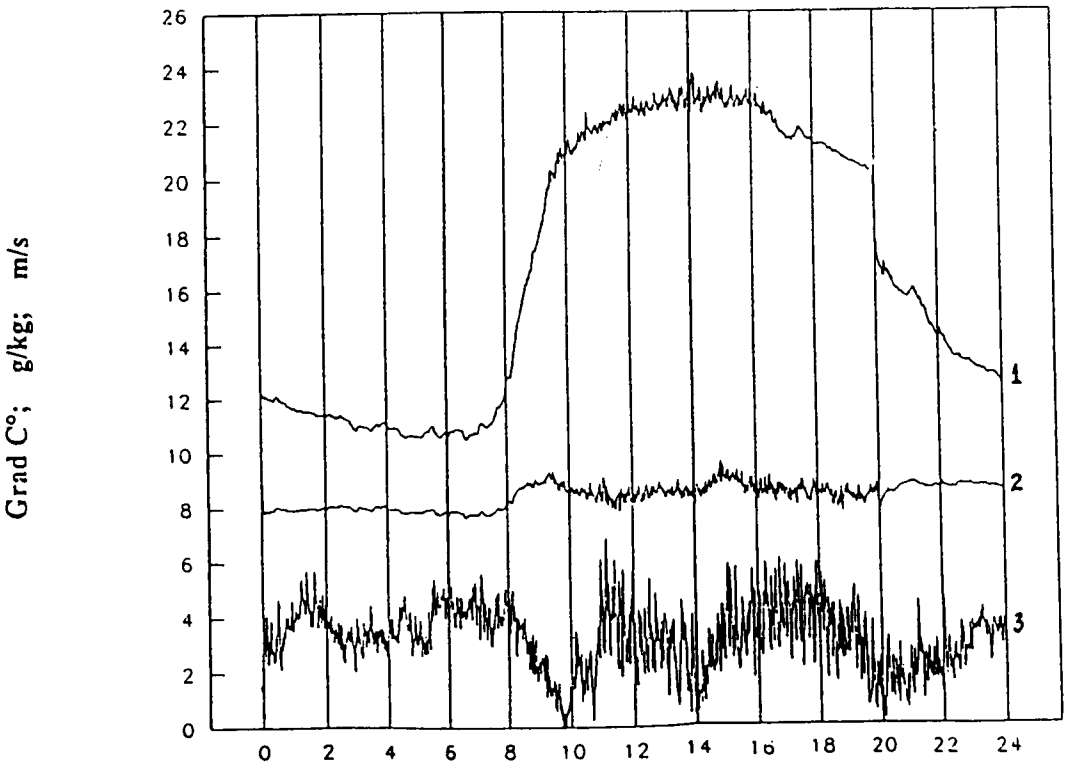


Fig.2 Diurnal behaviour of meteorological parameters taken on 12.09.1992;
1 - temperature, 2 - humidity, 3 - horozontal wind speed

of the sea-to land breeze is observed (fig.2). After the sun set (19:30) the temperature decreases and as one can see from the wind profiles the breeze changes it's direction: again after a calm period (fig.2, 19:00-20:00) a land-to-sea breeze is observed.

As it was reported (Kolev, 1994a) "the lidar images of the aerosol stratification in a coastal zone at presence of sea circulation enable one to distinguish between the cases of sea-to-land and land-to-sea breezes." Figures 3 and 4, presenting vertical scans from 14.09 and 12.09, azimuths Az=135° respectively, show the two different cases of breeze circulation.

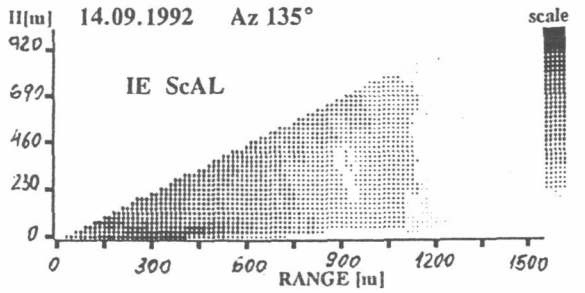


Fig.3 Lidar map presenting a vertical cross-section taken during 07:16-07:23 LST on 14.09.1992

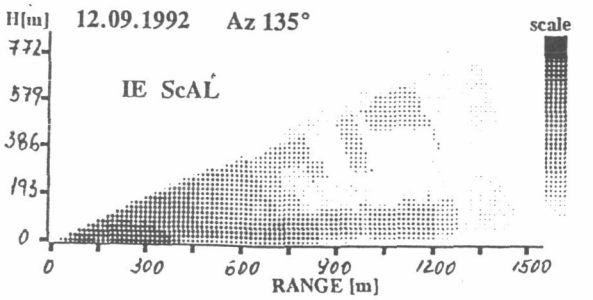


Fig.4 Lidar map presenting a vertical cross-section taken during 16:12-16:18 LSTon 12.09.1992

As one can see from the cross-sections, bearing in mind the wind profiles shown on fig 1a and 1b, the signal scattered backward by the aerosol within the sea-to-land flows is more intensive than the one obtained by scanning the aerosol within the land-to-sea flows. Taking into account the diurnal behavior of temperature and humidity, shown on fig.2 one may conclude that such a difference is due to the different humidity of the flows. The higher humidity of aerosol generated over the sea and transported towards the land effect the backscattered signal by watering the aerosol (the shape and refractive index of the particles most probably change) and/or by considerable (with respect to the wave length of the sounding radiation) increase of the size of the aerosol particles.

In case of well-presented breeze circulation the spatial resolution of the lidar at small step (3°) gives an opportunity to observe the influence of the underlying surface over the flow in direct contact with it. As a result of the circulation aerosol generated over one of the surfaces moves over the other one. In general, the part of the air flow influenced by the "new" underlying surface forms the so-called thermal internal boundary layer (TIBL) (Stull, 1990) the air above the TIBL is not influenced by the surfaces it is moving over.

In case of land-to-sea flow, as a result of the interaction between the cold air and warmer sea surface an increase of the air humidity and formation of fog (Parvanov, 1988), leading to corresponding increase of the backscattered signal is observed. Fig.5, presenting vertical scan from 14.09, azimuth Az=90°, illustrates the discussed situation.

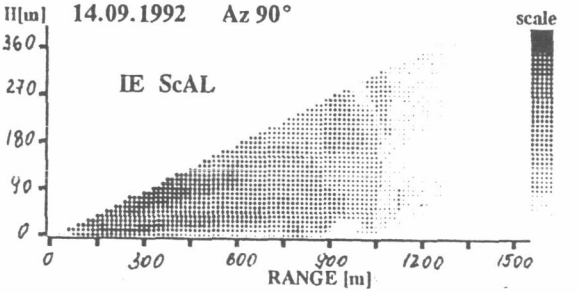


Fig.5 Lidar map presenting a vertical cross-section taken during 06:57-07:05 LST on 14.09.1992

The water surface is about 150 m away from the lidar. In the opposite case the part of the flowinfluenced by the heated land expands and the relative humidity decreases. The results are illustrated in fig.6, which represent data acquired on 12.09, azimuth Az=280° (over the land surface). As it can be seen from the figure the height of layer with lower contrast, identified with the TIBL increases and about 1300 m away from the shoreline it reaches about 150 m.

Around noon the influence of the underlying surface over the circulatory pattern reaches its maximum. The breeze cell turns to be destroyed, since the warmed up surface heats the air, above it. Under these unstable conditions the land- and sea-flow mix. As a result of the prevailing convective turbulence and heat fluxes the aerosol within the whole mixing layer is approximately uniformly distributed, which is illustrated in fig.7, presenting data from 14.09, azimuth Az=360° (parallel to the shoreline).

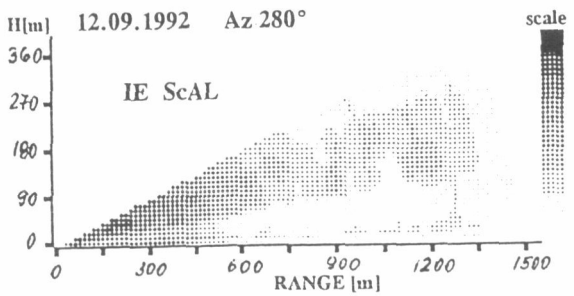


Fig.6 Lidar map presenting a vertical cross-section taken during 11:00-11:10 LST on 12.09.1992

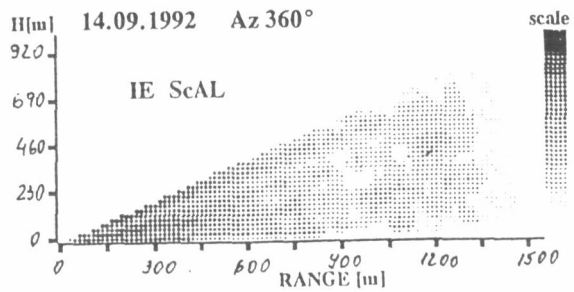


Fig. 7 Lidar map presenting a vertical cross-section taken during 13:07-13:21LST on 14.09.1992

4. Conclusion

In the present paper the variations of the optical characteristics of the atmospheric aerosol crossing the frontier of different underlying surfaces in case of breeze circulation are studied. The variances of relative humidity lead to changes in the amplitudes of the backscattered lidar signals, but without polarization studies it can not be unambiguously determined whether the watering of aerosol particles changes just the shape of the particles or their optical characteristics as well.

Basing on the changes of the backscattered coefficient of atmospheric aerosol generated over different underlying surfaces the height of the TIBL, formed in accordance with the breeze direction, was determined.

5. Acknowledgments

This experiment was performed under contract to the Ministry of Science and Technology, National Science Foundation

References

Wakimoto R. M and McElroy J. L. (1986), Lidar observation of elevated pollution layers over Los Angelis - *Journal of- Climate and Applied. Meteorology.*, Vol. 25, No.11, pp. 1583-1598

Melfi S. H., Spinhirne J. D., Chou S. H.and Paim S.P.(1985) Lidar observation of vertically organized onvectioon in the planetary boundary layer over the Ocean - *Journal of Climate and Applied Meteorology.*, Vol. 24, pp. 806-821

Kolev I., Parvanov O., Kaprielov B., Donev E., Ivanov D. (1994) Lidar Observations of Aerosol Stratification in the case of sea breeze circulation near the shore", *Comptus rendus l'Academie bulgare des Sciences*, Tome 47, No.11, pp. 21-24

Parvanov O., et al. (1988) "Lidar Observation of Air Mass Transformation et the Sea Coast", Lasers - Physics and Applications, Editor Spasov A., pp. 775-781, Singapour, WoreScience

R. Stull, *An Introduction t oBoundary Layer Meteorology*, lumer Academic Publishers, London, p.666, 1990

Long-term monitoring of aerosol and cloud in Sukhothai, Thailand and Chiba/Tsukuba, Japan

N. Takeuchi, H. Kuze, T. Uezono, A.Tadaishi
T. Takamura and T. Nakajima*

CEReS, Chiba University
*CCSR, Tokyo University

1- 33, Yayoi-cho, Inage-ku, Chiba 263-8522, Japan
Tel: +81-43-290-3849 Fax: +81-43-290-3857 e-mail : takeuchi@rsirc.cr.chiba-u.ac.jp

1. Introduction

Aerosol and cloud are important relating to not only air pollution and climate, but also earth radiation budget. Their coverage is usually monitored and analyzed using satellite data, but sometimes their vertical profile becomes very important. Its derivation is difficult by satellite monitoring, but is easy by lidar monitoring. Aerosol and cloud are spatially and temporally varied in short period, so that a long-term continuous monitoring with a short repetition time is significant. Along this line, we monitored the behavior of cloud ceiling height continuously for more than 3 months in Chiba and Tsukuba, both in Japan, and Sukhothai, in Thailand.

2. Monitoring

As a part of the GAME (GEWEX Asian Monsoon Experiment) activity, we installed a MPL (Micro Pulse Lidar), which was developed by Spinhirne [1], in Sukhothai, one of the AWS (Automatic weather Station) sites of GAME project from the end of June, 1997, and monitored the vertical profile of aerosol and cloud continuously with an integration time of 20 seconds. The lidar is operated at 523 nm (second harmonics of Nd:YLF laser pumped by a laser diode) with a repetition frequency of 2500 Hz. The sampling time is 200 ns, giving the spatial resolution of 30 m. The laser pulse energy is 5 μJ. The beam is expanded and emitted through a 20 cm diameter telescope, and the return signal is received through the same telescope. One half of the return signal is introduced to an APD detector and the signal is counted in the photon counting mode and is averaged for an integrated period (in our case 20 sec). Because the beam is expanded to a 20 cm diameter at the exit of the telescope, the laser beam satisfies eye-safety conditions.

The system was at first tested at Chiba University (35.7N, 140.1E) for the initial check from the end of January to the end of April. The ceiling height was measured and was analyzed in a form of one month average.

From the end of June, 1997, the system was transported to Sukhothai (17N, 100E), Thailand. In Fig. 1, the lidar housing is shown. It is settled just outside of the fence of the meteorological monitoring site. On the roof of the housing, a skyradiometer (aureolemeter) is located. In Fig. 2, the inside of the housing is shown. July is just the beginning of rainy season and the data were analyzed until October. We also analyzed the data in Tsukuba (36.1N, 140.2 E) provided by Meteorological Research Institute (MRI).

Radiation data, which are obtained from pyranometer, pyrageometer and aureolemeter, and other surface meteorological data are also available in Sukhothai.

In Tsukuba, radiosonde data is available twice a day (9 a.m. and 9 p.m., JST). The comparison with the radiosonde data will give a hint of cloud formation.

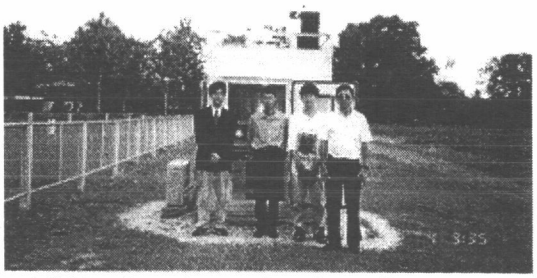


Fig. 1 Lidar housing and a skyradiometer on the roof.

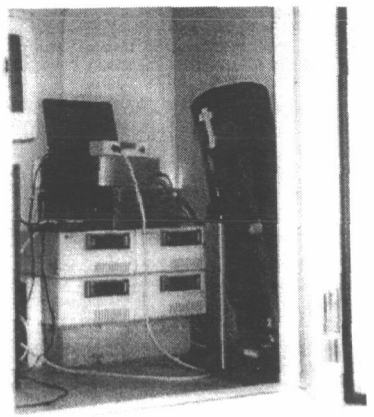


Fig. 2 Inside the lidar housing (it is air-conditioned to be not higher than 30 C)

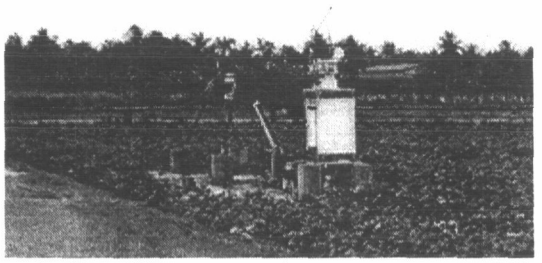


Fig. 3 Pyranometer and pyrageometer in an experimental farm.

3. Result

In Fig. 4a - c, range corrected data from June 28, 30, and July 2 are shown. The telescope was set at 19 degrees off from the zenith to prevent the direct incidence of solar light. This means the real altitude is 95 % of the distance. From Fig. 4, it is found that in the boundary layer active convection occurs and the layer is developed up to 5 km altitude in tropical region. Cloud is classified to three layers(<2km, 5 - 8 km, >10km). In each layer, cloud can be seen, but the existence probability in the lower two layers is larger. Especially in the middle layer, multi-layer cloud structure is clearly seen. It may give a large effect to the earth radiation budget.

In Figs. 5-7, we show the statistics of cloud ceiling height. Fig. 5 illustrates 24 hour integration of ceiling height in Chiba, April 1997. Though it is not readily clear from this figure, hourly statistics show normally cloud layer is split in two layers below 2 km and over 2 km. In Fig. 6, the cloud ceiling height in Sukhothai in June is shown. At the beginning of rainy season, lower layer cloud is not prominent. Every hour data of ceiling height also shows mostly single mode distribution, although middle layer cloud takes multilayer structure very frequently. In constrast, the September statistics (Fig. 7) in Sukhothai indicate apparent presence of the lower layer ceiling below 1.5 km , peculiar to the rainy season.

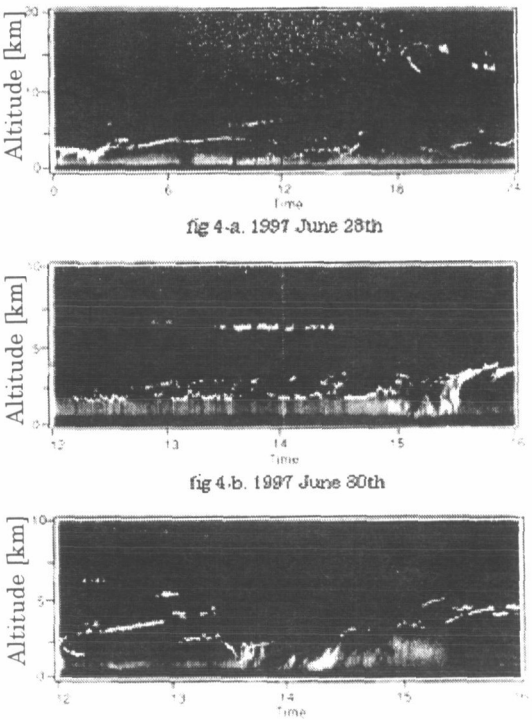


Fig. 4 Range corrected data in Sukhothai, Thailand, June - July, 1997

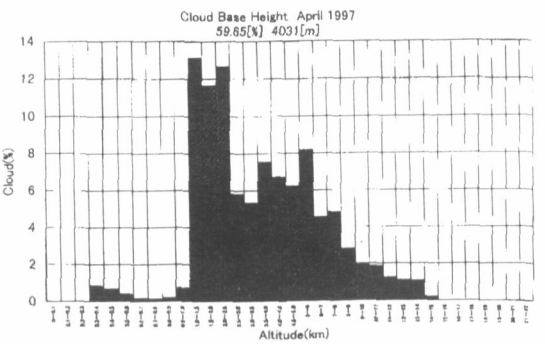


Fig. 5 Statistics of cloud ceiling height in Chiba, Japan, April, 1997.

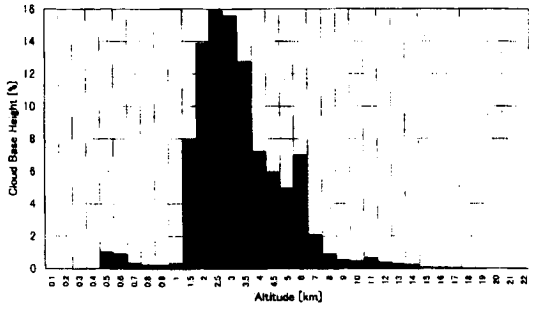


Fig. 6 Statistics of cloud ceiling height in Sukhothai, Thailand, July, 1997.

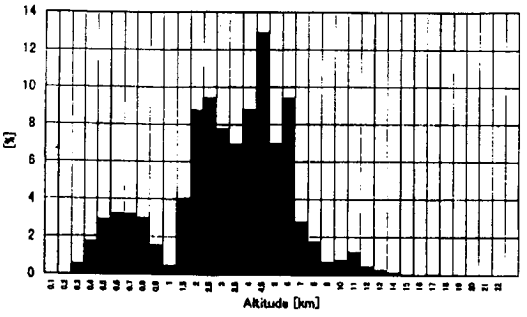


Fig. 7 Statistics of cloud ceiling height in Sukhothai, Thailand, September, 1997.

Here we did not show the data in Tsukuba. However the comparison of the lidar data and radiosonde data, it is infered that the cloud is generated at a range of the relative humidity (RH) over 80 %, in the lower atmosphere (inside the boundary layer), and in the middle layer over 5 km, sometimes the critical RH reduced down to 70 % (at the altitude and location of a radiosonde will be flown).

In this paper, we described a long-term monitoring of the aerosol and cloud using a MPL systems.

Finally we wish to express our thanks for Meteorological research people in Japan (MRI) and in Thailand (TMD).

References

1. J. Spinhirne: Micro Pulse Lidar , IEEE Trans. Geosc. Remote Sensing, 31, 48-54

Aerosol Analysis Techniques and Results from Micro Pulse Lidar

Dennis L. Hlavka, James D. Spinhirne, and James. R. Campbell
NASA/Goddard Space Flight Center, Laboratory of Atmospheres
Code 912, Greenbelt, MD 20771
Phone: (301) 286-5578, FAX: (301) 286-1762, E-mail: sgdlh@virl.gsfc.nasa.gov

John A. Reagan and Donna Powell
University of Arizona, Tucson, AZ

1. Introduction

The effect of clouds and aerosol on the atmospheric energy balance is a key global change problem. Full knowledge of aerosol distributions is difficult to obtain by passive sensing alone. Aerosol and cloud retrievals in several important areas can be significantly improved with active remote sensing by lidar.

Micro Pulse Lidar (MPL) is an aerosol and cloud profilometer that provides a detailed picture of the vertical structure of boundary layer and elevated dust or smoke plume aerosols. Refer to Spinhirne (1993). MPL is a compact, fully eyesafe, ground-based, zenith pointing instrument capable of full-time, long-term unattended operation at 523 nm. In October of 1993, MPL began taking full-time measurements for the Atmospheric Radiation Measurement (ARM) program at its Southern Great Plains (SGP) site and has since expanded to ARM sites in the Tropical West Pacific (TWP) and the North Slope of Alaska (NSA). Other MPL's are moving out to some of the 60 world-wide Aerosol Robotic Network (AERONET) sites which are already equipped with automatic sun-sky scanning spectral radiometers providing total column optical depth measurements. Twelve additional MPL's have been purchased by NASA to add to the aerosol and cloud database of the EOS ground validation network. The original MPL vertical resolution was 300 meters but the newer versions have a vertical resolution of 30 meters. These expanding data sets offer a significant new resource for atmospheric radiation analysis.

Under the direction of Jim Spinhirne, the MPL analysis team at NASA/GSFC has developed instrument correction and backscatter analysis techniques for ARM to detect cloud boundaries and analyze vertical aerosol structures. A summary of MPL applications is found in Hlavka (1997). With the aid of independent total column optical depth instruments such as the Multifilter Rotating Shadowband Radiometer (MFRSR) at the ARM sites or sun photometers at the AERONET sites, the MPL data can be calibrated, and time-resolved vertical profiles of aerosol optical depth as well as aerosol extinction can be calculated.

The techniques used to calibrate the lidar, calculate the aerosol extinction-to-backscatter ratio, and produce profiles of aerosol extinction and aerosol optical depths, will be described. Results using these techniques will be presented for case studies at the ARM site in the Tropical West Pacific and later in the Southern Great Plains.

2. Initial Data Analysis

Micro Pulse Lidar raw data sets must have three instrument characteristics corrected for before any aerosol analysis is performed. These corrections are described in detail in a separate article (Campbell (1998)) and are briefly summarized below:

Deadtime correction: A multiplicative factor dependent on signal strength applied to the raw data to correct for ineffective detector response when bombarded by photons at too close of time interval.

Afterpulse correction: A small subtraction to the deadtime corrected data which is a non-linear function of range from the instrument and represents the residual signal response which occurs due to pulse run-on of photoelectrons out of the detector.

Overlap correction: A range-dependent factor which is divided into the range-corrected signal to cancel signal degradation in the near range caused by field of view conflicts in the transmitter-receiver system.

The chosen starting point for the aerosol technique is after the above three corrections have been accounted for and the remaining signal

has been background subtracted, range corrected, and energy normalized:

$$P(r)=\frac{(n(r)dtc-n_b-n_{ap}(r))r^2}{oc(r)E}, \qquad (1)$$

where $P(r)$ is the resultant range dependent relative normalized backscatter, $n(r)$ is the range dependent raw signal in photoelectrons/μsec, dtc is the dead time correction factor, n_b is the measured background ambiant signal entering the receiver without the laser on, $n_{ap}(r)$ is the afterpulse correction, r is range from instrument, $oc(r)$ is the range dependent overlap factor, and E represents the laser pulse energy. The lidar equation furthermore shows that:

$$P(r) = C\beta(r)T^2(r), \qquad (2)$$

where C represents a dimensional system calibration constant, $\beta(r)$ is the range dependent backscatter cross section due to all types of atmospheric scattering, and $T(r)$ is the atmospheric transmittance out to range r.

3. Instrument Calibration Technique

Instrument calibration can be done during any 60 to 90 minute period where there is coincident clear sky MPL data and total column optical thickness measurements from sun photometers or the MFRSR. The total column optical thickness data must be converted to match the 523.5 nm wavelength of the MPL. Then the Rayleigh component must be subtracted out from knowledge of the atmospheric temperature and pressure structure. Finally, to obtain the needed aerosol optical thickness, an estimate of the ozone component (at 523.5 nm) must be subtracted. This can be estimated using known values of ozone absorption coefficient and ozone amount from the Total Ozone Mapping Spectrometer (TOMS) satellite given in Dobson units. MPL retrievals are calibrated by making the reasonable assumption that above a certain height (approximately 7 km) in the higher troposphere, almost all lidar backscatter at 523 nm stems from the molecular component alone. The attenuation in the signal caused by the lower tropospheric aerosols is calculated from the estimated aerosol optical depth. The attenuation-corrected integrated MPL signal in the upper troposphere is then fitted to the integrated molecular signal using an appropriate value of calibration. In equation form the process is:

$$C = \frac{\int_{rm}^{rt} P(r)dr}{T^2(rm)\int_{rm}^{rt} \beta_m(r)T_m^2(r)dr}, \qquad (3)$$

where $T^2(rm)$ is the two-way lidar transmittance from the instrument to range rm and includes both the molecular component and the aerosol component, rm is the range from the instrument to the estimated top of the aerosol layer and bottom of the upper tropospheric molecular fitting layer, rt is the range from the instrument to the top of the molecular fitting layer, usually around 12 km, $\beta_m(r)$ is the molecular backscatter cross section, and $T_m(r)$ is the molecular transmittance. The molecular components of Eq. 3 can be calculated based on the atmospheric temperature and pressure structure and the known estimate for molecular extinction / backscatter ratio. C is calculated for each MPL profile in the time period and then averaged.

4. Calculation of Aerosol Extinction / Backscatter Cross Section Ratio

Once the calibration has been calculated for the time period, the aerosol extinction-to-backscatter ratio (S_a) is estimated based on an iterative procedure which assumes S_a to be constant with height. Based on the work done by Spinhirne (1980), a differential equation has been developed which, when integrated vertically through the lidar profile, relates signal attenuation to an integration of the received signal return. This equation includes a separation of aerosol and molecular scattering terms. If one assumes for the MPL that the bottom of the integration layer is at the height of the instrument and that the instrument is pointing very close to zenith, then this equation takes the form:

$$T_a^2(rm)T_m^{2x}(rm) = 1 - \frac{2S_a}{C}\int_0^{rm} P(r)T_m^{2(x-1)}(r)dr, \qquad (4)$$

where $T_a(rm)$ is the aerosol transmittance from the instrument to range rm, $T_m(rm)$ is the molecular transmittance to rm, and $x=3S_a/8\pi$. By rearranging Eq. 4, solve for S_a:

$$S_a = C \frac{1 - T_a^2(rm) T_m^{2x}(rm)}{2\int_0^{rm} P(r) T_m^{2(x-1)}(r) dr} . \quad (5)$$

$T_a(rm)$ and $T_m(rm)$ can be calculated given the initial inputs of total column aerosol optical depth and the atmospheric temperature and pressure structure, respectively. Since the term x involves S_a, an iterative analysis must be done by first initializing x with a meaningful estimate, then calculating S_a by averaging the result for each profile in the time period, then plugging the new estimate for S_a into the x term and so on until the solution converges.

5. Calculation of Aerosol Optical Depth and Extinction Cross Section Profiles

A vertically -resolved profile of aerosol optical depth can be straight-forwardly produced from the MPL signal profiles once C and S_a are known. Solve Eq. 4 for $T_a^2(r)$, for all data points in each profile between 0 and rm, then find the average two-way aerosol transmittance for the time period. Multiple scattering effects are minimal with the MPL due to the very small receiver field of view of 100 μrad and are ignored. Next calculate the aerosol optical depth ($\tau_a(r)$):

$$\tau_a(r) = \frac{-\ln(T_a^2(r))}{2} . \quad (6)$$

The vertical profile of aerosol extinction cross section can then be found by differentiating $\tau_a(r)$ through the layer. The location of the top of the planetary boundary layer can be estimated accurately from a time series of these profiles.

6. Sample Results

Drought conditions and population pressures in Indonesia and surrounding areas of Southeast Asia sparked a massive biomass burning episode during September - November, 1997. Some of the smoky haze covered the ARM TWP site at Manus, Papua New Guinea from time to time. Five time periods were selected, mostly in September, where clear sky MPL profiles coexisted with MFRSR total column optical depth measurements. The MPL aerosol technique was used to process the five cases, which ranged in MFRSR aerosol optical depth from .06 to .40. A summary of the calibration and optical depth calculations for these cases are found in Table 1.

Date (local)	MPL C	MFRSR τ_a (523nm)	MPL τ_a
30Aug97 (pm)	120.5	.0645	.0320
03Sep97 (pm)	118.4	.1192	.1174
06Sep97 (pm)	111.7	. 2356	.2633
08Sep97 (pm)	103.6	.3958	.5980
20Sep97 (pm)	119.1	.1810	.2032

Table 1. Results of MPL aerosol technique using 90 minute time period averages at ARM's TWP site.

The MPL optical depths were determined by assuming a constant C for all the case studies. Usually the cleaner the boundary layer, the more accurate the C calculations. The C from September 3 was used here. The C calculations are in line with previous work and seem to oscillate by up to 10 percent on a day to day basis.

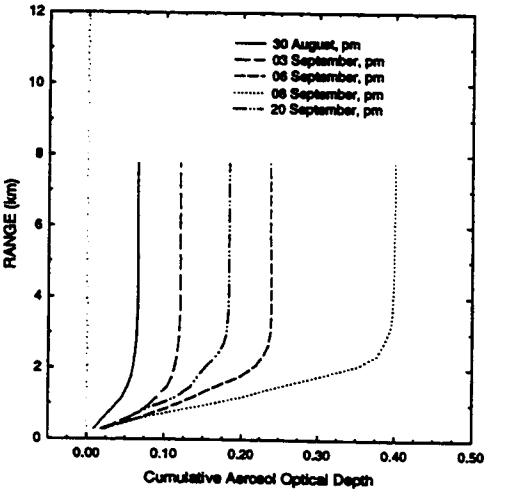


Figure 1. Average vertical profiles of aerosol optical depth at the TWP site in 1997 based on the results of Table 1.

Figure 1 shows the resultant average profiles of aerosol optical depth from the five cases. Notice that even with high aerosol loading, such

as on 08 September, the contributing aerosol layer did not extend above 4 km. In most cases, C was fitted to the molecular signal above 5 km. Figure 2 shows the corresponding aerosol extinction cross section average profiles for the five cases. Increased aerosol loading occurred over time until 20 September, when levels fell back to early September values. Double layers were observed on three of the days.

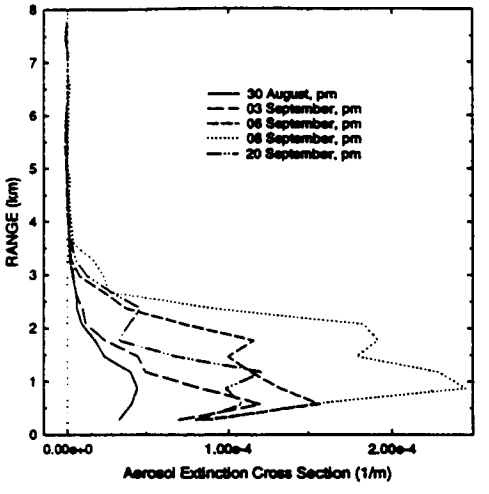


Figure 2. Average vertical profiles of aerosol extinction cross section at the TWP site in 1997 based on the results of Table 1.

Calculated aerosol extinction values are realistic for these cases. S_a ratios were lower than expected. More case studies will be analyzed to determine if there is a bias.

7. Summary

The MPL analysis team at NASA/GSFC has developed instrument correction, calibration, and aerosol structure analysis techniques with the aid of total column optical depth instruments such as the MFRSR. Test results involving five cases at the ARM TWP site successfully show the value of the technique, having calculated reasonable aerosol optical depths from the MPL alone when tied to one MFRSR measurement.

8. Acknowledgments

The authors wish to thank James Mather (PSU) and Jim Barnard (PNNL) for their timely calculation and distribution of MFRSR total column optical depths for the TWP instrument.

References

Campbell, J. R., D. L. Hlavka, J. D. Spinhirne, D. D. Turner, and C. J. Flynn, Operational Cloud Boundary Detection and Analysis from Micro Pulse Lidar Data, *Proceedings of the ARM Science Team Meeting, March, 1998*, Tucson, AZ

Hlavka, D. L., J. D. Spinhirne, and V. S. Scott, Full Time Lidar Cloud and Aerosol Height Distribution Data Sets to Support Radiation/Climate Forcing Studies, *Preprint Vol., 9th Conf. on Atmospheric Radiation*, AMS, Feb., 1997, Long Beach, CA.

Spinhirne, J. D., 1993: Micro pulse lidar, *IEEE Trans Geo. Rem. Sens.*, **31**, 48-55.

Spinhirne, J. D., J. A. Reagan, and B. M. Herman, 1980: Vertical Distribution of Aerosol Extinction Cross Section and Inference of Aerosol Imaginary Index in the Troposphere by Lidar Technique, *J. Appl. Meteor.*, **19**, 426-438.

LIDAR STUDIES OF CIRRUS CLOUDS ABOVE WESTERN SIBERIA

V. V. Zuev, M. I. Andreev, V. D. Burlakov, A. V. El'nikov, and S. V. Smirnov

Institute of Atmospheric Optics, SB RAS
1, Akademicheskii Ave., Tomsk, 634055, Russia
Phone: 7-3822-25-84-82; Fax: 7-3822-25-83-85;
E-mail: zuev@ldsa.tomsk.su

Abstract - A ground-based lidar for measuring characterictic of cirrus clouds are presented. Methods of measurement and processing optical characterictics are described. Some results of investigation of cirrus optical, geometrical and statistical characteristics over Western Siberia (56.5°N, 85.1°E) are illustrated.

Introduction

Current interest to the study of clouds is determined by their impact on a balance between the incoming solar radiation and the outgoing Earth's radiation. Cirrus clouds occupy a special place among the Earth's cloud formations. Their impact can be manifested through atmospheric warming or cooling [1]. Recurrence of cirrus clouds and their morphological and microphysical structures undergo significant variations as functions of latitude, season, orography, and underlying surface type. Tomsk (56.5°N, 85.1°E) is situated in Western Siberia – a large part of Eurasian continent covered by large forest areas far from seas and oceans. This introduces specific features in the formation of cirrus cloudiness above Western Siberia. Lidar studies of cirrus cloudiness were started in Tomsk in 1997.

Instrumentation and experimental procedure

A lidar system operating at the Siberian Lidar Station is capable of measuring the characteristics of cirrus cloudiness at night and in the daytime. A Nd-YAG laser is used as a transmitter. It generates laser pulses at the wavelength λ=1064 nm with energy 150 mJ per pulse. The pulse repetition frequency is 10 Hz.

The choice of λ=1064 nm was determined by the low level of the background daytime sky radiation at this wavelength, which is important for lidar observations of clouds in the daytime. Coaxial transceiver scheme is used in the lidar system. The backscattered laser radiation is received by a mirror with a diameter of 2.2 m and a focal distance of 10 m. A field stop, a collimating lens, a film polaroid, an interference filter, and a focusing lens are placed in the focal plane of the receiving mirror in front of a photomultiplier.

The signal-to-noise ratio was adjusted for daytime and night measurements by changing the diameter of the field stop and the area of the receiving mirror. In so doing, the entire area of the mirror was used for measurements at night, whereas for daytime measurements the receiving area of the mirror was decreased to that of the mirror 0.3 m in diameter. The field of view of the receiving system was 0.3 mrad. This small field of view was chosen to reduce the background illumination and the contribution of multiple scattering to a lidar return signal. The FEU-83 photomultiplier was used as a receiver. It was cooled by the Peltier elements to a temperature of -30°C to reduce its intrinsic noise level. Lidar return signals were recorded in the photon counting regime. Spatial resolution of the lidar system was 100 m and its temporal resolution was 3–4 s. The lidar system was equipped with a video camera. It was mounted parallel to the lidar optical axis near the focus of the lidar receiving telescope for monitoring of the sky cloudiness during lidar measurements. Video records were used to estimate the horizontal cloud sizes as well as the speed and direction of cloud motion.

We recorded clouds not only in the zenith, but also in the periphery of the sky. The lidar was oriented in the zenith and measurements were carried out only when clouds fell within the lidar field of view. Time series of lidar return signals were obtained. Each series

lasted ~30 min and comprised more than 256 individual vertical signal profiles. Every lidar return signal profile was averaged over 20–30 laser shots during 3–4 s. Figure 1 shows an example of cloud sensing above the measurement site during half an hour. Cirrus clouds were recorded in the absence of low cloudiness and through it.

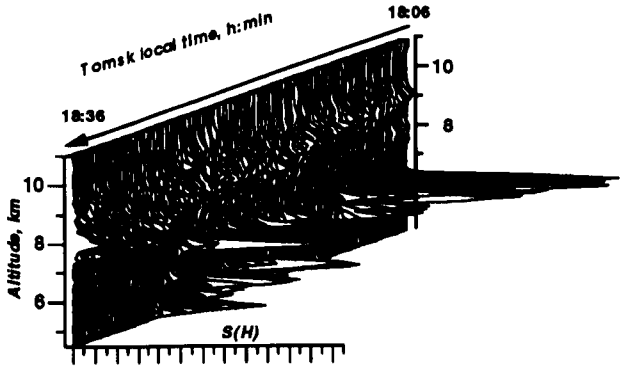


Fig. 1. Variations of the vertical structure of lidar return signals corrected for the sensing range during observations of cirrus, high-cumulus, and cumulus cloudiness on August 14, 1997 from 18:06 till 18:36, Tomsk local time.

To estimate qualitatively the phase state of clouds, in a number of experiments we measured the depolarization ratio of lidar return signals. In the present report we give only some preliminary results.

Some measurements of optical and geometric characteristics of cirrus cloudiness

Small field of view of the lidar receiving system (0.3 mrad) significantly decreased the relative contribution of multiple scattering to a lidar return signal. For this reason, the optical characteristics of clouds were reconstructed in the single scattering approximation. In this case the backscattering coefficient $\beta_\pi(H)$ can be calculated with the use of the well-known procedure for lidar return signal calibration against molecular scattering [1] under assumption of the absence of the aerosol at a given segment of the sensing path. The extinction coefficient $\alpha(H)$ was calculated by the method described in [2]. Under assumption of the constant ratio of the total backscattering coefficient to the total extinction coefficient, the formula for $\alpha(H)$ can be written as

$$\alpha(H) = S(H) \cdot \left[\frac{S(H_c)}{\alpha(H_c)} + 2 \cdot \int_H^{H_c} S(H')dH' \right]^{-1}, \qquad (1)$$

where H is the altitude, H_c is the calibration altitude, $\alpha(H_c)$ is the value of the extinction coefficient at the calibration altitude (it is considered to be known), $S(H)=[N(H)-N_{bg}]\cdot H^2$ is the lidar return signal $N(H)$ corrected for the sensing range, and N_{bg} is the background sky radiation.

An example of the reconstructed vertical profile of the extinction coefficient on December 22, 1997 is shown in Fig. 2 (at the center). This profile was averaged over 256 individual vertical profiles of lidar return signals accumulated from 19:13 till 19:40, Tomsk local time. This allowed us to follow the temporal variability of some parameters of the observed two-layer cloudiness. The heights of the lower (L) and upper (U) cloud boundaries calculated by the criteria of a) 10-fold excess of the backscattering coefficient at the boundary clear atmosphere-cloud (dots) and b) cloud halfwidth (circles) are also shown in Fig. 2.

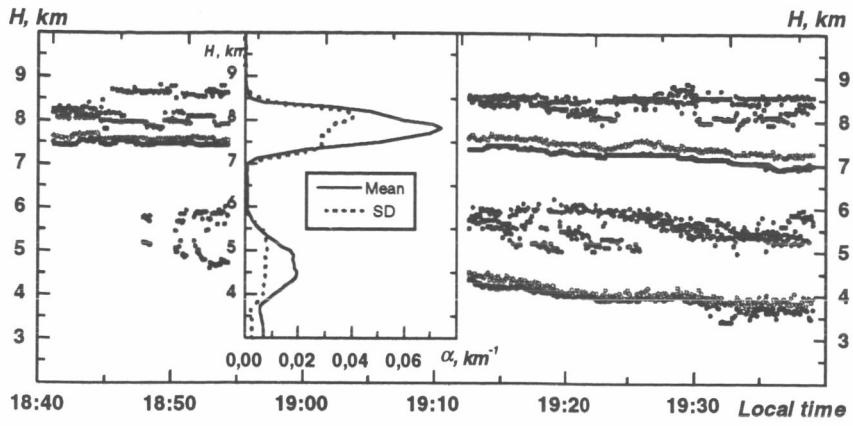


Fig. 2. Temporal behavior of the heights of the upper and lower boundaries of the two-layer cloudiness (calculated by the criteria mentioned in the text). The vertical profile of the extinction coefficient averaged over the period from 19:10 till 19:40 and its standard deviation (SD) are shown at the center of the figure.

Temporal variations of the optical thickness $\tau(t) = \int_L^U \alpha(t) \cdot dH$ of the upper and lower clouds are illustrated by Fig. 3a. Histograms of the distribution of their optical thickness are shown in Figs. 3b and c. It can be seen that the distribution of the optical thickness of the upper cloud is closer to the normal distribution in comparison with the lower cloud. The distribution of the optical thickness of the lower cloud is bimodal in character. Its main mode is centered at τ=0.04. The second mode of the distribution centered at τ=0.055 is less pronounced. It is likely that this mode is caused by a wave process, because the Fourier transform has the clearly pronounced maximum near 10^{-2} Hz (Fig. 3d). Judging from the autocorrelation functions of the optical thickness, the scales of inhomogeneities for the lower cloud are somewhat larger than for the upper cloud (Fig. 3e).

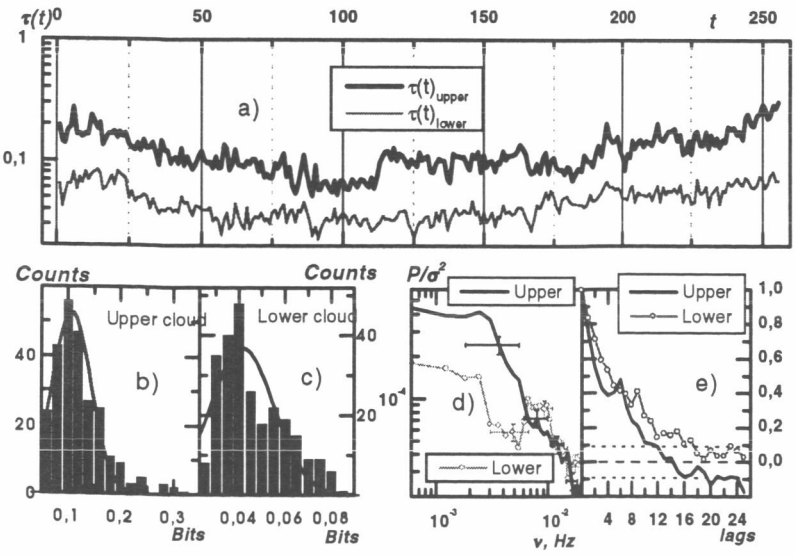


Fig. 3. Temporal variations of the optical thickness of the upper and lower clouds illustrated by Fig. 2 from 19:10 till 19:40 (a), histograms of distribution of their optical thickness (b and c), their Fourier transforms (d), and autocorrelation functions (e).

The depolarization ratios of lidar return signals $\delta(H) = P_\perp(H) / P_\parallel(H)$, where $P_\perp(H)$ and $P_\parallel(H)$ are the cross-polarized and parallel components of lidar return signals, respectively, were close to 0.8 for the upper and lower clouds.

The vertical profile $\delta(H)$ within the cloud extended from 6 to 10.5 km is shown in Fig. 4. The cloudiness can be classified as high cumulus by its lower boundary and as cirrus by its upper boundary.

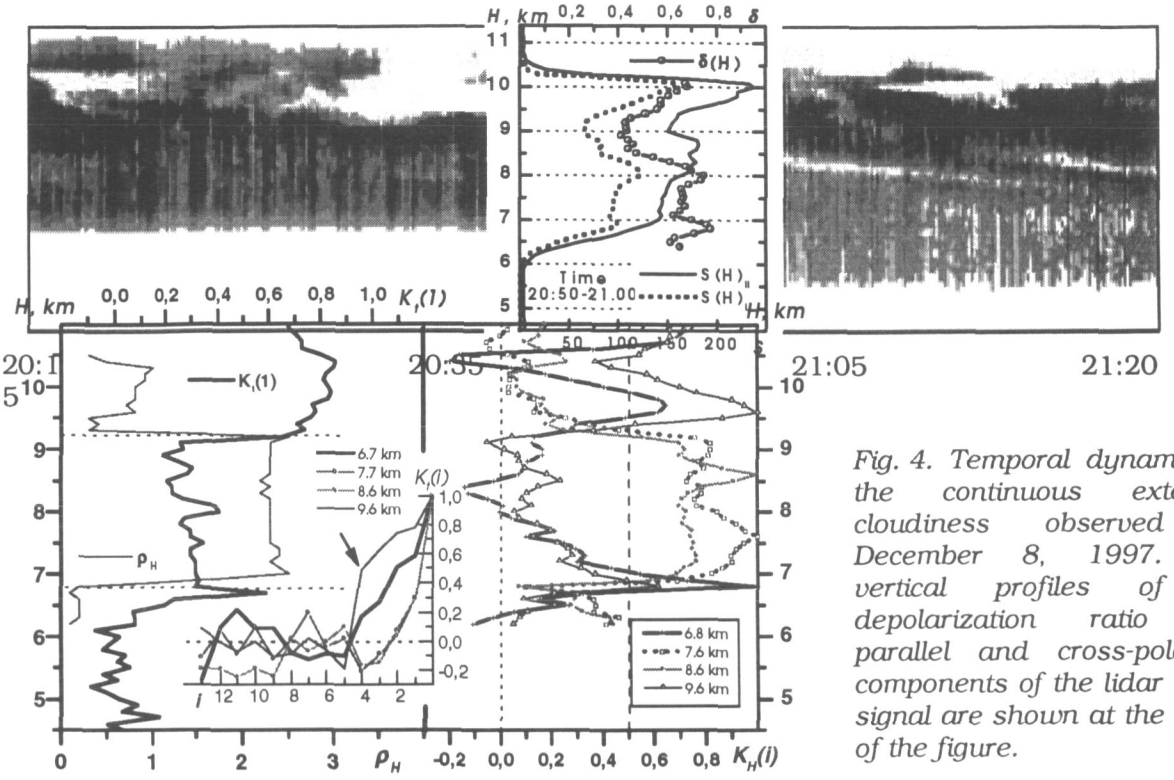


Fig. 4. Temporal dynamics of the continuous extended cloudiness observed on December 8, 1997. The vertical profiles of the depolarization ratio and parallel and cross-polarized components of the lidar return signal are shown at the center of the figure.

However, we did not observe any altitude dependence of the statistical or correlation characteristics of cloudiness. As an example, Fig. 5 shows the temporal autocorrelation functions $K_I(i)$ and the interlevel spatial correlation functions $K_H(i)$ for cloudiness observed from 20:15 till 20:35, Tomsk local time. Analogous functions were observed from 21:05 till 21:20, Tomsk local time. The vertical correlation radius ρ_H determined from the halfwidth of these correlation functions is shown in Fig. 5. We failed to estimate the correlation time, because already for the first lag the slope of the functions $K_I(i)$ exceeded 0.5. However, the first values of the temporal autocorrelation functions $K_I(1)$ that can be used to estimate the correlation time as a function of altitude are shown in Fig. 5. At the cloud bottom the correlation between the levels sharply decreased practically to zero in the directions from the cloud boundary toward the cloud depth and toward the clear atmosphere ($K_{6.8\ km}$). However, at the cloud top (near 9.5 km) the correlation function has the clearly pronounced maximum (~0.6). Analogous behavior has $K_{9.6\ km}$ at the cloud top. The internal cloud layers are closely correlated with the correlation coefficient >0.7 in the cloud depth ($K_{7.6\ km}$ and $K_{8.8\ km}$ in Fig. 5). The correlation sharply decreases at the cloud boundaries. Sharp difference between the interlevel correlation functions inside the cloud and at its boundaries (the decreased down to 0.5) was used as a criterion for the determination of the lower and upper cloud boundaries. The recurrence of clouds of all types (Ci+Cs+Cc) between 6-11 km was 55% over the observation period from August 8 till September 7, which slightly exceeded the reference data [4]. The recurrence of Ci was 48%, Cs – 29%, and Cc – 13%. Accoding to above-mentioned criterion, the recurrence of the cloud base height reached maximum between 7-10 km. Above 11 km, we did not observe the cloud base. Clouds moved preferably to the west with most probable velocities 10–20 m/s (in 70% of all cases). In 20% of all cases the cloud velocities exceeded 20 m/s and in 10% of all cases they were less than 10 m/s.

Fig. 5. Correlation characteristics of cloudiness displayed in Fig. 4 (from 20:15 till 20:35, Tomsk local time).

Acknowledgments The work was carried out at Siberian Lidar Station and supported by the Russian Ministry of Science (Reg. No. 01-64).

References

1. Cox S. K. , J. Atmos.Sci., 1971, v.28, p.1513-1515.
2. El'nikov A. V., Zuev V. V., and Marichev V. N. Atmospheric Optics, 1991, v. 4, No. 2, p. 201–209.
3. Zuev V. E., Kavkyanov S. I., and Krekov G. M. Izv. Akad. Nauk SSSR. FAO, 1983, v. 19, No. 3, p. 255–266.
4. Hahn C. J., Warren S. G., London J., Cherwin R. M., and Jenne R. Atlas of simultaneous occurrences off different cloud types over land. - NCAR Techn., Note TN241-STR, 21p.+188 maps.

Depolarization Measurements of Cirrus Cloud at Chung-Li (25 °N, 121 °E)

Wei-Nai Chen, Jan-Bei Nee
Department of Physics, National Central University
Chung-Li, Taiwan 32054
Phone: 886-3-427-6349, FAX: 886-3-425-1175, e-mail: wnchen@joule.phy.ncu.edu.tw

1. Introduction

Cirrus clouds play important role in determining the radiation budge of the earth's atmosphere. Many studies of cloud characteristics have been done by lidar. Polarization lidar is particularly useful for investigating the properties and compositions of ice particles in high cirrus clouds, which are known to contain a significant amount of non-spherical ice crystals. It is also known that cirrus clouds may contain water droplets which are spherical. The backscattering of liquid water droplets has very different polarization characteristics from the backscattering of ice crystals, and in many cases it is possible to use the polarization technique to distinguish between ice and water.

The depolarization ratio Δ for different types of cirrus cloud has been simulated by many people. Sun et al.[1], who gave $\Delta\approx0.8$ for clouds containing pure plates crystals and $\Delta\approx0.2$ for pure column crystals. For mixed-types of ice crystal, the depolarization ratio Δ ranged from 0.4 to 0.5[2].

We have used lidar to study high clouds since 1993. Recently, we have carried out the depolarization ratio measurements to understand the microphysics of cirrus clouds detected in the upper troposphere. This paper presents three cases of observations made in 1997.

2. Experiment and Result

Observations were made on 6/25/97, 8/22/97, and 9/3/97. Figure 1, 2, 3 show profiles for backscattering ratio and depolarization ratio. Each profile is progressively offset to show time evolution.

Figure 1 shows a cloud was located at the height between 12.1 km (about -50 °C) and 12.9 km (about -55 °C), but the depolarization ratio had a value only in the central part of cloud with a thickness of about 200 m. The center of the cloud with $\Delta\approx0.4$ should consist of ice particles, and the rest of the cloud with a $\Delta\approx0$ must consisted of water droplets.

Figure 2 shows a cloud was located at height between 13 km (about -55 °C) and 14.5 km (about -65 °C) with depolarization ratio $\Delta\approx0.2$. The maximum of depolarization ratio $\Delta\approx0.7$ was at the bottom. Since the depolarization ratio for pure column crystal is $\Delta\approx0.2$, and for pure plate crystal $\Delta\approx0.8$. That implies this cloud has the plate type crystals at the bottom and column type of crystals at the top.

Figure 3 shows consistent height profiles for both backscattering ratio and depolarization ratio, revealing the cloud was located at height between 15.6 km and 16.2 km an average value of $\Delta\approx0.25$. That suggests this cloud should consists of column type of crystals generally.

3. Reference

1. Y. Sun, Z. Li, J. Bosenber (1989), "*Depolarization of polarized light caused by high altitude clouds. 1: Depolarization of lidar included by cirrus*", Appl. Optics, 28, 3625-3632.
2. K. Sassen (1991), "*The Depolarization Lidar Technique for Cloud Research: A Review and Current Assessment*", Amer. Meteor. Soc., 72, 12, 1848-1866
3. L. Thomas, J. C. Cartwright and D. P. Wareing (1990), "*Lidar observations of the horizontal orientation of ice crystals in cirrus clouds*", Tellus, 42B, 2, 211-216

Figure 1, 2, 3. Cirrus cloud backscattering ratio R and depolarization ratio Δ measurements of selected case.

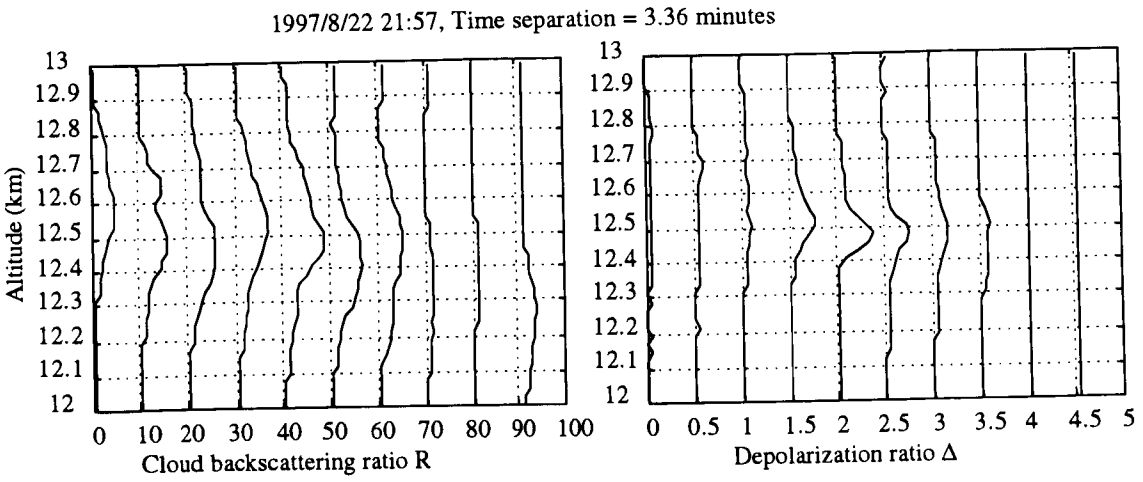


Figure 1. 8/22/97

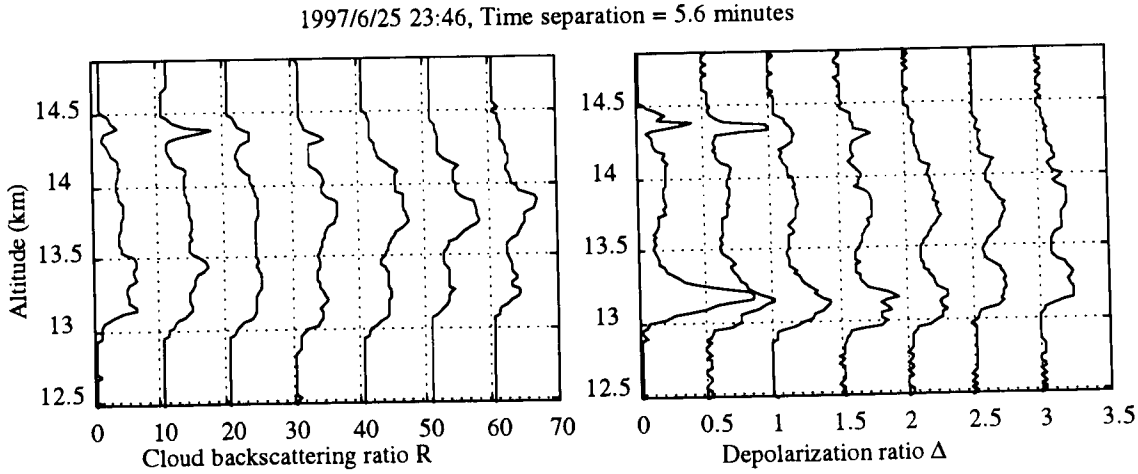


Figure 2. 6/25/97

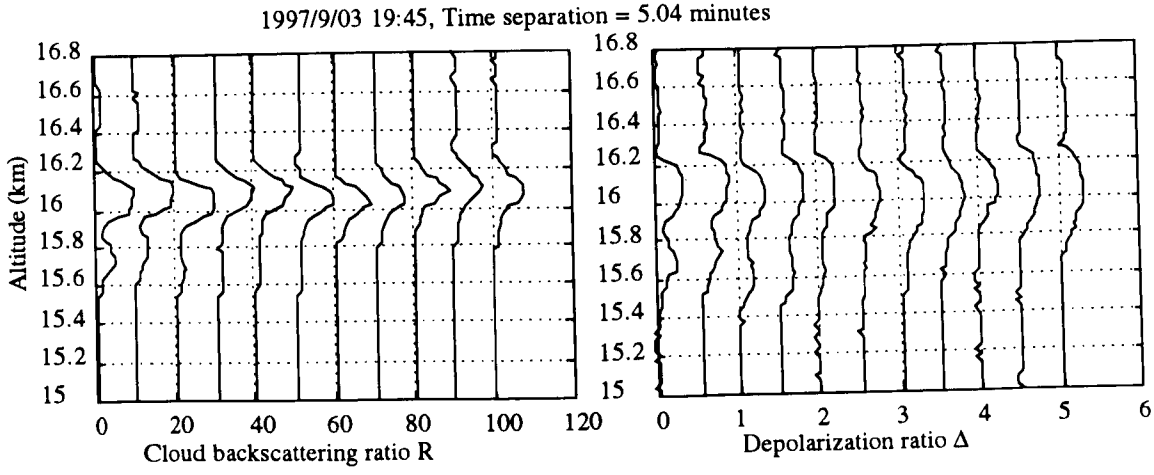


Figure 3. 9/3/97

Figure 1, 2, 3. Cirrus cloud backscattering ratio R and depolarization ratio Δ measurements of selected case.

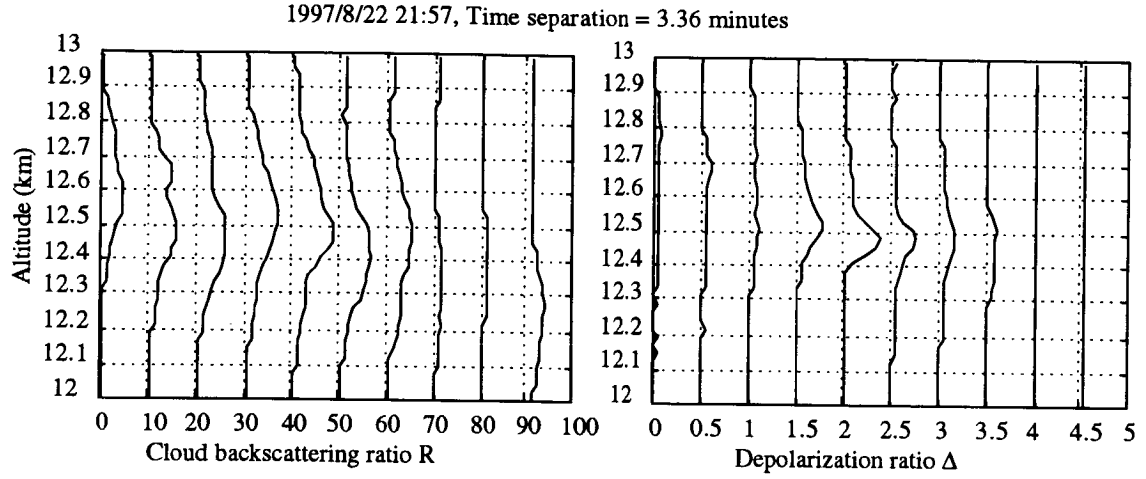


Figure 1. 8/22/97

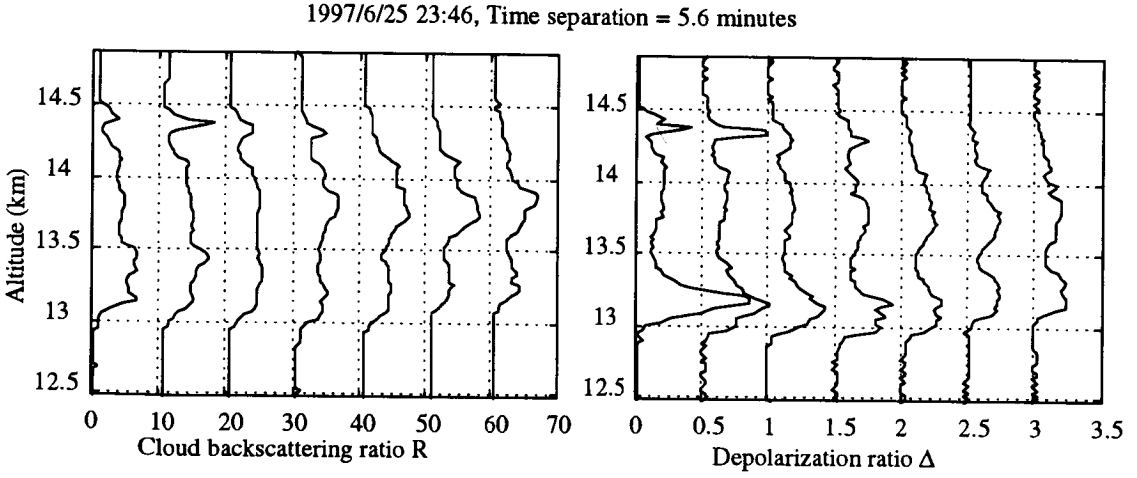


Figure 2. 6/25/97

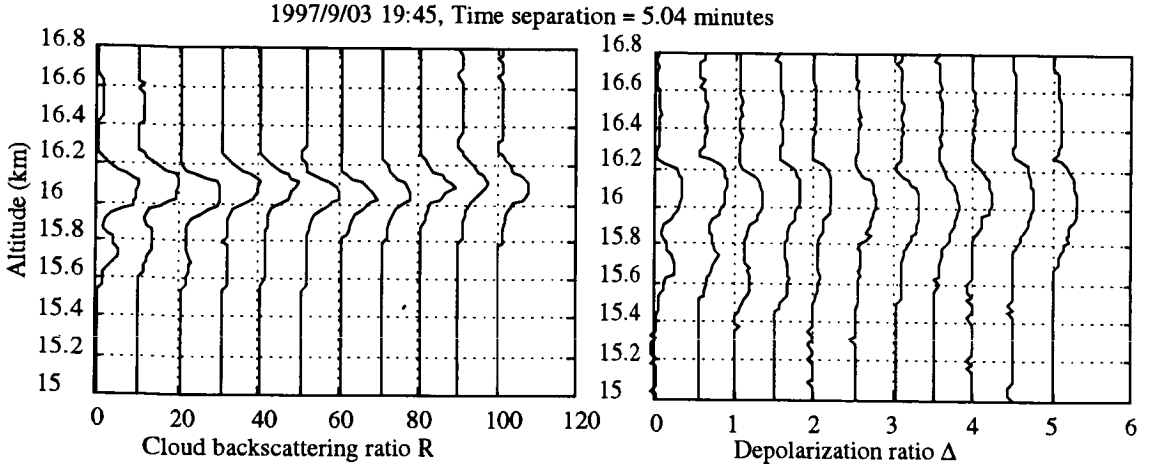


Figure 3. 9/3/97

Imaging of a Multiple Scattered Laser Beam Passing through Clouds: Experiment and Computer Simulation

Y. Saito, M. Ishizuka, S. Nagao, T.D. Kawahara, A. Nomura,
Shinshu University, 500 Wakasato, Nagano 380-8553, Japan
Phone: +81-26-226-4101, FAX: +81-26-223-4723, Email: saitoh@cs.shinshu-u.ac.jp

K. Noguchi
Chiba Institute of Technology, 2-17-1 Tsudanuma, Narashino, Chiba 275-0016, Japan

1 Introduction

Analysis of multiple scattering phenomena of a laser beam in dense materials such as clouds and fog is a troublesome. The effect causes uncertainty in the determination of the cloud base and depth for space lidar experiments, and of the cloud top even in ground-based lidar experiments. Some computer simulations of multiple scattering were reported, but there are a few experimental results and they only contained intensity data. We compare the multiple scattering distribution image of a laser beam passing through clouds obtained using a range-resolved imaging lidar with Monte-Carlo simulations.

2 Method

If multiple scattering occurred efficiently, the optical signal should spread into areas where the laser beam itself cannot exist. If the spread-signal could be detected as a two dimensional distribution image, the image will offer much more information for analysis than by using only the intensity data.

A highly sensitive CCD camera with an image intensifier was used as an imaging device. The photo-cathode of the intensifier was electrically gated to several hundreds nano-seconds and photo-electrons from the cathode were amplified enough to create images with a multi channel plate placed in the image intensifier. The gate operation was delayed by a circuit synchronized to the laser radiation. The delay time corresponds to the range from the system to the target and the gate time width corresponds to the range resolution. By changing the delay time, a range resolved image can be obtained. The distribution of the image from it's center corresponds to a multi-field view lidar signal with angular resolution.

The CCD camera used in this experiment had 756 (horizontal) x 485 (vertical) pixels that covered an area of 11.52 mrad in the field of view. Other system specifications were: 532 nm laser wavelength, 80 mJ pulse energy, 10 ns pulse width, 10 Hz repetition rate and 0.5 mrad beam divergence for the laser transmitter. A telescope camera lens with an 89 mm diameter and 500 mm focal length, and a 532 nm interference filter were placed in front of the camera to collect the scattered signal. The image was monitored on a TV screen which was useful to align the laser beam and the receiver. The image was recorded on a video tape. After the experiment, the data was reloaded into a computer and analyzed.

3 Experimental Results

The laser beam was directed vertically towards the clouds and passed through the clouds. Figure 1 shows examples of the range-resolved multiple scattering image at successive ranges inside the cloud. Although the images are represented as a horizontal image, multiple scattering in the vertical direction are also contained in the image. The image of (a) shows the Mie and Rayleigh scattering image before the laser beam hit the cloud. The image size is 15.36 m x 11.52 m in this case which depends on the delay time (range). The laser beam size in the figure is 1.4 m at a range of 1.02 km (6.8 μ s delay time) +15 m range width (100 ns gate time). When the laser beam hits the cloud base, the signal intensity suddenly increases and the beam size also enlarges (see (b)). As the laser beam passes through the cloud, the intensity of the laser beam that appears at the center of the image gradually decreases due to scattering by the cloud particles, and the multiple scattering signal spreads to the whole area of the image (c). After penetrating the cloud, the build-up of signal intensity was not seen any more but very small intensity signals still remained and were distributed

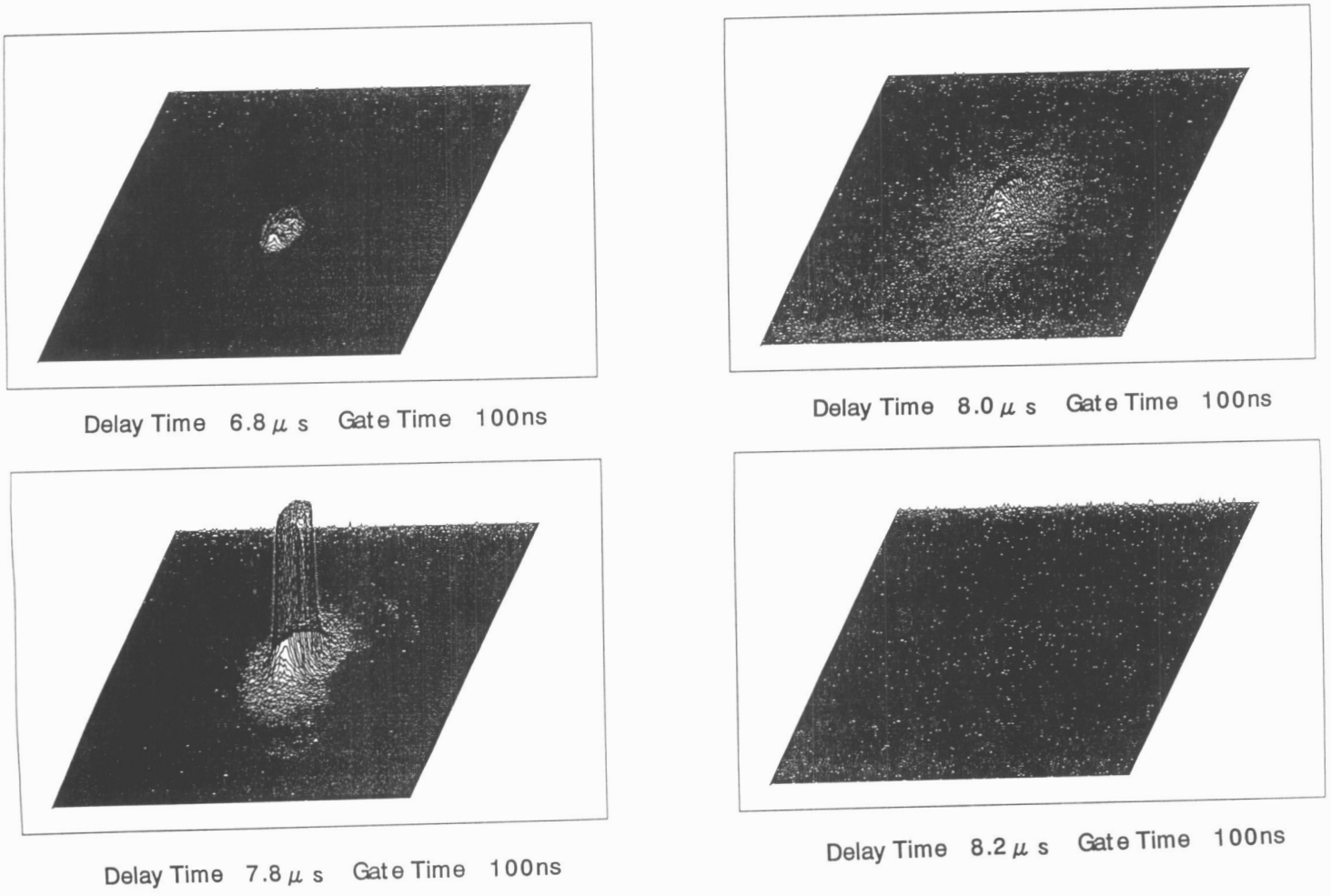


Fig. 1 Laser scattering image passing through cloud.

entirely in (d). The small signal seen on the upper area of each image is noise introduced when recording the data onto tape and reloading the data into the computer; the noise was too small to perturb the image signal. Figure 2 are cross-sections of the intensity images in Fig. 1. The range from the center of the image is converted to a field of view. The solid line corresponds to Fig. 1 (b), the broken line to (c), and the chain line to (d), respectively. The process of multiple scattering occurring inside the cloud is seen and the decrease of the peak intensity of the laser beam and the increase in the width of the distribution pattern as the laser beam passes through the cloud is clearly shown.

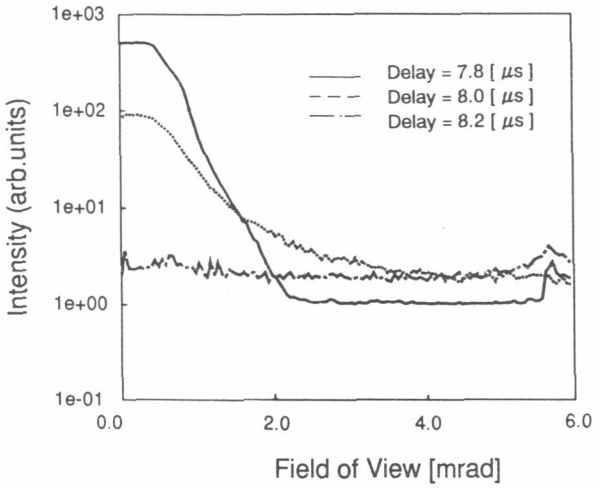


Fig. 2 Cross-sectional pattern of intensity of Fig. 1.

4 Comparison to Simulation Results

Monte-Carlo computer simulations were carried out to confirm the experimental results. The essential procedure is that described previously by Kunkel and Weinman (1976). After checking the appropriateness of the program performance by comparing the MUSCLE results to the simulation results for space lidar returns (Noguchi et al., 1997), the program was arranged to be able to make the distribution image of the multiple scattering signal. The trajectory of each scattered photon was followed and number of photons at the scattering place in the field of view was integrated within the gate time width. The parameters for the simulation were taken from the experiment and a small correction was made in the delay time to fit the simulated distribution pattern exactly to the experimental one. Figure 3 is an example of the simulated image for C1 clouds that corresponds to Fig. 1 (c) in which the envelope has a long tail. The image contains multiple scattering information with respect to time together with the range distribution. The cross-sectional patterns of the intensity distribution of simulated images of Fig. 3 and others in different delay time are shown in Fig. 4. Comparison of the image in Fig. 1 (c) to Fig. 3, Fig. 2 to Fig. 4 showed that the distribution patterns were reproduced by the simulation. As the simulation inside the clouds did not show the same pattern as Fig. 2 (d), it suggests that Fig. 2 (d) was obtained outside the clouds. Cloud models other than C1 clouds, i.e., Ns cloud, Haze C and Haze M, could not give good results in this case.

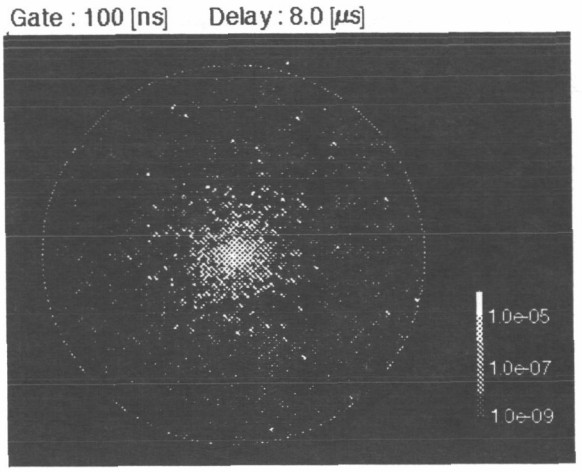


Fig. 3 Two dimensional distribution pattern of simulated multiple scattering image.

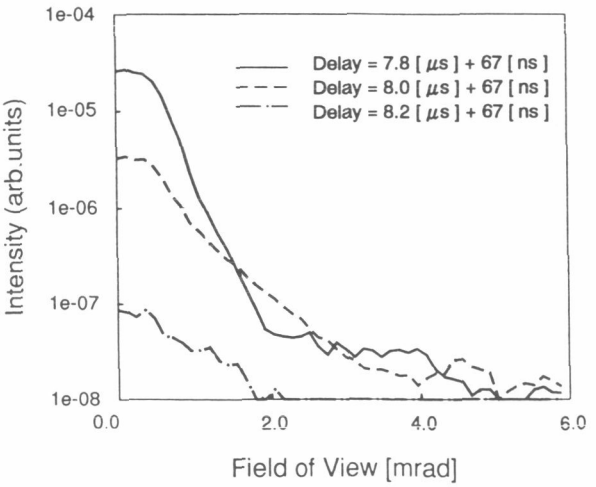


Fig. 4 Cross-sectional pattern of simulated signal intensity.

5 Conclusions

Use of a CCD camera offered a simple and easy way to add the capability of multi-field view observation with successive angular resolution to the lidar system. Both the experimental and simulation results clarified the multiple scattering process inside clouds. They supported the idea that imaging of multiple scattering was a useful method for cloud monitoring, i.e., to determine cloud depths and also to estimate cloud types.

Acknowledgments

We would like to express our thanks to Dr. T. Itabe (CRL, Japan) for supplying the CCD camera and to Dr. N. Sugimoto (NIES, Japan) for the telescope camera lens, and also thanks to Mr. K. Takahashi of our University for his helpful assistance.

References

Kunkel, K.E., J. Weinman (1976). Monte Carlo Analysis of Multiply Scattered Lidar Return. J. Atmos. Sci., 38, pp. 1772-1781, 1976.

Noguchi, K., Y. Saito, S. Nagao, and A. Nomura (1997). Simulation of Space Lidar Returns under Multiple Scattering from Cloud. In proceedings of *1997 OSA Winter Topical Optical Remote Sensing of the Atmosphere*, (Santa Fe, Feb. 9-14, 1997), OMD8, PP. 62-64.

Aerosols, cirrus clouds and temperature measurements with lidar in Camagüey, Cuba.

René Estevan, Roberto Aroche, Ismael Pomares and Sonia Cervantes
Camagüey Lidar Station, Centro Meteorológico, PO Box 134, Camagüey 70100, CUBA
Phone: (537) 322-61103, E-mail: rene@caonao.inf.cu

Juan Carlos Antuña
Meteorology Department, University of Maryland, College Park, MD 20742 USA
E-mail: antuna@atmos.umd.edu

1 Introduction:

The continuous monitoring of the atmosphere is an important component of the scientific community efforts to understand the climatic syatem and to determine the possible climate changes. Lidars play an important role in that way because of its capacity to make precisely and continuous measurements of different parameters and phenomena, its easy manipulation and its relatively low explotation cost.

There are only few lidars in the tropical zone, one of the less studied regions of the planet but at the same time a very important piece in our effort to undesrtand the climate system. One of those lidars is located in the Camagüey Meteorological Center (CMC), Cuba, (21°24´ N, 77°51´ W).

Here we report its applications to measurements of aerosols in the lower stratosphere and high troposphere, tropical night-time cirrus clouds and stratospheric temperature and density.

2 Camagüey lidar main features and data procesing.

The lidar was installed in 1988, as part of the Cuban-Soviet cooperation in tropical meteorology research, but only began regular operation in January 1992. Measurementswere carried out on cloud free nights. Table 1 shows its main parameters.

Parameter	Magnitude
Laser,λ	Nd:Yag, 532nm
Energy per pulse	300 mJ
P. R. F.	30 Hz
Mirror diameter	30 cm
Receiver	PMT FEU-136
Regimen	Photon Counting

Table 1. Lidar technical parameters.

Aerosol measurements are scheduled once a week at 300 m resolution. Some times, under apparently clear sky conditions the initial set of shots, used to check the functioning of the lidar, reveals the presence of cirrus clouds. In that cases, this set of shots is saved. Beginig in 1993, additional sets of measurements at 75 m resolution are done.

The aerosol backscattering coefficient (ABC) is calculated using the conventional algorithms as was reported before (Antuña, 1996b).

Cirrus cloud measurements bases and tops were determined using the enhancement of the backscatterred signal (photons) above the molecular backscattered signal . A cirrus multilayer strucuture was considered in the cases in which in the photons vs. height profiles the valley between two peaks (molecular backscattered signal) was less or equal than one third of the signal from the lower of the two peaks.

Considering the lower counts of photons above 30 km due to the construction limitations (mainly the optics) of our lidar, monthly photon vs,. height profiles were integrated. Then temperature and density profiles between 30 and 50 km were derived using the algorithms based in the single-frequency elastic backscattering (Chanin and Hauchecorne, 1991).

3 Stratospheric and high tropospheric aerosols.

The stratospheric aerosols lidar measurements from January 1992 to December 1993 provided information from the Mount Pinatubo volcanic aerosols. Partial results were published recently, showing the decay in time of the amount of aerosols at all levels (decaying ABC) as such as its descent in altitude. Derivations of the aerosol optical depth (AOD) from the lidar integrated ABC decreased from 0.14 in early 1992 to 0.03 by the end of 1993 (Antuña, 1996a, 1996b).

Figure 1 illustrates the mentioned aerosols amount decay and altitude descent. The four ABC profiles, with

6 months lag, show the decreasing in the ABC maximum from a value of 12.16 at 26 km in January 1992 to a value of 1.85 at 20 km in July 1993. It can be inferred from this figure the exponential time decay law typical of the stratospheric aerosol clouds originated by big volcanic eruptions.

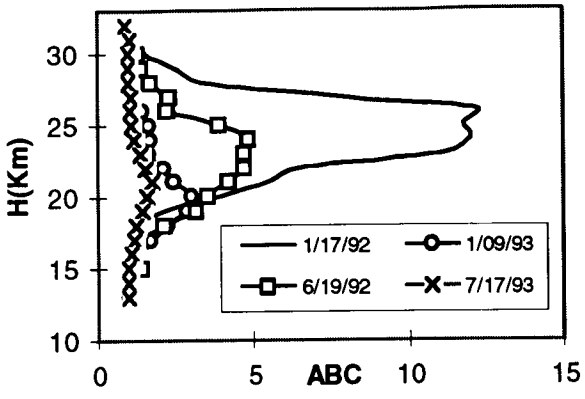


Figure 1. Selected aerosol backscattering coefficient (ABC) profiles from January 1992 to July 1993.

In figure 2 the ABC profiles for October 5th and 18th, 1994 reveals the presence of two narrow aerosol layers in the high tropical troposphere, in the vicinity of the tropical tropopause. The presence of such aerosols was confirmed by sunphotometer measurements in the south of the US made during the same period (Volz, 1994). From September to December 1995 aerosols layers with similar features were detected again in the lidar measurements. Also in this case measurements from sunphotometers located in the southern portion of the US corroborates the occurrence of such transient aerosol events, reporting values of the AOD which agree with lidar derived AOD values (Mims, 1996).

No volcanic eruption in the tropical zone capable to produce such aerosols were reported in both occasions, and no other event which could be the source of then was reported. One possible explanation to these events is that the aerosols may come from the tropical stratospheric reservoir (Grant et al., 1996).

It should be consider that the period of the year these events had been detected are associated in the CMC to the annual cycle descent of the tropopause and also that during the whole year around in the 30% of the days multiple tropopauses are present. Both features are associated with the stratosphere-troposphere airmasses transport, which can be responsible of carrying the aerosols from the tropical stratospheric reservoir to the high troposphere.

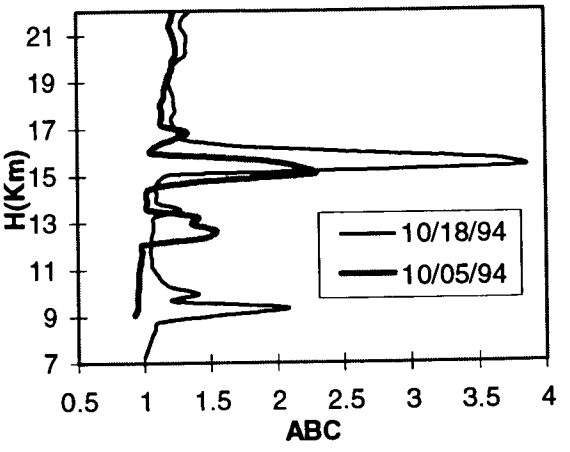


Figure 2. Aerosol backscattering coefficients (ABC) profiles for 5th and 18th October 1994.

4 Subvisible cirrus clouds.

The conditions under which cirrus cloud are measured, permit us to classify them as subvisible cirrus clouds. A total of 53 cirrus lidar measurements were made from 1992 to 1996. In general measurements showed that they were located at altitudes between 9 and 15 km. Under the mean sounding conditions of the atmosphere in Camagüey those altitudes are equivalent to temperatures in the range between -40 and -70 °C.

In Table 2 (Cervantes and Aroche, 1997) the mean vertical cirrus features are reported for the rainy (May - October) and low rainy seasons. It shows practically no differences between the bases in both periods but around 1 km difference in the tops (and consequently in the cirrus thickness). A possible explanation for that behavior is the high frequency of occurrence of depth convection in the rainy season. This will carry up moisture and cloud condensation nuclei (CCN) to the levels at which cirrus clouds forms. This phenomena take place in complex interaction with the 200 hPa circulation (Imasu and Iwasaka, 1991; Aroche et al., 1997). Another interesting feature is that in around the 40% of the cases there was a multilayer structure as has been reported in other tropical latitudes (Imasu and Iwasaka, 1991).

It was made a particular comparison between the

years 1992 and the years 1993 and 1994 together for the frequency of occurrence of only one layer and more than one. This classification was made considering the big differences in the stratospheric aerosol layer loading between both periods, which was shown in figure 1. It was found that in 1992 the 80% of the cases were only one layer cirrus and for 1993 and 1994 it was the 50% of the cases. Also in 1992 the mean top showed an increase in around 1 km (three times the resolution for that year) with respect to 1993 and 1994. These more thick cirrus during 1992 may be caused by the stratospheric aerosols seeding of cirrus clouds which is a potential phenomena mentioned by some authors (Sassen, 1992, Song et al, 1996). One possible mechanism to explain that feature is the increase of CCN in the high troposphere as result of the stratospheric aerosols falling into the troposphere through the tropopause. It will permit cirrus clouds to extent to altitudes normally scarce in CCN..

Cirrus Vertical Features	Season.	
	Rainy	Little Rainy
Base Height (Km)	11.54	11.22
Top Height (Km)	14.09	12.94
Thickness (Km)	2.56	1.72

Table 2. Tropical subvisible cirrus clouds features.

5 High stratosphere temperature and density.

The derivation of temperature and density in the high stratosphere (above 30 km) were not completely successful. It is known from the analysis of the algorithm used that it is very sensitive to the ratio of photon counting at each altitude and at the calibration height (Shibata et al, 1986; Chanin and Hauchecorne, 1991). This ratio depends on the product of the laser power and the receptor area. In our lidar this parameter has a value of 0.5 $W.m^2$, which is 20 times lower that the lidars used for density and temperature derivations. This low value is due to the low diameter of the receptor installed in our lidar (Pomares et al, 1997).

Figure 3 illustrates the high stratosphere temperature profile derived for one particular measurement (Tnov). Also the temperature profile for a composite of lidar measurements for the month of November (Tmedio) is shown. For comparison porpouses the mean temperature sounding for November in the CMC (Tsondeo) through the troposphere and lower stratosphere is drawn to show its matching with the tropical standard atmosphere temperature profile (Tt).

The derived profiles show an increasing trend of the temperature with height between 30 and 50 km, which agrees with the trend of the standard atmosphere, but below 40 km there are very big differences, with maximum values of around 200 °K. Above that altitude the differences are in the order 20 °K maximum and it can be appreciate the matching of profiles at some levels.

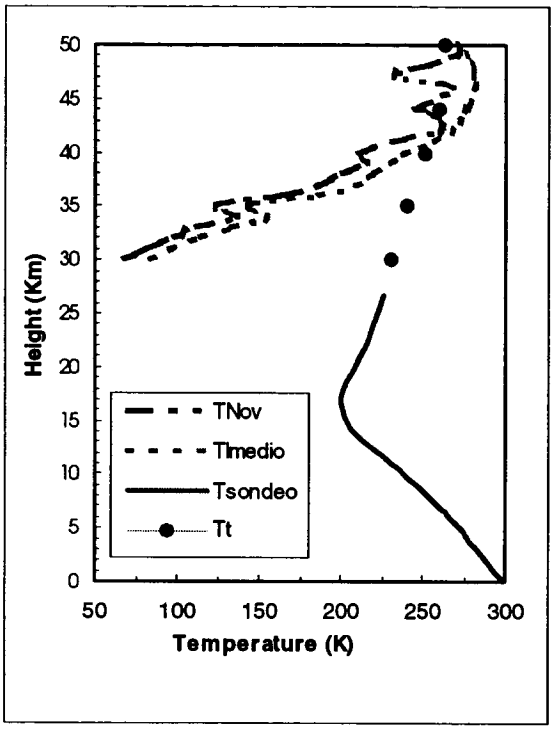


Figure 3. High stratosphere temperature profile derived from lidar. (See text for details.)

6 Summary.

Capabilities of the Camagüey lidar station for stratospheric and high tropospheric aerosols as such as subvisible cirrus clouds have been shown. This type of measurements have been taken regularly in the Caribbean by first time. Stratospheric aerosol measurements of the Mount Pinatubo volcanic cloud showed features of the decaying of the cloud. High tropospheric aerosols of unknown origin had been detected in the lidar soundings. They could be associated to stratosphere-troposphere airmasses transport phenomena that have not been detaliled documented yet. Subvisible cirrus clouds

geometrical properties have been studied. A possible evidence of the cirrus clod seeding by stratospheric aerosols have been found. The methodology for high stratosphere temperature and density derivation from lidar measurements was implemented. It was determined the technical limitation that should be solved in order to carry out this type of measurements in the near future.

7 Acknowledments.

Authors want to thanks the CMC engeeniering staff which have been providing technical support to the lidar station under very hard material limitations. Also to all the people from around the world which have been contributing with resources to maintaing the station in operation.

References.

Antuña J. C. (1996a). Lidar measurements of stratospheric aerosols from Mount Pinatubo at Camagüey, Cuba. *Atmos. Env.*, **30**, 10/11, pp. 1857-1860.

Antuña J. C. (1996b). Mount Pinatubo stratospheric aerosols decay during 1992 and 1993 as seen by Camagüey lidar station, Cuba. *in NATO ASI series, Vol. 42 "The effects of the Mt. Pinatubo eruption on the atmosphere and climate"* . pp 3-9.

Aroche R. R., et. al. (1997). Caracterización espacio-temporal de los radioecos de precipitación en el PMC. (Manuscript, unpublished). 16 pp.

Cervantes S. y R. Aroche (1997). Análisis de las Nubes Cirros Medidas por la Estación Lidar en Camagüey, Cuba, durante el Período de Marzo 1992 hasta Agosto de 1996. *Reporte Científico Técnico.* (Manuscript, unpublished). 19 pp.

Chanin M.L., A. Hauchecorne (1991). Lidar study of the structure and dynamics of the middle atmosphere. *Indian Journal of Radio & Space Physics,* **20**, pp 1-11.

Grant, B., E.V. Browell, C.S. Long, L.L. Stowe, R.G. Grainger and A. Lambert (1996). Use of volcanic aerosols to study the tropical stratospheric reservoir. *J. Geophys. Res.*, **101**, pp. 3973-3988.

Imasu R. and Y. Iwasaka (1991). Characteristics of Cirrus Clouds Observed by Laser Radar (Lidar) during the Spring of 1987 and the Winter of 1987/88. *Journal of the Meteorological Society of Japan.*, **69**, No. 3, pp. 401-411.

Mims, F., (1996). Bulletin of the Global Vulcanism Network. Vol. **21**, No. 2, pp.13.

Pomares I. y R. Aroche (1997). Sondeo láser para la determinación de la temperatura y densidad en la estratósfera alta. *Reporte Científico Técnico.* (Manuscript, unpublished). 27 pp.

Sassen, K. (1992). Evidence of liquid-phase cirrus cloud formation from volcanic aerosols: climate implications. *Science*, **257**, pp.516-519.

Shibata T., M. Kobuchi and M. Maeda (1986). Measurements of density and temperature profiles in the middle atmosphere with a XeF lidar. *App. Opt.*, **25**, pp 685-688.

Song, N., D. o'Starr, D. Wuebbles, A. Williams and S. larson (1996). Volcanisc aerosols and interanual variation of high clouds. *Geophys. Res. Let.*, **23**, pp. 2657-2660.

Volz F. (1994). Personal Comication.

STATISTICAL CHARACTERISTICS OF THE MARITIME CLOUD BASE HEIGHT

V. Shamanaev, G. Kokhanenko, and I. Penner

Institute of Atmospheric Optics,
1, Akademicheskii Ave, Tomsk 634055, Russia
Tel: +7 3822 258516
Fax: +7 3822 259086
E-mail: shvs@losa.iao.tomsk.ru

The scientific research vessel *Academician Mstislav Keldysh* had been sailing in the Atlantic (crossing it twice along 50°N latitude) and in Barents, Norwegian, and North seas for three months in 1995. The Makrel'-2 lidar [1] placed onboard the vessel was used for sensing of clouds from a cabin with the help of an external flat mirror.

Measurements were performed every day during 10 weeks. Individual runs lasted from 10 min to 1.5 h with a laser pulse repetition frequency of 1 Hz. The velocity of the vessel and the wind velocity at an altitude of 18 m above the water surface were measured independently. It was assumed that clouds drifted with the wind velocity. We measured the cloud base height above the sea surface and the radiation extinction coefficient at the cloud base.

Criteria for lidar determination of the cloud base height (CBH) were studied in [2]. In the present work we used two criteria based on an analysis of the lidar return signal derivative. The CBH was defined as a distance r_0 to the point at which the lidar return signal just started to increase when a laser beam entered the cloud after its propagation through the clear atmosphere or as a distance r_m to the point at which the signal reached its maximum.

The extinction coefficient $\varepsilon(r)$ at the distance r from the lidar was calculated from the measured lidar return signal power $P(r)$ by the formula

$$\varepsilon(r)=\frac{1}{2}\frac{P(r)r^2}{\int_{r_0}^{r_\infty}P(x)x^2dx-\int_{r_0}^{r}P(x)x^2dx}. \qquad (1)$$

Here, r_∞ is the maximum range from which the lidar return signal was still recorded. The condition of applicability of this asymptotic formula is $\int_{r_0}^{r_\infty}\varepsilon(x)dx \geq 3$.

The radiation extinction coefficient at the cloud base ε_b was calculated according to [2] as the value of $\varepsilon(r)$ averaged over the laser beam propagation path whose length is half the distance of signal accumulation, that is,

$$\varepsilon_b=\frac{2}{r_\infty-r_0}\int_{r_0}^{(r_0+r_\infty)/2}\varepsilon(x)dx. \qquad (2)$$

Figure 1 shows the results of sensing of low clouds having a trend of the CBH. Visually, they were stratocumulus clouds. The moon was seen through them. The lowest cloud layer vanished 30 min after the completion of this run and we investigated the cloud layer with H_{CBH}=570 m. Figure 1a illustrates the CBH profile calculated by the criterion r_m. In the presence of trend, the standard deviation was ΔH=25 m. After elimination of this trend, ΔH_0=14 m. The estimated spatial length of the sample was 26 km.

Empirical distribution of the CBH $n(H)$ before elimination of the trend is shown in Fig. 1b by small squares. The distribution is clearly bimodal with the asymmetry coefficient As=0.64 and the coefficient of excess E=2.0. After elimination of the trend As=–0.01 and E=–0.68. In this case, ΔAs=0.056 and ΔE=0.032; therefore, $n(H)$ cannot be classified as Gaussian: it is flatter.

As to the distribution of ε_b, it was markedly asymmetric. Its half-width from the modal value ε_{mod} toward greater ε_b are 16% of ε_{mod}. It is 42% of ε_{mod} toward smaller ε_b.

On the whole, for an ensemble of stratiform clouds with CBH ≤1 km we obtained the following. When the cloud base had a trend, its current average height could be represented as $H=H_0\pm\mu l$, where l is the distance from the initial measurement point and $\mu=(3.4\pm0.7)\times10^{-3}$ (assuming that the average wind velocity at the CBH was 10 m/s). Here and below the standard deviations of the measurable parameters are given. The maximum distance l was in the range 5–40 km.

The spread of the CBH with the trend in our experiments varied from 25 to 56 m with standard deviations (39±14) m, that is, the average variation coefficient was 36%. When the trend was eliminated, the spread of the CBH varied from 10 to 42 m with standard deviations (23±12) m, that is, the average variation coefficient was 52%.

The coefficient of asymmetry for the distribution $n(H)$ with CBH trend was negative in ~40% of all cases and equal to $As=-(0.36\pm0.49)$, that is, had moderate absolute values. Its extreme values were –0.01 and –0.70. In ~60% of cases the asymmetry was positive and equal to $As=(0.51\pm0.25)$, that is, slightly exceeded its moderate values. The extreme values of the asymmetry coefficient were 0.33 and 0.80.

After elimination of the trend, the distribution $n(H)$ symmetrized. Weakly pronounced negative asymmetry was observed in less than 20% of all cases with $As=-0.20$. In the remaining cases the asymmetry was positive, weak or moderate, with $As=(0.27\pm0.20)$.

Figure 2 shows rather smooth CBH distribution for high stratified clouds. These data were obtained on August 21, 1995 in the presence of thin maritime fog layer just above the water surface and the low cloud field that had disappeared by the start of sensing of higher clouds. The CBH was $H=(5424\pm223)$ m without trend. For the distribution $n(H)$, $As=0.69$, that is, the asymmetry was strong. The excess coefficient $E=0.24$ was typical of weakly pronounced flattop peaking. The distribution $n(\varepsilon)$ was similar to $n(H)$ and had the positive asymmetry coefficient as well.

On the whole, we did not record any trends of the CBH for these high clouds on measurable scales. The fluctuations of the CBH were $\Delta H=(115\pm95)$ m, varying from 11.7 to 264 m. The positive and negative asymmetry coefficients were observed equally often. In the first case, $As=(0.34\pm0.31)$, that is, the coefficient of positive asymmetry varied from small to moderate. In the second case, $As=-(0.75\pm0.42)$, that is, the coefficient of negative asymmetry varied from moderate to large. The negative excess coefficients were $E=-(1.0\pm0.81)$, that is, they were indicative of the bimodal character of the CBH distribution. In case of positive excess coefficients, $E=1.10\pm0.87$.

As to the scattering coefficient at the CBH, we did not observe any peculiarities of its behavior for low and high clouds. On the whole, $n(\varepsilon_b)$ was asymmetric. The halfwidth of the distribution $n(\varepsilon_b)$ at half ε_{mod} toward greater values of ε_b was (33±38)% of ε_{mod}. Once we recorded a shift by 110% from the modal value, that is, the distribution was very blurred but still remained nonuniform. To the left of ε_{mod}, that is, toward smaller ε_b, the halfwidth of $n(\varepsilon_b)$ at the same level was (41±17)% of ε_{mod}. The average width of the distribution $n(\varepsilon_b)$ can be written as $\varepsilon_{mod}{}^{+0.33\varepsilon_{mod}}_{-0.41\varepsilon_{mod}}$. To be objective, we note that up to 10% of the experimental distributions obeyed nearly uniform distributions of ε_b for the entire measurement range.

Thus, we can conclude the following. In the North Atlantic the CBH fluctuations of stratiform clouds obeyed most often asymmetric law rather than normal on horizontal scales between 10–70 km. The coefficient of asymmetry can be positive or negative. The extinction coefficient at the CBH, as a rule, also did not obey the normal law. Elimination of the low-frequency trend of the CBH decreases the degree of asymmetry of CBH distribution.

References

1. Abramochkin A.I., Zanin V. V., Penner I. E., Tikhomirov A. A., and Shamanaev V. S. Airborne polarization lidars for the study of the atmosphere and hydrosphere. Atmospheric Optics. V. 1, No. 3, 92–96 (1988).
2. Shamanaev V. S. Estimation of the radiation scattering coefficient at the cloud boundary. Atmospheric and Oceanic Optics. V. 5, No. 7, 702–706 (1993).

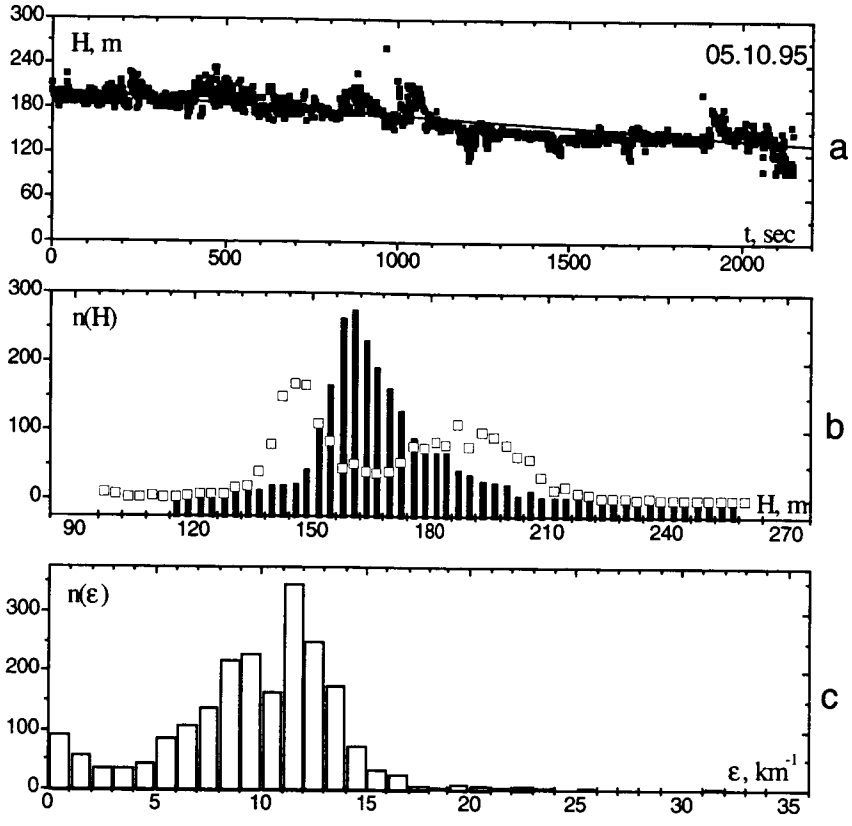

H, m
05.10.95
t, sec
a
n(H)
H, m
b
n(ε)
ε, km⁻¹
c

Fig. 1

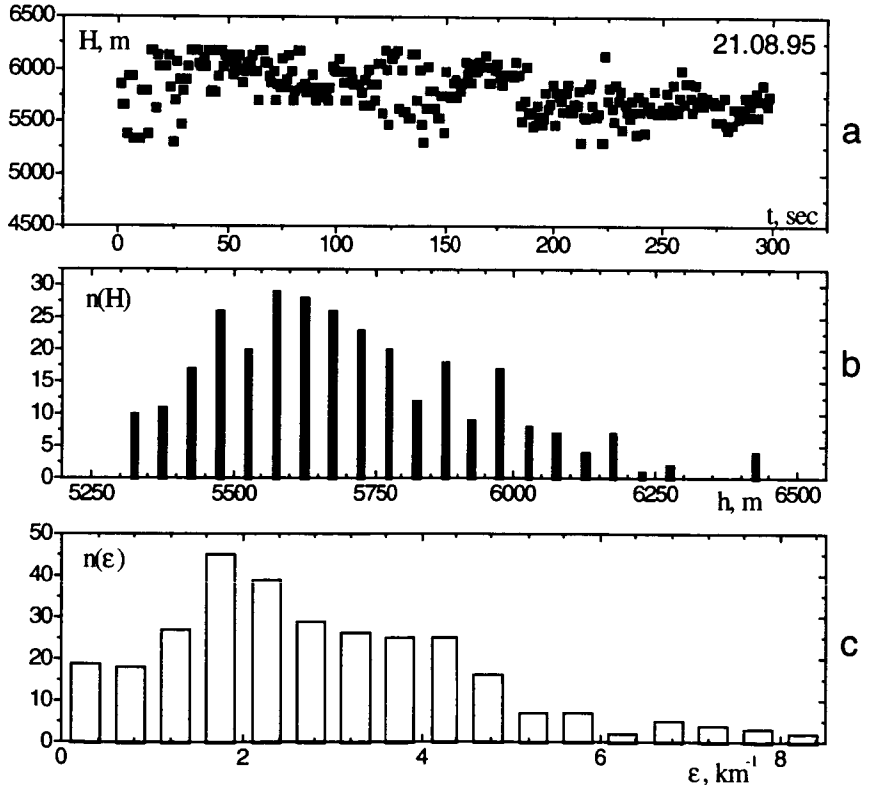

H, m
21.08.95
t, sec
a
n(H)
h, m
b
n(ε)
ε, km⁻¹
c

Fig. 2

AVERAGE AND FLUCTUATION CHARACTERISTICS OF THE TRANSPARENCY OF LAKE BAIKAL WATER FROM AIRBORNE LIDAR DATA

G. Ludbrook, [1] A. Scott, [1] G. Kokhanenko, [2] I. Penner, [2] and V. Shamanaev [2]

1. *Defence Evaluation and Research Agency*
St. Andrews R., Malvern Worcs, Malvern WR14 3PS, UK
Tel: +44 (0) 1684 894857
Fax: + 44 (0) 1684 896270
E-mail: gdlugbrook@dera.gov.uk

2. *Institute of Atmospheric Optics*
1 Akademicheskii Av., Tomsk 634055, Russia
Tel: 7 382 2 258516
Fax: 7 382 2 258895
E-mail: shvs@losa.iao.tomsk.ru

Corresponding author is V. Shamanaev

Lake Baikal is the world's largest reservoir of fresh water. By its area (its length is about 600 km) it can be classified as a small inland sea. Therefore, the interest to investigation of this unique water reservoir is understandable. A number of the parameters of Lake Baikal can be studied from aboard of an aircraft as was done earlier [1]. The water turbidity measurements are of interest not only for ecological researches but also for lidar pilot studies because of a wide range of variation of the transparency of upper water layers: from very turbid water of the Selenga to the clearest water of the Sargasso sea with the extinction index only slightly exceeding unity.

The Optik-E Antonov-30 aircraft laboratory of the Institute of Atmospheric Optics with the multipurpose Makrel'-2 lidar onboard flew above Lake Baikal in November 1996. Typical flight altitudes above the water surface were about 300 m. In the experiments, a Nd:YAG laser at λ=0.532 μm was used. Temporal resolution of a receiving system was 7.5 ns. A pulse repetition frequency of 25 Hz allowed us to perform bathymetric measurements with a horizontal resolution of 4 m.

The extinction index of water ε was calculated by the logarithmic derivative method for upper water layers to depths 5–15 m. Figure 1 illustrates one of the flight routes above the mouth of the Selenga with 10- and 50-m isobaths. Figure 2 shows cross-sectional mapping of the parameter ε along the flight line. The serial number of laser shot is indicated on the abscissa. A thousand shots correspond to a flight distance of 17.5 km for a pulse repetition frequency of 5 Hz. Here, arrows 1, 2, ... indicate the corresponding points of the flight route shown in Fig. 1. Significant spread of the values of ε near point 5 was due to the fact that laser beams there were incident not only on the water surface, but also on the swampy land of the river mouth. Near the mouth of the Selenga (at distances ≥10 km from the mouth) the extinction index monotonically increased from 0.14 to 0.35 m^{-1}. The Selenga runs off many suspended silt particles that deposited near the lake shore. There is a sharply pronounced interface between turbid river and clear lake waters, which was clearly observed from the aircraft. When we flew above these points, we recorded a sharp increase in the extinction index up to 0.5–0.6 m^{-1}. We also observed large spatial inhomogeneities of the water turbidity. Their horizontal sizes reached several kilometres. At a distance of ~40 km from point 6 water became increasingly clear. At a distance of ~100 km above the lake centre the mean values of ε reached 0.127±0.013 m^{-1}.

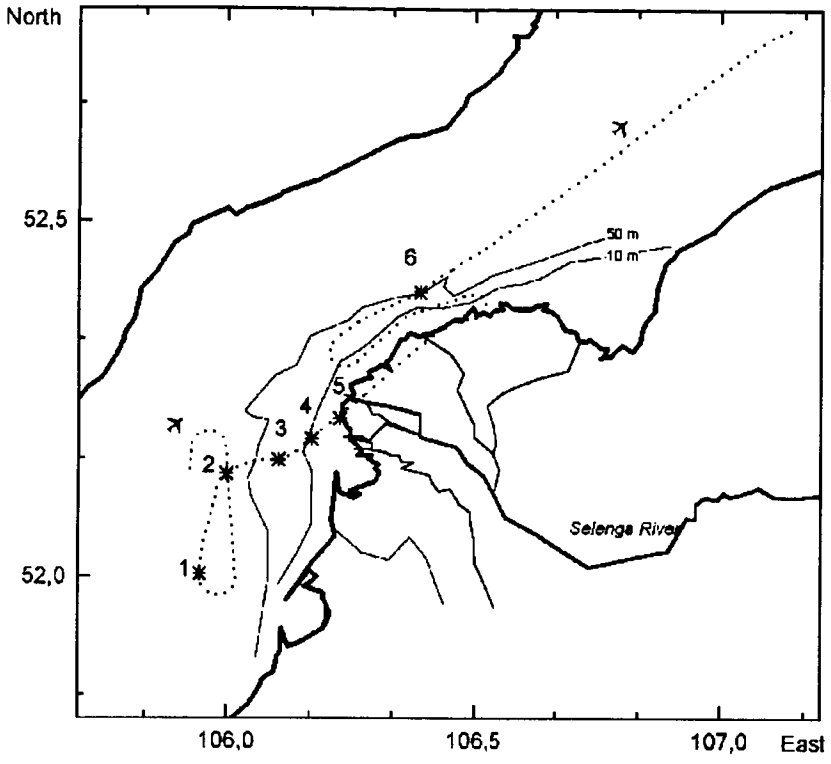
As can be seen from the calculated power spectra of the extinctione index fluctuations, the fluctuation intensity decreases by the power law. However, the spectral exponent varies as a function of spatial wavelength. In some cases, there arise the points of inflections on the curve of the spectral exponent at the wavelengths that correspond to certain characteristic scales of hydrophysical processes occurring within the water depth of Lake Baikal.

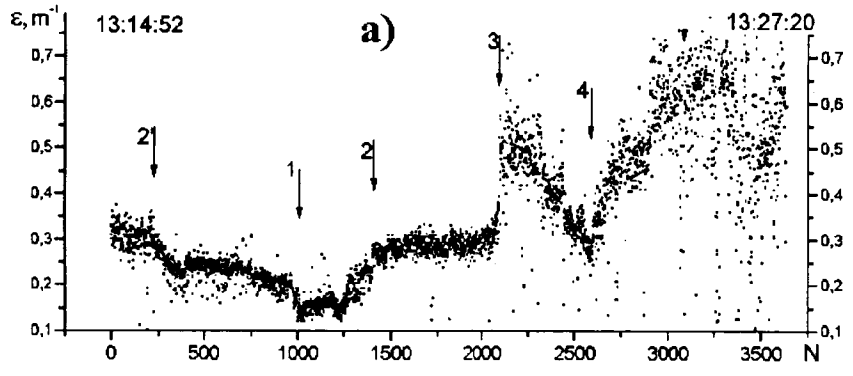
We estimated the minimum and maximum measurable depths of the bottom for our lidar. The minimum depth is determined by the laser pulse length, the lidar return signal power, and the dynamic range of the recording system. The best results can be obtained with the use of the cross-polarized component of a lidar returned signal, because the depolarization of signals coming from the upper water layers is insignificant, whereas signals reflected from the bottom are practically completely depolarized. The minimum measurable depth is 4 m.

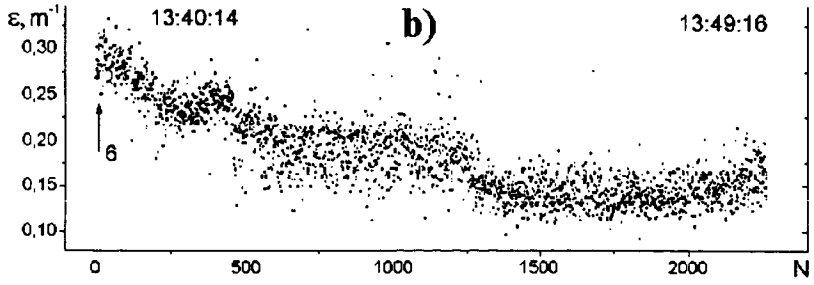
The maximum measurable depth of the bottom (for maximum lidar sensitivity and power per pulse) is primarily determined by the degree of water turbidity. We succeeded in recording the depths of the bottom as great as 40 m when we flew near the Bol'shoi Ushkanii island where the water extinction index was ~0.127 m^{-1}. When we flew above the northern part of the lake, we recorded the depths of the bottom as great as 19 m for waters with an extinction index of 0.184 m^{-1}. We failed to record the signals reflected from the bottom when we flew above the mouth of the Selenga.

Reference

1. Penner I. E. and Shamanaev V. S. Airborne Lidar Sensing of Lake Baikal Water Area. 17 ILRC, Sendai, Japan, July 25–29, 1994. Abstracts of Papers, pp. 73–75.


North
52,5
52,0
106,0
106,5
107,0
East
50 m
10 m
Selenga River
1
2
3
4
5
6


ε, m⁻¹
13:14:52
a)
13:27:20
0,7
0,6
0,5
0,4
0,3
0,2
0,1
0
500
1000
1500
2000
2500
3000
3500
N
1
2
3
4
5


ε, m⁻¹
13:40:14
b)
13:49:16
0,30
0,25
0,20
0,15
0,10
0
500
1000
1500
2000
N
6

Lidar Studies of the Cirrus Cloud Optical Properties Anisotropy

B.V.Kaul*, D.N.Romashov*, I.V.Samokhvalov**

*Institute of Atmospheric Optics, Siberian Branch of the Russian Academy of Sciences,
1 Akademicheskii Ave., 1, 634055 Tomsk, Russia
Phone: +7(3822) 25-98-86; Fax: +7(3822) 25-84-52; E-mail: arshinov@lwsa.tomsk.su
Tomsk State University, 36, Lenin Ave., Tomsk, 634050, Russia.
phone: +7(3822) 41 39 84; Fax: +7(3822) 22 61 62; E-mail: kvt@elephot.tsu.tomsk.su

Crystal clouds are an optically anisotropic atmospheric formation because the ice crystals, that make up the ensemble of cloud particles, may take some preferred orientation under the action of various natural factors. This fact often manifests itself in such optical phenomena in the atmosphere like halo, sun pillars, and the like.

From the standpoint of their participation in the radiation transfer in the atmosphere it is important that extinction of radiation by cirrus clouds depends on the radiation incidence angle. For instance, extinction of solar radiation by cirrus cloud layers may depend on the zenith and azimuth position of the Sun. This circumstance can not be allowed for in calculations based on model approach that uses representation of cloud particles by equivalent spheres. Besides, the model of equivalent spheres is unable to correctly describe the angular distribution of radiation scattered by crystals. The matter is that in this case the radiation transfer should be described by the radiation transfer equation in a vector-matrix form. In so doing one also should use such local properties of a medium as extinction and scattering phase matrices. Unfortunately, these characteristics of crystal clouds are yet poorly studied. However, at present there are certain grounds for making a mathematical modeling of these characteristics by assuming the ensemble of crystal cloud particle to be an ensemble of hexagonal plates and columns [1]. Such a modeling may also incorporate some *a priory* information on the shape, size, and orientation of particles, characteristic of cirrus clouds. As to the shapes and size of crystals in a cirrus cloud one can find a vast experimental material in literature collected using direct sampling data. Unfortunately, no so many data can be found on the particle orientation in a crystal cloud.

In our earlier studies we have developed a technique to remotely determine the direction and degree of preferred orientation of crystal particles in cirrus clouds based on lidar measurements of the cloud backscattering phase matrices (BSPM) [2,3].

In the course of grounding our approach we have derived a lidar equation in a vector-matrix form and some relations that enable calculation of the angles and degree of particle orientation.

Once the method for experimental determination of BSPMs of cirrus clouds is developed we could suggest the following scheme of mathematical modeling of the extinction and backscattering phase matrix. At the first stage one have to calculate BSPMs for model ensembles of crystal particles. The model ensembles are constructed in a wide range of such characteristics as particle shape, particle-size distribution, and the particle distribution over orientation angles. It is worth noting here that calculating BSPM is less laborious than calculating full scattering phase matrix.

Then, at the second stage, one makes a comparison between the experimentally measured and calculated BSPMs thus identifying, according to certain criteria [4], the nearest one, among the set of calculated matrices. From that comparison one also identifies the ensemble of crystals which then is used for calculating the full scattering phase matrix and an extinction matrix at the third and final stage of the scheme proposed. Following this scheme will require certain modifications in the calculation technique from Ref.1.

Below we present an example of the comparison made between the experimentally measured BSPMs and those calculated for ensembles of ice cylinders with a preset orientation parameters. The three-dimensional set of the orientation parameters has been being constructed as follows. The angle of radiation incidence onto the layer, γ, varied from 0° to 90° in a 10° step; the angle α of a preffered orientation was set from 0° to 180° with the step of 3°; the parameter k of the Mises distribution that characterizes the degree of particle orientation in the ensemble about the mode α varied from 0 to 3 at a step of 0.5. The rsults of the comparison are given in the Table.

Table Comparison between the experimentally measured (the upper line) and calculated (two lower lines) backscattering phase matrices.

N_0	γ^0	k	α^0	m_{22}	m_{33}	m_{44}	m_{12}	m_{13}	m_{34}	m_{24}	m_{23}	δ
	0	2.25	90	0.810	-0.600	-0.380	0.390	0.000	0.310	0.000	0.000	
1	30	3.0	90	0.867	-0.639	-0.507	0.433	-0.002	0.125	-0.004	0.000	0.31
	0	2.5	90	0.752	-0.439	-0.192	0.174	0.007	0.123	-0.002	0.001	0.48
	0	1.0	169.8	0.620	-0.550	-0.150	0.000	0.000	-0.320	-0.120	0.000	
2	10	1.0	168.0	0.534	-0.468	-0.012	-0.040	-0.015	-0.294	-0.124	0.031	0.20
	0	1.0	168.0	0.513	-0.423	0.044	-0.005	-0.002	-0.297	-0.117	0.022	0.25
	0	2.3	0	0.780	-0.550	-0.350	-0.430	0.000	-0.280	0.000	0.000	
3	30	3.0	0	0.870	-0.636	-0.507	-0.433	-0.015	-0.125	-0.005	-0.00	0.37
	0	3.0	0	0.784	-0.408	-0.192	-0.181	0.009	-0.130	-0.013	-0.004	0.46
	0	2.7	70.1	0.320	-0.100	0.580	0.560	0.380	-0.270	-0.200	0.210	
4	60	3.0	75.0	0.362	0.005	0.643	0.471	0.273	-0.150	-0.087	0.320	0.37
	0	2.0	75.0	0.525	-0.367	0.107	-0.025	-0.013	-0.238	-0.135	0.138	1.16
	0	-	172.6	0.650	-0.650	-0.350	-0.150	0.000	-0.100	-0.050	0.000	
5	0	1.5	177	0.716	-0.593	-0.310	-0.090	-0.011	-0.086	-0.034	0.006	0.13
	0	1.5	177	0.716	-0.593	-0.310	-0.090	-0.011	-0.086	-0.034	0.006	0.13

The criterion of closeness between the calculated and experimental values is the minimum in the discrepancy

$$\delta = \left(\sum_{i=1}^{4} \sum_{j=1}^{4} \left(m_{ij} - m'_{ij} \right) \right)^{1/2},$$

where m_{ij} and m'_{ij} are correspondingly the experimental and calculated elements of the matrix M_{ij} normalized, by its element M_{11}. Note that the parameters of particle orientation measured experimentally quite well agree with the calculated ones, even if the discrepancy is large. This may be explained by the fact that these parameters are expressed not through the absolute values of the BSPM's elements but through the ratios between them, the absolute values being stronger dependent on the particle size.

In conclusion note that the value k=3 observed in the experiments is indicative of quite a high degree of particle orientation, such that about 90% particles of the ensemble have their axes oriented within the sector α ±45° about the angle of preferred orientation.

References:

1. Ping Yang and K.N.Liou. *Geometric-optics-integral-equation method for light scattering by nonspherical ice crystals* Appl.Opt. Vol.35, No63, pp 6568-6584 1996.

2. B.V.Kaul, O.A.Krasnov, A.L.Kuznetsov, E.R.Polovtseva, I.V.Samokhvalov, and Stykon. *Lidar investigations of particles orientation in crystal clouds* Atm.Ocean.Opt. V10, No2, pp119-125, 1997.

3. B.Kaul, Yu.Arshinov, D.Romashov, I.Samokhvalov, Ch.Werner, J.Streicher, H.Herrmann, U.Oppel, H.Krasting *Lidar Studies of Crystal Clouds* (Scientific Report) Spektr, Tomsk, 1997.

4. J.W.Hovenier and C.V.M. van der Mee *Testing scattering matrices: a compendium of recipes* J.Quant.Spectrosc.Transfer, Vol.55, No5, pp649-661, 1996.

Synergetic Simulation of the Earth Radiation Mission Lidar and other Instruments

Shiv R. Pal, David Donovan, Mark Cann
Centre for Research in Earth and Space Technology (CRESTech)
4850 Keele Street, North York, Ontario, Canada, M3J 3K1
Tel: 416-665-5418, FAX: 416-665-2032, E-mail: pal@lidar.crestech.ca

Ralph Girard and P.S. Park
MPB Technologies Inc., 151 Hymus Blvd., Pointe Claire, Quebec, Canada, H9R 1E9

J.P. Blanchet and M. Laroque
Department de Physique,Universite du Quebec a Montreal(UQAM)
Case postale 8888, Succursale A, Montreal, Quebec, Canada, H3C 3P8

1 Introduction

Under an ESA contract, MPB Technologies, CRESTech, UQAM, Canada Centre for Remote Sensing (CCRS) and the Canadian Atmospheric Environment Service (AES) are conducting a synergy-study related to the proposed Earth Radiation Mission (ERM) satellite. The four instruments being considered are a Cloud Profiling Radar (CPR), a Backscatter Lidar (BL), a Broad Band Radiometer (BBR), and a Cloud Imager (CI). The forward model and inversion algorithms for the BL, BBR, and the CI were developed by CRESTech, while the CPR algorithms were developed by MPBT. These four sensors are applied to a model atmospheric 'scene' provided by UQAM. The model atmosphere is derived from a Regional Climate Model which is driven by an objective analysis from NMC.. The radiances from the scene to be utilized by the passive sensors are calculated using STREAMER/DISORT for the given satellite-solar geometry. The spectral resolution is 0.28 to 4.03μm (24 intervals) and 4.03 to 500 μm (105 intervals) for a total of 129 intervals. The algorithms for each instrument are linked together in a synergy master program.

The BL and CPR modules incorporate their respective transmit-receive functions and inversion algorithms which are relate to the cloud and atmospheric parameters. The passive instrument modules (BBR, CI) incorporate their own instrument specification and generation of output signals in response to an input radiation field produced by the model. A general structure of the synergy study is shown in the schematic given in Fig. 1.

As shown in Fig. 1, the input to the four sensors comes from the atmospheric model definition. Not all parameters generated by the model are utilized by all the four instruments. However, specific parameters are required by specific instrument. The inversion algorithms of these instruments extract specific atmospheric parameters as shown in the third row of blocks. The cloud physical as well as optical

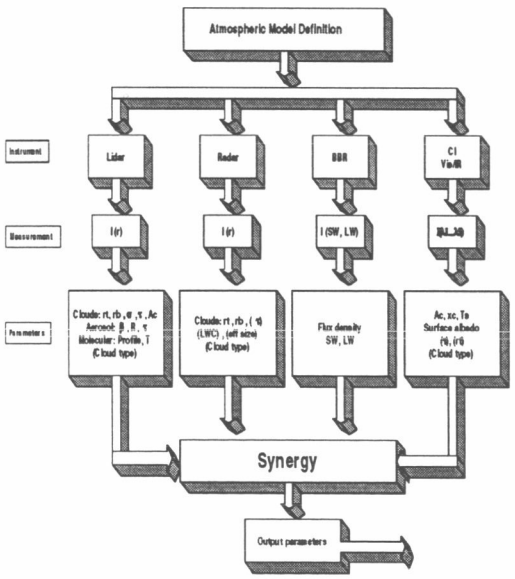


Figure 1: Synergy Schematic for BL, CPR, BBR and CI.

parameters such as lidar derived height of cloud top and bottom (r_t, r_b), extinction coefficient (σ), and those derived by other instruments are of interest in the ERM. The aim of this synergy study is to determine which parameters with what accuracy are accessible with the four instruments when all are synergistically linked while operating from the same satellite platform.

The results from all four sensors will be presented in this paper with emphasis on the BL.

2 Cloud Model

The cloud model is bound by the Latitude-Longitude coordinates (39.9°N, 294.6°) and (44.3°N, 300.6°) south of the Canadian province of Nova-Scotia on an 80x80 grid with pixel size resolution of approximately 7 km on a projected stereographic plane. In the vertical direction there are 30 levels (layers) from ground level up to about 30 km. The cloud parameters specified by the model are assumed to have a homogeneous distribution within each layer. Proper interpolation routines are utilized to generate profiles of these parameters with the range resolution required by the active sensors. The test trajectory runs through the middle of the model cloud scene which also coincides with the LITE orbit on Sept. 4, 1994 at 12Z.

3 Lidar and Radar

A Nd:YAG lidar (1064 nm) with ATLID specifications and microwave radar (94 GHz) complement each other for cloud measurements and form the set of active sensors on the ERM platform. A lidar provides efficient detection of thin and sub-visual clouds with cloud boundaries with insufficient pulse penetration in dense clouds. A Radar, on the other hand, does not detect the thin cirrus well but provides cloud bottom heights even for very dense clouds. The lidar simulation accepts several of the GCM provided average cloud parameters and outputs retrieved parameters for comparison with the parameters derived by the radar and other sensors. The lidar module requires microphysical parameters (size distribution, extinction and backscatter phase function) for its forward and retrieval models. Therefore for this study a parameterization scheme has been developed for the lidar. The instrument specifications and accuracy requirements are those prescribed in ESA's ERM mission.

4 BBR and CI

The BBR and the VisIR CI scan across the satellite track in order to measure and record upwelling radiation intensities in several visible and infrared bands from the Earth-atmosphere system. The BBR records the radiance in two channels, (short-wave) SW and (long-wave) LW. The pass-bands are selected so that the SW channel measures reflected solar radiation and the LW channel the thermal emission from the Earth's surface and atmosphere along with a small solar component. The derived brightness temperatures (IR channels), provide information on cloud cover, type and temperature. Some of these parameters also relate to the lidar and radar derived atmospheric parameters. The model comparisons are expected to provide cloud and aerosol optical depths also.

5 Parameterization for lidar

For the cloud extinction and backscatter the GCM provided cloud droplet effective radius and LWC are utilized in a cloud parameterization scheme where the ice/water fraction in the cloud is determined according to the parameterization based on the temperature (Rokel et al., 1991). The ice particle extinction and backscatter coefficients are determined using the parameterization of Ebert and Curry (1992). For the liquid water extinction and backscatter, a new parameterization was developed at CRESTech. The parameterized extinction for a wide range of effective droplet radius (normalized to 1 g m^{-3} of LWC), is shown in Fig.2.

The molecular backscatter and extinction related to the atmospheric density via Rayleigh scattering are derived from the GCM temperature and pressure profiles. These are interpolated for finer lidar vertical resolution. The background aerosol profile at the present time is similar to LOTRAN type.

6 Results

The trajectory chosen for this experiment was through the middle of the 80x80 grid. The GCM model-derived cloud liquid water content (LWC) along the trajectory is shown in Fig. 2. The LWC shows a very broad frontal system centered around an altitude of 9 km with narrow extensions below the main layer.

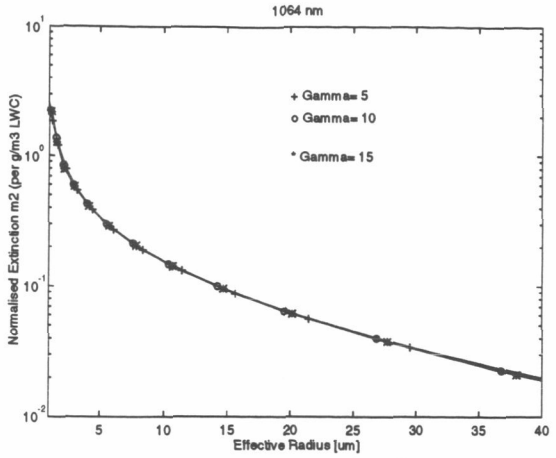


Figure 2. Cloud extinction cofficient as a function of cloud effective radius for three values of γ in the size distribution function (generalized gamma).

The radar retrieved LWC for the data in Fig. 2 is shown in Fig. 3. It is obvious that the cloud top and bottom are quite accurately detected by the radar with some small difference of a few range bins in cloud boundary.

The measured lidar signal along the trajectory is shown by the gray scale (white on black background) in the Fig.4. Also shown in this figure are the model cloud top (+) and bottom (—). The cloud here is very dense and the lidar signal disappears about half way through the cloud. The retrieved cloud top is within one range bin of the model cloud top. However, the lidar is not able to determine the cloud bottom due to incomplete pulse penetration.. Synergistically, the radar determined cloud bottom would be retained in this case. However for thin cirrus the lidar provides better cloud detection and renders cloud geometrical and optical parameters with higher precision. Such cases will also be presented

Fig. 6 shows a lidar retrieved cloud extinction profile (curve with noise in the cloud bottom) as compared to the one calculated from the model. Notice a good match between the two in the upper half of the cloud.

7 Conclusion

This synergy study provides insight into the effectiveness of system parameters of the sensors involved. The study will help determine how best to combine the output of the different sensors to create an optimum data set with the required accuracies. The lidar cloud parameterization and lidar application to different cloud scenarios will be presented.

The consultations provided by Z. Li from CCRS and L. Garand from AES are gratefully acknowledged.

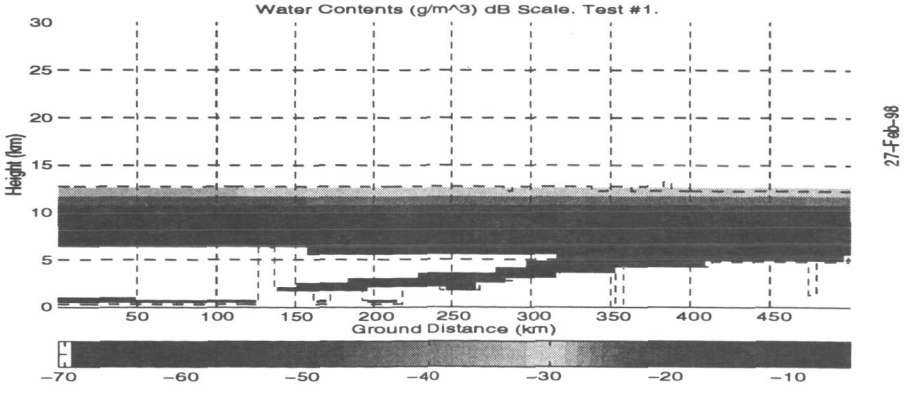


Figure 3: Gray scale plot of model LWC along the satellite track.

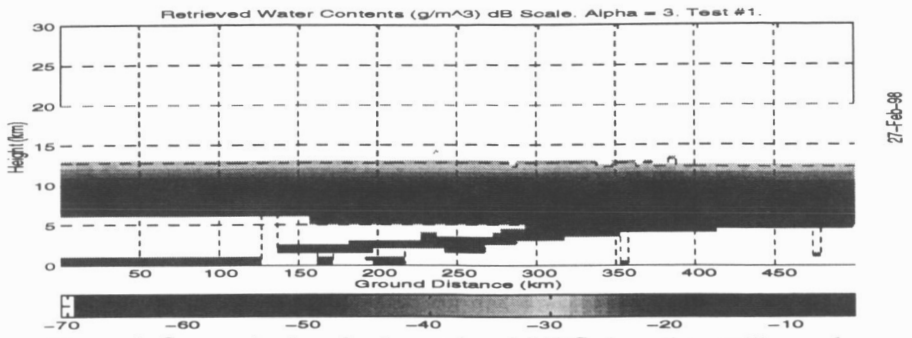


Figure 4: Gray scale plot of radar-retrieved LWC along the satellite track.

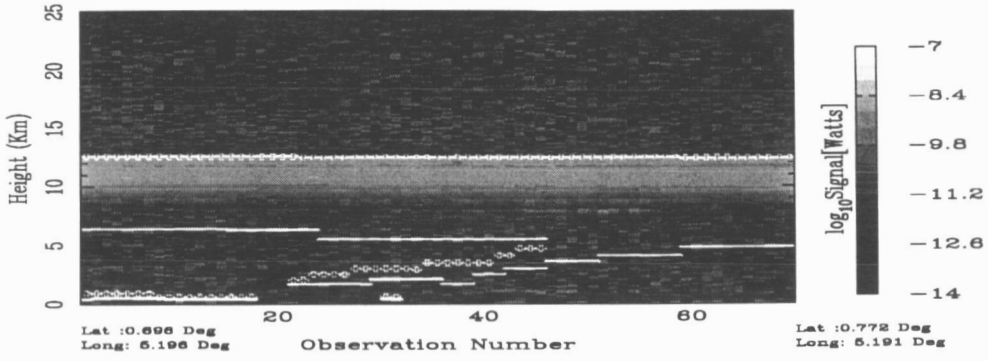


Figure 5: Lidar signal with model cloud tops (white +)and the bottoms (white —).

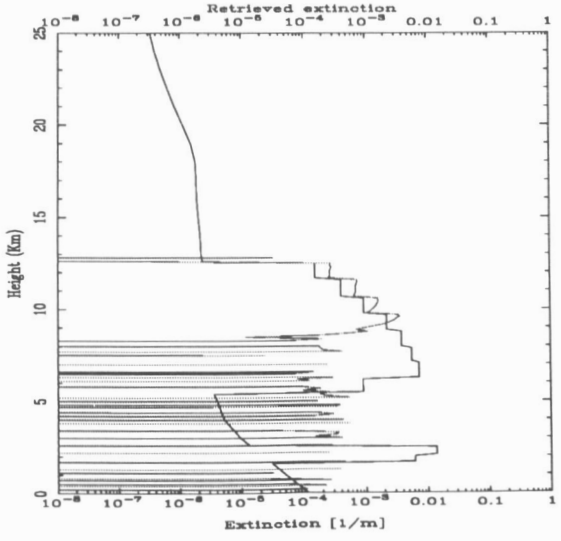


Figure 6: Model extinction profile and retrieved extinction profile for observation number 25.

8 References

Ebert, E., and J.A. Curry, ``A parameterization of ice cloud optical properties for climate models'', J. Geophys. Res., 97, 3831-3836, 1992.

Rockel B., Raschke. E. and Weyres B., "A parametrization of broad band radiative transfer properties of water, ice and mixed clouds", Beitr. Phys. Atm, 64, 1-12, 1991

OPTICAL EXTINCTION IN CLOUDS AT MULTIPLE WAVELENGTHS

G. L. Schuster*
Pennsylvania State University
Department of Meteorology
University Park, PA 16802
g.l.schuster@larc.nasa.gov

S. T. Esposito and C. R. Philbrick
Pennsylvania State University
Department of Electrical Engineering and
Applied Research Laboratory
University Park, PA 16802

SUMMARY
The Lidar Atmospheric Profile Sensor (LAPS) developed at Penn State University is used to measure the total atmospheric extinction coefficient at 284 nm, 530 nm, and 607 nm during the Southern California Ozone Study (SCOS). Extinction data at these wavelengths are presented during the development of a low-level cloud. While greater extinction at the ultra-violet (UV) wavelength is observed below the cloud (because of larger contributions of molecular Rayleigh scattering, small particle aerosol scattering and ozone absorption), the visible extinction becomes comparable to the UV extinction at cloud base. A time series of the visible extinction as the cloud grows is presented.

EXTINCTION RETRIEVAL
LAPS is a multi-wavelength Raman lidar with excitation wavelengths at 532 nm and 266 nm. The LAPS extinction retrieval technique has been described elsewhere (1), but we summarize it here. First, the Raman-shifted signals are range corrected and extinction at 530 nm is obtained with a least-squares fit of Beer's law compared to the expected gradient of the molecular profile. (The portion of the profile used for this analysis is beyond the region affected by the telescope form factor, or beyond about 800m). It is possible to assume that extinction coefficients at 530 nm (backscatter signal) and 532 nm (forward propagation) are nearly identical. Once the extinction at 530 nm is obtained it may be used to compute the attenuation of the forward beam, enabling the computation of the extinction of the return beam at the N_2 Raman-shift at 607 nm.

RESULTS
This paper presents extinction measurements of a cloud obtained during the Southern California Ozone Study (SCOS). Figure 1 shows a time sequence of the 530 nm extinction coefficient during the growth phase of a cloud. Lighter areas represent greater extinction coefficients than darker areas. The total optical depth between 2.3 km and 5 km at the

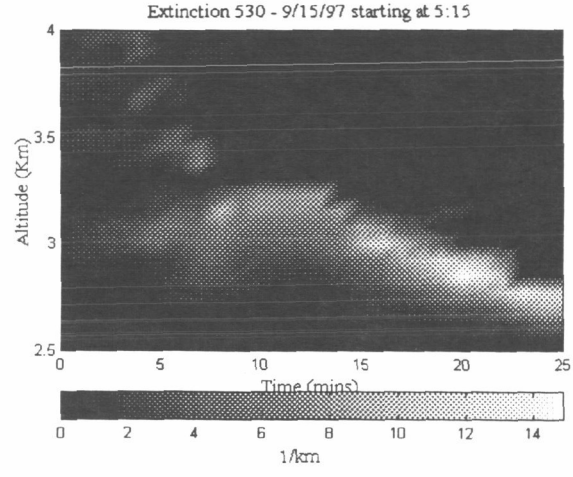


Figure 1 - Time series of extinction coefficient (km^{-1}) at 530 nm.

beginning of this time period indicated that a thick cloud was already present. (Note that the LAPS system is capable of penetrating optically thick clouds.) This cloud subsequently grows optically thicker and the cloud base decreases in altitude, as evidenced by the region of increased extinction in Figure 1. The dark region above cloud base after about 5:22 am (7 minutes into the sequence) is an area that was impenetrable by the lidar, and no information is retrieved beyond the indicated altitude.

A plot of multiple wavelength extinction coefficients averaged during the first 15 minutes of the same time period is shown in Figure 2. Ultra-violet extinction is greater than visible extinction below the cloud because of greater molecular Rayleigh scattering and ozone absorption. Scattering near the cloud base becomes more spectrally flat as cloud drops grow larger than both wavelengths. Probing further into the cloud reveals equal extinction at the red wavelength compared with the UV wavelength, consistent with expectations from Mie theory for spherical scatterers large compared with the wavelength.

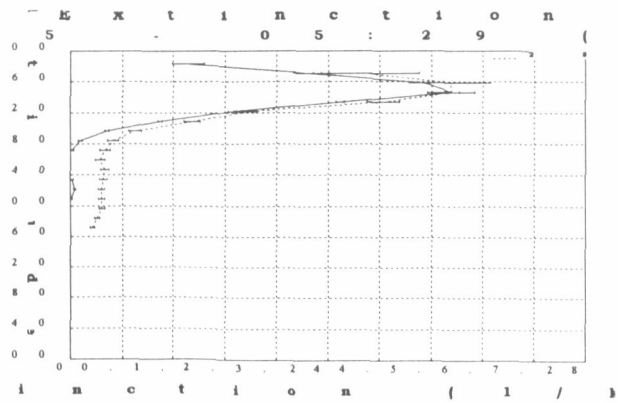


Figure 2 -- 284 nm and 530 nm extinction coefficients averaged for 15 minutes at 5:15 am.

ACKNOWLEDGEMENTS

Special appreciation for the support of this work go to SPAWAR PMW-185, California Air Resources Board (CARB), US Marine Corp at 29 Palms, the Mojave Desert Air Quality Management District, and the US EPA Monitoring Methods Research (Sect 8215). The efforts D.B. Lysak, Jr., T. Petach and Mike Zugger have contributed much to the success of the project. Conversations with Prof. Hans Verlinde of the P.S.U. Meteorology Department are also greatly appreciated.

*Permanent address for G. L. Schuster is NASA Langley Research Center, Mail Stop 420, Hampton, VA, 23681.

REFERENCES

1. Philbrick, C.,R., M. D. O'Brien, D.B. Lysak, T. D. Stevens, and F. Balsinger. "Remote sensing by active and passive optical techniques," Presented at the Advisory Group for Aerospace Research and Development, AGARD Conference Proceedings 582, p8-1, 1996.

Backscattering Mueller Matrix Derived from Lidar Polarization Measurements: Theory

Avishai Ben-David

Science and Technology Corporation
500 Edgewood Road, Suite 205, Edgewood, MD 21040 USA

Phone: (410) 612-6631, Fax: (410) 679-0369, Email: axbendav@apgea.army.mil

Mueller matrices and the Stokes vector are important tools for describing the scattering properties of aerosols. Although the study of Mueller matrices and Stokes vectors was introduced in the 19th century, and since then has been addressed in classical text books many new studies concerning symmetry relationship and the properties and structure of Mueller matrices for aerosols continue to appear in the literature, adding much more needed insight to aerosol research with polarized light. Polarization diversity lidars are used to study the shape, orientation, composition, and properties of scatterers in clouds (e.g., water droplets and ice crystals) by analyzing the polarized backscattering lidar measurements, measurements that can be described by appropriate Mueller matrices and Stokes vectors.

In this paper we develop a Mueller matrix $\tilde{M}(\tilde{S}(\theta),\theta,\phi,F)$ such that the irradiance Stokes vector $\vec{G}(\theta,\phi)=\tilde{T}(\phi_a)\tilde{M}\tilde{T}(\phi_p)\vec{u}$ (W m^{-2}) is measured with a detector with a field of view F and a pair of real polarizer-analyzer (i.e. a polarizer with a finite extinction ratio and a transmission less than 100%) with transmission Mueller matrix $\tilde{T}(\phi_p)$ and $\tilde{T}(\phi_a)$ from single scattering at angle (θ,ϕ) by a scattering medium characterized with a Mueller matrix $\tilde{S}(\theta)$ and illuminated with an incident irradiance $\vec{u}$. The matrix $\tilde{M}(\tilde{S}(\theta),\theta,\phi,F)$ can be viewed as a Mueller matrix for the scattering process that contains the information about the scattering aerosols. The various elements of $\tilde{M}$ can be deduced from polarized measurements by conducting a set of polarized measurements with a suitable combination of polarizer and analyzer fore and aft the scattering medium. In this work we also show how **all the 3X3** elements of $\tilde{M}$ that affect linear polarization measurements can be deduced by combining three azimuthally integrated measurements (the commonly made lidar measurements from which **only 3** elements of $\tilde{M}$ can be deduced) with eight azimuthally dependent measurements.

The scattering volume is illuminated with an incident irradiance Stokes vector $\vec{u}$ propagating along the z-axis. The incident Stokes vector $\vec{u}$ is transmitted through a linear polarizer with transmission Mueller matrix $\tilde{T}(\phi_p)$ whose maximum transmission $t_{\parallel}{}^{p}$ is oriented at azimuthal angle ϕ_p. A detector placed in the xy plane behind a linear analyzer, with transmission Mueller matrix $\tilde{T}(\phi_a)$ whose maximum transmission $t_{\parallel}{}^{a}$ is oriented at azimuthal angle ϕ_a, measures the irradiance I which is the first component of the Stokes vector $\vec{G}=(I,Q,U,V)$.

For scattering into the backward hemisphere, $\pi/2<\theta\le\pi$, a right-handed coordinate system for the scattering is the $\vec{x}\times(-\vec{y})=(-\vec{z})$. In this coordinate system the direction of propagation of the incidence (or scattering) is such that the cross product $(\perp)\times(\parallel)$ is the direction of propagation. The incidence $\vec{u}$ propagates along the positive z direction, and the scattering $\vec{G}$ propagates into the backward hemisphere toward the $(-\vec{z})$ direction. The measured irradiance $I(\theta)$ (and specifically the copolarized, cross-polarized and depolarization ratio) as a function of the polarizer and analyzer orientations (ϕ_p,ϕ_a) and their transmissions were developed. For scattering into the backward hemisphere ϕ_a is measured (in

the xy plane) counterclockwise from the (-y) axis (i.e., relative to the (||) direction of the scattered I_{-y}) and ϕ_p is measured (in the xy plane) clockwise from the y-axis (i.e., relative to the (||) direction of $\vec{u}$).

For an unpolarized incidence $\vec{u} = [1,0,0,0]$, we show that all co-polarization measurements are the same, and all cross-polarization measurements are the same (i.e., independent of the polarizer angle ϕ_p). For a linearly polarized incidence (which is usually the case in a lidar system) and with a perfect polarizer for which $t_\perp{}^p = 0$, the copolarized and cross-polarized measurements **are** a function of the polarizer angle ϕ_p. However the depolarization ratio remains independent of the polarizer angle. For backscattering ($\theta = \pi$) and for forward scattering ($\theta = 0$) a detector placed in the xy plane integrates the incoming radiance over the range of 2π azimuth ϕ within its field of view F. As a result of the azimuthal integration, the measured irradiance $I(\phi_p, \phi_a)$ contains information on only three quantities, m_{11}, m_{22}, and m_{23} of the Mueller matrix $\tilde{M}$, and **only these three quantities can be deduced** from the linear polarization measurements. For a small field of view F, such that contributions to the measured irradiance $I(\phi_p, \phi_a)$ from terms of second order and higher in F are neglected, m_{11}, m_{22}, and m_{23} are proportional to $S_{11}(\pi)$, $S_{22}(\pi) - S_{33}(\pi)$, and $S_{23}(\pi) + S_{32}(\pi)$ for backscattering and are proportional to $S_{11}(0)$, $S_{22}(0) + S_{33}(0)$, and $S_{23}(0) - S_{32}(0)$ for forward scattering.

However, by combining three azimuthally integrated measurements (i.e., the commonly made lidar measurements) and eight azimuthally dependent measurements made through a spatial filter of angular half-width $\Delta\phi$ placed in the focal plane at azimuthal angle ϕ (measured in the xy plane counterclockwise from the x-axis) in front of the detector such that only scattered radiance within $\phi \pm \Delta\phi$ will strike the detector, and scattered radiance at any other azimuthal angle is blocked by the spatial filter, all nine Mueller matrix elements ($S_{11}(\pi)$, $S_{12}(\pi)$, $S_{13}(\pi)$, $S_{21}(\pi)$, $S_{22}(\pi)$, $S_{23}(\pi)$, $S_{31}(\pi)$, $S_{32}(\pi)$, and $S_{33}(\pi)$) which affect linear polarized radiation, may be deduced from the 11 polarized backscattering measurements.

We combine a set of 11 measurements to produce 9 equations (noted as y_1 to y_9) from which the 9 Mueller matrix elements are derived as follows:

(1) Removing the spatial we make three azimuthally integrated measurements $I(\phi_p = 0, \phi_a = \pi/2)$, $I(\phi_p = 0, \phi_a = 0)$ and $I(\phi_p = \pi/4, \phi_a = 0)$ with the detector full field of view F. From y_1,

$$y_1 = [I(\phi_p = 0, \phi_a = \pi/2) + I(\phi_p = 0, \phi_a = 0)]/F = S_{11} t_\parallel{}^p (t_\parallel{}^a + t_\perp{}^a)/2$$

S_{11} is deduced. From y_2,

$$y_2 = [I(\phi_p = 0, \phi_a = \pi/2) - I(\phi_p = 0, \phi_a = 0)]/F = -(S_{22} - S_{33}) t_\parallel{}^p (t_\parallel{}^a - t_\perp{}^a)/4$$

the difference $(S_{22} - S_{33})$ is deduced. From y_3,

$$y_3 = I(\phi_p = \pi/4, \phi_a = 0)/F$$

$$= (S_{23} + S_{32})(t_\parallel{}^p - t_\perp{}^p)(t_\parallel{}^a - t_\perp{}^a)/16 + (t_\parallel{}^p + t_\perp{}^p) y_1 /(4 t_\parallel{}^p) - y_2 \sqrt{\frac{t_\perp{}^p}{4 t_\parallel{}^p}}$$

the sum $(S_{23} + S_{32})$ is deduced.

(2) Placing the spatial filter at an angle $\phi = 0$ (i.e., along the x-axis) in front of the detector we make four measurements with the field of view $F_{\Delta\phi}$ through the spatial filter: $I(\phi = 0, \phi_p = 0, \phi_a = \pi/4, \Delta\phi)$, $I(\phi = 0, \phi_p = 0, \phi_a = -\pi/4, \Delta\phi)$, $I(\phi = 0, \phi_p = \pi/4, \phi_a = \pi/4, \Delta\phi)$ and $I(\phi = 0, \phi_p = -\pi/4, \phi_a = -\pi/4, \Delta\phi)$. Then we rotate the spatial filter to an angle $\phi = \pi/8$ and repeat the previous four measurements: $I(\phi = \pi/8, \phi_p = 0, \phi_a = \pi/4, \Delta\phi)$, $I(\phi = \pi/8, \phi_p = 0, \phi_a = -\pi/4, \Delta\phi)$, $I(\phi = \pi/8, \phi_p = \pi/4, \phi_a = \pi/4, \Delta\phi)$ and $I(\phi = \pi/8, \phi_p = -\pi/4, \phi_a = -\pi/4, \Delta\phi)$.

From y_4,

$$y_4 = [I(0,0,\pi/4,\Delta\phi) + I(0,0,-\pi/4,\Delta\phi)]/F_{\Delta\phi}$$

$$= t_{\parallel}^{\,p}(t_{\parallel}^{\,a} + t_{\perp}^{\,a})[2\Delta\phi S_{11} - S_{12}\sin(2\Delta\phi)]/(2\pi)$$

and knowing S_{11} from y_1, S_{12} is deduced.

From y_5,

$$y_5 = [I(\pi/8,0,\pi/4,\Delta\phi) + I(\pi/8,0,-\pi/4,\Delta\phi)]/F_{\Delta\phi}$$

$$= t_{\parallel}^{\,p}(t_{\parallel}^{\,a} + t_{\perp}^{\,a})[4\Delta\phi S_{11} - 2^{1/2}(S_{12} + S_{13})\sin(2\Delta\phi)]/(4\pi)$$

and knowing S_{11} from y_1 and S_{12} from y_4, S_{13} is deduced. To deduce the matrix elements S_{22} and S_{33}, we solve simultaneously Eq. y_2 together with Eq. y_6 for the two unknowns S_{22} and S_{33}. Eq. y_6 is given by

$$y_6 = [I(0,-\pi/4,-\pi/4,\Delta\phi) + I(0,\pi/4,\pi/4,\Delta\phi)]/F_{\Delta\phi}$$

$$= (t_{\parallel}^{\,a} + t_{\perp}^{\,a})[\Delta\phi S_{11}(t_{\parallel}^{\,p} + t_{\perp}^{\,p}) - S_{12}(t_{\parallel}^{\,p}t_{\perp}^{\,p})^{1/2}\sin(2\Delta\phi)]/(2\pi)$$

$$+ (t_{\parallel}^{\,a} - t_{\perp}^{\,a})(t_{\parallel}^{\,p} - t_{\perp}^{\,p})[S_{22}(\sin(4\Delta\phi) - 4\Delta\phi) + S_{33}(\sin(4\Delta\phi) + 4\Delta\phi)]/(16\pi)$$

where S_{11} and S_{12} are already known. The matrix elements S_{23} and S_{32} are obtained by solving simultaneously Eq. y_3 together with Eq. y_7,

$$y_7 = [I(\pi/8,-\pi/4,-\pi/4,\Delta\phi) + I(\pi/8,\pi/4,\pi/4,\Delta\phi)]/F_{\Delta\phi}$$

$$= (t_{\parallel}^{\,a} + t_{\perp}^{\,a})[\Delta\phi S_{11}(t_{\parallel}^{\,p} + t_{\perp}^{\,p}) - (S_{12} + S_{13})2^{-1/2}(t_{\parallel}^{\,p}t_{\perp}^{\,p})^{1/2}\sin(2\Delta\phi)]/(2\pi)$$

$$+ (t_{\parallel}^{\,a} - t_{\perp}^{\,a})(t_{\parallel}^{\,p} - t_{\perp}^{\,p})[\sin(4\Delta\phi)(S_{23} - S_{32}) - 4\Delta\phi(S_{22} - S_{33})]/(16\pi)$$

where S_{11}, S_{12}, S_{13}, S_{22} and S_{33} are already known. From y_8,

$$y_8 = [I(0,0,\pi/4,\Delta\phi) - I(0,0,-\pi/4,\Delta\phi)]/F_{\Delta\phi}$$

$$= t_{\parallel}^{\,p}(t_{\parallel}^{\,a} - t_{\perp}^{\,a})[4\Delta\phi(S_{23} + S_{32}) - 4S_{31}\sin(2\Delta\phi) - (S_{23} - S_{32})\sin(4\Delta\phi)]/(8\pi)$$

we obtain S_{31}, where S_{23} and S_{32} are known. The remaining Mueller matrix element S_{21} is deduced from y_9,

$$y_9 = [I(\pi/8,0,\pi/4,\Delta\phi) - I(\pi/8,0,-\pi/4,\Delta\phi)]/F_{\Delta\phi}$$

$$= t_{\parallel}^{\,p}(t_{\parallel}^{\,a} - t_{\perp}^{\,a})[4\Delta\phi(S_{23} + S_{32}) - 2^{3/2}(S_{21} + S_{31})\sin(2\Delta\phi) + (S_{22} + S_{33})\sin(4\Delta\phi)]/(8\pi)$$

where S_{23}, S_{32}, S_{31}, S_{22}, and S_{33} are already known.

For randomly oriented aerosols characterized by the Mueller matrix

$$\tilde{S}(\theta) = \begin{bmatrix} S_{11}(\theta) & S_{12}(\theta) & 0 & 0 \\ S_{12}(\theta) & S_{22}(\theta) & 0 & 0 \\ 0 & 0 & S_{33}(\theta) & S_{34}(\theta) \\ 0 & 0 & -S_{34}(\theta) & S_{44}(\theta) \end{bmatrix}$$

$S_{11}(\pi)$, $S_{12}(\pi)$, $S_{22}(\pi)$, and $S_{33}(\pi)$ can be deduced from six measurements at backscattering angle: two azimuthally integrated measurements $I(\phi_p = 0, \phi_a = \pi/2)$ and $I(\phi_p = 0, \phi_a = 0)$ with the detector full field of view F and four azimuthally dependent measurements through a spatial filter with the field of view $F_{\Delta\phi}$ (at an angle ϕ) through the spatial filter: $I(\phi = 0, \phi_p = 0, \phi_a = \pi/4, \Delta\phi)$, $I(\phi = 0, \phi_p = 0, \phi_a = -\pi/4, \Delta\phi)$, $I(\phi = 0, \phi_p = \pi/4, \phi_a = \pi/4, \Delta\phi)$.

It should be noted that this set of measurements which can be implemented for a linearly polarized laser which is polarized along the y-axis is not a unique set and other sets of measurements can be used to derive the nine Mueller matrix elements. The choice between the possible measurements should be made based on; the expected signal-to-noise ratio in the measurements, the polarization of the laser source (e.g. for some lasers it is possible to rotate the incidence polarization and thus the laser incidence can be polarized along the x-axis as well as along the y-axis), the extinction ratio $t_{\perp}/t_{\parallel}$ of the polarizer and analyzer, and the effect of error propagation in the computation, especially when the deduced Mueller matrix elements are a result of subtraction of two large numbers.

Azimuthally dependent polarized backscattering measurements were previously (1985) demonstrated by Pal and Carswell[1] , using a pie-slice slit in the focal plane of the detector, where the co-polarized and cross-polarized backscattering from a cumulus cloud (as well as from a water cloud that was generated in the laboratory) were measured as a function of azimuth. Their lidar system employed three detectors fitted with polarizing optics and spatial filters were mounted on a slide so that different spatial filters were readily interchanged by moving the slide back and forth in front of each detector. In their paper, Pal and Carswell note that "the complex structure of atmospheric clouds and the large variation of their properties in space and time would complicate any application of this technique" due to the need of simultaneous polarization measurements. In a recent (1997) paper, Roy and Bissonnette[2] showed lidar backscattering measurements from clouds measured with nine fields of view within a period of 0.5 s , Roy and Bissonnette lidar system operated at 100 Hz and a dynamically controlled iris was used to define the field of view. Their measurements showed that "for most of the cloud events observed, the correlation of the time-dependent field of view lidar measurements was good enough over a period of 0.5s to allow lidar inversion of the data". Thus, the theory for azimuthal polarized backscattering measurements presented in this paper may be applied for a laboratory setup for which the temporal variations in scattering medium can be controlled, and the theory may also be implemented for atmospheric cloud measurements if the set of the proposed eleven measurements can be taken within 0.5 s.

A complete discussion and derivations of the Mueller matrices will appear in a future publication[3].

Acknowledgments

The author thanks Piero Bruscaglioni of the University of Florence for sharing his notes on depolarization during the 8th International Workshop on Multiple Scattering Lidar/Light Experiments (MUSCLE8). This work was supported by the U.S Army Edgewood Research, Development and Engineering Center, Aberdeen Proving Ground, Maryland, under grant DAAAM01-94-C-0079.

References

1. S. R. Pal and A. I. Carswell, "Polarization anisotropy in lidar multiple scattering from atmospheric clouds," Appl. Opt. **24**, 3464-3471 (1985).

2. G. Roy and L. R. Bissonnette, "Non-simultaneous measurements of multiple-field-of-view lidar returns in clouds: Time correlation length" in Advances in Atmospheric Remote Sensing with Lidar, A. Ansmann, R. Neuber, P. Rairoux and U. Wandinger, Eds, (Springer-Verlag, Berlin, 1997), pp 99-102 (1997).

3. A. Ben-David "Mueller matrices and derived information from linear polarization measurements with a lidar: Theory," to be published in Appl. Opt. (1998).

Lidar Observations at the Manila Observatory During the 1997 Indonesian Forest Fire

[1]Lorenzo de la Fuente, [2]Jaime Bucoy, [3]John Holdsworth and [3]Minella Alarcon

[1]Manila Observatory, Quezon City, Philippines
[2]Philippine Atmospheric, Geophysical and Astronomical Services Administration, Quezon City, Philippines
[3]Ateneo de Manila University, Quezon City, Philippines

1. Introduction

The impact of the regional haze generated by Indonesian forest fires in the fall of 1997 has been widespread and significant. Actual costs to the Philippines appear to be minimal, but anxiety about the effects has been disproportionately large. Monitoring the temporal and spatial distribution of the haze can provide information for contingency planning, and may provide scientific insights as well.

2. The lidar system and sample observations

The lidar site is located at 14.64 N 121.07 E within the Manila Observatory (MO). A Q-switched Nd-YAG laser transmits an expanded, collimated and linearly-polarized 532 nanometer beam at 20 hertz. The backscatter is collected by a 28 centimeter diameter Schmidt-Cassegraine telescope in a biaxial vertical configuration, and directed through a collimating lens and a bandpass filter. From there the signal goes through a beamsplitter where parallel and orthogonal beam polarization components are directed to separate photomultiplier tubes (PMT). The analog voltage output from the two PMTs are digitized and averaged by a storage oscilloscope and saved using a microcomputer. Details of earlier configurations may be found in Alarcon et al. (1996). A sample of lidar-derived

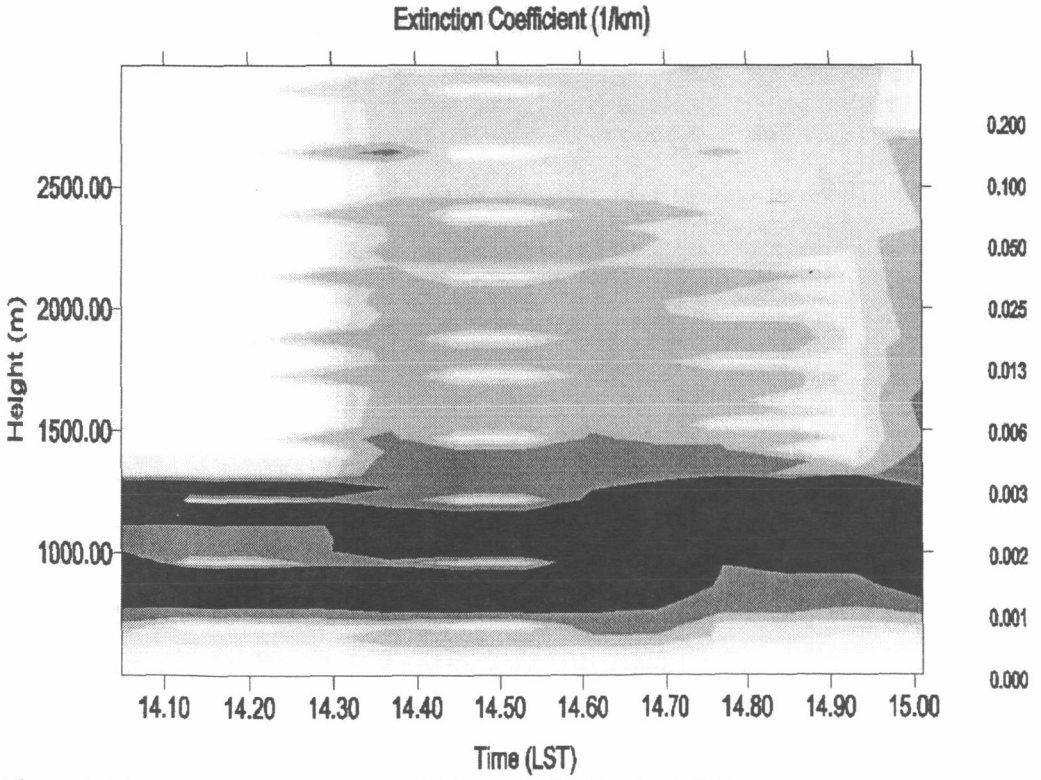


Figure 1. Time series of extinction coefficients for 02 October 1997

[1] Corresponding author address:
Lorenzo S. F. de la Fuente
Manila Observatory, Quezon City, Philippines 1108
Email: dfuente@admu.edu.ph

measurements of extinction coefficients are shown in Figure 1, from observations made between 28 September to 02 October 1997. The lidar return maxima are believed to be from scattering layers other than water clouds, since no visible water clouds relevant to the lidar signals were observed during the measurement period. In the calculations the system constant and backscatter to extinction ratio are calibrated using equations from Russell et al. (1979) and Fernald et al. (1972). Extinction coefficients for the overlap and extreme ranges are calculated following the method presented by Hughes et al. (1985), while the remaining coefficients are calculated using the stable equation developed by Klett (1981). A power law equation is used to calculate backscatter coefficients from extinction coefficients with the exponent set to unity.

3. Satellite and visual observations

GMS-5 satellite images from 30 September to 02 October 1997 show what appears to be a haze plume extending from Borneo to north of Palawan, visible in Figure 2. Features in the late September images correspond with

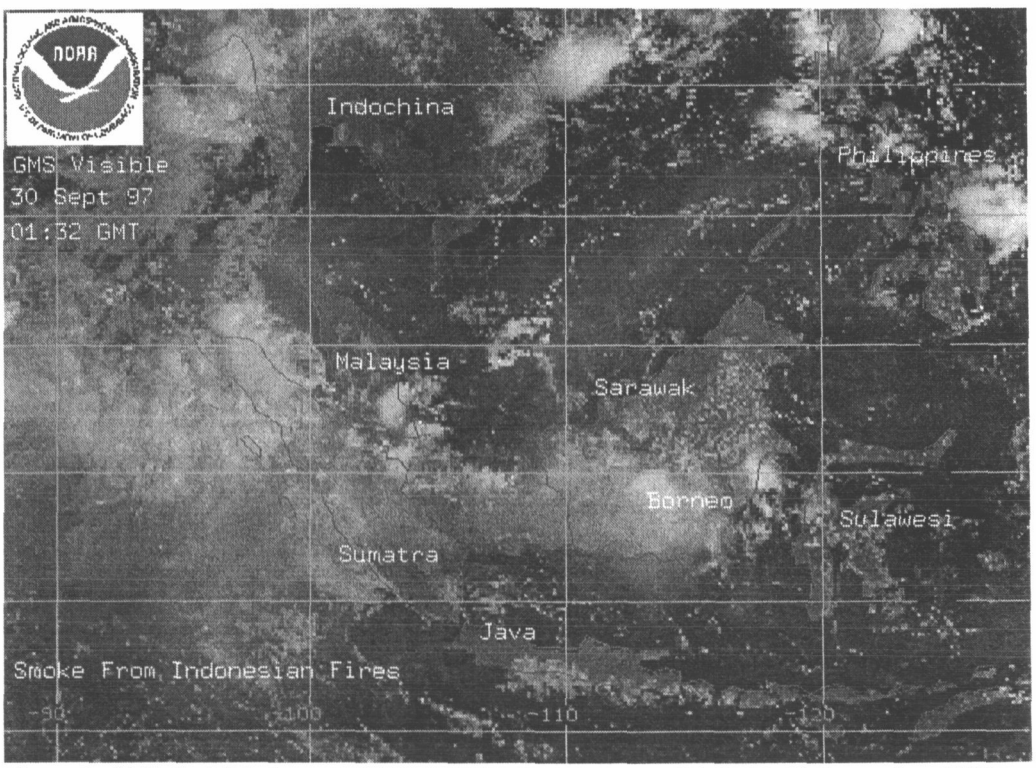


Figure 2. GMS-5 visible image with supposed haze plume at 0630 UTC, 30 September 1997

simultaneous AVHRR imagery showing the spatial boundaries of the haze plume, which were then monitored until early October. Unfortunately, the plume appeared to become less distinct in succeeding GMS-5 images as it approached Manila Bay by 02 October 1997, after which it became undistinguishable from the background. Visual observations from the Philippine Atmospheric, Geophysical and Astronomical Services Administration indicate that haze was observed over the Ninoy Aquino International Airport by 28 September 1997 when horizontal visibilities degraded to levels consistent with haze. This location was about 20 kilometers southeast and upstream of the lidar site, so there was a reasonable probability that the haze would also be observed over the lidar site. Photographs taken at the MO on 30 September 1997 also show that local visibility also decreased, although reduced visibilities unrelated to the regional haze were sometimes observed.

4. Discussion

On average, most aerosol particles generated by forest fires are larger than 5 micrometers (Wallace and Hobbs, 1977). These are within the detection limits of a 532 nanometer Mie-scattering lidar system, which can measure parameters such as aerosol plume altitude and thickness. Signal depolarization measurements provide information about scattering particle shape, which may in some cases indicate aerosol particle composition as discussed by Murayama et al. (1996). Figure 3 shows a sample profile of range-corrected power and linear depolarization ratio,

where the laser-telescope overlap range is about 500 meters. A lower plume appears to be centered around 1000 meters and an upper plume around 2000 meters based on the backscattered power profile, but the depolarization profile displays contrasting behavior. Outside the plumes where fewer depolarizing particles are expected the high computed values approach those characteristic of crystals or multiple scattering, while within the plumes where more depolarizing particles are expected the low computed values approach those of spherical droplets. These represent an unusual set of depolarization observations for MO lidar data, and given the uncertainty in identifying them as forest fire plume measurements no explanation for the discrepancies is offered at this time. Research is currently underway to obtain the information necessary to exclude the effects of aerosol scatterers from local sources, and establish positive identification of the forest fire haze plume.

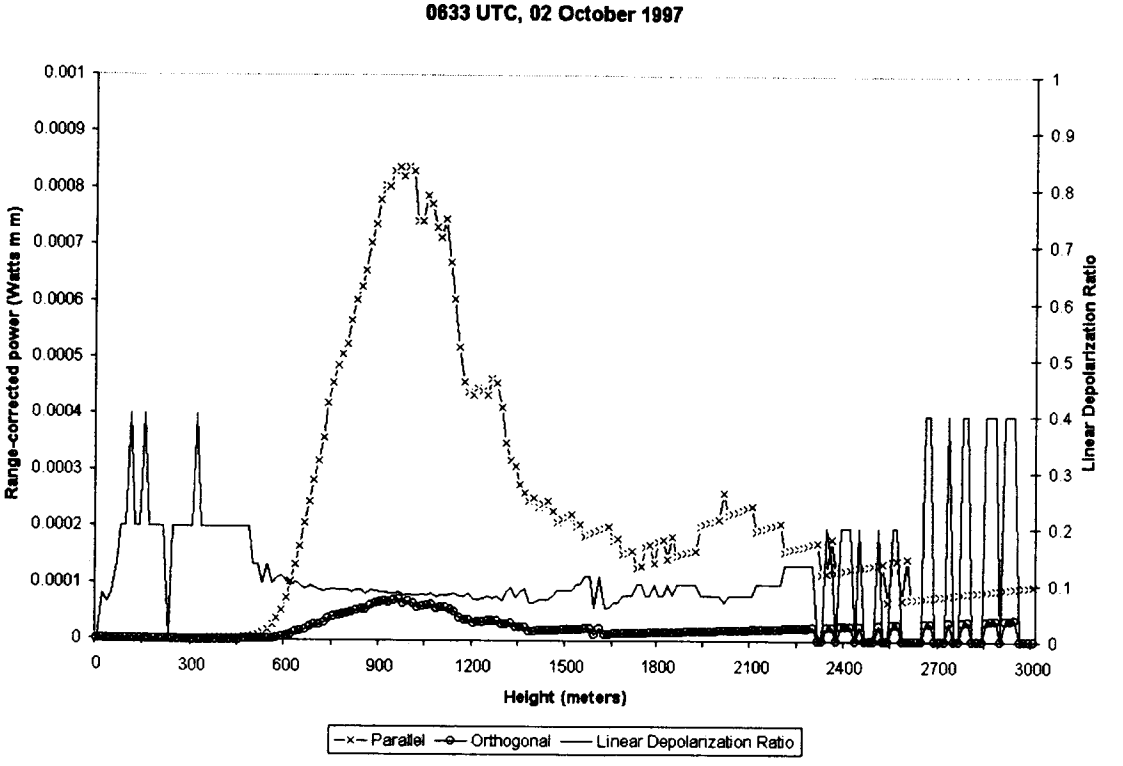


Figure 3. Comparison of range-corrected power with linear depolarization ratio

6. References

Alarcon, M., S. Dorado, J. Holdsworth, B. Sychingiok, and D. McNamara. 1996: Mie lidar measurements in Metro Manila (14.64 N, 121.07 E). 18th International Laser Radar Conference Abstract Book. Berlin, International Coordination Group on Laser Atmospheric Studies, 236 pp.

Fernald, F., B. Herman, and J. Reagan. 1972: Determination of Aerosol Height Distribution by Lidar. J. of Appl. Meteor. 11, 482-489

Hughes, H., J. Ferguson and D. Stephens. 1985: Sensitivity of a Lidar Inversion Algorithm to Parameters relating Atmospheric Backscatter and Extinction. Appl. Opt. 24, 1609-1613

Klett, J. 1981: Stable Analytical Inversion Solution for Processing Lidar Returns. Appl. Opt. 20, 211-220

Murayama, T., M. Furushima, A. Oda, N. Iwasaka and K. Kai. 1996: Depolarization Ratio Measurements in the Atmospheric Boundary Layer by Lidar in Tokyo. J. of the Meteor. Soc. of Japan. 74, 571-577

Russell, P., I. Swissler and M. McCormick. 1979: Methodology for Error Analysis and Simulation of Lidar Aerosol Measurements. Appl. Opt. 18, 3738-379

Wallace, J. and P. Hobbs. 1977: Atmospheric Science: An Introductory Survey. Academic Press. 467 pp.

Mie Backscatter Intensity and Depolarization Measurements of Tropical Clouds, 14.64 N, 121.07 E in the Philippines

Susana V. Dorado
Notre Dame of Marbel University, Koronadal, South Cotabato, Philippines
Phone: (063)-083-553-5724, E-mail: preledor@mozcom.com

Nofel C. Lagrosas, Emmanuel Agcopra and Jordan Cañete
Physics Department, Xavier University, Cagayan de Oro City, Philippines
E-mail: nofel@siki.eng.xu.edu.ph

Minella C. Alarcon
Physics Department, Ateneo de Manila University, Quezon City Philippines
E-mail: alarcon@pusit.admu.edu.ph

1. Introduction

The amount of solar radiation that reaches the earth's surface depends on the amount of coverage, type of clouds, and as well as their physical and optical properties. In particular, the optical depth distribution of clouds, which is derivable from extinction coefficient, is found useful in modeling transport of radiation in the atmosphere (Pal et. al.,1992). Lidar measurements with excellent spatial and temporal resolution over extended time periods and in different geographical regions prove to provide an instantaneous picture of the optical properties and behavior of clouds. Moreover, it is well acknowledged that there is paucity of ground based lidar data at low-latitude. Hence, extensive efforts from the international scientific community are being directed toward obtaining ground-based data from tropical sites.

A Mie lidar system was built for the first time at the Manila Observatory, (14.64° N, 121.07° E), Philippines with an aim of monitoring urban pollution and characterizing cloud properties in this part of the globe (Alarcon et.al.,1996). The basic system was calculated to reach up to 20 km under clear air conditions. In this paper, initial results of extinction coefficient and depolarization ratio calculations on tropical clouds are reported.

2. Intensity Measurements

A. Experimental Details

The basic lidar system used in this study is fixed, vertically pointing and biaxial in configuration and is composed of a laser transmitter, receiving telescope and signal processing system. The Nd:YAG laser operating at 20 Hz provides a 532 nm linearly polarized pulse output that is expanded, collimated and directed vertically upward by using a high-energy laser reflector. The backscatter is collected and focused by a telescope onto a photomultiplier tube (PMT) through a collimating lens and bandpass filter. The analog voltage output of the PMT is digitized and averaged by the digitizing

storage oscilloscope and stored to a computer.

Firing on a regular basis started in mid-August, once a week, 2h in the early morning and 2h in the early evening. This schedule coincided with the 0000 and 1200 UTC balloon soundings (0800 and 2000 local time) of the local weather bureau at a site 486 km from the lidar station.

B. Results

Lidar backscatter measurements made on a regular basis over a nine-month period, showed frequent occurences below 2.5 km of low-lying cloud layers which had relatively high backscatter intensity, on the wet months of August to November. The transition from wet to dry season was notable with the decrease in the frequency of cloud occurrence in the month of December and with cloud layers becoming thinner toward the end of January. In February, the air started to clear and gradually warmed up leading to the hot months of March and April. To date, signals from maximum altitudes of 15 km and 12 km were obtained during nighttime and daytime respectively.

The solution for single scattering lidar equation proposed by Klett (Klett, 1981) was used to derive the particulate extinction coefficient profiles, $\alpha(r)$. The second point at the end of the highest cloud layer was chosen as the calibration range where scattering was assumed to be mostly due to air molecules. A modeled molecular signal derived from the local weather bureau radiosonde data was used to calibrate the lidar data (Young, 1995). Most extinction coefficient profiles showed values ranging from 10^{-2} to 10^{-1} m^{-1}. An example in Figure 1 shows a maximum extinction coefficient values of 0.3 m^{-1} at an earlier time and about 0.34 m^{-1} at a later time of a persistent cloud layer with base altitude at about 8,600m and peak at about 8,800 m.

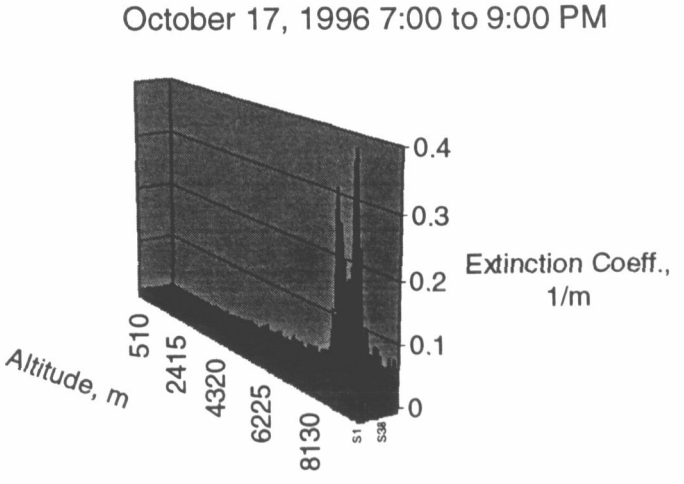


Figure 1. Time series of extinction coefficient profiles, sampled every 2 minutes over a period of 2 hours.

3. Polarization measurements

Polarization measurements started in mid-March 1997. The backscatter from the vertically polarized 532 nm laser pulse was collected by the telescope with 0.5 mrad field-of-view, transmitted through the iris, collimating lens, bandpass filter and polarizing beamsplitter which separated the signal into parallel and perpendicular components. The data acquired were hardware averaged over an integration time of 1minute corresponding to 1200 shots. The firing schedule was also changed to two hours a day (I h in the morning and 1 h in the afternoon), twice a week.

From these measurements, the depolarization ratio, δ, was calculated for a selected number of profiles containing cloud layers at different altitudes. The scatterplot of these values in Figure 2 reveals high values of δ (0.2 to 0.6) for cloud layers below 2.5 km. These low-lying clouds may be a mixture of liquid water droplets and irregularly shaped particles such as dust. For most clouds above 2.5 km, the values of δ obtained were $\delta < 0.1$ indicating pure water clouds (Derr, 1976). Moreover, the cloud layers at 3 to 4 km have values of $\delta > 0.1$ which may indicate smaller liquid water droplets present in the cloud (Pal, 1973). Radiosonde measurements 486 km from the lidar station report temperatures around -15 °C at altitudes of 7 km., and for clouds at the same height our calculated values of $0.2 > \delta > 0.05$ may indicate the presence of supercooled water droplets. Furthermore, it is generally observed that for low altitude clouds, δ increases with penetration depth indicating a decrease in droplet size with height.

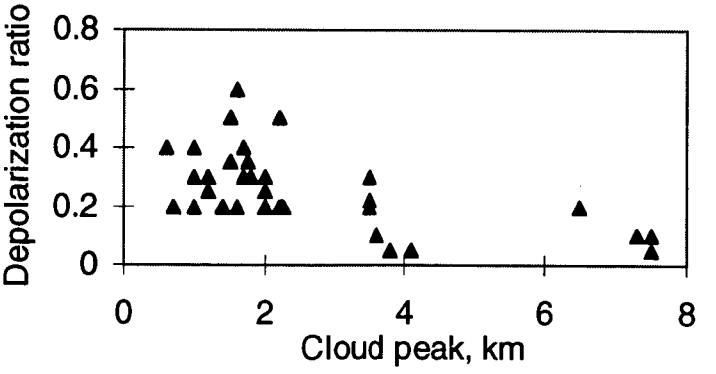


Figure 2. Scatterplot of depolarization ratio,δ, values at cloud peak for selected profiles from March to May, 1997.

4. Summary

For the first time, lidar returns are obtained in this part of the world. Information on cloud base location with range resolution of better than 3.5 m and the spatial extent of cloud layers is useful to our local weather bureau in verifying their independent visual

observations of clouds. Backscatter intensity measurements for nine months in our site reveal frequent occurrences of clouds from 1 km to 2.5 km. with marked differences in their optical properties with seasons. Extinction coefficient profiles showed values ranging from 10^{-2} to 10^{-1} m^{-1}. Moreover, depolarization ratio values ranging from 0.05 to 0.6 are obtained with generally higher values for low lying cumulus clouds than those observed for clouds at higher altitudes. A study conducted by our government showed that the bulk of ground level suspended particulates is dust (DENR, 1992). Finally, the initial results presented here cannot be taken as being widely representative of general cloud behavior. Rather, these initial results demonstrate the capability of the present lidar system in providing ground-based data on tropical clouds

Furthermore, the Philippine lidar group is determined to continue on with atmospheric studies. Future works will include the following areas: (a) multiwavelength system for temperature and particle size distribution measurements and, to explore the wavelength dependence of the extinction coefficient; (b) mixing layer and boundary layer measurements; and (c) multiple scattering from clouds.

5. Acknowledgments

The authors acknowledge the support and cooperation of the Philippine Department of Science and Technology, Manila Observatory, Ateneo de Manila University and the Philippine Atmospheric, Geophysical and Astronomical Services Administration.

References

Alarcon, M., S. Dorado, J. Holdsworth, B. Sychingiok, and D. McNamara.(1996). Mie Lidar Measurements in Metro Manila (14.64 N, 121.07 E). 18th International Laser Radar Conference Abstract Book, R. Neuber and P. Rairoux, eds., 167.

Department of Environment and Natural Resources. (1992). *1992 Report on Minima, Maxima, Average Concerntrations of TSP and SO2 in Air Monitoring Stations in MetroManila.*

Derr, V. E., N. L. Abshire, R. E Cupp, and G. T McNice. (1976). Depolarization of lidar returns from virga and source cloud. *J. Appl. Meteor.* **15**, 1200 -1203.

Klett, J. (1981). Stable analytical inversion solution for processing lidar returns. *Appl. Opt.* **20**, 211 - 220.

Pal, S. R. and A. I. Carswell. (1973). Polarization properties of lidar backscattering from clouds. *Appl. Opt.* **12**, 1530 - 1535.

Pal, S. R., W. Steinbrecht, and A. I. Carswell. (1992). Automated method for lidar determination of cloud-base height and vertical extent. *Appl. Opt.* **31**, 1488 - 1494.

Young, S. (1995). Analysis of lidarbackscatter profiles in optically thin clouds. *Appl. Opt.* **34**, 7019 -7031.

CART and GSFC Raman Lidar Measurements of Atmospheric Aerosol Backscattering and Extinction Profiles for EOS Validation and ARM Radiation Studies

R.A. Ferrare[1], D.D. Turner[2], S.H. Melfi[3], D.N. Whiteman[4], G. Schwemmer[5], K. D. Evans[6], J.E.M. Goldsmith[7], T. Tooman[8]

[1]NASA Langley Research Center, MS-401A, Hampton, Virginia 23681, 757-864-9443, 757-864-7790 (fax), r.ferrare@larc.nasa.gov

[2]Pacific Northwest National Laboratory, P.O. Box 999, MSIN K7-28, Richland, Washington 99352, 509-375-2590; 509-375-3641 (fax), dave.turner@pnl.gov

[3]University of Maryland Baltimore County, Baltimore, Maryland, 21228, 410-455-2186, 410-455-1072 (fax), melfi@umbc.edu

[4]NASA Goddard Space Flight Center, Code 924, Greenbelt, Maryland, 20771, 301-286-3115, 301-286-1761 (fax), David.N.Whiteman.1@gsfc.nasa.gov

[5] NASA Goddard Space Flight Center, Code 912, Greenbelt, Maryland, 20771, 301-286-5768, 301-286-1762 (fax), geary@virl.gsfc.nasa.gov

[6]University of Maryland Baltimore County, Code 912, NASA/GSFC, Greenbelt, Maryland, 20771, 301-286-9526, 301-286-1762 (fax), evans@agnes.gsfc.nasa.gov

[7]Sandia National Laboratories, PO Box 969, MS 9409, Livermore, California, 94551 510-294-2432, 510-294-3870 (fax), jgold@ca.sandia.gov

[8]Sandia National Laboratories, PO Box 969, MS 9056, Livermore, California, 94551 510-294-2752; 510-294-1559 (fax), tooman@ca.sandia.gov

Introduction

The aerosol retrieval algorithms used by the Moderate-Resolution Imaging Spectroradiometer (MODIS) and Multi-Angle Imaging SpectroRadiometer (MISR) sensors on the Earth Observing Satellite (EOS) AM-1 platform operate by comparing measured radiances with tabulated radiances that have been computed for specific aerosol models. These aerosol models are based almost entirely on surface and/or column averaged measurements and so may not accurately represent the ambient aerosol properties. Therefore, to validate these EOS algorithms and to determine the effects of aerosols on the clear-sky radiative flux, we have begun to evaluate the vertical variability of ambient aerosol properties using the aerosol backscattering and extinction profiles measured by the Cloud and Radiation Testbed (CART) and NASA Goddard Space Flight Center (GSFC) Raman Lidars. Using the procedures developed for the GSFC Scanning Raman Lidar (SRL), we have developed and have begun to implement algorithms for the CART Raman Lidar to routinely provide profiles of aerosol extinction and backscattering during both nighttime and daytime operations.

Aerosol backscattering and extinction profiles are computed for both lidar systems using data acquired during the 1996 and 1997 Water Vapor Intensive Operating Periods (IOPs). By integrating these aerosol extinction profiles, we derive measurements of aerosol optical thickness and compare these with coincident sun photometer measurements. We also use these measurements to measure the aerosol extinction/backscatter ratio S_a (i.e. "lidar ratio"). Furthermore, we use the simultaneous water vapor measurements acquired by these Raman lidars to investigate the effects of water vapor on aerosol optical properties.

Instruments

The CART Raman Lidar is an operational, autonomous system designed for unattended, continuous profiling of water vapor, aerosols, and clouds at the Department of Energy Southern Great Plains (SGP) site [1]. This system uses a tripled Nd:YAG laser, operating at 30 Hz with 400 millijoule pulses, to transmit light at 355 nm. A 61-cm diameter telescope collects the light backscattered by molecules and aerosols at the laser wavelength and the Raman scattered light from water vapor (408 nm) and nitrogen (387 nm) molecules. These signals are detected by photomultiplier tubes and recorded using photon counting with a vertical resolution of 39 meters. A beam expander reduces the laser beam divergence to 0.1 mrad, thereby permitting the use of a narrow (0.3 mrad) as well as a wide (2 mrad) field of view. The narrow field of view, coupled with the use of narrowband (~0.3-0.4 nm bandpass) filters, reduces

the background skylight and, therefore, increases the maximum range of the aerosol and water vapor profiles measured during daytime operations.

The SRL operates in a similar manner but differs in that it is a mobile, trailer-based system designed for research conducted during intensive operation periods. Unlike the CART Raman lidar, which measures only vertical profiles, the SRL uses a steerable elliptical flat which provides full 180 degree scan capability within a single scan plane. This scan capability is used to increase the vertical resolution and precision of the data at lower altitudes as well as to facilitate comparisons with tower and/or surface-based instrumentation [2].

Both Raman lidar systems measure the profiles of aerosol scattering ratio, which is defined as the ratio of aerosol+molecular scattering to molecular scattering, by using the Raman nitrogen signal and the signal detected at the laser wavelength. Aerosol volume backscattering cross section profiles are then computed using the aerosol scattering ratio and molecular scattering cross section profiles derived from atmospheric density data measured by coincident and co-located radiosonde data. Aerosol extinction cross section profiles are computed from the derivative of the Raman nitrogen signal with respect to range [3]. The aerosol backscattering and extinction profiles derived in this manner are then used to measure profiles of the aerosol extinction/backscattering ratio S_a. Aerosol optical thicknesses are derived by integration of the aerosol extinction profiles with altitude.

Measurements

Direct measurements of aerosol extinction using the Raman nitrogen channel are limited to ranges where the laser beam is fully within the field of view of the telescope so that the overlap function is unity. For the CART Raman lidar, which acquires only vertical profiles, this occurs for altitudes above about 800 meters. In contrast, aerosol backscattering profiles, which are computed using the ratio of the Rayleigh/Mie and Raman nitrogen return signals, are computed for altitudes above about 60 meters [2]. Therefore, as a first approximation, profiles of aerosol extinction below 800 meters are computed by multiplying the aerosol backscattering profiles by the aerosol extinction/backscattering ratio derived for altitudes between 800-1000 meters. This assumes that the aerosol extinction/backscatter ratio is constant within the lowest 1 km.

Aerosol extinction profiles computed from the CART Raman lidar are compared with aerosol extinction directly measured by the SRL. By scanning, the SRL acquires data at low elevation angles and can, therefore, directly measure profiles of aerosol extinction using the Raman nitrogen channel for altitudes as low as 100 meters. Aerosol extinction/backscattering profiles measured using scan data acquired in April 1994 at the SGP site have shown that in several cases S_a is constant to within about 10-20% in the lowest kilometer [4]. Figure 1 shows an example of the aerosol backscattering and extinction profiles measured simultaneously by both lidar systems at 02:25 UT on September 23, 1996 during the 1996 Water Vapor IOP. The CART Raman lidar aerosol extinction profile was derived from the aerosol backscattering profile using S_a=62 sr. We are continuing to use the SRL aerosol data sets in assessing the aerosol extinction computed using the CART Raman lidar data.

During the 1997 Water Vapor IOP, the CART Raman lidar measured aerosol and water vapor profiles between September 25 through October 6. Aerosol extinction/backscattering ratios derived from these data for altitudes between 0.8-1.4 km varied

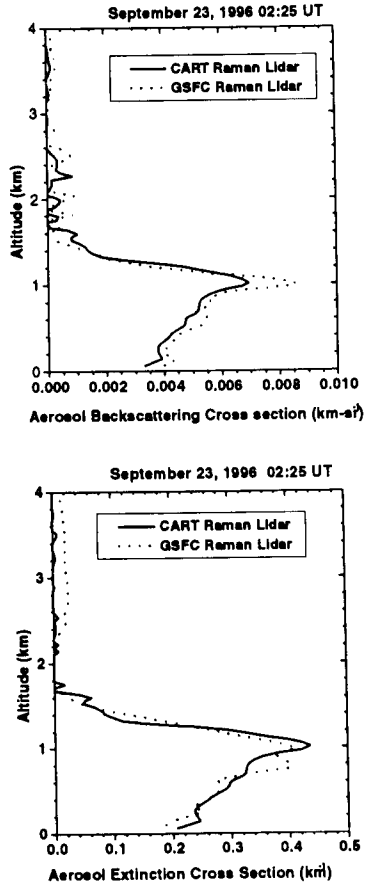


Figure 1. Aerosol backscattering (top) and extinction (bottom) profiles measured by CART and GSFC Raman Lidars at 02:25 UT on September 23, 1996.

between 45-75 sr, with an average value of 57 sr. These values are consistent with previous GSFC Raman lidar measurements [4] as well as the values reported by other investigators [5]. Preliminary investigations using the CART Raman lidar measurements have not revealed any significant relationships between S_a and either aerosol extinction or relative humidity.

The aerosol extinction profiles derived from the CART Raman Lidar data were integrated between 0 to 4 km to estimate the aerosol optical thickness. Figure 2 shows these values along with the aerosol optical thicknesses measured at 340 nm by a Cimel sun photometer located at the SGP site. The sun photometer measurements are restricted to cloud-free

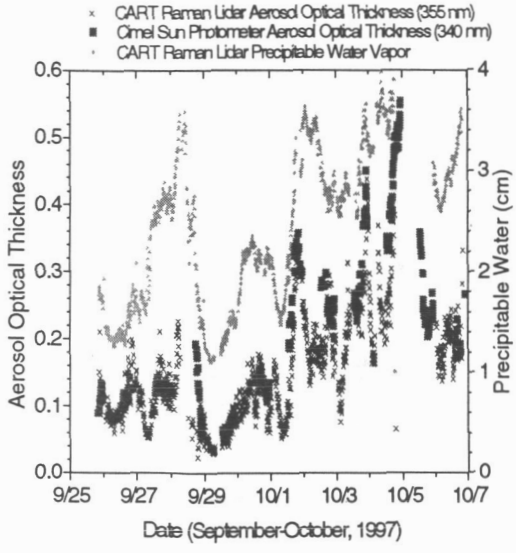


Figure 2. CART Raman Lidar and Cimel sun photometer aerosol optical thicknesses (left axis) and CART Raman Lidar precipitable water vapor (right axis) during the 1997 Water Vapor IOP.

daytime periods. The excellent agreement between the aerosol optical thickness measurements from the two instruments is also shown in figure 3. The sun photometer aerosol optical thicknesses at 355 nm were determined by interpolating between the sun photometer measurements at 340 nm and 437 nm. The results indicate that, for this period, aerosols above 4 km have a negligible contribution to the total aerosol optical thickness. Figure 2 also shows that the precipitable water vapor derived from the simultaneous CART Raman lidar water vapor measurements is highly correlated with aerosol optical thickness. This indicates: 1) aerosol and water vapor concentrations within various air masses were highly correlated over the SGP site during this experiment,

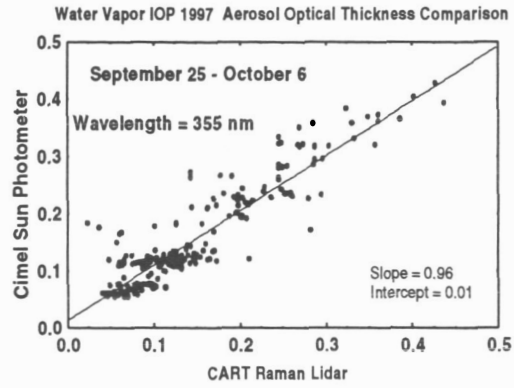


Figure 3. Correlation between CART Raman lidar and Cimel sun photometer aerosol optical thickness (355 nm) measurements during the 1997 Water Vapor IOP.

and 2) these aerosols tend to be hygroscopic so that the aerosol extinction increases with relative humidity.

The relationship between aerosol extinction and relative humidity over the SGP site on October 6, 1997 is shown in figure 4. Aerosol extinction profiles measured by the CART Raman lidar and relative humidity profiles derived from the CART Raman lidar water vapor mixing ratio profiles and radiosonde temperature profiles are shown. Temporal resolution is 10 minutes while the vertical resolution is 39 meters. An increase in aerosol extinction and relative humidity below about 0.3 km, which occurred shortly after sunset at 00 UT, is followed by a decrease in aerosol extinction and relative humidity after sunrise at 12:30 UT. The increase in aerosol extinction with relative humidity between 01:00-09:00 UT is plotted in figure 5. Since the water vapor mixing ratio was approximately constant in this region during this period, this increase in relative humidity is due to the decrease in temperature associated with radiational cooling. Under these conditions, the increase in aerosol extinction is due to the change in aerosol physical characteristics (i.e. size and composition) rather than variations in the aerosol number concentration associated with varying air mass characteristics.

Summary

CART Raman lidar data collected during the 1997 Water Vapor IOP were used to derive profiles of aerosol backscattering and extinction during both nighttime and daytime operations. While initial comparisons of aerosol extinction profiles measured by the CART Raman lidar and GSFC Scanning Raman lidar show good agreement, additional comparisons are required to more fully evaluate the

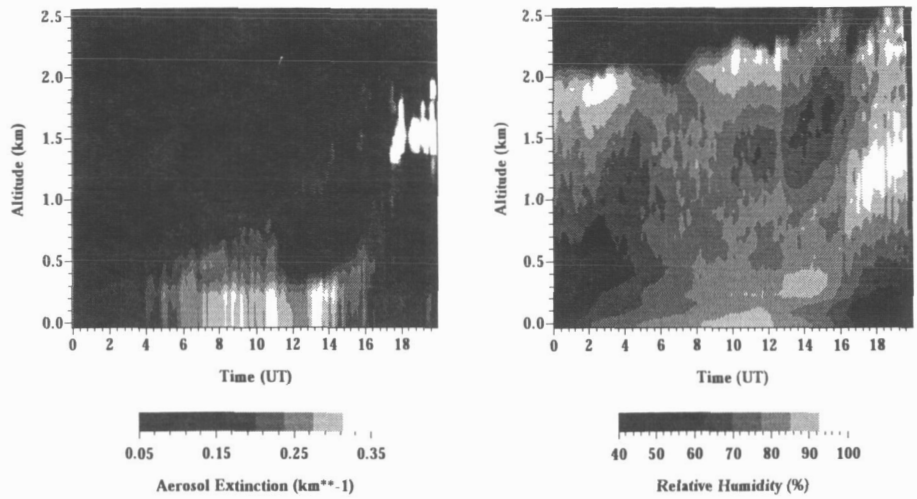


Figure 4. Aerosol extinction (left) and relative humidity (right) derived from CART Raman lidar measurements on October 6, 1997.

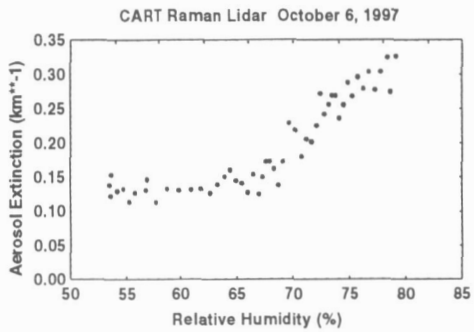


Figure 5. Aerosol extinction as a function of relative humidity derived for altitudes between 60-300 meters from CART Raman lidar measurements between 01:00-09:00 UT on October 6, 1997.

ability of the CART Raman lidar to measure aerosol extinction near the surface. Aerosol optical thicknesses derived from the aerosol extinction profiles measured by the CART Raman lidar in the daytime were shown to be in excellent agreement with those measured by a ground-based sun photometer. Aerosol extinction/backscatter ratios measured by the CART Raman lidar ranged between 45-75 sr, with an average value of 57 sr. The simultaneous aerosol and water vapor measurements were used to demonstrate how lidar data can be used to investigate the relationships between relative humidity and aerosol extinction and backscattering under ambient atmospheric conditions.

Acknowledgments

We wish to thank Brent Holben and Alex Smirnov (NASA/GSFC) for providing the cloud-screened Cimel sun photometer data.

References

1. Goldsmith, J.E.M., F.H. Blair, and S.E. Bisson, Implementation of a Turn-Key Raman Lidar for Profiling Atmospheric Water Vapor and Aerosols at the US Southern Great Plains Climate Study Site, Advances in Atmospheric Remote Sensing with Lidar, A. Ansmann, R. Neuber, P. Rairoux, and U. Wandinger, eds. Springer-Verlag, Berlin, (1997) 337-340.
2. Ferrare, R.A., S.H. Melfi, D.N. Whiteman, K.D. Evans, F.J. Schmidlin and D.O'C. Starr, A Comparison of Water Vapor Measurements made by Raman Lidar and Radiosondes, *J. Atmos. Ocean Tech.*, **12**, (1995) 1177-1195.
3. Ansmann, A., M. Riebesell, and C. Weitkamp, 1990: Measurement of atmospheric aerosol extinction profiles with a Raman lidar, *Optics Letters*, **15**, (1990) 746-748.
4. Ferrare, R.A., S.H. Melfi, D.N. Whiteman, K.D. Evans, R. Leifer, Y.J. Kaufman,: Raman Lidar Measurements of Aerosol Extinction and Backscattering - Part 1: Methods and Comparisons., submitted to *J. Geophys. Res.* (1997)
5. Takamura, T., Y. Sasano, and T. Hayasaka: Tropospheric aerosol optical properties derived from lidar, sun photometer, and optical particle counter measurements, *Appl. Opt.*, **33**, No. 30, (1994) 7132-7140.

THE GEOSCIENCE LASER ALTIMETER SYSTEM (GLAS)

James B. Abshire
James C. Smith
NASA - Goddard Space Flight Center
Laser Remote Sensing Branch, Code 924
Greenbelt MD 20771, USA
Phone: (301) 286-2611 Fax: (301) 286-0213

Bob E. Schutz
University of Texas at Austin
Center for Space Research, WRW 402
Austin, TX 78712, USA
(512) 471-4267

Abstract:
GLAS is a space-based lidar designed for NASA's Earth Science Enterprise's Icesat Mission. It is being designed to precisely measure the heights of the polar ice sheets, to determine the height profiles of the Earth's land topography, and to profile the vertical structure of clouds and aerosols on a global scale [1]. GLAS will fly on a small dedicated spacecraft in a polar orbit at 598 km altitude with an inclination of 94 degrees. The instrument is being developed to launch in July 2001 and to operate continuously at 40 Hz for a minimum of 3 years with a goal of 5 years.

Introduction:
Airborne and spaceborne lidar have demonstrated precise measurements of surface heights and atmospheric backscatter [2-4]. The GLAS instrument combines a 10 cm precision surface lidar with a dual wavelength cloud and aerosol lidar in a design for long-term continuous use in space.

The primary mission for GLAS is to measure the seasonal and annual changes in the heights of the ice sheets which cover Greenland and Antarctica. To do this, GLAS will measure the distance to the ice sheet from orbit at nadir with 1064 nm laser pulses. Each laser pulses results in a single range determination, and the single shot radial ranging accuracy is 10 cm for ice surfaces sloped < 3 degrees. Seasonal and annual fluctuations in regional ice sheet heights will be determined by comparing successive GLAS measurement sets. These should permit assessment of changes in the polar ice sheet topography on 3-6 month time scales. The planned series of 3 Icesat missions will monitor ice sheet heights over 15 years. The information gained from the Icesats will dramatically improve our knowledge of the short and long term changes of the Earth's major ice sheets and their possible contribution to the rise in global sea-levels.

GLAS will also determine the vertical distributions of clouds and aerosols below its flight path by measuring atmospheric backscatter profiles at both 1064 and 532 nm. The 1064 nm measurements will use an analog detector and profile of the height and vertical structure of thicker clouds. The measurements at 532 nm are more sensitive since they use photon counting detectors, and they will be used to measure the height distributions of very thin clouds and aerosol layers. With averaging these can be used to determine the height of the planetary boundary layer. The lidar measurements of the vertical aerosol distribution over a global scale will help improve understanding of aerosol-climate effects. The measurement performance of the altimeter and lidar have been estimated by using analysis and simulations. The mission, instrument and subsystem designs are briefly discussed in this paper.

Mission Overview:
GLAS is scheduled to be launched into a 598 km circular polar orbit in July 2001. The orbit and mission parameters are summarized in Table 1. The orbit's 94 degree inclination was selected to optimize the crossing ground track patterns over Greenland and Antarctica and to enable data comparison with other NASA Earth Science Enterprise instruments. The spacecraft has been selected as a commercial derivative. It will determine the orbit altitude, position and time from an on-board GPS receiver. The GLAS instrument utilizes the GPS receiver's orbit altitude for initial surface height estimates and the GPS 1 second time markers as a long term time standard. GLAS is being designed to operate continuously for 3 years with a goal of 5 years. NASA plans for two follow-on Icesat missions.

Table 1. GLAS Orbit & Measurements

Orbit altitude	598 km
Orbit inclination	94 degree
Orbit repeat tracks	1 km every 183 days
Ground track spacing	15 km at equator 2.5 km at 80 deg latitude
Post-Processed pointing knowledge	• 2 arcsec (all axes)
Position requirements: Radial orbit height Along-track	Post-processing: < 5 cm < 20 cm
Laser measurement direction	Nadir viewing (nominal)
Laser firing rate	40 pps

Measurement wavelengths: Surface & cloud tops Atmospheric aerosols	 1064 nm 532 nm
Spot diameter on surface	66 m (e-2 points)
Along-track laser spot separation	170 m (center to center)

Instrument Description:
The GLAS instrument specifications are summarized in Table 2. The instrument incorporates three diode-pumped Q-switched ND:YAG lasers, a 100 cm diameter Beryllium receiver telescope, a narrow (~25 pm) optical filter at 532 nm, Si APD detectors for 1064 and 532 nm, and a subsystem to measure the pointing angles of each laser firing to the arc-second level. The instrument components are mounted on an L-shaped optical bench, with one side of the L carrying the lasers and stellar reference system and the other side serving as the telescope interface and carrying the aft-optics and detector assemblies. In the present configuration, the instrument radiator is mounted in a separate plate which is parallel to the laser bench.

Table 2. GLAS Instrument Specifications

Laser Type	ND:YAG slab, 3 stage Q-switched, Diode pumped
Number of lasers	3 each, one operated at any time
Laser firing rate	40 pps
Laser pulse width	4-6 nsec
Laser Divergence angle	110 urad
Telescope diameter	100 cm
1064 nm detector	Si APD - analog (2 each)
532 nm detector	Si APD - Geiger (8 each)
Mass	300 kg
Power	300 W average
Instr. Duty cycle	100%
Data rate	~ 500 kbps (uncompressed)
Physical size	~ 110 x 140 x 110 cm
Thermal control	Radiators with variable conductance heat pipes

Surface Measurements:
The GLAS 1064 nm pulses will be used to measure the range to the surface, and from orbit illuminate the surface with footprints of 66 m diameter and 170 m center to center spacing. The error budget for the ice surface measurements is summarized in Table 3. Over ice surfaces with slopes < 2 deg., every laser measurement of range should have <10 cm resolution. When combined with 10 cm orbit uncertainty and up to 18 cm vertical uncertainty due to laser pointing biases over sloped surfaces, this results in measurement of the ice sheet vertical height with 20 cm accuracy. Subsequent data processing and averaging will grid crossing measurements over surface areas of 150 x 150 km to allow a determination of 1.5 cm height changes/year in these areas.

When over land GLAS will profile the heights of the topography and vegetation. The GLAS measurements will allow the Earth's land surface to be referenced, for the first time, to a common global grid with m-level accuracy. For its surface measurements, GLAS utilizes a single channel receiver with an 1064 nm detector. The detector signal is sampled by an all digital receiver which records each surface echo waveform with 1 nsec resolution and a length of either 200, 400, or 600 samples. Analysis of the echo waveforms permits discrimination between cloud and surface returns, measurements of the roughness or slopes of the surface and the vertical distributions of vegetation or trees illuminated by the laser beam.

Table 3. Ice Altimetry Error Budget

Source	Error Type	Magni-tude
Instrument	a. Single shot accuracy (3 deg. surface features) b. Range bias c. Laser beam pointing angle uncertainty (1 arcsec, 2 deg. surface) d. Radial orbit uncertainty e. Clock synchronization (<1 usec)	<10 cm <5 cm 18 cm 5 cm 1 cm
Spacecraft	Distance uncertainty from S/C POD to GLAS zero ref. point	0.5 cm
Environ-ment	Atmospheric error (10 mbar error, 0.23 cm/mbar)	2 cm
	RSS error	• 20 cm

Atmospheric Measurements:
GLAS will also measure atmospheric backscatter profiles at 1064 and 532 nm. These measurements share the transmitter, receiver telescope and the 1064 nm detector with the surface lidar. The 1064 nm atmospheric measurements will be used to profile the heights and vertical distribution of clouds and dense aerosols every shot, resulting in 75 m vertical and 175 m horizontal resolution.

The 532 nm atmospheric backscatter measurements are used to measure the vertical distribution of optically thin aerosols during both day and night. They utilize a frequency doubler in the laser, and a

dichroic beam splitter, narrowband filter and photon counting detectors in the receiver. The daytime background count rate is reduced by spatial and spectral filtering. The 532 nm field of view is 170 urad, and is kept aligned to the laser and accommodates the echo's lag angle by using a movable mirror assembly in the 532 nm receiver channel. A two stage optical bandpass filter is used to restrict the receiver's spectral bandpass to ~ 25 pm. In it a thermally tunable etalon is used to track the slow variations in the laser's 532 nm wavelength. After the filter, the optical signal is split equally to the eight identical Geiger-mode Si APD's used as the 532 nm photon counting detectors. At mid altitudes, GLAS will accumulate 20-40 consecutive 532 nm atmospheric measurements, producing an average 532 nm lidar profile at a 1 Hz rate with 75 m vertical and 3.5-7 km along-track resolution.

Laser Design:
In order to meet the mission lifetime requirements, GLAS uses 3 identical laser transmitters. One laser is used at any one time, the second is needed to meet the lifetime goal, and the third is available as a spare. There is one transmitter optical path, and the second and third lasers are optically selected as needed via flip mirror assemblies. The laser specifications are summarized in Table 4. The ND:YAG lasers are passively Q-switched, diode-pumped, conductively cooled and emit ~ 5 nsec wide pulses in a TEMoo beam [5,6]. The nominal transmitted pulse energy is ~ 75 mJ at 1064 nm and 30 mJ at 532 nm and the laser pulse rate is 40 Hz. The laser design uses a ~2 mJ energy Q-switched master oscillator to establish the pulse length and spatial beam quality, followed by two double-pass zig-zag slab laser amplifiers to increase the pulse energy, and a non-linear crystal to produce the 532 nm.

Table 4. Laser Specifications

Number of Flight Lasers	3
Energy/pulse (1064 nm) (532 nm)	75 mJ 35 mJ
Pulse Repetition rate	40 Hz
Pulse Shape/Width Stability	± 5%
Pulse width (FWHM)	4 - 6 nsec
Beam divergence	110 μrad
Spatial beam profile	Nominal Gaussian
Beam pointing stability*	± 10 μrad
Mass: (each laser)	12.7 kg
Size: (each laser)	< 18 x 30 x 15 cm
Power	< 105 W @ 28 V
Wall plug Efficiency	~ 6% from 28 V
Lifetime goal (3 lasers)	5 years continuous
Total laser shots in 5 years	6.3×10^9
Target lifetime per laser	3.15×10^9 shots

Laser Pointing Angle Determination:
Near their edges, the icesheets have sloped surfaces, and pointing of the laser beam away from nadir can bias the GLAS surface height measurements. For example over surfaces with 2 deg. slopes, knowledge to ~ 8 urad is required to achieve 10 cm height accuracy. As a consequence, accurate knowledge of the pointing angle for each laser firing is critical for the Icesat mission. GLAS uses a stellar reference system (SRS) to accurately determine the pointing angle of each laser firing relative to inertial space [7].

The GLAS SRS approach uses a high precision star camera oriented toward local zenith. Its measurements are coupled with a gyroscope to measure the inertial orientation of the SRS optical bench. The far field pattern of the laser beam is measured on every laser firing with a laser reference system (LRS). It incorporates a special camera which views zenith and digitizes images with a higher resolution and a narrower field-of-view than the star camera. The LRS folds a small fraction of the outgoing laser beam into the laser reference camera with two highly stable cube corner assemblies. The first cube corner, which has a transparent entry face, folds a small fraction of the laser beam angle into the second cube corner, which directs it into the laser reference camera. The laser reference camera digitizes each laser far field pattern along with several alignment markers. These are optical signals from the alignment reference surfaces of the star camera and gyroscope, which are folded via cube corners into the laser reference camera.

Optically measuring each laser far field pattern relative to the star camera and gyroscope alignment points permits the angular offsets of each laser pulse to be determined relative to inertial space in the ground-based data processing. The laser reference camera can also view stars which pass through its field of view. When these events occur roughly once every 8 minutes, they permit the alignment biases between the star camera and laser reference camera to be determined with sub-arcsecond precision.

Receiver Design:
The laser backscatter from clouds, aerosols and the surface are collected by the receiver telescope. The telescope is an all Beryllium Cassegrain design, with a diameter of 100 cm and a field-of-view of 350 urad. The 1064 nm detectors are a silicon avalanche photodiodes with ~ 200 MHz bandwidth. One serves as the prime detector and the backup unit can be switched into the path via a flip mirror assembly. The

1064 nm optical receiver is a larger higher performance version of the MOLA [9] receiver.

The 1064 nm surface echo is spread in time due to the slope and roughness of the terrain surface [10]. A fast electronics timing unit is used to measure the time of flight of the laser pulse. The GLAS 1064 nm electronics receiver uses an all digital approach, which digitizes and record both the transmit and echo signals at a 1 GHz rate. This permits post detection algorithms to search the digitized window, find the surface echo signal, and calculate the transmit and echo pulse energies and centroid occurrence times. This receiver approach permits a close approximation of a maximum likelihood estimator for range, and results in better performance and more flexible operation than the threshold, pulse width and energy measurements used on MOLA [10, 11]. The 1064 nm cloud lidar electronics utilize filter the echo waveform with 2 MHz (75 m) resolution, for the lowest 30 km in range. The atmospheric profiles at 1064 nm are reported for every laser firing.

To reject the daytime background light, the 532 nm lidar receiver uses a 170 urad field of view. A movable mirror assembly is used to keep this aligned with the laser signal A narrow band 532 nm filter and etalon are also used to reject background light. The etalon has a bandwidth of ~ 25 pm, and its center wavelength is thermally tuned to track the average laser wavelength. The received signals which pass through the filter are distributed via beam splitters to eight photon counting detectors. These operate in the Geiger mode and have > 50% photon counting efficiency. Using eight detectors permits > 80 MHz photon counting rates from the 532 nm receiver, which allows photon counting even with sunlit clouds in the telescope's field of view. At 532 nm, the sum of 40 individual lidar profiles measured by the photon counting detectors are reported once per second.

The measurement capabilities of the altimeter and lidar have been estimated by using analysis and simulations. Both the altimeter and lidar have > 3 dB performance margins. The details of the mission, instrument requirements, design and results of analysis and simulations will be presented.

Acknowledgments:
We would like to acknowledge the talented contributions of Ron Follas, GLAS Instrument Manager, Joe Dezio, Icesat Mission Manager and the entire GLAS Instrument Team.

References:

1. (1995) "Geoscience Laser Altimeter System," *1995 MTPE/EOS Reference Handbook*, NASA Washington DC, 132

2. Bufton, J.L. (1989) "Laser altimetry measurements from aircraft and spacecraft," Proc. IEEE, Vol 77, 463.

3. Bufton, J.L., J.B. Garvin, J.F. Cavanaugh, L. Ramos-Izquierdo, T.D. Clem and W.B. Krabill (1991) "Airborne lidar for profiling of surface topography," *Opt. Engr.*, Vol. 30, 72.

4. Gardner, C.S. (1992) " Ranging Performance of Satellite Laser Altimeters," IEEE Trans. *Geosc. Rem. Sensing*, Vol. 30, 1061.

5. Zuber, M.T., D.E. Smith, S.C. Solomon, D.O. Muhleman, J.W. Head, J.B. Garvin, J.B. Abshire and J.L. Bufton (1992) "The Mars Observer Laser Altimeter Investigation, " *J. Geo. Res.*, Vol. 97, 7781.

6. Afzal, R.S. and M.D. Selker (1994) "Design considerations for the GLAS laser transmitter," Processings, 1994 International Laser Radar Conference (ILRC) , Sendai Japan.

7. Afzal, R.S. "Diode-Pumped Solid State Lasers for Space-Based Applications," this conference.

8. Millar, P.S. and J. M. Sirota "The Geoscience Laser Altimeter System Stellar Reference System", this conference.

9. Ramos-Izquierdo, L., J.L. Bufton and P.Hayes (1994) "Optical System Design and Integration of the Mars Observer Laser Altimeter," *Appl. Optics*, Vol. 33, 307.

10. Abshire, J.B., S.S. Manizade, W. H. Schaefer, R.K. Zimmerman, J.S. Chitwood and J.C. Caldwell (1991) "Design and performance of the receiver for the Mars Observer Laser Altimeter," *Technical Digest* - CLEO'91, paper CFI4, *Opt. Soc. Amer*, Washington DC.

11. McGarry, J. F., L.K. Pacini, J.B. Abshire, and J.B. Blair (1991) "Design and performance of an autonomous tracking system for the Mars Observer Laser Altimeter receiver," *Technical Digest* - CLEO'91, paper CThR27, *Opt. Soc. Amer.*, Washington DC.

Laser Pointing Determination For The Geoscience Laser Altimeter System

Pamela S. Millar and J. Marcos Sirota*

NASA Goddard Space Flight Center, Laser Remote Sensing Branch, Code 924, Greenbelt, MD, 20771
* University of Maryland at Baltimore County
Phone: (301) 286-3793, FAX: (301) 286-0213, E-mail: pam@eib1.gsfc.nasa.gov

1 Introduction

The Geoscience Laser Altimeter System (GLAS) is a space-based lidar being developed to monitor changes in the mass balance of the Earth's polar ice sheets (Thomas *et al.* 1985). GLAS is part of NASA's Earth Observing System (Schutz 1995), and is being designed to launch into a 600 km circular polar orbit in the year 2001, for continuous operation over 3 to 5 years. The orbit's 94 degree inclination has been selected to allow good coverage and profile patterns over the ice sheets of Greenland and Antarctica. The GLAS mission uses a small dedicated spacecraft provided by Ball Aerospace, which is required to have a very stable nadir and zenith pointing platform which points to within ~100 urad (20 arcseconds) of Nadir.

Accurate knowledge of the laser beam's pointing angle (in the far field) is critical since pointing the laser beam away from nadir biases the altimetry measurements (Gardner 1992, Bufton *et al.* 1991). This error is a function of the distance of the laser centroid off nadir multiplied by the orbit altitude and the tangent of the slope angle of the terrain. Most of the ice sheet surface slopes are less than 1° resulting in pointing knowledge bias of only 7.6 cm with 7.3 urad accuracy, and overall single shot height accuracy of ~15 cm. However, over a 3° surface slope pointing knowledge to ~7.3 urad is the largest error source (23 cm) in achieving 26 cm height accuracy. The GLAS design incorporates a stellar reference system (SRS) to relate the laser beam pointing angle to the star field to an accuracy of ~7.3 urad. The stellar reference system combines an attitude determination system (ADS) operating from 4 to 10 Hz coupled to a 40 Hz laser reference system (LRS) to perform this task.

2 Stellar Reference System Description

The simplest approach for measuring the pointing of the GLAS laser beam with respect to the star field is to couple the laser directly into a star camera. Unfortunately this approach is not feasible with current star camera technology, regarding repetition rate (there are no cameras faster than 10 Hz), and angular resolution (the typical 8 x 8 degree field of view (FOV) would require centroiding to 1/60th of a pixel). Upgrades to star camera technology are being studied for a next generation (GLAS-II) SRS system. For these reasons an approach using a separate sensor to measure the pointing of the sampled laser beam at 40 Hz is baselined. The overall approach for the stellar reference system is shown in figure 1. The ADS measures the pointing of the instrument platform with respect to the star field while the LRS samples the laser beam and measures its alignment with respect to the components of the ADS.

In the SRS approach a small fraction of the GLAS laser beam is folded into the laser reference sensor's FOV with two lateral transfer retroreflectors (LTR's). LTR's have the same characteristics as retro-reflectors; they preserve the parallelism between the input and output beams as long as the alignment integrity between the three faces are maintained. The optic as a whole can move (within several degrees) and not affect the parallelism between the input and output beams. The first LTR encountered by the outgoing laser beam is constructed with a semi-transparent fused silica face and two other Zerodur faces which form the dihedral of the LTR. The fused silica output face is anti-reflective (AR) coated while the other two Zerodur faces have highly reflective coatings. The AR coatings on the output face ensures that at least 99% of the laser energy gets transmitted to Earth surface. The next LTR, constructed entirely of highly reflective coated Zerodur, relays the laser beam and other fiducial beams into the laser reference telescope where it is imaged for each laser shot fired.

The LRS consists of a (8.5 x 8.5 mrad) narrow FOV camera operating at 40 Hz frame rate. The camera includes a telescope, a charge coupled device (CCD) array, and ancillary electronics for imaging and computing the centroid locations of the GLAS laser beam and other fiducial reference images. There are 2 collimated (75 urad) reference beam sources attached to both the star tracker housing and gyro housing. The

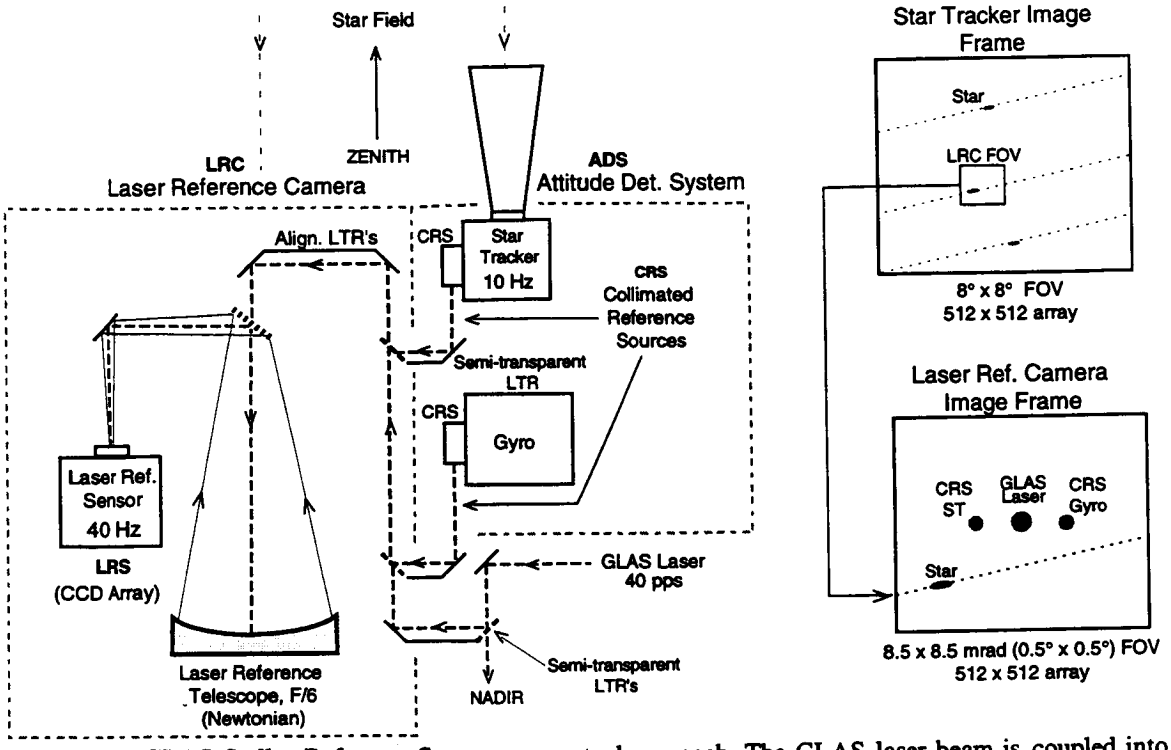


FIGURE 1. GLAS Stellar Reference System conceptual approach. The GLAS laser beam is coupled into the LRS along with collimated reference sources from the ADS components. All optical beams are introduced concentrically through the semi-transparent diagonal mirror of the telescope. They are spatially superimposed into the telescope but are offset in angle to avoid image overlap on the array focal plane.

optical beams generated by these sources are coupled into the newtonian telescope with LTR's to observe the alignment of the star tracker and gyro housings. The alignment and stability between the reference sources and the star tracker CCD array and gyro spin axis respectively, will influence how well the pointing of the GLAS laser beam can be determined, these error components are accounted for in the LRS error budget. The LRS will also be able to occasionally image stars which will enable a boresight check between the LRS and the larger FOV (8° x 8°) star camera. An annulus of 3.8 cm thickness with ~120 cm^2 total area is available for collecting star light. The relative movement between the far field pattern of the GLAS laser beam, reference sources from the ADS instruments, and an occasional star will be determined. This data combined with the processed ADS data will yield the pointing of the laser beam in inertial space. GPS and satellite laser ranging data, from the ground to a retroreflector target on the instrument, are used to determine the center of gravity (CG) orbit position of the spacecraft to ~5 cm. Knowledge of the laser footprint location on the ground is then determined by combining the pointing knowledge of the outgoing laser beam with the position of the spacecraft CG.

3 Performance

Error Budget Allotment

The error budget allotment of the SRS is shown in table 1. The overall system error in determining the laser pointing is estimated to be 6.7 urad, 1- sigma, (1.4 arcseconds) at 40 Hz. This value may be improved to 5 urad after post flight calibrations are performed. The ADS error component is derived by combining the performance specifications from a Litton HRG gyro and a commercial star tracker with Kalman filtering and smoothing. Unmeasured errors take into account any thermal distortions and high frequency (> 7 Hz) vibrations of the bench and components on the bench.

Details of the LRS error component are listed in table 2. This subsystem is the core instrument of SRS, it combines the laser reference camera (CCD array plus telescope) with coupling optics and collimated reference sources. The values listed for the lateral transfer retroreflectors and collimated reference sources are

based on finite element calculations assuming thermal gradients are limited to ±1°C. Recent tests on a prototype LTR show that gradients of ± 5°C can be tolerated. A description of the the laser reference camera performance is described in the following section.

Laser Reference Camera

To enable multiple co-alignment checks per orbit between the LRS and ADS, the laser reference camera (LRC) is required to detect stars of +8 magnitude, with centroid resolution of 2 urad while operating at 40 frames per second (the laser pulse rate). The LRC is also required to determine the ranging laser image and star camera and gyro fiducial image centroids to a resolution of at least 1 urad.

Operating the LRC at 40 Hz frame rate poses the most difficult challenge, since the integration and read-out time for detecting stars is < 25 msec. For comparison commercial star cameras typically operate at frame rates ≤ 10 Hz. The shorter integration times of the LRC are compensated for by using a larger collecting aperture, and a more suitable CCD array architecture for this application. This array is required to produce lower noise and be read out and processed with reasonable A/D speeds. For these reasons a dual frame transfer architecture with two clocked outputs is chosen. A 512 x 512 array provides high field resolution, while maintaining data rates at reasonable levels. The selected sensor is a multi-phase pinning (MPP) array with these characteristics, mounted on a thermo-electrically cooled package.

TABLE 1. GLAS SRS Error Budget Allotment

SYSTEM	ERROR MAGNITUDE (urad, 1 sigma)	FREQUENCY (Hz)	REFERENCE
Attitude Determination System	4.6	4	ADS ref. sources to star field
Laser Reference Sensor (LRS)	4.3	40	Laser beam to ADS ref. sources
Unmeasured Errors	2.2	7	Bench vibrations & Instrument angular disturbances
Stellar Reference System	6.7	40	Laser Beam to Star Field

TABLE 2. GLAS SRS laser Reference Camera (LRC) Error Budget Allotment

ERROR TYPE	ERROR (urad)	COMPONENT DESCRIPTION
Camera Centroid Resolution:	0.48	Laser image
	0.48	Star camera reference image
	0.48	Gryo reference image
	0.19	Star image (100 images averaged, worst case scenario)
Telescope Distortion:	1.45	Off-axis parabola
Coupling Optics Stability:	1.94	Star Camera LTR, Fused Silica (semi-transparent)
	1.94	Gyro LTR, Fused Silica (semi-transparent)
	1.94	Output Glas laser LTR, Fused Silica (semi-transparent)
	0.19	LTR obscuring Telescope, Zerodur (all reflective)
	1.45	Star Camera collimated reference beam stability
	1.45	Gyro collimated reference beam stability
Total LRS RSS Error	4.3	(1-sigma)

The telescope is an F/6 Newtonian with 15 cm aperature and 7.5 cm central obscuration (caused by the LTR and diagonal mirror of Newtonian). The smearing produced by the orbital motion corresponds to 2.3 pixels along track. Under these conditions, the noise equivalent angle (NEA) in the along-track direction for a star of magnitude +7.5 in the sensor becomes 1.2 urad. Readout noise, dark current, and photon noise are

included in this value. When accounting for estimated centroiding errors, optical error, and defocusing, a total RSS value of 1.9 urad per frame per star is obtained. Given the small FOV, statistics indicate that for most frames only one star will be visible in the field, therefore it will not be possible to average over multiple stars as is typically done by star trackers. However, an average star track in our camera FOV should produce approximately 100 images, which would yield a factor of 10 reduction in the overall error if averaged over the whole track. Sweep time for the 8.5 mrad FOV is approximately 4 sec. Averaging star images over the track over these periods will be valid for boresight verification assuming that variations of boresight between the star tracker and its corresponding collimated reference source a longer period. The validity of this assumption will be checked during engineering model testing late in 1998.

The laser ranging spot, as shown in figure 1, is imaged on a region of interest of 7 x 7 pixels wide. The incident power is limited by the well depth per pixel at the center of the beam. The NEA in this case is determined essentially by photon noise. The largest contribution to centroiding error is pixel response non-uniformity. The errors accrued in determining the location of the centroid of the ranging laser image and ADS fiducial images are much lower since the optical intensity of these sources are greater than dim stars. Preliminary calculations show that, accounting for all contributions, the required resolution (2 urad or 0.4 arcsec) per shot can be met.

4 Summary

The GLAS stellar reference system takes laser altimetry to a more accurate level (15-26 cm per measurement) which is a function of the slope angle of the terrain. We have developed an approach for relating the laser pointing angle to the inertial reference frame given the limits of current technology. The estimated pre-launch SRS performance of 6.7 urad is slightly better than the mission requirement. It is likely with the planned post-launch calibrations that the SRS will reach 5 urad accuracy while operating on-orbit.

5 Acknowledgments

This work is being funded by NASA's EOS Mission to Planet Earth. The authors would like to thank the GLAS SRS team with special thanks to Joe Garrick, Paul Hannan, and Jim Lyons for their contributions on the SRS instrument development.

References

Bufton, J.L., Garvin, J.B., Cavanaugh, J.F., Ramos-Izquierdo, L., Clem, T.D. and Krabill, W.B., (1991), "Airborne lidar for profiling of surface topography," *Opt. Engr.*, 30:72.

Gardner, C.S., (1992), "Ranging Performance of Satellite Laser Altimeters," *IEEE Trans. Geosc. Rem. Sensing*, 30: 1061.

Hofton, M. A., Ridgway, J. R., Minster, J. B., Williams, N., Bufton, J. L., Blair, J. B., and Rabine, D. L., (1996), "Repeat Airborne topographic survey of Long Valley, California, Using Scanning Laser Altimeters," EOS Trans., 77:S262.

Schutz, B. E., (1995), "GLAS Geoscience Laser Altimeter System," *MTPE/EOS Reference Handbook*, NP-215, 132.

Thomas, R. H., Bindschadler, R. A., Cameron, R. L., Carsey, F. D., Holt, B., Hughes, T. J., Swithinbank, C. W. M., Whillans, I. M., and Zwally, H. J., (1985), "Satellite Remote Sensing for Ice Sheet Research," in *Nasa Tech. Memo. 86233*, 17.

Zwally, H. J., (1994), "Detection of Change in Antarctica," in *Antarctic Science: Global Concerns*, Gotthilf Hempel, Ed., Springer-Verlag Berlin Heidelberg, 126-143.

Airborne Laser Mapping: Topographic and Bathymetric Applications

J. Green[1], A.G. Cunningham[2], etc.
Optech Incorporated
100 Wildcat Road
North York (Toronto), Ontario
Canada M3J 2Z9

1 jimg@optech.on.ca
2 grant@optech.on.ca

Introduction

Presently, the work in Airborne Laser Mapping distinguishes two clearly separate areas of study: terrestrial topography and underwater topography, or bathymetry.

Airborne Laser Topography (ALT) is a technique that collects from a number of sensors an all digital data stream aimed at producing accurate digital terrain models (DTMs) of overflown targets. Some areas of interest are, 1) topography for engineering, hydrology and slope studies, 2) corridor mapping for road and pipeline routing, 3) forestry applications for tree heights and contour generation beneath the canopy, and 4) coastal mapping for erosion, inundation and wetland studies. There are presently a number of ALT systems operating worldwide, from a number of manufacturers. To demonstrate the value of the ALT, this paper will summarize our experience with the development , capabilities and achievements of Optech's Airborne Laser Terrain Mapping (ALTM) system.

Airborne Laser Bathymetry (ALB) is a technique primarily aimed at augmenting nautical chart production and bathymetric mapping capability in relatively shallow coastal waters. The potential of water-penetrating airborne laser radar to provide cost effective characterization of underwater topography to depths as great as 50 meters, depending on water clarity, has triggered a number of research and development efforts worldwide over the past three decades. Early experimental prototypes in the 1970's were able to demonstrate the potential of the technique, and development soon progressed to the operational prototype stage by the early 1990's. Currently, there are several fully operational ALB tools in the world. This paper will summarize the development, capabilities and achievements of Optech's SHOALS system.

The motivation for operational usage of ALB is two-fold: the speeding up of surveying tasks currently mandated by various hydrographic agencies, and the realization of anticipated, significant cost savings for ALB as compared to conventional methods. Millions of square kilometers of uncharted waters exist worldwide, with depths less than 50 meters, which represent a backlog of hundreds of operational ship-years for traditional acoustic surveying. In addition, ALB offers the tangible benefits of rapid deployment, easy access to remote and hazardous areas, and flexibility of plan, which in concert act to increase the utility of ALB.

Airborne Laser Bathymetry Technique

Airborne laser topographers utilize a pulsed laser which is fired at a scanning mirror operating perpendicular to the line of flight, thereby creating a swath width which is typically user-definable. The laser pulse is then reflected back along the same path once contact occurs with the ground or any other object in the propagation direction. A precise time interval meter is used to measure the total elapsed time which is converted to a range. At the same time the laser pulse is fired, the position and attitude of the aircraft are precisely measured using a Differential Global Positioning System (DGPS) and an Inertial Reference System (IRS). All events are time referenced for post processing to create the final X,Y, Z ASCII output data.

Airborne laser bathymeters utilize the well-proven lidar technique to infer water depth from the time-of-flight difference of optical pulses scattered from the sea surface and sea bottom. Laser pulses of suitable wavelengths are transmitted from the aircraft to the water surface. A co-located optical receiver detects the two scattering events, and determines water depth from their relative timing after accounting for operating geometry, propagation-induced biases, instantaneous waveheight and tidal effects.

In the typical operating scenario a scanner system is used to sweep successive laser pulses across the track of the aircraft, thereby producing a wide swath of laser soundings with near-uniform spatial distribution. A positioning sub-system, combining both DGPS and an IRS, ensures accurate identification of each sounding's horizontal position. Data acquired with the airborne system is processed both in realtime (for data quality verification) and off-line using a dedicated post processing facility (for final, accurate depth determination).

Systems Development and Capabilities

The ALTM system was first developed in the early 1990's and has since undergone major improvements due to technological advances in pulsed lasers, GPS systems and Pentium computer processing capabilities. The first ALTM operated with a laser pulse rate of 2 kHz, a 40° scan angle and a maximum altitude of 1,000 m. The current systems operate at 10 kHz, a 40° scan angle and an altitude of 1,500 m. Testing is now underway for systems to operate at 15 kHz, 75° scan angle and an altitude of 6,000 m.

Compared to its predecessors the current generation of fully operational, Optech-developed ALB systems, represented by SHOALS, has incorporated certain key improvements which improve the accuracy, reliability and operational range of use of the system. A two-axis stabilized scanner, specially developed for use in ALB systems, compensates for pitch and roll of the aircraft platform, and assists in the generation of straight swaths of soundings which results in greatly increased data collection efficiency.

SHOALS utilizes multiple optical channels to locate the instantaneous water surface for each laser sounding, each exploiting a different scattering mechanism for signal generation. Since the depth measurement accuracy ultimately depends on the system's ability to accurately locate surface, this increases the accuracy and reliability of the depth soundings. For similar reasons, the system employs both deep- and shallow-optimized optical channels for detection of the water bottom, along with a sophisticated electronics pre-processing package. These features allow for compression and handling of the huge signal dynamic range exhibited by the backscatter waveforms, thereby extending the performance and utility of the system over a wide range of operational conditions.

An extensive development effort over many years has resulted in a flexible, robust post processing tool which combines the advantages of automation for efficiency, and manual processing for data editing and flexibility. A sophisticated wave corrector algorithm is employed in the automated post processor system to remove the effects of waves and long period swell from the measured depths.

Recently SHOALS has incorporated the capability for kinematic GPS (KGPS) with on-the-fly (OTF) ambiguity resolution. The primary purpose for operating in this mode is to obviate the need for collecting tidal data concurrent with the laser soundings.

The combination of a rugged, fully-operational airborne system and a sophisticated post processor yields a bathymetric surveying tool which acquires data at a rate of 200 soundings/sec, at altitudes between 200 and 400 m, and at area coverage rates up to 28 km^2/hr (with a nominal 4 x 4 m sounding density). SHOALS can measure in clear water to a depth of 40 m, and in more turbid coastal waters to commensurately lesser depths, with depth and positional accuracies of ± 20 cm and ± 4 m, respectively.

Systems Results and Achievements

The results and achievements of the current ALTM systems are assisting in the finding of many new applications. Since the initial flights in 1993, conducted in Germany, airborne laser scanning for topography has offered an exciting alternative to digital elevation data collection by other means.

In 1997 Opten Limited of Moscow, Russia, twice surveyed 2,500 km of existing power wires, for a total of 5,000 km, in under 10 days. This project was conducted through remote areas of Siberia, and their aim was to locate the position and separation of existing towers for future expansion. A helicopter platform was used to assist in following the existing power wires at a low altitude, and to ensure a high rate of laser returns from the individual cables.

In 1997 the University of Florida, in cooperation with the Ministry of the Environment, surveyed 350 km of shoreline in order to evaluate the extent of the damage caused by a hurricane. The ALTM was placed in a fixed wing aircraft and completed the survey in four hours. Traditional ground survey

crews had taken nine months to perform the same task. The results were subsequently compared and the differences found to be minimal.

In 1997 Fotonor AS of Norway surveyed ten separate areas for the UK Environment Agency to study the effects of ocean tides. For each of the areas tidal flats had to be surveyed during low tide, therefore the system required both daytime and nighttime operation capability. The ALTM was able to produce the required results and the UK Environment Agency has since purchased a system to continue their studies.

In 1996 the Rijkswaterstaat, a government agency in the Netherlands, conducted pilot projects to test the laser scanning technique. Their mandate was to create accurate DTMs of the dikes and surrounding countryside for flood control. Geodan Geodesie was selected to perform this test and were able to meet the very stringent demands put forth by the Rijkswaterstaat. In 1998 the Rijkswaterstaat has mandated that the whole country now be laser scanned in order to create a complete DTM of the Netherlands. Three separate companies have been awarded contracts to complete this task, Airborne Laserscanning International BV of the Netherlands, Fotonor AS of Norway, and Eurosense of Belgium.

SHOALS development was begun in the late 1980's, in order to augment the hydrographic surveying capabilities of the U.S. Army Corps of Engineers, and to provide speedier surveys at least as cost-effectively as with conventional techniques. Since its commissioning in 1994 the system has conducted numerous one-time, and some repeat, surveys in 17 states and the Yucatan Peninsula of Mexico. Approximately 220 survey projects have been completed, resulting in a total aerial coverage of more than 2,750 km^2.

When first envisioned, SHOALS' primary application was that of navigational channel inspections to facilitate their maintenance, with a secondary objective of nautical charting. However, the system has been successfully utilized for a variety of other applications such as beach nourishment monitoring and design, erosion monitoring, emergency response and damage assessment, sea-grass delineation, navigational hazard identification, military applications and others. Examples of certain of these applications will be discussed.

In 1993 the Town of Longboat Key, Florida, initiated a restoration project along 18 km of beach adjacent to Longboat Key utilizing over 1 million cubic meters of sand dredged from the nearby off-shore region. A large area survey of this region was the first operational mission flown by SHOALS in 1994, a project which was re-surveyed four more times over the next 32 month period. The combination of re-surveying over a large area with high density soundings, including both the near-shore and beach (above waterline) areas, allowed coastal engineers to accurately and quantitatively assess the movement of beach material during the surveyed period, thereby alleviating concerns that beach material was being continuously removed from the target area.

A beach area adjacent to Presque Isle, Pennsylvania on the Lake Erie shoreline is protected by a series of artificial breakwaters which are used to deflect and disperse the effects of high energy waves impacting on the beach area. Normally inspections of breakwater erosion are performed by divers, a costly, time-consuming and potentially dangerous task. However, with the SHOALS system inspections can be performed over the entire set of breakwaters (arrayed over > 1 km distance), in less than one hour flying time, with full three dimensional information both below and above the waterline at the time of surveying. Differencing of successive datasets yields quantitative data regarding changes to the structures.

In October 1995 Hurricane Opal devastated the Florida panhandle, causing extensive damage to both property and the environment. One of the areas affected most severely was East Pass, where overwash caused damage to dunes and jetty structures. SHOALS surveyed the area some 10 days after the storm, acquiring full data coverage in less than an hour and yielding final chart production with quantitative dredging estimates for the navigational passages within the same day as the survey mission was flown.

SHOALS' first international mission was conducted over a 2-1/2 month period in 1996, adjacent to Cancun on the Yucatan Peninsula, Mexico. The survey was performed in cooperation with the U.S. and Mexican Navies for purposes of nautical charting and hazardous object detection. The project resulted in a total area coverage of more than 800 km^2, consisting of 133 separate aircraft flights and more than 100 million individual laser soundings. This endeavor demonstrated SHOALS' ability to provide large area coverage: to collect, process and integrate large volumes of accurate, high resolution data seamlessly over a relatively extended time period.

One of the most stringent nautical charting requirements, as specified by the International Hydrographic Organization (IHO), concerns the capability for a charting methodology to detect hazardous objects which jut up from the surrounding sea bottom, and therefore to measure the minimum navigational depth in any given region. Optech-developed ALB systems, including both SHOALS and HawkEye variants, have undergone considerable testing on artificial sub-surface targets in order to determine the systems' ability to resolve hazardous objects in a variety of water depths and water clarities. In one particular test, HawkEye was able to discriminate a 1 meter cube positioned just above the surface of a 10 m by 10 m flat platform located in 6.5 meters of water.

Another successful application of SHOALS was in a very shallow area of Florida Bay (off the southern coast of Florida), known as "Little Rabbit Cuts". This entire area consists of shallow, turbid water less than 7 feet deep, with the central area generally less than 4 feet and consisting of a complex network of shallow channels, tidal pools and mud cuts. Previous mapping of this area had been performed manually using flat-bottomed boats and hand-held staffs to measure the water depth. SHOALS was able to quickly map the entire > 3 km^2 area with high resolution data in order to fully resolve, for the first time, this complicated subsurface topography which is suspected to play an important role in the exchange of water between Florida Bay and the Gulf of Mexico.

Conclusions

The examples discussed above for both the topographic and bathymetric applications of Optech's laser surveying systems indicate the considerable and varied utility of this airborne laser mapping technology. In this poster paper, details will be given of these and other examples of the performance of these systems.

New Instrumentation Developed for Mater Laser Ranging Observatory

M. Selden, C. Steggerda, R. Stringfellow, T. Oldham, D. McClure
AlliedSignal Technical Services Corporation
7515 Mission Drive, Lanham, MD 20706 USA

Dr. G. Bianco
Agenzia Spaziale Italiana
Center for Space Geodesy and Remote Sensing
"G. Colombo"
75100 Matera, Italy

AlliedSignal Technical Services Corp. (ATSC) began a partnership with the Italian Space Agency to develop a new state-of-the-art satellite laser ranging system. The system will be located in Matera Italy and will be capable of performing satellite and lunar laser ranging as well as supporting astronomical experiments. The Matera Laser Ranging Observatory (MLRO) was designed to be the best system of its type in the world for both the quantity and quality of its data and features a 1.5 meter astronomical quality telescope.

The MLRO system design required three new instruments with performance not commercially available. These were an event timer with picosecond resolution and accuracy to support time interval measurements to most SLR / LLR targets, a multi-channel range gate generator capable of providing range gate and simulation signals that can change dynamically at high (MHz) rates, and a multi-channel 1GHz bandwidth peak amplitude measurement device to allow for real-time laser diagnostics and modeling of amplitude-dependent systematic errors.

Event Timer

The event timer project was started in 1995 and completed in early 1998. The development was divided into two main phases: 1) the prototype development phase, which focused on developing a single-vernier prototype unit, and 2) the commercial instrument phase, which has resulted in a commercial-quality unit capable of supporting from one to four parallel verniers. Data from the prototype has been used extensively in the testing of the system and the new commercial version is currently being used in the system for operational testing.

The event timer can measure the epoch on events separated by at least 100 ns with sub-picosecond resolution with an RMS timing jitter of less than 5 picoseconds after instrument calibration.

Range Gate Generator

The Range Gate Generator (RGG) was developed to allow for computer-control of the detector and signal processing gates with low timing jitter and a rapid update rate. This instrument also provides precise simulation signals to the system to allow for automated diagnostics and troubleshooting of the large system.

The RGG has eight independent channels each channel can be individually updated at up to MHz rates

and offers timing jitter on the close order of 20 ps RMS with a timing resolution of 20 ps and gate width resolution of 500 ps.

The prototype was completed in early 1997 and the commercial version completed in the fall of 1997. This unit has been tested under both laboratory conditions and under operational satellite and lunar laser ranging.

Peak Amplitude Measurement

The peak amplitude measurement instrument was designed to allow the system to measure the amplitude of eight separate pulses at high (up to MHz) rates. Each channel can measure the amplitude of a pulse with 8 bit resolution and offers a 1 GHz analog bandwidth. The prototype was completed in mid 1997 and the commercial version was completed in the spring of 1998.

Summary

Three instruments have been developed to improve the ability and accuracy of laser ranging to targets at virtually all ranges. These are an event timer, range gate generator, and amplitude measurement instrument. All three instruments have been provided with automated diagnostic and calibration devices and software to maintain the quality of the data acquired by the MLRO system.

The MLRO system has been built in Greenbelt Maryland, the United States and will be installed near Matera Italy. The system is currently operational and will either be shipped this year or after receiving a dual wavelength ranging upgrade in 1999.

Reference:
Charles Steggerda, C. Bart Clarke, J. Michael Heinick, David McClure, Thomas Oldham, Michael Selden, Ray Stringfellow, Dr. Giuseppe Bianco (November 1996) "Instrumentation Development and Calibration for the Matera Laser Ranging Observatory" Laser Ranging Workshop Chinese Academy of Sciences, Shanghai China.

Development of a Medium Repetition Rate (10 Hz - 500 Hz) Diode Pumped Laser Transmitter for Airborne Scanning Altimetry

D. Barry Coyle, Steven J. Lindauer II and Richard B. Kay
Dept. of Physics, The American University
4400 Massachusetts Ave. NW, Washington, DC 20016
Phone: (301)286-0144, Fax: (301)286-1762, email: barry@eib1.gsfc.nasa.gov

Background:
Since the late 1980's, NASA has developed several small, all-solid state lasers of low repetition rates for use as transmitters in prototype LIDAR and raster scanned altimetry retrieval systems. Our early laser transmitters were developed for high resolution airborne altimetry which employed cavity dumping techniques to produce a pulse shape with a 1 ns rise time. The first such laser was the SUMR (Sub-millimeter resolution) transmitter which used a side pumped, D-shaped half-rod of Nd:YAG for the oscillator active media and produced ~3 ns pulses of 100 μJ energy at a 40 Hz repetition rate. (Coyle and Blair, 1993; Coyle et al., 1995) After several upgrades to improve rep rate and pulse energy, the final version produced 1.2 mJ pulses at 120 Hz with a 3.7 ns pulse width. The laser has become known as SPLT (Sharp Pulsed Laser Transmitter), and has flown successfully on a variety of airborne altimetry missions. (Coyle and Blair, 1995; Blair et al., 1994)

From building these systems, we have accrued valuable experience in delivering field-deployable lasers and have become aware of the advantages and disadvantages of employing new technologies. For example, even though the laser's main operating environment is in a "cold" aircraft during flight, the laser must still operate in very warm temperatures. This is important if the mission is based in the desert or a tropical climate since ground calibration data from stationary targets must be gathered before and after each data flight. Because conductive cooling is much more convenient than closed loop water flow, achieving the highest possible laser efficiency is becoming a high priority when designing a flight laser. This is especially true for lasers with higher pulse energies and repetition rates which are needed for high altitude scanning altimeters and LIDARs.

Application:
A pair of new laser diode array (LDA) pumped laser transmitters, shown in Figure 1a and 1b, are under development for the next generation scanning laser altimeter. This laser is to be a high efficiency, 5 ns pulsewidth, 2 mJ, 100-500 Hz transmitter for the Laser Vegetation Imaging System (LVIS).(Blair et al. 1996). Both of these lasers, which we will call LVIS IIIa and LVIS IIIb, are designed to be similar in performance, but they have different laser head geometries. The laser which exhibits the best efficiency, beam quality and reliability will be converted into an aircraft deployable unit. These differences will be discussed later. The LVIS platform is an airborne altimeter package consisting of a laser transmitter, a 6° FOV, 8" aperture all-refractive telescope and a waveform capture data system.(Blair and Coyle,

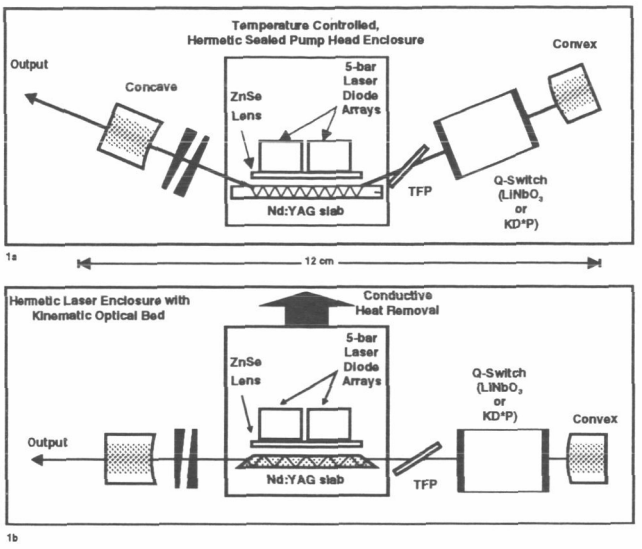


Figure 1a and 1b. Cavity layouts of parallel LVIS III laser transmitters under development. The main difference lies in the gain medium pumped volume overlap with the intracavity mode. The design which presents the best overall performance will be installed in a hermetic enclosure for aircraft use.

1996) Both the output mirror and an intra-telescope folding mirror are actively scanned by computer to coincide with the transmitted and imaged laser footprint on the ground. The laser footprint swath width is determined by the aircraft altitude, air speed and the laser repetition rate. In its present deployment, the LVIS system is capable of up to a 500 Hz repetition rate, but it does not have a conductively cooled laser transmitter. Instead, it is using a relatively large, water-cooled commercial system.

We have built two prior laser transmitters (LVIS I and LVIS II) for this effort over the past 2 years with mixed results.(Blair and Coyle, 1996) Neither was deployed with the LVIS aircraft instrument due to several factors involving poor Nd:YAG slab coatings, inefficient optical pump coupling, and assorted problems with heat pipe implementation. The LVIS III transmitter is a high efficiency design, employing the best aspects from each of the prior LVIS designs and optimized for low maintenance operation with conductive cooling and environment insensitive operation.

Laser Design: Diode Pumping
New LDA pumping technology involving patented collimating techniques, polarization beam folding and multi-pass pumping optics are underway, but a simple,

inexpensive and reliable method must be chosen for an aircraft laser, while still maximizing efficiency. When pumping with LDA stacks of 5 bars or more it has proven difficult to focus, or confine, the highly divergent light in a small volume in the laser crystal. This is needed for efficient TEM_{00} beam conversion. Many methods to solve this problem with various fiber coupling techniques, lens ducts, and micro-optics have been tried, (Morris et al. 1993; Beach, 1996; Bernard and Alcock, 1993) but there is yet no simple way for obtaining sub-mm pump beams from multi-bar stacks of pulsed LDAs. Similar methods are being studied at NASA but none are yet developed enough to employ in a deployable field laser. Furthermore, a stronger thermal lens is created when the pump light is confined to a smaller volume.

The simplest method to date for maximizing the inversion density in a laser slab is by mounting a cylindrical lens made of a high index material, such as undoped YAG (n = 1.82) or ZnSe (n = 2.5), in front of the multi-bar LDA facet to collect the light in a "sheet" of energy. Pump beam thicknesses can be produced as small as 0.4 mm for a 2-bar stack, which increase by about 0.2 mm for each extra bar in the LDA stack. The inter-bar spacing, or pitch, is typically 0.4 mm. We have obtained special 0.35 mm pitch LDAs, by-products from a recent SBIR for use in LVIS III. We have a smaller emitting source from our LDA package with which to focus into our laser crystal, however the maximum rated duty factor is inherently less than that of a 0.4 mm pitch LDA. The rated duty factor is determined by the packing density of the emitters per bar, (> 900/cm), and the effective heat flow from the bar to the heat sink. (SDL Inc. Catalog, 1996) Typical conduction cooled 60 W/bar LDAs are rated at 2% maximum duty factor before accelerated degradation is prominent.

Cavity Design:
A critical factor in obtaining high optical efficiencies in a laser system is accurately matching the intracavity beam diameter with the pumped volume in the active media. Several mirror configurations can be used to increase beam size, but the need for a relatively short cavity length, < 20 cm, limits the choices. The short cavity requirement comes from the round trip time T=2L/c, where L is the cavity length and c is the speed of light, which directly affects the Q-switched pulse width. The shorter the laser cavity, the shorter the Q-switched pulse and, generally, the smaller the intracavity beam.

Concave-Convex Cavity
A stable cavity can be formed by a concave-convex mirror combination which satisfies the central region of the Kogelnik stability criteria $0 < g_1g_2 < 1$, and is designed to have the requisite beam waist in the active media. Chesler and Maydan (1972) have shown that highly stable cavities result when the stability parameter parabola $g_1g_2 \sim 0.5$. We have tried several such cavities with the previous LVIS lasers and found them to show good stability in both axes. Thus, we are employing a concave-convex cavity for the LVIS III laser. Additionally, the concave-convex cavity can be designed to have a relative large beam waist near the concave mirror, which allows good coupling of the mode volume with the pumped volume, and also differentiates against higher order modes.

Q-Switching:
For Q-switching, a KD*P and $LiNbO_3$ are each being tested in the brass-board version of these LVIS III systems. The main differences between these materials is their respective optical damage thresholds and ¼ wave voltages. KD*P is a hygroscopic media which, for a typical 5 mm square x 20 mm long crystal, requires several kilovolts (kV) for adequate hold-off, however the optical damage levels are on the order of 2 GW/cm^2, about 4 times that of $LiNbO_3$. These crystals are also coated with a proprietary sol-gel(TM) antireflective coating which removes the need for index matching fluid. (see Cleveland Crystal product notes) On the other hand, $LiNbO_3$ requires about 1 kV, or 4 times less 1/4 voltage, than KD*P, thereby reducing the risk of HV arcing. Flight units of each are in hand and will be used and compared.

Laser Head Design:
Significant effort has been invested in the area of the laser head configuration and its pumping parameters. The geometry of the Nd:YAG slab is very important when designing for a laser's particular output energy and repetition rate. These output specifications fundamentally determine the number of LDAs that will be needed. Therefore, the slab must be large enough to couple in all the pump energy for absorption. Simultaneously, the slab must be as thin as possible to concentrate the pump energy and create a high inversion density. However, the thinner the slab, ie. the double-pass pump length, the smaller the total absorption efficiency. The absorption efficiency is further reduced with a higher number of LDAs due to the statistical broadening of the total pump bandwidth, when summed from all the bars. For these and other thermal reasons which we will not go into in this paper, we have arrived at two Nd:YAG slab designs, shown in Figures 1a and 1b.

The first is a total internal reflection (TIR) zig-zag slab with opposing Brewster cut faces (Figure 1b). The 809 nm LDA pump energy is sent through the AR coated short face and reflected off an HR coating on the rear face for double pass pumping. Great difficulty was involved in achieving this set of coating specifications while not inducing any TIR losses at 1064 nm. Our Slabs were produced by VLOC in Tarpon Springs, FL., one of only two companies in the USA which can reliably produce these coatings.

The second slab design was inspired by the TFR (Tightly Folded Resonator) cavity (Baer et al. 1990) where the zig-zag path length is lengthened and the volume swept out by the cavity beam (Figure 1a) is increased over the Brewster-cut trapezoid scheme. The beam enters and exits through the same face as the pump beam, somewhat reducing the coating costs. The difficulty in making this slab with low passive losses lies again with having long opposing faces for pump containment and high efficient TIRs. With the TFR concept, there must be a separate high

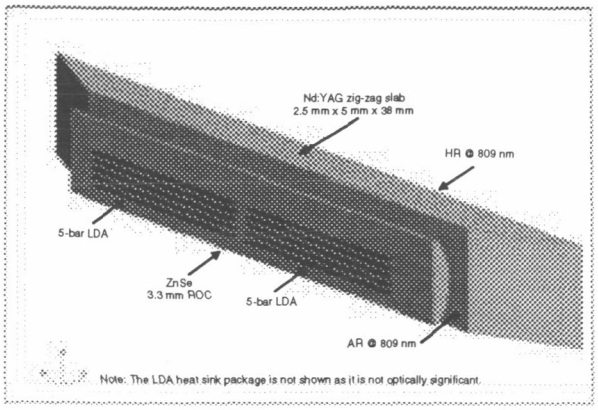


Figure 2. Computer modeled optical assembly of LVIS IIIa diode pumped head. Each component of the design is precisely reproduced in the optical software, including the LDAs for accurate pumping calculations.

reflective dielectric for both the pump LDA's and the Nd:YAG wavelengths. When designed correctly, the TIR angles produce an entry and exit angle equal to Brewsters. Therefore, no coatings are needed for these areas. For this paper, we will concentrate on data taken with the standard zig-zag slab design, or the LVIS IIIb slab.

Figure 2 shows a 3-D view of the laser head produced with OptiCAD, non-sequential optical ray tracing software, from which the optical pumping models were produced. Very few, if any, commercial software packages are available to accurately simulate the absorption distribution in a diode pumped laser crystal. We have developed an algorithm, combining commercial software packages and in-house routines, to numerically and graphically model the energy deposited within a laser crystal. Such calculations have been reported (Brioshi et al. 1992; Hanson and Haddock, 1988) but this effort may be the most simple and flexible yet developed. All the relevant parameters for virtually any diode pumped solid state crystal arrangement can be incorporated in the model. Such parameters include LDA pitch, x and y divergence, their relative gaussian

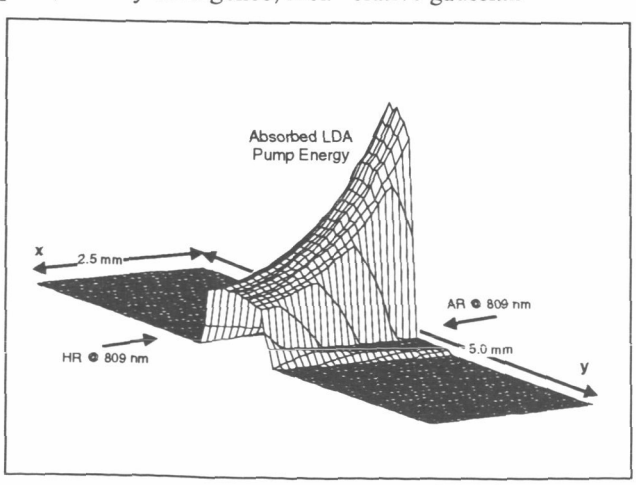


Figure 3. A 3-D plot from our model of the energy deposit in the LVIS III slab when pumped by a collimated 1-bar LDA. A double-pass path is used.

distributions and the LDA bar emitter density. This optical interchangability also applies to virtually any shape or material of collimation optics and laser crystal desired. For the LVIS III designs, various cylindrical lens shapes and materials were studied. A plano-convex cylindrical lens, 11 mm wide x 1 mm thick x 4.5 mm tall with 3.3 mm radius of curvature, made of ZiSe was chosen as the most effective LDA optic. Figure 3 shows the absorption in a 2.5 mm thick (x axis) by 5.0 mm tall (y axis) Nd:YAG slab from a single diode bar collimated with a ZnSe lens. The pump beam is reflected off the opposing face of the slab for a second pass. A 5-bar LDA configuration for the LVIS III head is shown in Figure 4. The average pumped volume thickness is about 2.0 mm. Figure 4b shows a CCD image of the actual pumped LVIS IIIa slab with the 5-bar configuration.

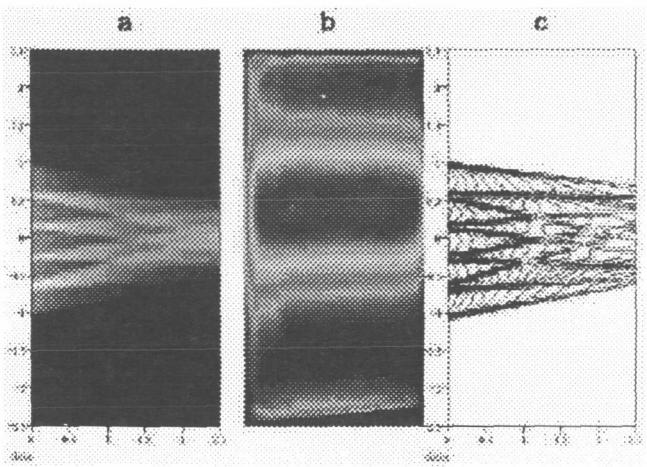


Figure 4a, 4b, 4c. Calculated contour image (left and right) of pumped volume in 2.5 mm by 5-bar LDA, and CCD image (center) of 1064 nm spontaneous emission of the actual LVIS IIIb slab.

Results:

We have some preliminary measurements of performance for LVIS IIIb. Figure 5 gives the single pass gain vs. LDA temperature while running at 20 Hz. There are 2 distinct peaks visible which can be used to an advantage. There are two 5-bar LDAs on the LVIS III head and each peak in the plot corresponds the different 809 nm emission temperatures for each stack. Our peak efficiency may be slightly reduced but the operating temperature range is increased, which is also important for aircraft based transmitters. We have long pulse lasing performance figures as of writing this paper. Figure 6 shows the pump pulse and output pulse using a +20 cm and -10 cm radii of curvature concave-convex cavity of 20 cm geometrical length, with the +20 cm radius mirror being the output coupler with reflectivity 60%. The energy is about 10 mJ per pulse, multimode. On the basis of experience with other similar lasers, we project a TEM_{∞} Q-switched output energy of ~ 3.5 mJ. This output is at 20 Hz repetition rate and 200 ms pump pulse. When operating at 250 Hz and 2 % diode duty cycle, which limits the pump pulse to 80 ms, a 1.7 mJ TEM_{∞} Q-switched output is projected. Note: All

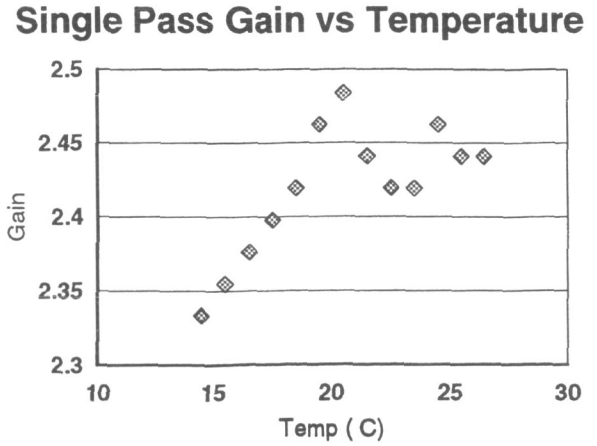


Figure 5. Plot of single-pass G_o vs. Temp for the LVIS IIIb laser head and two 5-bar LDAs, operated at 30 W/bar. Note: this is not the facet temperature, but the package temperature. As the LDA frequency and power is increased, these peaks will move to the left due to higher facet temperatures.

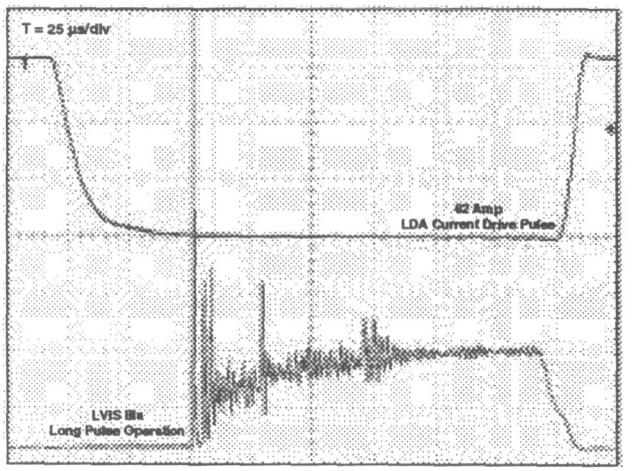


Figure 6. Oscilloscope trace of LDA current pulse and a long pulse output of a concave-convex cavity. Pulse energies of 11 mJ were achieved with multi-mode operation. Single-mode energies were 5.1 mJ.

data presented in this paper represents LDA powers of about 50 % of peak, due to the LDA's center wavelength dependence on temperature.

This work is being performed under a NASA Cooperative Agreement # CA-NCC-5-269 at The Goddard Space Flight Center's Laboratory for Terrestrial Physics. The authors wish to thank Dan Hopf and Gary Harris for their opto-mechanical expertise, without which this work could not succeed.

References:

Armandillo, E., Norrie, C., Cosentino, A., Laporta, P., Wazen, P. and Maine, P. (1997). Diode-pumped high-efficiency high-brightness Q-switched Nd:YAG slab laser. Opt. Lett. 15, **22**, 1168-1170..

Baer, T. M., Head, D. F., Gooding, P. (1990). High efficiency diode pumping of Nd:YLF. CLEO.

Beach, R. J. (1996). Theory and optimization of lens ducts. Appl. Opt. 12, **35**, 2005-2015.

Bernard, J. E. and Alcock, A. J. (1992). High- efficiency diode-pumped Nd:YVO_4 slab laser. Opt. Lett. **16**, 1850.

Blair, J. B., Coyle, D. B., Bufton, J. L., and Harding, D. J. (1994). A modified airborne laser altimeter for measurement of vegetation structure. IGARSS Proceedings.

Blair, J. B. and Coyle, D. B. (1996). Vegetation and topography mapping with an airborne laser altimeter using a high-efficency laser and a scanning field-of-view telescope. 2nd International Airborne Remote Sensing Conference.

Blair, J. B., Harding, D. J., and Coyle, D. B. (1996). Using laser echo recovery and a scannable field-of-view telescope to determine vegetation structure and sub-canopy topography over wide swaths, (LVIS). IGARSS.

Brioschi, F., Nava, E. and Reali, G. C. (1992). Gain shaping and beam quality in diode-laser multiarray side-pumped solid-state lasers. IEEE J. Q. E., 4, **28**, 1070-1074

Chesler, R. B. and Maydan, D. (1972). Convex- concave resonators for TEM_{00} operation of solid-state ion lasers. J. Appl. Phys. 5, **43**, 2254-2257.

Coyle, D. B. and Blair, J. B. (1993). Development of a diode-pumped, sharp-pulsed Nd:YAG laser for sub-meter resolution (SUMR) altimetry, CLEO **11**, 14.

Coyle, D. B. and Blair, J.B. (1995). Development of a Q-switched/cavity dumped sharp pulsed laser transmitter (SPLT) for airborne altimetry", OSA Proceedings of Advanced Solid State Lasers, **24**.

Coyle, D. B. Guerra, D. V., and Kay, R. B. (1995). An interactive numerical model of diode-pumped, Q-switched/cavity-dumped lasers. J. Appl. Phys. **28**, 452-62.

Hanson, J. and Haddock, D. (1988). Laser diode side pumping of neodymium laser rods. Appl. Opt., 1, **27**, 80-83.

Morris, P. J., Luthy, W., and Weber, H. P. (1993). High-intensity rectangular fiber-coupled diode laser array for solid state laser pumping.

SDL Inc. (1996). Product Catalog, 59-72.

Calculations of Multiple Scattering-Induced Errors in the GLAS Mission

David P. Duda
Universities Space Research Association
NASA Goddard Space Flight Center, Code 912, Greenbelt, MD 20771 USA
Phone: (301) 286-5495, FAX: (301) 286-1762, E-mail: David.P.Duda.1@gsfc.nasa.gov

James D. Spinhirne
Laboratory for Atmospheres
NASA Goddard Space Flight Center, Code 912, Greenbelt, MD 20771 USA

Edwin W. Eloranta
Space Science and Engineering Center, University of Wisconsin - Madison
1225 West Dayton Street, Madison, WI 53706 USA

1. Introduction

The Geoscience Lidar Altimeter System (GLAS) is a laser altimeter designed to measure temporal changes in the topography and mass balance of the Earth's ice sheets. GLAS is scheduled to be launched as part of the Earth Observing System (EOS) in 2001. Due to the large pulse width of GLAS and the slope (and roughness) of the ice sheets, the mean elevation of the laser's surface spot will be estimated from the centroid of the return pulse. While the accuracy of individual altimetry measurements is expected to be 15 cm, a cross-over technique that averages the elevation differences at selected points on the ice sheets will allow GLAS to detect mean ice elevation changes as small as 2 cm per year.

One factor that may degrade the proposed accuracy of the altimeter measurements is the effect of multiple scattering by thin clouds and aerosols over the ice sheets. In the return pulse, some photons from the lidar are slightly deflected by cloud particles but still return to the instrument detector. Since these photons travel a longer path than photons that pass directly to and from the surface, the mean travel time of the pulse is lengthened and the centroid of the return pulse is shifted toward a later time.

This study intends to determine the importance of this source of altimetry error in the GLAS measurements. Two methods will be used to estimate path delays in the GLAS lidar for a range of cloud conditions. An analytic expression of a doubly scattered return signal (Eloranta, 1972) will be compared to Monte Carlo simulations that estimate path delays by cloud, aerosol and molecular scattering. The results from both methods will be discussed in relationship to current knowledge of Arctic cloud climatology, and the impact of multiple scattering on GLAS altimeter measurements will be evaluated.

2. Analytic Model

Eloranta (1972) developed a lidar transfer equation to simulate the doubly scattered return of a lidar pulse. Figure 1 shows a schematic of the analytic model. Photons are assumed to be scattered only once in the atmosphere before returning to the lidar receiver. For a doubly scattered return, the additional path length (ζ) caused by the cloud scattering can be approximated as

$$\zeta = \frac{z\Theta_s^2}{2} \tag{1}$$

where z is the height of the scatterer and Θ_s is the scattering angle. By using diffraction theory to compute the mean scattering angle of the cloud particles and integrating the path delay over the field of view (FOV) of the lidar receiver, the mean path delay ($\bar{\zeta}$) of the doubly scattered return can be estimated as

$$\bar{\zeta} = \frac{z\langle\Theta_s^2\rangle}{2} - \exp\left[-\frac{(\tan^{-1}(\frac{c}{z}))^2}{\langle\Theta_s^2\rangle}\right] \times \left(\frac{z(\tan^{-1}(\frac{c}{z}))^2}{2} + \frac{z\langle\Theta_s^2\rangle}{2}\right) \tag{2}$$

where $\langle\Theta_s\rangle$ is the mean scattering angle (a function of particle size), z is the mean cloud height, and c is the distance at the surface from the lidar axis to the edge of the detector FOV ($c = 0.5 \times FOV \times$ (height of lidar)).

Figure 2 shows a plot of the mean path delay as a function of particle radius and mean cloud altitude for GLAS with a detector FOV of 350 μrad (the

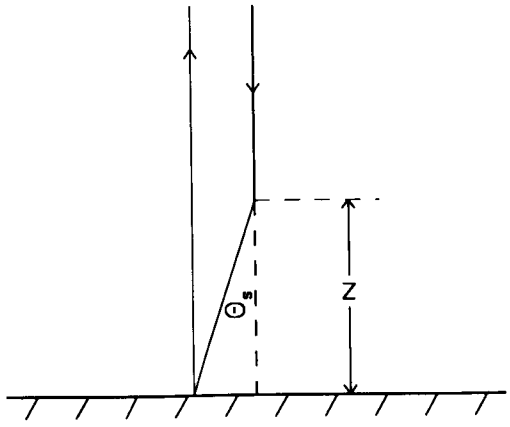


Figure 1: Schematic of double scattered return in Eloranta's analytic model.

nominal FOV of GLAS). The results show the greatest delays for low-level clouds composed of particles less than 50 microns in radius. Since such clouds are common in the Arctic, it is anticipated that significant path delays would also be common in the GLAS measurements.

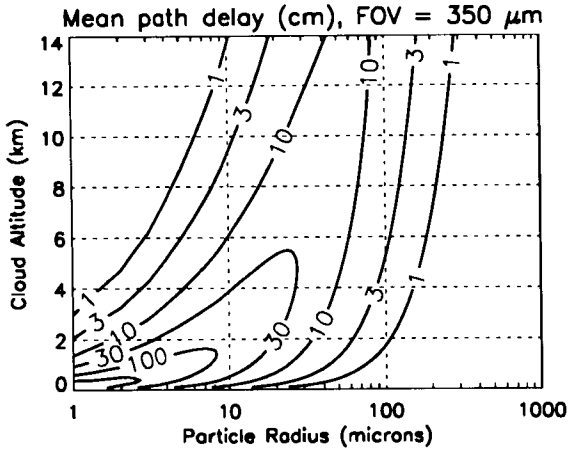


Figure 2: Mean GLAS lidar path delay derived from Eloranta (1972) as a function of mean cloud height and cloud particle size.

3. Monte Carlo Model

Estimates of mean path delays were also computed from Monte Carlo simulations of the GLAS lidar. The model used in the calculations was from Spinhirne (1982). The lidar was located 600 km above the surface in the model. The simulated lidar pulse was assumed to have a normal distribution of intensity with a pulse width (2σ) of 10 nanoseconds and a Gaussian-shaped beam divergence (2σ) of 100 μrad. The Monte Carlo model included Rayleigh scattering, aerosol properties derived from measurements by Spinhirne et al. (1980), and ice cloud optical properties. The cloud properties were computed from Lorenz/Mie scattering theory for gamma distributions of ice spheres with effective radii from 2 to 200 μm. A series of simulations were run assuming homogeneous clouds with a physical depth of 750 m and cloud tops at heights ranging from 0.750 to 8 km above the surface. The visible optical depths of all clouds was 0.5. The surface albedo was Lambertian and set to 0.30. For clouds with large particle sizes, the Monte Carlo calculations required several million photons because of the extremely sharp and narrow diffraction peak associated with the ice particles.

A typical simulated return pulse is shown in Figure 3. The most obvious effects of multiple scattering are evident in the tail of the distribution, but for clouds with small particles, even the peak of the return pulse lags slightly.

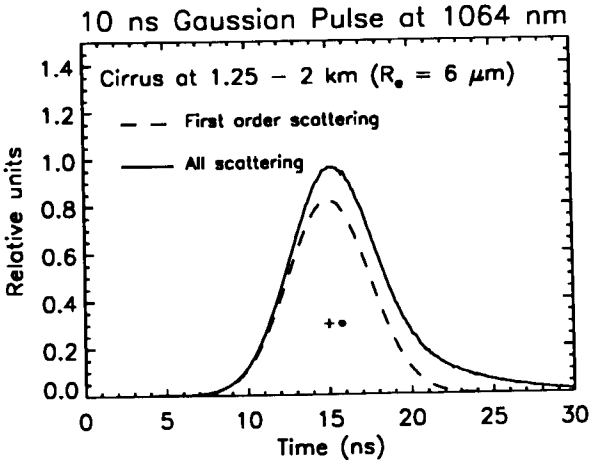


Figure 3: Plot of a typical simulated GLAS return pulse as function of time. The dashed line shows the singly-scattered part of the pulse, while the solid line shows the entire return. The centroid of the singly-scattered part of the pulse is shown as a plus sign, and the filled circle indicates the centroid of the entire pulse after truncation at 25 ns.

The results of the simulations are shown in Figure 4. To minimize ranging errors, the mean path delay was determined by computing the centroid of the return pulse truncated at 10 ns after the expected peak. The aerosol optical depth of the atmosphere was set to zero to match the conditions in

the analytic model more closely, although the Monte Carlo model still includes the effects of Rayleigh scattering.

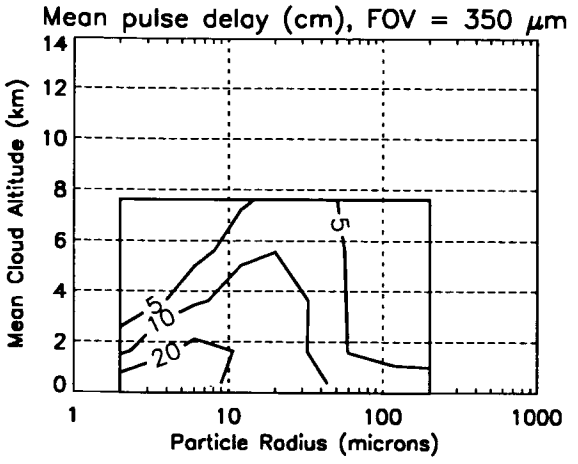


Figure 4: Mean GLAS lidar path delay derived from Monte Carlo simulations as a function of mean cloud height and cloud particle size.

4. Discussion

The results from the analytic model show a broad qualitative agreement with those from the Monte Carlo simulations, although the path delays in the Monte Carlo simulations are smaller due to the truncation of the simulated pulse returns. The agreement between the shapes of the path delay curves in Figures 2 and 4 is consistent with the expectation that the truncation of the pulses in the Monte Carlo simulations would eliminate most of the triple and higher-order scattered photons.

Since the path delays will depend on the height and the microphysical properties of the clouds, past surveys of Arctic cloudiness suggest that the path delay effects will vary both seasonally and spatially in response to changes in Arctic cloud cover. Curry et al. (1996) have reviewed several climatologies of cloud fraction over the Arctic. They note that cloud surveys based on surface observations show a seasonal cycle in cloudiness, with a maximum cloud cover as high as 90% during the summer and a minimum of 40 to 68% in the winter. In addition, during wintertime low-level ice crystal precipitation (diamond dust) is present 20 to 50 percent of the time during otherwise clear-sky conditions. Satellite climatologies of Arctic cloud fraction generally detect a smaller cloud fraction than surface observations, but they also show a similar seasonal cycle.

Curry et al. (1996) also report that summertime Arctic stratus have mean radii on the order of 2 to 7 microns, while the most comprehensive measurements of wintertime ice crystal distributions show modal radii between 10 to 80 μm, and an average effective radius of 40 microns for lower-tropospheric ice crystals. Considering the small particle sizes in summertime cloudiness, the path delays would be as large as 10 to 20 cm for low (1 to 2 km in height) stratus, while in the wintertime the delays would be 5 to 10 cm. Greater errors are expected for clouds with larger optical thicknesses. Given the difference between winter and summer Arctic cloudiness, it is likely that seasonal variations in ranging errors will have to be accounted for in the GLAS altimetry retrievals.

One problem that will complicate the correction of GLAS measurements is the lack of comprehensive information on Arctic cloud climatology. Even satellite determinations of polar cloudiness are difficult due to the low surface temperatures and solar illumination. Since the results shown above represent only a small portion of possible polar cloud conditions, more cases are to be studied. In particular, Monte Carlo simulations are planned for different cloud particle shapes and for multi-layer clouds.

Acknowledgments: This work is supported by USRA contract NAS5-32484.

REFERENCES

Curry, J. A., Rossow, W. B., Randall, D., and Schramm, J. L. (1996). Overview of Arctic cloud and radiation characteristics. *J. Clim.*, 9:1731-1764.

Eloranta, E. W., (1972). Calculation of doubly scattered lidar returns. Ph. D. thesis, University of Wisconsin.

Spinhirne, J. D., Reagan, J. A., and Herman, B. M. (1980). Vertical distribution of aerosol extinction cross section and inference of aerosol imaginary index in the troposphere by lidar technique. *J. Appl. Meteor.*, 19:426-438.

Spinhirne, J. D., (1982). Lidar clear atmosphere multiple scattering dependence on receiver range. *Appl. Opt.*, 21(14):2467-2468.

SLR2000: A MICROLASER-BASED SINGLE PHOTOELECTRON SATELLITE LASER RANGING SYSTEM

John J. Degnan and Jan F. McGarry
Code 920.3, NASA Goddard Space Flight Center, Greenbelt, MD 20771 USA
Phone: 1-301-286-8470; FAX: 1-301-286-0213; Email:JJD@LTPMAIL.GSFC.NASA.GOV

SLR2000 is an autonomous and eyesafe satellite laser ranging (SLR) station with an expected single shot range precision of about one centimeter and a normal point (time-averaged) precision better than 3 mm[1]. The system will provide continuous 24 hour tracking coverage for a constellation of over twenty artificial satellites. Replication costs are expected to be roughly an order of magnitude less than current operational systems, and the system will be about 75% less expensive to operate and maintain relative to manned systems. Computer simulations have predicted a daylight tracking capability to GPS and lower satellites with telescope apertures of 40 cm and have demonstrated the ability of our current autotracking algorithm to extract mean signal strengths below .001 photoelectrons per pulse from daytime background noise.

The dominant cost driver in present SLR systems is the onsite and central infrastructure manpower required to operate the system, to service and maintain the complex subsystems, and to ensure that the transmitted laser beam is not a hazard to onsite personnel or to overflying aircraft. To keep development , fabrication , and maintenance costs at a minimum, we adopted the following design philosophies: (1) use off the shelf commercial components wherever possible; this allows rapid component replacement and "outsourcing" of engineering support; (2) use smaller telescopes (<50 cm) since this constrains the cost, size, and weight of the telescope and tracking mount; and (3) for low maintenance and failsafe reliability, choose simple versus complex technical approaches and, where possible, use passive techniques and components rather than active ones. Adherence to these philosophies has led to the SLR2000 design described here.

A block diagram of the SLR2000 system is shown in Figure 1. SLR2000 consists of seven major subsystems: *(1) Time and Frequency Reference Unit; (2) Optical Subsystem; (3) Tracking Mount; (4) Correlation Range Receiver; (5) Meteorological Station; (6) Environmental Shelter with Azimuth Tracking Dome; and (7) Real-Time System Controller.*

The purpose of the ***Time and Frequency Reference*** is twofold: (1) to provide accurate on station epoch timing to simplify and accelerate the acquisition and tracking of the satellite targets; and (2) to provide an accurate frequency source for the pulse time-of-flight measurements. The Hewlett Packard Model HP58503A GPS Time and Frequency Reference Receiver has been selected to serve as the prototype station clock and frequency reference for SLR2000. The unit uses timing information from the Global Positioning System (GPS) constellation of satellites to automatically constrain the long term frequency drift in a crystal oscillator, which has excellent short term stability.

The ***Optical Subsystem*** consists of a 40 cm off-axis parabolic reflector telescope and associated transmit/receive optics, a passively Q-switched, frequency-doubled Nd:YAG microlaser operating at 2 KHz, a start detector, a photon-counting quadrant microchannel plate stop detector for simultaneous ranging and subarcsecond angle tracking, a CCD camera for automated star calibrations, and spectral and spatial filters to reduce the daylight background noise. The quadrant stop detector lies behind the telescope focal plane so that the incoming reflected laser energy and background noise is spread over the four quadrants, allowing estimation of the position of the satellite in the receiver field of view by the correlation range receiver. During star calibrations, collimated starlight is focused by a lens onto an Electrim Model EDC-1000M CCD array which measures the position of the star and provides pointing error information to the system computer for periodic mount modelling and pointing verification. The array is also used to periodically check and verify accurate system focus by minimizing the star spot diameter.

To achieve eyesafety at the exit pupil of the telescope, the laser pulse energy is reduced by almost three orders of magnitude relative to current systems (from 100 mJ to 133 μJ) and the transmit beam is magnified to fill the

available telescope aperture (40 cm). To compensate for this factor of 1000 reduction in signal strength , the repetition rate is increased from a nominal 5 Hz to 2 KHz (x 400) and the transmitter beam divergence is reduced from a nominal 25 arcseconds to about 10 arcseconds (x 6). The signal is extracted from the noise background using post-detection Poisson filtering. To attain the same ranging accuracy, pulsewidths comparable to modelocked lasers must be maintained. All of the laser specifications can be met by a passively Q-switched microlaser, which is an exceedingly simple, highly reliable, and extremely small device (on the order of a few mm in length) and operates in a TEM_{00} mode.

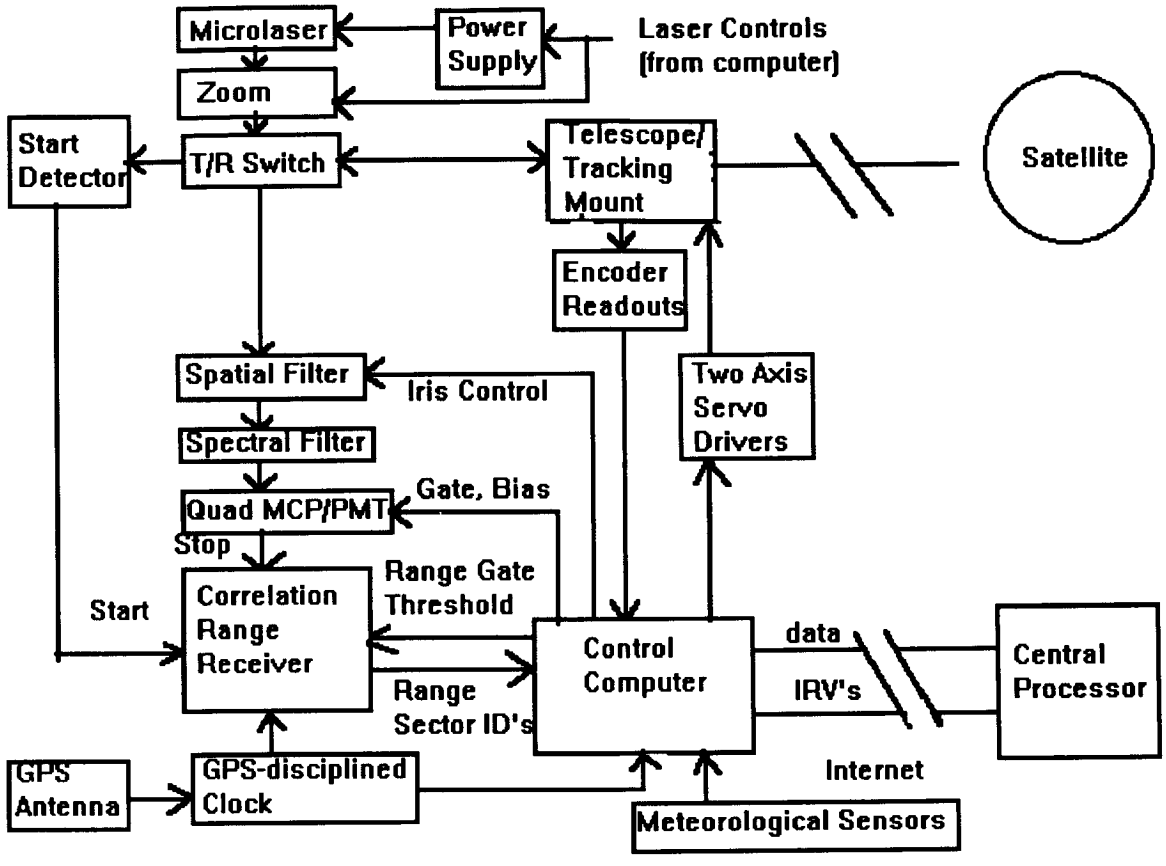


Figure 1: Simplified block diagram of the SLR2000 system.

Like the microlaser transmitter, the ***correlation range receiver*** (CRR) must also operate at KHz rates. All timing outputs from the CRR (starts, stops, and noise events) within a given range gate are transferred to the SLR2000 ranging computer which assigns them to "time bins". Signal counts from the satellite are bunched in a narrow time interval whereas dark current or background noise counts are spread over the full width of the range gate. The number of pulses over which the returns are counted is determined by the "frame interval". If the frame interval is too long, more noise collects in the bins, and the signal itself may eventually spill into an adjacent bin due to imperfect orbit predictions or onsite time bias. If the frame time is too short, there may be not enough signal returns to adequately discriminate against the noise background. When the bin width and frame interval are correctly chosen, the satellite returns will all fall within a single bin, resulting in a count that is significantly larger than the other bins. Following the filtering of noise counts based on time of arrival by this postdetection Poisson filter, a subarcsecond pointing angle correction can be computed by adding or subtracting the residual counts in each quadrant since the CRR also identifies which of the four quadrants the timing signal came from.

The SLR2000 ***Simulator*** permits testing of autotracking algorithms prior to hardware development. It models the relevant errors in the timing, tracking, receiver, laser and environment. The outer shell of the program keeps track of which returns are signal and which are noise and is therefore able to correctly assess the performance of the autotracking algorithms. Output is displayed in the form of an Observed minus Calculated (O-C) plot of the range data. Figure 2 shows the Correlation Range Receiver Single Frame Algorithm performance for a daylight pass of the LAGEOS satellite. Small dots indicate noise and darker squares are signal. Due to unmodellable errors in the mount pointing as well as small orbit prediction errors, the autotracking algorithm must first search for the satellite by scanning angularly. During the first 70 seconds, the system conducts a spiral scan searching outward from the satellite's predicted position which the simulator purposely caused to be in error by about a beamwidth. It is important to note that during this period the algorithm does not mistake noise for signal. Once the algorithm finds satellite returns, it calculates the required biases to both center the range returns in the window and the laser beam on the satellite. The CRR acquires the signal quickly following initial illumination of the target about 75 seconds into the pass, recognizes and corrects for a range bias of 0.5 μsec to center the signal in the gate, and continually narrows the width of the range gate from an initial value of ± 1 μsec until the background noise is nearly eliminated 140 seconds into the pass.

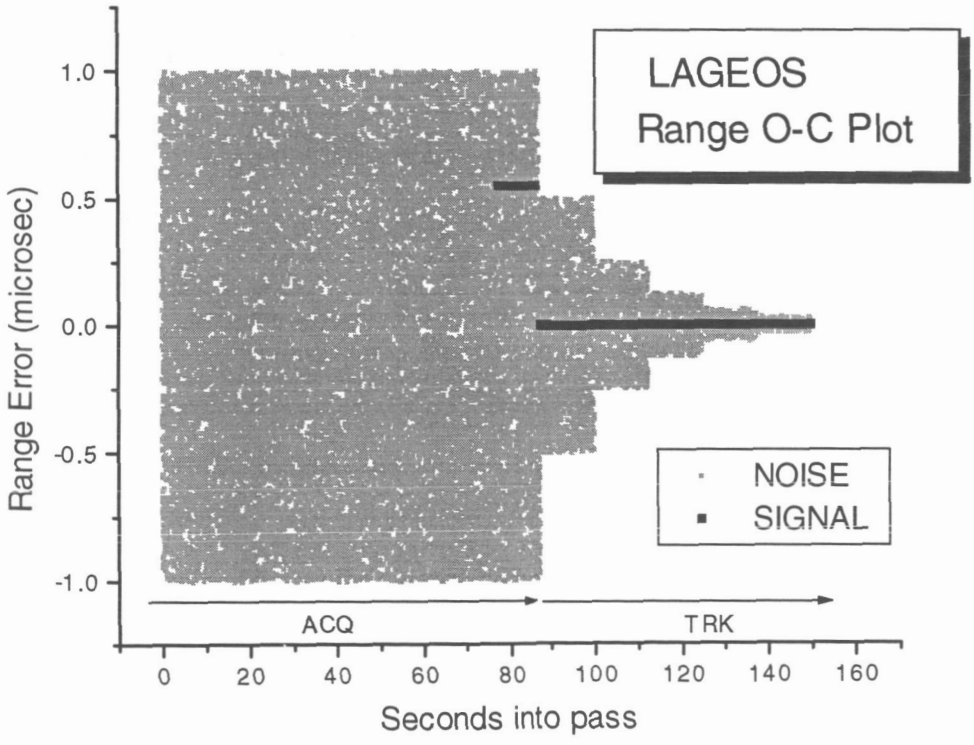


Figure 2: Simulated performance of SLR2000 acquiring the LAGEOS satellite in full daylight at an elevation angle of 20 degrees.

The telescope is mounted in the Aerotech Model AOM360-D ***tracking mount*** driven by direct-drive DC torque motors. The absence of gear trains and other drive mechanisms eliminates position error contributions due to mechanical hysteresis and backlash. The mount has a high axis positioning accuracy of one arcsecond, a bidirectional repeatability to one arcsecond, and a low axis wobble, also at the few arcsecond level. The use of Inductosyns, rather than optical encoders, for angle sensing allows the laser beam to be passed from the transceiver to the telescope through the center of the azimuth and elevation drive bases via a Coude system.

The SLR2000 ***controller*** consists of three Pentium-based processors, two UNIX-based processors in a VME backplane and the third in a PC/ISA crate. The VME bus was chosen for its higher bus speed (40MB/sec), while the ISA bus was needed to handle specialized interface cards for key components. The ISA computer functions as an Input/Output processor, passing data to and from the VME computers via shared memory. The VME processors perform all of the decision making, data analysis, and external communication. One of these processors, the "Pseudo-Operator", performs the functions of a human operator, making decisions on whether the weather permits opening the dome and tracking, which satellite should be tracked, and whether the returns in the ranging window are signal or noise. The Pseudo-Operator also acts to protect the system if it detects system health or safety problems. The second VME processor, called the Analysis CPU, processes and exchanges range and orbit prediction data with the central network archive. Human interaction with the SLR2000 system requires communicating with the Analysis CPU through the internet. A laptop PC running a special software package will allow personnel to monitor the operation of the system via graphical displays, get information from the system to analyze off-line, run diagnostic tests, and change system parameters.

The ***meteorological subsystem*** consists of four major components. A Paroscientific MET3-1477-001 Pressure, Temperature, and Relative Humidity Monitor measures pressure, temperature, and relative humidity with the requisite accuracy for supporting atmospheric models used in applying the atmospheric correction in subcentimeter laser ranging. The Belfort 200 Wind Monitor measures wind speed and direction. The Vaisala FD12P Precipitation and Visibility Sensor monitors the presence, type, and accumulation of various forms of precipitation (rain, snow, etc.);as well as local visibility out to 50 Km. Finally, an Inframetrics Thermasnap™ camera, containing an uncooled silicon thermoelectric IR detector array operating between 8 and 12 microns, is placed above a convex security mirror overcoated with gold in order to photograph the full sky cloud cover, day or night, down to 30 degrees elevation in a single frame. Each pixel senses the temperature of the sky within its field of view. Low lying cumulus cloud temperatures tend to follow the lapse rate with altitude and hence are at significantly higher temperatures (10-20°C) than the higher cirrus or clear sky backgrounds. The resulting "cloud mask" , combined with the wind, visibility, and precipitation sensors, assists the software "pseudo-operator" in deciding whether or not to open the observatory dome and begin laser operations. Based on cloud distribution, the "pseudo-operator" can also decide which satellites to track and over what portions of the orbit.

The SLR2000 system is protected by an ***environmental shelter and azimuth tracking dome***. The 2.5 meter diameter dome has a motorized open slit (shutter) and azimuth drive. Both are under computer control and the dome azimuth drive is slaved to the tracking mount azimuth. The electronics room is thermally isolated from the open dome area and maintained at nominal room temperature by an external heat pump. This stabilizes the temperature of critical elements in the optical transceiver and timing electronics and provides a comfortable workplace for visiting maintenance personnel. Outside ambient air and heated air from the electronics room are dehumidified and mixed to maintain the telescope near ambient when the dome is closed. Inexpensive security devices automatically detect and report threats to system security, via Internet and/or recorded phone messages. These include motion and intrusion sensors and surveillance cameras for detecting and reporting unauthorized personnel in the vicinity, thermal sensors for detecting heat pump failure, power/voltage monitors, etc. Key security components, such as the computer and selected sensors, are protected by UPS, and the safe default mode for key subsystems will be "Power Off" in the event of a power failure.

Clearly, many of the subsystems and software packages being developed for SLR2000 have applicability to remotely operated or autonomous lidars. High repetition rate microlasers and high sensitivity correlation receivers may also find application in the next generation of spaceborne altimeters where there is a need for greater spatial resolution and improved power efficiency and reliability.

REFERENCE

1. J. J. Degnan and J. F. McGarry, "SLR2000: Eyesafe and autonomous single photoelectron satellite laser ranging at kilohertz rates", in Laser Radar Ranging and Atmospheric Lidar Techniques, SPIE Vol. 3218, pp. 63-77, 1997.

The Detection of Clouds, Aerosols and Marine Atmospheric Boundary Layer Characteristics from Simulated GLAS Data

Stephen P. Palm
Science Systems and Applications Inc.
5900 Princess Garden Parkway. Lanham, Maryland 20706 USA
Phone: (301)286-4277 Fax: (301)286-1762 E-mail: spp@virl.gsfc.nasa.gov

James D. Spinhirne
Laboratory for Atmospheres, Code 912, NASA Goddard Space Flight Center
Greenbelt, Maryland 20771 USA

1 Introduction

Scheduled for launch in 2001 as part of NASA's Earth Observing System (EOS), the Geoscience Laser Altimeter System (GLAS) will provide continuous laser sounding of the earth's atmosphere from space for the first time. From its polar orbit about 600 km above the surface, GLAS will employ a 40 Hz solid state laser operating at 1064 nm to measure topography to an accuracy of 10 cm. Simultaneously, the atmospheric channels (1064 and 532 nm) of GLAS will provide profiles of atmospheric backscatter from 40 km to the ground with 75 meter vertical resolution (Spinhirne and Palm, 1996). These measurements will give scientists an unprecedented global data set on the vertical structure of clouds and aerosols which will greatly aid research efforts aimed at understanding their effects on climate and their role in climate change (Hartman, 1994).

To better understand and predict the performance of the GLAS atmospheric channels, a computer model was developed to simulate the type of signal that the instrument would likely produce. The model uses aircraft lidar data and provides realistic simulated GLAS data sets over large areas spanning a wide range of atmospheric conditions. These simulated GLAS datasets are invaluable for designing and testing algorithms for the retrieval of parameters such as cloud and aerosol layer height, optical depth and extinction cross section. This work is currently proceeding and in this paper we will present results of the cloud and aerosol detection algorithm with emphasis on the detection of Marine Atmospheric Boundary Layer (MABL) aerosol. In addition, we use a recently developed technique to ascertain the feasability of estimating MABL moisture and temperature structure from spaceborne systems such as GLAS.

2 Model Description

The GLAS Atmospheric Lidar Simulator (GALS) is a C program which produces simulated lidar data from an altitude of 40 km to the ground based on a series of input parameters which define the lidar transmitter and receiver characteristics. The details of the model are too numerous to describe at length and only a brief summary is given here. The simulations are based on lidar data from the high altitude ER-2 Cloud and Aerosol Lidar System (CALS) (Spinhirne et al. 1982, 1983, 1996). The CALS data sets are ideal for this purpose since they include the whole troposphere and lower stratosphere and cover very large distances. Analized data sets of attenuated backscatter cross section (βT^2) have been computed from numerous flights of the CALS system during the Tropical Ocean Global Atmosphere Coupled Ocean Atmosphere Response Experiment (TOGA COARE) and Central Equatorial Pacific Experiment (CEPEX). The background radiation (for day simulations) is based on simultaneous measurements from the MODIS Airborne Simulator (MAS) which also flew onboard the ER-2. This assures accurate and representative background values for the daytime simulations.

Table 1 lists the major input parameters to the program and their values for the current GLAS instrument configuration. The detector specifications are currently somewhat uncertain, but existing technology will provide quantum efficiencies approaching 70 percent. The green channel will use photon counting detectors, while the 1064 channel will use a solid state Avalanche Photo Diode (APD). This means that the green channel will be much more sensitive than the IR channel and will provide the highest quality data for aerosols and optically thin clouds. The high sensitivity of the 532 channel comes with a price, however.

It will be subject to saturation especially during the day with high background values. In an effort to circumvent this, GLAS will employ eight seperate photon counting detectors with each one receiving one eighth of the total incoming signal. This approach should keep most of the GLAS signals below the saturation value except for instances of optically thick clouds and high background values. When saturation does occur, the 532 signal can be computed from the 1064 channel. Thus, the occasional saturation of the 532 channel is not expected to present a problem.

The use of an efficient, very narrow band optical filter is critical to the performance of the system during daylight operation. The width of the optical filter, together with the telescope field of view determines the amount of background induced noise caused by ambient light. A sufficiently narrow optical filter will also help to keep the photon counting channel from reaching saturation during daytime operation. Based on results from GALS, it was determined that a filter width of 0.030 nm or less is required to insure adequate signal to noise for the daytime measurements. An example of a nighttime simulation produced using the specifications in Table 1 is shown in Fig 1.

The horizontal resolution of Fig 1 is 700 m (4 shot average). Plainly seen in the figure are cirrus clouds between 0 - 150 km along track, thicker mid-level clouds between 550 and 700 km, and the elevated aerosol backscatter associated with the MABL mainly between 100 and 550 km. This indicates that GLAS will successfully profile thin cirrus and typical MABL aerosol at sub-kilometer resolution.

3 Cloud and Aerosol Detection

Using the simulated GLAS data sets produced by the GALS, we have begun the development of rigorous, highly automated and reliable algorithms with which to process the GLAS data as it down-linked from the satellite. The objective is construct a set of algorithms which will produce near-real time retrievals of multiple cloud and aerosol layer heights (top and bottom), cloud and aerosol optical depth, backscatter and extinction profiles and boundary layer height. These products, together with color image cross sections of the data, will be available to researchers from a centralized data archival and distribution center most likely located at NASA Goddard. One of the most fundamental and important retrievals for any spaceborne lidar is the detection of cloud and aerosol layer heights. One promising approach to this problem utilizes an edge detection scheme which uses as input a cross sectional image of simulated GLAS data such as is shown in Fig 1. The algorithm breaks the image up into small, overlapping square boxes 12 pixels wide. Inside each box, the data is searched for edges by performing a series of statistical tests. The technique is based upon an edge detection technique originally developed for computer vision by Suk and Hong (1984). Applying the algorithm to the image in Fig 1 results in the detection of the cloud edges and MABL aerosol boundaries as shown in Fig 2. In general, this technique works very well with most clouds and MABL aerosol, but has difficulty with thin cirrus and very clean (optically thin) boundary layers.

4 MABL Characteristics

Recently, it has been shown that high resolution aircraft lidar data combined with infrared radiometer measurements of sea surface temperature can be used to derive the moisture and temperature structure of the MABL over tropical and subtropical oceans (Palm et al 1998). Such measurements would be of

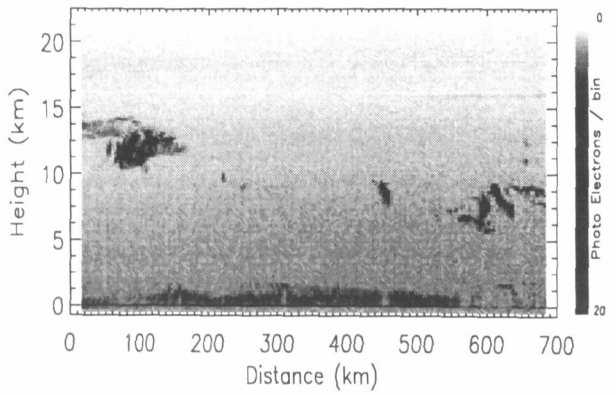


Figure 1: Example of output from the GALS program showing cloud and MABL structure over the tropical Pacific.

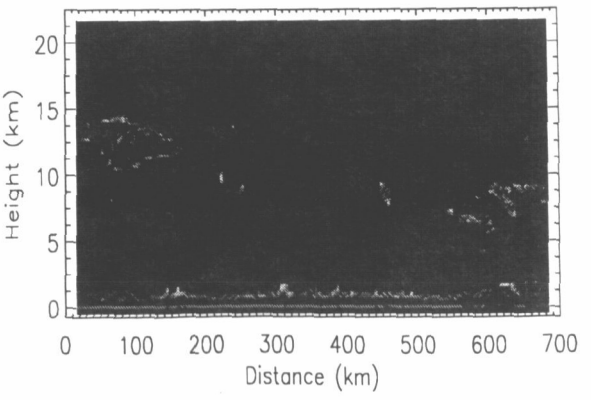


Figure 2: Cloud and MABL aerosol boundaries as retrieved by the edge detection algorithm for the simulated GLAS data shown in Fig 1.

great value if they could be made from a spaceborne system such as GLAS. There are three things which are critical to the technique: Sea Surface Temperature (SST), Lifting Condensation Level (LCL) and statistics on the height of the MABL. The later two can be derived from the lidar data, while the SST is obtained from orbiting infrared radiometers such as AVHRR (or in this case in-situ measurements). After retrieval of the MABL height from the edge detection algorithm, the LCL is determined from the MABL height data by first segregating the heights according to clear or cloudy. This is done by searching for a ground return for each MABL height. If a ground return is not found, then a MABL cloud is assumed. An example is shown in Fig 3. This represents all the MABL heights for the 700 km data segment shown in Fig 1. The LCL is defined as that height where 95 percent of the cloud top heights occur above and 5 percent occur below that level. The bulk MABL moisture is then derived from the height of the LCL (825 m) and an estimate of the near-surface air temperature. The later is assumed to be 0.8 ^oC less than the SST (which in this case, was measured by buoy and low-level aircraft flights as 29 ^oC).

Once the bulk MABL moisture is estimated, a profile of moisture and potential temperature can be contructed based on the statistics of the vertical distribution of MABL height. Details of the technique can be found in Palm et al, 1998. Figure 4 shows the retrieved profiles of mixing ratio and potential temperature (dashed) plotted with a radiosonde which was launched about 600 km southeast of the lidar flight track at 00 GMT, 1/8/93. This was the closest sounding to the ER-2 flight track which was launched from a research vessel (as opposed to an island radiosonde launch). The lidar data was acquired between 23:40 GMT, 1/7/93 and 00:20 GMT, 1/8/93. The lidar retrieved moisture and temperature agree well with observed values, except for close to the surface and between 500 and 800 m. The radiosonde indicates a shallower well-mixed layer and a large gradient of moisture in the surface layer (0-100 m). The difference in well mixed layer height could be due to the poor co-location of the radiosonde with respect to the lidar data.

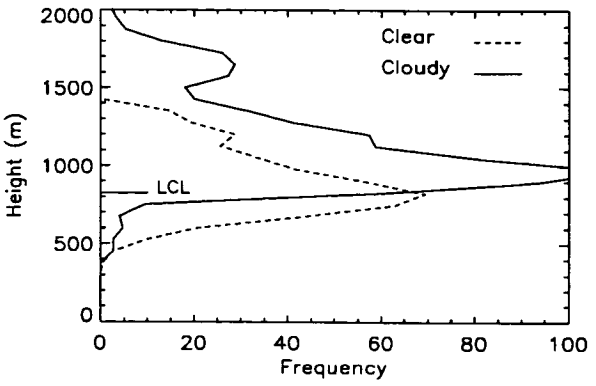


Figure 3: Lidar-derived MABL height frequency, segregated into clear (dashed) and cloudy. The LCL is shown at 825 m.

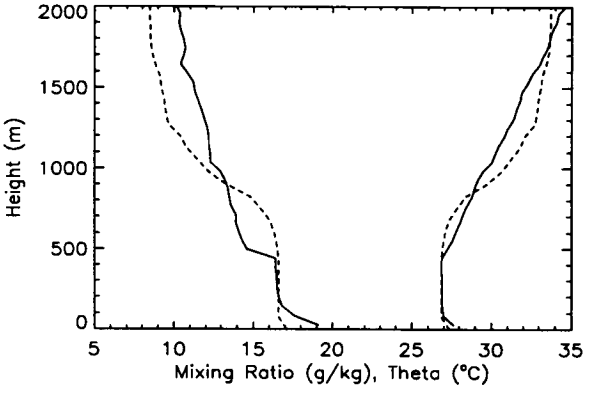


Figure 4: Lidar-derived profiles of mixing ratio and potential temperature (dashed) shown with observed radiosonde profile launched about 600 km east of the lidar flight track.

5 Summary and Conclusions

We have developed and used a model to simulate the expected GLAS atmospheric lidar performance for nighttime conditions. Using the simulated GLAS data, algorithms were designed and tested to retrieve cloud boundaries and MABL height using an edge detection approach. It was demonstrated that MABL height and cloud top and bottom height can be retrieved at sub-kilometer (700 m) horizontal resolution. This includes cirrus clouds and relatively clean (optically thin) MABL aerosol. We further demonstrated the feasability of retrieving the moisture and temperature characteristics of the MABL from simulated GLAS data. We conclude that similar measurements will be possible with actual GLAS data when it becomes available in the later half of 2001. These measurements, acquired on a global scale, will provide a significant advance in our ability to measure MABL characteristics and should be of great benefit to PBL research and numerical weather prediction models. Future work will include the generation of additional simulated GLAS data sets and the continued development and refinement of retrieval algorithms like the one presented here.

Table 1: Proposed GLAS system parameters.

Parameter	532 channel	1064 channel
Orbit Altitude	590 km	590 km
Laser Energy	36 mJ	73 mJ
Laser Beam Divergence	0.50 μ rad	0.50 μ rad
Laser Repetition Rate	40 Hz	40 Hz
Telescope Effective Diameter	97 cm	97 cm
Telescope Field Of View	150 μ rad	150 μ rad
Detector Quantum Efficiency	0.60	0.35
Detector Dark Current	$3.0\text{x}10^{-16}$	$50.0\text{x}10^{-12}$
RMS Detector Noise		$2.0\text{x}10^{-11}$ amps
Electrical Bandwidth	$1.0\text{x}10^{6}$	$1.0\text{x}10^{6}$
Optical Filter Bandwidth	0.030 nm	0.100 nm
Total Optical Throughput	0.33	0.30

6 References

Hartman, D. 1994: The Scientific Importance of GLAS Atmospheric Measurements. *The Earth Obs.*, **6**, pp 5-9.

Palm, S. P., D. Hagan, G. Schwemmer, and S. H. Melfi, 1998: Inference of Marine Atmospheric Boundary Layer Moisture and Temperature Structure using Airborne Lidar and Infrared Radiometer Data. *J. Appl. Meteor.* **37**, pp 308-324.

Spinhirne, James D, and S. Palm, 1996: Space Based Atmospheric Measurements by GLAS. *Selected Papers of the 18th International Laser Radar Conference (ILRC), Berlin,22-26 July 1996*, Springer-Verlag ISBN 3-540-61887-2 pp 213-216.

Spinhirne, James D, W. Hart and D. Hlavka, 1996: Cirus Infrared Parameters and Shortwave Reflectance Relations from Observations. *J. Atm. Sci.*, **53**, pp 1438-1458.

Spinhirne, James D., M. Hansen and J. Simpson, 1983: The Structure and Phase of Cloud Tops as Observed by Polarization Lidar. *J. Clim. and Appl. Meteor.*, **22**, pp 1319-1331.

Spinhirne, James D., M. Hansen and L. Caudill, 1982: Cloud Top Remote Sensing by Airborne Lidar. *Appl. Opt.*, **21**, pp 1564-1571.

Suk, M. and S. Hong, 1984: An Edge Extraction Technique for Noisy Images. *Computer Vision, Graphics and Image Processing*, **25**, pp 24-45.

Russian compact Lidar for NASA "Mars Surveyor Program 98"

A.V. Bukharin , V.M.Linkin , A.N.Lipatov , A.N. Lyash, V.S. Makarov, S.M. Pershin, A.V.Tiurin

Space Research Institute of Russian Academy of Sciences
117810 Profsoyuznaya st. 84/32, Moscow, Russia

Telephone (007-095) 333-3201, Fax 007-095-310-7023, e-mail: turin@mx.iki.rssi.ru

1.INTRODUCTION

Dust dynamic and atmosphere structure are the fundamental measurements required for the understanding of the dust storms evolution mechanism on the Mars. Daily and seasonally variation of the dust, haze and aerosol in the Mars atmosphere near the surface are frequently required in investigations of small dust storms. Dust is a crucial component of the Martian atmosphere at all times. Under the certain conditions, temperature gradients produced by the differential absorption of solar radiation can increase the wind and lead to raising of further large quantities of dust. Then, the dynamic of the aerosols and dust density in the layers over the Mars surface can be serve as a detectors before dust storms. Because of its general importance to solve the Martian dust storm mechanism, the detection and measurement of the vertical structure of the atmosphere near the surface and the dynamic of the dust, haze and aerosols density were advanced as a one of the fundamental goals of any lander on the Mars surface. It is well known that during the last Mars mission- the measurement of the vertical dust profile and its size distribution by sun limb sounding were very useful for improvement of the Martian atmospheric model (Moroz et al. 1991,[1]). But this technique cannot be used in lower, down the 5000m, atmosphere because of poor resolution and high dust [2] density. Backscattered light from groundbased pulsed Lidar has the potential to provide this and other information. To solve this problem, the miniature aerosol Lidar has been included in the scientific equipment of the meteorological complex of the Lander according to Mars Surveyor Program (MSP'98). The Lidar was developed by the Space Research Institute of Russian Academy of Sciences.

2. SCIENTIFIC OBJECTIVES

According to the Project schedule the Lander will be launched at 1998 December and will be landed on the planet surface near the South Pole (78°) at the beginning of the Mars summer [3].

The measurements of the Martian atmosphere parameters near the surface in South Pole region by using both an active and a passive remote sensing techniques are the scientific aims of the compact lidar device.

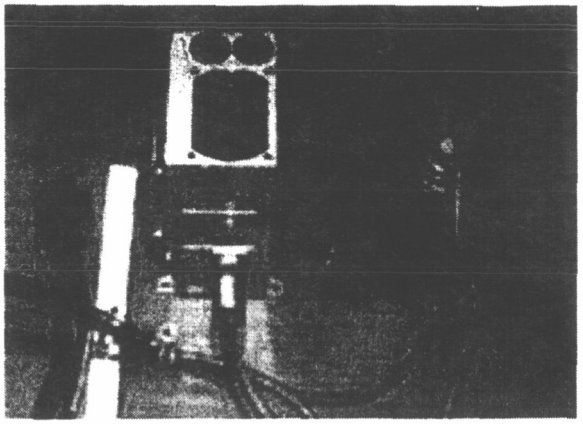
The scientific goals of the lidar are related to some fields of application: evolution of aerosols and stratification of the atmosphere, meteorology and environmental study. The main objective of lidar is to provide measurements of atmosphere parameters not attainable by other techniques, such as structure of near surface boundary layer and dynamic its scattering properties. These goals we may mentioned in the next priority:

- measurement of the daily and seasonally variability and dynamic of the vertical structure of the Martian atmosphere;
- detection of the cloud and fogs appearance;
- measurement of the incoming Solar radiation and its correlation with the atmosphere turbidity;
- measurement of the depolarization factor of the sky emission;

These observations are all well suited to our lidar.

3. INSTRUMENT DESCRIPTION

The instrument itself was designed and constructed under the philosophy of simplicity and reliability based on the standards and environment by R.Zurek (1996) for Mars-98 mission [3]. The main features are the using the full solid state elements and only digital exchange circuits without any preamplifiers. The Lidar was designed in a bistatic scheme with the separate transmitter and two receiver channels. It consists of three assemblies: a sensor assembly, an electronic assembly and the interconnecting cables (fig.1).



The total mass is 940 grams and total volume is 950 cm^3 in both assemblies. The power consumption provides only 4-Watt during 10 minutes measurements set. Lidar operates in the temperature range from +50°C to -100° C under lower pressure, near one mbar. The top view of scientific deck of the Lander-98 is presented on the fig.2.

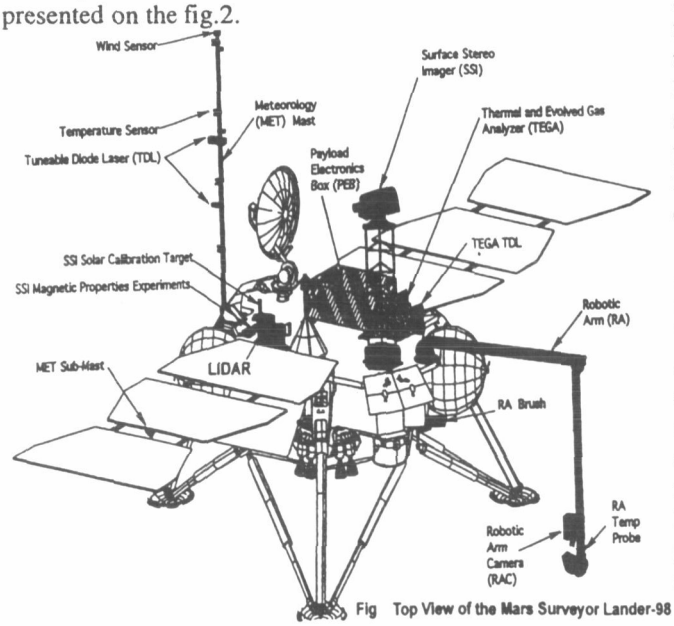


Fig Top View of the Mars Surveyor Lander-98

You can see here the two-lidar assemblies near the Solar panel. The Lidar is full autonomic device. It has internal processor and memory for data and program storage, connection with board processor by using of the RS-422 interface. Lidar gets the same commands from board and send it in 2046-bite telemetry frame. The Spacecraft shall be capable of storing Lidar science data up to a maximum of 25 600 byte per day for standard operation scenario. Note that the Lidar has mars sound microphone integrated into Lidar's unit.

The laser transmitter is a GaAlAs pulse laser diode emitting one microJoule in 20 nanosecond long pulses at 890-nanometer wavelength. Laser beam has a linear polarization. Lidar operates with repetition rate about 20-25 kHz. The laser beam has a 2-milliradian divergence with the output 54x34 mm^2 clear aperture. The Lidar's receiver channels consists of the objectives, interference filter and a gating; temperature compensated Single Photon Avalanche Diode (SPAD) (developed by Czech Technical University). It operates at low voltage no more then 30 V in a wide temperature range from +50° to -100°C. SPAD has 24% quantum efficiency at 890-nm and produces electrical pulse response on logical level without any preamplifier. Outside daylight background irradiance is the main source of noise inside the one mrad field-of-view of the receiver channel. The background irradiance is reduced by an optical interference filter having a bandwidth of 10 nm (FWHM) at 890 nm with 50% transmission and 15 mm clear aperture only. One of the receiver channels has polarizer. Its axes coincidence with the Lidar beam polarization.

. The Lidar's electronic circuit includes a time-of-flight counter, the programmable range gate generator, the control logic and an input/output interface to the board computer. It should be noted that the counter start pulse in this range is synchronized with the laser pulse, but the stop pulse is occasionally produced by noise or returns signal photons inside gate with 33 ns duration. The first 15 gates sequence is located along the 750m long trace with 330 pause between it. In this gate, position laser emits 65 000 pulses and detector registrate only some photocounts in different gates. Then the gate sequences are shifted toward on the one step (gate duration) and data storage returns. Then after 10 shifting the gate position covered full sounding distance 750m with 5 meters resolution along the trace. The 650 000 laser pulses is emitting for the 32 s total integrating time. It allows us to get a lot of return signal and representative statistics of photocounts [4]. The noise level and background scattered sunlight are measured the same technique without gate shifting. These data of measurement for the full cycle allow us to obtain the histograms of the distribution photon returns along the laser beam. In generally case, this histogram is proportional to the density probability function of a counter number along the beam and the backscatter coefficient profile [4]. The each spike indicate about obstacle on the laser beam, such as aerosol in inhomogeneous of the atmosphere, aerosol and other particles inside the tight layers, cloud boundary and hard target surface.

The single cycle has 10 minutes duration and consist of three active measurements by each channel simultaneously and 12 passive measurements of sky brightness. Single cycle measurements give us the next data:

a) sky brightness or incoming Solar radiation inside of the narrow field of view;

b) atmosphere backscatter coefficient profile inside the surface boundary layer.

The first parameter characterizes scattering properties of the whole atmosphere column; the second one characterizes scattering properties of the atmosphere layers near the lidar. By using and comparing the data of the both channels (with and without polarizer), we may obtain information about the non-spherical particles parameters and influence of the multiple scattering processes.

According to the main scenario, the Lidar will be operating 12 times per sol (every 2 hours). If it is necessary, we may change this scenario directly from Earth according to carent situation on Mars surface. The appearance of a dust storm and near-surface ice fog are very likely for place and time of landing and the Lidar can detect it.

4. LIDAR GROUND TESTS. EXPERIMENTAL DATA.

Using the Martian atmosphere model (Moroz et al. 1991), we estimate of the maximum sounding trace for the lidar. It strong dependence on the atmosphere state and its optical depth and solar background level. It should be note what the Sun will not setting during the Polar day for the all period of this mission. Its elevation angle will be change only from 10° to 40° over the horizon.

Calculations were done according to engineering model of the Martian atmosphere Below we give the base value of backscatter coefficient. Minimal level of the backscatter coefficient was estimated according to 3σ level signal to noise ratio on the distance 20 meters as $\beta_{Min} = 10^{-9}$ $1/m^2$ ster without background solar radiation and $\beta_{min} = 10^{-8}$ $1/m^2$ ster with solar radiation.

For instance, we may detect a cloud boundary with 10^{-5} $m^{-1}sr^{-1}$ backscatter coefficient up to 500 m height and with the atmosphere optical depth less then 0.1. It is clear that the background level depends on the optical depth. It distance is decreasing to 300 m with increasing of optical depth to 0.2 and increasing of scattered background light. These parameters may be improved if the photocounts number will be storage.
Figure 3 shows typical example of the time evolution of the lidar returns during 25 hours in Moscow in the geometry more close to the Mars mission-98 (see Pershin et al.) [4].

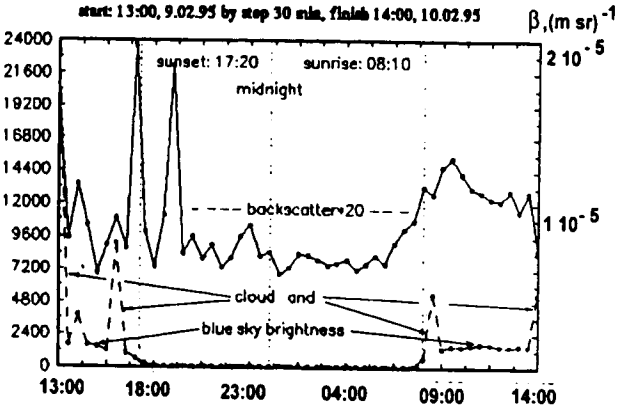


Fig LIDAR SENSING of AEROSOL & SKY BRIGHTNESS

Lidar was fixed at the elevation angle 45 deg. Experiment started at 13:00 and finished at 14:00 in February. All data were storage in automatic and autonomous version without the participant of investigator.
The aerosols density variation and clouds detection were made by using prototype of the compact lidar with 32000 laser pulses averaging in the each experimental points.

In active mode (see fig. 3 solid line) the backscatter lidar return was measured and detected the two sharp spikes of increasing the aerosol density at 17:00 and 18:30 - before and after sunset (17:20). This spike indicates the local processes of an aerosol condensation in according to the changing of the atmosphere parameters. At the midnight the aerosol density is decreasing and then twice increasing during sunrise period (near the 8:10). This may be effected by the morning fog appearance before sunrise as a similar in Mars morning (Pollack 1982)[5].

Taking into account that the sun will not setting during the mission in summer time we are going use it situation as the unique possibility to estimate of the atmosphere turbidity. The idea is based on the passive measurement through the polarizator of the halfday modulation of the sky brightness and its amplitude changing. So, the maximum intensity of the scattered light will be achieved twice per Martian sol in a case of high transparency atmosphere with a single scattering approximation when the Sun will crossing of the polarization plane.

5. CONCLUSION

We presented here the most as we know miniature aerosol backscattering Lidar for remote sensing of the Martian near surface boundary layers during the future Mars Surveyor Lander Mission in 1998-1999. This Lidar can operate under the extremely low temperature and low atmospheric pressure without special

container. The total Lidar mass is 940 grams and energy consumption not more then 4 Watts per measurement cycle.

5. REFERENCES

[1]. V.Moroz et al. "Engineering model of Martian atmosphere for Mars-96 project", Russ. "Space Research" 1991, v.29, pp.3-84.

[2]. O.Korablev, V.Krasnopolsky, A.Rodin, E.Chassenfiere, "Vertical structure of Martian Dust Measured by Solar Infrared Occultaions from the Fobos Spacecraft", ICARUS, 1993, v.102, pp.76-87.

[3]. R. Zurek, " Environmental Models for Support of Mars Surveyor '98 Lander Entry and Surface Operations. PDR Finel", private comm. May 20, 1996.

[4]. S.Pershin "A new generation of the portable backscatter Lidar with eye-safe energy level for environmental sensing" - in Proceeding of International Symposium "Aerospace Sensing", SPIE's v.2222, Orlando, Apr. 4, 1994

[5]. Properties of dust in the Martian atmosphere and its effect on temperature structure", Adv. Space Res. Vol.2, pp. 45-56,1982

Calibration of LITE Data

Mary T. Osborn
Science Applications International Corporation, NASA Langley Research Center
Mail Stop 475, Hampton, VA 23681-2199 USA
Phone:(757)864-2692, FAX:(757)864-2671, E-mail:m.t.osborn@larc.nasa.gov

1. Introduction

The Lidar In-space Technology Experiment (LITE) is a three-wavelength backscatter lidar developed by NASA Langley Research Center to demonstrate and explore the capabilities of space lidar. LITE was flown on Space Shuttle Discovery in September 1994. The LITE instrument was designed with the capability to measure tropospheric and stratospheric aerosols, clouds, height of the planetary boundary layer, temperature and density between 25 km and 40 km, and surface returns over both land and water. Not all science targets could be measured at the same time due to the large dynamic range of the return signal between the Earth's surface and the stratosphere. The LITE instrument was commandable and was operated in a variety of configurations to maximize science information. A description of the LITE instrument and the LITE mission are contained in Winker et al. [1996].

The determination of LITE system calibration constants, which include effective receiver aperture, nonvariable system parameters, and losses in the transmitting and receiving optics, is useful for retrieving aerosol data in the form of measurements of scattering ratio, aerosol backscatter, or aerosol extinction [Russell et al., 1979; Wiegner et al., 1989]. These constants would be especially useful if they could be applied to daytime or nighttime, low-gain data for which the signal-to-noise (S/N) is insufficient to perform high-altitude normalization or calibration. LITE calibration constants were calculated for all nighttime, high-gain data at 532 nm and 355 nm. (LITE data at 1064 nm do not have sufficient S/N to calibrate in the same manner.) The method used to calculate these factors and an examination of their variability are discussed below.

2. Calculations

The LITE calibration constant, C, for a given wavelength is defined as follows:

$$S(z)=C*el*gain*ff*af*ba(z)*10^{-\frac{att}{20}} *tr(z)/range^2,$$

where $S(z)$ is the background-subtracted signal at altitude z, *el* is the laser energy in Joules, *gain* is the PMT gain, *ff* is a filter function, *af* is an aperture function, $ba(z)$ is the aerosol plus molecular backscatter in units of 1/m-sr at altitude z, *att* is the attenuator setting in units of dB, $tr(z)$ is the two-way transmission between altitude z and the shuttle altitude, and *range* is the distance in meters between altitude z and the shuttle altitude. All system factors, such as detector quantum efficiency, that are constant over the LITE mission are included in C. The calibration constants were calculated using LITE data between 30 and 34 km, assuming that the backscatter at those altitudes is due almost entirely to molecular scattering, which is proportional to density. Density was obtained from the LITE meteorological data that were interpolated to the LITE locations using a gridded National Center for Environmental Prediction (NCEP) data product. Two-way transmission above 30 km is assumed to be 1. (Two-way transmission is in fact closer to 0.99, with the major contribution at 355 due to Rayleigh extinction and the major contribution at 532 nm due to ozone absorption.) Both *ff* and *af* are 1 during normal nighttime configuration. Values for C were calculated for each 200 shots of LITE high-gain, nighttime data at 532 nm and 355 nm.

Once C has been calculated, the only two unknowns in the above equation are $ba(z)$ and $tr(z)$. The transmission can often be adequately modeled, especially for the stratosphere, by using zonal mean measurements of aerosol extinction and ozone absorption from the Stratospheric Aerosol and Gas Experiment (SAGE) II. The remaining unknown, backscatter at altitude z, is usually the measurement being derived. Thus the calibration constant is potentially useful for deriving aerosol backscatter during daytime or low-gain periods. LITE daytime

measurements were made with an interference filter in place and a smaller aperture than used during nighttime measurements. Table 1 lists values for the reduction in signal due to the filter and smaller aperture.

Table 1. LITE Filter and Aperture Functions

	532 nm	355 nm
Filter function	0.65	0.30
Aperture function (Laser A)	0.90	0.95
Aperture function (Laser B)	0.74	0.83

An example of the calibration factors calculated using data from orbit 105 are shown in Figure 1. The top line corresponds to calibration factors for 532 nm and the bottom line to calibration factors for 355 nm. Each symbol represents a factor calculated from 200 laser shots. The line running through each set of symbols is the 1000 shot running mean.

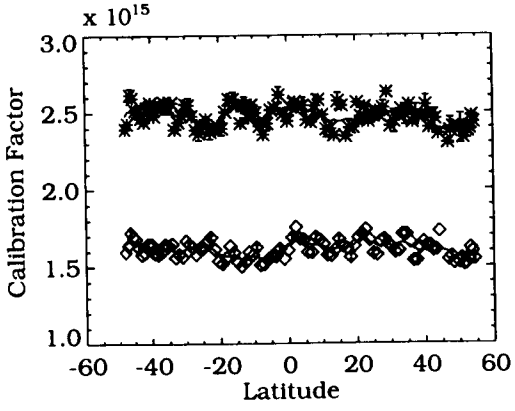


Figure 1. LITE calibration factors for orbit 105 based on 200 laser shots. The top row, values of approximately 2.5E15, corresponds to 532 nm; the bottom row, values of approximately 1.5E15, corresponds to 355 nm. A line representing the 1000 shot running mean runs through each set of symbols. Error bars representing the 1-sigma uncertainties are indicated on selected symbols.

To understand how constant the LITE calibration "constants" really are, average calibration factors were calculated for each LITE orbit with nighttime, high-gain data. Figure 2 is a plot of these average factors at 532 nm and 355 nm. The LITE instrument included two lasers, so different symbols have been used to identify orbits that used laser A (1-82 and 148-150) and orbits that used laser B (83-147). (Calibration factors would not be expected to stay constant with a change in laser.) As can be seen, there is a significant decrease with time. The calibration factors at 532 nm decreased approximately 15% and 20% for laser A and laser B, respectively. The calibration factors at 355 nm decreased approximately 20% and 28% for laser A and laser B, respectively. These decreases are assumed to be due, in large part, to decreases in optical throughput over the LITE mission, since changes due to diminishing laser energy have been compensated for.

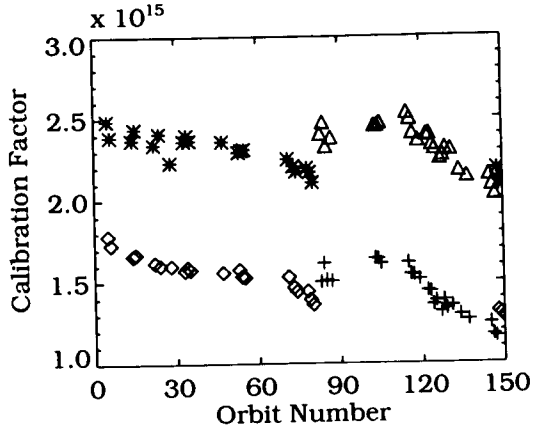


Figure 2. Average calibration factors for each orbit with nighttime, high-gain data. Symbols on the top and bottom rows correspond to calibration factors for 532 nm and 355 nm, respectively. Different symbols were used to differentiate laser A orbits (1-82, 148-150) from laser B orbits (83-147).

The variability of the LITE calibration factors within each orbit was analyzed by computing the percent difference from the mean for each orbit. The results of this analysis for laser A are shown in Figure 3. Results for laser B are similar. The within orbit variability for the 532 nm calibration factors, shown in Figure 3a, is generally within +/- 5% of the mean. Most of the points outside this range are from orbits 148-150, which are represented by + symbols. The laser energy was significantly lower during these orbits, resulting in lower S/N and greater variability in the calibration factors. The within orbit variability for the 355 nm calibration factors, shown in Figure 3b, is generally within +/- 3% of the mean, somewhat lower than for the 532 nm calibration factors.

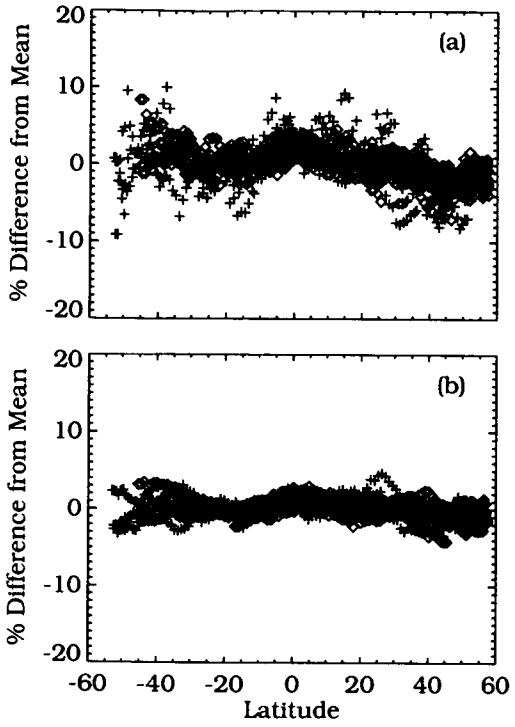


Figure 3. Percent difference from the orbital mean for laser A calibration factors based on 200 shots at a) 532 nm and b) 355 nm. Symbols represent 100*(calibration factor - mean) / mean. Values for orbits 148-150 are plotted using + symbols; earlier laser A orbits are plotted with diamond symbols.

As a result of the variability of the LITE calibration factors discussed above, the following procedure was adopted for including calibration factors in the LITE Level 1 data. For the portion of an orbit with nighttime, high-gain data, a calibration factor based on the running mean of 1000 laser shots is used. For the daytime or low-gain portion of an obit, the average calibration factor for that orbit is used. In the case of orbits with no nighttime, high-gain data, a calibration factor is interpolated from average factors for adjacent orbits.

3. Conclusion

Calibration "constants" provide useful information and are being included in the LITE Level 1 data that are being archived at the NASA Langley Research Center Distributed Active Archive Center (DAAC). The variability of these LITE calibration factors within and between orbits was studied. This analysis resulted in a better understanding of the LITE data and a reasonable method for calculating and reporting the calibration factors.

Acknowledgments. The author would like to thank G. S. Kent (STC) and W. H. Hunt (Wyle) for many informative discussions.

References

Russell, P.B., T.J. Swissler, and M.P. McCormick (1979). Methodology for Error Analysis and Simulation of Lidar Aerosol Measurements. *Applied Optics*, 18, 3783-3797.

Wiegner, M, M. Kästner, and H. Quenzel (1989). Comparison of Different Inversion Algorithms for Backscatter Lidar Measurements from Space. *Proceedings from IRS '88*, Lenoble and Geleyn (Eds.), A. Deepak Publishing, 534-535.

Winker, C. M, R. H. Crouch, and M. P. McCormick (1996). An Overview of LITE: NASA's Lidar In-space Technology Experiment. *Proceedings of the IEEE*, 84, 164-180.

LITE Data Processing

Kathleen A. Powell[1], David M. Winker[2]
[1]Science Applications International Corporation, NASA Langely Research Center
Mail Stop 475, Hampton, VA 23681-2199 USA
Phone: 757 864-2688, FAX: 757 864-2671, E-mail:k.a.powell@larc.nasa.gov
[2]NASA Langley Research Center
Mail Stop 475, Hampton, VA 23681-2199 USA
Phone: 757 864-6747, FAX: 757 864-2671, E-mail:d.m.winker@larc.nasa.gov

1. Introduction

The Lidar In-space Technology Experiment (LITE) was a payload onboard the Space Shuttle Discovery as part of the September 1994 STS-64 mission. LITE successfully made both atmospheric and surface measurements at the 355 nm, 532 nm, and 1064 nm wavelengths [Winker et al., 1996]. At mission completion, nearly 45 Gbytes of data had been obtained. As the data were collected they were organized into three data sets. The largest of these data sets contained the single-shot full resolution digitized lidar signals for all three wavelengths. The other two data sets contained the instrument status data block (ISDB) and the quick look science data (QLSD). ISDB information was generated once per second and contained timing parameters and engineering data related to the health, status, and configuration of the instrument. The QLSD are 100-shot averages of the 355 nm and 532 nm lidar signals and were generated at ten second intervals.

As the LITE data were generated, they were output to low-rate and high-rate telemetry streams. The low-rate data contained the ISDB and QLSD. The low-rate data were transmitted to the ground by the Shuttle S-band system through the Tracking and Data Relay Satellite System (TDRSS). The high-rate data contained the full resolution digitized lidar signals for all three wavelengths, the ISDB, and QLSD. The high-rate data were transmitted in real time by the Ku-band system through TDRSS downlink to the LITE operations center at the Johnson Space Center (JSC). High-rate data were only obtained when the orbiter and TDRSS telemetry link coincided with the real-time operations of LITE. The low-rate data were backed up by a Shuttle recorder during periods when the telemetry link was unavailable, and the entire low-rate data stream was transferred to the ground over the course of the mission. A total of 53 hours of low-rate data and 45.5 hours of high-rate data were acquired. All of the LITE raw telemetry data have been archived at the NASA Langley Research Center (LaRC), and the LITE high-rate data have been processed to the level 1 data product. This paper describes the data processing steps required to convert the LITE raw, high-rate telemetry data to the LITE level 1 data product.

2. Initial Data Processing

The LITE raw, high-rate telemetry data transferred from the orbiter to the LITE operations center at JSC were stored on optical platters in a PC format. After the mission was complete, the LITE data on the PC media were delivered to NASA LaRC for archive and post-processing. A Sun computer utilizing the UNIX operating system was designated to perform the LITE data processing. The first processing step was to error check the data and correct the data when possible. The data were then transferred from the PC media to an optical disk library.

The next step was to convert the LITE raw, telemetry data from its native form to a computer-compatible level 0 format. The level 0 data product was generated in several phases. The first phase was performed to decommutate the raw telemetry data, identify the telemetry frames containing ISDB and QLSD data, and to extract the time parameter from the ISDB. In combination, the QLSD location and the ISDB time parameter provided the necessary information to correlate ISDB and lidar profiles.

In the second phase, each lidar profile was time referenced and synchronized with an ISDB record. When ISDB information was missing due to gaps in the raw telemetry data stream, previously stored ISDB information was used as a substitute. This prevented the need to eliminate any lidar profiles from the level 0 product. Lidar profiles associated with repeated ISDB information were flagged.

In the third phase of level 0 processing, ISDB times were used to extract temperature and pressure profiles from the NMC data. These data were then merged into the level 0 data product.

The final phase was to geolocate each lidar profile. This required the use of ephemeris data from the Postflight Attitude and Trajectory History (PATH) product. The profile altitudes were defined in relation to a geoid model. A geoid was formed by adding undulations to an ellipsoid representation of the Earth, and served as an approximation to mean sea level. The position of the orbiter was specified by the Greenwich true of date (GTOD) geographic coordinate system. The attitude angles of the orbiter were specified as a set of Euler-like rotations which defined the orbiter orientation as a spacecraft maneuver sequence that aligned the three principal vehicle body axes with the corresponding GTOD axes. The Euler angles were used to form the transformation matrix that converts the LITE measurement geometry in the orbiter's body axes system to the GTOD coordinate frame. Through an iterative solution, the location of the lidar footprint and orbiter nadir point were defined relative to the geoid. Finally, the off-nadir angle was determined by the dot product of the lidar return and nadir vectors.

3. Final Data Processing

The level 0 data are an intermediate product and were used together with the raw telemetry data to form the level 1 data product, which is the intended distribution product. The level 1 data are organized as one data record per lidar pulse. Each data record contains header information and the lidar profiles for each wavelength. The organization of a level 1 data record is displayed in Table 1.

Table 1. LITE Level 1 Data Record Format

Header	1500 bytes
355 nm lidar profile	3000 bytes
532 nm lidar profile	3000 bytes
1064 nm lidar profile	3000 bytes
Total size	37500 bytes

The header contains 117 parameters and provides instrument settings and status, profile validity flags, profile processing status, and the time and location of each measurement. Several processing steps are applied to the level 0 profiles to obtain level 1 profiles. The steps, which are defined below, include removing fixed and random phase oscillations, performing offset subtraction, and interpolating the lidar profiles to a geolocated, constant altitude grid. The LITE system calibration constants have been determined and are reported for each lidar profile [Osborn, 1998].

The first level 1 processing step corrects the profiles for instrument artifacts. A fixed baseline correction was performed for every lidar profile. A second step then corrected for low-level, random phase oscillations found in the low-gain data. A processing status flag was set to indicate profiles having random phase oscillations removed.

In the second level 1 processing step, the DC offset was subtracted from each lidar profile. Two methods were used depending on lidar configuration. The methods and the criteria for selecting the methods are listed in Table 2.

Table 2. Offset Subtraction Methods

Method	Daytime	Nighttime
Slope		High-gain 355 and 532 nm
Averaged Signal	355, 532, and 1064 nm	1064 nm, Low-gain 355 and 532 nm

For the slope method, the offset value was calculated by matching the slope of the backscatter profile to the slope of a reference (density) profile over two high altitude regions. In the averaged signal method, the offset value was determined by averaging the signal over a single high altitude region The offset value and the method of offset subtraction are reported in the processing status flags.

The final step to processing level 1 lidar profiles was to interpolate the lidar profiles to a common altitude grid, which extends from -5.0 to 40.0 km with a 15 m vertical resolution. The level 1 lidar profiles were then combined with the header information and output as level 1 data records.

4. Concluding Remarks

The LITE data have been processed to level 1 and are being archived at the NASA LaRC Distributed Active Archive Center (DAAC). The level 1 data product contains lidar profiles that have been processed to remove the fixed and random phase oscillations, to correct for the offset, and to conform to a geolocated, constant altitude grid. A calibration constant has been supplied for each individual profile.

Associated with the level 1 data product are a metadata product and browse images. The metadata contain parameters which describe the measurement locations and instrument settings. The browse images are color-modulated plots of the LITE level 1 data. These products will be available through the LaRC DAAC and can be used to select the LITE level 1 data of interest. The LITE level 1 user's guide will also be available through the LaRC DAAC to provide more detailed information about the LITE level 1 parameters and their use.

Acknowledgements. The authors would like to acknowledge W. H. Hunt (Wyle) for defining the methods of offset subtraction and oscillation removal, M. A. Vaughan (SAIC) for developing a technique to remove the random phase oscillations, and M.C. Pitts (SAIC) for generating the NMC data.

References

Osborn, M. T. (1998). Calibration of LITE Data. Proceedings from the 19th International Laser Radar Conference, Annapolis, Maryland, 1998.

Winker, C. M., R. H. Couch, and M. P. McCormick (1996). An Overview of LITE: NASA's Lidar In-space Technology Experiment. Proceedings of the IEEE, 84, 164-180.

Observations of High Altitude Clouds Over the Equator in Regions Exhibiting Extremely Cold Temperatures

Ali H. Omar[1]
Department of Electrical & Computer Engineering
University of Illinois at Urbana-Champaign
1308 W. Main Street, Urbana, IL 61801-2307
Phone: 217-244-0612 Fax 217-3334303 email: a-omar@uiuc.edu

Chester S. Gardner
Department of Electrical & Computer Engineering
University of Illinois at Urbana-Champaign
1308 W. Main Street, Urbana, IL 61801-2307
Phone: 217-333-4682 Fax 217-3334303 email: cgardner@uiuc.edu

[1] Now at the Center for Atmospheric Sciences, Department of Physics, Hampton University, Hampton, VA

Introduction

The presence of cirrus clouds in upper troposphere near the Equator has implications for ozone chemistry and radiative transfer in this region. Cirrus clouds provide a surface area for the heterogeneous reactions of otherwise inert chlorine-containing compounds (e.g., HOCl, $ClONO_2$,HCl) into reactive forms of chlorine (ClO_y). The reactive forms of chlorine readily produce radicals that destroy ozone in repeated catalytic cycles analogous to ozone depletion reactions enhanced by polar stratospheric clouds in the stratosphere. By using a 2-D chemistry and dynamics model coupled with data from satellite observations, Solomon *et al.* (1997) show that such reactions could enhance the mixing ratio of ClO by up to 30-fold at mid-latitudes. Reactions on polar stratospheric cloud (PSC) surfaces have been used to explain the destruction of ozone observed above Antarctica each spring. Similar reactions can occur on cirrus cloud surfaces (Borrmann *et al.*, 1996; Solomon *et al.*, 1997).

Because these clouds are more persistent over time especially at the Equator (Wang *et al.*, 1996), the effects on the composition and ozone chemistry at and near the tropopause could be significant. The climatological studies of Wang *et al.* (1996) show that subvisual cirrus clouds are generally concentrated near the tropopause with frequencies as high as 70% in tropical regions. The appearance of these clouds is generally associated with the lowest water vapor mixing ratios. Given the high frequencies with which cirrus clouds occur and the continuous (in time) nature of these clouds, if $ClONO_2$ and HCl are present in sufficient quantities, the ensuing conversion to active chlorine radicals could contribute to ozone destruction near the tropical tropopause. For these reasons, interest in this phenomenon has intensified in recent years. There is, therefore, a need to determine the latitudinal distribution, vertical location, and temperatures of these cirrus clouds.

The use of lidar returns to determine the distribution and characteristics of cirrus and sub-visible cirrus clouds depends on the accurate determination of both the scattering ratio and the temperature profiles. In this study we show that the scattering ratio and corresponding temperature profiles for sections of Orbits 147-150 of the Lidar In-space Technology Experiment (LITE) mission are consistent with the presence of cirrus clouds in equatorial latitudes (15°S to 5°N).

Data Analysis and Temperature Retrieval

To calculate temperature profiles in the presence of aerosols, we take advantage of the difference in the wavelength dependence of aerosol and molecular backscattering to compensate for aerosol contamination of the backscattered molecular signal. The compensated (i.e., molecular) backscatter profile at λ_2 = 355 nm is calculated by subtracting a scaled version of the total backscatter profile at λ_1 = 532 nm from the total profile at λ_2 (Gu *et al.*, 1997) such that

$$\beta_m(\lambda_2, z) = \sigma_m(\lambda_2)p(z) = \frac{\beta_T(\lambda_2, z) - \left(\frac{\lambda_1}{\lambda_2}\right)^{\alpha(z)} \beta_T(\lambda_1, z)}{1 - \left(\frac{\lambda_2}{\lambda_1}\right)^{4.0117 - \alpha(z)}} \quad (1)$$

$\alpha(z)$ is the angstrom coefficient and $\beta_T(\lambda_n)$, $\beta_m(\lambda_n)$, $\beta_a(\lambda_n)$ are respectively the total, molecular, and aerosol backscatter profiles at wavelength λ_n. For large particles, the angstrom coefficient is near zero and scattering is only weakly dependent on wavelength (Hinds, 1982). The temperature profile was calculated from the density profile using the standard Rayleigh lidar technique for temperature retrieval.

Results

In this study, we assume clouds are present in the upper troposphere/lower stratosphere whenever the 532 nm-channel scattering is enhanced by more than 10%, i.e., the scattering ratio is greater than 1.1. Figure 1 shows the scattering ratios of the 532 nm and 355 nm channels for measurements of Orbit 150 at latitudes 6.2N to 3.4N corresponding to a ground track of 370 km in a North-to-South flight path of the space shuttle. Because aerosols enhance scattering to a much greater extent in the 532 nm channel than the 355 nm channel, regions in which large concentrations aerosols are present are characterized by peaks in the 532 nm channel scattering ratio profile. Two such peaks are depicted in Figure 1. The first peak is a cirrus cloud layer with a maximum scattering ratio of 2.4, a cloud thickness of 2.5 km at altitudes of 12.5-15 km. The second peak (~23 km) corresponds to the altitude of the stratospheric sulfate aerosol maximum. Another feature of these clouds is the small and variable angstrom coefficients in cloud layers. The angstrom coefficient profile varies from 1.0 at the cloud bottom to near 0.0 at the cloud top for the cloud layers in Orbit 150.

The corrected total backscatter profile was determined in the manner of Gu *et al.* (1997) using a fixed angstrom coefficient of α=1.5 which is characteristic of stratospheric aerosols. The corrected backscatter profile was then used to compute the temperature profile and the result is plotted in Figure 2. Using a fixed angstrom coefficient throughout the atmosphere in the presence of clouds does not properly compensate the data for aerosol scattering in the cloud layers which results in the discontinuous temperature profile as shown in Figure 2. This is because the fixed angstrom coefficient assumes that 1) the clouds are vertically homogenous both in composition and size distribution and 2) the fixed angstrom coefficient is known. Obviously, none of these assumptions is correct. A single angstrom coefficient has been used to compensate for aerosol backscatter and obtain accurate temperature profiles in the past (Gu *et al.*, 1997), but this has only been possible in the absence of clouds.

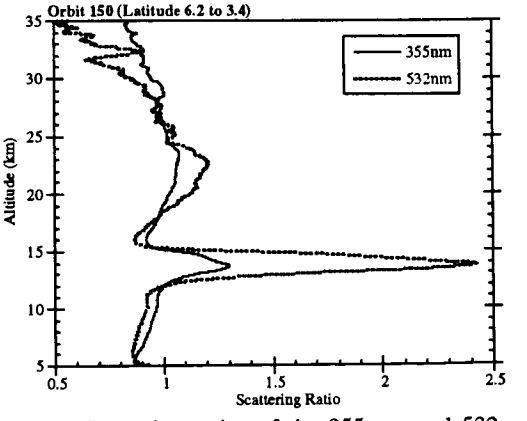


Figure 1. Scattering ratios of the 355 nm and 532 nm channels for a 50 second segment of Orbit 150. The scattering layers in the 532 nm channel at 14 km and 23 km denote a cirrus cloud and the stratospheric sulfate aerosol layer, respectively.

To properly compensate for aerosol scattering within the cloud layers, we computed the corrected backscatter profile using a variable angstrom coefficient determined analytically at each 15 m interval from cloud top to cloud bottom. The corrected backscatter profile was then used to obtain the more realistic temperature profile in Figure 2. This measured temperature profile compares favorably with the NMC-GOES7 model profile also shown in Figure 2. For altitudes between 10 km and 25 km, the root mean square (RMS) of the temperature difference ($\bullet T_{rms}$) between the LITE temperature profiles derived using variable angstrom coefficients and the NMC-GOES7 model profiles for all orbital segments is 4 K. The average RMS temperature difference in the cloud layers (for all orbital segments) only increases to about 5.5 K. This suggests that compensation for aerosol scattering using variable angstrom coefficients produces good temperature measurements within the cloud layers.

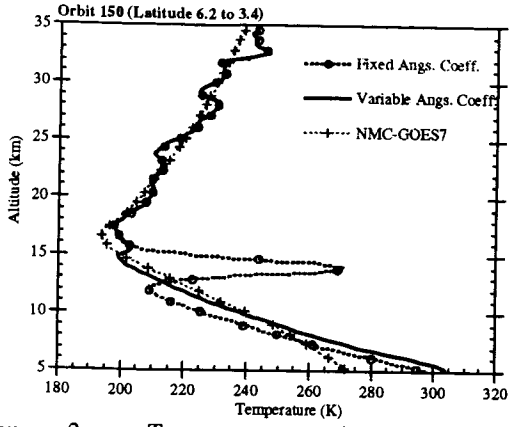
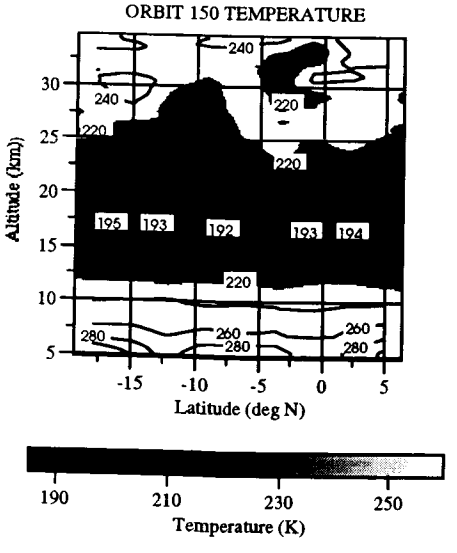


Figure 2. Temperature profiles from LITE measurements (using both fixed and variable Angstrom coefficients) and the NMC-GOES7 model for the data plotted in Fig. 1. In the vicinity of cirrus clouds (13-16 km), temperature profiles can be retrieved from LITE measurements using measured variable Angstrom coefficients.

Figure 3 is a plot of the LITE measurements of temperatures and scattering ratios for Orbit 150. There is a band of temperatures between 190-195 K collocated with scattering ratios greater than 1.1 at altitudes ranging from 15-20 km. The latitudinally-averaged cloud top and bottom height showed that the clouds lie on either side of the equatorial tropopause with a mean cloud geometric thickness of 2.9 ± 0.5 km.



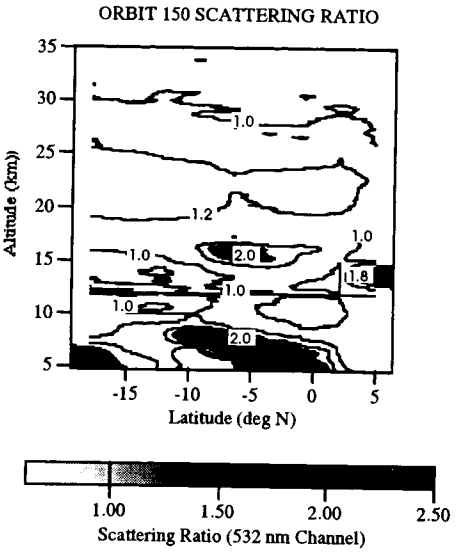


Figure 3. Temperature and scattering ratio profiles from LITE measurements of Orbit 150 showing a band of cold temperatures near the tropopause. A region of enhanced scattering between 10°S and 0° corresponds to a layer of cirrus clouds at temperatures of 192-193K.

Rosen *et al.*, 1997 used simulations of a H_2O-H_2SO_4-HNO_3 model to predict threshold temperatures at which PSCs form. In their study, PSCs were assumed to have formed when the scattering ratio (at 940 nm) doubles in a 1 K temperature drop. They found that the threshold temperature for the formation of PSCs near 15 km altitude when the water vapor concentration is 4-6 ppmv ranges from 192-196 K. These low water vapor concentrations are consistent with the Fall Stratospheric Aerosol and Gas Experiment (SAGE II) water vapor measurements near the tropopause over the Equator (Pan *et al.*, 1997). LITE measurements of the temperatures in the cloud layers of Orbits 147-150 show that the temperatures near the equatorial tropopause are comparable to the threshold temperatures of Rosen *et al.*, 1997.

A 6-year climatology of cloud occurrence frequencies from the SAGE II observations showed that a maximum in the subvisual cirrus cloud frequencies is found at 15 km near the Equator (Wang *et al.*, 1996). Though the LITE data set we used in this study (Orbits 147-150) is of much shorter duration, we found that the mid-point of the cirrus clouds is near 15 km. This is ~ 1 km below the tropical tropopause determined from the temperature profiles retrieved from the LITE data. Though the Equator is generally wetter than the higher latitudes, we do not believe that these clouds

are composed ice crystals because the tropical tropopause is likely to be relatively dry during the Fall months. SAGE II observations of seasonal variations of the water vapor content in the 345-355 K potential temperature surface (corresponding to 13-16 km range at the cloud temperatures) show that the Fall months have at least two orders of magnitude less water vapor (~20 ppmv) than the Winter months (~2000 ppmv) in this region (Pan *et al.*, 1997). The dry period coincides with the month during which the LITE experiments were conducted (September). The upper troposphere/lower stratosphere is therefore likely to have been too dry to form ice crystals and the particles we observed are more likely to be NAT. Measurements of the Halogen Occultation Experiment (HALOE) of the Antarctic vortex showed low concentrations of water vapor (1.5 - 4 ppmv), and that the observed aerosol extinction was more likely due Liquid Ternary Aerosol (LTA) and NAT than water ice (Hervig *et al.*, 1997). The possibility of ice clouds is excluded for temperatures above ~ 189K.

Conclusion

Compensation for aerosol contamination of the molecular backscatter profile using variable angstrom coefficients has been used to extend the Rayleigh lidar temperature retrieval using the LITE data to cloudy regions. Comparison of the LITE temperature measurements with NMC-GOES7 model data shows favorable agreement in both cloudy ($\bullet T_{rms}$= 5.5 K) and clear-sky ($\bullet T_{rms}$= 4 K) regions.

The LITE data has been used to determine the location of cirrus clouds near the Equatorial tropopause, their geometric thickness, scattering ratios, angstrom coefficients and temperature profiles. The optical properties of the clouds (scattering ratios and angstrom coefficients) show that the clouds are similar to those of Type 1a PSCs composed of NAT particles. These clouds, characterized by low temperatures (185 K-200 K), are ubiquitous in Equatorial regions at altitudes ranging from 11 km to 19 km. The temperatures are comparable to the threshold temperatures for the formation of PSCs composed of NAT. The relatively dry upper troposphere/lower stratosphere near the Equator during the Fall months supports the assertion that the particles observed in the clouds of Orbits 147-150 are not likely to be ice crystals but rather NAT particles.

References

Borrmann, S., S. Solomon, J. E. Dye and B. Luo (1996). "The potential of cirrus clouds for heterogeneous chlorine activation." Geophysical Research Letters **23**(16): 2133-2136.

Gu, Y. Y., C. S. Gardner, P. A. Castleberg, G. C. Papen and M. C. Kelley (1997). "Validation of LITE stratospheric temperature and aerosol measurements." Applied Optics **36**(21): 5148-5157.

Hervig, M. E., K. S. Carslaw, T. Peter, T. Deshler, L. L. Gordley, G. Redaelli, U. Biermann and J. M. R. III (1997). "Polar stratospheric clouds due to vapor enhancement: HALOE observations of the Antarctic vortex in 1993." Journal of Geophysical Research **102**(D23): 28185-28193.

Hinds, W. C. (1982). Aerosol Technology: Properties, Behavior, and Measurement of Airborne Particles. New York, John Wiley & Sons.

Pan, L., S. Solomon, W. Randel, J.-F. Lamarque, P. Hess, J. Gille, E.-W. Chiou and M. P. McCormick (1997). "Hemispheric asymmetries and seasonal variations of the lowermost stratospheric water vapor and ozone derived from the SAGE II data." Journal of Geophysical Research **102**(D23): 28177-28184.

Rosen, J. M., N. T. Kjome, N. Larsen, B. M. Knudsen, E. Kyro, R. Kivi, J. Karhu, R. Neuber and I. Beninga (1997). "Polar stratospheric cloud threshold temperatures in the 1995-1996 arctic vortex." Journal of Geophysical Research **102**(D23): 28195-28202.

Solomon, S., S. Borrmann, R. R. Garcia, R. Portmann, L. Thomason, L. R. Poole, D. Winker and M. P. McCormick (1997). "Heterogeneous chlorine chemistry in the tropopause region." Journal of Geophysical Research **102**(D17): 21,411-21,429.

Wang, P.-H., P. Minnis, M. P. McCormick, G. S. Kent and K. M. Skeens (1996). "A 6-year climatology of cloud occurence frequency from Stratospheric Aerosol and Gas Experiment II observations (1985-1990)." Journal of Geophysical Research **101**(D23): 29,407-29,429.

Global Tropospheric Ozone Investigations

Edward V. Browell
Atmospheric Sciences Division, NASA Langley Research Center
Mail Stop 401A, Hampton, Virginia 23681-0001 USA
Phone: 757-864-1273; Fax: 757-864-7790; E-mail: e.v.browell@larc.nasa.gov

1. Introduction

Ozone (O_3) is one of the most important trace gases in the troposphere, and it is responsible for influencing many critical chemical and radiative processes. Ozone contributes to the formation of the hydroxyl radical (OH), which is central to most chemical reactions in the lower atmosphere, and it absorbs UV, visible, and infrared radiation which affects the energy budget and atmospheric temperatures. In addition, O_3 can be used as a tracer of atmospheric pollution and stratosphere-troposphere exchange. At elevated concentrations, O_3 can also produce detrimental biological and human health effects.

The U.S. National Research Council (NRC) Board on Sustainable Development reviewed the U.S. Global Change Research Program (USGCRP) [NRC, 1995], and it identified tropospheric chemistry as one of the high priority areas for the USGCRP in the next decade. The NRC identified the following specific challenges in tropospheric chemistry.

- Although we understand the reason for the high levels of O_3 over several regions of the world, we need to better **establish the distribution of O_3 in the troposphere** in order to document and understand the changes in the abundance of global tropospheric O_3. This information is needed to quantify the contribution of O_3 to the Earth's radiative balance and to understand potential impacts on the health of the biosphere.
- Having recognized the importance of particles in the chemistry of the stratosphere, we must **determine how aerosols and clouds affect the chemical processes in the troposphere.** This understanding is essential to predict the chemical composition of the atmosphere and to assess the resulting forcing effects in the climate system.
- We must determine if the self-cleansing chemistry of the atmosphere is changing as a result of human activities. This information is required to predict the rate at which pollutants are removed from the atmosphere.

Over nearly two decades, airborne Differential Absorption Lidar (DIAL) systems have been used in over fifteen major field experiments conducted all over the world to address important atmospheric processes affecting the amount and distribution of O_3 and aerosols across the troposphere. This paper discusses some of these wide-ranging field experiments and their results and presents a direction for future global studies of O_3 and aerosols from space.

2. Airborne Ozone DIAL System

The DIAL technique has been used in airborne lidar measurements of tropospheric O_3 profiles since 1980 [Browell et al., 1983]. In 1988 the airborne DIAL system was modified to simultaneously measures O_3 and aerosol profiles above and below the aircraft for complete tropospheric coverage from near the surface to above the tropopause [Browell, 1989]. This system was recently upgraded with two new frequency-doubled Nd:YAG lasers and two new frequency-doubled dye lasers [Richter et al., 1997]. The four lasers are mounted on a structure that supports all of the laser power supplies, the laser beam transmitting optics, and the dual telescope and detector packages for simultaneous nadir and zenith measurements. In tropospheric O_3 investigations, one of the frequency-doubled dye lasers is operated at 289 nm for the DIAL on-line wavelength, and the other one is operated at 300 nm for the off-line wavelength. The DIAL wavelengths are produced in sequential laser pulses with a time separation of ~300 μs to ensure that the same atmospheric scattering volume is sampled at both wavelengths during the DIAL measurement. Half of the energy in each of the UV beams is transmitted in the zenith and nadir directions. The residual laser output at 600 and 582 nm from the frequency-doubling of the dye laser and the residual 1064-nm output from the frequency-doubled Nd:YAG laser are also transmitted for aerosol profile measurements. The output beams are transmitted out of the aircraft collinearly with the receiver telescopes through 40-cm-diameter quartz windows.

The backscattered laser energy at each laser wavelength is collected by two back-to-back 36-cm telescopes. The lidar returns in the UV, visible, and infrared are separated with dichroic optics and directed onto different detectors. The analog signals from the detectors are digitized at up to 10 MHz with 12-bit accuracy, and the average digitized signals are stored

every 1.5 seconds (average of 45 lidar returns) on 8-mm magnetic tape. Ozone concentrations and aerosol distributions are calculated in real time, and the output is displayed on a color monitor.

3. Global Tropospheric Investigations

Many investigations of O_3 and aerosols have been conducted with airborne DIAL systems over the last 16 years as part of NASA's Global Tropospheric Experiments (GTE). The first international field experiment was conducted over the tropical Atlantic from Puerto Rico during 1982-1983, and the first cross section of a tropopause fold event was obtained over the southwestern U.S. during the 1984 GTE Chemical Instrumentation Test Experiment (CITE-1). Airborne lidar investigations of O_3 and aerosols were conducted from Barbados over the Western Atlantic in 1984 (Atlantic Boundary Layer Experiment, ABLE-1) and in Brazil over the Amazon rain forest in the dry season of 1985 (Amazon Boundary Layer Experiment, ABLE-2A) and the wet season of 1987 (ABLE-2B). Airborne lidar measurements of O_3 and aerosols were also made over the tundra and ocean regions of the Arctic in 1988 (Arctic Boundary Layer Experiment, ABLE-3A) and the boreal forests and lowland regions of northern Canada in 1990 (ABLE-3B). Global tropospheric investigations over the western Pacific were conducted in the summer of 1991 (Pacific Exploratory Mission - West, PEM-West A) and the winter of 1994 (PEM-West B). The tropical Atlantic was investigated from Brazil and Africa in 1992 (Transport and Atmospheric Chemistry near the Equator - Atlantic, TRACE-A), and the tropical Pacific, primarily in the Southern Hemisphere, was studied in 1996 (PEM-Tropics A). This paper discusses the results from several of the most recent field experiments including TRACE-A, PEM-West B, and PEM-Tropics A.

3.1 TRACE-A

The TRACE-A field experiment was conducted during September-October 1992 to determine the source of high O_3 that occurs in the troposphere over the tropical Atlantic between Africa and Brazil during the late summer and early fall.

During TRACE-A, the airflow over the tropical Atlantic in the Southern Hemisphere was found to be predominantly from the east (Africa) in the lower troposphere (below 8 km) and from the west (Brazil) in the upper troposphere. Convective storms in Brazil transported the gases contained in extensive fire plumes from near the surface to the upper troposphere where O_3 was photochemically produced and advected eastward over the Atlantic. In central Africa, the fires were widespread, and in the absence of convective storms, the fire plumes were advected to the west over the Atlantic at altitudes below 6 km. Airborne DIAL measurements showed considerable variability in O_3 and aerosol distributions with strong dependence on transport of air masses from regions associated with biomass burning. Ozone and aerosols were positively correlated in plumes that were directly advected from the fire regions with O_3 frequently exceeding 75 ppbv (parts per billion by volume). In addition, O_3 often exceeded 100 ppbv in the upper troposphere from photochemical O_3 production in air from plumes that had been convectively lifted by storms over Brazil and Africa. The airborne DIAL data were used to help determine the relative contribution of the various processes on the buildup of high O_3 over the tropical southern Atlantic during TRACE-A.

3.2 PEM-West B

The airborne DIAL system was flown during PEM-West B to obtain distributions of O_3 and aerosols in the troposphere over the western Pacific during February-March 1994. This investigation was conducted as part of an investigation to determine the impact of continental sources of gases and aerosols on the air over the western Pacific during the late winter when the transport from Asia is at a maximum. The first field experiment over the Pacific was conducted in 1991 (PEM-West A) to examine the summertime period when the continental influence on the western Pacific is at a minimum [Browell et al., 1996a].

During PEM-West B, the airflow off Asia was found to be predominantly behind cold fronts and below 4 km. The continental air contained very high levels of aerosols and photochemically produced O_3 that sometimes exceeded 100 ppbv. The air in front of the cold fronts was usually clean with low levels of aerosols and low O_3 ($\leq$30 ppbv). At mid latitudes (north of ~30°N), O_3 was also enhanced in the middle and upper troposphere as a result of frequent stratospheric intrusions. The airborne DIAL data were used during PEM-West B to help determine the relative contribution of the various transport and chemical processes on determining the composition and chemistry of the air over the western Pacific during the wintertime [Fenn et al., 1996]. The average latitudinal O_3 distribution observed with the airborne DIAL system over the western Pacific during PEM-West B is shown in Figure 1. Many large-scale atmospheric features can be seen in this figure resulting from processes associated with convection in the tropics; advection between tropics and mid-latitudes; O_3 production and destruction; and stratosphere-troposphere exchange. This is an example of the complex combination of processes that contribute to the tropospheric O_3 budget.

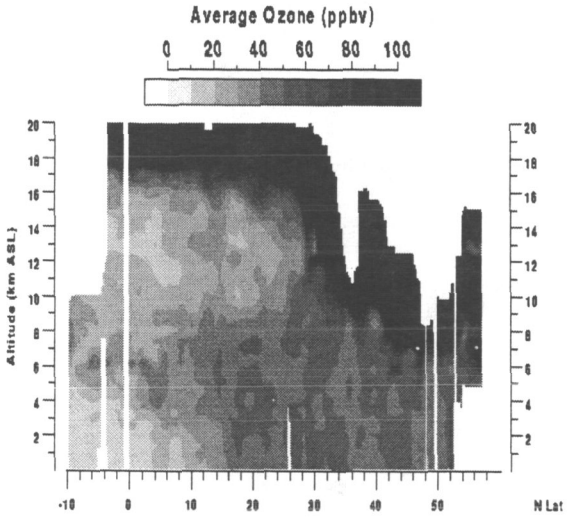


Figure 1. Average latitudinal O_3 cross section obtained in western Pacific during PEM-West B.

3.3 PEM-Tropics A

During PEM-Tropics A, a large number of plumes with high O_3 levels (>60 ppbv) were unexpectedly observed over the South Pacific. These plumes were often found in the 3-8 km region, and the chemical composition of these plumes and their backtrajectories indicated that many of them were due to biomass burning in Africa or Brazil. Biomass burning and urban/industrial plumes from closer sources, such as Indonesia, were also observed. Figure 2 shows a typical plume observed in the data from the airborne DIAL on the DC-8 during PEM-Tropics A. These data are from a latitudinal survey flight west of Tahiti. The enhanced O_3 in the figure is due to photochemical O_3 production in the biomass burning plume. The aerosol loading in the plume is low due to the loss of aerosols during convection and subsequent advection over at least 15,000 km. These plumes are thought to be over two weeks old based on the hydrocarbon concentrations found in the air. Airborne lidar measurements over the tropical Pacific were made from bases in Tahiti, Easter Island, New Zealand, and Fiji. The widespread impact of pollution from biomass burning in Africa and Brazil to this remote region was unexpected, but this just further emphasizes the interdependence of one region with another on this small planet. Additional details about this investigation are given by Fenn et al. [1998].

4. Global Ozone and Aerosol Investigations from Space

Science missions to investigate the global distribution of O_3 and aerosols with future space-based lidar systems are an important part of a comprehensive and integrated program to study the Earth's coupled land, ocean, and atmosphere system and the impact of human activities on our planet. The development of lidar systems for high vertical resolution measurements of these parameters would represent a revolutionary step toward the next generation of space-based remote sensors.

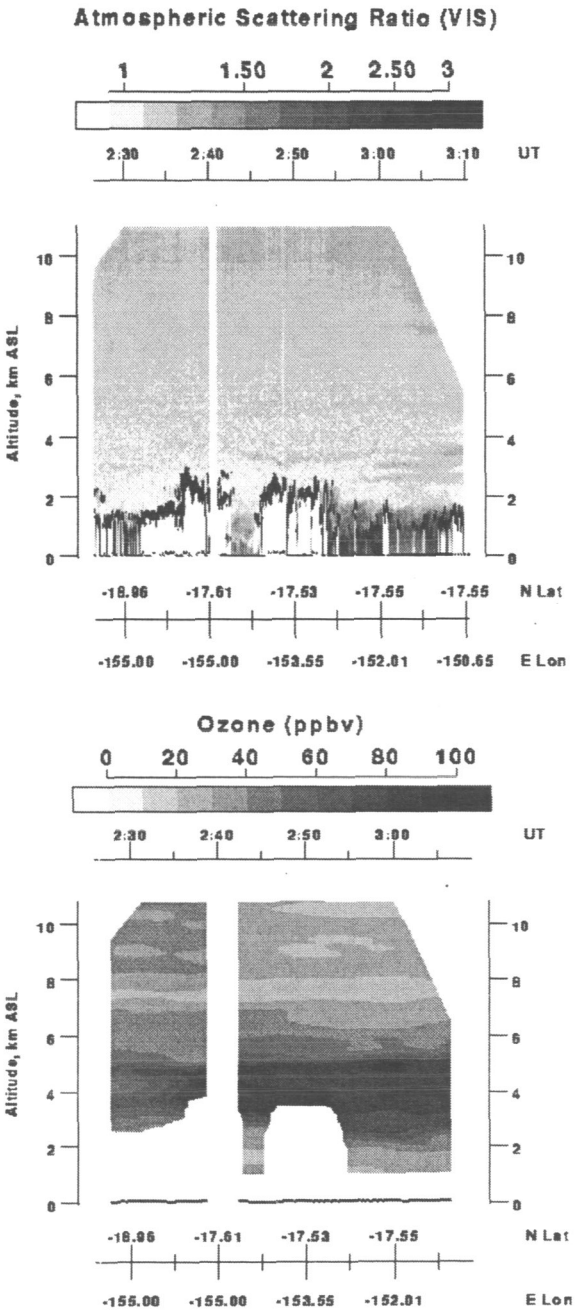


Figure 2. Aerosol (top) and O_3 (bottom) distributions observed on Sept. 6, 1996, during PEM-Tropics A.

NASA and the CSA (Canadian Space Agency) are jointly studying the development of a space-based lidar system for global measurements of O_3 and aerosol distributions in the troposphere and lower stratosphere. This lidar system called ORACLE (Ozone Research with Advanced Cooperative Lidar Experiments) will be capable of measurements of O_3 profiles and columns across the lower atmosphere with simultaneous measurements of aerosol and cloud profiles [Browell et al., 1997].

Airborne DIAL investigations of tropospheric O_3 and aerosols have shown that high-vertical-resolution simultaneous measurements of O_3 and aerosols are necessary to interpret the nature of remotely observed air masses. These air masses can be associated with boundary layer processes, elevated aerosol and cloud layers, natural and anthropogenic sources, long-range advection of air masses, vertical transport associated with clouds, and stratosphere-troposphere exchange. Ozone measurements are needed from space with vertical and horizontal resolutions of $\leq$3 km and $\leq$200 km, respectively, and with an accuracy of better than 10%, and aerosol and cloud measurements are needed with resolutions of 100 m and 1 km, respectively.

The NASA Earth Sciences Enterprise Strategic Plan for the next decade has a major science priority to provide global observations for the detection and scientific understanding of causes and consequences of changes in tropospheric O_3. It is recognized that there is a general lack of data on the global distribution of tropospheric O_3 and aerosols, and space-based active remote sensing measurements are an essential component of the measurement strategy. The combined use of active and passive measurements of O_3 and aerosols would provide important global data for addressing the key atmospheric science questions discussed in the Introduction.

5. Acknowledgments

The author thanks his colleagues in the Lidar Applications Group of the Atmospheric Sciences Division at the NASA Langley Research Center (LaRC) for their assistance in developing the airborne DIAL systems, in conducting the field experiments, and in processing the DIAL data presented in this paper. He also acknowledges the contributions made by the ORACLE study team at NASA LaRC and the CSA and with other associated Canadian and U.S. groups. The GTE investigations discussed in this paper were funded by the NASA Tropospheric Chemistry Program.

6. References

National Research Council, A review of the U.S. Global Change Research Program and NASA's Mission to Planet Earth/Earth Observing System, National Academy Press, Washington, DC, 1995.

Browell, E. V., A. F. Carter, S. T. Shipley, R. J. Allen, C. F. Butler, M. N. Mayo, J. H. Siviter, Jr., and W. M. Hall, NASA multipurpose airborne DIAL system and measurements of ozone and aerosol profiles, Appl. Opt., 22, 522-534, 1983.

Browell, E. V., Differential absorption lidar sensing of ozone, Proc. of the IEEE, 77, 419-432, 1989.

Browell, E. V., Ozone and aerosol measurements with an airborne lidar system, Optics & Photonics News, pp. 8-11, October 1991.

Browell, E. V., et al., Large-scale air mass characteristics observed over the Western Pacific during summertime, J. Geophys. Res., 101, 1691-1712, 1996a.

Browell, E. V., et al., Ozone and aerosol distributions and air mass characteristics over the South Atlantic Basin during the burning season, J. Geophys. Res., 101, 24,043-24,068, 1996b.

Browell, E. V., S. Ismail, T. C. McElroy, R. M. Hoff, and A. Dudelzak, Global Measurements of ozone and aerosol distributions with a space lidar system, EOS, 78, F89, 1997.

Fenn, M. A., E. V. Browell, and C. F. Butler, Airborne lidar measurements of ozone and aerosols during PEM-West A and PEM-West B, in Advances in Atmospheric Remote Sensing with Lidar, A. Ansmann, R. Neuber, P. Rairoux, and U. Wandinger, eds., pp. 355-358, Springer Verlag, New York, 1996.

Fenn, M. A., E. V. Browell, W. B. Grant, C. F. Butler, S. A. Kooi, M. B. Clayton, V. G. Brackett, and G. L. Gregory, Airborne lidar measurements of ozone and aerosols during the Pacific Exploratory Mission - Tropics A, Proc., 19thILRC, Annapolis, Maryland, July 6-10, 1998.

Richter, D. A., E. V. Browell, C. F. Butler, and N. S. Higdon, Advanced airborne UV DIAL system for stratospheric and tropospheric ozone and aerosol measurements, in Advances in Atmospheric Remote Sensing, A. Ansmann, R. Neuber, P. Rairoux, and U. Wandinger, eds., Springer-Verlag, Berlin, 395-398, 1997.

8. Additional Information

For detailed information on airborne DIAL data sets from these and other field experiments and for complete reference list please see our home page on the Internet at **http://asd-www.larc.nasa.gov/lidar/**.

LASE Measurements of Convective Boundary Layer Development during SGP97

Syed Ismail[1], Edward V. Browell[1], Richard A. Ferrare[1], Christoph Senff[2], Kenneth J. Davis[3], Donald H. Lenschow[4], Susan Kooi[5], Vince Brackett[5], Marian Clayton[5]

[1]NASA Langley Research Center, MS-401A, Hampton, Virginia 23681-0001, USA,
757-864-2719, 757-864-7790 (fax), s.ismail @larc.nasa.gov (e-mail)
[2]ETL, NOAA, Boulder, CO, USA
[3]University of Minnesota, St. Paul, MN, USA
[4]NCAR, Boulder, CO, USA
[5]Science Applications International Corporation, Hampton, Virginia, USA

Introduction

The Southern Great Plains 1997 (SGP97) field experiment [1] was conducted in Oklahoma during June-July 1997 to validate the models used for computing remote soil moisture using measurements by microwave radiometers. One of the objectives of SGP97 was to examine the effect of soil moisture on the evolution of the Atmospheric Boundary Layer (ABL) and clouds over the Southern Great Plains (SGP) during the warm season. The LASE (Lidar Atmospheric Sensing Experiment) airborne DIAL (Differential Absorption Lidar) system, which was flown autonomously on the NASA ER-2 aircraft during previous missions, was reconfigured to fly on the NASA P-3 research aircraft. During SGP97 LASE was used to study the morning evolution of the ABL, particularly as manifested in the development of the convective boundary layer, and to study the influence of soil moisture variations on the development of ABL. The ABL development is strongly influenced by the surface energy budget, which is in turn influenced by soil moisture, mesoscale meteorology, clouds, and solar insolation. LASE data acquired during this mission are being used to study the ABL water vapor budget, the development of the ABL, spatial and temporal variabilities in the ABL, and the meteorological factors that influence the ABL development. This field experiment also permitted comparisons of LASE water vapor measurements with water vapor profiles acquired by radiosondes launched at the DOE (Department of Energy) Atmospheric Radiation Measurement (ARM) Southern Great Plain (SGP) site and at NASA/Wallops Flight Facility, as well as with measurements from other SGP97 aircraft.

LASE Instrumentation

LASE is the first fully engineered, autonomous airborne DIAL system to measure water vapor, aerosols, and clouds throughout the troposphere [2,3]. This system uses a double-pulsed Ti:sapphire laser, which is pumped by a frequency-doubled flashlamp-pumped Nd:YAG laser, to transmit light in the 815-nm absorption band of water vapor. The Ti:sapphire laser wavelength is controlled by injection seeding with a diode laser that is frequency locked to a water vapor line using an absorption cell. LASE operates by locking to a strong water vapor line and electronically tuning to any spectral position on the absorption line to choose the suitable absorption cross-section for optimum measurements over a range of water vapor concentrations in the atmosphere. When flown on the ER-2 during the previous LASE Validation [2] and TARFOX [4] missions, LASE operated by alternating between strong (line center) and weak (side of strong line) water vapor cross sections for the on-line DIAL wavelength in order to measure water vapor throughout the troposphere. When flown on the P-3 during SGP97, the lower operational altitude (7-8 km) of the P-3 provided stronger near-field signal than from the ER-2 in the 4-8 km altitude region. This permitted the use of a single optimum absorption cross-section over the 0-8 km altitude region. This mode of operation not only facilitated data handling but also increased the horizontal resolution by a factor of two because twice as many shots are averaged in the low- and mid-tropospheric regions without the need to alternate between strong and weak cross-section between the DIAL pulse pairs. Typical horizontal and vertical resolutions for water vapor profiles extending between 0.2-7 km are 5 km and 200 m, respectively, with a predicted accuracy of better than 10% (random plus <5% systematic).

The LASE detector signal processor system was re-optimized to protect against the strong near-field signals when flown on the P-3. The laser beam was transmitted colinearly with the 15-inch diameter telescope. A 6-inch diameter mask was used around the laser beam axis to prevent the detection of strong near field signals and

to permit a more gradual lidar signal overlap region. The use of this mask reduced the effective area of the telescope by 18%.

The Spectra Diode Laboratory single mode laser that was used to seed the Ti:sapphire laser in earlier LASE missions was prone to mode hopping and necessitated a complex approach to achieve the desired water vapor line locking. It was changed to a David Sarnoff Labs distributed feedback diode (DFB) for the SGP97 Mission. The DFB has a strong side-mode suppression and operated without mode hopping over the operating temperature range resulting in fast tuning capability and nearly 100% reliability of reaching the desired absorption line [5]. The water vapor line at 816.1427 nm [6] was used, and the laser was operated in the sideline mode with an on-line cross section of 12.5E-24 cm^2.

Measurements and Analyses

During SGP97, LASE collected a total of 18 flight hours of data over 7 flights between July 11 and July 17, 1997. The flight plan that was most often used by the P-3 during SGP97 permitted measurements of water vapor and aerosol distributions covering a 50 x 260 km region over Oklahoma. The flights were conducted to capture the morning development of the ABL. These measurements were made in conjunction with the remote soil measurements made by the Electronically Scanned Thinned Array Radiometer (ESTAR) which was also on-board the NASA P-3 aircraft. The P-3 flights were coordinated with flights by other SGP97 aircraft including the

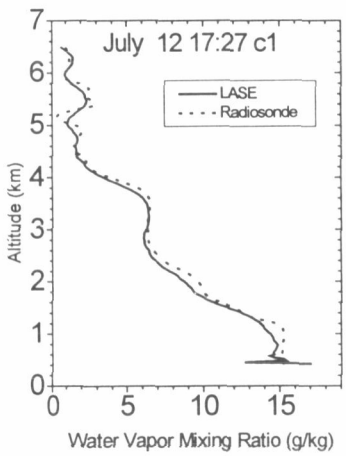


Figure 1. LASE and SGP CF radiosonde water vapor mixing ratio profiles acquired at 17:27 UT on July 12, 1997.

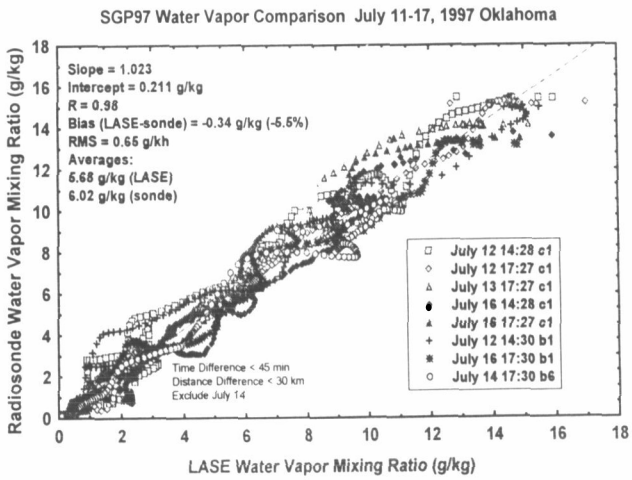


Figure 2. Comparison of LASE and ARM SGP radiosonde water vapor mixing ratios measured during SGP97.

Canadian NRC (National Research Council) Twin Otter and the NOAA (National Oceanic and Atmospheric Administration) Long-EZ. A detailed description of the SGP97 experiment is given in reference [1].

LASE profiles of water vapor mixing ratio were compared with those measured by Vaisala radiosondes launched at the DOE ARM SGP sites near Lamont, Oklahoma (C1); Hillsboro, Kansas (B1); and Purcell, Oklahoma (B6). Figure 1 shows an example of the water vapor mixing ratio profiles measured by LASE and the C1 radiosonde at 17:27 UT on July 12. These profiles show excellent agreement. Figure 2 shows a summary of the comparisons between water vapor mixing ratios measured by LASE and all the close-coincidence SGP radiosondes. Water vapor profiles measured by the two sensors within 45 minutes and 30 km of each other are included in this figure. LASE and radiosonde water vapor measurements agreed to within about 5% on average, which is within the uncertainty for each instrument.

In addition to measuring water vapor mixing ratio profiles, LASE simultaneously measures aerosol backscattering profiles at the off-line wavelength near 815 nm. Assuming a region with very low aerosol loading can be identified, profiles of the total scattering ratio, defined as the ratio of total (aerosol plus molecular) scattering to molecular scattering, are determined by normalizing the total atmospheric scattering in the region containing enhanced aerosol scattering to the expected scattering by the modeled molecular atmosphere at that altitude. The

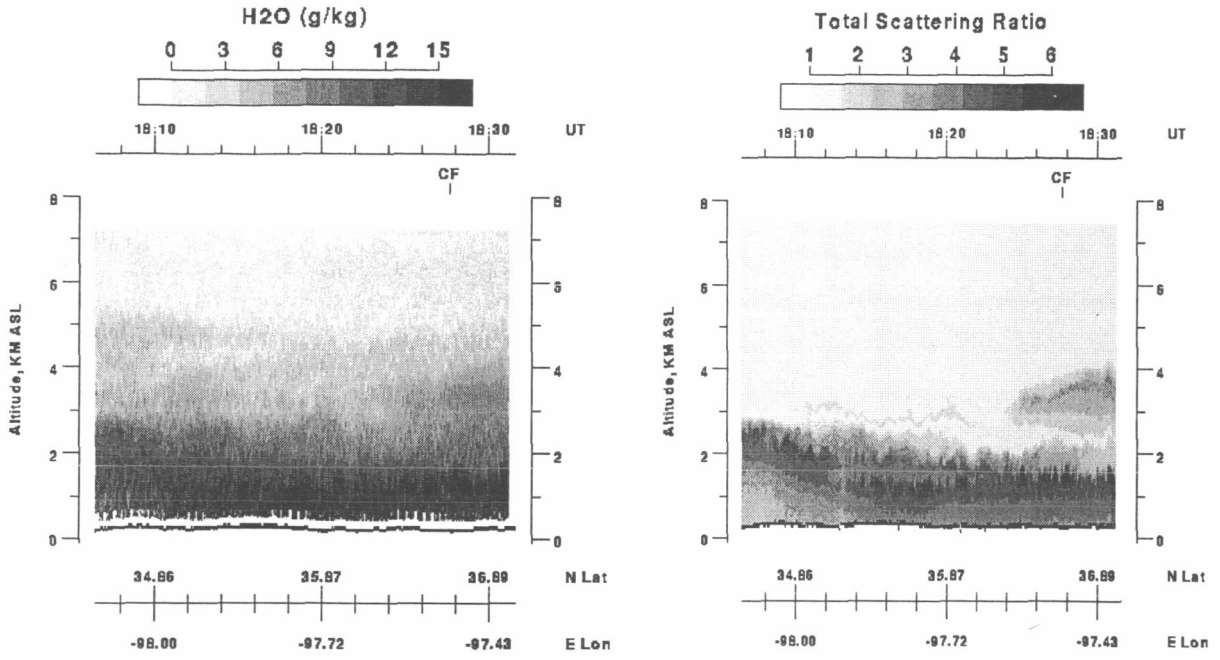


Figure 3. LASE measurements of water vapor mixing ratio (left) and total scattering ratio (right) during a north to south flight track on July 12, 1997. Note the variation in PBL characteristics during the flight.

aerosol backscatter coefficient is then computed from the total scattering ratio and the molecular backscattering cross section, which is derived from radiosonde and/or model pressure and temperature profiles. These aerosol profiles, which span the altitude range between 0.03-8 km, typically have horizontal and vertical resolutions of 200 m and 30 m, respectively.

LASE water vapor and aerosol profiles acquired on July 12, 1997 displayed heterogeneous development of the ABL. Figure 3 shows these profiles acquired during a north to south flight leg of the P-3 aircraft. High resolution aerosol and water vapor data indicate a high degree of correlation between aerosol and water vapor fields in the ABL. Individual convective cell features with vertical size variations of 100-200 m near the ABL top and < 1 km in horizontal size are clearly resolved by LASE aerosol measurements, which also show the very early stages of cloud development on top of a few of the individual cells (Figure 3b). The ABL in the southern end of the experiment region was substantially deeper (~ 2.5 km AGL (above ground level)) and drier (<10 g/kg) than the ABL in the northern region (1.2 km AGL and > 14g/kg). The cause of these variations is currently under

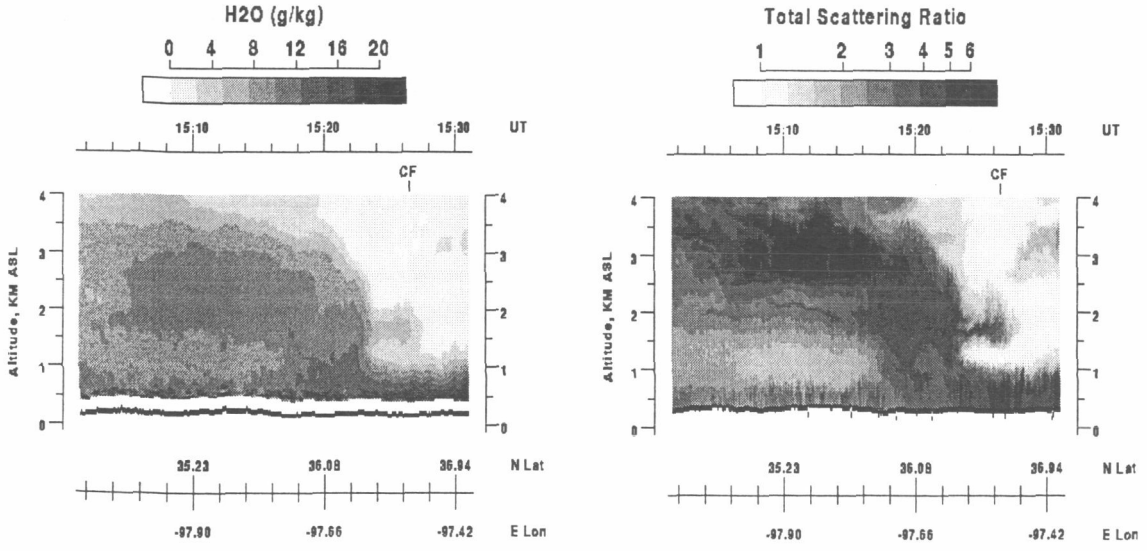


Figure 4. LASE water vapor mixing ratio (left) and total scattering ratio (right) measurements acquired during a south to north flight leg of the P-3 aircraft on July 14, 1997. These images show the passage of a cold front over the SGP97 region.

investigation. The segment of data from 18:15 to 18:31 UT, which covered about 180 km, showed a well developed homogeneous ABL that was used to estimate ABL characteristics using the statistical methods described in [7]. The boundary layer height z_i was estimated using the gradient function d/dR [ln ($P*R^2$)] where P is the lidar signal and R the range. The lowest aerosol layer was used to obtain an average z_i value of 1.2 km for this flight segment. Water vapor variance from the atmosphere was estimated using autocovariance functions to remove variance due to system noise. Using the water vapor variances measured by LASE in the upper third of the ABL, as discussed by [7], an average entrainment flux was calculated to be 0.20 g/kg m/s. This value of the entrainment flux is high but within range of entrainment fluxes measured previously under similar conditions. As part of the ABL water vapor budget study, we plan to compare LASE water vapor variance profiles and entrainment fluxes to those derived from in situ data from the flux measuring aircraft that participated in the SGP97.

LASE measurements made on July 14, 1997 show dramatically the passage of a cold front through the SGP97 region. Figure 4 shows the LASE water vapor and aerosol profiles acquired during a south to north flight leg. Here it can be clearly seen that a synoptic scale weather system (i.e., cold front) dominates the ABL heterogeneity. Within the synoptic regimes on either side of the front, the ABL appears homogeneous. LASE data also revealed other examples of heterogeneous ABL development and the impacts of synoptic scale meteorological features on the development of the daytime convective mixed layer. Progress in understanding the spatial and temporal development of the ABL and its relationship to the environmental factors will be discussed during this presentation.

Summary

NASA's Lidar Atmospheric Sensing Experiment (LASE) system was operated from the NASA P-3 aircraft during the Southern Great Plains 1997 (SGP97) Experiment to investigate the development of the ABL. LASE obtained high resolution measurements of atmospheric aerosol backscattering and water vapor profiles that are being used to study ABL development during seven flights between July 11-17, 1997. Segments of data show examples of homogeneous development over long ranges (>180 km). These data were used to estimate average boundary layer height, water vapor mixing ratio variances, and entrainment fluxes. LASE data also showed examples of heterogeneous ABL development and dramatic impacts of a cold front passage on the development of the ABL in the SGP97 region. LASE water vapor and radiosonde water vapor measurements were found to agree within about 5%. LASE data, along with measurements from the Canadian NRC Twin Otter and NOAA Long-EZ aircraft, will be used to derive the spatial variability of heat, moisture, and carbon dioxide fluxes.

References

1. Southern Great Plains 1997 (SGP97) Hydrology Experiment Plan, NASA, 177 pp. (1997) (see http://hydrolab.arsusda.gov/sgp97/explan/)
2. Browell, E.V., LASE Measurements of Tropospheric Water Vapor, Aerosols, and Cloud Distributions, OSA Optical Remote Sensing of the Atmosphere Technical Digest, Vol. 5, pp 2, (1997).
3. Browell, E. V., S. Ismail, W. M. Hall, A. S. Moore, Jr., S. A. Kooi, V. G. Brackett, M. B. Clayton, J. D.W. Barrick, F. J. Schmidlin, N. S. Higdon, S. H. Melfi, and D. N. Whiteman, LASE validation experiment, in Advances in Atmospheric Remote Sensing with Lidar, A. Ansmann, R. Neuber, P. Rairoux, and U. Wandinger, eds., Springer-Verlag, Berlin, 289-295, (1997).
4. Ferrare, R. et al., LASE Measurements of Aerosols and Water Vapor During TARFOX, 19th ILRC Proceedings, 1998.
5. Edwards, W. C., L. P. Petway, and C. W. Antill, 19th ILRC Proceedings, 1998.
6. Ponsardin, P. L. and E. V. Browell, J. Mol. Spec., 185, 58-70, 1997.
7. Kiemle, C., G. Ehret, A. Giez, K.J. Davis, D.H. Lenschow, and S.P. Oncley, Estimation of boundary layer humidity fluxes and statistics from airborne differential absorption lidar (DIAL), J. Geophys. Res., 102, 29189-29203, 1997.

Water vapor and aerosol distribution over the Atlantic Ocean as observed by LEANDRE II during ACE 2

Cyrille Flamant†, Jacques Pelon and Didier Bruneau

Service d'Aéronomie du CNRS, Paris, France
†Phone: 33-1-44274872, Fax:33-1-44273776, E-mail: cyf@aero.jussieu.fr

1. Introduction

The water vapor distribution over the Atlantic Ocean as been observed with the French airborne DIAL system LEANDRE II (Quaglia et al., 1996) flown onboard the F27/ARAT during the ACE-2 experiment. Detailled analysis of the vertical and horizontal water content fluctuations during a flight between Faro (Portugal) and Porto-Santo (Figure 1) on 7 July 1997 is presented. Remote sensing of the water vapor field in the troposphere is highly desirable for establishing the Earth's energy budget at the mesoscale and at the global scale. Given their spatial resolution (both horizontal and vertical), such airborne lidar systems can be used to improve latent heat flux parameterizations in mesoscale models and general circulation models (GCM). The objective is to study the impact of North-South water vapor and aerosol gradients observed over the Atlantic on the Earth's longwave budget at the mesoscale using the radiation scheme utilized in the European Center for Medium-range Weather Forcast (ECMWF). We have used the one-dimensional ECMWF radiation scheme (Morcrette et al., 1986) to calculate the up-going IR flux from temperature and water content profiles at each end of the flight track (during the ascent in Faro and the descent in Porto-Santo, see Figure 1). We have focused on up-going IR fluxes since they could directly be compared to measurements made an EPSLEY PSP Pyranometer (between 4 μm and 45 μm) located underneath the aircraft.

2. The airborne water vapor lidar LEANDRE II

LEANDRE II uses a single flash-pumped alexandrite laser developed at the Service d'Aéronomie (Bruneau et al., 1991). During ACE 2, DIAL measurements were performed using the 13717.175 cm^{-1} absorption line with a strength of $7.25\,10^{-24}$ $cm\,mol^{-1}$. In-situ water-vapor measurements were made with a dew-point hygrometer during aircraft ascent and descent. In the following, water vapor mixing ratio profiles are averaged by the hundred which, given the lidar repetition rate and aircraft true air speed, is representative of a horizontal resolution of about 1 km.

3. Water vapor and aerosol distribution in Faro and Porto-Santo on 7 July 1997

On Figure 2, we show the reflectivity profiles measured by LEANDRE II off-shore from Faro and Porto-Santo. The corresponding water vapor mixing ratios inferred from LEANDRE II and those measured in-situ are shown of Figure 3. As the aircraft was progressing away from Faro, the elevated aerosol layer observed between 1.5 and 2.3 km and advected from the continent gradually disparears. In Porto-Santo, the lower troposphere aerosol content is much less than near Faro except in the lower 500 m. The water vapor content is also seen to vary significantly. Lidar-inferred profiles shown on Figure 3 are located approximately 75 km away from the land in both cases, which may explain the large variability at a given end of the flight track.

4. Water vapor and aerosol impact on upward longwave fluxes

In the radiation scheme, longwave flux in clear-sky conditions are calculated using a broadband flux emissivity method with 6 intervals covering the spectrum beween 0 and 2620 cm^{-1}. The temperature and pressure dependence of the absorption in longwave radiation follows Morcrette et al. (1986). The absorption coefficients are fitted from AGFL (1982). Water vapor, carbon dioxyde as well as ozone absorption are accounted for. Absorption effects related to aerorols are accounted using an emissivity formulation. To carry the computation, an uniform sea-surface temperature (SST) of 17°C is assumed between Faro and Porto-Santo. Results are shown in Faro and Porto-Santo on Figures 4 and 5. Below 1 km, measured and modeled IR

fluxes cannot be compared because the surface temperature of the warm land controls the IR fluxes. In the relatively aerosol-free region of Porto-Santo, agreement between measured and modeled fluxes is within 10 W m^{-2}. More importantly, the slope with which the flux decreases are identical. The difference observed (which is constant with height) may be caused by an overestimated SST. We note that for an SST 5°C cooler measured and modeled fluxes would match exactly. In faro, however, the slopes are significantly different and this difference is most likely related to the presence of aerosols not properly taken into account in the model. Below 3 km, the fluxes modeled using in-situ and lidar-derived water vapor mixing ratio are in good agreement. Above, the lidar derived water vapor content oscillates around an average value of zero, causing the IR flux to increase artificially.

5. Conclusion

To the first order, the up-going IR flux is controlled by the temperature profile as well as the aerosol vertical distribution and their optical properties. The later are coarsly parametrized in the ECMWF radiation scheme and could induce important errors in longwave radiation budget at the mesoscale. A marine aerosol model, suited to a forward lidar data inversion scheme in the lower atmosphere, has been tested with the data acquired over the Azores during the SOFIA and SEMAPHORE experiments (Flamant et al., 1998). The vertical distribution of aerosol optical properties can be calculated using the forward integration scheme of Klett (1985) and the knowledge of a reference backscatter coefficient obtained from in situ extinction measurements around 0.5 μm by a nephelometer onboard the aircraft. They will be implemented in the radiation scheme in order to test the improvement on upward IR flux modeling at the mesoscale and at the synoptic scale.

Acknowledgments. This research was funded by CNRS through the Programme Atmosphère Océan à Moyenne Echelle and by the European Space Agency.

References

Bruneau, D., H. Cazeneuve, C. Loth, and J. Pelon, 1991: 'Double-pulse dual-wavelength alexandrite laser for atmospheric water vapor measurement'. *Appl. Opt.*, **30**, 3930-3937.

Flamant, C., V. Trouillet, P. Chazette, and J. Pelon, 1998: 'Wind speed dependence of atmospheric boundary layer optical properties and ocean surface reflectance as observed by airborne backscatter lidar'. *J. Geophys. Res.*, in revision.

Klett, J. D, Lidar inversion with variable backscatter/extinction ratios, Appl. Opt., 24, 1638-1643, 1985.

Morcrette, J.-J., L. Smith, and Y. Fouquart, 1986: 'Pressure and Temperature dependence of the absorption in longwave radiation parametrizations'. *Beitr. Phys. Atmosph.*, **59**, 455-469.

Quaglia, P. et al., 1996: 'The airborne water vapor lidar LEANDRE II: design, realization, tests et first validations'. In *Advances in atmospheric remote sensing with lidar*, A. Ansmann, R. Neuber, P. Rairoux and U. Wandinger Eds. (Springer), selected papers of the 18th ILRC, Berlin, 22-26 July, 1996.

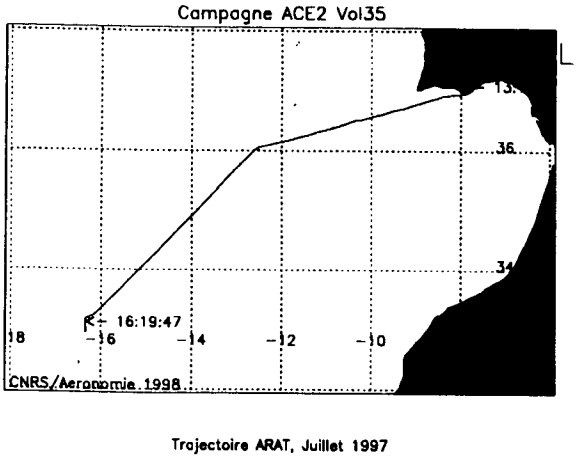


Figure 1: ARAT trajectory on 6 July 1997 between Faro (Portugal) and Porto-Santo.

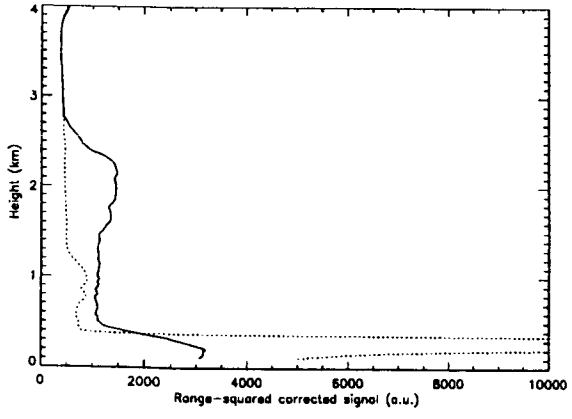


Figure 2: Atmospheric reflectivity at 0.73μm measured over the Atlantic by LEANDRE II close in Faro (solid line) and close to Porto Santo (dashed line).

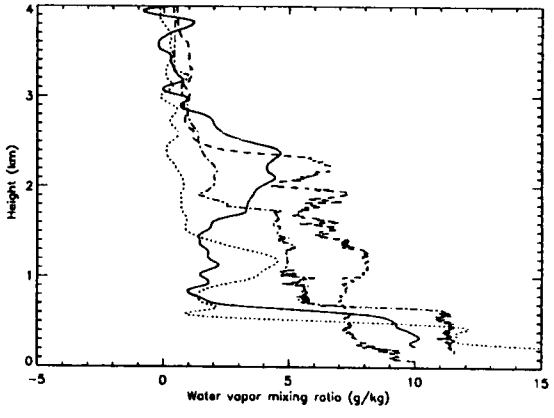


Figure 3: Water vapor mixing ratio ($g\,kg^{-1}$) measured over the Atlantic by LEANDRE II close in Faro (solid line) and close to Porto Santo (dotted line). Also shown is the water vapor mixing ratio measured by in-situ means during the ascent in Faro (dashed line) and the descent in Porto Santo (dashed-dotted line).

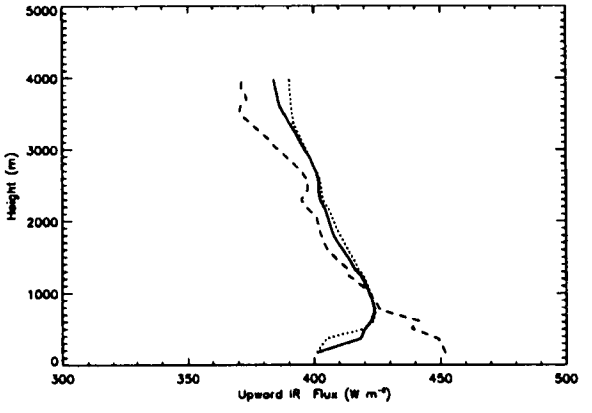


Figure 4: Upward IR flux measured onboard the ARAT (dahed line) and modeled using a temperature sounding and water vapor mixing ratio vertical distribution measured in-situ during the ascent in Faro (dotted line) and inferred fron LEANDRE measurements (solid line).

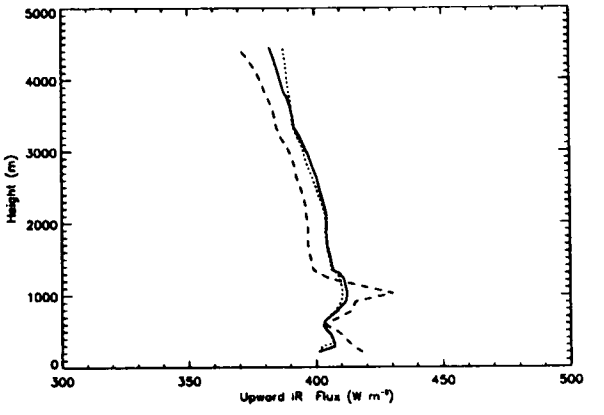


Figure 5: Upward IR flux measured onboard the ARAT (dahed line) and modeled using a temperature sounding and water vapor mixing ratio vertical distribution measured in-situ during the descent in Porto-Santo (dotted line) and inferred fron LEANDRE II measurements (solid line).

Airborne Lidar Measurements of Ozone and Aerosols During the Pacific Exploratory Mission-Tropics A

Marta A. Fenn[1], Edward V. Browell[2], William B. Grant[2], Carolyn F. Butler[1], Susan A. Kooi[1], Marian B. Clayton[1], Vincent G. Brackett[1], Gerald L. Gregory[2]

[1]Science Applications International Corporation, 1 Enterprise Parkway, Hampton, Virginia, 23665 USA
Phone: 757-864-2712; Fax: 757-864-7790; E-mail: m.a.fenn@larc.nasa.gov
[2]Atmospheric Science Division, NASA Langley Research Center, M S 401A Hampton, Virginia, 23681 USA

Abstract: Airborne lidar measurements of aerosol and ozone distributions from the surface to above the tropopause over the South Pacific Ocean are presented. The measurements illustrate large-scale features of the region, and are used to quantify the relative contributions of different ozone sources to the tropospheric ozone budget in this remote region.

1 Introduction

NASA Langley Research Center's Airborne Multiwavelength Lidar System made measurements of ozone (O_3) and aerosol distributions from the surface to above the tropopause over the South Pacific Ocean as part of a Global Tropospheric Experiment (GTE) Pacific Exploratory Mission , PEM Tropics A (PTA). PTA penetrated and explored one of the largest uncharted areas of the troposphere during August through October of 1996. A detailed survey of over 75 trace chemical species. The primary objectives of the PEM Tropics field experiment were to investigate the atmospheric chemistry of O_3 and its precursors in this photochemically and radiatively important region. The measurements obtained on this campaign provide a baseline against which future measurements can be compared in an area expected to show increased human influence in the next few decades.

2 Field Experiment

2.1 Airborne Instrumentation

The lidar flew on board the NASA DC-8 aircraft, transmitting 4 beams at 30 Hz both above and below the aircraft. The represented wavelengths included two in the ultraviolet at 288 and 300 n mfor the Differential Absorption Lidar (DIAL) measurement of O_3, as well as one in the visible at 600 nm and one in the infrared at 1064 nm. The latter two beams were used for the measurement of aerosol scattering ratio profiles. O_3 measurements were made with a vertical resolution of 300 m and a horizontal resolution of about 70 km. Measurement accuracy is 10% or 2 ppbv (parts per billion by volume) , whichever is larger, with a precision of 5% or 1 ppbv [1,2]. Aerosol scattering ratio measurements were analyzed at a vertical resolution of 60 m and a horizontal resolution of 470 m. The accuracy and precision of the aerosol measurements are 10% [2].

Additional instruments on board the DC-8 and P3-B made in-situ measurements of O_3, various O_3 precursors, and meteorological parameters. A fast response nitric oxide-chemiluminescence instrument measured in situ O_3 at aircraft altitude on board the DC-8.

2.2 Experiment Environment

During PTA, the lidar collected over 120 flight hours of data between the latitudes 72° S and 45° N and longitudes 152° E and 110° W, the vast majority of which was south of the equator. The DC-8 flew at several altitudes, often over the same ground track allowing the in-situ instruments to sample air which had been previously measured remotely by the lidar. After the first overflight of a ground track, lidar data served as a guide to the choice of subsequent flight altitudes for further sampling by in-situ instruments.

The meteorological conditions were considered typical during the campaign [3]. Prominent features that effect the Pacific circulation in the lower troposphere (below 3 km) are subtropical anticyclones, the Intertropical Convergence Zone (ITCZ) and the South Pacific Convergence Zone (SPCZ). The ITCZ crossed the entire Pacific Basin at an average latitude of 10° N. It defines a region of convection as the northeasterly winds of the northern tropics converge with the southeasterly winds of the southern tropics. Another zone of easterly confluent flow, the SPCZ, stretches southeastward from about 15° N near China to near Tahiti. In the mid-troposphere (above 3 km) there is no evidence of these zones in the wind fields. North of 20° N and south of 20° S, the winds are westerly with easterly flow in the intervening latitudes. Over the south Pacific, the winds poleward of 20 ° S remain westerly into the upper troposphere. The subtropical jet stream located at 30° S provided wind speeds in excess of 50 m s^{-1} in the upper troposphere over Australia, diminishing to 10 m s^{-1} over much of the south Pacific. A region of strong sinking motion occurred over Australia and the Indian Ocean.

3 Data Results

3.1 Instrument Intercomparison

The DIAL O_3 measurements were made remotely from the DC-8 aircraft which served as a platform for an in situ instrument that measured O_3 at a resolution of 10 seconds (approximately 25 m vertical resolution during ascents and descents). Measurements between the two instruments were compared at every opportunity; for a total of 34 vertical soundings. Comparisons made between the two instruments agreed to better than 5%.

3.2 Ozone Data

The O_3 cross section shown in figure 1 consists of DIAL remote measurements with in situ measurement at the aircraft altitude (10 km). The data-free zone surrounding the aircraft (1.5 km) is filled in using a third degree polynomial fit to the near field data, in each direction, plus the in situ measurement. The result is a field that completely covers the troposphere. This method of data analysis provides a much more complete picture of the state of the troposphere. On flight 8, the typical clean marine environment having O_3 values less than 50 ppbv is being intruded by stratospheric air from the south (left side of the image) providing elevated levels of O_3 down to the lower troposphere (value of more than 60 ppbv even down to 8 km). A limited region of O_3 having values above 60 ppbv can be seen at 9-10 km on the right side of the image. Meteorological back-trajectory analyses [3] indicate this pocket of high O_3 originated from South America, and represents a pollution plume. Outflow from the South American continent is responsible for the enhanced O_3 at 4 km altitude, as well.

3.3 Aerosol Data

Aerosol measurements have been used in the past to help distinguish the high O_3 from stratospheric origin from the elevated O_3 due to pollution [4,5]. In the tropical Pacific, the aerosols were largely confined to the boundary layer, making the remote differentiation of pollution plumes more difficult. The high-resolution lidar measurements have proven valuable in showing the structure of the marine boundary layer, and how shear induced transport of boundary layer material into the lower troposphere is an important process. However, aerosol loading in the free troposphere was insufficient to distinguish high O_3 air of stratospheric origin from high O_3 pollution plumes.

3.4 Airmass Classification

In an attempt to determine the origin of the high O_3 plumes observed in the remote south Pacific (0° to 40° S and 120° to 180° W) , we analyzed meteorological back trajectories, potential vorticity fields, and in-situ tracers of stratospheric air when available. Results of this analysis contradict the perception that the region is pristine, with 30% of the volume of air between 1 and 9 km receiving some contribution of O_3 from pollution sources. PTA occurred during the maximum season of biomass burning in the southern hemisphere. The strong westerly winds aloft along

with the regions of subsidence could have brought pollution to this remote region from as far away as South America and Africa. O_3 of stratospheric origin dominated above 9 km altitude; 26% of the volume of air between 9 and 15 km received the majority of its O_3 from the stratosphere.

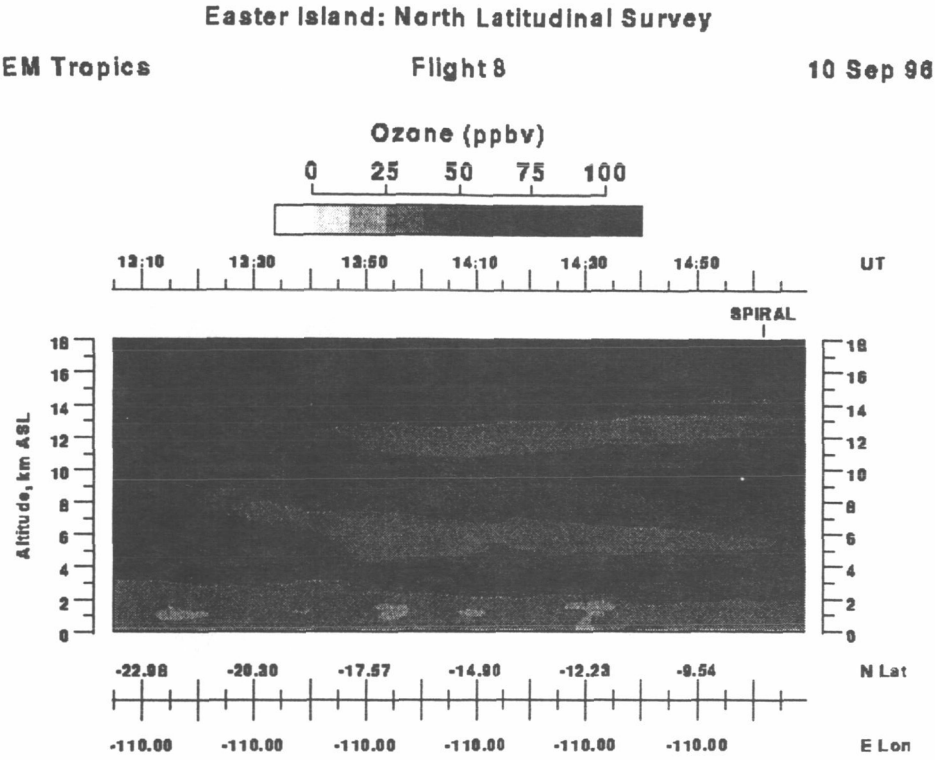


Fig. 1. Airborne lidar and in situ measurements of ozone distribution north of Easter Island, September 10, 1996.

References

1. Browell, E.V., Carter, A.F., Shipley, S.T., Allen, R.J., Butler, C.F., Mayo, M.N., Siviter, J.H., Hall, W.M.: NASA mulitpurpose airborne DIAL system and measurements of ozone and aerosol profiles. Appl. Opt. **22** (1983) 522-534
2. Browell, E.V.: Differential absorption lidar sensing of ozone. Proc. IEEE **77** (1989) 419-432
3. Fuelberg, H.E., Newell, R., Longmore, S.P., Zhu, Y., Westberg, D.J., Browell, E.V.: A meteorological overview of the PEM Tropics period. submitted to J. Geophys. Res.
4. Browell, E.V., et al.: Large-scale air mass characteristics observed over Western Pacific during summertime. J. Geophys. Res. **101** (1996) 1691-1712
5. Fenn, M.A., Browell, E.V., Butler, C.F.: Airborne Lidar Measurements of Ozone and Aerosols During PEM-West A and PEM-West B. Advances in Atmospheric Remote Sensing with Lidar. A. Ansmann, R. Neuber, P. Rairoux, U. Wandinger Eds. (1996) 355-358..

Rotational Vibrational–Rotational (RVR) Raman DIAL for Ozone Measurements in Clouds: Methodology and Experiment

Jens Reichardt[1], Scott E. Bisson[2], Susanne Krumbholz[3], Rudolf Baumgart[1], Claus Weitkamp[1], and Bernd Neidhart[1]

[1]GKSS-Forschungszentrum Geesthacht GmbH, Postfach 1160, D–21494 Geesthacht, Germany
Phone: +49 4152 871825, FAX: +49 4152 871888, E–mail: jens.reichardt@gkss.de

[2]Sandia National Laboratories, Livermore, CA 94551–0969, USA

[3]Max–Planck–Arbeitsgruppen c/o DESY, Notkestr. 85, D–22603 Hamburg, Germany

1 Introduction

Lidar remote measurements of ozone in cirrus clouds have recently been made at GKSS (Reichardt et al., 1996a). The lidar variant used for these observations is "conventional" Raman DIAL (McGee et al., 1993; Reichardt et al., 1996b), with two primary wavelengths transmitted into the atmosphere and ozone calculated from the differential absorption of the corresponding inelastic molecular return signals of nitrogen. A careful error analysis shows, however, that in the Raman–DIAL approach the wavelength dependencies of photon multiple scattering and of the atmospheric–particle extinction coefficient induce an uncertainty in the measured ozone molecule number density. This uncertainty can be substantial in thick water and ice clouds (Reichardt, 1997; Reichardt and Weitkamp, 1997).

To overcome this problem a novel technique has been developed that reduces these uncertainties and eliminates the need for a second laser. The approach is based on differential absorption by ozone of the purely rotational Raman return signals from nitrogen and oxygen as the on–resonance and the vibrational–rotational Raman return from nitrogen or oxygen as the off–resonance wavelength. Because of this combination, rotational vibrational–rotational, or RVR, Raman DIAL might be an appropriate term for the new method. The main advantages of the RVR Raman DIAL over a "conventional" Raman DIAL are a drastic reduction of the wavelength–dependent effects on the measured ozone concentration and reduced complexity of the lidar system. In this contribution the methodology as well as the setup of the RVR Raman DIAL are described. In a model calculation its performance is compared with conventional Raman DIAL for ozone measurements in upper–troposphere cirrus clouds, and a first measurement is presented.

2 Methodology

The radiation source of the RVR Raman DIAL is a tunable narrowband XeCl excimer laser injection–locked at a wavelength of $\lambda_e = 307.94\,\text{nm}$. For ozone measurements the anti–Stokes branch of the pure rotational Raman spectrum of oxygen and nitrogen and — in this work — the first (Stokes) vibrational–rotational Raman spectrum of nitrogen are filtered out of the atmospheric backscatter signal and registered as the on–line and off–line wavelengths λ_R and λ_{VR}, respectively. Setting the emission wavelength close to the short–wavelength boundary of the broadband excitation spectrum of XeCl and using the anti–Stokes Raman branch reduces the influence of possible unseeded laser pulses or amplified spontaneous emission (ASE) considerably.

For $\lambda_{VR} = 332\,\text{nm}$ the filter bandwidth is chosen to cover the full spectrum of the vibrational–rotational Raman transitions of nitrogen. For λ_R calculations were carried out to optimize the filter bandwidth and center wavelength for minimum dependency of the return signal on atmospheric temperature and maximum signal intensity. An important constraint to these considerations is the filter performance at wavelength λ_e because high suppression of elastically backscattered light is crucial for the ozone measurement. It turns out that filters with a center wavelength of 307.4 nm and a bandwidth between 0.3 and 0.5 nm are the best choice. Here, temperature effects are well below 1% for temperature differences of 50 K, and 60 to 80% of the intensity of the anti–Stokes branch lie within the bandpass of the filter. This is equivalent to 10 to 12 times the vibrational–rotational signal intensity of nitrogen. It is important to note that RVR Raman DIAL is a single–laser technique in contrast to conventional DIAL and Raman DIAL which both require two radiation sources.

Thus the proposed method promises a considerable reduction in system complexity.

Whereas differential absorption by ozone is roughly the same for both Raman DIAL and RVR Raman DIAL, the wavelength separation between the on–line and the off-line signals is much smaller in the case of the RVR Raman DIAL. The new technique is therefore far less sensitive to wavelength–dependent effects such as multiple scattering and particle extinction. This reasoning is substantiated in the following model calculation, for more details see Reichardt et al., 1997.

In the model atmosphere that was used for the comparison of the RVR Raman DIAL technique with conventional Raman DIAL the height of the tropopause was 11 km, and the ozone number density was assumed to be $0.8 \times 10^{12}\,\mathrm{cm}^{-3}$ throughout the troposphere. Between 9 and 11 km a homogeneous cirrus cloud with a particle extinction coefficient of $0.2\,\mathrm{km}^{-1}$ was present. The theoretical vibrational–rotational Raman return signals were calibrated at 8 km height with typical data of a 2–hour measurement with the present GKSS combined aerosol–ozone Raman lidar. The ratio of the effective on– and off–line Raman backscattering cross sections of the RVR Raman DIAL was used to calculate the number of rotational Raman return photons.

Under the assumption that the wavelength dependence of the particle extinction is $\propto \lambda^{\kappa}$, the relation between systematic ozone uncertainty, uncertainty of κ, and cloud particle extinction has been calculated for the cloud center (Fig. 1). For simplicity, the influence of multiple scattering was neglected here. Fig. 1 shows that the performance of the RVR Raman DIAL is superior to that of conventional Raman DIAL.

In order to assess the influence of particle multiple scattering on the ozone measurements in the model cloud, we carried out calculations with a multiple–scattering model (Shipley, 1978) modified and expanded for inelastic scattering processes (Reichardt and Krumbholz, 1998, to be published). The cloud was assumed to consist of ice spheres that are distributed in projection–area equivalence to cirrus particle size spectra measured in–situ (Heymsfield and Platt, 1984). The model results are shown in Fig. 2. 'Small particles' denotes a particle size spectrum with a high fraction of particles $< 20\,\mu$m, 'large particles' stands for a particle distribution with particles $> 20\,\mu$m. The RVR Raman DIAL reduces the effect of multiple scattering by a factor of 4 for both small and large particles. Thus for ozone measurements in clouds the RVR Raman DIAL promises to perform significantly better than the conventional Raman DIAL, and may well develop into a powerful technique for studies of particle–ozone interactions in the troposphere and lower stratosphere.

3 Experiment

A first experimental setup of the RVR Raman DIAL was installed in the trailer of the Sandia water–vapor Raman lidar (Bisson et al., 1998, submitted to *Appl. Opt.*). A Lambda Physik LPX 150 T MSC XeCl excimer laser serves as the light source, optionally a Lambda Physik LPX 220i XeCl excimer laser can amplify the output power of typically 12 W

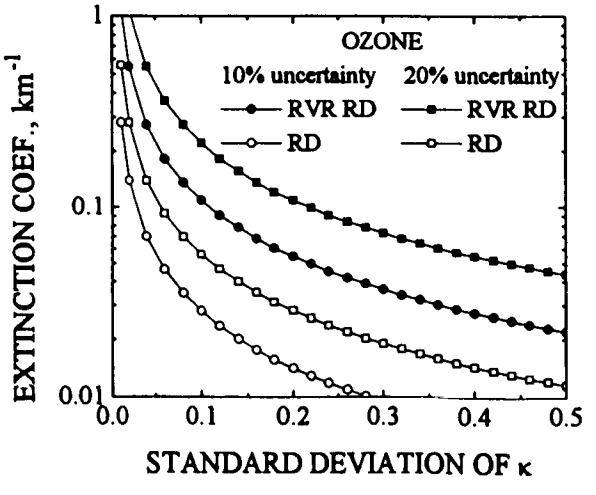


Figure 1: Relation between particle extinction coefficient and uncertainty in κ for a given ozone systematic uncertainty. RD — Raman DIAL.

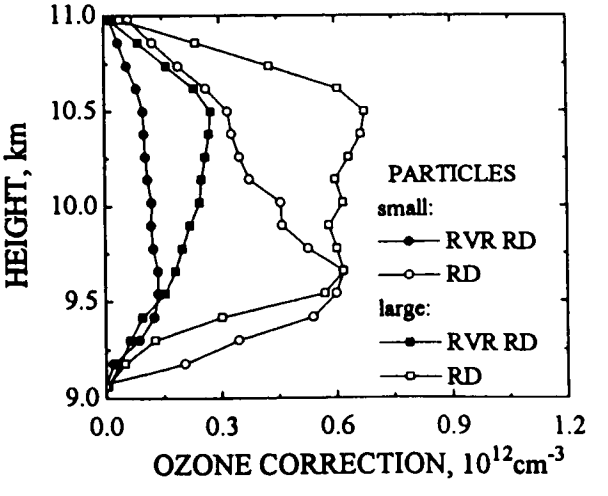


Figure 2: Ozone correction for the effect of multiple scattering. For the definition of 'small particles' and 'large particles', see text. RD — Raman DIAL.

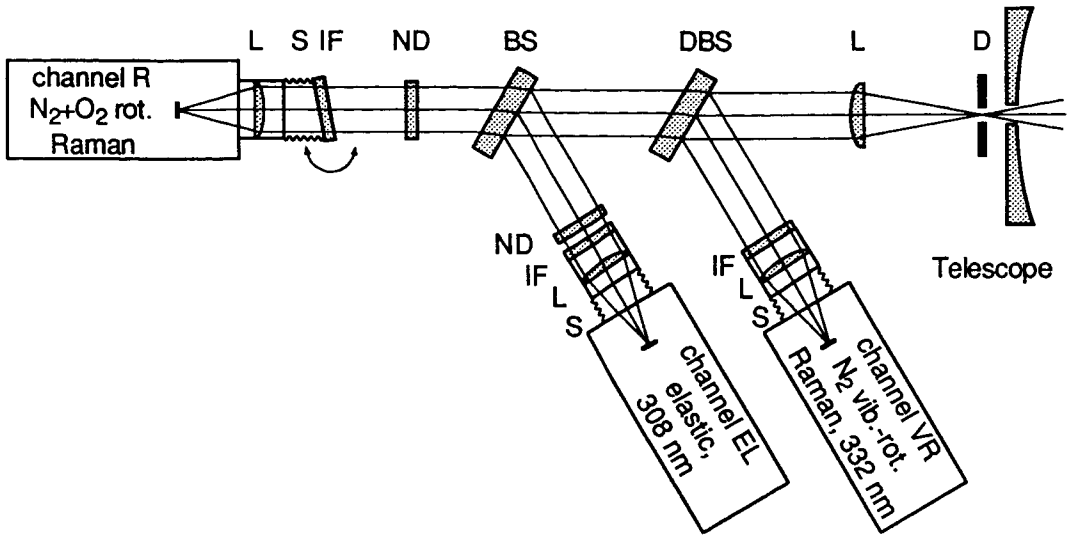


Figure 3: RVR Raman DIAL receiver: D, diaphragm; L, lens; DBS, dichroic beamsplitter; BS, beamsplitter; ND, neutral density filter; channel R, channel EL, channel VR, light–proof assemblies of photomultiplier tube, flexible shield S, lens L, and interference filter IF for the detection of atmospheric rotational Raman, elastic, and nitrogen vibrational–rotational Raman backscattering signals. The center wavelength of the channel–R interference filter can be tuned by rotating the filter around its vertical axis.

to over 40 W. After beam expansion by a factor of 5 the laser pulses are transmitted into the atmosphere. The spectral purity of the outgoing light is monitored on–line. Over hours of seeded laser operation neither build–up of scavanging side bands nor ASE could be observed. A schematic diagram of the receiving system is shown in Fig. 3. The atmospheric return signal is collected by a 760–mm–diameter Cassegrain telescope (f/4.5) and focused on an adjustable diaphragm serving as the field stop. Apertures of 1 to 3 mm and corresponding divergences of the collimated light inside the receiver of 6.3 to 19.0 mrad are usually chosen for the experiments. Light backscattered from nitrogen vibrational–rotational Raman scattering is separated from the return signals at shorter wavelengths by a dichroic beamsplitter and, after passing an interference filter (center wavelength (CWL) 332 nm, full width at half maximum (FWHM) 2 nm), is detected in channel VR. The atmospheric signal around 307.94 nm is divided by a beamsplitter (92% transmission) for the detection of elastical (channel EL; interference filter: 308 nm CWL, 2 nm FWHM) and rotational–Raman backscatter light (channel R; interference filter: 307.75 nm CWL at normal incidence, 0.4 nm FWHM). The channel–R interference filter is mounted on a precision rotary stage to allow fine tuning of the center wavelength by tilting. Both channel R and channel EL can be protected from the intense short–distance return signals by optional neutral density filters. The photomultipliers are operated in single–photon mode, the data acquisition electronics is triggered by straylight of the transmitted pulses. The range bins of the multichannel scalers are set to 75 m, 1000 range bins are stored on hard disc every 120 s of measurement time.

Fig. 4 displays a nighttime measurement of a cirrus cloud on 17 Sep 1997. Obviously, tuning the interference–filter center wavelength of channel R off the laser wavelength, i. e., increasing the tilt angle, reduces the contribution of the elastically backscattered light to the signal of channel R drastically. By use of the simultaneously measured backscatter ratios of the rotational Raman and the elastic signal, one can calculate the suppression of the elastic light in channel R. For filter tilt angles of 3°, 5°, and 7° a suppression of 5.8, 74, and 208 is found, respectively. Although these experimental values are smaller than theoretical estimates derived from the filter transmission curve, the measurement clearly demonstrates that interference filters can be used to separate rotational Raman from elastically backscattered light in the ultraviolet. Current work is aimed at further improving the receiver performance.

4 Acknowledgment

Our thanks to Phil Paul, Sandia National Laboratories, for supplying the laser spectrometer and for help on laser alignment.

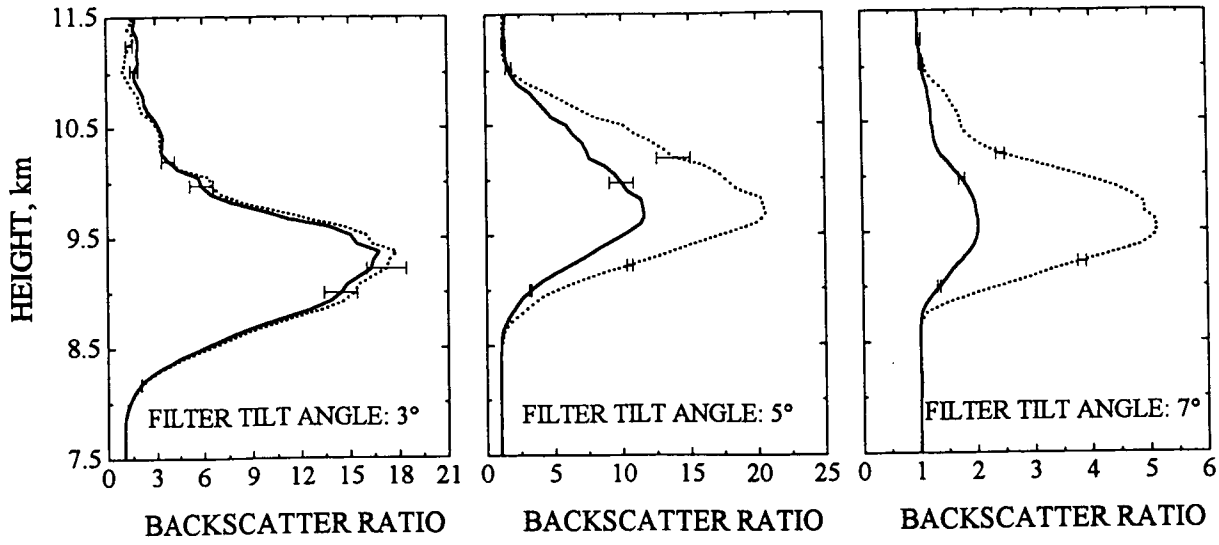


Figure 4: Backscatter–ratio time series of the rotational Raman (solid) and the elastic (dotted) signals measured during a cirrus event on 17 Sep 1997. From left to right, the tilt angle of the channel–R interference filter was 3°, 5°, and 7°, respectively. Temporal resolution of the profiles is 480 s, the lidar signals are smoothed with a sliding average window length of 600 m. Error bars indicate statistical noise.

References

Heymsfield, A. J. and Platt, C. M. R. (1984). A parameterization of the particle size spectrum of ice clouds in terms of the ambient temperature and the ice water content. *J. Atmos. Sci.*, 41(5):846–855.

McGee, T. J., Gross, M., Ferrare, R., Heaps, W., and Singh, U. (1993). Raman Dial measurements of stratospheric ozone in the presence of volcanic aerosols. *Geophys. Res. Lett.*, 20(10):955–958.

Reichardt, J. (1997). Optische Fernmessung von Ozon in Zirruswolken. Dissertation, University of Hamburg, Germany, 119 pp.

Reichardt, J., Ansmann, A., Serwazi, M., Weitkamp, C., and Michaelis, W. (1996a). Unexpectedly low ozone concentration in midlatitude tropospheric ice clouds: A case study. *Geophys. Res. Lett.*, 23(15):1929–1932.

Reichardt, J., Wandinger, U., Serwazi, M., and Weitkamp, C. (1996b). Combined Raman lidar for aerosol, ozone, and moisture measurements. *Opt. Eng.*, 35(5):1457–1465.

Reichardt, J. and Weitkamp, C. (1997). Raman–DIAL measurements in the upper troposphere and stratosphere: The effect of high–altitude ice clouds on ozone. *1997 OSA Technical Digest Series*, 5:208–211.

Reichardt, J., Weitkamp, C., and Krumbholz, S. (1997). Rotational vibrational–rotational (RVR) Raman DIAL: A novel lidar technique for atmospheric ozone measurements. *ESA SP-397*:237–241.

Shipley, S. T. (1978). The measurement of rainfall by lidar. PhD Thesis, University of Wisconsin, Madison, 187 pp.

Daytime Measurements of Aerosol Particle Extinction and Ozone Profiles with a Combined Elastic DIAL / Raman DIAL

Volker Matthias, Jens Bösenberg

Max-Planck-Institut für Meteorologie, Bundesstraße 55, D–20146 Hamburg
Phone: +49 40 4123-5087, Fax: +49 40 41173-269, E-mail: vom@lidar.dkrz.de

1 Introduction

Ozone DIAL is a technique which is capable of giving ozone density fields in the boundary layer and the lower free troposphere. The development of the ozone distribution in the boundary layer can be investigated during time episodes of several days with high resolution and accuracy. However, it remained difficult for all types of UV-DIAL-systems to get precise information about the ozone density in regions of strong gradients in the aerosol distribution [1]. The reason for this is that aerosol backscatter and extinction profiles can only be calculated with sufficient accuracy under cloud free conditions and with several assumptions (e.g. the lidar ratio) [2].
Additional Raman channels allow the independent measurement of the aerosol particle extinction, also at daytime if the Raman-backscattered light is in the solar blind region below 300 nm. With two Raman channels it is possible to calculate ozone density profiles which are independent of aerosol particle backscatter errors [3].

2 Calculation of ozone density and aerosol particle extinction and backscatter profiles

The aerosol particle extinction in the UV can be calculated modifying the equation given by *Ansmann* [4] and assuming that the ozone density is known:

$$\alpha_{aer}(\lambda_{on}) = \frac{1}{(1+(\frac{\lambda_R}{\lambda_{on}})^a)}\left(\frac{d}{dz}ln(\frac{N(z)}{P_R(z)z^2}) - \alpha_{ray}(\lambda_{on},\lambda_R,z) - \alpha_{O_3}(\lambda_{on},\lambda_R,z)\right) \quad (1)$$

Using two equations of this type, the aerosol particle extinction can be eliminated and the resulting equation can be solved for the ozone number density:

$$N_{O_3}(z) = \frac{1}{\Delta\sigma_{O_3}} \times \left(K_2\frac{d}{dz}ln(P_{R_2}(z)z^2) - K_1\frac{d}{dz}ln(P_{R_1}(z)z^2) + B + R\right) \quad (2)$$

This is the full Raman DIAL equation in which the corrections B for differential Raman backscatter and R for differential Rayleigh extinction have to be taken into account. The terms K_1 and K_2 contain the wavelength dependence of the aerosol particle extinction. The corrections are small and can be calculated with high accuracy if the air density is known from radiosondes or calculated out of ground data with standard atmosphere conditions. With this method, ozone profiles and aerosol particle extinction can be determined out of only two measured Raman signals and the assumption about the wavelength dependence of the aerosol particle extinction.
With the extinction information, it is possible to calculate aerosol particle backscatter profiles without assumptions about the lidar ratio. One gets the lidar ratio out of the measurements.
For calculating the aerosol particle backscatter, some assumptions about the total backscatter in a distinct height have always to be made. This is easy under cloud free conditions since in the free troposphere $\beta_{aer} \ll \beta_{mol}$ and $\beta(z_0) = \beta_{aer}(z_0) + \beta_{mol}(z_0) \approx \beta_{mol}(z_0)$ in the calibration height z_0. Rearranging two lidar equations in the UV (at z and z_0) leads to:

$$\beta_{aer}(z) = -\beta_{mol}(z) + \left(\beta(z_0)\frac{P(z)z^2}{P(z_0)z_0^2} \times e^{2\int_{z_0}^{z}(\alpha_{aer}(\zeta)+\alpha_{mol}(\zeta)+\alpha_{O_3}(\zeta))d\zeta}\right) \quad (3)$$

This formula is equivalent to that given by *Ansmann*, but easier to calculate since the Raman signals do not appear in this equation.

This method of retrieving the aerosol particle backscatter doesn't work below clouds, where it's very difficult to make a correct calibration under high aerosol loads in the PBL. In presence of single Cumulus clouds, one can make use of the information out of the calibration in the cloud gaps. The calibration equation contains information about the system constants and the transmission of the lowest part of the atmosphere.

$$\frac{P(z_0)z_0^2}{\beta(z_0)} e^{2\int_{z_{lh}}^{z_0}(\alpha_{aer}(\zeta)+\alpha_{mol}(\zeta)+\alpha_{O_3}(\zeta))d\zeta} = Ke^{-2\int_0^{z_{lh}}(\alpha_{aer}(\zeta)+\alpha_{mol}(\zeta)+\alpha_{O_3}(\zeta))d\zeta} = KT_{lh} \quad (4)$$

where z_{lh} is the lowest height in which information about the aerosol particle extinction is available and K stands for the system constants. Assuming that the transmission of the lowest part of the atmosphere doesn't change too much during the appearance of the cloud, one can calculate the aerosol particle backscatter below the cloud as follows:

$$\beta_{aer}(z) = -\beta_{mol}(z) + \frac{P(z)z^2}{KT_{lh}} \times e^{2\int_{z_{lh}}^{z}(\alpha_{aer}(\zeta)+\alpha_{mol}(\zeta)+\alpha_{O_3}(\zeta))d\zeta} \quad (5)$$

This gives more reliable results than a calibration somewhere below the cloud, where no information about the aerosol characteristics is available.

3 Systematical and statistical errors using the Raman technique

The main error doing measurements of the atmospheric Raman-backscattering is the statistical error due to the low signal intensities. For Raman-DIAL measurements with the MPI laser system, which emits laser light at 248 nm, 268 nm 292 nm and 320 nm, one has different possibilities to choose the detected Raman wavelengths. The O_2 and N_2 atmospheric backscattering of the 248 nm and the 268 nm offer four wavelengths in the solar blind region at 258 nm, 263 nm, 280 nm and 286 nm. The wavelength pair with the lowest statistical error is the 263/286 nm. These wavelengths have higher differential absorption than the 280/286 and higher backscattered intensities than the 258 nm and 280 nm because they use nitrogen Raman backscatter which is ca. 3 times higher than the oxygen Raman backscatter in the atmosphere (Figure 1).

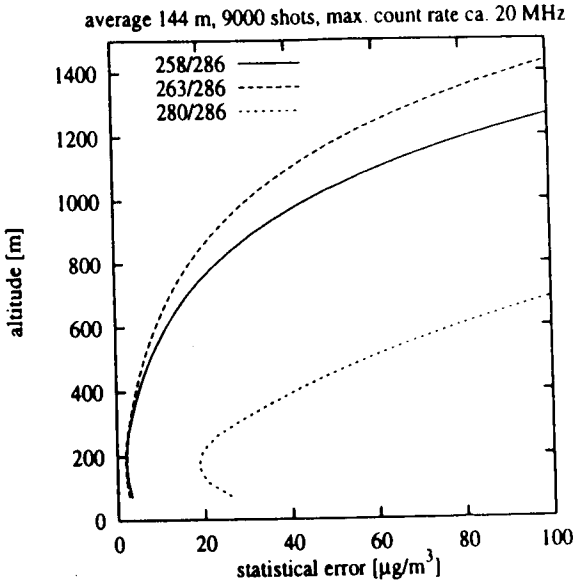


Figure 1: Statistical error for different Raman DIAL wavelength pairs. Model calculations for full overlap in 300 m and maximum signal in 200 m

Although maximum counting rates of ca. 20 MHz in 200 m were assumed for these calculations, the statistical error gets big in higher altitudes. This indicates, that high counting rates and repetition rates have to be achieved, to avoid too high averaging in time and space.

There additionally exist two main systematic errors using Raman backscattered signals which have to be avoided for correct results. These are

1. The dead time of the counting system is not considered.

2. Precise information about the starting of the laser pulse is not available.

The measured deadtime of the two photon counting channels of the MPI-UV-DIAL-system are 11.3 ns and 8.7 ns, respectively. The measurements where made with a method proposed by Johnson 1966 [5] and have an accuracy of better than 0.5 ns. Figure 2 shows the signal errors with and without dead time correction in dependence of the real counting rate.

If no dead time correction is applied, the error due to dead time effects gets bigger than 1 % at counting rates of more than 1 MHz. With dead time correction of accuracy better than 0.5 ns, the 1% limit is reached at 20 MHz. High counting rates cannot be achieved without dead time correction.

Attention has also be paid to the precise determination of the starting point of the laser. Photon counting data acquisition systems often have time resolutions

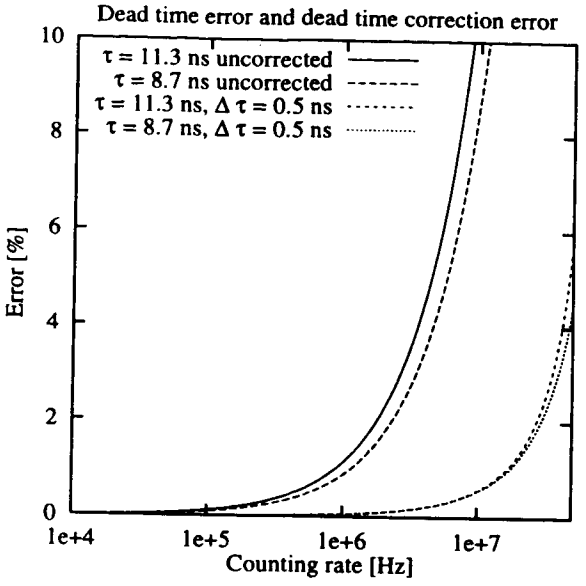


Figure 2: Dead time error with and without deadtime correction

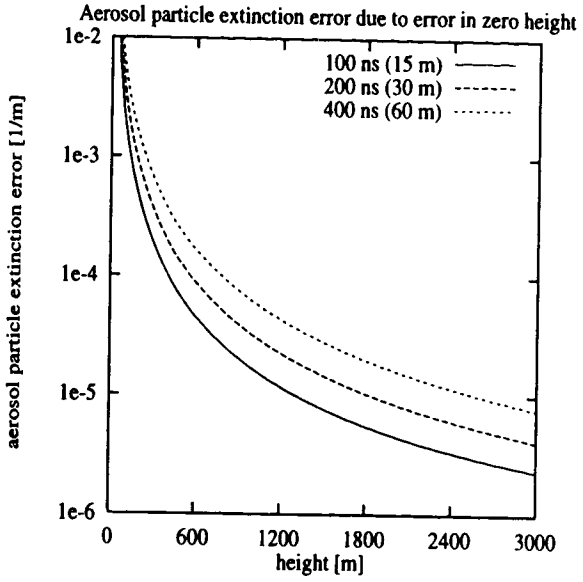


Figure 3: Aerosol particle extinction error at 351 nm due to incorrect range determination

of 200 ns or bigger. This can lead to errors in the determination of the distance z of the backscattered signal of 15 m or worse. Figure 3 shows the aerosol particle extinction errors due to this effect for 351 nm. In the lowest altitudes up to ca. 400 m, the error is ca. 100 % of typical aerosol particle extinction values ($1 \cdot 10^{-4}$ 1/m) even for a range error of only 15 m (= 100 ns). However, the effect on Raman DIAL measurements is very small since $K_1 \approx K_2$ so that the range z^2 almost disappears in the Raman DIAL equation (2).

4 Raman DIAL measurements

The UV-Lidar-system of the Max-Planck-Institut für Meteorologie is a combined Elastic DIAL / Raman DIAL. It is based on a KrF-Excimer-Laser (λ = 248 nm) with subsequent Raman shifting on D_2 (λ = 248 nm, 268 nm, 292 nm and 320 nm). The backscattered light is detected in 5 analog and 2 Raman channels, two telescopes cover a height range from 300 m to 3500 m.

Straylight of the elastic lidar returns in the Raman channels is suppressed by a factor of 10^{-8} by a spectrometer and small bandwidth interference filters (FWHM 1.5 nm). The N_2-Raman-Backscatter returns at 263.8 nm and at 286.4 nm are detected by photon counting PMTs (EMI 9893 QB 350) with subsequent 300 MHz discriminators and a two channel 700 MHz photon counter.

The elastic lidar returns at 268 nm, 292 nm (both telescopes) and 320 nm (far range telescope) are detected by a PMT with an DC-20 MHz amplifier and a 10 MHz ADC. They are than stored by a SUN workstation.

Ozone profiles have been measured with DIAL and Raman DIAL. They were calculated with the DIAL formula including aerosol correction, which uses a lidar inversion algorithm given by *Fernald* [6], and with the Raman DIAL formula (2) (Figure 4). The Raman signals were averaged over 240 m and 36000 shots to get the statistical errors below ca. 12 $\mu g/m^3$. The height resolution for the elastic signals was 120 m in the same time period. Substantial differences, bigger than the statistical uncertainties, appear at the top of the boundary layer (ca. 1100 m), the gradient in the ozone density is here sharper for the elastic signals. This can also be seen in the backscatter profile calculated with the lidar inversion algorithm, assuming a height constant lidar ratio of 35 sr (Figure 5). The aerosol particle extinction has been calculated for 286 nm following (1), the plotted statistical error includes the ozone error given in Figure 4 and the statistical error of the Raman signal. The aerosol particle backscatter was calculated following (3) with a calibration value of $\beta_{aer}/\beta_{ray} = 0.1$ in 1600 m.

The lidar ratio can be calculated out of the Raman data. In this case it suffers from high statistcal errors and low aerosol particle extinction values above 1 km. In 860 m the lidar ratio is $20 \pm 10 sr$.

In conclusion, one can say that the Raman DIAL technique gives promising results which are not influenced

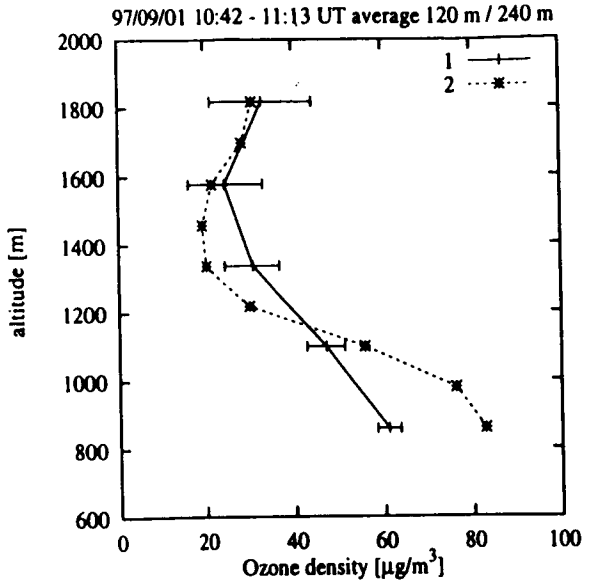


Figure 4: Ozone density profiles calculated with the Raman DIAL method (1) and the DIAL method with aerosol correction following *Fernald*'s inversion algorithm and a height constant lidar ratio (2).

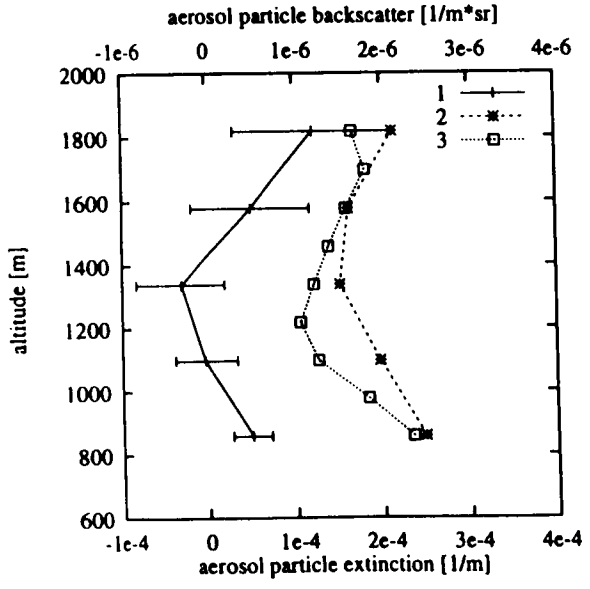


Figure 5: Aerosol particle extinction profile from the 286 nm Raman backscattered light (1), 292 nm backscatter with aerosol extinction and ozone correction (2) and 292 nm backscatter with lidar inversion algorithm and ozone correction (3).

by aerosol interference. It can be used to measure ozone density profiles under difficult conditions with high aerosol gradients or below clouds. The aerosol particle extinction and therefore the lidar ratio can also be calculated at daytime, which gives the possibility of a better understanding of the daytime aerosol processes.

Up to now, the method suffers from high statistical errors, but higher repetition rates of the laser system and a better detection efficiency can improve these first measurements substantially.

References

[1] Browell, E. V. , S. Ismail und S. T. Shipley : "Ultraviolet DIAL measurements of O_3 profiles in regions of spatially inhomogeneous aerosols", Applied Optics Vol. 24, No. 17, 1985, pp. 2827 - 2836

[2] Sasano, Y. , E. V. Browell und S. Ismail : "Error caused by using a constant extinction/backscattering ratio in the lidar solution", Applied Optics Vol. 24, No. 22, 1985, pp. 3929-3932

[3] Matthias, V., V. Wulfmeyer, and J. Bösenberg: "Comparison of Retrieval Methods in Tropospheric Ozone DIAL: The Impact of Raman Measurements", in: Advances in Atmospheric Remote Sensing with Lidar, 1996 pp. 403 - 406

[4] Ansmann, A. , U. Wandinger, M. Riebesell, C. Weitkamp und W. Michaelis : "Independent measurement of extinction and backscatter profiles in cirrus clouds by using a combined Raman elastic-backscatter lidar", Applied Optics Vol. 31, No. 33, 1992, pp. 7113-7131

[5] Johnson, F. A. , R. Jones, T. P.McLean, and E. R. Pike: "Dead-time corrections to photon counting distributions", Physical Review Letters Vol. 16, No. 13, 1966, pp. 589 - 592

[6] Fernald, F. G. , B. M. Herman und J. A. Reagan : "Determination of aerosol height distribution by LIDAR", Journal of Applied Meteorology Vol. 11, 1972, S.482 - 489

Daytime Raman Lidar Measurements of Water Vapor During the ARM 1997 Water Vapor Intensive Observation Period

D.D. Turner[1] and J.E.M. Goldsmith[2]

[1]Pacific Northwest National Laboratory, P.O. Box 999, MS K7-28, Richland, WA 99352
509-375-2590, 509-375-3641 (fax), dave.turner@pnl.gov

[2]Sandia National Laboratories, P.O. Box 969, MS 9409, Livermore, CA 94551
510-294-2432, 510-294-3870 (fax), jgold@ca.sandia.gov

INTRODUCTION

Water vapor is the most important greenhouse gas in the atmosphere, as it is the most active infrared absorber and emitter of radiation, and it also plays an important role in energy transport and cloud formation. Accurate, high resolution measurements (both temporally and spatially) of this variable are critical in order to improve our understanding of these processes and thus our ability to model them.

Raman lidars have been shown to provide these high resolution measurements in several experiments, but these measurements were primarily restricted to nighttime only, as Raman scattering is a weak process and the high solar radiation during the day tends to mask these signals. As part of an instrument development program for the Department of Energy's Atmospheric Radiation Measurement (ARM) program, a collaboration between Sandia National Laboratories and NASA Goddard Space Flight Center was funded to investigate recent improvements in lidar technology to address the ARM program's requirement for high resolution, 24-hour, automated water vapor measurements. The success of this project led to the decision to build this Raman lidar system, which was delivered to the ARM Cloud and Radiation Testbed (CART) site near Lamont, Oklahoma during the summer of 1996.

Because of the importance of water vapor, the ARM program initiated a series of three intensive operating periods (IOPs) at its CART site. The goal of these IOPs is to improve and validate the state-of-the-art capabilities in measuring water vapor. To date, two of the planned three IOPs have occurred: the first was in September of 1996, with an emphasis on the lowest kilometer, while the second was conducted from September - October 1997 with a focus on both the upper troposphere and lowest kilometer. These IOPs provided an excellent opportunity to compare measurements from other systems with those made by the CART Raman lidar. This paper addresses primarily the daytime water vapor measurements made by the lidar system during the second of these IOPs.

The ARM CART site is the home of several different water vapor measurement systems. These systems include the Raman lidar, a microwave radiometer, a radiosonde launch site, and an instrumented tower. During these IOPs, additional instrumentation was brought to the site to augment the normal measurements in the attempt to characterize the CART instruments and to address the need to improve water vapor measurement capabilities. Some of the instruments brought to the CART site include a scanning Raman lidar system from NASA/GSFC (which operated primarily at night), additional microwave radiometers from NOAA/ETL, a chilled mirror that was flown on a tethersonde and kite system, and dew-point hygrometer instruments flown on various aircraft.

LIDAR SYSTEM DESCRIPTION AND CALIBRATION

The CART Raman lidar (CARL) is an autonomous system that is permanently deployed at the site. It uses a tripled Nd:YAG laser (355 nm), with an average power of approximately 12 W and a repetition rate of 30 Hz. A 61 cm telescope directs the collected light into the detection optics, where the beam is split into two channels which have different fields-of-view. The wide field-of-view (WFOV) channel has a aperture of 2 mrad while the narrow field-of-view (NFOV) is 0.3 mrad. The WFOV channels are better suited to profile in the near field (up to approximately 1.5 km at night, lower during the day) as they admit more light than the NFOV channels at these low altitudes. After the field stops, the light is separated into three wavelengths (elastic backscatter and the two inelastic wavelengths associated with water vapor and nitrogen Raman backscatter) by dichroic mirrors. Narrow bandpass (0.3 nm) interference filters select only the desired wavelength, and the signal are detected using photon counting in approximately 0.25 microsecond bins, resulting in 39 m resolution. The narrow field of view coupled with narrow interference filters give the CARL system excellent nighttime and daytime abilities. System specifications are given in Table 1, and further details are given in [1].

Table 1. Lidar Specifications

Transmitter	
Laser	Nd:YAG third harmonic (355 nm)
Energy/pulse, rep. rate	400 mJ, 30 Hz
Beam Diameter, divergence	13 cm, ~0.1 mr
Receiver	
Telescope	61 cm diameter Dall-Kirkham
Channel bandpass	0.4 nm
Filter transmission	30-40%
Field of view	Dual, adjustable (typically 0.3 mr, 2 mr)
Channels	Rayleigh/aerosol (355 nm) Aerosol depolarization (355 nm) Water vapor (408 nm) Nitrogen (387 nm)
Electronics	Photon Counting, 39 m range resolution

Corrections for pulse pile-up (system dead-time), detector overlap, and differential attenuation at the different wavelengths are accounted for in the lidar system by techniques outlined in [1-2]. If these corrections are adequately specified, the resultant ratio of the water vapor and nitrogen signals are proportional to the water vapor mixing ratio. To calibrate these profiles, a height independent scale factor is derived to force the integrated precipitable water vapor measured by the Raman lidar to agree with that measured by the CART microwave radiometer. A single calibration scale factor was used the entire IOP lidar dataset.

COMPARISONS

One of the primary design goals was to build a Raman lidar system that was capable of making excellent daytime water vapor measurements without sacrificing the nighttime performance of the lidar. Figure 1 displays comparisons of 10 minute averaged nighttime and daytime CARL profiles to coincident radiosonde profiles, illustrating that the design goals of the lidar have been met. Melfi, et al. [3] further show that the nighttime abilities of the lidar in the upper troposphere are not hampered by this design by comparing profiles taken with the lidar to both radiosondes and dewpoint hygrometer measurements on an aircraft.

Since Raman scattering is a weak process, the high background radiance will affect the detected profiles most drastically during solar noon (approximately 1300 local, which is 1800 UTC). During the 1997 IOP, the Pacific Northwest National Laboratory (PNNL) Gulfstream aircraft

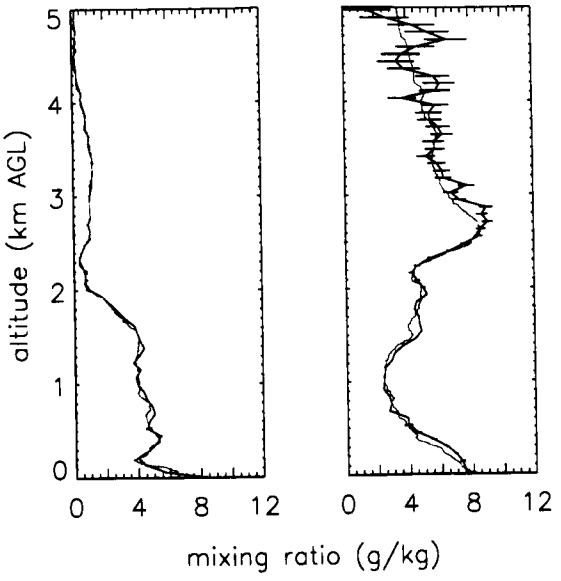


Figure 1. Comparisons of nighttime (left, 29 September at 0530 UTC) and daytime (right, 28 September at 1430 UTC) mixing ratio profiles from the CARL system (black with error bars) and coincident radisondes (gray) from the 1997 IOP. The lidar data have been averaged for 10 minutes with 78 m resolution. The error bars on both lidar profiles were calculated using Poisson statistics for the observed photon counts.

was at the CART site, and collected several profiles of water vapor near solar noon. Three of these profiles are shown in Fig. 2. During these flights, the aircraft flew stairstep ascents and then spiral descents. As the descents were always within approximately 5 km of the lidar, only the descents are shown. All three examples shown in Fig. 2 show remarkable agreement between the aircraft hygrometer and CARL measurements.

SUMMARY

The CARL system was designed to provide excellent daytime water vapor measurements without sacrificing its nighttime capabilities. Data collected during the 1997 water vapor IOP demonstrate that this design goal has been achieved using a dual field-of-view, narrowband approach. Together with the other design features of the CARL system [1], extended measurements spanning several days to weeks can be made with little or no operator interaction. An example of this is given in Fig. 3, where the evolution and passage of a cold front on 28 September 1997 was captured in fine detail. These measurements will better enable scientists to study the role of water vapor in the atmosphere and advance our understanding of its impact.

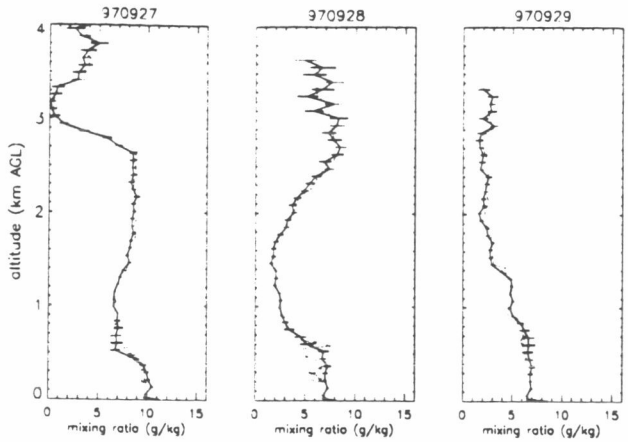


Figure 2. Comparison of daytime 10 minute profiles from CARL (black with error bars) with in-situ hygrometer measurements from the PNNL Gulfstream (gray) from the 1997 IOP. From left to right, the observation times are 27 September at 1700 UTC, 28 September at 1830 UTC, and 29 September at 20 UTC. The error bars on the lidar profiles were calculated using Poisson statistics for the observed photon counts.

REFERENCES

[1] J.E.M. Goldsmith, F.H. Blair, S.E. Bisson, and D.D. Turner, "Turn-key Raman lidar for profiling atmospheric water vapor, clouds, and aerosols," *Appl. Opt.*, in press.

[2] D.D. Turner and J.E.M. Goldsmith, "24 hour Raman lidar water vapor measurements during the Atmospheric Radiation Measurement Program's 1996 and 1997 water vapor intensive observation periods," *J. Atmos. Oceanic Technol.*, to be submitted.

[3] S.H. Melfi, D.D. Turner, K.D. Evans, D.N. Whiteman, G.K. Schwemmer, and R.A. Ferrare, "Upper tropospheric water vapor: A field campaign of two Raman lidars, airborne hygrometers, and radiosondes," *19th Int. Laser Radar Conf.*, Annapolis, MD, 1998.

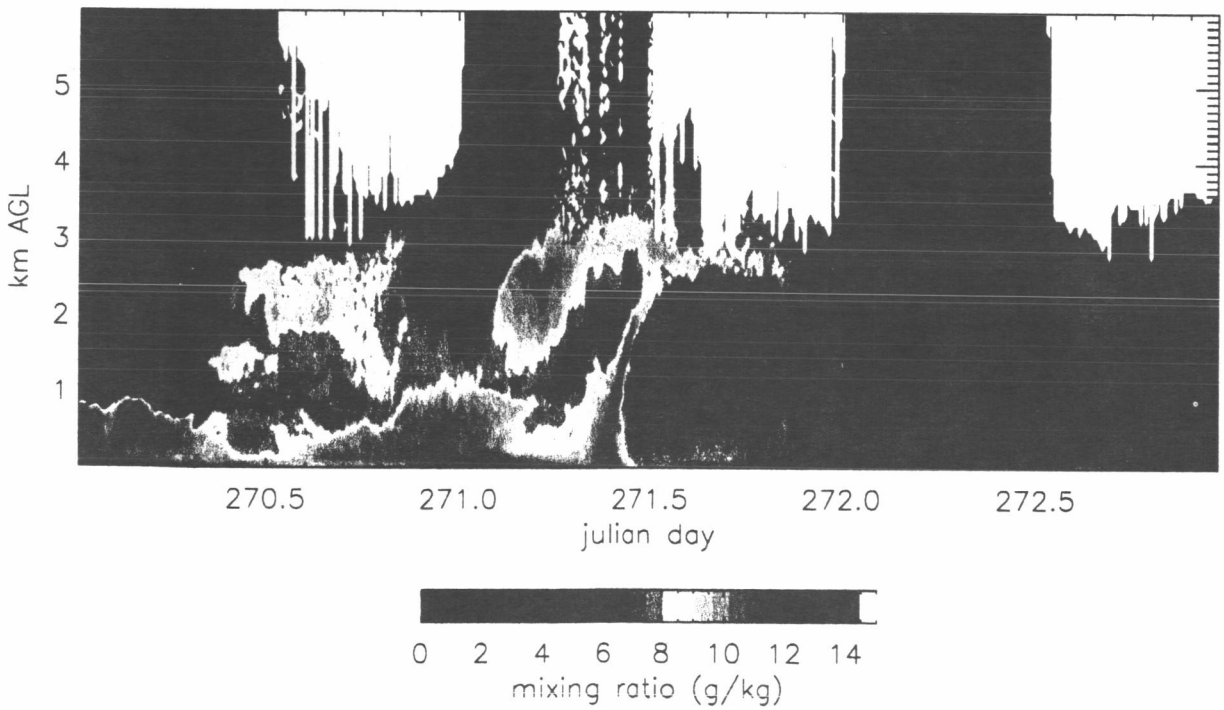


Figure 3. A false color image of water vapor mixing ratio measured by the CARL system on September 27-29, 1997, which shows the evolution of the water vapor field as a cold front passed over the ARM CART site. The front passed over the site on the 28th at approximately 10 UTC. The lidar profiles have 10 minute, 78 m resolution. The "whited-out" areas above 3.5 km occur during the daylight periods and denote regions where the signal-to-noise is approaching unity.

Comparison of Measurements by the NASA/GSFC Scanning Raman Lidar and the DOE /ARM CART Raman lidar

David Whiteman[1], David Turner[2], Keith Evans[3], Belay Demoz[3], Harvey Melfi[3], Geary Schwemmer[4], Martin Cadirola[3], Richard Ferrare[5], John Goldsmith[6], Tim Tooman[6], Stacy Wise[3]

[1] NASA/ Goddard Space Flight Center, Code 924, Greenbelt, Maryland 20771, 301-286-3115, 301-286-0213 (fax), david.whiteman@gsfc.nasa.gov, [2] Pacific Northwest National Laboratory, Richland, Washington, [3]Joint Center for Earth Systems Technology, Baltimore, Maryland, [4]NASA/GSFC, Code 912, [5]NASA/Langley Research Center, [6]Sandia National Laboratories, Livermore, California

Introduction

Latent heat transfer through evaporation and condensation of water vapor is the most important energy transport mechanism in the atmosphere. In addition, water vapor is the most active greenhouse gas. Any global warming scenario must take accurate account of the spatial and temporal variation of water vapor in order to account for both of these effects.

Due to the great importance of water vapor in atmospheric radiation studies, specific intensive operations periods (IOPs) have been hosted by the Department of Energy's Atmospheric Radiation Measurements (ARM) program. One of the goals of these IOPs has been to determine the quality of and explain any discrepancies among a wide variety of water vapor measuring instruments. Raman lidar systems developed by NASA/Goddard Space Flight Center and DOE/Sandia National Laboratories have participated in the two Water Vapor IOPs (WVIOPs) held at the Southern Great Plains (SGP) Cloud and Radiation Testbed Site (CART) site during 1996 (WVIOP1) and 1997 (WVIOP2). Detailed comparisons of these two systems is ongoing but this effort has already resulted in numerous improvements in design and data analysis for both lidar systems.

Lidar system descriptions

The NASA/GSFC Scanning Raman lidar (SRL) [1] is a mobile system which uses two laser transmitters: a XeF excimer laser (24 Watts - 351 nm) for nighttime measurements and a tripled Nd:YAG (9 Watts - 355 nm) for daytime measurements. Using a .76 m telescope, Rayleigh and Mie scattering from molecules and aerosols as well as Raman shifted signals from oxygen (1555 cm^{-1}), nitrogen (2329 cm^{-1}) and water vapor (3654 cm^{-1}) are measured. Interference filters and photomultiplier tubes (PMTs) are used to select and detect the desired wavelengths. Two PMTs are used for each signal; one for low altitude returns and the other for high altitude. A large scan mirror allows profiles to be acquired at any angle in a single scan plane and also allows improved measurements at low altitudes for comparison with tower or surface-based instruments.

The CART Raman lidar (CARL) [2] is an autonomous, operational lidar system permanently deployed at the SGP site. It has advanced the state of the art in Raman lidar system automation with its demonstrated ability to make unattended measurements for days at a time. It uses a tripled Nd:YAG laser (12 Watts - 355 nm), a .61 meter telescope and interference filters and PMTs. In addition to the Rayleigh/Mie, Raman water vapor and nitrogen signals, CARL also has the capability to measure depolarization in the Rayleigh/Mie channel. As in the SRL, CARL uses high and low channels for each signal.

Water Vapor Mixing Ratio Bias Versus Height

The ARM WVIOP held during September, 1996 provided the first opportunity for the Raman lidar systems from NASA and DOE to be carefully intercompared. Water vapor measurements were compared as a function of height using all times when both lidar systems were operated together and when radiosonde launches occurred. This allows the radiosondes to be used to determine the source of any systematic differences which might be found between the lidar systems. The first comparison of the lidars was performed shortly after WVIOP1 in 1996 and showed significant bias changes with height [3]. Work done since then has identified the sources of most of these differences. The most recently processed data from WVIOP1 implements a new lidar system overlap [2] correction for the CARL analysis which has removed most of the bias variation with height. The lidar systems now are in

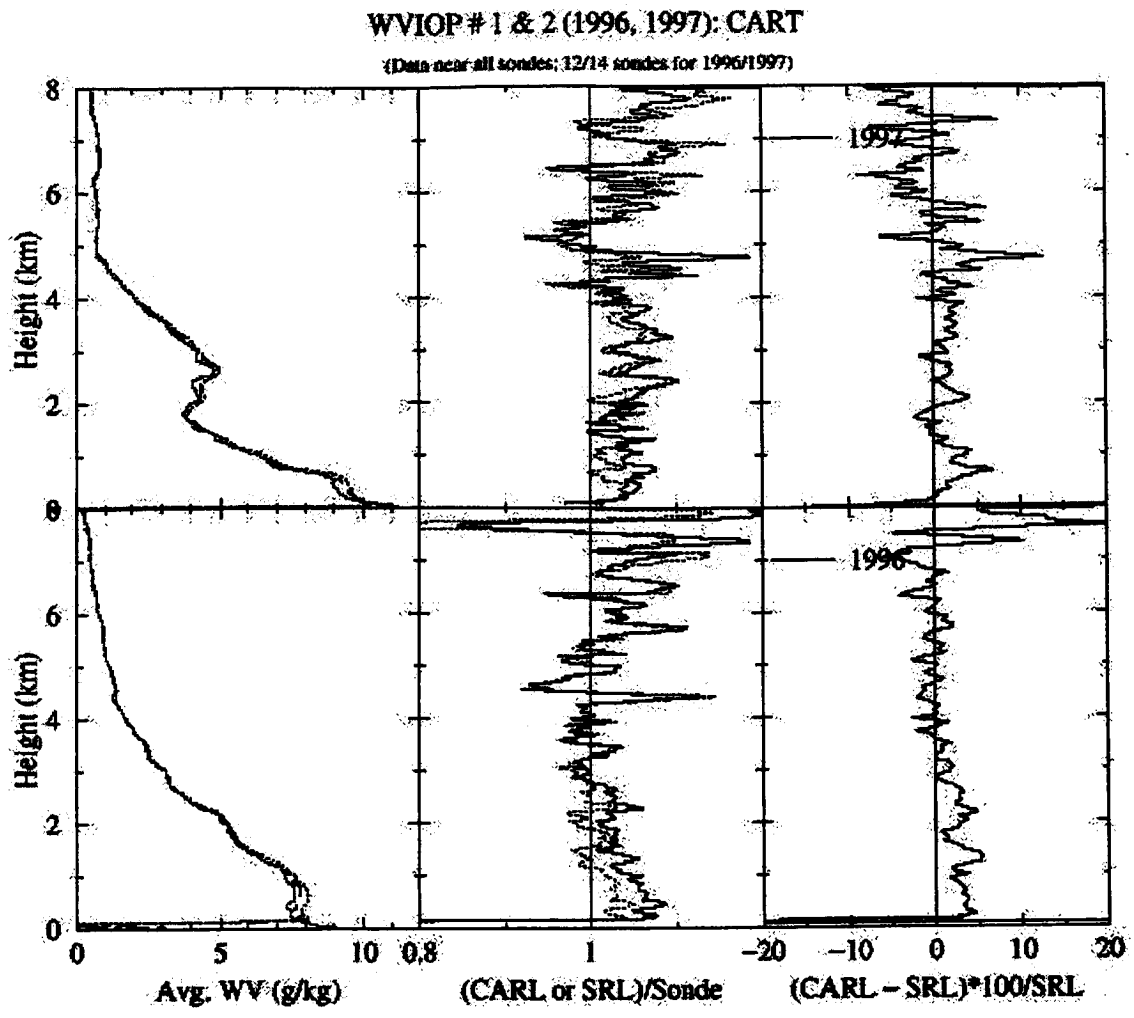


Figure 1. Synopsis of water vapor mixing ratio measurements versus height for both lidar systems and the Vaisala radiosondes averaged over both WVIOPs. In the left panels, the average radiosonde profile is represented by a solid curve, average SRL by a dashed curve, and the average CARL by a dotted curve. The overall agreement is excellent. In the center panel the ratio of these SRL and CARL averages to the average radiosonde profile is shown. The SRL ratio is represented by a dotted line, the CARL ratio by a solid line. The right panels are a comparison of average SRL to CARL percentage difference. The lower three panels present the most recently processed results from WVIOP1 (1996) while the results from WVIOP2 (1997) are presented on top. As explained in the text, the current analysis of SRL to CARL bias versus height for both WVIOPs shows that the lidars agree to within +/- 5% up to about 7 km for both experiments. The comparison with the average radiosonde profiles which is shown in the center panels indicates that there were small biases for both lidar systems during both WVIOPs; a sloping height dependent bias during 1996 and a constant offset bias during 1997.

agreement to generally better than +/- 5% from near the surface to about 7 km. The results from both IOPs are presented in figure 1.

The left panels of figure 1 present the average profiles of the SRL, CARL and Vaisala radiosondes for 12 cases during WVIOP1 and 14 cases during WVIOP2. These are the profiles used in the comparisons shown in the other panels of the figure. The results from WVIOP1 shown in the lower panels will be discussed first.

The lower right hand panel gives the water vapor mixing ratio bias versus height for WVIOP1 using the new overlap correction in the CARL analysis which has removed most of the height bias seen in earlier results [3]. There still remains up to a 5% bias between the two lidar systems between 0-4 km. The panel in the lower center of

the figure presents the ratio of the average lidar profile (both CARL and SRL) to the average radiosonde profile. This comparison shows that the lidars disagree with the radiosonde in the lowest part of the profile. Both the CARL and SRL curves slope toward the average radiosonde profile from the surface up to about 1.5 km in the case of the SRL and about 3.0 km in the case of the CARL. These differences require further study but are perhaps due to an equilibration time for the radiosondes or an incorrect lidar system overlap [2] in both lidar systems.

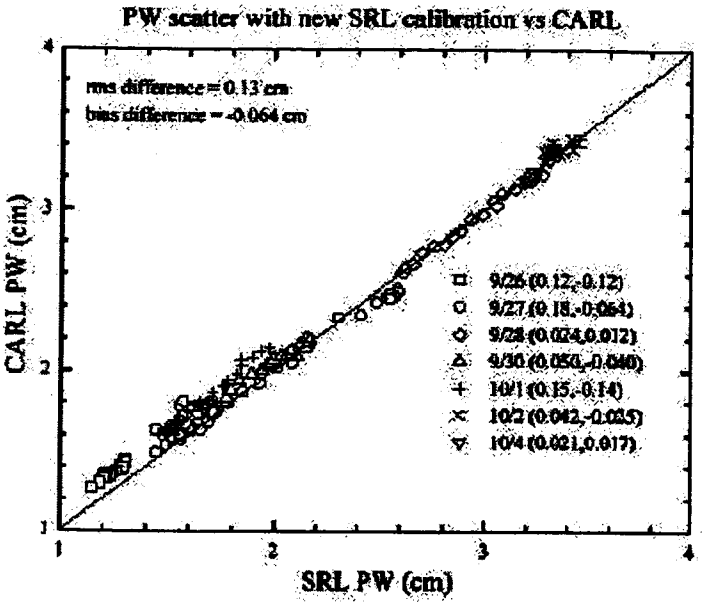


Figure 2. Precipitable water comparison of the CARL and the SRL from the 1997 WVIOP. Both lidars were calibrated with respect to the CART MWR precipitable water measurements. The agreement of the two systems is in general quite good. Discrepancies on the nights of September 26 and October 1 are under investigation.

The results from WVIOP2 are presented in the upper panels of figure 1. In general these comparisons indicate excellent agreement between the lidars. There is, however, an indication of a consistent difference of up to 5% between the lidars at about 1 km (upper right) which may be due to errors in the merging of the high and low channels. Otherwise, the average lidar profiles show little height dependent bias. The comparison of the lidars with radiosonde (upper middle), however, displays a consistent bias which is due to the fact that the lidars are calibrated with repect to the CART microwave radiometer (MWR) which in general measures a higher value of precipitable water than the radiosondes.

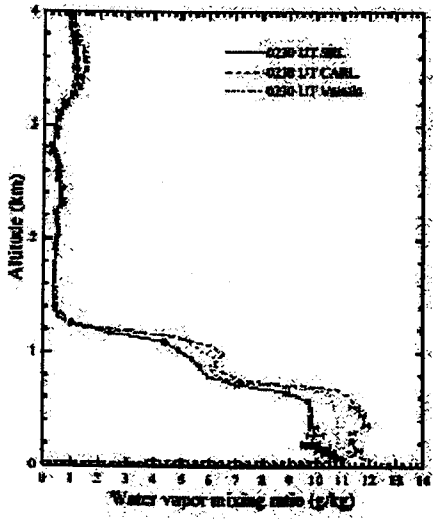


Figure 3. CARL, SRL and Vaisala radiosonde measurements of water vapor mixing ratio on the night of September 26. There are significant differences among all instruments in the first kilometer.

Precipitable water comparisons

For the precipitable water comparisons, the final calibration of the lidar mixing ratio for both systems has been performed by forcing the lidar integrated precipitable water (PW) to agree with that measured by the CART MWR. A single calibration constant for the entire IOP has been derived for each lidar system. Figure 2 shows the comparison of PW values for the two lidar systems over seven nights of measurement. The bias and rms differences between the two systems were -.06 cm and .13 cm, respectively, indicating that the lidars show good agreement with each other. The non-zero bias indicates that the calibration constants for the two systems were determined using a larger dataset than presented in these figures. On the evenings of September 26 and October 1, the SRL PW measurements were lower than the CARL measurements. On the 26th, the differences are due to substantially different mixing ratio profiles for both lidar systems. The radiosonde measurement made at this time did not agree with either lidar in the lowest 1 km as shown in figure 3. These differences in measurement have yet to be explained. On October 1, the SRL used a Nd:YAG laser for the transmitter due to an electrical problem in the excimer laser which is normally used for nighttime measurements. The differences on this night can be attributed to this substitution and the different calibration required.

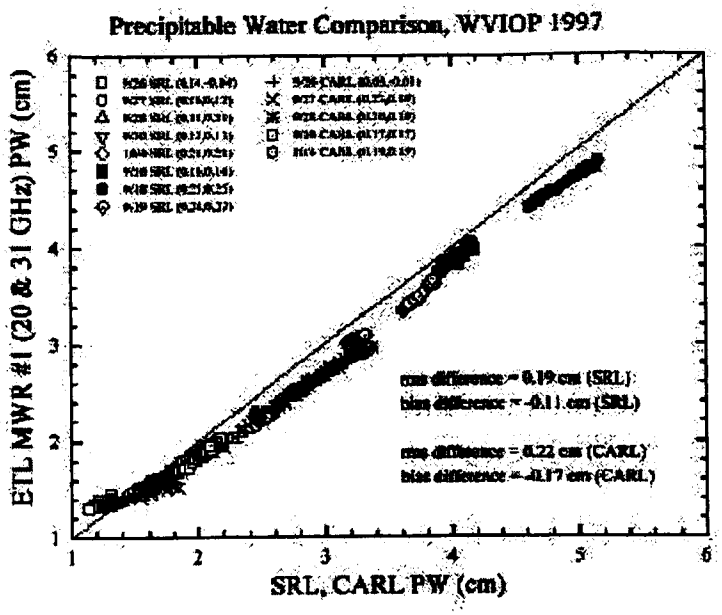


Figure 4. CARL and SRL measurements of PW compared with the ETL MWR. Notice the bias which changes as a function of PW. As the lidars are calibrated against the CART MWR, this curve reveals a PW dependent bias between the CART MWR and the ETL MWR.

As mentioned above, the calibration for both lidars is determined through comparisons with the CART MWR. Comparisons of the lidars with the CART radiometer thus show very good agreement and will be presented at the meeting. Figure 4 shows PW data from both lidars compared to ETL (NOAA/Environmental Technology Laboratory) MWR. The measurements are very consistent but show a bias which changes either as a function of PW or as a function of day of measurement. As will be shown at the meeting, this same bias change is present when a comparison of CART MWR PW versus this same ETL MWR is performed. It is clear from these comparisons that the standard to which the Raman lidar water vapor measurements is tied is crucial.

Other comparisons and testing

Comparisons have also been made between water vapor mixing ratio measurements at the 60 meter height by both lidars as well as the Vaisala in-situ sensor on the 60 meter tower at the CART site. These will be presented along with the results of other work that is ongoing between the two lidar groups including 1) linearity testing of both the CARL and the SRL photomultiplier tubes and 2) influence of high count rates on derived water vapor amount and improved techniques for processing these data.

Summary

Detailed comparisons of the water vapor measurements made by two Raman lidar systems during the two WVIOPs have been made. These comparisons have resulted in improvements in both the way that data are acquired and the way that the data are processed. Discrepancies in water vapor mixing ratio measurements between the two systems have been addressed and to a large degree resolved yielding excellent agreement between the lidar instruments. The small residual discrepancies between the lidars which are on the order of 5% or less are still under investigation. In addition, several other areas still require further study including 1) PMT detector linearity and 2) the influence of high signal levels and lidar system overlap function on derived water vapor values. Examples of this work will be presented at the meeting.

References

1. Ferrare, R. A., S. H. Melfi, D. N. Whiteman, K. D. Evans. F. J. Schmidlin and D. O'C. Starr, 1995: A comparison of water vapor measurements made by Raman Lidar and radiosondes. *J. Atmos. Oceanic Technol.*, 12, 1177-1195

2. Goldsmith, J.E.M., F.H. Blair, S.E. Bisson, and D.D. Turner, 1998:Turn-Key Raman Lidar for Profiling Atmospheric Water Vapor, Clouds, and Aerosols. *Applied Optics* (accepted for publication).

3. Turner, D.D., J.E.M. Goldsmith, 1998: CART Raman lidar measurements during the ARM 1996 water vapor IOP. Proceedings of the seventh Atmospheric Radiation Measurement (ARM) science team meeting, San Antonio, TX, 1998.

Raman Lidar Capability to Measure Tropospheric Properties

C. Russell Philbrick
Penn State University
Department of Electrical Engineering and
Applied Research Laboratory
University Park PA 16802
crp3@psu.edu

ABSTRACT

The Lidar Atmospheric Profile Sensor (LAPS) instrument is the fifth in a series of lidar instruments leading to a first operational prototype for obtaining meteorological profiles in the lower atmosphere. It was prepared and tested to determine its capability to provide automated shipboard operation for atmospheric properties under a wide range of meteorological conditions. The instrument measures the water vapor profile based on the vibrational Raman scattering and the temperature profile based on the rotational Raman scattering. Profiles of the Raman signals are obtained each minute with a vertical resolution of 75 meters from the surface to a user selected altitude. The measured 1 minute profiles are integrated for user selected intervals to simultaneously determine the real time atmospheric profiles for specific humidity, temperature, optical extinction and ozone. Daytime measurements of water vapor, extinction and ozone are made using the "solar blind" ultraviolet signals. The instrument includes a safety radar which detects aircraft as they approach and automatically shuts down the beam. The weather sealed instrument has been designed to include features such as real time data display/transfer, environment control, and performance self-tests to control many functions. Tests have proven the qualities of ruggedness, reliability and general performance of the LAPS lidar system.

RAMAN LIDAR TECHNIQUES

Raman scattering provides an important signal because it is unique to specific molecules. It is most useful because the vibrational Raman scattering provides distinct wavelength shifts for vibrational energy states of the different molecules and the rotational Raman scattering provides a signal with a wavelength dependence corresponding to atmospheric temperature. The ratio of Raman back scatter signals from the molecules of the water vapor at 660 nm and 294 nm from the 2nd (532 nm) and 4th (266 nm) harmonics of Nd:YAG laser and molecular nitrogen (607 nm and 284 nm) are at wavelengths that are widely separated from the exciting laser radiation and can be easily isolated for measurement using modern filter technology. The measurements are made using sensitive photon counting detectors. The ratios of rotational Raman signals at 528 nm and 530 nm provide a measurement that is sensitive to atmospheric temperature. Based upon accomplishments by several groups, we now have the capability for reliably profiling most of the important properties of the atmosphere with lidar [Ref 1 - 17]. In order to push the lidar measurement capability into the daylight conditions, the "solar blind" region of the spectrum between 260 and 300 nm has been used. Night time measurements are made using the 660/607 (H_2O/N_2) signal ratio from the doubled Nd:YAG laser radiation at 532 nm. Daylight measurements are obtained using the 294/284 (H_2O/N_2) ratio from the quadruple Nd:YAG laser radiation at 266 nm, where a small correction for the tropospheric ozone must be applied. That correction can be obtained from the ratio of the O_2/N_2 signals 278/284 and the ozone profile is also obtained in the lower troposphere. The temperature measurement is obtained from the ratio of 528 to 530 nm signals as a measure of the rotational state population distribution [17,18,19].

The Raman techniques use ratios of signals to measure water vapor and temperature and thus have a major advantage in removing essentially all of uncertainties, such as any requirement for knowledge of the absolute sensitivity and non-linear factors caused by aerosol and cloud scattering.

The optical extinction profiles from the LAPS instrument are determined from the gradients in the molecular profiles of the atmosphere caused by clouds and aerosol scattering. The gradient of the neutral density profiles can be used to directly determine the optical extinction. In general, optical extinction cannot be determined from the backscatter signal at the fundamental laser wavelengths [20]. However, the extinction profiles can be determined from the Raman

Table 1. LAPS Lidar Characteristics

Transmitter	Continuum 9030 -- 30 Hz 5X Beam Expander	600 mj @ 532 nm 130 mj @ 266 nm
Receiver	61 cm Diameter Telescope	Fiber optic transfer
Detector	Seven PMT channels Photon Counting	528 and 530 nm -- Temperature 660 and 607 nm -- Water Vapor 294 and 284 nm -- Daytime Water Vapor 278 and 284 nm -- Raman/DIAL Ozone
Data System	DSP 100 MHZ	75 meter range bins
Safety Radar	Marine R-70 X-Band	protects 6° cone angle around beam

shifted wavelengths of primary molecular species [21,22,23,24]. Measurements of optical extinction have been obtained from the 2nd harmonic of the Nd:YAG laser using the rotational Raman signal at 530 nm and the nitrogen vibrational Raman signals at 607 and 284 nm. Raman scatter signals measured at several wavelengths provides optical extinction profiles which can be used to estimate the changes in size distribution.

LIDAR ATMOSPHERIC PROFILE SENSOR

The objective of the LAPS Program was to develop a lidar profiler capable of providing real time profiles of atmospheric and meteorological properties, with emphasis directly measuring the RF refractivity which is directly determined from measurements of water vapor and temperature profiles. The LAPS instrument hardware was completed in mid-1996 and it was tested onboard the USNS SUMNER in the period August to October 1996. The LAPS instrument can obtain most of the measurements which are currently provided by radiosonde balloons. LAPS was preceded by the LAMP (Lidar Atmospheric Measurements Profiler) research instrument which was developed in 1990 and has been used to test the various measurement techniques that have been employed in the LAPS. Table 1 lists the primary characteristics of the LAPS lidar.

LAPS PERFORMANCE

Examples of the LAPS water vapor profiles compared to individual balloon rawinsondes are shown in Figure 1. During shipboard tests, the lidar measurements were compared to 97 standard rawinsonde balloons. Several balloon instruments failed to provide results but the average value of a ratio of the lidar and balloon results for each available flight are summarized in Figure 2. The lidar data are taken from the 30 minute integration at the time of the balloon release. Error in the balloon measurement, differences in the atmosphere between the vertical lidar profile and the balloon location (up to 50 km away during assent), or differences due to changes in the height of sharp profile gradients are factors which cause variations to be observed. The dynamics of the atmosphere causes differences between the point samples of the balloon measurements and the lidar vertically integrated 30 minute profile (note the profile in right panel of Figure 1). The differences observed between the lidar and the sonde result in an average difference of ±4.6% for the visible channels and 8.9% for the ultraviolet channels. The ultraviolet signal variations are larger because the error in the ultraviolet signals grows rapidly above 3 km and intermittent drifting of SO_2 emission from the ship's diesel engines across the lidar beam caused noticeable absorption at 294 nm. The lessons learned from the test included the following items:

- Flash lamps can provide long operation ~10^8 shots
- Operation can be conducted in all weather, clouds, rain, snow
- Radar can provide safe operation - no interference
- LAPS is a robust instrument - continuous measurements can be made
- Realtime data product - 1 minute update provides useful trend data
- SO_2 from ship stack causes an error in UV water vapor (294 nm)
- Gain stability requires protection of visible detectors in daylight

The LAPS instrument tests have demonstrated the measurements of the real time profiles of the properties which determine the RF-refractivity. The temperature and water vapor measurements are the critical parameters which weather balloons provide today and the lidar techniques will provide in the future.

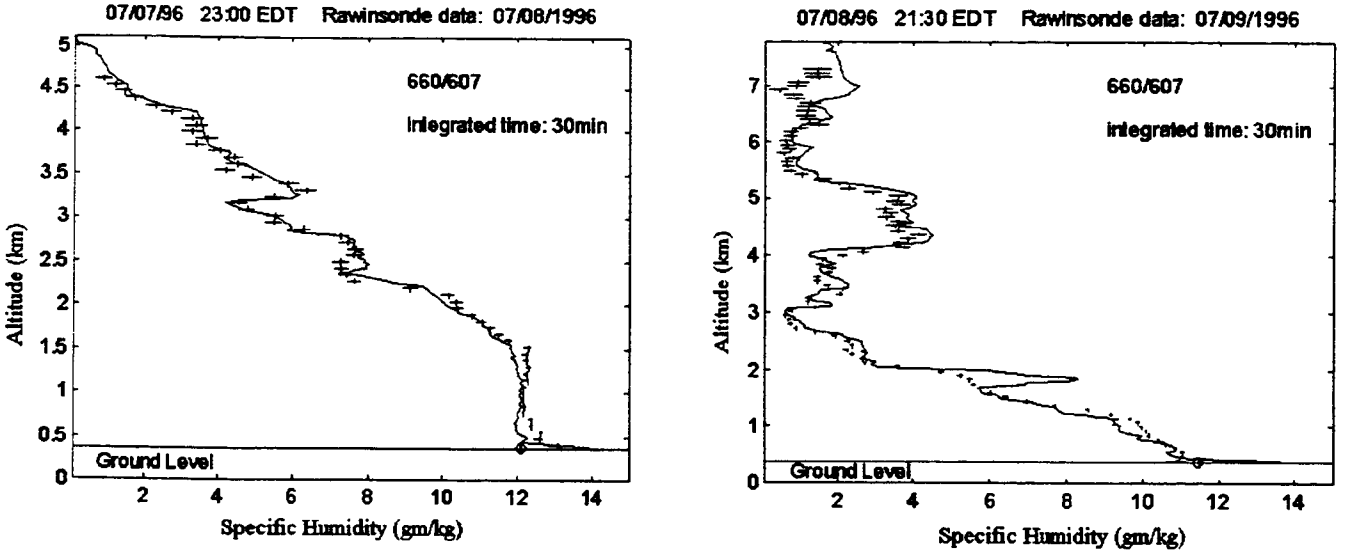


Figure 1. Two examples of LAP water vapor profiles are shown from measurements at State College PA on July 7 and 8 1996. The individual lidar points are shown with their ±1 σ error, the rawinsonde profiles are shown as a line and a point measurement at the surface is indicated.

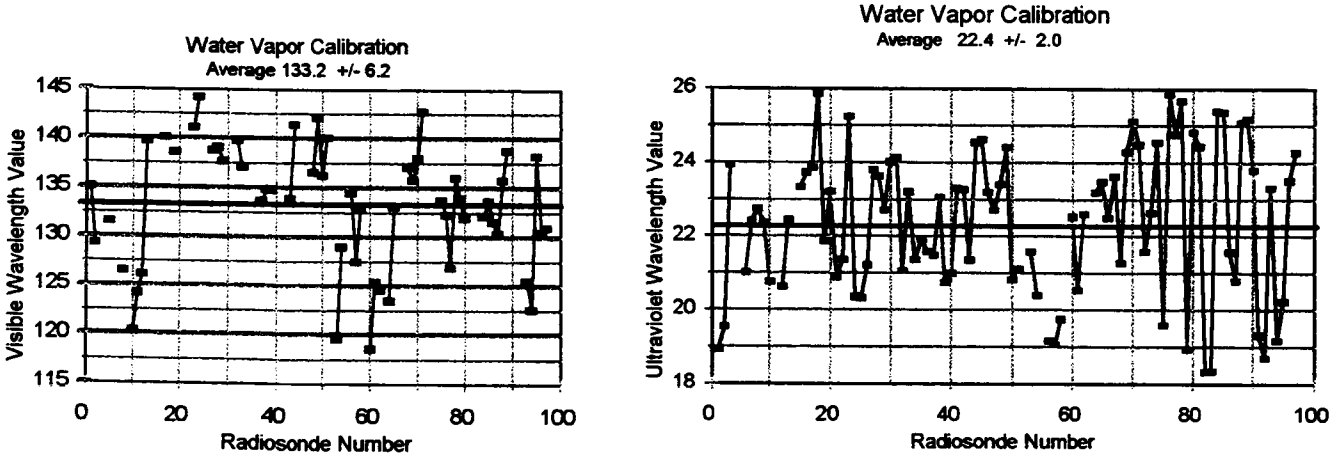


Figure 2. Summary of the comparison of ratio of the 30 minute lidar data to balloon data for each flight.

Thousands of profiles for water vapor, temperature, optical extinction and ozone have been measured and these are now being prepared in a data base to be used for investigations of atmospheric conditions.

SUMMARY

The LAPS instrument was operated and data were obtained on every operation attempted or planned during the period of the sea trial. Several scientific investigations have provided additional results during the past year. Investigations of the data show that the instrument was successful in demonstrating the capability to obtain the meteorological data and RF refractivity conditions during day and night conditions and in a wide range of weather conditions. The LIDAR system offers the capability to obtain high quality RF ducting prediction data with real time data products and routine update without the use of radiosonde expendables. We expect that the "operational environmental system" of the future will be based upon lidar profile data combined into a mesoscale grid model which is run to provide the spatial continuity, within constraints imposed by the

measured profiles, and provide the predictive conditions with products tailored to system, mission and scientific investigation requirements.

ACKNOWLEDGMENTS

The development of the LAPS instrument has been supported by the US Navy SPAWAR PMW-185 and ONR. The testing was carried out on the USNS SUMNER operated by NAVOCEANO. The METOC support for the rawinsonde balloons was coordinated by Prof. Ken Davidson and LCDR Dan Harrison of the Naval Postgraduate School. The LAPS development was made possible from the endeavors of D. B. Lysak, Jr., T. M. Petach and the engineering staff of the PSU Applied Research laboratory and P. A. T. Haris, T. D. Stevens, M. D. O'Brien and several additional graduate students of the PSU Department of Electrical Engineering.

REFERENCES

1. D. A. Leonard, "Observation of Raman scattering from the atmosphere using a pulsed nitrogen ultraviolet laser," Nature 216, 142-143, 1967.
2. J. A. Cooney, "Measurements on the Raman component of laser atmospheric backscatter," Appl. Phys. Lett., 12, 40-42, 1968.
3. S. H. Melfi., J. D. Lawrence Jr. and M. P. McCormick, "Observation of Raman scattering by water vapor in the atmosphere," Appl. Phys. Lett., 15, 295-297, 1969.
4. J. A. Cooney, "Remote measurement of atmospheric water vapor profiles using the Raman component of laser backscatter," J. Appl. Meteor., 9, 182-184, 1970.
5. R. G. Strauch, V. E. Derr and R. E. Cupp, "Atmospheric water vapor measurement by Raman lidar," Remote Sens. Envir. 2, 101-108, 1972.
6. G. Vaughan, D. P. Wareing, L. Thomas and V. Mitev, "Humidity measurements in the free troposphere using Raman backscatter," Q. J. R. Meteorol. Soc., 114, 1471-1484, 1988.
7. Yu. F. Arshinov, S. M. Bobrovnikov, V. E. Zuev and V. M. Mitev, "Atmospheric temperature measurements using a pure rotational Raman lidar," Appl. Optics 22, 2984-2990, 1983.
8. C. R. Philbrick, D. P. Sipler, G. Davidson and W. P. Moskowitz, "Remote Sensing of Structure Properties in the Middle Atmosphere Using Lidar," **Proceeding of OSA Topical Meeting on Lasers and Remote Sensing**, 120-124, 1987.
9. S. H. Melfi, D. Whiteman, and R. Ferrarre, "Observation of Atmospheric Fronts Using Raman Lidar Moisture Measurements," J. Appl. Met., 1989.
10. C.R. Philbrick, "Lidar Profiles of Atmospheric Structure Properties," in **Earth and Atmospheric Remote Sensing**, SPIE Vol. 1492, 76-84, 1991.
11. D. N. Whiteman, S. H. Melfi and R. A. Ferrare, "Raman lidar system for the measurement of water vapor and aerosols in the Earth's atmosphere," Appl. Optics 31, 3068-3082, 1992.
12. A. Hauchecorne, M. L. Chanin, P. Keckhut, and D. Nedeljkovic, "Lidar monitoring of the temperature in the middle and lower atmosphere," Appl. Phys. B55, 29-34, 1992.
13. D. Nedeljkovic, A. Hauchecorne and M. L. Chanin, "Rotational Raman lidar to measure the temperature from the ground to 30 km," IEEE Trans. Geos. Remote Sens. 31, 90-101, 1993.
14. C. R. Philbrick, "Raman Lidar Measurements of Atmospheric Properties," **Atmospheric Propagation and Remote Sensing III**, SPIE Volume 2222, 922-931, 1994.
15. C. R. Philbrick, D. B. Lysak, T. D. Stevens, P. A. T. Haris and Y.-C. Rau, "Lidar Measurements of Middle Atmosphere Properties during the LADIMAS Campaign," **Proc. 11th ESA Symp.**, SP-355, 223-228, 1994.
16. F. Balsiger and C. R. Philbrick, "Comparison of Lidar Water Vapor Measurements Using Raman Scatter at 266nm and 532 nm," in **Applications of Lidar to Current Atmos. Topics**, SPIE Proc. Vol. 2833, 231-240 1996.
17. F. Balsiger, P. A. T. Haris and C. R. Philbrick, "Lower-tropospheric Temperature Measurements Using a Rotational Raman Lidar," in **Optical Instruments for Weather Forecasting**, SPIE Proc. Vol. 2832, 53-60, 1996.
18. Paul A. T. Haris, "Pure Rotational Raman Lidar for Temperature Measurements in the Lower Troposphere," PhD Thesis for Penn State University, Department of Electrical Engineering, August 1995.
19. C. R. Philbrick and D. W. Blood, "Lidar Measurements of Refractive Propagation Effects," in **Propagation Assessment in Coastal Environments**, NATO-AGARD CP 567, Paper 3, 137 pg, 1995.
20. Y.-C. Rau, "Multi-Wavelength Raman-Rayleigh Lidar for Atmospheric Remote Sensing," PhD Thesis for Penn State University, Department of Electrical Engineering, May 1994.
21. C. R. Philbrick, M. D. O'Brien, D, B. Lysak, T. D. Stevens and F. Balsiger, "Remote Sensing by Active and Passive Optical Techniques," **NATO/AGARD Proceedings on Remote Sensing**, AGARD-CP-582, 8.1-8.9, 1996.
22. T. D. Stevens and C. R. Philbrick, "Particle Size Distributions and Extinction Determined by a Unique Bistatic Lidar Technique," **Proceeding of IGARSS96 Conference on Remote Sensing for a Sustainable Future** (International Geophysics and Remote Sensing Symposium) at Lincoln NB, May 1996, Vol II pg 1253-1256, 1996.
23. M. D. O'Brien, T. D. Stevens and C. R. Philbrick, "Optical Extinction from Raman Lidar Measurements," in **Optical Instruments for Weather Forecasting**, SPIE Proceedings Vol. 2832, 45-52, 1996.
24. Timothy D. Stevens, "Bistatic Lidar Measurements of Lower Tropospheric Aerosols," PhD Thesis for Penn State University, Department of Electrical Engineering, May 1996.

Raman-DIAL: Application to Areas Characterized by Varying Aerosol Burden

Arthur J. Sedlacek III and Mark D. Ray
Department of Advanced Technology
Brookhaven National Laboratory
Upton, NY, 11973-5000
Phone: 516-344-2404, FAX: 516-344-7650, E-mail: Sedlacek@bnl.gov

1 Introduction

With the rapid development in the areas of lasers, detectors, optical components, and computer algorithms, remote detection of airborne chemicals through the use of lidar has reached a state of maturity.[1] Of the physical phenomena exploited with these open-path sensors, DIAL has routinely achieved detection sensitivities on the order of low ppm to high ppb levels, depending on the absorption cross-section, albedo variation, atmospheric make-up (i.e., aerosol burden), laser pulse-to-pulse energy stability, and turbulence.[1]

In a typical application of DIAL, two probing laser lines are directed to the area of interest and their elastic return signals are monitored: λ_1 located at a highly-absorbing wavelength for the chemical species of interest and λ_2 in a non-absorbing spectral region, as shown in Figure 1.

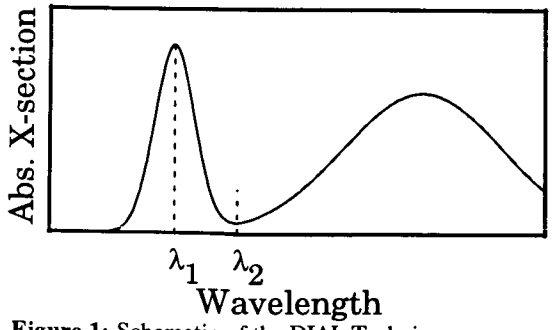


Figure 1: Schematic of the DIAL Technique

Elastic return of each outgoing laser line (λ_1 and λ_2) is provided through either a combination of Rayleigh scattering off air molecules and Mie scattering from the aerosols/particulates or, if range-resolved mapping is not important, hard-body return from a retroreflector [e.g., corner cube or a sand-blasted aluminum back-drop]. Despite the great sensitivity that the range-resolved lidar platforms offer, they suffer from data reduction and error analysis complications due to real world complexities.[1,2] This difficulty is inherent to classical DIAL because the technique derives the molecular absorption information from the elastic-return channel mentioned above. Consequently, the ability to distinguish variations in the return signal amplitude due to the presence or absence of the chemical species-of-interest from the unknown aerosol burden (which varies spatially and temporally) or from laser power fluctuations can be severely compromised. Although a variety of hardware and software techniques have been developed and implemented to confront these problems[3-6], the end result is typically an increase in the complexity of the DIAL platform.

In contrast to these approaches, the authors present a blueprint for a lidar platform that combines the strengths of two existing lidar techniques to produce a system that can potentially achieve DIAL sensitivities without the complex data and error analysis typical of this stand-off chemical detection platform This Raman-DIAL technique utilizes the inelastic Raman scattering returns from both atmospheric nitrogen and oxygen as the two *in situ* probing wavelengths for the DIAL-like measurement (λ_1 and λ_2 from the DIAL discussion), where one of the Raman returns is tuned to the peak of the molecular absorption and the other to a non-absorbing region. In this way, the traditional concerns of atmospheric turbulence, aerosol burden, and laser shot-to-shot energy variation in DIAL measurements completely disappear since the differential absorption measurement through this approach takes place at *exactly* the *same time*, in the *same volume* of space, and relies on return signals that propagate through the *same turbulence structure*. Consequently, this technique potentially offers a superior range-resolved chemical sensing scheme when accuracy is critical and in situations where the aerosol burdens are unknown.

In the 1980s, Renaut, Capitini and co-workers[7,8], while pursuing the development of the solar-blind Raman lidar (SBRL) for measuring the boundary-layer water vapor profiles, treated the strong Raman nitrogen and oxygen return signals as two pseudo-point sources to correct the Raman water vapor return signals for tropospheric ozone attenuation. In their study, a fourth-harmonic Nd:YAG laser (266 nm) was used, and the Raman nitrogen and oxygen returns at 277.5 nm and 283.4 nm, respectively, were exploited as the pseudo-DIAL wavelengths for subsequent measurement of the ozone. The fundamental assumption of Renaut and Capitini[7,8] was that tropospheric nitrogen and oxygen are well-mixed gases and, hence, the ratio of N_2 molecules to O_2 molecules is constant. Therefore, if during the analysis of the nitrogen and oxygen Raman return signals any deviation from the known N_2/O_2 ratio[9] of 3.7279 is

observed, the concentration of ozone can be determined through a DIAL-like measurement. Initial ranges were approximately up to 1500 meters. In 1996, Philbrick and co-workers[10] reported vertical water vapor profiles over 3.0 kms using higher-efficiency detectors and a higher power 266 nm laser system. In this work we have extend this idea beyond the measurement of atmospheric ozone and have successfully applied it to any chemical species possessing an absorption.

The strengths of this Raman-DIAL technique rest on a number of facts:

(i) This technique for chemical detection is based on the ratio of the atmospheric nitrogen and oxygen Raman (inelastically scattered) returns, one of which is set at the absorption peak of the chemical-of-interest while the other is nearly or completely off the peak. Both the N_2- and O_2-Raman lines are created by the same probing laser beam, at the same time and at the same location. Therefore any laser energy pulse-to-pulse fluctuation will cancel out when the ratio of the two signals is taken. As a result, the lidar data collection and reduction is simpler than with traditional DIAL.

(ii) Classical DIAL utilizes two wavelengths that are typically sent out in sequence. Therefore, any atmospheric parameters which have dynamic behavior, such as turbulence and aerosol burden, can result in signal fluctuations in the elastic channels. These fluctuations can cause severe problems in the data reduction. In contrast, the Raman-DIAL technique generates the two required wavelengths for the DIAL-like measurement simultaneously through the inelastic Raman scattering process of atmosphere nitrogen and oxygen. Furthermore, these two distinct beams are generated in the same spatial volume. Therefore, the dynamic effect of atmospheric turbulence on beam distortions, which are often encountered in horizontal interrogation of chemical plumes using ground-based lidar systems, can be greatly reduced.

(iii) The atmospheric nitrogen and oxygen Raman returns are strong because of their high concentrations. At sea level the air density is about 2.69×10^{19} cm^{-3}, 78.084% of which is nitrogen and 20.946% oxygen[9]. This opens the potential for long-range chemical detection, as evidenced by the work of McGee[5], in which the Raman return from atmospheric nitrogen has been exploited to ranges of 50 kms.

(iv) Finally, the recent availability and rapid development of tunable laser sources, (i.e. OPO/OPA based system), provide a means for tuning the excitation wavelength such that one of the inelastically scattered atmospheric Raman lines falls onto the peak of the molecular absorption band, while the other is off. The availability of these lasers along with the above arguments strongly suggest the application of the Raman-DIAL technique towards scenarios characterized by aerosol burden gradients, such as would be expected during rainy, or foggy atmospheric conditions, pollutant mapping around industrial parks, and volcanic eruptions. This technique offers the desired high sensitivity while keeping the data reduction straightforward.

2 Experimental Details

We recently conducted a series of field tests at the Nevada Test Site HAZMAT Spill Test Facility to explore the potential of the Raman-DIAL Technique. The laser source for all of our field experiments is a Spectra-Physics GCR170 Nd:YAG-pumped dye laser system (Quanta Ray PDL-1) which provides the required wavelength tunability. The Raman-DIAL return signals are collected by a 16-inch Cassegrain telescope and focused onto the slits of a single-grating spectrometer (2400 grooves/mm) and then detected by Oriel's Intaspec V intensified CCD (charge-coupled device). The collected Raman lidar return signals are curve fit to a Voigt lineshapes so that the N_2/O_2 ratio during data analysis. All timing aspects for distance ranging is based on a single-master oscillator.

3 Results

Shown in Figure 2 below is an example of some data collected from our field experiments. Acetone was poured into an open pan and allowed to evaporate. The laser operated at 266 nm thereby generating the probing Raman-DIAL wavelengths at 277.5 nm and 283.4 nm from atmospheric oxygen and nitrogen, respectively. At the beginning of the release, "baseline" data were collected at a distance of 1.05 km before the pan was loaded with the acetone. This was done to obtain an estimate of the tropospheric ozone loading. Once the pan was filled with the acetone, the range gating was changed to 1.37 km and the evolving acetone monitored as a function of time. Immediately after the start of the experiment, the measured nitrogen-to-oxygen ratio went up to ~3.1. After approximately 5 minutes the measured ratio began to decrease back to it's expected "no-release" level of 2.6. This decrease was due to the extensive evaporative cooling that took place during this portion of the experiment. For example, at the beginning of the experiment the temperature of the acetone was ~38° C and, through evaporative cooling, decreased to 3.7° C, consequently reducing the evaporation rate and, as a result, the measured nitrogen-to-oxygen ratio. A small "puff" was observed occurring at about 12:45 p.m., which is presumably due to re-heating of the now cooled acetone. At about 1:00 p.m., external heat was applied to the system thereby increasing the evaporation rate

and causing the nitrogen-to-oxygen ratio to go high. When all the acetone was used up (approximately 1:40 p.m.) the nitrogen-to-oxygen ratio returned to a new level dictated by the 1.37 km range and the 58 ppb loading of tropospheric ozone. Finally, it should be noted that in this spectral region, acetone is a weak absorber because the absorption is due to a n->π^* transition.

In addition this technique has also been successfully applied to the detection of SO_2 at a stand-off distance of 3.4 kms, as well as to nitrobenzene and the detection of emissions from a diesel generator. In contrast to ozone,

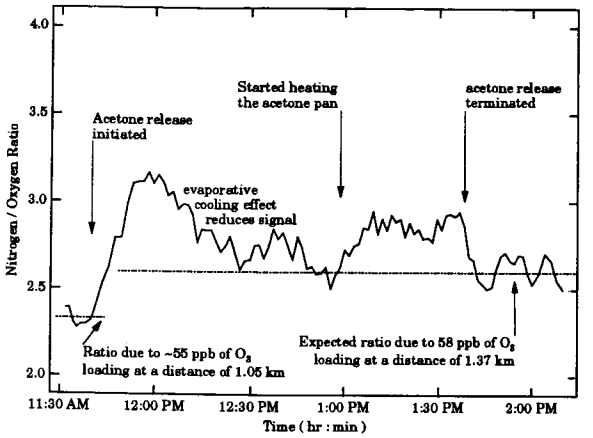


Figure 2: Raman-DIAL detection of an open-pan release of acetone at a distance of 1.37 kms.

sulfur dioxide represents a chemical species with a highly structured absorption as shown below in Figure 3.[11] The goal of the Raman-DIAL technique is to maximize the attenuation of either the nitrogen or oxygen Raman return while minimizing the attenuation of the companion Raman return signal. With a structured absorption, as is present with sulfur dioxide, the opportunity exists for observing great variation in the measured N_2/O_2 ratio as a function of excitation wavelength. An example of maximizing the attenuation of one of the Raman returns while minimizing the attenuation in the other is illustrated in Figure 3.

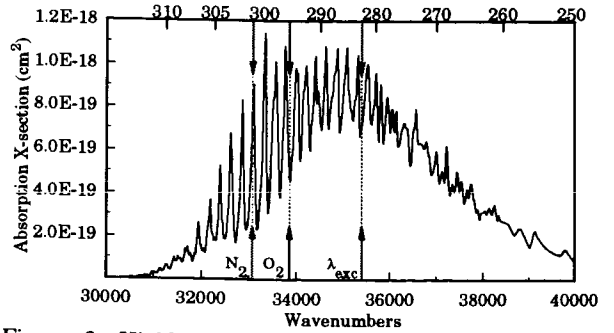


Figure 3: Highly Structured absorption of sulfur dioxide together with spectral locations for maximized Raman-DIAL sensitivity. (ref. 11)

Experiments involving SO_2 were also conducted at the HAZMAT Spill Facility. In contrast to the experiments with acetone, the SO_2. was released from a stack. The lidar platform stand-off distance was increased to 3.4 kms. The release plume was approximately 10 meters down wind from the stack orifice with a release concentration of SO_2 on the order of ~1000 ppm. For the purposes of this experiment, two laser wavelengths were used to maximize the attenuation of one of the Raman return signals relative to the companion return signal and visa versa. For the present experiments, the two laser wavelengths were 278.6 nm and 279.6 nm. A dependence of the measured N_2/O_2 ratio on laser excitation wavelength can be clearly observed in the data shown in Figure 4. Each point represents an integration of 6.5 minutes/point. Variation during a given excitation wavelength is attributed to fluctuations in the release plume's tail downstream due to variations in the wind direction. Since the volume of space interrogated during the course of this experiment remained constant, the potential existed for the wind to redirect the stack exhaust away from the analyzed volume. When this occurred, the measured N_2/O_2 ratio returned to the expected "no-release" value. This is clearly evident during the 279.6 nm excitation segment.

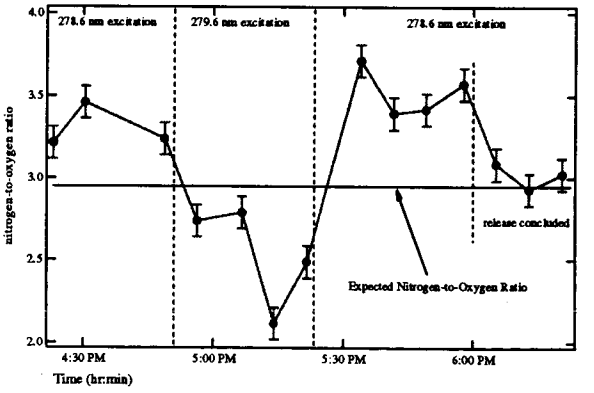


Figure 4: Raman-DIAL measurement of a sulfur dioxide stack release

Finally, it should be noted, that the number of laser excitation wavelengths required for the classical DIAL approach is two times the number of chemical species under investigation. For the Raman-DIAL , it is simply equal to the number of chemical species. For example, in the case of two chemical species, classical DIAL would require a minimum of four excitation wavelengths, since a pair of laser lines are necessary for a single DIAL measurement, whereas the Raman-DIAL would require a minimum only two excitation wavelengths.

4 Conclusions and Prognosis:

The Raman-DIAL technique exploits the Raman scattering off atmospheric nitrogen and oxygen, as a method of conducting a DIAL-like measurement. The strengths of this technique are its independence of return signal strength from aerosol loading, its insensitivity to laser pulse-to-pulse variations, and its use of two completely correlated wavelengths used for a DIAL-like absorption measurement. The basic premise of this technique is the constancy of the nitrogen-to-oxygen ratio. All of these advantages result in a simplification in the data reduction process while retaining the hallmark of DIAL: high sensitivity. This technique can be used to probe UV, VIS and near-IR absorptions through the use of tunable laser systems.

References

1. R. M. Measures, *Laser Remote Sensing: Fundamentals and Applications* (Krieger Publishing Co., Malabar FL, 1992, ISBN: 0-89464-619-2)
2. For example R. M. Schotland, J. Appl. Meteor. **13**, (1974) p 71; and J. C. Sentell, SPIE (W. Kamerman and W. E. Keicher editors *Industrial Applications of Laser Radar*) Volume 2271 (1994) page 2.
3. Z. Wang, J.Zhou, H. Hu and Z. Gong, Appl. Phys. **B 62**, (1996) 14.
4. J. Reichardt, U. Wandinger, M. Servazi and C. Weikamp, Opt. Eng **35**(5) (1996) 1457.
5. T. J. McGee, M. Gross, R. Ferrare, W. Heaps and U. Singh, Geophys. Res. Lett. **20** (10) (1993) 955.
6. R. V. Gathen, Appl. Optics **34** (3) (1995) 463.
7. D. Renaut, J.C. Pourny and R. Capitini, Optics Lett **5** (6) (1980) 233.
8. D. Renaut and R. Capitini, J. Atmos. Ocean. Tech. **5** (5) (1988) 585.
9. F. G.Smith (ed), *The Infared and Electro-Optical System Handbook, Volume 2, Atmospheric Propagation of Radiation* (1993) ISBN: 0-8194-1072-1, pp 9-10.
10. F. Balsiger and C. R. Philbrick SPIE (A. J. Sedlacek editor, Application of *Lidar to Current Atmospheric Topics*) Volume 2833 (1996) page 231.
11. S. Lanatt and A. Lane, J. Quant. Spectros. **50**, 267 (1993).

Tropospheric Temperature Profiling Based on Detection of Stokes and Anti–Stokes Rotational Raman Lines at 532 nm

Ulla Wandinger, Ina Mattis, Albert Ansmann
Institute for Tropospheric Research
Permoserstrasse 15, D–04318 Leipzig, Germany
Phone: ++49 341 235 2154, Fax: ++49 341 235 2361, E-mail: ulla@tropos.de

Yuri Arshinov, Sergey Bobrovnikov, Ilya Serikov
Institute of Atmospheric Optics
Siberian Branch of the Russian Academy of Sciences
634055 Tomsk, Russia

1 Introduction

In a German–Russian co–operation between the Institute for Tropospheric Research (IfT) at Leipzig and the Institute of Atmospheric Optics (IAO) at Tomsk a temperature measurement unit has been added to the IfT Raman lidar. This lidar is mainly used to study aerosol properties in the troposphere and stratosphere. It is part of the German aerosol lidar network (Mattis et al., 1998; Bösenberg et al., 1998). The light source of the Raman lidar is a Nd:YAG laser which emits pulses at 1064, 532, and 355 nm simultaneously. The three elastically backscattered signals — at 532 nm with polarization discrimination —, the vibrational–rotational Raman signals of nitrogen at 387 and 607 nm and of water vapor at 407 nm are detected. From these, particle backscatter coefficients at three wavelengths, particle extintion coefficients at two wavelengths, the water–vapor mixing ratio and the linear depolarization ratio at 532 nm are determined (Mattis et al., 1998). For the temperature measurements Stokes and anti–Stokes lines of the pure rotational Raman spectrum of nitrogen at 532 nm are used. Whereas the elastic and the vibrational–rotational Raman signals are discriminated with dichroic beamsplitters and interference filters, the rotational Raman spectrum is analyzed with a double–grating monochromator that has been developed at the IAO. The idea is based on former applications of the technique first described by Arshinov et al., 1983.

2 Experimental setup

Figure 1 shows a schematic view of the double–grating monochromator. The specifications of its components are given in Table 1. After passing the filter polychromator (Mattis et al., 1998, Fig. 2) about 90% of the light received at 532 nm is coupled into the double–grating monochromator with a monofiber. The monochromator consists of two separate chambers, in each of them one grating is mounted. The chambers are connected by monofibers the ends of which are mounted in solid monofiber blocks that are located in the focal planes of the gratings (see Fig. 1). Fig. 2 shows a cross section of the two monofiber blocks. With the first grating four portions of the rotational Raman spectrum corresponding to the 6th (near end, λ_1 and λ_2) and 12th lines (far end, λ_3 and λ_4) of both the Stokes

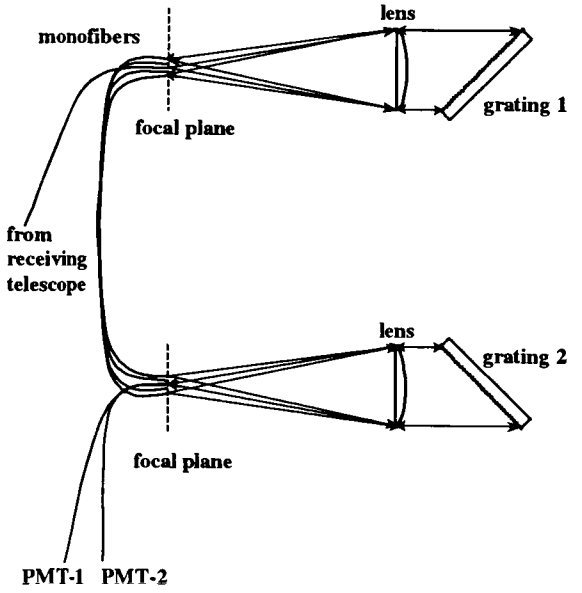


Figure 1: Schematic view of the double–grating monochromator.

Table 1: Specifications of the monochromator components.

Gratings (ruled)	
Grooves/mm	600
Diffraction order	5
Blaze angle, degs	53
Efficiency at 532 nm	0.4
Ruled area, mm^2	60×120
Lenses (quartz, aspherical)	
Focal length, mm	195
Diameter, mm	60
Reciprocal linear dispersion	1.05 nm/mm

and the anti-Stokes branches of N_2 are focused onto four monofiber ends (see upper part of Fig. 2, shaded circles). The opposite ends of the monofibers are geometrically arranged in the focal plane of the second grating (see lower part of Fig. 2, open circles) such that after passing the grating the light of the two near–end and the two far–end lines are focussed onto one monofiber each (see lower part of Fig. 2, shaded circles). In this way, an optical summation of the Stokes and anti-Stokes parts of the spectrum with nearly the same temperature behavior is performed, so that the signal intensity is almost doubled compared to conventional setups which use one side of the spectrum only.

At the same time, the background light due to the strong Rayleigh–Mie return that remains at the wavelengths λ_i after passing the first grating — indicated in Fig. 2 by ${}^i\lambda_0$ — is further suppressed (see lower part of Fig. 2, dashed circles). The overall suppression of the double–grating monochromator has been determined to be at least 10^6. From the monochromator two monofibers conduct the selected Raman signals to the photomultipliers (see Fig. 1).

3 Measurement example and calibration

Installation and performance tests of the temperature measurement unit were done in a common effort of the two lidar groups from Tomsk and Leipzig at the IfT in November and December 1997. Fig. 3 shows a temperature measurement taken on 17 December 1997 between 2100 and 2300 UTC. To get the lidar temperature profile one has to calibrate the measured ratio of the near– (6th lines) and far–end (12th lines) rotational Raman signals P_6 and P_{12}, respectively. From the temperature dependence of the rotational Raman spectrum one obtains a nonlinear calibration function of the form (Nedeljkovic et al., 1993):

$$T = \frac{A}{\ln(P_6/P_{12}) - B}. \qquad (1)$$

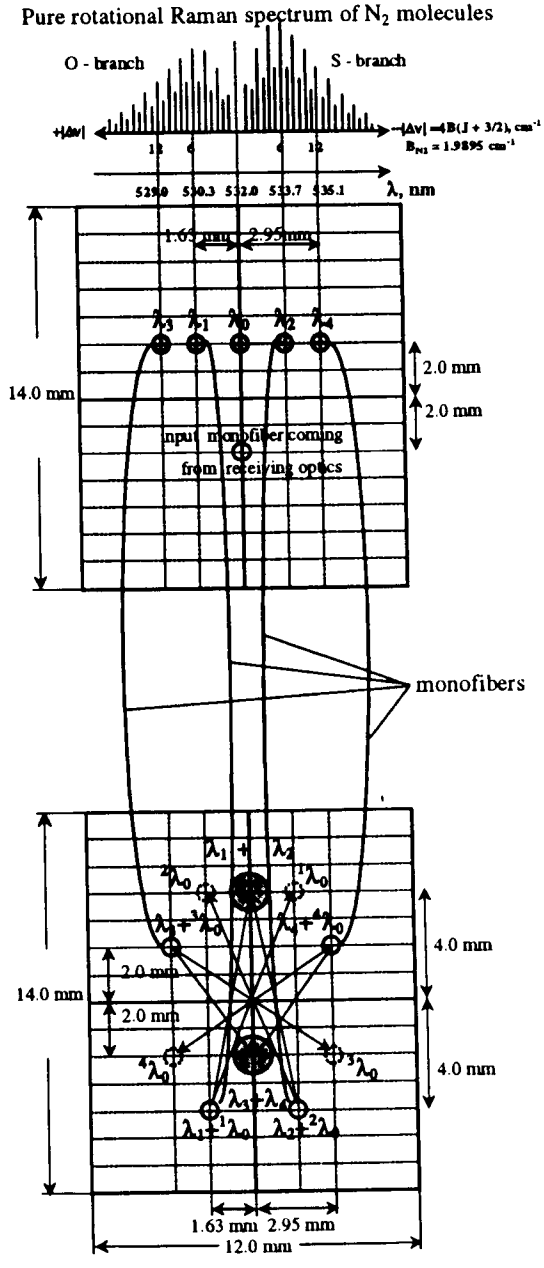


Figure 2: Cross section of the monofiber blocks located in the focal planes of the gratings.

The calibration constants can be determined either theoretically or experimentally by the use of the temperature profile measured with a radiosonde. In the present case, we used the profile provided by a radiosonde launched at the lidar site at 1955 UTC and obtained $A = -392.7$ and $B = 0.603$. In Fig. 3 the lidar profiles without smoothing (60 m vertical resolution, thin solid line) and with smoothing (vertical resolution 240 m below and 2400 m above 1800 m height, thick solid line) are compared to the radiosonde profile (dashed line). By smoothing, the statistical mea-

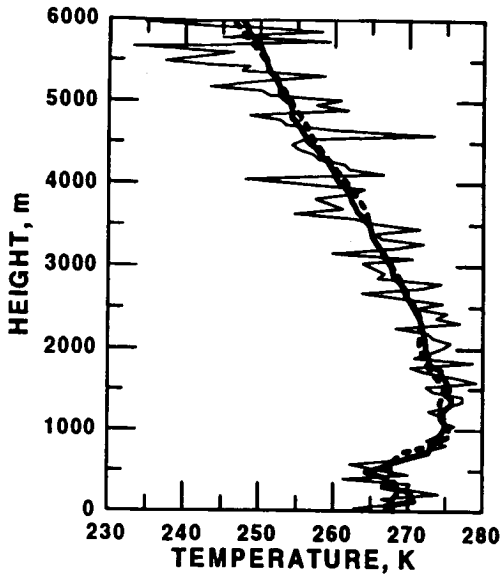


Figure 3: Temperature profiles taken with lidar (2100–2300 UTC, 60-m resolution, thin solid; smoothed with window lenghts 240 m below and 2400 m above 1800 m height, thick solid) and with radiosonde (dashed) on 17 December 1997.

surement error is reduced to below 0.3–0.6%, corresponding to 1–2 K, for the whole measurement range shown in the figure. The largest deviations between lidar and radiosonde profiles of up to 4 K were found below 800 m where near-field effects of the receiving optics play a role but which can be corrected for, if they are proved to be constant with time. Between 800 and 6000 m deviations of less than 2 K were observed. A second measurement example is shown in Mattis et al., 1998.

4 Summary and Outlook

We presented first measurements of tropospheric temperature profiles taken with the Raman lidar of the Institute for Tropospheric Research in Leipzig and a double-grating monochromator provided by the Institute of Atmospheric Optics in Tomsk. By several improvements of the system, such as an increased laser power (the system had to be run with only 25% output energy because of problems with the beam-expanding optics) and an anti-reflection coating of the fiber ends, we expect to increase the intensity of the measured rotational Raman signals by factor of 10 in the future. That will enable us to get temperature profiles with 1-h time and adequate spatial resolution up to the stratosphere at nighttime and up to about 6 km at daytime. The measurements will be especially used to study the development of temperature inversions in relation with the observations of aerosol properties in the lower troposphere.

Acknowledgment

We wish to thank the Deutsche Akademische Austauschdienst for supporting this German-Russian project.

References

Arshinov, Yu. F., Bobrovnikov, S. M., Zuev, V. E., Mitev, V. M. (1983). Atmospheric temperature measurements using a pure rotational Raman lidar. *Applied Optics* 22:2984–2990.

Bösenberg, J., Alpers, M., Böckmann, C., Jäger, H., Matthias, V., Wandinger, U., Wiegner, M. (1998). A Lidar Network for the Establishment of an Aerosol Climatology. *This proceedings.*

Mattis, I., Wandinger, U., Müller, D., Ansmann, A., Althausen, D. (1998). Routine Dual-Wavelength Raman Lidar Observations at Leipzig as part of an aerosol lidar network in Germany. *This proceedings.*

Nedeljkovic, D., Hauchecorne, A., Chanin, M.-L. (1993). Rotational Raman Lidar to Measure the Atmospheric Temperature from the Ground to 30 km. *IEEE Transactions on Geoscience and Remote Sensing* 31:90–101.

Initial Development of a Fiber-Based LIDAR System for Atmospheric Water Vapor Measurements

Liesl M. Little, Peter D. Dragic, S. David Roh, James J. Coleman, and George C. Papen
Department of Electrical and Computer Engineering, University of Illinois at Urbana-Champaign
Third Floor North, CSRL; 1308 West Main Street; Urbana, IL 61801-2307
Phone: (217) 333-4152, FAX: (217) 333-4303, E-mail: l-little@uiuc.edu

Introduction

Most current water vapor lidar systems use solid-state, dye, or excimer lasers and amplifiers [1, 2, 3]. These systems have excellent vertical and temporal resolution, but they tend to be expensive, bulky, and challenging to operate. For applications that require a large number of small lidar systems, such as ground-based meteorological stations [4], the system costs must be decreased and system operation must be simplified. Single diode systems, employing pseudo-noise coding to provide range resolution, have been reported [5, 6] to address this issue, but are peak power limited due to lack of an internal energy storage mechanism.

Here we report on a system using a semiconductor laser master oscillator and one or more fiber amplifier stages that provides moderate energy storage that substantially increases the peak power relative to systems based solely on semiconductor devices. These systems can be significantly less expensive and more efficient operate than large research systems while still producing peak powers an order of magnitude or more greater than existing diode-based systems. In addition, semiconductor lasers and fiber amplifiers can be completely fiber coupled to eliminate cavity absorption losses and external bulk optics. Thus once these systems are spliced together, there is no realignment required making it attractive for autonomous systems.

System Description

We focus on the system transmitter. Other components of the system are similar to existing small lidars [6]. The transmitter consists of a laser diode master oscillator, an acousto-optic modulator, an isolator, and one or more stages of fiber amplification. The semiconductor diode laser used as the master oscillator has been described elsewhere [7]. This laser is a ridge-waveguide, distributed-Bragg-reflector (DBR) laser with excellent spectral characteristics. Reported linewidths for lasers of this type have been in the range of tens of kilohertz [8], and the side-mode suppression is greater than 30 dB [7].

The lasers have two separate current paths, one through the gain region to provide gain and one through the DBR region to provide tuning. This additional current path adds a degree of freedom in tuning. Coarse tuning is acheived using the DBR while fine current tuning is done with the gain section. This combination can access any wavelength within the overall tuning range of the device without changing the substrate temperature, despite the occurrence of mode hops. Once the approximate wavelength has been reached, it is possible to tune on and off an absorption line or to scan through an absorption line using only DBR tuning.

The fiber amplifier stages are based on a three-level transition in neodymium that fluoresces around 935 nm [9]. This transition overlaps a strong water vapor absorption band. Although the fiber amplifier is not quite as efficient as the semiconductor amplifiers, Nd has a long upper state lifetime in silica fiber (~400 μs), which provides energy storage and enables higher peak powers than semiconductor devices used alone.

Initial Experimental Results

The system used for initial testing consisted of a single DBR laser and a single-stage neodymium-doped fiber amplifier. The fiber amplifier was pumped using a standard Fabry-Perot diode laser operating at 808 nm. The pump light and signal light were coupled into the amplifier using a wavelength-division-multiplexer.

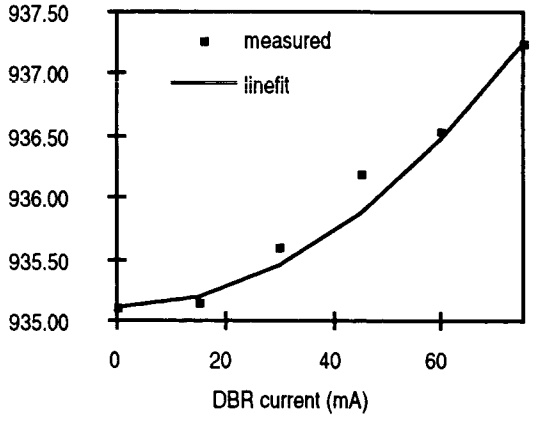


Figure 1 Measured wavelength tuning as a function of DBR current.

The wavelength tuning of the DBR laser as a function of the current on the DBR is shown in Figure 1. The wavelength variation follows roughly an I^2 dependence, implying that the DBR tuning is accomplished through thermal expansion of the DBR.

The fiber used for the amplifier had a numerical aperture of 0.19, and a core diameter of 5 μm. Other measured parameters for the fiber are listed in Table 1.

Table 1 Measured fiber parameters

σ_p^{abs} (cm^2)	4.2×10^{-21}
σ_s^{abs} (cm^2)	1.2×10^{-22}
σ_s^{em} (cm^2)+	1.8×10^{-21}
σ_p^{em} (cm^2)	~0 (forbidden)
Branching ratio $^4I_{9/2}$*	0.474
Branching ratio $^4I_{11/2}$*	0.428
Lifetime (μs)	372

+ Emission cross-sections were determined by fitting rate-equation-modeled amplification to measured amplification.

* Branching ratios are listed only for the two strongest transitions.

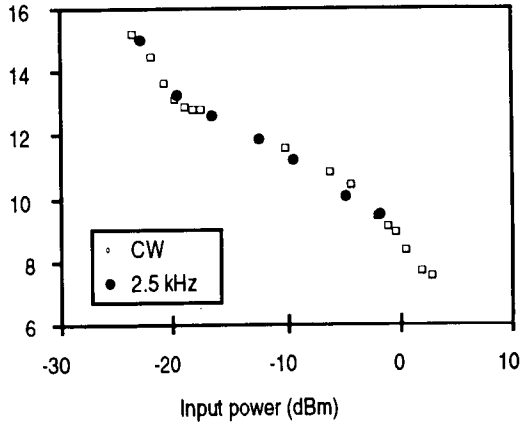


Figure 2 Gain as a function of average input power.

The ability of the neodymium-doped silica fiber to store energy and thus produce high pulse amplification was measured by plotting the small-signal gain as a function of average input power for a continuous input and for a series of pulses with a repetition frequency of 2.5 kHz. The results are shown on Figure 2. It can be seen that the gain depends only on average power not the peak power, which implies that energy is being stored and that high gain of pulses is possible. This is the first report of pulsed amplification for this transition in a Nd-doped silica fiber. For an input signal with a peak power of 2 mW, a pulse width of 1 μs, and a repetition rate of 2.5 kHz, the measured gain is ~15 dB for a single stage. With two stages the gain can be as high as 20 dB for a 1 μs pulse input with peak power of 1 mW and repetition frequency of 2.5 kHz. The second stage adds only 5 dB of gain because at higher powers the amplifier saturates and becomes more efficient. High peak power may be achieved by adding additional stages of amplification.

The linewidth of the signal after fiber amplification was tested by scanning a water vapor absorption line. The water vapor was contained in a multipass White cell. The solid line in the figure (which shows a slight amount of noise) is the measured absorption. The dotted line (which appears smooth because of the overlap with the measured data) is a linefit to the data. The absorption linewidth calculated from the measured data was 0.0946 cm^{-1}, which was within 1% of the HITRAN value (0.0937 cm^{-1}). This implies that the amplified signal spectral content is significantly less than the water absorption linewidth at ground level, which is a key system requirement of DIAL water vapor systems.

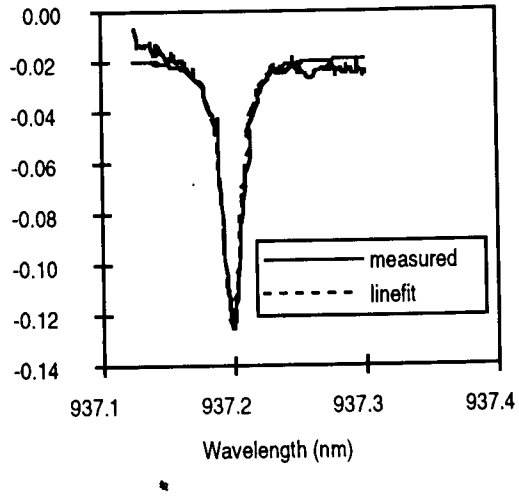


Figure 3 Measured water vapor absorption and Lorentzian linefit.

System Simulation

Based on our experimental results, a prototype water vapor system has been modeled to determine expected power returns and errors for water vapor density measurements in the boundary layer. The system parameters are listed in Table 2 and are based on initial results of a two stage amplifier system producing 100 mW of peak power. The expected error as a function of height is shown in Figure 4. The resulting error for a 30 minute integration was 10% at 2.7 km, assuming a photon-noise-dominated system with no background.

Table 2 Modeled water vapor system parameters

Peak pulse power	100 mW

Pulse width	1 μs
Repetition frequency	20 kHz
Absorbing wavelength	936.989 nm
Non-absorbing wavelength	936.518 nm
Telescope area	0.0507 m^2
Range bin	150 m

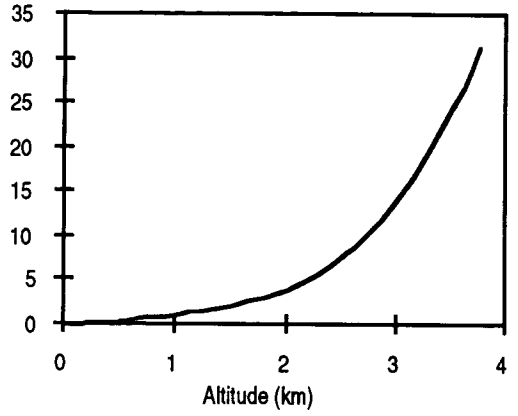


Figure 4 Expected error for a semiconductor master oscillator/fiber amplifier water vapor system with the parameters given in Table 2.

Conclusion

Distributed Bragg reflector lasers coupled with neodymium-doped pure silica fiber amplifiers have many desirable characteristics for compact water vapor lidar systems. We have presented the first demonstration of pulsed amplification in the three-level transition of neodymium-doped fiber and the first water vapor absorption line scan using a semiconductor DBR laser as master oscillator and neodymium-doped fiber amplifier. The absorption scan confirms the narrow linewidth of the amplified signal, and verifies the feasibility of using this system to measure water vapor in the atmosphere. Initial modeling of a lidar system based on this MOPA predicts a measurement error of 10% at 2.7 km, with significantly lower errors achievable by adding additional amplification stages. This novel combination of scaleable power, efficient operation and a fairly simple system design may provide a technology path for a variety of applications such a meteorological stations and autonomous systems.

References

1. A. S. Moore, K. E. Brown, W. M. Hall, J. C. Barnes, W. C. Edwards, L. B. Petway, A. D. Little, W. S. Luck, Jr, I. W. Jones, C. W. Antill, Jr, E. V. Browell, and S. Ismail, Advances in Atmospheric Remote Sensing with Lidar, Selected Papers of the 18th International Laser Radar Conference, Berlin, July 23-26, 1996, pp. 281-288.

2. M. Endemann and R. L. Byer, Applied Optics, vol. 20, no. 18, pp. 3211-7, 1981.

3. J. E. M. Goldsmith, F. H. Blair, and S. E. Bisson, Advances in Atmospheric Remote Sensing with Lidar, Selected Papers of the 18th International Laser Radar Conference, Berlin, July 23-26, 1996, pp. 337-340.

4. V. Wulfmeyer and J. Bosenberg, "Ground-based differential absorption lidar for water-vapor profiling: Assesment of accuracy, resolution, and meteorological applications," submitted to Applied Optics.

5. N. Takeuchi, H. Baba, K. Sakurai, and T. Ueno, Applied Optics, vol. 25, no. 1, pp. 63-67, 1986.

6. J. A. R. Rall, J. B. Abshire, D. Reusser, M. Humphrey, Conference Proceedings - Lasers and Electro-Optics Society Annual Meeting. Publ by IEEE, IEEE Service Center, Piscataway, NJ, USA, 94CH3463-7, vol. 8, pp. 196-198, 1994..

7. S. D. Roh, J. S. Hughes, R. M. Lammert, M. L. Osowski, K. J. Beernink, G. C. Papen, and J. J. Coleman, IEEE Photonics Technology Letters, vol. 9, no. 3, pp. 285-287, March 1997.

8. G. M. Smith, J. S. Hughes, R. M. Lammert, M. L. Osowski, G. C. Papen, J. T. Verdeyen, and J. J. Coleman, IEEE Photonics Technology Letters, vol. 8, no. 4, pp. 476-478, April 1996.

9. P. D. Dragic, L. M. Little, G. C. Papen, IEEE Photonics Tech. Lett. vol. 9, no. 11, 1478-1480 November 1997.

Water Vapour and Aerosol Observations by lidar in the Nocturnal Boundary Layer

Paolo Di Girolamo°, Paolo F. Ambrico, Aldo Amodeo,
Antonella Boselli, Roberta Capobianco, Gelsomina Pappalardo*, Nicola Spinelli°.

Istituto Nazionale per la Fisica della Materia
and
*Istituto di Metodologie Avanzate di Analisi Ambientale,
C.N.R.,Area della Ricerca di Potenza, via S.Loja, I-85050 Tito Scalo (Pz).
°Dipartimento di Ingegneria e Fisica dell'Ambiente,
Università della Basilicata, via della Tecnica 3 I-85100 Potenza.
Phone: 0039-971-427241, Fax: 0039-971-427222, e-mail: digirolamo@na.infn.it

1 Introduction

A ground-based lidar system capable to perform simultaneous measurements of atmospheric water vapour and aerosols in the nocturnal boundary layer has been developed in Potenza, Southern Italy (40°36'N-15°44'E, 820 m a.s.l.), in the context of a co-operation between Istituto Nazionale per la Fisica della Materia, Università della Basilicata and Istituto di Metodologie Avanzate di Analisi Ambientale (National Council for Research).

An intensive measurement campaign was performed in Potenza in the period 20 January-20 February 1997 aimed at the study of aerosol and water vapour in the nocturnal boundary layer for different meteorological regimes. Water vapour measurements are performed through the simultaneous application of the Raman and DIAL techniques, while aerosol backscattering profiles are obtained from lidar elastic echoes at 355 and 723.37 nm.

2 Experimental Set-up

The Potenza lidar system (Pappalardo et al., 1997) has been developed around a Nd:YAG laser source operating on both second and third harmonics (532 and 355 nm). The 355 nm laser beam, used to stimulate Raman scattering by water vapour and nitrogen molecules (λ = 407.5 and 386.6 nm, respectively), allows to perform humidity lidar measurements through the application of the Raman technique; the 532 nm beam is used to pump a Dye laser tuneable within a spectral region of major absorption for water vapour (690-730 nm) and capable to transmit two laser beams at two different wavelengths (λ_{on} and λ_{off}), the first one falling within a water vapour absorption line and the second one falling on the line shoulder. An intracavity rotating wedge allows the Dye laser to shift from λ_{on} to λ_{off}, with a repetition rate up to 20 Hz. In such a way λ_{on} and λ_{off}, together with 355 nm, are alternatively sent into the atmosphere through the same optical path. The selected absorption line (λ_{on}) is located at 723.29 nm, while the corresponding off-line (λ_{off}) is at 723.37 nm.

The receiver consists of a vertically pointing cassegrainian telescope (0.5 m diameter primary mirror, 5 m combined focal length). Spectral selection is performed by means of monochromators placed in the telescope focal plane. The selected radiation is detected by means of cooled photomultipliers, whose output signals are amplified and sampled by means of both photon counting and analog-to-digital conversion. Measurements at λ_{on} and λ_{off} are characterized by a vertical resolution of 3 m, corresponding to a time resolution of 20 ns, while measurements at 355, 386.6 and 407.5 nm are characterized by a vertical resolution of 300 m.

Water vapour DIAL measurements have been supported by a photoacoustic spectroscopy experiment in order to check laser tuning on the selected absorption line. The absorption line was carefully selected to minimize DIAL measurement uncertainties. In particular λ_{on} was selected in order to minimize interferences by molecular species different from the investigated one, to minimize the temperature variability for the water vapour absorption line strength and to meet the requirements in terms of optimal optical depth for the selected line (Ambrico et al. 1997).

3 Results and Discussion

Figure 1 illustrates a lidar measurement of the water vapour vertical profile as obtained through the simultaneous application of the Raman and DIAL techniques. The measurement, expressed in terms of water vapour mass density (g/cm^3), was carried out on January 30, 1997 (19:00-20:30 GMT). The Raman measurement is represented by the solid circles in the figure, while the open squares

correspond to the DIAL measurement. The vertical resolution of Raman data is 300 m; DIAL measurements have been acquired with a vertical resolution of 3 m, but the data have been vertically smoothed in order to reduce signal statistical fluctuations and to fit Raman data resolution.

The figure also shows (open circles) the humidity profile corresponding to the radiosonde launch performed on January 30, 1997 simultaneously to the lidar measurements (19:35 GMT).

All three independent measurements are reported with their error bars, the DIAL technique resulting to be affected by a larger uncertainty.

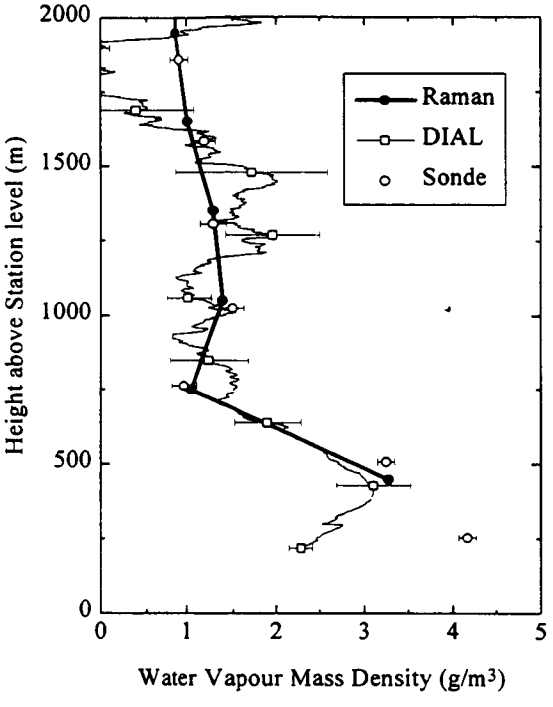


Figure 1. Simultaneous Raman (solid circles) and DIAL (open squares) measurements of the water vapour vertical profile in Potenza on January 30, 1997, 19:00-20:30 GMT; also reported is the simultaneous radiosonde profile (19:35 GMT).

The reported measurement was carried out in clear sky conditions few hours after sunset. A humidity layer extends throughout the boundary layer up to approximately 750 m a.s.l. Raman and DIAL measurements appear to be in good agreement up to 1700 m, with Raman data always falling within the error bars of corresponding DIAL data, while the accordance between radiosonde and lidar data is good above 500 a.s.l.

Raman and DIAL humidity measurements performed in the nocturnal boundary layer (NBL) on several nights have been compared with simultaneous radiosonde data obtained from both free and captive balloons. The agreement between Raman, DIAL and radiosonde data is good (within 30 % up to approximately 2 km above station level) for all considered cases.

Aerosol data are expressed in terms of the aerosol backscattering coefficient at 723.37 and 355 nm, $\beta_{A,723}(z)$ and $\beta_{A,355}(z)$. Lidar measurements of $\beta_{A,723}(z)$ have been compared with simultaneous radiosonde data expressed in terms of potential temperature and relative humidity.

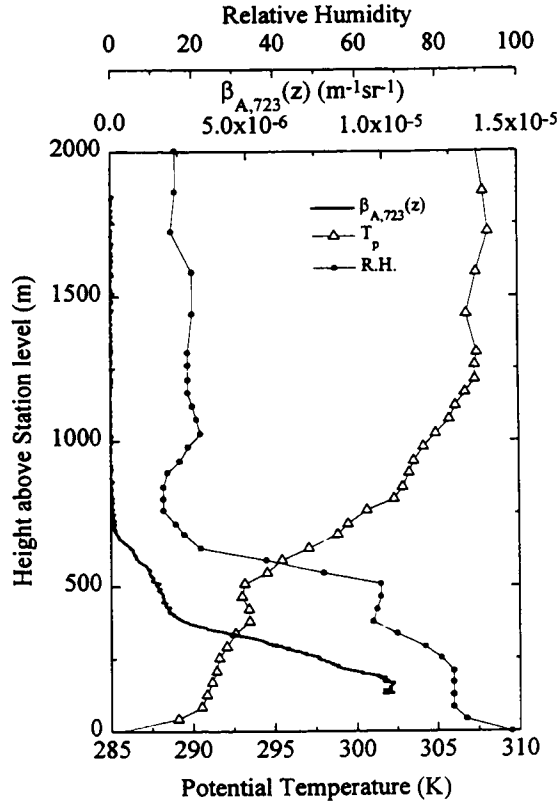


Figure 2. Vertical profile of $\beta_{A,723}(z)$ for 30 January 1997 and simultaneous profiles of potential temperature (open up triangles) and relative humidity (solid dots).

Figure 2 illustrates the vertical profile of $\beta_{A,723}(z)$ for January 30, 1997 (19:00-20:30 GMT), together with the profiles of potential temperature and relative humidity as obtained from the simultaneous radiosonde launch (19:35 GMT). The vertical profile of $\beta_{A,723}(z)$ evidences the presence of two distinct aerosol stratifications accompanied by a similar stratified structure in both the potential temperature

and the relative humidity profiles. The transition between the lower and the upper aerosol layers around 400 m is associated with a maximum in potential temperature and a minimum in relative humidity.

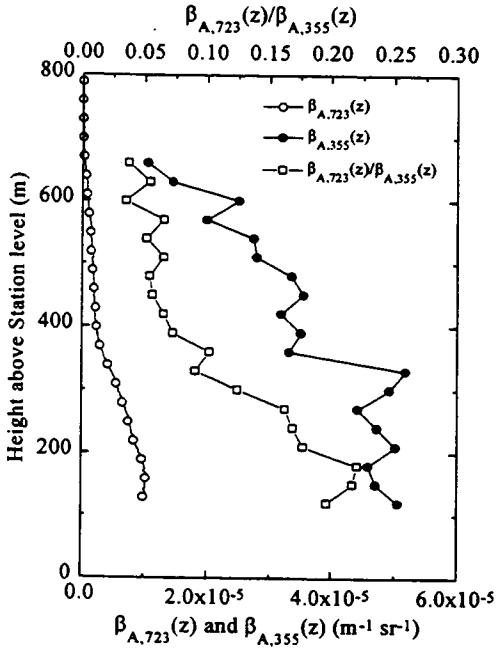


Figure 3. Simultaneous measurements of $\beta_{A,723}(z)$ (open circle) and $\beta_{A,355}(z)$ (solid circle) for 30 January 1997, together with the corresponding profile of the ratio $\beta_{A,723}(z)/\beta_{A,355}(z)$ (open square).

The comparison between profiles of $\beta_{A,723}(z)$ and simultaneous radiosonde data of potential temperature and relative humidity has been extended to 9 selected nights of measurements during the campaign period, covering a variety of boundary layer conditions. For all reported cases the NBL aerosol layer top appears to be located in coincidence with an increase of the potential temperature above a region of almost constant values for this parameter (residual layer); furthermore in most cases the NBL aerosol layer top results to be associated with a minimum in the relative humidity profile.

Aerosol average size characteristics have been determined from simultaneous measurements of $\beta_{A,723}(z)$ and $\beta_{A,355}(z)$. The method is based on the comparison between experimental and theoretical values of the ratio $\beta_{A,723}/\beta_{A,355}(z)$.

Figure 3 illustrates measurements of $\beta_{A,723}(z)$ and $\beta_{A,355}(z)$ for 30 January 1997, together with the profile of the ratio $\beta_{A,723}(z)/\beta_{A,355}(z)$. Theoretical values for $\beta_{A,723}(z)/\beta_{A,355}(z)$ are obtained through the application of the Mie scattering theory, assuming a trimodal lognormal aerosol size distribution (Jaenicke, 1988) and considering a variable accumulation mode mean radius (figure 4).

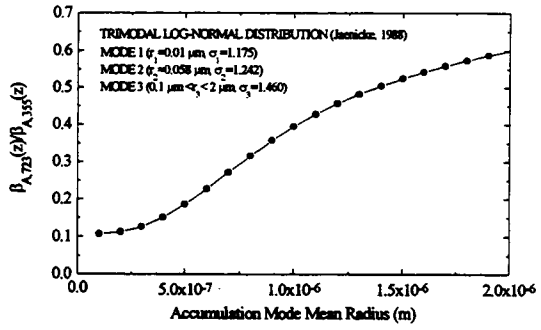


Figure 4. Theoretical values of the ratio $\beta_{A,723}(z)/\beta_{A,355}(z)$ as a function of the mean radius for the accumulation mode.

Measured values of $\beta_{A,723}/\beta_{A,355}(z)$ for 30 January 1997 range from approximately 0.05, at the NBL aerosol layer top, to 0.22 at an altitude of 200 m above station level. As evidenced by figure 4, values of $\beta_{A,723}(z)/\beta_{A,355}(z)$ decreasing with height are representative of aerosol dimensions decreasing with height, with the accumulation mode ranging from about 0.6 μm to about 0.1 μm. The study of the aerosol average size characteristics has been extended to the 9 selected nights of measurements.

References

Ambrico, P. F., Amodeo, A., Amoruso, S., Armenante, M., Berardi, V., Boselli, A., Bruzzese, R., Capobianco, R., Di Girolamo, P., Fiorani, L., Pappalardo, G., Spinelli, N., Velotta, R., (1997). A multiparametric lidar system spanning from UV to the mid IR, *Laser und Optoelektronik* (29) 62.

Jaenicke, R., (1988). In "Numerical Data and Functional Relationships in Science and Technology", Landolt-Börnstein New Series, V: Geophysics and Space Research, 4: Meteorology (G. Fisher, ed.) b: Physical and Chemical Properties of the Air, Springer, Berlin, 391-457.

Pappalardo, G., Ambrico, P. F., Amodeo, A., Berardi, V., Boselli, A., Capobianco, R., Di Girolamo, P., Spinelli, N., Velotta, R., (1997). Multiparametric tuneable lidar system based on IR OPO laser sources. *Lidar Atmospheric Monitoring EUROPTO, Proc. SPIE* (3104), 158-166.

Lidar Observations of a Land-Breeze Circulation

E. W. Eloranta, R. Kuehn and S. Mayor
University of Wisconsin
1225 W. Dayton Street, Madison, Wisconsin 53706, USA
Phone: 608-262-7327 Fax: 608-262-5974
Email: eloranta@lidar.ssec.wisc.edu

Abstract

Observations of a wintertime land-breeze along the shoreline of Lake Michigan are presented. Sequences of RHI, PPI, and three-dimensional scans with the University of Wisconsin Volume Imaging Lidar provide a detailed description of the flow of cold dense air out over the water in the face of an on-shore synoptic flow. Animations of the lidar data showing the surface outflow, the elevated return flow, gravity waves on the return flow boundary, the fluctuating frontal boundary and the eventual collapse of the front will be presented.

Background

The University of Wisconsin Volume Imaging Lidar (VIL) is designed to provide high spatial and temporal resolution images of atmospheric structure. It employs a Nd:YAG laser operating at a repetition rate of 100 Hz, 0.5-m diameter scanning optics, and a fast data acquisition system to generate two- and three-dimensional images. In typical operation the system records data to a range of 18 km with a range resolution of 15 m. The data system records profiles without averaging. Approximately 1 G-byte of data is recorded per hour of operation.

The VIL was operated as part of the Lake Induced Convection Experiment (Lake-ICE) at a site on the western shore of Lake Michigan from December 5, 1997 to January 19, 1998. Our lidar observations were designed to provide data on convective structures which develop over the lake when cold winter air flows over the unfrozen lake. The strong surface heat flux caused by the air-water temperature difference and the uniform lake surface provide a natural 'laboratory' setting which can be used to test computer models of convection in the atmospheric boundary layer. This paper presents lidar observations of a land-breeze circulation observed between 12:43 UT and 17:12 UT on December 21, 1997. A more complete description of VIL operations during the Lake-ICE experiment is contained in a paper by Mayor *et al.* (these proceedings).

Synoptic Conditions

A large high-pressure system centered northeast of Lake Huron moved slowly eastward during the observation period. The resulting pressure gradient supported a weak southeasterly (on shore) synoptic flow. Figure 1 shows the wind speed and direction measured at the Coast Guard station.

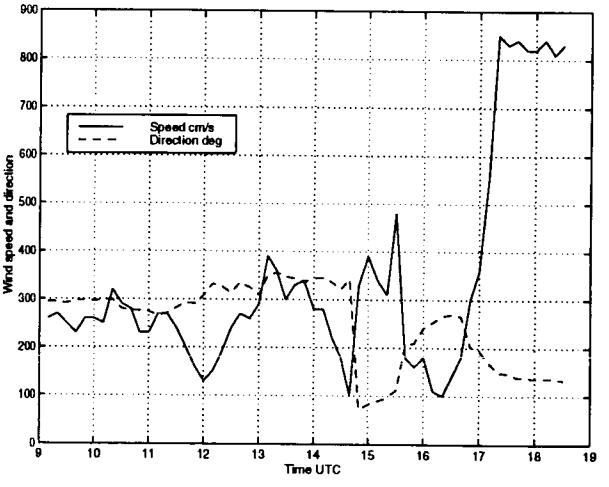


Figure 1. Wind speed and direction measured at the Sheboygan Coast Guard station between 9:00 and 18:30 UTC. The Coast Guard station is located 3/4-km North of the lidar site. Notice that the land-breeze front breaks down at 17:00 UTC under the influence of a weakening land-water temperature differential.

Except for a short period around 15:00 UTC, the offshore flow of the land-breeze is evident from 9:00

to 17:00 UTC. After 17:00 the onshore flow overwhelms the land-breeze flow.

The morning low temperature at the Sheboygan airport ($\sim$ 10 km inland from the lidar) was $-6°$ C and it occurred at 14:00 UTC. The airport temperature rose slowly to $-1°$ C by 17:00 UTC. The morning low temperature at the Sheboygan Coast Guard station (3/4 km north of the lidar on the shore line) was $-3.4°$ C at 11 UTC and the temperature rose to 1.6° C at 18 UTC. NOAA-satellite derived temperatures for the water offshore from the lidar were between 4° and 5° C.

Lidar Observations

Between 12:43 and 13:11 UTC the lidar scanned a three-dimensional volume between azimuth angles of 85° and 135° and elevation angles between 0° and 15°. This scan showed the presence of enhanced scattering close to the lidar and prompted a change in the scan pattern to better image structures near the shore. The new scan began at 13:12 UTC and ended at 15:21 UTC. Each volume scan provided 101 separate RHI scans (0 – 15° elevation) in the azimuth range between 126° and 176°. The volume scan was repeated at intervals of 187 seconds. Figure 2 shows a sample image derived from one of these scans. This image includes one RHI scan along with two constant-altitude cross section created from the same volume scan. Due to the small format available in these proceedings, the horizontal cross sections are enlarged to show only a small portion of the 12-km north-south extent of the lidar images.

The 10-m constant altitude scan shows the cold aerosol laden offshore flow in the land-breeze as an aerosol laden region which is roughly parallel to the shoreline of the lake. When a sequence of the 10-m altitude cross sections are animated, motions of the aerosol structures inside the lake-breeze front show a easterly outflow velocity of approximately 2 m/sec. With careful enhancement of this cross section we can also see aerosol inhomogeneities beyond the front. Animation shows an inflow velocity of 5 to 6 m/s from 130 – 140° on the lake-side of the front. This is roughly consistent with winds observed at the Coast Guard station after the front collapsed at 17:00 UTC (Fig. 1).

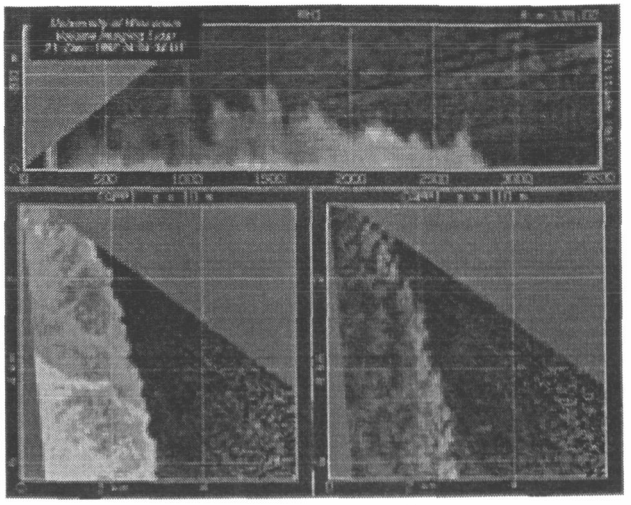


Figure 2. The land-breeze front observed at 14:04 UTC on December 21, 1997. The top panel shows a RHI cross section extending from the surface to an altitude of 300 m and a maximum horizontal range of 3500 m. The RHI is oriented at a compass heading of 134 degrees. The bottom panels show horizontal cross sections over a 6- by 6-km square area at altitudes of 10 m (left) and 110 m (right). North is at the top of the horizontal cross sections and the shoreline runs roughly along the left edge of the images.

The RHI image shows that the front decreases in depth with distance from the shore. It also shows the thin bright land-breeze outflow layer within $\sim$ 20 m of the surface; this is the cold layer of air sliding out over the water against the synoptic flow. Animation of the RHI cross section shows that the land-breeze outflow is confined to a thin layer near the surface. This air appears to flow along the surface to the front where it rises in a strong convergence zone and is then swept back inland in the layer above the outflow. This return flow appears to undergo strong mixing with the marine boundary layer as it is forced up over the land-breeze front. This mixing is evident in the decreased brightness of the upper part of the front near the shore. This decrease of brightness can also be seen in the 110-m cross section which is brightest at the outer edge for the front where air from the surface outflow is being lofted in the convergence zone. Animations show the presence of gravity-wave crests running parallel to the shoreline in the upper part of the front. Point-target-echos also indicate the presence of sea gulls soaring in the air lifted over the front.

Between 15:24 and 16:46 UTC the lidar was scanned back-and-forth to produce PPI scans at an elevation of 0.06° between an azimuth of 85° and 176°. These were acquired with an angular sep-

aration between profiles of 0.08° providing a scan time of 12 seconds. Animations of these scans show the position of the land breeze fluctuating in a series of surges and regressions. The outflow wind is made clearly evident by the motion of aerosol inhomogeneities. The signal strength was sufficient to provide usable images of the front out to a range of approximately 12 km south of the lidar. Visual observations during this period showed the lake to be calm without capillary waves near the shore. Offshore, at a distance which appeared consistent with the lidar imaged front, the water surface turned dark and disturbed by the on shore flow.

Between 16:51 and 17:12 UTC the lidar was programmed to repeatedly repeat an RHI scan between elevations of 0 and 15° with the azimuth held at 165°. The azimuth was selected from visual observations of the cloud motion; the lidar azimuth was set opposite to the wind direction in a newly formed stratocumulus cloud layer. This animation provides vivid images of the return flow even though the images are made more complex by the presence of extremely light snow showers which had begun to fall from an advancing stratocumulus cloud layer. This sequence documents the collapse of the land-breeze front. During the sequence, the frontal surface continuously retreats until it passes over the lidar's shoreline location. Small capillary waves began to build on the water near the shoreline as the front approached. After the frontal passage at 17:00 UTC the water became disturbed. Shortly afterward waves of approximately 30-cm height formed all along the previously calm shoreline.

This presentation will include animations of the lidar observed structure. We also hope to present lidar derived wind profiles in the frontal zone.

Acknowledgments

This research was supported under NSF Grant ATM-9707165 and Army Research Office Grant DAAH04-94-G-0195. Assistance in data acquisition and analysis was provided by P. Ponsardin, J. Hedrick and G. Tubal.

Contribution of Stratospheric and Mesospheric Lidar Measurements to Climate Issues

Philippe Keckhut & Alain Hauchecorne
Service d'Aéronomie du CNRS, BP3, 91371 Verrières-le-Buisson, France
keckhut@aerov.jussieu.fr, tel: (33) 1 64 47 43 11, Fax: (33) 1 69 20 29 99

1. Introduction

The actual and future climate result to some complex feedback that occur not only in the superficial atmospheric envelop but also in from its interaction with many other ecosystems such as ocean, biosphere and the upper atmosphere. Thermal effects which are primarily caused by radiative effects require that the radiation field be defined all along the atmosphere. Changes in radiation absorption induced by abundance modification of a chemical species at a given level may induced some effects which can exist far from the direct perturbation in order to maintain the global balance. On the basis of radiative transfer calculations, numerical simulations (Roble and Dickinson, 1989) reveal that the amplitude of the cooling of the middle atmosphere, induced by greenhouse gases increase, should be considerably greater than warming at the surface and in the troposphere. Some other climatic forcing such as those induced for example by the ozone depletion, the solar radiation change or the injection of volcanic aerosols occur directly in the stratosphere and may in turn influence ground climate.

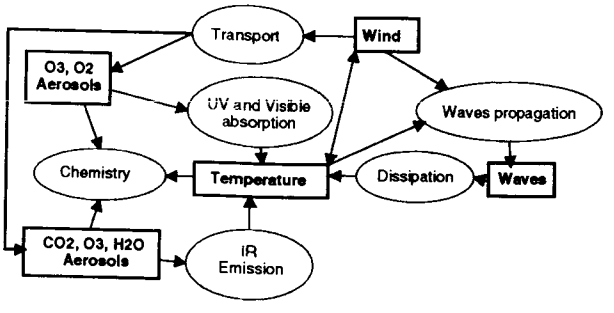


Figure 1. Schematic of the coupling between atmospheric parameters and physical mechanisms.

Despite ground-based lidar systems in routine operation can monitor only a single location, they provide many specific characteristics that let us expect a real and unique contribution on climate issues of the middle atmosphere. The middle atmosphere is driven by many chemical, dynamical and radiative processes linked together which lead to many feedback mechanism which need to be understood (Figure 1). There is a strong feedback of the temperature on the chemistry though the temperature dependence of many equilibrium. Dynamics have important consequences on the distributions of almost every chemical species though transport in the vertical, meridional or zonal directions. Also, temperature and its distribution play a key role in the wave propagation at almost every temporal and spatial scales. Dynamical parameters (Wind and temperature) and trace gases such as ozone appears as key parameters for the climate studies of the stratosphere.

2. Trend detection

Stratospheric lidar methods (Temperature, aerosols, ozone, wind) can provide absolute measurements free of any drift (Hauchecorne and Chanin, 1980; Pelon et al., 1986., Chanin et al., 1989; Keckhut et al., 1994; Souprayen et al., 1998). These methods are self-calibrated and then are not supposed to be sensible to instrumental changes such as rocket (Johnson and Gelman, 1985; Keckhut et al., 1998) balloon (Gaffen, 1994) and satellites (Gelman et al., 1986). These methods appear as well adapted for monitoring the middle atmosphere on a long-term basis. Some of the well improved lidar techniques (Rayleigh lidar, aerosol lidar, ozone DIAL lidar) have been proposed for the Network of Detection of Stratospheric Changes established in 1991 (Kurylo and Solomon, 1990). The Observatory of Haute Provence provide the longest data series of temperature and ozone and can exhibits preliminary trends results. Ozone trends (Guirlet et al., 1998) are in good agreement with other techniques in the upper stratosphere showing changes of 8-10%/decade at 35 km. While temperature trends are small (and even positive in winter) and not yet significant in the upper stratosphere, they are larger than expected from radiative models (Miller et al., 1995) in the mesosphere by a factor of 3-4 (Keckhut et al., 1995) probably due to some feedback effects induced by dynamic processes (Rind et al., 1990). In the Lower stratosphere, where large changes are reported, lidar measurements are more difficult to perform due to the presence of stratospheric aerosols. Raman techniques (Keckhut et al., 1989; McGee et al,

1993; Nedeljkovic et al., 1993) appears as very promising techniques for both ozone and temperature measurements, despite temperature measurements are not yet fully satisfactory for a long-term monitoring (Hauchecorne et al., 1992).

3. Waves studies

Lidar observations of stratospheric and mesospheric temperature has allowed to study waves activity with a height resolution not available from satellite data and with a quasi daily temporal coverage better than the one provided in rocket data base. Also, a temporal resolution, as small as several tens of minutes, not yet obtained with another technique in the same height range, can be achieved with lidars. The main features observed during the winter at mid-latitude are the anticorrelation of the mesospheric and upper stratospheric temperature perturbations and the succession at constant level of warmings and coolings reaching the largest amplitude in January (Hauchecorne and Chanin, 1982; 1983). Spectral analysis of the observed perturbations has shown the presence of specific periods. The 12 to 18 waves with a phase constant with height are attributed to the free Rossby waves. While longer periods from 25 to 40 days are associated with the succession of minor warmings. Planetary waves activity need to be better characterised because they modulate the mean temperature of the polar regions (and thus polar ozone decrease through the formation of PSC's), and to the intensity and permeability of the vortex (and thus to the horizontal transport from poles to the equatorial regions). Also planetary waves are suspected to play a main role in the generation of some climatic features such as the equatorial Quasi Biennial Oscillation that is not yet reproduced into climatic models.

The energy of the gravity waves is generally observed to propagate upward in the middle atmosphere suggesting that these waves are generated essentially in the troposphere and lower stratosphere due to orography, ageostrophy, wind shear or convection. Gravity waves amplitude grow with altitude as density is decreasing exponentially leading to instabilities in the mesosphere. The induced momentum deposition can explained the mesospheric features of the stratospheric jet and the positive temperature gradient between summer and winter hemisphere and probably the mesospheric inversion frequently observed at mid-latitude. Also, the atmosphere acts as a selective filter allowing or not vertical propagation of the different waves modes. Thus, it appears that gravity waves which are poorly parametrised in numerical climate models, can link the entire middle atmosphere through their propagation and act as a climate feedback in the mesosphere. Lidar is a well adapted technique for studying gravity waves, which has already provided numerous results through case studies (Wilson et al., 1991a) and local climatology (Wilson et al., 1991b) and which can help to develop realistic parametrisations.

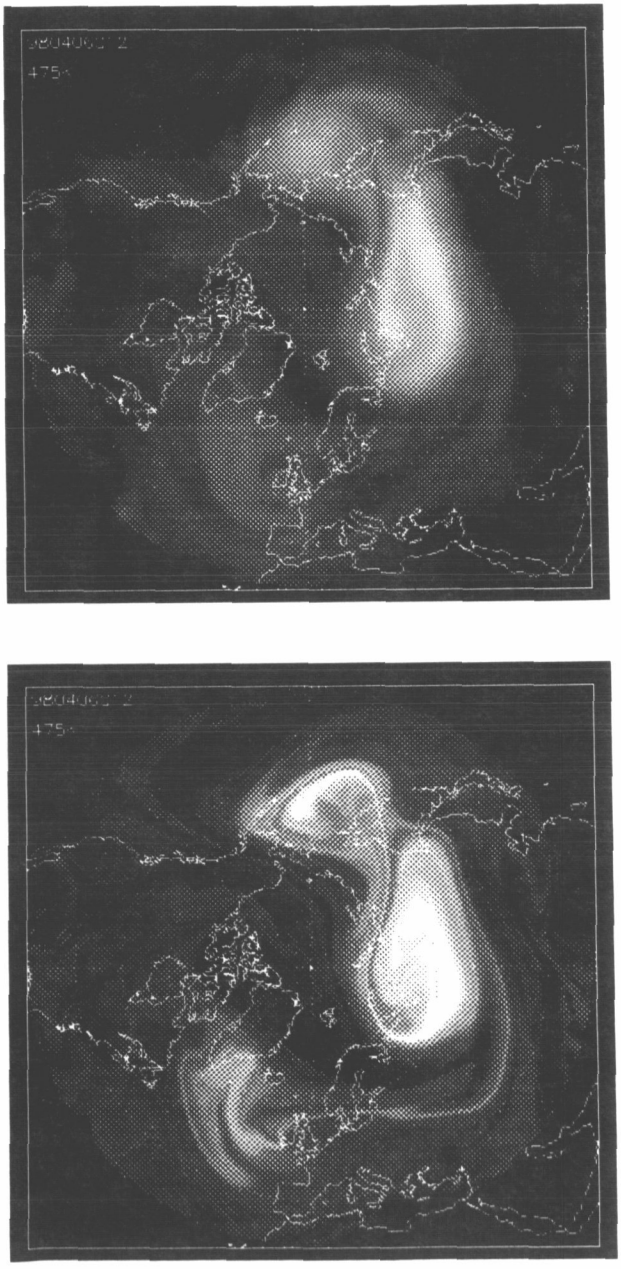


Figure 2. Potential Vorticity (PV) map at 475K level deduced from meteorological field (Top) and from advection simulation.

4. A new issue

The depletion of ozone in the lower stratosphere observed at mid-latitude could be due partly to horizontal transport of poor-ozone air from polar vortex to mid-latitude. Planetary waves breaking induce some air ejection from the vortex through filaments. Polar vorticity contours deduced from meteorological field can not reproduce those very narrow structures due to the size of the grid of the measurements provided by existing networks (Figure 2). These structures are expected to have continental extension and narrow sections of few tens of kilometres. Preliminary observations have revealed that such structures are real in ozone profiles and are not explained by vertical wave advection (Gibson-Wilde et al., 1997). A preliminary prevision of such structures can be obtained in advecting a tracer from meteorological fields. However, the correspondence between simulations and observations is not perfect and suffers to uncertainties about the mixing of the air filament with the background air and about the advection itself. The irreversibility of the transport and thus the possible decrease of ozone at mid-latitude induced by transport depend of this knowledge. Lidars can offer a good opportunity to observe these structures with airborne or ground instruments and can contribute to improve contour advection codes. High resolution vertical profiles of ozone can provide the quantification of the vertical size of these structures while the horizontal sections can be deduced by the continuous observations from the ground with high temporal resolution and collocated mean wind observations. Also the mixing is highly related to gravity waves activity which can be simultaneously observed with temperature and wind lidars. Finally planetary waves and their interactions with the mean flow need to be related to the generation of filament structures to be included into numerical models. Similar transport may exist between equatorial and mid-latitudes.

5. Summary and conclusion

Lidar are not only very exciting instrumental challenges. They had already have a significative contribution into our understanding of the stratosphere and mesosphere. This should continue in the future in providing absolute measurements easily and cheap to operate on a long-term basis, gravity waves characteristics and climatology, a better understanding of the interaction between waves and the mean flow, and understood the contribution of the sub-grid dynamic and transport to the stratospheric and mesospheric changes.

References

Chanin, M.L., Garnier, A., Hauchecorne, A. and Porteneuve, J. (1989) A Doppler lidar for measuring winds in the middle atmosphere, *Geophysical Research Letters* **16**, 1,273-1,276.

Gaffen, D.J. (1994) Temporal inhomogeneities in radiosonde temperature records, *J. geophys. Res.* **99**, 3.667-3.676.

Johnson, K.W. and Gelman, M.E. (1985) Trends in upper stratospheric temperatures as observed by rocketsondes (1965-1983), *Handbook for Map*, **18**, 24-27.

Gelman, M.E., Miller, A.J., Johnson, K.W. and Nagatani, R.M. (1986) Detection of long-term trends in global stratospheric temperature from NMC analysis derived from NOAA satellite data, Adv. Space Res, 6, 17-26.

Gibson-Wilde, D.E., Vincent, R.A., Souprayen, C., Godin, S., Hertzog A. and S.D. Eckermann (1997) Dual lidar observations of mesoscale fluctuations of ozone and horizontal winds, *Geophysical Research Letters* **24**, 1,667-1,630.

Guirlet, M., Keckhut, P., Godin, S., and Megie, G., Long-term monitoring of stratospheric ozone at the Observatoire de Haute-Provence using ground-based and satellite instrument, Solicited paper of the XXIII General Assembly of the European Geophysical Society, Nice, France 20-24 April 1998.

Hauchecorne, A. and Chanin, M.-L. (1980) Density and temperature profiles obtained by lidar between 35 and 70 km, *Geophys. Res. Lett.*, *7*, 565-568.

Hauchecorne, A. and Chanin M.-L. (1982) Midlatitude ground-based lidar study of stratospheric warmings and planetary waves propagation, *J. Atmos. Terr. Phys.*, ***44***, 577-583.

Hauchecorne, A. and Chanin M.-L. (1983) Mid-latitude lidar observations of planetary waves in the middle atmosphere during the winter of 1981-1982, *Journa l of Geophysical Research* **88**,.3.843-3.849.

Hauchecorne , A., Chanin, M-L., Keckhut, P., and Nedeljkovic D. (1992) Lidar monitoring of the temperature in the middle and lower atmosphere, *Appl. Phys.*, **B 55**, 29-34.

Keckhut P., Chanin, M-L. and Hauchecorne, A. (1990) Stratosphere temperature measurement using Raman lidar, *Appl. Opt.*, **29**, 5.182-5.186.

Keckhut, P., Hauchecorne, A. and Chanin M-L. (1993) A critical review of the database acquired for the long term surveillance of the middle atmosphere by the

French Rayleigh lidar, *J. Atmos. Oceanic. Technolo.*, **10**, 850-867.

Keckhut, P., Hauchecorne, A. and Chanin, M.L. (1995) Midlatitude long-term variability of the middle atmosphere: Trends and cyclic and episodic changes, *Journal of Geophysical Research* **100**, 18,887-18,897.

Kurylo, M.J. and Solomon S. (1990) Network for the Detection of Stratospheric Change, NASA Rep., Code EEU.

McGee, T.J., Gross, M.R., Ferrare, R., Heaps, W., and Singh, U.N. (1993) Raman DIAL measurements of stratospheric ozone in the presence of volcanic aerosols, *Geophys. Res. Lett.*, **20**, 955-958.

Miller, A.J., Tiao, G.C., Reinsel, C., Wuebbles, D., Bishop, L., Kerr, J., Nagatini, R.M., DeLuisi, J.J. and Mateer, C.L. (1995) Comparisons of observed ozone trends in the stratosphere through examination of Umkehr and balloon ozonesonde data, *Journal of Geophysical Research* **100**, 11,209-11,217.

Nedeljkovic D., Hauchecorne, A. and Chanin, M-L. (1993) Rotational Raman lidar to measure the atmospheric temperature from the ground to 30 km, *IEEE Trans. Geosci. Remote Sensing*, **31**, 90-101.

Pelon, J., Godin, S. and Megie G. (1986) Upper stratospheric (30-50 km) lidar observations of the ozone vertical distribution, *Journal of Geophysical Research* **91**, 8,667-8,671.

Rind, D., Suozzo, R., Balanchandra, N.K. and Prather, M.J. (1990) Climate change and the middle atmosphere, I, The doubled CO2 climate, *Jornal of the Atmospheric Sciences*, **47**, 475-494.

Roble, R.G. and Dickinson, R.E. (1990) How will change in carbon dioxide and methane modify the mean structure of the mesosphere and thermosphere?, *Geophysical Research Letters* **16**, 1,441-1,444.

Souprayen, C., Garnier, A., Hertzog, A., Hauchecorne, A. and Porteneuve, J., (1998) Doppler wind lidar for stratospheric measurements Part I: Instrumental setup-validation-first climatological results, submitted to *Applied Optics*.

Wilson, R., Chanin, M-L. and Hauchecorne , A. (1991a) Gravity waves in the middle atmosphere observed by Rayleigh lidar 1. Case studies, *Journal of Geophysical Research* **96**, 5.153-5167.

Wilson, R., Chanin, M-L. and Hauchecorne , A. (1991b) Gravity waves in the middle atmosphere observed by Rayleigh lidar 2. Climatology, *Journal of Geophysical Research* **96**, 5.169-5.183.

STUDY OF THE ARCTIC POLAR VORTEX EROSION FROM OZONE LIDAR MEASUREMENTS AT OHP (44°N, 6°E)

S. Godin and A. Hauchecorne
Service d'Aéronomie CNRS
Université P.M. Curie, B. 102, 4 Place Jussieu, 75230 Paris, Cedex
E-mail : sophie.godin@aero.jussieu.fr

1. Introduction

Systematic stratospheric DIAL ozone measurements are performed at the Observatoire de Haute-Provence (OHP - 44°N, 6°E) since the end of 1986. In 1994, the lidar system was improved in order to detect the 1st Stokes wavelengths in the Nitrogen vibrational raman spectrum of the emitted laser radiations at 308 nm and 355 nm [1],[2]. The backscattered signals related to these wavelengths are used to reduce the volcanic aerosol inference on the measured ozone number density and to provide measurements in the very low stratosphere. The final ozone measurement corresponds to a composite profile computed from the raman and the rayleigh signals which are detected simultaneously. The measurements range from 10 km to 45 km in average with a height resolution varying from 0.5 km at 10 km to 4.5 km at 45 km and a corresponding total uncertainty ranging from 5% to 15%. The number of measurements obtained at OHP since the implementation of the new system increased from 111 in 1994 to 202 in 1997.

2. Results

This system has participated to the various campaigns organized by the European Commission in order to study the impact of the arctic polar processes on the mid-latitudes ozone trends (EASOE, SESAME). In the frame of THESEO (Third European Stratospheric Experiment on Ozone) which is scheduled for the winter 1998-1999, it is involved in the METRO project whose objective is to study the mechanisms involved in the meridional transport of air from low and high latitudes to mid-latitudes region in the lower stratosphere, in order to understand the role of this transport in the ozone budget. One of the main points of this project is the study of the filamentation processes (or laminae) at the edge of the polar using a network of ground based lidar stations and an airborne ozone lidar. The interpretation of the filamentation events is made with a set of high resolution dynamical models. Since the implementation of the new lidar system at OHP, several events of this kind were detected, as illustrated in figure 1, which shows an ozone profile obtained at OHP on the night of December 4th - 5th 1997.

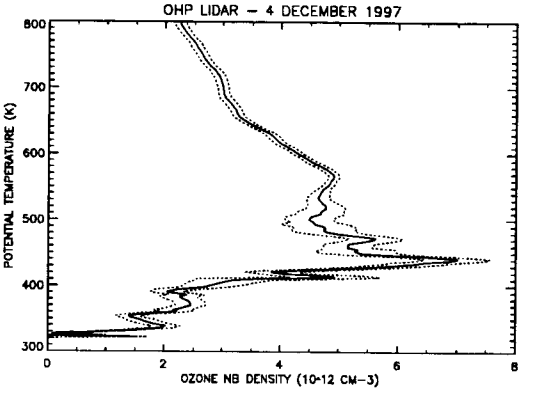


Figure 1. Ozone measurement at OHP on December 4th 1997.

The ozone-rich laminae is clearly visible around 450 K. The high resolution PV analysis at 435 K on the same night reveals the development of a large tongue of vortex air which stretches over Russia up to the southern France, Ireland and Greenland, as seen on figure 2. The dark area corresponds to high PV values characteristics of vortex air. One of the objectives of the METRO project is to compare the results of the high resolution dynamical models to the actual laminae observations provided by the lidar measurements. Besides, the analysis of the mesoscale fluctuations in the ozone and horizontal wind profiles obtained by the ozone lidar and a wind lidar located on the same site [3], allows to distinguish this type of laminae from the signature of gravity waves [4]. This presentation includes the description of the laminae occurrences as observed on the OHP ozone lidar measurements as well as the evaluation of

their potential impact on ozone trends at OHP. Besides, another type of event observed at this site is the detection of diluted vortex airmasses after the final break-up. Such events were observed in 1996 and 1997. The latter year was characterized by a very long lasting and cold vortex and the diluted airmasses were detected in May 1997 only. Such episodes are described in this presentation and the corresponding ozone loss is evaluated.

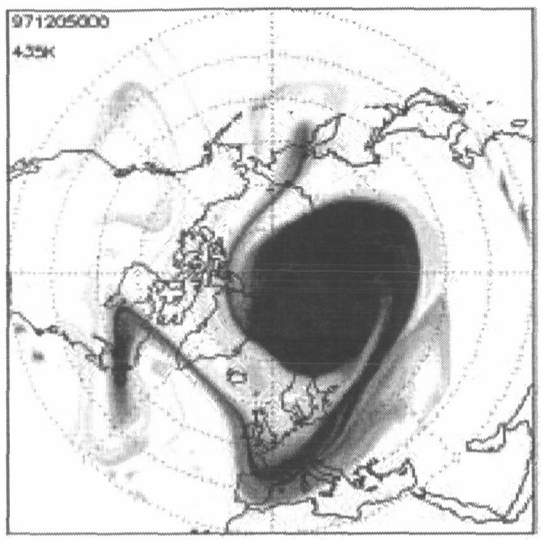


Figure 2. High resolution potential vorticity analysis showing the presence of an ozone-rich lamina around OHP on December 5th 1997 at 0h.

REFERENCES :

[1] Godin S., C. David, A.M. Lacoste, Systematic ozone and aerosol lidar measurements at OHP (44°N, 6°E) and Dumont d'Urville (66°S, 120 °E), 17th ILRC, Sendaï, Japan, 1994.

[2] Porteneuve J., A. Garnier, S. Godin, New Optics Of The Ozone Dial Lidar System at OHP (44°N, 6°E), 17th ILRC, Sendaï, Japan, 1994.

[3] Garnier A., and M.L. Chanin, Description of a Doppler Rayleigh Lidar for measuring winds in the middle atmosphere, App. Phys. B., 55, 35-40, 1992.

[4] Gibson-Wilde D.E, R.A. Vincent, C. Souprayen S. Godin, A. Herzog, S.D. Eckermann, Dual lidar observation of mesoscale fluctuations of ozone and horizontal winds, Geophys. Res. Lett., 24, 13, 1627-1630, July, 1, 1997.

Analysis of Record-Breaking Low Ozone Values During the 1997 Winter Over NDSC-Station Lauder, New Zealand.

E. J. Brinksma[1], Y. J. Meijer[2], B. J. Connor[3], G. L. Manney[4], J. B. Bergwerff[2],G. E. Bodeker[3], I. S. Boyd[3], J. B. Liley[3], W. Hogervorst[1], J. W. Hovenier[1], D. P. J. Swart[2]

[1] Vrije Universiteit, Faculty of Physics & Astronomy, De Boelelaan 1081, 1081 HV Amsterdam, The Netherlands (e-mail: ellen@nat.vu.nl, fax +31 20 444 7899).

[2] National Institute of Public Health and the Environment (RIVM), Air Research Laboratory, Bilthoven, The Netherlands.

[3] National Institute of Water and Atmospheric Research Ltd. (NIWA), Lauder, New Zealand.

[4] Jet Propulsion Laboratory, California Institute of Technology, Pasadena.

Abstract

During early August 1997, the ozone column density measured over Lauder was unusually low, with a minimum value of 222 Dobson Units (DU) at August 10. These observations are striking since in August, during the Austral winter, the ozone column density should be heading towards its yearly maximum; The August mean ozone column density measured over Lauder between 1987 and 1996 was 348 (±28) DU, the lowest monthly average in these ten years was 255 DU.

Regular altitude profile measurements of ozone, performed at Network for the Detection of Stratospheric Change (NDSC) station Lauder, make it possible to do a detailed, altitude-resolved, study of the low ozone observations. The measurements show ozone poor air in two altitude regions of the stratosphere: A 'high region', extending from the 600 K to the 1050 K isentrope (25 to 34 km), and a 'low region', below about 550 K (22 km).

High-resolution reverse trajectory maps of potential vorticity (PV) and ozone mixing ratio, based on the assumption of passive advection by the large-scale three-dimensional winds, show that in the 'high region' the ozone poor air was part of the polar vortex, which was centred off the pole and extended over Lauder for several days, while in the 'low region' the ozone poor air was mixed in from low latitudes. A rapid recovery of the ozone column density, by more than 110 DU within 24 hours, was observed when in the low region an ozone rich filament of the polar vortex moved over Lauder, while in the high region the (ozone poor) high part of the vortex moved away.

Introduction

The 1997 winter has been characterised by low ozone column densities (in comparison to the 10-year average) at mid-latitudes throughout the Southern Hemisphere and a much more irregularly shaped vortex edge than usual. The vortex was also observed to be centred off the pole several times.

Planetary wave activity can lead to peeling off of the vortex edge, redistributing the associated filaments over lower latitudes [Schoeberl et al., 1992]. Similarly, filaments can be peeled off the subtropical barrier. A previous study, for both hemispheres, links subtropical stratospheric mixing to disturbances in the polar vortices during the winter of 1990 [Waugh, 1993]. In this article, an analysis is presented that shows that both vortex and low latitude air were observed over Lauder in August 1997, at different altitudes. Likely, both were associated with the disturbed vortex and the associated increased planetary wave activity.

Over Lauder, three cases in which the ozone column density decreased suddenly and sharply, were observed in August, September and October of 1997. A study of the low ozone column densities that were observed over Lauder throughout the winter and springtime of 1997, and their relation to the ultraviolet levels, will be presented elsewhere [B. J. Connor et al., in preparation].

The amount of exchange between vortex and mid-latitude air is an important issue, because it influences the amount of chemical processing of ozone that takes place [Schoeberl, 1988]. In the literature, only very few cases of vortex filament observations at mid-latitudes have been reported for the Southern Hemisphere [Atkinson et al., 1989, Atkinson and Plumb, 1997].

Ozone Measuring Instruments at Lauder

The RIVM stratospheric lidar [Swart et al., 1994, 1995] has been operational at NDSC (Network for the Detection of Stratospheric Change) station Lauder, New Zealand (45°S, 170°E, time zone UT+12) since December 1994. Its major goal is to provide regular measurements of the stratospheric ozone profile over Lauder. In addition, measurements of the temperature in the middle-atmosphere, and of hydroxyl in the mesosphere [Brinksma et al, 1998] are also retrieved. An overview of the number of nights in which ozone

profile measurements have been performed is presented in Fig. 1. Until January 1998, 282 altitude profiles of ozone were measured. These lidar data have contributed to research comprised in several papers, including a study into the causes of record-breaking low ozone column densities measured over Lauder in the winter of 1997 [Brinksma et al., in preparation], which is presented in some detail below. Note the gaps in the data series in 1995, which were caused by laser problems. All RIVM lidar ozone measurements are available from the NDSC database.

Collocated with the lidar are the following other instruments which provide ozone profile measurements: Electrochemical concentration cell (ECC) balloon sondes, and a microwave radiometer [Parrish et al., 1988, 1992]. The ozone profiling instruments at Lauder have been intercompared during an official NDSC validation campaign in 1995 [I.S. McDermid et al., in preparation], in which collocated measurements by the NASA-GSFC mobile lidar system and two measurements by the satellite instrument SAGEII were also incorporated.

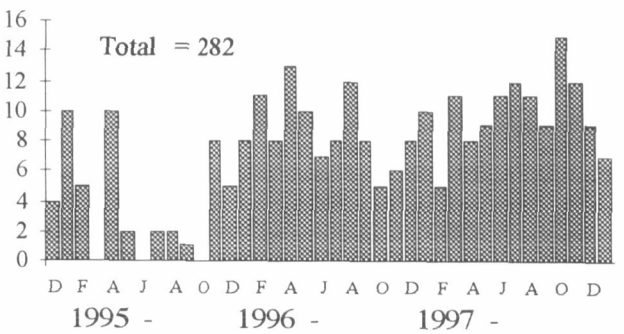


Fig.1: Overview of the number of nights with lidar measurements of ozone at Lauder, New Zealand, from December 1994 until January 1998.

Ozone column density measurements are performed at Lauder by a Dobson spectrometer and an ultraviolet scanning spectrometer (UVM). In addition, we also present ozone column density measurements taken by the Earthprobe TOMS satellite instrument, during overpasses within 0.25° of latitude and 0.30° of longitude from Lauder.

August '97 Observations.

An overview of the measured ozone column density over Lauder, compared to the daily average of the ozone column density in the 1978-1996 Lauder climatology, is presented in Fig. 2. Dobson ozone column density values shown are daily averages, UVM values are measured at local noon. Note that the ozone column density registered in August 1997 was over 2 standard deviations below the 1978-1996 daily average. In the day and night following, a rapid recovery was observed, leading to ozone column densities of 268 DU observed by the lidar at 10 PM local time, and 340 DU observed by several instruments during the next day.

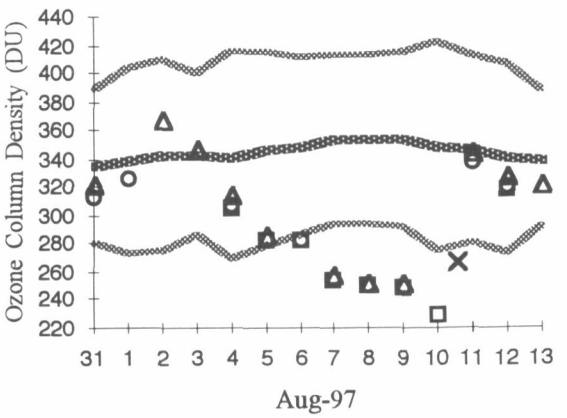


Fig. 2: Ozone column density measurements over Lauder by UVM (squares), Dobson Instrument (circles) and TOMS (triangles), compared to the average of the ozone column density values (grey line) of the 1978-1996 climatology. The lighter grey lines are at two standard deviations below and above this average. The ×-mark indicates the ozone column density derived from lidar measurement on Aug 10 in the local evening.

The lidar and sonde observations yield both ozone number density as a function of altitude (Fig. 3) and ozone mixing ratio as a function of potential temperature (Fig. 4). Since ozone column density equals the integral of ozone number density with respect to altitude, Fig. 3 illustrates more clearly the effect of changes in the ozone profile on the observed ozone column density. Since ozone mixing ratio is conserved on an isentropic surface, and mid-latitude air is well-mixed along isentropes, Fig. 4 is more suitable for unravelling the physical processes causing the decrease in ozone. The microwave measurements, which are available above 20 km (~480 K) and confirm the lidar observations, have been omitted for clarity.

Using the lidar measurements of ozone, potential temperature (θ) and air density, and assuming that ozone mixing ratios are conserved on θ-surfaces, we predicted the evolution of the ozone number density due to adiabatic processes only, and compared this to the observations. The influence of adiabatic processes on the ozone number density, and thus also on the ozone column density, was only significant between August 10 and 13, when adiabatic descent caused the increase in ozone density observed between 18 and 23 km.

Ozone poor air was observed in two regions. Most of the ozone density decrease was caused by advection of ozone poor air between potential temperatures of 350 to 550 K (~ 13 - 22 km, the lower boundary is determined by the start altitude of the lidar measurements.

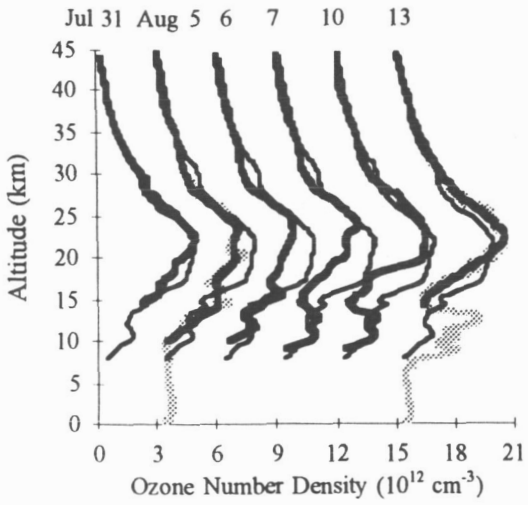


Fig. 3: Altitude profiles of ozone number density measured over Lauder, New Zealand, between July 31 and August 13, 1997. Thick black lines denote lidar measurements. Thick grey lines denote sonde measurements; On August 5 lidar and sonde measured simultaneously, on August 13 the lidar measurement was performed in the evening, while the sonde was launched the next morning (local time). The July 30 lidar measurement is superposed on all profiles as a reference, to guide the eye (thin line).

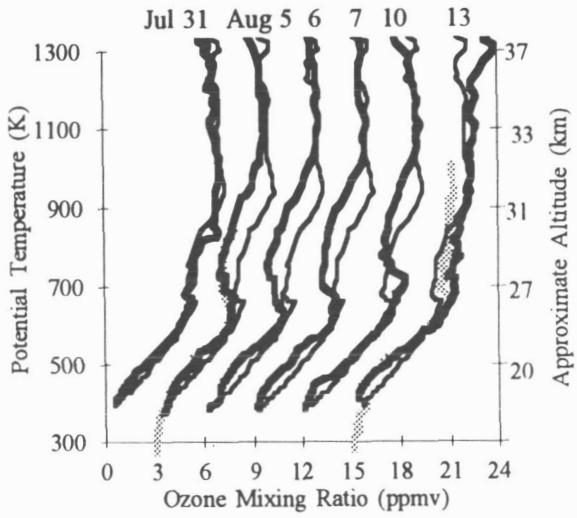


Fig. 4: Potential temperature against ozone mixing ratio is shown between July 31 and August 13, 1997. The same plotting conventions as in Fig. 3 are maintained. Here, the profiles have been offset successively by 3 ppmv. The indicative altitude scale on the right axis is derived from the lidar potential temperatures on August 5. The profiles have been offset successively by 3×10^{12} cm^{-3}.

Another region in which ozone depletion took place is between the 600 K and 1050 K isentropes (~ 25 to 34 km). Associated with the low ozone mixing ratios in this high region were unusually low temperatures in the middle and high stratosphere, and high mesospheric temperatures.

Analysis

To add to the understanding of the dynamical processes involved, high-resolution maps of the potential vorticity (PV) and ozone mixing ratio were calculated for August 4-10. PV is conserved on timescales of about a week, and thus can be used as a 'dynamical tracer' that indicates the origin of the air. The polar vortex is associated with high absolute values of PV, while low-latitude air will have low absolute PV values. For the PV maps, a reverse trajectory procedure was used [Manney et al, 1998, 1995] run and initialised with UKMO temperature and wind data. Similar maps of the ozone mixing ratio, initialised with ozone fields derived from MLS (Microwave Limb Sounder) and based on the assumption of passive advection by the large-scale three-dimensional winds, were also created.

The high-resolution PV and ozone maps at θ=420 and 500 K (not shown) indicate that patches of higher PV and ozone mixing ratios were replaced by low PV, ozone poor air from between August 6 and 7 until August 10. The ozone poor air was associated with a tongue of air from close to the subtropical barrier moving to mid-latitudes and mixing in. On August 10, abruptly, the ozone mixing ratios and PV in the top part of the low region, between 18 and 24 km (or θ=450 to 600 K) increased. The high-resolution maps at 420 K show clearly that this is due to a filament of ozone rich vortex edge air. The lidar observations on August 10 and 13 (Fig. 3) show that on August 10 the ozone number density between 19 and 24 km has increased significantly due to the filament. Below θ=450 K (or 18 km), the low ozone density due to the subtropical air remains until August 13.

The daily UKMO PV data, which are much coarser than the high-resolution PV maps, do not show the subtropical air moving in very well, but do show an overall decrease in PV at θ=420, 465 and 520 K (Fig. 5, lower panel). Around August 10, the PV increases significantly, likely due to the approaching vortex edge (= high absolute PV) filament which was over Lauder on August 10.

In the high region, the story is more straightforward. Between Aug 5 and 6, the vortex moved over Lauder, first above about θ=660 K, but on August 10 down to θ=600 K. Since the vortex at these potential temperatures is ozone poor, this explains the ozone decrease in the high region. Time series of the daily UKMO PV data (based on interpolations of measured temperature and wind fields) confirm that between August 5 and 10 high PV air is observed over Lauder, correlated to low

ozone mixing ratios (Fig. 5, top panel). Due to the low spatial and temporal resolution of the UKMO data the PV decrease lags behind the ozone mixing ratio recovery observed by lidar (on August 10).

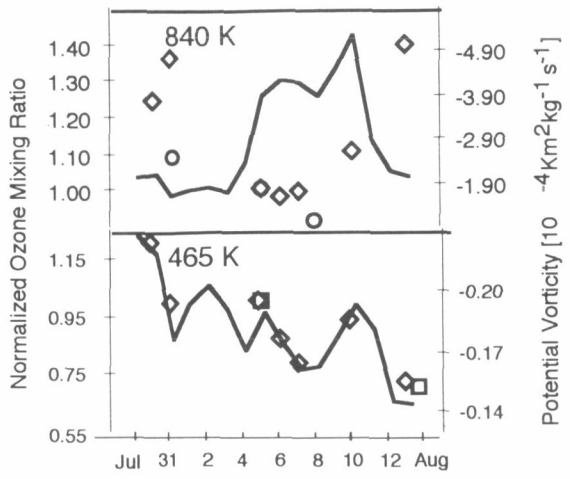


Fig. 5: Series of the daily UKMO PV above Lauder at 12 noon UT (solid line) compared to the ozone mixing ratio observed by lidar (diamonds), microwave (circles) and sondes (squares), at different θ-levels (top left corner labels). The ozone mixing ratios have been normalised to each instrument's August 5 measurement.

Simultaneous presence of low-latitude air in the low region and vortex air in the high region (above 600 K) led to the record-low ozone column observations. After August 10 the ozone poor vortex moved away, and lower down the ozone rich vortex edge filament moved over Lauder, replacing some of the ozone poor low PV air. The combination of these effects caused a rapid increase of the observed ozone column density on August 10.

Conclusions

We have shown that advection of ozone-poor air in two altitude regions caused record-low ozone values over Lauder. In the lower stratosphere, ozone poor air from low-latitude regions was advected from August 7 - 10. At higher altitudes vortex edge and vortex air was observed between August 6 and 10. The rapid recovery of the ozone column density on August 10 was caused by a filament of the polar vortex edge moving over Lauder at about 18.5 km (θ=460 K). Although only the August case was presented here in detail, two similar events happened over Lauder in September and October.

Acknowledgements

Thanks to the Microwave Limb Sounder team for making available maps of their ozone data. UVM-data were kindly provided by Dr. R. L. McKenzie. Drs. D. P. Donovan, J. F. de Haan, F. Alkemade, and G. J. M. Velders are thanked for useful discussions. The software used for generating lidar temperature and density data was written by K. F. Boersma. The sonde flight on August 5 was funded by the University of Wyoming.

References

Atkinson, R. J., W. A. Matthews, P. A. Newman, and R. A. Plumb, Evidence of the mid-latitude impact of Antarctic ozone depletion, *Nature*, 340, 290-294, 1989.

Atkinson, R. J., and R. A. Plumb, Three-dimensional ozone transport during the ozone hole breakup in December 1987, *J. Geoph. Res.*, 102, no. D1, 1451-1466, 1997.

Brinksma, E. J., et al., First lidar observations of mesospheric hydroxyl, *Geoph. Res. Letters*, 25, no. 1, 51-54, 1998. (Note: A correction was published in *Geoph. Res. Letters*, 25, no. 4, 521, 1998)

Manney, G. L., et al., Lagrangian transport calculations using UARS data. Part I: Passive tracers, *J. Atmos. Sci.*, 52, 3049-3068, 1995.

Manney, G. L., et al., Modeling ozone laminae in ground-based Arctic wintertime observations using trajectory calculations and satellite data, *J. Geoph. Res.*, in press, 1998.

Parrish, A., R. L. de Zafra, P. M. Solomon, and J. W. Barrett, A ground-based technique for millimeter wave spectroscopic observations of stratospheric trace constituents, *Radio Sci.*, 23, 106-118, 1988.

Parrish, A., B. J. Connor, J. J. Tsou, I. S. McDermid, and W. P. Chu, Ground-Based Microwave Monitoring of Stratospheric Ozone, *J. Geoph. Res.*, 97, 2541-2546, 1992.

Schoeberl, M. R., L. R. Lait, P. A. Newman, and J. E. Rosenfield, The Structure of the Polar Vortex, *J. Geoph. Res.*, 97, no. D8, 7859-7882, 1992.

Swart, Daan P. J., Jan Spakman, and Hans B. Bergwerff, RIVM's Stratospheric Ozone Lidar for NDSC Station Lauder: System Description and First Results. *Abstracts of Papers of the 17th International Laser Radar Conference*, Sendai, Japan, 405-408, 1994.

Swart, D. P. J., J. Spakman, J. B. Bergwerff, E. J. Brinksma, F. T. Ormel, RIVM Stratospheric Ozone Lidar for NDSC Station Lauder, New Zealand, *NOP Report*, RIVM, Bilthoven, The Netherlands, 57 pages, 1995.

Waugh, D.W., Subtropical stratospheric mixing linked to disturbances in the polar vortices, *Nature*, 365, 533-535, 1993.

Comparison of airborne Lidar measurements with Contour Advection simulations

H. Flentje, M. Wirth and W. Renger
Deutsches Zentrum für Luft- und Raumfahrt, DLR
D-82234 Oberpfaffenhofen, Germany
E-mail: harald.flentje@dlr.de

W.A. Lahoz
Centre for Global Atmospheric Modelling
University of Reading, PO Box 243, Reading, UK

1 Introduction

The depletion of stratospheric ozone observed in northern hemisphere midlatitudes during the past decade [10], [11] is discussed to be at least partly due to transport of chemically perturbed air-masses from the polar vortex to midlatitudes [14]. By breaking planetary waves narrow filaments of vortex air may be peeled off the vortex edge and subsequently transported meridionally mixing into the surrounding surf zone [4], [5], [9]. Intrusions of air into and ejections out of the polar vortex have been observed in high resolution numerical simulations with Contour Advection and Domain Filling Trajectory codes during various periods, see e.g. [8], [14] and references cited therein. However since the spatial resolution of the structures produced by these models is much finer than that of the meteorological analyses taken for their initialization the reality of the produced filaments might be questionable [6]. The reliability of occurrence and placing of the filaments will depend on their scales as well as model run parameters like run time or optional removal of very fine scale structures and may be investigated by comparison with accordingly high resolved experimental data.

Detailed insight into the fine scale structure of lower stratosphere tracer transport has been gained through measurements with an airborne Lidar system in several campaigns during the Second European Arctic and Mid-latitude Experiment (SESAME). During the winter 94/95 a number of measurements with the airborne DLR Lidar OLEX have been carried out [15]. During five campaigns from December 94 to April 95 in all 24 flights with 140 flight hours were performed on board a Transall aircraft. The investigated area extended from the east coast of Greenland (20°W) to Novaja Semlja (50°E) and from 85°N to 48°N where along flight track measurements within the vortex core outside the vortex and across the vortex boundary were possible. The ozone and aerosol distributions measured during these flights frequently show pronounced small scale horizontal and vertical inhomogeneities with blob- and tilted stripe structures occurring throughout the winter in the lower stratosphere indicating filamentation. The relatively high resolution of the Lidar measurements allows to validate the output of the Contour Advection Model treated by this article.

2 The analyzing procedure

Since the Contour Advection technique developed by Dritschel [1] has been described by various authors e.g. [7], [13], [3] only a brief description is given here. The code is run on specified levels of potential temperature from 350K to 600K on which it is initialized by fields of Ertl's potential vorticity ((E)PV) and driven by daily isentropic winds both produced by UKMO data assimilation [12]. The analyzed UKMO fields are available at a horizon-

tal resolution of 3.75°longitude by 2.5°latitude and at a vertical resolution of about 2.5km, extending from 1000 hPa to 0.32 hPa with 22 levels equally spaced in log pressure. Contour Advection traces the evolution of specified PV contours which are each represented by a number of material particles and advecting these particles by the winds interpolated to the step time and location from the gridded UKMO distribution. Optionally a "surgery" procedure may be included which disconnects and reconnects contours when the scale of features is below some prescribed value.

To investigate the reality of the fine-scale structure shown by the CA simulation case studies have been carried out for a couple of days on which the Lidar data of ozone and/or aerosol exhibit appropriate features. From the winter 94/95 campaigns the measurements from January 11, February 7, March 21, March 27 and April 4, 5, 8 were suitable for the comparison. Since the Lidar data range approximately from 350K up to 600K the Contour Advection code was run over this range for 11 levels equally spaced by 25K in height. From the calculated high resolved PV-fields the values along the flight path are extracted for the selected isentropic surfaces. The ability of the simulation to reproduce the filaments observed by Lidar is then investigated with regard to height, scale, model run time since initialization and "surgery".

The model validation by correlating the PV simulations with the measured ozone and aerosol distributions is based on the fact that each of these quantities under certain conditions tracer vortex air-masses. Potential vorticity generally exhibits high values within the vortex surrounded by a steep isentropic gradient at its edge and low values outside. The ozone concentration within the undisturbed lower stratospheric polar vortex is markedly higher than outside due to mid-stratospheric poleward transport of equatorial ozone rich air combined with strong subsidence inside the vortex. However this does not hold above 450-500K since in high latitudes this is approximately the lower boundary of the meridionally sloping equatorial air-masses (see e.g.[2]). Analogously the particle concentration inside the vortex is far lower due to subsidence of upper stratospheric and mesospheric air. However chemical depletion may cause vortex air-masses to contain relatively few ozone inverting the correlation and in case of an unstable vortex with strong intrusions into the vortex combined with mixing inside the tracer characteristics get lost no definite relation between ozone, aerosol and PV can be expected at all.

3 Discussion

In this section the measured ozone and aerosol distributions are compared to the CA simulations for two representative days which shows that the air-mass transport indicated by the model is in a relatively good agreement with the measured tracers distributions.

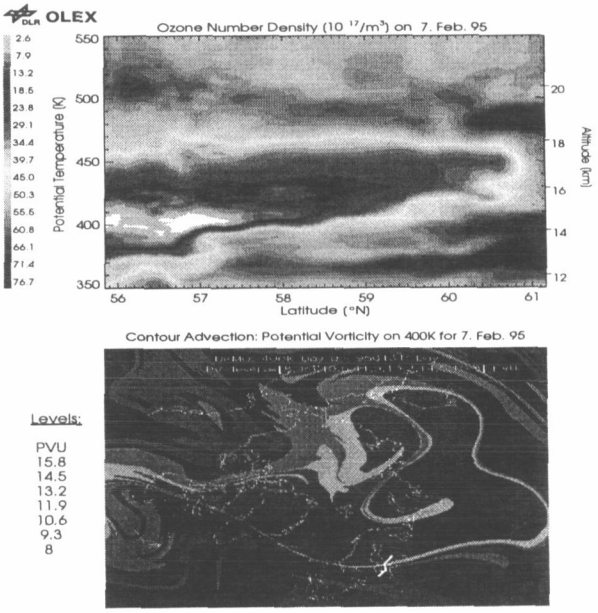


Figure 1: *7 February 1995:* Vertical distribution of ozone number density along the flight path above the Baltic sea marked bold white in lower panel and PV field from 7 day-Contour Advection simulation on the 400K level.

7 February 1995: On 7 Feb 95 a track outside the vortex from 55.8°N, 16.5°E to 61.2°N, 25.4°E was flown. The measured ozone distribution given in Figure 1 upper panel shows a low-ozone-layer with a tilted lower boundary extending from below 56°N to nearly 61°N centered around 400K near 56°N to 440K at 60°N. Between 56°N and 57.5°N at 400K almost no ozone was present which coincides precisely with a tongue of lower latitude air

on that level appearing in the Contour Advection simulation run for either 3, 5, 9 (not shown) and 7 Days (Figure 1 lower panel). On the 400K level the strong gradient of both PV and ozone near the transition zone at 57.5°N confirms that air-masses of different origin are here mirrored correspondingly by the Lidar measurement and the CA simulation. This correlation of low ozone with low PV is valid for the other height levels below 475K as well while above as quoted the meridional ozone gradient vanishes and the air-masses cannot be separated by their ozone content.

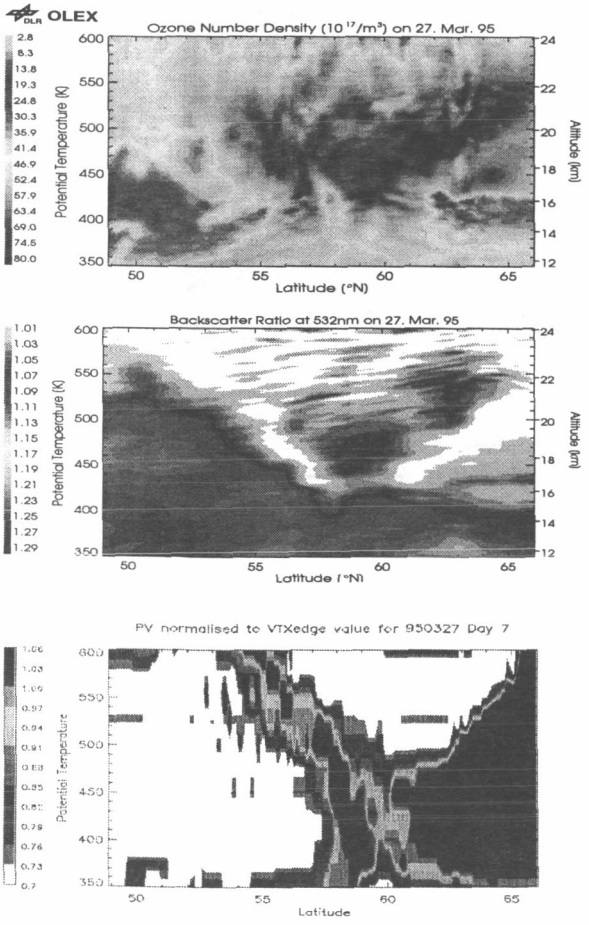


Figure 2: *27 March 95:* Upper panels: Ozone number density and aerosol backscattering ratio at 532nm measured by the DLR Lidar OLEX. Below: Along-flight-path crossection through the polar vortex visualized by PV normalized to the vortex edge value.

27 March 1995: The next example from 27 March 95 deals with a vertically tilted sheet of air which is peeled off the vortex and than transported meridionally as shown by the Contour Advection simulation Fig. 2 lower panel. The signature of this filament appears in either the ozone and especially pronounced in the aerosol distribution over a large horizontal and vertical range (Fig. 2 upper panels). On this day the flight path went from Kiruna (67.9°N, 21.1°E) roughly along the Norwegian coast, over southern Denmark to Munich. The along-flight-path cut through the vortex boundary Fig. 2 is visualized by potential vorticity normalized to the vortex edge value to remove the height dependence of PV. On the uppermost panel the vertical distribution of ozone inside the vortex exhibits a layer with remarkably low ozone concentration extending poleward from 62°N between 390K and 430K which was subject to chemical ozone depletion during the first weeks of March [15]. Note the narrow blob (≈1°lat) in the ozone distribution near 58°N around 420K indicating a cut through the mentioned filament that spirals out of the vortex. As confirmed by CA simulations this low ozone air-mass originates from the ozone depleted layer within the vortex being transported isentropically to lower latitudes. There it is mixed and thus contributes to the observed mid-latitude ozone loss. The aerosol backscatter ratio $\gamma := \frac{\beta_{Mie}+\beta_{Rayl.}}{\beta_{Rayl.}}$ stays below 1.01 in a v-like zone of vortex air with low particle loading enclosing an area of mid-latitude air containing more particles which is in good qualitative agreement with the shown CA simulation. A small latitudinal offset appears between the measurements and the simulation because there is a time shift between the flight (1400-1800 UT) and the shown PV-distribution (0 UT). Further the lower boundary of the vortex as visualized by Fig. 2 depends critically on the definition of the height dependent vortex edge value which below 400K is ill defined and its placing should thus be given less significance.

April 95: In the begin of April 95 the vortex had started to break down indicated by fine scale inhomogeneous distributions of ozone and aerosol below 500K. While most of the observed filaments are reproduced in some cases their vertical tilt differs and some structures are not duplicated on all height levels by the simulated PV distribution. Whether

these discrepancies are due to shortcomings of the model is difficult to decide since the vortex air has already been mixed by that time.

4 Summary

For two representative days of winter 1994/95 the qualitative agreement between Contour Advection simulations with airborne Lidar measurements of ozone and aerosol has been shown. For other days as well most observed filaments are represented and positioned "accurately" by CA runs over 5 up to 9 days down to the confidence scale of about 1°lat ([6]). However some filaments have been observed that do not appear in the calculated PV field. This is attributed to the fact that ozone and aerosol do not unequivocally tracer vortex air especially after mixing across the vortex boundary occurred. This mainly limits the validation since it may cause or mask deviations as well as correspondence between model and measurement. Additionally the importance of dynamical effects for the exchange across the vortex boundary has been demonstrated and an example for meridional transport of a chemically disturbed vortex air mass to lower latitudes has been given.

References

[1] Dritschel, G.D., Contour dynamics and contour surgery: Numerical algorithms for extended, high resolution modeling of vortex dynamics in two-dimensional, inviscid, incompressible flows, *Comput. Phys. Rep.*, *10*, 77-146, 1989.

[2] Holton, J.R., Meridional distribution of stratospheric trace constituents, *J. Atmos. Sci.*, *43*, 12, 1238-1242, 1986.

[3] Lahoz, W.A., et al., Vortex dynamics and the evolution of water vapour in the stratosphere of the southern hemisphere, *Q.J.R. Meteorol. Soc.*, *122*, 423-450, 1996.

[4] McIntyre, M.E., and T.N. Palmer, Breaking planetary waves in the stratosphere, *Nature*, *305*, 593-600, 1983.

[5] McIntyre, M.E., and T.N. Palmer, The 'surf zone' in the stratosphere, *J. Atmos. Terr. Phsy.*, *46*, 825-849, 1984.

[6] Methven, J., and B. Hoskins, On the advection of high resolution tracers by low resolution winds, submitted to *J. Atmos. Sci.*1998.

[7] Norton, W.A., Breaking Rossby waves in a model stratosphere diagnosed by a vortex following coordinate system and a contour advection technique, *J. Atmos. Sci.*, *51*, 654-673, 1994.

[8] O'Neill, A., W.L. Grose, V.D. Pope, H. MacLean, and R. Swinbank, Evolution of the stratosphere during northern winter 1991/92 as diagnosed from U.K. meteorological analyses, *J. Atmos. Sci.*, *51*, 20, 1994.

[9] Orsolini, Y.J., On the formation of ozone laminae at the edge of the Arctic polar vortex, *Q.J.R. Meteorol. Soc.*, *121*, 1923-1941, 1995.

[10] Stolarski, R.S., P. Bloomfield, R.D. McPeters, and J.R. Herrman, Total ozone trends deduced from Nimbus 7 TOMS data, *Geophys. Res. Letters*, *18*, 1015-1018,1991.

[11] Stolarski, R.S., R. Bojkov, L. Bishop, C. Zerefos, J. Staehelin, and J. Zawodny, Measured trends in stratospheric ozone, *Science*, *256*, 342-349, 1992

[12] Swinbank, R., and A. O'Neill, A stratosphere-troposphere data assimilation system, *Mon. Weather Rev.*, *122*, 868-702, 1994.

[13] Waugh, D.W. et al., Transport out of the lower stratospheric Arctic vortex by Rossby wave breaking, *J. Geophys. Res.*, *99*, D1, 1071-1088, 1994.

[14] Waugh, D.W., et al., Mixing of polar vortex air into middle latitudes as revealed by tracer-tracer scatter plots, *J. Geophys. Res.*, *102*, D11, 13119-13134, 1997.

[15] Wirth, M. and W. Renger, Evidence of large scale ozone depletion within the arctic polar vortex 94/95 based on airborne Lidar measurements, *Geophys. Res. Letters*, *23*, 8, 813-816, 1996.

Lidar Measurements of Stratospheric Ozone at the Eureka NDSC Station, 1993 to 1998

A. I. Carswell, J. C. Bird, D. P. Donovan, T. J. Duck, S. R. Pal and D. Velkov
Center for Research in Earth and Space Technology
and the Department of Physics and Astronomy, York University, Toronto, Ontario, Canada M3J 3K1
Phone: (416) 736-2100 x77755, Fax: (416) 736-5516, Email: carswell@lidar.crestech.ca

1. Introduction

Since January of 1993 lidar measurements of stratospheric ozone have been made at Eureka (80° N. 86° W) in the Canadian High Arctic. At this location the Canadian Atmospheric Environment Service has provided an observatory which is part of the international Network for the Detection of Stratospheric Change (NDSC). A UV DIAL system has been operated at this location for the last six winters. Although this lidar has been developed to measure ozone it is also used for measurements of stratospheric aerosol, temperature and gravity waves (Carswell *et al.*, 1993). This facility has provided an unprecedented observational record of these important atmospheric properties throughout the recent Arctic winters.

In this paper, a summary of the ozone observations is presented and other results from this system are discussed elsewhere in these proceedings. During this extended period of observations the stratospheric ozone has exhibited widely varying properties in both space and time. The specific behaviour of the ozone has been observed to be strongly affected by the dynamical behaviour of the polar vortex which forms around the pole in the winter months. This high speed wind jet circulates around the poles at velocities in excess of 80 m/s and serves as a barrier to air exchange between the polar region and mid-latitudes. As the winter progresses, regions of very low temperature develop within the vortex leading to the formation of polar stratospheric clouds (PSCs) and a resultant depletion of the ozone (Manney *et al.*, 1996).

Since the lidar measures only the ozone profile directly over the Eureka site, the concentrations measured depend strongly on the position of the vortex relative to Eureka. The location at Eureka has been found to be particularly advantageous since during a typical winter the jet can pass over the site several times permitting measurements of the stratospheric properties both inside and outside of the vortex. This movement also provides opportunities to study the detailed structural behaviour of the jet at the vortex edge as it passes over the lidar line of sight. The excellent spatial and temporal resolution of the lidar data are providing important new information on the vortex structure.

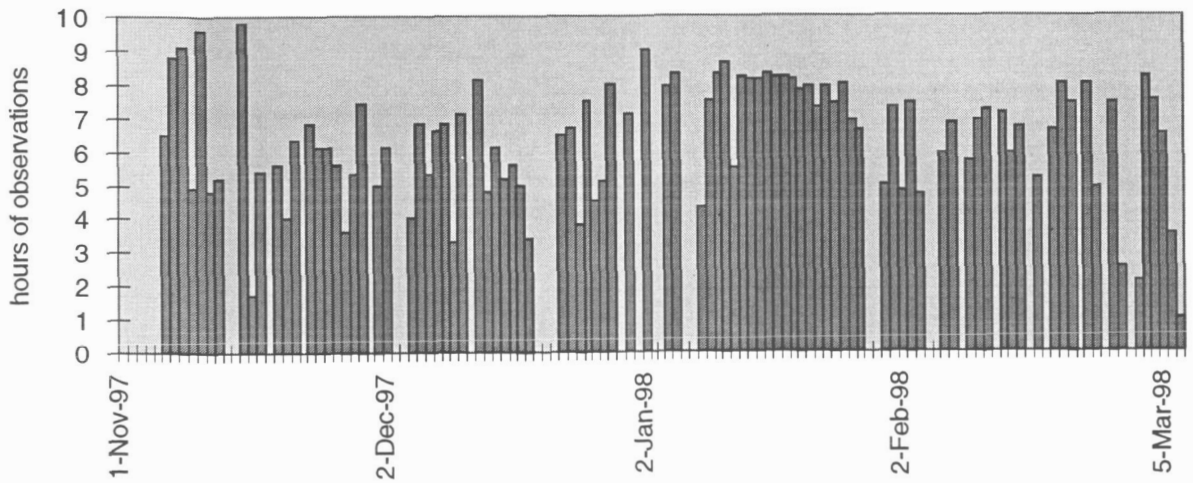


Figure 1. Hours of observation for each night in the 1997-98 winter season at Eureka

winter season	1993	93-94	94-95	95-96	96-97	97-98
number of observation days	30 days	83 days	79 days	76 days	92 days	110 days
obs. days/days on site	62%	63%	81%	67%	84%	88 %

Table 1. Summary of lidar observation days at Eureka with observations as a fraction of the number of days with Crestech personnel on site.

The Eureka location has also proven to have excellent visibility conditions for stratospheric observations during the winter months. In Figure 1 is shown the observational record for the 1997-98 winter and in Table 1, the record for all six winters is summarised. The start and stop dates of our annual campaigns have varied somewhat but overall a detailed time series of ozone profiles has been obtained for the November to March period.

2. Observations

Ozone values over Eureka are highly variable on a year to year basis. The main variations are dominated by the location and motion of the polar vortex wind pattern (sample seen in Figure 2). The location and evolution of the vortex is revealed by the potential vorticity field which also serves as a tracer for conservative motions for frictionless adiabatic flow as air parcels will flow between potential temperature surfaces conserving PV. Furthermore, horizontal PV gradients indicate the presence of a barrier to mixing, so ozone depleted air tends to remain confined within the vortex until it breaks up in the spring.

Ozone mixing ratios measured throughout the observation season of 1996-97 along with the PV values at various levels of potential temperature are shown in Figure 2. The low PV values in early December indicate that during this period Eureka was outside the vortex. The sonde and lidar ozone data are seen to be in good agreement. The consistent decrease of ozone mixing ratio during February and March is indicative of chemical depletion within the vortex during the period. As expected, the relationship between PV and ozone mixing ratio shows positive correlation below 550 K and negative correlation above 550 K (Donovan, et al. 1996).

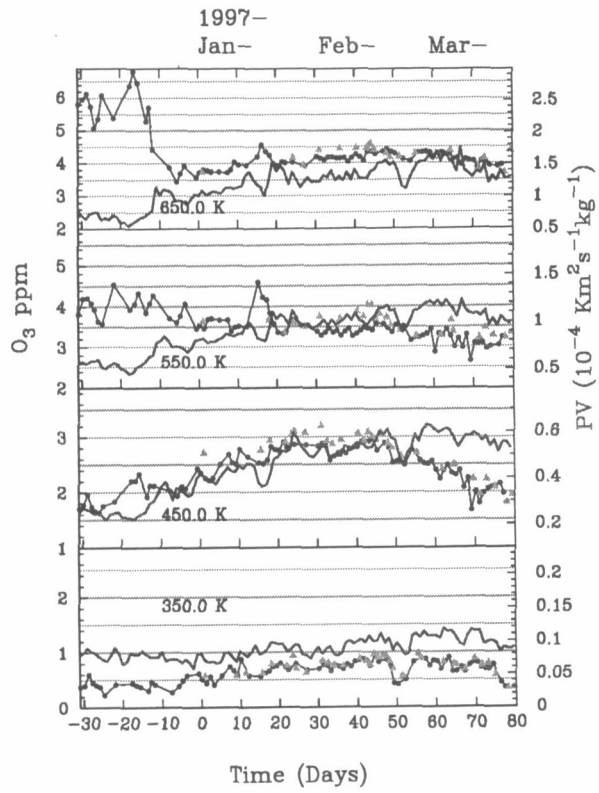


Figure 2. Ozone mixing ratio (dark line) during the 1997 season, and potential vorticity for different potential temperature levels. Ozonesonde values are shown as triangles.

During the winter strong diabatic descent generally occurs within the confines of the polar vortex. As a result, in the lower stratosphere ozone mixing rations tend to increase throughout the season as ozone rich air is transported downwards across isentropic surfaces. This increase is seen in Figure 3 for recent years but only at higher elevations (above about 550 K).

Below this level a similar increase would also be expected. However there is a consistent trend each year for a definite decrease in ozone mixing ratios at lower altitudes (below about 550 K). These decreases are consistent with chemical depletion of the ozone.

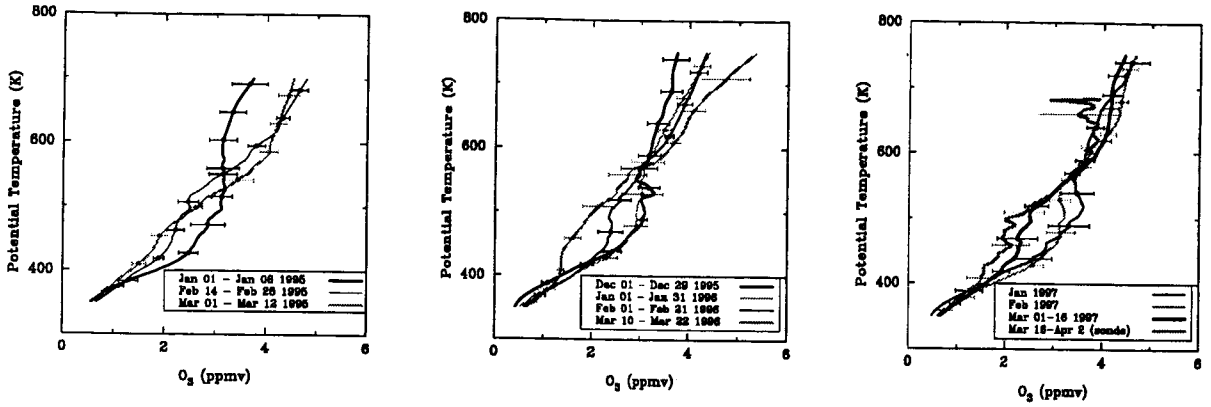


Figure 3. Average intra-vortex ozone mixing ratio profiles during the springs of 1994-95, 95-96, and 96-97. The error bars show the standard deviation of the mean profiles

Specifically, a loss of 35% at 500 K or 1.7-1.8 % per day between mid-February and late-March 97 was observed (Donovan *et al,* 1997). This compares to a higher loss during 1995-96 of 50% between mid-January and mid-March described by Donovan *et al.*, (1996), and 30 % from early January to mid March 1994-95 (Donovan *et al.*, 1995). Similar declines within the vortex have also been reported in other studies using the UARS/MLS satellite data described by Manney *et al.* (1996).

The highly structured nature of the ozone profiles have also been studied in some detail. A sample of such profiles is shown in Figure 4. In this figure ozone profiles on three consecutive days are displayed (over an altitude range from about 0 to 45 km). These profiles show the existence of laminated structure. Laminated structures in ozone profiles have been associated with the dynamic excursions of the polar vortex as shown by Bird *et al.*, (1997). They have been attributable to filaments, vortex edge structure, and low ozone pockets. Transport through the vortex edge region has been an important topic receiving much attention recently in part due to the implications for ozone reductions at midlatitudes. Laminations have been associated with intrusions of midlatitude air into the vortex edge as shown by Orsolini *et al.*, (1995).

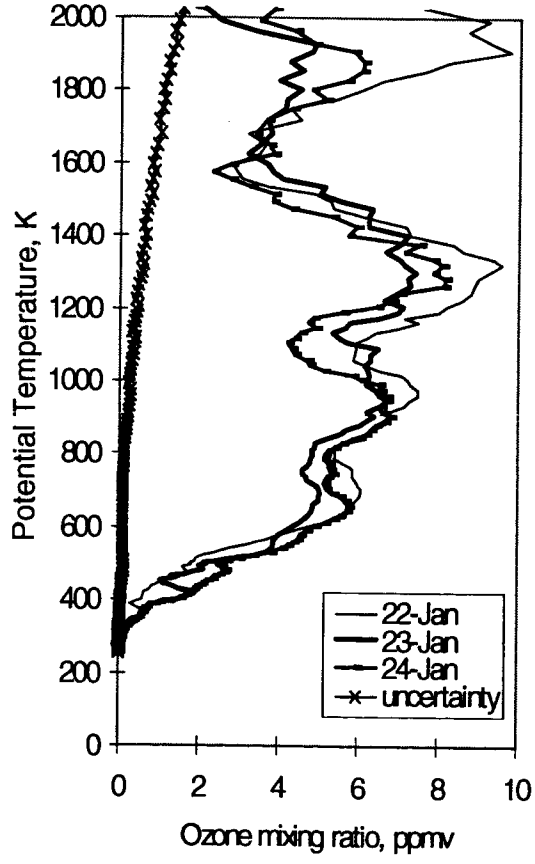


Figure 4. Development of Ozone Laminae during late January, 1995 from DIAL observations. The numbers are the dates from January 22 to Jan 24, 1995.

4. Conclusion

Measurements by lidar and ozonesondes have provided valuable data for the study of the arctic polar stratosphere and in particular, the relationship between the ozone distribution and the polar vortex. It has been shown that ozone mixing ratios below 500 K in the polar vortex have declined during the recent spring seasons. Data for the 1997-98 season is currently being analyzed and will be presented. Overall there have been indications of substantial amounts of chemical depletion of ozone during the winters of our observations at Eureka. Ozone structures or laminations have been seen in the ozone profiles and are attributed to filaments both around and within the vortex.

Polar stratospheric clouds (PSCs) that occur at very low stratospheric temperatures have also been observed on a number of occasions. In addition to ozone structures in the form of minima and maxima in the lower stratosphere, our observations at Eureka show structures in the upper stratosphere at 30-40 km.

5. Acknowledgments

This work was carried out as part of the research program of the Center for Research in Earth and Space Technology at York University. Financial support was also provided by the Atmospheric Environment Service of Canada and the Natural Sciences and Engineering Research Council of Canada.

References

Bird, J. C., *et al.*, Observations of Ozone Structures in the Arctic Polar Vortex, *J. Geophys. Res., 102*, pp10,785-10,800, 1997.

Carswell, A.I., A. Ulitsky and D.I. Wardle, Lidar Measurements of the Arctic Stratosphere, *SPIE, 2049*, 9-23, 1993.

Donovan, D.P. *et al.*, Lidar Observations of Stratospheric Ozone and Aerosol, *Geophys. Res. Lett*, 22, 3489-3492, 1995.

Donovan, D. P. *et al.*, Ozone and aerosol observed by Lidar in the Canadian Arctic during the winter of 1995/96, *Geophys Res. Lett. 23*, pp 3317-3320, 1996.

Donovan, D. P. *et al.*, Ozone, Colunm ClO, and PSC measurements made at the NDSC Eureka observatory (80° N, 86° W) during the spring of 1997, *Geophys Res. Lett. 24*, pp 2709-2712, 1997.

Manney, G. L. *et al.*, Arctic Ozone Depletion Observed by UARS MLS during the 1994-95 Winter, *Geophys. Res. Lett. 23(1)*, 85-88, Jan. 1, 1996.

Orsolini, Y., P. Simon, D. Cariolle, Filamentation and layering of an idealized tracer by observed winds in the lower stratosphere, *Geophys. Res. Lett.*, 22, 839-842, 1995.

Integrated experiment on optical monitoring of atmospheric ozone at the Siberian Lidar Station

V. V. Zuev, M. V. Grishaev, A. V. El'nikov, V. N. Marichev, and S. V. Smirnov

Institute of Atmospheric Optics of the SB RAS
1, Akademicheskii Ave., Tomsk 634055, Russia
7-3822-25-84-82
7-3822-25-83-85 (fax)
zuev@ldsa.tomsk.su

Abstract. Results of integrated experiment on optical monitoring of atmospheric ozone at the Siberian Lidar Station are presented. Monitoring includes lidar measurements of vertical profiles of ozone and temperature in the stratosphere as well as spectrophotometric measurements of total ozone and vertical distribution and total content of nitrogen dioxide. An analysis of the obtained results has shown that the occurrence and evolution of ozone anomalies depend on the anomaly of evolution of global circulation and synoptic processes. Anomalous vertical distribution of nitrogen dioxide was observed during positive ozone anomalies. During negative ozone anomalies ozone and nitrogen dioxide were uncorrelated. Planetary waves with wave number 3 or 4 were observed during ozone anomalies. The duration of ozone anomaly increased with the decrease of the wave number.

Introduction

Frequent occurrence of ozone anomalies in recent years has stimulated strong interest to the study of reasons for their formation and evolution. Experimental observations and their subsequent analysis [1-9] demonstrate that negative ozone anomalies in winter and spring are closely correlated with anomalous evolution of atmospheric circulation during these periods as well as with possible intensification of catalytic decomposition of the stratospheric ozone.

Investigations of stratospheric ozone at the Siberian Lidar Station (56.5°N, 85.0°E) are integrated in character. They are based on regular lidar measurements of the vertical ozone distribution (VOD) and the vertical temperature distribution (VTD) in the stratosphere and on spectrophotometric measurements of the total ozone (TO) as well as the vertical distribution (VD) and total content (TC) of nitrogen dioxide (NO_2). The first results of the integrated experiment on optical monitoring of atmospheric ozone were reported in [10-12].

In the present paper, the results of analysis and interpretation of lidar and spectrophotometric observations, performed as part of the integrated experiment in 1996, are presented.

Results and their discussion

Figure 1 shows the time series of the total content of ozone and nitrogen dioxide from spectrophotometric observations in 1996. Their 6- and 20-day sliding average values that characterize the average synoptic period and the average half-period of long atmospheric waves typical of the global atmospheric circulation are also shown in Fig. 1.

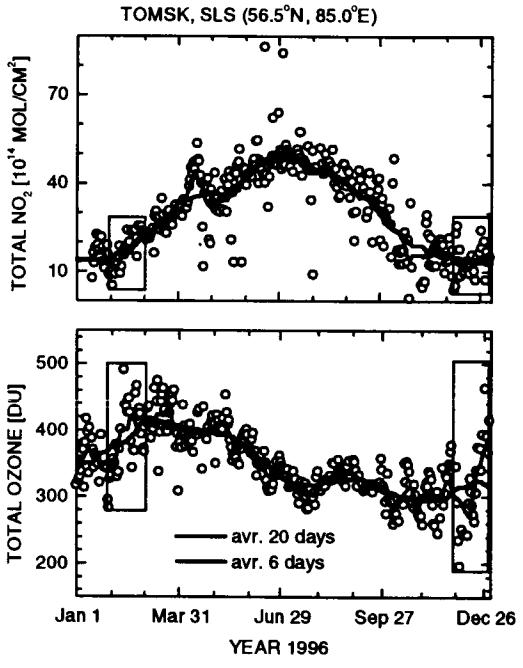


Fig. 1. Time series of total content of ozone and nitrogen dioxide in Tomsk in 1996.

Two periods in February and December framed in Fig. 1 were most informative for an analysis from the viewpoint of the accumulated data volume. In these periods of 1996 we recorded the highest TO values (490, 455, and 456 Dobson unit (DU) on February 12, 22, and 23, respectively, and 464 DU on December 27) as well as unique short-

period TO decay down to 196 DU on December 5. Lidar-derived VOD and VTD for these periods are shown in Fig. 2.

Synoptic analysis of situations demonstrated that the difference between VOD and VTD is caused by different scenarios of evolution of circulation and synoptic processes in the stratosphere. The increase of the ozone content and the temperature increase in the lower stratosphere on February 12 were caused by displacement of the Arctic air mass to the south and by downward vertical flows at the warm core of the circumpolar cyclonic vortex. The simultaneous increase of ozone in the lower and middle stratosphere and of the temperature in the middle stratosphere on February 22 was caused by stratospheric warming. The significant zonal distortion in the middle stratosphere led to high advection of the tropical air mass and transformation of the VOD above the climatic ozone peak. On December 27 high ozone content and very low stratospheric temperature were caused by the cold portion of the circumpolar cyclonic vortex that displaced at our latitudes. On the whole, this case is a continuation of anomalous evolution of the situation observed during the first two weeks in December when on December 5 we recorded anomalously low TO.

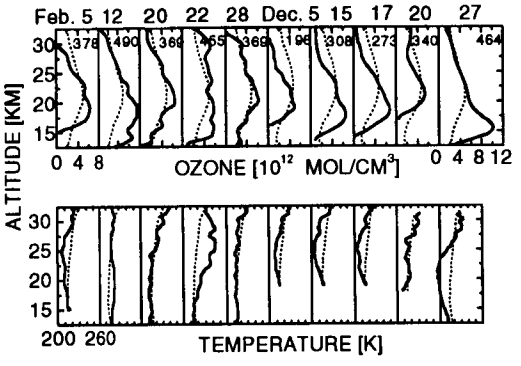


Fig. 2. Vertical ozone and temperature profiles (solid curves) from lidar measurements at the Siberian Lidar Station in February and December 1996. The corresponding model profiles according to [13, 14] are shown by dots. Figures adjacent to the upper plots indicate the total ozone (in Dobson unit) from spectrophotometric measurements.

In [1, 2, 4, and 5] it was shown that analogous synoptic situations, VOD, and VTD in winter and spring were caused by intrusions of the tropical air masses in temperate or polar latitudes as a result of the displacement to the north and subsequent stabilization of high blocking anticyclones (or high crests) and of the corresponding displacement of the circumpolar stratospheric cyclone at lower latitudes. Under these conditions the ozone decay in the lower stratosphere was caused by advective substitution of the air mass in the high baric crest. In the upper stratosphere the ozone decay was caused by upward vertical flows in the cold core at the periphery of the circumpolar vortex.

In these three cases with positive anomalous deviations of the TO and VOD, we also observed some anomalies in the behavior of the VD of NO_2. Figure 3 shows the vertical profiles of NO_2 from twilight spectrophotometric measurements (using methodology according to [15]) in the morning and evening hours that illustrate transformations of the NO_2 distribution during positive ozone anomalies. As can be seen, the NO_2 content in the lower stratosphere sharply increased 2-4 days ahead of the occurrence of the maximum in the TO from evening measurements. This was accompanied by the formation of the maximum of NO_2 content between 10-15 km typically observed between 25-30 km. In a day the VD of NO_2 recovered and then its behavior became unstable. After the occurrence of the maximum TO, the VD of NO_2 became completely stable.

We did not observe any significant changes in the behavior of the VD/TC of NO_2 during the first two weeks of December associated with the anomalous decay of the TO on December 5.

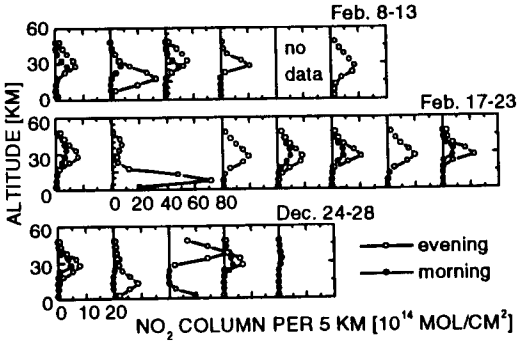


Fig. 3. NO_2 profiles from spectrophotometric measurements during the positive ozone anomalies in February and December 1996.

We believe that the observed trends in the behavior of NO_2, in analogy with the anomalous deviations of the total ozone, are caused by atmospheric dynamics and peculiarities of the latitudinal distribution of NO_2 in winter. When the

cold Arctic air masses with low content of NO_2 but high content of compound-reservoirs ($ClONO_2$, N_2O_5, and so on) from the polar night zone intrude deep into the sunlit temperate latitudes, intense photolysis proceeds of the compound-reservoirs with the formation of NO_2 in the first light day after intrusion. Because in the Arctic air mass the mixing ratios for $ClONO_2$ and N_2O_5 are several times higher than in the temperate air mass, after intrusion the amount of NO_2 is first increased in the upper troposphere and lower stratosphere.

An analysis of synoptic information also confirmed that the positive ozone anomalies were connected with frontal zones of high slightly mobile central cyclones displaced at lower latitudes. The negative ozone anomalies were connected with frontal zones of high blocking anticyclones or high crests displaced at higher latitudes. Planetary waves with wave number 3 or 4 were observed during ozone anomalies of tropospheric circulation. The intensity and duration of ozone anomaly increased as the wave number decreased.

Statistical analysis of lidar measurements of stratospheric aerosol and ozone in summer 1995 - summer 1997 demonstrated that the variability of these atmospheric components for background state of the stratospheric aerosol layer was determined by the same processes. Figure 4 shows the first three eigenvectors S (i=1÷3) of the correlation matrices calculated from lidar measurements. The similarity of the vectors S_i that specify the interlayer correlation for the vertical distributions of ozone and aerosol is indicative of the common mechanism of their variability formed by atmospheric dynamics.

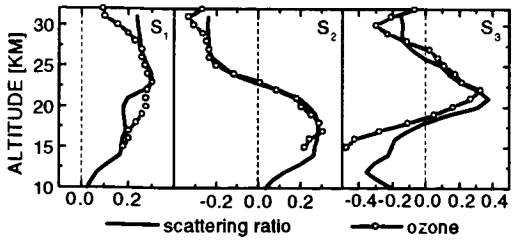


Fig. 4. Interlevel correlation for the vertical distributions of ozone and aerosol in the form of eigenvectors S_i.

Conclusions

Our investigations have demonstrated that the main reason for the formation of ozone anomalies is the advection of air masses caused by displacement of high extensive baric formations. The largest local ozone anomalies are connected with zones of intense vertical flows in contrast frontal zones of baric formations in the lower stratosphere above the tropospheric baric systems.

Our results agree well with the data of investigations reported in [1, 2, 4, and 5] which indicate that local ozone anomalies are closely correlated with the behavior of such centers of atmospheric activity as circumpolar cyclonic vortex, permanent anticyclonic centers of activity - Azores and North Pacific anticyclones, and seasonal Asian (Siberian) anticyclone, whose displacement and intensity, in their turn, are caused by climatic changes in the regime of global atmospheric circulation.

Acknowledgments. We are grateful to our colleagues for technical support of measurements and help in processing of the observations. The work was supported in part by the Russian Fund for Basic Researches (Grant No. 96-05-64282).

References

1. Bekoryukov, V. I., I. V. Bugaeva, G. R. Zakharov, et al., Azores high, ozone, and meteorological parameters of the troposphere and stratosphere, *Meteorology and Hydrology*, *7*, 40-47, 1995 (in Russian).
2. Bekoryukov, V. I., G. R. Zakharov, A. A. Kukoleva, and V. E. Fioletov, About connections of anomalous low ozone content with a synoptic situation, *Meteorology and Hydrology*, *12*, 103-105, 1990 (in Russian).
3. Zhadin, E. A., Anomalies of ozone layer and stratospheric angular momentum, *Meteorology and Hydrology*, *7*, 48-55, 1995 (in Russian).
4. Kruchenitsky, G. M., V. I. Bekoryukov, V. M. Voloshchuk, et al., On dynamic factors contribution into formation of anomalously low total contents of ozone in the Northern Hemisphere, *Atmospheric and Oceanic Optics*, *9*, 1233-1242, 1996 (in Russian).
5. Bekoryukov, V. I., I. V. Bugaeva, G. R. Zakharov, et al., Long-period oscillations of ozone and meteorological parameters of the troposphere and stratosphere as a result of evolution of climato-forming centres of atmospheric activity, *Atmospheric and Oceanic Optics*, *9*, 1243-1249, 1996 (in Russian).
6. Petzoldt, K., B. Naujokat, and K. Neugebohren, Correlation between stratospheric temperature, total ozone, and troposheric weather systems, *Geophys. Res. Lett.*, *21*, 1203-1206, 1994.

7. Randall, C. E., D. W. Rusch, R. M. Bevilacqua, et al., Preliminary results from POAM II: Stratospheric ozone at high northern latitudes, *Geophys. Res. Lett.*, *22*, 2733-2736, 1995.
8. Dorokhov, V. M., T. E. Potapova, F. Goutail, and J.-P. Pommereau, Studying a negative ozone anomaly in the East Siberian ozone maximum in winter and spring of 1995, *Meteorology and Hydrology*, *6*, 53-62, 1996 (in Russian).
9. Browell, E. V., C. F. Butler, S. Ismail, et al., Airborne lidar observations in the wintertime arctic stratosphere: ozone, *Geophys. Res. Lett.*, *17*, 325-328, 1990.
10. Marichev, V. N., V. V. Zuev, M. V. Grishaev, and S. V. Smirnov, Lidar and spectrophotometric measurements of vertical distributions of ozone, nitrogen dioxide, and temperature in the stratosphere over Tomsk (Western Siberia), In: *Advances in atmospheric remote sensing with lidar*: selected papers of the 18th Int. Laser Radar Conf., Berlin, 22-26 July 1996 / A. Ansmann, R. Neuber, P. Rairoux, U. Wandinger (eds.), Springer-Verlag, Berlin, 549-552, 1997.
11. Zuev, V. V., S. V. Smirnov, V. N. Marichev, and M. V. Grishaev, Results of integrated experiment on optical monitoring of the ozonosphere at the Siberian Lidar Station, *Atmospheric and Oceanic Optics*, *10*, 1170-1180, 1997 (in Russian).
12. Zuev, V. V. and S. V. Smirnov, Results of integrated observations of ozone anomalies at the Siberian Lidar Station, *Atmospheric and Oceanic Optics*, *10*, 1400-1414, 1997 (in Russian).
13. Krueger, A. J. and R. A. Minzner, *J. Geophys. Res.*, *81*, 4477, 1976.
14. Ippolitov, I. I., V. S. Komarov, and A. A. Mitzel, Optometeorological model of the atmosphere for a simulation of lidar measurements and a calculation of radiative transfer, In: *Spectroscopic methodologies for sensing of the atmosphere*, Novosibirsk, Nauka, 4-75, 1985 (in Russian).
15. McKenzie, R. L., P. V. Johnston, C. T. McElroy, et al., Altitude distributions of stratospheric constituents from ground-based measurements at twilight, *J. Geophys. Res.*, *96*, 15,499-15,511, 1991.

A New Aerosol Background Level in the Stratosphere? Lidar Observations of the Period 1976 to 1997

H. Jäger and F. Homburg
Fraunhofer Institute for Atmospheric Environmental Research, IFU,
Kreuzeckbahnstr. 19, D-82467 Garmisch-Partenkirchen, Germany
Phone: +49-8821-183-193, Fax: +49-8821-73573, E-mail: jaeger@ifu.fhg.de

1 Introduction

The investigation of the stratospheric aerosol layer by lidar remote sensing began with the pioneering measurements of Fiocco and Grams in 1964. Since then the lidar technique has proved to be invaluable in detecting and monitoring the occurrence, magnitude, spread and decay of numerous volcanic eruptions perturbing the stratosphere. The interest in stratospheric aerosol grew considerably in the past when heterogeneous ozone destruction mechanisms were proposed to take place on aerosol particles even under moderate stratospheric conditions in addition to the highly effective reactions on PSCs.

The program in laser remote sensing of the stratospheric sulphate aerosol layer by ground-based lidar began at the IFU at Garmisch-Partenkirchen (47.5°N, 11.1°E) in 1976. Since then an almost uninterrupted record exists at this midlatitude station.

2 Observations

Until 1990 a ruby laser had been used (694.3 nm), since 1991 a frequency doubled Nd:YAG laser transmitting at 532 nm has been in operation as the lidar emitter. Aerosol size distributions derived from balloon-borne particle counter data from Laramie, WY, are used by a conversion model to calculate height and time resolved ratios of extinction and mass to lidar backscatter and backscatter wavelength exponents. These results are then used to calculate the extinction correction in the lidar equation, to convert 532 nm backscatter measurements to backscatter at the ruby wavelength at 694.3 nm, and to infer the particle mass from lidar backscatter data. The method has been described by Jäger and Hofmann (1991) and by Jäger et al. (1995).

The perturbation of the stratosphere following the Pinatubo eruption in June 1991 was studied in detail by lidar at Garmisch-Partenkirchen, including: the build-up of the perturbation in 1991, the maximum in early 1992, the exponential decay until 1995 (Jäger et al., 1997), and finally the gradual transition to a background situation in 1996 and 1997. Figure 1 indicates that the backscatter integrals measured by lidar decayed to values below the pre-Pinatubo level in 1996.

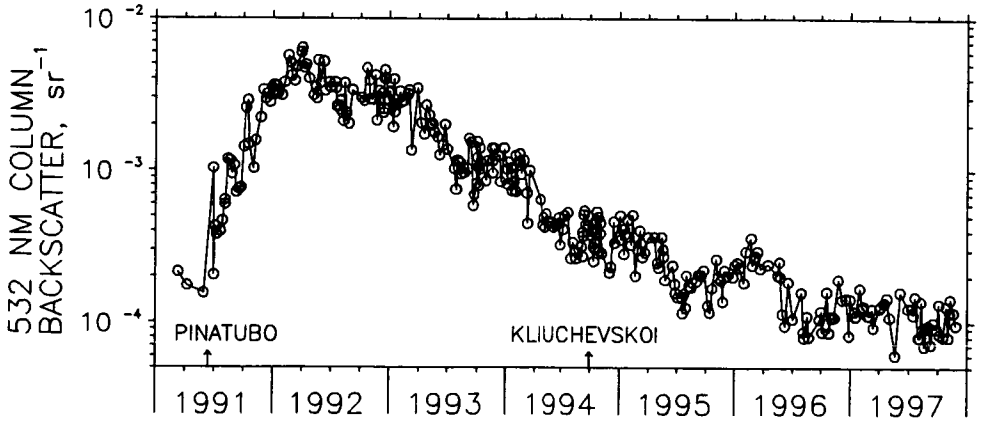


Figure 1. Lidar measurements at Garmisch-Partenkirchen: integral particle backscatter coefficient at 532 nm between the tropopause and the top of the layer. Volcanic eruptions are indicated.

3 Discussion

To examine the present situation of low stratospheric aerosol load, comparisons with previous measurements with the ruby lidar system have been made. The following aspects of the longterm record 1976 to 1997 will be presented:

o The integral backscatter (1 km above the tropopause to the top of the aerosol layer) at 694.3 nm (Figure 2);

o the peak aerosol scattering ratio or optical mixing ratio (ratio of particle to Rayleigh backscatter) at 694.3 nm (Figure 3), which is found in the 15 to 20 km height range and typically at 18 to 20 km in background periods; and

o the column mass in the 15 to 20 km height range (Figure 4).

The aerosol model, mentioned above, was used to calculate the wavelength conversion 532 nm to 694.3 nm (data 1991 to 1993) and the conversion of lidar backscatter to aerosol mass (data 1976 to 1993). More recent Laramie size distributions (T. Deshler, personal communication) were used to treat lidar data 1994 to 1997.

Figures 2 to 4 indicate that the stratosphere at northern midlatitutes was severely perturbed during

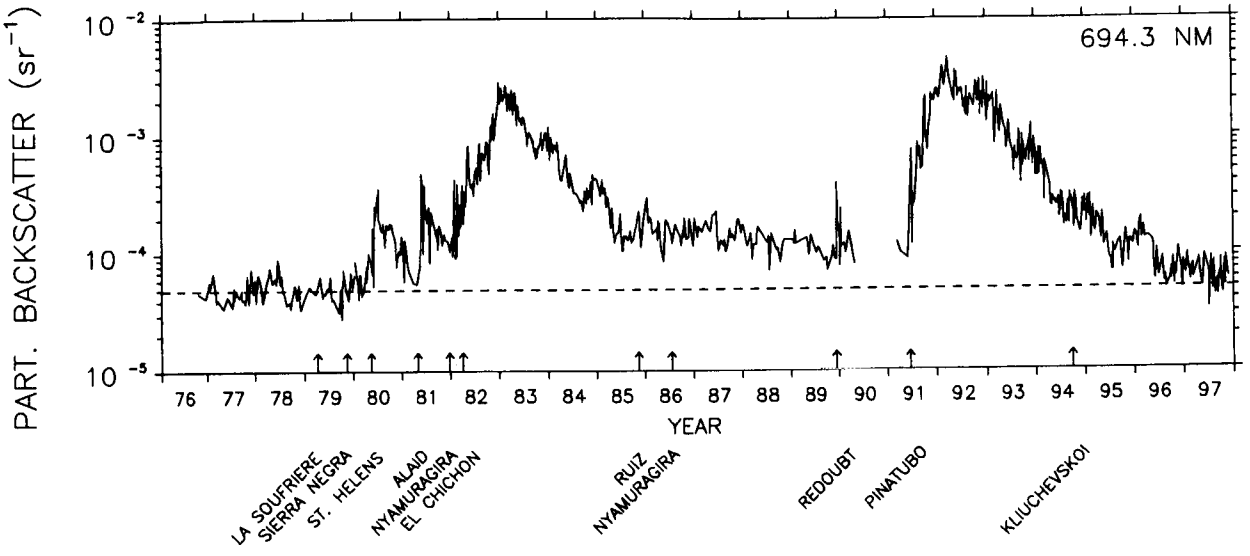


Figure 2. Integral particle backscatter coefficient at 694.3 nm in the height range tropopause plus 1 km to the top of the layer. Volcanic eruptions are indicated.

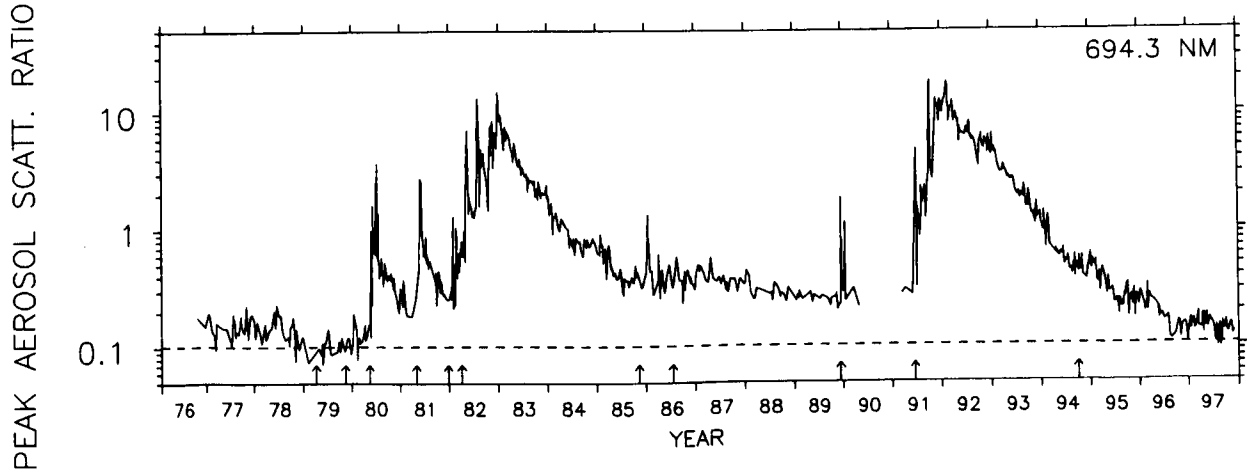


Figure 3. Peak aerosol scattering ratio at 694.3 nm.

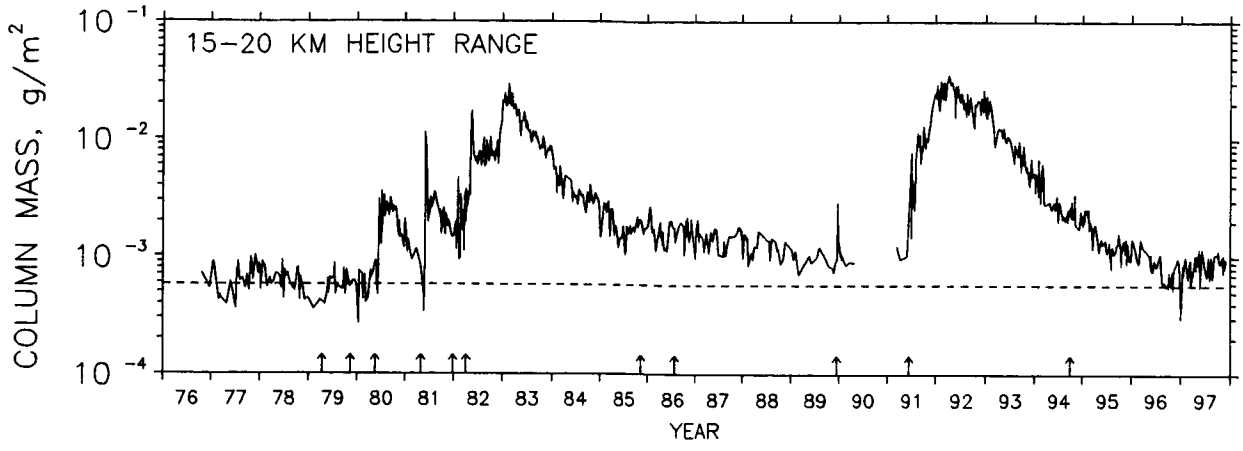


Figure 4. Column aerosol mass in the height range 15 to 20 km.

the years 1980 to 1986 (mainly by the eruptions of St. Helens, Alaid, and El Chichón) and since mid-1991 (Pinatubo eruption). The years 1977 to 1979 were a volcanically quiet period as has been the most recent years. In the years following the eruptions of Nevado del Ruiz (1985) and Nyamuragira (1986) a decay to values comparable with the late 70's or 90's could not be observed. Hofmann (1991) and Jäger (1994) discussed the possibility of air traffic exhaust contaminating the lower stratosphere, whereas Thomason et al. (1997) pointed to the fact that the stratosphere had not recovered completely from the eruptions of Ruiz and Kelut (1990, not detected in the IFU lidar record) when Pinatubo erupted in 1991. The marginal eruptions of Redoubt (1989) and Kliuchevskoi (1994) were rather insignificant episodes.

Therefore, only observations of the late 70's should be compared with the present stratospheric situation. However, during this long period the technique of observation and data retrieval underwent changes due to technical progress (e.g. the change of laser and wavelength) and better understanding of the stratospheric aerosol layer. Most lidar profiles measured during 1976 to early 1980 had been matched with a calculated Rayleigh backscatter profile at a backscatter minimum between the tropopause and the aerosol layer near 12 to 15 km, under the assumption that no aerosol was present at this level. This aerosol minimum can be found in the Laramie balloon data (Hofmann and Rosen, 1981). All profiles after January 1980 had been normalized above the aerosol layer. This change in the treatment of lidar data does not allow a direct comparison of the background period 1977/79 with present data. To allow better inter-comparison within the time series all 1976 to 1980 profiles had been recalculated assuming a reasonable aerosol minimum concentration at the matching level (Jäger, 1994).

In each of the Figures 2 to 4 the 1979 average value is marked by a dashed line. Especially the peak aerosol mixing ratio indicates that 1979 can be regarded a reference background year. All three quantities shown here did not return to the 1979 level until end of 1997. But one has to consider that at background level considerable uncertainties in the single measurements have to be taken into account. These were during 1977/79 about 40% in the aerosol scattering ratio and about 50% in integral backscatter and mass. The respective values are about 25% and 30% at present.

4 Conclusions

Although none of the three quantities of Figures 2 to 4 has returned to the 1979 minimum values, two of them, the particle backscatter integral and the peak aerosol mixing ratio seem to indicate further decay. The aerosol mass in the 15 to 20 km height range, however, seems to have stabilized in 1997 at a value about 50% above the 1979 value.

In 1994 the comparison of the stratospheric background situations of the late 70's and the late 80's indicated a 5 ± 2 % per year increase of the aerosol mass in the 15 to 20 km height range of the lower stratosphere (Jäger, 1994). This finding was compared to the 3% per year increase in fuel consumption of commercial air traffic (Schumann, 1994) pointing to a possible major contribution of

aircraft exhaust to an increase in the aerosol content of the lower stratosphere. It is, however, not possible to conclude that aircraft have caused this dramatic effect because the stratospheric aerosol layer was volcanically loaded during the pre-Pinatubo period.

The 1997 level of aerosol mass in the 15 to 20 km height range, if it remains constant, would indicate a 2% per year increase since 1979, and following the error estimates in Jäger (1994) the uncertainty should be in the same order as the per year increase, namely 2%.

The data presented here describe the situation at a location at northern midlatitudes. It can be argued that findings at one station might be not too represenative. On the other hand, the geographic location of Garmisch-Partenkirchen at 47.5°N and 11.1°E is in very close proximity to major air traffic corridors and in the lee of the West Europe and North Atlantic air traffic. This is obviously a very suitable place to investigate a stratospheric change if it should result from the still growing air traffic in the northern hemisphere.

The question regarding the existence of an anthropogenic signal in the aerosol content of the lower stratosphere will remain open for years to come. It can only be answered conclusively by further observations of the stratospheric aerosol background undisturbed by major volcanic injections.

Acknowledgements

This research has been supported by the German Bundesministerium für Bildung, Wissenschaft, Forschung und Technologie (BMBF) and by the Commission of the European Union.

References

Fiocco, G. and G. Grams (1964). Observations of the aerosol layer at 20 km by optical radar. *J. Atmos. Sci.*, 21: 323-324.

Hofmann, D.J. and J.M. Rosen (1981). On the background stratospheric aerosol layer. *J. Atmos. Sci.*, 38: 168-181.

Hofmann, D.J. (1991). Aircraft sulphur emissions. *Nature*, 349: 659.

Jäger, H. and D. Hofmann (1991). Midlatitude lidar backscatter to mass, area, and extinction conversion model based on in situ aerosol measurements from 1980 to 1987. *Appl. Opt.*, 30: 127-138.

Jäger, H. (1994). Anthropogenic source of observed change in stratospheric background aerosol? In *Impact of Emissions from Aircraft and Spacecraft upon the Atmosphere, DLR Mitteilung* 94-06, pp 461-466, DLR, D-51140 Köln, Germany.

Jäger, H., T. Deshler, and D.J. Hofmann (1995). Midlatitude lidar backscatter conversion based on balloonborne aerosol measurements. *Geophys. Res. Lett.*, 22: 1729-1732.

Jäger, H., T. Deshler, F. Homburg, and V. Freudenthaler (1997). Five years of lidar observations of the Pinatubo eruption cloud. In *Advances in Atmospheric Remote Sensing with Lidar*, pp 485-488, Springer-Verlag Berlin Heidelberg.

Schumann, U. (1994). On the effect of aircraft engines on the state of the atmosphere. *Ann. Geophys.*, 12: 365-384.

Thomason, L.W., G.S. Kent, C.R. Trepte, and L.R. Poole (1997). A comparison of the stratospheric aerosol background periods of 1979 and 1989-1991. *J. Geophys. Res.*, 102: 3611-3616.

Temperature climatology of the middle atmosphere from long-term lidar measurements at mid- and low-latitudes.

I. Stuart McDermid, Thierry Leblanc
Jet Propulsion Laboratory, California Institute of Technology, Table Mountain Facility, Wrightwood, CA 92397
mcdermid@tmf.jpl.nasa.gov, Tel: +1 760 249 4262, Fax: +1 760 249 5392

Philippe Keckhut, Alain Hauchecorne
Service d'Aéronomie du CNRS, 91371 Verrières-le-Buisson, France

C. Y. She and David A. Krueger
Department of Physics Colorado State University Fort Collins, CO 80523

1. Introduction

The temperature structure of the middle atmosphere has been studied for several decades using a variety of techniques. However, temperature profiles derived from lidar measurements can provide improved vertical resolution and accuracy [*Hauchecorne and Chanin*, 1980]. Lidars can also provide long-term data series relatively absent of instrumental drift, and integration of the measurements over several hours removes most of the gravity wave-like short-scale disturbances.

This paper describes a seasonal climatology of the middle atmosphere temperature derived from lidar measurements obtained at several mid- and low-latitude locations. Results from the following lidars, which have all obtained a long-term measurement record, were used in this study: the two Rayleigh lidars of the Service d'Aéronomie du CNRS, France, located at the Observatoire de Haute Provence (OHP, 44.0°N) and at the Centre d'Essais des Landes (CEL, 44.0°N), the two Rayleigh/Raman lidars of the Jet Propulsion Laboratory, USA, located at Table Mountain, California (TMF, 34.4°N) and at Mauna Loa, Hawaii (MLO, 19.5°N), and the Colorado State University, USA, sodium lidar located at Fort Collins, Colorado (CSU, 40.6°N). The overall data set extends from 1978 to 1997 with different periods of measurements depending on the instrument. Three of the instruments are located at primary or complementary stations (OHP, TMF, MLO) within the Network for Detection of Stratospheric Change (NDSC). Several aspects of the temperature climatology obtained by lidar in the middle atmosphere are presented, including the climatological temperature average through the year; the annual and semi-annual components, and the differences compared to the CIRA-86 climatological model.

2. The instruments, database and data processing.

The Rayleigh/Raman and sodium fluorescence lidar techniques for measuring temperature profiles are well established and have been described in detail by numerous authors. Some details of the lidar techniques used in this study can be found in *Hauchecorne and Chanin* [1980], *Leblanc et al.* [1998a], *She et al.* [1992], *McDermid et al.* [1995].

At mid-latitudes the CNRS-SA Rayleigh lidar at OHP (44.0°N, 6.0°E) has obtained more than 1240 nighttime temperature profiles between 30 and 95 km from 1978 to the present with 75 to 300 m vertical resolution, and 670 profiles at CEL (44.0°N, 1.0°W) from 1986 to 1994 with 300 m vertical resolution. The total estimated error at the top of each profile is about 20-25 K. This error drops to less than 1 K at mid-range (typically 55 km) and below. The CSU (40.6°N, 105.1°W) Na lidar has obtained nearly 250 temperature profiles in the Na layer between 80 and 110 km since 1989 with an initial 75 m vertical resolution smoothed over 3 km. The total estimated error is less than 4 K and 8 K at the top and bottom of the profiles respectively, dropping to 0.6 K at mid-range (typically 90 km). At lower latitudes, the JPL Rayleigh/Raman lidars [*McDermid et al.*, 1995] located at TMF (34.4°N, 117.7°W) and MLO (44.0°N, 155.6°W) have obtained more than 685 and 410 temperature profiles from 30 to 80 km since 1988, and from 15 to 90 km since 1993 respectively. Most of the routine measurements comprise a 1.5-2.0 hour integration experiment, usually at the beginning of the night. The associated temperature errors are similar to those of the French Rayleigh lidars but the top of the profiles are slightly lowered.

For all instruments, each individual temperature profile was interpolated to obtain data points every one kilometer. Then, all temperature profiles were merged into a composite single year of data. A weighted running average with a triangular 33-day width filtering scheme was applied to each day of the composite year that a profile was available. No removal of tidal structures was performed. At MLO the role of the diurnal and semidiurnal tides may not be negligible above 80 km and similarly for the diurnal component at CSU above 90 km.

3. Results

a. Climatological temperatures.

The mean annual temperature climatologies obtained are presented in Figure 1(a) and (b) for OHP+CEL together (same latitude), and MLO. A distinctly defined temperature pattern is observed at both sites. For

OHP+CEL [Fig.1(a)] a familiar mid-latitude warm summer and cool winter stratosphere is observed with a maximum of 272 K in May-June and a minimum of 255 K in early November at the stratopause altitude of 47 km. A characteristic warm winter/cold summer mesosphere is also observed with a maximum of 220 K in December and January, and a minimum of 195-200 K in May-June at 75 km, which is in good agreement with previous climatologies [*Hauchecorne et al.*, 1991]. The weak negative vertical temperature gradient observed in winter is the consequence of the seasonal average of the so-called mesospheric temperature inversions occurring during the entire winter at OHP and CEL, and more specifically in February at TMF (not shown).

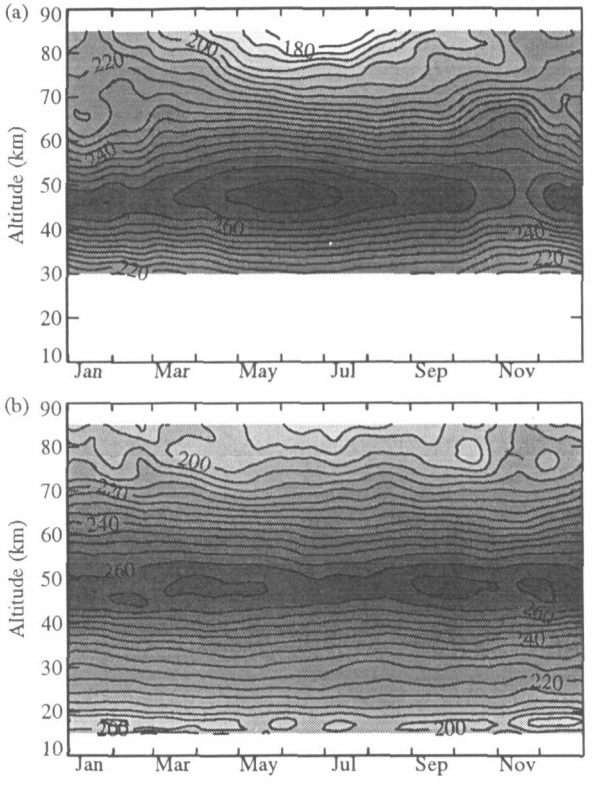


Figure 1. Climatological temperatures obtained from lidar measurements at (a) OHP+CEL (44.0°N), and (b) MLO (19.5°N, 155.6°W). Contour interval is 5 K.

Figure 1(b) (MLO) clearly shows a semiannual cycle at the stratopause and an annual cycle in the lower stratosphere with a very cold minimum of 190 K at 17 km identified as the tropical tropopause. As expected at these latitudes, the amplitude of the seasonal variations is weak. At the top (80-85 km), where the effect of the mesospheric tides is the largest, the measured cold temperatures are more representative of early night temperatures than nightly (or even a 24-hour) mean temperatures.

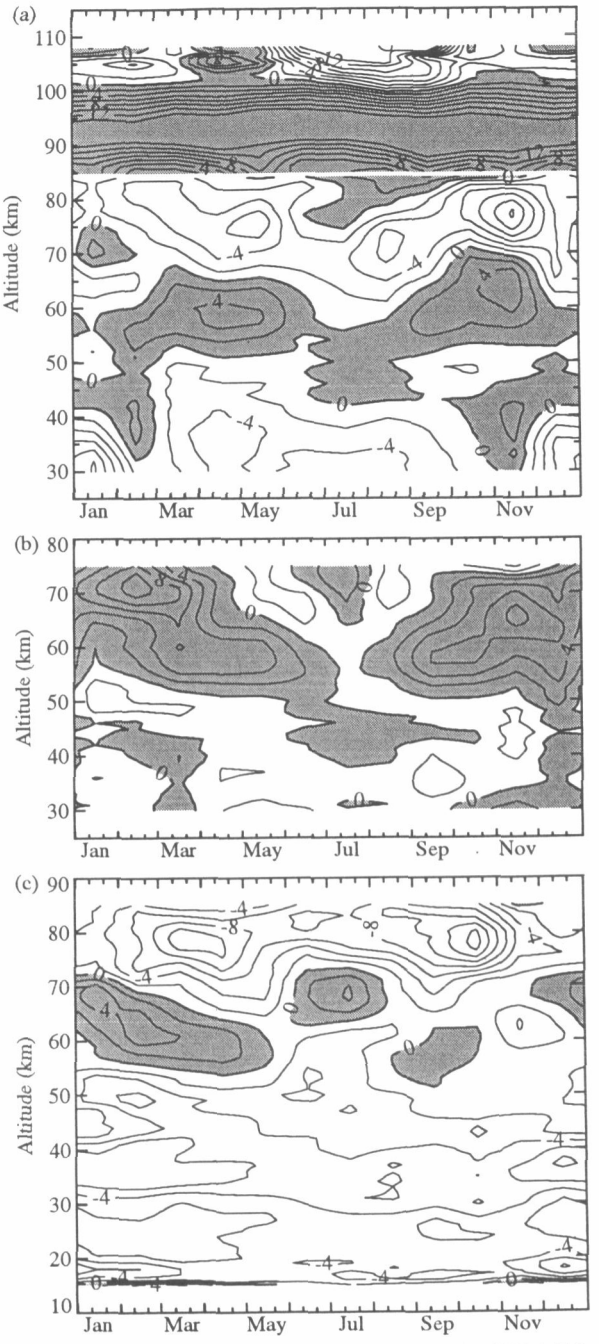


Figure 2. Monthly mean differences from the CIRA-86 temperatures for (a) OHP+CEL and CSU, (b) TMF, and (c) MLO. Contour interval is 2 K.

b. Difference from CIRA-86

The monthly mean lidar temperatures were subtracted from the monthly mean CIRA-86 temperatures [*Fleming et al.*, 1990]. The temperature difference between the observed lidar and the CIRA-86 climatologies is plotted in Figure 2(a) OHP+CEL and CSU, (b) TMF and (c) MLO. Since they have quasi-separated altitude ranges, OHP+CEL and CSU are

presented on the same plot, Figure 2(a), with a separating altitude of 84-85 km.

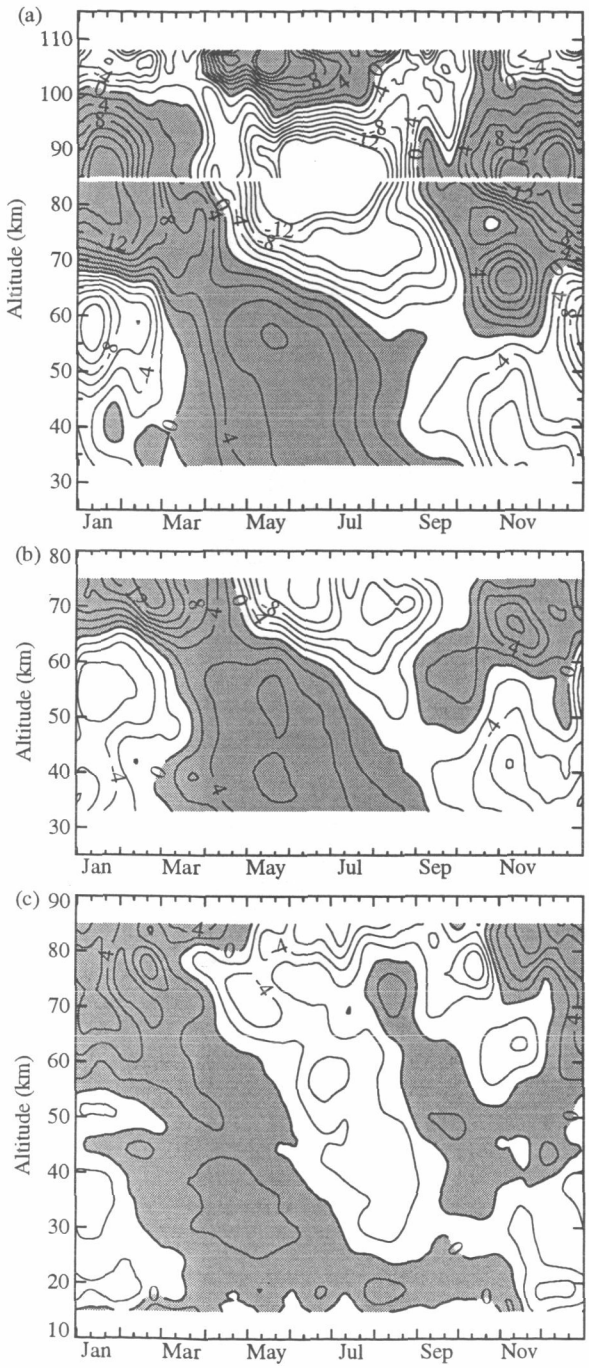


Figure 3. Daily mean deviation from the annual mean temperature (from the temperature climatology shown in Figure 1). (a) CSU and OHP+CEL, (b) TMF, (c) MLO. Contour interval is 2 K.

At OHP and CEL [Fig.2(a)] the observed temperatures are systematically 2-4 K colder than CIRA between 30 and 40 km, especially in summer, and 2-6 K colder between 70 and 80 km, while no systematic error is observed at stratopause altitudes. For MLO [Fig.2(c)] the entire region between 15 and 55 km is colder than the CIRA; up to 4 K in the upper stratosphere. In the stratosphere the systematic departure is about 2 K. At mesopause altitudes the systematic error is remarkably large at mid-latitudes as illustrated by the difference CSU-CIRA [Fig.2(a)] where a very large positive departure of more than 16 K is observed in the entire mesopause region (90-95 km). *Clancy et al.* [1994] reported similar SME/CIRA-86 departures suggesting that the CIRA is definitely too cold at these heights and latitudes.

In addition to the systematic errors, observed temperatures are up to 10 K colder than CIRA in December and January below 40 km at OHP+CEL. This can be explained by the out-of-phase occurrence, between late January and February, of stratospheric warmings at OHP and CEL and its equivalent occurring earlier in the CIRA model (December-January). Consequently the CIRA is too warm in December and January.

In the lower mesosphere OHP+CEL and TMF temperatures are warmer than CIRA. A maximum departure of 10 K near 70 km is observed in February at TMF, 4 K at 60 km in April-May for all mid-latitudes sites, and 4 K (respectively 8 K) at 60-70 km in November above OHP/CEL (respectively TMF). In the mid-mesosphere OHP/CEL temperatures are colder than CIRA with a maximum departure of 10 K in November at 75-80 km. At MLO [Fig.2(c)] the temperature departures are smaller than at mid- and subtropical-latitudes. This is not surprising since the variability is itself smaller at low-latitudes. Consequently the errors due to the annual and semi-annual amplitudes, and due to the seasonal transitions, are minimized. In the entire middle atmosphere the CIRA model is warmer except at two times of the year between 60 and 70 km. At 80 km a maximum negative departure of 10 K can be observed. In the 60-70 km region CIRA is colder as already observed at mid-latitudes [Fig.2(a),(b)]. Also, a very special pattern is observed at the beginning of the year; a negative departure is propagating downward from 80 km associated with a positive departure around 65 km and another negative departure between 50 and 55 km.

c. Temperature deviations from the annual mean

The annual mean temperature profile was then subtracted from each available daily composite profile to obtain the daily deviation from the annual mean. Figure 3 represents this deviation for (a) CSU and OHP+CEL, (b) TMF, and (c) MLO. As expected for CSU, OHP+CEL, and TMF [Fig.3(a),(b)] an annual cycle is clearly dominant in both the stratosphere and mesosphere. At 67-70 km its phase is inverted compared with the solar flux leading to the classic

warm summer stratosphere and cold summer mesosphere and vice-versa in winter. A second phase inversion is clearly observed at CSU [Fig.3(a)] around 95-100 km, marking the transition between the dynamically and chemically or radiatively driven upper mesosphere. These plots, in particular Figure 3(a), also show a warm late-winter centered at 35-40 km. This is the signature of the stratospheric warmings occurring from January to March at mid- and high-latitudes. This signature is still observable in Figure 3(b) but with a weaker magnitude. Another warm spot is observed at 65-67 km in November reaching 11 K for OHP/CEL and 8 K for TMF. This feature can also be observed in Figure 1(a) as a bulge of warm temperatures in November between 60 and 70 km.

In contrast to the mid-latitudes sites MLO [Fig.3(c)] primarily exhibits a semi-annual cycle between 25 and 80 km altitude. This is not surprising since MLO is located at 19.5°N and is influenced by the equatorial dynamical pattern which in turn is affected by both northern and southern hemispheres. The semi-annual cycle observed here is almost a continuous downward propagating oscillation with an approximate vertical speed of 12 km/month and can be identified as the thermal semi-annual oscillation (SAO). The so-called mesopause and stratopause SAOs appear here as a combined single SAO propagating downward from the mesopause to 30 km with minimum amplitude at 45 km. A phase inversion is observed near 82 km similar to that observed by SME at 83 km [*Garcia and Clancy*, 1990]. The oscillation is strongly modulated with the first cycle being stronger than the second.

4. Summary

Long term measurements from several lidar instruments (Rayleigh/Raman and sodium) located at 44.0°N, 40.6°N, 34.4°N, and 19.5°N have been used to develop a new climatology of the middle atmosphere temperature. The climatologies for each lidar were first compared to the CIRA-86 model. Large differences between the lidar temperatures and the CIRA-86 temperatures are identified and explained. When compared to all instruments, CIRA-86 appears systematically too cold between 90 and 95 km, by 20 K or more, and possibly 6-8 K too warm around 80 km, making its use as a reference atmosphere model questionable at these altitudes. The annual and semi-annual components of the seasonal variability were investigated. An annual cycle with 6-7 K amplitude in the upper stratosphere, increasing to 15-20 K at 80 km, is observed at mid-latitudes. This cycle is in phase with the solar flux in the stratosphere and in opposite phase in the mesosphere with a very cold summer mesopause at 85 km, in good agreement with previous climatologies. At lower latitudes, a semiannual oscillation (SAO) propagates downward from 85 to 30 km and is characterized by a stronger first cycle than the second (4 K and 2 K amplitude respectively). Finally, sudden seasonal transitions, highly consistent between all instruments, have been observed (not shown here). In particular, in the early winter mid-latitudes a two-step warming of the winter mesosphere between 65 and 85 km as well as a cooling of the lower mesosphere appear to be real climatological events rather than some short-term geophysical or instrumental random variability.

Acknowledgements

The work described in this paper was carried out, in part, at the Jet Propulsion Laboratory, California Institute of Technology, under an agreement with the National Aeronautics and Space Administration.

References

Clancy, R. T., D. W. Rush, and M. T. Callan, Temperature minima in the average thermal structure of the middle atmosphere (70-80 km) from analysis of 40- to 92-km SME global temperature profiles, *J. Geophys. Res.*, *99*, 19,001-19,020, 1994.

Fleming, E. L., S. Chandra, J. J. Barnett and M. Corney, COSPAR International Reference Atmosphere, Chapter 2: Zonal mean temperature, pressure, zonal wind and geopotential height as functions of latitude, *Adv. Space Res.*, *10* (12), 11-59, 1990.

Garcia, R. R., and R. T. Clancy, Seasonal Variation in equatorial mesospheric temperatures observed by SME, *J. Atmos. Sci.*, *47*, 1666-1673, 1990.

Hauchecorne, A., and M. L. Chanin, Density and Temperature Profiles obtained by lidar between 35 and 70 km, *Geophys. Res. Lett.*, *7*, 565-568, 1980.

Hauchecorne, A., M. L. Chanin, and P. Keckhut, Climatology and trends of the middle atmospheric temperature (33-87 km) as seen by Rayleigh lidar over the south of France, *J. Geophys. Res.*, *96*, 15,297-15,309, 1991.

Leblanc, T., I. S. McDermid, A. Hauchecorne, and P. Keckhut, Evaluation and optimization of lidar temperature analysis algorithms using simulated data, JGR In Press, 1998.

McDermid, I. S., T. D. Walsh, A. Deslis and M. L. White, Optical systems design for a stratospheric lidar system, *Appl. Opt.*., *34*, 6201-6210, 1995.

She C. Y., J. R. Yu, H. Latifi, and R. E. Bills, High-spectral-resolution fluorescence light detection and ranging for mesospheric sodium temperature measurements, *Appl. Opt.*, *31*, 2095-2106, 1992.

Lidar Temperature Measurements at Ny-Ålesund (79N) during Winter, 1998

T. J. McGee[1], M. Gross[2], P. Newman[1], G. Beyerle[3], I. Beninga[3], A. Dahl[3], R. Neuber[3], P. Wahl[3], and O. Schrems[3]

1. Goddard Space Flight Center
Atmospheric Chemistry and Dynamics Branch
Code 916
Greenbelt, MD 20771
Phone: 301-286-5645 FAX: 301-286-1754
mcgee@aeolus.gsfc.nasa.gov
2. University of Maryland - Baltimore County
3. Alfred Wegner Institute for Polar and Marine Research
Bremerhaven and Potsdam, Germany

Abstract. During January and February, 1998, a measurements campaign was held at the Network for the Detection of Stratospheric Change (NDSC) Arctic site at Ny-Ålesund (78.9N). Lidar measurements of ozone, temperature and aerosol parameters were made along with balloon sonde and microwave measurements of ozone. Atmospheric temperatures were measured between 10 and 70 km. During the time of the campaign an strong warming occurred at the stratopause, elevating the measured temperature by as much as 80 K. The height of the stratopause descended at this time to below 40 km.

Introduction

During the winter of 1997-98 the Goddard Space Flight Center deployed the Stratospheric Ozone Lidar to Ny Ålesund, on Spitsbergen Island (78.9N) to participate in the Ny Ålesund Ozone Measurements Intercomparison (NAOMI). This was a Network for the Detection of Stratospheric Change (NDSC) Validation Campaign for the permanently-based ozone lidar and microwave instruments there as required by the NDSC Validation Protocols. In addition, temperature and aerosol measurements were made by several instruments at the time of the ozone campaign. This paper will discuss the temperature results from the GSFC lidar, the Mobile Aerosol Raman Lidar (MARL) deployed at the site by the Alfred Wegner Institute (AWI), and the temperature results from radiosondes launched by AWI. The data discussed was obtained during January and February, 1998.

The GSFC Stratospheric Ozone Lidar is mounted in a trailer and has been transported to several locations around the world. It is a Differential Absorption Lidar (DIAL) transmitted at 308 nm and 351nm; the wavelengths are generated by two excimer lasers, XeCl for 308 nm and XeF for 351 nm. Four backscattered wavelengths are collected, the two elastically scattered signals at 308 and 351nm, as well as the N_2-Raman scattered signals at 332 and 382 nm. In a relatively clean atmosphere temperature can be retrieved from approximately 10 km up to over seventy km using both the elastic and inelastically scattered lidar returns from the transmitted 351 nm radiation. Power for the lidar instrument was provided by a 50KW diesel-powered generator.

The MARL instrument uses a Nd-YAG laser and transmits 532 and 355 nm. It collects the elastic wavelengths as well as the N_2 Raman wavelengths at 607 and 387 nm. Depolarization data is collected for each of the transmitted wavelengths. The system operates at 30 Hz. Although these lidar instruments were positioned within 30 meters of each other, there was no evidence of

interference at the UV wavelengths, and it was therefore possible to operate the lidars simultaneously.

The AWI ozone lidar system is similar in many ways to the GSFC ozone lidar. This lidar transmits 308 nm and 353 nm radiation - the 353 nm radiation is generated by stimulated Raman scattering in a high pressure H_2 cell. Because of the proximity of the GSFC lidar to the AWI lidar, and the fact that both lidar instruments transmit and collect virtually the same wavelengths, it was not possible to operate these two lidars simultaneously. While this interference makes an intercomparison more difficult, it does provide for a more complete temporal series of temperature, since temperature is retrieved from the 353 return.

Results

The Goddard lidar began operation on January 19, 1998, but after two days encountered generator problems which were related to the cold weather. This shut the instrument down for three days. Beginning on January 26, measurements were made daily until February 9 when the campaign officially ended. This paper will report on the temperature data obtained between 1/26 and 2/9.

Figure 1 is a contour plot of the GSFC temperature data from this time period. This is made up of 35 individual temperature profiles obtained at Ny-Ålesund. Each profile is an integration of nearly two hours of data. The individual contours represent changes of 20 K. By far the most obvious feature is the rapid onset of an intense warming at the stratopause beginning on February 3 (day 34). On this day there was an increase in temperature at the stratopause of more than 40K compared to the previous day's measurement. During subsequent days this

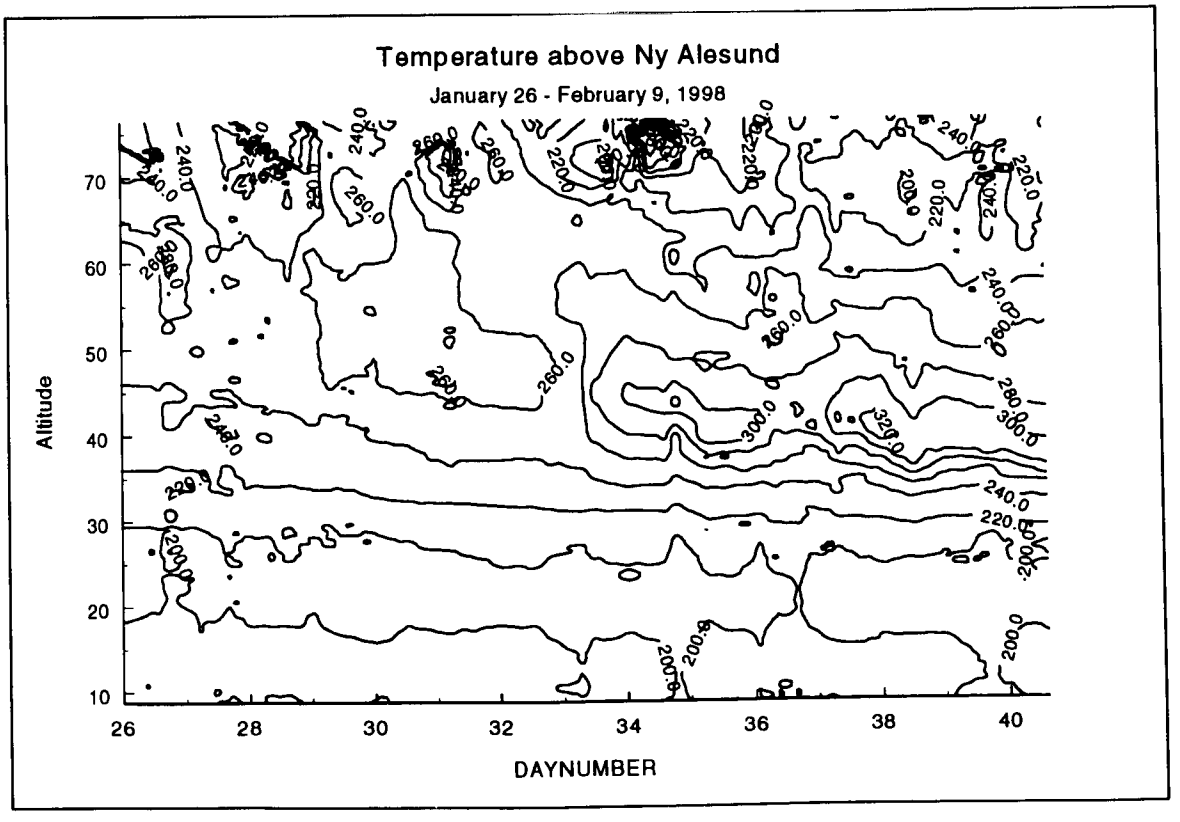


Figure 1. Contour plot of GSFC lidar temperatures obtained between Jan. 26 and Feb. 9, 1998 .

warming difference increased to over 70 K more than on Feb 2. The maximum temperature observed at the stratopause was 332 K on the morning of February 7. The last measurements on the evening of February 9, 1998 observed a stratopause temperature still over 300 K. Also apparent from the Figure is the descent of the stratopause. In late January, the observed stratopause height was near 50 km. During this warming, the height of the stratopause was seen to descend to below 40 km on several days in February.

Figure 2 shows temperature profiles obtained on February 1, 1998. Included on the plot are profiles from the GSFC lidar, the MARL instrument, the AWI Ozone lidar, a local balloon sonde and the NCEP data for that day. The lidar profiles extend down to just below 10 km and up to over 70 km. There is excellent agreement among the sonde and lidar profiles; both the sonde and the lidar pick up the inversion at 10 km. The lidar captures the amplitude of the inversion as well as the sonde does. There is a definite time dependence of the temperature at the stratopause.

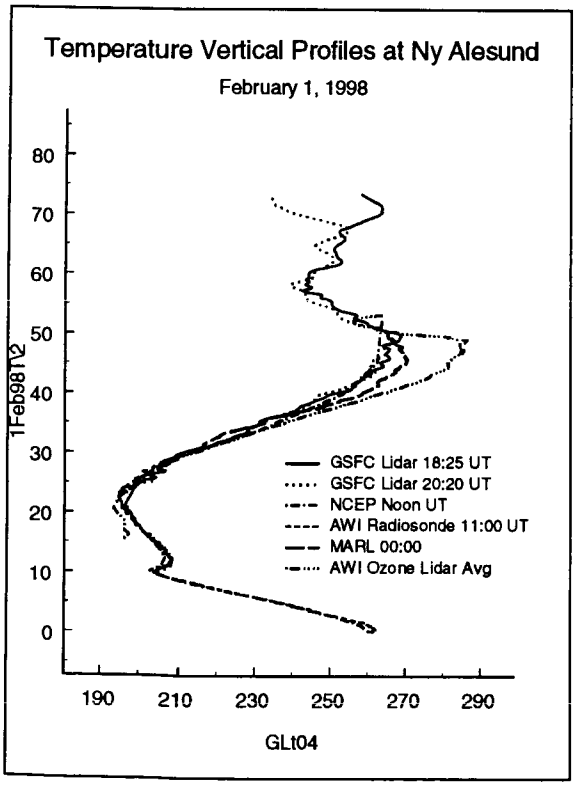


Figure 2 Vertical profiles of temperature measured on February 1, 1998.

References

Schaefer, H.-J. , O. Schrems, G. Beyerle, B. Hofer, W. Mildner, F. A. Theobold, W. Lahmann, C. Weitkamp, and M. Steinbach, A modular and mobile multi-purpose lidar system for observation of tropospheric and stratospheric aerosols *SPIE EurOpto Series 2581*, 128 - 136, 1995

M. R. Gross, T. J. McGee, R. A. Ferrare, U. Singh, and P. Kimvilakani, Temperature Measurements Made with a Combined Rayleigh-Mie/Raman Lidar, *Applied Optics*, **24**, 5987-5995, 1997.

Results of The Ny-Ålesund Ozone Measurements Intercomparison NAOMI

W. Steinbrecht[1], M. Gross[2], T. McGee[2], R. Neuber[3], P. v.d. Gathen[3],P. Wahl[3], U. Klein[4], J. Langer[4]

1 Introduction

Worldwide, about ten Differential Absorption Lidars are used for long-term monitoring of stratospheric ozone. These systems are an important component of the Network for the Detection of Stratospheric Change. Although DIALs are self-calibrating in principle, regular intercomparisons with other ozone-lidars, microwave radiometers or ozone-sondes are highly desireable to ensure high data quality at a well known level. The NDSC validation policy suggests that such intercomparisons be "blind", meaning all participants submit their data to an impartial referee, without seeing results from the other participants. Here we report on the "blind" intercomparison taking place from January 20th to February 10th 1998 at Ny-Ålesund, Spitsbergen (78.92°N, 11.95°E). Participating groups were from the Alfred Wegener Institute, Potsdam, operating the NDSC DIAL system at Ny-Ålesund [*v.d. Gathen et al.*, 1994], from the University of Bremen operating the NDSC microwave radiometer for ozone profiling at Ny-Ålesund [*Langer et al.*, 1998], and the NASA Goddard Space Flight Center group with the "NDSC travelling standard" STROZ-LITE [*McGee et al.*, 1995]. The first author acted as the impartial referee. Also used for the intercomparison were data from ECC-6A/Vaisala RS80 ozone sondes routinely launched at Ny-Ålesund by the AWI group. A 1 % KI solution (3 ml) and the 1986 ECC pump correction (1.092 at 5 hPa) are used. The ECC-data were available to all participants during the campaign and thus were not "blind". Table 1 summarizes the expected performance of the instruments participating in the ozone intercomparison reported in this paper. An overall description of the entire NAOMI campaign is given in the companion paper by *Neuber et al.*

Altitude range		AWI Lidar	GSFC Lidar	UBremen µWave	AWI ECC
20 to 30 km	altitude resolution	0.6 to 2 km	1.2 to 2 km	10 km	300 m
	precision	1 to 4 %	1 to 3 %	3 %	3 to 5 %
30 to 40 km	altitude resolution	2 km	1.6 to 3 km	14 km	500 m
	precision	4 to 30 %	1 to 5 %	3 %	3 to 10 %
40 to 50 km	altitude resolution	2 to 6 km	3 to 6 km	20 km	X
	precision	>50%	5 to 100 %	3 %	X

Table 1. Typical performance of the ozone instruments participating in the NAOMI campaign.

2 Experimental details

The different measurement times are plotted in Figure 1. To avoid interference between the two lidars, they were run at interleaving times. Combined, the two lidars provided measurements for about 41 % of the time for a period of 3 weeks - a remarkable achievement. Excellent is also the very even temporal coverage of the microwave instrument, which took measurements for about 12 minutes every hour (18 % coverage). With coverage of 3.5 % of the time the sondes only provide snapshots. However, sondes and microwave operate independent of cloud conditions, whereas the lidars require a cloud free sky. The sondes are also the only instrument providing good tropospheric ozone data.

An important consideration is the natural coordinate system in which ozone profiles are measured by the different instruments. The lidars measure ozone number density as a function of geometric altitude. The ECC-sondes measure ozone partial pressure which is easily converted to number density using the temperature measured by the accompanying radiosonde. The radiosonde also provides the geopotential altitude. These conversions contribute no appreciable error to the number density profile derived from the ECC/Vaisala RS80 sondes. More problematic are the microwave data. First, only preliminary data derived using standard profiles of pressure and temperature were available for this paper.

[1] DWD, 82383 Hohenpeißenberg, Germany, +49-8805-9200-15, FAX -46, wolfgang@mohp.dwd.d400.de
[2] NASA Goddard, [3] AWI Postdam, [4] Bremen University

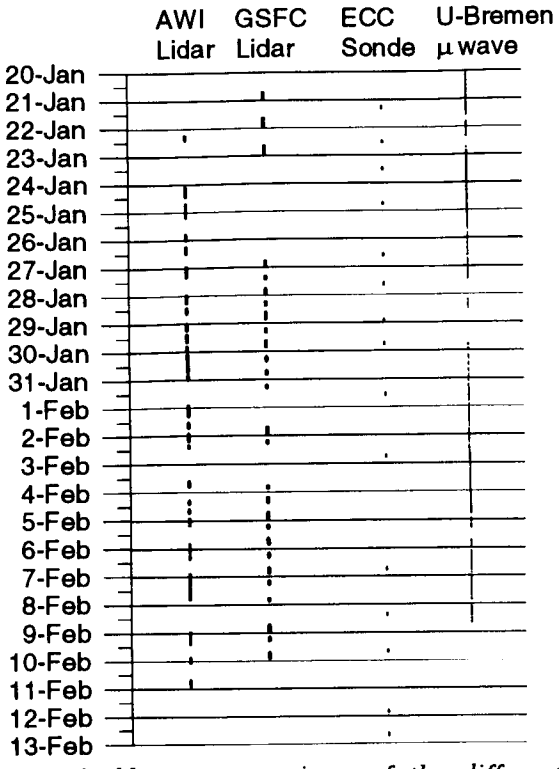


Fig. 1. Measurement times of the different instruments during NAOMI for each ozone profile.

Second, the microwaves natural measurement, ozone mixing ratio vs. some vertical coordinate, was converted to number density using the same standard profiles. This procedure may have introduced errors of several percent into the microwave number density profiles. Results for the microwave instrument in this paper, therefore, have to be treated with caution.

3 Results

Figure 2 shows time series of ozone number density at selected altitude levels, as measured by the different instruments. The levels demonstrate various aspects of the intercomparison. Between 17 km and 24 km all instruments recorded a 5 to 6 day periodic oscillation of the ozone number density. This oscillation is most likely driven by changes in tropospheric and lower stratospheric circulation. Below 25 km instrumental noise was found to be small compared to natural ozone variability. At 21 km, the two lidars and the ECC sondes track each other very well. The microwave data, sometimes, show different results, e.g. on January 26/27 or February 7/8. However, this could be an artefact due to the use of preliminary data. At 35 km the lidar data have become noisier, especially for the AWI lidar, which also tends to report lower ozone density (e.g. February 2nd to 6th) at this altitude. The microwave data exhibit less noise than the lidars. It remains to be seen, whether using varying atmospheric profiles will introduce additional variability into the microwave time series. Because of balloon burst, no ECC sonde data are available above 32 km. At 41 km, the lidar data also appear noisier than the microwave results. The AWI lidar is coming close to its upper measurement range, as demonstrated by the large scatter at the end of the time series. Only a few ozone profiles from the AWI-lidar exceeded 45 km. The more powerful GSFC lidar still gives very good results at 41 km, exemplified by the excellent agreement with the microwave data from February 4th to 8th. Most profiles from the GSFC lidar reach up to 47 km.

In order to reduce statistical noise and to detect possible systematic differences, average profiles were determined for each instrument. Averages were taken for the time period from January 26th to February 9th, where both lidars were running at nearly the same times. For the two lidars and the ECC sonde, Figure 3 shows the average profile from all measurements between January 26th and February 9th. Individual lidar profiles were weighted with the number of laser shots acquired. For clarity and because of their preliminary nature, the average microwave profile is not shown in Figure 3. The average profiles confirm impressions from the time series in Figure 2. Above 42 km, where the AWI data become very noisy, the average AWI profile deviates

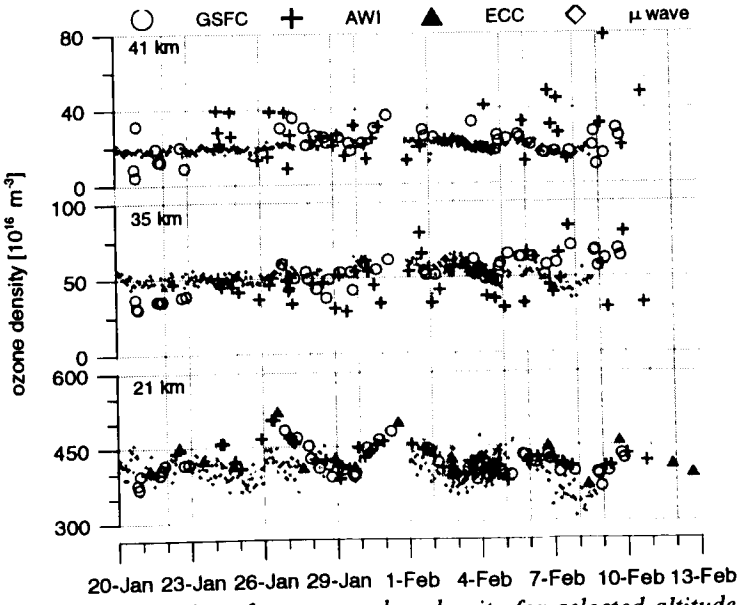


Fig. 2. Time series of ozone number density for selected altitude levels. Small diamonds are for the microwave instrument.

from the GSFC profile towards unrealistically high ozone values. Such behaviour is often seen for lidar ozone profiles at the upper end of their range. Around 35 km, the GSFC profile shows higher ozone densities than the AWI profile. Between 25 and 30 km the two lidar- and the ECC average profiles agree very well. However, between 15 and 25 km only the AWI and ECC profiles match very well. Compared to these profiles, the GSFC profile is shifted to lower altitudes. We have to caution against overinterpreting this apparent shift. It may be an artefact caused by different phases of the AWI and GSFC measurement times with respect to the atmospheric oscillation apparent in the lower panel of Figure 2. Similarly, the good agreement between the AWI lidar and the ECC profile may just be coincidental, because the frequency of sonde measurements is not high enough to properly sample the observed atmospheric oscillation. Deleting one or two sondes from the record could change the average sonde profile. Therefore, below 25 km, the simple averages presented in Figure 3 will have to be supplemented by a more careful analysis in the future.

Profiles of the relative differences are shown in Figure 4. The average profile from the GSFC lidar was arbitrarily chosen as a reference. This choice does not imply that the GSFC lidar gives "truer" values than the other instruments. To give a rough indication of the significance of the differences, the standard error σ_M of the mean profile is plotted in Figure 4 (67 % confidence interval). It was estimated from standard deviation σ and number n of individual profiles using $\sigma_M=\sigma/\sqrt{n}$. In the altitude range 15 to 28 km, differences between the AWI, ECC and GSFC profiles are small, under 5 %, and hardly significant. The slightly larger difference for the GSFC profile is connected to the afore mentioned shift. Agreement between the AWI and ECC profiles is excellent over the entire range from 15 to 31 km, better than 3 %. However, between 30 and 40 km the AWI profile is up to 12 % lower than the GSFC profile. This could be caused by a systematic bias between the differential filters used by the AWI and GSFC groups. In recent ESMOS/NDSC algorithm intercomparisons [*Godin et al.*, 1998], algorithm induced biases of the order of 10 % have been found. Unfortunately none of the algorithms currently used by the AWI and GSFC groups participated in the last ESMOS/NDSC intercomparison. Above 40 km, the average ozone values reported by the AWI lidar are substantially higher than for the GSFC lidar. As mentioned, such behaviour is often seen at the upper end of the measurement range of an ozone DIAL.

Most notable for the preliminary microwave data is the good agreement in the altitude range 22 to 33 km, where all average profiles agree within 5 %. Below 20 km the microwave profile is substantially lower than the other

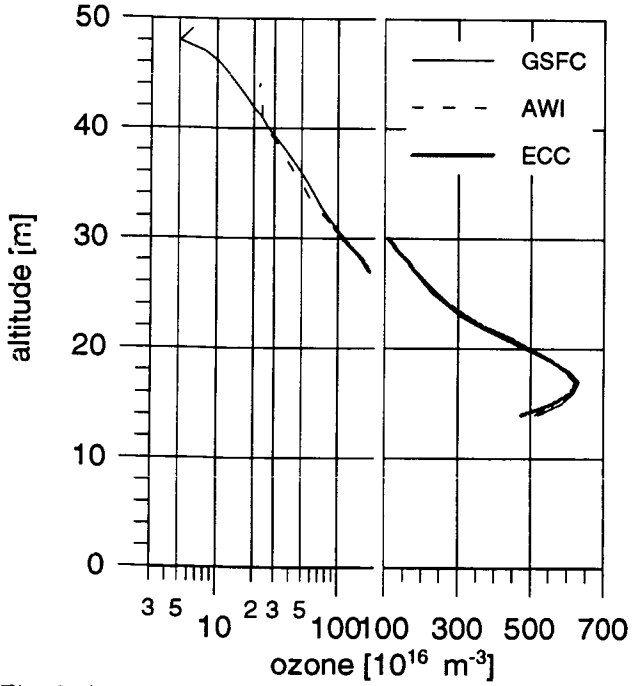


Fig. 3. Average profiles for the period Jan. 26th to Feb. 9th. Note the split scale. Left: Logarithmic. Right: Linear.

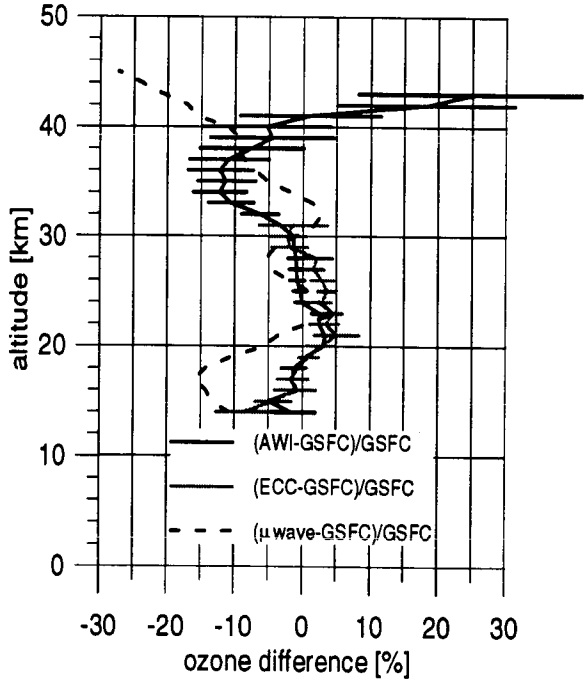


Fig. 4. Relative difference of average profile for each instrument with respect to the average GSFC profile. The microwave profile is preliminary and no error bars are shown for it.

profiles. This is most likely a consequence of the lower altitude resolution of the microwave instrument, of the order of 10 km, compared to 1 km at these altitude for the other instruments. This coarser resolution reduces the ozone maximum at about 18 km. At this point of the analysis no attempt has been made to degrade the altitude resolution of the ECC sondes or the lidars. Above 40 km the microwave shows substantially lower ozone values than the GSFC and AWI lidars. It remains to be seen whether this feature is also found for the final microwave data, and whether it is related to a different altitude resolution, or indication of a systematic bias.

Summary

The Ny-Ålesund Ozone Measurements Intercomparison has very successfully demonstrated the high level of accuracy of ozone profiles measured by the AWI and GSFC-lidars, ECC sondes and the Uni-Bremen microwave radiometer. Except for the preliminary microwave data, the average profiles from each instrument agree within 5 % between 15 and 32 km. Lower values seen by the microwave at 20 km are likely a consequence of its coarser altitude resolution. Particularly good agreement is found between the AWI lidar and the ECC sondes. An apparent shift of the GSFC profile around 20 km will have to be investigated in the future. It may result from the relative phase of the individual sampling times with respect to an observed 5 to 6 day oscillation of the ozone density. Further analysis, including the final microwave data, should help to explain the 10 % difference seen between the two lidars at 35 km.

Acknowledgements

We wish to thank Tine Weinzierl and Ingo Beninga for their never ending support to keep the lidars running and Bodo Wichura and Dirk Roemermann for their skillful ozone sonde handling.

References

Gathen, P. von der, B. Heese, G. Beyerle, and R. Neuber: Multi-wavelength LIDAR configurations for polar stratospheric research, in: Abstracts of Papers, 17th Intern. Laser Radar Conf., Sendai, Japan, 422-423, 1994.

Godin, S., A. Carswell, D. Donovan, H. Claude, W. Steinbrecht, S. McDermid, T. McGee, O. Uchino, D. Swaart, H. Nakane, P. von der Gathen, and R. Neuber: DIAL ozone algorithm intercomparison, manuscript in preparation, contact sophie.godin@aero.jussieu.fr

Neuber, R., G. Beyerle, I. Beninga, P. von der Gathen, O. Schrems, P. Wahl, M. Gross, Th. McGee, Y. Iwasaka, M. Fujiwara, T. Shibata, U. Klein, and W. Steinbrecht: The Ny-Ålesund Aerosol and Ozone Measurements Intercomparison campaign 1997/98 (NAOMI-98), this issue

McGee, T.J., M. Gross, U.N. Singh, J. J. Butler, and P. Kimvilakani: Improved stratospheric ozone lidar. *Opt. Eng.*, **34**, 1421-1430, 1995.

Langer, J., U. Klein, K.F. Kuenzi, U. Raffalski, B.-M. Sinnhuber: A Versatile Millimeter Wave Radiometer for Spectroscopic Measurements of Atmospheric Trace Gases, Proc. XVIII Quadrennial Ozone Symp., L'Aquila, Italy, 1996, in press 1998.

Resonance Lidar and Airglow Observations of Wave Activity in the Arctic Mesopause

Richard L. Collins and Roger W. Smith
Geophysical Institute, University of Alaska Fairbanks
903 Koyukuk Drive, Fairbanks, AK 99775-7320 USA
Phone: (907) 474-7607, FAX (907) 474-7290, E-mail: rlc@gi.alaska.edu

1 Introduction

Interest in the aeronomy of the mesopause (70-110 km) is spurred in large part because the circulation of this region is maintained far from radiative equilibrium by dynamic and chemical heating effects (Andrews et al., 1987). As mean wind and temperature climatologies of the middle atmosphere have been established, attention has turned to the role of gravity waves in the general circulation. Interest has focused on seasonal and geographical variations in the characteristics of the gravity wave field. Recent midlatitude radar measurements of the mean wind (Franke and Thorsen, 1993) and lidar measurements of the mean temperature (Yu and She, 1995) show a mesopause structure that is consistent with our current understanding of a large-scale circulation modified by gravity-wave mean-flow interactions. The physical mechanisms through which these interactions occur are not precisely understood. At high latitudes the inertial period approaches the minimum value of 12 hours and the presence of waves with periods of several hours raises a variety of questions about the structure of the tides and the role of wave-wave interactions (Waltershied et al., 1986; Collins et al., 1992; Hernandez et al., 1993).

This work presents new lidar and airglow measurements of wave activity in the mesopause region over Poker Flat Research Range (PFRR), Alaska (65°N, 147°). Simultaneous lidar and airglow observations are used to study distinct wave events, while the lidar measurements is used to compare the observations with earlier lidar measurements at another high-latitude site, South Pole (90°S), and a midlatitude site, Urbana, IL (40°N, 88°W) (Collins et al., 1994; 1997). A variety of studies have shown the relative sensitivities of the gravity wave measurements when made by different instruments and when employing different retrieval algorithms (e.g. Burrage et al., 1996; Gibson-Wilde et al., 1996). In this study the earlier lidar measurements have been reworked and reduced in precisely the same way as these new measurements.

2 Experimental Details

A sodium resonance lidar system has been operated at PFRR since the spring of 1995. The lidar system consists of a flashlamp-pumped dye laser and a 0.35 m Schmidt-Cassegrain receiving telescope. The average laser power is 0.5 W. The sodium concentration profiles are determined from the sodium photon count profiles with the standard inversion techniques (e.g., Tilgner and von Zahn, 1988) using meteorological data from the local radiosonde releases 50 km away at Fairbanks. The lidar observations are made at a resolution of 100 s and 75 m and yield sodium profiles at a resolution of 15 min and low-pass filtered at 2 km. The temperature of the hydroxyl (OH) layer is measured with an Michelson interferometer. The interferometer has a 10 cm aperture beamsplitter that records the airglow in the OH Meinel bands from 1.0 to 1.6 μm. Temperature measurements are made every 2-3 minutes with an accuracy of 2 K.

The quality of the lidar data is significantly reduced in the summer when the concentration of sodium is at its seasonal minimum, and the background noise is a maximum during the perpetual twilight. Accordingly, we present measurements from the winter, spring and fall.

3 Observations

A typical sequence of sodium profiles measured by the lidar on November 15, 1995 is plotted in Figure 1. These measurements show two distinct features associated with the data. There are downward phase progressions associated with upwardly propagating gravity waves and tides. There is also a strong oscillation in the bottomside of the sodium layer. Figure 2 shows the OH temperature measurements and the contour of constant sodium density. A coherent oscillation is present throughout the observation period.

Both waves are consistent with a long wavelength (≈20 km) gravity wave propagating through the sodium and OH layers. The 6.5 hr wave on 6-7 November 1995 has an rms horizontal wind amplitude of at least 12 m/s. Analysis of the sodium perturbations at higher altitudes do not yield a dominant 6.5 hr wave. These oscillations have been observed during other periods at PFRR. Similar observations have also been reported in other high-latitude sodium lidar observations, where strong oscillations in the bottomside of the sodium layer appear not to propagate to higher altitudes (Collins et al., 1992).

This lidar data, obtained over a two year period of approximately 45 nights of observations, is used to quantify the gravity wave activity over PFRR. The sodium fluctuations are used to infer the variance of the density perturbations associated with the gravity wave (Senft and Gardner, 1991). The variation of the wave variance with altitude provides a measure of the interactions between the gravity waves and the background atmosphere. These data will be compared with the set of 20 observations from South Pole site and the set of 57 observations from Urbana.

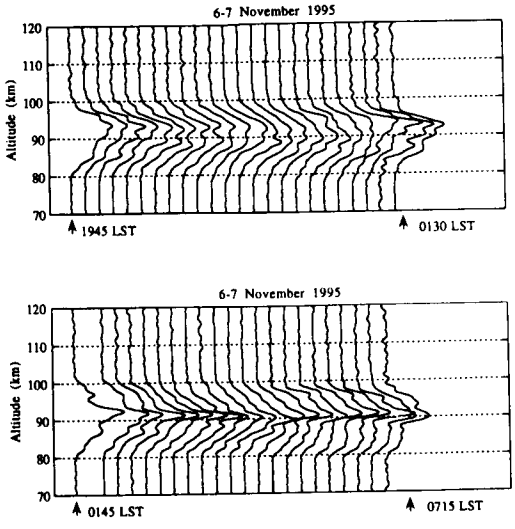


Figure 1. Sequence of sodium density profiles. The individual profiles represent 15 minutes of observations and have been low-pass filtered with a 2 km cutoff.

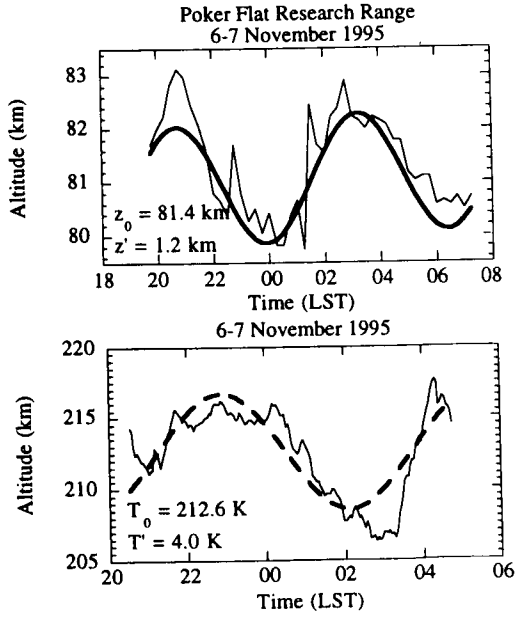


Figure 2. Upper plot shows contour of constant sodium density (fine) with 6.5 hour harmonic fit (bold). Lower plot shows OH temperature measurements (fine solid) with a 6.5 hour harmonic fit (bold broken).

3 Summary

The analysis of a new data set of new of high-latitude resonance lidar observations is currently under examination. The combination of simultaneous sodium density lidar and OH temperature allows us to study the vertical structure of long-period waves, and

explore the role of wave-wave interactions. The sodium lidar density data is also been compared with sodium lidar observations at two other sites to assess the geographical variability of gravity wave activity.

References

Andrews, D. G., J. R. Holton, and C. B. Leovy, *Middle atmosphere dynamics*, Academic Press, Orlando, 1987.

Burrage, M. D., D. A. Gell, A. R. Marshall, D. A. Ortland, W. R. Skinner, S. J. Franke, D. C. Fritts, P. Hoffman, A. H. Manson, C. McLandress, R. Niciejewski, F. J. Schmidlin, G. G. Shepherd, W. Singer, T. Tsuda, and R. A. Vincent, 1996, Validation of mesosphere and lower thermosphere winds from the High Resolution Doppler Imager on UARS, *J. Geophys. Res.*, 101:10365-10392, 1996.

Collins, R. L., D. C. Senft, and C. S. Gardner, Observations of a 12 h wave in the mesopause region at the South Pole, *Geophys. Res. Lett..*, 19:57-60, 1992.

Collins, R. L., A. Nomura, and C. S. Gardner, Gravity waves in the upper mesosphere over Antarctica: Lidar observations at the South Pole and Syowa, *J. Geophys. Res.*, 99:5475-5485, 1994.

Collins, R. L., D. Thorsen, and S. J. Franke, Comparative MF radar and Na lidar measurements of fluctuating winds in the mesopause region, *J .Geophys. Res.*, 102:16,583-16,591, 1997.

Franke, S. J., and D. Thorsen, Mean winds and tides in the upper middle atmosphere at Urbana (40°N, 88°W) During 1991-1992, *J. Geophys. Res.*, 98:18,607-18,615, 1993.

Gibson-Wilde, D. E., I. M. Reid, S. D. Eckermann, and R. A. Vincent, Simulation of lidar measurements of gravity waves in the mesosphere, *J. Geophys. Res.*, 101:9509-9522, 1996.

Hernandez, G., G. J. Fraser, and R. W. Smith (1993), Mesospheric 12-hour oscillation near South Pole, Antarctica, *Geophys. Res. Lett.*, 20:1787-1790.

Senft, D. C., and C. S. Gardner, Seasonal variability of gravity wave activity and spectra in the mesopause region at Urbana, *J. Geophys. Res.*, 96:17,229-17,264, 1991.

Tilgner, C. and U. von Zahn, Average properties of the sodium density distribution as observed at 69°N latitude in winter, *J. Geophys. Res.*, 93:8,349-8,454, 1988

Yu, J. R., and C. Y. She, Climatology of a midlatitude mesopause region by a lidar at Fort Collins, Colorado (40.6°N, 105°W), *J. Geophys. Res.*, 100:7441-7452, 1995.

Walterschied, R. L., G. G. Sivjee, G. Schubert, and R. M. Hamwey, (1986), Large amplitude semidiurnal temperature variations in the polar mesopause: evidence of a pseudotide, *Nature*, 324:347-349.

Comparison of an Fe Boltzmann Lidar with a Na Narrowband Lidar

George C. Papen, Daniel Treyer
Department of Electrical and Computer Engineering
University of Illinois at Urbana-Champaign
Address: 1406 W. Green St.,Urbana, IL 61801 USA
Phone:(217)244-4115, *Fax:*(217)333-4303, *e-mail:*g-papen@uiuc.edu

The performance of an Fe Boltzmann lidar is compared to existing Na narrow-band techniques. It is shown that the two systems yield similar performance, but the Fe system allows the use of more broadband lasers.

For both techniques, the sensitivity is defined as the normalized change in the ratio per degree temperature change [1]

$$S_T = \frac{(\partial R_T/\partial T)}{R_T} \tag{1}$$

Using Eq. (1),the RMS temperature error due to photon noise can be written as [1]

$$\Delta T = \frac{1}{S_T}\sqrt{\frac{1+1/R_T}{N}} = \frac{Q_T}{\sqrt{N}}. \tag{2}$$

where ${Q_T}^2$ is the number of photon counts N required for 1 K of temperature accuracy.

The Na narrow-band technique exploits the temperature dependence of the absorption cross section of Na. An increase in temperature results in a broadening of the absorption line. The shape of the cross section can be measured by tuning a laser to selected frequencies within the absorption feature (sub-Doppler probing). For a two frequency technique for temperature measurements, the ratio can be written as [1]

$$R_T(z,t) = \frac{N_{f_c}(z,t)}{N_{f_a}(z,t)} = \frac{\sigma_{\text{eff}}(f_c,T)\,\rho(z,t)}{\sigma_{\text{eff}}(f_a,T)\,\rho(z,t)} \tag{3}$$

where $\rho(z,t)$ is the Na density, f_a is a frequency near the peak of the Na D_{2a} resonance and f_c is near the local minimum of the effective absorption cross section $\sigma_{\text{eff}}(f,T)$. Thus N in Eq. (2) is N_{f_a} for the case of Na with Q_T being calculated numerically.

The Fe Boltzmann technique relies on the temperature dependence of the ratio of the ground state populations of two closely spaced Fe lines. At thermal equilibrium, this ratio is the Boltzmann factor $e^{\Delta E/kT}$ [2]. The Fe system utilizes two separate transitions at 372 nm and 374 nm and thus the laser linewidth can be broadband relative to Na narrowband systems. This relaxation of the system linewidth is the principle reason why Boltzman Fe systems are being developed.

The ratio of the photon counts at the two wavelengths is

$$R_T = \frac{N_{374}}{N_{372}} = \frac{\sigma_2\lambda_2 g_2}{\sigma_1\lambda_1 g_1}\exp\left[-\frac{\Delta E}{kT}\right] = C_1\exp\left[-\frac{C_2}{T}\right]. \tag{4}$$

Here, the σ_i are the peak values of the effective Fe cross sections, the λ_i are the center wavelengths of the Fe transitions, and the g_i are degeneracies. At T = 200 K and σ_l = 800 MHz FWHM (full width at half maximum), the peak values of the cross section become $\sigma_1 = 0.759 \times 10^{-16}$ m^2, and $\sigma_2 = 0.704 \times 10^{-16}$ m^2. Using $g_1 = 9$, $g_2 = 7$, λ_1 = 371.993 nm, λ_1 = 373.713 nm, and energy difference $\Delta E = 415.9$ cm^{-1}, the constants in Eq. (4) are C_1 =0.725 and $C_2 = 598.446$ K^{-1}, and the ratio $R_T = 0.0364$.

The sensitivity, as defined by Eq. (1), becomes

$$S_T = \frac{C_2}{T^2} \approx \frac{600}{T^2} \qquad \text{(at 200 K)}. \tag{5}$$

Using Eqs. (4) and (5), Q_T becomes

$$Q_T = \frac{T^2}{C_2}\sqrt{1 + \frac{1}{C_1}\exp\left[\frac{C_2}{T}\right]}. \tag{6}$$

Using Eq. (6) with $N = N_{374}$ in Eq. (2) yields the temperature error for the Fe technique.

Over typical mesospheric temperatures (100–250 K), the sensitivity of the Na technique is about half that of the Fe technique. For both techniques, as the temperature increases,the ratio approaches unity and S_T decreases. To achieve 1 K accurate temperatures at T = 200 K, the ratio R_T must be known to an RMS accuracy of 0.83% with the Na technique and to 1.5% with the Fe technique.

Figures 1 and 2 show ${Q_T}^2$, the required number of return counts for a 1 K temperature accuracy at $N = N_{f_a}$ and N_{374} respectively. At low temperatures, Q increases because the photon error is dominated by the frequency that has the lowest signal and both N_{f_a} and N_{374} decrease. At high temperatures, Q increases because the sensitivity decreases. The optimum point for the Fe system is roughly T = 150 K whereas for the Na system, the optimum lies at T = 80 K. At T = 200 K, ${Q_T}^2 = 64 \cdot 10^3$ for the Na system, whereas for ${Q_T}^2 = 127 \cdot 10^3$ the Fe system.

The compare the systems using commerically available laser technology, we use the values from Table 1. The main difference between the two systems is that the Fe system power is assumed to be *8x* of the Na system power because of the increase in linewidth tolerance for the Fe system. Thus, for a 1-K accurate temperature measurement with a column height Δz = 3 km, the integration times at T = 200 K for the two systems become 389 s and 352 s for the Fe and Na systems respectively indicating comparable system performance.

References

[1] Papen, G. C., W. M. Pfenninger, and D. M. Simonich, Sensitivity analysis of Na narrowband wind-temperature lidar systems, *Applied Optics, 34 (3)*, 480–498, 1995.

[2] Gelbwachs, J. A., Iron Boltzmann factor lidar: Proposed new remote-sensing technique for mesospheric temperature, *Applied Optics, 33*, 7151–7156, 1994.

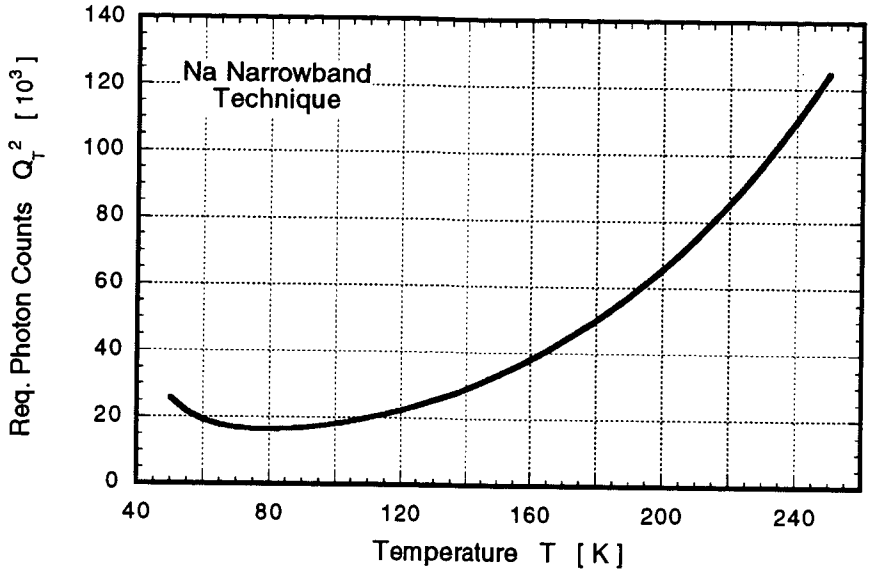


Figure 1: Required number of return counts for 1-K temperature accuracy with the Na narrow-band technique. Optimum is at $T = 80$ K. Background noise N_B is neglected.

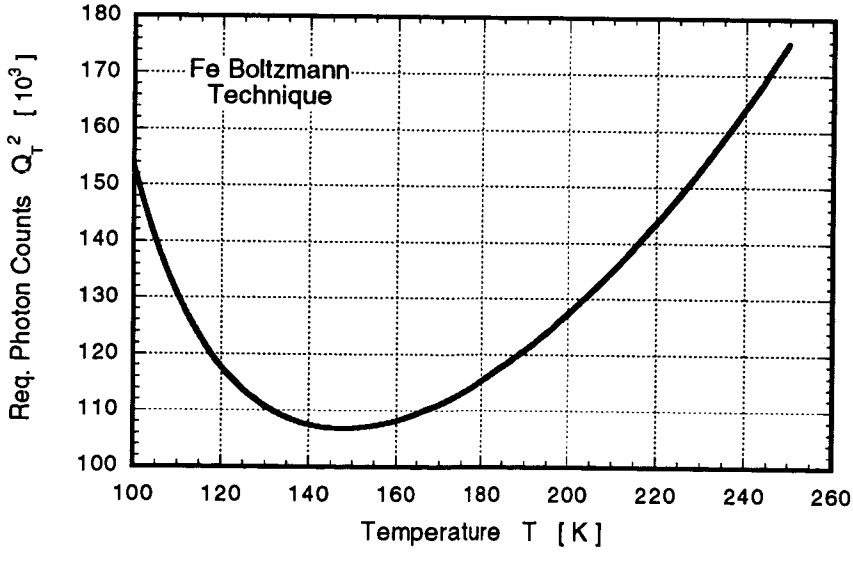


Figure 2: Required number of return counts for 1-K temperature accuracy with the Fe Boltzmann technique. Optimum is at $T = 144$ K. Background noise N_B is neglected.

Table 1: System parameters used in the simulation of the current two frequency Na narrow-band system and the Fe Boltzmann system.

		Na Narrow-Band System	Fe Boltzmann System
Layer Parameters (Annual mean at 40° N, Urbana)			
Transition Wavelengths (air)		$\lambda_{\mathrm{Na}D_2} = 589.15826$ nm	$\lambda_1 = 371.993$ nm $\lambda_2 = 373.713$ nm
Total Abundance	C_ρ	$5.35 \cdot 10^9$ cm^{-2}	$10.6 \cdot 10^9$ cm^{-2}
RMS Width	σ_ρ	4.42 km	3.41 km
Peak Density	ρ_{pk}	$4.83 \cdot 10^9$ m^{-3}	$12.4 \cdot 10^9$ m^{-3}
Altitude	z_{pk}	92.1 km	88.1 km
Atmospheric Transmittance (one-way)	T_a	0.7	0.5
Laser Parameters			
Effective Backscatter Cross Section ($T = 200$ K)		$\sigma_{\mathrm{eff},f_a} = 9.49 \cdot 10^{-12}$ cm^2 $\sigma_{\mathrm{eff},f_c} = 2.80 \cdot 10^{-12}$ cm^2	$\sigma_{\mathrm{eff},1} = 0.759 \cdot 10^{-12}$ cm^2 $\sigma_{\mathrm{eff},2} = 0.704 \cdot 10^{-12}$ cm^2
Linewidth	σ_l	60 MHz *RMS*	800 MHz *FWHM*
Total Power	P_l	1 W	8 W (both lines)
Receiver Parameters			
Receiver Aperture	A_R	0.130 m^2 (0.099 m^2 actual)	0.130 m^2
Receiver Optics Transmittance	η_R	19 %	19 %
Detector Quantum Efficiency	η_{QE}	11 %	28 %

Mesopause temperature variations from observations of more than 24 hours

David A. Krueger, Huailin Chen and C. Y. She
Physics Department, Colorado State University, Fort Collins, CO 80523
Phone: (970) 491-7381, FAX: (970) 491-7947, E-mail:krueger@lamar.colostate.edu

1. Introduction

Temperatures in the mesopause region of the atmosphere have been measured by lidars primarily during night over the past seven years. These measurements have been used to study seasonal changes of the vertical structure (She and von Zahn) and episoidic variations (She, et.al., 1998). Extraction of the effects of tides (e.g. with periods of 24, 12, 8, ... hours) is problematical from observations lasting less than 12 hours. Only more recently has technology advanced to allow measurements during the daytime (Chen, et. al., 1996; States and Gardner). Here data is presented for three campaigns with 31, 45 and 61 hours of observation. Contour plots show the measurements, the Lomb normalized periodograms show spectral content of variations of periods from 1 to 60 hours, a least squares fit of periodic functions gives an alternate view, and the effect of using 10 hour subsets of the data is discussed.

2. Temperature Measurements

Temperatures measured in February and March, 1997, are shown in Figure 1 along with those measured in October, 1995, which were reported earlier (Krueger, et. al. 1997). There are regions that display variations with periods around 24 and 12 hours which are expected because of the thermal driving of the atmosphere by the sun.

3. Lomb power

The Lomb method (Press, et. al., 1994) yields not only the spectral power as a function of angular frequency $\omega = 2\pi f = 2\pi / P$, but also allows an estimate of the significance of that power compared to what would obtain if the variation of the signal were simply due to random Gaussian noise. Figure 2 shows the Lomb power for three altitudes for periods equal to 1, 2, ... 60 hours.

Also shown are the powers that would be expected with probabilities of 0.5, 0.05, and 0.005 (=50%, 5% and 0.5%) from Gaussian noise. These powers equal ln(M/probability) where M is the number of independent frequencies. M values, calculated using a Monte Carlo technique, are 21, 17.7, and 14.4 for the Feb, Mar, and Oct observations respectively. The peaks about periods of 12 and 24 hours are significant. There is little indication of waves with other periods. The widths of the peaks can be estimated from Kovacs (1981) as $0.75\ P^2\sigma_N / (\tau\ A\ N^{1/2})$ where σ_N is the variance of the noise after a signal has been subtracted out, τ is the length of the data set, A is the amplitude of the signal, and N is the number of observations. Thus, going from a period of 12 hours to 24 hours, the width would increase by a factor of four consistent with Fig. 2.

4. Fits to periodic functions

The time variation of the temperature was analyzed by assuming a periodic functional form, $T(z,t_i)$, containing a constant and a sum of $\cos(2\pi\ t / P_k)$ and $\sin(2\pi\ t / P_k)$ terms where P_k takes on the values 24, 12, 8, and 6 hours if we use all the data and just 12 hours if we use 10 hour intervals of the observations. The amplitudes are determined by minimizing the weighted chi-square (Press, 1994)

$$\chi^2 = \Sigma_{i=1}^{N}\ W_i\ \{\ T_{exp}(z, t_i) - T(z, t_i)\ \}^2$$

where W_i^{-1} is equal to the estimated variance in the experimental values, $T_{exp}(z, t_i)$. Typical night-time measurements will have up to 10 hours of observations. Fitting to tides over a limited time range has been seen to contribute to more structure in the mesopause than if one takes data over 24 hours. (States and Gardner). Thus it is of interest to do the least squares fitting or averaging over 10 hours during the night or day to compare with the full data set.

February campaign results are presented in the amplitude and phase form, $A_k \cos(2\ \pi\ [t - \tau_k]/ P_k)$ in Fig. 3. We have also included plots of the average temperature over all the observations as well as over daytime (7 am to 5 pm) and nighttime (7 pm to 5 am). For data taken during the night, the profiles of the averages have somewhat more "structure" than the profiles of the constant term in the fits. Results from the gobal-scale wave model (GSWM) of Hagen et. al. (1995) are also shown. The GSWM diurnal

(semidiurnal) amplitudes for April and October are about 2 K larger (5 K smaller) than those shown for January. The measured diurnal amplitude is decreasing with altitude whereas the model is mostly increasing. There are some differences in the semidiurnal tides from night and day but they are less than the differences compared to the model. The phases of the semidiurnal variation are in better agreement.

For comparison, the constants from the fits and amplitudes and phases for the diurnal and semidiurnal waves are shown in Figure 4 using all the data for the February, March, and October campaigns. The diurnal and semidiurnal amplitudes for the three nights exhibit significantly different behaviors, but all have values up to 10-15 K. The associated phases have greater similiarities. The 8 and 6 hour amplitudes are not shown but are less than 6 K except for the 88 to 94 km region in October where the 8 hour amplitude peaks at about 8 K. The small values are consistent with the periodogram results. Since there are more than 24 hours of observations with few missing hours, the amplitudes are almost independent of each other.

5. Acknowledgment

The work presented here has been partially supported by the National Science Foundation, under grants ATM-9415853 and ATM-9714676.

References

Chen, H., M. A. White, D.A. Krueger, and C.Y. She, "Daytime mesopause temperature measurements with a sodium-vapor dispersive Faraday filter in a lidar receiver", Optics Lett. 15, 1093-5, (1996).

Hagen, M.E., J.M. Forbes, and F. Vial, "On modeling migrating solar tides", Geophys. Res. Lett., 22, 893-6 (1995).

Kovacs, G. Ap. Space Sci. 78, 175, (1981).

Krueger, D.A., H. Chen, and C.Y. She, "Mesopause temperature and sodium density variations over 35 hours during October, 1995, at 4059N, 105.14W", Proc. 13th ESA Symp., Oland, Sweden, 495-8, May, (1997).

Press, W.H., S.A. Teukolsky, W.T. Vetterling, and B.P. Flannery, Numerical Recipes in C, 2nd Ed. Cambridge U. Press, (1994).

She, C.Y. and U. von Zohn, "The concept of two-level mesopause: Support through new lidar observation", J. Geophys. Res. (in press).

She, C.Y., S.W. Thiel, and D.A. Krueger, "Observed episodic warming at 86 and 100 km between 1990 and 1997: Effects of Mount Pinatubo eruption", Geophys. Res. Lett. 25, 497-500, (1998).

States, R.J., Gardner, C.S., "Influence of the diurnal tide and thermospheric heat sources on the formation of mesospheric temperature inversion layers", (in press).

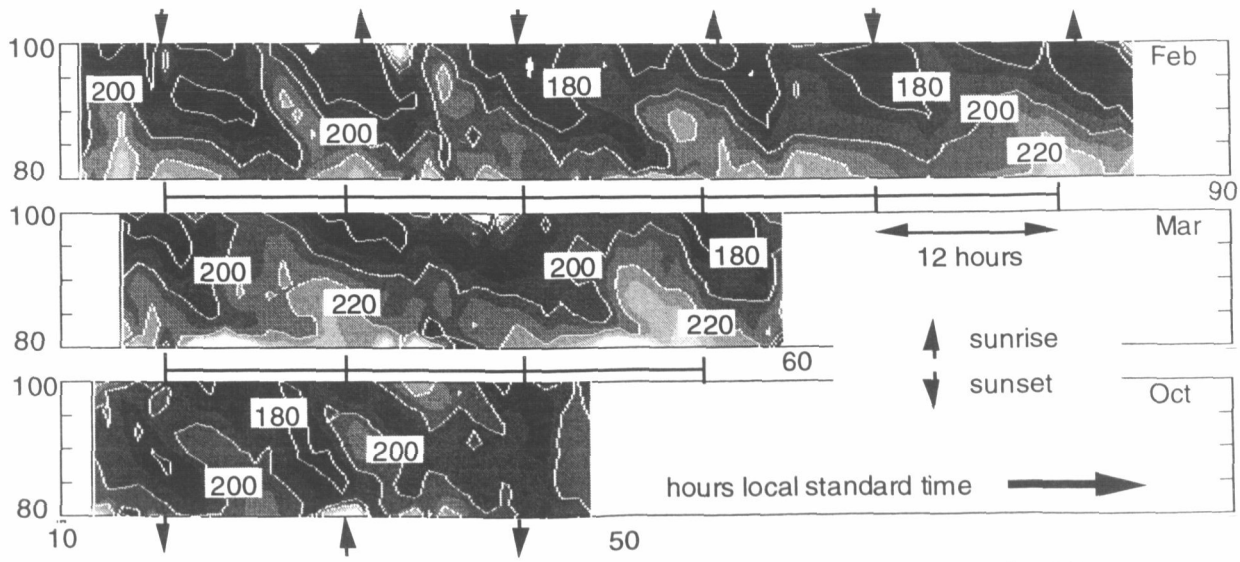


Figure 1. Contours of temperature from 80 to 100 km for campaigns in February and March in 1997 and October in 1995. Sunrise and sunset are marked by vertical arrows and are essentially the same for February and March.

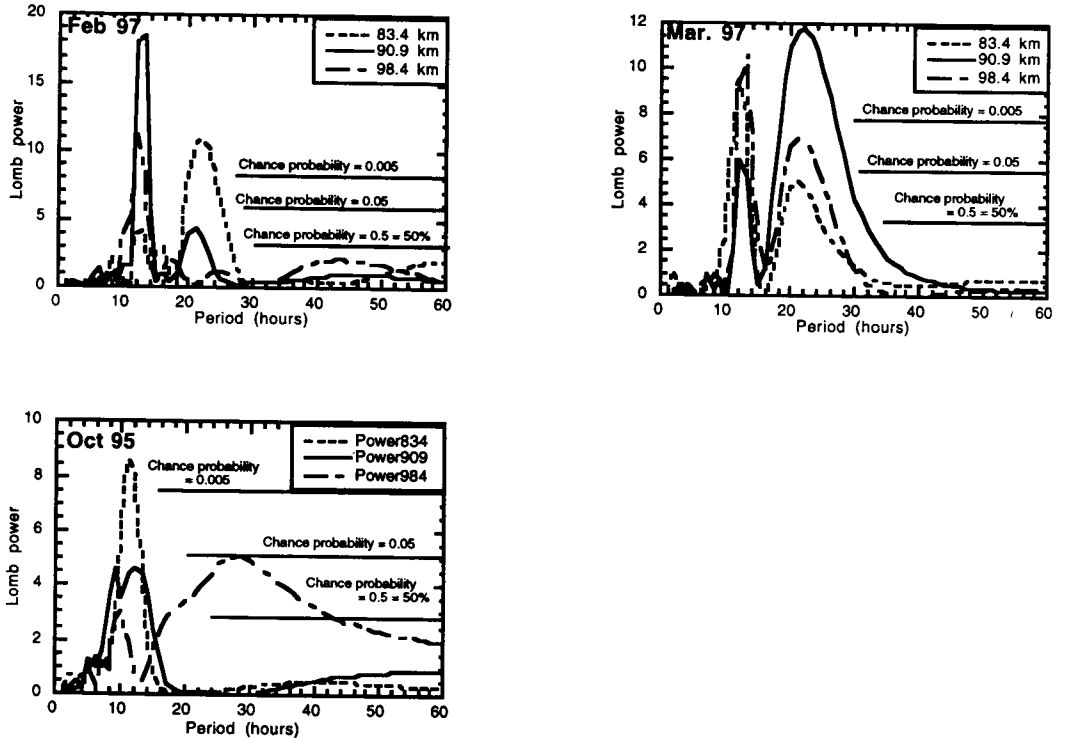


Figure 2. Lomb spectral power for Feb, Mar, and Oct. for altitudes of 83.4, 90.9, and 96.4 km.

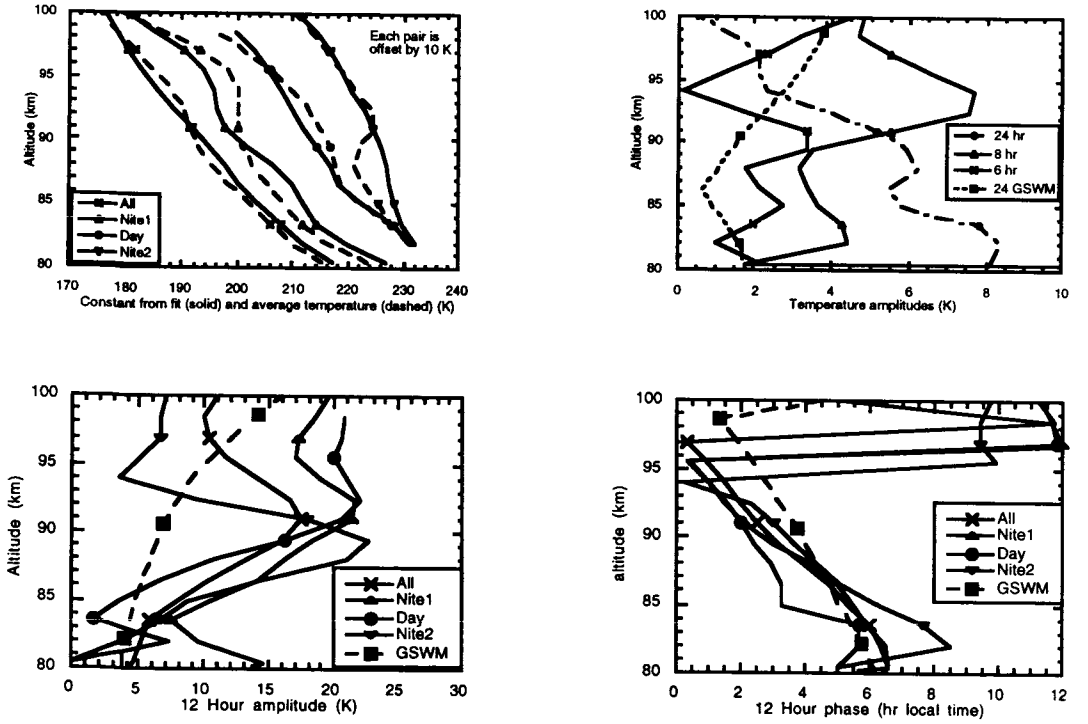


Figure 3. Results of fitting February temperatures to a periodic function. All indicates using all 61 hours. Nite1 and Nite2 (Day) include 10 hours of observation from 7 pm to 5 am local time (7 am to 5 pm). Sunrise was 6:33 am and sunset was 5:56 pm. Also shown is the simple average over the interval.

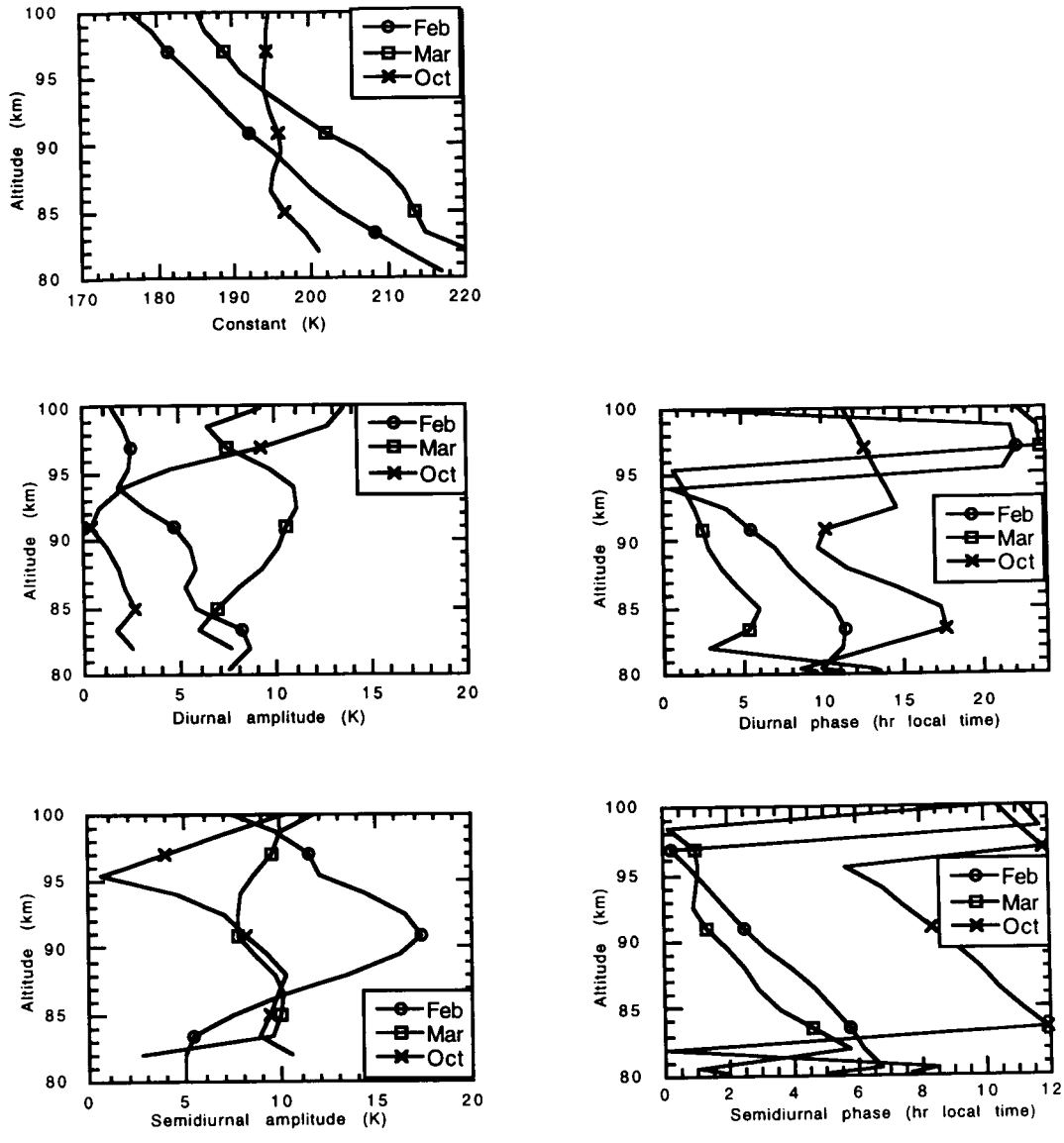


Figure 4. Results of fitting all data for Feb, Mar, and Oct campaigns to periodic functions with periods of 24, 12, 8, and 6 hours. The 8 and 6 hour results are not shown.

A frequency-agile lidar with concurrent frequency monitor for simultaneous measurement of temperature and line-of-sight wind in the mesopause region

Michael White, David A. Krueger and C. Y. She
Physics Department, Colorado State University, Fort Collins, CO 80523
Phone: (970) 491-5424, FAX: (970) 491-7947, E-mail:mawhite@lamar.colostate.edu

1. Summary

To achieve simultaneous measurement of temperature and line-of-sight wind, Colorado State University's two-frequency narrowband lidar has been modified for three-frequency operation. The application of a tandem acousto-optical modulator system permits rapid frequency-shifting, resulting in measurements free of contamination from atmospheric Na density fluctuations. Simultaneous temperature and vertical wind profiling data taken during 1996-97 have revealed a possible systematic frequency shift between the pulsed transmitter output and that of the c.w. seed laser used for frequency selection. Although this frequency shift impacts temperature measurements negligibly, it gives rise to a systematic bias in the vertical wind of ~ -8 m/s depending on the condition of dye laser amplifier. In this paper, we discuss a technique that may be used to monitor such a frequency shift, as well as its implementation into routine data acquisition.

2. The Narrowband Na Lidar

Lidar techniques for routine measurement of temperature and wind profiles in the mesopause region have become increasingly interesting as the study of thermal and dynamical structures of this region have become increasingly topical. In order to determine Doppler broadening (thus temperature) and Doppler shift (thus wind) of laser induced fluorescence from atmospheric metal atoms, a narrowband (~100 MHz) and tunable laser system is required. For over six years Colorado State University has utilized a narrow-band lidar for mesopause temperature profiling over Fort Collins, CO (41°N, 105°W) and considerable new geophysical information has been obtained. The transmitter includes a pulsed dye amplifier seeded by a c.w. ring dye laser tuned to the Doppler-free D_{2a} peak and cross-over features, at which frequencies Na fluorescence is temperature sensitive (located respectively at ν_a = - 651.4 MHz and ν_c = 187.8 MHz relative to the Na D_2 transition at 589.158 nm) (She et al., 1992). The measured fluorescence intensity ratio at these two frequencies is used to determine the atmospheric temperature in the mesopause region.

But studies of the middle atmosphere are incomplete without detailed knowledge of its wind structure. Since the absorption frequency (mean wavelength λ_o) of an atmospheric Na atom with radial velocity V_R is shifted by V_R/λ_o, line-of-sight winds can also be measured by a narrowband lidar provided that Doppler shift, in addition to Doppler broadening of atmospheric Na atoms, is monitored. To do this, an additional fluorescence ratio excited at frequencies sensitive to Doppler-shift (wind speed) is required from the lidar return. Using a Fabry-Perot interferometer as an additional frequency marker, the Illinois group has employed a four-frequency (ν_a - Δf and ν_a + Δf, with Δf = 600 MHz in addition to ν_c and ν_a) scheme and made the first lidar horizontal wind measurement in the mesopause region (Bills et al., 1991). Using a single acousto-optic frequency shifter to shift to a third frequency, initial observation of temperature and radial wind have also been made with a three-frequency (at ν_a, ν_a + 480 MHz and ν_c) scheme (She and Yu, 1994)

However, a limitation of schemes which use a Fabry-Perot or a single-modulator becomes clear. Data collection requiring integration at successive frequencies and laser tuning between Doppler-free features necessitates a time delay between successive

signal returns significant compared to the timescale of sodium density fluctuations in the atmosphere. Therefore, both the wind and temperature measurements are subject to contamination by these density fluctuations. For this reason, systems at both Colorado State (White et al., 1996) and Illinois (Yu et al., 1997) were upgraded using two acousto-optic (AO) modulators in tandem. In this system, the C.W. seed laser remains locked to the peak of Na D_{2a} spectrum (ν_a), and the tandem AO modulator system is used to provide the additional two frequencies ($\nu_\pm = \nu_a \pm 630$ MHz) necessary for the simultaneous temperature and line-of-sight wind measurements.

3. Initial Temperature and Vertical Wind Measurements

With this tandem AO system we opted to point the lidar at zenith for initial measurements at Colorado State; the higher accuracy required for vertical wind measurements providing a more stringent test of the lidar system's accuracy. The system has been in regular operation, and a typical result giving hourly averaged temperature and vertical wind profiles are shown in Fig. 1. The hourly temperature profiles are seen to display expected range of temperatures and variations. However, the vertical winds show a systematic bias of roughly 8 m/s, a value considerably larger than expected and likely indicative of an instrumental problem.

It should be pointed out that the lidar transmitter beam is the output of a pulsed dye amplifier (PDA) which is injection seeded by a single-mode c.w. dye laser tuned to the Na D2 resonance line. Up to this point, we have assumed the centroid frequency of the pulsed output to be identical to the frequency of the c.w. ring laser which serves as the frequency marker (She et al., 1992) via Doppler-free fluorescence spectroscopy (She and Yu, 1995). Calculations show (White et al., 1996) that if the centroid frequency of the pulsed output is blue shifted from that of the c.w. laser by 13 MHz, a bias in the vertical wind velocity of -8 m/s results, consistent with Fig. 1. The same frequency shift will give a temperature bias of less than 0.5 K. The simultaneous temperature and line-of-sight measurement technique has therefore been implemented for our routine lidar operation, yielding accurate temperature measurements for our long-term study of the thermal structure of the mesopause region (She et al., 1998). To most accurately measure vertical wind, we have pursued the investigation of the observed bias with the intention to monitor this frequency shift in real time to allow corrections to be made for its effect.

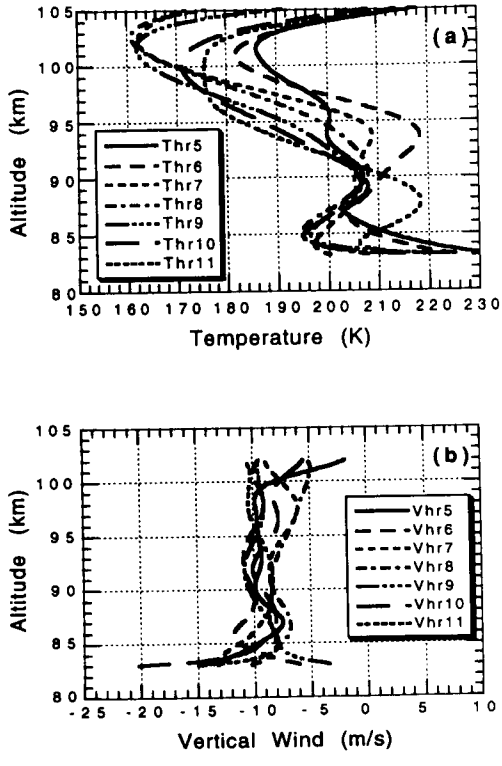


Figure 1: Analyzed three-frequency lidar data from the night of March 18, 1997, UT. (a). hour-averaged temperature profiles and (b). hour-averaged vertical wind profiles display systematic offset from 0 m/s, the accepted theoretical value.

4. The Frequency Shift Monitor

It is well known that there exist ample absorption lines of iodine vapor in the visible wavelengths, both the center and width of which depend upon the temperature of the iodine cell. It is our intention to use an iodine vapor cell to monitor the frequency of the transmitter pulses. Shown in Fig. 2 is the transmission curve of an iodine cell held at 80°C along with the Doppler-free fluorescence spectrum of a Na vapor cell, with the locations of the operating frequencies at ν_a, and $\nu_\pm = \nu_a \pm 630$ MHz indicated. The spectra were taken simultaneously by scanning the c.w. seed laser, with the iodine spectrum subsequently broadened by a computation taking into account the lineshape function of the PDA output pulses, measured previously. By monitoring the transmittance of pulsed laser light through the iodine cell, we can experimentally determine the frequency shift of the transmitter pulses. This may be done during data acquisition by sending a small portion of the transmitter laser pulse into a monitoring setup, similar to that employed by the edge technique (Korb et al., 1992) for wind measurement. Shown in Fig. 3, a transmitter pulse is divided into a monitor and a reference channel, measuring its transmission through the iodine cell and its pulse energy, respectively. The ratio of the intensities, appropriately scaled, gives the fractional transmittance through the cell. During data acquisition, the iodine transmittance may then be monitored in real-time and the mean transmittance at the three operating frequencies recorded for each set of photocount profiles, to be used for the correction of any present frequency shift. In this manner, even if the conditions (pump power and dye quality) of the PDA are changed during data acquisition, the corresponding frequency shift can be determined and its effect properly assessed and corrected. When this is implemented, the lidar return may be adjusted to provide accurate temperature and line-of-sight wind measurements to within 0.5 K and 1 m/s accuracy. With both vertical winds and temperatures precisely measured the profile of heat flux, for example, can be experimentally determined.

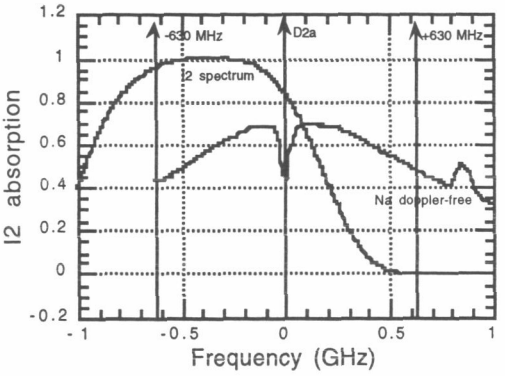


Figure 2: Transmission curve of the Iodine vapor cell held at 80°C, along with a Na doppler free spectrum and indicated lidar operating frequencies.

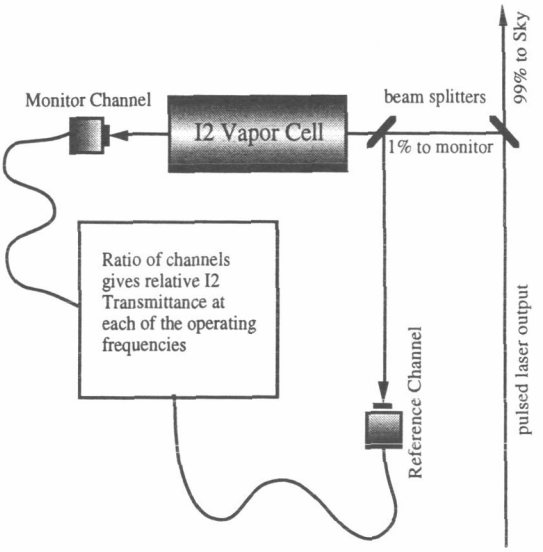


Figure 3: Schematic of the frequency monitoring system.

5. Acknowledgment

The work presented here has been partially supported by the National Science Foundation, under grants ATM-9415853 and ATM-9714676.

References

Bills, R. E., C. S. Gardner, and S. J. Franke, "Na Doppler/temperature lidar: Initial mesopause region observations and comparison with the Urbana medium frequency radar", J. Geophys. Res., 96, 22,701-22,707, 1991.

Korb, C. L., B. M. Gentry, and C. Y. Weng, "Edge technique: theory and application to the lidar measurement of atmospheric wind", Appl. Opt. 31, pp. 4202-4213 (1992).

She, C. Y., J. R. Yu, H. Latifi, and R. E. Bills, High-Spectral-Resolution Fluorescence Lidar for Mesospheric Sodium Temperature Measurements," Appl. Opt. 31, 2095-2106, 1992.

She, C. Y., and J. R. Yu, "Simultaneous three-frequency Na lidar measurements of radial wind and temperature in the mesopause region', Geophys. Res. Lett., 21, 1771-1774, 1994.

She, C. Y., and J. R. Yu, "Doppler-Free Saturation Fluorescence Spectroscopy of Na Atoms for Atmospheric Applications", Appl. Opt., 34, 1063-1075, 1995.

She, C. Y., S. W. Thiel and D. A. Krueger, Observed episodic warming at 86 and 100 km between 1990 and 1997: Effects of Mount Pinatubo eruption, Geophys. Res. Lett. 25, 497-500, 1998.

Tao, X. and C. S. Gardner, "Heat flux observations in the mesopause region above Haleakala," Geophys. Res. Lett. 22, 2829-2832, 1995.

White, M. A., D. A. Golias, D. A. Krueger, and C.Y. She, A frequency-agile lidar for simultaneous measurement of temperature and radial wind in the mesopause region without sodium density contamination, in p.p. 136-140, Application of Lidar to Current Atmospheric Topics, Sedlacek Ed., SPIE Proceedings 2833 (1996).

Yu, J., W. Yang and C. S. Gardner, A novel acousto-optic modulation technique for Na wind/temperature lidars, in Advances in Atmospheric Remote Sensing with Lidar, , p.p. 573-576, Eds. Ansmann, Neuber, Springer-Verlag, 1997.

Upper Tropospheric Water Vapor: A Field Campaign of Two Raman Lidars, Airborne Hygrometers, and Radiosondes

S. Harvey Melfi[1], Dave Turner[2], Keith Evans[3], Dave Whiteman[4], Geary Schwemmer[5], Richard Ferrare[6]

[1]University of Maryland Baltimore County, Baltimore Maryland 21228, 410-455-2186 410-455-1291 (fax), melfi@umbc.edu
[2]Pacific Northwest National Laboratory, P.O. Box 999, MSIN K7-28, Richland, Washington 99352, 509-375-2590, 509-375-3641 (fax), Dave.Turner@pnl.gov
[3]University of Maryland Baltimore County, Code 912, NASA/GSFC, Greenbelt, Maryland 20771, 301-286-9526, 301-286-1762 (fax), evans@agnes.gsfc.nasa.gov
[4]NASA Goddard Space Flight Center, Code 924, Greenbelt, Maryland 20771, 301-286-3115, 301-286-1761 (fax), David.N.Whiteman.1@gsfc.nasa.gov
[5]NASA Goddard Space Flight Center, Code 912, Greenbelt, Maryland 20771, 301-286-5768, 301-286-1762 (fax), geary@virl.gsfc.nasa.gov
[6]NASA Langley Research Center, MS-401A, Hampton, Virginia 23681, 757-864-9443, 757-864-7790 (fax), r.ferrare@larc.nasa.gov

Water vapor in the atmosphere plays an important role in radiative transfer and the process of radiative balance so critical for understanding global change. It is the principal ingredient in cloud formation, one of the most difficult atmospheric processes to model, and the most variable component of the Earth-atmosphere albedo. And as a free molecule, it is the most active infrared absorber and emitter, thus, the most important greenhouse gas. The radiative impact of water vapor is important at all levels of the atmosphere. Even though moisture decreases by several orders-of-magnitude from the Earth's surface to the tropopause, recent research has shown that, from a radiative standpoint, a small percentage change in water vapor at any level is nearly equivalent (Arking, 1998). Therefore accurate and precise measurements of this important atmospheric constituent are needed at all levels to evaluate the full radiative impact. The need for improved measurements in the upper troposphere is particularly important because of the generally hostile (very dry and cold) conditions encountered.

Because of the importance of water vapor to the understanding of radiative transfer, the Department of Energy's Atmospheric Radiation Measurements (ARM) program initiated a series of measurement campaigns at the Cloud And Radiation Testbed (CART) site in Oklahoma, especially focused on atmospheric water vapor. Three water vapor intensive observation period (water vapor IOP) campaigns were planned. Two of the water vapor IOP campaigns have been completed: the first IOP was held during the fall of 1996 with a focus on boundary layer water vapor measurements, and the second was conducted during the fall of 1997 with a focus on both boundary layer moisture and moisture in the upper troposphere.

This paper presents a review of the intercomparisons of water vapor measurements in the upper troposphere acquired during the second water vapor IOP. Data to be presented include water vapor measurements from: two Raman Lidars, the NASA Goddard Scanning Raman Lidar (SRL) and the CART Raman Lidar (CARL), a number of Vaisala radiosondes launched during the IOP campaign, and a dew point hygrometer flown on the University of North Dakota Cessna Citation Aircraft.

The water vapor IOP campaign was conducted over the period September 15 to October 5, 1997 at the CART site near Lamont, OK. During the IOP there were 10 nights where the meteorological conditions (thin or no cloud cover) allowed for lidar measurements up to and including the upper troposphere. Data acquired during these nights will be discussed after a brief description of the two lidar systems.

The Scanning Raman Lidar was developed in the early 1990's and was first deployed in the fall of 1991 in the SPECTRE/FIRE campaign in Coffeyville, KA (Whiteman *et al.*, 1992). The SRL consists of an XeF excimer laser aligned with a 0.76 m diameter telescope. The average output of the laser is 24 W at a wavelength of 351 nm at a repetition rate of 400 Hz. The system has four spectral channels: the laser wavelength, and the Stokes shifted Raman wavelengths associated with oxygen, nitrogen, and water vapor. Photon counting data is recorded simultaneously from the PMT's in the four channels in sequential 0.5 microsecond bins, corresponding to a range resolution of 75 m. Data is

typically accumulated from 23,200 laser shots (approximately one minute at 400 Hz) before being stored for real-time analysis. The SRL was optimized for nighttime operation.

The CART Raman Lidar, CARL, was developed during the mid 1990's and was delivered to the Oklahoma site during the summer of 1996 (Goldsmith *et al.*, 1998). The CARL system uses a tripled Nd-YAG laser aligned with a 0.61 m telescope. The laser generates 12 W average power at the tripled wavelength of 355 nm, at a repetition rate of 30 Hz. It is a three spectral channel lidar (Raman scattering by oxygen is not observed), with the channel locations appropriate to the output frequency of the tripled Nd-YAG laser. The system acquires photon counting data in 0.25 microsecond bins (37.5 meter range resolution) typically accumulating data from 1740 laser shots before storing (corresponds to one minute of operation). The CARL system was optimized for daytime operation with narrow spectral channels and a narrow field-of-view, thus giving it outstanding characteristics for nighttime operations.

Both lidars routinely provide vertical profiles of water vapor mixing ratio, aerosol scattering ratio, and aerosol optical depth. Figures 1 and 2 show typical profile comparisons of water vapor mixing ratio data from the various measurement techniques during two different observation periods. The profiles shown in the two figures include integrated SRL data at full vertical resolution to an altitude of 8 km with smoothing to 300 m resolution above, average CARL data with vertical smoothing to 312 m above 9 km, data from two sondes launched during each observation period, and Citation data from the dewpoint hygrometer during both ascent and descent of the aircraft.

Data in figure 1 were acquired during the observation period of Sept. 26, 1997 between 0230 and 0430 UTC (between 2130 and 2330 CDT on the evening of Sept. 25, 1997). Independent synoptic meteorological information indicates that during the observation period there was moistening in the altitude range 9 to 12 km, which is consistent with data from the two sondes given in the figure. Comparison of the data from all the measurements up to an altitude of 8.5 km shows good agreement. Above 8.5 km and up to 11 km, we see reasonable agreement between the two lidars and the aircraft measurements, with the SRL data slightly wetter than CARL, and the aircraft data wetter than SRL. These profiles lie between the measurements from the two sondes, which is consistent with the moistening of the atmosphere during the observation period.

Figure 2 shows data acquired during the observation period between 0100 and 0400 UTC on October 4, 1997. Independent observations indicate that the upper troposphere moisture was essentially unchanged during the observation period. Comparison of the profiles from all the measurement systems show good agreement from 6 to 12 km with the exception that the SRL data indicates wetter conditions above 10 km.

The wet bias seen in the SRL data when compared to the CARL data, shown in both figures, could be due to a positive bias in the water vapor channel of the SRL, introduced by signal-induced-noise (SIN). The SRL has a larger field-of-view than the CARL and therefore, when the laser pulse first crosses into the field-of-view of the telescope, the PMTs in the water vapor channels of the SRL would be exposed to a relatively larger backscatter than the corresponding PMTs in the CARL. This relatively high exposure at short range (low altitude) would be more likely to produce SIN in the SRL water vapor data at high altitudes, where the backscatter from water molecules is low, leading to a wet bias in the upper troposphere.

Figure 3 is a summary of the comparison of the CARL data with the sonde data from the nine clear sky nights of observation between September 26 and October 4, 1997. Shown in the figure is the mean percentage difference between the CARL and the sondes, for 29 independent comparisons, calculated using the following relationship: (CARL-Sonde)/CARL. The bars in the figure represent the standard deviation of the mean difference. For the comparisons, CARL data was accumulated over a thirty minute period after the launch of each sonde. The timing difference allows for the balloon to rise to the upper troposphere so as to assure the best spatial and temporal overlap of the two measurements. In the comparison only CARL data with a signal-to-noise greater than 4 was used. The figure shows a gradually increasing trend in the mean difference between the two measurements. The trend is seen as a wet bias in the CARL data compared with the sonde data. The wet bias could be due to a small amount of SIN in the CARL data and/or a dry bias of the sonde data. A dry bias in sonde data in the upper troposphere has been reported by other investigators (Soden *et al.*, 1994).

We must continue our focus on upper tropospheric moisture observations until we are confident of the accuracy and precision of the measurements, and we come to understand the spatial and temporal variability of naturally occurring moisture. Until then we cannot be certain of our predictions of the radiative effects of atmospheric water vapor.

References

Arking, Alan, 1998: private communication.

Goldsmith, J.E.M., F.H. Blair, S.E. Bisson, and D.D. Turner, 1998: Turn-key Raman lidar for profiling atmospheric water vapor, clouds, and aerosols, *Appl. Opts.*, (accepted for publication)

Soden, B.J., S.A. Ackerman, D.O'C. Starr, S.H. Melfi, and R.A. Ferrare, 1994: Comparison of upper tropospheric water vapor from GOES, Raman lidar, and cross-chain loran atmospheric sounding system measurements, *J of Geophys. Res.*, **99**, No. D10, 21005-21016.

Whiteman, D. N., S. H. Melfi, and R. A. Ferrare, 1992: Raman lidar system for the measurement of water vapor and aerosols in the Earth's atmosphere, *Appl. Opts.*, **31**, 3068-3082.

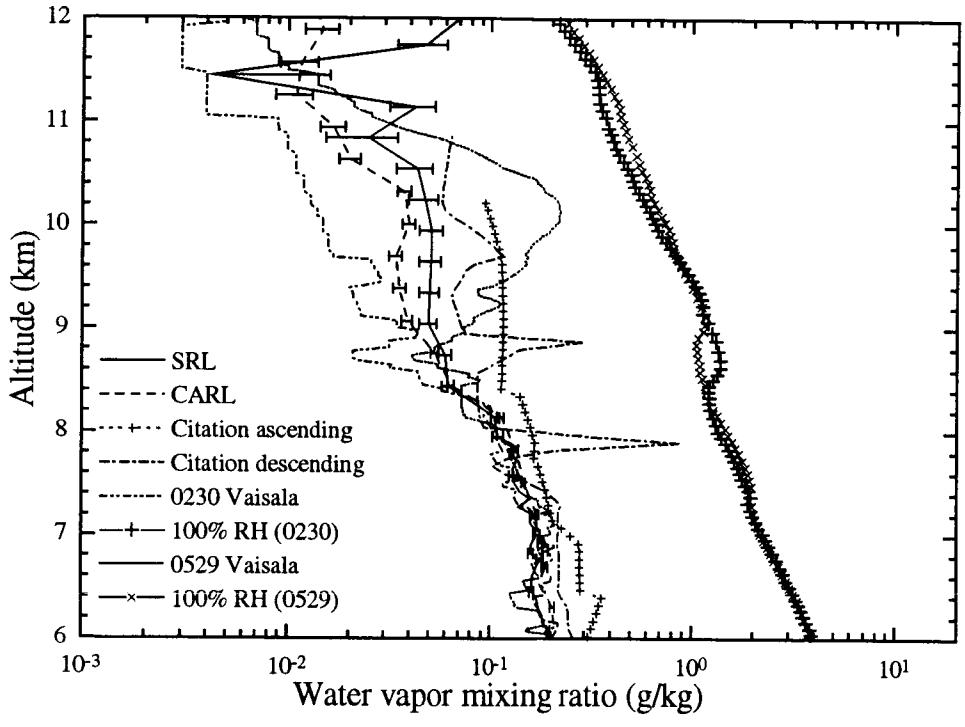


Figure 1. SRL and CARL on September 26, 1997, integrated from 0230-0430 UTC compared to the Citation dewpointer, during ascent and descent, and to the Vaisala radiosondes. Also shown for comparison is the water vapor mixing ratio profile for 100% relative humidity derived from the sonde temperatures and pressures.

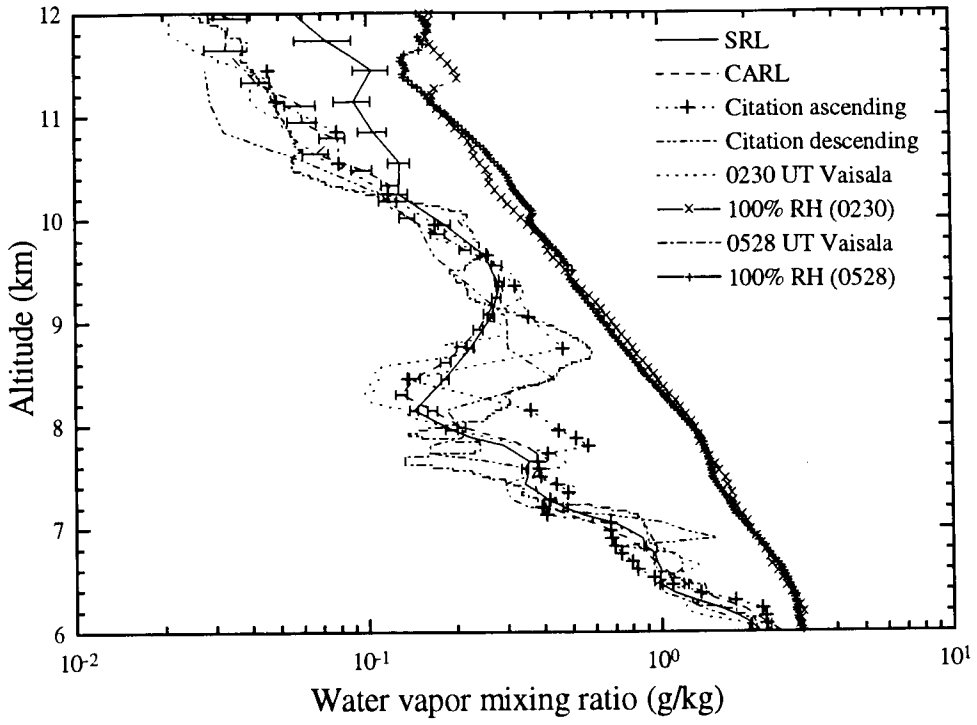


Figure 2. Same as Figure 1 except these data are from October 4, 1997, 0100-0400 UTC. Note the scale on the abscissa.

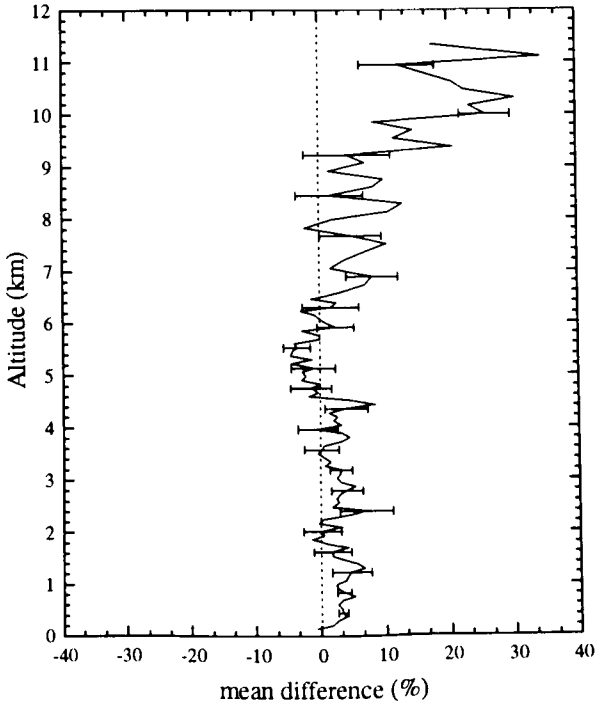


Figure 3. Mean difference profile, in percent, comparing CARL to radiosondes for the 1997 water vapor IOP.

A Compact Water Vapor Raman Lidar

Coorg R. Prasad, and **Savyasachee Mathur**
Science and Engineering Services, Inc., 4032 Blackburn Ln., Burtonsville, MD 20866-1166,
Ph: 301-989-1896, Fax: 301- 421-4137, e-mail: sesi@erols.com

Introduction

A compact Raman lidar for the remote measurement of atmospheric water vapor and aerosols is described here. Continuous measurements of tropospheric water vapor profiles over all temporal and spatial scales are required for meteorological and climate studies, and lidars are the most convenient instruments for this task. Lidars based on either Raman scattering or differential absorption technique [Grant, 1991] are commonly utilized for measurement of water vapor. Although the Raman lidar is conceptually a much simpler instrument compared to the differential absorption lidar (DIAL), practical Raman lidars are bulky, expensive and operate mostly at night, because of the low Raman signal levels. The compact Raman lidar (CRL) will overcome many of these limitations by utilizing the Micro Pulse Lidar [Spinhirne, 1992] concept, and will result in a rugged, affordable lidar with routine day and night operational capability. A compact, high repetition rate, diode-pumped, frequency quadrupled Nd:YAG laser (266nm) is the laser source. By operating in the solar blind wavelength region, the solar background is reduced to allow daylight operation. A moderate sized telescope (35cm aperture) collects the weak signal and efficient detection is achieved with photon counting after blocking elastic scattering with rejection filters. An aperture placed at the telescope focus is used to reduce the field of view and further reduce the background radiation reaching the detector. Water vapor mixing ratios can be obtained with vertical resolution of 100-200m, for 1mJ/pulse laser energy, for up to 3km altitude. An averaging period of ten minutes is adequate to yield high accuracy (5%) and good signal to noise ratio (~20) at 2 km altitude.

Although the early Raman lidar water vapor measurements were demonstrated in the late sixties and early seventies, this technique was not exploited greatly until recently. This was primarily because of the very small Raman scattering cross section for the atmospheric species compared to the molecular scattering (about 4 orders larger) or particulate scattering CS, thus requiring a high energy laser and large telescope, and resulting in a large and complex lidar instrument. Since the Raman scattering cross section increases as the inverse fourth power of the laser wavelength, the Raman signal is increased by using shorter wavelength lasers. Hence improvements in the performance of lasers and the commercial availability of high energy short wavelength pulse lasers such as the third and fourth harmonic of Nd:YAG at 355 and 266 nm, and excimer lasers (e.g., XeCl and KrF at 308 and 248 nm) made Raman lidars attractive once again. A number of Raman lidars have been built [Melfi et al, 1985, Whiteman, et al, 1992, Philbrick, 1996] and have established their ability to make accurate water vapor measurements up to 10 km. However, these Raman lidar systems are still large, complex, expensive and in many cases function only at night and are not eye-safe.

The Raman Lidar described here is a significant departure from the others in being compact, robust, and even more importantly it is eye-safe, and by effectively discriminating against the background radiation continuous day and night measurements can be obtained. The keys to the simplification are: the compact, efficient diode pumped laser in place of the large excimer or flash-lamp pumped lasers; a low cost astronomical Cassegrainian telescope with a narrow field of view; a high sensitivity photon counting detection system equipped with solar blind detectors and blocking filters for daytime measurements with adequate spatial and temporal resolution; a robust, user-friendly system design, control and data acquisition electronics. Although the altitude range is rather limited, it may be pointed out that the bulk of the water vapor is contained in the bottom 3 km of the atmosphere. In addition, this instrument will also provide ozone concentration profiles and aerosol distributions(to a much higher altitude). Unlike the differential absorption lidar (DIAL) for water vapor measurement which needs two lasers, one of which has to be a narrow bandwidth high stability source, the Raman lidar is a much simpler instrument requiring only a single laser with reasonable stability and linewidth.

Raman Lidar Technique

During Raman scattering, the frequency of a small fraction of the exciting radiation ν_L is shifted down (Stokes shift) or up (Anti-Stokes) by the rotational or vibration-rotational energies $\nu_{R,m}$, of the molecules interacting with the radiation. Although the Raman cross section increases as the fourth power of frequency, both laser and Raman scattered wavelengths are increasingly absorbed in the UV by ozone and oxygen. In addition, there is increased extinction due to Rayleigh scattering which also increases as the fourth power of frequency. The shortest wavelength where the optimum performance

occurs was shown to be near 265 nm [Renaut and Capitini, 1988]. Thus the fourth harmonic of Nd:YAG at 266 nm is well suited for Raman lidar and is chosen. Table 1 lists the Raman frequency shift $\nu_{R,m}$, the Stokes shifted wavelength of Raman scattering $\lambda_m = 1/(\nu_L - \nu_{R,m})$, and the differential backscattering cross sections $(d\sigma/d\Omega)_\pi$ for O_2, N_2 and H_2O for an excitation wavelength $\lambda_L = 266$ nm (i.e., $\nu_L = 37593$ cm^{-1}). [Renaut and Capitini, 1988].

Raman shift & cross section for excitation at 266 nm.

Specie (m)	Vibrat. shift $\nu_{R,m}$ (cm^{-1})	Raman W/length λ_m (nm)	CS $(d\sigma/d\Omega)_\pi$ cm^2 sr^{-1}
Oxygen	1556	277.5	2.0×10^{-29}
Nitrogen	2330	283.6	9.7×10^{-30}
Water vapor	3653 (ν_1 band)	294.6	3.0×10^{-29}

Most of the Raman lidars detect the Stokes shifted vibrational Raman bands of the species of interest. The Raman scattering cross sections are very small, being about 3 to 4 orders lower than that for Rayleigh scattering. Hence blocking the Rayleigh and the even stronger particulate scattering, is crucial for detecting the weak Raman scattered radiation. Raman band pass filters pass the Raman radiation, but block scattered light at the laser wavelength by over 8 orders. The bandwidth of the filter is chosen to optimize the Signal to Noise Ratio (SNR) while making the measurement insensitive to temperature [Whiteman, et al, 1992] over the full temperature range of the atmosphere over which water vapor measurments are made. Such special filters are commercially available [Barr Associates].

A direct determination of the water vapor mixing ratio is made by taking the ratio of the measured intensities of the Raman scattered radiation in the vibrational bands of water vapor and nitrogen. Recent measurement campaigns have demonstrated 5% measurement accuracy for altitudes up to 3 km with a few minutes of signal integration for nighttime operation [Melfi et al, 1992]. The low signal intensity makes it hard to perform daytime Raman measurements [Goldsmith and Ferrare, 1992] in the presence of strong background solar radiation. But daytime Raman measurements in the solar blind UV region (where the background solar radiation is attenuated strongly by O_3 and O_2) have been demonstrated [Balsiger, et al, 1996]. In such a system, however the differential ozone absorption at the N_2 and H_2O Raman wavelengths [Renaut, et al, 1988, Whiteman et al., 1996] has to be corrected before the water vapor mixing can be determined. This is achieved by including a third Raman channel for O_2, and using the O_2 and N_2 signals to determine the ozone density [Balsiger, et al, 1996].

Compact Raman Lidar

The CRL described above is in the initial stage of development at SESI. It is based on the aerosol and cloud micro-pulse lidar demonstrated first by Spinhirne [1993], modified and improved [Lee, et al, 1997] into a commercial instrument by SESI.

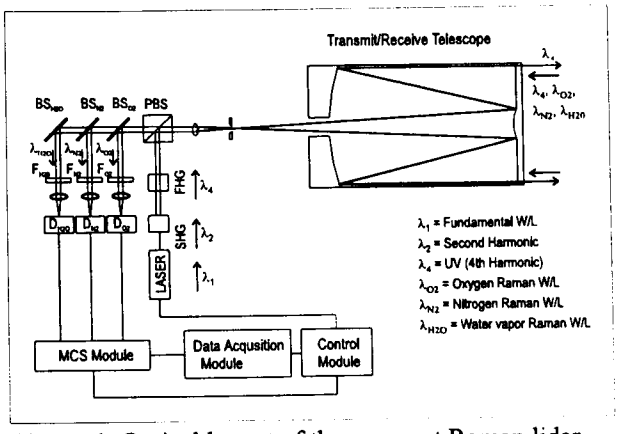


Figure 1. Optical layout of the compact Raman lidar

Figure 1 shows a schematic diagram of the CRL. The lidar system consists of three sub-systems: a. the transmitter, b. multi-channel receiver, detectors with multi-channel scalers, c. data acquisition, recording and a control system. A 35 cm aperture, f/10.2 Cassegrain optical telescope collects the Raman and elastic backscattered signals. The telescope does double duty as the transmitter and expands the laser beam to its full aperture so as to reduce the power density of the transmitted beam to below the eye-safe limit. The polarized output of a frequency quadrupled DPSS Nd:YAG (about 1 mJ/pulse, 1 kHz) laser reflects off a polarizer beam splitter before entering the telescope through a mode matching lens, and a pinhole. A small portion of the outgoing beam is collected for laser energy monitoring required for signal normalization.

The receiver subsystem consists of the telescope, pre-detection relay optics, photodetectors, optical and electronic filters, power supplies and gating electronics. The transmitting vector is located co-axially with the receiver axis. This configuration allows the lidar to stay aligned and to accommodate a significant level of mechanical vibration during operation. By using a small field stop, and reducing the field of view (FOV) of the telescope, the solar background noise can be reduced substantially so that daytime operation is possible by using the blocking and narrow bandpass filters.

The return signal passes through the polarizing

beam splitter (PBS) where it is separated into multiple detector channels by the dichroic beam splitters BS_m. The separated signals pass through bandpass interference filters F_m, before being focused on the photodetectors D_m. The filters serve the dual function of blocking the elastic scattered laser wavelength by 10^9 orders for the O_2 and N_2 channels and by $>10^{10}$ orders for the H_2O channel, in addition to blocking the ambient solar background radiation. Compact photomultiplier tubes (PMT) will be used for detection in the photon counting mode. The output of the PMT is fed into programmable multichannel scalers [SESI, Model 1003] that will range resolve the photoelectron counts into bins of desired spatial resolution and also accumulate the counts for a predetermined number of shots. The PC also serves as the data system together with the multichannel scalers, whose range bin is selectable between 100 nsec and 2 μsec. The time integration of the return signal is performed by the MSC and the data is read out at a predetermined rate by the PC.

Eye Safety Considerations

Eye safety criteria of the laser exposure is defined in terms of the maximum permissible exposure (MPE) for the naked eye according to the American National Standards Institute (ANSI Z136, 1986). The MPE for a pulse laser is based on the peak power of the pulse while the MPE for a cw system concerns the total energy for an extended exposure period of a few seconds. The MPE for a number N of repetitive pulses that are viewed within the exposure period, is reduced from the MPE of a single pulse by a factor of $(N)^{-1/4}$. Since the reduction of MPE is a rather slow function of the pulse repetition rate while the average power (and hence the signal information content) increases linearly with the rep rate, an eye safe lidar can use a high PRF low pulse energy laser transmitter. For an exposure of 10 s for the human eye staring at the UV beam, the MPE is calculated for a 1 kHz laser at 266 nm is 3×10^{-4} J/cm^2. Thus when the laser beam is expanded by the telescope, this transmitter will readily satisfy the ANSI eye safety requirement for the 1mJ, 1 kHz pulses at 266 nm, as opposed to 532 nm where the maximum pulse energy is limited to about 120μJ.

Analysis

For a lidar transmitter with a laser wavelength λ_L, and pulse energy E_L, the signal $S_m(R)$ at the Raman shifted wavelength λ_m collected by the telescopefrom a layer of thickness $\Delta R = c\,\Delta T/2$, at a range $R = ct/2$:

$$S_m(R) = B(\lambda_m) + \eta_{\lambda_m}\phi(R)N_m(R)\left(\frac{d\sigma_m}{d\Omega}\right)_{\pi} E_L \frac{A\Delta R}{R^2} \cdot \exp\left[-\int_0^R [\alpha(\lambda_L) + K(\lambda_L) + \alpha(\lambda_m) + K(\lambda_m)]\,dz\right]$$

where $B(\lambda_m)$ is the background radiation, η = term including the system optical efficiency and the detector quantum efficiency, $\phi(R)$ = geometric overlap function, $\alpha(\lambda)$= attenuation coefficient due to scattering and continuum absorption effects, $K(\lambda)$ = resonant absorption (by O_3, O_2, etc), A = area of receiver telescope, $N_m(R)$ = number density of the species m, and the subscript m identifies the species. The water vapor mixing ratio $w(z)$ defined as the ratio of the mass of water vapor to that of dry air in a given volume is given by:

$$w(z) = \frac{N_{H_2O}(z)\,M_{H_2O}}{N_{D.Air}(z)\,M_{D.Air}} \approx C_1 \cdot \frac{S_{H_2O}(z)}{S_{N_2}(z)}$$

where C_1 = system calibration constant and M are the molecular weights. Since the proportion of nitrogen in air is constant, the mixing ratio is proportional to the ratio of the water vapor and nitrogen Raman signals. However, this is only approximately correct because the attenuation and absorption coefficients at the two Raman shifted wavelengths are not the same. Rayleigh scattering is calculated at the two wavelengths and used for correction.

A major source of error for the UV Raman lidar is absorption by ozone. O_3 absorption spectrum covers the 240 to 340 nm wavelength region. Both the H_2O and N_2 Raman vibration bands are positioned on the sloping side of the Hartley absorption band of ozone, the tropospheric O_3 causes a differential absorption [Renaut and Capitini, 1988], which if left uncorrected can significantly affect the water vapor mixing ratio. Furthermore concentration of O_3 varies considerably both spatially and over all time scales ranging from hours to months and years. Its concentration ranges from 2 to 6 × 10^{11} cm^{-3} near the surface [Profitt and Langford, 1997]. Therefore it is necessary to determine the ozone density N_{O3} in the measurement range. This is accomplished by including another channel for measuring the Raman signal from oxygen at 279 nm. Taking the ratio of the oxygen and nitrogen return signals, the expression for the integrated ozone column density is obtained as:

$$\frac{S_{O_2}(z)}{S_{N_2}(z)} = C_2 \frac{N_{O_2}(z)}{N_{N_2}(z)} \exp\left(-\left[\sigma(\lambda_{O_2}) - \sigma(\lambda_{N_2})\right]\int_0^z N_{O_3}(\zeta)\,d\zeta\right)$$

where $\sigma(\lambda_{O2})$ and $\sigma(\lambda_{N2})$ are O_3 absorption cross sections at the O_2 and N_2 Raman wavelengths. Since the ratio $N_{O2}(z)/N_{N2}(z)$ is constant through the lower atmosphere this equation can be solved to obtain the column density of ozone. The ozone density $N_{O3}(z)$ is directly obtained by taking the derivative of the equation. After applying the ozone correction the water vapor mixing ratio is:

$$w(z) = C_3 \frac{S_{H_2O}(z)}{S_{N_2}(z)} \left[\frac{S_{O_2}(z)}{S_{N_2}(z)}\right]^{\Delta\sigma_{O_3}} ; \quad \Delta\sigma_{O_3} = \frac{\sigma_{N_2} - \sigma_{H_2O}}{\sigma_{N_2} - \sigma_{O_2}}$$

where C_3 is the new calibration constant.

Performance Simulation

A performance simulation was conducted for the proposed CRL system which is under development at SESI. We have assumed a laser energy of 1mJ/pulse at 1 kHz, 35 cm aperture receiver, a 15% detector quantum efficiency. A standard tropical atmosphere model with a 23 km visibility was used for the simulation. Extinction of the laser beam and the backscattered signals by ozone absorption and Rayleigh and aerosol scattering are included. Since the low Raman scattering cross sections yield very low photo-electron counts, fairly long signal integration times are required. Figures 2 and 3 show the number of photoelectrons detected in each 1 μs bin (150 m resolution) for a 10 minute observation period. Here the signal is accumulated over 6×10^5 shots (10 min) to yield 10^4 counts for H_2O and 10^5 counts for N_2 at 1 km altitude. Uncertainties in lidar measurements come from two main sources: the signal detection random error; uncertainties in the knowledge of scattering cross section and O_3 concentration. The signal to noise ratio of the photon counting detector depends on photon statistics, and the dark noise of the PMT and the background radiation falling on the PMT. For the low dark noise and background in this lidar, photon statistics dominate the source of noise and the SNR is then proportional to the square root of the photon counts. At 1km, from the photon counts in figure 1, the SNR is approximately 100 for H_2O and 315 for N_2, and the mixing ratio SNR ~ 95. At 2 km however, the corresponding values are 19, 100 and ~17. Vertical range of up to 3 km may be profiled with a somewhat coarser vertical resolution and longer averaging period. Reducing the FOV by inserting a 1 mm aperture to limit the background radiation affects only the signal in the first 1.2 km as seen in figures 2 and 3. The SNR of the measurement can be improved further by reducing the FOV and increasing the averaging time.

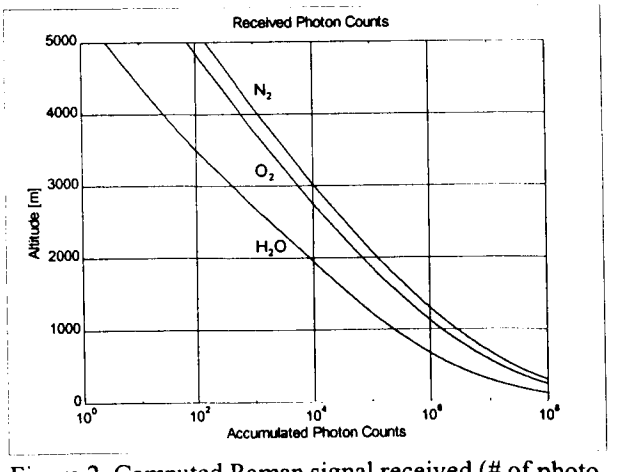


Figure 2. Computed Raman signal received (# of photo-electrons) in the 3 channels for 10 min averaging.

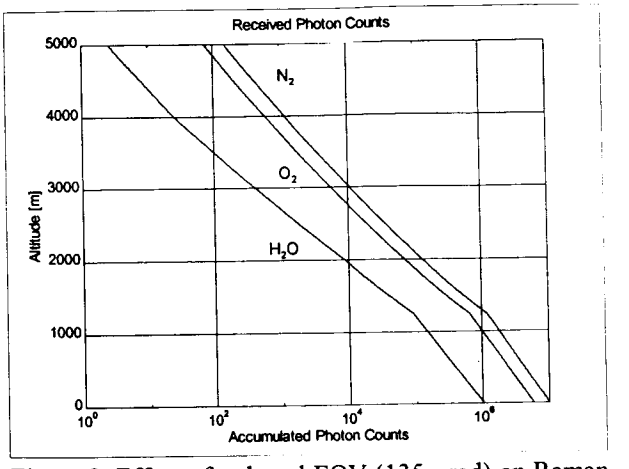


Figure 3. Effect of reduced FOV (135 μrad) on Raman signal. Signal is reduced for only the first 1.2 km.

It is seen thus the CRL described here is an eye-safe lidar capable of providing continuous water vapor mixing ratios in the lower troposphere.

References

Balsiger, F and C.R.Philbrick, *Proc SPIE*, vol **2833**, 231-240, 1966.

Goldsmith, J. E. M. and R. A. Ferrare, *16th International Laser Radar Conference,* NASA Conf. Pub. **3158**, pp. 667-670, 1992.

Grant, W.B., Opt. Engineering, **30**, 40-48, 1991.

Lee, H.S., I.H.Hwang, J.D.Spinhirne and V.S.Scott, *Advances in Atmospheric Remote Sensing with Lidar*, pp 7-10, A.Ansmann, Ed., Springer Verlag, Berlin, 1997.

Melfi, S. H. and D.Whiteman, *Bull. Am. Meteorol. Soc,* **66**, 1288-1292, 1985.

Philbrick, C.R., in *Atmospheric Propagation and Remote Sensing III*, SPIE vol **2222**, 922-931, 1994.

Renaut, D., and R.Capitini, *J. Atmospheric Oceanic Technology*, **5**, 585-601, 1988.

Spinhirne, J.D., "Micro Pulse Lidar," *IEEE Trans. on Geosci. and Remote Sens.*, **31**, pp 48-55, 1993.

Whiteman, D.N., S.H. Melfi, R.A. Ferrare, *Appl. Optics*, **31**, pp 3068-3082, 1992.

Whiteman, D. N., S. H. Melfi, R.A. Ferrare, K.D. Evans, *Advances in Atmospheric Remote Sensing with Lidar*, Ed. A.Ansmann, pp 317-320, Springer, 1997.

LIDAR PROFILING OF OZONE AND AEROSOL IN THE SCOS97-NARSTO EXPERIMENT

Y. Zhao, R. D. Marchbanks, C. J. Senff, H. D. Johnson
CIRES/NOAA
Environmental Technology Laboratory
Atmospheric Lidar Division

Mail address: NOAA/ERL/ETL, R/E/ET2, Boulder, CO 80303.
Telephone and e-mail address:
(303) 497-6567, yzhao@etl.noaa.gov (Zhao),
(303) 497-7755, rmarchbanks@etl.noaa.gov (Marchbanks)
(303) 497-6823, csenff@etl.noaa.gov (Senff)
(303) 497-6858, hjohnson@etl.noaa.gov (Johnson)
FAX: (303) 497-5318

and

L. Dolislager
California Air Resources Board
Research Division

Mail address: California Air Resources Board, 2020 L Street, Sacramento, CA 95812
Telephone: (916) 323-1533, e-mail address: ldolisla@arb.ca.gov, FAX: (916) 322-4357

1. Introduction

Although ambient ozone concentrations have declined significantly as a result of major reductions in the emission of volatile organic compounds and nitrogen oxides, southern California continues to have the worst ozone problem in the United States. The complex meteorological and chemical processes taking place in the region are not fully understood. The 1997 Southern California Ozone Study (SCOS97)[1] was planned to provide a new milestone in the understanding of relationships between emissions, transport, ozone standard exceedances in southern California, as well as to facilitate modeling to refine estimates of the additional emission reductions required to attain the National Ambient Air Quality Standard. The study was conducted in coordination with the North American Research Strategy for Tropospheric Ozone (NARSTO). Thus, the experiment is known as SCOS97-NARSTO.

The study's modeling domain of southern California and adjoining environs includes the rectangular area between approximately 32.3°N and 36°N latitude and between 115°W and 121°W longitude, an area of 205,000 square kilometers. The data collected will be extensively analyzed to determine how reductions in emissions might impact air quality, and also to quantify transport of pollutants between neighboring air basins.

The field activity started June 16 and ran through October 15, 1997. The existing monitoring network was supplemented with additional sites for the collection of continuous air quality and meteorological data. Moreover, during selected periods (2-4 days) when high ozone concentrations were forecast, additional monitoring and sampling occurred. During these intensive operation periods (IOPs), four to six aircraft, instrumented with ozone monitors and other monitoring equipment, made two to three flights per day; up to 75 balloon soundings were made per day; and additional samples of volatile organic compounds and carbonyls were taken

As a high technology remote sensing instrument, the NOAA Environmental Technology Laboratory (NOAA/ETL)'s ozone profiling atmospheric lidar[2,3] (OPAL) was deployed in the Los Angeles urban area. During IOPs, OPAL operated continuously for more than 20 hours per day, providing vertical profiles of ozone and aerosol in an area important for understanding ozone evolution and transport, as well as for air quality model performance validation.

The lidar was located at the El Monte Airport, about 15 km south of the foothills of the San Gabriel Mountains, which have a ridge line north of El Monte at altitudes about 2-2.5 km. The intent of choosing this site was that the polluted air mass in the return flows from the San Gabriel mountains

could be detected by the lidar. The site elevation is 90 m (msl).

2. The OPAL System

The ETL's OPAL transmits three UV wavelengths (266, 289, and 355 nm) in an eye-safe manner. The first two are for ozone and the third is for aerosol profiling. The innovative hardware design of this lidar makes it efficient, compact, and easily transportable. Prior to the SCOS97-NARSTO experiments, a redesigned 2-dimensional scanner was installed on the lidar. The vertical scanning capability provides a valuable internal system check, frequent calibration, and was desired for both monitoring and modeling studies.

The lidar has the unique capability of measuring profiles of ozone concentrations from near the surface to 2-3 km above the ground level and aerosol profiles up to 10 km. The raw data were recorded with a signal sampling interval of 5 m. With an averaging of 600-1200 pulses (5-10 min), the retrieval of ozone concentrations has a range resolution from a few tens of meters in the lower boundary layer to 150-200 m at about 3 km. Range resolution decreases with height because the signal-to-noise ratio is lower at farther ranges. The aerosol profiling at 355 nm has a maximum range of about 10 km with a range resolution of 15 m.

3. Lidar Observations in SCOS97

In the SCOS97-NARSTO experiment, OPAL detected persistent ozone and aerosol layers aloft on most days during the IOP's. A lower layer of ozone and aerosol at 1000-1500 m (msl) and a higher layer of ozone and aerosol at 2000-2500 m (msl) were frequently observed by the lidar. These distinctly separate layers existed simultaneously during a time period from the late afternoon till midnight, when they started to dissipate. Sometimes, they persisted through the night and could be seen in the early morning.

An example of the ozone and aerosol layers aloft are shown in Figs. 1 and 2, respectively. Ozone and aerosol vertical profiles are plotted against time in a contoured time-height chart. The profiles were taken on August 4, 1997, from 17:12 to 22:52 PST (Pacific Standard Time). Two layers of ozone and aerosol aloft are shown clearly in the figures. The following day featured the highest ozone surface concentration observed during an IOP (≈190 ppb)

To show the two ozone layers aloft more distinctively using a black-and-white contour, the contours in Fig. 1 begins at 60 ppb. The lower layer at about 1000-1500 m lay just above the top of the marine boundary layer. According to the temperature soundings, the top of the boundary layer decreased from about 800 msl at 1700 PST to about 500 m at midnight. The altitudes of the lower ozone layer decreased simultaneously with the underlying boundary layer. The peak ozone concentrations in this layer were 90-105 ppb in the early evening, and decreased to about 70 ppb at midnight. The ozone layer at higher altitudes was at about 2000 to 2500 m, the same altitudes as the ridge line of the San Gabriel Mountains. Ozone peak concentrations in this layer were higher than those in the layer below, started from 110-130 ppb in the early evening, decreased to about 90 ppb at midnight.

Ozone concentrations below 500 m were high in the mid afternoon (≈110 ppb), decreased in late afternoon, and dropped to less than 20 ppb after about 20:30 PST. The surface ozone concentration decreased even more rapidly, from 42 ppb at 17:12 PST, to 0 after 20:20 PST.

The two aerosol layers aloft shown in Fig. 2 were at the same height as the ozone layers. There was also a dense aerosol layer below 500 m. In the 2-2.5-km layer, the upper boundary extended up to 4500 m in the early evening and gradually became lower in late evening. The lower boundary of this layer was parallel to that of the ozone layer. The peak aerosol extinction coefficients in this layer increased from about 0.26 km^{-1} to about 0.34 km^{-1}. The 1000-1500-m layer was at first detached from the lower boundary layer. After about 1900 PST it merged with the layer below 500 m. The upper boundary of this layer was also parallel with the ozone layer. The peak value of extinction coefficients increased from 0.22 km^{-1} to 0.28 km^{-1}. In the layer below 500 m, the aerosol extinction coefficient was high. The peak value increased from 0.3-0.4 km^{-1} in the early evening, to 0.5-0.6 km^{-1} at midnight.

The increase of the 355-nm extinction coefficient with time from the surface to 3 km may imply an increase in the aerosol size due to the increase in relative humidity at night. Because 355 nm is close to the peak of an NO_2 absorption band, a portion of the increase in the extinction coefficient may also be attributed to additional absorption by NO_2 which was created when ozone was scavenged

by nitric oxide emissions. Ozone scavenging is indicated by the decrease of ozone concentrations at all altitudes, but especially at the lower level. However, the NO_2 absorption would only be about 10-20% of the 355-nm aerosol extinction coefficients in this particular case, even if we assume NO_2 concentrations were as high as 100 ppb.

Various nitrogen compounds (e.g., NO_2 N_2O_5) and radicals act as reservoirs of potential oxygen atoms which are necessary for the formation of ozone. Any such compounds available in the morning would enhance ozone formation after sunrise.

4. Summary and Discussion

Layers of high ozone concentrations aloft in the South Coast Air Basin (SoCAB) in California have been reported by many measurement projects. These layers may result from complex mesoscale flows in the basin, including sea breezes and thermally forced daytime up-slope flow in the mountains.

It is hypothesized that these high-concentration ozone layers aloft may contribute significantly to ozone standard exceedances in the basin by recycling pollutants from previous days, and/or increase ozone concentrations in downwind basins by transport.[4,5] During the 1987 Southern California Air Quality Study experiment, trajectory studies in two cases showed an upper level recirculation in the middle of the SoCAB.[6]

During the SCOS97-NARSTO experiment, NOAA/ETL's OPAL detected persistent ozone and aerosol layers aloft in the SoCAB. One layer was just above the top of the marine boundary layer, the other was at the same altitudes of the mountain ridge line north of the site. The continuous lidar observations during high ozone episodes in this experiment provided time variations of ozone and aerosol vertical profiles that were not previously available. Further analysis of the lidar data, combined with wind and other observational data, would contribute significantly to the understanding of the formation and transport of the ozone layers, and bring new insight into important issues in air quality research in Southern California.

5. Acknowledgment

The authors wish to thank K. W. Koenig, J. L. George, K. R. Healy, D. J. Greenstone, and L. D. Olivier for field support and/or software/hardware support, and to B. L. Weber for providing vertical profiles of atmospheric temperature and wind in SoCAB. The experiment in SCOS97-NARSTO was sponsored by CARB under contract 95-337.

References

1. E. M. Fujita, J. Bowen, M. C. Green, and H. Moosmüller (1997 draft) 1997 Southern California Ozone Study (SCOS97) Field Study Plan. Report prepared by Desert Research Institute for California Air Resources Board, Sacramento, CA. Contract No. 93-326. (see *http://www.arb.ca.gov/scos/scos.htm*)

2. Yanzeng Zhao, J. N. Howell, and R. M. Hardesty, "Transportable Lidar for the Measurement of Ozone Concentration and Aerosol Profiles in the Lower Troposphere," A&WMA/SPIE *International Symposium on Optical Sensing for Environmental Monitoring*, October 11-14, 1993, Atlanta, Georgia, pp.310-320.

3. Yanzeng Zhao, Richard D. Marchbanks, and R. M. Hardesty, "ETL's Transportable Lower Troposphere Ozone Lidar and Its Applications in Air Quality Studies, " 42nd SPIE Annual meeting, 31 July 1 - 1 August, 1997, San Diego, California, *Application of Lidar to Current Atmospheric Topics II,* Proceedings of SPIE #3127, pp.53-62.

4. J. L. McElroy and T.B. Smith, "Creation and fate of ozone layers aloft in southern California," *Atmospheric Environment* **27A**, No. 12, pp. 1917-1929 (1993).

5. R. Lu and R.P. Turco, "Ozone distributions over the Los Angeles basin: 3-dimensional simulations with the SMOG model," *Atmospheric Environment* **30**, No. 24, pp. 4155-4176 (1996).

6. S. G. Douglas, R. C. Kessler, C. A. Emery, and J. I. Burtt, "Diagnostic Analysis of Wind Observations Collected During the Souther California Air Quality Study, Final Report." Prepared under Contract No. A832-133, for California Air Resources Board, Sacramento, CA, by Systems Applications International, San Rafael, CA.

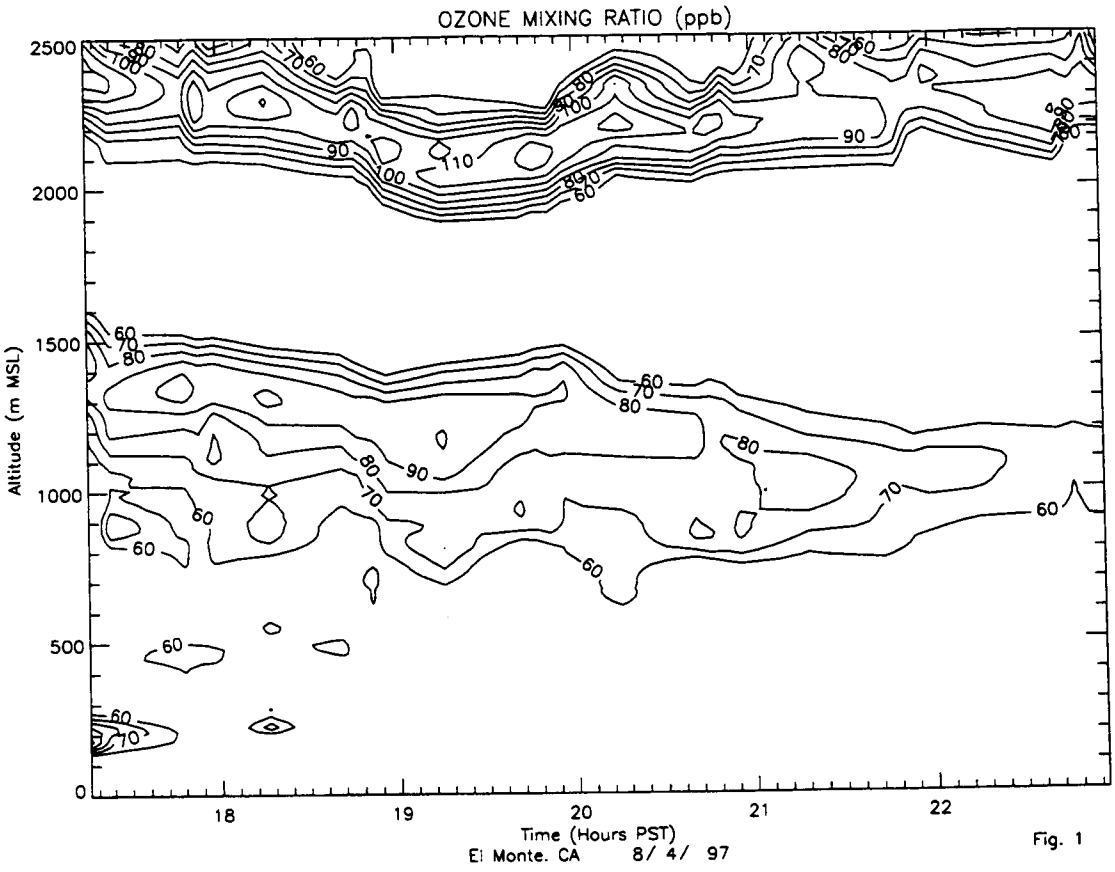

OZONE MIXING RATIO (ppb)
Altitude (m MSL)
2500
2000
1500
1000
500
0
18
19
20
21
22
Time (Hours PST)
El Monte. CA 8/ 4/ 97

Fig. 1

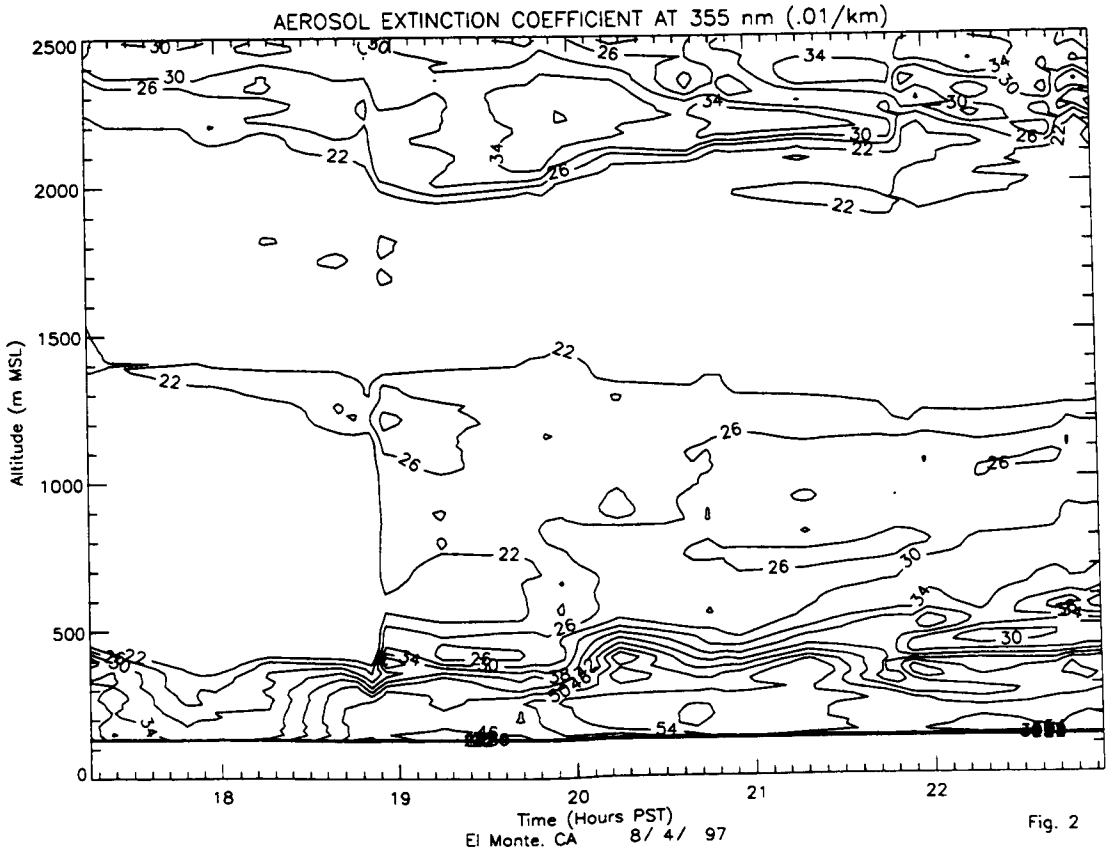

AEROSOL EXTINCTION COEFFICIENT AT 355 nm (.01/km)
Altitude (m MSL)
2500
2000
1500
1000
500
0
18
19
20
21
22
Time (Hours PST)
El Monte. CA 8/ 4/ 97

Fig. 2

Chemistry and dynamics of the lower troposphere over North America and the North Atlantic Ocean in fall 1997 observed using an airborne UV DIAL system

William B. Grant[1], Carolyn F. Butler[2], Marta A. Fenn[2]
Susan A. Kooi[2], Edward V. Browell[1] and Henry Fuelberg[3]

[1] Atmospheric Sciences Division, NASA Langley research Center, MS 401A, Hampton, VA 23681 USA; Phone: 757-864-5846; fax: 757-864-7790; E-mail; w.b.grant@larc.nasa.gov
[2] Science Applications International Corporation (SAIC), 1 Enterprise Parkway, Hampton, VA 23665.
[3] Meteorology Dept., Florida State University, Tallahassee, FL 32306-3034.

1. Introduction

The NASA Langley Research Center's airborne UV DIAL system [Richter et al., 1997] participated in the Subsonic Assessment, Ozone and Nitrogen Oxide Experiment (SONEX) mission from October 13 to November 12, 1997. The purpose of the mission was to study the upper troposphere/lower stratosphere in and near the North Atlantic flight corridor to better understand this region of the atmosphere and how civilian air travel in the corridor might be affecting the atmospheric chemistry. Bases of operations included NASA Ames, California (37.4°N, 122.1°W); Bangor, Maine (44.8°N, 68.8°W); Shannon, Ireland (52.7°N, 8.9°W); and Lajes, Terceira Island, Azores (38.8°N, 27.1°W). Since the UV DIAL system observes in the nadir as well as the zenith, aerosol and ozone data were obtained from near the Earth's surface to the lower stratosphere. A number of interesting features were noted relating to both chemistry and dynamics of the troposphere, which are reported here.

2. Measurements and discussion

Plumes from urban/industrial areas were observed on flights over populated regions. For example, on the transit flight from NASA Ames to Bangor, Maine on October 13, a haze cloud was seen above the Rockies near Aspen, Colorado (39.2°N, 106.8°W), a thick haze cloud over Denver (39.7°N, 105°W) (Figure 1), sometimes referred to as the "Denver Brown Cloud," as well as thin haze plumes near Grand Junction, Colo. (39°N, 108.5°W) and Richfield, Utah (38.7°N, 112°W). The westerly wind speeds were relatively low so the aerosols were not transported away rapidly.

Mountain waves were observed while crossing the Rocky Mountains on October 13. The Front Range (39° 35'N, 105° 40'W) gave the largest effect, with one dip observed just prior to the ridge followed by another dip just past the ridge (Figure 1). The peak-to-peak separation was 10 km, and the amplitudes were 1-1.5 km. There were also minor waves associated with other nearby peaks. Mountain waves are a well-known phenomenon [Ralph et al., 1997a, b], but this image may represent the first time they have been studied using airborne aerosol lidar.

Several examples were found of unseasonably high ozone in the boundary layer from pollution sources. The first was between Pittsburgh, Pennsylvania (40.4°N, 80°W) and Albany, New York (42.6°N, 73.8°W), on October 13 between 1940 and 2010 UT. Values of 60-75 ppbv from 1.3 to 2.6 km were seen during most of this portion of the flight track. This is a region of concern about ozone pollution, with the ozone precursor hydrocarbons and NO generated in the Ohio Valley and points east, then transported eastward through this region, but such values are not usually seen into autumn.

Enhanced aerosols and ozone were observed during flights over New England and Quebec on November 10 and from New York to Kansas on November 12. The aerosols and clouds extended from 3-10 km, and ranged from optically thin to optically thick, indicating that they had picked up considerable moisture during transit. The elevated ozone was observed as high as 8 km, and was associated with the aerosols. The air mass back trajectories indicated that the air had recently come from the Ohio Valley. On November 10 at the lower altitudes (surface and 700 hPa), the streamlines were westerly, while for the higher ones (500-200 hPa), the winds were southwesterly, which explains why the pollution was seen only at the higher altitudes (there is little urban/industrial activity to the west of the region). Both conditions point to convective pumping from the lower troposphere followed by long-range transport.

Another example of pollution transport was found off the coast of Ireland on October 18 from 1400 to 1700 UT. Pollution from Portugal was wheeled up to

there by the low pressure system off the coast of Portugal. The Iberian Peninsula could represent a significant pollution source for the British Isles, when the winds are from the south.

Evidence of even longer range transport of pollutants was found on the flight from Shannon to the Azores on October 28. Continental pollution from the U.S. reached out to 38°-42°N, 17°-21°W, a distance of at least 4,700 km from the eastern U.S. at that latitude, assuming straight line transport. A low pressure system was located over New Brunswick, which diverted some of the continental flow a bit to the south as it exited the U.S. in the mid-Atlantic states region, and a high pressure system over the center of the North Atlantic near 40°N, 35°W diverted the flow to the south before pulling it back to the north. Such long-range transport over the oceans has been observed before, such as over the western Pacific [Browell et al., 1996a; Jaffe et at., 1997] and tropical South Atlantic [Browell et al., 1996b]. Evidently once plumes get transported to the ocean, they can often travel quite large distances due to the reduced frequency of convective activity over oceans compared to over land, except during hurricane season.

A large number of stratospheric ozone intrusions were observed during SONEX, with at least one observed on 10 of 14 flights. These flights were primarily in the latitude range from 39°N to 53°N. This period is between the period of maximum northern midlatitude stratospheric intrusions (June-July) and minimum intrusions (December-February), based on ozonesonde climatologies for Uccle (51.8°N, 4.35°E) and Observatoire de Haute Provence (43.9°N, 5.75°E) [Van Haver et al., 1996]. The intrusions reached as low as 4 km, where further descent was blocked by an inversion layer at the top of a stable boundary layer. One was seen to stop at the top of the Denver haze layer. Another intrusion disappeared into a convective storm, which is one way they get mixed into the troposphere. They can also just slowly dilute into the troposphere once they are cut off from the stratosphere. During PEM West A, which was conducted from September 16-October 22, 1991 [Browell et al., 1996a], stratospheric intrusions made significant contributions down to 5-6 km in the 40°N-60°N region, and less significant contributions down to 4-5 km in the 20°N-40°N region.

Two jet streaks were crossed during the mission. In the classic jet streak, which often occurs during a straight leg of the jet stream, the winds accelerate along the jet, thereby pulling up lower-tropospheric air and pulling down stratospheric air through the Venturi effect [Blaustein, 1993]. This situation was observed on the flight from the Azores to Bangor on October 31 near 48°-49°N, 45°-48°W. A high pressure system was found near 43°N, 18°W, with low pressure systems found near 56°N, 82°W and 67°N, 0°W, all of which contributed to the path of the sub-polar jet stream, although the jet streak was closest to the low pressure system. A 4-km thick, optically-thin (the surface could still be detected) cloud developed below the jet streak, and aerosols formed streamlines to the cloud boundary from lower altitudes 200-500 km away, showing the direction of air mass flow. The tropopause was depressed as determined by in situ instruments onboard the NASA DC-8. Another jet streak was observed near 66°N, 10°W soon after leaving Shannon on October 25, but the tropopause depression was not as evident (Figure 2).

3. Summary

The NASA Langley UV DIAL system participated in the SONEX mission in October-November 1997 over mid-latitude North America and the North Atlantic Ocean. During the mission, a number of interesting chemical and dynamical features in the troposphere were found, including unseasonably high ozone levels in the boundary layer, haze above urban areas, long-range transport of pollutants, stratospheric intrusions, convective outflow, mountain waves, and jet streaks. These observations provide further evidence that an airborne lidar/DIAL system can find interesting atmospheric phenomena during an extended field mission, even in areas not identified in advance as part of the major objectives of the mission.

4. Acknowledgements

The authors thank G.E. Lockard, W.J. McCabe, A. Notari (SAIC), L.W. Overbay, and J.A. Williams for technical support in the field.

References

Blaustein, H.B., Synoptic-Dynamic Meteorology in Midlatitudes, Vol. II Observations and Theory of Weather Systems, Oxford Univ. Press, New York, 1993.

Browell, E.V., et al., Large-scale air mass characteristics observed over Western Pacific during summertime, J. Geophys. Res., 101, 1691-1712,

1996a.

Browell, E.V., et al., Ozone and aerosol distributions and air mass characteristics over the South Atlantic Basin during the burning season, J. Geophys. Res., 101, 24,043-24,068, 1996b.

Jaffe, D., A. Mahura, J. Kelley, J. Atkins, P.C. Novelli, and J. Merrill, Impact of Asian emissions on the remote North Pacific atmosphere: Interpretation of CO data from Shemya, Guam, Midway and Mauna Loa, J. Geophys. Res., 102, 28,627-28,635, 1997.

Ralph, F. M., P. J. Neiman, T. L. Keller, D. Levinson, and L. Fedor, Observations, simulations, and analysis of nonstationary trapped lee waves, J. Atmos. Sci., 54, 1308-1333, 1997.

Ralph, F. M., P. J. Neiman, and D. Levinson, Lidar observations of a breaking mountain wave associated with extreme turbulence, Geophys. Res. Lett., 24, 663-666, 1997.

Richter, D.A., E.V. Browell, C.F. Butler, and N.S. Higdon, Advanced airborne UV DIAL system for stratospheric and tropospheric ozone and aerosol measurements, in A. Ansmann, R. Neuber, P. Rairoux, and U. Wandinger, (eds.), Advances in Atmospheric Remote Sensing with Lidar, Springer-Verlag, Berlin, 395-398, 1997.

Van Haver, P., D. De Muer, M. Beekmann, and C. Mancier, Climatology of tropopause folds at midlatitudes, Geophys. Res. Lett., 23, 1033-1036, 1996.

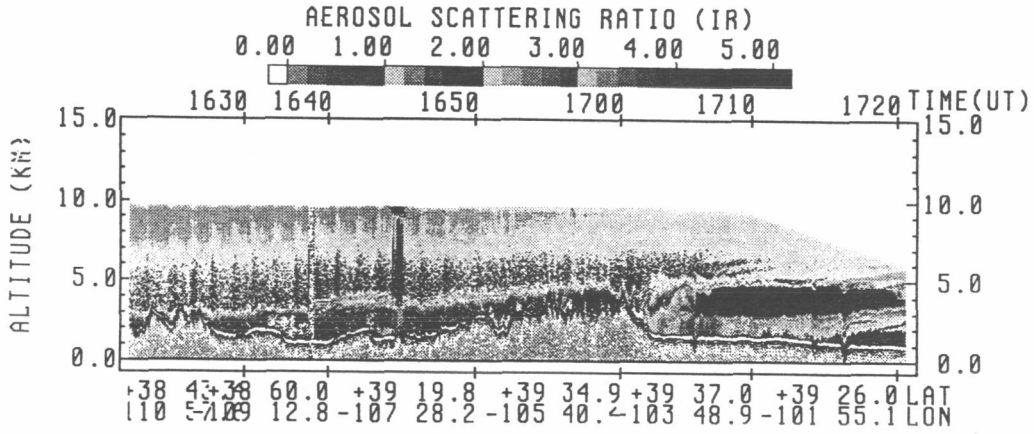


Figure 1. Aspen, Colorado haze, mountain waves, and the Denver "Brown Cloud" observed on October 13, 1997. The terrain is represented by the white region, while the atmospheric scattering ratio is represented by various shades of gray. The aircraft was travelling about 750 km/hour.

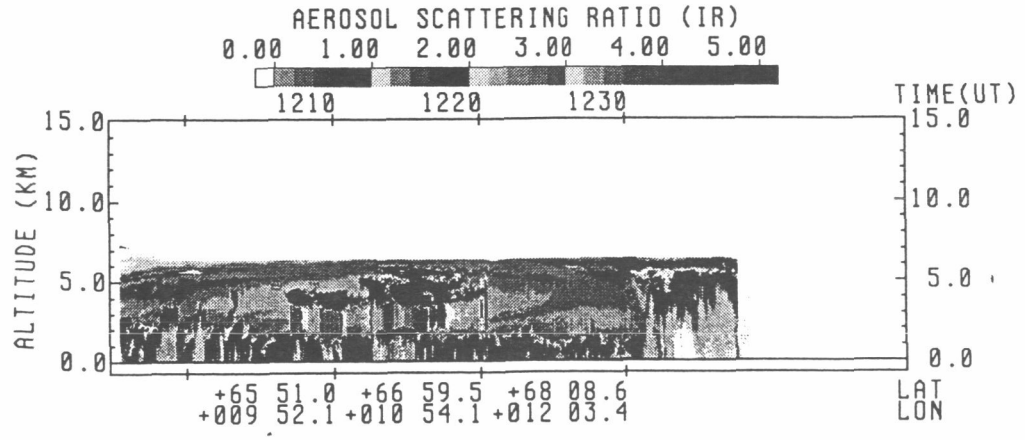


Figure 2. Jet streak-induced aerosol distributions observed northeast of Shannon, Ireland on October 25, 1997. The cloud in the center is just below the jet streak, and the aerosol distributions to either side of the cloud show horizontal transport induced by the jet streak.

Measurement of Various Minor Species Near Ground Surface Using Differential Absorption Lidar

S.L. Jain, B.C. Arya, S.Sharma and Arun Kumar
Radio & Atmospheric Sciences Division
National Physical Laboratory
New Delhi-110 012 (India)
Fax: 091 11 5752678 /091 11 576 4189
E-Mail: sljain@csnpl.ren.nic.in

1. INTRODUCTION :

The nonmethane - hydrocarbons such as alkanes, alkenes, alkynes, etc. are pollutants, and their concentrations depend on complex balance between their sources, their transport and their sinks. A number of phenomenon, including biomass burning, deforestation, fossil - fuel burning and agriculture practices are altering appreciably their concentrations in the atmosphere. These hydrocarbons together with oxides of nitrogen are also recognised the important precursors of ozone in the lower troposphere. Thus the monitoring of nonmethane - hydrocarbons along with surface ozone, water vapor etc are important for a better understanding of the tropospheric chemistry. New Delhi (28.7° N, 77.2° E) is considered to be one of the cities severely hit by anthropogenic activity. In view of the above a Differential Adsorption LIDAR (DIAL) using a tunable CO_2 laser has been designed and developed at National Physical Laboratory, New Delhi, to monitor various minor constituents in the atmosphere. In this paper some preliminary results of measurements of surface ozone, water vapour and ethene using DIAL are presented.

2. EXPERIMENTAL SET UP :

The set up consists of a continuous wave tunable CO_2 laser as transmitter, CO_2 laser spectrum analyser, Hg Cd Te detector, lock-in-amplifier , He-Ne laser, Chopper etc. The CO_2 laser beam is aligned with the help of a Helium-Neon laser. A 4" diameter mirror is used to reflect back the laser beam to the receiver. The total horizontal path-length is 210 m. The returned signal is sensed by a liquid nitrogen cooled HgCdTe detector and synchronously detected using a lock-in-amplifier. The technical specifications of the system are presented in Table I.

3. *RESULTS AND DISCUSSION* :

The DIAL technique involves differential absorption of laser radiation by a molecular species. It employs two laser wavelengths, one overlapping with the strong absorption features of the species of interest (called ON line), while the other being non-resonant (OFF line). By comparing the attenuation of the two beams one can get the concentration of the species. Interference due to the other species, scattering from the other particles and aerosols can be eliminated by choosing the two wavelengths at a very close interval. The concentration of the constituent of interest can be computed using the DIAL equation.

The CO_2 laser is a suitable source of radiation because there is a good spectral coincidence between laser emission lines and the absorption lines of many gases of interest. In the present investigation the DIAL has been used to monitor surface ozone, water vapour and ethene concentrations. The 'on' and 'off' lines used are given in the table. The typical diurnal variation of surface ozone obtained using differential absorption lidar at NPL is depicted in the figure. The maximum ozone concentration was observed around noon local time and it decreases towards the evening. The Lidar derived surface ozone is also compared with that measured by a in situ ozone analyzer. The surface ozone measurement are being made on round the clock basis using ozone analyzer to study the diurnal as well as seasonal variation. Very high values ie more than 140 ppb of surface ozone have been found on some days during summer June-July 1997 which is health hazard. In the present communication the salient features of the DIAL system and the results obtained will be discussed in detail.

DIURNAL VARIATION OF SURFACE OZONE AT NEW DELHI ON APRIL 6, 1997

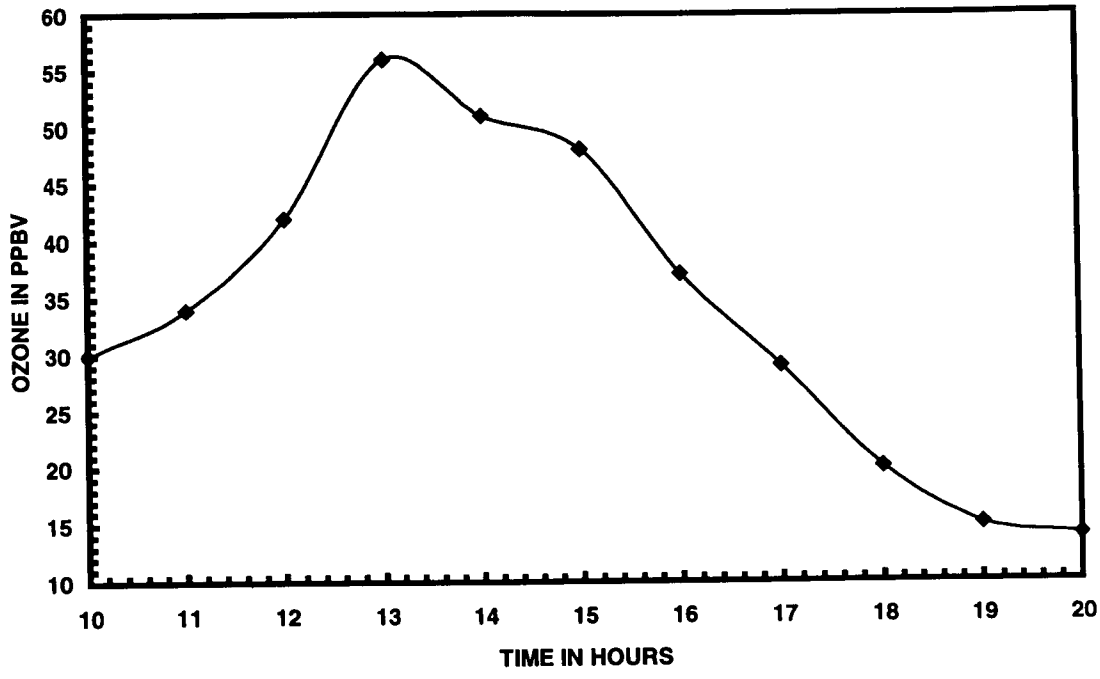


TABLE 1

TRANSMITTER	RECEIVER
Laser Type - Grating Tuned CO_2 Laser Edinburgh Instruments Model WL8 - GT Wavelength Range - 9-11 μm Power - 2- 3 watt CO_2 Spectrum Analyzer - Optical Engg. Optics - ZnSe (Lenses, B.S. etc) He-Ne Laser - 5 mw LINES USED FOR 1.OZONE IN 9 μm BAND λ_{on} =P(14), λ_{off} =P(24) 2.WATER VAPOUR IN 10 μm BAND λ_{on} =R(20), λ_{off} =R(16) 3.ETHYLENE IN 10 μm BAND λ_{on} =P(14), λ_{off} =P(16)	Detector - Cooled HgCdTe (PV) Santa Barbara Model 40742 / SAT PV 708 P Lock-in-Amplifier - Stanford Research Model SR510 Chopper - EG&G PARC, Model 192 Power Meter - Scientech Model 372 Chart Recorder IBM PC/AT 586

4. ACKNOWLEDGEMENT:

The authors are thankful to Director, NPL and Dr. K.K. Mahajan, Head, RASD for their keen interest during the progress of the work.

Lidar Observation of the Nocturnal Inversion Transition in the Lower Atmosphere over Hong Kong

T.M. Mok[1], K.M. Leung[1,2], J.C.L. Chan[1,2], A.H.P. Ho[1], and C.N. Ng[1,2]

[1]Department of Physics and Materials Science
[2]Centre for Environmental Science and Technology
City University of Hong Kong
83 Tat Chee Avenue, Kowloon
Hong Kong, China
Phone: 2788 7707
Fax: 2788 7830
e-mail: aptmok@cityu.edu.hk

Abstract. The time evolution of the vertical lidar profiles during a typical winter evening transition period over Hong Kong, a subtropical coastal city is presented. Results indicate that the nocturnal planetary boundary layer is more stratified under strong radiative cooling conditions. The formation of the nocturnal inversion and the overlying residual layer were also observed. In this study, comparisons between the result and radiosonde sounding data will also be discussed.

1 Introduction

There are many criteria in determining the height h of nocturnal boundary layer (NBL). The dynamical height scale as the low-level wind maximum [1], the thermal height scale that is the height of the ground-based stable layer [2], and also the level which turbulent kinetic energy decreases to 5 percents of its surface values [3]. To understand the behaviour of h is important as it plays a significant role in atmospheric and environmental research, for example h can be a basic input parameter to meso- and synoptic-scale numerical weather forecasting models.

For the past two decades, many researchers have successfully demonstrated the capability of using lidar to study the structure of the daytime convective boundary layer [4, 5, 6, 7], but relatively few nighttime lidar measurements of the PBL have been reported [8, 9, 10]. It is very difficult to determine h based on a single monitoring method.

In this paper, we focus on the temporal evolution of the PBL two hours before and after sunset using a Mie lidar system developed at City University of Hong Kong, Hong Kong. The result presented here is a typical case showing the stratification of the PBL and the formation the NBL during a winter evening under clear sky condition. The distinct features of the nocturnal PBL observed by lidar reveal that it is feasible to use lidar to probe the NBL.

2 Lidar Monitoring Arrangement

The City University of Hong Kong lidar [11] consists of a frequency doubled Nd:YAG laser (output wavelength at 532 nm with a repetition rate of 10 Hz). The output beam axis was aligned colinearly with the optical axis of a 0.25-m diameter Newtonian telescope. A 0.30 m diameter reflecting mirror mounted on a computer-controlled stepping motor is used to redirect the laser beam into the atmosphere from a dome on top of a nine-storey building (about 57 m AMSL). The expanded laser beam is 30-mm in diameter with 0.2-mrad divergence. The telescope collects the backscatter radiation from atmospheric molecules and aerosols. As a light signal is spatially and optically filtered to minimize background noise and then detected by a photomultiplier tube (PMT). The output of the PMT is converted to voltage and then digitized for every 0.02 microseconds (6-m range-resolution) on a digital storage oscilloscope. The digital signals are transferred to the hard disc of a Pentium-Pro PC via GPIB interface. In addition, a CCD camera is used for viewing where the target of the laser beam is pointing in the atmosphere.

For data comparison, we used radiosonde measurements taken by the Hong Kong Observatory, which is 3 km Southeast from our lidar site. The lidar profile is range-corrected by multiplying each data point to the square of its corresponding range value. The inversion algorithm of Klett's [12] is applied to derive the extinction coefficient

3 Results and Discussion

The observation was performed in the clear sky winter evening on 9 December 1997. In Figure 1, a comparison of the lidar and the radiosonde profiles shows that the two sounding systems are consistent in determining the inversion height in the nocturnal PBL. In the lidar profile (figure 1a), we determine the first decrease of the extinction coefficient as the top of the inversion. Conversely, the radiosonde defines the region where the first increase in potential temperature (figure 1b) and coincide as decrease in relative humidity (figure 1c) over isothermal layer [13]. Figure 1 also depicts the formation of the NBL height h at 450 m, which is very much related to the rate of the radiative cooling. Above the NBL the residual layer and capping inversion can be identified.

Figure 2 depicts the time evolution of the vertical lidar profiles, started at local time two hours before (17:00 hr) and ended at two hours after (21:00 hr) sunset. The level at which a sharp decrease in aerosol signals appears indicates the height of the mixed layer; in this case strong mixing occurred during daytime. At LT 2000 hour, the 'ripples' signals at an even low level replaced the previous 'sharp decrease' signal. This can be largely explained the thickening of the entrainment zone. As the night progressed further the layer became more stratified. The NBL depth is about 450 m from ground and the residual layer overlying the NBL has an approximate depth of 650 m. Thus the mixed layer depth decreased at an averaged rate of 50 m per hour at this evening transition period.

This is a preliminary study of the evening transition nocturnal inversion over a subtropical coastal city. The first result is promising in using lidar technique to probe the nocturnal PBL. Detailed data analysis will be presented.

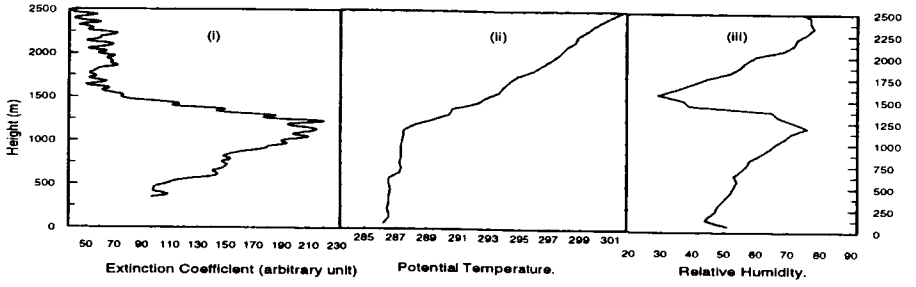


Fig. 1. Data comparison between lidar (i) and radiosonde (ii) and (iii) at LT 20:00 on 9 December 1997.

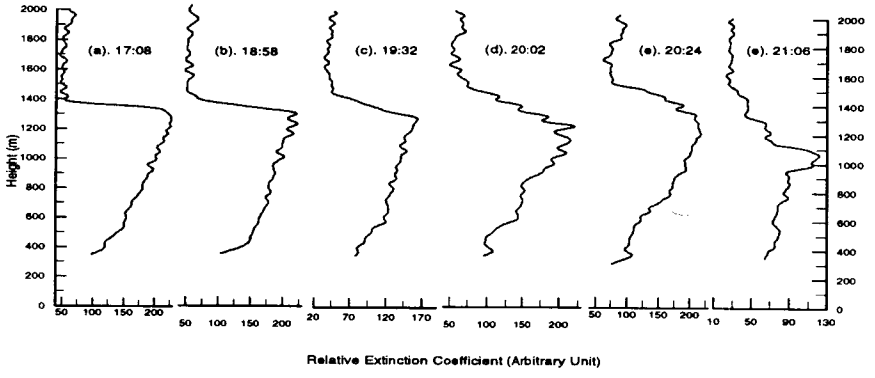


Fig. 2. Lidar signal profile: evolution of evening transition PBL at 20:00 on 9 December 1997.

Acknowledgements The authors are grateful to Mr. K.Y. Chan for his help in preparation of the data and the Hong Kong Observatory for providing the radiosonde data. This work was supported by the Strategic Research Grants 7000429 and 7000646 and the Faculty of Science and Technology, City University of Hong Kong, Hong Kong, China.

References

1. Nieuwstadt, F.T.M., and Driedonks, A.G.M., 1979: The Nocturnal Boundary Layer: A Case Study Compared with Model Calculations. J. Appl. Meteor.,18, 1397-1404.
2. Garratt, J.R., 1992: The Atmospheric Boundary Layer. Cambridge Atmospheric and Space Science Series, Cambridge University Press.
3. Grant, A.M.L., 1997: An observational study of the evening transition boundary-layer. Q. J. R. Meteorol. Soc., 123, 657-677.
4. Kunkel, K.E., Eloranta, E.W., and Shipley, T., 1977: Lidar Observation of the Convective Boundary Layer. J. Appl. Meteor., 16, 1306-1311.
5. Hooper, W.P and Eloranta, E.W., 1986: Lidar Measurements of Wind in the Planetary Boundary Layer: The Method, Accuracy and Results from Joint Measurements with Radiosonde and Kytoon. J. Climate Appl. Meteor., 25, 990-1001.
6. Glaser, E., Dagan, N., Furer, O., Gamliel, M., Yogev, A., Fastig, S., Dayan, U., and Benayahu, Y., 1993: A Comparison of Balloon Soundings and Lidar Scans for Measuring the Height of the Turbulent Mixed Layer at a Coastal Site in Israel. Wat. Sci. Tech., 27, 271-278
7. Marsik, F.J., Fischer, K.W., Mcdonald, T.D.,and Samson,P.J., 1995: Comparison of Methods for Estimating Mixing Height Used During the 1992 Atlanta Field Intensive. J. Appl. Meteor., 34, 1802-1814.
8. Anfossi, D., Bacci, P., Longhetto, A., 1974: An application of lidar technique to the study of the nocturnal radiation inversion. Atmos. Environ. 8, 537-541.
9. Devara, P.C.S., Ernest Raj, P., Murphy, B.S., Pandithurai, G., Sharma, S., and Vernekar, K.G., 1995: Intercomparison of Nocturnal Lower-Atmospheric Structure Observed with Lidar and Sodar Techniques at Pune, India. J. Appl. Meteor., 34, 1375-1383.
10. Ernest Raj, P., Devara, P.C.S., Maheskumar, R.S., Pandithurai G., and Dani K.K., 1997: Lidar Measurements of Aerosol column content in an urban nocturnal Boundary Layer. Atmos. Research, 45, 201-216.
11. Leung, K.M., Lin, T.J., and Chan, J.C.L., 1994: Lidar measurement of wind velocity by tracking a single cloud movement, Abstracts of Papers of the 17th international laser Radar conference, 575-577, Sendai, Japan, 25-29 July, 1994.
12. Klett, J.D., 1981: Stable analytical inversion solution for processing lidar returns. Applied Optics, 20, 211-220, and 1981.
13. Wyngaard, J.C., 1986: Probing the Atmospheric Boundary Layer. Edited by D.H. Lenschow, American Meteorological Society, Boston, Mass..

Multiwavelength DIAL for Trace SO_2 Measurement

Tetsuo Fukuchi, Naohiko Goto, Takashi Fujii, and Koshichi Nemoto

Electrical Physics Department, Komae Research Laboratory
Central Research Institute of Electric Power Industry
2-11-1 Iwado-kita, Komae-shi, Tokyo 201-8511, Japan
TEL: +81 3 3480 2111, FAX: +81 3 3480 3401
E-mail: fukuchi@criepi.denken.or.jp, naogoto@criepi.denken.or.jp,
fujii@criepi.denken.or.jp, nemoto@criepi.denken.or.jp

I. INTRODUCTION

Vertical concentration profiles of approximately 100-300 m range resolution and ppb-order concentration resolution for substances causing acid rain, such as SO_2, are considered necessary for validation of emission and transport models. These profiles can be measured by *in situ* sampling using aircraft, or more conveniently and economically by a ground-based differential absorption lidar (DIAL).

Localized, relatively high concentrations of SO_2, such as smokestack exhaust or volcanic emission have been measured by DIAL in the past [1, 2, 3, 4]. In these cases, the SO_2 concentrations were in the order of 100 ppb with range resolution in the order of 10 m. Range-resolved DIAL measurements of ambient SO_2, whose concentration is in the order of several ppb, have been very few in number [5].

In order to improve the resolution of DIAL measurement of SO_2, a multiwavelength method making use of two DIAL pairs is presented. Calculations of SO_2 measurement error show that multiwavelength measurement is effective in removing the effects due to other species, especially O_3.

II. MULTIWAVELENGTH DIAL

The lidar equation gives the number of backscattered photons received from range between R and $R+\Delta R$:

$$N(R,\lambda_i) = \frac{E_0 \eta A}{E_p} \frac{\Delta R}{R^2} \beta(R,\lambda_i) \exp\left[-2\int_0^R n(R')\sigma_0(\lambda_i) + \alpha_x(R',\lambda_i)dR'\right] \tag{1}$$

Here λ_i is the illumination and detection wavelength, E_0 is the laser pulse energy, η is the optical efficiency of the receiver, A is the effective area of the receiver, $E_p = hc/\lambda_i$ is the energy per photon, ΔR is the range resolution, β is the backscatter coefficient, n and σ_0 are the number density and absorption cross section of the measurement target species, and α_x is the extinction coefficient due to other molecules and particles. The laser pulse width (typically 10 ns) is considered to be much shorter than the time interval $\Delta t = 2\Delta R/c$ corresponding to the range resolution ΔR (typically $\Delta t = 670$ ns for $\Delta R = 100$ m).

The extinction coefficient due to constituents other than SO_2 is given by $\alpha_x = \alpha_M + \alpha_R + \sum_j n_j\sigma_j$ where α_M, α_R are the extinction coefficients due to Mie and Rayleigh scattering, respectively, and n_j, σ_j are the number density and absorption cross section of the interfering atmospheric constituents. The Mie extinction coefficient (at sea level) can be approximated by $\alpha_M(\mathrm{km}^{-1}) \simeq (3.91/R_v)(550/\lambda)^q$ where R_v is the visibility of the atmosphere in km, λ is in nm, and $q = 1 \sim 1.30$ [6]. The principal interfering species in the 300 nm wavelength region is O_3.

The backscatter coefficient is given by $\beta = \beta_M + \beta_R$, where β_M and β_R are the Mie and Rayleigh backscatter coefficients, respectively. Rayleigh backscatter is dominant for heights above ~2 km.

The range-resolved concentration profile of the measurement target species can be found from the number of backscattered photons at the different wavelengths (m total wavelengths):

$$n = \frac{1}{2\Delta R\sigma_0'}\left[\sum_{i=1}^{m} e_i Z(R,\lambda_i) - \sum_{i=1}^{m} e_i B(R,\lambda_i)\right] - \frac{\alpha_x'}{\sigma_0'} \tag{2}$$

where

$$Z(R,\lambda_i) = \ln\left[\frac{N(R,\lambda_i)}{N(R+\Delta R,\lambda_i)}\right], \qquad B(R,\lambda_i) = \ln\left[\frac{\beta(R,\lambda_i)}{\beta(R+\Delta R,\lambda_i)}\right],$$

$e_i = +1$ for large values of $\sigma_0(\lambda_i)$ (corresponding to the "on" wavelengths, at which the absorption by the measurement target species is large) and $e_i = -1$ for small values thereof (corresponding to the "off" wavelengths, at which the absorption is small), and

$$\sigma_0' = \sum_{i=1}^{m} e_i \sigma_0(\lambda_i), \qquad \alpha_x' = \sum_{i=1}^{m} e_i \alpha_x(\lambda_i)$$

σ_0', α_x' reduce to the differential absorption cross section and differential extinction coefficient for the two wavelength case ($m = 2$).

Considering the multiwavelength case to be a superposition of two or more DIAL pairs, m is an even integer and $\sum_{i=1}^{m} e_i = 0$. For $\beta(R,\lambda_i) = \lambda_i^{\nu} f(R)$ where ν = constant, $\sum_{i=1}^{m} e_i B(R,\lambda_i) = 0$. The measurement wavelengths λ_i can suitably be chosen so that $n\sigma_0' \gg \alpha_x'$, in which case eq.(2) yields

$$n = \frac{1}{2\Delta R \sigma_0'} \sum_{i=1}^{m} e_i Z(R,\lambda_i) \tag{3}$$

Table 1: Cases considered for SO_2 measurement.

	DIAL		3 wavelength dual-DIAL				4 wavelength dual-DIAL			
i	1	2	1	2	3	4	1	2	3	4
λ_i (nm)	299.35	300.05	298.65	299.35		300.05	298.05	298.75	299.35	300.05
e_i	-1	+1	+1	-1	-1	+1	+1	-1	-1	+1
σ_0' (m^2)	98.0×10^{-24}		131×10^{-24}				148×10^{-24}			
$n\sigma_0'$ (m^{-1})	2.5×10^{-6}		3.3×10^{-6}				3.8×10^{-6}			
α_x' (m^{-1})	-3.7×10^{-6}		0.83×10^{-6}				0.094×10^{-6}			

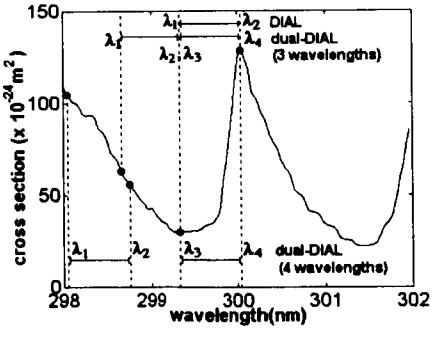


Figure 1: Absorption cross section of SO_2 indicating wavelengths used in DIAL and dual-DIAL

The DIAL wavelength pair ordinarily used for SO_2 measurement is in the vicinity of 299.35 and 300.05 nm. The absorption cross section of SO_2 and the DIAL wavelengths are shown on Figure 1 [7]. The uncertainty in the cross section values is quoted to be $\sim 2\%$. The attenuation coefficients for this pair, for a typical O_3 concentration of 30 ppb, atmospheric visibility of 20 km, and a SO_2 concentration of 1 ppb, are shown on Table 1. Note that the assumption $n\sigma_0' \gg \alpha_x'$ does not hold, indicating that 1 ppb is below the detection limit by two wavelength DIAL.

In order to suppress the effects due to O_3 and aerosols, we consider multiwavelength DIAL measurement consisting of a combination of two DIAL pairs (dual-DIAL). We consider two dual-DIAL cases, as shown on

Table 1 and Figure 1, which are obtained by a combination of two DIAL pairs, one being the ordinary DIAL pair at 299.35 and 300.05 nm. For 3 wavelength dual-DIAL, the "off" wavelengths for each pair are equal ($\lambda_2 = \lambda_3 = 299.35$ nm). For 4 wavelength dual-DIAL, both the "on" and "off" wavelengths are different, the pairs being chosen so that α'_x is minimized. The separation between the "on" and "off" wavelengths is kept constant at 0.7 nm for each pair.

III. ERROR ANALYSIS

The principal sources of noise for a lidar are counts due to detector noise, counts due to background radiation, and statistical noise. In addition to random noise, there are errors in the cross section of the measurement target species and errors due to the existence of interefering species in the atmosphere. In the UV region, the detector noise is not significant, and the background radiation ($S_\lambda = 10^{-6}$ W/cm^2-sr-μm at $\lambda = 300$ nm) need only be considered for large range, for which the number of backscattered photon count N (per time bin) is comparable to the background photon count N_B. Ignoring detector noise, the statistical error for the detected photon counts is given by $\delta N = \sqrt{N + N_B}$. The error in n can be then found from (2):

$$(\delta n)^2 = \left(n\frac{\delta\sigma'_0}{\sigma'_0}\right)^2 + \frac{1}{(2\Delta R\sigma'_0)^2}\sum_{i=1}^{m}\sum_{j=1}^{2}\left[\frac{N_{ij}+N_B}{N_{ij}^2} + \left(\frac{\delta\beta_{ij}}{\beta_{ij}}\right)^2\right] + \left(\frac{\delta\alpha'_x}{\sigma'_0}\right)^2 \tag{4}$$

where $j = 1, 2$ stand for range R and $R + \Delta R$, respectively.

Measurement error based on (4) was calculated using the following system parameters: laser pulse energy $E_0 = 30$ mJ, effective receiver area $A = 0.2$ m^2, receiver optical efficiency $\eta = 0.05$, receiver bandwidth $\Delta\lambda = 5$ nm. The number of measurement sets (for averaging) was variable, $N_s = 100 - 3000$. To calculate the Mie extinction coefficient, we set $\alpha_M(\text{km}^{-1}) = (3.91/R_v)(550/\lambda)^{1.3}$ and used R_v as a variable parameter ranging from 5 to 30 km. The height dependence of α_M was taken from ref. [6]. The concentration of O_3 is not known *a priori*, so we used this as a variable parameter ranging from 0 to 100 ppb.

The following assumptions were made for calculating the measurement error: (1) the laser pulse energy is the same for all wavelengths, (2) the set of shots consisting each DIAL measurement have perfect correlation, and (3) successive measurement sets are independent (uncorrelated) so that the statistical error decreases as $\sim 1/\sqrt{N_s}$ where N_s is the number of measurement sets. Assumption (2) is based on a two laser system, with the "on" and "off" wavelength lasers fired within 1 ms of each other, during which the atmosphere can be considered frozen. To satisfy (3), the pulse repetition rate should be sufficiently low in order for successive pulse pairs to be uncorrelated.

The concentrations of SO_2 and O_3 were taken to be uniform with respect to height and invariant within the integration time. The visibility R_v and background radiation level were also considered to be invariant within the integration time.

Figure 2[a] shows the SO_2 measurement error of two wavelength DIAL and multiwavelength dual-DIAL as a function of vertical range for atmospheric visibility 20 km, ozone concentration 30 ppb, SO_2 concentration 10 ppb, range resolution 100 m and 300 m. The dotted traces represent measurement error in the absence of statistical error (in the limit $N_s \to \infty$). Figure 2[b] shows SO_2 measurement error as a function of vertical range and atmospheric visibility for a fixed ozone concentration of 30 ppb. A similar plot for SO_2 measurement error as a function of vertical range and ozone concentration for a fixed atmospheric visibility of 20 km is shown on Figure 20[c]. The effectiveness of dual-DIAL methods in removing the effects due to ozone can be seen. Figure 2[d] shows the dependence of SO_2 measurement error on the vertical range resolution ΔR at 1 km range, i.e. for $R, \Delta R$ such that $R + \Delta R/2 = 1000$ m. The concentration of SO_2 and O_3 are 10 ppb and 30 ppb, respectively, and the visibility is set to 20 km.

The use of multiwavelength DIAL results in considerable reduction in measurement error over ordinary two wavelength DIAL, especially in the lower range where the statistical error is not dominant. There is no significant difference between three and four wavelength dual-DIAL except for the case of high O_3 concentration.

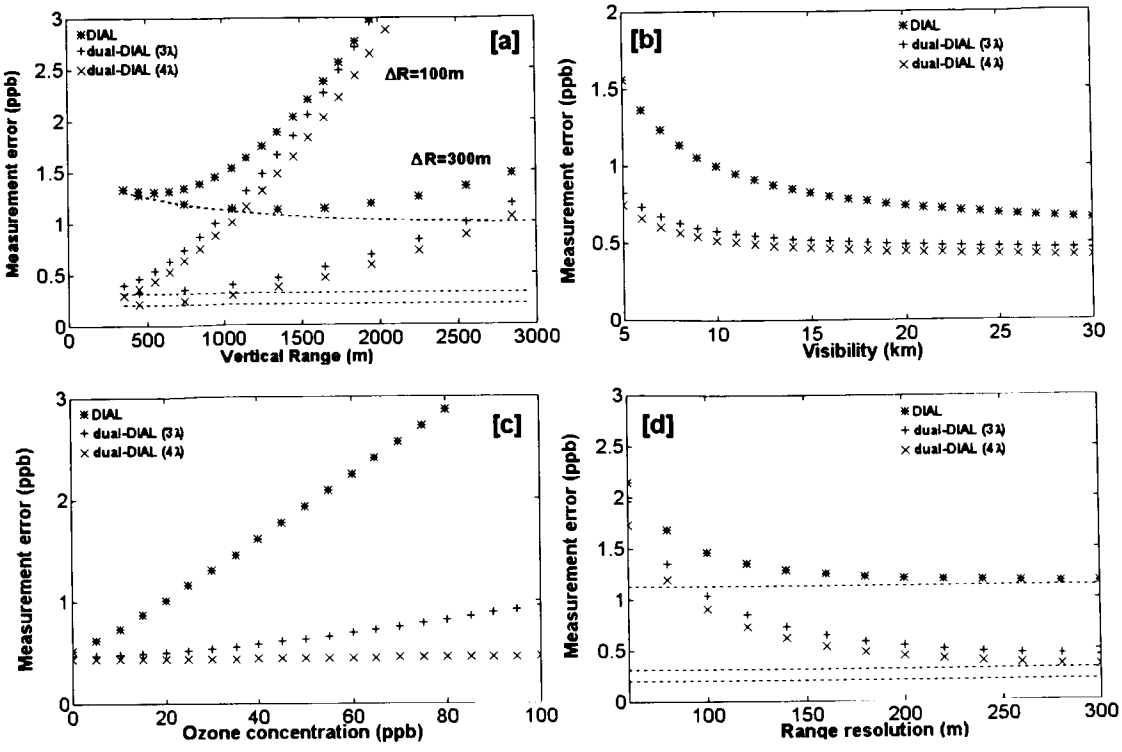


Figure 2: SO_2 measurement error of DIAL and dual-DIAL as a function of variable parameters.

IV. CONCLUSION

In conclusion, a multiwavelength DIAL method consisting of a superposition of two DIAL pairs to improve the accuracy of SO_2 measurement in the lower atmosphere is presented. The effects of ozone and aerosols can be minimized by an appropriate choice of wavelengths. In principle, the measurement accuracy can be improved to below 1 ppb for 100-300 m range resolution. On the basis of this estimation, a multiwavelength DIAL system is currently under development at this laboratory.

References

[1] R. Adrain, D. Brassington, S. Sutton and R. Varey, *Opt. Quant. Electr.* **11**, 253 (1979).

[2] H. Edner, K. Fredriksson, A. Sunesson, S. Svanberg, L. Unéus, and W. Wendt, *Appl. Opt.* **26**, 4330 (1987).

[3] H. Edner, P. Ragnarson, S. Svanberg, E. Wallinder, R. Ferrara, R. Cioni, B. Raco, and G. Taddeucci, *J. Geophys. Res.* **99**, 18827 (1994).

[4] K. Fredriksson, B. Galle, K. Nyström, and S. Svanberg, *Appl. Opt.* **18**, 2998(1979).

[5] J. P. Wolf, H. J. Kölsch, P. Rairoux, and L. Wöste, in *Applied Laser Spectroscopy*, W. Demtöder and M. Inguscio, eds., Plenum, New York (1990), pp.435-467.

[6] R. M. Measures, *Laser Remote Sensing*, John Wiley & Sons, New York, 1984.

[7] D. J. Brassington, *Appl. Opt.* **20**, 3774 (1981).

Airborne Lidar Studies of the Entrainment Zone

Christoph Kiemle and Gerhard Ehret
Lidar Group
Deutsches Zentrum für Luft- und Raumfahrt (DLR)
D-82234 Oberpfaffenhofen, Germany
E-mail: Christoph.Kiemle@dlr.de

Kenneth J. Davis
Department of Soil, Water, and Climate
University of Minnesota, St. Paul, MN 55108

1 Introduction

The entrainment zone is the region of the atmospheric boundary layer where parcels of air from the overlying free troposphere are entrained into the boundary layer as a result of convective thermals impinging upon the capping inversion and generating turbulent mixing. The convection and the resulting turbulence within the boundary layer and the entrainment zone are driven by solar heating of the earth's surface. The entrainment zone is the least well understood portion of the boundary layer. Measurements are sparse because of the altitude above ground and the great spatial and temporal variability of the interface. Model predictions of entrainment vary widely [1] because of the irregular nature of the interface, the lack of data to guide model development, and the small turbulent scales which may be important within the entrainment zone. The entrainment zone is important because the exchange of air between the boundary layer and the free troposphere has a significant impact upon climate, weather and air quality. A better understanding of entrainment processes through lidar observations can improve our understanding of these important issues.

An open question is whether entrainment occurs mostly on a small scale due to mixing at the very top of thermals, or whether most of the mixing is due to engulfment between rising thermals. The scales and mechanisms of entrainment are likely to vary depending upon the depth of the boundary layer, the strength of the convection, the strength of the capping inversion, and wind shear across the boundary layer top.

The boundary layer is characterized by high aerosol and moisture loading, originating from the surface. The aerosol and moisture content is generally much lower in the free troposphere, and a sharp change in the aerosol and humidity profile occurs at the boundary layer top within the entrainment zone. Thus, the boundary layer top, the entrainment zone, and its variability can often be accurately detected with high spatial and temporal resolution by means of a downward-looking airborne lidar system.

2 Experimental Details

A near infrared airborne water vapor DIAL instrument has been developed at the DLR [3]. It uses a narrow-band tunable dye laser for sequentially generating the on-line and off-line wavelengths around 724 nm. The dye laser is pumped by a frequency doubled Nd:YAG laser which operates in Q-switch mode providing 6 nanoseconds short pulses with a repetition rate of 9 Hz. The wavelength calibration is performed by use of the water vapor absorption spectrum from a photo-acoustic cell. The systems' receiver consists of a 35 cm diameter Cassegrain telescope. The backscattered photons are detected with a photomultiplier and digitized at a resolution of 12 bits and a sampling rate of 20 MHz for each laser shot. A micro computer controls the data ac-

quisition and stores all data on a removable disk for further processing on ground.

The system, which is currently being replaced by a new, OPO-based concept, successfully participated in several field campaigns. The largest one was the 1994 Boreal Ecosystem-Atmosphere Study (BOREAS) in central Canada [5], during which the DLR lidar was mounted on board the National Center for Atmospheric Research (NCAR) Electra research aircraft. The Electra made turbulent flux, radiation and lidar observations in and just above the boundary layer along a transect extending across the entire boreal forest biome and into the subarctic tundra. The Electra frequently flew repeated passes of approximately 100 km length over the same flight track but at multiple altitudes. These altitudes were mostly within the boundary layer, with one leg just above so that the downward looking lidar could gather boundary layer aerosol and water vapor data.

Water vapor DIAL results from the BOREAS campaign have already been shown [4]. Also, an analysis of boundary layer top statistics derived from the lidar data has recently been published [2]. We focus here on the entrainment zone backscatter returns from these measurements. Since the aircraft was flying just above the top of the boundary layer, the signal-to-noise ratio for returns from the entrainment zone was optimal. At a typical aircraft speed of 120 m/s, the horizontal lidar resolution is 13 m. The vertical resolution is 7.5 m.

3 Results

Figure 1 shows a lidar backscatter cross section through the top of the convective boundary layer, with an aspect ratio of around 2:1. It is part of a lidar measurement of 60 km length. In the center a strong uprising thermal, around 3 km broad, is detected through relatively strong and homogeneous backscatter. The strong gradient at its top suggests that its vertical motion was strong enough to reach and locally lift the inversion. The surrounding boundary layer top shows a smoother backscatter transition towards the nearly aerosol-free atmosphere above, indicating that mixing processes have already taken place there. To the left and right of the well defined, sharp top of the thermal, slightly weaker backscatter regions are found, probably due

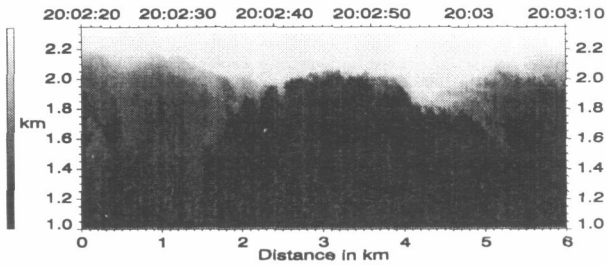


Figure 1: Lidar backscatter cross section of the entrainment zone from a BOREAS flight on August 4, 1994. Darker shades are stronger backscatter and the grey scale is linear. The upper abscissa is time (UT) which corresponds to about noon local solar time.

to engulfment of tropospheric air.

Figure 2, a 4:1 aspect ratio zoom into a measurement spanning a distance of 80 km, shows a morning boundary layer with a mean depth of around 400 m. The very irregular boundary layer top is caused by early morning growth coupled with strong wind shear across the entrainment zone. Winds of 17 m/s were measured above the boundary layer on this day, blowing from left to right, in contrast to 11 m/s winds within the boundary layer. The tops of what we believe are thermal plumes appear slightly tilted in the plot. At 16:29:56, what appears to be an overturning thermal plume is visible at the boundary layer top.

In contrast, Figure 3 shows the early morning boundary layer, before convection has been established. A residual well-mixed boundary layer extends from the ground to about 0.5 km. From about 0.5 to 2.5 km, several smooth haze layers of varying thickness are evident. These layers were evident to the naked eye. Later in the day, boundary layer turbulence significantly perturbs these layers, though not to the point of breaking them up.

Since low backscatter most often stems from free atmosphere air and high backscatter from boundary layer air, intermediate backscatter intensities can be attributed to a mix of free atmosphere and boundary layer air which is mostly likely, in the convective case, entrained air. By defining two thresholds for low and high backscatter in the lidar plots, air parcels belonging to the entrainment zone can be separated from pure free atmosphere and

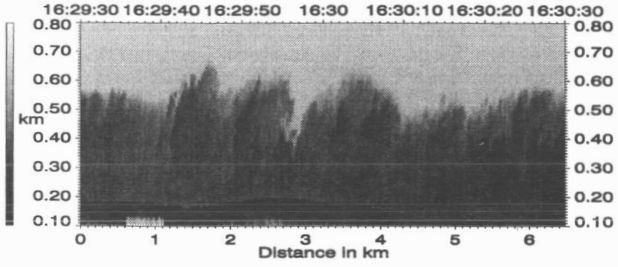


Figure 2: Backscatter cross section of a BOREAS flight on September 3, 1994, about local 10:00. The black curve in the bottom is the ground return. Clearly visible is the irregular top of the aerosol-laden boundary layer.

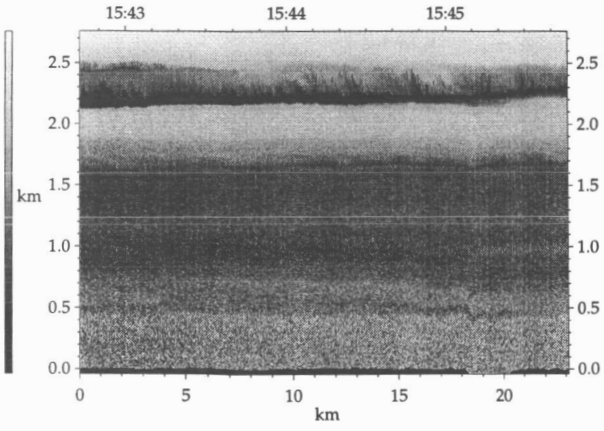


Figure 3: Lidar plot for July 30, 1994, about local 9:00. The strong backscatter at the top comes from a smoke layer. Forest fires were frequently observed during BOREAS.

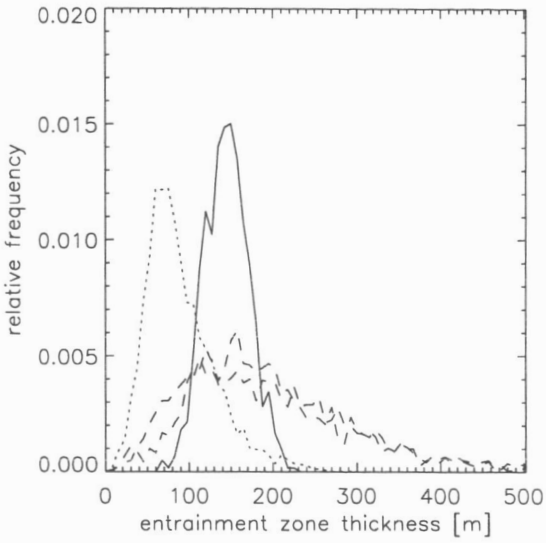


Figure 4: Frequency distribution of entrainment zone thickness for three convective boundary layer (dashed) and one stable layer interface (solid).

pure boundary layer air. Their vertical extent is a measure of the entrainment zone thickness. This method works as long as backscatter behaves like a conserved quantity. In order to check the applicability and validity of this entrainment zone detection method, we tested it on four different boundary layer top measurements including three convective boundary layer tops and one stable interface, lying between 1.5 and 2.0 km altitude in Figure 3.

The result can be found in Figure 4 where integral normalized histograms of entrainment zone thickness series determined via the above mentioned method are compared. The method has been applied to a midday convective boundary layer measurement of which Figure 1 is a subset (dashed curve), to a measurement performed one and a half hours earlier at the same site (superposed dashed), to a morning convective boundary layer measurement, of which Figure 2 is a subset (dotted), and to the stable layer transition of Figure 3 (solid).

The good match of both dashed histograms belonging to two different but in time and space neighboring measurements indicates a robust behavior of the entrainment zone detection method. A statistical analysis of these two entrainment zone

depth time series yields a mean of 207 (193) m, a standard deviation of 117 (101) m and a skewness value of 1.7 (0.9). A positive skewness means an asymmetric histogram with a smoother slope towards larger values, as seen in Figure 4. This is related to deep entrainment events into the boundary layer occurring between the relatively sharply defined thermal tops.

The morning boundary layer case, while exhibiting a much thinner entrainment zone due to the small boundary layer depth (only 90 m mean thickness and 42 m standard deviation), has a comparable skewness of 1.1. In contrast to these convective cases, the solid curve is nearly gaussian as expected for a stable layer transition, with a skewness of only 0.1. This demonstrates the ability of the method to discriminate various transition zones. Although few cases have been examined up to now, we have confidence in these results because we obtained fairly good agreement between the method described here and another entrainment zone extraction scheme based on fitting a line to the backscatter slope at the boundary layer top, and because the results of Figure 4 look internally consistent and match our expectations.

4 Summary

The method presented gives a means of quantitatively describing the entrainment zone and of discriminating different boundary layer regimes using entrainment zone thickness series derived from lidar data. Boundaries between stable layers can be distinguished from convective layers through the skewness of the entrainment zone thickness. We note that this way of determining the entrainment zone from lidar data is only feasible when the atmospheric backscattering is horizontally homogeneous and when there is a backscatter gradient across the entrainment zone. The method fails if the aerosol concentration is vertically homogeneous and horizontally heterogeneous, as was sometimes the case during BOREAS due to forest fires. It also fails when hygroscopic aerosol growth is prevalent in the boundary layer and causes rapid and extreme increases in backscatter.

A next step will be to apply the method to the whole BOREAS lidar data base to obtain relationships between entrainment zone thickness and classical boundary layer parameters derived from the BOREAS *in situ* measurements such as convection, inversion and wind shear strengths. Enlarged and improved by data from other campaigns, these relationships will hopefully enable us to set up a rough classification of boundary layers simply using backscatter lidar measurements of the entrainment zone and of boundary layer depth. On a long term perspective such a classification could, applied to data from future operational spaceborne lidars, help improve boundary layer parameterization in weather or climate forecasting models. Another goal is to compare these observations to large-eddy simulations of entrainment which utilize nested grids to achieve hight spatial resolution in the entrainment zone. Data which can be used to validate the predictions of these models is lacking.

References

[1] Ayotte, K. W., P. P. Sullivan, A. Andren, S. C. Doney, A. M. Holtslag, W. G. Large, J. C. McWilliams, C.-H. Moeng, M. J. Otte, J. J. Tribbia, J. C. Wyngaard, An evaluation of neutral and convective planetary boundary-layer parameterizations relative to large eddy simulations, *Bound. Layer Meteor.*, *79*, 131-175, 1996.

[2] Davis, K. J., D. H. Lenschow, S. P. Oncley, C. Kiemle, G. Ehret and A. Giez, Role of entrainment in surface-atmosphere interactions over the boreal forest, *J. Geophys. Res.*, *102*, D24, 29219-29230, 1997.

[3] Ehret, G., C. Kiemle, W. Renger and G. Simmet, Airborne Remote Sensing of Tropospheric Water Vapor Using a Near Infrared DIAL System, *J. Appl. Opt.*, *32*, 4534-4551, 1993.

[4] Kiemle, C., G. Ehret, A. Giez, K. J. Davis, D. H. Lenschow and S. P. Oncley, Estimation of boundary-layer humidity fluxes and statistics from airborne differential absorption lidar (DIAL), *J. Geophys. Res.*, *102*, D24, 29189-29203, 1997.

[5] Sellers, P. J., et al., The Boreal Ecosystem-Atmosphere Study (BOREAS): an overview and early results from the 1994 field year, *Bull. Amer. Meteor. Soc.*, *76*, 1549-1577, 1995.

The EPFL UV Ozone DIAL: results and upgradings

Valentin Simeonov, François Jeanneret, Philippe Quaglia, Hubert van den Bergh,
and Bertrand Calpini.
Swiss Federal Institute of Technology DGR Laboratory of Air and Soil Pollution
CH 1015 Ecublens VD Switzerland
Phone:++41(0)21 693 5789, Fax:++41(0)21 693 3626, E-mail: valentin.simeonov@epfl.ch

1. Introduction

The EPFL Ozone DIAL was built mainly to supply data for 3D Eulerian mesoscale chemical transport model developed at our institute. The latter are used for simulating pollutant dynamics over regions like Athens Greece, Milan Italy or Geneva and Obwalden in Switzerland [1,2] and providing technical guidance to air quality management agencies. The domain covers typically ranges in the order of 100x100 km horizontally, and up to 6 km vertically. The horizontal grid resolution is 1 to 5 km, with a vertical resolution of some tens of meters for the lowest layer of the model up to 500 meters for the top layer. Our ozone DIAL data are first used to test the accuracy of the model, and also to supply data for the model boundary conditions.

2. The Ozone DIAL System

The optical layout of the system is shown in Figure 1. The transmitter consists of two solid state NdYAG laser sources which emit sequentially at 266 nm (NdYAG 4th harmonic generation) with a delay of 300 μs, an energy per pulse of 100 mJ at 10 Hz.

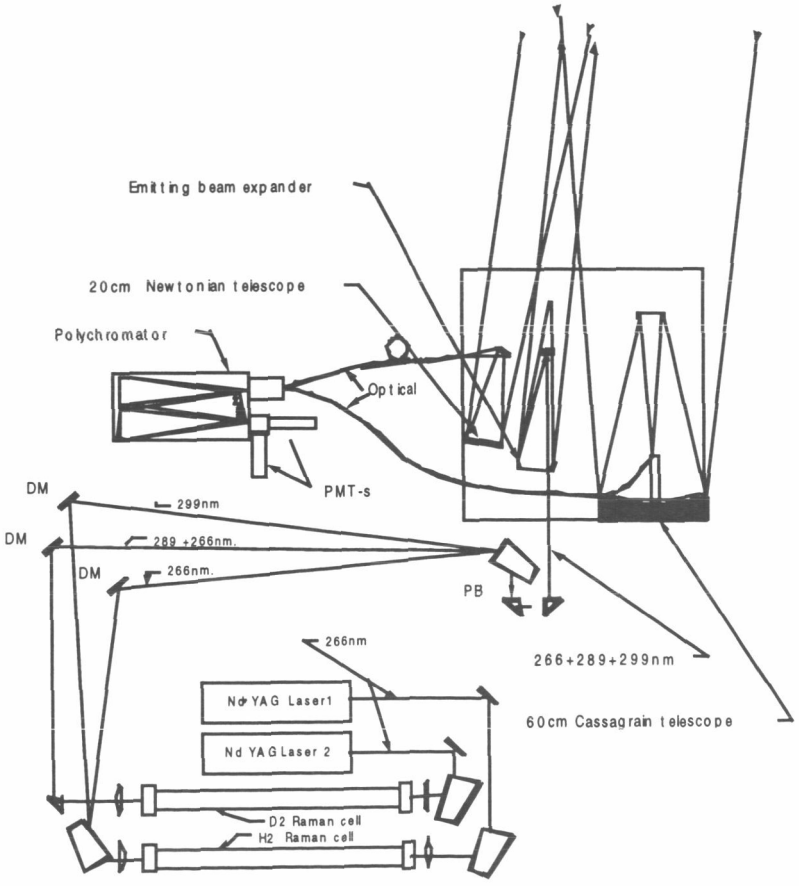


Figure1. Lidar optical layout.

The laser emission is converted in 289 and 299nm by two low pressure single pass Raman cells filled respectively with D_2 and H_2. The 1st Stokes from the cells and the residual pump from the H_2 cell are combined in one beam using a scheme based on a Pellin Broca prism (PB) and three dichroic mirrors (DM). Because of the time delay between the laser pulses, it is possible with this combining scheme to obtain two DIAL wavelength pairs 266-289nm and 289-299nm. This three wavelengths emitter offers the possibility to optimize the choice of the DIAL wavelength pairs needed for different air quality conditions (ozone smog episode and low visibility, or clean atmospheric conditions) and for different ranges [2,3]. The lidar receiver is based on the use of two telescopes operating simultaneously: a "short range" Newtonian telescope with a primary mirror diameter of 20 cm and a 60 cm focal length for DIAL measurements between 50 and 600 m, and a "long range" Cassegrain telescope with a primary mirror diameter of 60 cm and a 460 cm focal length for measurements from 500 m up to the free troposphere (typ. up to 3 km AGL). The spectral separation of the different lidar signals is carried out by a SPEX 500 monochromator. To separate the long and short range signals, the light from the two telescopes is applied by optical fibers at different heights on the entrance of the monochromator, symmetrically to its optical axis. The two PMT's (Thorn EMI 9829 QB) at the exit of the polychromator detect the light from each telescope, and the analog signals from the PMTs are preamplified, and captured with an 8-bits 500 MHz transient digitizer with a special shot per shot electronics [4].

3 Results and Discussion

As a first example, Figure 2 shows time series of ozone vertical profiles measured with the short range telescope in the center of Geneva on July 18th 1996. The lidar ozone concentrations are presented from 120 up to 700 m AGL between 3 and 9 p.m. The same figure shows also DOAS data at 20m AGL. Relatively high ozone concentrations, around 80 ppb, are measured with a well mixed layer before 16 h over the range presented here, thus revealing essentially constant ozone concentrations from the ground level up to 700 m. From 17 to 20 h, this situation changes rapidly and a strong increase in ozone concentration is measured between 450 and 600 meters, with values reaching 120 ppb. Around 21 h., this episode is over and the ozone concentrations return to about 70 ppb, as measured by DOAS at ground level, and with maximum values around 90 ppb at higher altitudes.

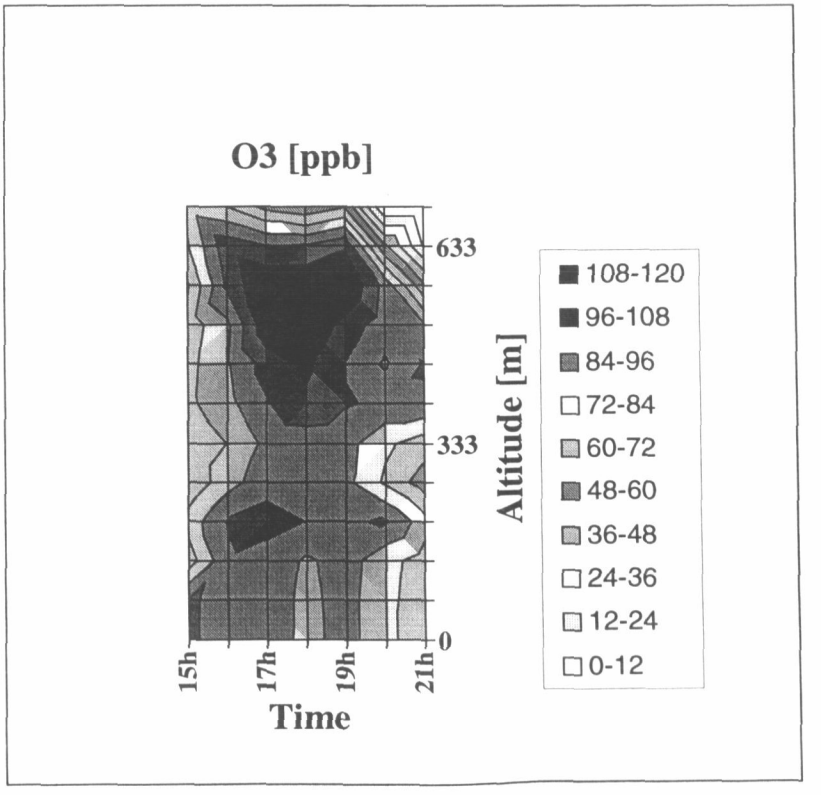


Figure 2. Ozone DIAL time series and ground DOAS data measured in Geneva town July 18th 1996.

One should note that above 600 m, these measurements with the smaller of the two telescope systems are hampered by an insufficient signal to noise ratio for the more absorbed wavelength λ_{on}.

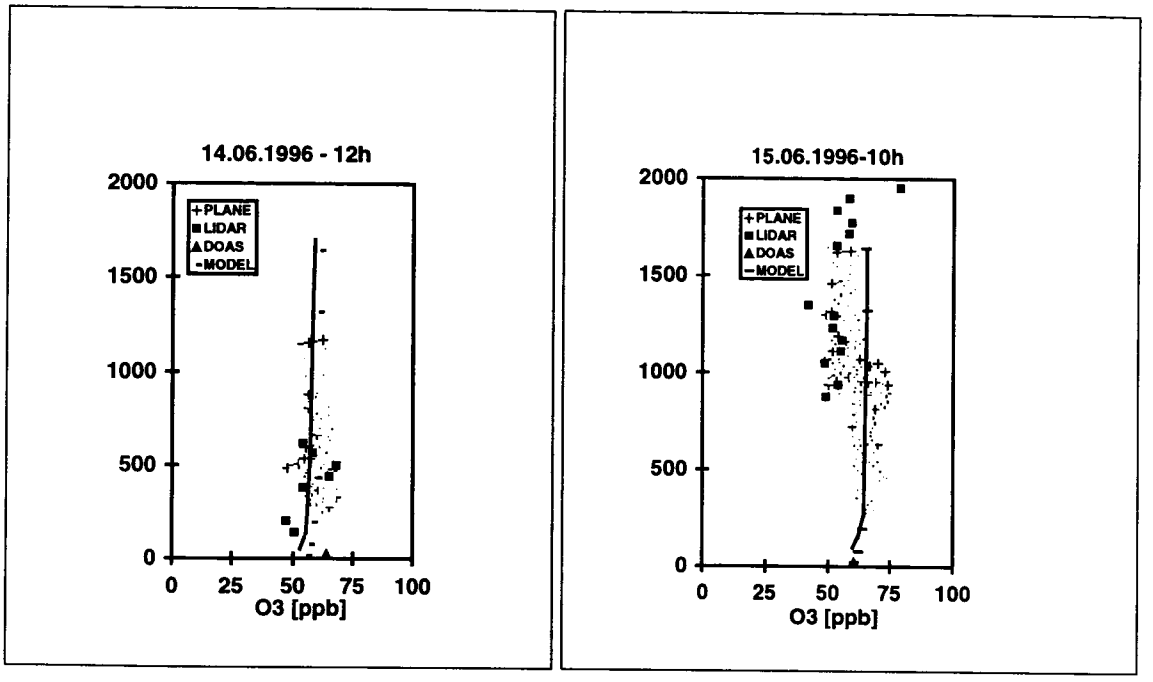


Figure 3: Comparison between DIAL, air plane, ground based DOAS, and model prediction for the ozone concentration above Changins during the Geneva field campaign. Left: short range DIAL. Right: long range DIAL

The profiles presented in Figure 3 were taken in Changins near Nyon at the NE border of the model domain. They are shown together with a motorglider ozone data and the model prediction. The ozone values measured by the motorglider in a radius of 4 km around the lidar vertical axis are plotted here, ranging from 300 to 1'600 m, and for a time window of 1 h around noon on July 14th and respectively 10 a.m. on July 15th.. The model was applied for the episode between July 13th and July 16th. Results of the model show good agreement with the measurements. Nevertheless, the model result at ground level slightly underestimates the effective ozone concentration measured by the DOAS for the 14.06 at 12 p.m, while the top of the mixing layer is well defined around 900 m AGL by the airplane and the lidar data, but is not well retrieved on the simulated profile.

4 Recent developments

The EPFL DIAL system has been continuously upgraded between the different field campaigns. For the emitter, D_2 was replaced by the cheaper and more efficient $CH_4/H_2/Ar$ mixture [5] that produces predominantly Ist CH_4 Stokes at 289.4 nm. In the receiving part, the monochromator was replaced by 3 solar blind Corion filters which have high enough rejection for solar radiation. It is possible to use this configuration only if the 2 DIAL wavelengths are emitted sequentially, thus making the acquisition system simpler, but no more able to acquire simultaneously the 3 different wavelengths. The replacement of the EMI PMTs with Hammatsu R5600 has been recently done. The latter PMTs have extended linearity, no detectable afterpulse effect and are far more compact. Unfortunately they suffer from some spacial inhomogenity of the photocathode sensitivity. This affects strongly the short range lidar signal, but we managed to reduce this inhomogenity to an acceptable level by using suitable diffusers. The complete results of this work will be published soon, and part of it will be presented at the 19th ILRC.

References

1.B. Calpini, V. Simeonov, F. Jeanneret, J. Kuebler, V. Sathya, and H. van den Bergh "Ozone LIDAR as an A nalytical Tool in Effective Air Pollution Management: The Geneva 96 Campaign Chimia" 51 (1997) 700-704, Neue Schweizerische Chemische Gesellschaft ISSN 0009-4293.

2. L. Schoulepnikoff, V. Mitev, H. van den Bergh, B. Calpini, "Lidar for tropospheric air pollution monitoring", review article submitted to *Encyclopedia of Environmental Analysis and Remediation*, John Wiley & Sons, Ed. Robert A. Meyers, in press 1998.

3. L. Schoulepnikoff, V. Mitev, V. Simeonov, B. Calpini, H. van den Bergh, "High -power single-pass Raman shifters in the ultraviolet" *Applied Optics*, Vol. 36, pp 5026-5043, 1997

4. L. Fiorani, B. Calpini, L. Jaquet, H. van den Bergh, E. Durieux, "A correction scheme for experimental biases in DIAL tropospheric ozone measurements, based on the analyses of shot per shot data samples", *Applied Optics*, 1997 Vol 36, No 21 pp 6857-6863,1991

5. V.Simeonov, V.Mitev, B.Calpini, H. van den Bergh. "Raman frequency shifting in CH_4:H_2:Ar mixture pumped by the fourth harmonic of Nd:YAG" submitted to *Applied Optics* 1998

Towards Quantifying Mesoscale Flows in the Troposphere Using Raman Lidar and Sondes

B. Demoz,[1] D. Starr,[2] K. Evans,[1] D. Whiteman,[2] S. Melfi[1], D. Turner,[3] R. Ferrare,[4] J. Goldsmith,[5] G. Schwemmer,[2] and M. Cadirola,[1]

1. INTRODUCTION

Water vapor plays an important role in the energetics of the boundary layer processes which in turn play a key role in regulating regional and global climate. It plays a primary role in Earth's hydrological cycle, in radiation balance as a direct absorber of infrared radiation, and in atmospheric circulation as a latent heat energy source, as well as in determining cloud development and atmospheric stability. Water vapor concentration, expressed as a mass mixing ratio ($g\ kg^{-1}$), is conserved in all meteorological processes except condensation and evaporation. This property makes it an ideal choice for studying many of the atmosphere's dynamic features.

Raman scattering measurements from lidar also allow retrieval of water vapor mixing ratio profiles at high temporal and vertical resolution. Raman lidars sense water vapor to altitudes not achievable with towers and surface systems, sample the atmosphere at much higher temporal resolution than radiosondes or satellites, and do not require strong vertical gradients or turbulent fluctuations in temperature that is required by acoustic sounders and radars.

Analysis of highly-resolved water vapor profiles are used here to characterize two important mesoscale flows: thunderstorm outflows and a cold front passage. The data were obtained at the Atmospheric Radiation Measurement Site (CART) by the ground-based Department of Energy/Sandia National Laboratories lidar (CART Raman lidar or CARL) and Goddard Space Flight Center Scanning Raman Lidar (SRL). A detailed discussion of the SRL (Ferrare et. al., 1995) and CARL (Goldsmith et al., 1998) performance during the IOPs is given by others in this meeting.

[1]University of Maryland Baltimore County, Baltimore, MD; bdemoz@climate.gsfc.nasa.gov; (301) 286-2930
[2]NASA/Goddard Space Flight Center, Greenbelt, MD
[3]Pacific Northwest National Laboratory, Richland, WA
[4]NASA/Langley Research Center, Hampton, VA
[5]Sandia National Laboratories, Livermore, CA

2. THUNDERSTORM OUTFLOW

Two cases of thunderstorm outflows from the 1994 Remote Cloud Sensing Intensive Operation Period (RCSIOP) are presented. At about 1200 on 27 April 1994, a thunderstorm moved into the CART region from the Texas panhandle and Oklahoma border. Low level clouds were found (satellite) in advance of the storm. A wind shift, from SW to NNE, at about 0300 indicated arrival of an "inflow" region over the CART site. The associated low clouds were obaserved after about 0500. As evident in the SRL observations (Fig. 1), the cloud layer was thin, extending from 1 to 1.5 km, and exhibited a very flat base. This feature is common to pre-storm environments. Fankhauser (1976) showed that the inflow of an ordinary multicell hailstorm was derived from a layer which, at 20 km ahead of the storm, was restricted to below 1 km above ground level.

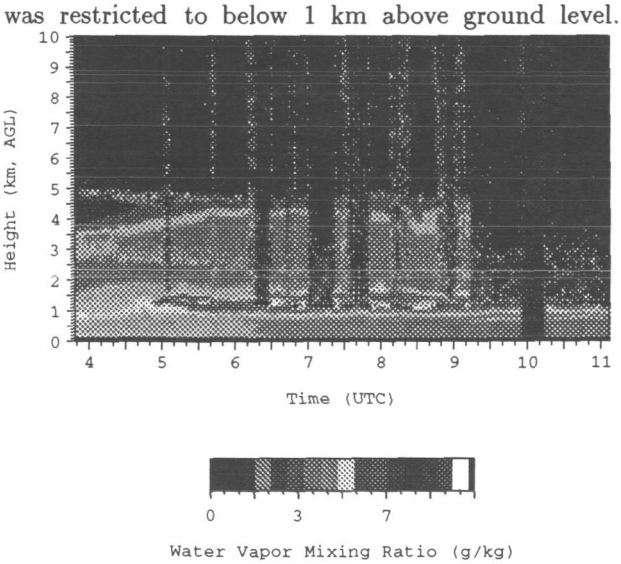


Figure 1. SRL-sensed water vapor mixing ratio ($g\ kg^{-1}$) profiles on 27 April 1994 over the CART station. Note the vertical stipling, which indicates attenuation by cloud, and the data gap around 1000.

Marwitz et al. (1972) also reported that a distinct cloud base associated with an organized updraft can be detected up to 30 km away from an approaching storm. Here, however, the low level cloud deck ex-

tended more than 100 km ahead of the storm and persisted until the storm passed overhead after 1500. In this case, attenuation by the low level cloud deck limited the SRL observations of water vapor structure at middle and upper-tropospheric levels after 0900. However, the advance of the upper level moisture and outflow (anvil) is captured by the rawinsonde observations at 1200 (Fig. 2). In addition, to showing the sub-sounding (less than 3hr) details of the lower cloud the SRL reveals atmospheric structure above cloud and details of the boundary layer moisture stratfication (drying with time and storm proximity).

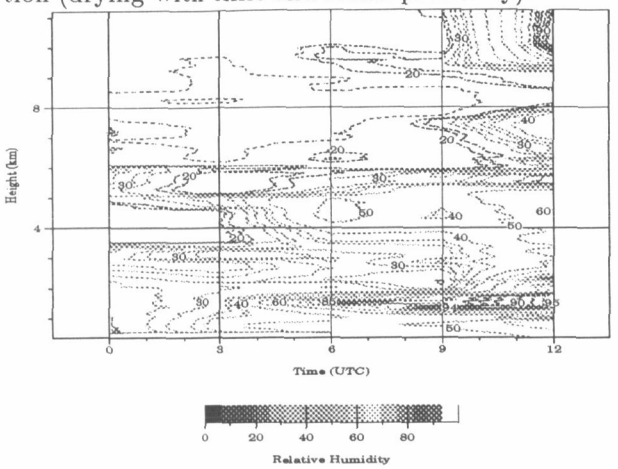


Figure 2. Time-height contour of rawinsonde derived profiles of relative humidity for 27 April 1994.

Another example of thunderstorm outflow and anvil clouds is shown in Fig. 3. This occurred on 29 April 1994. The low-level moisture was capped by a relatively dry atmosphere. Below about 2km, wind direction changed from westerly at 0000 to NE and became stronger with time in agreement with thunderstorm inflow observations (Frankhauser 1976). A moist layer at 3-4.5 km, and another in the upper troposphere were detected. The latter agrees well with the expected structure and location of anvil plume formation according to the models of Browning (1977). The anvil (usually composed of broad cirrus shields and mamma clouds) forms as air diverges horizontally in all directions and carries small ice crystals away from the top of the main updraft core into the down-shear direction.

SRL data for this night are shown in Fig. 4. The figure is remarkably similar to the soundings, but of much higher resolution. The vertical structure of the continuous decrease in moisture in the lowest 2 km, indicated by the soundings, is well documented. The SRL observations also capture the mid-tropospheric and upper tropospheric moist layers. The anvil moisture plume outflow is shown as a continuously lowering base similar to what is often observed by radars, visually. The Pennsylvania State University radar (not shown here) detected the first anvil cloud echo at about 1500, about 4 hours later.

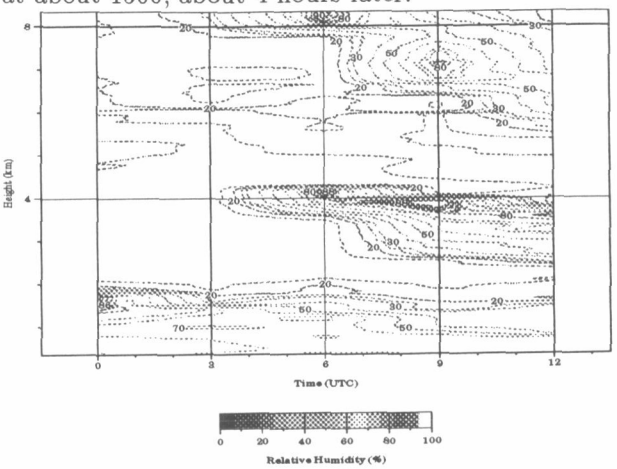


Figure 3. Same as Fig. 2, except for 29 April 1994. Note the data gap centered on the 1800 sounding above 6.0 km.

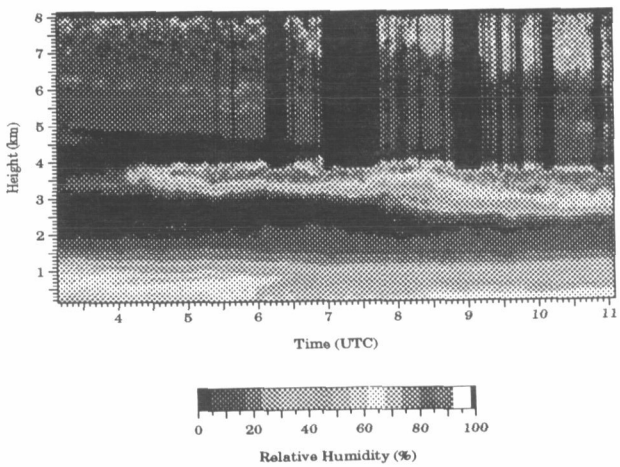


Figure 4. SRL derived relative humidity (%) profiles on 29 April 1994 over the CART station. The RH is derived using the 3hr sonde profiles of temperature and pressure. Note the continously lowering anvil in the upper right corner.

2.1. Cloud-Base Measurements

A comparison of the SRL derived cloud base heights (derived using data from the aerosol channel), to those measured by a Belfort Laser Ceilometer (BLC, usually limited to below 3-4 km) and by a Micro Pulse Lidar (MPL; Spinhirne 1993) are shown in Fig. 5. The figure shows the excellent correlation between these instruments in detecting cloud base altitudes in both

cases. Average cloud base altitudes (km) on 27 April (top figure) were 1.3(±0.08), 1.15 (±0.07), and 1.15 (±0.07) for the BLC, MPL and SRL aerosol channel, respectively. Altitudes of 80-90% relative humidity derived from the SRL water vapor channel data are also shown in Fig. 5. These data sets also reveal a moist layer "cloud" at about 7.5 to 8 km altitude. This is possible because the SRL laser signal is capable of acquiring information above cloud level provided the cloud is not very thick and/or through gaps in the overhead cloud, which was apparently the case. Note that the high altitude moisture detected by the SRL was absent in Fig. 2 because the sonde had wandered far from the site. A very good correlation betweeen the instruments is also shown for the 29 April case (lower part of Fig. 5).

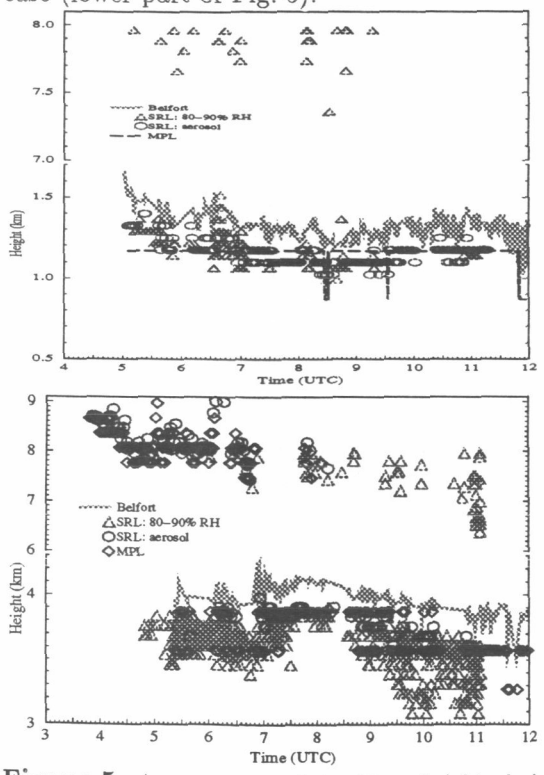


Figure 5. A comparison of cloud base heights derived from measurements made by the SRL aerosol (circle) and water vapor (triangle) channels, Belfort ceilometer (solid line), and the Micro-Pulse Lidar (dotted line) over the CART station on 27 and 29 April 1994.

Average cloud heights (km) of 3.71 (±0.16), 3.79 (±0.09), and 3.96 (±0.11) were detected by the MPL, SRL, and BLC aerosol channel, respectively. The MPL and SRL also show the presence of upper tropospheric clouds with continuosly lowering bases until 0700. But, only the SRL detects this moisture associated with the anvil outflow past 0700.

3. NON-PRECIPITATING COLD FRONT

Fronts, three-dimensional zones demarcating air masses of different origin and characteristics, are one of the main weather-producing atmospheric structures. As such, considerable effort has been devoted in documenting frontal organization and structure. Most studies of cold fronts use data from rawinsondes, satellite, tower and surface mesonets (dense network of meteorological instruments). Most of these instruments are limited in the information they provide on frontal structure and dynamics. Radars are good at locating clouds and precipitation zones but are unable to provide data in regions where clouds or high concentrations of relatively large aerosols are absent. Tower and acoustic radars do provide valuable data sources in the analysis of cold front dynamics (Shapiro et al. 1985), but are limited to altitudes of less than about 600 m. Instruments capable of acquiring continuous and high vertical resolution data (e.g Raman lidar) are required for a detailed study of frontal slope, thickness, cross-front mixing and many other issues. Below, we present analysis of a cold front observed on 28 September 1997 by both the CART Raman lidar and the SRL.

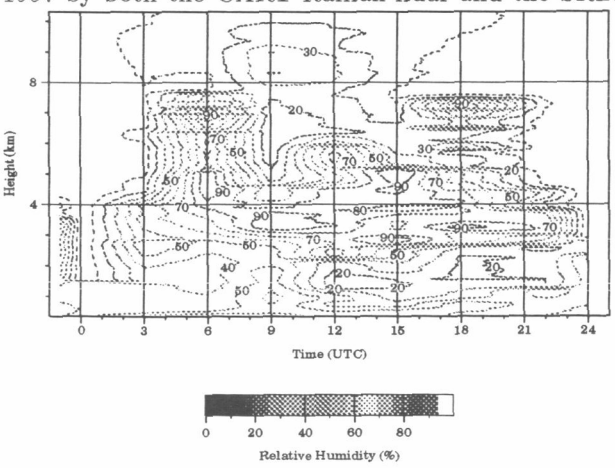


Figure 6. Same as Fig. 2, except for 28 September 1997.

A contour of relative humidity (Fig. 6) derived from the soundings (3hr) reveals the atmospheric structure, albeit crude, including the moist boundary layer prior to frontal passage (0900) and the drying in post-frontal conditions at low levels. It also shows the saturated elevated layer (cloud) with base at 2.5 km, following the data gap at 0300-0600. This 3-hr resolution of the structure of the atmosphere during the cold frontal passage, however, does not show the fine scale

dynamics and structure nor does it capture any cross-front mixing events that may be taking place. On the other hand, at 75 m vertical and 1-2 minute temporal resolution the CARL measured mixing ratio profiles (Fig. 7), detail the atmospheric structure to about 8 km altitude. This images of Raman lidar includes daylight operation (1200-2400), a recently added advantage. Note that during day-time operation, the signal-to-noise ratio is very low above about 5 - 6 km.

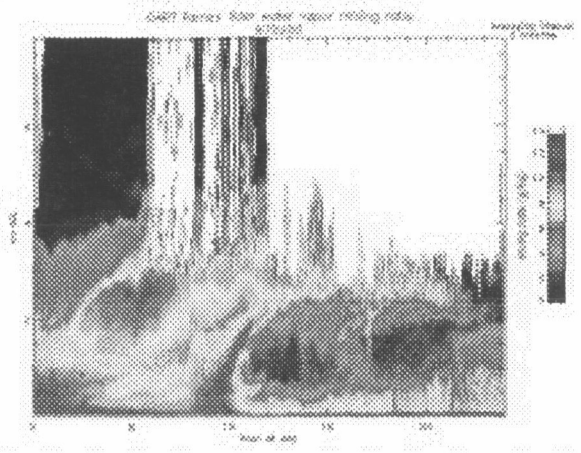


Figure 7. CART Raman Lidar sensed water vapor mixing ratio ($g\ kg^{-1}$) profiles on 28 September 1997 over the CART site. Note again that the vertical stipling indicates attenuation by cloud and information is lost above 5-6 km after about 1600 due to low signal-to-noise ratio.

The passage of the front at the surface was determined to be a little past 1000, indicated by the drying of the boundary layer to mixing ratios of less than about 4 $g\ kg^{-1}$. The leading edge of the cold front resembles the structure of a gravity current (Smith and Reeder 1988) with the leading edge of the front forming a nose-like structure (gravity "head") and buffered from the ground by a slightly moist layer (friction layer). Other interesting features include, the elevated moist region (at 2 - 3 km and around 0500) leading the frontal surface. From Fig. 7 and wind profiler measurements (not shown), it was found this moisture originated at near-surface (below mainly about 1 km) and was a back-flow of the airmass that was lifted by the frontal surface. Note that these features and many others can not be deduced from the 3-hourly soundings or any other conventional meteorological instrument but are readily observed using Raman lidar.

4. SUMMARY

The results shown here demonstrate the Raman lidar system's superb capability in visualizing the detailed vertical and horizontal stratification of the atmosphere to more than 8 km altitude. Fine-scale structures in the boundary layer and/or between air mass boundaries were easily detected and the dynamic processes involved in generating this structures inferred. The water vapor mixing ratio images also compare well to the prevailing conceptual models of fronts or gravity currents and thunderstorm outflows. The moisture "shadow" of the anvil (evaporated and/or sub-visual) is detected well before (3-4 hrs) the presence of ice (detection by radar). Comparisons of cloud base data derived from the Raman lidar (SRL), a micro pulse laser, and a ceilometer were also in excellent agreement.

5. REFERENCES

Ferrare, R. A., S. H. Melfi, D. N. Whiteman, K. D. Evans. F. J. Schmidlin and D. O'C. Starr, 1995: A comparison of water vapor measurements made by Raman Lidar and radiosondes. *J. Atmos. Oceanic Technol.*, **12**, 1177-1195.

Browning, K.A., 1977: The structure and mechanisms of hailstorms. *Meteor. Monogr.*, **38**, 1-43.

Fankhauser, J.C., 1976: Structure of an evolving hailstorm, Part II: Thermodynamic structure and airflow in the near environment. *Mon. Wea. Rev.*, **104**, 576-587.

Goldsmith, J.E.M., F.H. Blair, S.E. Bisson, and D.D. Turner, 1998: Turn-Key Raman Lidar for Profiling Atmospheric Water Vapor, Clouds, and Aerosols. In Press. *Applied Optics.*

Marwitz, J.D., A.H. Auer, and D.L. Veal, 1972: Locating the organized updraft on severe thunderstorms. *J. Appl. Meteor.*, **11**, 236-238.

Shapiro, M.A., T. Hampel, D. Rotzoll, and F. Mosher, 1985: The frontal hydraulic head: A meso-α scale (1 km) triggering mechanism for mesoconvective weather systems. *Mon. Wea. Rev.*, **113**, 1166-1183.

Smith, R.K., and M.J. Reeder, 1988: On the movement and low-level structure of cold fronts. *Mon. Wea. Rev.*, **113**, 1166-1183.

Spinhirne, J. D., 1993: Micro pulse lidar. *IEEE Trans*, **31**, 48-55.

Raman/DIAL Technique for Ozone Measurements

Steven T. Esposito and C. Russell Philbrick
The Pennsylvania State University
Department of Electrical Engineering and
Applied Research Laboratory
University Park PA 16802
ste101@psu.edu and crp3@psu.edu

Abstract

The Lidar Atmospheric Profile Sensor (LAPS) instrument is capable of simultaneously measuring profiles of ozone, water vapor, temperature, and optical extinction. The measured profiles are integrated, for user selected intervals, to calculate and display the real-time atmospheric profiles with their associated errors, $\pm 1\sigma$ standard deviation. Profiles of ozone are obtained from a Differential Absorption Lidar (DIAL) analysis of the Raman shifted scatter of N_2 and O_2. The LAPS instrument uses the "solar blind" portion of the ultraviolet spectrum to obtain measurements during daytime periods when large background limits visible measurements.

Introduction

Penn State University has developed the Lidar Atmospheric Profile Sensor (LAPS) as a prototype instrument for the U.S. Navy. The LAPS instrument is capable of providing real-time data products of meteorological properties to determine the refractive conditions in the atmosphere. Several sub-systems have been specifically designed into the LAPS instrument in order to make the instrument simple to operate. User friendly software has been written for the LAPS instrument to constantly monitor the subsystems as well as display a real-time data product. With little training an individual can operate the instrument effectively to produce a data output.

The LAPS instrument uses molecular scattering properties of the species in the lower atmosphere to simultaneously measure profiles of ozone, water vapor, temperature, and optical extinction due to aerosol/particle contributions [1,2]. The profiles are currently obtained each minute, with a vertical resolution of 75 meters from the surface to 7 km. In the near future, the vertical resolution will be improved to the range of 3 to 15 meters using a new fast electronics package that has been demonstrated as a single channel prototype in our laboratory.

Measurement Technique

Ozone profiles are obtained from a DIAL (Differential Absorption Lidar) analysis of the Raman shifted scatter of N_2 (285 nm) and O_2 (276 nm) which occur on the steep side of the Hartley absorption band of ozone (see Figure 1). The tropospheric ozone can be measured during both the daytime and nighttime because of the capability of the instrument to use the "solar blind" portion of the ultraviolet spectrum from the 4th harmonic of the Nd:YAG laser. The day sky background wavelengths are dark because of stratospheric ozone absorption The process used to obtain the ozone profile is illustrated in Figure 2. First, The integrated ozone profile is obtained by taking the ratio of the O_2/N_2 signals. This can be seen in the left panel of Figure 2. .Since photo-multiplier tubes (PMT) are used to detect the backscattered photons, the error bars seen in the left panel of Figure 2 are associated with Poisson statistics, that is, the error is determined from the square-root of the number of photon counts [3]. The ozone profile comes from the differentiation of this integrated measurement and can be seen in the right panel of Figure 2. The ozone profiles must be integrated for 15 to 30 minutes to obtain an acceptable signal to noise ratio.

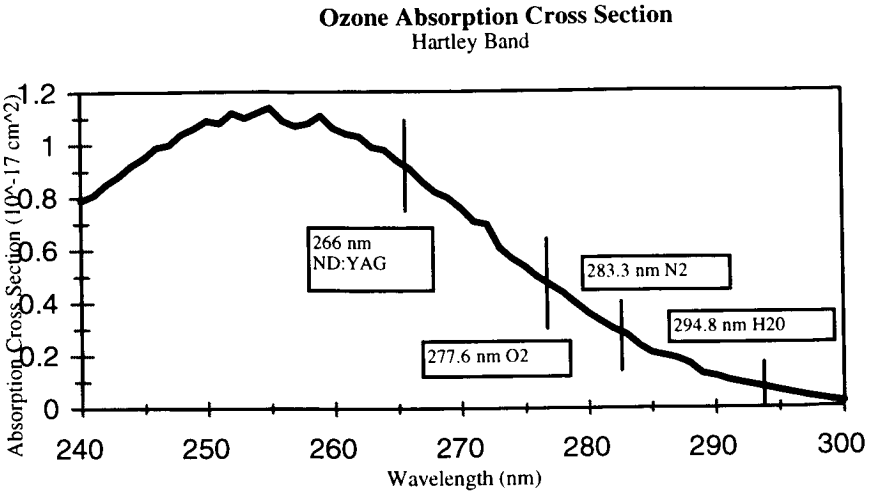


Figure 1. The Hartley band absorption cross-section of ozone is shown with the location of the wavelengths of the 4th harmonic of the ND:YAG laser and Raman shifted wavelengths for N_2, O_2, and H_2O are indicated.

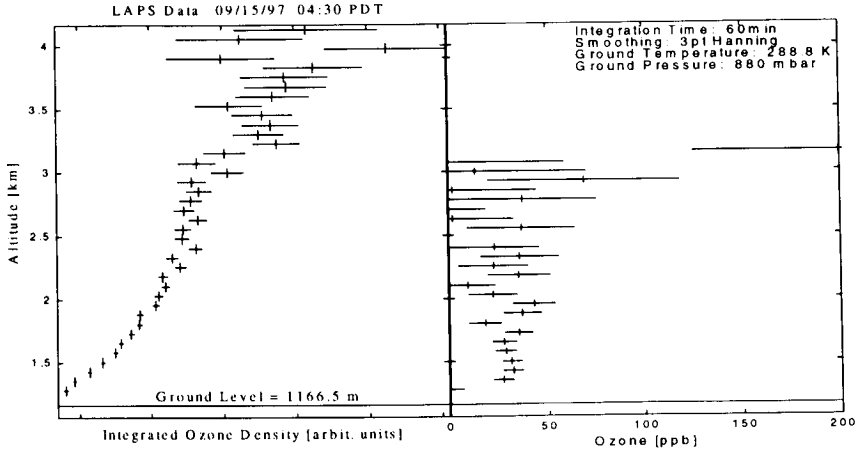


Figure 2: A data sample is used to show how lidar data is analyzed to obtain an ozone profile. The left panel of the figure is the integrated ozone density with arbitrary units. The right panel of this figure illustrates the differentiation to get the final profile.

Experimental Data

During August and September 1997 the LAPS instrument was used in the SCOS (Southern California Ozone Study) program to investigate the urban pollution in the Los Angeles area. The PSU lidar field measurement activity in the SCOS'97 program was undertaken to investigate the ozone production in the Los Angeles basin and subsequent transport into the high desert that lies to the east. The instrument was co-located at a site with a RASS (Radio Acoustic Sounding System) instrument at a meteorological station of Radian International Corporation located in Hesperia, California. This site was located in the high desert at the top of the Cajon Pass and was chosen because the Cajon Pass is believed to be a passage which allows ozone to flow from Los Angeles out into the high desert.

During the SCOS campaign the LAPS instrument collected data for nearly 10 hours per day. This was just one of many instruments collecting data during the SCOS '97 campaign. A sample of an ozone profile from the LAPS real-time data display can be seen in Figure 3. This profile was integrated for 60 minutes from 04:30 PDT to 05:30 PDT on 15 September 1997. Figure 4 shows a time sequence plot of ozone for data also obtained on the morning of 15 September. This data was integrated for 30 minutes and updated every 10 minutes. This display illustrates the vertical changes in ozone density as a function of time. The ozone density is ascending as time progresses and is attributed to the lee waves coming from the mountains in the Cajon Pass.

Also during the SCOS'97 campaign, three sets of coordinated measurements were obtained using the LAPS lidar instrument in conjunction with instruments on a University of California, Davis aircraft. On the 18th and 19th of September, the aircraft performed ascending and descending flights which approximately mapped the sides of a square box about 2 km on each side of the lidar beam. Each ascent and descent took approximately 15 minutes. A comparison of the data from LAPS and the airplane can be seen in Figure 5. The LAPS data is integrated for 30 minutes and is centered around the time of ascent for the airplane.

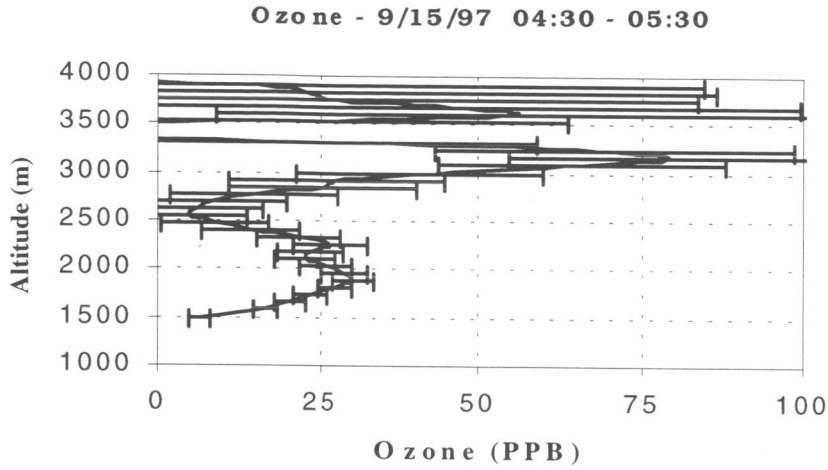


Figure 3: An example of the real-time display of ozone density shows the graph a controller would see on the LAPS console on 15 September 1997.

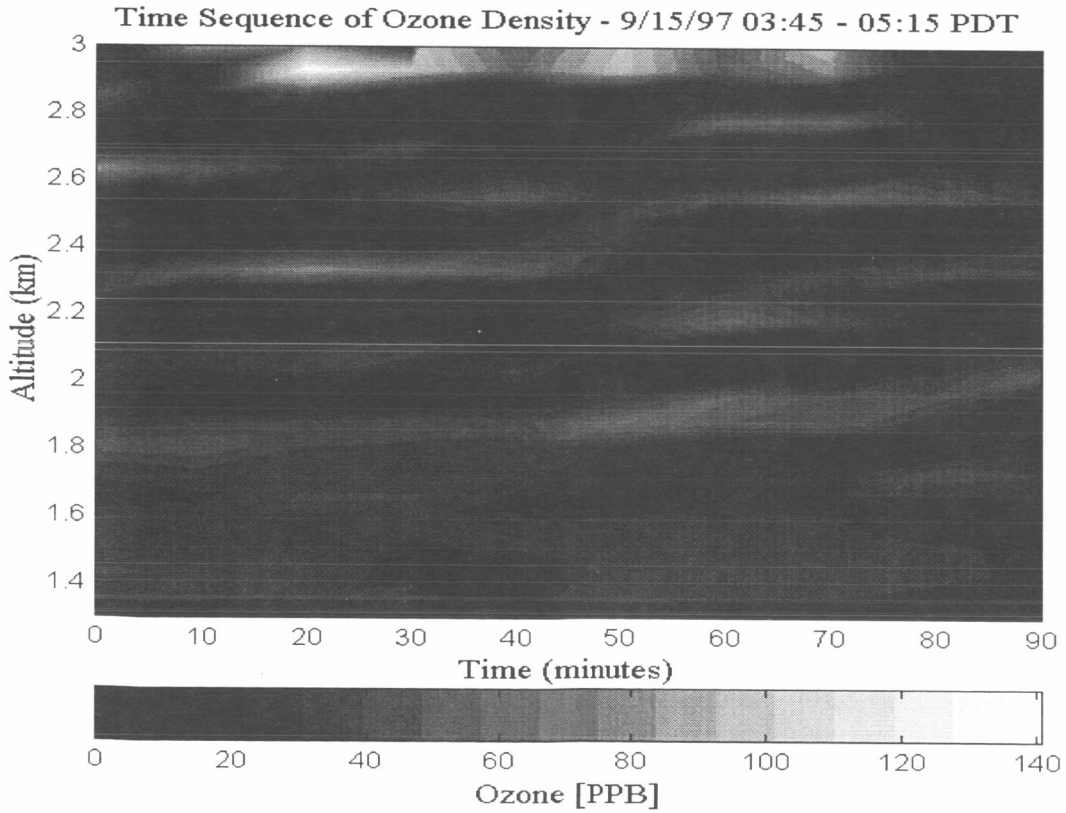


Figure 4: This display shows a time sequence ozone density starting at 03:45 PDT on 15 September 1997 from the LAPS instrument located at the Hesperia, CA site.

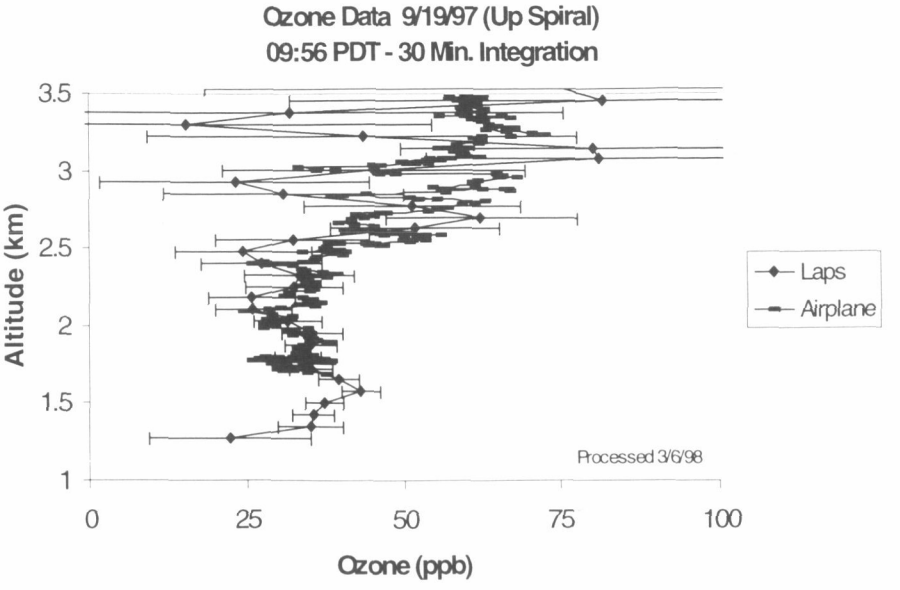


Figure 5: A comparison of ozone data from the LAPS instrument and the University of California, Davis aircraft from 19 September 1997.

Summary

The LAPS instrument uses a DIAL analysis of the Raman shifted scatter of N_2 (285 nm) and O_2 (276 nm) to obtain real-time profiles of ozone density, with a vertical resolution of 75 meters. The minimum integration time for these profiles is 15 to 30 minutes depending on atmospheric conditions. The "solar blind" spectral region is used to obtain profiles of ozone absorption in intense daylight. The LAPS instrument has been compared with other instruments that measured the same atmospheric properties using different techniques and has performed well. This instrument is able to constantly monitor and display absorption properties of tropospheric ozone. This paper shows the preliminary results from the major data set obtained. Simultaneous measurements of water vapor, temperature and optical extinction at three wavelengths was obtained.

Acknowledgments

Special appreciation for the support of this work go to SPAWAR PMW-185, California Air Resources Board (CARB), US Marine Corp at 29 Palms, the Mojave Desert Air Quality Management District, and the US EPA Monitoring Methods Research (Sect 8215). The efforts of Prof. John Carroll from the University of California, Davis, D. B. Lysak, Jr., T. Petach and Mike Zugger have contributed much to the success of this project.

References

1. C. R. Philbrick and D. B. Lysak, "Measurement Capability of the LAPS Lidar," Proceeding of the Battlespace Atmospheric Conference, San Diego, California, December 1997.
2. C. R. Philbrick and D. B. Lysak, "Atmospheric Optical Extinction Measured By Lidar," Proceeding of the Battlespace Atmospheric Conference, San Diego, California, December 1997.
3. W. Durbin, "Lidar Measurements of Ozone in the Lower Atmosphere," Masters Thesis, Department of Electrical Engineering, Penn State University, 1997.
4. Balsiger, Franz and C. Russell Philbrick, "Lower-tropospheric Temperature Measurements Using a Rotational Raman Lidar," Optical Instruments for Weather Forecasting, SPIE Proceedings Vol 2832, pg 45-52, 1996.

Lidar Observation of the Atmospheric Boundary Layer over Jakarta, Indonesia

Mego Pinandito, Imam Rosananto, Ii Hidayat, Muharyan Syamsudin, and Santoso Sugondo
Reaearch & Development Center for Calibration, Instrumentation & Metrology
Indonesian Institute of Science (KIM-LIPI), Kompleks Puspiptek Serpong Tangerang, Indonesia
Phone 62-21-7560562 ext.3063, Fax 62-21-7560568
E-mail mego@kim-server.iptek.net.id

Nobuo Sugimoto and Ichiro Matsui
National Institute for Environmental Studies, 16-2 Onogawa, Tsukuba 305 Japan
Phone 81-298-50-2459, Fax 81-298-51-4732, E-mail nsugimot@nies.go.jp

Takao Kobayashi
Fukui University, 3-9-1 Bunkyo, Fukui 910 Japan
Phone 81-776-27-8557, Fax 81-776-27-8557
E-mail kobayasi@optele.fuee.fukui-u.ac.jp

1. Introduction

Air pollution in Jakarta is getting worse due to the growth of urban populations, increasing number of cars and traffic congestion, and the expansion of industry. Jakarta faces Sea of Java in the north, and it is considered that a typical air pollution phenomenon which is generated by photochemical reactions of pollutants and the transportation by sea/land breeze is occuring in Jakarta. In fact, high concentration of ozone is often recorded in an inland part of the Jakarta area. The wind system in Jakarta is a combination of seasonal wind and sea/land breeze. The seasonal wind is westerly in wet season and easterly in the dry season. During transition period, seasonal wind is weak and heavy air pollution is often observed.

In order to study the air pollution in Jakarta, the lidar network system consisting of two Mie scattering lidars and one differential absorption lidar was constructed in a cooperative project of the New Energy and Industrial Technology Development Organization (NEDO) of Japan and the Indonesian Institute of Science (LIPI). The lidar network system consists of three lidars, two Mie scattering lidars and one differential absorption lidar (DIAL). Three lidar are installed at three locations in Jakarta along a line perpendicular to the coastline to observe transportation by sea/land breeze (Sugimot et al. 1997). In this paper, we report on the measurement of atmospheric boundary layer structure over Jakarta using the lidar network system.

2. Lidar System

The lidar network system consists of two Mie scattering lidars and one DIAL. The Mie scattering lidars employ compact flashlamp pumped Nd:YAG lasers operated at 1064 nm fundamental. The lidars are installed in shelters and directed vertically. It can be operated automatically for a long period. One of the Mie lidar has a rotating wedged window for scanning conically to measure wind velocity with a correlation method (Matsui et al 1990).

The DIAL system is a multipurpose lidar fasility which employs two Nd:YAG laser pumped optical parametric oscillators. The system is also installed in a shelter. It is designed for measuring distribution of ozone and sulfer dioxide in the near UV region, and nitrogen dioxide in the 450-nm region. It has full scanning capability. It can be also operated as a vertically looking Mie lidar. Specifications of the DIAL and Mie lidars are listed in Table 1 and 2.

Table 1 Specification of the DIAL

Laser	Nd:YAG laser pumped OPO (SpectraPhysics MOPO730 x2) Compact Nd:YAG for Mie mode			
Target	O_3	SO_2	NO_2	aerosol
Wavelength(nm)	(on/off)			
	280 /285	300.1 /299.5	448.1 /446.6	1064
Differential absorption cross section (10^{-23} m^2)				
	20	98	2.2	
Output energy (mJ)				
	10	10	50	100
Pulse repetition (Hz)		20		20
Receiver diameter (cm)		25		
Receiver FOV (mrad)		0.5 - 2		
Filter bandwidth (nm)				
	10(or 35)	4(or 35)	4	9
Detector		Photomultiplier (DIAL) APD (Mie at 1064 nm)		
AD converter sampling rate (Msamples/s)		20		
ADC accuracy (bits)		12		
Scanner		two mirror two axes scanner		
Measurement mode		scan/slant/vertical		

Table 2 Specification of the Mie lidar system.

Laser	Compact flash lamp pumped Nd:YAG laser	
	Wavelength (nm)	1064
	Output energy (mJ)	300
	pulse repetition (Hz)	10
Receiver telescope diameter (cm)		25
	Field of view (mrad)	0.5 - 2
	Filter bandwidth (nm)	9
Detector	Si Avalanche photodiode (APD)	
Analog to digital converter (ADC)		
	sampling rate (Msamples/s)	20
	ADC accuracy (bits)	12
Measurement mode		vertical

3. Observation of the Atmospheric Boundary Layer

The locations of the three lidars are indicated in Fig. 1. An example of diurnal variation of aerosol profile (range-corrected time-height indication) at the three locations in Jakarta city is shown in Fig. 2.

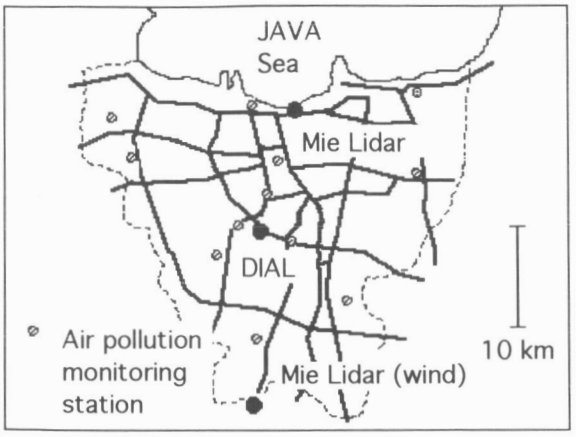


Fig. 1 Locations of the three lidars in Jakasrta.

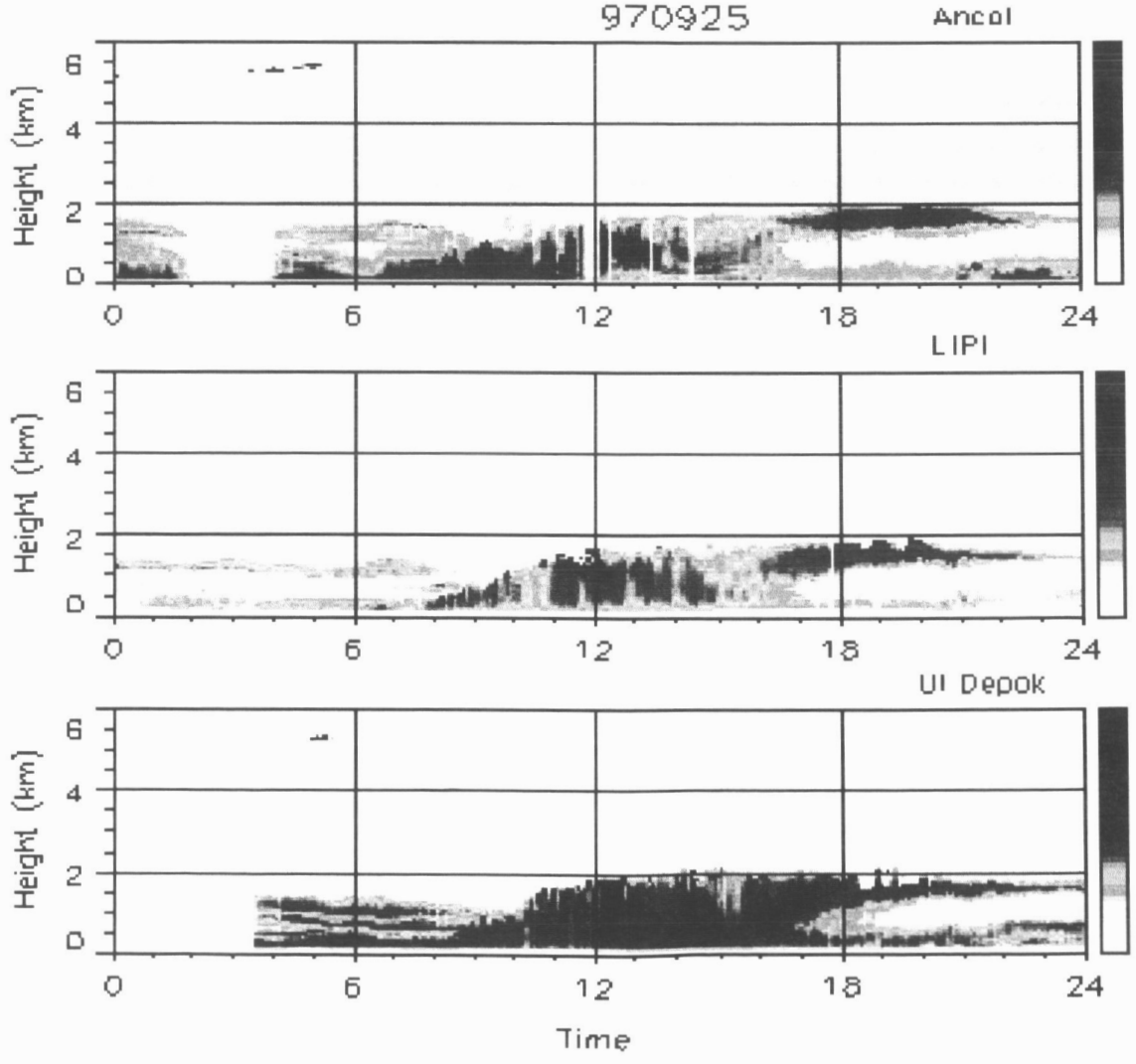


Fig.2 Diurnal variation of aerosol profiles measured at the three locations in Jakarta.

The top panel of Fig.2 indicates the observation at the location close to the coast, the middle and the bottom indicate locations approximately 10 km and 20 km inland. The structures are similar, but it can be seen that boundary layer height is higher in inland. Also, time delay in the structures are seen. We are studying the observed boundary layer structure by comparing with radio sonde measurements carried out by LAPAN in the same period in Jakarta.

Figure 3 shows boundary layer structure in the wet season (upper panel) and dry season (lower panel). It is seen that the structure is very different in the wet and dry seasons. The boundary layer height seems higher in the wet season. We plan to continue observation and carry out climatological study using lidar data.

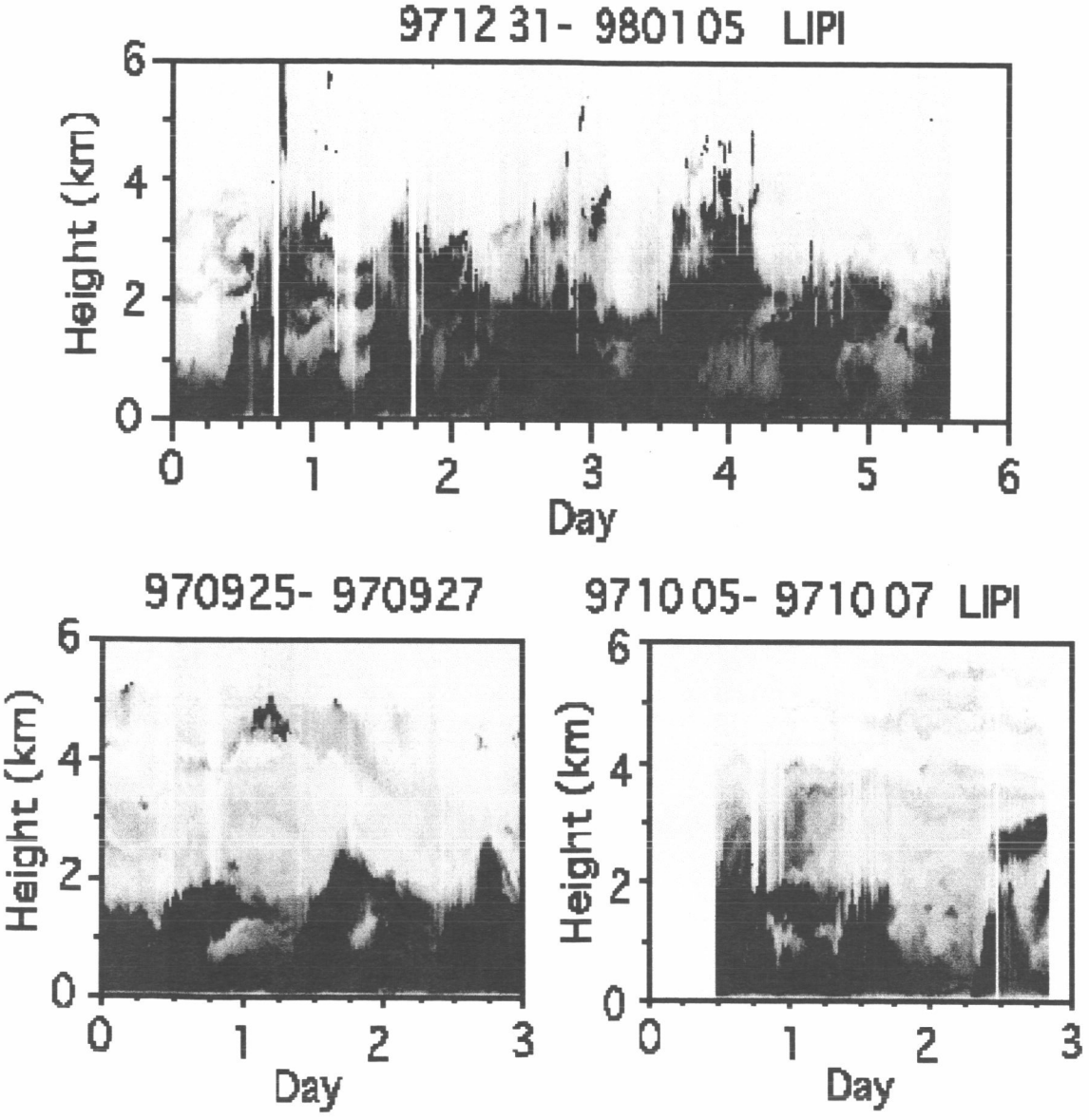


Fig.3 Difference in boundary layer structure in the wet season and the dry season in Jakarta.

References

Matsui, I., Sugimoto, N., Sasano, Y., Shimizu, H. (1990). Wind Profiling by a Conical-Scanning Time-Correlation Lidar. Jpn. J. Appl. Phys. 29, 441

Sugimoto, N., Matsui, I., Kobayashi, T., Ishii, T., Murata, S., Yasuda, N., Takano, H., Pinandito, M., Rosananto, I., Hidayat, I., Syamsudin, M. (1997). Development of a Lidar Network System for Monitoring Atmospheric Environment in Jakarta City, CLEO Pacific Rim '97, Chiba./ Also on a web page at http://wwwris.nies.go.jp/LIPILRtest/LIPILRe.htm

Lidar Measurements of the Atmospheric Boundary Layer (ABL) dynamics at Buenos Aires (Argentina).

Javier Fochesatto, Mario Lavorato, Pablo Cesarano, Eduardo Quel
División Radar Láser-CEILAP (CITEFA-CONICET)
Zufriategui 4380-1603 Villa Martelli-Argentina
lavorato@udceilap.edu.ar.

Cyrille Flamant, Jacques Pelon
Servicie d'Aeronomie du CNRS. Universitè Paris-6. France
jacques.pelon@aero.jussieu.fr

Pierre Flamant
Laboratoire de Météorologie Dynamique. Ecole Polytechnique.Palaiseau. France.
flamant@lmdx04.polytechnique.fr

Abstract. Since mid 1995 until now, an effort has been undertaken at CEILAP in Argentina to document the ABL in a urban area in the Buenos Aires suburb (34.6S, 58.5W), characterized by a complex terrain with industrial districts, motor highways, large forested parks and the Río de la Plata river. A backscatter lidar with a Nd:YAG laser transmitter (0.532 nm) pointed vertically was used to conduct the measurements. Later on a pyranometer was installed at the same site. Meteorological information from radiosoundings at the nearby international airport are also collected on a regular basis. The results, i.e. the height of the ABL and the entrainment zone, show different behaviors according to the meteorological conditions and display large day-by-day fluctuations. The development of a convective ABL reaching 1300 m in summer and 700 m in winter was measured in clear day, in absence of clouds. This summer the height of the ABL is lower than usual due to the meteorological conditions prevailing in the Buenos Aires geographical area. It show a connection between the ABL dynamics and El Niño 1997 event.

Water Vapour Mixing Ratio Measurements using the Purple Crow Raman-Scattering Lidar

C. Bryant, P. S. Argall, R. J. Sica
Department of Physics and Astronomy, The University of Western Ontario
London, Ontario, Canada N6A 3K7
Phone: (519)661-2111 ext 6509, Fax: (519)661-2033, E-mail: chadb@lucille.physics.uwo.ca

R. M. Hoff
Atmospheric Environment Service
Downsview, Ontario, Canada

Introduction

The Purple Crow Lidar is located at the Delaware Observatory, 30 km southwest of London, Ontario, Canada. The lidar is currently undergoing modifications to allow continuous nighttime measurement of water vapour mixing ratio in the troposphere and stratosphere, density fluctuations from 1 to 100 km and temperature from the tropopause to 100 km. Temperature in the upper mesosphere and lower thermosphere are measured by both Rayleigh-scattering and sodium fluorescence. Rayleigh-scatter measurements have been taken since 1994, while the first measurements of sodium and water vapour have been made recently.

The Purple Crow Raman-Scattering Lidar uses a frequency doubled, 20 Hz pulsed Nd:YAG at 532 nm as its transmitter. A 2.65 meter diameter liquid mercury mirror is used to collect the backscatter from the lidar [*Sica et al*, 1995]. An optical fibre, placed at the focus of the mirror, directs the returned photons to the detector table. On the detector table, two photomultipliers, one with a filter for Raman scattering from molecular nitrogen (607.3 nm), the other from water vapour (660.3 nm) measure the backscattered photons. Both filters have a bandwidth of one nanometer.

Rationale for the Water Vapour Measurements

The study of water vapour may lead to a better understanding of cloud formation, storm development and the hydrological cycle in climate modelling. In addition, the exchange of air between the stratosphere and troposphere can be observed. This exchange is important for studying the transport of pollutants in the atmosphere. Lidars are a good choice for such studies as they have, in general, a greater spatial-temporal resolution then radiosondes and, therefore, allow both the study of synoptic and small scale exchanges of air parcels. Measuring the water vapour mixing ratio means that molecular nitrogen is also measured. This allows the temperature to be found down to the tropopause, as well as measurements allowing density perturbations down to 1 km for gravity wave source studies.

Data Processing

The lidar equation can be written

$$N(z) = O(z)\eta T^2 \Delta t \frac{P_L}{hc/\lambda} \frac{A(r)}{4\pi} \frac{\sigma_R n(z)}{z^2} \Delta z + B \quad (1)$$

The number of photocounts returned to the system $N(z)$ is directly proportional to the area of the telescope, power of the laser, and the time span over which a reading is taken. Because the area of the liquid mercury mirror telescope is large (2.65 m) and the transmitted power is high (600 mJ @ 20 Hz), a large number of counts can be collected over a one minute scan. Each one minute scan can be statistcally added with others to get different temporal resolutions. The overlap function, for which photons are lost due to the backscatterred light being blocked out by the instrumentation at the focus of the mirror, is negated by using the mixing ratio of the gas.

In our intial measurements, only a small amount of nitrogen scans were taken and, during the processing, were averaged together. In the two datasets we have collected, over 120 minutes of water vapour were acquired. The photocounts were coadded together so that spatially the resolution was 144 meters.

The mixing ratio is found using

$$W = \frac{k_{N_2}}{k_{H_2O}} \cdot \frac{\sigma_{N_2}}{\sigma_{H_2O}} \cdot \frac{M_{H_2O}}{M_{dry}} \cdot \frac{n_{N_2}}{n_{dry}} \cdot \Delta_q \cdot \frac{N_{H_2O}}{N_{N_2}} \quad (2)$$

where σ is the Raman differential backscatter cross-section, M is the molecular mass, Δ_q is the ratio of atmospheric transmissivities, k represents the photomultiplier quantum efficeincies and N is the returned counts from the lidar [*Whiteman et al.*, 1992]. The

power and telescope area are important as they increase the signal-to-noise ratio by increasing the number of counts returned. The ratio $\frac{n_{N_2}}{n_{H_dry}}$, the amount of nitrogen in the atmosphere at a given altitude, is assumed constant.

The atmospheric transmissivities are dependent on both the wavelength of the light and altitude. Intially we have assumed the transmissivities based on the equation

$$q(\lambda_z, z_o, z) = exp(-\int_{z_o}^{z} \alpha_{\lambda_z}(z')dz') \qquad (3)$$

where α_{λ_z} is the extinction coefficient due to wavelength λ_z. After estimating q_{N_2} and q_{H_2O}, Δ_q is calculated from

$$\Delta_q = \frac{q_{N_2}}{q_{H_2O}} \qquad (4)$$

As our measurements are still in the preliminary stages, we hope to be able to improve the estimates of atmospheric transmissivity and perhaps measuring them using the scattering from the sodium and the Rayleigh-scatter beams.

Results

Figure 1 shows the average water vapour profile for the night of December 16, 1997, the first night of measurements. The original profile was in 24 meter bins. The data was coadded by 6 bins and smoothed by 3s and 5s [*Hamming*, 1977]. The bars indicate the photocount error according to Poisson statistics. Structure can be seen in the water vapour below 9 km. Above 9 km the mixing ratio is fairly constant, which is consistent with previous measurements of lower stratospheric water vapour [*Kley et al*, 1980].

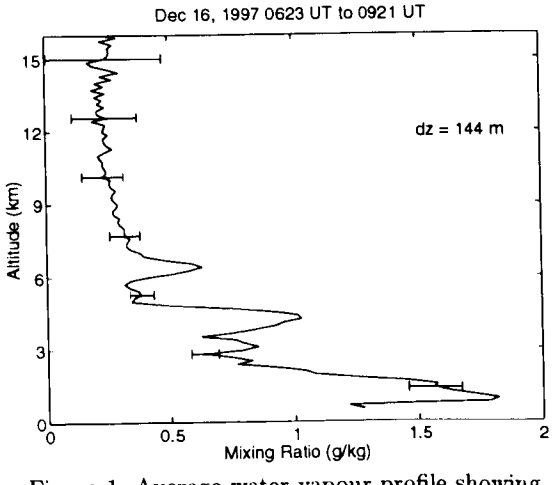


Figure 1: Average water vapour profile showing statistical errors with altitude.

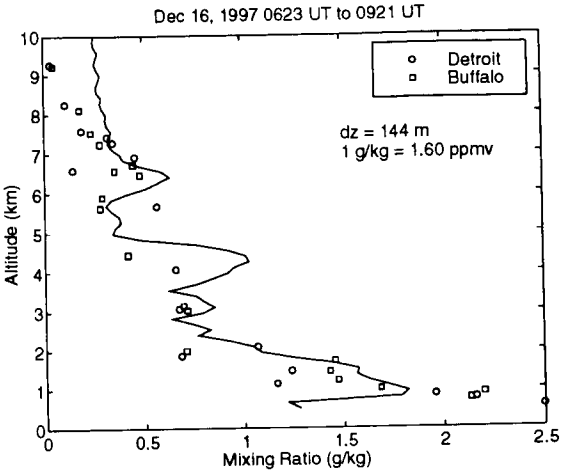


Figure 2: Comparison of radiosonde measurements with lidar measurements on December 16, 1997.

Figure 2 is a comparison of the lidar measurements with radiosondes launched from Buffalo and Detroit at roughly the same time of day. Considering the distance between London, Detroit, and Buffalo (approximately 160 km to either), the data all appear to match well, easily within an order of magnitude of each other. We hope to fly our own radiosondes from the Delaware Observatory in order to make a more accurate calibration of the lidar, in addition to improving our estimate of the atmospheric transmission.

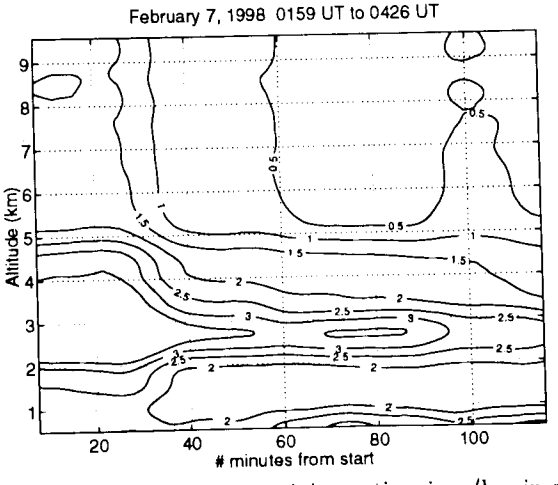


Figure 3: Water vapour mixing ratios, in g/kg, in a contour plot. The error at 9 km is about 15% while near 3 km the error is only about 5%.

Figure 3 shows the mixing ratios with a spatial resolution of 48 meters, a temporal resolution of 2 minutes, and smoothing bandwidths of 14 minutes and 1008 meters. Between two and three kilometers there is a maximum throughout the entire night. Plots like this may allows us to study the movement of air parcels, whether dry or wet, through the night.

Conclusions

It has been demonstrated with these two preliminary data sets that we can get profiles useful for studies of stratosphere-troposphere exchange. The mixing ratios calculated from the lidar data are on the order of radiosonde mixing ratios from Detroit and Buffalo taken in the same time period. We hope to perform radiosonde launches from the Delaware Observatory this summer to verify the calibration of the measurements. Finally, we have shown changes in the mixing ratio at high temporal-spatial resolution.

Acknowledgements

The authors would like to thank the Atmospheric Environment Service, CRESTech and the National Science and Engineering Research Council (NSERC) of Canada for their support of the Purple Crow Lidar Water Vapour project.

References

Sica, R. J., S. Sargoytchev, P. S. Argall, E. F. Borra, L. Girard, C. T. Sparrow, and S. Flatt, Lidar Measurements taken with a large-aperture liquid mirror, *Applied Optics, 34*, 6925-6936, 1995

Whiteman, D. N., S. H. Melfi, and R. A. Ferrare, Raman lidar system for the measurement of water vapour and aerosols in the Earth's atmosphere, *Applied Optics, 31*, 3068-3081, 1992

Hamming, R. W., Digital Filters, Prentice-Hall, Inc Englewood Cliffs, New Jersey, 1977

Kley, W., J. W. Drummond and A. L. Schmeltekopf, On the structure and microstructure of stratospheric water vapour, in Atmospheric Water Vapour A. Deepak, T. D. Wilkerson and L. H. Ruhnke (eds.), Academic Press, New York, New York, 1980

Issues effecting the signal-to-noise ratio for airborne CO_2 DIAL measurements

Richard G. Vanderbeek[1], Avishai Ben-David[2], and Francis M. D'Amico[1] Steven W. Gotoff[1]
[1]U.S. Army Chemical and Biological Defense Command, APG, Md. 21010
[2]Science and Technology Corporation, Edgewood , Md. 21040

1. INTRODUCTION

The effects of signal averaging and time-lag correlation on differential-absorption lidar (DIAL) systems were studied by Menyuk et al.[1] for a horizontal path of a medium range (2.7 km) from a diffuse target (flame-sprayed aluminum). Menyuk et al. showed that the signal averaging does not reduce the standard deviation of the dial measurements by the expected $n^{-1/2}$, where n is the number of pulses that were averaged (a running mean), because of the presence of a long-term temporal fluctuations in the atmospheric transmission. In our work the effect of flight geometry, signal averaging, and time-lag correlation coefficient on airborne dial measurements is presented. In DIAL measurements the concentration of a trace gas of interest is deduced from the time series measurements $z(t)$ which is given by the vector $\vec{z} = \ln(\vec{x}/\vec{y})$ which is the log of the ratio of a lidar measurements $x(t_i)$ measured at wavelengths λ_1 and the lidar measurement $y(t_i + \Delta t)$ measured at wavelengths λ_2 where Δt depends on how fast the lidar can switch between wavelengths. The vector $\vec{z}$ is proportional to the trace gas concentration as a function of time. The accuracy of the deduced trace gas concentration is directly proportional to the standard deviation σ_z which is effected by the signal fluctuations of the lidar measurements $\vec{x}$ and $\vec{y}$. The signal fluctuations in $\vec{x}$ and $\vec{y}$ are caused by the following processes: system noise (e.g., detector and amplifier electronic noise), spatial scintillation in the measured signal due to speckle and glint of the topographic target, temporal scintillation due to atmospheric turbulence, temporal fluctuations of the atmospheric extinction coefficient due to aerosols moving across the lidar field of view (FOV). In addition, the angle of incidence, ground albedo and range change in time due to the airplane flight geometry, resulting in further signal fluctuations. The reduction of σ_z can be achieved by signal averaging of n pulses (i.e., a smoothing operation by a running mean) on the time series vectors $\vec{x}$ and $\vec{y}$ and by increasing the correlation coefficient ρ_{xy} between $\vec{x}$ and $\vec{y}$. Let $w_n(\vec{x})$ (and similarly $w_n(\vec{y})$) be a smoothed version of $\vec{x}$ by applying a running-mean window with a width of n points. The standard deviation of the smoothed signals, $\sigma_{w_n(x)}$ and $\sigma_{w_n(y)}$, decreases with increasing n . The behavior of ρ_{xy} as a function of signal smoothing depends on the time Δt between wavelengths as well as on the long term fluctuations of the lidar signals. In addition ρ_{xy} depends on the relative magnitude of all sources of signal fluctuations and their corresponding time scales. When the variance due to a temporal drift in the atmospheric transmission is significant, signal averaging will reduce σ_x and σ_y while increasing the correlation between the smoothed vector $w_n(\vec{x})$ and the smoothed vector $w_n(\vec{y})$ and thus σ_z will be further reduced. In addition, the ratio $[w_n(\vec{x})/w_n(\vec{y})]$ will normalize (i.e., cancel) the long term fluctuation of the atmosphere and thus will also cause σ_z to decrease.

In our CO_2 lidar system up to twenty different wavelengths can be transmitted sequentially with 5 ms between adjacent wavelengths, and a new (or the same) group (burst) of wavelengths can be transmitted again at a burst repetition frequency (BRF) of 1-4 Hz.. The time Δt between wavelengths for which the atmospheric transmission drift is correlated between the lidar signals $\vec{x}$ and $\vec{y}$ has consequences on the number of different wavelengths that can be used in one burst. This has implications for multi-vapor measurements and also for measuring a single vapor with a wide absorption spectra for which one would like to make DIAL measurements at many wavelengths across the absorption spectra of the gas. Thus it is of interest to know how many wavelengths and how many groups of wavelengths can be used effectively in DIAL measurements. It is important to note that if the trace gas of interest is in the form of a moving cloud with a finite size through the lidar FOV, smoothing (averaging) over n pulses will reduce the unwanted fluctuations in $[w_n(\vec{x})/w_n(\vec{y})]$. However, at the same time the smoothing process will also reduce the desired information inherent in the fluctuations of the vapor cloud density. Thus, the signal-to-noise ratio (SNR) will be reduced if n is too large. In fact, there is an optimal amount of averaging for which the SNR is maximum. This effect will be discussed further in the next section.

2. MEASUREMENTS AND SIMULATION

In our application we are concerned with detecting the presence of non-naturally occurring vapors against a background of naturally occurring gasses. Therefore, for the purpose of this discussion, the signal is taken to be the fluctuation in the return due to absorption by the vapor of interest. Any fluctuation in the return due to other sources of absorption is taken to be noise. In our measurements there are only naturally occurring gasses present, therefore it is strictly a measurement of the background noise. We define the SNR to be the absorption due to the vapor of interest divided by the standard deviation of all the other sources of fluctuation. Since there is no signal present in our measurements we cannot show the effect of signal averaging and taking the DIAL ratio on SNR directly, it can only be inferred based on the observed effect on the noise. To better understand how the signal component of the SNR will be effected a simulation was performed in which normally distributed white noise was superimposed onto a gaussian shaped signal. The resultant data simulates a plot of absorption as a function of time from measurements taken of a cloud with a gaussian shaped density that passes the FOV at a constant velocity. The SNR is defined as the peak of the gaussian signal divided by the standard deviation of the noise. The signal was then smoothed with a moving average filter with a window of width n. The plot of SNR as a function of the filter window width is shown in Fig. 1. The gaussian width (2σ) is 40, 80, and 120 points in the bottom, middle, and top curve respectively. A peak SNR of 38, 54, and 66 was achieved at a filter width of 53, 113, and 173 points in the bottom, middle, and top curves respectively. The figure shows that the wider the cloud is, the more filtering that can be done without reducing the desired information. The figure also shows that the more filtering done (assuming the cloud is wide enough) the larger the resulting SNR will be. Because of this result flight geometry will have a profound influence on the optimally achievable SNR in that it will, in part, determine the observed cloud width (i.e. the number of data points that contain information about the cloud). Lets assume a cloud of width 1000 m, a nominal wind velocity of 3 m/s, an airplane speed of 200 m/s, a burst rate of 2 Hz, and that the lidar FOV is much smaller than the cloud. If one employs a "push broom" geometry, i.e. the lidars angle with respect to the plane remains constant, then the cloud will be in view of the lidar for (1000 [m] 2 [burst/s]) / 200 [m/s] = 10 bursts. On the other hand, if the lidar were tracking a point on the ground while the plane circles it, then the cloud would be in view of the lidar for (1000 [m] 2 [burst/s]) / 3 [m/s] = 666 bursts. In the first case very little averaging could be done and the resulting SNR would be relatively low, but in the latter case one could average many bursts and the resultant SNR would be relatively high.

In the lidar measurements taken the signal is composed of fluctuations with three time scales: a very short time scale due to system noise which is faster than the data acquisition sampling rate (MHz) of the receiver, a medium time scale (KHz) due to atmospheric turbulence, and a long time scale (Hz) due to slow atmospheric transmission drift from aerosol inhomogeneities. In our lidar system the receiver waveform sampling rate is 40 MHz and the shortest possible time between wavelengths is 5 ms, which is usually longer than the turbulence time scale (i.e., turbulence fluctuations and speckle noise are decorrelated between any two wavelengths). The burst rate is 1-4 Hz for which the atmospheric transmission drift due to aerosol inhomogeneities is partially correlated between bursts, but is completely correlated for any two wavelengths within a burst (which contains up to 20 wavelengths , i.e., a duration of up to 100 ms). The smoothing process, $w_n(\bar{x})$, where n is the number of bursts, will reduce the variance due to turbulence, speckle and system noise by 1/n because their decorrelation time-scales are much shorter than the time between bursts (i.e., all the signal fluctuations with short and medium decorrelation time scales are sampled at a low frequency of few Hertz, and thus become independent samples whose variances is reduced by 1/n). The ratio process $[w_n(\bar{x})/w_n(\bar{y})]$ will reduce the variance due atmospheric extinction fluctuations in the DIAL signal $\bar{z}$ because the time-lag in sampling the wavelength-pair (x_i, y_i) is short (5 ms up to 100 ms) and the decorrelation time of the atmospheric extinction fluctuations due to aerosol inhomogeneities is much longer (seconds) and therefore this source of fluctuation will be effectively "frozen" and will be greatly reduced in the ratio operation.

We present one example (Fig. 2) of airborne DIAL measurements. In this example $\lambda_1 = 10P12$ $\lambda_2 = 10P22$ and the burst was transmitted at a frequency of 3.3 Hz. The time between two adjacent wavelengths in a group was 5ms. Low frequency (few tens to few hundreds of Hz) periodic fluctuations in the lidar system were reduced with the use of band-pass filters. The system noise was sampled and was shown to have very good agreement to noise sampled from a normal distribution, and is independent from point to point. The lidar pointing did vary during the flight and as a result the long-term fluctuations in the lidar signals $\bar{x}$ and $\bar{y}$ is due to desert terrain reflectivity changes as well as to atmospheric extinction fluctuations from aerosol inhomogeneities traversing the lidar beam. The measured lidar signals $\bar{x}$ and $\bar{y}$ were corrected by the effect of the instantaneous angle and range to the target as a function of time along the flight. In Fig. 2 the measurements $\bar{x}$ where arbitrarily displaced

vertically from the measurements $\bar{y}$ to enhance visualization. The correlation coefficient between the smoothed vectors $w_n(\bar{x})$ and $w_n(\bar{y})$ increases from 0.6 when there was no smoothing to above 0.9 for n=10.

The effect of increasing the time-lag Δt between λ_1 and λ_2 on the standard deviation σ_z is shown in Fig. 3. As the time-lag Δt increases, the signal fluctuations between λ_1 and λ_2 due to aerosol inhomogeneity become uncorrelated , and these fluctuations will not "cancel" out by the ratio $w_n(\bar{x})/w_n(\bar{y})$. Thus, the standard deviation σ_z increases with increasing Δt. However, σ_z will always decrease as a function of n for which the variance in $w_n(\bar{x})$ and $w_n(\bar{y})$ will be reduced. The time separation Δt in these figures and the effect on σ_z is directly related to the question of how many wavelengths one can use for DIAL measurements. For example, Fig. 3 indicates that 80 wavelengths (i.e. about 4 bursts) can be used for DIAL measurements assuming a steady state cloud (i.e. the vapor cloud is always present within the lidar F.O.V). This is concluded because the overlapping lines indicate that the long time scale fluctuations did not decorrelate significantly, thus the ratio reduced this source of fluctuation.

3. CONCLUSIONS

The effects of flight geometry, signal averaging and time-lag correlation coefficient on airborne CO_2 dial lidar measurements are shown using field measurements. These factors have implications for multi-vapor measurements and also for measuring a single vapor with a wide absorption spectra for which one would like to make DIAL measurements at many wavelengths across the absorption spectra of the gas. Thus it is of interest to know how many wavelengths and how many groups of wavelengths can be used effectively in DIAL measurements. Our data indicate that for our lidar about 80 wavelengths (i.e., about 4 groups of wavelengths, each contains 20 wavelengths, transmitted at a group repetition frequency of 2-4 Hz) can be used for DIAL measurements of a stationary vapor. The lidar signal is composed of fluctuations with three time scales: a very short time scale due to system noise which is faster than the data acquisition sampling rate (MHz) of the receiver, a medium time scale (KHz) due to atmospheric turbulence, and a long time scale (Hz) due to slow atmospheric transmission drift from aerosol inhomogeneities traversing the lidar beam. The decorrelation time scale of fluctuations for airborne lidar measurements depends on the flight geometry. More information and a more detailed description of most of these results is available in a previously published paper[2].

REFERENCES

1. N. Menyuk , D. K. Killinger and C. R. Menyuk, "Error reduction in laser remote sensing: combined effects of cross correlation and signal averaging", Appl. Opt. **24**, 118-131. 1985.
2. A. Ben-David, R. G. Vanderbeek, S. W. Gotoff, and F. M. D'Amico, "The effect of spectral time lag correlation and signal averaging on airborne CO_2 DIAL measurements", Proceedings of SPIE Application of Lidar to Current Atmospheric Topics II, Vol. 3127, 234-246. 1997.

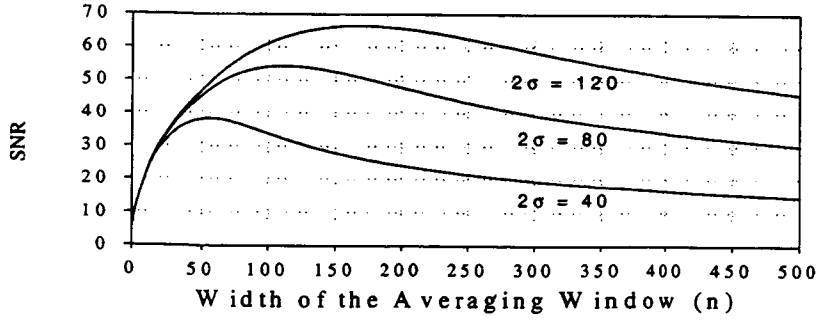


Fig. 1 - SNR as a function of the moving average filter window width.

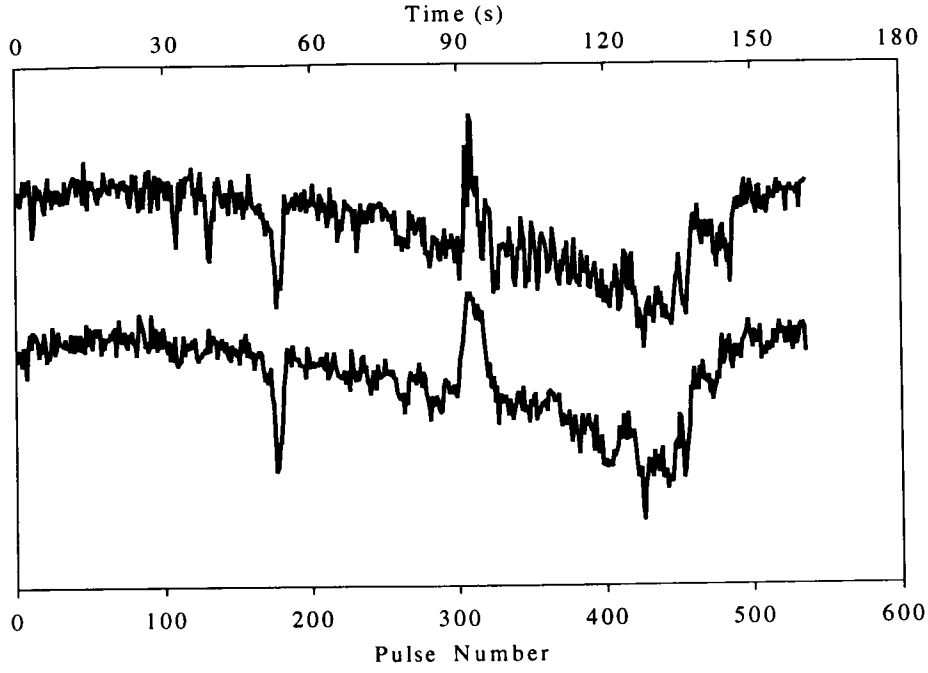


Fig. 2 - Time dependent lidar measurements $\bar{x}$ and $\bar{y}$

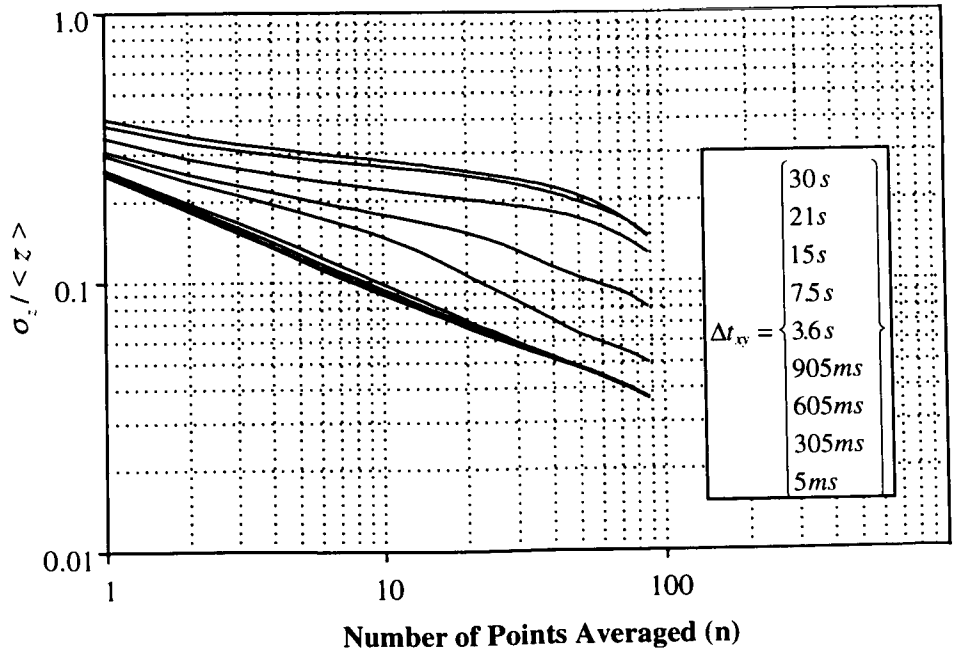


Fig. 3 - The effect of increasing the time-lag Δt_{xy} between λ_1 and λ_2 on the standard deviation σ_z, $\bar{z} = w_n(\bar{x}) / w_n(\bar{y})$, as a function of the number of pulses that were averaged.

Multiple Wavelength Rotational Raman Lidar For Calibration Free Determination of Tropospheric Temperatures

D. Waite, S. Frey, F. Immler, M. Mueller, P. Rairoux†, M. Rodriguez, B. Stein, C. Wedekind, H. Wille, L. Wöste, W. Zimmer

Freie Universität Berlin, Institut für Experimentalphysik
Arnimallee 14, D-14195 Berlin, Germany
Phone: +49-30-838-4776, Fax: +49-30-838-5567, E-mail: waited@physik.fu-berlin.de

†Alfred Wegner Institut
Telegrafenberg A43, D-14473 Potsdam, Germany

I. Introduction

The study of atmospheric temperatures using rotational Raman lidar was first proposed by Cooney (1972) and has been investigated by a number of groups (Cohen, Arshinov, Vaughan). Because the entire return spectrum is focused on the PMT, in these experiments a suppression of Rayleigh return of the laser on the order of 6 magnitudes is needed. Thus, commonly two narrow band filters are used in conjunction with PMTs to measure a near and a far channel. Due to the breakthrough of the laser line and the sensitivity of the filters to ambient temperature changes, calibration of the instrumentation is necessary. In order to overcome these limitations, a new system based on direct analysis of the resolved rotational Raman spectrum is currently under development.

The system, based on a CCD camera coupled with a spectrometer allows for the resolution of the individual lines. Through direct intercomparison between the return spectrum and the theoretical spectrum temperature can be determined. Preliminary studies for this experiment were made in Berlin, Germany at the beginning of November, 1997. In these studies, Raman spectra were able to be taken even during daytime through the use of a gated CCD camera which reduces background solar radiation. Construction of the new system is underway and is expected to be running by April 1998.

II. Experimental Setup

A block diagram of the system is shown in Fig. 1. The laser system consists of the second harmonic of a seeded Q-switched Nd:YAG (Quanta Ray DCR-3) which is beam expanded by a factor of eight to reduce divergence. The receiver system is a 40cm f/3 telescope with polarizing cubes mounted on top to separate the return signal into polarized and depolarized components. The entire polarization optic (L1-L3, P1-2, PMT) can be turned to chose which polarization is coupled into the cable. Due to the 99.635% polarization of the Rayleigh return, the use of the polarizers increases the Raman to Rayleigh signal ratio by a factor of 136. The depolarized signal is coupled to a spectrometer by a 1mm round to 8.5mm line fiber optic bundle with 100μ fibers to increase optical throughput. The holographic grating with 1800l/mm suppresses stray light by at least 5 orders of magnitudes. An image intensified gated CCD camera (Oriel Instaspec V), cooled to -40C, is used to record the spectra.

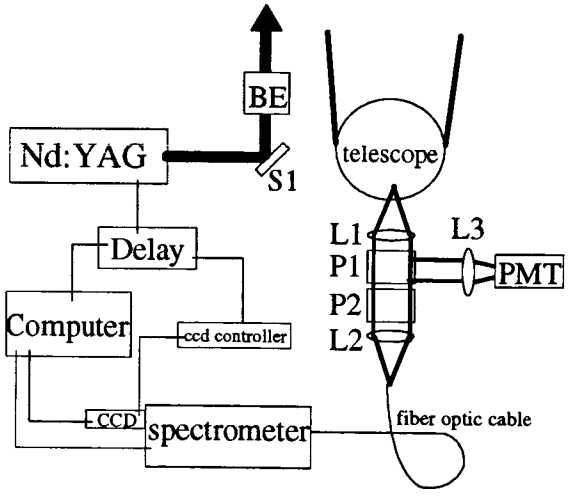


Figure 1: Block Diagram of Experimental Setup
L=lens, P=polarizer, S=mirror,
BE=Beam Expander

The camera is based on an S25 photocathode which is intensified by a MCP coupled through fiber optics to an EEV 40-11 CCD. A computer controls the spectrometer, the delay generator used to trigger the camera, and reads the data from the camera. A CCD controller converts the trigger from the delay for the camera.

The other signal can be coupled into a PMT connected to a transient recorder which allows for simultaneous measurement of Rayleigh backscatter.

III. Methods and Results

A series of measurements for various heights has been made by integrating over a 750m path length for 1000 shots. A typical result can be seen in figure 2, demonstrating that even daytime measurement of rotational Raman spectra are possible using the current setup.

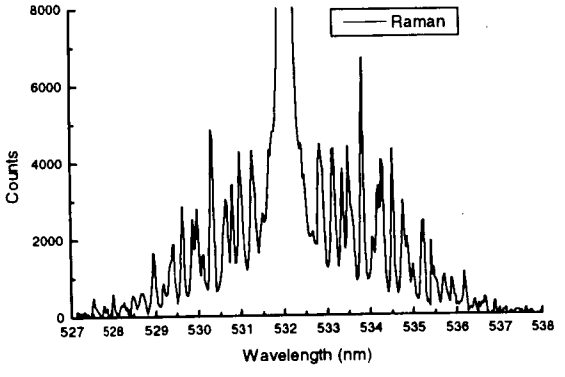


Figure 2: Daytime Rotational Raman Spectrum

The spectrum consists of interleaved O_2 and N_2 Raman lines shifted to the left and right of laser wavelength. For the Stokes shift, the power of the Jth line of an individual molecular species is given by (Penney):

$$P_J = \frac{3hcB_0(J+1)(J+2)}{kT(2J+3)(2I+1)^2}\omega_J^4\gamma^2 g_J \times \exp-\left(\frac{hcB_0J(J+1)}{kT}\right)$$

B_0 is the rotational constant for the molecule, I is the nuclear spin, ω_J is the wave number of the Jth Raman line, γ is the anisotropy of the molecular polarizability tensor, and g_J is the statistical weight of the line. One of the greatest sources of uncertainty in this distribution is due to the uncertainties in the value of $\gamma^2(O_2):\gamma^2(N_2)$ (Vaughan). Values of this ratio at 488nm and 647nm are between 2.47 and 2.61(Buldakov, Penney, Rowell). Studies at 532nm are unknown to the authors and thus the data must be extrapolated. Uncertainty in the anisotropy values introduces an uncertainty of ~1C.

Subtraction of the Rayleigh scattering from the signal is possible either by turning the entire polarizing optic and measuring the parallel polarization. Due to the high polarization of the Rayleigh return, Rayleigh to Raman signal strength is increased by 272. The measured signal can be scaled appropriately to the signal in the depolarized channel or by modeling.

To measure temperature a fit of the measured spectrum to calculations is made. The weighted fractional difference between the measured and theoretical spectra is given by:

$$\Delta = \sum_J g_J^N g_J^T \ (P_J^c - P_J^m)^2 / P_J^c$$

where P_J^c and P_J^m are the powers of the individual lines of the calculated and measured spectra respectively. g_J^N is a weighting factor for the reliability of the lines due to signal to noise considerations and g_J^T is a weighting factor for the sensitivity of the lines to temperature changes.

The temperature can be determined from the corrected spectrum by minimizing the difference between the measured spectrum and the theoretical spectrum. At the present time, software is being developed to analyze the signal.

IV. Future Work

In addition to software development, at the current time, we are working on a new system based on a non-intensified CCD camera. The recent advancement of CCD technology has made low cost low noise CCD cameras readily available. The system under development will also use a 1m spectrometer to increase resolution. Redesign of the polarizer should increase optical throughput

enormously. The system is expected to be operational by April 1998.

V. Summary

A new method for determination of tropospheric temperatures from rotational Raman spectra returns has been developed and tested. The main advantage of this system is that it allows calibration free temperature measurements. Due to a lack of filters, the system is also insensitive to temperature changes. Through the use of a polarization system and a gated camera, it is possible to increase optical throughput to levels that allow not only nighttime operation, but daytime as well. Continuing advances in CCD technology due to digital photography will allow for the development of a low cost system.

S Acknowledgments

The authors would like to thank G. Vaughan for his helpful correspondence.

References

Arshinov, Y.F. (1983). Atmospheric Temperature Measurements Using a Pure Rotational Raman Lidar. Applied Optics, 22.

Buldakov, M. A., Matrosov, I.I., Popova, T.N. (1979). Determination of the Anisotropy of the Polarizability Tensor of the O_2 and N_2 Molecules. Optika i Spektroskopiya, 46.

Cohen, A., Cooney, J.A. and Geller, K.N. (1976). Atmospheric Temperature Profiles from Lidar Measurements of Rotational Raman and Elastic Scattering. Applied Optics, 15.

Cooney, J.A. (1972). Measurement of Atmospheric Temperature Profiles by Raman Backscatter. Journal of Applied Meteorology, 11.

Penney, C.M., St. Peters, R.L., Lapp, M. (1974). Absolute Rotational Raman Cross Sections for N_2, O_2, and CO_2. Journal of the Optical Society of America, 64.

Rowell, R.L., Aval, G.M. (1971). Rayleigh-Raman Depolarisation of Laser Light Scattered by Gases. Journal of Chemical Physics, 54.

Vaughan, G., Wareing, D.P., Pepler, S., Thomas, L., Mitev, V. (1993). Atmospheric Temperature Measurements Made by Rotational Raman Scattering. Applied Optics, 1993.

Atmospheric Lidar EXperiment (ALEX): A New Raman Lidar System at the University of Maryland Baltimore County

Martín P. Cadirola, S. Harvey Melfi, David N. Whiteman, A. Dan Wooten
Joint Center for Earth Systems Technology, University of Maryland Baltimore County
1000 Hilltop Circle, Baltimore, Maryland 21250, USA
Phone: (410)-455-2715, Fax: (410)-455-1072, E-mail: mcadir1@umbc.edu

I. Introduction

A Raman Lidar system has been constructed at the Department of Physics of the University of Maryland Baltimore County (UMBC). This system, also known as Atmospheric Lidar EXperiment (ALEX), observes the Raman scattering produced by water vapor and nitrogen molecules, as well as Rayleigh scattering by molecules and Mie scattering by aerosols.

This paper describes the modules of the system, such as laser, interference filters, photomultiplier tube and the discriminator-multichannel scaler system, with an emphasis on the software application used to record the observations of the experiment. The software is based on National Instrument's LabVIEW, an application we found useful for developing a complete acquisition and processing capability.

II. System Description

The block diagram of the system is shown in Figure 1. A diagram of the one channel ALEX system is shown in Figure 2.

The laser is a high power Q-switched Nd:Yag provided with doubling and tripling crystals which allow simultaneous output at wavelengths of 1064, 532 and 354.7 nanometers. Only the UV portion of the output is used to maximize the scattering return. Each pulse sent to the atmosphere has a maximum energy of 200 mJ and a temporal width of 4 to 6 nanoseconds while the pulse repetition frequency is 10 Hz.

The transfer mirrors provide transmission at 1064 and 532 nanometers while reflecting at 354.7 nanometers. Thus, they filter out the fundamental and second harmonic while maintaining horizontal polarization at 354.7 nm.

The telescope used to collect the scattered radiation is a 14 inches Schmidt Cassegrain f/11. It is also positioned on a micrometer adjustable mount designed by the author.

A 5 mm diameter fiber optic bundle is composed of fibers of 200 μm in diameter. These fibers are arranged in a scrambled manner to provide maximum transmittance for our spectral range (67% from 380 to 420 nm). One end of the bundle is located at the focal point of the telescope and the other end has a collimator which allows light to exit as uniformly and as parallel as possible to the interference filters and then to the photomultiplier tube.

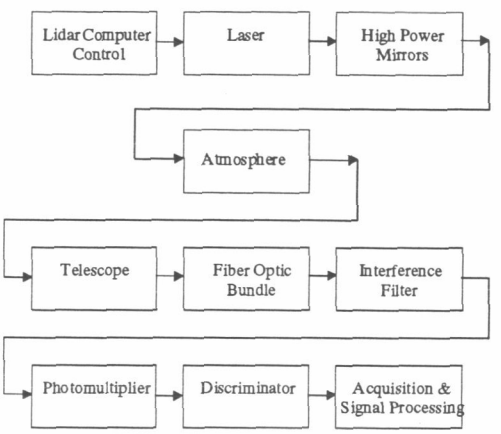


Figure 1. ALEX System block diagram

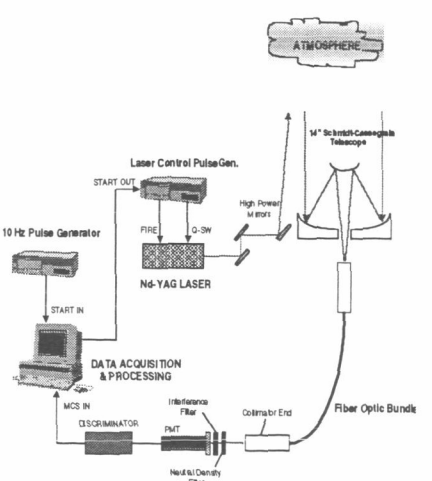


Figure 2. ALEX one channel configuration system

The narrow band interference filters provide the wavelength selection corresponding to the Raman scattering shift due to the atmospheric molecules. These result from illumination with a laser beam at

354.7 nm. These shifts are studied and described in detail by Inaba and Kobayasi. Also, a filter tuned at the laser wavelength is provided for observing aerosols.

The photomultiplier tube (PMT) has high gain (71 x 10^6) and low noise (dark current 10 nA) characteristics. This tube is working in the photon counting mode.

A 300 MHz count rate discriminator allows the accurate counting of pulses coming out of the PMT and conditions the signal for computer acquisition. The selection of the discriminator threshold is of importance as noted by Donovan *et al.* and Cadirola. An appropriate value will minimize the pulse pile-up effect found in photon counting systems. The value of the discriminator threshold used in our observations was chosen according to linearity tests made on the PMT (Cadirola). It is important to note that each discriminator threshold will depend on the particular PMT used in the detection, even if the same model and manufacturer is used. Therefore, a linearity test should be performed for each tube used in the system.

The multichannel scaler (MCS) is able to acquire pulses of the discriminator in sequential bins in order to provide a range resolved profile of the atmosphere. The bin size is 250 nanoseconds which defines a spatial resolution of 37.5 meters. The laser will fire synchronously at a fixed time after the start of a multichannel scaler sweep. To improve the statistics of the observation a further number of multichannel scaler sweeps is required. Therefore after M sweeps the MCS will contain a profile of the range resolved accumulation of counts for the total number of laser shots. This profile is then used in the processing and analysis of experimental data.

The computer data acquisition system is based on an IBM/PC compatible with Windows 95 and National Instruments' LabVIEW software. This software is used to control the laser firing, acquisition, processing, displaying and storing the range resolved counts.

III. Signal Processing

The signal processing performed for each raw Lidar return is performed on-line with a personal computer IBM/PC compatible using Windows 95 and running National Instruments' LabVIEW version 4.1. The data acquired is saved to a file and later processed using the same software.

It is useful to know the expected number of counts per bin calculated by a simplified version of the Lidar equation (Melfi). This equation will be used for comparison of experimental data. This can be shown as:

$$i(z) = \frac{E \times c \times q(\lambda_{Laser}, z) \times \left.\frac{d\sigma}{d\Omega}\right|_{\lambda Raman} \times n(z) \times q(\lambda_{Raman}, z) \times A \times \gamma(\lambda_{Raman}) \times \eta(\lambda_{Raman}) \times G}{2 \times z^2}$$

where

i(z): photomultiplier cathode current per laser pulse

E: total laser energy per pulse at λ_{Laser} (J)

c: speed of light (m/s)

$q(\lambda_{Laser}, z)$: atmospheric transmissivity for the laser wavelength

$\left.\frac{d\sigma}{d\Omega}\right|_{\lambda Raman}$: total effective backscatter crosssection (m^2/sr)

$n(z)$: number density of Raman scattering molecules ($1/m^3$)

$q(\lambda_{Raman}, z)$: atmospheric transmissivity for the Raman scattering wavelength

A: area of receiver telescope (m^2)

$\gamma(\lambda_{Raman})$: system optical efficiency

$\eta(\lambda_{Raman})$: pmt's cathode spectral sensitivity (A/W)

G: gain of the photomultiplier

z: altitude = c*t/2 (m)

Further schemes used in the processing of raw Lidar profiles can be summarized as: (a) background subtraction and range square correction, (b) count rate and (c) signal to noise ratio. In addition, water vapor mixing ratio and aerosol scattering ratio are performed.

Background subtraction consists of removing the DC component contained in the raw data. This DC component is due to sky background light that enters the photomultiplier. It is calculated by averaging the total number of counts over a period of approximately 200 µs before the laser is fired for the total number of laser shots acquired. This average is then adjusted to obtain an equivalent background per 250 ns bin. This can be shown as:

$$N_{ave_back} = \frac{1}{L_2 - L_1 + 1} \sum_{i=L_1}^{L_2} N(i)$$

$$N_{back_sub}(i) = N(i) - N_{ave_back}$$

where

i = bin number

L_1 = initial bin

L_2 = final bin

N_{ave_back}= calculated average background per bin

N_{back_sub} = background subtracted lidar data

N (i) = total raw counts per bin

Range square correction consists of multiplying each bin by the corresponding squared altitude or range since, as seen from the Lidar equation, all returns are affected by the factor due to the change in

the receiver telescope solid angle as referred to the laser pulse. It is also very important to apply this correction to background subtracted returns since a DC component contained in the data would give an apparent increase in signal with increasing altitude.

Knowing that each bin contains information from a height layer 37.5 m thick, we can assume that the number of counts in that bin will correspond to a height equal to 37.5m times 2i - 1 where i is the bin number. Thus, the calculation can be summarized as:

$$N_{range_corrected}(i) = N_{back_sub}(i) \cdot (\frac{bsr}{2} \cdot (2i-1))^2$$

where
i = bin number
bsr = bin spatial resolution = c x bin_width/ 2 = 37.5 m
N_{back_sub} *= background subtracted lidar data*
$N_{range_corrected}$ *= range squared corrected lidar data*

The count rate shows how close the photomultiplier tube is to saturation levels, being a very important evaluation tool, given that the PMT output is not already saturated. It can be calculated as:

$$M(i) = \frac{N(i)}{250 \cdot 10^{-9} \cdot S}[Hz]$$

where
i = bin number
N(i) = total number of counts per bin for S number of laser shots
M(i) = count rate per bin
S = total number of laser shots

The PMT pulse height distribution showed the experimental maximum count rate for the tube used has a value of approximately 10 MHz. It can be seen that for the measured profiles (where saturation is not ocurring) the count rate values are mostly within the linear operation of the tubes. However, since at low altitude (within the first kilometer) the count rate is larger than the maximum value the tube can handle, we assume all our Lidar observations are useful above the first kilometer ($\cong$ 25 MCS bins).

The signal to noise ratio can be calculated as:

$$SNR = \frac{S(i)}{N(i)} = \frac{N(i) - N_{ave_back}}{\sqrt{N(i)}}$$

where
N (i): total raw counts per bin
N_{ave_back}*: average background per bin*

This calculation is based on the assumption that the probability of observing any specific number of counts in a Lidar profile is given by the Poisson probability distribution. Therefore, the counts found in each bin represent an estimate of the mean of a Poisson distribution for that bin (Bevington). Hence the variance σ^2 equals the number of counts N in that bin i, and the uncertainty in the number of counts per i bin is given by:

$$\sigma(i) = \sqrt{N(i)}$$

The water vapor mixing ratio is the mass of water vapor divided by the mass of dry air in a given volume and usually expressed as grams per kilogram (g/Kg). Its calculation basically is the ratio of the water vapor to the nitrogen Lidar profiles. Similarly, the aerosol mixing ratio can be found by calculating the ratio of the aerosol to molecular scattering, i.e., rationing the aerosol with the nitrogen Lidar returns. These calculations are described in more detail by Whiteman *et al.*

IV. Experimental Data Acquisition and Analysis

The operation of ALEX consists of (a) an alignment procedure and (b) a data acquisition and processing scheme.

The alignment procedure is performed to intersect the laser beam with the center-on-axis of the field of view of the telescope. The idea is to maximize the long range return for any specific wavelength.

The data acquisition and processing scheme provides the final step in observing and recording the Lidar profiles.

The acquisition and processing software, based on LabVIEW, uses the concept of modular programming in which an application is composed of a series of tasks which can also be divided in subtasks. It also has extensive library functions for applications like data acquisition, analysis, presentation and storage. In addition, development tools provide easy debugging and program development. LabVIEW philosophy considers routines or modules as *virtual instruments* (VIs) with the idea of constructing instruments that perform a certain function within the program. These VIs consist of two components: a *front panel*, which acts as an interface with the user, and a *diagram*, in which the programmer writes the VI's commands. This arrangement permits clear and conceptual understanding of the operation of the software program. Each component of the program is then implemented as a virtual instrument.

Each Lidar return corresponding to nitrogen, water vapor and aerosols is recorded sequentially. All data shown in this paper are averaged 15 minutes. After storing all the different profiles, the processing software allows the computation of water vapor

mixing ratio and aerosol scattering ratio, including a qualitative comparison of the water vapor mixing ratio with radiosonde data.

The advantage of having a real-time acquisition and processing software is the ability to evaluate the Lidar profiles qualitatively and quantitatively on the fly, so that any extra corrections to alignment, signal attenuation or others can be made at the time of the measurement.

For example, in order to know if the system is properly aligned a qualitative analysis can be made by comparing the acquired nitrogen Lidar profile with the number density of nitrogen molecules described in the U.S. Standard Atmosphere Tables. This is shown in the right graph of Figure 3.

Similarly, a quantitative analysis of the system performance can be made by comparing the acquired nitrogen Lidar profile with the expected number of counts calculated theoretically using the Lidar equation. This is shown in the left graph of Figure 3.

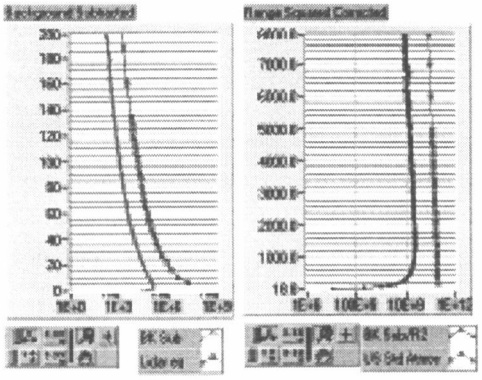


Figure 3. (Left) Plot of Nitrogen profile vs. expected counts calculated by Lidar equation (MCS bins vs. Counts per shot);(Right) Range square corrected nitrogen profile vs. US Standard Atmosphere tables (Range in meters vs. Total counts).

In the same way, a qualitative comparison of the water vapor mixing ratio with radiosonde data can be made. As shown in Figure 4, our computed water vapor mixing ratio shows good agreement with the radiosonde.

V. Summary

The UMBC's Atmospheric Lidar EXperiment (ALEX) has demonstrated the capability of remotely sense the atmosphere by measuring nitrogen, water vapor and aerosol concentrations in the troposphere with acceptable noise characteristics. The versatility and simplicity of the application software LabVIEW allows both the programmer and the end user to easily interact with the computer and datasets. The experimental analysis of Lidar data is greatly simplified due to the powerful built-in graphs which allow the operator to obtain faster study and therefore better instrument data analysis performance.

Future capabilities of the data acquisition and processing software include database and Matlab interfaces as well as remote control and operation of mobile systems.

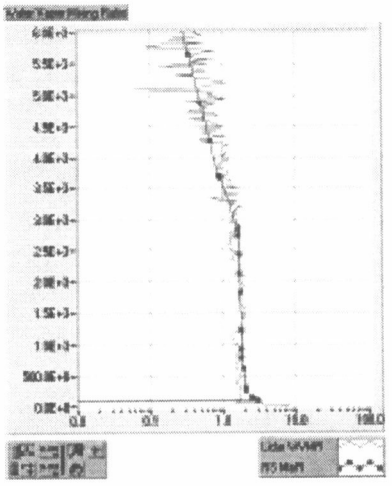


Figure 4. ALEX Water vapor mixing ratio observation vs. radiosonde data. Radiosonde data was taken from Washington Dulles airport on December 17, 1997 at 0000z, approx. 4 hours away from acquisition time

VI. References

Bevington, P.R., Robinson D.K. *Data Reduction and Error Analysis for the Physical Sciences.* McGraw Hill, New York (1992).

Cadirola, M. P. *Remote Sensing of the Atmosphere using a Raman Lidar.* M.S. Thesis, University of Maryland Baltimore County, Baltimore, Maryland, USA (1997).

Donovan, D.P., Witeway, J.A., Carswell A.I., "Correction for nonlinear photon counting effects in Lidar systems," Appl. Optics, Vol. 32, 6742-6753 (1993).

Inaba, H., Kobayasi T., "Laser Raman Lidar," Opto Electronics, Vol. 4, 101-123 (1972).

Melfi, S. H. *Raman Backscatter of Laser Radiation in the Earth's Atmosphere.* Ph.D. dissertation, College of William and Mary, Virginia, USA (1970).

Whiteman, D.N., Melfi, S.H. and Ferrare R., "Raman Lidar System for the measurement of water vapor and aerosols in the Earth's atmosphere," Appl. Optics, Vol. 31, 3068-3082 (1992).

Retrieval of ozone and water vapor in the lower troposphere by Raman DIAL

Benoît Lazzarotto, Valentin Simeonov, Philippe Quaglia,
Gilles Larcheveque, Hubert van den Bergh and Bertrand Calpini
Laboratory for air pollution / Lidar group
EPFL, Swiss Federal Institute of Technology. 1015 LAUSANNE. SWITZERLAND
Phone: ++41 (0) 21 693.61.71. Fax: ++41 (0) 21 693.36.26. email: benoit.lazzarotto@dgr.epfl.ch

Max Frioud and Valentin Mitev
Lidar group.
Observatory of Neuchâtel. 2000. NEUCHATEL. SWITZERLAND
Phone: ++41 (0) 32 889.88.23. Fax: ++41 (0) 32 889.62.81. email: max.frioud@on.unine.ch

1. Introduction

We propose a new and more accurate way of measuring ozone and water vapor in the Planetary Boundary Layer (PBL), two important components for both chemistry and meteorology. The method is based on the Raman scattering in the UV, measured simultaneously on O_2, N_2 and H_2O. The Raman shifted wavelengths from O_2 and N_2, with well known Raman cross sections and constant mixing ratio, are well suited for differential ozone measurements in Hartley band. Furthermore, water vapor mixing ratio can be retrieved using the classical Raman method [1, 2].
The Raman DIAL was already successfully performed in the stratosphere at night time conditions for ozone [3]. We propose to adapt this technique for monitoring ozone in the PBL by using a single probing wavelength at the 4th harmonic of a Nd:YAG laser. In this case, the Raman shifted wavelengths are situated in the solar blind region, which makes possible daytime measurements.

2. The experimental setup

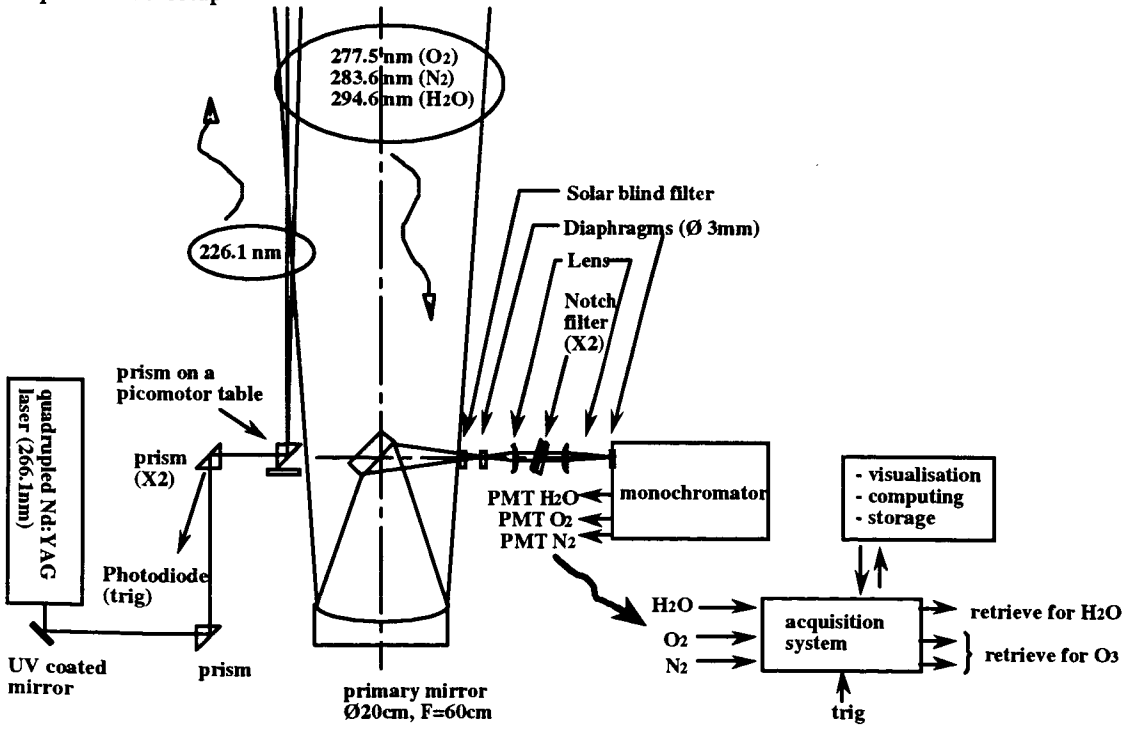


Figure 1. Experimental setup

The optical layout is shown in Figure 1. The system is based on a quadrupled Nd:YAG laser which emits the 266.1 nm radiation at a maximum power of 120 mJ and 10 Hz, with a beam divergence of 0.5 mrad. We use a non coaxial configuration without beam expansion. The three backscattered Raman signals are collected by a Newtonian telescope with a 20 cm diameter primary mirror, 60 cm focal length and 5 mrad divergence. The Raman signals are spectrally separated by a single 500 mm optical path monochromator with 10^5 background noise rejection. The monochromator has a 1.1 nm / mm resolution using a 1'800 gr./mm grating.
The additional rejection of the pump beam is performed by two custom designed holographic Notch filters, with a typical 2.6 OD at 266 nm for each filter with up to 80% transmission for the three Raman wavelengths. The Notch filter transmission curves for a tilt of 0 and 20 degrees are shown in Figure 2.

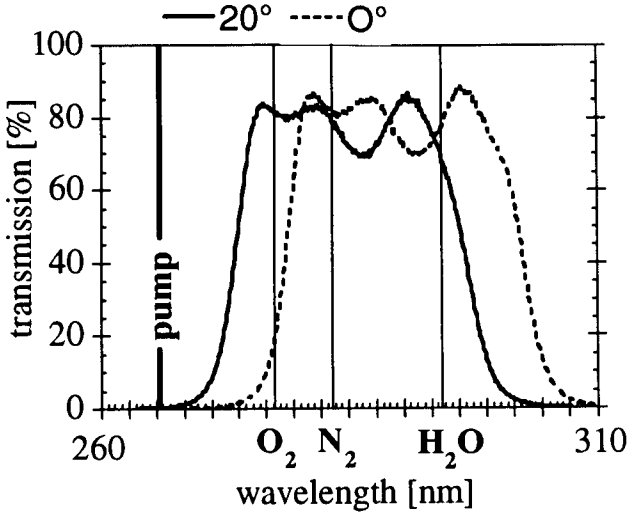


Figure 2. Notch filter transmission curve between 260 - 310 nm, at 2 different angles.

With the combination of the monochromator and the two Notch filters, we obtain over 10^{10} rejection ratio at 266 nm. Adding a solar blind filter at the output of the telescope performs additional day light suppression. With this configuration, daytime measurements are achieved easily. The F number of the monochromator and telescope is fitted using two positive lenses, a 40 mm to collimate the light in the Notch filters and a 60 mm at the entrance of the monochromator. The three Raman shifted wavelengths at the output of the monochromator are simultaneously detected by three PMTs, and the signals are recorded with 12 bits 20 MHz transient ADC recorder, with the control of the acquisition and treatment of the data performed by a PC.

3. Data analysis

The analysis of the Raman data is similar to that described earlier in McGee et al [3] but applied here for a single wavelength. The ozone number density can be obtained from the following equation:

$$n_{O_3}(R) = \frac{\frac{d}{dr}(S_{N_2}(R)) - \frac{d}{dr}(S_{O_2}(R)) - \left[\alpha_{O_2}(R) - \alpha_{N_2}(R)\right]}{\sigma_{O_2}(R) - \sigma_{N_2}(R)}$$

with $S_x = \ln(R^2 P_x(R))$ the logarithm of the range corrected Raman signals, $\alpha_X(R)$ the extinction coefficient and $\sigma_X(R)$ the ozone absorption cross section related to the Raman shifted wavelengths. The Raman shifts are 1555 cm^{-1} for O_2, 2331 cm^{-1} for N_2 and 3651 cm^{-1} for H_2O. With the 266.1 nm pump beam, the vibrational Raman wavelengths are 277.5 nm for O_2, 283.6 nm for N_2 and 294.6 nm for H_2O [3]. The corresponding ozone cross section for Raman shifted wavelengths are $490.6*10^{-20}$ cm^2/mol for O_2 and $296.3*10^{-20}$ cm^2/mol for N_2 [5].
In addition to the ozone retrieval, the is capable to detect the Raman signal at 294.6 nm from H_2O and to provide the water vapor profile by applying the method proposed in [1, 3].
4. Results and discussion

With this rather simple configuration, Raman signals are acquired in the analog detection mode for altitude up to 1000 m. The high rejection ratio was proved by the absence of the elastic lidar echo in O_2 and N_2 Raman signals from low level clouds. Two range corrected signals obtained with the system are presented in Figure 3, for the O_2 and N_2 Raman shift, on 4000 shots average. The graph directly show the difference in the slopes of the curves due to different ozone absorption cross-sections, the "Raman O_2" corresponding to the *on* wavelength and the "Raman N_2" to the *off* wavelength. The corresponding ozone profile is shown in Figure 4. It is a preliminary result, with the data points obtained with a binning of 30 meters (4 x 7.5 m) and the linear fit showing a reasonable 30 ppb mean ozone concentration between 90 and 450 m above the ground level. Water vapor Raman signals have been observed but not yet processed.

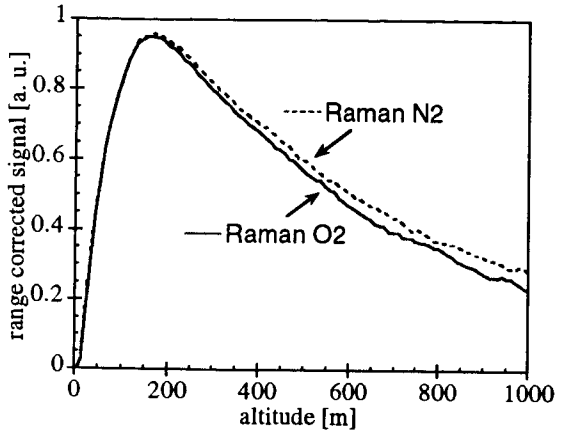


Figure 3. Range corrected Raman for N_2 and O_2 signals.

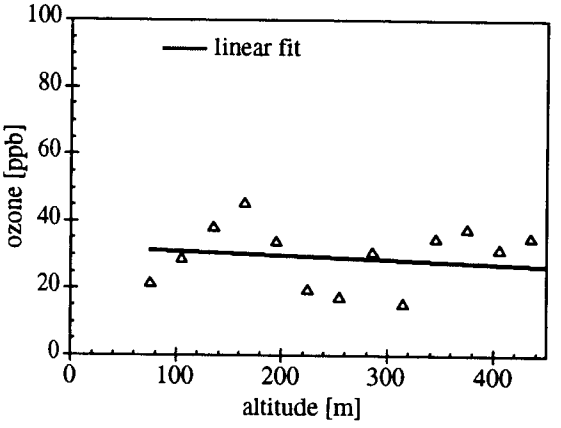


Figure 4. Extracted concentration from the two Raman signals presented in Fig. 3.

We may expect that working in photon counting mode, the range will be extended up to the free troposphere. Water vapor retrieve will be performed soon, and ozone and water vapor intercomparison is on the way. The exchange of the monochromator by a filter based system will be investigated.

6. References

[1]. S.H. Melfi, J.D. Lawrence Jr, and M.P. Mc Cormick, "Observation of Raman scattering by water vapor in the atmosphere", Appl. Phys. Lett., 15, 295-297 (1969).

[2]. G. Vaughan, D.P. Wareing, L. Thomas, V. Mitev, "Humidity measurements in the free troposphere using Raman backscatter", Q. J. R. Meteorological Society, vol. 114, 1471-1484 (1988).

[3]. T.J. Mc Gee, M. Gross, R. Ferrare, W. Heaps & U. Singh, "Raman DIAL measurements of stratospheric ozone in the presence of volcanic aerosols", Geophysical Research Letter, vol. 20, 955-958 (1983).

[4]. W.K. Bishel and G. Black, "Wavelength dependence of Raman scattering cross-sections from 200 - 600 nm, in excimer lasers", edited by C.K. Rhodes, H. Egger and H. Pummer, American Institute of Physics, New York, 181-194 (1983).

[5]. "Laser monitoring of the atmosphere", Ed. E. David Hinkley, Springer (1976).

Raman Lidar Calibration of the DMSP SSM/T-2 Microwave Water Vapor Sensor

John Wessel, Steven Beck, Yat Chan, Robert Farley, and Jerry Gelbwachs
The Aerospace Corporation, P.O. Box 92957,Los Angeles, CA 90009
Phone: (310) 336-6599, FAX: (310) 336-6801, Email: John.E.Wessel@aero.org

1. Introduction.

Two campaigns were conducted at the Pacific Missile Range Facility, Barking Sands Kauai (PMRFK), investigating Raman lidar as a method to improve calibration of the DMSP SSM/T-2 microwave water vapor profiling instruments. A transportable Raman lidar developed at the Aerospace Corporation was deployed to an island test site at Barking Sands, Kauai, following launch of DMSP F-14. The site was selected for a tropical atmosphere, minimal cloud cover, and water surrounding. The lidar operated in conjunction with AIR and Vaisala radiosondes and was supported by downlinked satellite data and surface measurements from a regional buoy network. Raman lidar profiles extending from <0.5 to >10 km altitude were obtained on 34 of 37 available nights during the two campaigns, June-July and September, 1997 respectively.

2. Experimental.

The lidar transmitted 355 nm output from a frequency-tripled Nd:YAG laser (Spectra Physics GCR290-50, injection locked), and received with a f/6.5 0.8 m diameter (primary) Cassegrain telescope employed in coaxial configuration. Laser, telescope, detection optics, and electronics were installed in a 30 foot container that was transported by air to PMRFK. In the second campaign, a high speed ferroelectric liquid crystal shutter was added to the optical train in order to suppress spurious signal-induced noise in high altitude measurements. A ferroelectric liquid crystal was chosen because it switches at higher speed than conventional liquid crystal media, while retaining the large acceptance angle and aperture of these devices.

3. Results.

Lidar calibration constants, relating the ratio between water and nitrogen signals to the water vapor mixing ratio, were derived from simultaneous radiosonde measurements. An AIR GPS 77 radiosonde system supplied temperature, relative humidity, and wind measurements. Polymeric film humidity sensors were used in Kauai, in contrast to recently published work (Ferrare et al.; Wang et al.) which employed AIR radiosondes equipped with carbon hygristors. Sondes were launched from the lidar site approximately 15 minutes prior to satellite overpass. Viewing conditions were generally extremely clear. Vaisala radiosondes with polymeric humicap sensors were launched simultaneously from an adjacent side at PMRFK on five nights of the September campaign. Vaisalas were also flown about 7 hours after satellite overpass on eleven nights during June-July.

The lidar calibration constant was reproduced to about ±2 percent from day to day by performing system alignment using a large corner cube retroreflector. Calibration constants for the photon counting mode were derived from 3 to 6 km altitude data. This was based on the expectation of good photon counting statistics, reasonable signal linearity, moderately reliable operation of the radiosondes at prevailing temperatures, and relatively stable moisture profiles during observation periods. The lidar calibration constant was obtained by minimizing RMS difference between "good" AIR profiles and the lidar mixing ratio profiles (~1.6% RMS in RH in typical cases). In all cases, the calibration constants so derived yielded realistic saturation at cloud levels. Minimized RMS differences were larger for the Vaisala radiosondes and the changes in RH with altitude reported by the Vaisalas were physically inconsistent with changes in the water Raman channel. This indicates that a systematic bias occured in the Vaisala measurements at low RH, therefore AIR profiles were used for lidar calibration. The Vaisala profiles were persistently moister than AIR profiles for 3 to 9 km at RH below 20 percent. The difference accounts for the poorer corre-

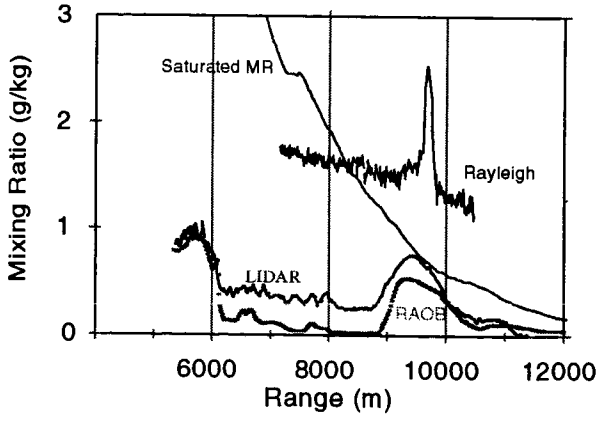


Figure 1. Water vapor mixing ratio measured by lidar (heavy black line), AIR radiosonde (gray squares), Rayleigh-Mie (gray line), and saturated mixing ratio (MR).

spondence between Vaisala-based forward calculations and SDRs than for AIR or lidar measurements.

Figure 1 presents data recorded in the presence of thin cirrus clouds at 9 km altitude. In this typical case, the radiosonde did not report saturation at cloud level, whereas the lidar, which was adjusted to agree with the RAOB at 3-6 km, indicated a saturated mixing ratio (relative to ice) at the cloud base. RAOBs typically varied, reporting from 40 to 60 percent RH within clouds above 6 km, which is shown for five nights in Figure 2. RAOBs failed to resolve structure in profiles above 9 km (<-25C). The large discrepancies are in the direction consistent with reference to a liquid water vapor pressure curve extrapolated below freezing temperature.

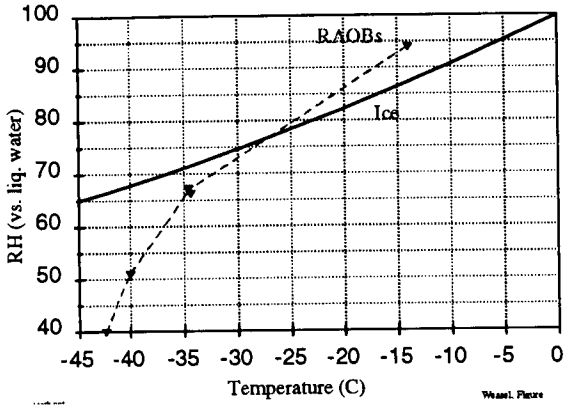


Figure 2. Relative humidity referenced to liquid water at cloud level, versus cloud temperature as measured by AIR radiosondes (triangles).

At large ranges, lidar signals were observed to have anomalous behavior, such that background-corrected signals remained high relative to the expected exponential decrease in water vapor. This is indicative of signal-induced photomultiplier noise known as after-pulsing (Campbell; Lee, et al.). For ratio signals, the anomaly was essentially independent of overall signal level. The effect was investigated in detail during the September campaign.

On several evenings, thick low clouds drifted in and out of view during observations. This was exploited in order to determine the effect of the intense low altitude signals on the high altitude measurements. Cases were examined in which Rayleigh and nitrogen channels indicated optically thick clouds. In these situations, signals should be essentially zero for range bins beyond clouds. In every case, slowly decaying signals were recorded in water range bins above cloud level. The waveform of the spurious signals was stable and the shape was relatively independent of signal level. A waveform derived from the average of cloud-blocked measurements was used for after-pulse correction (APC). The correction is significant beyond 5 km range. It is scaled in order to achieve convergence to zero water vapor above 14 km. In most cases, the combination of a constant dark current baseline subtraction and a scaled APC correction are required, particularly in the presence of moonlight. The APC signals generally had correct asymptotic behavior and in all cases, correct saturated mixing levels were indicated at the bases of high thin clouds.

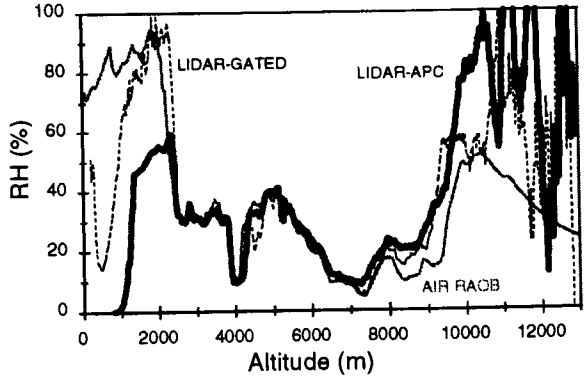


Figure 3. The solid line is an after-pulse corrected profile with a cloud base at 10.3 km. The dashed line corresponds to data obtained using the electro-optical shutter 23 minutes later. The region from 0 to 1.5 km is modified by transient switching.

Uncertainties associated with APC correction were reduced by use of an electro-optic shutter. Results are illustrated in Figure 3. The ratios are not corrected for wavelength and time dependent retardation at short times following the on-pulse for the device. Therefore, ratio measurements are only reliable beyond 2 km. Measurements obtained with the electro-optic shutter are nearly free of the slowly decaying APC waveform. Nonetheless, a small APC correction (10 percent of that needed in the absence of the shutter) improved the agreement between lidar and AIR RAOBs over the range from 7 to 9 km. The gated measurements at long range were generally similar to those made without a gate using optimized APC corrections. The shutter was not used routinely because it attenuated the water signals by about 80 percent in the open state.

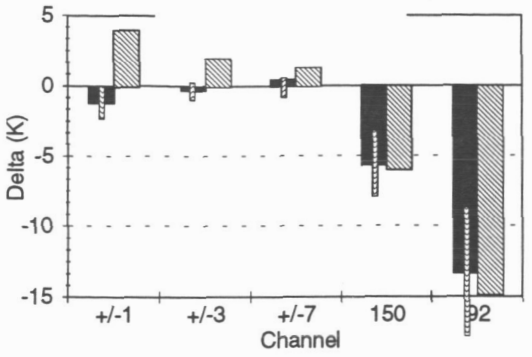


Figure 4. Difference between radiative transfer calculation and satellite measurements for the 10 best collocations. Black rectangles refer to lidar-based profiles, stripes to AIR radiosonde profiles, and thin gray lines to statistical uncertainty. The channels correspond to upper, mid-, and lower troposphere (183+/-1, +/-3,+/-7 GHz) and to lower troposphere plus surface (150 GHz) and, surface (92 GHz), respectively.

Differences between forward calculations and satellite measurements (SDRs) are presented in Figure 4. Generally, the correspondence is excellent, except for surface sensitive 92 and 150 GHz channels. The discrepancies are discussed below. At first, it was thought that acceptable agreement would be confined to relatively cloud-free nights. Later, it was established that agreement was excellent on most nights, provided after-pulse corrections were made. SSM/T-2 imagery did not reveal the influence of land in the vicinity of Kauai, therefore land does not account for the surface discrepancies. Land area is too small relative to the 92 GHz footprint. Land and orographic clouds, clearly influence the 92 GHz channel in the vicinity of the large island, Hawaii. Examination of collocated mid-infrared imagery from the DMSP OLS imager and SSM/T-2 imagery indicated that the microwave signals were not significantly influenced by cloud structure during the Kauai campaign. Based on differences in moisture and wind soundings between the windward and leeward sides of Kauai, we tentatively suggest that the large surface channel discrepancies are associated with an orographic drying effect in the vicinity of PMRFK. Additional evidence will be presented.

4. Summary

Forward calculations based on lidar data accurately predict SDRs observed in the atmospheric channels, provided account is taken of photomultiplier after-pulsing. For a given instrumental setup, it is possible to correct for this effect by scaling an after-pulse waveform to the overall amplitude of the signals integrated over the range profile.

For the Kauai experiments, the RMS difference between the reliable AIR and lidar measurements for altitudes 2 to 6 km corresponds to ~2 percent. Although our radiosonde data appears to be unreliable above 9 km, it was possible to extend RH measurements to higher altitude using lidar. This was based on the observation that the lidar constant is stable and independent of altitude. The accuracy required to calibrate SSM/T-2 atmospheric channels is based on this capability. Additional studies are needed to resolve substantial surface channel discrepancies.

5. Acknowledgments.

The authors express appreciation to supporting staff for design, construction and deployment activities. Particularly important contributions were made by David Hinckley, James Skinner, Steven LaLumondiere, and for deployment, Michael Zellmer and the Hawaiian Air National Guard. Thanks are also due to Dr. Carol Selvey, Arlene Kishi Donald Boucher and Lt. Lynda Wilson for supporting the effort. Generous advice provided by Dr. Harvey Melfi and coworkers is also gratefully acknowledged. The work was funded by the POESS Program Office and USAF under Contract F04701-96-C-0097.

References

Campbell, L. (1992). Afterpulse Measurement and Correction, *Rev. Sci. Instrum.* 63, 5794-5798.

Ferrare, R. A., Melfi, S.H. , Whiteman, D. N., Evans, K. D., Schmidlin, F. J., and O'C. Starr, D. (1995). A Comparison of Water Vapor Measurements made by Raman Lidar and Radiosondes," *J. Atm. and Oceanic. Technology*, 12, 1177-1195.

Lee, H. S., Schwemmer, G. K., Korb, C. L., Dombrowski, M., and Prasad, C. (1989). Gated Photomultiplier Response Characterization for DIAL Measurements, Appl. Opt. 29, 3303-3315.

Wang, J. R. , Melfi, S. H., Racette, P., Whitemen, D. N., Chang, L. A., Ferrare, R. A, Evans, D. D., and Schmidlin, F. J. (1995). Simultaneous Measurements of Atmospheric Water Vapor with MIR, Raman Lidar, and Rawinsondes, J. Applied Meteorology, 34, 1595-1607.

Is the PBL height well determined by aerosol lidar in very clean boreal conditions?

G. Larchevêque, V. Simeonov, H. Van den Bergh and B. Calpini
Swiss Federal Institute of Technology (EPFL), DGR-Laboratory of Air and Soil Pollution
CH-1015 Lausanne, Switzerland
Phone: ++41 (0) 21 693 6185, Fax: +41 (0) 21 693 3626, E-mail: gilles.larcheveque@epfl.ch

1. Introduction

Elastic backscatter lidar is known to be a very efficient and rather standard technique for the remote sensing of aerosol in the Planetary Boundary Layer (PBL), in particular for regions and meteorological conditions for which high load of particulate matters are present in the air and essentially trapped into the PBL [1]. Moreover, the top of the PBL is very often associated with a change in the temperature gradient versus altitude and the formation of an inversion layer. The aerosols are condensed at this height and their presence induces a very clear "signature" on the lidar signal showing the top of the PBL.

This paper report on the WINTEX pilot study: WINTEX (Land-surface-atmosphere interactions in a wintertime boreal landscape) is an EU Environment project which focuses on the study of land-surface-atmosphere exchange at high latitude and during winter time, under conditions for which the largest influences about likely climatic changes can be expected. This implies that studies of land-surface-atmosphere exchange should be concentrated to high latitudes and winter time, which was not the case up to the present WINTEX study. For both practical and theoretical reasons, such studies were essentially concentrated to the warm and biologically most active part of the year.

Our task in this project was to demonstrate the possibility to use an aerosol lidar in these very rude conditions, and especially for very low particulate matter concentration in the air. The EPFL trailer was installed during March 1997 in Marsta-Uppsala - Sweden, and recorded different meteorological events, in particular between March 12-17. At these days, other instrumental technique like scintillometer, meteo balloon soundings, and wavelengths resolved direct and diffused solar fluxes were engaged by different groups within the WINTEX project, as well as airborne data acquired by the STAAARTE British Hercule airplane.

2. Methodology

To fulfil the requirement of the present study, the performances of the EPFL lidar prototype were adapted in order to be used as a multi-wavelength backscatter lidar , with two beams set at 355 and 532 nm from a YAG laser source, with respectively 100 and 150 mJ/pulse at 10 Hz. The two beams are emitted in parallel, between the two receiving telescope, as shown in Figure 1. The first telescope is a newtonian type with a diameter of 200 mm for the primary mirror, thus unabling a detection range from typically 50 to 1'500 m. This telescope corresponds to the "short range telescope". The second telescope is a Cassegrain type telescope with a diameter of 600 mm and a measuring range from 0.4 to 14 km. It corresponds to the "long range telescope". Measurements were recorded simultaneously with the two telescopes, and polarized measurements were obtained from the 355 nm channel. At this point of the study, the data treatment is mainly

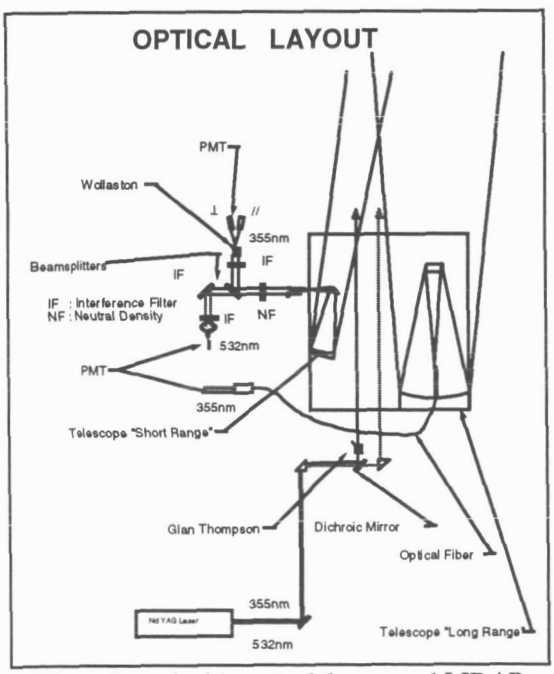


Figure 1: optical layout of the aerosol LIDAR

centered on the range corrected data. The analysis of the 355 nm signals and the 532 nm signals from the short range telescope shows that they coincide well with the signals from the long range telescope. The Klett algorithm allows us to invert the lidar signal and to extract the atmospheric volume backscatter.

3. Results

One example of the results obtained during this field study is presented in Figure 2. It is a time series of the range corrected of the total backscatter signals versus the altitude above ground level (AGL). In this figure the 355 and the 532 nm channels were measured alternatively, on a basis of typically 15 minutes, and are both normalized so to be combined on the same graph. These data were obtained with the short range telescope, each single profile being recorded and stored on a 12 bits 20 Mhz ADC converter within less than 2 minutes averaging time (1'000 shots per profile). No binning is applied on the data, and the range resolution is 7.5 m in this case. Even if the meteorological conditions were very clean and without cloud coverage in the morning, a well defined and stable mixing layer is seen with almost constant thickness form 0 to 8 h, while a fast development of the mixing layer in altitude from 9 to 18 h can be depicted. The two "spikes" around 15 and 16 h are due to the saturations of the PMTs because of the appearance of a cloud layer at the top of the PBL at that time, while after 18 h and due to a very rapid change in the weather conditions, snow falls started and therefore prevented any further lidar measurements.

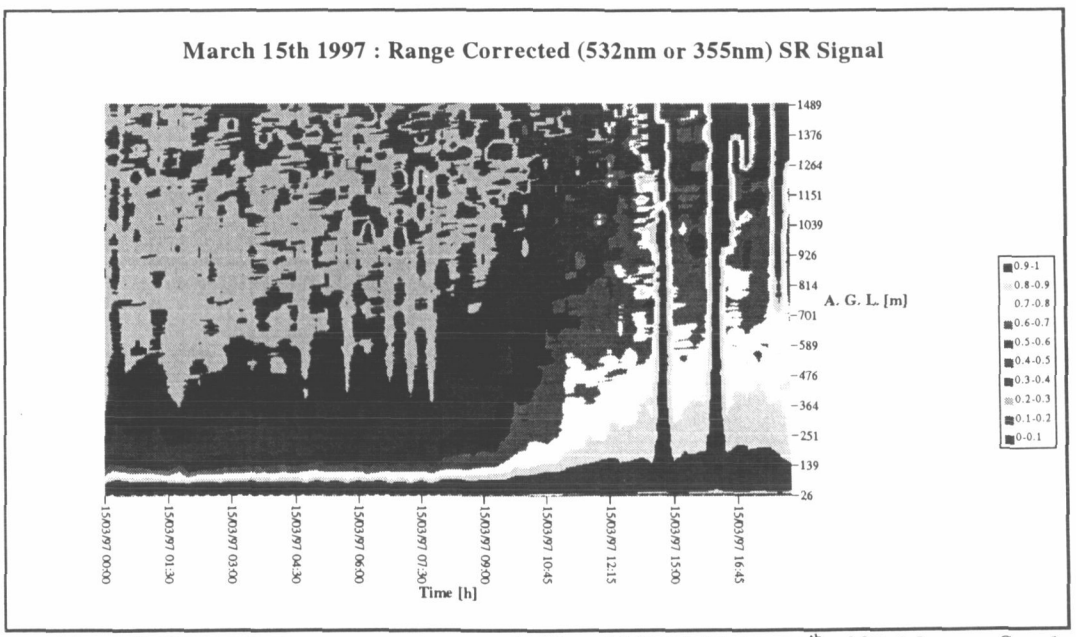


Figure 2: Range corrected signal between 0h00 and 18h00, March 15th 1997, Marsta - Sweden

From the results in Figure 2, it is possible to reconstruct the height of the top of the PBL, which is presented in Figure 3. In that case the data treatment consists in filtering and defining the intensity level corresponding to the transition between the lower altitude region with higher particle density (the PBL region) and the higher altitude region with lower particle density. Our estimate of the height of the PBL was further confirmed by balloon soundings launched close to the lidar trailer. This transition is shown by the "Mean" value presented in Figure 3, while the "Min" and "Max" curves correspond to respectively + and -16% of the mean signal intensity. This criteria indicates that the PBL height under night time conditions is very well defined (the inversion layer is very close to the ground) , while the PBL height is defined with a lower accuracy for day time conditions for where the aerosol load is diluted in a wider mixing layer. This example proves that it is possible to follow the daily evolution of the PBL in boreal conditions.

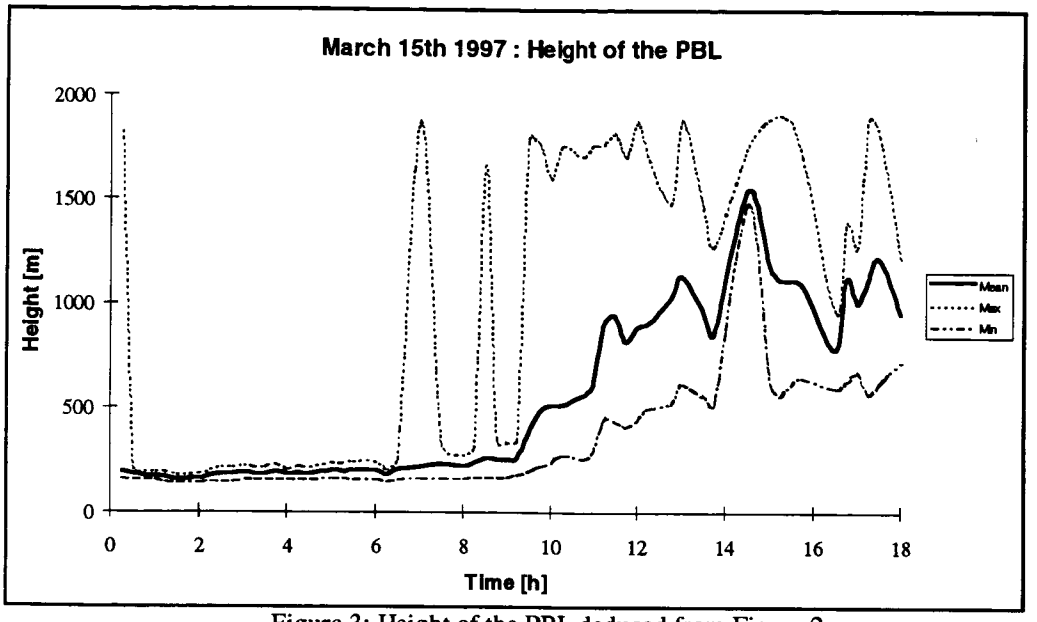


Figure 3: Height of the PBL deduced from Figure 2

4 Conclusion

During this WINTEX study, we demonstrated that even in very clean air conditions, the retrieve of the PBL height can be achieved, and gives similar results than well calibrated balloon soundings, with the advantage of continuous monitoring. A further analysis of the backscattered coefficient and the analysis of the polarised measurements at 355 nm will be presented, the latter giving more information about the particles optical properties. A comparison of our results with the measurement obtained by the sun photometer and the scintillometer is also foreseen.

Acknowledgement

Our thanks to the Swiss Federal Office for Science and Education (OFES) for the funding support of this project.

Reference

1 *The role of urban and suburban aerosols on solar UV radiation over Athens, Greece* (A. Papayannis, B. Calpini, A. Bais, D. Balis, H. van den Bergh, E. Durieux, L. Fiorani, L. Jaquet, I. Ziomas, C.S. Zerefos) Atmospheric Environment, Special issue on MEDCAPHOT, in press 1998.

Modeling Technique of Processing Raman-Lidar Returns from a Stack Emission to Extract Data on Its Composition and Total Outcome

I.B.Serikov, Yu.F.Arshinov, S.M.Bobrovnikov, and A.I.Nadeev

Institute of Atmospheric Optics, Siberian Branch of the Russian Academy of Sciences,
1 Akademicheskii Ave., 1, 634055 Tomsk, Russia
Phone: +7(3822) 25-98-86; Fax: +7(3822) 25-84-52; E-mail: arshinov@lwsa.tomsk.su

1. Introduction

Use of the Raman spectroscopy to analyze the composition of gas mixtures in the atmosphere still attracts much attention of researchers. The reasons for this are certain favorable, from the stand-point of constructing a measurement technique, features of the Raman scattering process. It is important that the Raman lines of molecular species present in a mixture are observed simultaneously, with the line of atmospheric nitrogen being among them. Ratios of the Raman line intensities of contaminating gases to that of nitrogen make a good basis for constructing a closed technique of spectroscopic gas analysis of such atmospheric formations as emissions from plant stacks.

However, Raman light scattering is an extremely weak effect what imposes a strong restriction on its use in spectral analysis of atmospheric formations. Most practical seems to be the Raman-lidar detection of contaminating gases in atmospheric emissions from plant stacks[1]. First of all this is caused by high concentration of gases in such emissions, especially at the stack mouth.

In this connection it is worth noting that along with the emission gas composition it is desirable to measure the velocity of the emission jet outflow to be able to estimate the emission gross yield.

Earlier[1,2] we have discussed a possibility of estimating the velocity of the emission outflow from a stack using the Raman-lidar return signal along sounding path that pierces the stack plume near the stack mouth. Unfortunately, the approach proposed in these papers strongly depends on conditions to be fulfilled for the assumptions made to work.

Besides, the possibility of calibrating Raman-lidar returns from contaminating gases by that from nitrogen within the volume inside the emission from a stack is not so trivial because the temperature inside the emission jet is higher than in the ambient air and, as a result, the concentration of nitrogen is also to be determined. Therefore certain methodical efforts are needed to make use of simple relations between the ratios of the Raman-lidar returns and the concentration of the contaminating gases sought.

Strictly speaking, when constructing a technique for extracting parameters of an object under study from data of sensing, for example with a lidar, one certainly uses, either directly or indirectly, some models of the object itself or of its interaction with the sounding beam. In the case of lidar sensing one must add to this the models of optical and electronic channels of the lidar complex that are also necessarily involved into the final consideration. As a result, the sought parameters of an object under study and physical quantities measured with a lidar are related by expressions that involve many optical and other characteristics of the instrumentation used, just in accordance with those explicit or implicit models.

According to the above consideration one may state that the inverse problem of determining the parameters of atmospheric formations sounded from the lidar response may be reduced to constructing relevant models of the object and of the response detection system. Such a modeling is aimed at finding the best fit of the model response to the actual one acquired with a lidar. In so doing the parameters of an object model that provide the best fit may be interpreted as the object parameters sought. Using such an approach to solving the inverse problem one may avoid certain troubles, normally met in the processing of experimental data, that are connected, for example, with the necessity of their differentiation.

2. Basic relations

Normally, optical power of a lidar return collected with its receiving antenna from a scattering volume at a distance R is described by the so called lidar equation

$$P_{\lambda_i}(R) = P_0 \frac{c\tau}{2} G(R) \frac{A}{R^2} \beta_\pi^{\lambda_i}(R) T_{\lambda_0}(R) T_{\lambda_i}(R), \qquad (1)$$

where is $P_{\lambda_i}(R)$ is the power received at the wavelength λ_i of a Raman line from the ith gas component; P_0 is the laser pulse peak power; c is the speed of light; τ is the pulce duration; $G(R)$ is the lidar geometric (overlap) function; A is the receiving area; $\beta_\pi^{\lambda_i}(R)$ is the the Raman backscattering coefficient of ith gas; $T_{\lambda_0}(R) T_{\lambda_i}(R)$ is the product of atmospheric transmission at the wavelength of sounding radiation, λ_0, and at the wavelength of the $i$thRaman line, λ_i.

The backscattering coefficient $\beta_\pi^{\lambda_i}(R)$ if the ith gas component the product of the corresponding diffrential Raman cross-section, σ_π^i and number density, $N_i(R)$, of molecules at the range R ($\beta_\pi^{\lambda_i}(R) = \sigma_\pi^i(R) N_i(R)$.

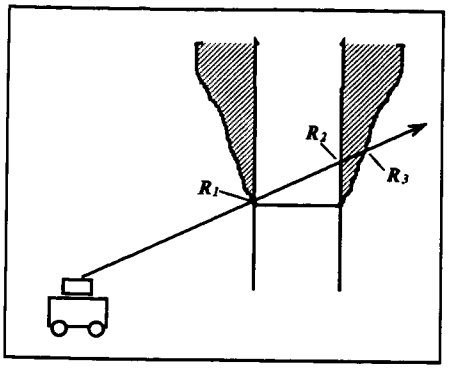
In reality any lidar return recorded with a recording system is a convolution of the function (1) and a pulse transient function, $\phi(r)$, of that system. So, the signal at a recording system output may be written as follows

$$S_{\lambda_i}(R) = \int_0^R \phi(R - r) P_{\lambda_i}(r)\, dr. \qquad (2)$$

As a consequence, when determining the concentration of a gas component from lidar return signal, we have to solve the equation (2). In the general case no exact solution of this inverse problem exists, though in some particular cases it may be solved analytically, under certain assumptions on the emission jet flow. For instance, in Ref.1 a technique is proposed for reconstructing the concentration of the emission components if the flow is nearly laminar. Therefore the search for possible algorithms to solve this problem is being done among numerical methods.

3. Technique for reconstructing the concentrations

In this paper we propose an algorithm for solving the above stated problem that is based on modeling the formation of lidar response from a gas component of an atmospheric emission from a stack. Basic assumptions that make up the approach being discussed are as follows. First we consider the case when sounding path pierces the emission jet just above the stack mouth. It is important since in that case we may consider the emission to be uniformly mixed regarding the distribution of its components over its cross section, while being not yet mixed with the ambient air. From what we just have said naturally follows the assumption that the function $N_i(R)$, entering the lidar equations (1) and (2), is a step-wise function of range along the sounding path, with the step being exactly above the stack mouth. However, the latter assumption should necessarily be modified because in practice the laser beam is incident onto an actual emission, sounded with a ground-based lidar, along a slant path (see Fig.1). As a result, the assumption on a step-wise behavior of $N_i(R)$ function is true only at the front boundary of the emission coming out from the stack since at the rear portion of the jet there may occur essential washing out of its boundary due to turbulent mixing with the ambient air. To allow for this effect we will model it as a gaussian process that yields a diffuse trailing edge of the otherwise rectangular pulse response. It is important to note that in the case of hot emissions from stacks the Raman-lidar return from nitrogen should have a dip in the range interval above the stack mouth[3], in contrast to a step in corresponding return signals from other molecular species. Taking this into account we write the models of $N_i(R)$ function for nitrogen and contaminating gases as follows

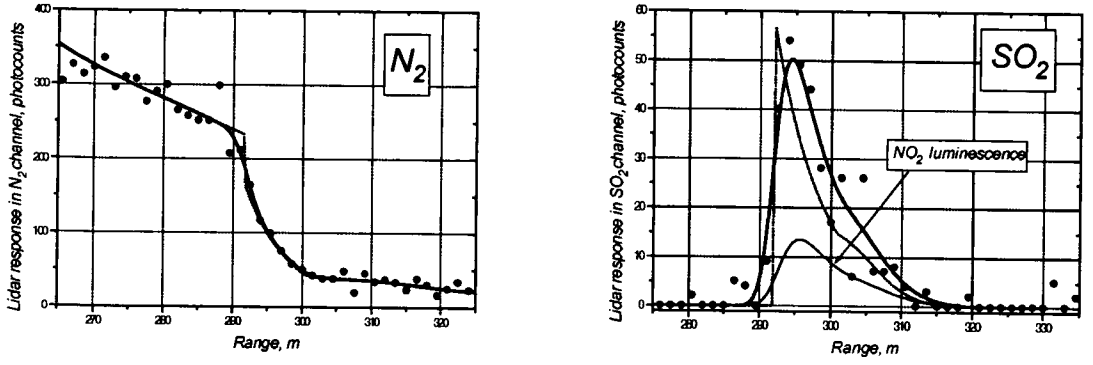


$$N_{N_2}(r)=\begin{cases} N_{N_2}^{atm} & for \quad r\in[0.R_1] \\ N_{N_2}^{atm}(1-A_{N_2}) & for \quad r\in[R_1,R_2] \\ N_{N_2}^{atm}[1-A_{N_2}\exp(-\dfrac{(r-R_2)^2}{2\sigma_R^2})] & for \quad r\in[R_1,\infty] \end{cases}$$

$$N_i(r)=\begin{cases} 0 & for \quad r\in[0.R_1] \\ A_i & for \quad r\in[R_1,R_2] \\ A_i\exp(-\dfrac{(r-R_2)^2}{2\sigma_R^2}) & for \quad r\in[R_1,\infty] \end{cases}$$

Fig.1. optical scheme of sounding

From these expressions one may readily see that the parameters of the model that must be fitted numerically are the distance R_1 to the emission, the amplitude or level of the emission A_i, and the width of the mixing region in the far end of the sounding path within the emission jet. In actual emissions from stacks, especially if they are hot, there is certain amount of nitrogen dioxide that contributes to almost all Raman lines from other gases due to the broad-band and long-lived luminescence[3]. In our model we allow for this factor by adding a corresponding model of this process the input data for which are the experimental data on the luminescence return at a wavelength in a region between Raman lines. An example of such modeling performed to achieve the best fit to experimentally measured lidar responses from nitrogen and SO_2 in the emission from an electric power plant is shown in Fig.2.



a *b*

Fig.2. Lidar responses from nitrogen (*a*) and SO_2 (*b*) in a stack emission from an electric power plant. Dashed curves present model responses prior to convoluting them with the lidar pulse transient function; bold solid lines show the best fit model of the total lidar responses, including the luminescence from NO_2 molecules.

Thus it is seen from these data that the modeling approach to Raman-lidar data processing provides for obtaining the estimates of the gas species concentration in the stack emissions since when achieving the best fit of a model to the actual lidar data we automatically determine the amplitudes of the gas concentrations in the emission jet as it is among the model parameters that are being involved in the fitting process.

4. Estimating the emission jet outflow velocity

In contrast to more or less clear physical grounds for extracting information on atmospheric emission gas composition from Raman-lidar returns the problem of estimating the outflow velocity of the emissions from lidar returns is not yet well understood. In this paper we are going to discuss in a more detail the approach that is based on detecting fluctuations of the emission jet boundary and relating their properties to the velocity sought. Figures 3,*a* and *b* show two versions of optical arrangement that may be applied to detection of the emission boundary fluctuations. The first one assumes measuring return signals with two beams from two points on the boundary, while the second one suggests to optically isolate two sub-volumes in a scattering volume from a single sounding beam.

Thus recorded returns from the two spots on the emission boundary will bear information on the boundary fluctuations either through varying distance to the boundary directly, or through the fluctuations in the return power, if a photon counting is used to integrate the return power within a single time gate centered at the boundary. It may be shown that correlating the time series of thus recorded return signals one may estimate the outflow velocity of the emission jet. Moreover the estimates that we have already done in a model experiment show a good promise for making this approach practicable.

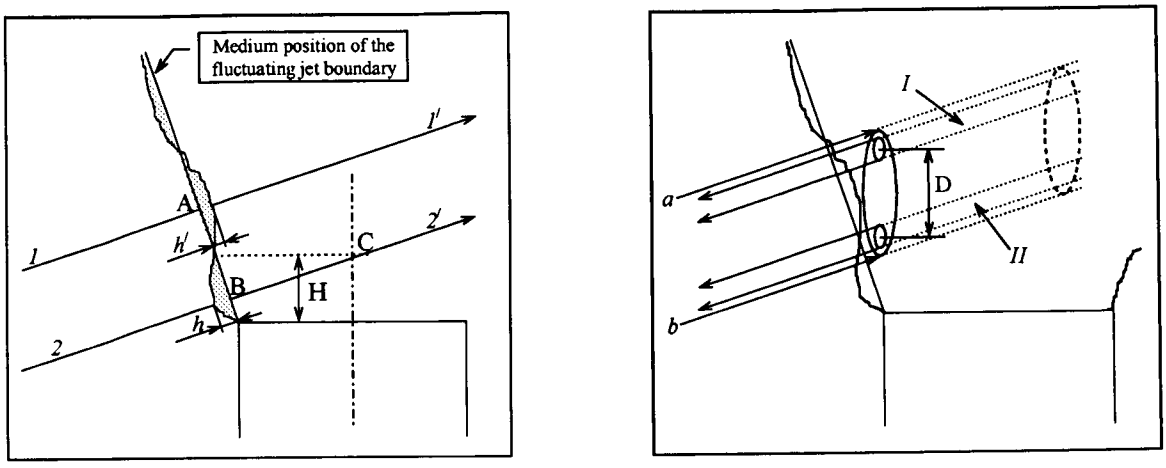


Fig.3. two versions of the optical arrangement for lidar detection of the emission boundary fluctuation; using two spaced beams (*a*) and two spots from one and the same beam (*b*)

The model estimates have been done with the allowance for the following factors that may affect the measurement accuracy:

- statistical nature of the interaction between the laser radiation and the aerosol in the emission;
- uncorrelated behavior of random variations in the recording system parameters;
- fluctuations in the tangential component of the jet outflow velocity that may result in deformations of the correlation function shape;
- random fluctuations in time of the recording system triggering;
- fluctuations of the electron travel time through a PMT's dynode system;
- finite length of the laser pulses.

The numerical simulations that we have performed show that it is quite realistic to achieve the accuracy of the velocity measurements within several per cent error interval.

References:

1. Yu.F.Arsinov, S.M.Bobrovnikov, V.K.Shumskii, A.G.Popov, I.B.Serikov *Remote determination of the composition, temperature, and velocity of outflow of the atmospheric emission from plant stacks using a Raman lidar*. Atmos. Ocean. Opt. V5, No.5, pp323-328 (1992

2.Yu.F.Arsinov, S.M.Bobrovnikov, V.K.Shumskii, A.G.Popov, I.B.Serikov *An extension of the Raman-lidar technique to measure the velocity and temperature of the atmospheric emission jets from stacks* 16th International Laser Radar Conference. Conf. Abstracts, pp.239-242.Cambridge, Massachusetts, USA, 20-24 July, (1992)

3. Yu.F.Arshinov, S.M.Bobrovnikov, I.B.Serikov, D.I.Shelefontyuk, V.K.Shumskii, P.V.Bazylev, V.A.Lugovoi, N.N.Stolyarov. *Calibration of a Raman-lidar gas analyzer of atmospheric emissions from plant stacks using a remote gas chamber* "Advances in Atmospheric Remote Sensing with Lidar" Selected papers of the 18th International Laser Radar Conference (ILRC), pp. 427-430. Springer,Berlin,22-26 July (1996)

Towards water vapor profiling with BELINDA

Holger Flint, Felix A. Theopold, and Claus Weitkamp

GKSS-Forschungszentrum Geesthacht GmbH, D-21494 Geesthacht, Germany

Phone: +49 4152 87 1836, Fax: +49 4152 87 1888, E-mail: holger.flint@gkss.de

1. Motivation

Moisture and temperature are important properties of the atmosphere. The study of dynamical processes in the planetary boundary layer requires the capability of daylight measurements of these parameters with high spatial and temporal resolution.

Differential-absorption lidar can meet these requirements (Browell et al., 1979; Bösenberg, 1997). However, DIAL measurements are strongly affected by gradients in the Mie-to-Rayleigh scattering ratio (Ansmann, 1985; Theopold et al., 1993), as they occur in smokestack plumes and at cloud boundaries. Problems are also caused by slightly different fields of view that originate in imperfect alignment of the laser beams. To reduce the influence of these effects, the BELINDA concept (Theopold et al., 1992) has been developed.

2. Principle of measurement

In BELINDA, or **B**roadband **E**mission **LI**dar with **N**arrowband **D**etermination of **A**bsorption, the basic idea is to perform the spectral separation of the on-resonance and off-resonance signals in the receiving part of the system, in contrast to the usual DIAL setup with two lasers or one laser with wavelength switching. For the implementation of BELINDA, one laser is needed with a linewidth of approximately twice the width of the absorption line of the gas that is to be measured. For the determination of water vapor at wavelengths around 730 nm the required linewidth is around 0.4 cm^{-1} FWHM. Calculations show that the required smooth lineshape is only necessary on the average, not for every individual laser pulse.

At the receiving end a polychromator with special features must be available. The device currently used is a combination of a Fabry-Perot interferometer for the detection of backscattered radiation in the wings of the absorption line which corresponds to the "off-line" signal of a conventional DIAL, and a special double-cavity etalon (Linow, 1994) with two closely-spaced transmission peaks on either side and close to the center of the absorption line, which transmits the "on-line" lidar signal (Theopold et al., 1996).

3. Experimental setup

In the actual BELINDA setup (Fig. 1) a tunable flashlamp-pumped Ti:sapphire laser (modified Elight, 410HR) is used.

A small fraction of the outgoing laser light is extracted for beam analysis. We currently monitor the temporal behavior, the energy, the center wavelength and the spectral shape of the laser pulses. The wavelength is measured with a commercial instrument (ATOS Lambdameter) that in our application provides the absolute value to an accuracy better than 3 pm or 0.05 cm^{-1} (only three of the four Fizeau interferometers of the Lambdameter are used). In addition, a photoacoustic cell filled with water vapor is used to determine whether the emission wavelength coincides with the center of the absorption line. The linewidth and the spectral shape are

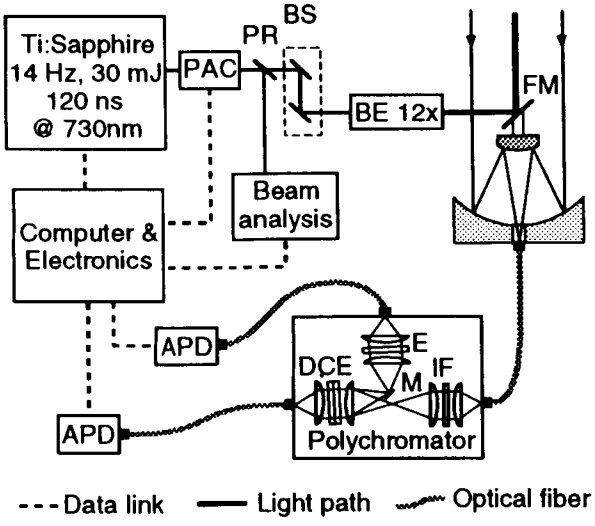


Figure 1. Experimental setup of BELINDA, PAC: photoacoustic cell, PR: partial reflector, BS: beam steering optics, BE: beam expander, FM: folding mirror, IF: interference filter, DCE: double-cavity etalon, M: mirror, E: Fabry-Perot interferometer, APD: avalanche photodiode.

monitored in real time with an etalon with a finesse of 38 and a free spectral range of 1.2 cm^{-1} in combination with a CCD camera.

After twelvefold expansion with a Galilean telescope the beam has a diameter of 80 mm and a divergence of 0.1 mrad. It is transmitted into the atmosphere via an Al-coated folding mirror.

The backscattered light is collected with a commercial 280 mm (11″) diameter Cassegrain telescope (Celestron C11) and directed into the polychromator through an optical fiber. After spectral separation with the interferometers inside the polychromator the light is detected by Si avalanche photodiodes (APDs, EG&G C30921E).

Digitizing of the signals is carried out with a specially designed 12 bit, 40 MSamples/s transient recorder, jointly developed and built with the GKSS electronics department.

The whole system is controlled by one Macintosh Computer with a user-friendly graphical user interface, written mainly in LabVIEW. It is used for system alignment and data acquisition, data visualization, and data storage. It also allows the on-line control of all relevant parameters and keeps a protocol of every action, particularly the change of parameter settings, in order to facilitate quality assurance.

4. Results

At 729.6 nm an output of 30 mJ could be achieved. Under these conditions the measured temporal width of the laser pulse is 120 ns corresponding to a minimum spatial resolution of 18 m. The spectral distribution is smooth on a 50-pulse average (≈ 4 s) yielding a linewidth of 0.38 cm^{-1}. After a warm-up time of 20 minutes the drift of the laser wavelength is stable to ± 0.05 cm^{-1} which is sufficient BELINDA.

In order to improve the signal-to-noise-ratio (SNR) we cooled one of the APDs with a thermoelectric cooler, thus increasing the gain. A first analysis shows a slightly better SNR, but this result must be confirmed by additional measurements.

The system is now capable of performing routine measurements of water-

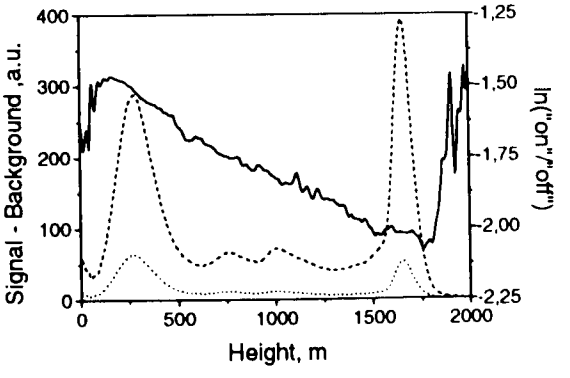


Figure 2. BELINDA measurement of 6.3.1998, 17:30 CET, with a gliding average of 75 m and temporal resolution of 120 s. The „on-line" and „off-line"-signals are scaled at the left and given by the dotted and dashed lines, respectively. The solid line represents the optical depth and is scaled at right.

vapor optical depths as shown in Fig. 2.

The figure shows an almost constant slope between 150 and 1800 m. The average slope is in very good agreement with the one calculated from the ground values of temperature and humidity and a standard atmospheric model. The increase beyond 1800 m is caused by lack of signal and has no physical significance.

As predicted by theory strong gradients in the backscatter ratio have little effect on the measured optical depths. The minimum distance from which the signal can be evaluated without perturbation is about 150 m. This is well within the region of partial overlap of the laser beam with the receiver field of view.

5. Conclusion and future prospects

The work described in this contribution shows that the problems associated with the implementation of the BELINDA concept could all be solved. Several of the predicted advantages have been demonstrated and thus a significant improvement over conventional water vapor DIAL has been achieved.

However, the temporal and spatial resolution is not yet sufficient for flux measurements. To improve the resolution an increase of the signal-to-noise-ratio is necessary. Several steps towards this aim are planned, e.g., injection seeding of the Ti:sapphire laser with a suitably chosen laser diode to increase the output power, more sensitive APDs, and an amplifier with less noise. The greatest effect is expected from an increase of the free aperture of the interferometers inside the polychromator, without change of the achieved transmission characteristics. This now seems possible due to progress in the technology of grinding, polishing, and coating of optical surfaces.

References

Browell, E. V., Wilkerson, T. D., McIrath, T.J. (1979). Water vapor differential absorption lidar development and evaluation. *Appl. Opt.*, 18: 3474-3483

Bösenberg, J. (1997). Remote Sensing of the Troposphere Using Differential Absorption Lidar. *Report No. 236*, Max-Planck-Institut für Meteorologie.

Ansmann, A. (1985). Errors in ground-based water-vapor DIAL-measurements due to Doppler-broadenend Rayleigh backscattering, *Appl. Opt.*, 24: 3476-3480

Theopold. F. A., Bösenberg. J. (1993). Differential absorpion lidar measurement of atmospheric temperature profiles: Theory and experiment. *J. Atm. Oc. Tech.*, 10: 165-179

Theopold. F. A, Weitkamp, C., Michaelis, W. (1992). BELINDA: Broadband Emission Lidar with Narrowband Determination of Absorption. A new concept for measuring water vapor and temperature profiles. *NASA CP-3158* :671-674

Linow, S. (1994). Drei-Spiegel-Interferometer für ein DAS-Lidar mit breitbandiger Emission und schmalbandigem Nachweis. Diplomarbeit, Fachbereich Physik, Universität Hamburg, GKSS 94/E/62.

Theopold, F. A., Behrendt, A., Flint, H. Weitkamp, C. (1996). First Results of the BELINDA Approach. In: Ansmann, A. Neuber, R. Rairoux, P. Wandinger, U., eds.: *Advances in Atmospheric Remote Sensing with Lidar*. Springer, Berlin Heidelberg New York: 325-328.

Broadband lidar measurements of tropospheric constituent profiles

I. M. Povey, A. M. South, C. Hill, and R. L. Jones
Centre for Atmospheric Science, University Chemical Laboratory, University of Cambridge,
Lensfield Road, Cambridge CB2 1EW, United Kingdom
Tel:+44 1223 336521, Fax:+44 1223 336362, E-mail: imp20@hermes.cam.ac.uk

1. Introduction.

Absorption spectroscopy in the UV-visible region of the electromagnetic spectrum is now a well-established method for measuring the atmospheric concentrations of a range of different constituents. In the troposphere the technique has been used to obtain surface concentrations of a number of species using long path differential optical absorption spectroscopy (DOAS). However, while offering high species selectivity, the DOAS method generally suffers from the limited spatial resolution obtainable in comparison with lidar. Differential absorption lidar (DIAL) and Raman lidar systems used in constituent profiling are also subject to limitations. Vibrational Raman lidar is restricted by the extremely small Raman cross sections of most molecules, a consequence of which is that only in the study of atmospheric water vapor have significant advances been made. DIAL is at present limited to measuring single atmospheric species with well-resolved spectral features and relatively large differential absorption cross sections (H_2O, O_3, and, at very short range and high levels of pollution, NO_2 and some hydrocarbons). The presence of aerosol in significant amounts (as are frequently observed in the troposphere) also leads to substantial errors in DIAL methods. By comparison, DOAS offers a means for the simultaneous detection of many atmospheric trace species. With DOAS, spectrally resolved measurements over a wide bandwidth enable the unambiguous identification of several species even where absorptions overlap. A further advantage is that the method is very insensitive to the presence of Mie and Rayleigh scattering, due to the high-pass filtering technique used to obtain differential spectra. However, DOAS measurements to date have provided only extremely limited vertical resolution in the troposphere, and generally only path-averaged measurements are possible by this method.

We present a development of both DOAS and DIAL in which the advantages of both methods (spatial resolution of DIAL and species discrimination of DOAS) are combined. The method employs a broadband laser, an imaging spectrometer and a CCD camera used in a novel mode, permitting simultaneous altitude- and wavelength-resolved measurements of backscattered photons. We present the principles of a broadband lidar, including the critical element: the use of a CCD detector and present examples of measurements.

2. Principles of Combining DOAS and DIAL

The basis of the development described here is to combine the advantages of both the DIAL technique and DOAS methodology in which a multiwavelength and time-resolved detection system is coupled to a broadband short-duration light source. The aim is to obtain altitude-resolved broadband spectra to which the DOAS technique can be applied to directly derive high-resolution vertical profiles. Central to the operation of such a system is the detector which must combine high wavelength and time discrimination. As the backscattered light must be spectrally resolved (generally at higher resolution than 1 nm full width at half maximum (FWHM) to avoid degrading the magnitude of the differential cross sections of the species to be measured), a grating spectrometer is required; this necessity coupled with the need for "whole spectra" acquisition rates of 10^5 s^{-1} rules out the use of the traditional lidar detector, the photomultiplier tube (PMT). Similarly, the slow readout time of a photodiode array (often used in DOAS instruments) makes their use unsuitable. However, the use of a charge- coupled device (CCD), coupled with an imaging spectrometer, allows both criteria to be met. A CCD is essentially a two-dimensional array of electrodes that are insulated from a light sensitive silicon thin film and from each other by a metal oxide layer. The incident light is converted to photocharge in the silicon layer and is constrained in potential wells. By applying suitably phased voltages to the electrodes along one of the axes of this pixel array, charge can be transferred efficiently between rows of CCD pixels in either direction. The timing

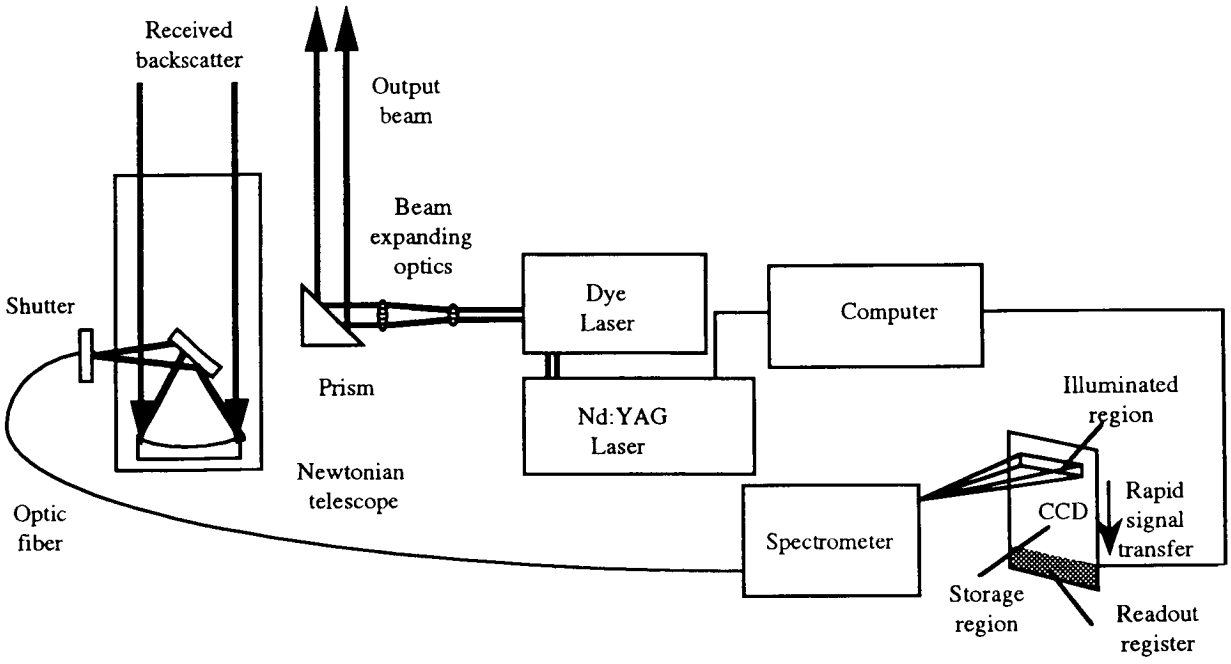


Figure 1. Schematic diagram of the broadband lidar system. Radiation from the Nd:YAG pumped broadband dye laser is expanded and collimated by a Galilean telescope and directed into the atmosphere via a right-angled prism. The receiving optic consists of a 40 cm Newtonian telescope, the output of which is focused into an optic fiber and transferred to an astigmatic Czerny-Turner spectrometer. The wavelength-dispersed light is imaged across the unmasked region of the CCD perpendicular to the axis of fast charge transfer.

and sequence of these phased voltages along the time axis of the CCD are referred to as a clocking sequence. When the photocharge reaches the edge of the array, it can be read out.

In the present application the CCD is positioned in the focal plane of an imaging spectrometer, which disperses the spectrum across rows of the CCD, the CCD is itself masked to prevent illumination of the unexposed parts of the CCD and to improve the definition of the exposed area. The spectrum accumulated within this illuminated region is then transferred along the time axis by a clocking sequence, allowing subsequent spectra to be recorded by the exposed rows. The current system employs a Nd:YAG pumped broadband dye laser with a pulse duration of 6-8 ns. The short pulse duration of the laser means that the maximum obtainable altitude resolution is dictated by the time gate of the CCD detector, defined by the number of exposed rows and clocking rate of charge transfer. In the prototype instrument, for throughput considerations the exposed region has been set at 10 rows; thus, with a maximum clocking rate of 1 μs per row, an altitude resolution of 1.5 km is obtainable.

As the CCD is capable of efficiently transferring data in both directions on the CCD, the altitude-resolved spectra can be returned to the starting position after one laser pulse to await the next, allowing on-CCD integration of laser pulses. What is thus obtained is a series of time- and thus altitude-resolved spectra, to each of which the standard DOAS analysis method can be applied using the first return signal as a zero altitude reference spectrum. Subtraction of line-of-sight amounts then allows the vertical profile to be determined, as with a conventional lidar.

3. Instrument Details

The Cambridge lidar (Figure 1), employs a Q-switched (Spectron SL803-G) Nd:YAG laser

operating at 20 Hz with a nominal divergence of 0.5 mrad. This laser source provides 900 mJ per pulse at 1064 nm, with a 6-8 ns pulse duration. The Nd:YAG second and third harmonics are employed to transversely pump a dye laser (Spectron SL4000B) from which the dispersive element in the laser cavity has been removed to give a broadband spectral output. By selecting suitable dyes, an output pulse with a FWHM of 10-20 nm can be achieved at the required wavelength in the visible spectrum (400-750 nm), pulse energies at 20 Hz are typically in the range 50-150 mJ. The beam divergence of the dye output is 0.8 mrad, although with appropriate beam expansion optics this can be reduced to 0.1 mrad to match the field of view of the detection system. The laser output is directed vertically into the atmosphere via a turning prism 0.25 m from the central axis of a 0.4 m diameter standard *f*/4 Newtonian telescope of 1.6 m focal length. The backscattered light received by the telescope is focused to a shuttered optical fiber, which in turn relays the light to the entrance slit of an astigmatic imaging Czerny-Turner spectrometer (Chromex 250 IS) with a 250 mm focal length and an *f*/4 aperture to match the receiving telescope output. The flat field image of the spectrometer is projected onto the CCD perpendicular to the fast charge transfer axis. The CCD camera employed in these studies is an Astrocam 4201 fitted with a TE3A head, which is Peltier air cooled to >40°C below ambient temperature. The CCD itself (EEV 37-10) is an UV-coated 512 times 1024 array of 15 μm square pixels.

4. Observations

The first results with a broadband laser are presented, measurements being performed across the 715-730 nm absorption band for H_2O profiles, and the 650-670 nm spectral region for simultaneous detection of H_2O and NO_3.

4.1 Retrieval of H_2O (715-730 nm). Water vapor is the most variable of the major molecular constituents of the atmosphere and plays a primary role in many atmospheric processes; hence measurement of its spatial and temporal distribution is of paramount importance. Because of their large and highly structured absorption cross sections the visible absorptions corresponding to the 4ν vibrational overtone bands of H_2O are suitable spectral features for broadband laser ranging.

A laser output centered at 715 nm (FWHM 12 nm) was generated by 532 nm pumping of a Pyridine II methanol solution to give a pulse energy of 40 mJ. Spectra averaged over 1 hour periods were accumulated throughout the night of 15 October 1996 (2230-0600 G.M.T.). U.K. Meteorological Office (UKMO) radiosonde data (Vaisala RS80L device) were obtained from the British Atmospheric Data Centre for comparison, from the closest stations in the UK Upper Air Network - Shoeburyness (51.55N, 0.83E) and Herstmonceux (50.90N, 0.33E) - both within 125 km of the lidar location (52.12N, 0.08E).

Zero-altitude spectra (reference spectra) were recorded by sampling the expanded laser beam prior to output to the atmosphere. This was necessary for lower troposphere measurements because the non-coaxial nature of the output and detection systems with the prototype design resulted in poor overlap of the transmitted beam and detector field of view at low altitudes.

The measurement of water vapor profiles employing the 4ν vibrational overtone bands of H_2O is complicated by the narrowness (<10 pm) and intensity of individual ro-vibrational transitions, so that the Beer-Lambert law may not be directly applied to the measured lower-resolution backscatter absorption spectra. Instead, a line-by-line calculation at high spectral resolution is made using HITRAN data [*Rothman et al.*, 1992]; the resulting transmission is smoothed to the instrument resolution before fitting to the measured absorption spectra. By starting with the lowest-altitude return, and incorporating the fitted amounts of water vapor

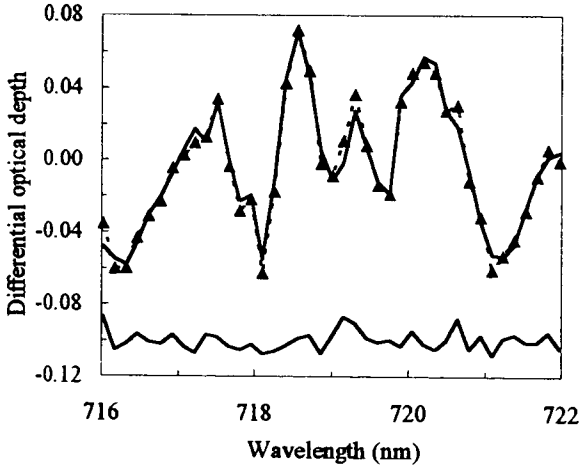


Figure 2. The observed (triangles on dotted line) and fitted (solid line) differential optical depths for water vapor, with the residual displaced for clarity. The backscatter spectrum was recorded on 10/15/1996 (integration time, ~1 hour) and has a scattering altitude of ~1.8 km. The rms residual is 0.006 (0.6%).

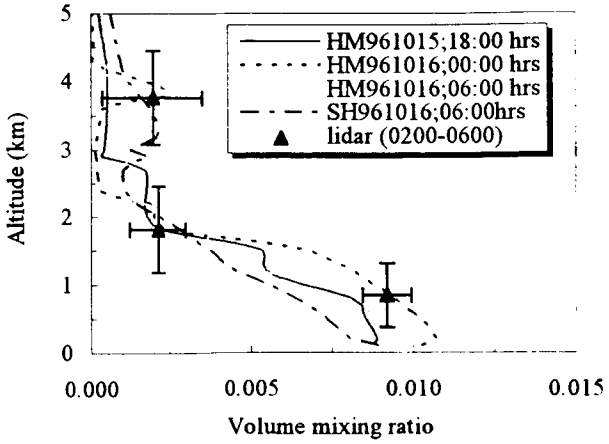


Figure 3. Water vapor mixing ratio for 15-16 October 1996, measured by the broadband lidar over Cambridge (solid triangles) and by radiosondes released from Shoeburyness (SH) and Herstmonceux (HM).

in the calculation of the transmission for higher altitudes, an H_2O number density profile is obtained. This is converted to a mixing ratio profile by assuming, in this case, the U.S. Standard Atmosphere (1976) temperature profile. An example of the quality of the spectral fit obtained is shown in Figure 2, and the corresponding water profile up to an altitude of ~4 km is shown in Figure 3 with (UKMO) radiosonde data for comparison. It is evident from the presented data that the potential of the lidar system to profile water vapor from the ground to at least the middle troposphere is excellent.

4.2. Simultaneous Retrieval of NO_3 and H_2O (650-670 nm). The broadband lidar has also been used to study the much weaker features of the $4\nu+\delta$ overtone region of the H_2O spectrum and the NO_3 absorption centered at 662 nm. A consequence of the atmospheric importance of NO_3 is that this spectral region has been studied extensively by DOAS, zenith sky and moon-pointing instruments. Despite the extensive measurements, tropospheric, or indeed boundary layer, profiling of NO_3 has yet to be obtained.

To maximize the signal-to-noise ratio, the backscatter spectra from each night were averaged over the whole measurement period and in the altitude axis to give a single profile point relative to the zero-level reference. Spectral fits for H_2O and NO_3 were performed across the 651-668 nm region applying functions derived from literature cross sections. The total fit obtained for August 19, 1996

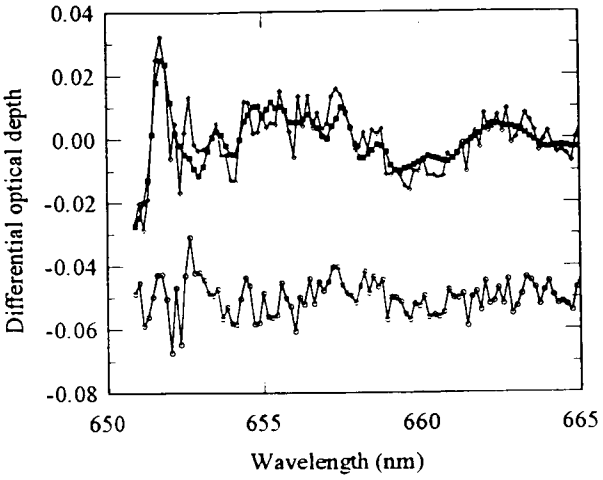


Figure 4. The observed (open diamonds) and fitted (solid squares) total differential spectra of August 19, 1996, with the residual (open circles) displaced for clarity. Spectral features due to NO_3 (centered at 662 nm) and H_2O (652-660 nm) are present; the rms residual is 0.0056 (0.56%).

data is illustrated in Figure 4, from which it is clearly evident that the two species NO_3 and H_2O are present. The corresponding mixing ratios of the two species are 211±51 pptv and 0.95±0.09 % respectively. The high NO_3 concentration is indicative of a polluted boundary layer.

5. Summary

It has been shown that the broadband lidar technique is viable for nighttime range-resolved visible absorption spectroscopy in the troposphere. Vertical profiling of water vapor up to ~4 km has been achieved by monitoring spectral features due to the 4ν vibrational overtone bands. It has also been demonstrated that the broadband lidar is capable of multiple species determination, monitoring the $4\nu+\delta$ vibrational overtone band of H_2O and the NO_3 radical.

References

I. M. Povey, A. M. South, C. Hill, A. t'Kint de Roodenbeke, R. A. Freshwater and R. L. Jones, A broadband lidar for the measurement of tropospheric constituent profiles from the ground, *J. Geophys. Res.*, **103**, (D3), 3369-3380, 1998.

Rothman, L.S. *et al.*,The HITRAN molecular database: editions of 1991 and 1992, *J. Quant. Spectrosc. Rad. Transfer, 48*, 469-507, 1992.

South, A. M., I. M. Povey, R. L. Jones, Broadband lidar measurements of tropospheric water vapor profiles, *J. Geophys. Res.*, submitted 1998.

Comparison of Aerosol Properties Derived from Lidar, Sun Photometer, and *in situ* Observations During the Aerosol Characterization Experiment 2

Frank Wagner, Detlef Müller, Albert Ansmann, Diana Weise, Dietrich Althausen
Institute for Tropospheric Research (IfT)
Permoserstr. 15, 04303 Leipzig, Germany
Phone: ++49 (0)341 235-2941, Fax: ++49 (0)341 235-2361, E-mail: frank@tropos.de

1 Introduction

Atmospheric aerosol particles influence the Earth's radiation balance both directly by scattering and absorption of light and indirectly by acting as cloud condensation nuclei, thereby influencing the albedo and lifetime of clouds. The Aerosol Characterization Experiments (ACE) are a series of international field studies to understand the combined chemical and physical processes that control the evolution of those aerosol properties that are relevant to radiative forcing and climate. ACE-2 focused on anthropogenic aerosols from the European continent and desert dust from the African continent as they move out over the North Atlantic Ocean.

In ACE-2 we have used the IfT scanning six-wavelength lidar, an 18-channel sun and sky photometer, and a DMPS/APS (Differential Mobility Particle Sizer/Aerodynamic Particle Sizer) system to determine aerosol optical properties and aerosol size distributions. The instruments were operated at Sagres, Portugal, on more than 40 days during the ACE-2 intensive field campaign held in June and July 1997.

In this contribution we show measurements of optical and microphysical particle properties obtained with the aforementioned systems in the case of a well-mixed marine boundary layer. Microphysical particle properties derived from multiwavelength- lidar and sun-photometer measurements with two different inversion techniques and the *in situ* measured size distributions are compared.

2 Instruments

The IfT scanning six-wavelength lidar uses two Nd:YAG and two dye lasers to emit light simultaneously at 355, 400, 532, 710, 800, and 1064 nm (Müller et al., 1996). Signals elastically backscattered by molecules and particles at these wavelengths as well as Raman-scattered light from nitrogen at 607 nm and from water vapor at 660 nm are detected. From these, six backscatter coefficients and one extinction coefficient and the water-vapor mixing ratio are determined. From measurements at two different zenith angles optical thicknesses of aerosol layers at all six measurement wavelengths can be estimated in addition (Gutkowicz-Krusin, 1993; Ansmann et al., 1998).

The sun photometer (company Dr. Schulz & Partner, Germany) is a compact system which automatically tracks the sun. A silicon diode permits one to measure both direct solar and sky radiance, and thus column-integrated optical depths and sky-brightness phase functions, at 18 wavelengths between 351 and 1064 nm. The wavelengths are selected with interference filters with halfwidths smaller than 5 nm. The instrument was calibrated at the high-mountain site Zugspitze in the German Alps before the ACE-2 intensive field campaign.

Ground-based measurements of aerosol size distributions were carried out with a DMPS for particles in the size range from 3 to 860 nm (mobility diameter) and with an APS in the range from 800 to 10000 nm (aerodynamic diameter). Larger particles were cut off with a pre-impactor at the inlet.

3 Measurement example

In order to make the results of the three very different – profile, path, and point – measurements comparable we chose a measurement taken in the early morning of 20 June 1997. On that day a fairly well-mixed boundary layer was present and no additional aerosol layers above that could be observed. Thus, one can expect that all three devices observed nearly the same aerosol features. In the early morning one can use, on the one hand, data from Raman measurements at night and, on the other hand, sun-photometer almucantar measurements taken shortly after sun rise.

Figure 1 shows the lidar backscatter profiles and the humidity profile calculated from the Raman measurement of the water-vapor mixing ratio and the temperature profile of a radiosonde launched at the field site at 06:10 UTC. The lidar was operated under a zenith angle of 60°. The top of the boundary layer at 550 m can clearly be seen. The profiles indicate a fairly good mixing. The relative humidity increased slightly from the surface to the top of the mixing layer. Some change in the spectral behavior of the backscatter coefficients at different heights was present. Backscatter values below about 250 m are not reliable because of the high uncertainty in the correction of the incomplete overlap between the laser

beam and the receiver field of view. Looking at time series of meteorological data and of measured signals from the three systems one can conclude that the conditions were nearly constant during the measurement period.

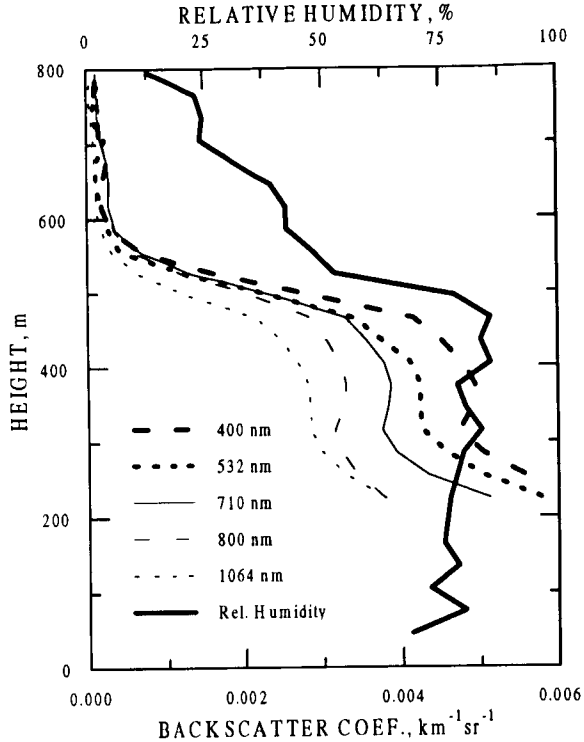


Fig. 1: Vertical profiles of backscatter coefficients and relative humidity measured with lidar on 20 June 1997, 02:00 - 05:00 UTC.

The aerosol backscatter coefficients were computed with the Klett method (Fernald, 1984). This method needs a proper set of reference backscatter coefficients and of lidar ratios. Here, for each wavelength a mean boundary-layer lidar ratio was estimated by using the Klett solutions and optical-thickness values obtained from measurements at two different zenith angles (30°, 60°) (Gutkowicz-Krusin, 1993; Ansmann et al, 1998).

The optical data measured with the lidar were inverted into microphysical particle parameters with the method of inversion via regularization (Müller, 1997). We chose two heights, 375 and 465 m. As necessary input data served the five backscatter coefficients shown in Fig. 1, an extrapolated backscatter value at 355 nm (because of detector problems that value could not be measured correctly below about 1000 m on this day) and boundary-layer mean extinction coefficients at 355 and 532 nm determined from the measurements at two zenith angles. From the inversion, that considers particle sizes between 10 nm and 10 µm, effective radius, total number, surface-area, and volume concentrations as well as mean complex refractive index are determined. An initial guess of the shape of the aerosol size distribution is not needed.

Fig. 2 shows the spectral optical thickness measured with the sun photometer, Fig. 3 the normalized sky-brightness phase function at 779 nm derived from the almucantar measurement. The agreement between the particle optical depths determined from the scanning-lidar and the sun-photometer observations was good. Only at short wavelengths the lidar-derived optical depth was lower by about 0.02 at 400 nm and 0.05 at 350 nm. This may indicate the influence of small particles in the free troposphere and in the stratosphere on the sun photometer measurements. In addition, photometer values at short wavelenghts seem to be slightly erroneous.

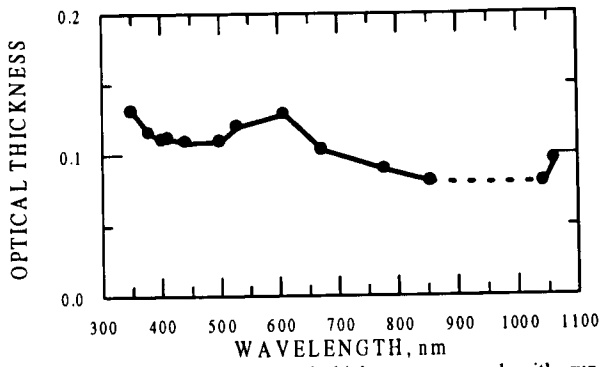


Fig. 2: Rayleigh-corrected optical thickness measured with sun photometer on 20 June 1997, 06:30 UTC. The ozone absorption band can clearly be seen between about 500 and 650 nm. The water-vapor absorption channels around 940 nm are excluded.

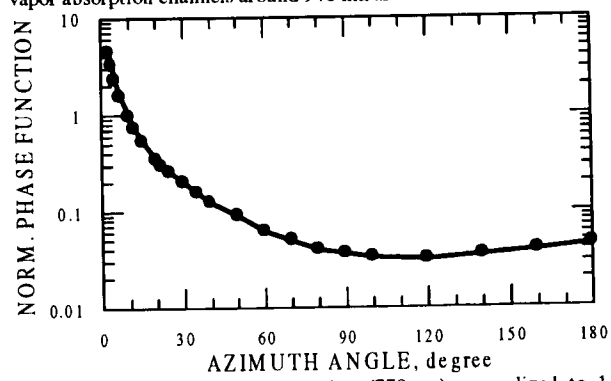


Fig. 3: Sky-brightness phase function (779 nm) normalized to 1 measured with sun photometer on 20 June 1997, 06:30 UTC. The strong increase of the scattered intensity in the forward direction indicates the existence of large particles.

Again, from the optical data physical particle properties were calculated. Here, the program CIRATRA (Coupled Inversion Radiation Transfer) developed by von Hoyningen-Huene and Wendisch (1994) was used. The CIRATRA method derives the discrete aerosol size distribution between about 64 nm

and 10 μm and the real part of the refractive index without any *a priori* guess of the shape of the size distribution.

The results for refractive index, effective radius, total number, surface-area, and volume concentrations as they were obtained from the three systems are shown in Table 1. As mentioned above, one should keep in mind that lidar retrievals are valid for the heights of 375 m and 465 m, sun-photometer-based retrievals represent mean aerosol properties of the whole atmospheric column, and the DMPS/APS provides *in situ* data at the ground. Thus, in a strict sense, the three systems did not observe the same aerosol. However, because of the well-mixed boundary layer the aerosol properties should be comparable.

Tab.1: Mean particle properties derived from lidar, sun-photometer, and DMPS/APS measurements. n corresponds to the total number, a to the total surface-area, and v to the total volume concentration, r_{eff} denotes the effective radius, and m_r and m_i the real and imaginary part of the refractive index. The integration limits of the DMPS/APS-derived values are 64 nm and 3.5 μm.

	LIDAR		SPM	DMPS/ APS
	375 m	465 m		
n cm^{-3}	278 ± 58	352 ± 163	522 ± 99	478 ± 48
a $\mu m^2 cm^{-3}$	58 ± 3	62 ± 2	133 ± 9	92 ± 9
v $\mu m^3 cm^{-3}$	13 ± 1	12 ± 2	35 ± 5	18 ± 2
r_{eff} μm	0.7 ± 0.1	0.6 ± 0.1	0.8 ± 0.1	0.6 ± 0.1
m_r	1.450 .. 1.475	1.400 .. 1.450	1.375 .. 1.425	
m_i	0.005 .. 0.01	0.005 .. 0.01		

The table shows a good agreement for the effective radius and the real part of the refractive index within the error limits. These two quantities are characteristic for a particle ensemble and do not depend on the actual number concentration in the measurement volume. But also the values for number, surface-area, and volume concentrations are of the same order of magnitude for the three different measurements. The slightly larger sun-photometer- derived effective radius compared to the lidar- derived value may be caused by larger particles near the ground. The slightly smaller DMPS/APS-derived effective radius might also be due to the cut-off at 5-μm aerodynamical radius which leads to a lack of measured large particles.

Finally, the retrieved sun-photometer aerosol size distribution was compared to the size distribution measured with the DMPS/APS system. This is shown in Fig. 4. The sun-photometer retrieved number concentrations are slightly higher than the *in situ* measured values at the ground, but nevertheless the agreement is good over a wide range of radii and over about four orders of magnitude. The comparison of the volume concentration (not shown) gives the same good agreement.

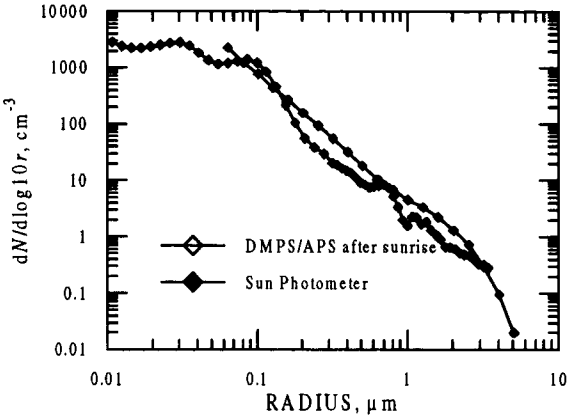


Fig. 4: Comparison of *in situ* measured (DMPS/APS system) and inverted (using sun-photometer data) aerosol number size distribution on 20 June 1997, 06:30 UTC.

5 Summary

We have compared particle optical and microphysical properties derived from profile, path, and point measurements. In the case of a single, well-mixed aerosol layer, mean particle properties (real part of the refractive index, effective radius, number, surface-area, and volume concentrations) determined from different sets of optical data, measured with lidar and sun photometer, and inverted with different algorithms show a good agreement. The comparison confirms that the new lidar inversion scheme works well and shows further that sun-photometer-derived particle properties are reliable, if the optical information is strongly determined by a well-mixed boundary layer.

References

Ansmann, A., Althausen, D., Müller, D., Mattis, I., Wagner, F., Wandinger, U. (1998). Role of Lidar in Climate-related Aerosol Characterization Experiments. *This issue.*

Fernald, F.G. (1984). Analysis of atmospheric lidar observations: some comments. *Appl. Opt.* 23: 652-653.

Gutkowicz-Krusin, D. (1993). Multiangle lidar performance in the presence of horizontal inhomogeneities in atmospheric extinction and scattering. *Appl. Opt.* 32:3266-3272.

Müller, D., Althausen, A., Wandinger, U., Ansmann, A. (1996). Multiple-Wavelength Aerosol Lidar. *In: Ansmann, A,. Neuber, R., Rairoux, P., Wandinger, U.: Advances in Atmospheric Remote Sensing with Lidar, Springer.*

Müller, D. (1997). Inversionsalgorithmus zur Bestimmung physikalischer Partikeleigenschaften aus Mehrwellenlängen-Lidarmessungen. *Ph.D. Dissertation, University of Leipzig.*

von Hoyningen-Huene, W., Wendisch, M. (1994). Possibility of refractive index determination of atmospheric aerosol particles by ground based solar extinction and scattering measurements. *Atmos. Environ.* 28:785-795.

A New Technique to Derive Mixed Layer Depth and Entrainment Zone Thickness from Lidar Profiles

D. G. Steyn[1], M. Baldi[2] and R. M. Hoff[3]

[1] Atmospheric Science Programme, Department of Geography, The University of British Columbia, Vancouver, Canada 604-822-6407, fax: 604-822-6150, email: douw@geog.ubc.ca.
[2] Institute for Atmospheric Physics, IFA-CNR, Rome, Italy
[3] Atmospheric Environment Service, Egbert, Ontario, Canada

Introduction

The detection of mixed layer depth has been a frequently derived product from both ground-based and airborne lidar [1-3]. The detection of the mixed layer has been based on discontinuities in the aerosol backscatter coefficient (β_a) immediately above the boundary layer and relies on sufficient aerosol production in the surface layer to delineate the ML inversion. We will use the lidar backscatter ratio, b = 1 + β_a/β_R, in this paper as a measure of the lidar backscatter.

Traditional detection techniques have been based on a measure of the discontinuity in the profile, typically a maximum of -db/dz. Endlich [1] used a pattern recognition algorithm to match adjacent values of -db/dz which were similar and thus provide horizontal continuity in the boundary layer height even with a noisy signal. Melfi et al. [3] used an automated detection technique based on a critical absolute backscatter value and also examined the variance of -db/dz which should maximized at the point where convective entrainment is largest.

These techniques are often not reliable. With a noisy signal or low aerosol scattering in the boundary layer, detection of the gradient in backscatter is not always a unique measure of the mixed layer height. In a study from an aircraft mission in the Lower Fraser Valley (Vancouver), British Columbia [4,5], a smoothed set of lidar profiles was used along with a simple derivative technique to determine MLDs. The lidar data were taken at 1s averages (10 shots) with 12m vertical resolution. Even where the aerosol concentration was uniform in the ML, this technique worked adequately only as long as there was a significant horizontal (10 profiles, or about 2km of flight leg) and vertical (5 points or 60 m) smoothing of the data. This smoothing not only decreased the value of the high resolution airborne lidar data, but also opened the possibility of aliasing the data. This is especially problematic in cases where horizontal discontinuities existed (near the shoreline where Thermal Internal Boundary Layer, TIBL, development was seen, for example). For this reason, we have developed a new technique to better retrieve the MLD on the unaveraged lidar data.

The New Technique

We have examined wavelet techniques to extract the MLD from the lidar profiles. Wavelet transforms have been found not to be well suited to the form of the backscatter profile near the mixed layer. In formal wavelet analysis [6], one requires convergence of the integral over all space of the modulus of a wavelet. This requires that the wavelet goes to zero at $\pm\infty$. This can be accomplished by subtracting the Rayleigh value to have the backscatter ratio go to zero at $+\infty$. There is the problem that the wavelet is not defined for negative values and therefore, it would have to be synthetically reflected in the negative domain.

We have chosen a technique which is much simpler and, therefore, easier to automatically process over large volumes of data. This technique fits an idealized backscatter ratio profile <b(z)> to the observed data and using a minimization technique to reduce the variance between the two profiles. The idealized profile is one which fits our expectation of the mixed layer, containing a gradient in backscatter from a mixed layer value, b_m, to the value above the ML, b_u. The idealized profile used is:

$$< b(z) >= \frac{(b_m + b_u)}{2} - \frac{(b_m - b_u)}{2} erf(\frac{z - z_m}{s})$$

where z_m is the mixed layer depth height and s is a measure of the width of the entrainment zone. With the definition of the entrainment zone being that region where the aerosol concentration is between the 5th and 95th percentile of the mixed layer value [7], the entrainment zone thickness, EZT, is 2.77s. It should be noted that the z_m and s parameters correspond to translation and dilation factors in formal wavelet analysis. In this technique, we fit only one daughter function (wavelet) to the observed profile. Figure 1

shows the idealized profile with z_m = 500m, s = 100m, b_u = 2 and b_m = 10.

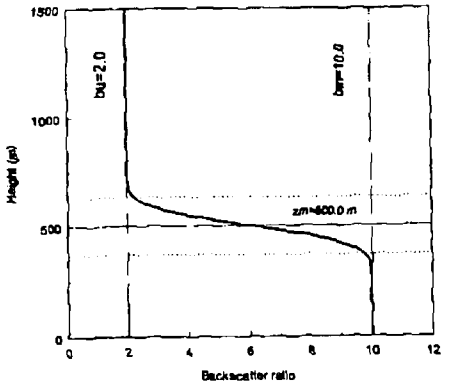


Figure 1: Idealized backscatter profile used in the model.

A process of multidimensional minimization is needed to find "best fit" values of the profile parameters. Initial attempts to use the downhill simplex method [8] in multidimensions proved unreliable. Implementation of the method of "simulated annealing" achieves very satisfactory results with relatively little computational cost. Routines for implementation of this method are described and presented in Press *et al.* [8].

Results using Airborne Lidar Data

The lidar data used in this work were obtained from 21 missions carried out over the Lower Fraser Valley of British Columbia during July and August 1993 [4,5]. The AES elastic lidar operated at 1.064 um from the National Research Council of Canada's Convair 580 aircraft. The lidar was flown at a nominal altitude of 4300m and operated at 10 Hz. The data was stored as 10 shot averages giving a horizontal resolution of 1s or approximately 200m and a vertical resolution of 12m.

Figures 2-6 show five profiles from the August 3 mission. Figures 2 and 3 show typical mixed layer profiles which are well delineated and nearly constant under the inversion. Figures 4-6 show profiles which give problems with the traditional retrieval algorithm. In Figure 4, the mixed layer has a layer of relatively cleaner air within the boundary layer. This is believed to be due to advection of the overlying more polluted air over a relatively clean region of the valley. Figures 5 and 6 were obtained closer to the colder waters of the Georgia Straight and thus have shallower boundary layer features. Figure 5 shows an overlying plume over the main portion of the mixed layer. Figure 6 shows a profile which is much shallower than those shown in the other retrievals and has an increasing aerosol content right down to the surface.

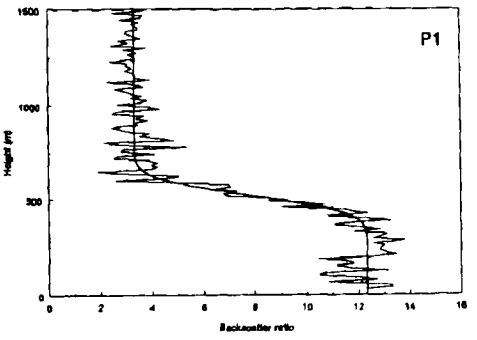


Figure 2a: Well mixed profile from line L6N

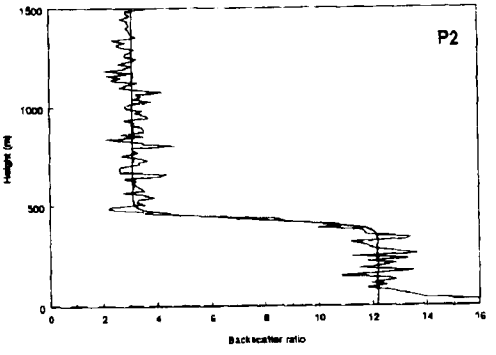


Figure 3: Well mixed profile from line L8N

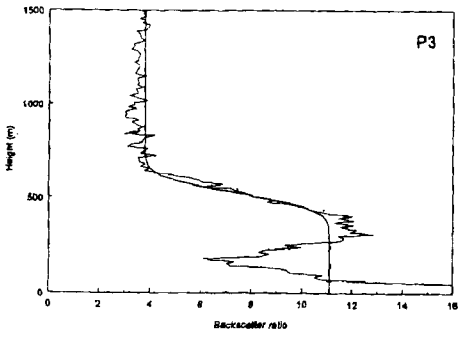


Figure 4: More difficult profile to retrieve containing cleaner air below the inversion.

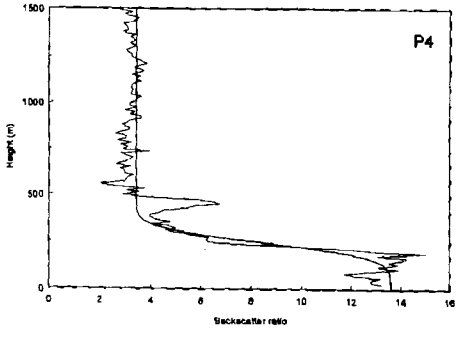


Figure 5: Profile containing plume aloft on line L9S (closer to Georgia Straight).

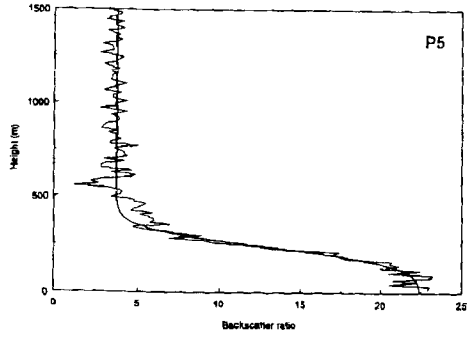


Figure 6: Shallow profile on line L9S.

The results of these retrievals showed that there was reasonable agreement between the gradient technique (552 m) and the one proposed here (521) only for the first profile (Figure 2). In fact, Figures 3 and 4 show profiles for which the gradient retrieval found large increases near the surface and identified them as very shallow boundary layers (0 m), while the new technique gave more correct heights of 425 and 534m. In Figures 5 and 6, the gradient retrieval identified the mixed layer height at 170m where it was more closely determined to be 246 and 236m, respectively, by the wavelet technique used here.

A fuller discussion of this technique can be found in [9]. Copies of this work can be obtained by contacting the first author.

Acknowledgements

This work was funded by grants awarded by the Atmospheric Environment Service of Environment Canada and by the Natural Science and Engineering Research Council of Canada. MB was able to participate through funding from the NATO/CNR senior fellowships programme.

References

1. Endlich, R.M., F. Ludwig and E. E. Uthe, 1979: An automated method for determining the mixing depth from lidar observations. *Atmos. Environ.* **13**, 1051-1056.

2. Boers, R., E. W. Eloranta, and R. L. Coulter, 1984: Lidar observation of mixed layer dynamics: Tests of parameterized entrainment models. *J. Clim. Appl. Met.*, **23** , 246-266.

3. Melfi, S. H., J. D. Spinhire, S.-H. Chou, and S. P. Palm, 1985: Lidar observation of vertically organized convection in the planetary boundary layer over the ocean., *J. Clim. Appl. Meteorol.*, **24**, 806-821.

4. Hayden, K.L., K.G. Anlauf, R.M. Hoff, W.J. Strapp, J.W. Bottenheim, H.A. Wiebe, F.A. Froude, J.B. Martin, D.G. Steyn and I.G. McKendry, 1997: The vertical chemical and meteorological structure of the boundary layer in the Lower Fraser Valley during PACIFIC '93. *Atmospheric Environment*, 31 (4), 2089-2106..

5. Hoff, R.M., M. Harwood, A. Sheppard, F. Froude, B.A. Martin and W. Strapp, 1997: Use of airborne lidar to determine aerosol sources and movement in the Lower Fraser Valley (LFV), British Columbia. *Atmospheric Environment*, 31 (4), 2123-2134.

6. Meyer, Y., 1993: *Wavelets, Algorithms and Applications* (Translated and revised by R. D. Ryan) SIAM Press, 133p.

7. Nelson, E., R. Stull and E. Eloranta, 1989: A prognostic relation for entrainment zone thickness. *J. Appl. Met.*, **28**, 885-903.

8. Press, W. H., S. A. Teukolsky, W. T. Vettering and B. R. Flannery, 1992: Numerical Recipes in FORTRAN: The art of scientific computing, 2nd ed.) Cambridge University Press, 963p.

9. Steyn, D., M. Baldi, and R. M. Hoff, 1998: The detection of mixed layer depth and entrainment zone thickness from lidar backscatter profiles. *J. Atmos. Ocean. Tech.* (submitted).

LASE Validation Experiment: Preliminary Processing of Relative Humidity from LASE Derived Water Vapor in the Middle to Upper Troposphere

Vincent G. Brackett[1], Syed Ismail[2], Edward V. Browell[2], Susan A. Kooi[1], Marian B. Clayton[1], Richard A. Ferrare[2], Patrick Minnis[3], Brian J. Getzewich[4], and Jennifer Staszel[5]

[1]Science Applications International Corporation (SAIC), NASA Langley Research Center, Mail Stop 401A, Hampton, VA 23681, USA, Phone: 757-864-5854, Fax: 757-964-7790, email: v.g.brackett@larc.nasa.gov
[2]NASA Langley Research Center, Mail Stop 401A, Hampton, VA 23681, USA
[3]NASA Langley Research Center, Mail Stop 420, Hampton, VA 23681, USA
[4]Computer Science Corporation (CSC), NASA Langley Research Center, Bldg 1268, Room 1317, Hampton, VA 23681, USA, (NASA LARSS 97 Program Summer Student)
[5]University of Michigan, Department of Atmospheric, Oceanic, and Space Science, Ann Arbor, Michigan, 48109, USA, (NASA LARSS 97 Program Summer Student)

Introduction

LASE is the first fully engineered, autonomous airborne DIAL (DIfferential Absorption Lidar) system to measure water vapor, aerosols, and clouds throughout the troposphere [1,2,3]. This system uses a double-pulsed Ti:sapphire laser, which is pumped by a frequency-doubled flashlamp-pumped Nd: YAG laser, to transmit light in the 815-nm absorption band of water vapor. LASE operates by locking to a strong water vapor line and electronically tuning to any spectral position on the absorption line to choose the suitable absorption cross-section for optimum measurements over a range of concentrations in the atmosphere. During the LASE Validation Experiment, which was conducted over Wallops Island during September, 1995, LASE operated on either the strong water line for measurements in middle to upper troposphere, or on the weak water line for measurements made in the middle to lower troposphere including the boundary layer. Comparisons with water vapor measurements made by airborne dew point and frost point hygrometers, NASA/GSFC (Goddard Space Flight Center) Raman Lidar, and radiosondes showed the LASE water vapor mixing ratio measurements to have an accuracy of better than 6% or 0.01 g/kg, whichever is larger, throughout the troposphere [4].

In addition to measuring water vapor mixing ratio profiles, LASE simultaneously measures aerosol backscattering profiles at the off-line wavelength near 815 nm from which atmospheric scattering ratio (**ASR**) profiles are calculated. **ASR** is defined as the ratio of total (aerosol + molecular) atmospheric scattering to molecular scattering. Assuming a region with very low aerosol loading can be identified, such as that typically found just below the tropopause, then the **ASR** can be determined. The ASR profiles are calculated by normalizing the scattering in the region containing enhanced aerosols to the expected scattering by the "clean" atmosphere at that altitude. Images of the total **ASR** clearly depict cloud regions, including multiple cloud layers, thin upper level cirrus, etc., throughout the troposphere.

New data products that are being derived from the LASE aerosol and water measurements include: 1) aerosol extinction coefficient, 2) aerosol optical thickness [5], 3) precipitable water vapor [5], and 4) relative humidity (**RH**). These products can be compared with airborne in-situ, and ground and satellite remote sensing measurements. This paper presents a preliminary examination of **RH** profiles in the middle to upper troposphere that are generated from LASE measured water vapor mixing ratio profiles coupled with rawinsonde profiles of temperature and pressure.

Data Processing

LASE post processing provides profiles of **ASR** every 3 seconds (the average of 15 laser shots), with a horizontal and vertical resolution of 600 and 30 meters, respectively. The horizontal resolution for the water vapor profiles is 600 meters; the vertical resolution is 330 meters for the weak line (0.2-7 km), and 510 meters for the strong line (7-16 km). Figure (1) shows the ER-2 aircraft track in the vicinity of Wallops Island, Virginia during LASE Validation flight 3, which was conducted on September 13, 1995. Figure (2) shows the corresponding

measurements of ASR (left) and water vapor mixing ratio (right) profiles between 00:00 UT and 01:15 UT from this flight leg.

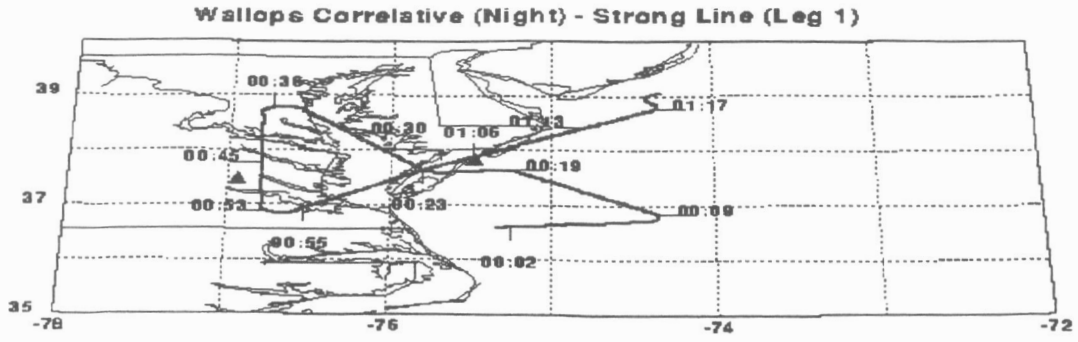


Figure 1. LASE ER-2 Track (Flight 3) on September 13, 1995.

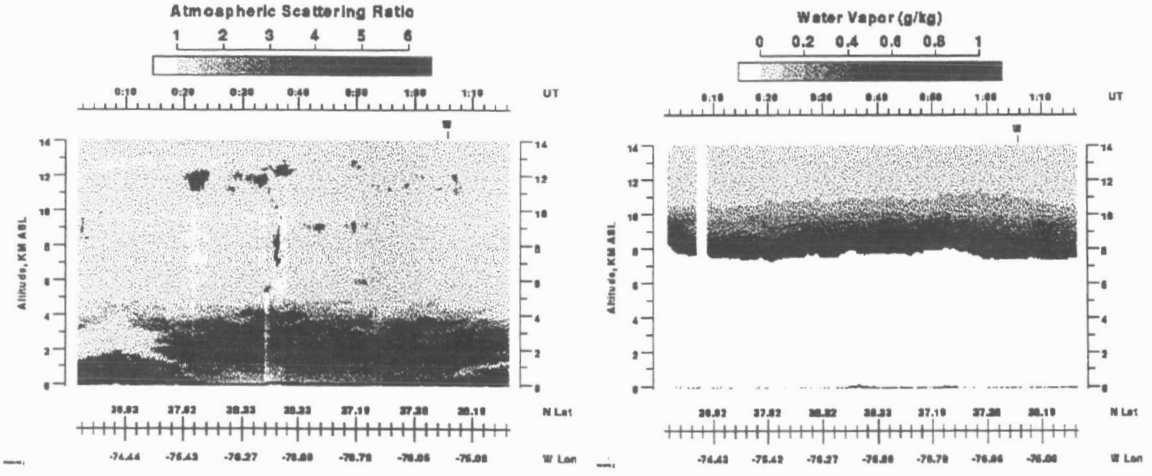


Figure 2. Atmospheric Scattering Ratio (left) and water vapor mixing ratio (right) measured by LASE on September 13, 1995 during the LASE Validation Experiment. LASE operated using the strong water vapor absorption line during this portion of this flight. Mid and high-level cirrus clouds can be seen in the atmospheric scattering ratio image.

Relative humidity (**RH**) with respect to water (or ice) is the ratio (in percent) of the water vapor mixing ratio (W_v) to the saturation mixing ratio of water (W_s) with respect to water (or ice) at the same temperature and pressure. There are various methods used, depending on the parameters available, to calculate **RH**. The following equation was used to calculate **RH:**

$$RH = \frac{W_v / 1000 * (P - V_p)}{0.00622 * V_p} \quad (1)$$

where **RH** = relative humidity (%)
W_v = water vapor mixing ratio (g/kg)
V_p = saturation vapor pressure (mb)
P = pressure (mb)

Profiles of temperature, which are required to compute the saturation vapor pressure, and pressure are required. Two different approaches were used to obtain these profiles.

1) Single Point Method

Vaisala radiosondes, which were launched at Wallops Island in support of LASE operations, were used to construct individual profiles of temperature and pressure. Both profiles were interpolated to match the vertical resolution of the LASE water vapor mixing ratio data. These profiles were then used in equation (1) to calculate **RH.** This point method was considered a viable first order calculation of **RH** when LASE was within 100 km of Wallops Island.

2) Curtain File Method

Rawinsondes, launched from Upper Air (UPA) sounding stations surrounding Wallops (7 sites), were obtained from the SSEC (Space Science and Engineering Center) at the University of Wisconsin in McIDAS (Man-computer Interactive Data Access System) format for the appropriate LASE flight days. Using McIDAS, contour grids of pressure and temperature at 00Z and 12Z were developed for the radiosonde specified reporting altitudes. Additional McIDAS algorithms were then developed to interpolate these grids in time and space to obtain corresponding profiles of temperature and pressure, for every LASE water vapor profile. These "curtain files" containing temperature and pressure profiles were then used in equation (1) to calculate the **RH** profiles.

Relative humidity with respect to both water and ice were computed using both methods.

Results

Figure (3) and (4) are images of **RH** profiles using the two different calculation methods described above.

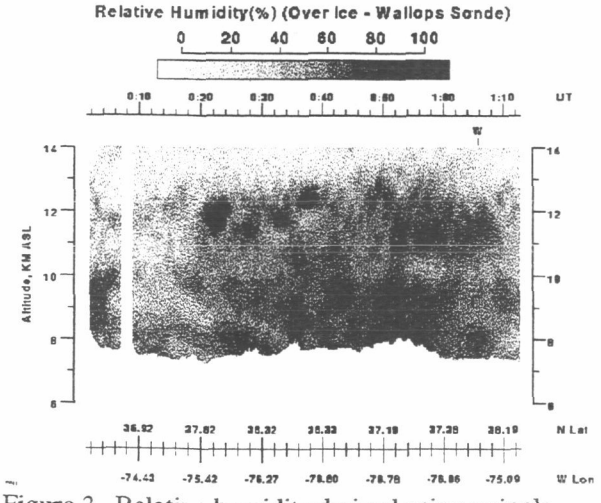


Figure 3. Relative humidity derived using a single Wallops Island rawinsonde profile of temperature and pressure.

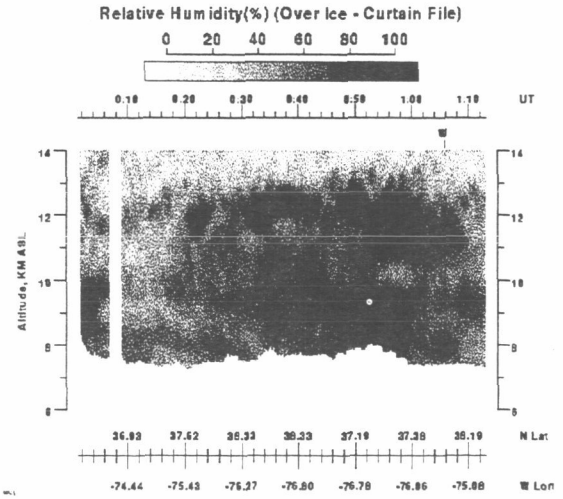


Figure 4. Relative humidity derived using "curtain" files of pressure and temperature..

Regions where the relative humidity with respect to ice is above 98%, which are shown in black in figure (3) and (4), are well correlated with the regions of middle to high-level cirrus clouds shown in figure (2). In general, horizontal gradients of relative humidity are better preserved when curtain files were used. For the data shown in figure (3), the "Single Point" method has a high degree of correlation also since LASE remained in the vicinity of Wallops Island during this period. This would not hold true for transit flights or operations over large geographical

Summary of Volume Imaging Lidar (VIL) Preliminary Results from the Lake-Induced Convection Experiment (Lake-ICE)

Shane D. Mayor, Edwin W. Eloranta, Ralph Kuehn, and Patrick Ponsardin
Department of Atmospheric and Oceanic Sciences, University of Wisconsin
1225 W. Dayton St., Madison, Wisconsin, 53706, USA
phone: 608-263-6847, fax: 608-262-5974, e-mail: shane@lidar.ssec.wisc.edu

Introduction

The University of Wisconsin's Volume Imaging Lidar (UW-VIL) [1] was deployed in Sheboygan, Wisconsin, for the Lake-Induced Convection Experiment (Lake-ICE) during December of 1997 and January of 1998. The site (43°44′N, 87°42′W, 176 m ASL) was located within 10 m of the western shore of Lake Michigan for the purpose of measuring the 4-dimensional (space and time) structure of the upwind edge of the unstable thermal internal boundary layer (TIBL) [2] that forms over the relatively warm lake during cold air outbreaks (CAOs).



Figure 1. Map of the region. For Lake-ICE, the VIL was located in Sheboygan, WI.

During CAOs, the air temperature typically drops to -15 to -30° C while the temperature of the lake water remains a few degrees above freezing. This temperature difference generates large surface heat fluxes which creates a convective boundary layer over the lake. Because the large-scale air flow is from the land to the lake and considering the diffusive nature of turbulence, the TIBL becomes deeper with increasing offshore distance. Stratocumulus clouds form offshore, and steam fog often forms over the lake surface. Futher downwind, the convection can become intense enough to produce lake-effect snow.

Despite the 1997-1998 midwest US winter being one of the mildest on record, we still experienced a few CAOs that were strong enough to enable us to meet our objective. Furthermore, in addition to the TIBLs we observed, we gathered VIL data on many other very interesting phenemona at the edge of the lake, including a land-breeze (see Eloranta *et al.*, this conference), microscale linear and cellular patterns in shallow convection [3], steam-fog, steam-devils, and gravity waves.

We collected data on 9 days during Lake-ICE, which took place from December 5 until December 22, 1997, and from January 9 until January 22, 1998. The experiment included flights of the NCAR Electra and the University-of-Wyoming King-Air aircraft for in situ boundary layer measurements. Three NCAR integrated sounding systems (ISS) stations and five fixed and one mobile cross-chain loran atmospheric sounding system (CLASS) stations provided additional wind and thermodymanic soundings in the surrounding states. The only ISS in Wisconsin was located about 10 km west of the VIL. Measurements of wind and temperature mentioned here are from the National Data Buoy Center's SGNW3 weather station which was located about 750 m north of the VIL. The air temperature and wind were measured at 15.5 m and 19.2 m above the site elevation, respectively.

Motivation

Large eddy simulations (LESs) provide an attractive way of developing parameterizations for large-scale models such as global climate and weather forecast models. This is because they provide 4-D information which can potentially be used to compute fluxes with sampling errors that are much smaller than those made from in situ measurements. LESs, however, are only viable if we have confidence in their solutions. In particular, high resolution 4-D measurements are needed to test the LES.

The UW-VIL is uniquely suited to measure the 4-D structure of aerosol backscatter in the atmo-

Summary of Volume Imaging Lidar (VIL) Preliminary Results from the Lake-Induced Convection Experiment (Lake-ICE)

Shane D. Mayor, Edwin W. Eloranta, Ralph Kuehn, and Patrick Ponsardin
Department of Atmospheric and Oceanic Sciences, University of Wisconsin
1225 W. Dayton St., Madison, Wisconsin, 53706, USA
phone: 608-263-6847, fax: 608-262-5974, e-mail: shane@lidar.ssec.wisc.edu

Introduction

The University of Wisconsin's Volume Imaging Lidar (UW-VIL) [1] was deployed in Sheboygan, Wisconsin, for the Lake-Induced Convection Experiment (Lake-ICE) during December of 1997 and January of 1998. The site (43°44'N, 87°42'W, 176 m ASL) was located within 10 m of the western shore of Lake Michigan for the purpose of measuring the 4-dimensional (space and time) structure of the upwind edge of the unstable thermal internal boundary layer (TIBL) [2] that forms over the relatively warm lake during cold air outbreaks (CAOs).



Figure 1. Map of the region. For Lake-ICE, the VIL was located in Sheboygan, WI.

During CAOs, the air temperature typically drops to -15 to -30° C while the temperature of the lake water remains a few degrees above freezing. This temperature difference generates large surface heat fluxes which creates a convective boundary layer over the lake. Because the large-scale air flow is from the land to the lake and considering the diffusive nature of turbulence, the TIBL becomes deeper with increasing offshore distance. Stratocumulus clouds form offshore, and steam fog often forms over the lake surface. Futher downwind, the convection can become intense enough to produce lake-effect snow.

Despite the 1997-1998 midwest US winter being one of the mildest on record, we still experienced a few CAOs that were strong enough to enable us to meet our objective. Furthermore, in addition to the TIBLs we observed, we gathered VIL data on many other very interesting phenemona at the edge of the lake, including a land-breeze (see Eloranta *et al.*, this conference), microscale linear and cellular patterns in shallow convection [3], steam-fog, steam-devils, and gravity waves.

We collected data on 9 days during Lake-ICE, which took place from December 5 until December 22, 1997, and from January 9 until January 22, 1998. The experiment included flights of the NCAR Electra and the University-of-Wyoming King-Air aircraft for in situ boundary layer measurements. Three NCAR integrated sounding systems (ISS) stations and five fixed and one mobile cross-chain loran atmospheric sounding system (CLASS) stations provided additional wind and thermodymanic soundings in the surrounding states. The only ISS in Wisconsin was located about 10 km west of the VIL. Measurements of wind and temperature mentioned here are from the National Data Buoy Center's SGNW3 weather station which was located about 750 m north of the VIL. The air temperature and wind were measured at 15.5 m and 19.2 m above the site elevation, respectively.

Motivation

Large eddy simulations (LESs) provide an attractive way of developing parameterizations for large-scale models such as global climate and weather forecast models. This is because they provide 4-D information which can potentially be used to compute fluxes with sampling errors that are much smaller than those made from in situ measurements. LESs, however, are only viable if we have confidence in their solutions. In particular, high resolution 4-D measurements are needed to test the LES.

The UW-VIL is uniquely suited to measure the 4-D structure of aerosol backscatter in the atmo-

spheric boundary layer. By rapidly moving the laser beam in a series of RHIs, each with a slightly increased azimuth angle, we can measure the 3-D structure within a few minutes. For example, a volume which spans 40° in azimuth and 15° in elevation angle requires about 2 minutes and contains about 80 RHIs. The change in elevation angle between two laser pulses during an RHI is 0.23°. By repeating such volume scans, we can also monitor the temporal evolution of the structures. This is possible because the lifetimes of the individual thermals and large-eddies within the boundary layer are long compared to the time it takes to complete one volume scan.

In addition to volume-scans, we also repeated RHI scans at constant azimuths and PPI scans at constant elevations to obtain high temporal resolution 2-D animations of the boundary layer. For example, RHIs (between 0° and 15° elevation) at a constant azimuth direction allow us to produce animations of a vertical slice of the atmosphere with new frames every 2 s. The configuration of the VIL used in Lake-ICE allowed us to transmit 400 mJ/pulse at 100 Hz, and record backscatter intensity at 15-m intervals out to a range of 18 km.

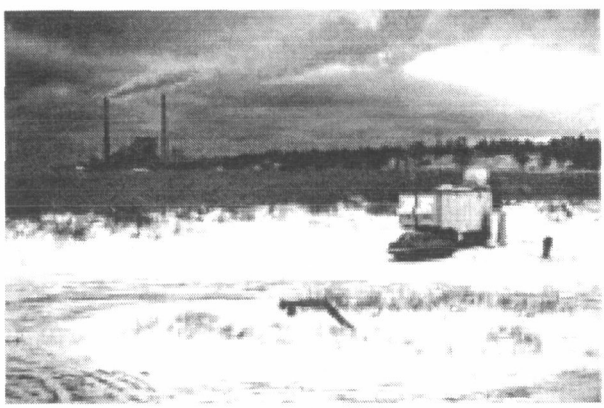


Figure 2. Photograph (looking south) showing the UW-VIL trailer in the foreground on the right and the Edgewater electric power plant in the background on the left. Stack plumes in this photo are blowing to the west.

Interesting observations

Perhaps the most interesting VIL observation during Lake-ICE was open-cell convection patterns in the steam-fog about 5 meters above the surface of the lake on 10 and 13 January 1998. Cold air advection was occurring on both of these days and visual observations confirmed clear skies over the lidar site and steam fog on the surface of the lake. On 10 January the minimum temperature reached -16.7° C at 14 UTC with the wind from 236° at 6.5 m s^{-1}.

The VIL's beam-steering-unit (the point at which lidar beam is transmitted from) was located approximately 5 m above the lake surface. Thus, PPI scans at 0° elevation allowed us to map the horizontal distribution of steam-fog in a plane approximately 5 m above and parallel to the surface of the lake. Figures 3 and 4 are PPI scans of this type. In figure 3, the data range from 5 to 10 km offshore. RHI scans within an hour of this image show that the steam-fog did not rise above ~50 m on this day.

The narrow walls of the cells, where the steam is concentrated, is probably a region of convergence and upward motion with weaker compensating sinking motion in the larger clear interior of the cell. The cells appear to be slightly elongated in the direction of the wind. Their somewhat hexagonal shape allows any one cell to share most of its walls with neighboring cells. The horizontal cell dimensions increase with increasing offshore distance. Cells on the left side of the image range from approximately 200-500 m wide while the cells on the right range from 500-1000 m wide. The streaks across the image are caused by attenuation from the steam fog.

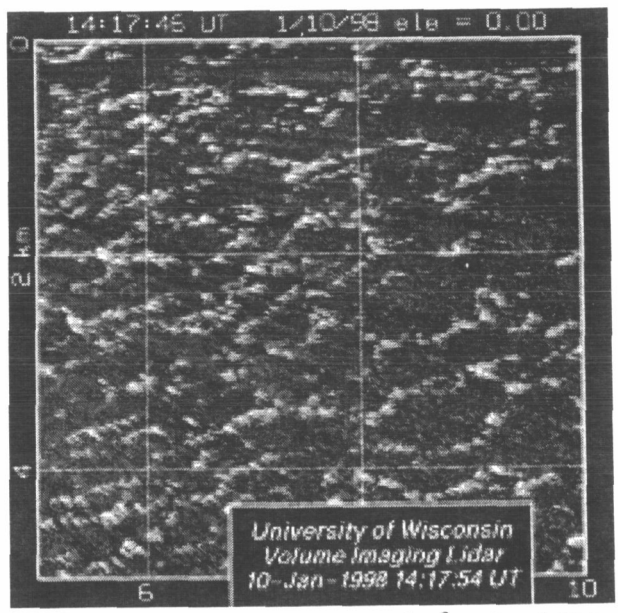


Figure 3. Enlargement of a 25-km^2 region 5-10 km offshore from a PPI image of range-corrected backscatter intensity. The image shows open-cell organization of convection in the steam-fog over the lake during a cold air outbreak on 10 January 1998. Note the approximately hexagonal shape of the cells. At the shore, the mean wind during this time was from 236° at 6.5 m s^{-1} and the air temperature was -16.7° C. The streaks across the image are caused by attenuation from the steam fog.

While the steam on the 10th did not appear to rise more than about 50 m above the lake, RHI scans from 13 January reveal narrow rising columns of steam which sometimes extend to the top of a 400-

m deep mixed-layer. The minimum temperature on the morning of the 13th was -20° C and the wind was from 280-290° at 5-10 m s^{-1}. The columns are very bright near the surface and decrease in intensity with altitude. In figure 5, there is one such feature at about 4.4 km range that extends from the surface up to about 200 m. Some of these features may be steam devils and we hope that the VIL observations of them will enable us to quantify their size and number density.

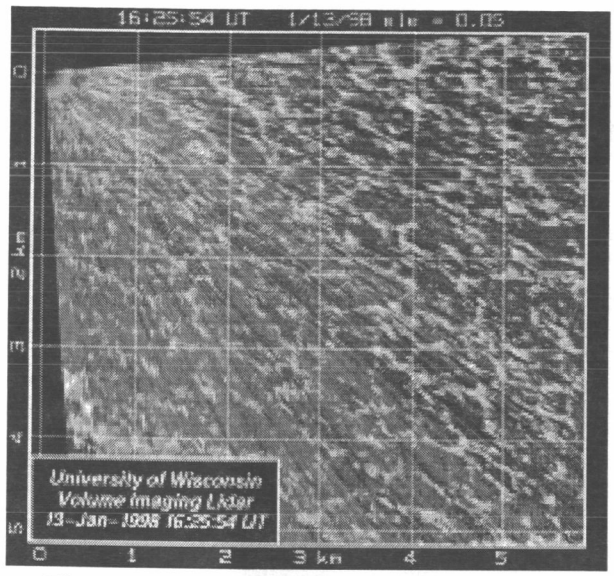


Figure 4. PPI of range-corrected backscatter intensity showing the open-cell organization of the steam fog on 13 January 1998 from a few hundred meters to 5.9 km offshore. At the shore the mean wind during this time was from 280-290° at 5-10 m s^{-1} and the air temperature was -20° C. The open-cells range in horizontal size from about 100 m at 1 km offshore to about 500 m at 5.9 km offshore.

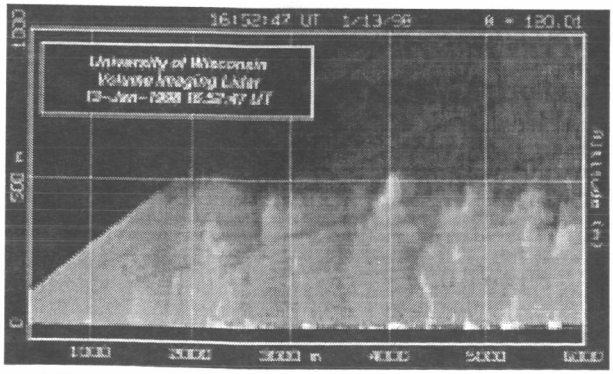


Figure 5. RHI of range-corrected backscatter intensity showing the vertical structure of the steam fog and TIBL over the lake on 13 January 1998.

We saw evidence of lake-induced unstable TIBLs on most of the days we operated the VIL at Lake-ICE. Our first operational day, 5 December 1997, showed a complex boundary layer in which snow caused the air above the TIBL to be higher in scattering than the thermals with origins over the lake.

Figure 6 shows the vertical structure of the lower atmosphere over the lake on 19 January 1998. A shallow mixed layer can be seen from the surface up to about 100 m. A residual layer, or mixed layer produced from the land, which is lower in scattering, can be seen from 100 to 200 m. Gravity waves can be seen between 500 and 600 m above the lake. The waves have an amplitude of approximately 50 m and a wavelength of about 500 m.

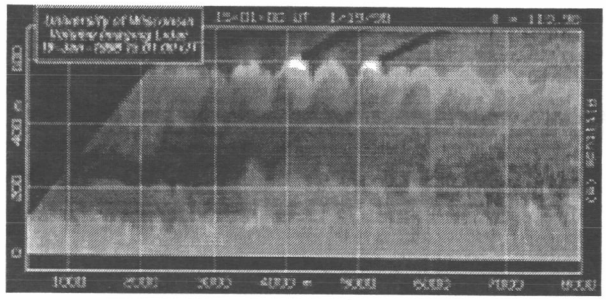


Figure 6. RHI aligned downwind (120° azimuth). This vertical cross-section of the atmosphere over the lake on 19 January 1998 shows gravity waves above a shallow mixed layer.

On 14 December 1997, we observed a "criss-cross" pattern of waves, or waves and linear convective features, within a 100-km^2 area on PPI displays. The linear features (or waves) with crests that were oriented north-south were moving toward the east and the linear features with crests oriented approximately west-east were moving to the north. The result is a pattern which resembles a "waffle" and is shown in figure 7. The coherent structures are much more obvious in animated color images. The wavelength of both features is 400-500 m. The animation also reveals some counter-clockwise turning of the flow field which may be related to the terrain causing a coastal eddy.

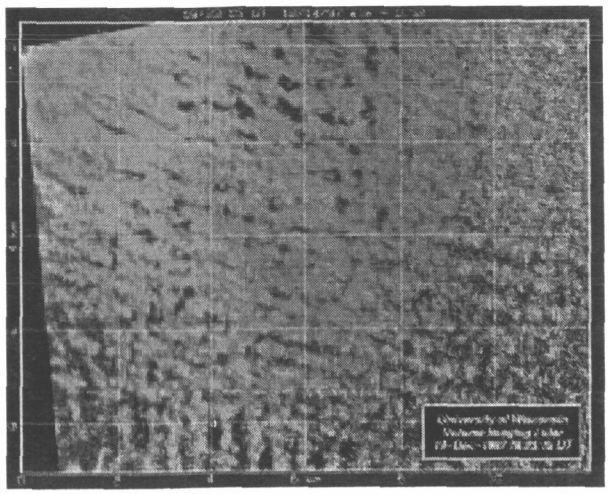


Figure 7. PPI of range-corrected backscatter intensity showing a "criss-cross" of waves or waves and linear coherent structures over the lake on 14 December 1997.

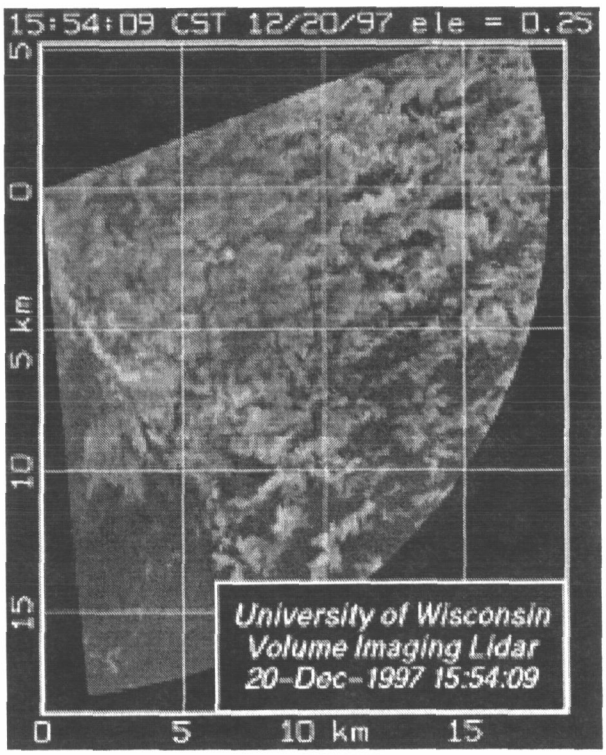


Figure 8. Snow acting as a tracer as it falls into the mixed layer over the lake.

Figure 8 shows patterns in a light snowfall on 20 December 1997. Surface measurements indicated the wind was from 310° at 3-5 m s^{-1} and the air temperature was near 0° C. Animations of the lidar data show structures flowing from the north and a convergence band along a line from approximately 3 km south of the lidar site to a point 5 km east and 10 km south of the lidar. This case was particularly impressive because the signal-to-noise ratio at 18 km was still very high.

While light snow acted as a tracer on a few days, we found the coastal environment near Sheboygan to offer high contrast in the aerosol scattering. Even on days with very high visibility, there was abundant scattering to resolve boundary layer structure. Steam-fog over the lake also provided a high scattering tracer in extremely shallow convection.

All the images shown here are frames extracted from high-resolution color animations. These MPEG movies can be downloaded from our website at http://lidar.ssec.wisc.edu.

Summary

Deployment of the UW-VIL in Lake-ICE during the winter of 97-98 allowed us to collect a rich set of unique measurements of atmospheric boundary layer structures. Our next steps include using the VIL data to quantitatively estimate the shapes of the structures and to compute wind profiles as a function of offshore distance. We also plan to compare these measurements with LES of intense cold-air advection over warm water.

Acknowledgments

This work was made possible by NSF grant number ATM9707165 and ARO grant number ARO DAAH-04-94-G-0195. Thanks to Jim Hedrick and Toby Schwalbe for preparation and maintance of the lidar.

References

[1] E. W. Eloranta and D. K. Forrest. Volume imaging lidar observations of the convective structure surrounding the flight path of a flux-meausring aircraft. *J. Geophys. Res.*, 97:18383–18393, 1988.

[2] R. B. Stull. *An Introduction to Boundary Layer Meteorology*. Kluwer Academic Publishers, 1988.

[3] E. M. Agee. *An Introduction to Shallow Convective Systems*, chapter in Cloud Dynamics, pages 3–30. D. Reidel Publishing Company, 1982.

On the Contribution of Water–Vapor DIAL to the Investigation of Turbulent Transport Processes

Volker Wulfmeyer

NOAA/ERL/ETL, NCAR
325 Broadway, Boulder, CO 80303, USA
Phone: (303) 497-6094, FAX: (303) 497-5318, Email: vow@ucar.edu

1 Introduction

The investigation of exchange processes between the earth's surface, the boundary layer, and the free troposphere is essential for the understanding of weather and climate. The vertical transport of water–vapor is an especially important issue which is dealt with in several projects of the World Climate Research Programme (WCRP) (see e. g. [1, 2]).

In previous publications it was shown that water–vapor differential absorption lidar (DIAL) has the potential to make important contributions to this research due to its high accuracy and resolution (see [3, 4] and references within). However, only recently an experimental proof of this potential became possible as operational DIAL systems which fulfil all requirements for accurate water–vapor measurements became available [5, 6, 7, 8].

This paper focuses on the investigation of transport processes using the ground–based water–vapor DIAL system of the Max–Planck–Institute for Meteorology (MPI) in Hamburg, Germany [9]. This system demonstrated a high absolute accuracy of the water–vapor profiles which is typically better than 5% in the whole troposphere. Furthermore, the statistical error of the DIAL measurements was extensively characterized and is about $0.1\,g/m^3$ using a vertical resolution of 75 m to 150 m and a time resolution of 1 min up to 2 km [9]. This is to our knowledge to date the lowest statistical error of a water–vapor remote sensing instrument for day– and nighttime measurements. These specifications will be confirmed at the conference both theoretically and experimentally.

The MPI DIAL system is transportable, operational and was deployed during two field campaigns. A 150–h dataset is available with the above mentioned accuracy and resolution which allows for a detailed investigation of boundary layer processes.

2 Measurements

Data are presented which were collected during a field experiment performed within the scope of the Baltic Sea Experiment (BALTEX) [2]. An overview on the results is given in [10]. The measurement site was located at the eastern coastline of Gotland, a Swedish island in the Baltic Sea, at 57:24 N and 18:55:30 E. The site was equipped with the DIAL system, a Radar–Radio Acoustic Sounding System (Radar–RASS) of the University of Hamburg, a rain radar, and a ceilometer. Furthermore, a group from the University of Uppsala, Sweden, and the Risø National Laboratory, Roskilde, Denmark, performed in–situ surface flux measurements on the island of Östergarnsholm 6 km northeast of our measurement site.

The data analyzed here were extracted from a 24–h continuous measurement on September 13, 1996. During the whole measurement period cold air was advected from the Baltic Sea to our site so that the measurement was performed in the convective marine boundary layer. The horizontal wind velocity was about 9 m/s, the absolute humidity in the boundary layer $\approx 6\,g/m^3$, and the surface temperature amounted to about 13°C. The boundary layer had a depth of $z_i \approx 700$ m.

Mainly three scientific questions will be addressed in this paper:

- What accuracy can be expected with respect to noise and sampling errors for the determination of turbulent quantities in the boundary layer? To address this question profiles of second to forth–order moments of the water–vapor fluctuations are shown including a detailed error analysis (see sections 2.1 and 2.2).
- Can a comparison of the measured variance profiles with published large eddy simulation (LES) model results be applied to determine of surface and entrainment latent heat fluxes (see section 2.1)? An introduction to this method

which is referred to as the *variance method* is found in [11].

- Does a relationship between the water–vapor flux divergence and the skewness exist to help distinguish between entrainment drying and moistening boundary layers as suggested by Mahrt [12] (see section 2.2)?

2.1 Water–vapor variance and dissipation profiles

Water–vapor variance profiles will be shown for four different 1–hour time periods. The statistical errors were estimated using the high–frequency wing of the variance spectra [13] in combination with the error propagation of the equation for the atmospheric variance. The sampling error was estimated directly by the determination of the integral scale in combination with the error propagation formulas found in [14, 15, 16].

Fig. 1 shows an example of a variance profile measured on 13 September 1996 between 4.5 UT and 5.5 UT using a vertical resolution of 60 m and a gliding average of 15 m. The noise error is $< 10\,\%$ in the entire range, and the sampling error is about 20 %. A least–squares–fit to LES model results [17, 18] is also indicated. In the mixed layer the fit reproduces the shape of the variance profile well up to $0.7\,z/z_i$. It will be shown that this result led to a promising agreement between in–situ surface latent heat fluxes and the surface flux estimated with the variance method. However, the small error bars allow the conclusion that a significant deviation between the LES model results and the measurements is found in the entrainment zone.

The first attempt of a comparison of water–vapor DIAL data with LES model results was reported in [19]. Kiemle et al. also found strong deviations of up to 60 % between fluxes derived using the variance method and in–situ measurements in the entrainment zone. However, they did not investigate whether this discrepancy was due to errors in the DIAL data or if the applicability of the LES model results should be questioned. Fig. 1 shows clearly that the published LES model results cannot be applied generally for comparisons with water–vapor variance profiles in the entrainment zone. The reasons are discussed in detail at the conference and in [20, 21, 22].

In a further step a method is presented to determine experimentally the shape of the top–down variance function calculated with the LES models.

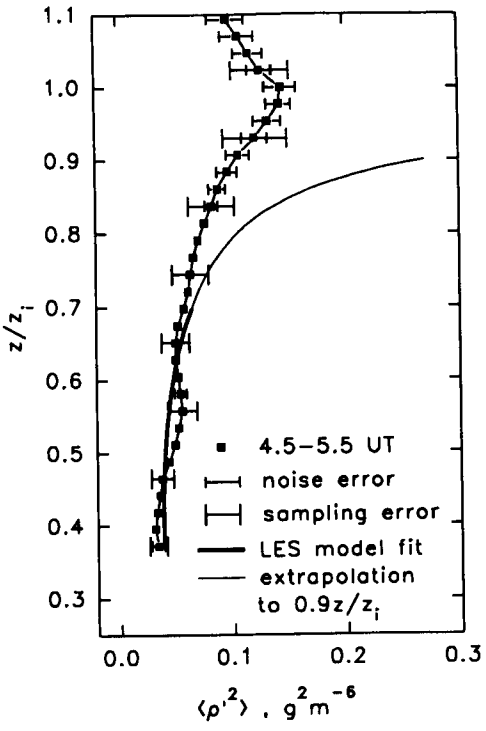


Figure1.
Water–vapor variance profile including noise and sampling errors in comparison with LES model results. The fit was only possible up to $0.7\,z/z_i$; otherwise the fitted profile did not resemble at all the shape of the measured profile (thin line extending to $0.9\,z/z_i$).

This can be an important tool to investigate the applicability of model results.

A fit of the structure function to the humidity autocovariance yields water–vapor dissipation rate profiles which will be presented and discussed.

2.2 Water–vapor skewness and kurtosis profiles

The calculation of profiles of the third and forth–order moments is more sophisticated as higher–order noise terms have to be removed. It is far beyond the scope of this paper to discuss the methodology which will be presented at the conference [22]. For four time periods skewness and kurtosis profiles will be shown including an error analysis with respect to noise and sampling errors. An example is shown in fig. 2.

During the experiment high–resolution vertical wind data were measured using the Radar–RASS

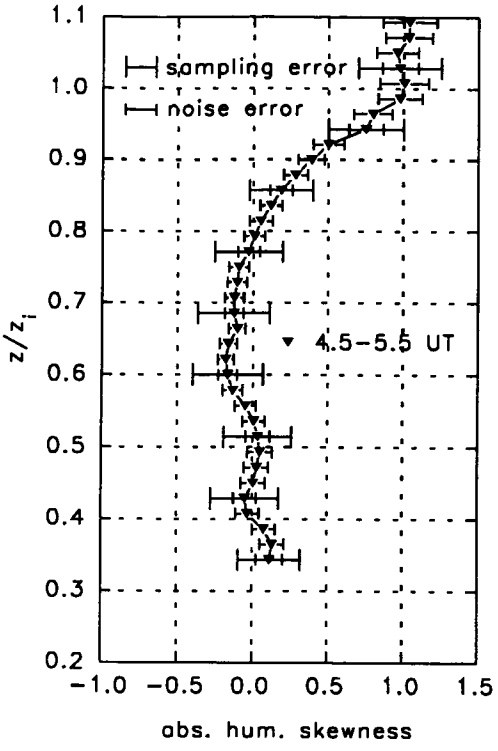


Figure2.
Water–vapor skewness profile including noise and sampling errors. The same resolution is used as in fig. 1. The profile shows no indication for a skewness in the mixed layer but a significant increase to positive values in the entrainment zone.

so that water–vapor flux profiles could be measured simultaneously to the higher–order humidity moments. Comparisons of skewness with water–vapor flux profiles will be presented. It is shown that a clear relationship between the water–vapor flux divergence and the sign of the skewness was not found in contrast to the suggestion of Mahrt [12]. Further applications of higher–order moments for the investigation of the structure of the water–vapor transport will be discussed.

3 Conclusion and outlook

High–resolution water–vapor profiles measured with ground–based DIAL make an important contribution in boundary layer research. The measured water–vapor variance profiles can be used to investigate and to improve LES models. It is demonstrated that the application of the variance method for the determination of surface latent heat fluxes yields a promising agreement with in–situ surface fluxes. However, the variance method cannot be applied generally for the determination of entrainment fluxes. The results of high–resolution models – even if these were derived from LES models – still have to be interpreted and applied with care when comparisons with "real–world" data are performed. Furthermore, suggested flux–gradient as well as similarity relationships can be investigated.

In the future it is planned to contribute to the improvement of small–scale parameterizations in mesoscale models by intercomparison of the collected data sets with model runs.

Acknowledgements

Various contributions to this research from the lidar group of Jens Bösenberg, the Radar group of Gerhard Peters, Ann–Sofi Smedman, Jørgen Højstrup, Don Lenschow, Christoph Senff, and Chin–Hoh Moeng are greatly acknowledged.

The author would like to express his appreciation to Mike Hardesty, Peter Hildebrand, Walt Dabberdt, and the Alexander von Humboldt Foundation for giving him the opportunity to perform this research during a research stay at NOAA and NCAR, Boulder, CO, USA.

References

1. World Climate Research Programme, "Scientific plan for the Global Energy and Water Cycle Experiment", *WMO/TD–No. 376*, WMO, Geneva, Switzerland (1990)
2. "Baltic Sea Experiment BALTEX initial implementation plan", *International Baltex secretariat publication no. 2*, GKSS Research Center, Geesthacht, Germany (1995)
3. S. Ismail, and E. V. Browell, "Airborne and spaceborne lidar measurements of water vapor profiles: a sensitivity analysis", *Appl. Opt.*, **28**, 3603–3615 (1989)
4. J. Bösenberg, "Ground–based differential absorption lidar for water–vapor and temperature profiling: Methodology", *Appl. Opt.*, in press (1998)
5. D. Bruneau, H. Cazeneuve, C. Loth, and J. Pelon, "Double–pulse dual–wavelength alexandrite laser for atmospheric water vapor measurement", *Appl. Opt.*, **30**, 3930–3937 (1991)
6. V. Wulfmeyer, J. Bösenberg, S. Lehmann, C. Senff, and S. Schmitz, "Injection–seeded alexandrite ring laser: performance and application in a water–vapor differential absorption lidar", Opt. Lett., **20**, 638–640 (1995)
7. E. V. Browell, and S. Ismail, "First lidar measurements of water vapor and aerosols from a high–altitude aircraft", in Optical Remote Sensing of the

Atmosphere, OSA Technical Digest Series Vol. 2, 212–214 (1995)
8. V. Wulfmeyer, "Ground–based differential absorption lidar for water–vapor and temperature profiling: Development and specifications of a high–performance laser transmitter", *Appl. Opt.*, in press (1998)
9. V. Wulfmeyer, and J. Bösenberg, "Ground–based differential absorption lidar for water–vapor profiling: Assessment of accuracy, resolution and meteorological applications", *Appl. Opt.*, in press (1998)
10. V. Wulfmeyer, F. Jansen, J. Bösenberg, L. Hirsch and G. Peters, "Investigation of turbulent processes in the lower troposphere with water–vapor DIAL and Radar–RASS", *J. Atmos. Sci.*, submitted for publication (1998)
11. K. J. Davis, "Surface fluxes of trace gases derived from convective–layer profiles", *Ph.D. thesis*, University of Colorado, Boulder, USA (1992)
12. L. Mahrt, "Boundary–layer moisture regimes", *Quart. J. Roy. Meteor. Soc.*, **117**, 151–176 (1991)
13. C. Senff, J. Bösenberg, and G. Peters, "Measurement of water vapor flux profiles in the convective boundary layer with lidar and Radar–RASS",*J. Atmos. Oceanic Technol.*, **11**, 85–93 (1994)
14. D. H. Lenschow, and L. Kristensen, "Uncorrelated noise in turbulence measurements", *J. Atmos. Oceanic Technol.*, **2**, 68–81 (1985)
15. D. H. Lenschow, and B. B. Stankov, "Length scales in the convective boundary layer", *J. Atmos. Sci.*, **43**, 1198–1208 (1986)
16. D. H. Lenschow, J. Mann, and L. Kristensen, 1994, "How long is long enough when measuring fluxes and other turbulence statistics?", *J. Atmos. Oceanic Technol.*, **11**, 661–673 (1994)
17. C.–H. Moeng, and J. C. Wyngaard, "Statistics of conservative scalars in the convective boundary layer", *J. Atmos. Sci.*, **41**, 3161–3169 (1984)
18. C.–H. Moeng, and J. C. Wyngaard, "Evaluation of turbulent transport and dissipation closures in second–order modeling", *J. Atmos. Sci.*, **46**, 2311–2330 (1989)
19. C. Kiemle, G. Ehret, A. Giez, K.J. Davis, D. H. Lenschow, and S. P. Oncley, "Estimation of boundary–layer humidity fluxes and statistics form airborne DIAL", *J. Geophys. Res.*, **102, D24**, 29189–29204 (1997)
20. Z. Sorbjan, "Effects caused by varying the strength of the capping inversion based on a large eddy simulation model of the shear–free convective boundary layer", *J. Atmos. Sci.*, 2015–2024 (1996)
21. Z. Sorbjan, "Similarity of scalar fields in the convective boundary layer", *J. Atmos. Sci.*, submitted for publication (1997)
22. V. Wulfmeyer, "Investigations of humidity skewness and variance profiles in the convective boundary layer and comparison with large eddy simulation results", *J. Atmos. Sci.*, submitted for publication (1998)

First results from the aerosol lidar and backscatter sonde intercomparison campaign STRAIT'97 at Table Mountain Facility during February–March 1997

G. Beyerle[1,5], M. R. Gross[2], D. A. Haner[3], N. T. Kjome[4], I. S. McDermid[1], T. J. McGee[2], J. M. Rosen[4], H.-J. Schäfer[5,6], and O. Schrems[5]

(1) Jet Propulsion Laboratory, California Institute of Technology
P.O.Box 367, Wrightwood, CA 92397-0367, ph.: (760) 249-6176
fax: (760) 249-5392, e-mail: beyerle@tmf.jpl.nasa.gov
(2) Goddard Space Flight Center, Greenbelt MD, USA
(3) California State Polytechnic University, Pomona CA, USA
(4) University of Wyoming, Laramie WY, USA
(5) Alfred Wegener Institute for Polar and Marine Research, Bremerhaven and Potsdam, Germany
(6) now at Forschungszentrum Jülich, Germany

1 Abstract

First results of an intercomparison measurement campaign between three aerosol lidar instruments and in-situ backscatter sondes performed at Table Mountain Facility (34.4°N, 117.7°E, 2280 m asl) in February–March 1997 are presented. During the campaign a total of 414 hours of lidar data were acquired by the Aerosol-Temperature-Lidar (ATL, Goddard Space Flight Center) the Mobile-aerosol-Raman-Lidar (MARL, Alfred Wegener Institute), and the TMF-Aerosol-Lidar (TAL, Jet Propulsion Laboratory), and four backscatter sondes were launched. From the data set altitude profiles of backscatter ratio and volume depolarization of stratospheric background aerosols at altitudes between 15 and 25 km and optically thin high-altitude cirrus clouds at altitudes below 13 km are derived. On the basis of a sulfuric acid aerosol model color ratio profiles obtained from two wavelength lidar data are compared to the corresponding profiles derived from the sonde observations. We find an excellent agreement between the in-situ and ATL lidar data with respect to backscatter and color ratio. Cirrus clouds were present on 16 of 26 nights during the campaign. Lidar observations with 1–7 minute temporal and 120–300 m spatial resolution indicate high spatial and temporal variability of the cirrus layers. Qualitative agreement is found between concurrent lidar measurements of backscatter ratio and volume depolarization.

2 Introduction

Ground-based lidar observations of the stratosphere are an integral part of the Network for the Detection of Stratospheric Change (NDSC). The high quality level of the NDSC data set is guaranteed by periodic intercomparisons between measuring instruments [e.g., *McDermid et al.*, 1995]. Here we report on results from an intercomparison campaign which has taken place at the NDSC complementary station Table Mountain Facility in southern California (34.4°N, 117.7°E, 2280 m asl) between February 19 and March 18, 1997. Three aerosol lidar instruments participated in the campaign:

- a mobile aerosol Raman lidar (AT-Lidar or ATL) *Gross et al.* [1995] from Goddard Space Flight Center (GSFC), USA,
- a mobile aerosol Raman lidar (MARL) [*Schäfer et al.*, 1995] from Alfred Wegener Institute for Polar and Marine Research (AWI), Germany, and
- an aerosol lidar (TAL) from Table Mountain Facility / Jet Propulsion Laboratory, USA.

Four balloon-borne backscatter sondes (BKS) [*Rosen and Kjome*, 1991] from University of Wyoming were launched to provide independent data on aerosol backscatter coefficient.

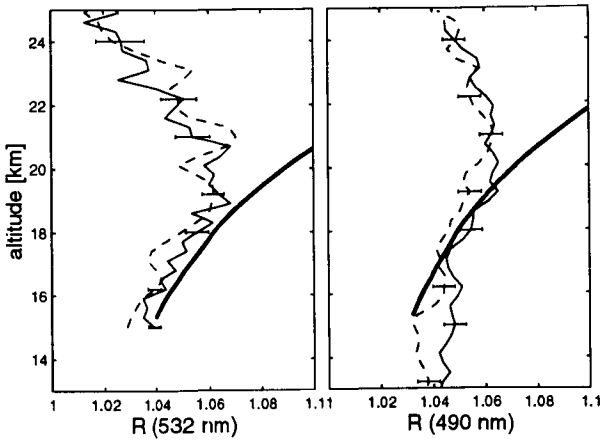


Figure 1: Backscatter ratio at 532 nm (AT-Lidar, left panel) and 490 nm (BKS, right panel) as observed on March 11 (full line) and March 13, 1997 (dashed line). The thick lines give the result obtained by the aerosol model.

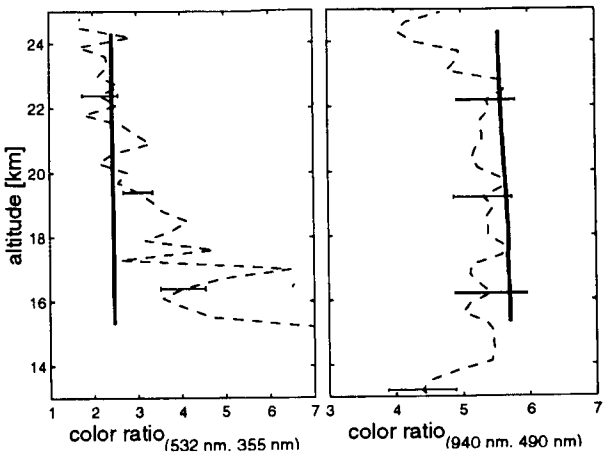


Figure 2: Color ratio at 532 nm, 351 nm (AT-Lidar, left panel) and at 940 nm, 490 nm (BKS, right panel) as observed on March 13, 1997 (dashed line). The thick lines give the result obtained by the aerosol model.

3 Results and discussion

The three aerosol lidar systems were placed in close vicinity. The distance between MARL and TAL was about 30 m, the AT-Lidar was located at a distance of about 500 m. Test measurements showed that all three aerosol lidar could be operated simultaneously with no detectable interference or cross-talk between the instruments. During the campaign a total of 413.6 hours of lidar data were acquired by the three instruments.

3.1 Stratospheric background aerosol

In order to compare the lidar observations of the stratospheric background aerosol (SBA) layer with the in-situ data an aerosol model is used [*Steele and Hamill*, 1981]. The model is based on the assumption that SBA consists of H_2SO_4/H_2O droplets in equilibrium with 5 ppmv ambient water vapor mixing ratio [*Hamill et al.*, 1997]. The size distribution dN/dr is assumed to follow a log-normal distribution,

$$\frac{dN}{dr} = \frac{N_0}{\sqrt{2\pi}\, r \ln \sigma_g} \exp\left(-\frac{\ln^2(r/r_m)}{2 \ln^2 \sigma_g}\right) \qquad (1)$$

where N_0, r_m, and σ_g denote the particle number density, the median radius, and the geometric standard deviation, respectively. *Pinnick et al.* [1976] give the parameterization $N_0 = 10$ cm^{-3}, $r_m = 0.075$ μm, and $\sigma_g = 1.86$. We assume N_0, r_m, and σ_g to be constant throughout the aerosol layer.

The wavelength dependence of the aerosol backscatter coefficient β^A can be expressed in terms of the color ratio

$$C_{\lambda_1,\lambda_2} = \frac{R(\lambda_1) - 1}{R(\lambda_2) - 1} = \frac{\beta^A(\lambda_1)}{\beta^A(\lambda_2)} \left(\frac{\lambda_2}{\lambda_1}\right)^k . \qquad (2)$$

Here, R is the backscatter ratio at wavelength λ and $k = -4.13$ denotes the wavelength dependence of molecular scattering [*Ciddor*, 1996].

In Figure 1 the enhancement of backscatter ratio due to the presence of the SBA as observed by AT-Lidar and BKS sonde on March 11 and 13, 1997 is shown. The lidar measurement time periods were 6.5 h and 5.5 h, respectively. Both, the lidar and sonde observations are in good agreement with the model results (thick lines) at altitudes between 15 and 19 km.

Figure 2 shows the color ratio calculated from the lidar and in-situ data at 532 nm, 351 nm and 940 nm, 490 nm, respectively. We find a good to excellent agreement between observations and the model calculations (thick lines). As color ratio does not depend on particle number density N_0 (Equation 2) the agreement with respect to C (Figure 2) above 19 km and disagreement with respect to R (Figure 1) suggests that $N_0 < 10$ cm^{-3} above 19 km.

3.2 High-altitude cirrus

During the campaign cirrus clouds were observed on 16 of 26 nights. Analysis of high temporal resolution data (6.6 and 1 minute for MARL and TAL, respectively) reveals a strong spatial and temporal variability of the observed cirrus clouds.

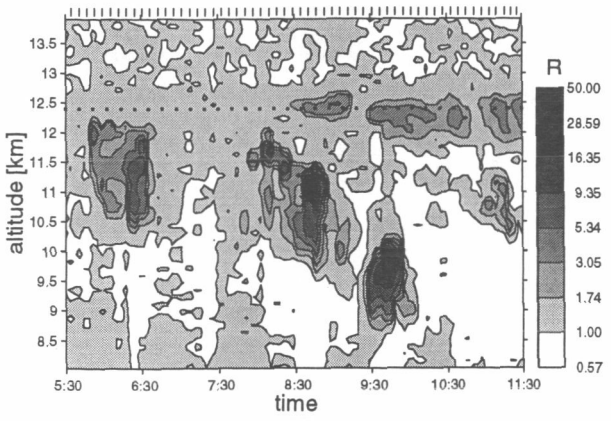


Figure 6: Temporal development of backscatter ratio at 532 nm on March 13, 1997 as observed by MARL. The tropopause altitude is marked by a dotted line.

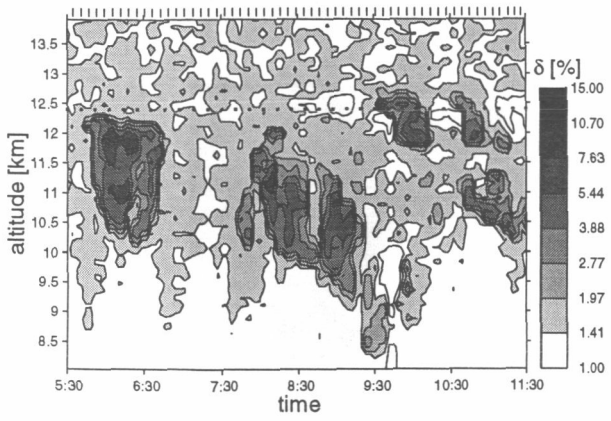


Figure 7: Temporal development of volume depolarization at 532 nm on March 13, 1997 as observed by MARL. The tropopause altitude is marked by a dotted line.

- Frequently cirrus clouds are observed in close vicinity below and at the tropopause. There is no indication that cirrus cloud occur in the lower stratosphere.

- The cirrus layers exhibit a high degree of spatial inhomogeneity.

- In-situ and lidar observations show vertical scales on the order of several tens of meters.

- The vertical and horizontal extend of cirrus clouds can accurately be mapped by the high-resolution lidar data set.

5 Acknowledgments

Financial support by Alfred Wegener Institute, Germany and the National Aeronautics and Space Administration is gratefully acknowledged. The work described in this paper was carried out at the Jet Propulsion Laboratory, California Institute of Technology, through an agreement with the National Aeronautics and Space Administration. GB thanks National Research Council for the award of an associateship.

References

Ciddor, P. E., Refractive index of air: new equations for the visible and near infrared, *Appl. Opt.*, *35*, (9), 1566–1573, 1996.

Gross, M., T. J. McGee, U. N. Singh, and P. Kimvilakani, Measurements of stratospheric aerosols with a combined elastic-Raman-backscatter lidar, *Appl. Opt.*, *34*, (30), 6915–6924, 1995.

Hamill, P., E. J. Jensen, P. B. Russell, and J. J. Bauman, The life-cycle of stratospheric aerosol particles, *Bull. Amer. Meteor. Soc.*, *78*, (7), 1395–1410, 1997.

McDermid, I. S., S. M. Godin, and T. D. Walsh, Results from the Jet Propulsion Laboratory stratospheric ozone lidar during STOIC 1989, *J. Geophys. Res.*, *100*, (D5), 9263–9272, 1995.

Pinnick, R. G., J. M. Rosen, and D. J. Hofmann, Stratospheric aerosol measurements III: Optical model calculations, *J. Atmos. Sci.*, *33*, 304–314, 1976.

Rosen, J. M., and N. T. Kjome, Backscattersonde: A new instrument for atmospheric research, *Appl. Opt.*, *30*, (12), 1552–1561, 1991.

Schäfer, H.-J., O. Schrems, G. Beyerle, B. Hofer, W. Mildner, F. A. Theopold, W. Lahmann, C. Weitkamp, and M. Steinbach, A modular and mobile multi-purpose lidar system for observation of tropospheric and stratospheric aerosols, *SPIE EurOpto series*, *2581*, 128–136, 1995.

Steele, H. M., and P. Hamill, Effects of temperature and humidity on the growth and optical properties of sulphuric acid-water droplets in the stratosphere, *J. Aerosol Sci.*, *12*, (6), 517–528, 1981.

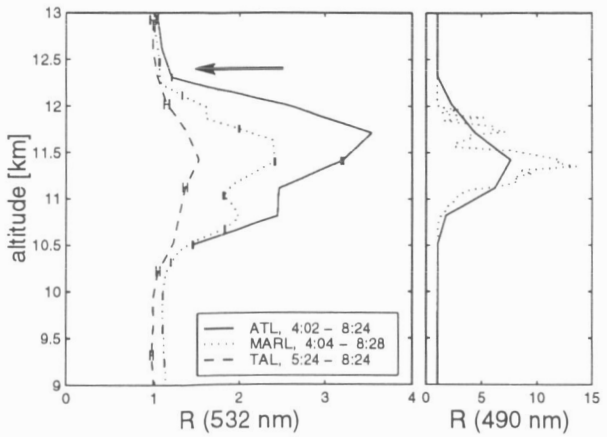


Figure 3: Cirrus cloud observation by lidar (left panel) and in-situ sonde (right panel) on March 11, 1998. All profiles have been converted to a common altitude resolution of 600 m. Lidar integration times vary between 3 and 4.5 h. (The dotted line in the right panel marks the original profile.) Tropopause altitude is marked by an arrow.

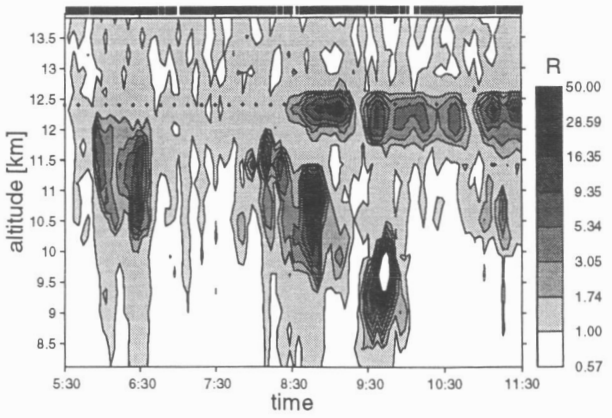


Figure 4: Temporal development of cirrus layers on March 13, 1997 as observed by TAL. Backscatter ratio at 532 nm is shown as a function of altitude and time. The tropopause altitude is marked by a dotted line. Bars above the figure indicate the time of the individual measurements.

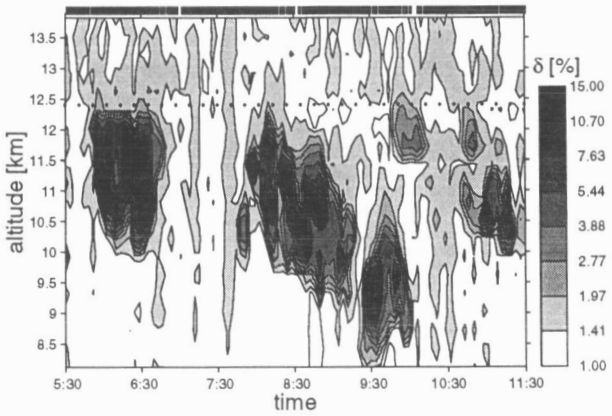


Figure 5: Temporal development of volume depolarization at 532 nm on March 13, 1997 as observed by TAL. The tropopause altitude is marked by a dotted line.

In general, the layers extend vertically over 1–2 km; occasionally, clouds appear in several distinct layers separated by 1–2 km. Cirrus clouds are found in close vicinity below and at tropopause altitudes. There is no indication for cirrus occurrence in the lower stratosphere.

Figure 3 shows the cirrus cloud observation of March 13, 1997. The tropopause altitude is derived from the in-situ temperature profile. In order to facilitate the comparison all backscatter ratio profiles are converted to a common altitude resolution of 600 m. We find substantial differences not only between sonde and lidar profiles but also between lidar observations. For example, values of R obtained by ATL and MARL deviate by almost 50% despite an almost identical measurement period and an integration time of several hours.

These deviations are caused by a strong temporal and spatial variability of cirrus clouds as can be seen from Figure 4-7. In Figures 4 and 6 the temporal evolution of backscatter ratio at 532 nm is plotted as a function of altitude and time. The tropopause altitude is derived from the in-situ temperature profile. Taking into account that the temporal and vertical resolutions of the underlying data set are not identical (1 minute/300 m and 6.6 minutes/120 m for TAL and MARL, respectively) a general similarity between Figures 4 and 6 is observed. We note that for the graphical representation the data sets have been interpolated in time using Gaussian weights with a standard deviation of 1.5 minutes.

Likewise, the temporal evolution of volume depolarization $\delta = \beta_{\perp}/\beta_{||}$ show qualitative agreement (Figures 5 and 7). ($\beta_{||,\perp}$ denote the backscatter coefficient in the aligned- and cross-polarization detection channel, respectively.)

4 Conclusions

Based on our observations we draw the following conclusions.

- Good or excellent agreement is found between lidar and in-situ measurements of the stratospheric background aerosol.

Evaluation and optimization of lidar temperature analysis algorithms using simulated data.

Thierry Leblanc, I. Stuart McDermid
Jet Propulsion Laboratory, California Institute of Technology, Table Mountain Facility, Wrightwood, CA, USA.
leblanc@tmf.jpl.nasa.gov, Tel: +1 760 249 1070, Fax: +1 760 249 5392

Alain Hauchecorne, and Philippe Keckhut
Service d'Aéronomie du CNRS, BP 3, 91371 Verrières-le-Buisson, France

1. Introduction

The middle atmosphere (20 to 90 km altitude) has received increasing interest from the scientific community during the last decades, especially since such problems as polar ozone depletion and climatic change have become so important. Temperature profiles have been obtained in this region using a variety of satellite-, rocket-, and balloon-borne instruments as well as some ground-based systems. One of the more promising of these instruments, especially for long-term high resolution measurements, is the lidar. Measurements of laser radiation Rayleigh backscattered [*Elterman*, 1951], or Raman scattered [*Moskowitz*, 1988], by atmospheric air molecules can be used to determine the relative air density profile and subsequently the temperature profile if it is assumed that the atmosphere is in hydrostatic equilibrium and follows the ideal gas law [*Hauchecorne and Chanin*, 1980]. The high vertical and spatial resolution make the lidar a well adapted instrument for the study of many middle atmospheric processes and phenomena as well as for the evaluation and validation of temperature measurements from satellites, such as the Upper Atmosphere Research Satellite (UARS). In the Network for Detection of Stratospheric Change (NDSC) [*Kurylo and Solomon*, 1990] lidar is the core instrument for measuring middle atmosphere temperature profiles. Using the best lidar analysis algorithm possible is therefore of crucial importance.

In this work, the JPL and CNRS/SA lidar analysis softwares were evaluated. The results of this evaluation allowed the programs to be corrected and optimized and new production software versions were produced. First, a brief description of the lidar technique and the method used to simulate lidar raw-data profiles from a given temperature profile is presented. Evaluation and optimization of the JPL and CNRS/SA algorithms are then discussed.

2. Determination of the atmospheric temperature profile from lidar measurements.

Laser radiation transmitted into the atmosphere is backscattered by the air molecules and collected by the lidar telescope. The number of photons received from a scattering layer δz, at a mean altitude z, is proportional to the number of photons emitted in the laser pulse and to the number of molecules or air density. Mie scattering by aerosols is typically only important below 25-30 km and can be neglected for the air density derivation above 30 km. However, following volcanic eruptions particular care is required to ensure that the density derivation is not corrupted by aerosol scattering. Then, the temperature is derived from the air density assuming hydrostatic equilibrium and the ideal gas law [*Hauchecorne and Chanin*, 1980].

3. Simulation of lidar raw-data.

Starting with known, user-defined temperature profiles the corresponding pressure and density profiles can be deduced and, in turn, theoretical or simulated raw-data profiles can be calculated using the known or measured characteristics of any specific lidar instrument. Simulated raw-data profiles are generated and then analyzed using the standard analysis algorithms as though they were measured profiles. The 'retrieved' temperature profiles are compared to the 'original' simulated ones. In this section, the simulation process is briefly described. Comparisons between retrieved and the original profiles will be presented in the next sections.

The first step in the data simulation procedure is the creation of the initial temperature profile. The CIRA-86 model was chosen as the climatological reference and as the starting point for the generation of test profiles. This model includes the zonal and monthly mean temperature between 0 and 100 km. The January-mean temperature profile at 44°N, 6°E was chosen as the basic reference profile. Various disturbances to this profile were introduced to simulate non-climatological profiles for the case studies described below.

The second step is to create the pressure-density profile associated with the generated temperature profile. A 2.7 hPa reference pressure at 40 km has been used to compute these profiles using the hydrostatic equilibrium and ideal gas law. The simulated interdependent temperature-pressure-density profile is then used to compute the theoretical number of photons that would be received by a given lidar instrument taking into account the known parameters of that

instrument. This is the main part of the simulation process.

1) The Rayleigh lidar equation is first evaluated, considering only the atmospheric backscattering and the constant terms relevant to the emitting system.

2) The Rayleigh extinction and ozone absorption corrections are then applied to the signal for the round-trip of the light between the instrument and the altitude of measurement. It is assumed here that no aerosols contribute to the signal extinction or backscattering, allowing comparisons of Rayleigh temperatures well below 30 km.

3) The signal is then corrected by the solid angle formed between the altitude of measurement and the telescope surface.

4) Then a noise from the sky background light must be added to the signal. When several independent channels are used, the sky background noise should be normalized by the fov of the telescopes when different.

5) The signal and sky background light are then transmitted between the receiving and counting systems. An efficiency coefficient has to be introduced to account for the optical transmission between the telescope surface and the photomultiplier detectors, and for the quantum efficiency of the counting system.

6) The photomultiplier and the counting system then translate the photons received into electronic pulses which are counted by the MCS. Due to the high dynamic range of the signal, the system can be either saturated if too many photons arrive in a short period or under-saturated if the magnitude of the electronic pulse caused by a low signal is too small to be retained [see for example, *Donovan et al.*, 1993]. The number of photons counted is therefore different from the true number of photons received. The correction applied is function of the maximum counting rate of the electronics and level of discrimination of the electronic pulses.

7) Finally, an instrumental noise has to be added. This so called signal-induced-noise is a reaction of the photomultipliers to the very strong signal received from the lower altitudes which results in a time dependent enhancement of the background counts.

The number of photons finally obtained is assumed to be the raw-data, as if it were really measured by the instrument. The output data must present signal levels similar to those obtained with real measurements since the analysis algorithms typically use these levels in various steps of the temperature derivation. To ensure that the results were not dependent on the simulations themselves, the latter were performed using characteristics typical of several different existing lidar systems. The simulated data are analyzed and the temperature results are compared to the original simulated temperature profiles.

The simulation of vibrational Raman lidar temperature measurements was also performed. The methods and equations used are similar to the Rayleigh simulation, except for few points (nitrogen density instead of air density, wavelengths and cross sections). Only the results from the Rayleigh simulations will be shown, since the results for the Raman case are strictly similar.

4. Evaluation of the JPL and CNRS/SA temperature lidar algorithms.

The simulation procedure described above was used to evaluate the temperature retrieval algorithms of the JPL and CNRS/SA lidar systems, and to diagnose inaccuracies or identify limitations in these analysis methods. Simulations were performed taking into account the actual characteristics of three different lidar systems: the Table Mountain Facility (TMF) and Mauna Loa Observatory (MLO) lidars of JPL, and the Observatoire de Haute-Provence (OHP) Rayleigh lidar system of CNRS/SA, France. Because the same analysis software is used for both TMF and MLO lidar systems, only MLO results will be shown, together with the OHP results.

As a starting point, a standard CIRA [*Fleming et al.*, 1990] temperature profile was used in the raw-data simulation. Since the lidar algorithms necessarily use model information in at least one part of the analysis, a simulated profile taken from a climatological model allows the study of analysis errors independent of the model errors. Raw data profiles corresponding to the CIRA-86 temperature profile at 44°N, 6°E in January were simulated and retrieved. Realistic experimental noise was included in the raw-data profiles to simulate a real data acquisition. The retrieved and original temperature profiles were compared. Both retrieved profiles remained close to the original, at least below 70 km (not shown). The MLO profile was systematically cut-off at 80 km, while the OHP profile was cut-off at a given signal to noise ratio. Some significant differences between the original and retrieved profiles appeared below 40 km for both the JPL and CNRS/SA profiles. These departures were much greater than the one sigma standard deviation, especially for the JPL profile below 25 km and were indicating that there were some problems with these versions of the algorithms.

To help identify the source(s) of the errors leading to such departures the same profile was simulated but without instrumental noise. Figures 1(a) and (b) show the difference between the retrieved and original simulated temperature profiles. At this point, the shape of the departures is clear, and the departures are apparently of different origin for OHP and MLO.

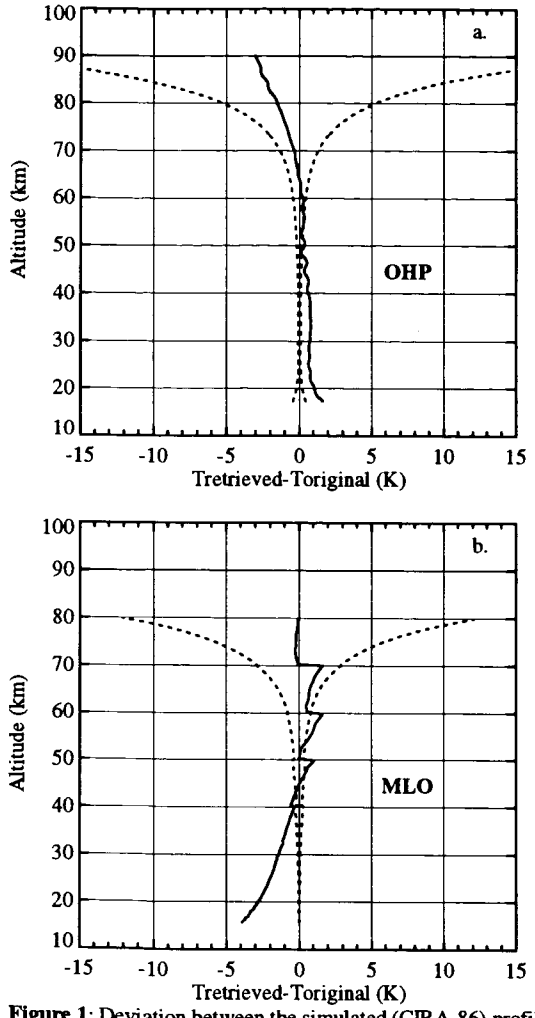


Figure 1: Deviation between the simulated (CIRA-86) profile and the OHP (a) and MLO (b) retrieved profiles. The dotted lines indicate the temperature error at one standard deviation

Large steps are observed every ten kilometers on the MLO which were not clear with the profiles containing instrumental noise. These steps were easily identified as being related to the smoothing part of the algorithm since they occur at the altitudes, every ten kilometers above 40 km, where the vertical smoothing range was increased. Review of the JPL algorithm revealed that a linear smoothing function was applied to the density signal which is actually an exponential function, decreasing with height. This source of inaccuracy was removed by applying the same smoothing method to the logarithm of the density which can be considered as a nearly linear function of altitude. Repeating the analysis with the corrected smoothing routine completely removes the steps (not shown here).

Several other departures were identified and corrected using the simulated data. Some of the errors identified have been summarized below:

- An error of few hundred meters in the site altitude assignment produces a maximum error of 5 K at 15 km, 2 K at 30 km, decreasing to near-zero as the altitude increases to 80 km.
- An error of a factor 2 in ozone vertical distribution causes a temperature error reaching more than 1 K at 20 km.
- An inaccurate background extraction (especially in the presence of non-linear signal induced noise) can lead to some errors reaching 5 K in the 10 upper kilometers of the profile.

5. Optimization of the JPL and CNRS/SA temperature lidar algorithms.

The simulation was then used to optimize the temperature retrievals of the JPL and CNRS/SA lidar systems. In this work, we will focus on a specific subject: The effect of introducing *a priori* information into the instrumental data, and the effect of smoothing. For lidar temperature retrievals, *a priori* information is necessary at two different steps in the data processing:

1) when normalizing the signal (relative density) to an *a priori* density taken from a CIRA-like climatological model or from a NCEP analysis.

2) when starting the downward integration of the temperature profile from the top.

Figure 2 illustrates, using the MLO retrieval, the effect of the temperature initialization at the top of the profile. The lidar temperature retrievals always need such an initialization which can be made by taking an *a priori* temperature and density or pressure at the top. The temperature profile is then integrated downward. In the case of Figure 2, the simulated profile is 15 K warmer than the CIRA profile at all altitudes. Therefore, when initializing at 90 km to the CIRA temperature, T_{TOP}, a -15 K departure is observed. Then, the error quickly decreases as we integrate downward because of the quasi-exponential growth of the density. Starting with a 15 K error at 90 km, it drops to 4 K at 80 km and 1 K at 70 km and becomes negligible below this. This error cannot be removed and can be a significant limitation of the lidar temperature analysis, especially near the mesopause which is a region with large temperature variability. However, Figure 2 illustrates the worst condition of using the *a priori* information since real temperature profiles are never 15 K hotter than the climatology throughout the entire profile (15-90 km). Even if deviations of 25-30 K occur at mesospheric heights, small vertical scale wave structures allow the real temperature to reach climatological values in several kilometers, making the

convergence from the outlying *a priori* values to the real values much faster.

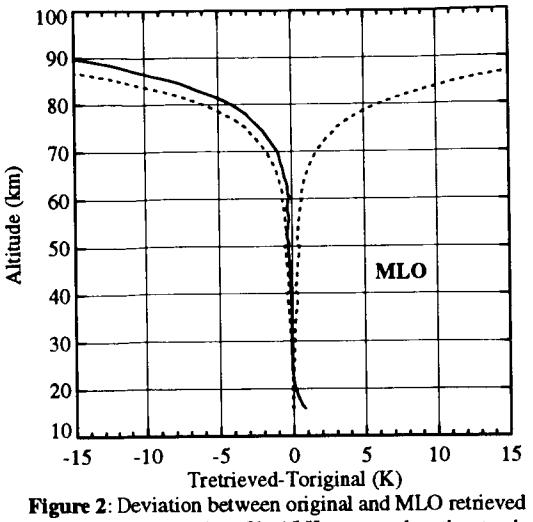


Figure 2: Deviation between original and MLO retrieved profiles for a simulated profile 15 K warmer than the standard CIRA profile.

6. Conclusion.

The use of simulation has been shown to be useful for testing the lidar analysis algorithms. Using known temperature-pressure-density profiles some typical raw-data profiles were simulated and then analyzed by different lidar softwares as if they had been obtained by real measurements. The retrieved temperature profiles were then compared to the simulated original profiles. By using different analysis methods, or by purposely introducing inaccuracies, the effects on the error related to different parts of the lidar analysis could be determined. Different error sources have been identified and quantified.

When the simulated profile is far from a climatological profile the most dramatic departures are located in the first 10 kilometers from the top due to the necessary initialization by model data (20 K departure of temperature is frequently observed). Also, the accuracy of the smoothing method and background subtraction are of crucial importance. A secondary effect is the inaccurate normalization of density, used in the extinction correction at UV wavelengths, leading to departures up to 3 K at the very bottom for UV wavelengths. Finally, range correction errors or altitude shifts can lead also to significant departures in the lower part of the profiles.

After these errors have been corrected the difference between retrieved and original profiles remained very small (< 0.5 K, not shown here), illustrating the usefulness of such approach. Other useful tests, concerning notably noise and saturation correction effects, can be investigated in the future simulations. The simulations presented in this work demonstrate the capability to evaluate lidar temperature analysis programs and to diagnose typical problems. Application of this technique to evaluate the different temperature analysis programs used by most of the lidar groups within the NDSC is planned.

Acknowledgments

The work described in this paper was carried out at the Jet Propulsion Laboratory, California Institute of Technology, under an agreement with the National Aeronautics and Space Administration.

References

Donovan, D. P., J. A. Whiteway, and A. I. Carswell, Correction for non-linear photon-counting effects in lidar systems, *Appl. Opt.*, *32*, 6742-6753, 1993.

Elterman, L. B., The measurement of stratospheric density distribution with the searchlight technique, *J. Geophys Res.*, *56*, 509-520, 1951.

Fleming, E. L., S. Chandra, J. J. Barnett, and M. Corney, COSPAR International Reference Atmosphere, Chapter 2: Zonal Mean Temperature, Pressure, Zonal Wind, and Geopotential Height as a Function of Latitude, *Adv. Space Res.*, *10*, 11-59, 1990.

Hauchecorne, A., and M. L. Chanin, Density and Temperature Profiles obtained by lidar between 35 and 70 km, *Geophys. Res. Lett.*, *8*, 565-568, 1980.

Kurylo M. J., and S. Solomon, Network for the Detection of Stratospheric Change: a status and implementation report, *NASA. Upper Atmosphere Research Program and NOAA Climate and Global Change Program*, NASA, Washington D.C., 1990.

Moskowitz, W. P., G. Davidson, D. Sipler, C. R. Philbrick, and P. Dao, Raman augmentation for Rayleigh lidar, 14th ILRC, Conference Abstracts, 284-286, 1988.

High-resolution Lidar Studies of Stratospheric Air Intrusions

Holger Eisele, Rudolf Sladkovic, and Thomas Trickl
Fraunhofer-Institut für Atmosphärische Umweltforschung (IFU), Kreuzeckbahnstr. 19,
D-82467 Garmisch-Partenkirchen
Phone: (+49)-8821-183-209, FAX: (+49)-8821-73573, E mail: trickl@ifu.fhg.de

1 Introduction

There has been a long tradition of Alpine monitoring stations, such as Zugspitze, in the investigation of stratospheric air parcels descending down to these height levels (e.g., Reiter et al., 1971). The analysis of these processes has been based on the measurement of tracers such as ozone, ^{7}Be, humidity and temperature. Tropopause folds have been associated with anticyclonic bending of the jet steam over Central or North-west Europe. A long record exists for the IFU stations Zugspitze and Wank near Garmisch-Partenkirchen. The data of these two monitoring stations were recently partly re-analysed by Elbern et al. (1997) who point out that for a selected period of ten years 195 stratospheric events could unambiguously be identified for the Zugspitze summit (2962 m a.s.l.), 85 of which reaching even the Wank station (1776 m a.s.l.). In no case stratospheric air could be verified in the valley (IFU, 730 m a.s.l.). The fraction of intrusions not reaching 3 km a.s.l. as well as the stratospheric ozone fluxes to the troposphere above and below this height remained unknown.

In order to obtain additional information we have attempted a better approach based on sufficiently dense sounding with an ozone lidar. The lidar method has been demonstrated to be a powerful technique for the investigation of stratospheric air intrusions (Browell et al., 1987; Ancellet et al., 1991; Ancellet et al., 1994; Langford et al., 1996). The upgraded ozone lidar at IFU offers a unique detection range between 0.2 km above the ground and least 4 km above the tropopause and is, consequently, an ideal tool for such investigations. Dense long-term series of soundings may be carried out under automatic control. The lidar measurements since January 1996 have revealed a lot of interesting details on stratospheric air intrusions. Although the data are far from being sufficient for an attempt to determine fluxes, we are able to give a first estimate of the fraction of stratospheric air intrusions reaching the Zugspitze summit. In this contribution we give just a brief overview of the work done. A full description, including colour plots of two longer time series, was recently submitted for publication (Eisele et al., 1998). This work forms a part of Work Package one of the VOTALP project (Vertical Ozone Transport in the Alps, funded by the European Union).

2 Description of the Experimental Approach

The stationary ozone lidar at IFU, after its modification in 1995 (Eisele and Trickl, 1997), is operated with three laser wavelengths, 277, 292 and 313 nm. The ozone distribution may be separately evaluated from the atmospheric backscatter signals for two different wavelength pairs, usually 277/313 nm and 292/313 nm. The comparison of the ozone data for these two pairs yieds an ideal system performance check. Under optimum conditions the results for different wavelength pairs agree to within 5 % which is comparable to the accuracy of in-situ instruments. This error limit, which was verified by numerous intercomparisons, is achieved with a vertical resolution dynamically varied from 50 m next to the ground to about 0.5 km near the tropopause, thus compensating the declining signal-to-noise ratio of the backscatter signals, and a signal averaging time as short as 40 s. The vertical resolution is selected by setting the interval size of a sharp-edge numerical low-pass filter to the ozone densities calculated from the backscatter signals. It could be demonstrated by comparisons with station and sonde data that stratospheric ozone tongues, wich may be in some cases as narrow as 300 m, may be correctly reproduced. Details of the lidar and the data evaluation will be published separately.

It has long been known that ^{7}Be peaks at Zugspitze are correlated with the occurrence of clear, cloud-free air, nicknamed ^{7}Be weather. In fact, only very few such episodes have escaped lidar sounding due to non-dissipating low lying clouds in two years. Long-term observations with the lidar are facilitated by the option of automatic system control.

The meteorological prediction of stratospheric air intrusions is based on the criteria mentioned in the introduction. In addition, a custom-made model package has been applied which yields quick-look

analyses of radio-sonde and meteorological data as well as trajectory calculations.

3 Results and Discussion

During a total of 43 stratospheric episodes in 1996 and 1997 lidar soundings were carried out. The events were mostly predicted by the meteorological analysis, but also identified later on from a more intense data inspection. In 1996, due two periods of system shutdown, the number of episodes with lidar soundings were limited to 16 mostly due to two periods of system shutdown, but also due to less concentrated efforts at the beginning of the project. The lidar method has been applicable in almost all cases since the residual, low-lying clouds above the valley usually dissipate quite rapidly. However, during quite a few of these episodes they do not dissipate before the stratospheric air reaches the Zugspitze summit.

Not in all cases a unambiguously discernible ozone peak was verified, mostly due to a late or early period of .observation. However, such peaks were seen at the Zugspitze station in all but one case, together with elevated ^{7}Be and a humidity dip. For that case elevated ozone was, nevertheless detected with the lidar above the Zugspitze height. One intrusion proceeded all the way down to the ground the final step very likely being supported by convective mixing (May 29, 1996).

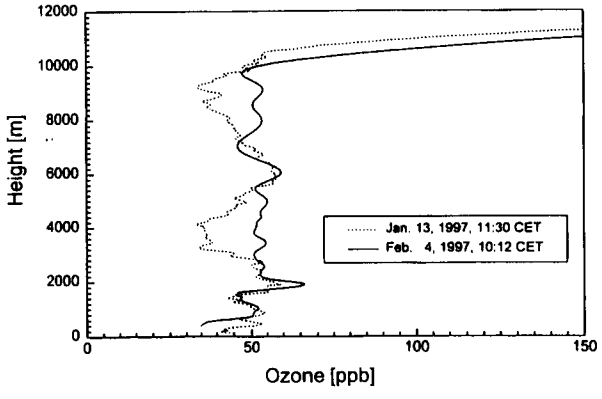


Figure 1. Two examples of ozone distributions during tropopause folding events showing different cases of ozone peaks in the lower troposphere; for details see text.

Figure 1 shows two examples of vertical ozone distributions during tropopause folding events. The narrow peak at 1.9 km above the ground on February 4, 1997, descended with a speed slightly below 100 m/h and corresponded to a 3.5-h ozone rise (f.w.h.m.) at the Zugspitze summit (relative height 2.22 km with respect to the lidar zero). The Zugspitze mixing ratios before and after the passage of the stratospheric layer, 47 and 52 ppb, repectively, agree well with the ozone values measured with the lidar below and above the peak. The peak mixing ratio of the lidar exceeds the Zugspitze value by 4 ppb which demonstrates the absence of smoothing errors during the data evaluation. The example of January 13, 1997, corresponds to the intrusion generating the second highest ^{7}Be peak (21 mBq m^{-3}) in 1997. No large ozone peak is seen. However, the vertical width of the stratosperic layer around 3 km is about 1.5 km. Although the background mixing ratio (35 to 40 ppb is a typical winter-time value) is exceeded by just 10 to 15 ppb a lot of stratospheric air is contained in that layer and causes the pronounced increase in radioactivity (24-h accumulation).

An important result of our work has been the observation that in a surprisingly high number of cases intrusions of stratospheric air into the troposphere are not confined to a single, primary tropopause fold. Quite frequently secondary ozone tongues occur which subside towards the lower troposphere with similar speed as the primary fold and may contain a substantial amount of ozone. In a series started on May 29, 1996, the secondary structures were traced over a total of four days after the occurrence of the fold, with lidar running under automatic control during the entire period of observation (Eisele et al., 1998). In this case the secondary peaks did not penetrate the troposphere below 4 km. However, also the Zugspitze data show multiple ozone peaks (humidity dips) during several extended periods of stratospheric air intrusions during which the jet stream position was almost fixed for several days in a row.

Figure 2 shows examples from a series of lidar measurements between May 28, 1997, 4 p.m. and May 29, 1997, 6 p.m.. Starting at 6 p.m. on May 28 every third profile is displayed, i.e., at intervals of three hours. The distributions are mutually shifted by 50 ppb in order to make the time dependence visible.

Two main conclusions can be drawn from this series of vertical soundings. First of all it is the only case in two years for which we were able to register a tropopause-folding event from its very beginning. Secondly, again two secondary ozone tongues are

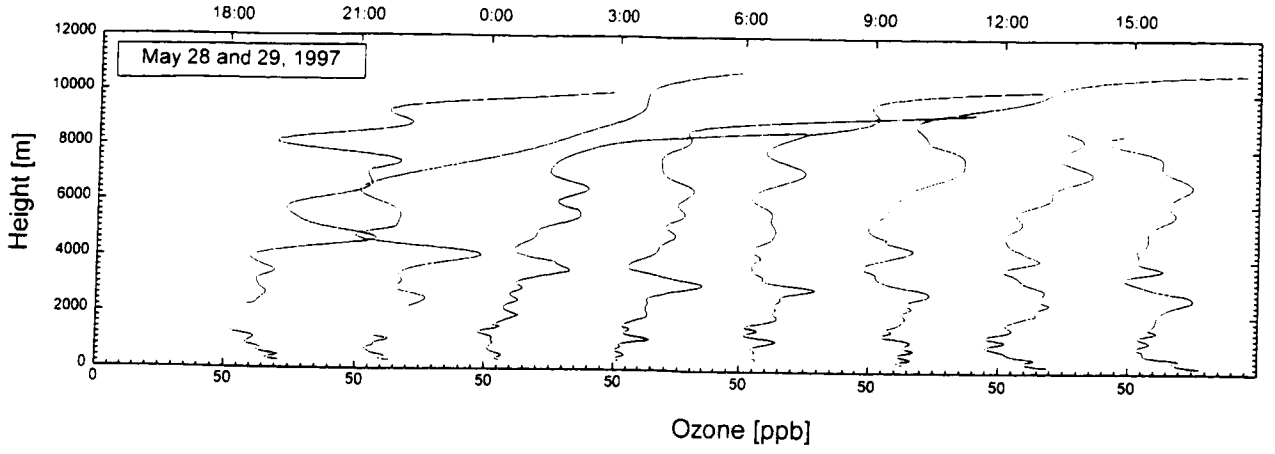


Figure 2. Ozone profiles selected from the series of lidar soundings during the stratospheric air intrusion on May 28 and May 29, 1997; the tropopause fold was completely mapped and is seen as a series of ozone peaks descending to 2.8 km above the ground (lidar: 740 m a.s.l.) and to below 2 km later on. In addition, the formation two secondary ozone tongues is observed.

seen, the first one starting at about 7 km above the ground near 22:00 CET (Central European Time) and descending to about 3.8 km in the final ozone profile shown in Fig. 2, the second one at about 8 km near 7:00 CET. on May 29 and reaching 6.8 km at 15:00 CET.

Quantitative flux determinations involving experimental data have so far been concentrated on tropopause folds, which form isolated features with rather defined boundaries (for a recent review see (Beekmann et al., 1997)). It is obvious that a quantitative evaluation of the contribution of the secondary structures to the stratosphere-troposphere ozone flux will be substantially more difficult. Even criteria for a prediction of their occurrence are currently missing. These structures may contain even more stratospheric ozone than the primary fold. Consequently, their analysis is an important task. Some information is expected to be contributed from ongoing model calculations within the VOTALP project based on both MM5 and trajectory model approaches.

Finally, we have derived a value for the fraction of the deep stratospheric air intrusions reaching the Zugspitze summit. Between January 1996 and November 1997 a total of 59 folding events associated with anticyclonic jet bending over Europe north or north-west of us yielded enhanced ozone and ^{7}Be concentrations as well as low humidity. Discarding 5 cases for which the relative humidity dip ended near the 40 % level and considering a single case in which the lidar revealed an intrusion not reaching 3000 m a.s.l. the fraction of those episodes successfully registered at the Zugspitze station is 98 %.

This high value is remarkable, in particular since less than 50 % of the intrusions have been found to reach the Wank station at 1780 m a.s.l. (Elbern et al., 1997). However, it underlines the significance of the continuous measurements made at high mountain peaks. The ten-year analyis published by Elbern et al. would suggest just 37 stratospheric episodes for the Zugspitze station in 23 months. We tentatively ascribe the difference to our higher value by our different approach to select the cases (Eisele et al., 1998).

4. Conclusions

The lidar measurements of tropopause-folding events have revealed a number of interesting details not easily accessible with other experimental techniques. Several more years of concentrated data acquisition will be necessary before a meaningful analysis can be made. A lot of questions need to be answered, dealing with the duration of stratospheric air intrusions, the height-dependence of the flux, the nature of the secondary ozone maxima in the upper troposphere, the effective width of a layer of stratospheric air, which starts to mix with the surrounding troposphere during the penetration process, as well as the total flux.

5 Acknowledgements

The authors would like to thank Prof. W. Seiler for supporting this work and H.-J. Kanter for providing the beryllium data. The fruitful exchange of information within the VOTALP project is gratefully

acknowledged, in particular with Dr. H. Feldmann, Dr. M. Memmersheimer and Dr. H. E. Scheel. This work has been supported by the European Union (VOTALP) and by the German Umweltbundesamt.

References

Ancellet, G., Pelon, J., Beekmann, M., Papayannis, A., and Mégie, G. (1991). *J. Geophys. Res., 96(D12)*: 22401-22421.

Ancellet, G., Beekmann, M., and Papayannis, A. (1994). *J. Geophys. Res.*, 99(D2): 3451-3468.

Beekmann, M., Ancellet, G., Blonsky, S., De Muer, D., Ebel, A., Elbern, H., Hendricks, J., Kowol, J., Mancier, C., Sladkovic, R., Smit, H. G. J. , Speth, P., Trickl, T., and Van Haver, P. (1997), Regional and global tropopause fold occurrence and related cross tropopause flux, *J. Atmos. Chem.*, 28: 29-44

Browell, E. V., Danielsen, E. F., Ismail, S. Gregory, G., and Beck, S. M. (1987). Tropopause Fold Structure Determined from Airborne Lidar and in Situ Measurements. *J. Geophys. Res.*, 92(D2): 2112-2120.

Eisele, H., Sladkovic, R., and Trickl T., (1998). High-resolution Lidar Measurements of Stratosphere-troposphere Exchange. Submitted for publication.

Eisele, H., and Trickl, T. (1997). Second Generation of the IFU Stationary Tropospheric Ozone Lidar. In *Advances in Atmospheric Remote Sensing with Lidar* A. Ansmann, R. Neuber, P. Rairoux and U. Wandinger, Eds., pages 379-382, Springer (Berlin, Heidelberg).

Elbern, H., Kowol, J., Sladkovic, R., and Ebel, A. (1997). Deep Stratospheric Intrusions: A Statistical Assessment with Model Guided Analysis. *Atmospheric Environment*, 31: 3207-3226.

Langford, A. O., Masters C. D., and Proffitt, M. H. (1996). Ozone measurements in a tropopause fold associated with a cut-off low system. *Geophys. Res. Lett.*, 23: 2501-2504.

Reiter, R., Sladkovic, R., Pötzl, K., Carnuth, W., and Kanter, H.-J. (1971). Studies of the influx of stratospheric air into the lower troposphere using cosmic-ray-produced radionuclides and fallout. *Arch. Met. Geophys. Biokl.*, 20 (Ser. A): 211-246.

TOR (1997). *Transport and Chemical Transformation of Pollutants in the Troposphere (EUROTRAC), Vol. 6, Tropospheric Ozone Research*, O. Hov, Ed., Springer (Berlin, Heidelberg): 499 pages.

Comparison of Temperature and Ozone Profiles Derived from DIAL and SAGE II Measurements over Toronto

J. C. Bird, D. Velkov, D. P. Donovan, A. I. Carswell, S. R. Pal, Center for Research in Earth and Space Technology and the Department of Physics and Astronomy, York University, North York, Ontario, Canada M3J 3K1
Phone: (416) 665-5415 Fax: (416) 665-5032 Email: bird@lidar.crestech.ca

S. Guo, Kunming Dobson Ozone Observatory and Department of Earth Science, Yunnan University, Kunming, Yunnan Province, China

1. Introduction

Based on the observational data of the CRESTech (Center for Research in Earth and Space Technology) Differential Absorption Lidar (DIAL) and the NASA Stratospheric Aerosol and Gas Experiment II (SAGE II) in 1994 and 1995, the temperature and ozone profiles derived from the two measurement systems over Toronto region are analyzed and compared in this paper

The SAGE II limb-scanning solar photometer instrument is part of the Earth Radiation Budget Satellite. It was designed to observe atmospheric O_3, H_2O, NO_2, and aerosol profiles at wavelengths between 0.385 and 1.02 μm. It is a multi-channel spectral radiometer that measures the attenuation of solar radiation at seven wavelengths (1020, 940, 600, 525, 453, 448 and 385 nm) as they pass through the earth's atmosphere during the spacecraft's sunrises and sunsets. SAGE II performs 15 sunrise and 15 sunset measurements each day around the globe and covers a latitudinal range from approximately 70° S to 70° N over a period of about one month [11] . The temperature is measured using the a band of O_2.

Studies using the SAGE II ozone data set have included analyses of the ozone quasi-biennial and semiannual oscillations, Antarctic and Arctic springtime ozone variabalities, and global ozone trends Zowodny (1991). Comparison of SAGE II ozone and temperature profiles with ground-based and other satellite measurements have been reported by, Tsou (1995), Veiga (1995), Margitan (1995) and others.

Veiga (1995) pointed out that the best ozonesonde / satellite comparisons were found in the altitude range near the ozone maximum (21 ~ 26 km), where essentially all comparisons showed the median percentage differences less than 5%. The largest median percentage differences ranged between -5 and -30% were found between 15 and 20 km (Vegia, 1995). Some of these assessments showed that ozone trends derived from SAGE data agree well with SBUV trends in the lower to middle stratosphere but that the results disagreed in the upper stratosphere McPeters (1994) .

The DIAL system at CRESTech (Carswell et al., 1991) uses a high-power xenon chloride (XeCl) excimer laser that operates at a wavelength of 308 nm for the ozone probing, with the reference beam at 353 nm (Raman 1st Stokes in H_2). The laser beams at two wavelengths are transmitted simultaneously in time and coincidentally in space. The backscatered radiation is collected with a 100 cm telescope, and the two wavelengths are separated by a series of dichroic mirrors and interference filters. The signal is then measured with photomultipliers and photon-counting methods. The observational data set can be archived by a 66 MHz AST 486 computer. The computer is also connected to the SUN 3/280 network server for data processing.

How to further assess the precision and reliability of SAGE II and DIAL systems is of great significance for improving their observational quality and is very useful for our atmospheric ozone research. In this paper, the data preprocessing and a detailed intercomparison between these two measurements are presented. The differences in vertical resolution and spatial sampling are also taken into account. Furthermore, some characteristics for stratospheric temperature and ozone are discussed and analyzed.

2. Data Comparison Technique

For the investigations, we use coincidence criteria of ±2.5 degrees Latitude, ±12 degrees Longitude, ±1, ±2, ±3 days time-lag. We then obtain a rectangular region of 41.3N ~ 46.3N and 67.5W ~ 91.5W, centered around Toronto. Our comparisons take into consideration all SAGE II data points within this range.

In 1995 within the measurement region around Toronto there were 14 events of SAGE II data. Among them there are 6 events which are comparable to the DIAL data, but they cover only 4 months (February, March, April, and June), hence we cannot present the whole year's evolution. For the data of 1994, there were 38 events of SAGE II data and among them 13 events are comparable, and they covered almost whole 1994. The following discussion is mainly based on the data set for 1994 and 1995.

The SAGE II data sets were provided by the NASA Langley Research Center, Hampton, Virginia. All of the published comparisons mentioned above were performed using versions of the SAGE II data set earlier than that used here. The improvements for the version used here (version 5.93) include the aerosol correction to the ozone below 15 km, a long-term time-varying mirror reflectivity correction which affects ozone concentration above 50 km, and some recent corrections to the ozone below 30 km.

3. DIAL / SAGE II Temperature and Ozone Profiles Comparison

Temperature and ozone number density profiles are compared from DIAL and SAGE II data sets. It is clear that atmospheric variability has always been a problem that has affected the measurement intercomparison. In order to minimize this effect here, the data to be compared measurements. in this section are primarily from the measurements during the summer seasons as summer is a period of the reduced variability.

3.1 Temperature Profiles Comparison

Our analysis results show that both DIAL and SAGE II measurements can give a complete temperature profile, including inversion structure. The degree of the lidar and SAGE II temperature agreement depends largely upon the distance from SAGE II data points to the lidar observatory position (Toronto), especially on their latitude difference (absolute latitude difference, from Toronto to SAGE II point).

Now considering the data of 1994 and 1995 where our time-lag selection is firstly restricted to less than 1 day which means the time difference between a pair of comparable DIAL and SAGE II data must be less than 2 days, we have five comparable profiles.

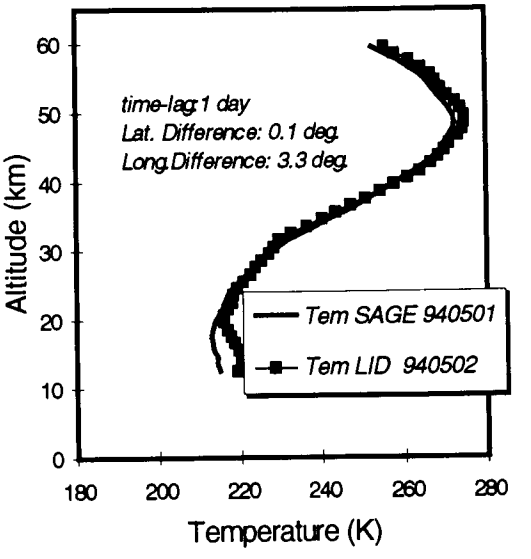


Fig. 1 Example of DIAL/SAGE II temperature profile comparison.

As for the profile shown in Fig. 1 on May 1, 1994, the nearest point to Toronto ($|\Delta Lat.| = 0.1$ degrees), the agreement between the profiles is excellent. Furthermore, we found that the corresponding relative difference between SAGE II and DIAL, from 20 km to 50 km, is roughly within ±1 %.

For 1994 and 1995 we selected fourteen cases from SAGE II and DIAL data sets from 15.5 to 40.5 km. It was found that when both time-lag and the latitude difference between the measurements was relatively small (with a latitude difference of less than 0.8 degrees and a time-lag of less than 1 day, the profiles were found to be in good agreement. Also, when the distance between Toronto and SAGE II point is relatively small the profiles were in good agreement.

3.2 Ozone Number Density Profiles Comparison

Because the DIAL system is designed to measure profiles of the stratospheric ozone concentration at altitudes between about 15 km to 40 km, our attention in following intercomparison will be mainly focused on this vertical range.

An example measurement for May 6, 1995 is shown in Figure 2. The deviation is relatively small in the vertical region of about 18.5 km ~ 32.5 km, where both systems have higher precision. Over the altitude range from 18.5 km ~ 32.5 km, the averaged relative difference value is (5.2 ± 4.4) % (1σ). Below 18.5 km and above 32.5 km, the averaged relative difference values are (9.8 ± 5.8) % and (15.0 ± 11.1) % respectively.

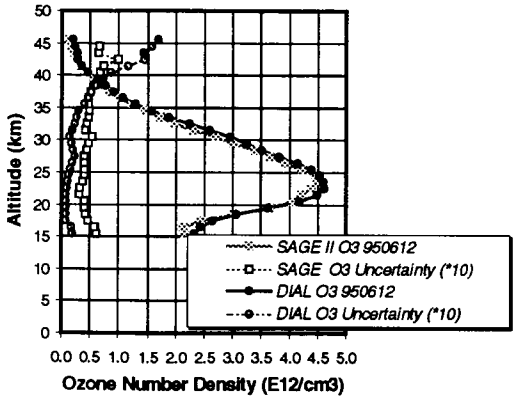


Fig.2 Example of ozone comparison.

It can be seen from Fig. 3 that most of the points fall into the 1 σ uncertainty margin, and from about 20 km to 36 km the relative difference values are quite close to zero. Below 21 km some points exceed the uncertainty margin

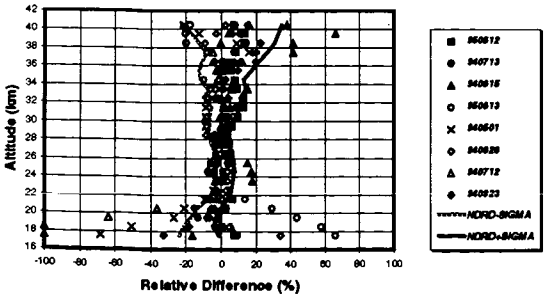


Fig. 3 Relative Difference for 8 days ozone number density profiles, 1994-1995.

4. Annual Variation of Maximum Ozone Number Density and its Corresponding Height

In order to see whether there is any correlation between maximum number density and maximum number density height in 1994, we used our DIAL data and all SAGE II data that fall into the defined Toronto region (41.3 N ~ 46.3 N, 67.5W ~ 91.5W). Using these data sets we plotted annual variation curves of maximum number density and maximum number density height, as shown in Fig. 4.

Both SAGE II and DIAL measurements demonstrate that the height of maximum ozone number density has a distinct seasonal variation. Their polynomial curve which looks like a standard sine curve, reaching its minimum value during winter/spring and maximum value during summer/fall period. More precisely, the minimum is at about 21 km, occurring during February and March 1994; and the maximum value is about 24 km, occurring during September and October 1994. This result is consistent with Kerr et al. (1991).

From Fig. 4 it can be seen that, both the DIAL and SAGE II data sets show that the maximum ozone number density itself has an evident one-year oscillation. During January and February 1994, the maximum value is about 6.0×10^{12} mol·cm^{-3}; and during August and September 1994 it became close to 4.5×10^{12} mol·cm^{-3} That is to say, the maximum value is relatively higher in winter/spring and lower in summer/fall period.

Generally speaking, at the altitude of the ozone peak, the maximum ozone content derived from the DIAL system is higher than that from the SAGE II measurement, although we do not have the lidar data set for December, 1994. However, during January to March, the time-lag between two systems is usually larger than 2 days.

Thus we can conclude that there is roughly an anticorrelation between the maximum number density and the maximum number density height. Both maximum ozone number density and their corresponding height have a one-year oscillation. This is an interesting phenomenon, because the tropopause height will increase with the solar altitude and solar radiation, that can play an important role in ozone photochemical reaction process in the stratospheric atmosphere.

Moreover, we can deduce that when a maximum ozone layer descends or ascends, a notable vertical exchange will take place, the lower the maximum ozone height, the much more strongly the downward ozone transport occurs. Of course, a further, more detailed investigation of this phenomenon needs to be done.

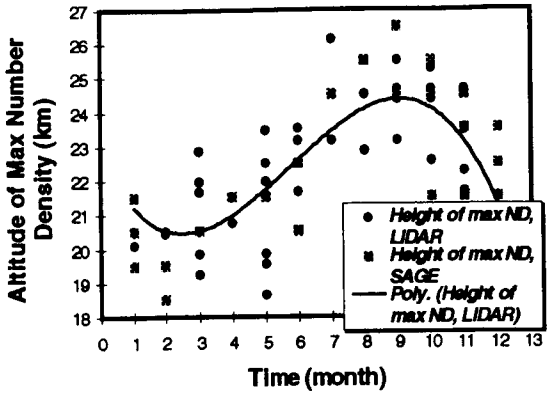


Fig. 4 Comparison of Max. Number Density, SAGE/DIAL, 1994.

Summary

The results indicate that: (1) temperature profiles from the SAGE II data files are in good agreement with those from DIAL measurements, especially in the vertical range of 15.5 km - 35.5 km, in which the relative difference between two measurements, defined as (DIAL - SAGE II)/SAGE II, ranges from -4.35 % to +4.32 %, and the mean value of those differences is only 0.2% ; (2) in the vertical range of 15.5 km - 40.5 km the absolute difference between DIAL and SAGE II ozone mixing ratio is at most ±1 ppmv, and the mean value of those absolute differences is only 0.137 ppmv. This means that these two ozone measurements are, generally, in agreement with each other; (3) under usual conditions, below 35 km or so, ozone number density profiles derived from DIAL measurements possess higher precision than those from SAGE II measurements, and above this altitude, vice versa. Especially in the altitude range 21.5 km ~ 35.5 km, including the maximum O_3 number density layer, the 8-profile-averaged relative difference is extremely close to zero, and the vertical mean value is 0.96 %; (4) the agreement degree for the two measurements is mainly affected by the latitude difference between Toronto and concerned SAGE II data points; (5) both DIAL and SAGE II measurements show that the maximum ozone content and its corresponding height have a one-year-oscillation feature which is accompanied with the tropopause seasonal variation. A negative correlation was found between the ozone maximum content and the maximum height of ozone maximum; (6) during 1994 and 1995 averaged column ozone values for DIAL and SAGE II (altitude range 13.5 to 45 km) are 268 and 285 Dobson Units respectively and their relative difference is about -5.9% .

References

Carswell, A. I., S. R. Pal, W. Steinbrecht, J. A. Whiteway, A. Ulitsky, and T. Y. Wang, (1991), Lidar measurements of the middle atmosphere, *Can. J. Phys., 69*, p1076-1086.

Kerr, J. B., Trends in Total Ozone at Toronto Between 1960 and 1991, (1991), *J. Geo. Res 96*, p20,703-20,709.

Margitan, J. J., et al., (1995), Stratospheric Ozone Intercomparison Campaign (STOIC) 1989: *Overview, J Geo. Res, 100*, p9193-9207.

McPeters, R. D., T. Miles, L. E. Flynn, C. G. Wellemeyer, and J. M. Zawodny, (1994), Comparison of SBUV and SAGE II ozone profiles: Implications for ozone trends, *J. Geophys. Res.* **99**, 20,513-20,524.

Reinsel, G. C., et al., (1994), Seasonal trend analysis of published ground-based and TOMS total ozone data through 1991, *J. Geo. Res. 99*, P5449-5464.

Tsou, J. J., B J. Connor, A. Parrish, I. S. McDermid, and W. P. Chu, (1995), Ground-based microwave monitoring of middle atmosphere ozone: Comparison to lidar and Stratospheric and Gas Experiment II satellite observations, *J. Geophys. Res. 100*, 3005-3016.

Veiga, R. E., D. M. Cunnold, W. P. Chu, and M. P. McCormick, (1995), Stratospheric aerosol and gasexperiments I and II comparisons with ozonedondes, *J.Geo. Res. 100*, p9073-9090.

Zawodny, J. M., and M. P. McCormick (1991), Stratospheric Aerosol and Gas Experiment II measurements of the quasi-biennial oscillations in ozone and nitrogen dioxide, *J. Geophys. Res., 96*, 9371-9377.

The Winter Evolution of the Polar Stratospheric Vortex Thermal Structure

Thomas J. Duck*, James A. Whiteway†, and Allan I. Carswell*

* Centre for Research in Earth and Space Technology and the Department of Physics and Astronomy, York University, 4700 Keele Street, Toronto, Ontario, Canada, M3J 1P3.
Phone: (416) 736-2100 x77748, Fax: (416)736-5516, Email: tomduck@lidar.crestech.ca

† Department of Physics, University of Wales, Aberystwyth, Ceredigion, SY23 3BZ, UK

1 Introduction

Measurements of temperature in the middle atmosphere have been obtained by a Rayleigh lidar in the Canadian High Arctic at Eureka (80°N, 86°W) each winter since the 1992/93 season. High Arctic observations are of particular interest because of the influence of the polar stratospheric vortex, an immense cyclone some 4000 km across with peak winds in excess of 80 m/s. Perturbations, by way of planetary wave disturbances (McIntyre and Palmer, 1983) and interactions with deep vortices produced in the mid-latitude buckling (surf) zone (O'Neill and Pope, 1988), may displace the vortex from its quiescent position over the pole. The choice of Eureka as a location for a stratospheric observatory was fortuitous, since the vortex may be positioned so that Eureka is beneath the vortex core, below the vortex jet, or outside of the vortex altogether (see Fig. 1).

Internal gravity waves (Hines, 1960) have a profound effect on the thermal and dynamical structure of the Arctic middle atmosphere. Gravity waves that propagate upward from tropospheric sources grow in response to the decreasing background density and break when they induce unstable temperature gradients (Hodges, 1967). In the mean, the drag induced by breaking gravity waves forces flow into an adjacent region where it descends and warms adiabatically, an effect recently referred to as "downward control" (Haynes et al., 1991). The climatological warm Arctic winter mesopause (Lindzen, 1981; Holton, 1982) and the separated polar stratopause (Hitchman et al., 1989; Garcia and Boville, 1994) are thought to be formed in this manner.

In this paper, we present observations of thermal structure from the lidar at Eureka that show an annual warming of the upper stratospheric vortex core. The warming propagates down into the lower stratosphere and is sustained through the winter. Coincident with the warming onset is an increase in gravity wave activity in the jet of the stratospheric vortex. These observations are interpreted as evidence of downward control extending deep into the stratosphere. Since the midwinter formation of polar stratospheric clouds (which are thought to begin the ozone depletion process) is very sensitive to the temperatures within the lower stratospheric vortex core (Schoeberl and Hartmann, 1991), a detailed understanding of the processes that control intra-vortex temperatures is important.

2 Measurement Technique

The lidar at Eureka is a pulsed ozone-DIAL system operating in the ultra-violet at 308 and 353 nm. Approximately 10% of the power of the 308 nm XeCl laser source is Raman shifted via an H_2 cell to 353 nm, the Rayleigh (elastic) backscattered wavelength that we use for temperature measurements. The receiver optics consist of a 1 m Newtonian telescope coupled to a set of photomultiplier tubes (PMTs). Tropospheric signal is blocked via the use of a mechanical chopper in order to ensure PMT linearity. Stratospheric signal is accumulated for ten minute durations, and then stored off-line for processing. Temperatures are derived according to the standard method described by Hauchecorne and Chanin (1980). Technical details of the lidar at Eureka are given by Carswell et al. (1991) and Pal et al. (1996).

Gravity waves are observed by the fluctuations that they induce in ten-minute average temperature profiles. The wave perturbations are extracted from each profile by using a series cubic polynomial fits to estimate a background profile. The gravity wave potential energy density, our measure of the gravity wave activity, is then given by $E_p=(g/N)^2\cdot(T'/T)^2$, where g is the gravitational acceleration, N is the atmospheric buoyancy frequency, and $(T'/T)^2$ is the

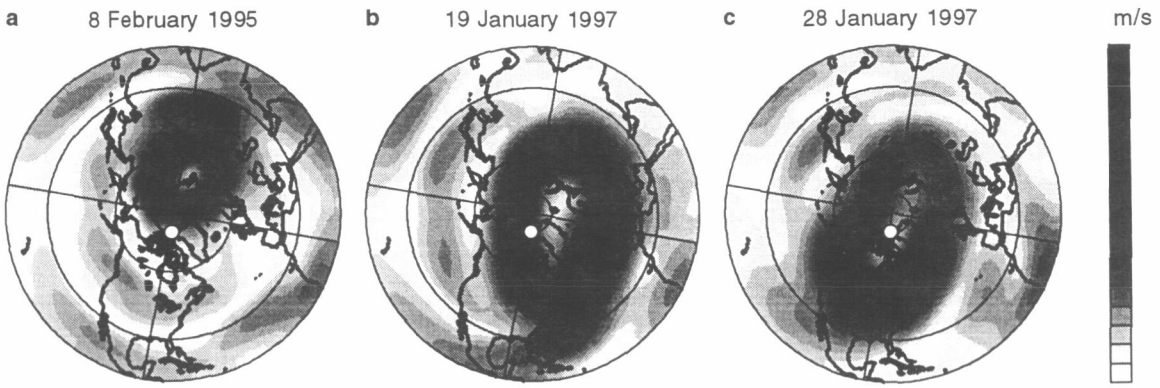


Figure 1. Maps of geostrophic wind speed in the Northern Hemisphere at the 10 hPa pressure level (about 30 km in altitude) for **a** 8 February 1995, **b** 19 January 1997, and **c** 28 January 1997. The dark ring of high wind speed is the polar stratospheric vortex (counter-clockwise motion). The position of Eureka is given by the white dot.

nightly average variance of the fractional temperature fluctuations. Gravity wave studies at Eureka have previously been conducted by Whiteway and Carswell (1994), Whiteway and Duck (1996), and Whiteway et al. (1997).

3 Observations

The measurements at Eureka reveal that the stratospheric temperatures are highly dependent on the location of the polar vortex. Fig. 2 shows two contrasting temperature profiles that are representative of observations within the vortex core and outside of the vortex respectively. As illustrated in Fig. 2, the upper stratosphere of the vortex

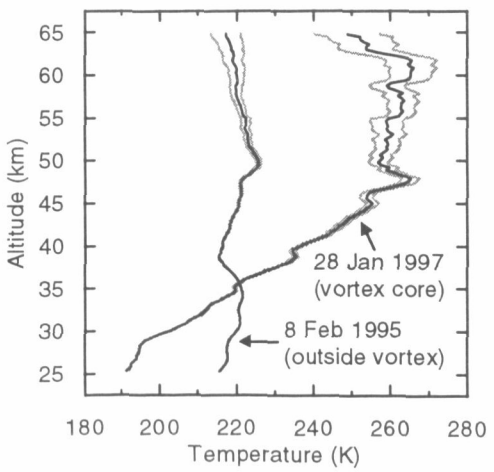


Figure 2. Nightly average temperature profiles for 8 February 1995 (outside vortex) and 28 January 1997 (within vortex core). Grey lines represent the uncertainty in each measurement.

interior is very warm and the lower stratosphere is very cold relative to the temperatures obtained outside of the vortex. That the upper stratospheric intra-vortex temperatures are so warm is at first surprising, since the air mass contained in the vortex core is isolated from the rest of the atmosphere during the mostly sunless High Arctic winter. The peak temperature in the vortex core profile is perhaps 80 K warmer than expected from radiative considerations alone (Fels, 1985).

In order to examine the winter evolution of this upper stratospheric intra-vortex warm pool, all of the nightly average temperature profiles measured within the vortex core were separated for further investigation. A strong annual warming of the upper stratosphere that commences in late December was found. To illustrate, a selection of profiles obtained within the vortex core during the 1996/97 season are given in Fig. 3. Note that the temperature at 45 km increases by about 30 K during the eighteen days between the first and last profiles.

To better visualize the average altitude-dependent magnitude of the annual warming, all of the temperature profiles obtained within the vortex core were collected and arranged by date (without considering the year they were obtained). Radiosonde temperatures were used at altitudes inaccessible to our lidar (i.e. below 25 km). A temperature profile representative of mid-December was subtracted from each daily profile. The results are shown in Fig. 4a, which depicts the daily temperature deviation by altitude from the mid-December temperature profile.

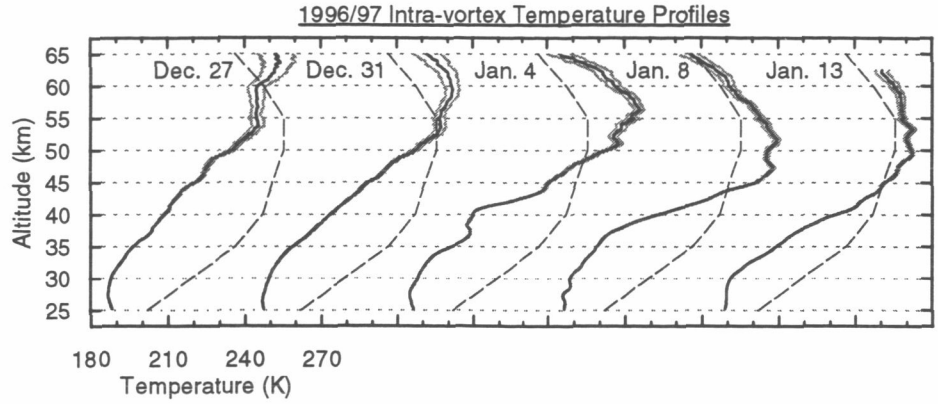


Figure 3. Selected nightly average temperature profiles measured within the vortex core during an 18 day span of the 1996/97 winter season (solid lines). Successive profiles are shifted by 60 K. The dashed line is the CIRA reference atmosphere temperature profile for January at 80 °N. Note the strong warming at 45 km in altitude.

As shown in Fig. 4a, stratospheric temperatures within the vortex core slowly decrease through November and until late December, when a strong warming of the upper stratosphere occurs. A smaller but significant cooling is also observed above 60 km in altitude. The warming propagates down into the lower stratosphere, and is sustained through the winter. Since radiative calculations indicate that high latitude upper stratospheric temperatures should decrease until late February (Shine, 1987), we anticipate a dynamical origin for this warming.

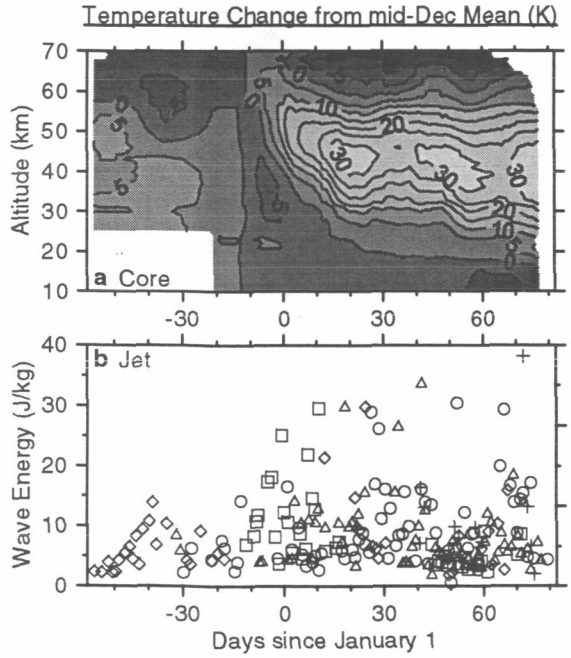


Figure 4. **a** The average daily temperature deviation from the mid-December mean temperature profile within the core of the vortex as measured above Eureka. **b** The average daily gravity wave potential energy densities from 30 to 35 km within the vortex jet. Each symbol represents a different measurement season: + 1992/93, ◊ 1993/94, □ 1994/95, ○ 1995/96, and Δ 1996/97.

The average gravity wave potential energy densities measured between 30 and 35 km in altitude within the jet of the vortex are arranged by date in Fig. 4b. Since observations within the vortex core yield consistently low gravity wave energies (Whiteway et al., 1997), they were not considered in this analysis. Measurements beyond the jet maximum were also excluded due to their distance from our region of interest (i.e. the vortex core).

As shown in Fig. 4b, the gravity wave energies during November and until late December are generally low. However, coincident with the warming onset in late December are episodes of increased gravity wave activity. The variance of the wave energy distribution before the warming is 11 J^2/kg^2, and after the warming onset it is 47 J^2/kg^2. These variances are significantly different, which emphasizes the fact that the wave activity after the warming onset is statistically spread to higher energy values.

4 Discussion

The observed late December increase in gravity wave activity was not anticipated, and appears to be (at least partially) associated with a change in gravity wave transmission due to critical level filtering (see, for example, Whiteway and Duck,

1996, and Whiteway et al., 1997). We interpret the coincidence of increased gravity wave activity within the vortex jet and warming of the vortex core as evidence of "downward control" extending deep into the stratosphere. We propose that the late December increase in gravity wave activity is accompanied by vigorous breaking above the vortex jet. The resulting gravity wave drag increase will force flow into the vortex core where it descends and warms adiabatically.

That the vortex interior experiences an annual warming extending down into the lower stratosphere is of interest with respect to the ozone depletion problem. The formation of polar stratospheric clouds (which begin the ozone depletion process) within the lower stratospheric vortex core is temperature sensitive. Reproducing the observed gravity wave activity distribution and annual intra-vortex warming should be a goal for global circulation models in any effort to predict the future state of the ozone layer and the stratospheric circulation in general.

5 Acknowledgments

The authors wish to thank the National Centers for Environmental Prediction for the use of their temperature and height global analyses This work was carried out as part of the research program of the Centre for Research in Earth and Space Technology at York University. Financial support was provided by the Atmospheric Environment Service of Canada and the Natural Sciences and Engineering Research Council of Canada.

References

Carswell, A. I., Pal, S. R., Steinbrecht, W., Whiteway, J. A., Ulitsky, A., and Wang, T. Y. (1991). Lidar measurements of the middle atmosphere. *Can. J. Phys.*, 69: 1076-1086.

Fels, S. B. (1985). Radiative-dynamical interactions in the middle atmosphere. *Adv. Geophys.*, 28: 277-300.

Garcia, R. R., and Boville, B. A. (1994). "Downward control" of the mean meridional circulation and temperature distribution of the polar winter stratopause. *J. Atmos. Sci.*, 51: 2238-2245.

Hauchecorne, A., and Chanin, M. L. (1980). Density and temperature profiles obtained by lidar between 35 and 70 km. *Geophys. Res. Lett.*, 14: 565-568.

Haynes, P. H., Marks, C. J., McIntyre, M. E., Shepherd, T. G., and Shine, K. P. (1991). On the "downward control" of extratropical diabatic circulations by eddy-induced mean zonal forces. *J. Atmos. Sci.*, 48: 651-678.

Hines, C. O. (1960). Internal atmospheric gravity waves at ionospheric heights. *Can. J. Phys.*, 38: 1441-1481.

Hitchman, M. H., Gille, J. C., Rodgers, C. D., and Brasseur, G. (1989). The separated polar stratopause: a gravity wave driven climatological feature. *J. Atmos. Sci.*, 46: 410-422.

Hodges, R. R. (1967). Generation of turbulence in the upper atmosphere by internal gravity waves. *J. Geophys. Res.*, 72: 3455-3458.

Holton, J. R. (1982). The influence of gravity wave breaking on the general circulation of the middle atmosphere. *J. Atmos. Sci.*, 40: 2497-2507.

Lindzen, R. S. (1981). Turbulence and stress owing to gravity wave and tidal breakdown. *J. Geophys. Res.*, 86: 9707-9714.

McIntyre, M. E., and Palmer, T. N. (1983). Breaking planetary waves in the stratosphere. *Nature*, 305: 593-600.

O'Neill, A., and Pope, V. D. (1988). Simulations of linear and nonlinear disturbances in the stratosphere. *Q. J. R. Meteorol. Soc.*, 14: 1063-1110.

Pal, S. R., Carswell, A. I., Bird, J., Donovan, D., Duck, T., and Whiteway, J. (1996). Lidar measurements of the stratosphere at the Eureka and Toronto NDSC stations. *SPIE*, 2833: 28-39.

Schoeberl, M. R., and Hartmann, D. L. (1991). The dynamics of the stratospheric polar vortex and its relation to springtime ozone depletions. *Science*, 251: 46-52.

Shine, K. P. (1987). The middle atmosphere in the absence of dynamical heat fluxes. *Q. J. R. Meteorol. Soc.*, 113: 603-633.

Whiteway, J. A., and Carswell, A. I. (1994). Rayleigh lidar observations of thermal structure and gravity wave activity in the high Arctic during a stratospheric warming. *J. Atmos. Sci.*, 51: 3122-3136..

Whiteway, J. A., and Duck, T. J. (1996). Evidence for critical level filtering of atmospheric gravity waves. *Geophys. Res. Lett.*, 23: 145-148.

Whiteway, J. A., Duck, T. J., Donovan, D. P., Bird, J. C., Pal, S. R., and Carswell, A. I. (1997). Measurements of gravity wave activity within and around the Arctic stratospheric vortex. *Geophys. Res. Lett.*, 24: 1387-1390.

Rayleigh/Raman Scattering Lidar for measuring atmospheric parameters

Shunsheng Gong, Wengang Zheng, Hongjun Li, Guotao Yang

Wuhan Institute of Physics & Mathematics
The Chinese Academy of Sciences
Wuhan, 430071, P.R.China
Email: gongss@nmr.whcnc.ac.cn

Introduction

Based on the technique and equipment of the sodium fluorescence Lidar which we established earlier in our Institute[1], We have recently developed a Rayleigh/Raman scattering Lidar for measuring atmospheric parameters of troposphere, stratosphere, and mesosphere over Wuhan, China(30.6N 114.4E). As well known, the Rayleigh scattering Lidar is the best candidate for the atmospheric parameter measurements of the mesosphere and the upper stratosphere[2,3]. The highest altitude that a modern Rayleigh Lidar can reach is up to the mesopause region, but the lowest measurable altitude of the Rayleigh Lidar is limited, usually to about 25~30Km. The reason for this is that the Rayleigh scattering signal will be contaminated by the stronger Mie scattering below this altitude range, and no atmospheric parameters can be obtained from Rayleigh scattering directly. There are two methods that can be used to solve this problem. One is using high spectral resolution technique to separate the contributions from Rayleigh and Mie scatterings[4], and the other is using Raman scattering to extract the atmospheric molecular scattering only[5]. We chose to use the Raman Lidar for measuring atmospheric parameters below about 25Km because of its technical simplicity.

Lidar equipment

Our Rayleigh/Raman Lidar uses one laser beam as the common emitting beam for both Rayleigh and Raman scatterings. The beam at wavelength 532nm is from the second harmonic output of an YAG laser (DCR-2) working at a repetition rate of 20Hz. The energy and the divergence of the beam are about 150mJ per pulse and 0.5 mrad respectively. An homemade transmitting type telescope is used as the receiving optics of the Lidar, and it consists of a Φ40Cm, f/3-8 non-spherical lens, an variable

field stop and a collimating lens. We choose to use transmitting type telescope is because that it is easier to make and its light collecting efficiency is higher than the reflecting type telescope with the same diameter. By using the non-spherical main lens, the optical quality of our telescope is high, and its field of view can be controlled down to smaller than 1 mrad. The photon detection system is consists of a cooled PMT(RCA31034), a preamplifier (bandwidth 300MHz, Gain 25), and a photon counting scaler(SR-430). The synchronization of the system is realized by optical triggering, the system control and automatic data acquisition is accomplished by a computer. For the Rayleigh detection, a filter with λ_0=532.5nm, bandwidth=1nm, and peak transmission = 40% is used; for the Raman detection, we use a combination of an interference filter and two color filters to get about 10^8 rejection of 532nm. The combined filter has a peak wavelength of 607.2nm and a bandwidth of 3nm to transmit the rotational band of N_2 Raman v=0-1 vibration transition, which is shifted from emitting wavelength by 2330.7 cm^{-1}.

Preliminary results

The high optical efficiency and low noise level of the system is most important for the Rayleigh operation of the Lidar. Besides the careful control of the receiving field of view and the interference from electrical and optical sources, more attention was put on the accurate alignment of the emitting beam to the receiving axis throughout the detection altitude range. At present, the detectable altitude range of our Rayleigh Lidar is about 25~70Km(Fig.1), and thus the information about density and temperature profiles of the atmosphere in this altitude range can be obtained[6]. For the Raman version of the Lidar operation, most critical problem is the disturbance of the weak Raman signal by the much stronger Mie scattering and the light induced fluorescence of the filters. We have tried various filter combinations, and changed the sitting order of the filters to

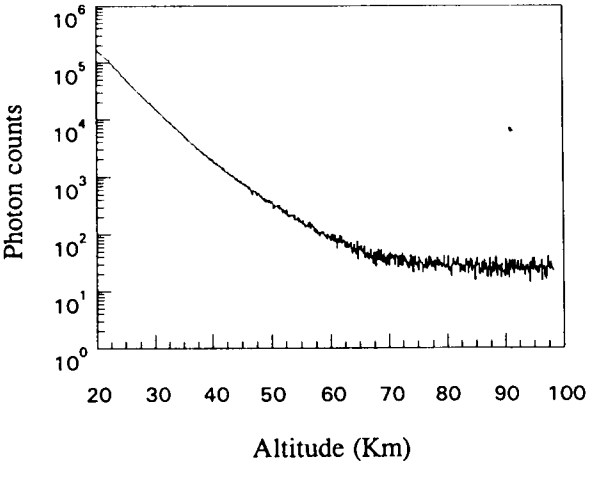


Figure 1, Raw data of Rayleigh Lidar

make sure that thisdisturbance was below the detectableRaman scattering level. At the present time, the detectable altitude range of our Raman Lidar is about 2~10Km(Fig.2), and so the atmospheric parameters in this altitude range can be obtained. We are now trying to extend the detectable range of both Rayleigh and Raman versions of our Lidar to cover most altitude range from lower troposphere to the mesopause region.

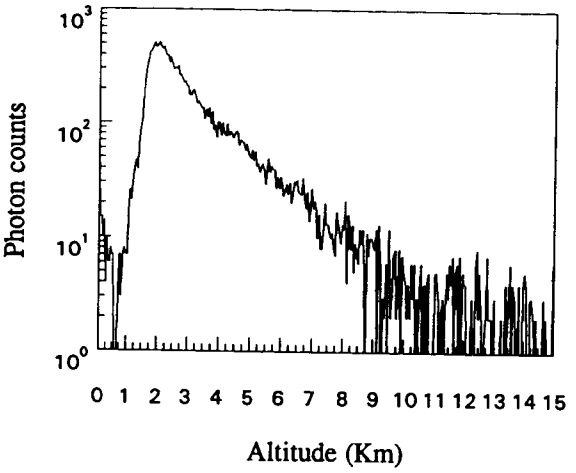


Figure 2, Raw data of N_2 Raman Lidar

References:

[1] S.S.Gong, X.Z.Zeng, X.J.Xue, and W.G.Zheng, "The preliminary observation of the sodium layer over Wuhan using a Na fluorescence Lidar", the 18th International Laser Radar Conference(1996)

[2]M.L.Chanin and A.Hauchecorne, "Lidar Study of Temperature and Density using Rayleigh Scattering", Hand. MAP 13, 87(1984)

[3]T.Shibata, M.Kobuchi, and M.Maeda, "Measurements of Density and Temperature Profiles in The Middle Atmosphere with a XeF Lidar", Applied Optics, 25, 685(1986)

[4]C.Y.She, R.J.Alvarez II, L.M.Caldwell, and D.A.Krueger, "High-spectral-resolution Rayleigh-Mie Lidar measurement of aerosol and atmospheric profiles", Optics Letters, 17, 541(1992)

[5]P.Keckhut, M.L.Chanin, and A.Hauchecorne, "Stratosphere Temperature Measurement using Raman Lidar", Applied Optics, 29, 5182(1990)

[6]W.G.Zheng, H.J.Li, G.T.Yang, and S.S.Gong, "The Lidar detection of the Atmospheric Density and Temperature over Wuhan",(accepted by Atmosphere Science (China))

STRATOSPHERIC AEROSOL CLIMATOLOGY IN NORTH AND SOUTH HEMISPHERE

Donatella Guzzi, Marco Morandi, Vincenzo Santacesaria, Leopoldo Stefanutti
Istituto di Ricerca sulle Onde Elettromagnetiche "Nello Carrara" (IROE-CNR)
Via Panciatichi 64, 50127, Florence, Italy
Phone: +39 55 42351, FAX: +39 55 410893 e mail: guzzi@iroe.fi.cnr.it

Pietro Agostini, Vincenzo Cuzzola
ENEA –Brasimone,
P.O. BOX n°1, 40032 CAMUGNANO (Bologna), Italy
Phone: +39 534 801280, FAX +39 534 801400

Using lidar data collected at the following sites: Northern Finland, Sodankyla (67°N, 26.50^{o}E); New Zealand, Lauder (45°S, 170°E); Antarctica, Dumont d'Urville (66.41^{o} S, 140°E); Italy, Florence/Brasimone (43.5^{o}N, 11°E), we obtained a three-year stratospheric aerosol climatology for the northern and southern hemispheres.

This analysis will provide stratospheric aerosol loading trends, which can be used to include aerosol corrections in the algorithms employed to produce a long-term homogeneous large-scale data set of vertical ozone profiles or to verify aerosol impact on climate modifications.

At the Arctic site of Sodankyla a four wavelength - depolarisation lidar has been operating since 1991. Three winter campaigns were carried out from December 1991 to March 1992, from late November 1994 to April 1995,and from late November 1996 to April 1998. The aim of these campaigns was the monitoring of stratospheric aerosol loading and the evolution of PSCs formation during the Arctic winter.

The two-wavelengths depolarisation lidar place in Florence, has been collecting monthly background aerosol measurements since February 1996. The lidar station of Brasimone, that has been operating since 1994, is close to Florence. Therefore, the two data sets were used together, in order to obtain more extensive information on stratospheric aerosol loading at mid latitude in the Northern hemisphere.

In the southern hemisphere, at the mid-latitude site of Lauder, since January 1994 a two wavelengths depolarisation lidar has been carrying out routine measurements of stratospheric aerosols, while at Dumont d'Urville, Antarctica, a single-wavelength depolarisation lidar has been working since 1989. Year-round lidar measurements were carried out in order to study stratospheric aerosols and PSCs evolution.

PTU soundings are available for almost all measurements.

Even if three of the four lidars have more then one wavelength, for aerosol climatology we used only the second harmonic of Nd:YAG laser, 532 nm, to monitor the changes in the mean scattering ratio, integrated backscattering and aerosol mass content above the four sites.

The philosophy of lidar measurements strictly depends on both the parameters to be measured and the type of aerosol loading to be investigated. Other constraints derive from the features of the lidar system (i.e. laser pulse energy and repetition rate, optical efficiency).

From lidar profiles, the backscatter and extinction coefficient, the depolarization, and the scattering ratio (SR) were retrieved. Inversion algorithms and software codes were carefully tested, using both computer simulation and real lidar profiles. The procedures involved are: a modified backward Klett method and an iterative numerical solution developed at IROE-CNR[1]. Both methods compute the profiles of the aerosol backscatter and extinction coefficients and of the depolarization ratio.

Not all the sites started their operation during the same period. We choose therefore, for uniformity in data representation, a three-year period, from 1.1.1994 to 31.12.1996 to monitor the dissipation of the Pinatubo aerosol.

With regard to the evolution in aerosol loading after the volcanic eruption of Pinatubo, the aerosol decay time constant was evaluated for the January 1994 – December 1996 period. The decay time was obtained by linearly interpolating the logarithm of the integrated backscattering value. The results are summarised in table 1.

AEROSOL DECAY TIME CONSTANT			
Sodankyla (Finland)	Lauder (New Zealand)	Firenze-Brasimone (Italy)	Dumont d'Urville (Antarctica)
2.54 years	2.39 years	2.47 years	2.23 years

Table 1 Evaluated aerosol decay time constant for the period 1994-1996

Calculations show a shorter time constant for the Antarctica station compared to the one observed in the Arctic region. For mid-latitude sites, the time decay was almost the same. In any case, it seems to be consistent with the value of sedimentation velocity for sulfuric aerosol particles, with a mean radius of around 0.3-0.4 microns.

Under the assumption that aerosol particles are a homogeneous sphere, the backscattering efficiency may be approximated as a linear function of the particle size parameter [2], x:

$$4\pi Q_{bs}(x,n) \approx C(n)x$$

where $x=2\pi r/\lambda$, r is the particle radius and n is the refractive index of the particle.

Using such an assumption, it is possible to relate the aerosol mass content, M, to the integrated backscattering coefficient β, regardless of the dependence on size distribution as follows:

$$M \approx 8\rho\lambda\beta / (3C(n))$$

with ρ, is the density of the aerosol droplets and λ, is the wavelength of the incident radiation.

The linear coefficient C(n) is dependent on particle composition. It was evaluated for different refractive index and aerosol particle composition, linearizing the computed Mie backscattering efficiencies[3] with respect to their size parameter.

The composition of sulfuric acid aerosols as a function of temperature and water vapour pressure was derived by Steele and Hamill[4]. We combined their results with the information coming from the PTU soundings to determine the refractive index and density of aerosol sulfuric acid droplets. These data and the values of integrated backscattering were employed to evaluate the aerosol mass loading for all the lidar sites when temperature and humidity information was available.

In figure 1 we plotted the integrated backscattering between 10-25 km. The columnar mass content reported in figure 2 was evaluated using mean values for both temperature and humidity. As shown in figure 1-2, the columnar aerosol mass evolution follows the integrated backscattering trend, but differences may be noted between the different sites, with higher values at the Antarctica site compared to the Arctic and Mid-latitude stations.

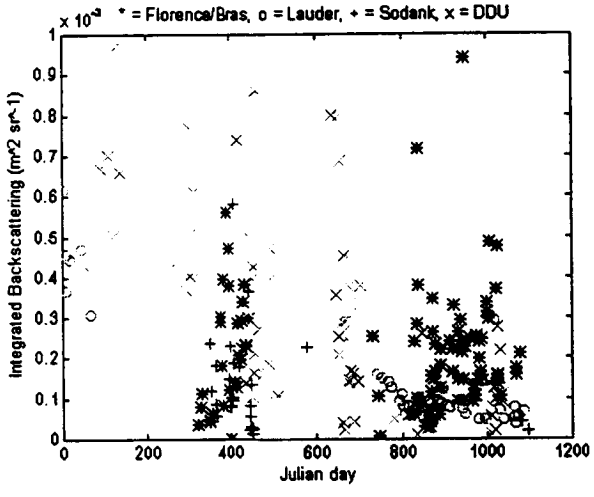


Fig.1 Integrated backscattering for the four stations since 1.1.1994

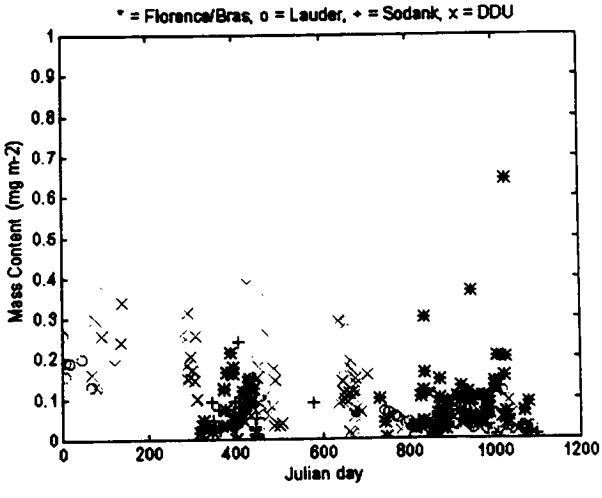


Fig.2 Aerosol mass content for the four stations since 1.1.1994

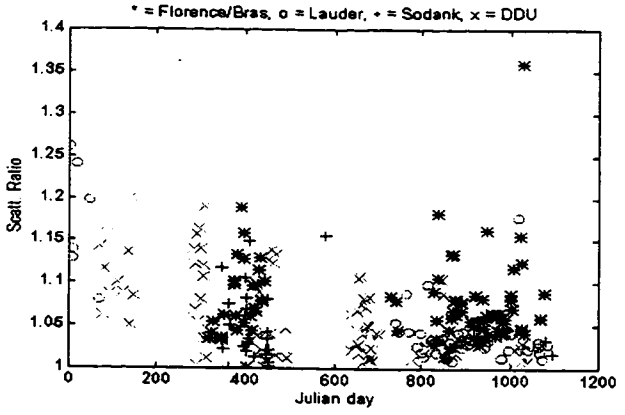


Fig.3 Mean scattering ratio for the four stations since 1.1.1994

For mid-latitude stations, the northern site of Florence/Brasimone shows values for the aerosol mass content that are higher then the ones measured in the southern station of Lauder. With regard to the evolution of aerosols loading above these sites, both aerosol mass content and mean scattering ratio (see fig. 4 and 5) showed during 1995-1996, some peaks above the general decreasing trend. In particular a strong increase could be noticed in the aerosol loading during September 1996.

During 1994 the aerosol mass content at mid-latitude ranged from the 0.20 mg m^{-2} for Lauder to the 0.30 mg m^{-2} for Florence/Brasimone. For the polar site of Dumont d'Urville it reached a value of 0.40 mg m^{-2}. Starting from 1995, a decreasing trend could be noticed which continued during 1996, with values, for the aerosol mass content, of less than 0.10 mg m^{-2} for the Lauder and Sodankyla stations and around 0.10-0.15 mg m^{-2} for Dumontd'Urville and Florence/Brasimone.

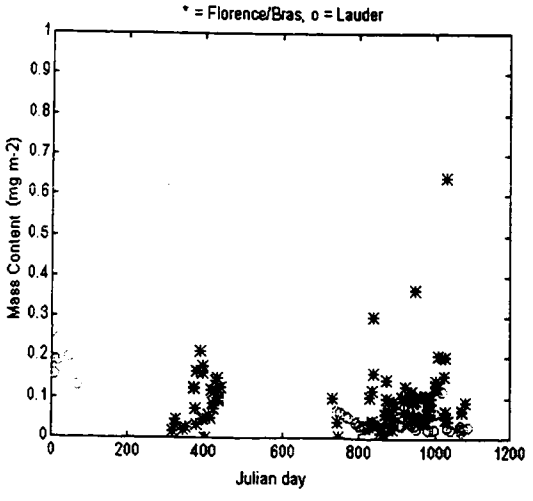


Fig.4 Aerosol mass content above mid-latitude sites since 1.1.1994

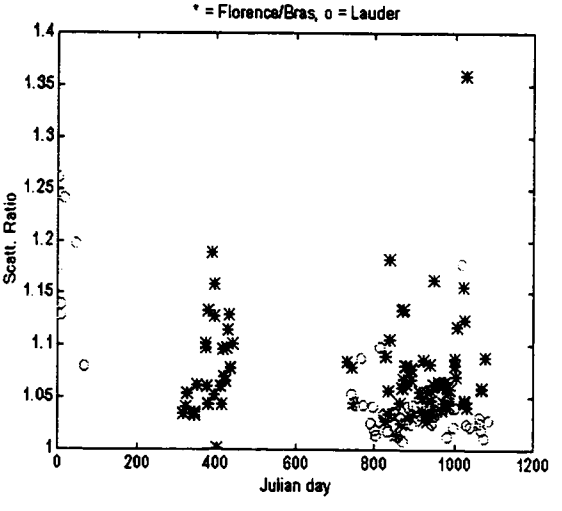


Fig.5 Mean scattering ratio above mid-latitude sites since 1.1.1994

These preliminary observations, which are consistent with the ones reported by the NDSC sites of Garmish- Partenkirken and Muana Loa[5] , may show that the aerosol layer is reaching a situation like the one observed before the eruption of Mt. Pinatubo on June 1991.

References

[1] Morandi M, *"A complete procedure for inverting backscattering lidar returns"*, IROE Internal Report n. RR/GCF/92.11, 1992

[2] Pinnick, R.G. , S.G. Jennings, P. Chylek, *"Relationship between extinction, absorption, backscattering and mass content of sulfuric acid aerosols"*, J. Geoph. Res. Vol. 85, pp.4059-4066, 1980

[3] Guzzi D. , *" FORTRAN programs for the determination of the scattering properties of spherical particulate"*, IROE Internal Report n. RR/POE/93.18, 1993

[4] Steele, H.M., P. Hamill, *" Effects of temperature and humidity on the growth and optical properties of sulfuric acid water droplets and Stratosphere"*, J. Aerosol Sci., Vol. 12, pp. 517-528, 1981

[5] Bulletin of the Global Volcanism Network, vol. 22 (5), pp. 13-14, 1997

ILE Lidar Measurements of Ozone Concentration over Suwon, Korea

Chan Bong Park, Choo Hie Lee
Dept. of Electronic Engineering, Institute for Laser Engineering
Kyung Hee University
Kiheung-Eup, Yongin-Si, KyungKi-Do, 449-701
TEL : 82-0331-201-2126, 2250 FAX : 82-0331-202-7657
E-mail : Ilekhu@nms.kyunghee.ac.kr

- ABSTRACT -

We have been measured tropospheric and stratospheric ozone profiles at Suwon(37N/140E) Korea from October 1992 to July 1997. For these experiments, ILE combined ozone lidar system are used. Here, we reports the variation of ozone concentration in stratosphere and troposphere during last 5 years.

Ⅰ. Introduction

Recently, The decrease of ozone concentration in northern hemisphere have been reported[1]. So, many scientists in the regions focus their interesting on variation of ozone in stratosphere and troposphere. DIAL measurements is known as one of the most effective and accurate method for ozone measurements. Since October 1992, we have been measured atmospheric ozone concentration from 5 km upto 30 km over Suwon, Korea by Combined Lidar [2,3,4]. We used 308/353 nm and 292/319nm pair for stratospheric and tropospheric simultaneous ozone measurements. Here we reports the time variation of ozone concentration from 5 km upto 30 km and annual variation of partial ozone column (D.U.) from 10 km upto 30 km.

Ⅱ. Instrumentation and Data processing

The ILE Ozone Lidar system described in Fig. 1. comprises two transmitting system and one receiving system for the simultaneous DIAL measurement of tropospheric ozone from 5 to 15 km and stratospheric ozone from 10 to 30 km. We use two excimer laser pumping stimulated raman lasers to generate two wavelength pairs, and one receiving system which is consist of telescope, 4 channel optical spectrometer, detector, photon-counter and data processing system. After sounding two wavelength pair into atmosphere inturn with 10 ms, then backscattered 4-wavelength signals are processed by one receiving system. So, we can measure stratospheric and tropospheric ozone concentration profiles simultaneously.

308/353 nm generated by XeCl excimer laser pumping H_2 Raman laser and 292/319 nm generated by KrF excimer laser pumping D_2 Raman lasers is used for stratospheric and tropospheric measurements respectively. The output energy of each wavelength pair are 32/10 mJ and 8/4mJ. The beam divergency are in 0.5 mrad and size of beam is 20 x 8 mm^2.

The backscatterd light collected by cassegrain telescope consisted of 600mm primary mirror and 200mm secondary mirror. To cut-off the unwanted strong signal from low altitude, the chopper is installed behind the input pin-hole. The light passed throught the pin-hole seperated into same wavelength as transmitting wavelength by spectrometer. This spectrometer have 4 channels of 319nm, 353nm and two 292/308nm channel. The spectrum bandwidth of Interference filter at each channels are 8 nm (292/308nm), 5 nm (319 nm), 5 nm (353 nm). The signals after optical parts are detected by PMT, then digitised by amplifier and discriminator. These digitised signals are transmitted to photon counter. The main function of synchronisation system is control of the trigger circuit of the lasers to sounding the 5 pulses in turn with 10msec delay.

For the data processin of ozone concentration, we used well known Browell's equation [5]. Because

of the effect on ozone data processing by Pinattubo aerosol is not so negligable, we corrected the aerosol backscattering and extinction term with the equation of transmission method[6]. For the calculation of backscattering term, we used 353nm return signal. Lastly, we eliminate the data which have the stastical error over 30%.

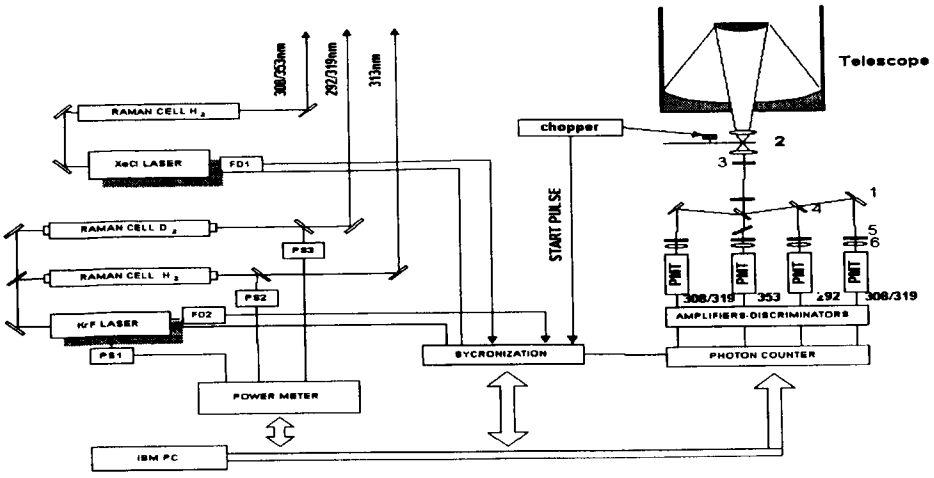


Fig. 1. Block diagram of Combined Ozone Lidar

III. Measurements

3-1. Time variation of vertical ozone concentration profile.

Fig. 2. Show the the variation of stratospheric and tropspheric ozone measured during 3 hours on November 21, 1993. 3 times stratospheric measurments are performed marked as ST in Fig. 3. The time difference between first and second is 5 min. and second and last is 2 hours. The time diferences on each tropspheric measurements marked TR are 15 min. The temporal resolution on each experiments are 15 minutes. in stratosphere and 5 minutes in troposphere

As a results, the small variation in stratosphere less than 10 % over 10 km altitude are measured. But, in torophere lower than 10 km, the dynamic variation more than 30 % are measured. In this experiments, we can estimate the bounday layer between stratospher and tropspher is about 10 km around.

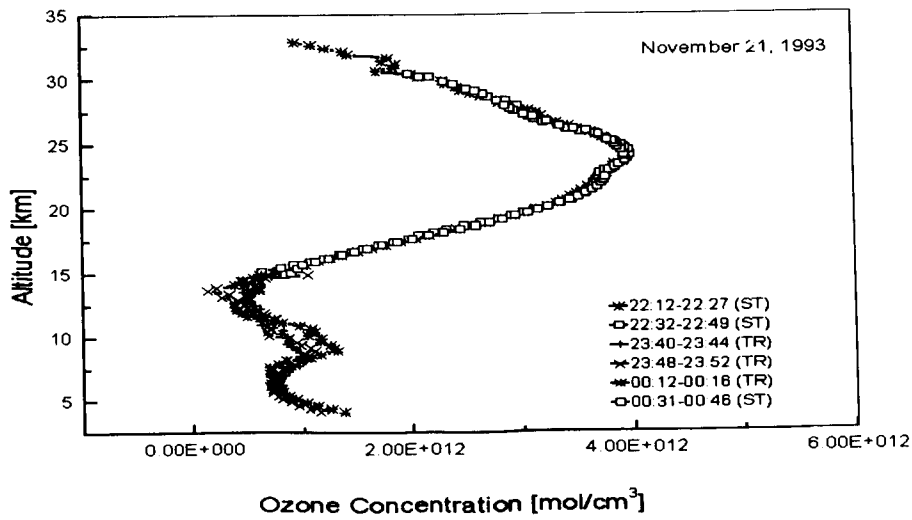


Fig. 2. Time variation of vertical ozone concentration over Suwon

3-2 Annual variation of column ozone (D.U.)

Fig. 3. show the yearly periodic variation of column ozone Dobson unit from 10 km upto 30 km measured by lidar from October 1993 to July 1997. the dot line is a averaged value (183 D.U.) of each daily measurements data during last 5 years. The error bar mean the statistical error of lidar measurements. As a results of this analysis, we can see the seasonal variation ozone concentrarion in each year are very similar except winter of 1992. From December to May, almost data show the higer value than averaged value. On June, July and August are similar with averaged value The maximum value is in 220 to 240 D.U. on spring. Otherwise, the minimum is in 140 to 160 D.U. on autumn (September and October). Especially, September and October in 1992, the value of column ozone is lower 40 D.U. than others. It's results are know as the effects of Pinatubo eruption. It is very difficult to say the annual trends of decrease or increase because of lack of measurements cases. So, our future goal are day-time and night-time routine measurements and construction of database of ozone measurements.

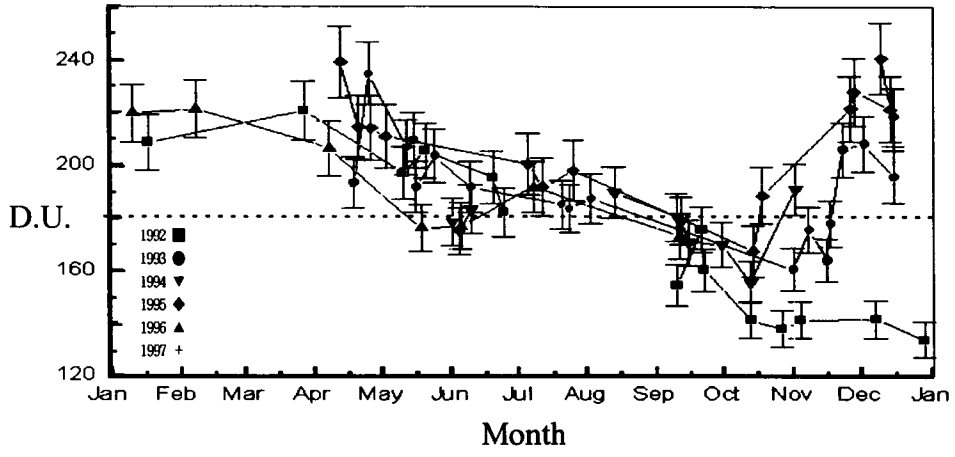


Fig. 3. The annual variation of column ozone (D.U.) from 1992 to 1997

References.

[1]. J. R. Herman, D. Larko : Low Ozone amount during 1992-1993 from NIMBUS7 and Meteor 3 Total Ozone Mapping Spectrometer Jounal of Geophysivcal Research, 99, D2, 3483-3496, (1994)

[2] C. B. Park, C. H. Lee : The Development of DIAL Ozone Lidar using Excimer Laser" Proceedings of 8th Conference on Waves and Lasers, II-14, .33 (1993.2), Optical Society of Korea (in Korean).

[3] C. B. Park, C. H. Lee, S. S. Khmelevtsov :Measurement of tropospheric and stratospheric Ozone using Combined UV DIAL system. CLEO'94, 1994 Technical Digest Series, 8, CWD6, 425-426 (1994.5)

[4] C. B. Park, C. H. Lee : Differential Absorption Lidar Measurements of Tropospheric and Stratospheric Ozone at Suwon, Korea from 1992 to 1997, JGR, Submitted.

[5] Browell E. V., James S., :Ultraviolet DIAL Measurement of O3 Profile in Region of Spatially Inhomogeneous Aerosols. Appl. Opt. 24, 17, 2827-2836 (1985).

[6] Russell P. B. :Meteodology for Error Analysis and Simulation of Lidar Aerosol Measurement. Appl. Opt., 18 (1979).

RESULTS OF LIDAR DATA APPLICATION TO CLIMATIC STUDIES OF THE STRATOSPHERIC OZONE FIELD ABOVE WESTERN SIBERIA

Komarov V. S., Zuev V. V., Lomakina N. Ya., Marichev V. N., and Popov Yu. B.

Institute of Atmospheric Optics,
1, Akademicheskii Ave, Tomsk 634055, Russia
Tel: + 7 3822 258616
Fax:+ 7 3822 259086
E-mail: shvs@losa.ioa.tomsk.ru

Current interest to lidar studies of stratospheric ozone above Western Siberia is caused by its role in the formation of the Earth's climate and by the lack of any information about the vertical ozone distribution (VOD) above the vast territory of the Asian part of Russia. Therefore, occasional lidar sensing of ozone was started in Tomsk (56.5°N, 85°E), Western Siberia, in 1989. Regular lidar sensing of ozone has been performed since 1995 with the use of a XeCl excimer laser and a mirror of a receiving telescope 1 m in diameter. Lidar measurements have been performed between 12 and 40 km, with vertical resolutions of 100-200 m below 24 km and 400 m above 24 km and with the relative measurement error less than 12%. The results of the preliminary analysis of the ozone vertical distribution are described in Ref. 1.

By now we have accumulated about 115 vertical profiles of ozone concentration. This allowed us for the first time to perform climatic studies of the state of the stratospheric layer above Western Siberia.

Statistical analysis of the VOD with the use (as in Ref. 2) of average values, variances, autocorrelation functions, eigenvectors, and eigenvalues of covariance matrices $|S_{n_3 n_3}|$ revealed its features typical of the examined region.

In particular, it was demonstrated:
– the maximum ozone concentration at the mean profile is observed at 18–22 km altitudes (Fig. 1);

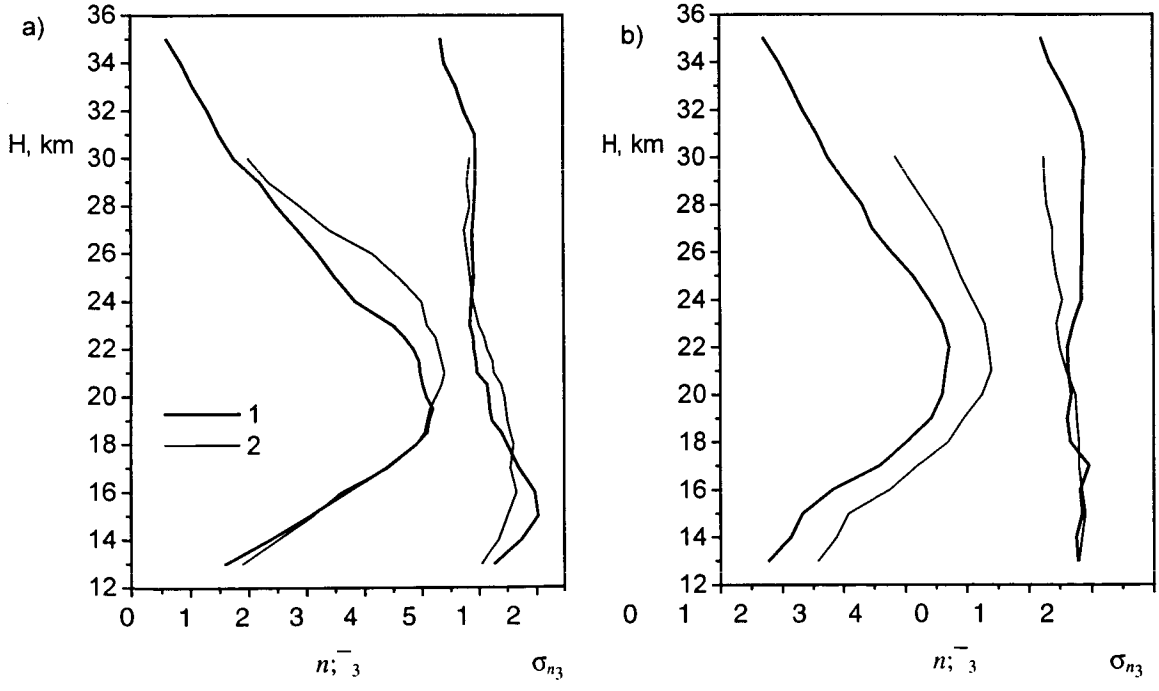


Fig. 1. Vertical distributions of the average values ($n_3 \times 10^{18}$, mol×m^{-3}) and standard deviations ($\sigma_{n_3} \times 10^{18}$, mol×m^{-3}) of the stratospheric ozone concentrations above Tomsk (1) and the station Legionovo (2) in winter-spring (a) and summer-fall (b).

– the decreased ozone content in the layer between 21 and 27 km recorded in winter and spring above Western Siberia (in comparison with Eastern Europe – st. Legionovo, 52°N and 21°E) is caused by specific features of the stratospheric meridional circulation which brings an ozone-poor air in this region;

– the average stratospheric ozone concentrations above Western Siberia, in analogy with other regions located at the moderate latitudes of the Northern Hemisphere (Ref. 2, 3), exhibit clearly pronounced annual behavior. The maximum ozone concentration (~5.0–5.2×10^{18} mol×m^{-3} between 18 and 22 km) was observed in winter and spring, whereas the minimum ozone concentration (~3.6–3.71×10^{18} mol×m^{-3} between 20 and 23 km) was observed in summer and fall.

– the variability of ozone, i.e., its rms deviation σ_{n_3}, has its maximum values in winter-spring, when large day-to-day variations of the ozone contents are caused by the intensive cyclogenesis, typical of the this period of the year;

– the degree of ozone interlayer correlation above the ozone peak (that is, above 19-22 km) depends on the season (it is sufficiently high in winter and spring when ascending air flows predominate; vice versa, it is very low in summer and fall when descending air flows predominate);

– the first three components of the vector $F_\alpha(\alpha=1, 2, 3)$ and the corresponding eigenvalues λ_α of the covariance matrix $\|S_{n_3 n_3}\|$ used to investigate the properties of the natural orthogonal components of vertical profiles of the stratospheric ozone concentration and the quality of their representation by the first terms of the expansion. The first eigenvectors of the covariance matrix $\|S_{n_3 n_3}\|$ in the examined seasons have some common features and noticeable differences. In particular, both in winter-spring and summer-fall the first eigenvectors reach their maxima (~0.30–0.31) somewhere above the stratospheric ozone peak, namely, near 23 and 21 km, respectively. At the same time, whereas in winter and spring the eigenvector F_1 remains positive between 15–30 km, in summer and fall it is negative above 28 km. This specific feature in the behavior of the eigenvector F_1 in summer and fall is due to the fact that above 28 km the correlation functions of the stratospheric ozone $r_{n_3 n_3}$ that determine the shape of the first eigenvectors pass through zero.

– the first three eigenvectors of the matrix $\|S_{n_3 n_3}\|$ (from n=16) contribute 90–91% to the total variance in both examined seasons. Four eigenvectors describe the profiles $n_3'(H_i)$ with the relative error ≤5%.

From this it follows that few-parameter models can be used to describe the realistic vertical profiles of the stratospheric ozone concentration due to sufficiently fast convergence of their expansion in the natural orthogonal components. At the same time, the main components of this expansion also can be used to construct regional statistical prognostic models of the stratospheric ozone.

References

1. Zuev V.V., Dolgii S.I., El'nikov A.V., Marichev V.N. Preliminary Statistical Analysis of the Stratospheric Ozone Lidar Sounding. Atmos. Oceanic Opt. 10, 1613–1615 (1997).
2. Zuev V.E., Komarov V.S. Statistical Models of the Temperature and Gaseous Components of the Atmosphere. Reidel, Dordrecht, The Netherlands, 1987, 306 p.
3. Spankuch D. and Dohler W., 1975: Statistische Characteristika der Vertical Profile von Temperatur und Ozon und ihre Kreuzkorrelation uber Berlin. *Geod. Geophys. Veroff*, 2, 132.

Observations of Gravity Waves in the Stratospheric Polar Vortex

James A. Whiteway[1], Thomas J. Duck[2], and Allan I. Carswell[2]

1. Department of Physics, University of Wales, Aberystwyth.
Tel:(01970) 621197, Fax: (01970) 622826, Email: jjw@aber.ac.uk

2. Department of Physics and Astronomy, York University, Toronto.

Summary

Lidar measurements of gravity wave activity have been conducted throughout each winter since 1993 at the Arctic Stratospheric Observatory in the Canadian High Arctic. The observatory is located on a mountain ridge near Eureka Weather Station (80° N, 86°W) on Ellesmere Island. The lidar system is based on a XeCl excimer laser that emits 70 Watts at a wavelength of 308 nm and this is partially converted to 353 nm by stimulated Raman scattering in a Hydrogen gas cell. The receiver detects backscatter at four wavelengths corresponding to elastic (308 nm, 353 nm) and Raman (from N_2 : 332 nm, 385 nm) scattering for measurements of ozone, aerosol and temperature (Pal et al. 1996). The 353 signal is used for conventional Rayleigh lidar measurements of temperature in the upper stratosphere and mesosphere (Hauchecorne and Chanin 1980).

Gravity waves are observed by the fluctuations they induce in temperature. Figure 1 shows a measured temperature profile which clearly exhibits perturbations that were induced by a large amplitude gravity wave. The wave induced fluctuations are isolated for analysis by subtracting an estimate of the unperturbed background state (a combination of cubic polynomial fits to the night's mean temperature profile). The corresponding profile of wave induced temperature perturbation is shown in Fig. 1b. In this case there is a dominant wave with amplitude growing exponentially with height - as expected when a wave is not dissipated. The exponential growth appears to cease above 43 km where the dominant wave is inducing a marginally unstable temperature gradient (-10 deg/km as illustrated in Fig 1a). Also, waves with smaller vertical scales appear to be combining with the dominant one to induce marginal convective instability (eg. at 37 km).

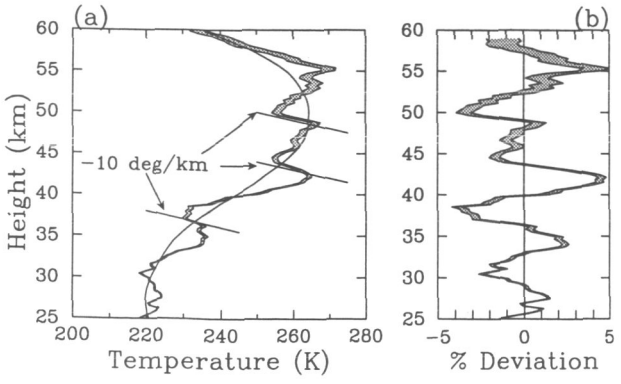


Figure 1. (a) A half hour average temperature profile measured at Eureka on 14 Feb. 1993. The smooth line is the estimated unperturbed background state. (b) The corresponding profile of fractional temperature perturbation from the background state. Shading indicates the limits of uncertainty in the measurement.

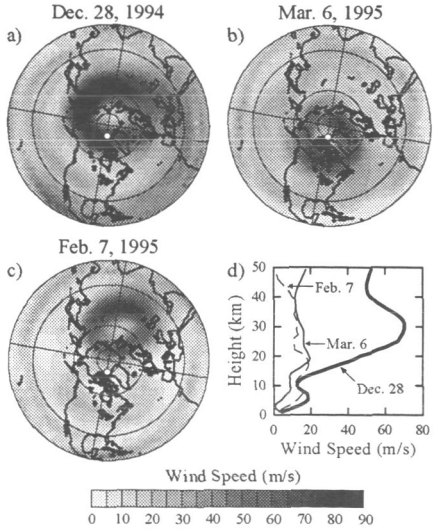


Figure 2. Maps of Geostrophic wind speed computed from the NCEP analysis at the 10 hPa pressure level (height approximately 30 km) above the northern hemisphere for a) 28 Dec. 1994, b) 6 Mar 1995, and c) 7 Feb. 1995. The position of Eureka is indicated by the white dot. The dark ring is the westerly (eastward) jet of the polar vortex (counter-clockwise motion). The corresponding height profiles of wind speed above Eureka are shown in d).

The location of Eureka is ideal for ground based studies of stratospheric dynamics since a wide range of meteorological conditions can be observed as the polar vortex changes position. As demonstrated in Fig. 2, the vortex position may change such that Eureka is situated beneath: a) the westerly jet (vortex edge), b) the vortex core, and c) outside of the vortex. The measurements at Eureka have sampled each of these distinct stratospheric conditions and there is a clear pattern in the distribution of gravity wave activity within and around the polar vortex.

The amount of wave activity was gauged by the potential energy density associated with the wave induced temperature fluctuations. The gravity wave potential energy density is determined by multiplying the fractional temperature variance by $(0.5)(g/N)^2$, where g is acceleration due to gravity and N is the buoyancy frequency (which is derived from the night's mean temperature profile). Figure 3 shows profiles of gravity wave potential energy density that were averaged separately according to the different positions within and around the polar vortex. The gravity wave activity was greatest within the westerly jet (Fig. 2a) of the polar vortex and the minimum was in the core (Fig. 2b) of the vortex. This pattern has been observed each winter since 1993.

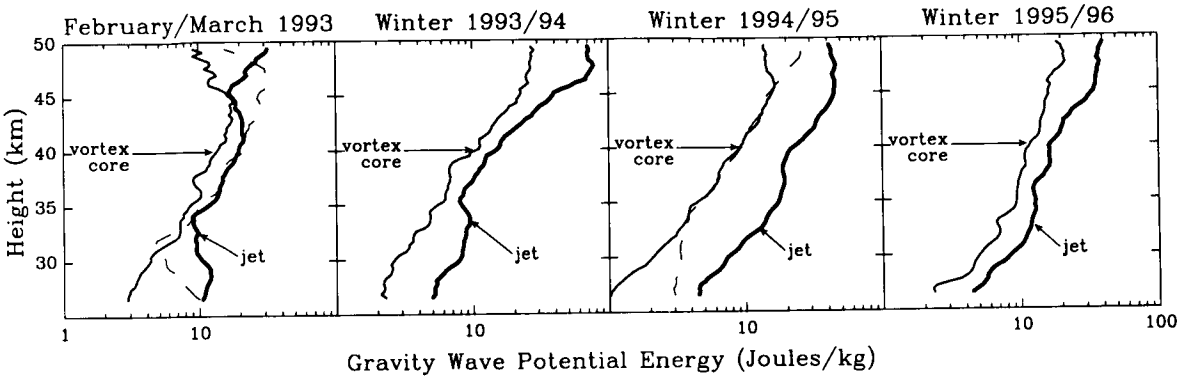


Figure 3. Profiles of mean gravity wave potential energy density averaged separately according to vortex position: inside core (thin), jet (thick), and outside (dashed).

This research is continuing with the aim of investigating the link between polar vortex dynamics and gravity wave activity. Further analysis has shown that the enhancement of wave activity in the jet corresponds to meteorological conditions that are favourable for vertical propagation of gravity waves from the troposphere (Whiteway et al., 1997). Also, there is new evidence which indicates that thermal structure in the vortex core is influenced by gravity wave activity in the vortex jet (Duck et al. 1998).

Acknowledgements

The Arctic Stratospheric Observatory and Eureka Weather station are operated by the Atmospheric Environment Service of Canada. This work was carried out as part of the research program at the Centre for Research in Earth and Space Technology at York University. Global analysis of the stratospheric height and temperature (for wind calculation) were provided by the National Centers for Environmental Prediction.

References

Duck, T. J., J. A. Whiteway, and A. I. Carswell, 1998: Observations of gravity waves and Arctic vortex core warming. Submitted to *Geophys. Res. Lett.*.

Hauchecorne, A., and M. L. Chanin, 1980: Density and temperature profiles obtained by lidar between 35 and 70 km. *Geophys. Res. Lett.*, vol. 7, pages 565-568.

Pal, S. R., A. I. Carswell, J. Bird, D. P. Donovan, T. J. Duck, and J. A. Whiteway, 1996: Lidar measurements of the stratosphere at the Eureka and Toronto NDSC stations. *SPIE*, vol. 2833, pages 28-39.

Whiteway, J. A., T. J. Duck, and A. I. Carswell, 1997: Measurements of gravity wave activity within and around the Arctic stratospheric vortex. *Geophys. Res. Lett.*, vol. 24, pages 1387-1390.

Observation of the middle atmospheric thermal tides using lidar measurements over Mauna Loa Observatory (19.5°N, 155.6°W).

Thierry Leblanc and I. Stuart McDermid
Jet Propulsion Laboratory, California Institute of Technology, Table Mountain Facility, Wrightwood, CA, USA.
leblanc@tmf.jpl.nasa.gov, Tel: +1 (760) 249 1070, Fax: +1 760 249 5392

1. Introduction

Temperature measurements in the middle atmosphere using Rayleigh lidars have been performed for several decades now. The high accuracy and vertical resolution provided by lidars allow to study the temperature variability at various scales with high confidence levels. One of the numerous applications is the study of the middle atmospheric thermal tides. Although Rayleigh lidar measurements are basically possible only at nighttime, diurnal and semidiurnal components can often be extracted if the results are taken with care and correctly interpreted.

Using results from more than 200 hours of nighttime measurements obtained by lidar in October 1996 and 1997 at Mauna Loa Observatory, Hawaii, a study of the middle atmospheric (25-90 km) thermal tides is presented in this paper. The amplitudes and phases of the diurnal and semidiurnal components were calculated for some altitudes where the fits converged significantly, and compared to that of the Global Scale Wave Model (GSWM).

2. Lidar principle, data sets and data analysis.

Laser radiation transmitted into the atmosphere is Rayleigh backscattered by the air molecules and collected by a telescope. The number of photons received is proportional to the number of photons emitted and to the number of molecules i.e. air density. Except following volcanic eruptions when particular care is required, Mie scattering by aerosols is only important below 25-30 km and can be neglected for the air density derivation above 30 km. Then, the temperature is derived from the air density assuming hydrostatic equilibrium and the ideal gas law [*Hauchecorne and Chanin*, 1980].

10 nights of measurements (typically 11-hours per night from 19:00 to 5:00 Local Solar Time) obtained by the Jet Propulsion Laboratory (JPL) Rayleigh/Raman lidar [McDermid et al., 1992] at Mauna Loa (19.5N) between October 3-16, 1996, and 10 nights obtained between October 2-11, 1997 were used for this study. For both October 1996 and 1997 periods, the raw signal taken every night at a given Local Solar Time (LST) has been summed into a composite raw signal and analyzed to obtain 11 hourly-mean composite temperature profiles (15-95 km). Also, the nightly average temperature profile over the 10 nights in October 1996 and that over the 10 nights in October 1997 has been calculated. The temperature determination by Rayleigh lidar requires an a priori initialization at the top. For the two nightly average profiles the CIRA-86 temperature at 103-105 km was used. Then, for each 1996 hourly-average profile the 1996 nightly average temperature at 93.4 km has been used, and for each 1997 hourly-average profile, the 1997 nightly average temperature at 94 km has been used. Thus it is certain that at these tie-on altitudes the temperature will remain constant throughout the night and the calculated fits for both diurnal and semidiurnal components will result in zero-amplitudes. Then, a few kilometers lower the calculated amplitudes are expected to rapidly increase to their observed values as the temperature is calculated downward and converges into its true value. The total error at the top of a typical temperature profile is about 20 K, rapidly decreasing to few Kelvin 10-15 km below and to less than 1 K 25 km below.

3. Results.

In a first step, for each given LST the temperature difference between the composite profile and the nightly average profile has been calculated. These temperature differences were seen to be LST dependent and were fitted temporally using 2 cosine functions to represent the diurnal and semidiurnal components only. When the nightly average temperature is close to the true 24-hour-average temperature the calculated fits will give correct and significant results. However, this is not true when the nightly average is far from the true 24-hour-average. For this reason, some estimated components were taken from GSWM [*Hagan et al.*, 1995].and introduced to calculate an estimated 24-hour-average to be subtracted from the LST composite profiles. Figure 1 gives the results of the calculated diurnal and semidiurnal amplitudes and phases between 25 and 95 km for the 1996 period, using the phases given by GSWM, and twice the amplitudes given by GSWM for the estimation of the 24-hour average. Unlike GSWM, the calculated amplitudes (in K) and phases (LST) are given with their 1σ standard deviation (horizontal bars). The effect of an 11-hour wide measurement window is clearly seen. The semidiurnal component can be retrieved correctly but the diurnal component can not be well identified at all altitudes.

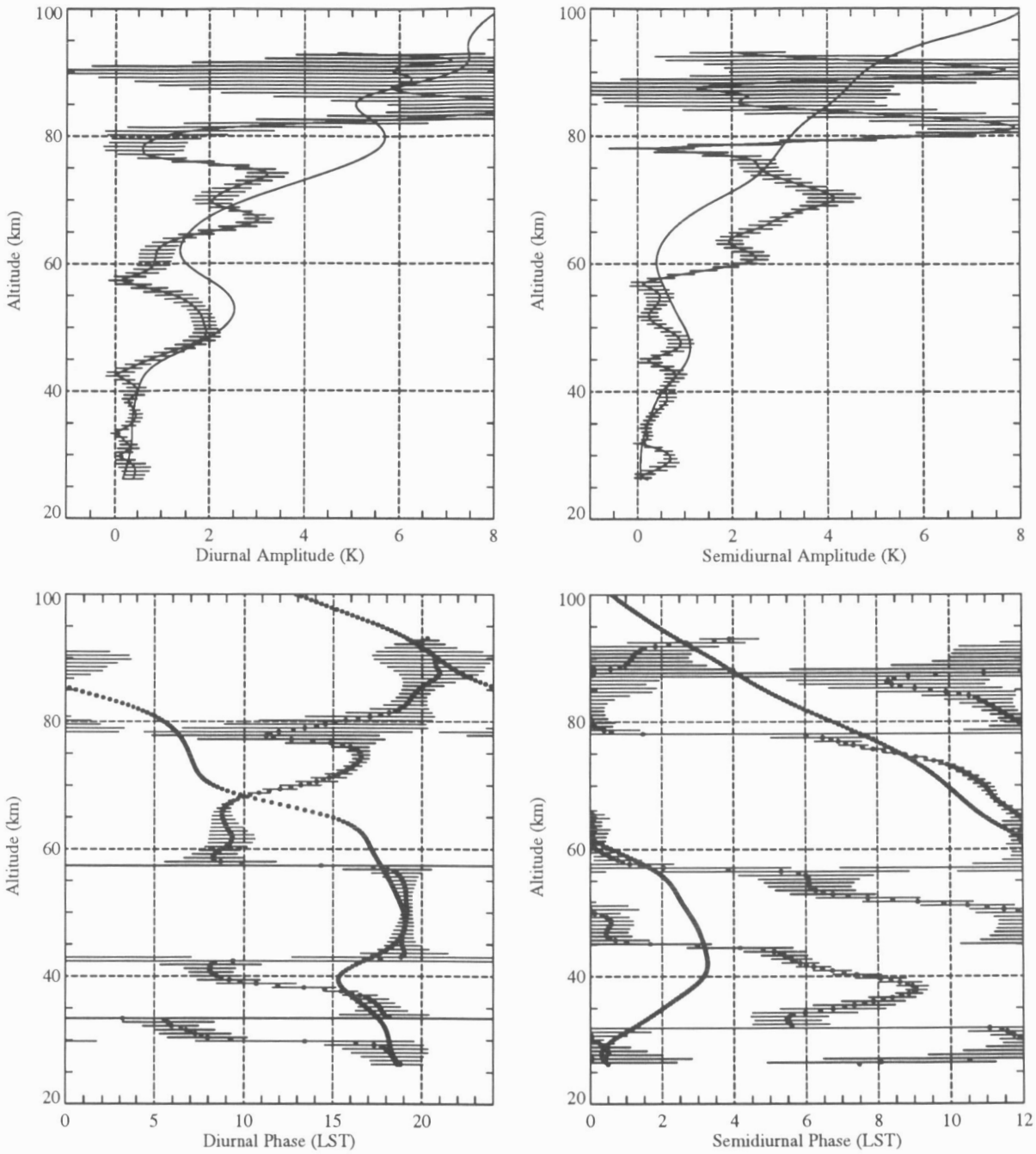


Figure 1: Amplitude (top) and phases (bottom) of the diurnal (left) and semidiurnal (right) components calculated for 10 nights of October 3-16, 1996. The amplitudes and phases are plotted with their 1σ standard deviation (horizontal bars) while twice the GSWM amplitudes and the GSWM phases are represented by single lines and dots.

Basically, the significant results are:

For the semidiurnal component:

a) A small amplitude (< 1K) below 60 km.

b) A maximum amplitude of 4 K at 70 km, with a corresponding phase around 10:00 - 11:00, 2 hours away from the theoretical model GSWM.

c) A minimum of amplitude corresponding to an out-of-phase transition (from 6:00 to 12:00) just below 80 km.

d) An 8 K maximum amplitude at 82 km, with a corresponding phase of 11:00-12:00.

For the diurnal component:

e) A small amplitude (< 1K) below 45 km.

f) A maximum amplitude of 2 K around 47-51 km, with a corresponding phase around 18:00 - 19:00, in good agreement with GSWM.

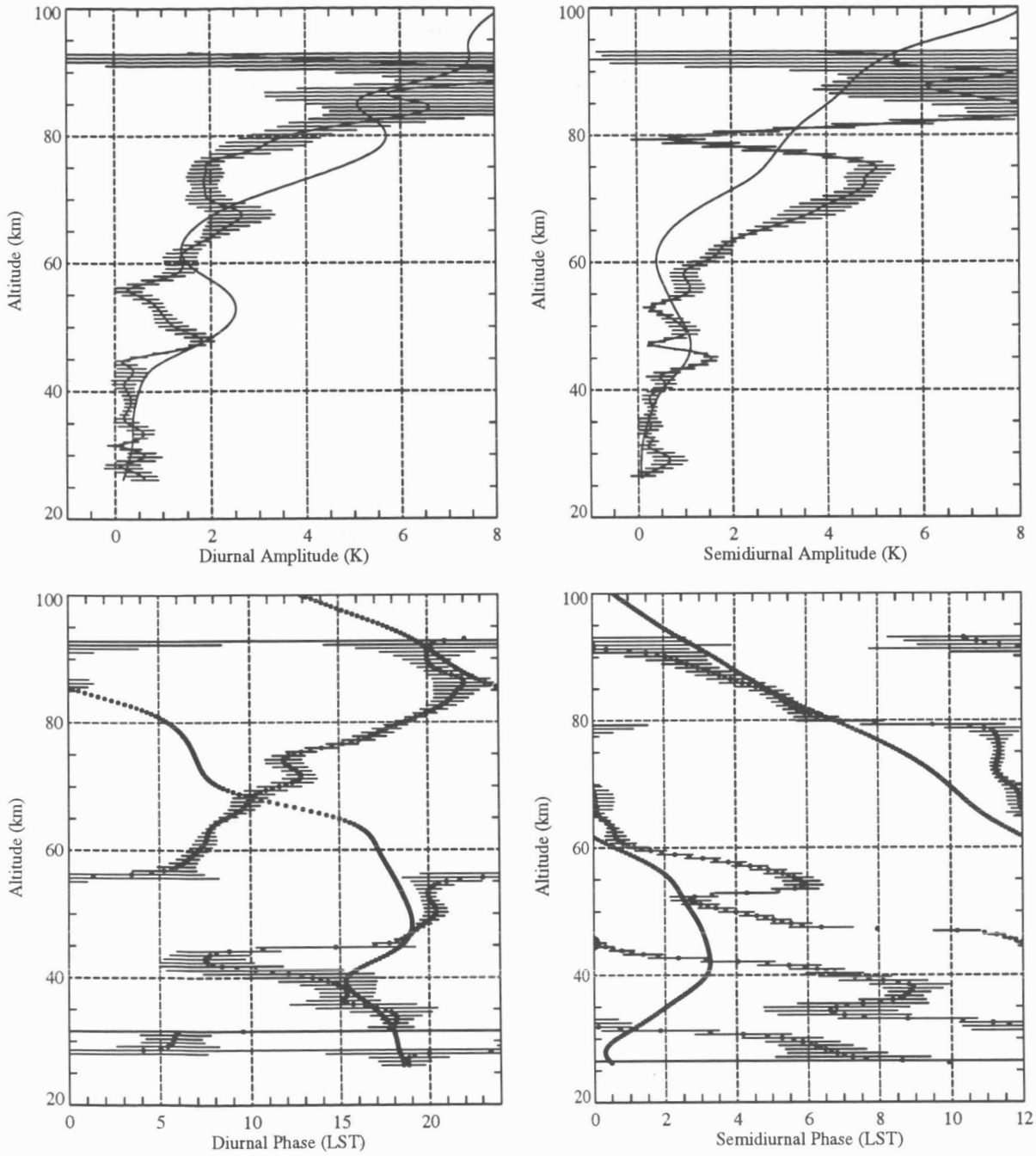


Figure 2. Same as Figure 1 but for the 10 nights of October 2-10, 1997.

g) A minimum amplitude corresponding to an out-of-phase transition (from 19:00 to 7:00) at 57-58 km. This may indicate an actual phase around 12:00 at this altitude.

h) A double maximum of 3 K at 66 and 73 km. The phase corresponding to the upper maximum occurs at 16:00, which is in total disagreement with the 7:00 phase of GSWM.

i) A minimum amplitude at 78 km. Once again, this may indicate an actual phase around 12:00 at this altitude.

First, all results show that the observed amplitudes appear to be twice as large than predicted by GSWM (the modeled amplitudes plotted in Figure 1 are equal to twice the GSWM). Results b) shows that a maximum in the semidiurnal amplitude has not been predicted by the model. Results c) f) g) h) and i) together may suggest the presence of a locally forced diurnal mode at 78 km not predicted by the model, or that the diurnal mode propagating from below 50 km has a near-20-km

vertical wavelength, much shorter than predicted and already suggested by [*Dao et al.*, 1995].

Figure 2 is similar to Figure 1 but for the October 1997 period. When compared to the October 1996 period, some remarkably consistent results are found.

For the semidiurnal component:

j) Same as a) with a first secondary maximum in amplitude (1.5 K) around 45 km.
k) Same as b), a maximum amplitude of 5 K around 70-75 km, analog to the result b)
l) A minimum amplitude corresponding to an out-of-phase transition (from 12:00 to 6:00) just below 80 km, but in out-of-phase compared to 1996.

For the diurnal component:

m) Same as e): small amplitude below 45 km.
n) Same as f): Maximum amplitude of 23 K but at 46-47 km instead of 47-51 km, with a corresponding phase around 18:00 - 19:00, in good agreement with GSWM.
o) Same as g): A minimum amplitude corresponding to an out-of-phase transition (from 19:00 to 7:00) at 56 km. Once again, this may indicate an actual phase around 12:00 at this altitude.
p) A phase located at 15:00 around 75 km, once again in total disagreement with GSWM.

6. Summary.

More than 200 hours of nighttime measurements obtained by the Jet Propulsion Laboratory (JPL) Rayleigh/Raman lidar in October 1996 and 1997 located at Mauna Loa Observatory (19.5°N) have been used to extract the diurnal and semidiurnal components in the middle atmospheric temperature (15-95 km) and to compare them to the Global Scale Wave Model (GSWM). Despite a short 11-hour wide measurement window, some significant results have been obtained:
- Both observed diurnal and semidiurnal amplitudes appeared to be twice as large as predicted by GSWM.
- Both diurnal and semidiurnal amplitudes are less than 1 K below 40 km.
- The calculated semidiurnal amplitude has a maximum at 70-75 km, not predicted by GSWM. The corresponding phase is around 11:00 – 12:00, in good agreement with GSWM.
- The calculated diurnal amplitude has a maximum at 45-50 km, with a phase around 19:00, in good agreement with GSWM.
- For both 1996 and 1997 periods, a minimum in the calculated diurnal amplitude associated with an out-of-phase transition from 19:00 to 7:00 is clearly observed at 55-58 km. Since the 11-hour measurement window is centered on 00:00 LST, the diurnal phase at this altitude is likely to be around 12:00 and the true amplitude is likely to be larger than calculated. This minimum, together with the maximum found at 45-50 km and a well defined 16:00 diurnal phase at 75 km may suggest the presence of an upward propagating diurnal mode from below 50 km with a vertical wavelength of approximately 20-km, or the presence of a forced mode trapped around 75 km.
- For both 1996 and 1997 periods, a minimum in the semidiurnal amplitude associated with an out-of-phase transition from 6:00 to 00:00 in 1996, and from 12:00 to 6:00 in 1997 is clearly observed just below 80 km.
- Unlike the diurnal minimum at 55-58 km, the out-of-phase transition at this altitude and the 12 hours difference observed between 1996 and 1997 can not be explained at this date. However, the nightly averaged profiles calculated for 1996 and 1997 appeared to be extremely different especially above 80 km, and may play a major role in modulating and/or ruling the semidiurnal and diurnal components.

More investigations and observations are necessary to confirm these results. In particular, the use of simulated data and the refinement of estimated components for the calculation of a correctly estimated 24-hours average profile should give some important answers for a better understanding of the thermal tides in the middle atmosphere.

Acknowledgments

The work described in this paper was carried out at JPL, California Institute of Technology, under an agreement with the National Aeronautics and Space Administration.

References

Dao, P. D., R. Farley, X. Tao, and C. S. Gardner, Lidar observations of the temperature profile between 25 and 103 km: evidence of strong tidal perturbation, *Geophys. Res. Lett.*, *22*, 2825-2828, 1995.

Hagan, M. E., J. M. Forbes and F. Vial, On modeling migrating solar tides, *Geophys. Res. Lett.*, *22*, 893-896, 1995.

Hauchecorne, A., and M. L. Chanin, Density and Temperature Profiles obtained by lidar between 35 and 70 km, *Geophys. Res. Lett.*, *7*, 565-568, 1980.

McDermid, I. S., T. D. Walsh, A. Deslis and M. L. White, Optical systems design for a stratospheric lidar system, *Appl. Opt.*, *34*, 6201-6210, 1995.

The Ny-Ålesund Aerosol and Ozone Measurements Intercomparison campaign 1997/98 (NAOMI-98)

R. Neuber[1], G. Beyerle[2], I. Beninga[1], P. von der Gathen[1], P. Rairoux[1], O. Schrems[1], P. Wahl[1], M. Gross[3], Th. McGee[3], Y. Iwasaka[4], M. Fujiwara[5], T. Shibata[4], U. Klein[6], W. Steinbrecht[7]

1. Alfred Wegener Institute for Polar and Marine Research, Bremerhaven and Potsdam
Telegrafenberg A43, D-14473 Potsdam, Germany
Phone: +49-331-288-2129, Fax: +49-331-288-2137, E-mail: neuber@awi-potsdam.de
2. AWI, currently at JPL-Table Mountain Facility, CA USA
3. Goddard Space Flight Center, Greenbelt, MD 20771 USA
4. Solar Terrestrial Environment Laboratory, University of Nagoya, Japan
5. University of Fukuoka, Japan
6. Institute of Environmental Physics, University of Bremen, Germany
7. Deutscher Wetterdienst, Meteorological Observatory Hohenpeißenberg, Germany

Abstract

An intercomparison campaign for Lidar measurements of stratospheric ozone and aerosol has been conducted at the Primary Station of the NDSC in Ny-Ålesund/Spitsbergen during January-February 1998. In addition to local instrumentation, the NDSC mobile ozone lidar from NASA/GSFC and the mobile aerosol lidar from AWI participated. The aim is the validation of stratospheric ozone and aerosol profile measurements according to NDSC guidelines. This paper briefly presents the employed instruments and outlines the campaign. Results of the blind intercomparison of ozone profiles are given in a companion paper by Steinbrecht et al. (1998) and temperature measurements are described in this issue by McGee et al. (1998).

1 Introduction

Ny-Ålesund/Spitsbergen (79°N, 12°E) is a primary site within the Network for the Detection of Stratospheric Change (NDSC). Lidar observations of the stratosphere are performed with a multiwavelength lidar facility for observations of ozone, aerosols, and temperature. To maintain the high standards of data quality required within the NDSC, regular intercomparisons are conducted within the network. Here we describe an intercomparison campaign in winter 1997/98 for measurements of stratospheric ozone, temperature, and aerosol profiles. The intercomparison focused on ozone measurements of the lidar instrument at Ny-Ålesund and the NDSC travelling ozone lidar maintained by NASA's Goddard Space Flight Center (GSFC). In addition the Rayleigh temperature and aerosol profiles are compared between the above mentioned lidar systems, the new Mobile Aerosol and Raman Lidar (MARL) of AWI, and the aerosol lidar of the Universities of Nagoya and Fukuoka. Additional techniques used on site for the ozone intercomparisons are the ozone microwave radiometer and balloon borne ECC ozone sondes. Planning of this campaign resulted from contacts at the 1994 and 1996 Int. Laser Radar Conferences (ILRC) and NDSC-Lidar-Meetings.

Lidar algorithm intercomparisons recently carried out for the retrieval of aerosol profiles and for ozone profiles give are basis for this on site instrument intercomparison. The algorithm intercomparisons were presented by Steinbrecht et al. (1996) at the 18. ILRC for aerosol retrievals and by S. Godin at the NDSC-Lidar-PI-Workshop 1996 (Godin et al., 1998) for ozone profile evaluations.

2 Experimental procedures

The intensive measurement period for the campaign started on 19 January and ended on 10 February 1998. Weather conditions have been extremely favorable, with cloud cover never preventing measurements for more than 24 h. Accordingly lidar measurements could be taken on every day.

Due to optical interference problems, the two ozone lidars had to operate alternately on interleaving times. The Rayleigh lidar systems could measure independently from each other. Due to high background levels of the approaching daylight, measurements were prevented around local noon.

Raw data for the ozone profiles were integrated over 2 - 6 hours and the retrieved ozone profiles transferred via internet to the referee. The intercomparison of the ozone profiles was conducted blindly. Data from ozone sondes, however, which were performed almost daily during the intensive measurement period, are publicly available and accessable to the participants.

Ozone profiles of the microwave radiometer on the other hand are compared blindly as well. They were recorded semi-automatically for 12 min. on every hour. As the ozone microwave radiometer is practically insensitive to clouds, this instrument has the best overall measurement statistics.

Although usually the January-February period is the high season for observations of Polar Stratospheric Clouds (PSCs) by aerosol lidar, only one minor PSC event occurred during the intercomparison period, limiting the aerosol intercomparison to this one case.

On the other hand, the absence of large aerosol signals allows to derive atmospheric temperature data

from elastically scattered laser lines e.g. at 353 nm in addition to the temperature data collected by Raman channels.

3 Instrumentation for the intercomparisons

The following paragraph gives an overview of the instruments, which are summarized in table 1.

The Ny-Ålesund Multiwavelength Lidar facility

The ozone- and aerosol-lidar instruments at Ny-Ålesund are realized as one combined multi-wavelength system. It comprises a XeCl-Excimer laser for UV-wavelengths, running at 90 Hz and a Nd:YAG-laser for near IR- and visible wavelengths running at 30 Hz pulse repetition. Laser pulses are emitted into the atmosphere with dedicated 'sender-optics' consisting of beam expanders and steerable mirrors. During the campaign the 'old' 60 cm and a recently installed 150 cm telescope were alternately used to collect the return signals. The new large telescope focuses received light into a glas fibre, which guides it into a two channel detector, which can be equipped with Fabry-Perot etalons for daylight suppression at the ozone DIAL wavelengths of 308 and 353 nm. As the measurements reported here were taken in the polar night, no etalons were installed. The smaller telescope is the standard used since lidar operations began on Spitsbergen. It is coupled to the multi channel detection system used during the polar night for simultaneous detection of elastically and inelastically scattered signals (Neuber et al., 1991, 1994, von der Gathen et al., 1994). Aerosol data is obtained at the wavelengths 353 nm, 532 nm, and 1064 nm with additional depolarization measurements at 532 nm (Beyerle et al., 1994), and the ozone measurements are performed using the DIAL principle and employing the signals at 308 and 353 nm. In addition to the emitted wavelengths also the wavelengths of nitrogen Raman scattered light are recorded at 607 nm.

The Ny-Ålesund Microwave Radiometer

The Radiometer for Atmospheric Measurements (RAM) has been developed by the Institute of Environmental Physics of the University of Bremen as an instrument for ground-based millimeter-wave observations of trace gases in the stratosphere and lower mesosphere in the frequency range from 100-300 GHz. As part of the German ozone research program (OFP) and the European Stratospheric Monitoring Stations projects (ESMOS/Arctic I & II) this instrument is operated continuously according to the requirements for a primary NDSC station.

The RAM is a heterodyne receiver consisting of two front-ends for the observation of ozone at 142 GHz and chlorine monoxide (ClO) at 204 GHz, which are operated in a time-sharing mode. Both front-ends consist of a rotatable mirror for calibration, a quasi-optics and a mixer-HEMT pre-amplifier stage which is cryogenically cooled to about 12 K.

The back-end consists of a 2048 channel acousto-optical spectrometer (AOS) with a center frequency of 2.1 GHz, a bandwidth of 945 MHz and a frequency resolution of ~1.3 MHz. This allows to retrieve trace gas volume mixing ratio profiles in the altitude range from 15 to 60 km from the shape of the observed signal. The whole system is computer controlled and can operate automatically (Langer et al., 1998).

The Ny-Ålesund ozone sonde facility

At Ny-Ålesund ECC ozone sondes of type 6A from Science Pump Corp. are launched with RS80 radiosondes from VAISALA. A recently modernized VAISALA DigiCORA receiver is used for collection of

Table 1 Participating institutes and instruments

Instrument	Spezies measured	Operating institution	Validation history
(i) regularly in Ny-Ålesund:			
multiwavelength lidar for aerosol and ozone	ozone, temperature, aerosols	AWI	algorithm intercomparisons for aerosol and ozone profiles
Microwave Radiometer for Atmospheric Measurements (RAM)	ozone	Univ. Bremen	
ozone sondes	ozone	AWI	
aerosol lidar	aerosols	Univ. Nagoya	
(ii) campaign operation:			
NDSC Mobile Ozone Lidar	ozone, temperatures	NASA/GSFC	NDSC traveling intercomparison standard
MARL (Mobile Aerosol Raman Lidar)	aerosols, temperatures	AWI	on site intercomparison with NDSC aerosol lidars during winter '96/97 at JPL/TMF Calif.

Fig. 1a

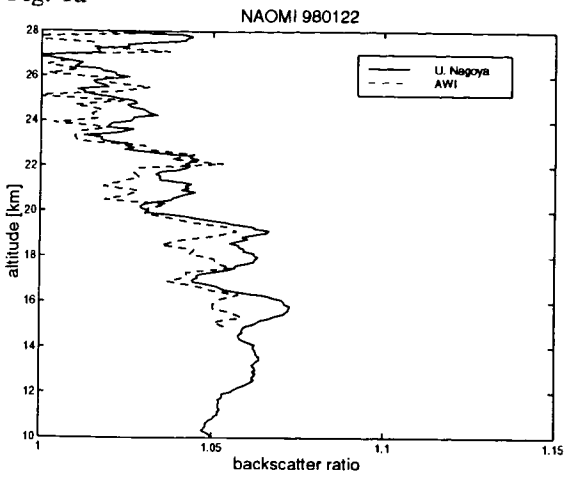
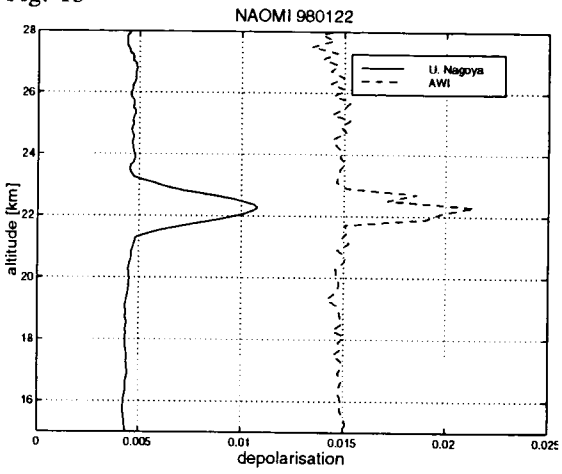


Fig. 1b



data. The sondes are flown with Totex rubber balloons, which are pre-treated during periods of low stratospheric temperatures resulting in burst altitudes usually above 30 km. Altitude resolution of the data transmittance is approximately 50 m depending on the balloon ascent rate. The altitude resolution, however, is reduced to about 300 m due to the response time of the sensor, which is filled with 3 cm^3 of 1 % KI solution. The ECC data is treated according to the manufactorer's instructions, which follow those by Komhyr (1986), including the tabled pump correction factors given there (that is e.g. 1.054 at 10 hPa). Due to polar night conditions for about half of the year no total ozone correction by a Dobson spectrometer is performed.

The Univeristy of Nagoya lidar at Ny-Ålesund

The lidar operated by the Universities of Nagoya and Fukuoka is a conventional Nd:YAG laser based aerosol lidar. Two wavelengths at 1064 and 532 nm of the laser are used in the lidar system. The vertical profiles of backscattering coefficient at the two wavelengths and the depolarization profiles at 532 nm are measured for the observation in the stratosphere. The echo, Raman-shifted from 532 nm, at 607 and 660 nm by N_2 and H_2O molecules are also detected for the observation in the troposphere. The laser energy is 200 mJ/pulse at each wavelength, and the pulse repetition is 10 pps. The diameter of the telescope is 35 cm.

The NASA/GSFC lidar

The Goddard Space Flight Center mobile Stratospheric Ozone Lidar was developed under the auspices of the Network for the Detection of Stratospheric Change (NDSC). It is a DIAL instrument capable of making measurements of the vertical profiles of temperature, ozone and aerosols simultaneously (McGee et al 1995). The lidar instrument uses excimer lasers with 200 Hz pulse repetition rate to generate the two wavelengths (308 and 351 nm) which are transmitted into the atmosphere. A 30" Dall-Kirkham telescope collects the backscattered radiation, and a series of beamsplitters spectrally separate the light into four wavelengths; the elastically backscattered signal from each of the transmitted laser beams, and the N_2 Raman shifted wavelengths for each laser wavelength. The combination of Raman scattered, and elastically scattered signals yields aerosol information as well as returning a more accurate ozone measurement in regions of heavy aerosol loading. The GSFC lidar has been used extensively in NDSC, and satellite validation intercomparisons, most recently at the Observatoire de Haute Provence in southern France. The 1998 NAOMI campaign at Ny-Ålesund was the first set of measurements under extreme weather conditions.

The Mobile Aerosol Raman Lidar (MARL)

The MARL consists of a high power Nd:YAG laser emitting at 532 and 355 nm wavelengths with 30 Hz repetition rate. The laser light is polarized to a high degree (>99.65%) and has a low divergence (< 50 micro rad). A quasi Cassegrainian telescope assembly collects the return signals and feeds them into a polychromator detector, which simultaneously records the laser wavelengths in both planes of polarization, the vibrational N_2-Raman scattered light from the air at 387 and 607 nm and of water molecules at 408 nm. The instrument is designed as an autonomous system installed in a 20 ft laboratory container. It only needs hook-ups for power and communication lines.

4 Examples of data sets

The results of the ozone measurement intercomparison are presented by Steinbrecht et al. in this issue. As it is a blind intercomparison no results can be shown here. The night of 21./22. January was a typical measurement period with all lidars operating and covering many hours. It was a non-typical night in so far, as it was the only night, when signals of Polar Stratospheric Clouds (PSCs) could be recorded. Still, the signature was very weak and practically only detectable in the depolarisation channels of the Rayleigh lidars operating

in the visible. Figures 1a and 1b display the backscatter ratios and total depolarisations averaged over several hours during that night as they were recorded by the Univ. Nagoya lidar and the AWI-NDSC-Lidar. In both cases the 532 nm wavelength of the Nd:YAG lasers is employed. Fig. 1a shows that both lidars track the very small backscatter ratio quite well, with the fine structure seen in both profiles. With a backscatter ratio around 1.05, however, this signal is practically that of the stratospheric background ('Junge') layer. The PSC only shows up in the depolarisation channels between 21.5 and 23 km (Fig. 1b). While the Junge layer between 12 and 20 km displays no depolarisation (spherical particles), the PSC clearly stands out. This is a good example of the necessity to operate depolarisation channels when searching for PSCs. The systematic difference in the depolarisation values is due to the fact that the U. Nagoya lidar employs a small bandwidth filter centered on the Cabannes line, while the AWI system records the complete Rayleigh spectrum.

Data of the same night is used to derive temperatures from the tropopause up to the mesosphere, as displayed in figure 2. Here the data from the AWI Nd:YAG system is shown together with the high altitude profile of the MARL (both at 532 nm) and the GSFC lidar. The later uses the N_2-Raman line at 382 nm for the lower part of the profile and the DIAL reference line at 351 nm for the upper part. Data shown here is an average of several hours during the night 21./22. January. Between 30 and 50 km all systems agree very well, above 50 km both AWI lidars retrieve with high uncertainty only. Below 25 km the AWI NDSC lidar records temperatures considerably lower than the GSFC system, which can be attributed to the backscatter signal enhancement by the background aerosol layer.

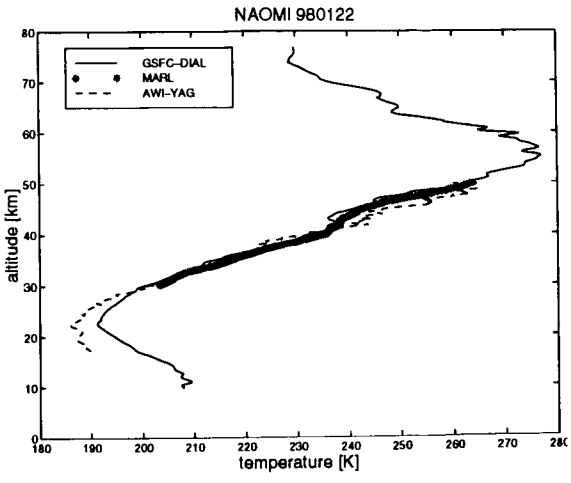
Acknowledgements

The personell of the Koldewey-Station, Tine Weinzierl and Bodo Wichura, as well as the personell of Kings Bay Kull Compagnie, Ny-Ålesund, were extremely helpful during preparation and realization of the campaign. D. Römermann and B. Wichura performed the ozone sonde launches. This research was partly supported by the European Commission (project ESMOS/Arctic II) and performed as a NDSC activity. AWI contribution no. 1383.

References

Beyerle, G., et al., Multiwavelength lidar measurements of stratospheric aerosols above Spitsbergen during winter 1992/93, Geophys. Res. Lett., 21, 57-60, 1994.

Fig. 2 Night average temperature profiles 21/22 Jan. 98



McGee, T.J., et al., Improved stratospheric ozone lidar, Opt. Eng., 34, 1421-1430, 1995.

Neuber, R., B.C. Krüger, and O. Schrems, Remote measurements of ozone concentration and aerosols in the Arctic stratosphere, Proc. of the symposium "Spuren von Elementen und Verbindungen in der Atmosphäre", Fresenius J. Anal. Chem. 340, 650-653, 1991.

Neuber, R., et al., Aerosol, ozone, and temperature measurements with a multi-wavelength LIDAR at Spitsbergen, *in:* Abstracts of Papers, 17th Intern. Laser Radar Conf., Sendai, Japan, 1994.

Gathen, P. von der, et al., Multi-wavelength LIDAR configurations for polar stratospheric research, *in:* Abstracts of Papers, 17th Intern. Laser Radar Conf., Sendai, Japan, July 25-29, 1994.

Godin S., et al., DIAL Ozone Algorithm Intercomparison, in preparation, 1998.

Komhyr, W., Operations Handbook - Ozone Measurements to40 km Altitude with 4A Electrochemical Concentration Cell (ECC) Ozonesondes, NOAA Technical Memo. ERL ARL-149, 1986.

Langer, J., et al., A Versatile Millimeter Wave Radiometer for Spectroscopic Measurements of Atmospheric Trace Gases, Proceedings of the XVIII Quadrennial Ozone Symp. L'Aquilla, Italy, 1996

Steinbrecht, W., et al., NDSC Intercomparison of Stratospheric Aerosol Processing Algorithms, *in:* A. Ansmann, R. Neuber, P. Rairoux, U. Wandinger, edts, Advances in Atmospheric Remote Sensing with Lidar, Springer Verlag Heidelberg, 1996.

Steinbrecht, W., et al, Results of the Ny-Ålesund Ozone Measurements Intercomparison NAOMI, this issue, 1998

Multiwavelength Measurements of Arctic Lower Stratospheric Aerosol at Eureka.

D.P. Donovan[1], J.C. Bird[1], A.I. Carswell[1], T.J. Duck[1], T. Itabe[2], T.Nagai[3], , S.R. Pal[1], O. Uchino[4],T. Shibata[5], and J.A. Whiteway[6]

[1] Center for Research in Earth and Space Technology and the Department of Physics and Astronomy, York University, 4700 Keele Street, North York, Ontario, Canada, M3J IP3.
Phone: (416) 665-5417, Fax: (416) 665-2032, e-mail: donovan@lidar.crestech.ca

[2] Communications Research Laboratory, 2-1, Nukuikita-machi 4-chome, Koganei, Tokyo 184, Japan
[3] Meteorological Research Institute, 1-1, Nagamine, Tsukuba, Ibaraki 305, Japan
[4] Japan Meteorological Agency, 3-4, Ohtemachi 1-chome, Chiyoda-ku, Tokyo 100, Japan
[5] Solar-Terrestrial Environmental Laboratory, Nagoya University, Furo-cho, Chikusa-ku, Nagoya, Aichi 464-01, Japan
[6] Now at: Department of Physics, University of Wales, Aberystwyth, Ceredigion, SY23 3BZ, UK

1 Introduction

Stratospheric aerosols play a number of important roles in the winter polar stratosphere. In particular, they play a key role in polar ozone chemistry. At temperatures below around 195 K, heterogeneous reaction probabilities associated with the "background" mainly sulphate/water aerosol greatly increase, leading to significant conversion of chlorine from inactive to active forms (Del Negro et al. 1997). At temperatures below around 193 K, the sulphate/water aerosol may grow significantly via increased absorption of HNO_3 and water (Carslaw et al. 1994) leading to polar stratospheric cloud (PSC) formation. Stratospheric aerosols can also serve as tracers of air motion. To a first approximation they are passivily carried along by the winds and as such their distribuion can often be useful in dynamical studies.

In order to study the role of stratospheric aerosols it is necessary to be able to make quantitative measurements of the aerosol size distribution. With respect to lidar measurements this implies inverting a collection of aerosol backscatter and/or extinction measurements in order to extract information about the aerosol size distribution. In general, it is not possible to extract reliable detailed size distribution information from a few lidar backscatter and/or extinction measurements (Müller and Quenzel, 1985) . However, it is possible to make reliable estimates of such quantities related to the lower moments of the size distribution namely; surface area density, volume density, and aerosol effective radius.

In this paper Priciple Component Analysis (PCA) is applied to a large time series of multiwavelength lidar measurements. The lidar measurements were made during Janurary to March of 1995 at the Eureka NDSC (Network for Detection of Stratospheric Change) observatory in the Canadian high Arctic. The work presented in this paper demonstrates the application of a recently developed extention of PSA to the case of lidar signals (Donovan and Carswell, 1997). PSA had been previously applied to the case of the SAGE II aerosol extinction measurements (Thomason and Osborn, 1992).

2 Principle Component Analysis

Here a brief overview of the theory relating to PCA as employed in this work is given. A more detailed account is given in Donovan and Carswell, 1997 (see also Twomey, 1977).

In general, the the aerosol extinction or backscatter for a wavelength of λ_i at a given altitude is given by

$$g_i = \int_0^\infty K_i(r)\frac{dV(r)}{dr}dr \qquad (1)$$

where $dV(r)/dr$ is the aerosol volume size distribution. g_i is either a backscatter or extinction measurement and K_i is the appropriate Mie backscatter or extinction kernel which is equal to $3Q_{\alpha,\lambda_i}(r)/4r$ for extinction or $3Q_{\beta_\pi,\lambda_i}(r)/4r$ for backscatter. Here N $(i = 1 \ldots N)$ is the number of extinction and/or backscatter measurements.

After applying an appropriate quadrature rule Eqn. 1 can be re-written in matrix form as

$$\bar{\mathbf{g}} = \mathbf{K}\bar{\mathbf{v}} \qquad (2)$$

where $\overline{\mathbf{g}}$ is the measurement vector and $\overline{\mathbf{v}}$ is the volume size distribution vector. A principle c omponent retrival may then used to invert Eqn. 2 to recover an estimate of $\overline{\mathbf{v}}$.

Any estimate of an intergral properity of the size distribution (such as total aerosol volume) can be expressed as a wighted sum of the elements of the size distribution vector

$$P = \overline{\mathbf{w}}^{\mathbf{t}}\overline{\mathbf{v}} \tag{3}$$

$\overline{\mathbf{w}}$ is the weighting vector for the property in question. For example, in the case of aerosol volume $w_j = 1$, for surface area $w_j = 3/r_j$ and for aerosol extinction at a given wavelength $w_j = 3Q_{\alpha,\lambda}(r_j)/4r_j$. It can be shown that Eqn. (3) can be written as

$$P = \overline{\mathbf{a}}^{\mathbf{t}}\overline{\mathbf{g}} \tag{4}$$

where

$$\overline{\mathbf{a}}^{\mathbf{t}} = \overline{\mathbf{w}}^{\mathbf{t}}\mathbf{K_t}\mathbf{U}\mathbf{L}^{-1}\mathbf{U}^{\mathbf{t}}. \tag{5}$$

where $\mathbf{U}$ is a matrix containing, as its columns, the eigenvectors of the kernal covariance matrix and $\mathbf{L}$ is a matrix containing the corresponding eigenvalues as its diagonal elements. Thus the estimated value of any integral parameter can be expressed as a linear combination of the N measurements without explicitly evaluating the size distribution ($\overline{\mathbf{v}}$). Once the coefficients (the elements of $\overline{\mathbf{a}}$) have been calculated for a given aerosol refractive index they can be stored and conveniently applied to a given data set.

In general, a given set of aerosol and or extinction measurements can often be strongly correlated. This leads to sometimes large error magnifications associated with the PCA parameter estimates. To reduce the degree of error magnification here usually only the first two lowest order component functions are retained in Eqn. 5.

In the previous discussion the size distribution was formulated in terms of the volume size distribution. In practice, it was found that by reformulating the problem in terms of the surface area size distribution it was possible to make more accurate estimates of the total surface area than by using the volume formulation alone.

3 Lidar Measurements and Observations

Two seperate lidars are located at Eureka, the AES/CRESTech Raman DIAL and the MRI/CRL Nd:YAG system. The DIAL system is designed around a XeCl laser and makes measurements of the aerosol backscatter and extinction using the elastic and Raman 'off' wavelength pair (353/385nm). The system is described in detail elsewhere (Donovan et al., 1995). The Nd:YAG system makes aerosol backscatter and depolarization measurements at both 532 and 1064 nm. The YAG system is described by Nagai et al. (1997) in detail.

Figure 1 shows an example of a set of backscatter ratio ($R = 1.0 + \beta_{\pi,aerosol}/\beta_{\pi,molecular}$) and extinction measurements made at Eureka on the night of March 04, 1995. The observations shown here were taken when the stratosphere above Eureka was within the polar vortex. This is consistent with the fact that very little aerosol was present above about the 450 K potential temperature (θ) surface. The observations shown here are an average of the night's data (typically several hours worth). Aerosol extinction effects in the backscatter retrivals were accounted for in a consistent manner by using PCA relationships to predict the aerosol extinction at 532 and 1064 nm. The temperature and density profiles used were deduced from local radiosondes which were launced at least twice daily. In order to deduce the the refractive index of the aerosol a constant water vapor mixing ratio of 5 ppm was assumed (Russel and Hamill, 1984).

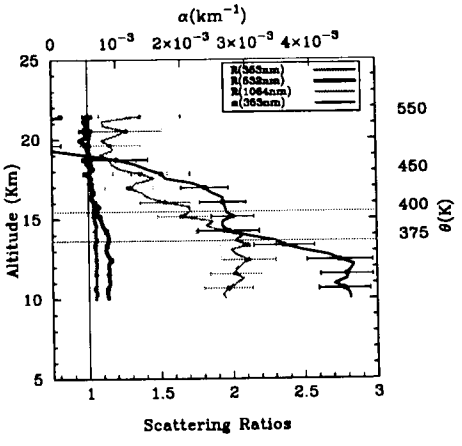


Figure 1: Lidar scattering ratios and 353nm extinction measured over Eureka March 4th, 1995.

Figure 2 shows the volume density (V), surface area density (S), and the effective radius ($3V/S$) predicted using the data shown in Figure 1. Above 450 K there is very little aerosol so it is difficult to make reliable estimates of aerosol parameters in this region. Below 400 K in the lowermost vortex and sub-vortex regions reliable estimates can be made. The error bars denote the statistical error

limits ($\pm 1\sigma$) while simulations indicate that the estimates are likely biased by no more than 30 % (Donovan and Carswell, 1997).

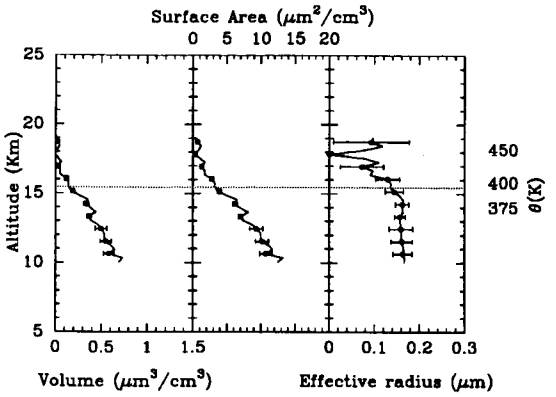


Figure 2: PCA estimates of aerosol volume, surface area, and effective radius for the data shown in Figure 1.

Unfortunatly, no other instruments to compare results with, such as optical particle counters, were operated at Eureka during the 1994/95 season. However, the results were tested for self-consistency. As mentioned previously PCA can be used to predict the optical properties of the aerosol as well as physical properties. Simulations have indicated that for aerosol size distributions where the majority of particle radii are in the 0.1-0.5 μm range that it should often be possible to predict the aerosol scattering properties at a single measurement wavelength using PCA analysis applied to the remaining measurements. Figure 3 shows a typical example of the measured aerosol scattering ratio at 532 nm compared with the scattering ratio profile predicted using PCA and the measured aerosol backscatter and extinction at 353nm together with the measured backscatter at 1064 nm. The comparision between the measured and predicted scattering ratios are typicaly good indicating that the calculations are self-consistent and that perhaps in many cases one of the backscatter measurments can be considered somewhat redundent as far as adding new information about the aerosol size distribution.

Figure 4 shows the average surface area density profiles deduced for periods where Eureka was clearly outside (Jan 20–Feb 07) or clearly inside of the polar vortex (remaining profiles). Only cases where no strong depolarization signatures were present (which would indicate the presence of non-spherical particles) were used here. Non-

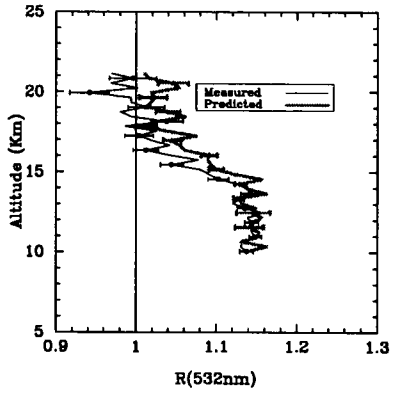


Figure 3: Comparision of the measured green backscatter ratio for 04 March 1995 and that predicted from PCA using the remaining measurements.

spherical PSC scatterers were indeed found to be present over Eureka in mid December 1994 and early Janurary 1995 (Nagai et al. 1997). The error bars in Figure 4 show the standard deviation of the average surface area density at that level. Corresponding to Figure 4, Figure 5 shows the average aerosol volume.

In Figures 4 and 5, the Jan 20–Feb 7th data were acquired when Eureka was well outside of the polar vortex, correspondingly there are significant levels of aerosol surface density present above 450 K compared to the periods when Eureka was inside of the vortex. Comparing the Jan 01–Jan 08 profile with the Mar 01–Mar 12 profile shows a substancial decrease in aerosol surface area and volume at all levels. This is likely due to the effects of diababtic descent which would tend to 'shift' the profiles downward (Rosenfield et al. 1994) and possibly aerosol sedimentation.

4 Summary

The application of PCA to the Eureka lidar systems has enabled us to make estimates of the lower stratospheric liquid aerosol bulk physical properties. Because of the low amount of aerosol above 450 K within the polar vortex it is hard to comment reliably on the aerosol physical characterists above this level. However, the Eureka data are useful in studying the morphology of the stratospheric aerosol within the lowermost vortex (where ozone destruction still occurs) and sub-vortex regions.

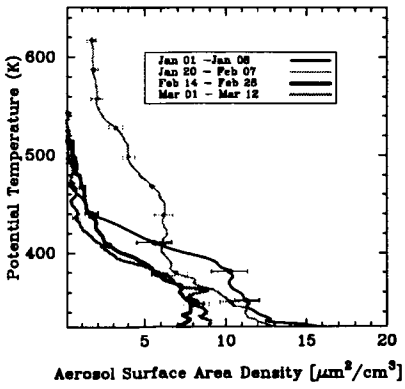


Figure 4: PCA estimated aerosol surface area density measured througout the first few months of 1995.

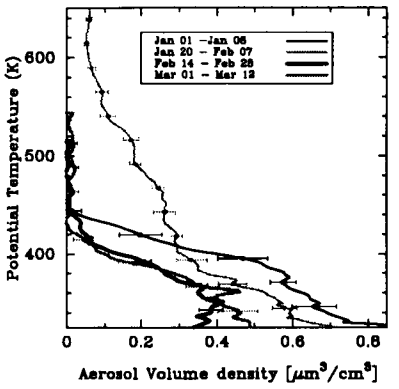


Figure 5: PCA estimated aerosol volume density measured througout the first few months of 1995.

The interpretation of the Eureka multiwavelength data for the 1994/95 season is still ongoing. Lidar PCA estimates have not yet been compared directly with in-situ sensors. However, the results using actual data are self-consistent and are consistent with previous simulation studies. Moreover, the PCA results in the context of SAGE II aerosol extinction measurements have been shown to agree well with other sensors (Yeu et al. 1995).

Acknowledgments

Financial and technical support was provided by CRESTech and by the Canadian Atmospheric Environment Service. The financial support of the Science and Technology agency of Japan is also greatfully acknowledged.

References

Carslaw, K.S. et al., Stratospheric aerosol growth and HNO_3 gas phase depletion from coupled HNO_3 and water uptake by liquid particles, *Geophys. Res. Letts., 23*, 2479-2482, 1994.

Donovan D.P. and A.I. Carswell, Principle component analysis applied to multiwavelength lidar aerosol backscatter and extinction measurements, *Appl. Opts. 36*, 9406–9424, 1997.

Donovan D.P., J.C. Bird, J.A. Whiteway, T.J. Duck, S.R. Pal, and, A.I. Carswell, Lidar Observations of Stratospheric Ozone and Aerosol above the Canadian High Arctic During the 1994-95 Winter, *Geophys. Res. Letts., 22*, 3489-3492, 1995.

Del Negro L.A. et al., Evaluating the role of NAT, NAD, and liquid $H_2SO_4/H_2O/HNO_3$ solutions in Antarctic polar stratospheric cloud aerosol: Observations and implications, *J. Geophys. Res., 102*, 13225-13282, 1997.

Müller H. and H. Quenzel, Information content of multispectral lidar measurements with respect to the aerosol size distribution, *Appl. Opts. 24*, 648–654, 1984.

Nagai T., O. Uchina, T. Itabe, T. Shibata, K. Mizutani, and T. Fujimoto, Polar stratospheric clouds observed at Eureka (80°N, 86° W) in the Canadian Arctic during the 1994/95 winter, *Geophys. Res. Letts., 24*, 2243–2246, 1997.

Rosenfield J.E., P.A. Newman, and M.R. Schoeberl, Computations of diabatic descent in the stratospheric polar vortex, *J. Geophys. Res. 99*, 16677-16689, 1994.

Russell P.B. and P. Hamill, Spatial variation of stratospheric aerosol acidity and model refractive index: Implications of recent results, *J. Atmos. Sci., 41*, 1781-1790, 1984.

Thomason L.W. and M.T. Osborn, Lidar conversion parameters derived from Sage II extinction measurements, *Geophys. Res. Letts., 19* 1655–1658, 1992.

Twomey S.A., *Introduction to the mathematics of inversion in remote sensing and indirect measurements*, (Elsevier Scientific Publishing Co., New York, 1977.

Yeu, G.K., L.W. Thomason, L.R. Poole, P.-H. Wang, D. Baumgardner, and J.E. Dye, Aerosol surface areas deduced from early 1993 SAGE II data and comparisons with stratospheric photochemistry, aerosols, and dynamics expedition measurements, *Geophys. Res. Letts. 22*, 2933–2936, 1995.

Japanese Mesopause Physics Program with a Sodium Temperature Lidar at Syowa Station, Antarctica

T.D.Kawahara, A.Nomura, T.Kitahara, F.Kobayashi and Y.Saito
Shinshu University, 500 Wakasato, Nagano, 380-8553, Japan
Phone:+81-26-226-4101, Fax: +81-26-223-4723, e-mail: kawahara@cs.shinshu-u.ac.jp

1. Introduction

Physics and chemistry of mesopause region are thought to be complex and interesting. Recently, experimental approach to this region with sodium or potassium temperature lidars have been carried out and a lot of important results are reported (von Zahn *et al.*, 1996; She *et al.*, 1994). Though the temperature lidar technique is quite powerful to probe the mesopause region, no observation has been conducted over Antarctic stations because the systems are quite large and need continuous maintenance. Newly developed sodium temperature lidar based on injection-seeded Nd:YAG lasers will start observation at Japanese Syowa station, Antarctica, from 1999. This paper presents an overview of the Japanese Antarctic physics program and the sodium temperature lidar system.

2. Antarctic Physics Program with the Lidar

The 5 year observation campaign of Japanese Antarctic Research Expedition started at Syowa Station (60°00'S, 39°35'E) from 1996. The main objective of this campaign is to study the energetic coupling processes between the upper mesosphere and the lower thermosphere through the mesopause region over Antarctica. During this campaign, the sodium temperature lidar measurements are programed from 1999 to 2001. The lidar measures the vertical structure of temperature and sodium density variation in the height region from 85 km to 105 km. Daytime (summertime) observation is also carried out with an extremely narrowband Faraday filter. Further, HF and MF radars, a Fabri Perot Doppler imager and several kinds of auroral imagers will be cooperatively operated (see Fig.1). These radar and optical measurements are complementary with each other, and combined observations of them are expected to give us useful data set for better understandings of polar middle atmosphere.

3. Temperature Measurement Technique and the Lidar System

Our temperature measurement technique is the same as that of Bills *et al.* (1991). Because the D_{2a} peak and the intermediate minimum between the D_{2a} and D_{2b} peaks are particularly sensitive to temperature, the ratio of the minimum to the peak can be used to accurately derive the sodium temperature. By collecting lidar photocount profiles with a narrowband lidar at each of these two wavelengths, then taking the ratio of the photocounts collected at each altitude, one can derive the vertically resolved temperature structure throughout the sodium layer region.

One of the interesting coincidence of nature is that the sum frequency of two appropriately tuned Nd:YAG lasers near 1064 nm and 1319 nm can generate resonant wavelength of the sodium D_2 transition (589.158 nm). Using non linear optical crystals such as Lithium Triborate (LBO) or Barium Borate (BBO), 589 nm pulse laser can be generated from the two wavelengths of the Nd:YAG lasers. To make the spectral width narrow and to tune the wavelength finely, seed lasers for the each infrared wavelengths are necessary. The injection seeding technique is much superior to that using etalons because of no energy loss. Chiu *et al.* (1994) built the transmitter with injection-seeded Nd:YAG lasers with the LBO crystal. The spectral linewidth was quite narrow, less than 100 MHz (0.1 pm), which is enough for the temperature observation from the Doppler broadened sodium D_2 cross section (~3 pm). Our transmitter is basically following the Chiu's system and constructed in HOYA Continuum, Inc.

Fig. 2 shows an overall layout of the lidar system. Two seed lasers are used to characterize the spectral

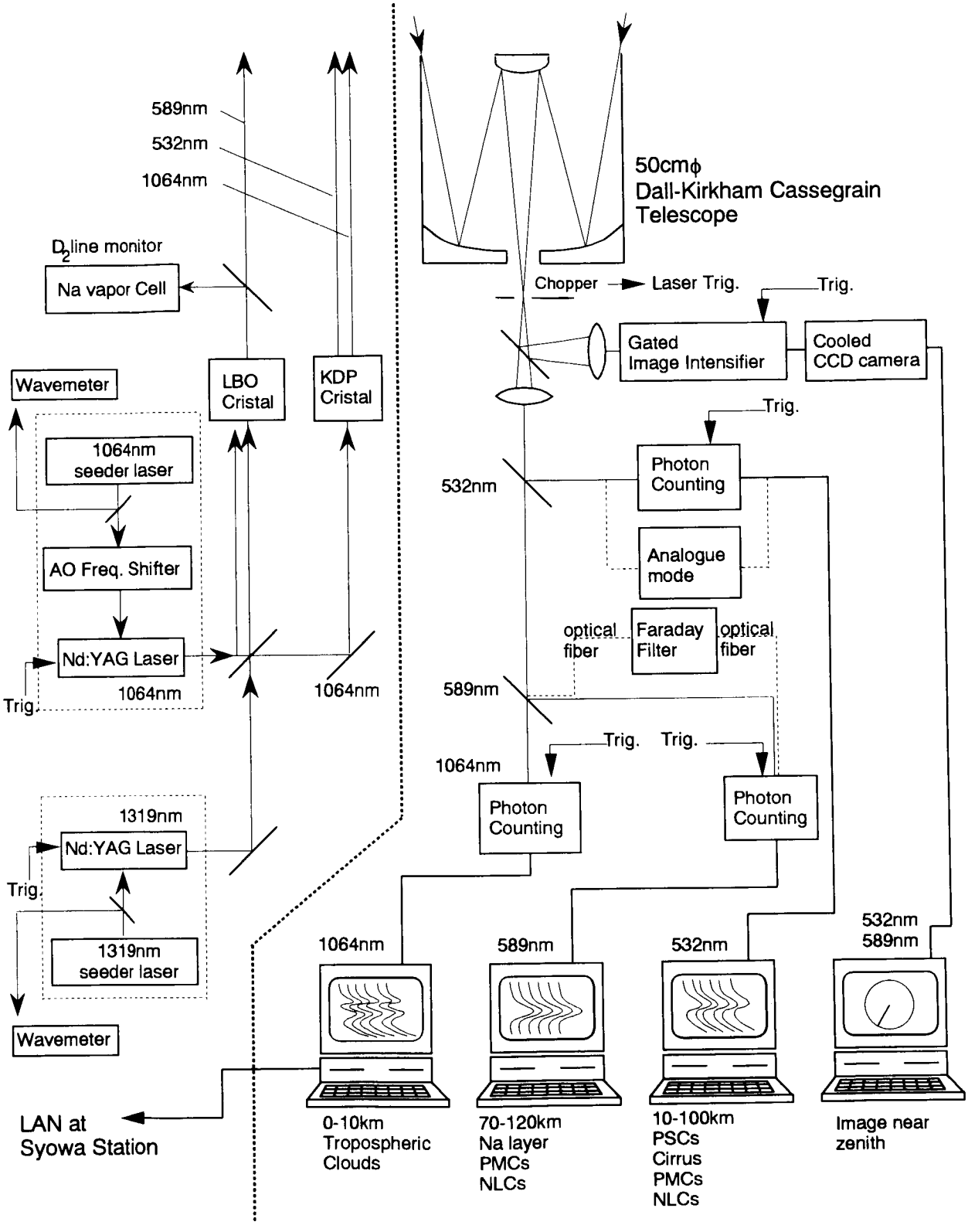


Fig.1 Schematic diagram of the sodium temperature lidar system.

profiles of the laser pulses. The laser can be tuned to the sodium D_{2a} resonance peak by monitoring resonance scattered light intensity from the sodium vapor cell. For the switching of the frequency between the D_{2a} peak and the minimum between the peaks (about 850MHz), an AO frequency shifter (N17425, Neos) is used in the laser line of the 1064 nm seed laser. The retro-reflected seed laser goes through a +425 MHz AO driver again and the frequency is finally shifted by +850 MHz. In the actual operation, for example, 10 second accumulation at each frequency may be repeated to obtain one temperature profile and after totally 10 minute accumulation, a ten minute averaged temperature profile is calculated and saved to a computer. This procedure can make less error caused by even a short period temporal variation of the mesospheric temperature. Together with 589 nm, the transmitter also emits 1064 nm and 532 nm laser pulses for the observation of polar stratospheric clouds or cirrus. The 532 nm channel is used as a Rayleigh lidar to obtain temperature profiles between 35 - 60 km height.

Scattered light is collected by a 0.5 m diameter Dall-Kirkham Cassegrain telescope (Kiyohara Optical Lab.) by pulse to pulse shot. The light is focused through a field stop iris and collimated by a lens. After separated by dichroic mirrors, the light passes through an interference filter centered at the each laser wavelength and is photocounted by a cooled low-noise photomultiplier tube (R943-02, Hamamatsu Photonics Co.). The PMT pulse current is processed to produce digital pulsescorresponding to each photon received, and these pulses are counted over 96 m range intervals by Multichannel Scaler (SR430, Stanford Research Systems, Inc.). The MCS integrates the range-gated photocounts over many laser pulses to generate photocount profiles. For the 589 nm channel for the temperature measurement, a couple of MCSes

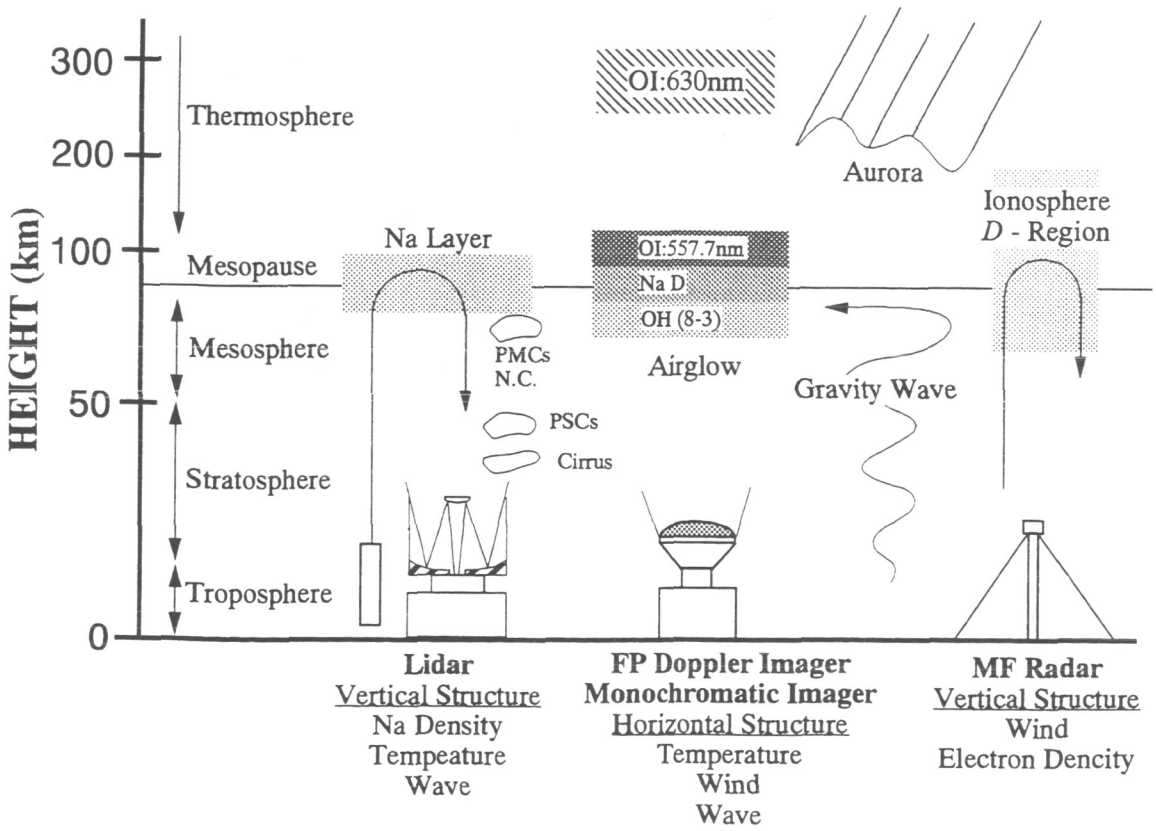


Fig. 2 Schematic drawing of observational height region with optical instruments and an MF radar at Syowa station.

are independently used for the integration at the original and shifted frequency. The profile data are transferred to a computer to display real-time A-scope and for further processing. All the system is controlled by personal computers through GPIB interface. The PMT is gain switched to prevent saturation by the strong returns below 15 km. Further, because the strong scattered light gives damage to the photoelectric surface of the PMT, the low altitude returns (< 10 km) are masked by an optical chopper. The chopper also gives laser trigger timing. A cooled CCD camera (CV-04, Mutoh) images zenith direction to align the axes of the telescope and the laser beams easily.

A fiber coupled dispersive sodium Faraday filter is installed for the daytime observation of mesospheric temperature. A Colorado State University group has already fabricated the Faraday filter and made successful wind/temperature observations in daytime and nighttime (Chen *et al.*, 1993; Chen *et al.*, 1996). The FWHM transmission of the filter is quite narrow, 2 pm which is comparable to the width of sodium D_2 resonance spectrum of 3 pm and the peak transmission is quite high, 86%. Sky background light is effectively rejected to 2×10^{-5}. The Faraday filter consists of a temperature controlled (~170°C) sodium vapor cell (ϕ25mm, l = 25mm, Opthos Instruments, Inc.) between a pair of crossed polarizers (03PTH403/A, Melles Griot), and rare-earth magnets which make a strong axial magnetic field in the cell position. Because of Faraday rotation and Zeeman effect, near sodium resonance light is alternatively pass through the crossed polarizers. Since strong magnetic field of ~1800 G is achieved, the Faraday filter is connected with optical fiber cable and placed away from the PMTs. The Faraday filter enables us to make summertime observations as well as wintertime observations with HF and MF radars and is expected to reveal seasonal variations of mesospheric temperature and wind.

4. Conclusion

We presented in this paper the sodium temperature lidar system and the future lidar observation plan at Syowa Station, Antarctica. The daytime and nighttime temperature observations will be the first ever made of the mesopause region in Antarctica. The injection-seeded Nd:YAG laser base transmitter is newly developed for the sodium D_2 resonant wavelength. It is a reliable and easily operated system for the continuous observation. Moreover, the combined operation with MF and HF radar and other optical instruments at Syowa Station would provide us invaluable information about atmospheric dynamics in vertically and horizontally wide spatial area.

Acknowledgment

It is our great pleasure to thank Prof. C.S.Gardner of University of Illinois and Prof. C.Y.She of Colorado State University for their useful comments and discussions.

References

Bills, R.L., C.S. Gardner and C.Y. She (1991): Narrowband lidar technique for sodium temperature and Doppler wind observations of the upper atmosphere, Opt. Engineering, **30**, 13-21.

Chen, H., C.Y. She, P. Searcy and E. Korevaar (1993): Sodium-vapor dispersive Faraday filter, Opt. Lett., **18**, 1019-1021.

Chen, H., M.A. White, D.A. Krueger and C.Y. She (1996): Daytime mesopause temperature measurements with a sodium-vapor dispersive Faraday filter in a lidar receiver, Opt. Lett., **21**, 1093-1095.

Chiu, P.H, A. Magana, and J. Davis (1994): All solid-state single-mode sum frequency generation of sodium resonance radiation, Advanced Solid-State Lasers, **20**, 367-371.

She, C.Y. and J.R. Yu (1994): Simultaneous three-frequency Na lidar measurements of radial wind and temperature in the mesopause region, Geophys. Res. Lett., **21**, 1771-1774.

von Zahn, U., J. Hoffner, V. Eska and M. Alpers (1996): The mesopause altitude: only two distinctive levels worldwide?, Geophys. Res. Lett., **23**, 3231-3234

The Purple Crow Lidar at the University of Western Ontario

P.S. Argall, R.J. Sica, A.R. Russell, O.N. Vassiliev, C.R. Bryant
Department of Physics and Astronomy,
The University of Western Ontario,
London, Ontario, Canada, N6A 3K7
Phone (519) 661-2111 x6509, Fax (519) 661-2033, Email sargall@lucille.physics.uwo.ca

Introduction

The Purple Crow lidar (PCL) is a high power-aperture product lidar that is used for lower and middle atmospheric studies. The PCL utilizes Rayleigh, Raman and sodium-resonance fluorescence scattering to measure atmospheric parameters from a few kilometers to over 100 km in altitude.

This presentation will give a description of the instrumentation, focusing on some of the unique features of the PCL and present result obtained with this instrument.

The PCL transmitter is a 12 W frequency-doubled Nd:YAG and a 1.2 W tunable pulse-dye-amplifier (PDA). The YAG is used for mesospheric and stratospheric Rayleigh temperature measurement as well as tropospheric and lower stratospheric vibrational Raman-water-vapor measurements. The PDA is used to obtain measurements of the temperature in the mesosphere utilizing the sodium resonance fluorescence technique. The PCL utilizes a 2.65 m diameter liquid mirror telescope as the collector for the detector system.

Instrumentation

Transmitter

The PCL transmits two laser beams into the sky. The more powerful of these is the 20 Hz, 12 W injection-seeded, frequency-doubled YAG that provided the light source for the Rayleigh and water vapor systems.

The transmitter used for the sodium system consists of a tunable ring-dye-laser that is pumped by an Ar^+ laser. This ring laser is used to "seed" a pulsed dye amplifier which is pumped by a 12 W injection-seeded frequency doubled YAG. The maximum average output power of the PDA is 1.8 W at Pulse repetition frequency of 20 Hz.

Both laser beams are transmitted into the sky coaxial with the field-of-view of the detector system. This arrangement ensures that the laser beams are fully contained within the field of view of the detector system at all altitudes.

Telescope

The large power aperture product of the PCL is due in large part to the large liquid mirror telescope (LMT). A LMT in its simplest form consists of a spinning dish with a thin layer of mercury covering the surface. The rotation of the dish naturally forms a parabolic surface on the liquid mercury. The LMT technology is being developed[1] principally by a group at Universite Laval headed by Dr. Borra. The development of LMT's has been mainly for astronomical use. However, our experience over more than five years has shown the value and advantage of using an LMT as a part of a lidar. LMT's can be produced at a fraction of the cost of conventional glass telescopes of the same size.

A major limitation of the LMT technology is that it is difficult to use the telescope to view off-zenith. Many other lidar systems are imposed with the same zenith pointing restriction due to the difficulty in maintaining the alignment between the transmitted laser beam and the field-of-view of the detector system when changing viewing direction.

A high speed rotating shutter is used to block the low level high intensity returns for both the Rayleigh and sodium systems. The PCL data collection system uses photon counting to record the intensity of the backscattered light. Due to the high power-aperture product of the Purple Crow Lidar, significant counting losses occur in the data collection system of the Rayleigh channel at altitudes below about 45 km. The efficiency of the data collection system has been measured as a function of input light intensity and so this inefficiency can for the most part be corrected.

Rayleigh Scatter Lidar

The PCL Rayleigh system has been in routine operational since the summer of 1994. Since that time temperature profiles have been measured on approximately 100 nights. The length of these data set varies from about one hour up to twelve or more hours. Most of these measurements have been made between late spring to early fall due mainly to local weather conditions. Some of the

more interesting temperature profiles, those which show significant variations from models such as CIRA or MSIS, can be seen in the limited winter measurement that have been made.

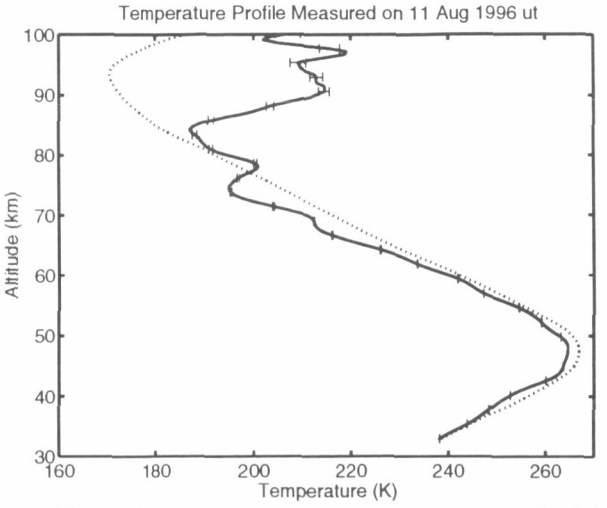


Figure 1. The average temperature measured with the PCL Rayleigh lidar between 1:35 and 9:10 UT. The densities were coadded to 240 m and smoothed with a 5 point filter before the temperatures were calculated. The temperature retrieval algorithm was started at 108 km. The dotted line shows the MSIS temperatures for comparison.

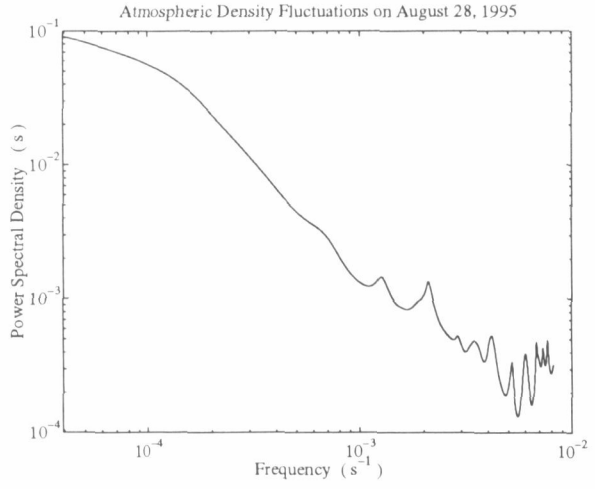


Figure 2. Average power spectral density from 32.5 to 37.6 km calculated from PCL Rayleigh scatter density fluctuation measurements between 2:44 to 9:45 UT on 28 August 1995. The density fluctuations were obtained from 1 minute scans which had a height resolution of 48 m and were smoothed with a digital filter of 1000 m bandwidth. Note the excess of energy past the measured buoyancy frequency, which is 2.7 x 10^{-3} s^{-1}.

On average temperature profiles for the summer months are a few degrees Kelvin cooler than predicated by the MSIS model from 30 km up to about 80-85 km (figure 1). At higher altitudes the monthly average Rayleigh lidar temperature profiles are much warmer than those for the model, up to 25 K. This difference is in agreement with sesonally averaged sodium lidar measurement from other locations.[2]

The lidar has been used for the study of super adiabatic lapse rate in the middle atmosphere (Figure 2; Sica et. al.[3&4]). These studies have shown "whitecaps" in the atmosphere due to the passage of gravity waves through the atmosphere. Indications of seasonal variations of the regions is also evident.

The high temporal-spatial resolution measurements of density fluctuation can be used to study the spectrum of gravity waves. An example of a temporal spectrum from the upper stratosphere is shown in Figure 3. Spatial and temporal spectra are being used to study the intermittancy of the spectrum as well as the energy deposited by gravity waves in the middle atmosphere[5&6].

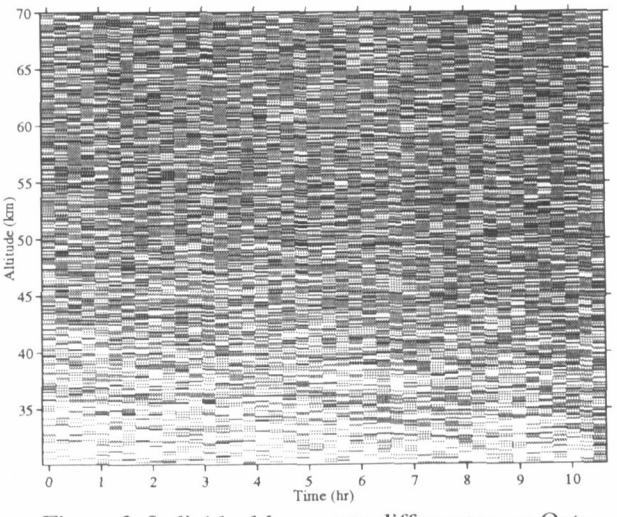


Figure 3. Individual lapse rate differences on October 17, 1995. Positive regions are white, indeterminate regions are grey and negative regions black. Zero time on ordinate is 2009 EDT.

Sodium Lidar

The PCL sodium system is used to measure the temperature in the mesosphere sodium layer. This temperature measurement is achieved by determining the spectral width of the resonance scatter from the sodium atoms in this layer, as described by Bills et. at.[7] and She et. al.[8]

In order to determine the spectral width of the light

backscattered from the sodium atoms the laser is alternately tuned to two very precisely determined wavelengths within the sodium D_2 line. The backscattered intensities are then measured at these two wavelengths. The ratio of these intensities is equal to the ratio of the scattering cross-sections at the two wavelengths, which is a function of temperature. This enables temperature measurement using this two-wavelength technique.

For the practical application of this technique it is necessary to tune the transmitted laser wavelength alternately, quickly and with high precision to two well known wavelengths within the sodium D_2 line. This is achieved by actively locking the laser wavelength to the sharp spectral features obtained using a technique known as Doppler-free-saturation spectroscopy. This technique uses a cell containing sodium vapor and two counter propagating beams of light derived from the same tunable laser. If the intensity of the beams is selected appropriately for the density of vaporized sodium atoms in the cell, sharp spectral features can been seen in the fluorescence from the cell. Figure 4 shows a measurement a spectra containing these Doppler-free features. The Doppler-free-features are sharp enough and spaced appropriately so that they allow tuning of the laser as required for atmospheric temperature measurement. (Also see the paper by Vassiliev et. al. in this volume.)

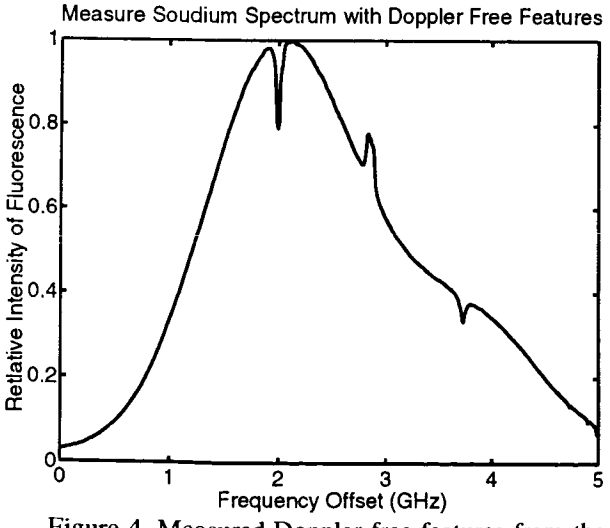


Figure 4. Measured Doppler-free features from the sodium cell which forms part of the PCL sodium lidar transmission system.

Water Vapor

The third part of the PCL is the tropospheric water vapor systems. The water vapor system uses the same 12W, 532nm transmitted laser beam as the Rayleigh temperature system and the same 2.65m diameter LMT. Water vapor mixing ratios can be determined by measuring the Raman component of the backscatter from both nitrogen and water vapor molecules and taking the ratio of these two measurements as described by Melfi et al[9]. (Also see the paper by Bryant et. al. in this volume.)

Initial measurements (figure 5) have been made using this system and these have been compared to radiosonde measurements and shown good agreement.

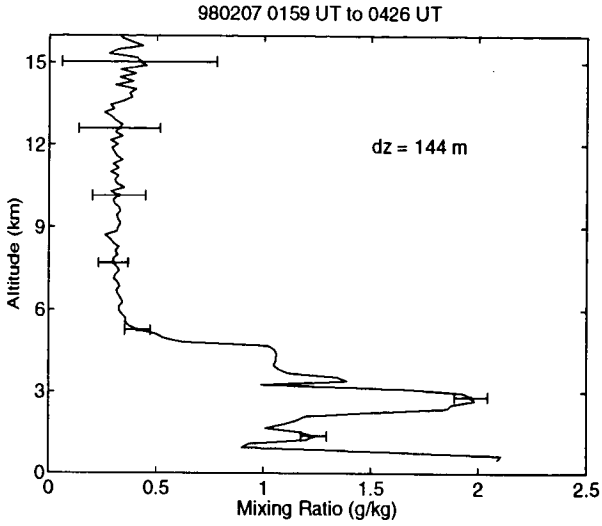


Figure 5. Water vapor mixing ratio profile measured using the PCL.

It is expected that the PCL water vapor system will have to ability to measure water vapor profile up to at least the tropopause with temporal and spatial resolution adequate to measure tropospheric-stratospheric exchange processes using water vapor as a tracer.

Future

Further work on this system is required in order to make these water-vapor-mixing-ratio profiles on a routine basis. Current work on a detector system upgrade will give an increase in the efficiency of the detector system by about a factor of 2 and will also allow all three parts of the PCL, Rayleigh, sodium and water vapor, to operate simultaneously.

The simultaneous operation of these thee system will allow a large improvement in the measurement of atmospheric temperature profiles. The sodium system measures temperature profiles from about 85 to 105 km. These temperatures can then be used to "seed" the temperature retrieval algorithm for the Rayleigh temperatures. This will eliminate the usual uncertainty inherent in this type of temperature measurement. The lower limit of the Rayleigh temperature profiles is abut 30km.

This limit is imposed by the ability of the detection system to adequately cope with the larger number of photons being detected from below this altitude. Below 30 km the Raman component of the backscatter from nitrogen molecules can then be used to extend these temperatures profiles down to approximately the altitude of the tropopause. Again, the Rayleigh scatter temperatures can be used to seed the vibrational-Raman-scattering temperatures.

Conclusion

The Purple Crow Lidar (PCL) is routinely used to measure temperature profiles throughout the stratosphere and mesosphere using the Rayleigh lidar technique. The data set for the measurements starts in the summer of 1994 and contains temperature profiles from approximately 100 nights.

Both sodium resonant fluorescent and Raman water vapor measurement have been demonstrated with the PCL. The implementation of these measurements on a routine basis along with planned improvements instrumentations will make the PCL a powerful tool for study of atmospheric dynamics and thermodynamics.

Acknowledgments

We would like to thank the Canadian National Science and Engineering Research Council (NSERC), the Atmospheric Environment Service (AES) and the Center for Research in Earth and Space Technology (CRESTech) for their support of this work.

References

1. Borra E.F. "Liquid Mirrors" Scientific American February 1994, 76

2. She, C.Y., J.R. Yu, and H. Chen, "Observed thermal structure of a midlatitude mesopause", Geophys. Res. Lett., **20**, 567-570, 1993.

3. Sica, R.J., and M.D. Thorsley, "Measurements of intermittency in the upper stratosphere and mesosphere", in "Gravity Wave Process Their Parameterization in Global Climate Models". Hamilton, K. (Ed.), Springer-Verlag, New York, NATO ASI Series, Vol I 50: 27-44, 1997.

4. Sica, R.J., and M.D. Thorsley, "Measurement of superadiabatic lapse in the middle atmosphere", Geophy. Res. Lett., **23**, 2797-2800, 1996.

5. Sica, R.J., and A.R. Russell, "Measurement of the effects of gravity waves in the middle atmosphere using parametric models of density fluctuations. 1: Vertical wavenumber and temporal spectra.", J. Atmosph. Sci. (submitted).

6. Sica, R.J. "Measurement of the effects of gravity waves in the middle atmosphere using parametric models of density fluctuations. 2: Energy dissipation and eddy diffusion.", J. Atmosph. Sci. (submitted).

7. Bills, R.E., C.S. Gardner, and C.Y. She, "Narrowband lidar technique for sodium temperature and Doppler wind observations in the upper atmosphere," Opt. Eng., **31**, 13-21, 1991.

8. She, C.Y., J.R. Yu, H. Latifi, and R.E. Bills, "High-spectral-resolution fluorescence light detection and ranging for mesospheric sodium temperature measurement," Appl. Opt., **31**, 2095-2106, 1992.

9. Whiteman, D.N., S.H. Melfi, and R.A. Ferrare, "Raman lidar system for the measurement of water vapor and aerosols in the Earth's atmosphere," Appl. Opt., **31**, 3068-3081, 1992.

The Purple Crow Sodium Resonance Fluorescence Lidar

O.N.Vassiliev, P.S.Argall, M.Mwangi, and R.J.Sica

Department of Physics and Astronomy, The University of Western Ontario
London, Ontario, N6A 3K7, Canada
Phone: (519)661-3521, FAX: (519)661-2033, E-mail: sica@physics.uwo.ca

1. Introduction

Narrowband sodium lidar systems have been shown to provide high resolution temperature profiles for the upper mesosphere and lower thermosphere [*Fricke et al., 1985, Gardner et al.,* 1989, *She et al.,* 1992].

The lidar at the University of Western Ontario uses the two-frequency technique for measurement of the temperature. The technique is based on the fact that Doppler broadening makes the cross section of Na D_2 transition a sensitive function of temperature. The lidar transmitter can be tuned to two frequencies: f_a near the D_{2a} resonance, and f_c near the midpoint between the D_{2a} and D_{2b} transitions. This choice of the frequencies is optimal in terms of the accuracy of transmitter tuning and temperature retrieval. The temperature is determined from the ratio of the fluorescence signals registered at the two frequencies.

2. Lidar description

The lidar is located at the Delaware observatory ($42°52'N, 81°23'W$), ~30 km southwest of London, Ontario.

The transmitter frequency is determined by a tunable ring-dye laser. A small fraction of the beam is forwarded to an intensity stabilizer and then split into two beams so that to illuminate a sodium vapour cell by two counter-propagating overlapping beams. The fluorescence spectrum of the cell then exhibits the Doppler-free features. The fine structure of the features provides a reference for the laser tuning and for absolute calibration of its frequency. The fluorescence signal from the cell is monitored continuously and processed by a computer that controls laser parameters to lock it at the required frequency. Switching from one of the two frequencies to another takes about 5 s.

A greater fraction of the beam is forwarded to a pulse dye amplifier. The latter is pumped by a powerful Nd:YAG laser (600 mJ/pulse at 20 Hz). The amplified beam is directed vertically to the sky. A small fraction of the outgoing beam is forwarded to a spectrum analyzer, that provides the measurement of the output beam shape necessary for the temperature retrieval.

The axis of the outgoing beam coincides with the optical axis of a 2.65-m-diameter liquid mirror. Fluorescence photons emitted by the atmospheric sodium and collected by the mirror are registered by a photomultiplier. The signal from the photomultiplier is processed using a multichannel scaler-averager. A complete description of the receiver is given elsewhere [*Sica et al.,* 1995].

3. Determination of Absolute Transmitter Frequency

Parameters of the Na D_2 hyperfine transitions are well known. However, the fine structure of the Doppler-free features depends on the actual system set-up. For this reason a theoretical calculation of the fluorescence spectrum can improve significantly the accuracy of the transmitter frequency calibration and, as a result, the accuracy of the measured temperatures. It has been estimated that the corresponding contribution to the total uncertainty can be reduced from 1-2 K to 0.2-0.4 K using the model to be described.

To calculate the spectrum we use a procedure based on a model by *Papen et al.* [1995] that takes into account excitation, relaxation, stimulated emission of six major transitions of the Na D_2 doublet and motion of atoms across the area illuminated by the beam. Fig. 1 and 2 show comparisons between the calculated and measured spectra at frequencies near f_a and f_c respectively. Some differences in the amount of fluorescence can be attributed to the model limitations discussed by *Papen et al.* [1995]. Beam frequency and intensity fluctuations as well as magnetic fields in the vicinity of the cell can also contribute to the calculation uncertainties. However, the most important quantity, the location of the features, is particularly stable with respect to reasonable variations in the system

parameters. Variations in calculated frequencies f_a and f_c are less than 2-4 MHz.

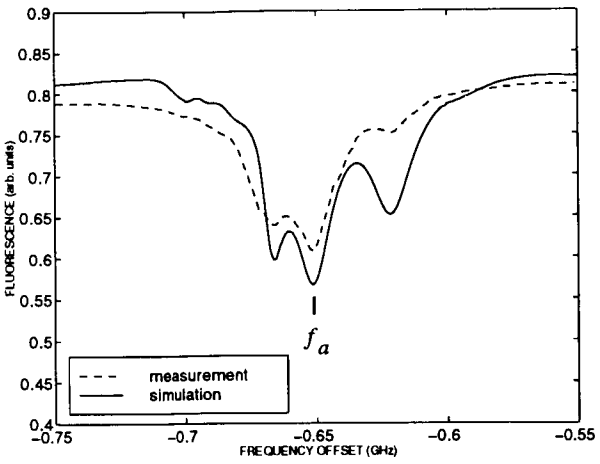


Figure 1. Fine structure of the sodium cell fluorescence spectrum near the frequency f_a . The vertical bar indicates the locking position used by the lidar control software.

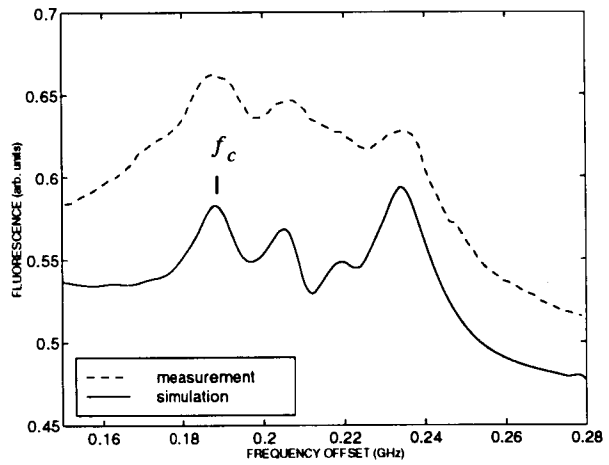


Figure 2. Fine structure of the sodium cell fluorescence spectrum near the frequency f_c . The vertical bar indicates the locking position used by the lidar control software.

4. Observation data

The sodium temperature lidar is presently making its initial measurements which are currently being analyzed. A representative sodium density profile is shown in Fig. 3. The data were acquired during the night of March 6, 1998. The profile is the average of 23 scans of 30s duration at the frequency f_a. Each of the scans was converted to a density profile with 48-m height resolution and was low-pass filtered with a bandwidth of 1 km. Estimated photocount uncertainty for the shown profile is less than 3% in the region 85-98 km. The profile generally agrees with the similar data reported by *Gardner et al.* [1989].

Fig. 3 also shows the RMS magnitude of the density variations during the observation period. The variations have the time scale of tens of minutes and may be associated with gravity wave activity. The study of gravity waves and related phenomena in this region of the atmosphere is the intended focus of the lidar operation.

The temperature retrieval procedure is currently being tested using the real observation data. More comprehensive data, including observed temperature profiles, will be presented in our talk.

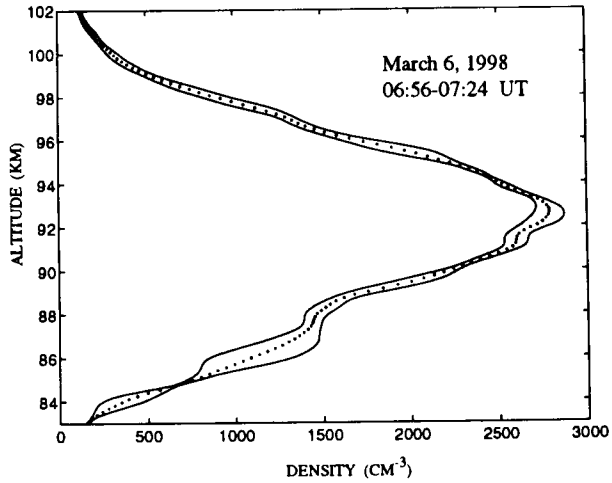


Figure 3. Average sodium density profile (dotted line) and RMS variations in the density (solid lines) during the observation period.

5. Summary

The Purple Crow sodium resonance fluorescence Lidar has started acquiring measurements which will allow routine high resolution studies of the temperature and sodium density in the middle atmosphere. In preparation is a modification of the transmitter that allows tuning to additional two frequencies for simultaneous measurements of the wind velocity.

6. Acknowledgments

We would like to thank the Natural Science and Engineering Research Council of Canada for their support of the project.

You can learn more about the Purple Crow Lidar on our web page:

http://pcl.physics.uwo.ca/

References

Fricke, K.H., and von Zahn, U. (1985). Mesopause temperature derived from probing the hyperfine structure of the D_2 resonance line of sodium by lidar. *J. Atmos. Terr. Phys.*, **47**, 499-512

Gardner, C.S., Senft, D.C., Beatty, J., Bills, R.E., and Hostetler, C.A. (1989). Rayleigh and sodium lidar techniques for measuring middle atmosphere density, temperature and wind perturbations and their spectra. In *World Ionosphere/Thermosphere Study Handbook*, (Scientific Committee on Solar Terrestrial Physics, Urbana, Ill.) Vol.2, Chap. 6

Papen, G.C., Pfenninger, W.M., Simonich, D.M. (1995). Sensitivity analysis of Na narrowband wind-temperature lidar systems. *Appl. Opt.* **34**, 480-498

She, C.Y., Yu, J.R., Latifi, H., and Bills, R.E. (1992). High-spectral-resolution fluorescence light detection and ranging for mesospheric sodium temperature measurements. *Appl. Opt.* **31**, 2095-2106

Sica, R.J., Sargoytchev, S., Argall, P.S., Borra, E.F., Girard, L., Sparrow, C.T., and Flatt, S. (1995). Lidar measurements taken with a large-aperture liquid mirror. 1. Rayleigh-scatter system. *Appl. Opt.* **30**, 6925-6936.

Rayleigh Lidar Observations of Temperature and Gravity Waves in the Middle Atmosphere

S. P. Namboothiri, N. Sugimoto, H. Nakane, and I. Matsui
National Institute for Environmental Studies
16-2 Onogawa, Tsukuba, Ibaraki 305, Japan
Phone: 81-298-50-2393, FAX: 81-298-51-4732, E-mail: nambooth@nies.go.jp

Y. Murayama
Communications Research Laboratory, Koganei, Tokyo 184, Japan

1. Introduction

Lidar technique has been used for atmosphere probing for many years and proved itself as an excellent technique for investigating the middle atmosphere. By making use of a variety of scattering and absorption processes it is possible to obtain a great deal of information about the atmosphere, its constituents and their changes in both time and space (eg., Chanin and Hauchecorne, 1981; Hauchecorne and Chanin, 1983; Shibata et al., 1986). Lidar, in addition to its important DIAL measurement of ozone and other trace gas concentration in the atmosphere, measurements of density and temperature at the altitude range 30-65 km, in particular, have provided immense information of this region, which is known as the gap region. Even high powered radars are blind to this region and balloon, rocket, and satellite observations were the main sources of information of this region. However, these datasets showed many discrepancies and suffered deficiencies due to poor vertical resolution and sporadic nature of the observations. To this respect Rayleigh lidar complements to the other techniques; it is capable to make measurements of a number of the atmospheric parameters with excellent space and time resolution.

Density and temperature profiles are widely used to study phenomena such as tides, planetary and gravity waves, sudden warmings and chemical equilibria (Chanin and Hauchecorne, 1981; Gardner et al., 1989; Hauchecorne and Chanin, 1982; Whiteway and Carswell, 1994; Wilson et al., 1991). The ozone lidar observation at the National Institute for Environmental Studies (NIES) is continuing on routine basis, providing high quality data on the ozone concentration, aerosol, and neutral air density. Density measurements are used to calculate the temperature in the 30-70 km height region. In the present study data collected for 33 nights during the winter seasons of 1995 and 1996 have been used to study the winter thermal structure over Tsukuba (36°N). First, an effort has been taken to validate the temperature profiles with other observations/models. Temperature profiles are further used to study the dominant gravity wave activity in the height region.

2. Technical Summary and Methodology

NIES ozone lidar system is comprised of two subsystems, a low altitude system (LA) for the troposphere observation and a high altitude (HA) system for the stratosphere and mesosphere. In the present use of high altitude sounding the system employs the XeCl and XeF excimer lasers to emit light with wavelengths of 308, 339 and 351 nm, and a receiving telescope with a diameter 2m. The laser beam at each wavelength is detected by photomultiplier (PMT) tubes which are used for high sensitivity and low sensitivity channels to maintain a wide dynamic range of detectable signal. To avoid strong background echoes, which results in a saturation of PMTs and signal induced noise, the HA system is equipped with a mechanical chopper rotating at a frequency 188 Hz, which

provides timing signals for other instruments in the lidar system. A detailed account of the system can be seen elsewhere (Sugimoto et al., 1989).

Basically, at altitudes above 30 km Mie-scattering from the aerosol component is reduced to a negligible level and above this altitude the atmosphere scatters essentially as a molecular gas. A propagating laser beam undergoes Rayleigh scattering in this gaseous medium and the backscattering detected by the lidar receiver is directly proportional to the molecular density. Thus density profiles can be derived directly from the scattered intensity if the density values at a reference altitude is known. The temperature values are derived from the density profiles by assuming that the atmosphere is in hydrostatic equilibrium and obeys the perfect gas equation.

3. Results

The observed temperature profiles (figure not given) show the typical pattern of winter variability. The stratopause near 44-50 km is clearly evident in the profiles. The observed stratopause temperature is typical for this latitude and season. However, we have observed few days in Jan/Feb 1995 with increasingly warm stratopause. We have checked the occurrence of any major stratospheric warming during this period. But no major warming implying the reversal of the stratospheric temperature gradient between 60°N and 90°N and reversal of stratospheric winds were recorded during this period of lidar observations. The increase in temperature may be due to planetary wave activity or minor warmings at the poles. Another feature observed in the profiles is the presence of temperature inversions on some days at heights above 65 km. This phenomenon is interpreted as being a result of gravity wave breaking within and above this inversion.

For the purpose of validation/comparison of our temperature profiles we have used different datasets based on measurements/models. These datasets include rocket measurements at Ryori (39°N), Solar Mesosphere Explorer (SME) spacecraft measurements and CIRA 86 model.

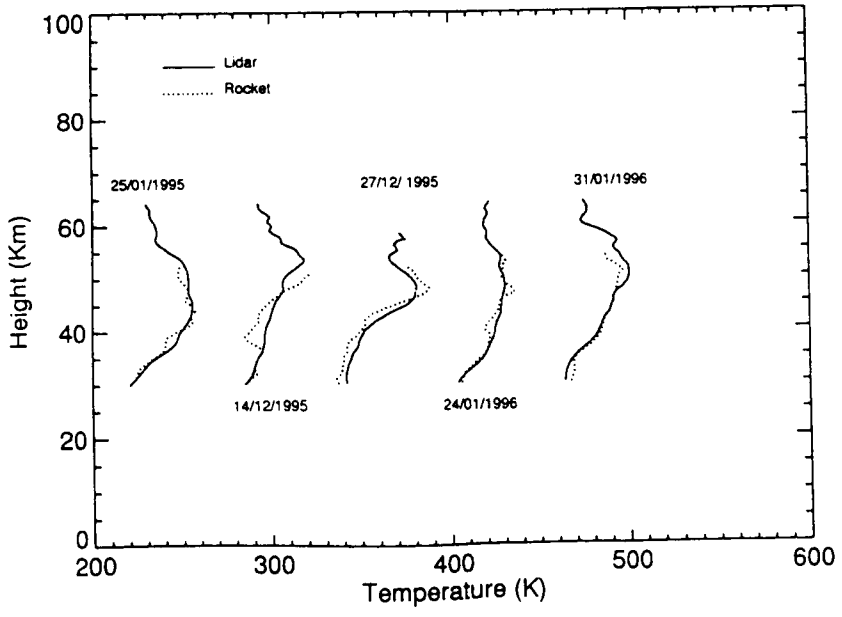


Figure 1. Lidar and rocket temperature profiles for 5 individual days. Solid and dotted lines represent the lidar and rocket profiles, respectively.

The databases of lidar and rocket observations have been examined and fortunately we found 5 dates for which both the observations were conducted. Although these measurements were conducted on the same date, there is a time difference between the observations; rocket launchings were carried out during daytime at around 11 AM and the lidar observation was conducted between 1700 LT and 2200 LT.

Figure 1 shows the temperature profiles obtained by lidar and rocket soundings on the same dates. From the figure it is clear that there is encouraging agreements between the two observations. Except the case for 14 December 1995, all the profiles show very good resemblance. The stratopause is situated at the same altitude in both the observations. Any small differences observed can be attributable to the difference in the time of observation or the location of the two measurements. The overall scenario is promising and it can be concluded that the lidar produces absolute temperature values.

Comparisons were performed between monthly mean temperature profiles obtained by lidar and other datasets. Figure 2 depicts the results for the month of February. SME and CIRA-86 temperature profiles are representative for 35°N. Excellent agreement is evident in the case of February. For all the plots temperature values show good resemblance in the entire height region. Stratopause is located at around 48 km in each plots and the temperature is about 260 K.

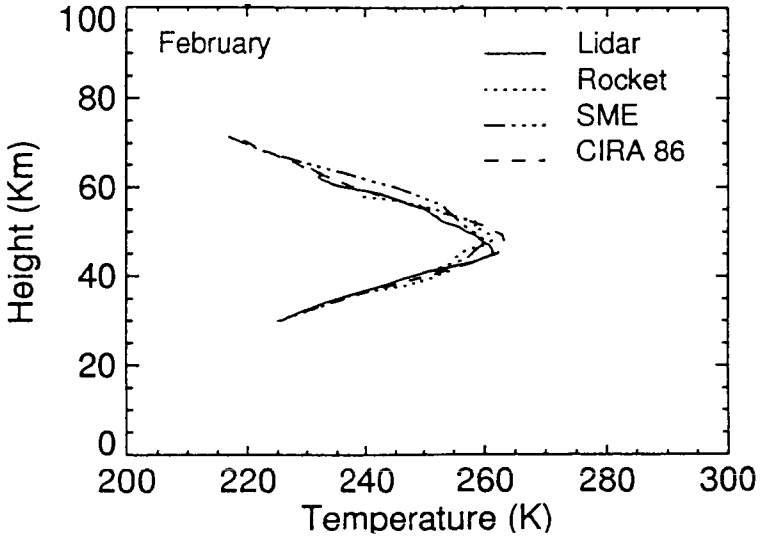


Figure 2. Monthly mean temperature profiles for February. Various datasets such as lidar, rocket, SME and CIRA 86 are presented.

We also have studied the results obtained for other winter months (figs. not shown). Climatological trends observed in the plots are very interesting.

The temperature profiles are further used to study the gravity wave activity. The nightly mean vertical wavenumber potential energy spectra, calculated for 24 Jan. 1995, over the altitude intervals 30-45 and 45-60 km are shown in Figure 3. The model spectrum is also plotted (dashed line) using the observed values of N^2. Spectral amplitudes for small wavenumbers for example, m = 2 x 10^{-4}cyc/m (or 5 km in wavelength) showed an increase from the lower altitude interval to the upper interval. By comparing the observed values with the model prediction, it can be suggested that the wave components with m = 2 x 10^{-4}cyc/m were able to increase in amplitude in the

stratosphere and shows signs of saturation in the mesosphere. Spectra computed for individual profile of certain nights showed considerable variability in the distribution of spectral energy over the period of observations indicating one or more dominant gravity wave components.

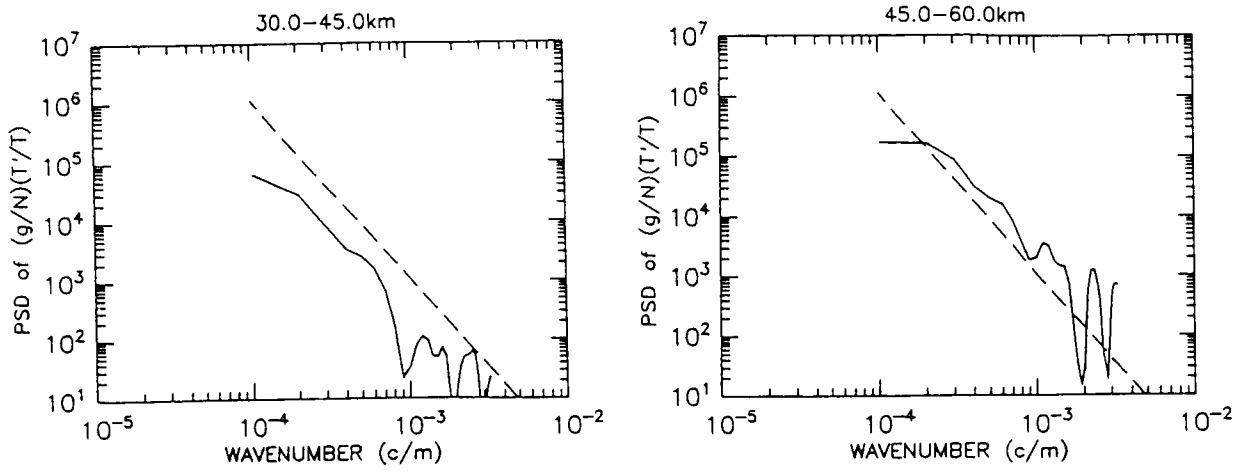


Figure 3. Nightly average vertical wavenumber potential energy spectra computed for 24 Jan. 1995, from the altitude regions 30-45 km and 45-60 km. The straight dashed line represents the broadband convective instability limit.

4. Concluding Remarks

In the present study we have focussed on the validation/comparison results of the temperature profiles derived by using the ozone lidar system at the National Institute for Environmental Studies, Tsukuba. Temperature profiles of the winter season of 1995 and 1996 are used in this study. Validation/comparison of the temperature profiles are carried out using other datasets such as rocket, SME and CIRA 86. Lidar and rocket observations of the same dates show encouraging agreements between the profiles. Climatological comparison of the lidar temperature with other databases also shows a high level of consistency in their trends. Gravity wave analysis identified the dominant wave field and suggests the growth of wave amplitude from the lower atmosphere to the upper atmosphere.

References

Chanin, M. L., and A. Hauchecorne, *J. Geophys. Res., 86*, 9715-9721, 1981.

Chanin, M. L., et al., *J. Geophys. Res., 92*, 10933-10941, 1987.

Gardner, C. S., et al., *J. Atmos. Sci., 46*, 1838-1854, 1989.

Hauchecorne, A., and M. L. Chanin, *J. Atmos. Terr. Phys., 44*, 577-583, 1982.

Hauchecorne, A., and M. L. Chanin, *J. Geophys. Res., 88*, 3843-3849, 1983.

Shibata, T., et al., *Appl. Opt., 25*, 685-688, 1986.

Sugimoto, N., et al., *Oyobutsuri*, 56, 1385-1397, 1989.

Whiteway, J. A., and A. I. Carswell, *J. Atmos. Sci., 51*, 3122-3136, 1994.

Wilson, R., et al., *J. Geophys. Res., 96*, 5153-5167, 1991.

Observations of Mesospheric Sodium over Italy.

Piero Di Carlo, Vincenzo Rizi, Guido Visconti
Dipartimento di Fisica
Università degli Studi, Via Vetoio Località Coppito, 67010 L'Aquila, Italy
Phone:+39 862 433083, FAX: +39 862 433033, E-mail: vincenzo.rizi@aquila.infn.it

1. Introduction

The Na layer is generally found at an altitude range from 80 to 110 Km and the density peak close to the mesopause (~90 Km) is of the order of 10^3 to 10^4 atoms per cm^3 (Richter et al., 1981)
Since this region is relatively inaccessible to in situ measurements, most studies have relied on remote sensing, although at the far range of these techniques.
The accuracy, the spatial and temporal resolutions of the LIDAR observations have allowed the study of the seasonal, daily and small scale variations of the Na layer (Simonich, et al., 1979).
The Na layer is, also, a good tracer to determine mesospheric wave activity. Actually, it is very sensitive to perturbations of atmospheric tides and gravity waves (Gardner and Schelton, 1985). Moreover, the Na layer is confined in a definite zone with large density and this amplifies the observed wave perturbations.
LIDAR measurements of the Na layer are conducted in different sites in the world, since the late the 60s, but in Southern Europe they are absent. This gap is filled up with the development of the LIDAR of University of L'Aquila. In this work we presents the features and the capabilities of the system and some preliminary results.

2. System configuration and performances.

This system is situated at 42.35°N and 13.38°E, and it is set up in a monostatic configuration. For this type of measures the emission laser wavelength is matched up the wavelength of the Na transition from the ground state to the first excited state (resonance transition). The radiation emitted by the excited sodium atoms (resonance scattering) is detected. Actually, the cross section of resonance scattering is many order of magnitude larger than the Rayleigh cross section. The atomic and molecular densities of the upper atmosphere is so low that the transition linewidth of the Na is only Doppler broadened.
The transmitter part of the system consists of a tunable dye-laser pumped by a frequency doubled Nd:YAG laser. The dye-laser uses a solution of Rodamine 590 and 610 and it can be tuned to the D_2 line of Na using a computer-controlled grating in the laser cavity. The emission linewidth is about $0.05cm^{-1}$. The Nd:YAG and dye-laser main characteristics are reported in Table 2.1. 1% of laser energy is used to illuminate a hollow cathode Na lamp. The fed back of the induced opto-galvanic signal allows to keep the tuning to the D_2 line of Na within 0.1pm during the measurements.

Table 2.1.

Nd:YAG-Laser- Continuum NY80	
Repetition rate	10 Hz
Energy	~400 mJ
Divergence	<0.5 mrad
Energy Stability	3.5 %
Pulse width	5 ns
Dye-Laser-Continuum ND60	
Dual Grating	2x2400 lines/mm
Precision	1 pm
Divergence	<0.5 mrad
Linewidth	$0.05\ cm^{-1}$
Stability	$0.05cm^{-1}\ ^0C^{-1}\ hours^{-1}$

A Cassegrain telescope, coupled with field lens to an interference filter and a photomultiplier is used as receiver. The characteristics of the receiving part of the system are reported in Table 2.2. The mechanical chopper, between the telescope and the field lens, prevents saturation effects by the low altitude backscattering. The chopper is also used to synchronize the laser with the receiving electronics.

Table 2.2

Telescope	
Primary mirror	50 cm (diameter)
Total focal length	540 cm
Field of view	0.5 mrad
Interferential filter	
CW	589.6 nm
FWHM	2.5 nm
Peak transmission	~71%
PMT- Thorn Emi 9202B	
Spectral response	S20
Efficiency	21% (peak)
Gain	$8\ 10^4$

The data acquisition chain consists of a preamplifier, a pulse discriminator, an EG&G multi-channel scaler card and a computer. The photon-counting sampling gate is 2μsec large, corresponding to an altitude resolution of 300m.

An example of backscattering profile is reported in Figure 2.1; it has been obtained accumulating the signals from 2000 laser shots. There are evident two altitude regions, the lower (30 to 60km) is the signature of the molecular backscattering (below 25km the PMT is obscured by the chopper wheel), while the higher (between 80 and 110Km), is the resonant signal of Na atoms.

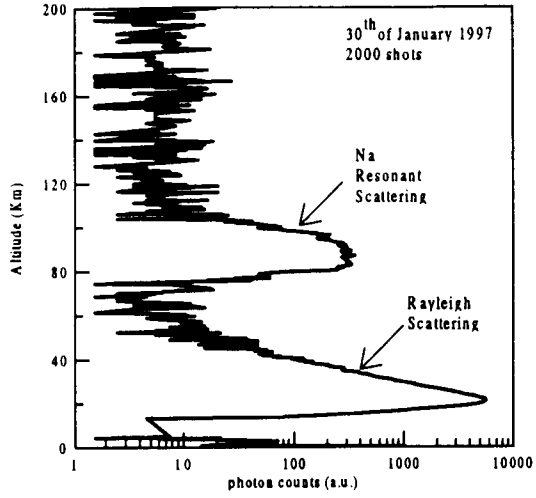


Figure 2.1. *Backscattering profile obtained accumulating the signals from 2000 laser shots.*

From this sort of profile, it is possible to retrieve the Na density profile (Figure 2.2) according to standard algorithm (i.e.: Mégie, et al., 1978, Measures, 1988).

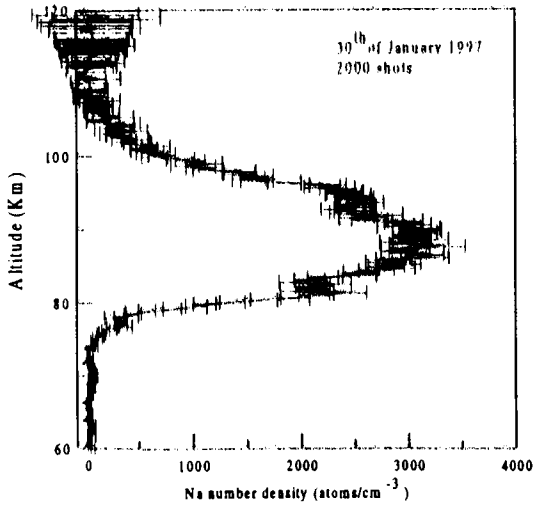


Figure 2.2. *The Na number density profile retrieved from the backscattering signal shown in Figure 2.1. The error bars indicate 3 times the standard deviation.*

The calibration of the resonant backscattering signal over the altitude range where the molecular backscattering is dominant (usually between 35 and 50km) eliminates the dependencies from the laser power fluctuations, the optical transmission of the lower atmosphere and the efficiency of the receiving chain.

The relative Na density values are affected by the uncertainty of the atmospheric density, the statistic fluctuation of the signals, the saturation and the absorption of the Na layer. The dominant error is the former and is roughly of 10%.

3. Preliminary analysis.

Figure 3.1. shows the time series of the Na number density profiles collected during 7 hours measurement session. Each profile is obtained each 200sec. In this series, it is evident a time dependent perturbation in the Na layer, that it is likely originated by the interaction of the atmospheric wave activity with the Na atoms. The response of the Na layer to a quasi-monochromatic wave propagating in the atmosphere can be determinated solving the continuity equation for the Na number density profile, with the assumptions that the diffusion and chemical effect are negligible and the imperturbed layer is horizontal homogeneous. This solution (Gardner and Shelton, 1985) makes possible to estimate the wave number of the propagating waves with a simple spectral analysis of spatial variations of Na profiles (Gardner and Voelz, 1987).

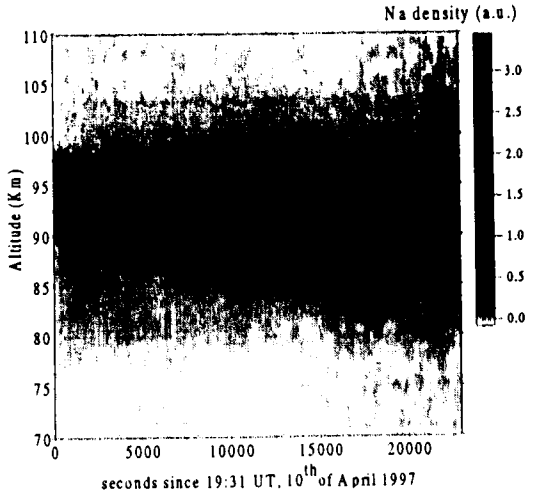


Figure 3.1. *Na number density profiles plotted versus time, during 7 hours measurement session. The time and altitude resolution are respectively 200sec and 300m.*

As an example, we have calculated the spatial spectra for the Na profiles, by means of standard FFT, in a time window of 10 minutes (Figure 3.2). According to Gardner and Voelz (1987) technique, both the Na profiles and their vertical wave number spectra can be inspected to identify a quasi-monochromatic gravity wave that might be present. The values of the vertical wavelength can be determined from the position of the

notch between two peaks in the spectrum; the value of the vertical phase velocity of the wave can be estimated looking at the motion of successive peaks in the Na profiles.

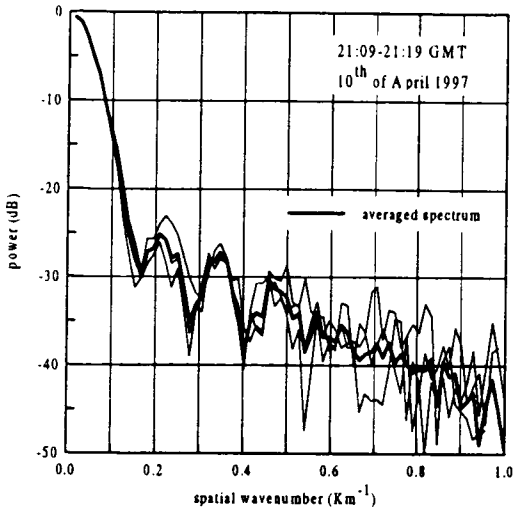


Figure 3.2. *The spatial power spectra and average spectrum (bold line), calculated from the Na profiles in a period of 10min. The dashed line indicates the noise level.*

Although Gibson-Wilde et al., (1996) have well evidenced that there is a limit on the gravity wave information which can be extracted from Na LIDAR data, we get spectra with the signature of wavelike propagating perturbation in the measured Na profiles. In the mean spectrum, we can identify a wavenumber $k=0.28Km^{-1}$ (corresponding to a vertical wavelength of 3.6Km), with an apparent phase velocity of 1.7Km/h, thus the wave period is about 2.1h. The spectrum in Figure 3.2 also suggests the presence of a shorter $k=0.40km^{-1}$ wave (non linear interaction). Because this spectral signature is close to the noise level, the calculated parameter may contain substantial errors.

5. Conclusions and perspectives

In this work we report the status and the performances of a LIDAR system for mesospheric Na sounding. We show that our system, based on standard techniques, has the capabilities for detecting the Na number density profile with an accuracy that allows the study of the small scale variability of the mesospheric Na content.
The system is in routine operation and is now making observation during night. With an extended collection of measurements, we can start a finer data analysis.

References

Gardner, C. S. and J. D. Shelton, Density Response of Neutral Atmospheric Layers to Gravity Wave Perturbations. *J. Geophys. Res., 90,* 1745-1754, 1985.

Gardner, C. S. and D. G. Voelz, Lidar Studies of Nighttime Sodium Layer Over Urbana, Illinois. Gravity Waves. *J. Geophys. Res., 92,* 4673-4694, 1987.

Gibson-Wilde, D. E., et al., Simulation of LIDAR measurements of gravity waves in the mesosphere, *J. Geophys. Res., 101,* 9509-9522, 1996

Measures, M. M., Editor, *Laser Chemical Analysis, John Wiley & Sons, New York,* 1988.

Mégie, G., et al., Simultaneous Measurements of atmospheric Sodium and Potassium. *Planet. Space Sci., 26,* 27-35, 1978.

Richter, E. S., et al.., LIDAR observation of the mesospheric sodium layer over Urbana, Illinois. *J. of Atmos. and Terr. Phys., 43,* 327-337, 1981.

Simonich, D. M. et al., The mesospheric sodium layer at 23°S: nocturnal and seasonal variations, *J. Geophys. Res., 84,* 1543-1550, 1979.

Lidar Measurements of Mesospheric Potassium Layers with a Injection Seeded Flashlamp Pumped Ti:Sapphire Laser

Tatsuya Kyomitsu, Makoto Abo, Chikao Nagasawa, and Yasukuni Shibata
Graduate School of Electrical Engineering, Tokyo Metropolitan University
1-1, Minami-Ohsawa, Hachioji-shi, Tokyo 192-0397, Japan
Phone:+81-426-77-2740, FAX:+81-426-77-2756,E-mail: abo@eei.metro-u.ac.jp

1 Introduction

A Titanium-doped sapphire (Ti:Al_2O_3) laser has a very wide tuning range from 700 nm to 1000 nm. Usually, Ti:sapphire pulse lasers are pumped by frequency doubled Nd:YAG lasers, and the tunable laser systems become complicated considerably because they need to prepare the oscillator-amplifier systems to get the large energy. A flashlamp pumped alexandrite laser is also a similar tunable solid state laser, however, its tuning range of the wavelength is very narrow (720-800 nm), and it needs to warm the laser rod. On the other hand, the flashlamp pumped Ti:sapphire laser with solid-state fluorescence conversion, cw-simmer and prepulse technique achieves the high efficient pulse oscillation.

We are developing the resonance scattering lidar system for measurement of mesosphric metallic atoms and ion such as K, Fe, Ca^+ and so on. It is necessary for the resonance scattering observation to lock the laser wavelength at the resonance wavelength and to reduce the linewidth of the laser. Some methods of locking the laser wavelength and spectral narrowing have been proposed, such as putting a etalon into the cavity of the laser, injection seeding (Vasa et al., 1997) and so on. In these methods, we adopt the method of the injection seeding for locking and narrowing of the laser line. Injection seeding has the merit that the internal loss of the laser cavity is smaller than any other methods. So, we have developed the injection laser that consists of a external cavity laser diode (ECLD) (Duarte, 1995; Sun et al., 1995) and constructed the flashlamp pumped Ti:sapphire laser seeded by the ECLD. It is possible to lock the wavelength of the injection laser to the center of the resonance line by feedbacking the optogalvanic signal from potassium atoms (Green et al., 1976; Ikegami et al. 1995) to the ECLD.

2 Injection Seeder Using ECLD

Figure 1 shows setup of the injection seeding laser system. It consists of two parts, namely an external cavity laser diode and a frequency tuning-locking system. This system can tune and lock to the resonance wavelength of the potassium.

The ECLD consists of a laser diode (SDL-5401-G1), a diffraction grating and a tuning mirror. The external cavity length is about 25 cm. The zero order diffraction beam of the grating is the output beam. The first order diffraction beam of the grating is incident on the tuning mirror. Then, this beam is reflected by the mirror back to the grating and produces another first order diffraction beam that is fed back to the LD. The wavelength tuning is realized by adjusting the tuning mirror angle instead of the grating angle. The mirror is adjusted by a piezoelectric device for fine tuning. The ECLD has the property of mode-hopping suppression that is suitable for the injection laser. But the disadvantages are higher coupling losses (also due to two diffractions) and increase in number of elements that must be properly aligned. The external cavity mode spacing is much smaller than the intrinsic cavity mode spacing, because the external cavity length is much longer than that of the LD cavity. But the ECLD doesn't oscillate with the external cavity mode spacing but with the LD mode spacing. Because our LD doesn't have anti-reflection coating on its facet. So, the wavelength tuning is realized by the tilt control of the tuning mirror, the temperature control of the LD and the current control of the LD. The temperature and the current controls of the LD are equal to adjusting the apparent cavity length of the LD by changing the refractive index of the active region.

A 11 nm tuning range (from 769 to 780 nm) was obtained from this ECLD with current of about 60 mA, and the output power (zero-order diffraction beam power) was about 6 mW. The linewidth of the ECLD that we measured with a scanning etalon (Free Spectral Range =3.8 pm) was about 0.3 pm(FWHM) at the resonance wavelength of the potassium (769.898 nm).

The frequency stabilization system consists of a lock-in amplifier, an oscillator and a hollow cathode lamp with potassium cahtode, as shown in Figure 1. The zero order diffraction beam that produced by the beam from the tuning mirror is guided into the hollow

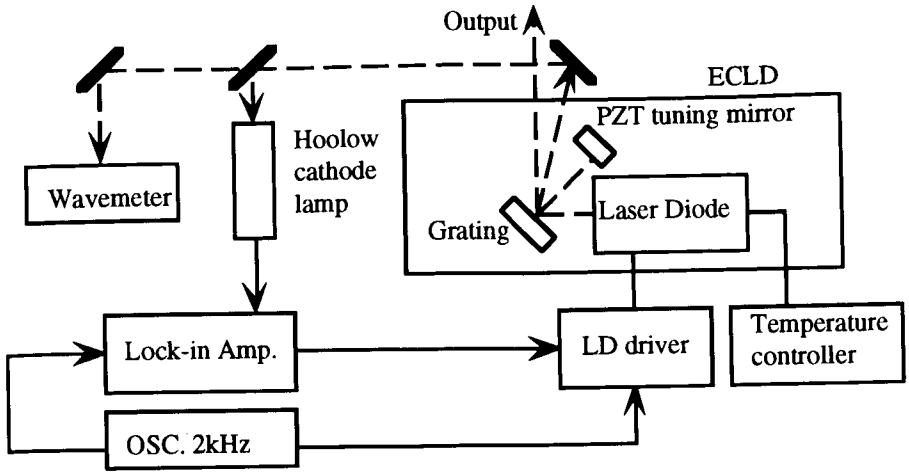


Figure 1. Experimental setup of a ECLD with a frequency stabilization system.

cathode lamp to stabilize the oscillation frequency of the ECLD. We use the optogalvanic signal as a reference signal for the laser stabilization. Optogalvanic effect can be described as change in the electrical properties of discharge caused by illuminating atoms or a molecules with radiation having a wavelength corresponding to an atomic or a molecular transition in the discharge. The 2 kHz rectangular current with small amplitude of 1 mAp-p is added to the current of the LD to modulate the laser frequency, and the error signal from the lock-in amplifier is fed back to the LD. Figure 2 shows the wavelength stability of the injection laser system. The wavelength has been locked by this system during 45 to 60 minutes.

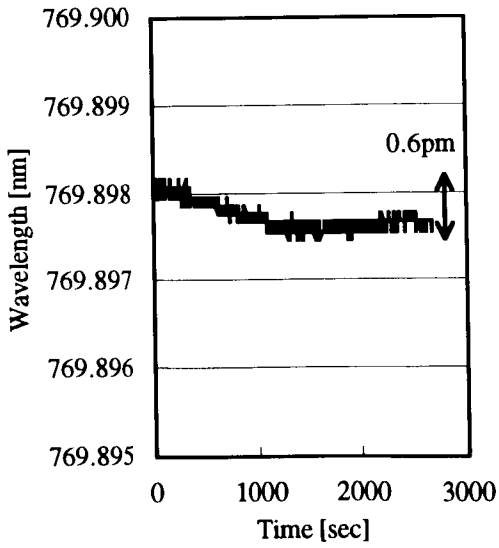


Figure 2. Wavelength stability of the ECLD.

3 Seeded Ti:sapphire Laser

The experimental setup of the injection seeding is illustrated in Figure 3. It was based on a commercial flashlamp pumped Ti:sapphire laser (Elight Laser Systems, Ti:Flash series). The Ti:sapphire rod (8 x 150 mm; doped with 0.1 wt.% Ti) was pumped by three flashlamps driven by a 2 kW power supply. A multistep simmering circuit was used to reduce the discharge duration in the lamps and extend their lifetime. The resonator of a flashlamp pumped Ti:sapphire laser is constructed by an output coupler and a high reflectance mirror. The reflectance of the output coupler is 65%. The end reflector is a concave mirror with 10m radius of curvature whose reflectance is greater than 99% at 770 nm. A pin hole with 2.5 mm radius is inserted into the resonator, because the radius of the output beam of the ECLD is smaller than the radius of the Ti:sapphire rod. The pockels cell consists of a KD*P crystal with anti-reflection coatings. The output beam of the ECLD was passed through three Faraday isolators and was guided into the cavity of the Ti:sapphire laser using a polarizing prism. The isolation of each isolator is 20 dB. They were used to prevent the seeding laser from strong radiation of the Ti:sapphire laser.

The Fabry-Perot interference fringe pattern of the flashlamp pumped Ti:sapphire laser with injection seeding is obtaioned by the CCD camera. The free spectral range of the Fabry-Perot interferometer was 2.0 pm. The Ti:sapphire laser without injection seeding had broadband spectrum and no visible fringe pattern was obtained. The measured linewidth (FWHM) of the flashlamp pumped Ti:sapphire laser with injection seeding was 0.55 pm. The output power was about 35 mJ at 10 Hz, and the pulse width was about 50 ns.

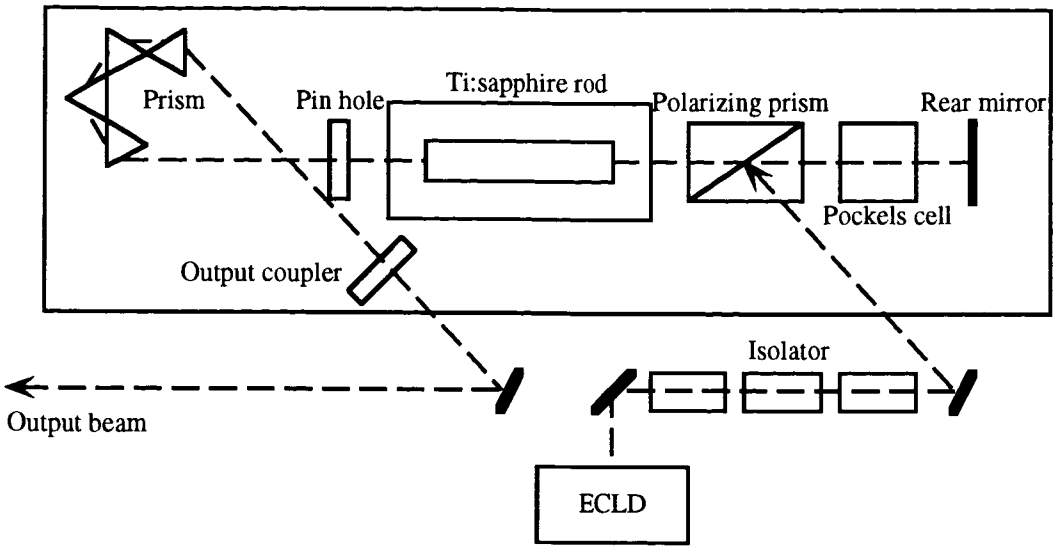


Figure 3. Experimental setup of the flashlamp pumped Ti:sapphire laser seeded by the ECLD.

4 Measurements of Mesospheric Potassium Layer

Table 1 shows the specification of the resonance scattering lidar system. The measurement has performed at the campus of Tokyo Metropolitan University (Japan). Final laser pulse energy was about 35 mJ and the repetition rate was 10 Hz at 769.89 nm of the resonance line of the potassium. The receiver has the diameter of 350 mm and the field of view of 1mrad. The measured density profiles of potassium atoms on the night are plotted in Figure 4. Each profile is derived from the photon counting accumulated from 36,000 laser shots. The potassium layer at 80-100 km altitude is evident clearly and the peak density of the potassium atoms was 25cm^{-3} at 93 km.

5 Conclusion

The characteristics of the flashlamp pumped Ti:sapphire laser seeded with a external cavity laser diode has been presented. The linewidth (FWHM) of the ECLD is about 0.3 pm with an output power of 6 mW and the wavelength tuning range is 11 nm from 769 nm to 780 nm. It is demonstrated experimentally to lock the wavelength of the injection laser to the resonance peak by feedbacking the optogalvanic signal from potassium atoms to the ECLD. The linewidth (FWHM) of the flashlamp pumped Ti:sapphire laser seeded by the

Table 1. Specification of the potassium lidar

Location		
	Tokyo Metropolitan University	
	35N,139E	
Transmitter		
	Laser type	Injection seeded flashlamp pumped Ti:sapphire laser
	Energy	35mJ/pulse
	Repetition rate	10Hz
	Wavelength	769.898nm
	Linewidth	0.55pm
	Pulse length	50ns
	Beam divergence	0.5mrad
Receiver		
	Diameter	350mm
	Field of view	1mrad
	Detector	PMT (R943-02 Hamamatsu)
Data Acquisition		
	Type	Photon counting
	Range resolution	200m
	Shot number	18,000 (30min)

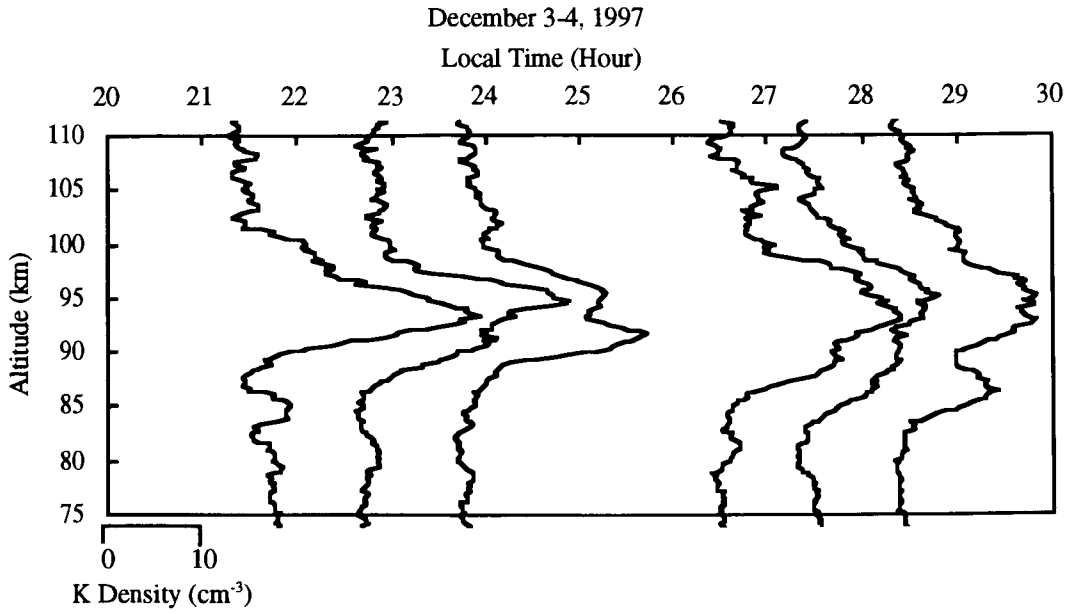


Figure 4. Potassium density profiles measured on the night of December 3-4, 1997.

ECLD was about 0.55 pm and the output power was about 35 mJ consequently. We think that it is possible to increase this laser output power by improving the flashlamp pumped Ti:sapphire laser. It is achieved to measure potassium atom layers in the mesopause region by using the lidar system with the laser developed here. It is certified that the flashlamp pumped Ti:sapphire laser seeded by an external cavity laser diode is useful for resonance lidar applications.

This lidar system will applied for the mesospheric Fe(372nm), Ca(423nm) and Ca^+ (393nm) layer measurements and Fe Boltzmann factor lidar (374 and 372nm) for mesospheric temperature measurement (Gelbwachs, 1994) using second harmonic generator.

References

Duarte, F. J. (1995). *Tunable Lasers Handbook*, Academic Press.

Gelbwachs, J. A. (1994). Iron Boltzmann factor LIDAR: proposed new remote-sensing technique for mesospheric temperature. *Appl. Opt.*, 33: 7151-7156.

Green, R. B., Keller, R. A., Luther, G. G., Schenck, P. K., and Travis J. C. (1976). Galvanic detection of optical absorptions in a gas discharge. *Appl. Phys. Lett.*, 29: 727-729.

Ikegami, T., Sudo, S., and Sasaki, Y. (1995). *Frequency Stabilization of Semiconductor Laser Diodes*. Artech House.

Sun, H., Menhart, S., and Adams, A. J. (1995). Development of a tunable, grating external cavity, strong feedback semiconductor laser with real-time wavelength monitoring. *Opt. Eng.*, 34: 2993-2997.

Vasa, N. J., Morishita, K., Parhat, H., Okada, T., Maeda, M., and Uchino, O. (1997). Tunable Single-mode Pulsed Ti:sapphire laser injection-seeded by a continuous-wave Cr^{3+}:$LiSrAlF_6$ Laser. *Opt. Review*, 4: 176-179.

FARADAY METAL VAPOR FILTERS FOR DAYTIME OBSERVATION OF THE MESOPAUSE REGION

Songsheng Chen, David A. Krueger and C. Y. She
Physics Department, Colorado State University, Fort Collins, CO 80523
Phone: (970) 491-0681, FAX: (970) 491-7947, E-mail: schen@lamar.colostate.edu

Introduction

To measure temperatures in the mesopause region in the daytime with a lidar, an ultra-narrowband filter with a bandwidth between 1 and 100 GHz is needed to reject sky background and at the same time to pass the desired signal. That a circular birefringent, diachronic medium between crossed polarizers would work was demonstrated by Ohman [1956] before the laser was invented. Later in 1975, a Faraday filter with a magnetic field of 1500 G was constructed by Agnelli et al. [1975] for the observation of solar sodium D lines. Their filter gave a full width of ~ 15 GHz and a maximum transmission of 25%. During the late 80's, the interest in Faraday filters has been revived for the detection of narrowband laser radiation, unrelated to temperature measurements.

Briefly, a Faraday filter consists of a vapor cell in an axial magnetic field between two crossed polarizers. After passing through the first polarizer, light is linearly polarized and it can be considered as a linear superposition of two counter-rotating circularly polarized components. Under a strong axial magnetic field, the absorption line is Zeeman shifted by more than two Doppler line widths for each circular polarization in the opposite directions; near unity transmission occurs at the line-center when the vapor density is adjusted to give a $\pi/2$ Faraday rotation. Near the absorption peaks, now Zeeman shifted away from the line-center, the transmission drops sharply to roughly 0.25 because one or the other circularly polarized component is completely absorbed. Further away from the center, the transmission falls to zero because of two crossed polarizers.

We have developed and tested in the laboratory an ultra-narrow dispersive Faraday filter [Chen et al., 1993] resulting in a band-pass filter of 86% peak transmission and 1.9 GHz FWHM. Later, we have constructed a longer sodium cell (1 inch long) in an axial magnetic field of 1800 G and in an oven operated at a lower temperature of 168 °C. The cell windows in a cooler oven have less chance of being attacked by metal atoms in the cell, thereby prolonging the life of the Faraday filter, an absolutely necessary requirement for routine lidar operation. We have incorporated this Faraday filter into our lidar receiver for daytime operation on campaign basis since late 1995 [Chen et al., 1996[. Such a receiver is termed Faraday receiver (as opposed to the Regular receiver).

We have also constructed a potassium Faraday filter that may be used in other observatories with narrowband K lidar for daytime temperature measurements. In this paper, we discuss the figure of merits of both Na and K Faraday filters, the performance enhancement on narrowband lidar with a Na Faraday filter, permitting daytime operation, and the plan for integrating a K Faraday filter into a lidar receiver with a large aperture.

Characterization of Faraday Filters

The transmission function of a Faraday filter may be derived from quantum mechanical calculations [Chen et al., 1993]; its functional form depends on effective optical depth and applied external axial magnetic field. By choosing an axial magnetic field in an appropriate range and adjusting the oven temperature, one can "engineer" the Faraday filter to have a very narrow passband and respectable peak transmission at the same time. For lidar applications, Na D_2 line and K D_1 line are used. Although the line strength of the D_2 transition of an alkali atom is a factor of 2 stronger than that of the D_1 transition, due to competing oxygen absorption at the K D_2 transition frequency, the K D_1 transition at 770 nm is chosen for K lidar operation. Since the hyperfine splitting of the Na ground state (1.8 GHz) is much wider than that of the K ground state (0.46 GHz), a much higher magnetic field (~ 1800 G) is needed for the Na filter than for the K filter (~ 700 G) to achieve comparable peak transmission of ~ 85%. The larger splitting of the ground state and the higher magnetic filed result in a wider central passband width, defined as full width of half maximum transmission (FWHM), for the Na filter than the K filter.

The measured transmission functions of a Na D_2 and a K D_1 Faraday filter with near maximum peak transmission are shown in Figure 1(a) and 1(b) respectively. The characteristics of these filters is summarized in Table 1, where the values for the Na D_1 and K D_2 transitions were calculated the operational oven temperatures and magnetic fields. Both D_1 and D_2 transmission functions are required for the assessment of skylight background passing through the filters.

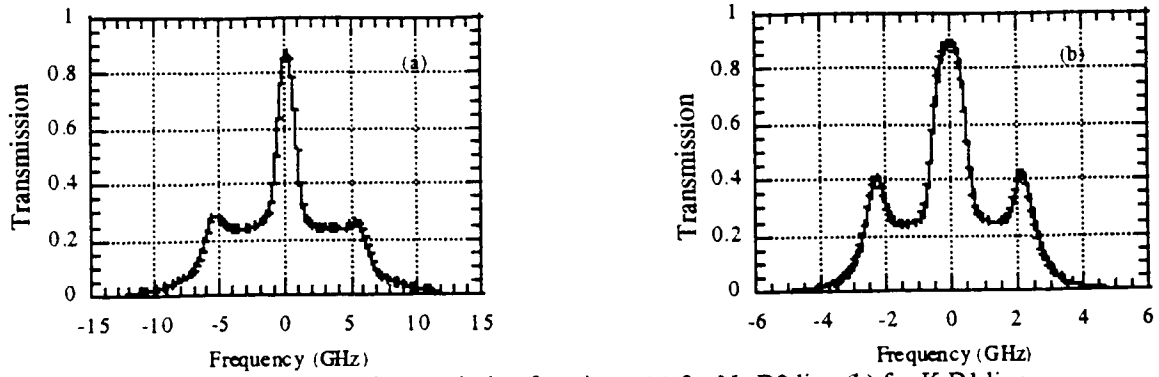


Figure.1 Measured transmission functions. (a) for Na D2 line (b) for K D1 line

Table 1 Typical characteristics of Na and K filters

	Operation Temperature (°C)	Operation Magnetic Field (Gauss)	Maximum Transmission (%)	Passband Width (FWHM, GHz)	Equivalent Noise Bandwidth* (GHz)
NaD_1	189	1850	38	10.9	0.6
NaD_2	189	1850	86	1.9	0.5
KD_1	90	700	89	1.2	0.7
KD_2	90	700	56	1.1x2**	0.05

*The area of the product of Faraday filter transmission and Fraunhofer absorption
** The two obvious peaks of the Faraday filter transmission at KD_2 line

The broadband sky-light background (45° from Zenith) with a typical spectral radiance of 8×10^{-7} $Wcm^{-2}sr^{-1}A^{-1}$ for Na and 1.2×10^{-7} $Wcm^{-2}sr^{-1}Å^{-1}$ for K (before receiving telescope) is reduced by Fraunhofer absorption near the D_1 and D_2 resonance, with frequency-dependent transmission functions, $T_{H1}(\nu)$ and $T_{H2}(\nu)$, respectively for the D_1 and D_2 transition regions. For the Faraday receiver, the detected background is further reduced by the dispersive Faraday filter with the associated transmission functions, $T_{F1}(\nu)$ and $T_{F2}(\nu)$. Ignoring the off-resonance contribution, an effective noise bandwidth, B_F and B_R, respectively for Faraday and Regular receivers may be defined to compare the performances of respective receiving system as:

$$B_F = \int [T_{H1}(\nu)T_{F1}(\nu) + T_{H2}(\nu)T_{F2}(\nu)]d\nu \quad (1a)$$

and

$$B_R = \int [T_{H1}(\nu) + T_{H2}(\nu)]d\nu \quad (1b)$$

The off-resonance transmission of the Faraday receiver depends on the quality of the crossed polarizers used; it is measured to be 2×10^{-5}. In addition to the B_F given in Eq. (1a) and listed in Table 1, the off resonance contribution to B_F for a 10 nm bandwidth determined by a commercial interference filter and Fraunhofer absorptions was estimated to be 0.17 GHz and 0.10, giving rise to total B_F of 1.3 GHz and 0.90 GHz for Na and K Faraday receivers. The corresponding values for the Regular receivers, B_R, are 8.6×10^3 GHz and 5.1×10^3 GHz, resulting in enhancement for sky background rejection by a factor of 6.6×10^3 and 5.7×10^3 for Na and K Faraday receivers, respectively. These enhancement factors made daytime temperature measurements possible.

Application to Sodium Temperature Lidar

Atmospheric temperatures in the mesopause region may be determined from the measured intensity ratio, $R(z) = I_C(z) / I_a(z)$, by means of calibration curves, the calculated intensity ratio as a function of temperature, where $I_C(z)$ and $I_a(z)$ are, respectively, the Na resonance scattering photocount

profiles at the crossover (ν_c) and the D_{2a} peak (ν_a) frequencies between 80 and 110km[She et al., 1992].

As discussed in a recent publication (Chen et al., 1996), in the daytime receiver, the collected light from the telescope is fiber-coupled after an interference filter into a light-tight box containing the Na Faraday filter and a photomultiplier (PMT). The effectiveness of the Faraday filter in rejecting skylight background may be appreciated by the high quality data obtained, shown in Figure 2. These are hourly photocount profiles taken at (a) high noon with the Faraday receiver for the two operating lidar frequencies, and (b) night with the Regular receiver. A mean detected background counts from sky background radiance, averaged photocounts between 120 and 155 km, at high noon with Faraday receiver is much lower than that detected at night with the Regular receiver.

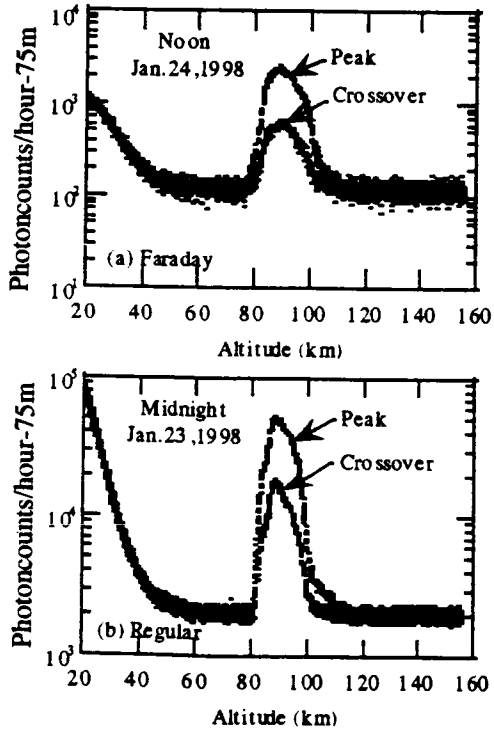


Figure 2. Raw lidar returns taken at Fort Collins, CO (41°N, 105°W) on January 23-24, 1998 with 1 hour integration, at (a) high noon (12 MST) from Faraday receiver, (b) midnight (0 MST) from Regular receiver.

The use of polarizers and fibers in addition to a Na vapor cell reduces the detected signal to 12 %. Our receiver area is about 950 cm^2 and resolution bin length 75 m (0.5 μs). The transmitting laser has a repetition rate of 20 Hz with pulsed energy of 30 mJ at 589 nm (photon energy = 3.4×10^{-19} J). The detection efficiency of our Regular receiver system is about 7.5% (15%, 70% and 70% for PMT, optics and interference filter). With typical Na abundance of 2×10^{13} m^{-2}, the Na signal should be ~125 counts/pulse, giving ~1000 counts/min-75m at the peak of the Na layer. Since the Faraday receiver is only 12% efficient, it should have 15 counts (per pulse) of signal and ~120 counts/min-75m at the Na peak. In practice, the measured signals as shown in Figure 2 are the sum of 24 files during one hour, which give about 50 counts/min-75m and 750 counts/min-75m averaged peak signals over the sodium layer, respectively for Faraday and Regular channels. A factor of (1.3-2) less than the rough estimation could be the fluctuation of the sodium density. The measured sky background of about 5 counts/min-75m for the Faraday channel is about a factor of 3 less than the estimated of 17 counts/min-75m with the effective noise bandwidth of 1.3 GHz, which could be the fluctuation of the sky background radiance.

The temperature profiles, shown in Figure 3, may be derived form the photocount profiles, shown in Figures 2. Also shown in Figure 3(b) is the temperature profile simultaneously measured by the Faraday receiver operated at night. They are seen to agree with each other within the error bars.

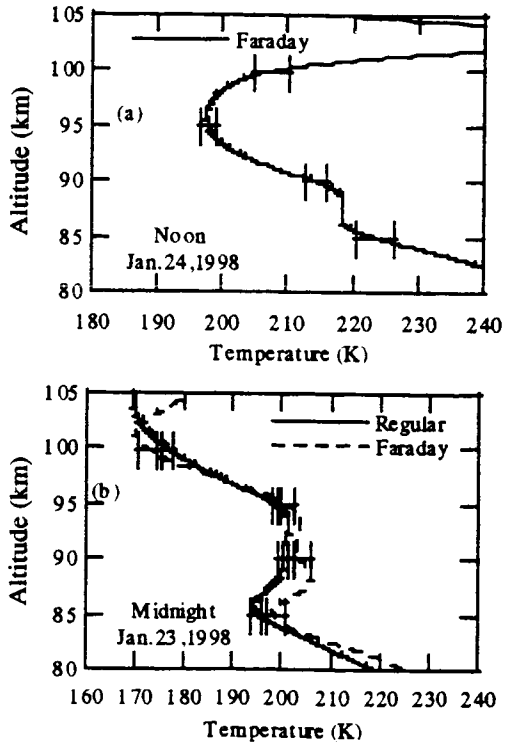


Figure 3 Temperature profiles taken at Fort Collins, CO (41°N, 105°W) on January 23-24, 1998 with 1 hour integration, at (a) high noon (12 MST) from Faraday receiver and (b) midnight (0 MST) from both Regular and Faraday receivers

Future Prospects

To study the latitude dependence, daytime capability is required for lidar observatories at both equatorial and polar latitudes [She and von Zahn, 1998] as well. The existing narrowband lidars at Kühlungsborn, Germany (54°N) and Arecibo, Pueto Rico (18°N) are based on mesopause potassium detection [von Zahn and Höfner, 1996]. These observatories employ receiving telescopes with much larger aperture, ~ 1m in diameter. Methods to adopt the K Faraday filter we constructed for 14" telescope are being investigated. A tighter focussing into the filter cell may be a way to accept photons from a wider field of view. Alternatively, a K Faraday filter with a larger optical aperture may be designed for an individual telescope for the global interrogation of daytime thermal and dynamical structure of the mesopause region.

It should be pointed out that our receiver aperture that produces photocount profiles shown in Fig. 2 is only 14 inches. For a telescope with larger aperture, the signal-to-background ratio will remain the same, but the signal and signal-to-noise will be much improved. The signal-to-background ratio shown in Fig. 2 is large enough, and the system should be capable of making simultaneous daytime temperature and line-of-sight wind measurements [White et al., 1996] in the mesopause region.

Acknowledgement

The work presented here has been partially supported by the National Science Foundation, under grants ATM-9523689 and ATM-9714676.

References

Angnelli, G., A. Cacciani, and M. Fofi, Solar Phys. 44, 509, 1975.

Chen, H., C. Y. She, Paul Searcy and Eric Korevaar, "Na Vapor Dispersive Faraday Filter", Opt. Lett. 18, 1019-1021, 1993.

Chen, H., M.A. White, D.A. Krueger, and C.Y. She, "Daytime mesopause temperature measurements with a sodium-vapor dispersive Faraday filter in a lidar receiver", Optics Lett. 15, 1093-5 (1996).

Ohman, Y., Stockholm Obs. Ann. 19, 3, 1956.

She, C. Y., J. R. Yu, H. Latifi, and R. E. Bills, "High-Spectral-Resolution Fluorescence Lidar for Mesopheric Sodium Temperature Measurements," Appl. Opt. 31, 2095-2106, 1992.

She, C. Y. and U. von Zahn, "The concept of two-level mesopause: Support through new lidar observation", J. Geophys. Res. (in press).

White, M. A., D. A. Golias, D. A. Krueger, and C.Y. She, "A frequency-agile lidar for simultaneous measurement of temperature and radial wind in the mesopause region without sodium density contamination", in p.p. 136-140, Application of Lidar to Current Atmospheric Topics, Sedlacek Ed., SPIE Proceedings 2833 (1996).

von Zahn, U., and J. Höffner, "Mesopause temperature profiling by potassium lidar", *Geophys. Res. Lett., 23*, 141-144, 1996.

APPENDIX
AUTHOR INDEX

Boldface session numbers indicate first author; *indicates abstract not available at time of publication.

Author	Session-Paper No.	Page No.
Abo, Makoto	PS1.1-15	107
	PS1.1-22	131
	PS2.2-19	545
	PS2.2-21	*
	PS3.2-21	827
Abshire, James B.	**OS7-1**	925
	PS1.2-1	211
	PS3.2-15	803
Afzal, Robert S.	**OS5-4**	613
	OS7-1	925
Agcropra, Emmanuel	PS1.1-40	203
Agostini, Pietro	PS2.2-7	501
Ahl, Jeffrey	OS6-5	669
Al-Habash, A.	PS3.2-3	755
Alarcon Minella C.	PS1.1-39	199
	PS1.1-40	203
Alpers, Matthias	OS1-5	23
Althausen, Dietrich	OS1-1	7
	OS1-7	29
	PS2.1-24	457
	PS3.2-23	833
Alvarez, J.M.	OS8-4	983
Alvarez, Raul J., II	OS5-11	639
Ambrico, Paola F.	PS3.2-33	871
	OS2-13	305
Amodeo, Aldo	PS3.2-33	871
	OS2-13	305
Amoruso, S.	PS3.2-33	871
Amzajerdian, Farzin	**PS3.1-4**	703
Andreev, M.I.	PS1.1-29	159
Andrews, L.	PS3.2-3	755

Author	Session-Paper No.	Page No.
Ansmann, Albert	**OS1-1**	7
	OS1-7	29
	OS2-11	297
	PS2.1-24	457
	PS3.2-23	833
Antill, C.W., Jr.	PS3.2-18	815
Antuña, Juan Carlos	PS1.1-32	173
Aoki, Tetsuo	OS7-5	935
	PS1.1-16	111
Apituley, Arnoud	**PS1.1-24**	139
Argall, P.S.	PS2.1-14	417
	PS2.2-15	529
	PS2.2-16	533
Armenante, M.	PS3.2-33	871
Aroche, Roberto	PS1.1-32	173
Arshinov, Yu. F.	OS2-11	297
	PS2.1-21	445
Arya, B.C.	PS2.1-5	383
Astafurova, Tatjana P.	PS3.3-2	897
Austin, R.T.	PS1.1-7	77
Baldi, M.	PS2.1-25	461
Ball, Donald J.	OS7-8	945
Banakh, V.A.	**PS3.1-10**	727
	PS3.1-11	*
	PS3.1-12	731
Barker, Ben C., Jr.	**OS6-8**	681
Barnes, James C.	**OS5-6**	619
	PS3.2-30	861
Barnes, Norman P.	OS5-2	603
Barnett, Jennifer M.	OS1-11	45
Barrie, L.A.	OS7-11	959

Author	Session-Paper No.	Page No.
Bastille, Christian	PS3.2-6	767
Baumgart, Rudolf	OS2-5	273
Beck, Steven	PS2.1-19	437
Behrendt, Andreas	**OS5-9**	631
Ben-David, Avishai	OS6-5	669
	PS1.1-38	195
	PS2.1-15	421
Beninga, I.	OS3-9	343
	PS2.2-12	517
Berardi, V.	PS3.2-33	871
Bergwerff, J.B.	OS3-3	319
Bernutat, Claudia	**PS1.1-1**	59
Beyerle, G.	OS3-9	343
	PS2.2-1	477
	PS2.2-12	517
Bianco, G.	PS1.2-4	223
Bird, J.C.	OS3-5	327
	PS2.2-13	521
	PS2.2-4	489
Bisson, Scott E.	OS2-5	273
Bissonnette, Luc R.	**OS1-13**	51
	PS1.1-23	135
	PS3.2-6	767
Blackwell, Timothy S.	PS3.1-4	703
Blamont, Jacques-Emile	OS7-4	931
Blanchet, J.P.	OS7-11	959
	PS1.1-36	189
Bobrovnikov, Sergey M.	OS2-11	297
	PS2.1-21	445
Böckmann, Christine	OS1-5	23
	PS1.1-1	59
Bodeker, G.E.	OS3-3	319
Boitel, C.	PS3.1-5	707
Boselli, Antonella	OS2-13	305
	PS3.2-33	871

Author	Session-Paper No.	Page No.
Bösenberg, Jens	**OS1-5**	23
	OS2-6	277
	PS3.2-4	759
	PS3.2-5	763
Bousek, Ronald R.	OS5-14	651
	0S6-2	657
Boyd, I.S.	OS3-3	319
Brackett,Vincent G.	OS1-2	11
	OS2-2	261
	OS2-4	269
	PS2.1-26	465
Brasseur, Guy	**PL-2**	*
Brewer, W. Alan	OS4-2	557
	OS4-4	565
	OS4-6	573
Brinksma, E.J.	**OS3-3**	39
Brogniez, G.	OS1-6	25
Browell, Edward V.	OS1-2	11
	OS2-1	257
	OS2-2	261
	OS2-4	269
	OS6-9	685
	OS7-8	945
	PS1.1-12	95
	PS2.1-26	465
	PS2.1-4	379
Bruneau, Didier	OS2-3	265
	PS3.2-16	807
Bryant, C.R.	**PS2.1-14**	417
	PS2.2-15	529
Buchhold, Michael	OS4-5	569
Bucoy, Jaime	PS1.1-39	199
Bufton, Jack L.	OS7-2	927
Bukharin, A.V.	**PS1.2-9**	241
Bundas, David J.	OS7-6	939

Author	Session-Paper No.	Page No.
Bundschuh, Bernhard	**PS3.2-23**	833
Burlakov, V.D.	PS1.1-29	159
Butler, Carolyn F.	OS2-4	269
	PS2.1-4	379
Cadirola, Martín P.	OS2-8	285
	PS2.1-10	403
	PS2.1-17	429
Cahalan, Robert F.	PS1.1-11	91
Calpini, Bertrand	OS6-4	665
	PS2.1-18	433
	PS2.1-9	399
	PS2.1-20	441
Campbell, James. R.	OS1-11	45
	PS1.1-19	119
	PS1.1-28	155
Cañete, Jordan	PS1.1-40	203
Cann, Mark	PS1.1-36	189
Capobianco, Roberta	PS3.2-33	871
	OS2-13	305
Cardell, Greg	OS7-3	929
Carnahan, Timothy M.	OS7-6	939
Carrasco, I.	OS1-4	19
Carswell, Allan I.	**OS3-5**	327
	PS2.2-13	521
	PS2.2-4	489
	PS2.2-10	511
	PS2.2-5	493
Cervantes, Sonia	PS1.1-32	173
Cesarano, Pablo	PS1.1-6	75
	PS2.1-13	415
Cess, Robert	**PL-3**	*
Chaikovsky, A.P.	**PS1.1-4**	69
Chan, J.C.L.	PS2.1-6	387
	PS3.2-22	829
Chan, Yat	PS2.1-19	437
Chanin, Marie-Lise	OS7-4	931

Author	Session-Paper No.	Page No.
Chaudhuri, Sandipan S.	PS3.2-35	879
Chazette, P.	**OS1-4**	19
Chen, Huailin	OS3-13	359
	OS4-10	587
	PS3.1-1	691
	PS3.3-6	915
Chen, Songsheng	**PS2.2-20**	549
Chen, Wei-Nai	**PS1.1-30**	165
Chepfer, Hélène	**OS1-6**	25
	PS1.1-18	115
Cheung, Eric C.	PS3.1-13	735
Chicklis, Evan	OS5-5	617
Chou, H.	OS5-13	647
Chyba, T.H.	**PS3.2-9**	779
	PS3.2-28	853
Clappier, Alain	OS6-4	665
Clarke, Antony D.	OS6-6	673
Clayton, Marian B.	OS1-2	11
	OS2-2	261
	OS2-4	269
	PS2.1-26	465
Clemesha, B.R.	PS1.1-3	65
Coleman, James J.	OS2-12	301
Collins, Richard L.	OS1-12	47
	OS3-11	351
Connolly, Patrick	OS6-3	661
	PS3.3-4	905
Connor, B.J.	OS3-3	319
Corbett, F.	OS5-13	647
Cornwell, Donald M., Jr.	**OS4-8**	581
	PS3.2-15	803
Coyle, D.B.	**PS1.2-5**	225
	PS3.2-37	887
Cunningham, A.G.	PS1.2-3	219
Cutten, Dean R.	PS3.1-9	723

Author	Session-Paper No.	Page No.
Cuzzola, Vicenzo	PS2.2-7	501
D'Amico, Francis M.	OS6-5	669
	PS2.1-15	421
Dabas, Alain M.	PS3.1-5	707
	PS3.1-7	715
	PS3.1-8	719
Dahl, A.	OS3-9	343
Dallas, J.L.	OS5-4	613
Dani, K.K.	PS1.1-20	123
Danne, Olaf	OS1-10	41
Dao, Phan D.	**OS6-3**	661
	PS3.3-4	905
Davidson, Gilbert	OS6-3	661
	PS3.3-4	905
Davis, Anthony B.	**OS1-14**	55
	PS1.1-11	91
Davis, Kenneth J.	OS2-2	261
	PS2.1-8	395
Day, R.	OS5-5	617
de la Fuente, Lorenzo	**PS1.1-39**	199
Dean, David R.	OS5-14	651
Degnan, John J.	**PS1.2-7**	233
Delaval, A.	PS3.2-3	755
Delmonte, Stéphane	PS3.2-16	807
Delville, Patricia	**PS3.1-5**	707
Demoz, Belay	OS2-8	285
	PS2.1-10	403
Dentamaro, Anthony V.	OS6-3	661
	PS3.3-4	905
Desbois, Michael	OS7-4	931
Devara, P.C.S.	**PS1.1-20**	123
DeYoung, Russell J.	OS5-12	643
	PS3.2-2	751
	PS3.2-26	845
	PS3.2-27	849
	PS3.2-29	857
	PS3.2-31	863
	PS3.2-38	891
	PS3.3-7	919
Di Carlo, Piero	**PS2.2-18**	541
Di Girolamo, Paola	**OS2-13**	305
Dinolfo, Christian	**PS3.2-12**	791
Disselkamp, Robert S.	OS1-12	47
Dolislager, L.	PS2.1-3	375
Donnier, J.M.	PS3.1-5	707
Donovan, David P.	OS3-5	327
	PS1.1-36	189
	PS2.2-13	521
	PS2.2-4	489
Dorado, Susana V.	**PS1.1-40**	203
Dowling, James A.	OS5-14	651
Dragic, Peter D.	OS2-12	301
Drobinski, Philippe	PS3.1-5	707
	PS3.1-7	715
	PS3.1-8	719
Duck, Thomas J.	OS3-5	327
	PS2.2-5	493
	PS2.2-13	521
	PS2.2-10	511
Duda, David P.	**PS1.2-6**	229
Dudelzak, Alexander E.	OS7-8	945
Dulac, F.	OS1-4	19
Eberhard, Wynn L.	**OS5-11**	639
Edwards, W.C.	**PS3.2-18**	815

Author	Session-Paper No.	Page No.
Ehret, Gerhard	**OS5-10**	635
	PS2.1-8	395
	PS3.2-14	799
Eickel, Karl-Heinz	PS3.2-7	771
Eisele, Holger	**PS2.2-3**	485
El'nikov, A.V.	OS3-6	331
	PS1.1-29	159
Elivert, R.	PS3.2-9	779
Eloranta, Edwin W.	**OS2-14**	309
	PS2.1-27	469
	PS1.2-6	229
Elouragini, Salem	PS1.1-18	115
Emmitt, G. David	OS4-1	553
Eng, R.	OS5-13	647
Esposito, Steven T.	PS1.1-37	193
	PS2.1-11	407
Esproles, Carlos	OS7-3	929
Estevan, René	**PS1.1-32**	173
Evans, Keith D.	OS1-2	11
	OS2-8	285
	PS2.1-10	403
	PS1.1-41	207
	PS2.1-1	367
Ewing, J.J.	**OS5-3**	609
Fan, T.Y.	OS5-3	609
Farley, Robert	OS6-3	661
	PS2.1-19	437
	PS3.3-4	905
Favreau, X.	PS3.1-5	707
Fenn, Marta A.	**OS2-4**	269
	PS2.1-4	379

Author	Session-Paper No.	Page No.
Ferrare, Richard A.	**OS1-2**	11
	OS2-8	285
	PS2.1-10	403
	PS1.1-41	207
	PS2.1-1	367
	OS2-2	261
	PS2.1-26	465
Fix, Andreas	OS5-10	635
	PS3.2-14	799
Flamant, Cyrille	**OS2-3**	265
	PS2.1-13	415
Flamant, P.H.	OS1-3	15
	OS1-6	25
	OS4-7	577
	PS1.1-6	75
	PS1.1-18	115
	PS2.1-13	415
	PS3.1-5	707
	PS3.1-7	715
	PS3.1-8	719
Flentje, H.	**OS3-4**	323
Flesia, Cristina	OS4-9	585
	OS7-13	967
	PS3.1-1	691
	PS3.1-2	695
Flint, Holger	OS1-10	41
	PS2.1-22	449
Fochesatto, Javier	PS1.1-6	75
	PS2.1-13	415
Forouhar, Siamak	OS7-3	929
Fox, Jay	**OS6-5**	669
Fox, Marsha J.	OS5-14	651
	OS6-2	657
Frederick, S.	PS3.2-3	755

Author	Session-Paper No.	Page No.
Frelin, Ronald	OS6-3	661
	PS3.3-4	905
Freudenthaler, Volker	PS1.1-21	127
Frey, S.	PS2.1-16	425
Frioud, Max	PS2.1-18	433
Fuelberg, Henry	PS2.1-4	379
Fujii, Masamitsu	PS1.1-15	107
	PS1.1-22	131
Fujii, Takashi	PS2.1-7	391
	PS3.2-13	795
Fujimoto, Toshifumi	OS1-8	33
	PS1.1-16	111
Fujiwara, M.	PS2.2-12	517
Fukuchi, Tetsuo	**PS2.1-7**	391
	PS3.2-13	795
Fuller, W.H., Jr.	OS8-4	983
Gainey, Kathleen	PS3.3-5	909
Gao, J.L.	**PS3.2-22**	829
Gardner, Chester S.	PS1.2-12	253
Garner, Richard	OS6-3	661
	PS3.3-4	905
Garvin, James B.	OS7-2	927
Gathen, P.v.d.	OS3-10	347
Geary, Joseph M.	PS3.1-4	703
Gelbwachs, Jerry	OS6-3	661
	PS2.1-19	437
	PS3.3-4	905
Gentry, Bruce M.	**OS4-10**	587
	PS3.1-1	691
	PS3.3-6	915
Getzewich, Brian J.	PS2.1-26	465
Girard, Ralph	PS1.1-36	189
Glesne, T.R.	OS5-13	647
Godin, S.	**OS3-2**	317
Goldschmidt, Soendeke	**PS3.3-7**	919

Author	Session-Paper No.	Page No.
Goldsmith, J.E.M.	OS2-7	281
	OS2-8	285
	PS1.1-41	207
	PS2.1-10	403
Goloub, P.	OS1-6	25
Gong, S.L.	OS7-11	959
Gong, Shunsheng	**PS2.2-6**	497
Goto, Naohiko	PS2.1-7	391
Gotoff, Steven W.	PS2.1-15	421
Grant, William B.	OS6-9	685
	OS2-4	269
	PS1.1-12	95
	PS2.1-4	379
Green, J.W.	**PS1.2-3**	219
	OS5-4	613
Gregory, Gerald L.	OS2-4	269
Grigorov, Ivan V.	PS1.1-2	63
Grishaev, M.V.	OS3-6	331
Grishin, Anatolii I.	PS3.3-2	897
Gross, M.R.	OS3-10	347
	OS3-9	343
	PS2.2-1	477
	PS2.2-12	517
Grund, Chris	OS4-6	573
Guerra, David V.	**PS3.2-35**	879
Gultepe, I.	PS3.2-17	811
Guo, S.	PS2.2-4	489
Guzzi, Donatella	**PS2.2-7**	501
Hair, Johnathan	**PS1.1-13**	99
Hamdi, Saipul	OS1-8	33
	PS1.1-16	111
Hamilton, Carla M.	OS5-14	651
Hammond, Marc	PS3.3-8	923
Hamonou, E.	OS1-4	19

Author	Session-Paper No.	Page No.
Haner, David A.	PS2.2-1	477
	PS3.2-25	841
Hara, Hiroshi	PS1.1-15	107
	PS1.1-22	131
Hardesty, R. Michael	**OS4-2**	557
	OS4-4	565
	OS4-6	573
Harper, David B.	**PS3.2-27**	849
Hart, William D.	**PS1.1-10**	87
Harwood, Michael G.	**PS3.2-8**	775
	PS3.2-17	811
Hasson, V.	**OS5-13**	647
Hauchecorne, Alain	OS3-1	313
	OS3-2	317
	OS3-8	339
	OS7-4	931
	PS2.2-2	481
Healy, Kathleen R.	OS5-11	639
Hemmati, Hamid	OS7-3	929
Hidayat, Ii	PS2.1-12	411
Higdon, N. Scott	**OS5-14**	651
	OS6-2	657
	PS3.2-9	779
Hignett, Philip	OS1-2	11
Hill, C.	PS2.1-23	453
Hirota, Michio	OS1-8	33
	PS1.1-16	111
Hlavka, Dennis L.	PS1.1-19	119
	PS1.1-28	155
Ho, A.H.P.	PS2.1-6	387
	PS3.2-22	829
Ho, Cheng	OS1-14	55
Ho, James G.	PS3.1-13	735
Hoang, Ngoc	**PS3.2-38**	891
Hobbs, Peter V.	OS1-2	11
Hoff, R.M.	**OS7-11**	959
	PS2.1-14	417
	PS2.1-25	461
Hogervorst, W.	OS3-3	319
Holben, Brent N.	OS1-2	11
Holdsworth, John	PS1.1-39	199
Homburg, F.	OS3-7	335
Hopt, D.	PS3.2-37	887
Hovenier, J.W.	OS3-3	319
Howell, James	OS6-6	673
Howell, Jim	OS4-6	573
Hu, Huanling	**OS1-9**	37
Hua, Dengxin	OS4-3	561
Hwang, I.H.	**OS8-3**	979
Immler, F.	PS2.1-16	425
Intrieri, Janet M.	OS5-11	639
Ishizuka, M.	PS1.1-31	169
Ismail, Syed	OS1-2	11
	OS2-2	261
	OS7-8	945
	PS2.1-26	465
Itabe, Toshikazu	OS1-8	33
	OS7-5	935
	PS1.1-16	111
	PS2.2-13	521
Ivanov, A.P.	PS1.1-4	69
Iwasaka, Yasurobu	OS1-12	47
	PS2.2-12	517
Jäger, Horst	OS1-5	23
	OS3-7	335
Jain, S.L.	**PS2.1-5**	383
Jansen, Friedhelm	PS3.2-5	763
Jeanneret, François	**OS6-4**	665
	PS2.1-9	399

Author	Session-Paper No.	Page No.
Jinhuan, Qiu	**PS3.1-15**	743
	PS1.1-17	113
Johnson, H.D.	PS2.1-3	375
Jones, R.L.	PS2.1-23	453
Kai, Kenji	**PS1.1-15**	107
	PS1.1-22	131
Kałoka, Sri	OS1-8	33
	PS1.1-16	111
Kane, Timothy J.	PS3.1-3	699
Kaprielov, Boiko	PS3.1-14	739
	PS1.1-26	147
	PS3.2-10	783
Karyampudi, V. Mohan	**OS6-9**	685
Kaufman, Yu. G.	PS 1.1-5	73
Kaul, B.V.	**PS1.1-35**	185
Kavaya, Michael J.	**OS4-1**	553
Kawahara, T.D.	PS1.1-31	169
	PS2.2-14	525
Kay, R.B.	PS3.2-37	887
Kay, Richard B.	PS1.2-5	225
Keckhut, Philippe	**OS3-1**	313
	OS3-8	339
	PS2.2-2	481
Kelly, Brian T.	OS6-2	657
	OS5-14	651
Kelly, D.	PS3.2-3	755
Ketteridge, P.A.	OS5-5	617
Kharchenko, Olga V.	PS3.3-2	897
Khmelevtsov, S.S.	**PS 1.1-5**	73
Khmelevtsov, A.S.	PS 1.1-5	73
Kiemle, Christoph	**PS2.1-8**	395
Killinger, Dennis	PS3.2-24	837
Kinjo, Hideki	**PS1.1-25**	143
Kirchner, Frank	OS6-4	665
Kitahara, T.	PS2.2-14	525

Author	Session-Paper No.	Page No.
Kjome, N.T.	PS2.2-1	477
Klein, U.	OS3-10	347
	PS2.2-12	517
Klimkin, Vladimir M.	PS3.3-2	897
Klingenberg, H.H.	PS3.2-11	787
Kobayashi, F.	PS2.2-14	525
Kobayashi, Takao	**OS4-3**	561
	PS2.1-12	411
Koch, Grady J.	OS6-8	681
Koenig, Keith W.	OS5-11	639
Koga, Nobuhiko	OS7-5	935
Kokhanenko, G.	PS1.1-8	79
	PS1.1-33	177
	PS1.1-34	181
	PS3.2-1	747
	PS3.3-1	895
	PS3.3-3	901
Kolarov, George V.	**PS1.1-2**	63
Kolev, Ivan	PS1.1-26	147
	PS3.1-14	739
	PS3.2-10	783
Komarov, V.S.	**PS2.2-9**	503
Kooi, Susan A.	OS1-2	11
	OS2-2	261
	OS2-4	269
	PS2.1-4	379
	PS2.1-26	465
Köpp, F.	PS3.1-10	727
Korb, C. Laurence	**OS4-9**	585
	OS4-10	587
	PS3.1-1	691
	PS3.1-2	695
	PS3.3-6	915
Korol, M.M.	PS1.1-4	69
Kovacs, M.	OS5-13	647
Krainak, Michael A.	PS3.2-15	803

Author	Session-Paper No.	Page No.
Krishnamurti, T.N.	**OS6-1**	655
Krivolutsky, N.P.	PS3.1-10	727
	PS3.1-12	731
Krueger, David A.	OS3-8	339
	OS3-13	359
	OS3-14	363
	PS1.1-13	99
	PS2.2-20	549
Krumbholz, Susanne	OS2-5	273
Kuehn, Ralph	OS2-14	309
	PS2.1-27	469
Kumar, Arun	PS2.1-5	383
Kunimori, Hiroo	OS7-5	935
Kushina, Mark	**PS3.2-12**	791
Kuze, Hiroaki	PS1.1-25	143
	PS1.1-27	151
Kyomitsu, Tatsuya	**PS2.2-19**	545
Lagrosas, Nofel C.	PS1.1-40	203
Lahmann, Wilhelm	OS1-10	41
	PS3.2-7	771
Lahoz, W.A.	OS3-4	323
Langer, J.	OS3-10	347
Larchevêque, Gilles	PS2.1-18	433
	PS2.1-20	441
Laroque, M.	PS1.1-36	189
Laufer, Gabriel	PS3.2-38	891
Laurent, Sauvage	**PS1.1-18**	115
Lavorato, Mario	OS1-6	25
	PS1.1-6	75
	PS2.1-13	415
Lawerence, R.M.	OS8-4	983
Lazzarotto, Benoît	**PS2.1-18**	433
Leblanc, Thierry	OS3-8	339
	PS2.2-11	513
	PS2.2-2	481

Author	Session-Paper No.	Page No.
Lee, Choo Hie	PS2.2-8	505
Lee, H.R.	PS3.2-9	779
Lee, Ian	OS5-5	617
Lee, S.W.	PS3.2-28	853
Leete, Stephen J.	**OS7-6**	939
Lehmann, Stefan	**PS3.2-5**	763
Lehner, Susanne	OS4-5	569
Lenschow, Donald H.	OS2-2	261
Leung, K.M.	PS2.1-6	387
	PS3.2-22	829
Lewis, P.	OS5-13	647
Li, Hongjun	PS2.2-6	497
Li, S. Xingfu	PS3.1-1	691
Li, Steven X.	OS4-10	487
	OS4-11	591
	PS3.3-6	915
Li, Ye	PS3.1-4	703
Lienert, Barry R.	OS6-6	673
Liley, J.B.	OS1-8	33
	OS3-3	319
Lindauer, Steven J., II	PS1.2-5	255
Linkin, V.M.	PS1.2-9	241
Linné, Holger	**PS3.2-4**	759
	PS3.2-5	763
Lipatov, A.N.	PS1.2-9	241
Liquang, Yang	PS3.1-15	743
Little, Liesl M.	**OS2-12**	301
Liu, P.	OS7-11	959
Liu, Zhaoyan	**PS1.1-14**	103
Livingston, John M.	OS1-2	11
Lomakina, N. Ya.	PS2.2-9	509
Lomonosov, M.V.	PS3.1-16	745
Lonn, Fredrik	**PS3.2-29**	857
Loth, Claude	**OS4-7**	577
	PS3.1-5	707

Author	Session-Paper No.	Page No.
Love, Steven P.	OS1-14	55
Luck, William S., Jr.	PS3.2-26	845
Ludbrook, G.	**PS1.1-34**	181
	PS3.3-1	895
Lukemire, A.	OS5-4	613
Lyash, A.N.	PS1.2-9	241
Maganova, M.S.	**PS3.1-16**	745
Magee, Eric P.	**PS3.1-3**	699
Maheskumar, R.S.	PS1.1-20	123
Makarov, V.S.	PS1.2-9	241
Malique, Christian	OS7-4	931
Mamakos, W.	OS5-4	613
Mamidipudi, Priyavadan	**PS3.2-24**	837
Manney, G.L.	OS3-3	319
Manome, Kazunobu	PS1.1-22	131
Marchbanks, Richard D.	OS4-6	573
	PS2.1-3	375
Marichev, V.N.	OS3-6	331
	PS2.2-9	509
Marinov, Vladimir Stoykov	**PS3.1-6**	711
Marsh, Waverly	PS3.2-30	861
Martino, Anthony J.	OS7-6	939
Mathews, W. Andrew	OS1-8	33
Mathur, Savyasachee	OS4-10	587
	PS2.1-2	371
	PS3.1-1	691
	PS3.3-6	915
Matsui, Ichiro	PS2.1-12	411
	PS2.2-17	537
Matthews, Leroy F.	PS3.2-19	819
Matthey, Renaud	PS3.2-32	867
	PS3.2-36	883
Matthias, Volker	OS1-5	23
	OS2-6	277
Mattis, Ina	OS1-1	7
	OS1-7	29
	OS2-11	297
Matusi, Ichiro	PS1.1-14	103
Matvienko, Gennadii G.	**PS3.3-2**	897
Mayor, Shane D.	OS2-14	309
	OS4-6	573
	PS2.1-27	469
McCarthy, J.C.	**OS5-5**	617
McClure, D.	PS1.2-4	223
McCormick, M. Patrick	**OS7-7**	943
McCray, C.L.	PS3.2-9	779
McDermid, I. Stuart	**OS3-8**	339
	PS2.2-1	477
	PS2.2-2	481
	PS2.2-11	513
McGarry, Jan F.	PS1.2-7	233
McGee, T.J.	**OS3-9**	343
	OS3-10	347
	PS2.2-1	477
	PS2.2-12	517
McGill, Matthew J.	**OS4-11**	591
	PS3.2-34	875
McKay, Jack A.	**OS4-12**	595
Meijer, Y.J.	OS3-3	319
Mel, S.	PS2.1-10	403
Melfi, S. Harvey	OS1-2	11
	OS2-8	285
	OS6-9	685
	PS1.1-41	207
	PS2.1-1	367
	PS2.1-17	429
Melnikov, Vladimer	OS7-4	931

Author	Session-Paper No.	Page No.
Menzies, Robert T.	**OS7-3**	929
	PS3.1-9	723
	PS3.2-25	841
Mileti, G.	PS3.2-32	867
Millar, Pamela S.	**PS1.2-2**	215
Minato, Atsushi	OS7-5	935
Minnis, Patrick	PS2.1-26	465
Minomura, Mitsuo	PS1.1-25	143
Mitev, Valentin	PS2.1-18	433
	PS3.2-36	883
	PS3.2-32	867
Mizutani, Kohei	OS1-8	33
	PS1.1-16	111
Moidek, Mariusz J.	OS4-8	581
Mok, T.M.	**PS2.1-6**	387
Moody, Stephen E.	**OS8-1**	971
Moore, Alvah S., Jr.	**PS3.2-19**	819
Morandi, Marco	PS2.2-7	501
Mordaunt, David W.	**PS3.1-13**	735
Moulton, P.F.	**OS5-1**	601
Mueller, M.	PS2.1-16	425
Müller, Detlef	OS1-1	7
	OS1-7	29
	PS2.1-24	457
	PS3.2-23	833
Murae, Takeshi	OS4-3	561
Muramatsu, Daisuke	PS1.1-15	107
	PS1.1-22	131
Murayama, Toshiyuki	PS1.1-15	107
	PS1.1-22	131
Murayama, Y.	PS2.2-17	537
Mwangi, M.	PS2.2-16	533
Nadeev, A.I.	PS2.1-21	445

Author	Session-Paper No.	Page No.
Nagai, Tomohiro	**OS1-8**	33
	PS1.1-16	111
	PS2.2-13	521
Nagao, S.	PS1.1-31	169
Nagasawa, Chikao	PS1.1-15	107
	PS1.1-22	131
	PS2.2-19	545
	PS2.2-21	*
	PS3.2-21	827
Nakajima, Hayato	PS1.1-15	107
Nakajima, T.	PS1.1-27	151
Nakane, H.	PS2.2-17	537
Nam, Matthew K.	OS8-3	979
Namboothiri, S.P.	**PS2.2-17**	537
Nedeljkovic, Dusan	OS7-4	931
Nee, Jan-Bei	PS1.1-30	165
Neidhart, Bernd	OS2-5	273
	OS5-9	631
Nemoto, Koshichi	PS2.1-7	391
	PS3.2-13	795
Nessler, Phillip J., Jr.	**OS8-2**	975
Neuber, R.	OS3-9	343
	OS3-10	347
	OS5-8	627
	PS2.2-12	517
Newman, P.	OS3-9	343
Ng, C.N.	PS2.1-6	387
	PS3.2-22	829
Nguyen, D. Chi	OS6-8	681
Niedermeier, S.	OS5-8	627
	PS3.2-20	823
Nikowa, Ljuba	PS3.2-7	771
Niwano, Keiko	PS1.1-15	107
Noguchi, K.	PS1.1-31	169

Author	Session-Paper No.	Page No.
Nomura, Akio	OS7-5	935
	PS1.1-31	169
	PS2.2-14	525
Nuryanto, A.	PS1.1-16	111
Ohno, Yuichi	PS1.1-22	131
Okada, Kikuo	PS1.1-15	107
Oldham, T.	PS1.2-4	223
Omar, Ali H.	**PS1.2-12**	253
Osborn, Mary T.	OS7-12	963
	PS1.2-10	245
Osipenko, F.P.	PS1.1-4	69
Otaguro, Wilfred	**PS3.3-5**	909
Ozawa, Kenichi	OS7-5	935
Pal, Shiv R.	OS3-5	327
	PS2.2-13	521
	PS2.2-4	489
	PS1.1-36	189
Palese, Stephen P.	PS3.1-13	735
	PS1.2-8	237
Palm, Steve	OS6-9	685
Pandithural, G.	PS1.1-20	123
Papen, George C.	OS2-12	301
	OS3-12	355
Pappalardo, Gelsomina	OS2-13	305
	PS3.2-33	871
Park, Chan Bong	**PS2.2-8**	505
Park, P.S.	PS1.1-36	189
Parvanov, O.	PS1.1-26	147
	PS3.1-14	739
Patel, C. Kumar N.	**PL-1**	1
Pelon, Jacques	**OS1-3**	15
	OS1-4	19
	OS1-6	25
	OS2-3	265
	OS4-7	577
	PS1.1-6	75
	PS1.1-18	115
	PS2.1-13	415
	PS3.1-5	707
	PS3.1-8	719
	PS3.2-16	807
Penner, I.	PS1.1-33	177
	PS1.1-34	181
	PS1.1-8	79
	PS3.2-1	747
	PS3.3-1	895
	PS3.3-3	901
Périn, Julie	PS3.1-8	719
Pershin, S.M.	PS1.2-9	241
Peters, Bruce R.	PS3.1-4	703
Petros, Mulugeta	OS5-2	603
Petway, L.P.	PS3.2-18	815
Philbrick, C. Russell	**OS2-9**	289
	PS1.1-37	193
	PS2.1-11	407
Phillips, Mark W.	OS5-2	603
Phillips, R.	PS3.2-3	755
Pickett, M.C.	PS1.1-7	77
Pierce, Harold	OS6-9	685
Pierrottet, Diego K.	OS5-14	651
Pinandito, Mego	**PS2.1-12**	411
Platt, C.M.R.	**PS1.1-7**	77
Poberaj, G.	**PS3.2-11**	787
Pohle, R.	OS5-13	647
Pomares, Ismael	PS1.1-32	173
Ponsardin, Patrick	PS2.1-27	469

Author	Session-Paper No.	Page No.
Popov, Yu. B.	PS2.2-9	509
Porter, John N.	OS6-6	673
Povey, I.M.	**PS2.1-23**	453
Powell, Donna	PS1.1-28	155
Powell, Kathleen A.	**PS1.2-11**	249
Prasad, Coorg R.	**PS2.1-2**	371
	PS3.2-38	891
Pratt, Lee	PS3.3-5	909
Pueschel, R.F.	PS1.1-12	95
Qirong, Huang	PS3.1-15	743
Quaglia, Philippe	PS2.1-9	399
	PS2.1-18	433
Quante, Markus	OS1-10	41
Quel, Eduardo	PS1.1-6	75
	PS2.1-13	415
Rahm, Stephan	**OS4-5**	569
Rairoux, P.	**OS5-8**	627
	PS2.1-16	425
	PS2.2-12	517
	PS3.2-20	823
Raj, P.E.	PS1.1-20	123
Rall, Jonathan A.R.	PS3.2-15	803
Ramlau, Ronny	PS1.1-1	59
Ranganayakamma, Belthur	OS8-3	979
Ray, Mark D.	OS2-10	293
	OS6-7	677
Reagan, John A.	OS6-9	685
	PS1.1-28	155
Redemann, J.	**PS1.1-12**	95
Rees, David	**PS2.2-22**	*
Refaat, Tamer F.	**PS3.2-26**	845
Reichardt, Jens	**OS2-5**	273
	OS5-9	631
Remer, Lorraine A.	OS1-2	11
Renger, W.	OS3-4	323
Richter, Dale A.	OS5-14	651
	PS3.2-9	779
Richter, Holger	PS3.2-23	833
Richter, Ron	OS4-6	573
Rizi, Vincenzo	PS2.2-18	541
Ro, C.	OS7-11	959
Rodriguez, M.	OS5-8	627
	PS2.1-16	425
	PS3.2-20	823
Roh, S. David	OS2-12	301
Romand, B.	PS3.1-5	707
Romashov, D.N.	PS1.1-35	185
Ronneberger, F.	OS5-8	627
	PS3.2-20	823
Rosananto, Imam	PS2.1-12	411
Rosen, J.M.	PS2.2-1	477
Ross, Martin	OS6-3	661
	PS3.3-4	905
Roy, Gilles	OS1-13	51
	PS1.1-23	135
	PS3.2-6	767
Ruffatto, D.	OS5-13	647
Russell, A.R.	PS2.2-15	529
Russell, Philip B.	OS1-2	11
Rye, Barry J.	OS4-2	557
	OS4-4	565
Saito, Yasunori	OS7-5	935
	PS1.1-31	169
	PS2.2-14	525
Samokhvalov, I.V.	PS1.1-35	185
Sandberg, Scott P.	OS5-11	639
Santacesaria, Vincenzo	PS2.2-7	501
Sasano, Yasuhiro	**OS7-9**	949
Sassen, Kenneth	**OS1-11**	45
Sauerbrey, R.	OS5-8	627
	PS3.2-20	823

Author	Session-Paper No.	Page No.
Sauvage, Laurent	OS1-6	25
	PS1.1-6	75
Savov, Plamen	PS3.2-10	783
Schafer, H.J.	PS2.2-1	477
Schillinger, H.	OS5-8	627
	PS3.2-20	823
Schrems, O.	OS3-9	343
	PS2.2-1	477
	PS2.2-12	517
Schroeder, B.	OS5-4	613
Schuster, G.L.	**PS1.1-37**	193
Schutz, Bob E.	PS1.2-1	211
Schwemmer, Geary K.	OS1-2	11
	OS2-8	285
	OS5-7	623
	PS2.1-1	367
	PS1.1-41	207
	PS2.1-10	403
	PS3.2-35	879
Scott, A.	PS1.1-34	181
	PS3.3-1	895
Scott, V. Stanley, III	PS1.1-19	119
	PS3.2-34	875
Sedlacek, Arthur J., III	OS6-7	677
	OS2-10	293
Selden, M.	**PS1.2-4**	223
Sellar, G.	PS3.2-3	755
Senff, Christoph	OS2-2	261
	OS4-6	573
	PS2.1-3	375
Senft, Daniel C.	**OS6-2**	657
	OS5-14	651
Serikov, I.B.	OS2-11	297
	PS2.1-21	445
Shamanaev, V.	**PS1.1-8**	79
	PS1.1-33	177
	PS1.1-34	181
	PS3.2-1	747
	PS3.3-1	895
	PS3.3-3	901
Sharma, S.	PS2.1-5	383
Sharma, Shiv K.	**OS6-6**	673
Shcherbakov, V.N.	PS1.1-4	69
She, C.Y.	OS3-13	359
	OS3-14	363
	OS3-8	339
	PS1.1-13	99
	PS2.2-20	549
Shen, Chyau	PS3.3-5	909
Shibata, Takashi	OS1-8	33
	OS1-12	47
	PS2.2-12	517
	PS2.2-13	521
Shibata, Yasukuni	PS2.2-19	545
	PS3.2-21	827
Sica, R.J.	PS2.1-14	417
	PS2.2-15	529
	PS2.2-16	533
Simeonov,Valentin	**PS2.1-9**	399
	PS2.1-18	433
	PS2.1-20	441
Simonich, D.M.	**PS1.1-3**	65
Singh, Upendra N.	**OS5-2**	603
Siping, Zheng	PS3.1-15	743
Sirota, J. Marcos	PS1.2-2	215
Situ, Wen	**OS5-12**	643
Skakalova, T	**PS1.1-26**	147
Sladkovic, Rudolf	PS2.2-3	487

Author	Session-Paper No.	Page No.
Smalikho, I.N.	PS3.1-10	727
	PS3.1-11	*
	PS3.1-12	731
Smirnov, S.V.	OS3-6	331
	PS1.1-29	159
Smith, James C.	PS1.2-1	211
Smith, Roger W.	OS3-11	351
Smoak, M.C.	**PS3.2-37**	887
Sok, Ronald	PS1.1-24	139
Sokovikov, Vladimir G.	PS3.3-2	897
Soletsky, Philip	OS6-3	661
	PS3.3-4	905
South, A.M.	PS2.1-23	453
Spacek, L.	OS7-11	959
Spiers, Gary D.	PS3.1-4	703
Spinelli, Nicola	OS2-13	305
	PS3.2-33	871
Spinhirne, James D.	OS1-6	25
	PS1.1-10	87
	PS1.1-19	119
	PS1.1-28	155
	PS3.2-34	875
	PS1.2-6	229
	PS1.2-8	237
Stadler, John H.	OS7-8	945
Starkov, A.V.	**OS7-13**	967
Starr, D.	PS2.1-10	403
Staszel, Jennifer	PS2.1-26	465
Stefanutti, Leopoldo	PS2.2-7	501
Steggerda, C.	PS1.2-4	223
Stein, B.	OS5-8	627
	PS2.1-16	425
	PS3.2-20	823
Steinbrecht, W.	**OS3-10**	347
	PS2.2-12	517
Steyn, D.G.	**PS2.1-25**	461
Storm, Mark E.	**PS3.2-30**	861
Stoyanov, Dimitar Vassilev	PS3.1-6	711
Strawbridge, Kevin B.	PS3.2-8	775
	PS3.2-17	811
Stringfellow, R.	PS1.2-4	223
Stryjewski, J.	PS3.2-3	755
Sugimoto, Nobuo	OS1-6	25
	OS7-5	935
	PS1.1-14	103
	PS2.1-12	411
	PS2.2-17	537
Sugondo, Santoso	PS2.1-12	411
Sun, Xiaoli	OS7-1	925
Swart, D.P.J.	OS3-3	319
Swim, Cynthia	OS6-5	669
Switzer, Gregg W.	**PS3.2-15**	803
Syamsudin, Muharyan	PS2.1-12	411
Tadaishi, A.	PS1.1-27	151
Takamura, T.	PS1.1-27	151
Takeuchi, Nobuo	PS1.1-25	143
	PS1.1-27	151
Tanaka, Ryuzo	OS4-3	561
Tatarov, Boyan	PS3.2-10	783
Testud, Jacques	OS4-7	577
Theopold, Felix A.	OS1-10	41
	PS2.1-22	449
Thomas, B.	PS3.2-9	779
Tiurin, A.V.	PS1.2-9	241
Tooman, Tim	OS2-8	285
	PS1.1-41	207
Tratt, David M.	OS7-3	929
	PS3.1-9	723
Treyer, Daniel	OS3-12	355
Trickl, Thomas	OS1-5	23
	PS2.2-3	485

Author	Session-Paper No.	Page No.
Trouillet, V.	OS1-3	15
	OS1-4	19
Tulinov, Gueorguï	OS7-4	931
Turco, R.P.	PS1.1-12	95
Turner, David D.	**OS2-7**	281
	OS2-8	285
	PS1.1-19	119
	PS1.1-41	207
	PS2.1-1	367
	PS2.1-10	403
Uchino, Osamu	OS1-8	33
	PS1.1-16	111
	PS2.2-13	521
Uezono, T.	PS1.1-27	151
Ulbricht, Matthias	PS3.2-7	771
van den Bergh, Hubert	OS6-4	665
	PS2.1-9	399
	PS2.1-18	433
	PS2.1-20	441
van Lammeren, André	PS1.1-24	139
Vanderbeek, Richard G.	OS6-5	669
	PS2.1-15	421
Vandermeer, A.	OS7-11	959
Vankov, Orlin I.	PS1.1-2	63
Vassiliev, O.N.	PS2.2-15	529
	PS2.2-16	533
Veefkind, J. Pepijn	OS1-2	11
Velkov, D.	OS3-5	327
	PS2.2-4	489
Velotta, R.	PS3.2-33	871
Vet, R.	OS7-11	959
Visconti, Guido	PS2.2-18	541
von der Gathen, P.	PS2.2-12	517
Wagner, Frank	OS1-1	7
	PS2.1-24	457
Wahl, P.	OS3-9	343
	OS3-10	347
	PS2.2-12	517
Waite, D.	OS5-8	627
	PS2.1-16	425
	PS3.2-20	823
Wakiyama, Kanji	PS1.1-15	107
Wandinger, Ulla	OS1-1	7
	OS1-5	23
	OS1-7	29
	OS2-11	297
Wang, Y.	OS5-13	647
Weber, Konradin	PS3.2-7	771
Wedekind, C.	OS5-8	627
	PS2.1-16	425
	PS3.2-20	823
Weib, V.	OS5-10	635
Weickmann, Ann	OS4-6	573
Weidauer, Derk	**PS3.2-7**	771
Weise, Diana	PS2.1-24	457
Weitkamp, Claus	**OS1-10**	41
	OS2-5	273
	OS5-9	631
	PS2.1-22	449
	PS3.2-7	771
Wendt, R.	OS5-13	647
Werner, Christian	OS4-5	569
	PS3.1-10	727
	PS3.1-12	731
Wessel, John	**PS2.1-19**	437
White, Michael	**OS3-14**	363

Author	Session-Paper No.	Page No.
Whiteman, David N.	OS1-2	11
	OS2-8	285
	PS1.1-41	207
	PS2.1-1	367
	PS2.1-10	403
	PS2.1-17	429
Whiteway, James A.	PS2.2-5	493
	PS2.2-10	511
	PS2.2-13	521
Wickwar, Vincent B.	PS3.3-8	923
Wiegner, Matthias	OS1-5	23
	PS1.1-21	127
Wilkerson, Thomas D.	**PS3.3-8**	923
Wille, H.	OS5-8	627
	PS2.1-16	425
	PS3.2-20	823
Williamson, Cynthia K.	**PS3.2-2**	751
	PS3.2-31	863
Winker, David M.	**OS7-10**	955
	OS7-7	943
	PS1.2-11	249
Wirth, M.	OS3-4	323
Wise, Stacy	OS2-8	285
Wolf, Jean-Pierre	PS3.2-7	771
Won, Jae Gwang	PS1.1-9	83
Woodard, Ryan	**OS1-12**	47
Wooten, A. Dan	PS2.1-17	429
Wooten, Albert D., Jr.	PS3.2-35	879
Wöste, L.	OS5-8	627
	PS2.1-16	425
	PS3.2-20	823
Wulfmeyer, Volker	OS4-4	565
	OS4-6	573
	PS2.1-28	473
Xu, J.	**PS3.2-3**	755
Yang, Guotao	PS2.2-6	497
Yasui, Motoaki	OS1-8	33
	PS1.1-16	111
Yokozawa, Takeshi	PS1.1-22	131
Yoon, Soon-Chang	**PS1.1-9**	83
Young, Stuart A.	PS1.1-7	77
	OS7-12	963
Yu, A.W.	OS5-4	613
Yu, Jirong	OS5-2	603
Zenker, T.	PS3.2-28	853
	PS3.2-9	779
Zhao, Y.	**PS2.1-3**	375
Zheng, Wengang	PS2.2-6	497
Zimmer, W.	PS2.1-16	427
Zuev, V.V.	**OS3-6**	331
	PS1.1-29	159
	PS2.2-9	509
Zukowski, Barbara J.	OS7-6	939

REPORT DOCUMENTATION PAGE

Form Approved
OMB No. 07704-0188

Public reporting burden for this collection of information is estimated to average 1 hour per response, including the time for reviewing instructions, searching existing data sources, gathering and maintaining the data needed, and completing and reviewing the collection of information. Send comments regarding this burden estimate or any other aspect of this collection of information, including suggestions for reducing this burden, to Washington Headquarters Services, Directorate for Information Operations and Reports, 1215 Jefferson Davis Highway, Suite 1204, Arlington, VA 22202-4302, and to the Office of Management and Budget, Paperwork Reduction Project (0704-0188), Washington, DC 20503.

1. AGENCY USE ONLY *(Leave blank)*	2. REPORT DATE	3. REPORT TYPE AND DATES COVERED
	July 1998	Conference Publication

4. TITLE AND SUBTITLE
Nineteenth International Laser Radar Conference

5. FUNDING NUMBERS
WU 258-70-21-08

6. AUTHOR(S)
Upendra N. Singh, Syed Ismail, and Geary K. Schwemmer, Editors

7. PERFORMING ORGANIZATION NAME(S) AND ADDRESS(ES)
NASA Langley Research Center
Hampton, VA 23681-2199

8. PERFORMING ORGANIZATION REPORT NUMBER
L-17738A

9. SPONSORING/MONITORING AGENCY NAME(S) AND ADDRESS(ES)
National Aeronautics and Space Administration
Washington, DC 20546-0001

10. SPONSORING/MONITORING AGENCY REPORT NUMBER
NASA/CP-1998-207671/PT1

11. SUPPLEMENTARY NOTES
Singh and Ismail: Langley Research Center, Hampton, VA; Schwemmer: Goddard Space Flight Center, Greenbelt, MD.

12a. DISTRIBUTION/AVAILABILITY STATEMENT
Unclassified–Unlimited
Subject Category 35 Distribution: Standard
Availability: NASA CASI (301) 621-0390

12b. DISTRIBUTION CODE

13. ABSTRACT ***(Maximum 200 words)***

This publication contains extended abstracts of papers presented at the Nineteenth International Laser Radar Conference, held at Annapolis, Maryland, July 6–10, 1998; 260 papers were presented in both oral and poster sessions. The topics of the conference sessions were Aerosol Clouds, Multiple Scattering; Tropospheric Profiling; Stratospheric/Mesospheric Profiling; Wind Profiling; New Lidar Technology and Techniques; Lidar Applications, Including Altimetry and Marine; Space and Future Lidar; and Lidar Commercialization/Eye Safety.

This conference reflects the breadth of research activities being conducted in the lidar field. These abstracts address subjects from lidar-based atmospheric investigations, development of new lasers and lidar system technology, and current and future space-based lidar systems.

14. SUBJECT TERMS
Lidar; Laser radar; Remote sensing; Atmospheric measurements

15. NUMBER OF PAGES
523

16. PRICE CODE
A22

17. SECURITY CLASSIFICATION OF REPORT	18. SECURITY CLASSIFICATION OF THIS PAGE	19. SECURITY CLASSIFICATION OF ABSTRACT	20. LIMITATION OF ABSTRACT
Unclassified	Unclassified	Unclassified	